Carnegie Institution

OF WASHINGTON

Year Book 79

1979–1980

Director's Office

Carnegie Institution

OF WASHINGTON

Year Book 79

1979–1980

Library of Congress Catalog Card Number 3-16716
International Standard Book Number 0-87279-653-1
Composition by Action Comp Co. Inc., Baltimore
Printing and Binding by Rose Printing Co., Tallahassee
December 1980

Contents

Officers and Staff	v
Report of the President	*1*
Reports of Departments and Special Studies	1
Department of Embryology	3
Department of Plant Biology	101
Developmental Biology Research Group	207
Geophysical Laboratory	225
Department of Terrestrial Magnetism	429
Hale Observatories	589
Administrative Reports	651
Office of Administration	653
Bibliography	655
Report of the Executive Committee	657
Abstract of Minutes of the Eighty-Third Meeting of the Board of Trustees	659
Financial Statement	661
Articles of Incorporation	679
By-Laws of the Institution	683
Index of Names	689



Digitized by the Internet Archive
in 2012 with funding from
LYRASIS Members and Sloan Foundation

http://www.archive.org/details/yearbookcarne79197980carn

President and Trustees

PRESIDENT
James D. Ebert

BOARD OF TRUSTEES
William R. Hewlett[1]
Chairman

William C. Greenough
Vice-Chairman

William T. Golden
Secretary

Philip H. Abelson
Robert O. Anderson
Lewis M. Branscomb
William T. Coleman, Jr.[2]
John T. Connor[3]
Edward E. David, Jr.[4]
John Diebold
Gerald M. Edelman[4]
Michael Ference, Jr.[5]
Carl J. Gilbert
Robert G. Goelet[4]
Crawford H. Greenewalt
Caryl P. Haskins
Richard E. Heckert[4]
William McChesney Martin, Jr.
Antonia Johnson Mörner[4]
Franklin D. Murphy
Robert M. Pennoyer
Richard S. Perkins
Robert C. Seamans, Jr.
Frank Stanton[6]
Charles H. Townes
Juan T. Trippe
Trustees

Henry S. Morgan
Garrison Norton
Charles P. Taft
James N. White
Trustees Emeriti

[1]Elected Chairman May 2, 1980.
[2]Elected December 17, 1979.
[3]Resigned January 1, 1980.
[4]Elected May 2, 1980.
[5]Resigned January 1980.
[6]Chairman to May 2, 1980.

Former Presidents and Trustees

PRESIDENTS

Daniel Coit Gilman	1902–1904
Robert Simpson Woodward	1904–1920
John Campbell Merriam	1921–1938
Vannevar Bush	1939–1955
Caryl P. Haskins	1956–1971
Philip H. Abelson	1971–1978

TRUSTEES

Alexander Agassiz	1904–1905
Lord Ashby of Brandon	1967–1974
J. Paul Austin	1976–1978
George J. Baldwin	1925–1927
Thomas Barbour	1934–1946
James F. Bell	1935–1961
John S. Billings	1902–1913
Robert Woods Bliss	1936–1962
Amory H. Bradford	1959–1972
Lindsay Bradford	1940–1958
Omar N. Bradley	1948–1969
Robert S. Brookings	1910–1929
Vannevar Bush	1958–1971
John L. Cadwalader	1903–1914
William W. Campbell	1929–1938
John J. Carty	1916–1932
Whitefoord R. Cole	1925–1934
John T. Connor	1975–1980
Frederic A. Delano	1927–1949
Cleveland H. Dodge	1903–1923
William E. Dodge	1902–1903
Charles P. Fenner	1914–1924
Michael Ference, Jr.	1968–1980
Homer L. Ferguson	1927–1952
Simon Flexner	1910–1914
W. Cameron Forbes	1920–1955
James Forrestal	1948–1949
William N. Frew	1902–1915
Lyman J. Gage	1902–1912
Walter S. Gifford	1931–1966
Cass Gilbert	1924–1934
Frederick H. Gillett	1924–1935
Daniel C. Gilman	1902–1908
Hanna H. Gray	1974–1978
Patrick E. Haggerty	1974–1975
John Hay	1902–1905
Barklie McKee Henry	1949–1966
Myron T. Herrick	1915–1929
Abram S. Hewitt	1902–1903
Henry L. Higginson	1902–1919
Ethan A. Hitchcock	1902–1909
Henry Hitchcock	1902
Herbert Hoover	1920–1949
William Wirt Howe	1903–1909
Charles L. Hutchinson	1902–1904
Walter A. Jessup	1938–1944
Frank B. Jewett	1933–1949
Samuel P. Langley	1904–1906
Ernest O. Lawrence	1944–1958
Charles A. Lindbergh	1934–1939
William Lindsay	1902–1909
Henry Cabot Lodge	1914–1924
Alfred L. Loomis	1934–1973
Robert A. Lovett	1948–1971
Seth Low	1902–1916
Wayne MacVeagh	1902–1907
Keith S. McHugh	1950–1974
Andrew W. Mellon	1924–1937
John Campbell Merriam	1921–1938
Margaret Carnegie Miller	1955–1967
Roswell Miller	1933–1955
Darius O. Mills	1902–1909
S. Weir Mitchell	1902–1914
Andrew J. Montague	1907–1935
William W. Morrow	1902–1929
Seeley G. Mudd	1940–1968
William I. Myers	1948–1976
William Church Osborn	1927–1934
Walter H. Page	1971–1979
James Parmelee	1917–1931
Wm. Barclay Parsons	1907–1932
Stewart Paton	1916–1942
George W. Pepper	1914–1919
John J. Pershing	1930–1943
Henning W. Prentis, Jr.	1942–1959
Henry S. Pritchett	1906–1936
Gordon S. Rentschler	1946–1948
David Rockefeller	1952–1956
Elihu Root	1902–1937
Elihu Root, Jr.	1937–1967
Julius Rosenwald	1929–1931
William M. Roth	1968–1979
William W. Rubey	1962–1974
Martin A. Ryerson	1908–1928
Henry R. Shepley	1937–1962
Theobald Smith	1914–1934
John C. Spooner	1902–1907
William Benson Storey	1924–1939
Richard P. Strong	1934–1948
William H. Taft	1906–1915
William S. Thayer	1929–1932
James W. Wadsworth	1932–1952
Charles D. Walcott	1902–1927
Frederic C. Walcott	1931–1948
Henry P. Walcott	1910–1924
Lewis H. Weed	1935–1952
William H. Welch	1906–1934
Andrew D. White	1902–1916
Edward D. White	1902–1903
Henry White	1913–1927
George W. Wickersham	1909–1936
Robert E. Wilson	1953–1964
Robert S. Woodward	1905–1924
Carroll D. Wright	1902–1908

Under the original charter, from the date of organization until April 28, 1904, the following were *ex officio* members of the Board of Trustees: the President of the United States, the President of the Senate, the Speaker of the House of Representatives, the Secretary of the Smithsonian Institution, and the President of the National Academy of Sciences.

OFFICE OF ADMINISTRATION

1530 P Street, N.W., Washington, D.C. 20005

James D. Ebert	*President*
Robert N. Kreidler	*Vice President*[1]
James W. Boise	*Bursar; Executive Secretary to the Finance Committee*
Christopher Wright	*Staff Member (Science Policy and Institutional Development)*
Franklin H. Portugal	*Historian*
Ray Bowers	*Publications Officer; Editor*
Kenneth R. Henard	*Assistant Bursar*
Susan Y. Vasquez	*Assistant to the President*
Joseph M. S. Haraburda	*Assistant to the Bursar*
Richard E. Hewitt	*Administrative Officer for Services*

Marshall Hornblower	*Counsel*

STAFF MEMBER IN SPECIAL SUBJECT AREA

Roy J. Britten

DISTINGUISHED SERVICE MEMBER IN SPECIAL SUBJECT AREA

Barbara McClintock

RESEARCH ASSOCIATE AT LARGE

Harry E. D. Pollock

[1]Effective November 1, 1980.

Carnegie Institution of Washington adheres in all phases of its operations, including employment and educational programs, to a policy barring discrimination on the basis of race, religion, color, national or ethnic origin, sex, or physical handicap. In its educational programs it admits qualified students as fellows without regard to race, religion, color, national or ethnic origin, sex, or physical handicap to all the rights, privileges, programs, and activities generally accorded or made available to fellows at the Institution. It does not discriminate on the basis of race, religion, color, national or ethnic origin, sex, or physical handicap in administration of its educational policies, admissions policies, fellowship programs, and other Institution-administered programs.

Report OF THE *President*

I remember how in my youth, in the course of a railway journey across Europe from Brindisi to Calais, I watched with keen delight and wonder that continent flowing with richness under the age-long attention of her chivalrous lover, western humanity . . . the heroic love-adventure of the West, the active wooing of the earth.

Rabindranath Tagore
Towards Universal Man

. . . . Earth has potentialities that remain unexpressed until properly manipulated by human labor and imagination. But work is not enough to discover and bring to light the hidden treasures of Earth; it also takes love.

We cannot escape from the past, but neither can we avoid inventing the future.

René Dubos
The Wooing of Earth

I COMPLETED MY READING of the Annual Reports of the directors of the Institution's Departments nearly two months ago. Individually and collectively they held immense interest for me, for they provided penetrating and specific insights into some of the central problems of our time. Yet until only a fortnight ago I found myself groping for a unifying theme for this essay. Then I read, and re-read, René Dubos' paean to the symbiosis of humankind and the Earth, *The Wooing of Earth*, and I knew that my task must be to explore the Institution's role in "inventing the future," in providing the scientific understanding that will open new perspectives on man's use of Nature. I knew, too, that I must accentuate the positive, that I must emphasize the resilience of science and the richness of new opportunity. For I am firm in my belief that we can improve on Nature.

Scarcely anyone would deny the immense promise of the emerging gene technology; yet throughout the world there is widespread apprehension about both its costs and possible unfortunate social consequences. Some fear it may be used unwisely to tinker with human heredity or to produce unforeseen and unwanted changes in animals or plants. Such fears were recently fueled by a possibly premature attempt at gene therapy in humans—the treatment of thalassemia by inserting copies of the human gene for beta-hemoglobin into a patient's bone-marrow cells—a procedure undertaken before it had been shown by animal experiments that such gene transfers could be done successfully.

But whether or not the treatment was medically appropriate, the

episode illustrates that it is the national, indeed world, mood to dwell on risk rather than benefit, on the possibility of failure rather than on that of success. In my view, this prevailing atmosphere of pessimism must be reversed, lest it dampen the spirit of pioneering independence so crucial in research.

The promise of genetic research is great, but we still know so very little. As Lederberg has emphasized, over 99 percent of the human genome remains a mystery. We must continue then, not only to isolate and characterize genes, but also to probe more deeply into the ways genes interact with each other and with the cellular environment. Indeed, this last phrase, "interact with each other and with the cellular environment," encompasses a wide range of critical problems. Among them, none loom larger than our need to understand the mechanism whereby blocks of genetic information move within the chromosomal complement. We are at last beginning to appreciate fully the remarkable pioneering contributions of Barbara McClintock, who described the transposable elements of maize in the 1950's, and to recognize that there may be, in John Abelson's words, "a unity in the mechanism by which transposable elements function" in bacteria, yeast, *Drosophila*, and in immunocompetent cells.

The search for gene control mechanisms is equally compelling. Nowhere is it better exemplified than in the role of the Department of Embryology in the emergence of developmental biology as an exact science.

In the late 1950's, we at Baltimore were convinced that the immediate future of developmental biology in part lay in isolating genes, in studying their arrangement and organization within the chromosome, and in discovering the mechanisms regulating their action. We had no timetable, but we were surprised when we and workers elsewhere achieved the first steps toward this goal as early as 1970. We believed that we should begin by attempting to define the final gene products, the proteins, and by using them as markers to move closer to the genes themselves. It was a field wherein we had already contributed. As it turned out, the technology for studying direct gene products, the ribonucleic acids—especially the ribosomal RNAs—developed more rapidly than we anticipated, thus opening the way for today's direct attack on the gene.

Over the years, Donald Brown and more than a score of colleagues have pioneered in the isolation and characterization of animal genes and their immediate products, the ribonucleic acids; these studies have, in turn, made possible major advances in understanding the mechanisms of gene regulation. Brown's study with Carnegie Fellow John Gurdon of an anucleolate mutant strain of the South African clawed toad *Xenopus* constitutes a modern landmark, offering decisive

proof of the role of the nucleolus in the synthesis of ribosomal RNAs. By further exploiting the anucleolate mutant, Brown was able to map the genes encoding these RNAs. He and his co-workers then proved that during oogenesis the genes for ribosomal RNAs are amplified into hundreds of copies. This research then evolved to the point where it became possible to isolate the genes coding for the 28S and 18S ribosomal RNA fragments—the first genes to be isolated from any eukaryotic cell. The further extension of these techniques culminated in the isolation and characterization of the genes coding for 5S ribosomal RNA.

Brown and his co-workers then turned to the question whether the amplification of specific genes can be demonstrated in specialized cell types. Together with Yoshiaki Suzuki (now at the National Institute of Basic Biology, Okazaki, Japan), he isolated the messenger RNA coding for the silk protein, fibroin, in the larval silkworm, *Bombyx mori*. Using this mRNA as a probe, they were able to show that the fibroin gene is not amplified in the cells of the silkglands. Suzuki's further studies have provided what may be the most complete account thus far available of the waxing and waning of gene action during development.

The concept of gene amplification continues to be a prime focus of research in the Department, where Allan Spradling studies the genes that encode a group of eggshell (chorion) proteins in the fruit fly, *Drosophila melanogaster*. The power of using *Drosophila* lies in its suitability for traditional genetics as well as for the newer methods of gene isolation, characterization, and function. Recently, Spradling has shown that genes for chorion proteins are amplified in follicle cells just before the genes are expressed—the first reported example of amplification for protein genes that is programmed into normal development. Mutants have already been found that affect this amplification.

In the most recent and perhaps most promising development in the field of gene control, Brown and colleagues have isolated from ovarian tissue a protein that interacts specifically with a control region located in the center of the 5S RNA gene. This protein has the remarkable property of binding the gene product, 5S RNA, and forming a stable particle with it. The synthesis of this protein almost certainly accounts for the activation of 5S RNA genes in early oocytes. This is the first discovery of a control protein that is specific for one eukaryotic gene and at least partly responsible for the differential expression of that gene in development.

The consequences of this latest discovery may be far-reaching. But I would emphasize not the discovery itself nor the decade of discovery leading up to it. What is important here is that the Department of Embryology has proven itself able to take advantage of new opportunities as they unfold. It has its priorities straight. The age structure of the

Department is becoming younger, and there is a healthy turnover of uncommonly promising young men and women. The freedom to recruit the brightest young minds is always an advantage, but it is especially significant in fields like developmental biology which are idea- rather than instrument-limited. Opportunity for expansion of the Department in the foreseeable future of "steady-state budgets" is limited, indeed almost nonexistent; thus the flexibility of mind to shift into new ventures, whether in the fields of gene regulation, transmitters and receptors, or cell communication, is essential.

But if the Department of Embryology is clearly positioned to exploit new opportunities to improve on Nature, is this also the case in our other departments? The answer is unhesitating: Yes. For in fact two Carnegie departments, the Geophysical Laboratory and Department of Terrestrial Magnetism, focusing as they do on the mobile Earth, stand at critical junctions not only in the whole course of basic research but also with respect to the nation's future needs. As Hatten Yoder wrote in reviewing the work of the Geophysical Laboratory:

> Opportunities for basic research remain almost unlimited in spite of recent major advances and, indeed, are often created by such advances. The staff continue to uncover and delineate new areas for expanded effort. The key appears to be in asking significant and fundamental questions and in having courage to try unconventional approaches. The continued growth of geology as a science seems assured as nations become more responsive, within economic constraints, to the complex problems of natural resources and hazards.

Conceptual advances, particularly the theory of plate tectonics, and the development of new instruments have proceeded apace over the past two decades. As a consequence, the Geophysical Laboratory and DTM are poised to contribute significantly to efforts to deal with the nation's fuel shortage and especially its potential nonfuel mineral shortage. Studies of the fluid dynamics of magma bear on the accumulations of the mineral ores in layered intrusions that yield chromium, titanium, vanadium, nickel, copper, and platinum. In fact, nearly every endeavor at the Laboratory, in Yoder's view—from measurements of mineral solubilities to studies of organic substances in ore deposits—can be perceived as contributing to an understanding of the principles whereby elements are accumulated in ore deposits.

Throughout the history of DTM, the principal focus of its work has been on the Earth, particularly in its global aspects. Today, the overall goal of the Department is to advance fundamental understanding of the essential nature and history of the Earth, planets, stars, and galaxies, and to explore the ways wherein these systems and their histories

are interrelated. George Wetherill, the Department's director, has written:

> Our goal is obviously an ambitious one and an approach toward it is possible only by drawing upon and synthesizing the much larger body of related work being carried out in other institutions. Yet we have found that an approach to such broad questions within a small and interactive staff has proven fruitful in the past, and we expect that this will remain true in the future.

Earlier, we described developmental biology as more dependent on ideas than on instruments. There is no dearth of ideas among earth scientists, but advances in instrumentation loom large in their most promising endeavors. Consider the seismological work at DTM, which addresses the nature of the earthquake source mechanism and the distribution and migration of stress within the Earth. An important tool is the Sacks-Evertson strainmeter, which provides a simple, sensitive, and accurate means of measuring changes over very long periods, i.e., at very low seismic frequencies. Networks of these strainmeters have been deployed in Japan and Iceland, and another network is being installed in the San Andreas fault zone in California. Smaller numbers of instruments have been installed elsewhere.

Wetherill has noted that when observations are extended to a new frequency band (in this case, to zero hertz) there is often a discovery of new phenomena. In the case of the strainmeters, the new phenomenon is the "slow earthquake." These are episodic releases of stored seismic strain energy, unaccompanied by the damaging strong accelerations that accompany more familiar, higher-frequency earthquakes. Events of this kind have been detected for a number of years by DTM strainmeters, and Sacks, Suyehiro, Linde, and Snoke have discussed the possible role of slow earthquakes in "invisibly" redistributing and concentrating stresses, and in thereby triggering damaging earthquakes.

These scientists have now analyzed data showing the first seismic evidence for the simultaneous occurrence of a normal earthquake and an accompanying slow earthquake in Japan in 1978. A normal earthquake of magnitude 7.0 was confined to the offshore area. However, geological observations on land indicated movements along a fault extending inland. These observations were confirmed by data from three nearby strainmeters, which recorded strain steps associated with both the offshore and inland fault motions. Slow strain changes occurred for about an hour after the normal earthquake and indicated that the energy associated with the slow earthquake was similar in magnitude to that of the normal earthquake. The fact that the first normal aftershock did not occur until after this slow release and redistribution of stress emphasizes the coupling of the events.

To a large extent the global-scale motions described by plate tectonics are but the accumulation over hundreds of millions of years of the fault motions associated with ordinary earthquakes. These investigations raise the possibility that plate motions accompanying these episodic but very low frequency, slow earthquakes may play a tectonic role comparable to that of normal earthquakes.

Our attention to the Earth's resources leads us naturally to their overuse and misuse, and to the environmental degradation and pollution that may result. Fortunately, there is increasing awareness worldwide of the fragility of the environment, and new technologies are evolving both to reduce pollution and to provide remedial action. In this context, the Geophysical Laboratory's efforts in biogeochemistry deserve special mention.

Concern about pollution of the environment has led to widespread effort to measure specific pollutants and certain classes of organic compounds in natural water systems, sediments, and soils. Certain natural organic polymers are of particular biological and environmental importance because they can absorb, chelate, and transport essential trace metals as well as toxic organic substances. Relatively little is known, however, of their actual compositions.

The organic material in aquatic systems is a complex mixture of biological decomposition and resynthesis products. Because of this complexity, no simple procedure for complete characterization exists, although recent work by Sigleo, Hoering, and Hare suggests that aquatic organic material is derived primarily from aquatic microorganisms *in situ*. These workers developed a procedure for obtaining dissolved and colloidal organic material from fresh and saline waters with commercially available ultrafiltration techniques. They tested their method using samples from the Chesapeake Bay and Patuxent River, in Maryland. This water system is ideal for the purpose because it provides an easily accessible variety of environments, including a salinity gradient varying from freshwater to nearly seawater.

Sigleo first analyzed the final dried organic matter for more than 30 elements by instrumental neutron activation analysis at the University of Maryland. The group then characterized aliquots of the same samples by temperature-controlled stepwise pyrolysis. The volatile products of pyrolysis were separated by gas chromatography and identified by use of a mass spectrometer.

A number of natural and synthetic polymers give characteristic pyrolysis products that can serve as "fingerprints" of the original polymer. Many oxygen-containing compounds produced by the pyrolysis are characteristic of carbohydrate thermal decomposition. A series of nitrogen-containing compounds are typical pyrolyzates from pro-

teins and smaller peptides. The Carnegie researchers have verified and precisely quantified the proteinaceous component in the samples by amino acid analyses. These analyses were made with the state-of-the-art ion exchange chromatographic system developed at the Geophysical Laboratory by Hare.

The indication that colloidal aquatic material is composed primarily of proteinaceous material (amino acids) and carbohydrates is significant because both contain numerous active functional groups capable of complexing and transporting trace metals. The methods developed during the last year will be useful not only for documenting the distribution of these compounds in aquatic and sedimentary systems, but also for ultimately determining the role of organic compounds in the transport and deposition of trace metals in the environment. Because over half the ore deposits of the world are in sedimentary material, these studies may be significant with respect to the growing mineral-resource problem.

Deforestation and the burning of fossil fuels have an important part in the evolution of research in the Department of Plant Biology as well as in the Geophysical Laboratory.

During the past few years, the physiological ecology group of the Department of Plant Biology has concentrated its studies of acclimation almost exclusively to a single factor: temperature. In numerous experiments, investigators made certain that water supply was not a limiting factor and that saturating levels of CO_2 were available when appropriate so that the intrinsic responses of the system to temperature changes could be isolated and studied. Interest focused on the upper end of the temperature range. This year, the Department's Report contains descriptions of research on two other factors, carbon dioxide enrichment and water stress, as well as on the phenomenon of chilling sensitivity.

Evidence is strong showing a significant increase in carbon dioxide in the atmosphere as a consequence of the burning of fossil fuel and deforestation. It is thus essential to determine the long-term effects on photosynthesis of high carbon dioxide partial pressures. Björkman and his colleagues have investigated the effect of CO_2 enrichment lasting weeks or months on several C_3 and C_4 plants. Not surprisingly, they found very little effect on the C_4 plants, since a distinctive feature of C_4 photosynthesis is that it concentrates carbon dioxide for fixation by ribulose bisphosphate carboxylase. In C_3 plants, however, CO_2 enrichment produced strong increases both in light-limited and light-saturated photosynthetic rates and significant enhancement in dry matter production. Perhaps the most impressive consequence of CO_2 enrichment on both C_3 and C_4 plants was a dramatic increase in the water-use efficiency (carbon dioxide fixed per unit of water lost

through transpiration). Though other aspects of a CO_2-enriched atmosphere may not necessarily be beneficial, the effects reported here could have a positive impact on agricultural productivity.

Studies of the effect of water stress on the desert shrub *Nerium oleander* are also under way. The shrub is highly tolerant to water stress. Contrary to expectations, *Nerium* makes no osmotic adjustment in response to gradually imposed water stress. There is a reduction in intrinsic photosynthetic capacity, however, a response expected on the basis of previous studies at the Department and elsewhere, and possibly accounted for entirely by a decrease in the capacity for photosynthetic electron transport and photophosphorylation in the stressed plants. These studies mark the onset of a new program of investigating the interaction of stress factors on photosynthetic systems.

Provocative results have come, too, from studies on the interactions between light and temperature on chilling-sensitive plants. Such plants (beans and tomatoes are examples) are simply unable to tolerate temperatures below 10 °C in normal air and high light intensity, conditions producing damage to the photosynthetic apparatus. Such damage does not occur, however, if the oxygen tension is lowered or if the light intensity is reduced. While details of the mechanism of injury remain to be resolved, the results could have significant agricultural implications.

Of all the manifestations of Nature, none is more basic to our well-being, now and in the future, than our own star, the Sun. In this year of maximum sunspot activity, general interest in solar research has been widespread. Coincidentally, a program of data collection long under way at Mount Wilson led to one of the year's most significant discoveries in solar physics.

Since 1966, scientists at Mount Wilson have been making daily measurements of the magnetic and velocity fields at some 24,000 positions on the Sun's surface. Last year, Howard and LaBonte began a systematic reduction and analysis of the massive data, which resided on more than 150 computer tapes. They discovered that the solar surface has zones, or currents, of fast and slow rotational velocity. At any time, there are two fast and two slow currents in each hemisphere, symmetrically distributed about the solar equator. Zones of fast velocity appear near the poles every 11 years and gradually migrate equatorward, to reach the equator 22 years later. The movements appear synchronized with the 11- and 22-year sunspot cycle. Even more remarkably, the area of greatest sunspot activity coincides and migrates with a border region between fast and slow current. The whole phenomenon is clearly related to the same subsurface dynamo that generates the magnetic fields accounting for the sunspots and the basic solar cycle. Howard and LaBonte cautiously write that their results represent

"the first evidence of the association of mass motions with large-scale characteristics of the solar activity cycle." Their discovery, which rests on more than a decade of observation, illustrates the significance of long-term and stable funding for research.

Energy, Economics, Education: Science in the 1980's

> For one person time is a scale along which events are measured. For another it is events themselves in their ceaseless flow. For another it is the sum of hope, fear, doom, and joy, all in turbulent motion.
>
> David Park
> *The Image of Eternity*

"Events . . . in their ceaseless flow"—nearly 80 years of discovery—bring the scientists of Carnegie Institution to the 1980's full of hope and poised to exploit new opportunities. For in its lifetime the Institution has often played seminal and catalytic roles in "inventing the future." We come to this position neither entirely by chance nor entirely by design. Although the contemporary portrait of the Institution differs in many details from that of the past, there has been one constant theme: to offer opportunities to those rare individuals who have gifts of critical judgment and rigor, who are able and eager to select problems for their importance, not for their ease. The Institution preserves this spirit of inquiry.

Actually, I am less concerned about the Institution's ability to contribute to the course of science than I am about the effect on the Institution of larger forces over which it has no immediate control, especially energy and the economy. (I write "no *immediate* control" because in the long run our research in the earth and plant sciences may contribute tellingly to meeting the world's energy and mineral needs.)

I spoke earlier of the realities of steady-state budgets in the Department of Embryology. Such fiscal limitations are compounded in instrument-dependent fields, of which astronomy and geology are prime examples.

We have made substantial strides in improving our short-term financial position, thanks in larger part to the generosity of our own trustees and to the recognition by a number of the nation's major philanthropic foundations—among them the Ahmanson, Charles E. Culpeper, Exxon Education, Fleischmann, Andrew W. Mellon, Jessie Smith Noyes, Alfred P. Sloan, and Whitehall Foundations, and the Commonwealth Fund—that our departments are deserving of unrestricted support.

But now our attention must be focused on the longer term. Two years ago I set a goal, one upon whose attainment may depend the survival of the Carnegie idea. We propose to—in fact we must—increase our endowment twofold. Further, we must achieve this in the foreseeable future.

Toward this end we will be calling increasingly on the corporate, as well as the foundation, sector. The development of creative interactions with industry will be crucial. I am especially heartened to report that even as this essay is in press, Mr. Robert Kreidler is joining us as vice president, to strengthen our efforts in assuring the Institution's financial stability.

But even so remarkable a national resource as Carnegie Institution may not succeed in overcoming financial restrictions if we fail to reverse the tide of doubt and pessimism in society about the values of science and technological innovation. In his Trueman Wood Lecture, "Making Our Institutions Work," John Diebold spoke of the widening gap between what is *possible* in the improvement of mankind's condition given our present means and what we are actually able to turn to *reality*. Diebold stressed the need for constructing a new general scheme—in Elting Morison's words, "an attracting vision."

There is no simple prescription to alter the national mood. But I believe that "the attracting vision" must include, as its centerpiece, the reorganization of our educational system in the sciences and technology. On Thursday, October 23, a *New York Times* article was captioned "U.S. Report Fears Most Americans Will Become Scientific Illiterates." It cited a report, prepared by the Department of Education and the National Science Foundation, entitled "Science and Engineering Education for the 1980's and Beyond." The report, while assuring us that our eminence in basic research is still secure and that the best of our students are learning about as much as they ever did, concludes that *most* students learn less and less.

We must reverse the deterioration of our educational system, for we cannot afford even another year, let alone a decade of decay. In 1945, James B. Conant wrote, ". . . the future of science in this country will be determined by our basic educational policy." Today, Conant's statement must be broadened—our economy, our jobs, our security, our very lives depend on a sound educational system.

We sense the consequences of our failure at every turn: our capabilities have been reduced in our high-technology industries and our armed forces, both seriously dependent on the contributions of our engineers and scientists. Our domestic economy and our competitive position in international markets has been weakened. And the problem is not confined to the professional level. Trained technical personnel are scarce at every level, a condition caused by our failure to teach the

fundamentals of mathematics and science in the primary and secondary schools, and by a mistaken idea that machines will replace skilled personnel. It is sometimes true that it is possible to use modern equipment without knowing how it works. But machines are no better than the men and women who design, program, and maintain them.

Our society will be asking much from our scientists, engineers, and technical people. We must develop our energy resources—sufficient and affordable. We must at the same time preserve our natural environment, ensuring food from our seas and the blooming of our deserts. We must ensure our security. And if we are to justify our privileged place in history, we must move ahead in the explorations of space and the recesses of the human mind, toward the great discoveries of tomorrow that cannot even be conceived today. But scientists, engineers, and technicians are not enough. We need a well-educated, scientifically literate public, a public able to comprehend the workings of the modern world and willing to make the sacrifices that surely lie ahead.

What must we do? Some remedies are clear. We must continually replace our obsolete instructional equipment, just as we must renew equipment for research.

Even more important are matters of educational content. We must renew our curricula in mathematics and the sciences at every level. For the very heart of science is change; the fruits of our research in science and engineering must be incorporated fully and rapidly into the curriculum. The necessary planning cannot be narrowly based: new findings are often controversial. They may even appear to be esoteric, yet within a few short years they may have a profound impact on our lives. Controversy will always be with us; even today, local school districts and states are again wrestling with the problem of "scientific creationism" versus evolution. Thus, a national curriculum study—one emphasizing the consequences of discovery, with input from all responsible levels and sectors—is crucial.

The nation has supported curriculum development before, in the 1950's and '60's; and some of those programs, for example the Biological Sciences Curriculum Studies, were highly successful. What, then, went wrong?

It was not that the federal role in education was decreasing—it did not. Its shape was changed significantly, however. Emphasis became less on increasing the quality of education and more on equality of opportunity. Somehow, the nation could not comprehend that equality and quality must go hand in hand. Our children are not well served by an educational system that is primarily a vehicle for addressing the full range of the nation's social problems.

Even more distressing was the absence of continuity of support.

Education received only sporadic bursts of attention—in response to Sputnik and alternating gluts and shortages of personnel in several fields.

Granted, in *The Image of Eternity* David Park observed that it is hard to imagine what our civilization would have been like without the continued expenditure of quixotic effort, pointing to recurring "projects that seem out of proportion to necessity"—the pyramids, the Imperial Court at Peking, the walk on the Moon.

But a revitalization of our educational system cannot depend upon quixotic effort. Yet in recent decades education, not just in science and engineering but the entire system, has been treated in just that way. There has been neither a clearly stated national policy nor continuing review to make the system responsive to changing needs; nor has there been a stable floor of financial support.

Where should responsibility for continuity lie? Neither the Department of Education nor the National Science Foundation appears to be strategically placed to command the attention required from all federal sectors; moreover, too often their interests appear to be competing. And while I agree fully with William Golden, who has called for the reestablishment of the President's Science Advisory Committee (*Science, 210*, 145), I doubt that PSAC would meet this need. Reluctant as I am to see the creation of a new office (at least without a compensating reduction), I must argue for the establishment, within the Executive Office, of a Council for Education in Science and Technology, to give continuing heed to our vital human resources, which surely deserve as much attention as our financial resources.

HIGHLIGHTS OF THE YEAR

Discovery—and Change—in Pasadena

I have already sketched (p. *10*) Howard and LaBonte's major contribution to our understanding of the solar cycle. This is but one of several discoveries at the Hale Observatories this year deserving special mention.

The Magellanic Clouds, observable only from the Southern Hemisphere, are our nearest neighbors in extragalactic space, some 200,000 light years away. They allow more detailed study of their stellar make-up than do other galaxies. For this reason, the Clouds are a favorite target for astronomers having access to southern telescopes. Searle, with Althea Wilkinson of the University of Manchester and William G. Bagnuolo, a former graduate student at the California In-

stitute of Technology, recently completed a study of the integrated light of populous star clusters in the Clouds. Their purpose was to investigate correlations between cluster age and metal abundance in order to develop classification schemes for the integrated spectra of clusters.

Searle, Wilkinson, and Bagnuolo find from inspection of the Magellanic spectra obtained with the Swope reflector at Las Campanas that age and metal abundance are correlated, such that the metal abundance is lower in older star clusters. A correlation is also known for clusters of our Galaxy and is attributed to the gradual enrichment in metals of the interstellar gas as products of nuclear burning in the interiors of stars are returned to the interstellar medium. However, the correlation in the Magellanic Clouds differs from that found in our Galaxy, as the histories of chemical enrichment appear to have been qualitatively different. Recent observations obtained with Shectman's Reticon detector at the du Pont Telescope should allow the observers to put the age–metal abundance relation in the Magellanic Clouds on a quantitative basis.

The large field of the du Pont Telescope, covering in excess of two square degrees on each 50 × 50 cm plate, has allowed Sandage and Gustav A. Tammann of the Astronomical Institute of the University of Basel, Switzerland, to undertake a photographic survey of the Virgo cluster of galaxies. Sandage and Brucato have obtained half of the required plates over two observing seasons. A catalog of all possible cluster members in these fields is nearing completion, with a principal goal of studying the distribution of dwarf galaxies. These galaxies are generally of the dwarf elliptical type with a smooth luminosity profile and no suggestion of current star formation. They are distributed throughout the cluster region outlined by the bright galaxies, but do not extend southward into the so-called Southern Extension. Sandage and Tammann conclude that this appendage to the Virgo cluster proper does not form a dynamical unit with it.

Robert Shaw has traced the plates for all possible cluster members, using the large microphotometer at the European Southern Observatory headquarters in Geneva (now in Munich). Preliminary results show that the surface brightness of the galaxies decreases monotonically with absolute luminosity. Thus, the very low surface brightness of the dwarf elliptical permits separation of the faint cluster members from the numerous distant elliptical galaxies in the background field. Spectra obtained for 43 of the dwarfs by Sandage and Dressler using the Gunn SIT detector at the Cassegrain spectrograph of the Palomar 5-meter reflector confirm that all have radial velocities less than around 2000 km/sec, proving cluster membership. The fainter dwarf galaxies show spectroscopic evidence for the presence of A-type

stars, suggesting that star formation in these systems took place until as recently as one billion years ago. This may be due to the slow collapse of these dwarf galaxies caused by their very low mean density.

Another group of observers, including Shectman, Robert Kirshner of the University of Michigan, Augustus Oemler, Jr., of Yale University, and Paul Schechter of Kitt Peak National Observatory, have discovered a volume of space conspicuously empty of galaxies. This is the largest feature yet found in the distribution of matter in the universe. They studied three fields near the north galactic pole to avoid the patchy dust obscuration observed near the galactic plane. The fields, each of two square degrees, were separated from each other by about 35 degrees. Redshifts were measured for more than 100 galaxies brighter than red magnitude 17.

The striking result is that not a single galaxy shows a velocity of recession between 12,500 and 18,500 km/sec, whereas the most likely velocity (on the basis of the range of brightness surveyed) was expected to be 15,000 km/sec. The gap is common to all three fields; hence its width on the sky is comparable to its depth. The gap spans a diameter 100 times our distance to the nearest major galaxy, Andromeda, and six times our distance to the nearest major cluster of galaxies, Virgo. A supercluster associated with the very rich Coma cluster of galaxies may be responsible for a clear peak in the observed velocities below 12,500 km/sec.

Ever since quasars were discovered in the early 1960's, their nature has been a matter of intense investigation. Part of the inquiry has concerned the relation between quasars and galaxies or clusters of galaxies. Kristian, Young, and Westphal, in order to search for faint associated galaxies, have now investigated the vicinity of 16 quasars having redshifts from 0.3 to 1.4 (in z, the fractional shift in wavelength $\Delta\lambda/\lambda_0$). On the basis of deep two-hour red CCD exposures at the 5-meter Hale Telescope, they conclude that galaxies cluster around most of the quasars, even those with redshift in excess of 1.0. (CCD is an abbreviation for charge-coupled device, a new highly quantum efficient photon detector with potential for broad applications in astronomical research.) To explain such a degree of clustering, it is required that the tendency for a quasar to be located near a galaxy be much stronger than the corresponding tendency for a galaxy to be located near another galaxy. An alternative explanation is that galaxies at a redshift of 0.75 would have to be 40 times more luminous than nearby galaxies.

Among the most significant events this year in astronomy was the confirmation of a gravitational lens. The story of this discovery has been told on several occasions, perhaps most effectively in Frederic H. Chaffee, Jr.'s, fascinating account in *Scientific American* (November 1980).

A pair of quasars of identical redshift, 1.41, was discovered in 1979 at the Steward Observatory of the University of Arizona. Only six arcseconds apart, the two quasars were thought possibly to be gravitationally lensed images of a single object. Young and Kristian observed the object Q0957+561, with a CCD system built by Gunn and Westphal (*Year Book 78*, p. 779). They discovered that the object lay behind a cluster of galaxies: the brightest galaxy in this cluster lay only one arcsecond north of the southern quasar image. Multichannel and CCD spectra by Oke and Gunn gave a redshift of 0.36 for this galaxy. Theoretical calculations by Young and Gunn demonstrated that the galaxy and cluster of galaxies acting together produced the gravitational lens effect. The southern quasar image was observed to brighten by 30 percent in January 1980. If the gravitational lens geometry can be understood well enough, then the time delay between the light variations of the two quasar images will allow an independent determination of the Hubble constant.

Reorganization of the Observatories. Thus far I have focused attention on *discovery*: First things first. On July 1, 1980, the Hale Observatories, formerly administered jointly by the Institution and California Institute of Technology, were dissolved, and each institution assumed responsibility for managing its own facilities. Each now has its own Acting Director: George Preston for Carnegie's Mount Wilson and Las Campanas Observatories, and Gerry Neugebauer for Caltech's Palomar Observatory. I would emphasize that the separation is administrative, not scientific. Collaboration in research and in instrument development will continue, not only between Caltech and Carnegie astronomers but with visiting scientists as well. As Maarten Schmidt observed in his final Report as director of Hale Observatories: "Time on telescopes of both institutions will be assigned jointly on the basis of scientific merit and without regard to institutional affiliation."

Astronomy at DTM

Research in the Department of Terrestrial Magnetism ranges from studies of distant galaxies to investigations of isotope compositions in materials raised from the Earth's interior. As Wetherill observes, the astronomical studies at DTM, in addition to their intrinsic importance, are relevant to the Department's studies of the solar system and Earth history in several ways. For example, many of the isotopic anomalies in the early solar system probably have their origin in supernova ejecta heterogeneously mixed into the solar system during its formation,

possibly including material from a supernova which triggered the collapse of the interstellar molecular cloud that evolved into the Sun and other stars.

Another connection between stellar and planetary science is the use of the abundances of naturally occurring and extinct radioisotopes, determined from meteorite data, to determine details of the time scale for solar system formation and its relationship to prior Galactic history. Such calculations involve assumptions as to the rate of star and element formation in the Galaxy during its evolution.

Galaxies are the largest systems in the visible universe. They are the "factories" within which stars are produced. Our inadequate understanding of the dynamical processes controlling the evolution of galaxies seriously hampers our interpretation of the record of the early solar system revealed by lunar and planetary exploration and studies of meteorites.

Rubin, Ford, Thonnard, and their colleagues are carrying out a long-range program in optical and radio astronomy, relating types of galaxies (under the classification system developed by Hubble) to observable parameters of physical significance such as the distribution of mass, rotational velocity, and luminosity of individual galaxies. A sample of 50 galaxies has now been studied in this way, and more will be studied in the years ahead. This work has disclosed an unexpected phenomenon: unlike their luminosities, the masses of galaxies are not concentrated toward the galactic centers. Mass falls off much more slowly with distance from the center, and a considerable fraction of the mass of a galaxy lies even beyond the edge of its optical image. This phenomenon is common to all the morphological types studied to date. In more detailed work, Rubin and colleagues have found significant differences among galactic types. One of these is the very abrupt increase of rotational velocity found near the centers of the most luminous galaxies. A by-product of this discovery will be its use as a distance indicator for identifying very luminous but distant galaxies among faint galaxies.

This work establishes fundamental data upon which future syntheses of galactic evolution must be based. We may suppose that, as in stellar evolution, galactic evolution is largely an internal playing out of events predestined by the initial state of the galaxy in accordance with the fundamental laws of physics and chemistry. But this is probably not the whole story. Recent work by a number of investigators has emphasized the role of catastrophic events, such as a collision and merger of two galaxies. Research by Rubin, Ford, and their collaborator, M. S. Roberts of the National Radio Astronomy Observatory, on the giant galaxy NGC 1961, for example, has indicated that a great burst of star

formation occurred only about 100 million years ago during a violent dynamic event of this kind.

The Earth and Planets; Meteors and Meteorites

DTM scientists have continued to give attention to a star-forming event 4.5 billion years ago in our own galaxy—the formation of the Sun and its planetary system including the Earth. Such studies afford a special approach to a central problem in stellar astronomy, the history and nature of star-forming processes in galaxies.

In his introduction to the DTM Report, Wetherill addresses the fundamental question of the age of the Earth. A good approximation was set at 4.55 billion years by Patterson in 1956; when corrected to the uranium-lead decay constants and other parameters in current use, the value becomes 4.45 billion years. More recent calculations with newer data and a more sophisticated approach to the problem have given similar results. On the other hand, meteoritic data, based on a consistent set of decay constants, give an age of 4.56 billion years. A number of workers have discussed the 100-million-year difference in these two values. Some authors assume as axiomatic that the Earth and meteorites must have an identical age. But if one considers various plausible physical processes by which meteorites and the Earth may have formed, it becomes quite possible, and even probable, that about 100 million years were required to form the Earth from bodies similar in size to the parent bodies of the meteorites, thus reconciling the seeming discrepancy in Earth ages. However, the same physical processes also determine the thermal history of the Earth and indicate that the mean time of uranium-lead fractionation that accompanied the formation of the Earth's core corresponds to a shorter interval of from 10 to 30 million years. The age of the Earth calculated from lead isotope data, *probably actually dates the mean age of core formation.* For this reason, an age of the Earth 100 million years later than the age indicated by meteorite data raises some difficulties for quantitative theories of planet formation.

Tera has now presented data strongly suggesting that the actual time of core formation is in approximate agreement with the theoretical expectation, namely about 4.54 billion years. These data are obtained from lead-bearing minerals more than 2.6 billion years old. Tera discerns regularities in the lead isotope ratio from these ancient minerals and infers that for the first two billion years of its history, the mantle source of these minerals had a uranium-lead ratio about 15% lower than that usually accepted. Use of this value leads to a consis-

tent result for both the age of the Earth and the value of this ratio, whereas other combinations are not consistent. It also appears likely that the source of lead minerals of this kind became more enriched in uranium relative to lead about 2.6 billion years ago. Use of younger samples which had experienced this more complex history leads to a younger, and probably incorrect, value for the age of the Earth.

Among the more significant potential sources of information about the early solar system are detailed laboratory studies of meteorites. A major difficulty is our uncertainty as to the parent bodies of most meteorites. Of particular interest in facing this question are the "brecciated" meteorites, which consist of broken fragments of meteoritic material more or less bonded together to form again a solid rock. Many of these breccias have features also found in brecciated lunar rocks, produced by high-velocity meteoritic bombardment of the surface of this airless planetary body. It can be shown quite clearly that meteorites do not actually come from the Moon. It is very likely that some of these brecciated meteorites are samples of the surfaces of similarly atmosphere-free asteroids. Fundamental uncertainties remain, however. Superficially similar breccias can be produced by a number of differing circumstances. These include the relatively prosaic production of such rocks on the surface of bodies in the present-day asteroid belt. They may also constitute a record of events early in solar system history associated with the primordial acceleration of asteroids to their present high-velocity orbits, or during the still earlier accumulation of the asteroids from interplanetary dust and small planetesimals.

Several investigations on these "regolithic" meteorites are being carried out at DTM, directed toward the goal of interpreting their brecciation history, and in particular trying to understand which phenomena should be attributed to early solar system events and which to more prosaic processes occurring on the surface of a modern asteroid.

Last year Scott and Rajan, using metallographic data, showed that the xenolithic brecciated meteorites can be subdivided into two types: those that were first metamorphosed and cooled rapidly through 400 °C prior to brecciation and final compaction, and those that were first brecciated and compacted and then subsequently cooled very slowly through 400 °C. This year Kothari and Rajan have extended this work by study of the fission tracks and silicate minerals produced by the extinct radioisotope ^{244}Pu in adjacent phosphate mineral grains in some of these same meteorites. The work is directed toward understanding the time in solar system history at which these metamorphic cooling, brecciation, and compaction events took place.

One of these meteorites, Bhola, belongs to the group that was metamorphosed and cooled after brecciation. Kothari and Rajan find that ^{244}Pu (82 m.y. half-life) was still present in Bhola after the se-

quence of brecciation, metamorphism, and cooling. Quantitatively it is calculated that all of these events occurred prior to 4.01 billion years ago—relatively early in solar system history. Two other meteorites, Weston and Fayetteville, belong to the group that were brecciated and formed in a regolith subsequent to their early metamorphic history. These meteorites also contain phosphate grains which experienced ^{244}Pu decay over a range of times that average about 4.25 billion years. In this case, however, because of track annealing and retention properties of the minerals, it is unclear whether the age represents the time of metamorphism or resulted from the subsequent history of brecciation, and further work is necessary to make this distinction.

The most common view is that essentially all meteorites are derived from the asteroid belt, either directly or indirectly via Apollo objects. However, as discussed by Wetherill and ReVelle this year, there is some evidence that meteoroids with physical properties similar to some meteorites are arriving on the Earth from beyond Jupiter, and thus at least for these objects, a relation to comets is probable. In addition, there is still a problem of reconciling astronomical spectral data on asteroids with the most common types of meteorites. Therefore, while it is highly plausible to consider asteroids as prime candidates for meteorite sources, it is thought premature to regard these questions as settled at the present time.

Geochemistry and Seismology at DTM

Much remains to be learned about the present state of the Earth and its internal processes. The enormous implications of the plate tectonic concept of a dynamic planet have just begun to be understood. Most of the geochemical and seismological work at DTM is currently directed toward increasing that understanding.

A large fraction of the geodynamic "action" takes place near the descending plates of oceanic lithosphere. The most extensive earthquake and volcanic belts are found there, and these regions probably represent the principal sites where new continental crust is being formed. As Wetherill has observed, the most straightforward way to study the oceanic plates would be to actually sample them by drilling a number of holes into them. In practice, only the upper 300 meters of the oceanic crust have been directly sampled in this way. However, there are rare occurrences where portions of oceanic crust have been elevated and preserved above sea level, and therefore have become amenable to normal geological study. One such area is on Gorgona Island, off the Pacific coast of Colombia. Last year Echeverría described the occurrence on Gorgona of komatiite, a lava with a very high

melting point and a very magnesium rich composition, more characteristic of the Earth's mantle than the crust. The discovery was particularly noteworthy because all other well-established occurrences of komatiite were in rocks 2.6 billion years of age or older, and it was often surmised that such high-temperature lavas could have been produced only at an early time in Earth history when near-surface temperatures were probably higher. The discovery of very young komatiite afforded an opportunity to study in detail the occurrence of a geological phenomenon generally characteristic of an earlier stage in Earth history.

This opportunity has now been pursued and the results described in this year's Report. It might have been supposed that the magnesium-rich composition of komatiite represented the parental oceanic mantle material which partially melted to form oceanic basalts. In a combined experimental and theoretical geochemical study, Echeverría and Hofmann show that this is not the case. The pattern of rare earth element concentrations shows that there is nothing primitive or primary about Gorgona komatiite. It is strongly depleted in the light rare earth elements and was probably formed by the partial melting of depleted oceanic mantle a considerable time after basaltic melts had already been extracted from it. These workers also showed that the geochemical processes that produce komatiites, demonstrably lavas, are closely related to those that generate other relatively young rock of high melting point which occur in Iceland and Spain, for which there has been disagreement about whether or not they were true melts, or rocks brought to the surface as solids. Their demonstrated relationship to komatiites thereby extends further the case for high-temperature melts late in Earth history.

Direct sampling of a geologically observable section of oceanic crust is rarely possible; thus one must make inferences concerning the oceanic crust and mantle from the thick sequences of volcanic rocks found on oceanic islands, in island arcs, and in mountain chains located above subducting slabs, such as the Andes.

The volcanic systems associated with subducted plates are of great geological importance because, among other things, they appear to represent a major and quite possibly the dominant process whereby low-density, highly buoyant continental material is formed. It is this high buoyancy that permits continents to resist subduction and remain on the surface for billions of years, in contrast to oceanic crust which will survive for only about a hundred million years before it is destroyed by subduction. In order to understand how continents are formed, DTM scientists are studying the source of the magma which erupts as lava from the Andean volcanoes above the subduction zone on the west coast of South America.

For several years, James has devoted his attention to the use of the

isotopic composition of oxygen and strontium in the Andean rocks to determine the extent to which they bear a "crustal signature" or appear to be pristine mantle material lacking a previous crustal history. Oxygen which has had a crustal history and consequently has been involved in processes of interaction with the atmosphere and surface water is characteristically enriched in the heavy oxygen isotope ^{18}O. This year, James reports the early results of a more extensive investigation on volcanic rocks from the central Andes. The enrichment in ^{18}O that is observed demonstrates the presence of a crustal component in these lavas, established either by assimilation of crustal material during ascent or by subduction of sediments of continental origin. Further investigation may distinguish between these two alternatives and permit more quantitative assignment of the relative importance of these various possible sources.

An innovative study directed toward gathering the basic data needed to identify the contribution of the subducted slab to volcanic lavas is being developed by Brown, Sacks, and Tera and their collaborators Klein and Middleton at the University of Pennsylvania. This work involves the use of radioactive isotope ^{10}Be as a tracer to identify subducted material in volcanic rocks. ^{10}Be, produced in the atmosphere by cosmic rays, settles in oceanic sediments, which form the uppermost portion of the subducted plate. Techniques have been developed to use the University of Pennsylvania tandem Van de Graaff accelerator as an extremely sensitive mass spectrometer capable of measuring ^{10}Be even if its isotopic abundance is as small as 10^{-13}. If the subducted oceanic crust contributes a major portion of the trace elements to the volcanic rocks on a time scale comparable to or shorter than the 1.5-million-year half-life of ^{10}Be, then this isotope should be detected in the erupted lavas. ^{10}Be has already been identified in natural materials, including oceanic sediments, by this group. Extraction of beryllium from volcanic rocks is now under way.

Mineral Resource Problems and the Geophysical Laboratory

> . . . . Practically every endeavor at the Geophysical Laboratory can be perceived as contributing to an understanding of the principles whereby elements are accumulated in ore deposits.
>
> Hatten S. Yoder, Jr.

In a prescient article written in 1974, Elburt Osborn observed that the state of our mineral supply is precarious. The United States consumes over four billion tons of new mineral material annually, twice

the consumption of two decades ago. Our dependence on foreign sources is increasing—we import nearly 90 percent of our aluminum ores and 70 percent of our nickel requirements, nearly all our manganese, cobalt, and chromium. A widening gap between need and supply would have a severe effect on our future way of life.

There are no instant solutions to such matters. But from basic research in the earth sciences, such as the work in progress at the Geophysical Laboratory, will come a better understanding of the Earth—its complex history, composition, and dynamics. And from such knowledge may come better ways of finding and recovering minerals, and new ideas for discovering metal substitutes and new metals.

Fluid flow during metamorphism. Fluids flow through rocks during regional metamorphism: Shales lose water and become schists; basalts gain water to become amphibolites; and siliceous limestones and dolomites are decarbonated to form calc-silicate minerals. Fluid flow during regional metamorphism has an effect on mineral isograds, the most commonly mapped metamorphic structural element. Several effects on isograds are possible: (1) Fluid flow may change the composition of the intergranular fluid phase, thereby altering the breakdown temperature of dehydration or decarbonation reactions. The result of this process would be to shift the location of mineral isograds relative to the position of isothermal surfaces. (2) Fluid flow can also change the location of isothermal surfaces from the position they would otherwise occupy as a consequence of conductive heat transfer. (3) The absence of fluid flow, as in impermeable rocks, results in local buffering of fluid composition by mineral assemblages. Such local control of fluid composition may lead to a variety of seemingly incompatible mineral assemblages not provided for in conventional isograd or facies classification schemes.

Rumble of the Geophysical Laboratory has determined the nature and extent of fluid flow during metamorphism by comparing the isotopic composition of vein fluids to the composition of fluids in equilibrium with adjacent country rocks. The infiltration of hydrothermal solutions from the vein into the country rocks results in large changes in oxygen isotope composition, for example. These changes cannot be due just to the release of oxygen as CO_2 or H_2O from the rocks themselves, because that oxygen represents only a small fraction of the total oxygen in the rocks. Rumble believes that large changes in isotopic composition are clear evidence that hydrothermal solutions have invaded the rocks. Analyses of some fossiliferous calc-silicate rocks depleted in the ^{18}O isotope suggest to Rumble that volumes of fluid from four to six times greater than that of the rocks flowed through during metamorphism. The relative permeability of the rocks

through which the fluids flowed was ascertained by the degree of equilibrium attained between layers. If fluid components failed to attain isotopic equilibrium within a series of layered rocks, it may be inferred that the fluid components were not free to move and equilibrate during metamorphism. With this technique it should be possible to map the major pathways of fluid flow and eventually correlate the pathways with element transport and deposition.

Ore mineralization and organic matter. There are numerous examples of the close relationship between ore mineralization and organic matter. These include the gold of the Witwatersrand deposits of South Africa and the Carlin District of Nevada, the mercury deposits of California and Yugoslavia containing organic "minerals," the uranium and thorium of the Blind River and Witwatersrand associated with organic matter in ores such as thucolite, and the lead-zinc deposits of the Mississippi Valley Type occurring with bituminous material. The processes that led to these associations are not evident, and it is reasonable to ask if the organic matter has played a role in the concentration of metallic ions, their transport, and subsequent precipitation into an ore body.

Gize and Hoering have characterized the organic matter in a Mississippi Valley Type, lead-zinc deposit at the Shullsberg mine in southwestern Wisconsin. Deposits of this type (found worldwide, but named after their classic locality) are major sources of these metals, but the details of their genesis remain enigmatic. Mississippi Valley Type deposits usually occur in dolomitized carbonates, and appear to have formed at temperatures less than 200°C. The ore minerals are typically galena (PbS), sphalerite (ZnS), fluorite (CaF_2), barite ($BaSO_4$), and minor sulfides such as millerite (NiS) and siegenite $(Ni,Co)_3S_4$; of special interest is the ubiquitous organic matter.

Gize and Hoering analyzed the saturated hydrocarbons and fatty acids in the host rocks by gas chromatography–mass spectrometry, and showed that most of the organic material is indigenous, having been derived from marine microorganisms. The hydrocarbons are sensitive indicators of the thermal history of the rocks, and the relative proportions of biogenically derived molecules and those molecules produced by thermal cracking suggest that the average temperature of the host rock, 60°–70°C, has prevailed since the Ordovician. This result is supported by the yellow color of the kerogen, indicating an exceptionally low temperature. It is evident that the formation of the Wisconsin District did not involve hidden igneous bodies, a view advanced by some other investigators.

Petroleums and bitumens contain significant concentrations of porphyrins derived from chlorophyll. Early in diagenesis the magnesium

in chlorophyll is replaced by nickel, vanadium, or other metals. In the Wisconsin District, Gize and Hoering found that the ratio of nickel to vanadyl in a neutral porphyrin increased eightfold in the host rock as the ore body was approached, and that the concentration of nickel porphyrin alone increased fifteenfold. These results indicate that some of the metals may have been introduced in the ore-forming solutions as organo-metallic complexes. The low solubilities of lead, either as the chloride or bisulfide complex ions (which would produce lead concentrations too low to form the Wisconsin deposits) also support the possibility that this metal has been partly introduced as an organo-metallic complex.

The effects of temperature and pressure on crystal structures. The extreme conditions of the interior of the Earth result in unique atomic arrangements and interatomic forces affecting all physical and thermochemical properties of minerals. An understanding of the effects of temperature and pressure on crystal structures is, therefore, essential in studies of the solid Earth. Knowledge of how matter is altered by heating and compression is also of central concern to solid-state industries, such as metals manufacturing, chemical synthesis, and electronics development, where crystalline components must function under nonambient conditions.

Advances at the Geophysical Laboratory and elsewhere during the past decade have led to the routine determination of crystal structures at either elevated temperature or elevated pressure. The study of crystal structures at *combined P* and *T*, however, has proved far more difficult. Nevertheless Hazen and Finger of the Geophysical Laboratory have designed and successfully operated a miniature resistance heater placed around the diamonds of a high-pressure, diamond-anvil cell. Hazen and Finger used this "*PT* cell" to perform the first single-crystal x-ray study of any material at both high temperature and high pressure.

After the first experiments on the simple cubic mineral fluorite (CaF_2), which is used as an internal pressure standard in the *PT* cell, Hazen and Finger determined crystal structures on the more complex pyroxene diopside ($CaMgSi_2O_6$), which is a major calcium-bearing phase in the Earth's crust and mantle. The structure of diopside, as of most solids, varies continuously with changes in temperature and pressure. At combined high temperature and high pressure, however, these changes may cancel each other out. Thus, diopside at 375 °C and 14 kbar was found to have the same molar volume, and very nearly the same structural details, as diopside under room conditions.

Data on diopside and other mineral structures at high *P* and *T* may

be used to plot crystal structure variations along the geotherm—the pressure-temperature profile of the Earth with increasing depth. It is surprising that diopside (and most other rock-forming minerals) becomes *less* dense with increasing depth for at least the first few hundred kilometers of the Earth, because thermal expansion is greater than compression in this region. Observed density increases with depth are thus due to either phase transitions to denser phases or compositional changes to heavier elements, rather than to simple compression of a fixed assemblage of minerals.

Planetary gases at high pressure. The advent of experiments at ultrahigh pressures in the megabar range has provided numerous opportunities for research in totally unexplored areas. One fruitful area is in the confinement of gases and determination of their properties under extreme pressure where they transform to crystallize solids (and, at some point as yet unattained, to metals). This work has potential applications not only in the fields of solid-state physics and electronics, but also in the fundamental study of the solar system.

In 1976, R. Smoluchowski of Princeton University concluded that the chemical composition and internal structure of planets could be uniquely determined when they are large and have low density (from "Origin and Structure of Jupiter and Its Satellites," in *Jupiter*, T. Gehrels, ed., University of Arizona Press, Tucson, pp. 3–21, 1976). The reasons for such optimism stemmed from chemical models of the major planets Jupiter and Saturn as well as Uranus and Neptune. These planets are composed mostly of the very lightest elements in the solar system, captured by huge gravitational fields. The proportional abundances of the elemental and molecular gases that form most of these planets and their thermodynamic properties are relatively well known or, presumably, can be obtained by experiment. Needed are better observations of the surface boundary conditions of the major planets and their gravitational fields, and experimental data on the properties of light-element gases at high pressures and temperatures. With these data, reasonably accurate models of the major planets can be formulated.

The first of these required parameters, surface conditions and gravity, are being obtained now by the Pioneer and Voyager space probes to a degree of accuracy far greater than Smoluchowski—and anyone else four years ago—would have imagined. At the same time, high-pressure experimental advances are now being employed at the Geophysical Laboratory and elsewhere to test properties of the abundant light-element gases, such as H_2, He, NH_3, and CH_4, under extreme conditions that duplicate their formation in the solid state. The first

experiments with hydrogen ranged to 700 kbar, a pressure a factor of almost 10^2 higher than had been previously attained with hydrogen. Recent experiments with He, NH_3, and CH_4 by Hazen, Mao, Finger, and Bell at the Geophysical Laboratory have revealed that each of these gases crystallizes in the cubic form and that all are the most compressible solids ever observed. These data are being used with the space-probe results to construct the first chemical/physical models of the other planets.

Instrumentation. Earlier I wrote of the critical role of new instrumentation in the earth sciences, citing as one example the Sacks-Evertson strainmeter. No less important have been the continuous improvements in the diamond-window, high-pressure apparatus. Study of crystal structures at the temperatures and pressures of formation is critical to understanding the relationships between structure, thermochemical properties, and stability of minerals. Such experiments can be used to study the differential expansion and compression of bonds with changing temperature and pressure, and hence the nature of interatomic forces. Hazen and Finger describe the design of a simple and inexpensive, heated diamond-anvil cell, which is easily adapted to x-ray diffractometry and photography. Maximum conditions of 450 °C and 40 kbar have been sustained; thus, conditions within much of the Earth's crust may now be duplicated in single-crystal, x-ray experiments.

Mao and Bell have modified a diamond-window, high-pressure apparatus for studies of single crystals of solidified gases. Samples are loaded into the cell as fluids at cryogenic temperatures. This new device has been used successfully in obtaining single-crystal, x-ray diffraction data. For example, high-quality, single-crystal data were obtained on solidified argon and other gases *in situ* at high pressure after short exposure times. They have also made an improved design of the diamond-window, high-pressure cell that contains apertures for 20 nonredundant scattering directions. In studies of Brillouin scattering it is desirable to measure simultaneously several orientations of longitudinal and transverse acoustic wave velocity in order to define the elastic moduli for a single crystal under pressure. In some instances it is possible to measure the acoustic velocity in certain directions and utilize other apertures in combination to obtain the refractive index of the pressurized crystal. The multiple apertures of this cell result in measurements of the Raman spectra of a pressurized sample free of fluorescent interference originating in the diamonds. Furthermore, the dependence of the Raman spectra of a pressurized sample on scattering direction can be determined.

Underexploited Resources

The use of underexploited resources is one of Alexander Hollaender's favorite themes, which he treated so admirably in editing two recent books, *The Biosaline Concept* and *Genetic Engineering of Osmoregulation* (the latter with D. W. Rains and R. C. Valentine). It is also one of the driving forces in the Department of Plant Biology: to understand and, through understanding, to overcome the barriers to productivity in plants grown under environmental stress. Increasingly we see convergence of the Department's principal research tracks: photosynthesis and photomorphogenesis, physiological ecology, and molecular biology.

It is particularly gratifying to record the advances in plant molecular biology by Thompson and his colleagues, who have exploited cloning techniques to do several things: to obtain information at a high level of resolution on genome organization, to follow transcriptional changes during development, and to study evolutionary relationships and organization of organelle genomes from a number of species. Equal emphasis is being given to studies of the organization of plant genomes and the regulation of their expression.

The successful cloning of plant DNA was reported last year by Cuellar, Selker, Jorgensen, and Thompson. The group described considerable progress in developing and characterizing cDNA clones and in using them to follow developmental changes in the RNA sequences of greening pea seedlings. They have also developed techniques to permit accurate measurements of the concentrations of large numbers of different RNA sequences. Thus, the hope of following in detail transcriptional changes during development is now much closer to reality.

Palmer and Thompson have made significant progress in their studies of chloroplast and mitochondrial DNA in plants. In addition to determining the relative amounts of chloroplast (5–15%) and mitochondrial (1–2%) DNA in the total genome, they have shown homology of 60% or greater between chloroplast DNAs from plants as distantly related as corn and spinach, with the homologies between the mitochondrial DNAs being much lower (as low as 27%). The mitochondrial genomes show unexpectedly large kinetic complexity. To account for this complexity, Palmer and Thompson hypothesize that the mitochondrial genome may consist of a number of different circular molecules of different sizes, sharing little sequence homology. Finally, they have constructed complete clone banks of the chloroplast genomes from mung bean, pea, and spinach. These banks should provide powerful tools for the study of a wide range of problems in the molecular biology of chloroplasts.

Murray, Peters, and Thompson have continued their investigations into the organization of pea and mung bean genomes. They have found, surprisingly, that if the criteria for reassociation of single-stranded DNA are somewhat relaxed, virtually all pea DNA can form duplexes, including almost all of that normally classified as single copy. Both reassociation and melting (thermal dissociation) techniques clearly indicate that the DNA actually expressed in messenger RNA is indeed single copy. However, a much larger class of pea DNA, which behaves as though it were single copy under normal reassociation conditions, in fact consists of distantly diverged repeated sequences. Murray and his colleagues have applied to it the term "fossil repeats." Mung bean, in contrast to pea, contains much less DNA in this fraction. Most of the mung bean DNA that appears as single copy under normal reassociation criteria behaves as single copy under the relaxed criteria as well.

Like the departments in the earth sciences, the Department of Plant Biology has a fine tradition in developing new instruments. This year, Melis and Hart designed and built a spectrophotometer, which has the capability of measuring very small absorbance changes in the ultraviolet (a difficult measurement because of the extremely high background absorption of any biological materials below 400 nm). It was only because of this instrument that Melis and Brown could for the first time obtain quantitative information on the relative numbers of reaction centers in each of the two photosystems of photosynthesis. Contrary to expectation, the ratio of the two was not unity, and when chloroplast membranes were appropriately fractionated, it was possible to obtain fractions differentially enriched for one of the two systems; this result clearly indicates some spatial differentiation within the chloroplast and is consistent with other studies. Finally, the ratio does not remain constant for a given plant but changes during development. These studies have uncovered an unexpected and important aspect of chloroplast organization, which should have a substantial effect on the course of a number of research efforts at the Department and elsewhere.

The year has been a highly productive one for the rest of the photosynthesis group as well, with Fork's versatile use of fluorescence to approach questions of photosynthetic unit size, water stress, and mechanisms of resistance to dessication.

Malkin and Fork used the fluorescence technique they developed two years ago to determine the sizes of photosynthetic units—expressed as total number of chlorophyll molecules per photosystem II reaction center—for a number of different sun and shade plants. All the sun plants yielded values between 220 and 540, and all the shade plants yielded values from 630 to 940. Fork and Govindjee also measured the time of appearance of a transient peak in chlorophyll *a* fluorescence in

most of the same plants, and found a general inverse correlation between time of appearance of the peak and photosynthetic unit size. The technique should be adaptable to nondestructive field estimates of photosynthetic unit size if this inverse relationship holds up in other plants.

In studies complementary to those of the physiological ecology group, Fork and his associates have used fluorescence to study the effects of water stress both in the desert shrub *Nerium oleander* and in an intertidal alga *Porphyra perforata.* In the oleander studies, they again concentrated on a fluorescence transient, studying the effect of water potential on the ratio of maximum to minimum fluorescence in the transient. They found an excellent correlation between decrease in water potential and decrease in this ratio. Again, the method should be readily adaptable to field measurements, providing a rapid, simple, and nondestructive indicator for water stress effects.

Öquist and Fork used fluorescence at low temperature to study the effects of dessication on the photosynthetic apparatus of *Porphyra.* Like any intertidal alga, this species is exposed to air drying during low tide, and must somehow avoid photodynamic damage when this drying occurs during periods of high light intensity. The studies showed that dessication led to a loss of photosystem II emission with a concomitant increase in photosystem I fluorescence, changes rapidly reversed on rehydration. Öquist and Fork hypothesize that photosystem I may be far better suited to dissipating excitation energy as heat than photosystem II, and that the change in energy distribution between the two photosystems may provide a possible mechanism to avoid photodynamic damage.

In the area of photomorphogenesis, Briggs and his colleagues have continued to focus on photosensitive molecules, both phytochrome, sensitive to radiation at the red end of the spectrum, and blue light photoreceptors. As in the past, studies have been both physiological, with intact seedlings, and biochemical, on isolated and purified subcellular fractions. Mandoli has now obtained detailed characterization of the responses of dark-grown oat seedlings to light. Surprisingly, these seedlings are extraordinarily sensitive. Their growth pattern is significantly changed when they receive an amount of light equivalent to one second of full moonlight. In order to do the experiments at all, Mandoli had to develop techniques for handling the plants in complete darkness, since even dim green "safelights" would transform enough phytochrome in a few minutes to yield a substantial response. Both coleoptiles and mesocotyls showed not one but two distinct responses, one of them almost four orders of magnitude more sensitive than the other. For the less sensitive response, irradiation of the node between coleoptile and mesocotyl was most effective in obtaining responses

from either organ, although growth of tissues at some distance from the node is what was affected.

In other plant research of outstanding merit, Leong has successfully isolated and characterized a blue-light-sensitive cytochrome-flavin complex from corn and has separated the photoactivity into what is probably a plasma membrane fraction. Following work initiated by Goldsmith and Caubergs (reported in last year's *Year Book*), he succeeded in separating completely the membrane fraction containing the light-sensitive complex, which contains both a cytochrome and a flavin, from other cytochrome-containing fractions. He showed that the photoactivity co-purified with activity of a putative marker for the plasma membrane. With Caubergs, he also succeeded in solubilizing the photoactivity from the purified membrane fraction, using a mild detergent. Because photoactivity was virtually unchanged by solubilization, it seems likely that both flavin and cytochrome are on the same protein. Room temperature spectra for this cytochrome clearly distinguished it from the other well-known extramitochondrial cytochrome, cytochrome b_5 of the endoplasmic reticulum. This distinction was seen even more dramatically in low-temperature spectra taken by Leong in collaboration with Richard Vierstra of Michigan State University.

In Winslow Briggs' words, the plants of Death Valley and the Arizona desert continue to provide "fertile ground" for the physiological ecologists' studies of acclimation to stress. I have already discussed the observations of Björkman and co-workers on the long-term effects of higher carbon dioxide partial pressures on photosynthesis. Seemann, Berry, and Downton have followed acclimation of photosynthesis through a Death Valley growing season for a group of annual species, and they found that all these species increase their tolerance to high temperature as the cool weather accompanying the winter rains is replaced by intense summer heat. Desert perennials showed the same flexibility as those winter annuals investigated. By contrast, a group of summer annuals growing in the Arizona desert where the rains come in summer, not in winter, showed a significantly lower capacity to acclimate. Though all the summer annuals were tolerant of high temperatures, they had a more limited capacity for adjustment than the other groups of species investigated. The range of high-temperature acclimation observed over a growing season for plants in the field was matched very well by plants grown in laboratory cabinets, where temperature alone was varied. Thus the range of adjustment found in the field is probably a response to changes in temperature during the season. This physiological change in the capacity to tolerate high temperatures may enable the plants to extend their growing season into the hotter parts of the year.

Roberts and Berry have continued monitoring membrane changes

occurring in mature leaves of *Nerium oleander* when it is shifted from a cool to a hot regime. There are several dramatic changes in the lipid species found in the chloroplast membranes, some of them clearly apparent after a single day at the high-temperature regime. There is a general decline in unsaturated and an increase in saturated fatty acids, as might be expected from work on other systems. Surprisingly, the abundances of specific fatty acids change in opposite directions in the galactolipids and the phospholipids. The control mechanisms for these changes are completely unknown and clearly merit further study. Both of these studies underscore dramatic increase in our understanding of thermal acclimation, much of it having its origins in this Department.

On Becoming An Exact Science

> That the fundamental aspects of heredity should have turned out to be so extraordinarily simple, supports us in the hope that nature may, after all, be entirely approachable. Her much-advertised inscrutability has once more been found to be an illusion due to our ignorance. This is encouraging, for if the world in which we live were as complicated as some of our friends would have us believe we might well despair that biology could ever become an exact science.
>
> Thomas Hunt Morgan

In writing earlier (p. *5*) of the role of the Department of Embryology in the emergence of developmental biology as an exact science, I cited recent discoveries in the field of gene regulation by Donald Brown and his colleagues and by Allan Spradling. However, the isolation and characterization of genes, and studies of their control, are but one aspect of the Department's significant contributions in the reshaping of developmental biology over the past 25 years.

In the early years after the founding of the Department in 1914, there were three parallel streams of inquiry in embryology. Carnegie scientists—Franklin P. Mall, then George Streeter, and later Carl Hartman—led the "anatomy-physiology" stream. The "mechanics of development" stream, emphasizing cell and tissue interactions, was led by Hans Spemann and Ross Harrison and included Carnegie's Warren and Margaret Lewis. Almost completely separate was the "biochemical embryology" stream, for which Joseph Needham became the principal spokesman. There were few points of contact between the three streams.

During the same period the field of genetics was exploding. How remarkable it is that these two fields, embryology and genetics, which are today almost one, so long continued on their separate ways. Pio-

neers like Goldschmidt, Wright, Brachet, Caspersson, and Schultz attempted a synthesis. But even Morgan's career was "compartmentalized": embryology— genetics—embryology. As late as the late 1940's, a student might study embryology with only casual reference to genetics. Slowly, however, the remarkable achievements first of Ephrussi and Beadle, and then of Beadle and Tatum, in elucidating the one gene–one enzyme hypothesis, became a part of the literature of both embryology and genetics. Students of development began to perceive that it should be possible ultimately to understand the factors regulating the synthesis of specific products and their assembly during the shaping of a new organism.

The Department of Embryology was for five decades the world's leading center for the study of the human embryo. It pioneered in the development of primates for research, having one of the earliest and most successful monkey breeding colonies. In studies using these animals, large strides were made toward understanding menstruation and cyclic changes in the ovaries and uterus, laying much of the groundwork for today's advances in population control. Earlier studies, culminating in Ramsey's classic works, set the standard for work on the primate placenta, and Burns' studies of sex transformation similarly provided a standard in the field of sex differentiation.

But by the mid-1950's the field and the Department were ripe for change. Just as we had agreed that the mechanisms of gene action were a "prime target," we firmly believed that a second clear objective was to find ways of studying the manner in which cells impinge upon and influence each other. Cell and tissue interactions are the hallmark of development. How are the inner controls of one cell regulated by contact with another? To understand these problems, it would first be necessary to perfect techniques for analyzing cell differentiation in clonal cultures thereby to make it possible to study the genetics of somatic cells. Ultimately attention would have to be paid to the genesis, structure, and functioning of cell membranes themselves.

Several of the Department's contributions over the years have had a profound impact on our understanding of cellular differentiation, and work currently in progress offers similar promise. Here I shall refer only briefly to past events however significant, preferring to concentrate on recent findings.

Of the Department's achievements in the 1960's, one stands out—Konigsberg's clonal analysis of myogenesis. His was the first clonal study of any differentiating cell. Puck first developed the "feeder layer" technique, enabling the cloning of established cell lines, but Konigsberg modified the technique and applied it significantly. It deserves mention, too, that two other members of the Department, Coon and Kaighn, have followed Konigsberg's initial success with un-

commonly important clonal analyses of chondrocytes and liver, and that a former Carnegie Fellow, Tokindo Okada (now at Kyoto University), has used his experience in the Department to great advantage in his studies, with Eguchi, of "transdifferentiation" of pigmented retinal cells to lens cells.

Several years ago Fambrough and his colleagues developed methods for measuring the metabolism of a membrane protein, the acetylcholine (ACh) receptor of muscle cells. They studied the rates of synthesis and degradation, and the route by which these molecules moved from their sites of synthesis to their final destinations in the cell surface. These studies were the first detailed biochemical analyses of a membrane component of muscle with a known function. Essential to this research was the availability of a specific assay system that could detect only the ACh receptor and nothing else.

Fambrough recognized that the new and powerful method of monoclonal antibody production could provide specific probes enabling him to extend his observations to other membrane proteins. This year, he and his associates have characterized several of the monoclonal antibodies that they have made against cell surface components. The antibodies have diverse, and in some cases surprising, characteristics. One reacts with and kills fibroblasts without affecting muscle cells, solving in an original way the age-old problem of ridding pure muscle cultures of fibroblasts.

Another key objective in the Department is to amass fundamental knowledge of the synthesis, degradation, and functional role of phospholipids in cell membranes. As Pagano and his colleagues have recognized, this will require new techniques of introducing tagged molecules into membranes, localizing them, and following their fate with time. Molecules inserted into cell membranes can be traced by fluorescence energy transfer and the use of haptenated lipids detectable with antibodies. They apply these methods to problems in membrane "capping," in the separate metabolism of the inner and outer leaflets of the membrane, and in the flow of lipids relative to fixed structures in the lipid bilayer.

Ward and his colleagues study spermiogenesis and fertilization in the simple nematode *Caenorhabditis elegans*. To probe the details of fertilization, they use a wide variety of biochemical, genetic, and morphological methods. The sperm moves by extending a pseudopod from one side, an action correlated with fertility. Last year, Ward and associates increased their interest in this morphological change in motile sperm. They have learned how to maintain and monitor sperm movement in vitro, and they now describe morphological and some biochemical features characterizing this asymmetric flow of membranes.

Muller and colleagues use the leech nervous system because of its

great simplicity and experimental accessibility. Its essential components—neurons, glial cells, synapses, and the like—are similar in important ways to their counterparts in the vertebrate nervous system. Yet Muller has been able to map the connections of single neurons in a kind of detail impossible for more complex nervous systems. Elliott and Muller have begun a study of the role of glial cells in influencing regeneration of the axons they surround. Although glial cells can survive for months in their experimental preparations, these cells do not seem able to regenerate like neurons.

LOSSES

Two trustees of the Institution, Michael Ference, Jr., and John T. Connor, resigned in January. Dr. Ference was elected to the Board in May 1968. A Ph.D. in physics (University of Chicago, 1936), he became associated with the Ford Motor Company in 1953, serving first as Chief Scientist and eventually becoming Vice President for Research. John T. Connor, a trustee since May 1975, was a former Secretary of Commerce (1965–1967) and, during his five-year tenure at Carnegie, was Chief Executive Officer and Chairman of the Board of Allied Chemical Corporation.

Richard Roberts, who worked in the nuclear physics group at the Department of Terrestrial Magnetism for 38 years, died on April 4, 1980. While at DTM, he worked in the development of the proximity fuze during World War II, in the pioneering work of the DTM biophysics group, and in projects dealing with the detection of hidden nuclear explosions. Described in 1937 as "an indefatigable worker," Roberts visited DTM on the day he died, discussing with some of the astronomers there his recent calculations analyzing the density of the universe at the time of the Big Bang.

On November 24, as this essay was nearing completion, we received the unexpected news of Henrietta Swope's death. Even after her 16-year career at the Institution, Miss Swope remained a devoted friend of the Mount Wilson and later Hale Observatories. Because of her generosity, the Institution was able to design and build a 40-inch telescope at the Las Campanas Observatory. Miss Swope, herself a dedicated researcher, is perhaps best known for her distance calculations to faint stars and galaxies—celestial "yardsticks" that, in the words of Barnard College where she only recently received a Medal of Distinction, "serve as a standard of excellence against which all others can be judged."

With the administrative separation of the Hale Observatories, Carnegie loses the Observatories' director, Maarten Schmidt. Schmidt

began his association with Carnegie soon after taking his Ph.D. in astronomy at the University of Leiden, The Netherlands, in 1956. A professor of astronomy at the California Institute of Technology since 1964, Schmidt was appointed director of the Hale Observatories in 1977. Schmidt's many contributions to astronomy, especially his work in identifying the spectral characteristics of quasars, have won him wide acclaim as a leader in his field.

Harry E. D. Pollock, former director of the Carnegie Department of Archaeology (earlier the Division of Historical Research) from 1951 to 1958, and a Research Associate since 1958, formally severed ties with the Institution in May 1980. Dr. Pollock had been associated with the Department of Archaeology since 1931. His researches in the archaeology of Yucatan and other Middle American regions had been concerned primarily with architecture in its relation to the development of the Maya Indian culture.

Sheila McGough, editor at the Institution since 1968 and publications officer since 1971, departed in September 1979 for full-time study at the Law School of George Mason University.

Bessie Smith retired from the Department of Embryology in December 1979 after 15 years as a laboratory helper, 12 of them in Ebert's laboratory, where she was appreciated not only for her devotion and technical skill, but also for her generosity and warmth toward scholars from distant lands.

Herman Carpentier, who started working at Mount Wilson in 1968 as a carpenter and eventually became Superintendent of Buildings and Grounds responsible for facilities at the Santa Barbara Street office and on Mount Wilson, retired in June 1980.

Samuel Callaway, former Secretary to three Carnegie presidents, died on December 13, 1979, in Venice, Florida. Callaway, who was a recipient of a Presidential Certificate of Merit for assisting Vannevar Bush during World War II, served the Institution for 40 years.

Floyd E. Day, former optician with the Hale Observatories, died on April 8, 1980. Day made optical components for hundreds of astronomical instruments during his 33-year career at the Observatories.

. . . AND GAINS

Six distinguished individuals in fields ranging from science to law were elected to the Board of Trustees this year. The Honorable William T. Coleman, Jr., a senior partner in the law firm of O'Melveny and Myers in Washington, D.C. and a former Secretary of the U.S. Department of Transportation, was elected to the Board in January. The five trustees elected to the Board at the May Annual Meeting were: Gerald

M. Edelman, a professor of immunology and protein chemistry at Rockefeller University and a Nobel laureate (1969); Edward E. David, Jr., President of the Exxon Research and Engineering Company and a former Science Advisor to the President and Director of the Office of Science and Technology (1970–1972); Robert G. Goelet, President and Director of the Goelet Realty Company and President of the American Museum of Natural History and the New York Historical Society; Richard E. Heckert, Director, Senior Vice President, and member of the Executive Committee of the du Pont Company; and Antonia Johnson Mörner, an executive officer with A. Johnson and Company, one of Sweden's premier privately owned companies.

Robert N. Kreidler joins the Carnegie Institution as vice president, effective November 1, 1980. Having worked with the Alfred P. Sloan Foundation, first as Director of Educational Affairs (1962–1965), then as Vice President (1965–1968), and finally as Executive Vice President (since 1968), Kreidler brings 20 years of foundation experience to his initial roles at Carnegie in the general areas of financial development and planning.

Gerald Rubin has been appointed Staff Member of the Department of Embryology beginning August 1980. Rubin worked at the Sidney Farber Cancer Institute of Harvard Medical School after doing postgraduate work at Stanford University, graduate work at Cambridge University, and undergraduate work at the Massachusetts Institute of Technology. At Carnegie, he will be investigating transposable genetic elements in *Drosophila.*

Alan Dressler has accepted an appointment to the Mount Wilson and Las Campanas Observatories' staff, effective September 1, 1981. Dressler, who has held a Carnegie–Las Campanas Fellowship since 1978, received his Ph.D. from the University of California at Santa Cruz in 1976. From then until 1978 he worked at the Observatories as a Carnegie Fellow. For the last several years his research has been exclusively extragalactic, with a heavy emphasis on clusters of galaxies. He has been collaborating with Allan Sandage obtaining rate curves for about 30 S0 galaxies and with Stephen Shectman studying galaxy morphology and rich clusters.

The following honors were awarded to individuals during the year.

Maarten Schmidt, director of the Hale Observatories, received the 1980 Gold Medal of the Royal Astronomical Society.

Bjørn O. Mysen, Staff Member, Geophysical Laboratory, was awarded the 1979 Reusch Medal of the Norwegian Geological Society on April 16 for studies on CO_2 solubility in silicate melts.

Ho-Kwang Mao of the Geophysical Laboratory received the Annual

Award of the Mineralogical Society of America in San Diego, November 6, 1979, for outstanding research at ultrahigh pressures.

Henrietta Swope, former Research Fellow at the Mount Wilson and Palomar Observatories (1952–1968), was awarded a Barnard Medal of Distinction at the College's 88th Commencement, May 14, 1979, for developing careful and precise methods for the measurement of faint stars.

Samuel R. M. Reynolds, former Staff Member of the Department of Embryology (1941–1955), received the 1979 Distinguished Service Award for Contributions and Service to the American College of Obstetricians and Gynecologists.

Halton Arp of the Hale Observatories was named president-elect of the Astronomical Society of the Pacific.

Winslow Briggs, director of the Department of Plant Biology, has just assumed the presidency of the American Institute of Biological Sciences for 1980–1981. He has been on the Executive Committee of the AIBS since 1978.

James D. Ebert

FACULTY, FELLOWS, AND STUDENTS

1979–1980

DEPARTMENT OF EMBRYOLOGY
Baltimore, Maryland

Director

Donald D. Brown

Staff Members

Douglas M. Fambrough
Nina V. Fedoroff
Kenneth J. Muller
Richard E. Pagano
Allan Spradling
Samuel Ward

Staff Associate

Patricia Gearhart

Research Associates and Fellows

M. John Anderson
Ellen Bayne
Daniel Bogenhagen
Ellen Elliott
Dick Hoekstra
Sheila McCormick
Steven McKnight
Wylie Nichols
Hugh Pelham
Ronald Peterson
Thomas Roberts
Richard Rotundo
Alan Schroit
Sheryl Scott
Mavis Shure
Barbara Sollner-Webb
Douglas Struck
Eric Wakshull
Susan Wessler
Michael Wormington

Visiting Investigators

Charles Emerson
Suzanne Emerson
Hyun Shin

Students

Yair Argon
Dan Burke
John M. Gardner
Elizabeth Gavis
Gregory A. Nelson
Shigeru Sakonju
Heidi Schaeffer

DEPARTMENT OF PLANT BIOLOGY
Stanford, California

Director

Winslow R. Briggs

Director Emeritus

C. Stacy French

Emeritus

William M. Hiesey

Staff Members

Joseph A. Berry
Olle Björkman
Jeanette S. Brown
David C. Fork
Malcolm A. Nobs
William F. Thompson

Research Associate

Michael G. Murray

Senior Fellows

W. J. S. Downton
Govindjee
George E. Hoch
Jacob Levitt
Shmuel Malkin
Gunnar Öquist
Peter H. Quail

Fellows

Paul A. Armond
Geoffrey W. Harvey
Richard A. Jorgensen
Ta-Yan Leong
Anastasios Melis
Stephen B. Powles

Thomas D. Sharkey
Christer Sundqvist
Gijsbert van Ginkel

Students

Michael R. Blatt
Richard E. Cuellar
Holly L. Gorton
Dina F. Mandoli
Jeffrey D. Palmer
Richard S. Preisler
Jeffrey R. Seemann
Celia M. Smith
William E. Williams

GEOPHYSICAL LABORATORY
Washington, D.C.

Director

Hatten S. Yoder, Jr.

Emeritus

Gordon L. Davis
Elburt F. Osborn
Emanuel G. Zies

Staff Members

Peter M. Bell
Francis R. Boyd, Jr.
John R. Brady
Felix Chayes
Marilyn L. F. Estep
Larry W. Finger
John D. Frantz
P. Edgar Hare
Robert M. Hazen
Thomas C. Hoering
T. Neil Irvine
Ikuo Kushiro
Ho-Kwang Mao
Tsutomu Murase
Bjørn O. Mysen
Douglas Rumble III
David Virgo

Research Associates

Robert K. Popp
Bruno A. Simons

Fellows

Timothy M. Benjamin
Nabil Z. Boctor
Donald L. Elthon
Hiroyuki Fukuyama
Andrew P. Gize
Wendy J. Harrison
Richard H. Kingsley
Steven W. Lonker
Joseph F. Mammone
Shirley A. Rawson
Shiv K. Sharma
Eiichi Takahashi

Students

Halina Dabrowski
Roshini Ponnamperuma
Antonio M. G. Possolo
Allan Rubin

DEPARTMENT OF TERRESTRIAL MAGNETISM

Director

George W. Wetherill

Distinguished Service Member

Merle A. Tuve

Emeritus

Scott E. Forbush
Richard B. Roberts[1]

Staff Members

L. Thomas Aldrich
George E. Assousa
Louis Brown
W. Kent Ford, Jr.
Albrecht W. Hofmann
David E. James
Typhoon Lee
Alan T. Linde
R. Sundar Rajan
Vera C. Rubin
I. Selwyn Sacks
Fouad Tera
Norbert Thonnard

[1]Deceased April 4, 1980.

Research Associates
Albert Jambon
Leonidas Ocola
Rambabu P. Ranganayaki
Frederick J. Ryerson

Senior Fellow
Edward R. D. Scott

Fellows
Marie-France Bugnon
David Burstein
Bruce W. Carney
Lina María Echeverría
Mark Feigenson
W. Daniel Heinze
Esther M. Hu
Emi Ito
Brajesh K. Kothari
Richard A. Lux
Kiyoji Shiono
Robert J. Stern
William M. White

Visiting Investigators
Akira Hasegawa
Douglas G. Mose
Volker von Drach

Student
Morgan I. Granger

HALE OBSERVATORIES

Director
Maarten Schmidt

Staff Members
Halton C. Arp
Horace W. Babcock
Judith D. Cohen
Jesse L. Greenstein
James E. Gunn
Robert F. Howard
Jerome Kristian
Robert B. Leighton
Gerry Neugebauer
J. Beverley Oke
S. Eric Persson
George W. Preston
Allan R. Sandage
Wallace L. W. Sargent
Leonard Searle
Stephen A. Shectman
Arthur H. Vaughan
James A. Westphal
Peter Young
Harold Zirin

Staff Associates
Robert J. Brucato
Charles T. Kowal
Jean J. Lorre
Keith Matthews
Thomas G. Phillips
B. Thomas Soifer
John T. Trauger
Michael W. Werner

Senior Fellows
Alan M. Dressler
Thomas R. Geballe
Ronald Moore
Robert J. Zinn

Fellows
Thomas B. Ake III
Peter L. Cottrell
Gary S. DaCosta
Debra Meloy Elmegreen
Howard B. French
Richard F. Green
John G. Hoessel
Frank P. Israel
Robert C. Kennicutt
Barry J. LaBonte
Stefan Mochnacki
Jeremy R. Mould
Anneila I. Sargent
Horace A. Smith

Carnegie-Chilean Fellow
Guido Garay

Student Observers
Graham Berriman
Kirk D. Borne
Alexi Filippenko
Keith Horne
Stephen M. Kent
Matthew Malkan

Daniel Nadeau
Jeffrey R. Pier
Douglas M. Rabin
Abhijit Saha
Donald P. Schneider
William L. Sebok
Richard A. Wade
Howard K.-C. Yee

President and Trustees

PRESIDENT
James D. Ebert

BOARD OF TRUSTEES
William R. Hewlett[1]
Chairman

William C. Greenough
Vice-Chairman

William T. Golden
Secretary

Philip H. Abelson
Robert O. Anderson
Lewis M. Branscomb
William T. Coleman, Jr.[2]
John T. Connor[3]
Edward E. David, Jr.[4]
John Diebold
Gerald M. Edelman[4]
Michael Ference, Jr.[5]
Carl J. Gilbert
Robert G. Goelet[4]
Crawford H. Greenewalt
Caryl P. Haskins
Richard E. Heckert[4]
William McChesney Martin, Jr.
Antonia Johnson Mörner[4]
Franklin D. Murphy
Robert M. Pennoyer
Richard S. Perkins
Robert C. Seamans, Jr.
Frank Stanton[6]
Charles H. Townes
Juan T. Trippe
Trustees

Henry S. Morgan
Garrison Norton
Charles P. Taft
James N. White
Trustees Emeriti

[1]Elected Chairman May 2, 1980.
[2]Elected December 17, 1979.
[3]Resigned January 1, 1980.
[4]Elected May 2, 1980.
[5]Resigned January 1980.
[6]Chairman to May 2, 1980.

OFFICE OF ADMINISTRATION

1530 P Street, N.W., Washington, D.C. 20005

James D. Ebert	*President*
Robert N. Kreidler	*Vice President*[1]
James W. Boise	*Bursar; Executive Secretary to the Finance Committee*
Christopher Wright	*Staff Member (Science Policy and Institutional Development)*
Franklin H. Portugal	*Historian*
Ray Bowers	*Publications Officer; Editor*
Kenneth R. Henard	*Assistant Bursar*
Susan Y. Vasquez	*Assistant to the President*
Joseph M. S. Haraburda	*Assistant to the Bursar*
Richard E. Hewitt	*Administrative Officer for Services*

Marshall Hornblower	*Counsel*

STAFF MEMBER IN SPECIAL SUBJECT AREAS

Roy J. Britten

DISTINGUISHED SERVICE MEMBER IN SPECIAL SUBJECT AREA

Barbara McClintock

RESEARCH ASSOCIATE AT LARGE

Harry E. D. Pollock

[1]Effective November 1, 1980.

Bibliography

PUBLICATIONS OF THE INSTITUTION

Carnegie Institution of Washington Year Book 79, viii + 47 + 846 pages, 394 figures, December 1979.

Carnegie Institution of Washington Newsletter. Issued in December 1979, March and May 1980.

Ceramics for the Archaeologist. Anna O. Shepard. Publication 609. xxvi + 414 pages, 59 figures. Reprint. May 1980.

PUBLICATIONS BY THE PRESIDENT OF THE INSTITUTION*

James D. Ebert

The importance of basic research to the users of the sea: some biological concerns, in *Marine Sciences and Ocean Policy Symposium, June 17–20, 1979*, University of California, Santa Barbara, David S. Simonett, ed., 1979.

Epidemic of life, Editorial essay in *BioScience, 30*, p. 503, August 1980.

*Scientific publications by Staff Members and Fellows of the Institution are listed in the reports of the several departments.

Carnegie Institution of Washington adheres in all phases of its operations, including employment and educational programs, to a policy barring discrimination on the basis of race, religion, color, national or ethnic origin, sex, or physical handicap. In its educational programs it admits qualified students as fellows without regard to race, religion, color, national or ethnic origin, sex, or physical handicap to all the rights, privileges, programs, and activities generally accorded or made available to fellows at the Institution. It does not discriminate on the basis of race, religion, color, national or ethnic origin, sex, or physical handicap in administration of its educational policies, admissions policies, fellowship programs, and other Institution-administered programs.

Reports of Departments and Special Studies

Department of Embryology

Department of Plant Biology

Developmental Biology Research Group

Geophysical Laboratory

Department of Terrestrial Magnetism

Hale Observatories

Department of Embryology

Baltimore, Maryland

Donald D. Brown
Director



Department of Embryology staff, June 1980. *Left to right, bottom row:* M. John Anderson, Jeffrey Mauvais, Sheila McCormick, John Pazdernik, Ellen Elliott, Pat Gearhart, Audrey Sheppard, Douglas Fambrough, Kenneth Muller. *Second row:* Richard Grill, John Gardner, Pat Chase, Leslie Pedersen, Eileen Hogan, Betty Phebus, Ellen Bayne, Ernestine Flemmings, Ben Nathans, Sue Wessler, Pat Schmidt, Sue Satchell, Dan Bogenhagen. *Third row:* John Jones, Eric Wakshull, Tom Roberts, Thomas Miller, Wylie Nichols, Richard Pagano, Rick Rotundo, William Duncan, Nina Fedoroff, Dick Hoekstra, Sam Ward, Donald Brown, Nadine Nivera, Ron Peterson, Allan Spradling, Alice Mabin, Joe Vokroy, Hugh Pelham, Bob Kingsbury, Mike Wormington, Shigeru Sakonju, Dan Burke.

Contents

Introduction 7

Nerve Cell–Synaptic Target Interactions and Nerve Repair 9
Regeneration in the absence of the target neuron 11
Terminal sprouting of an intact axon 12
Behavior of glial cells following injury 13
Removal of single glial cells 15
Function of a "coupling interneuron" 16

Cell Surface and Secretory Glycoproteins of Skeletal Muscle 19
Metabolism of chick embryo muscle acetylcholinesterase 20
Preparation of pure muscle cultures and analysis of secretion products . . . 22
Control of muscle cell surface structure during development 26
Some other interesting monoclonal antibodies 27

Organization, Dynamics, and Metabolism of Cell Surface Lipids 28
Kinetics of phospholipid transfer between vesicles 29
Assay of membrane interactions using fluorescence energy transfer 30
Topology of membrane fusion 32
Lipid capping in lymphocytes 34

Genetic Specification of Cellular Morphology 37
The ionophore monensin triggers spermiogenesis in vitro 37
The development of wild-type and mutant sperm 38
Actin in sperm 41
Membrane mobility in nematode sperm 42

Expression of Antibody Variable and Constant Regions During the Immune Response 46
Diversity in the V regions of anti-PC antibodies 47
Successive switching of heavy chain classes expressed with the cell lines of a B-cell clone 49

Molecular Studies on the Controlling Elements of Maize 51
Anthocyanin pigment pathway 52
Starch biosynthesis 53
A1 locus 53
Bronze locus 55
Shrunken locus 57
Shrunken 2 locus 60
Waxy locus 61
Maize tissue culture 61

Studies on the Thymidine Kinase Gene of Herpes Simplex Virus 62
Microinjected frog oocytes will express the HSV tk gene 62
Construction and analysis of deletion mutants of the HSV tk gene 64
Structural studies of the HSV tk gene 66

Initiation and Termination Signals of *Xenopus* Ribosomal DNA 70
Mapping the transcription initiation and termination signals of *Xenopus laevis* ribosomal DNA 70
The *Xenopus laevis* ribosomal DNA transcription termination signal is correctly read by RNA polymerase III 72

The Structure and Expression of *Drosophila* Chorion Genes 73
Mechanism of chorion gene amplification 74
Effect of mutations on chorion gene amplification and expression 74

The Dual 5S Gene System in *Xenopus* 79
A transcription factor binds to the control region of 5S DNA 80
The 5S DNA transcription factor is the same protein that complexes 5S RNA in oocytes 82
Quantitation of in vitro transcription by "competition" of 5S RNA genes . . . 85
Partial purification of a factor for 5S DNA transcription 88
In vitro transcription with extracts from tissue culture cells 89
Nucleotide sequences required for termination of 5S RNA synthesis 89
Abundance and chromosomal arrangement of three 5S DNA multigene families in *X. laevis* 92

The Collection of Human Embryos 93
Placentology 93
Developmental stages in human embryos 93
Development of the nervous system 93
Visitors 94

Staff Activities 94

Bibliography 95

Personnel 98

INTRODUCTION

"It was 1:10 P.M. on the 15th day of March, nineteen hundred and thirty in the Carnegie Laboratory of Embryology in Baltimore, Maryland, that there was recovered from the Fallopian tube of a cow a two-celled egg."

And so a writer from the Ayrshire Cattle Society's *Journal* (*4*, no. 3, 1932) described for the farmers that made up his readership "a fine adventure in scientific research" by Carl Hartman and his colleagues—an adventure that he likened to reaching the top of the Matterhorn. Hartman and his associates, by isolating early embryos at different stages of development from cows bred at specified times, determined that the bovine egg could be fertilized only during a few hours after shedding. "It puts us right on the threshold of finding out more about the time to serve cows if you want to get calves . . .," concluded the Ayrshire writer. Today, the methods of embryo transfer and artificial insemination with farm animals owe their widespread success in part to Hartman's research.

On this fiftieth anniversary of Hartman's important discovery, research on eggs and sperm remains an active part of this Department's work; it is the major interest of three Staff Members (Ward, Spradling, and Brown). In the tradition of Carl Hartman, our current research is not directed toward practical goals. However, we are aware that an important discovery, like Hartman's, is almost certain to have an impact on practical problems.

Samuel Ward and his colleagues study spermiogenesis and fertilization in the simple nematode, *C. elegans*. To probe the details of fertilization, they use a wide variety of biochemical, genetic, and morphological methods. The sperm moves by extending a pseudopod from one side, a movement correlated with fertility. This year, Ward and associates have become increasingly interested in this morphological change in motile sperm. They have learned how to maintain and monitor sperm movement in vitro, and they now describe morphological and some biochemical features that characterize this asymmetric flow of membranes.

This is the first Report describing work by Allan Spradling, who joined the Department in January 1980. Spradling received his Ph.D. in cell biology from the Massachusetts Institute of Technology in 1975 and then carried out three years of postdoctoral work as a Helen Hay Whitney Fellow in the Zoology Department of Indiana University. He studies the genes encoding a group of eggshell (chorion) proteins in the fruit fly *Drosophila melanogaster*. These genes are under developmental control. The power of using *Drosophila* is that its suitability for traditional genetics can now be coupled with the new methods for gene isolation, characterization, and function. Recently, Spradling showed that genes for chorion proteins are amplified in follicle cells just before they are expressed. This is the first reported example of amplification for protein genes programmed into normal development. Mutants have already been found that affect this amplification.

The simple genes for 5S ribosomal RNA in *Xenopus* have been useful for analyzing gene function. A protein has been isolated from ovarian tissue that interacts specifically with a control region located in the center of the 5S RNA gene. This protein has the remarkable property of binding the gene product, 5S RNA, and forming a stable particle with it. The synthesis of

this protein almost certainly accounts for the activation of 5S RNA genes in early oocytes. This is the first discovery of a control protein that is specific for one eukaryotic gene and at least partly responsible for the differential expression of that gene in development.

Steven McKnight has developed a powerful system for probing the expression of a protein gene. He has cloned the gene for thymidine kinase from Herpes simplex virus and shown that it is expressed when injected into *Xenopus* oocyte nuclei. McKnight has deleted gene segments from both ends and delimited small regions that must contain the initiation and termination sites. He will soon be able to identify regions in and around the gene that affect its expression.

Nina Fedoroff is applying molecular methods to problems of gene control in maize. Previously, genes that caused some visible change, such as those involved in the anthocyanin pigment pathway, were studied. Unfortunately, these genes do not encode a large quantity of gene products, which must be characterized for complete understanding of the gene controls. Fedoroff outlines some of her strategies for overcoming these serious technical problems in this Report.

Several years ago Douglas Fambrough and his colleagues developed methods for measuring the metabolism of a membrane protein, the acetylcholine receptor. They studied the rates of synthesis and degradation as well as the route by which these molecules went from their sites of synthesis to their final destination in the cell surface. These were the first detailed biochemical analyses of a membrane component with a known function. The essential key to these studies was the availability of an absolutely specific assay system that could detect only the ACh receptor and nothing else. Fambrough recognized that the new and powerful method of monoclonal antibody production could provide specific probes enabling him to extend his observations to other membrane proteins. In this Report, Fambrough and his associates characterize several of the monoclonal antibodies that they have made against cell surface components. The antibodies have diverse and in some cases surprising characteristics. One, for example, reacts with and kills fibroblasts without affecting muscle cells, solving in an original way the age-old problem of ridding muscle cultures of fibroblasts.

One of the great biological detective stories has been the genetic basis of the extraordinary diversity of the immune system. Even a homogeneous antigen can elicit the synthesis of several different kinds of antibody molecules. Gearhart has begun an analysis of the diversity of antibodies formed following the administration of a single simple antigen, phosphorylcholine. This can be done by the monoclonal antibody technique, since each secreting hybridoma line produces only one single homogeneous antibody. The result is that one antigen produces an array of antibodies even more varied than originally predicted. Gearhart is investigating the structural relationship of different antibodies with the same antigenic specificity.

Biological advances so often result from new methods that in many cases biological theories seem trivial: theories are only tolerated if they can be tested experimentally. Richard Pagano and his colleagues have recognized that fundamental knowledge of the synthesis, degradation, and functional role of phospholipids in cell membranes requires new techniques—ways of introducing tagged molecules into membranes, localizing them, and following their fate with time. They describe how they can transfer and trace molecules inserted into cell membranes by fluorescence energy transfer and how they use haptenated lipids detectable with antibo-

dies. They apply these methods to investigations of membrane "capping," the separate metabolism of the inner and outer leaflets of the membrane, and the flow of lipids relative to fixed structures in the lipid bilayer.

Muller and his colleagues use the leech nervous system because of its great simplicity and experimental accessibility. Its essential components—neurons, glial cells, synapses, and the like—are similar in important ways to their counterparts in the vertebrate nervous system. Yet Muller has been able to map the connections of single neurons in a kind of detail that is impossible with more complex nervous systems. Ellen Elliott and Muller have begun a study of the role of glial cells in influencing regeneration of the axons they surround. Although glial cells can survive for months in experimental preparations, these cells do not seem able to regenerate like neurons.

Gerald Rubin has been appointed Staff Member beginning in August 1980. Dr. Rubin, currently at the Sidney Farber Cancer Institute of Harvard Medical School, received his undergraduate education at the Massachusetts Institute of Technology and his Ph.D. from Cambridge University. He then did postdoctoral work at Stanford University, where he became convinced that the application of modern genetic methods to *Drosophila* has enormous promise for solving biological problems. Upon his arrival we will have five Staff Members interested primarily in genetics—either asking how genes work or using genetic mutations to solve complex developmental problems. This reflects a tradition strong in the Institution's history, since three of its departments (Embryology, Genetics, Terrestrial Magnetism) have made major contributions to genetics research.

Bessie Smith retired in December 1979, after 15 years as a laboratory helper with the Department. Her good nature and forthright personality encouraged many research fellows and students whom she assisted and befriended.

The research of Brown, Gearhart, Muller, Pagano, Spradling, and Ward has benefitted from grant support by the National Institutes of Health. Fedoroff has been supported by grants from the National Science Foundation and the U.S. Department of Agriculture. Fambrough receives a grant from the Muscular Dystrophy Association. Departmental research has been assisted greatly by grants from the Commonwealth Fund, the Culpeper Foundation, and the Fleischmann Foundation, as well as by a Biomedical Research Support Grant from the National Institutes of Health.

Donald D. Brown

NERVE CELL-SYNAPTIC TARGET INTERACTIONS AND NERVE REPAIR

K. J. Muller, E. J. Elliott, S. A. Scott, and B. E. Thomas

Nerve cells, or neurons, form connections with one another in the nervous system in a manner that provides specific networks of communication between cells. In many cases the connections, or synapses, formed during the development of the organism can regenerate if later disrupted by injury, although the degree of recovery depends upon the extent and location of the lesion in the particular species studied.

In man's central nervous system, for example, neurons are for unknown reasons rarely able to regenerate nerve fibers, or axons, and form synapses

with their normal targets. In many lower vertebrates and invertebrates, however, central neurons can grow new and seemingly appropriate connections. To show that individual nerve cells can grow and functionally reconnect with their normal target neurons, researchers have turned to the simpler nervous systems of certain invertebrates, particularly that of the medicinal leech. We have focused on the leech in our studies of the mechanisms by which growing neurons select their synaptic targets and establish functioning contacts with them.

Several features of the leech nervous system make it favorable for study. It has a small number of neurons—only about 350 in each of 21 segmental ganglia forming a chain along the length of the animal, and half again as many in fused ganglia that form brains at the head and tail. Nearly a third of the neurons have been identified as to function. Leech neuron synapses resemble those in human brains: both consist of chemical synapses, where transmitter molecules released by one cell diffuse a short distance to the next cell to activate receptor molecules in its membrane, and electrical synapses, which carry currents directly from one neuron to the next. As in higher animals, leech neurons and their axons are ensheathed by non-neuronal glial cells; in the leech these are unusually accessible for physiological study with intracellular microelectrodes. This has allowed us to look from a new vantage point at the role of the glial cells in axonal growth and synapse regeneration.

We have previously shown that if a nerve axon in the leech is severed, the cut end of the axon will sprout and grow along its original pathway, thereby regenerating connections with its normal target neuron at the normal site of synapse. By selectively destroying single target neurons with intracellular injection of a protease, we found somewhat surprisingly that the target is not necessary for accurate regeneration to the normal site of synapse. Furthermore, the regenerating axon will not synapse with other targets. This year we used a variety of techniques to confirm the earlier findings and to examine them in detail. Work has also begun on selectively removing from the nervous system another possible guide for the growing axon—its severed distal stump. In addition, we obtained a better understanding of the interaction that we previously demonstrated exists between a neuron and its target, namely the target's ability to inhibit axonal growth.

When axons of neurons in the leech regenerate, they grow within a sheath formed by the glial cell, which itself has been injured by the lesion that prompts regeneration. Because of the intimate relationship between neurons and glia, and because of the suspicions stretching back to the turn of the century that glia may account for the specificity of regenerated connections, we have sought to determine exactly how glial cells respond to injury and how the destruction of ensheathing glial cells (as by intracellular injections of protease) affects regenerating axons. The use of techniques previously applied only to neurons has produced several novel and exciting results. The severed, anucleate pieces of glia can survive independently of their cell bodies for months, as can severed axons in the leech, but glial cells do not seem to repair themselves in the same fashion as neurons.

To study the accuracy and mechanisms of regeneration it is essential to know the normal arrangement of contacts between neurons. We have therefore continued to examine the spatial distribution of synapses between identified sensory neurons, motor neurons, and interneurons and to look at the effect of the distribution of synapses between pairs of cells on synaptic transmission between them. Of particular interest has been the discovery reported last year of a pair

of neurons interposed between two other neurons that by ordinary criteria would be considered to be in direct contact at an electrical synapse. Such a formerly hypothetical and difficult-to-detect "exception" may be more widespread in nervous systems than has been generally acknowledged.

Regeneration in the Absence of the Target Neuron

K. J. Muller, S. A. Scott, and B. E. Thomas

One particular neuron, the S-cell, has provided us with considerable information on the details of synapse regeneration. The single S-cell in each segmental ganglion extends a recognizable axon halfway to the next ganglion anteriorly and posteriorly along the axon bundles (called connectives) that link ganglia. At the halfway point along the connectives the axon makes an electrical synapse with the next S-cell. The axon bundle in which the S-cell travels, called Faivre's nerve, lies between the paired lateral connectives. If the S-cell axon is severed, as happens if the connectives are crushed with forceps, the cell grows a new axon from its cut end until it reconnects with the adjacent S-cell at the normal site of synapse. We have now examined 39 preparations, nearly twice as many as reported last year, in which the target S-cell was destroyed by protease in order to determine the role of the target in regeneration (Fig. 1). We have confirmed that during the second month growth stops at the normal site of synapse, and the regenerating neuron does not grow beyond the end of its severed distal stump. Thus, regeneration proceeds normally. The distal stump of the severed axon degenerates after several months, but the regenerated axon does not either retract or make synapses with other axons. In older preparations the axon

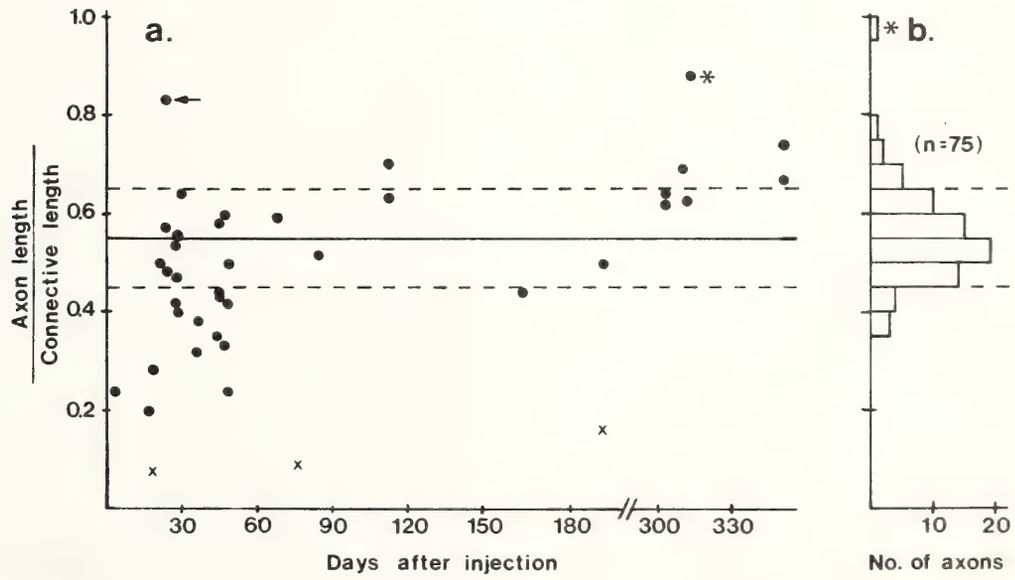


Fig. 1. (a) Growth of severed axons of S-cells after protease injection of their targets was assayed and normalized by dividing the length of the regenerated axon by the distance to the next ganglion (the connective length). Control S-cells, shown in (b), extend each axon about halfway to the next ganglion. The solid line in (a) indicates the mean relative axon length of control S-cells from (b) (mean = 0.55), and the dashed line indicates the standard deviation (S.D. = 0.1). Each dot represents one regenerated axon. When their target was destroyed, most severed axons grew to within one standard deviation of the control mean axon length, and very few grew farther. The dot marked with an arrow had not grown beyond the end of its distal stump, and the dot marked with an asterisk (whose distal stump had degenerated) was from the same leech as the control axon marked with an asterisk, suggesting that neither of these two long axons had grown beyond their old synaptic region. The ×'s represent axons that had not regenerated across the crush.

is typically surrounded by numerous glial wrappings (Fig. 2).

Our present hypothesis is that either the glial cell or the severed distal stump may provide an important guide for the growing axon and a signal to stop its growth. Because the distal stump is less than 10 μm in diameter, it has not been possible to penetrate it reliably and inject it with protease to destroy it. The technique that may provide us with a solution to the problem is to inject the adjacent S-cell with a fluorescent dye, such as Lucifer Yellow (MW ~ 450). The small molecule of dye is able to pass between cells that are electrically coupled; thus it can pass from the injected S-cell into the severed distal stump of an adjacent S-cell to which the injected cell remains electrically coupled. By irradiating the dye with intense light of suitable wavelength, photodynamic effects have been used successfully to destroy the severed distal stump in vitro. It remains to apply the method in vivo, and then to trace the extent of regeneration.

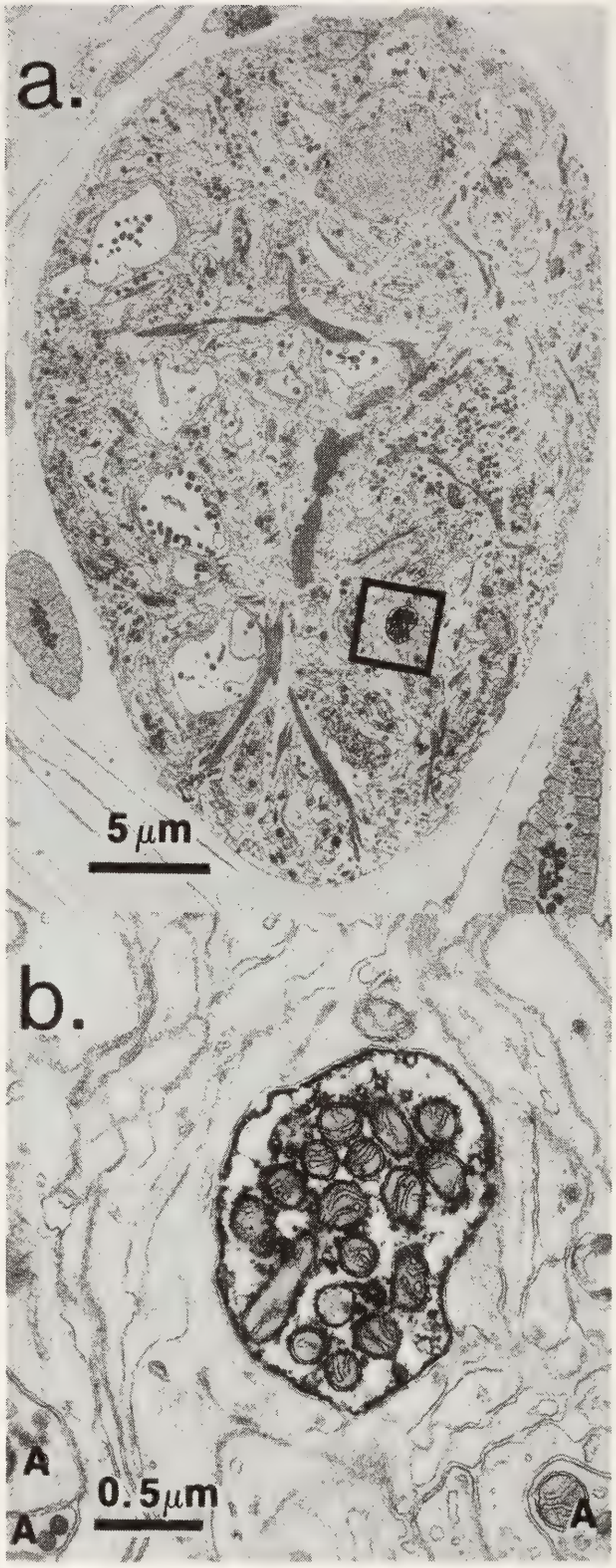


Fig. 2. The tip of the regenerated axon of an S-cell injected with horseradish peroxidase (HRP) as a marker, in a box in (a) and at higher magnification in (b), is surrounded by glial processes 44 weeks after the axon was severed and its target eliminated with protease. Few other axons (A) are near the regenerated axon tip.

Terminal Sprouting of an Intact Axon

K. J. Muller, S. A. Scott, and B. E. Thomas

S-cell axons in the nervous system of the adult leech do not normally grow or retract, even when their synaptic targets have been destroyed with protease (Fig. 3). In developing nervous systems, axons typically grow until they reach their normal targets. If those target cells are missing or have been destroyed, the axon may contact alternative targets or the cell may die. One obvious difference between adult and developing neurons is that adult neurons are no longer growing. Last year we reported that injury to an adult S-cell could trigger its intact axon to grow once its adjacent target S-cell had been destroyed, as if the axon were growing in search of the lost

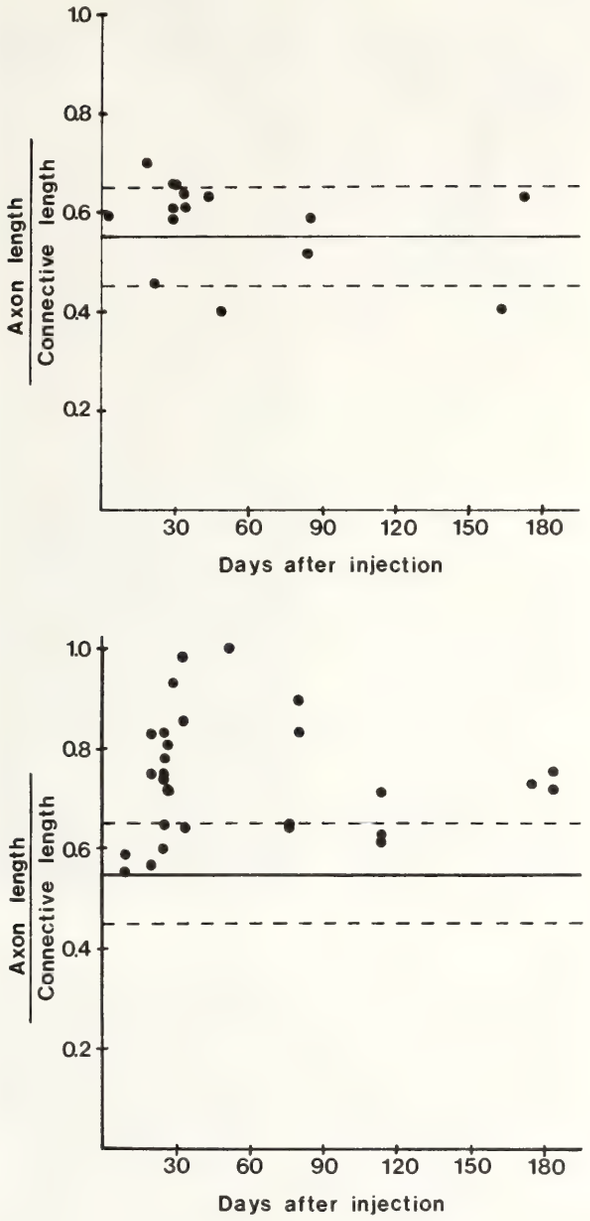


Fig. 3. *Upper.* Intact axons next to an S-cell killed by protease injection do not measurably change length. The solid and dashed lines are the mean length, normalized, of control axons and the standard deviation, respectively, from Figure 1b. The intact axons, each denoted by a dot, were of normal length, and neither grew nor retracted. *Lower:* Relative length of intact axons of injured cells increases when their target is eliminated. The solid and dashed lines represent the mean length, normalized, of control axons and the standard deviation, respectively, from Figure 1b. During the first two months after surgery the intact axons, each denoted by a dot, extend beyond the connective midpoint, but they later appear to retract.

target. Thus, removing the target removes an inhibition of axon growth. No alternative synapses are made by the growing axon. This year we extended our study from 11 cells to 28 (Fig. 3b), confirming the conclusions drawn previously. In addition, it has become clear that it takes longer after cellular injury for the intact axon to sprout (about three weeks) than for a regenerating axon to begin growing (less than two weeks).

After several months the sprouted axons retract somewhat, forming retraction bulbs of the type in the mammalian peripheral nervous system described by Cajal more than 50 years ago (*Degeneration and Regeneration of the Nervous System*, R. M. May, ed. and tr., Hafner, New York, p. 600, 1928). The clublike morphology of the retraction bulbs is different from that of the growth cones with filopodial extensions that tip the sprouting axons, but both are filled with a smooth membranous reticulum that may be related to turnover of membrane at these structures.

Further experiments, designed to determine whether sprouting is prompted by the loss of physical contact with the adjacent S-cell or some other aspect of target removal, such as an interruption of impulse traffic along the nerve cord, have shown that terminal sprouting occurs consistently only when the target is completely destroyed rather than when the target cell's axon is simply severed. This has suggested that a loss of physical contact is required for sprouting to occur.

Behavior of Glial Cells Following Injury

E. Elliott

As a first step in determining the role of glia in nerve regeneration, we have studied the behavior of the glial cell itself following injury. In the vertebrate nervous system, some glia (astrocytes) may divide and proliferate after injury, while others (oligodendroglia) do not divide but are capable of some measure of self-repair. The

large glial cells of the leech are all of one basic type, and their responses to injury have not been studied previously.

Each of the two lateral connectives of the leech nervous system is ensheathed by a single large glial cell which extends the entire distance (~5 mm) between ganglia. The median connective, which contains the S-cell axon, is ensheathed by one or both of the two connective glial cells. It is convenient in studying nerve regeneration to injure the connectives by crushing them. A crush between two ganglia severs axons and also divides each of the two connective glial cells into two parts—a portion containing the nucleus, which lies midway between the ganglia, and an anucleate glial stump.

We have found that the nucleated glial segment remains intact, with no sign of degeneration or cell division. Surprisingly, the anucleate glial stump also stays intact for months, maintaining its resting potential and normal morphology. During this time the stump is isolated from its nucleated portion, as is demonstrated by intracellular injection of two different markers. One marker is the enzyme horseradish peroxidase (HRP) (MW ~40,000), which can be reacted to give a stain visible in the light and electron microscopes; the other is the small (MW ~450) fluorescent dye Lucifer Yellow, which, unlike HRP, can pass between electrically coupled neurons or between glia in the leech. When injected into the stump, HRP diffuses readily throughout the stump but does not travel beyond the crush into the nucleated segment (Fig. 4). Lucifer Yellow also does not cross the crush when it is injected into either the stump or the nucleated portion of the glial cell. This indicates that the glial cell does not form electrical junctions with its stump, as does at least one type of neuron in the leech, the S interneuron (*Year Book 76, 78*). The absence of electrical junctions between the glial stump and glial nucleated portion was confirmed by electrical recordings.

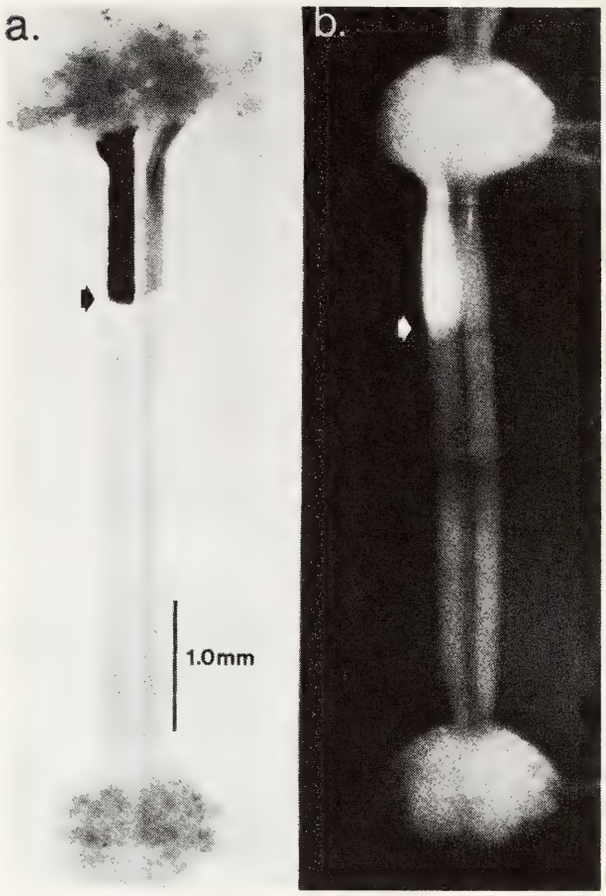


Fig. 4. Anucleate glial stump survives for months and remains isolated from nucleated glial segment. (a) Two months after the connectives have been crushed (at arrow), one connective glial stump has been injected strongly with HRP and the other very faintly. The HRP reaction product fills each stump and does not cross the crush into the nucleated glial segments. (b) A fluorescent micrograph shows that Lucifer Yellow injected into the glial stump also does not cross the crush. Calibration is approximately the same in (a) and (b). Anterior ganglion is at top.

Glial cells in the leech are normally coupled by electrical ("gap") junctions to the neighboring glial cells with which they are in contact. Thus, when a glial stump is formed by a single crush, the stump is isolated from the nucleated portion of the cell but is still electrically coupled to glial cells of the ganglion. It seemed possible that the stump might obtain metabolites and other molecules needed for survival via

its electrical junction with the adjacent intact glial cell. However, we have found that completely isolated anucleate glial segments formed by two crushes can also survive for months.

At times exceeding about three months after crushing, most anucleate glial stumps begin to deteriorate. Their glial cytoplasm shrinks, the normally numerous glial filaments diminish, and electrode penetration becomes difficult (Fig. 5). Small "microglia" invade or proliferate within the connective. We find that these cells, which seem to be phagocytic as judged by their lysosomal inclusions, can ensheathe axons. Their ensheathment does not appear completely to replace that of the atrophying glial stump. In a few preparations, sprouting of the nucleated glial segment across the crush has also been seen.

In summary, nucleated and anucleate glial segments both survive after crushing and retain their normal physiology and morphology throughout the period (3–8 weeks) required for functional axonal regeneration. This leaves open the possibility that the glial cell may physically guide growing axons or may contribute in other ways to nerve regeneration.

Removal of Single Glial Cells

E. Elliott and K. Muller

As a second step in determining the role of glia in nerve regeneration, we are studying the effect on axon growth of selective removal of the glial cell. We have succeeded in killing single glial cells by intracellular injection of a protease, a method used previously in this and other labs for selectively eliminating single neurons (*Year Book 77*). Injecting glial cells is more easily done in nerve preparations that have been removed from the animal than in the intact animal. For this reason, we be-

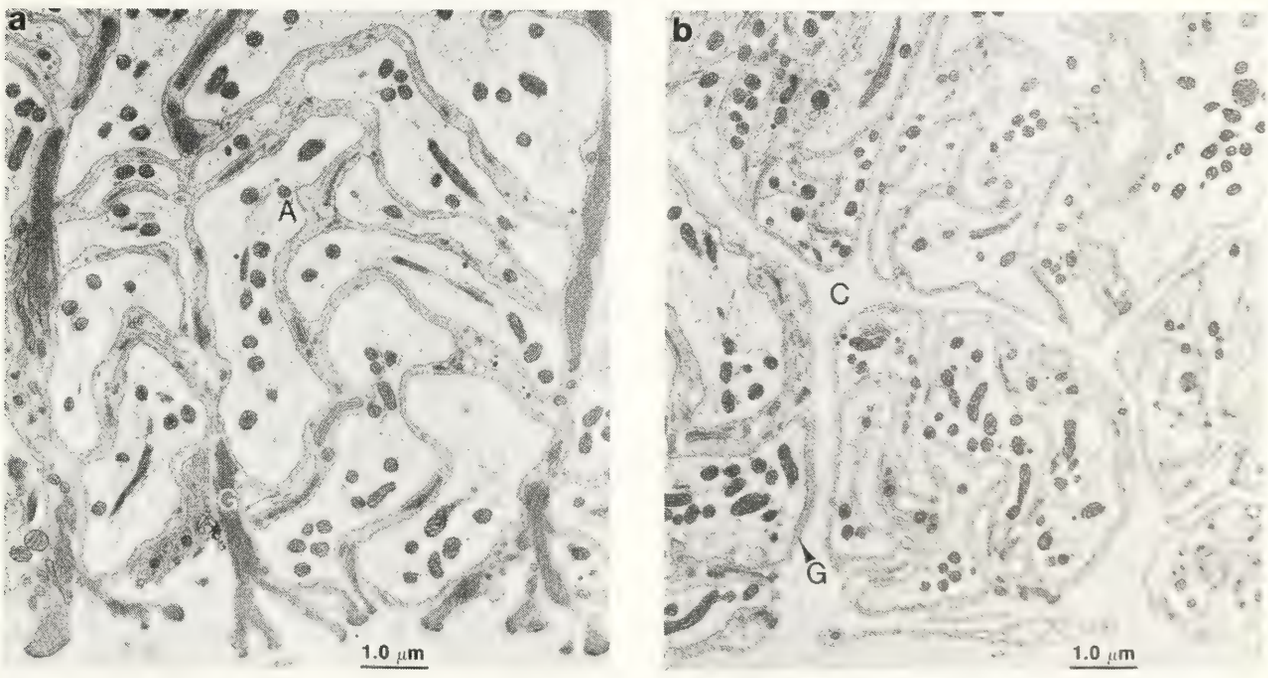


Fig. 5. Anucleate glial stump eventually atrophies. (a) A cross section of a normal connective shows axons A surrounded by thin, branching sheets of glial cell G. The axons contain mainly mitochondria and microtubules; the glial cell is distinguished by dark patches of glial filaments. (b) Ten months after the connective has been crushed, the anucleate glial stump G has atrophied, creating large channels C of extracellular space throughout the connective. The normally abundant glial filaments have virtually disappeared.

gan our glial-killing experiments in cultured preparations. Pairs of ganglia with the joining connectives were removed from the animal under sterile conditions. One of the two large connective glial cells was injected with a protease, and the preparation was then placed in modified L-15 culture medium for up to two weeks. Within three days the protease-injected glial cell had been destroyed, although some glial debris was still present after two weeks (Fig. 6). Axons that had been surrounded by the killed glial cell continued to conduct impulses for at least two weeks and appeared morphologically normal in the electron microscope.

Axon regeneration was examined in cultured preparations in which connectives were doubly crushed. In these experiments, one glial segment between the two crushes was injected with protease, while the other lateral connective served as a control. After one or two weeks in culture, selected sensory neurons in the ganglia were injected with HRP and stained to determine the extent of axon regeneration across the crushes. Injured axons sprouted and grew along the connectives toward the next ganglion in both the pronased side and the control side (Fig. 7). In some preparations, the extent of sprouting was greater in the pronased side than in the control side.

These experiments with cultured preparations demonstrated that single glial cells can be killed, that the axons they ensheathed can remain intact for at least two weeks, and that injured axons will still grow in a directed fashion. We have now begun similar experiments in the intact animal, which allows experiments to be carried out for much longer times than in culture and provides a better opportunity to follow regeneration functionally as well as morphologically. Functional regeneration normally requires that the growing axon reach its target in the next ganglion, which may require 3–8 weeks. Moreover, regeneration of the S interneuron, which has been intensively studied by this laboratory, occurs reliably only in vivo.

With the longer studies in vivo, we have found that from three to four weeks after glial cells are killed with protease, the glial debris is apparently completely removed. By this time, many microglia are present, and they extensively ensheathe the axons. The axons continue to conduct impulses and appear morphologically normal up to six weeks after glial killing, the longest time studied. Experiments to trace functional regeneration in vivo after killing one connective glial cell and then crushing the connectives have just begun. Preliminary results corroborate the findings of similar experiments in culture; that is, axons whose glial cell has been killed are still able to regenerate across a crush.

Function of a "Coupling Interneuron"

K. J. Muller, S. A. Scott, and B. E. Thomas

Whereas sensory neurons carry signals into the central nervous system and motor neurons and other effector cells conduct impulses to the periphery, many neurons are confined entirely within the central nervous system. These are called interneurons. We have reported that touch sensory neurons produce electrical synaptic excitation of the S-cell, which is itself an interneuron, but that the touch and S-cells do not make contact. A pair of interneurons described last year (*Year Book 78*) which we have called "coupling interneurons" provide the missing link. One reason these cells are of interest is that cells of this type may be abundant within the nervous system but would normally be difficult to detect. Their role is uncertain. By recording with pairs of microelectrodes from touch cells, coupling in-

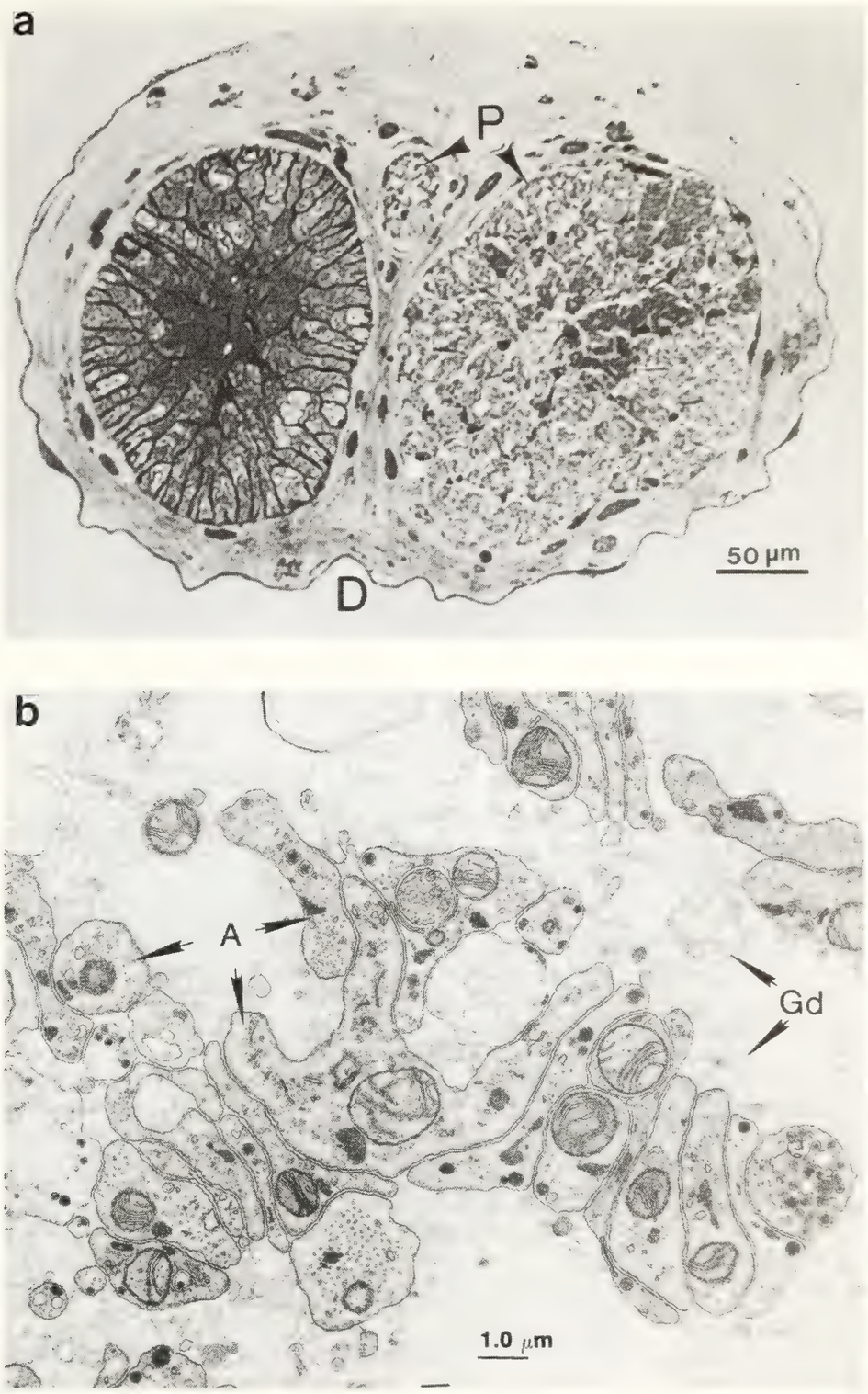


Fig. 6. Protease-killed glial cells in culture. (a) One week after protease has been injected into the right connective glial cell, the right lateral connective (P, right arrow) and the much smaller median connective (P, left arrow) both show signs of glial cell death. This indicates that the right connective glial cell also ensheathed the median connective (or Faivre's nerve) in this region. The glial cell of the left lateral connective has a normal, branched appearance. Section 2 μm thick was stained with Toluidine Blue. (b) At higher magnification, a lateral connective whose glial cell has been injected with protease two weeks earlier contains axons (A) which appear normal and debris remaining from the killed glial cell (Gd). Preparations in both (a) and (b) were maintained in culture after protease injection of glia.

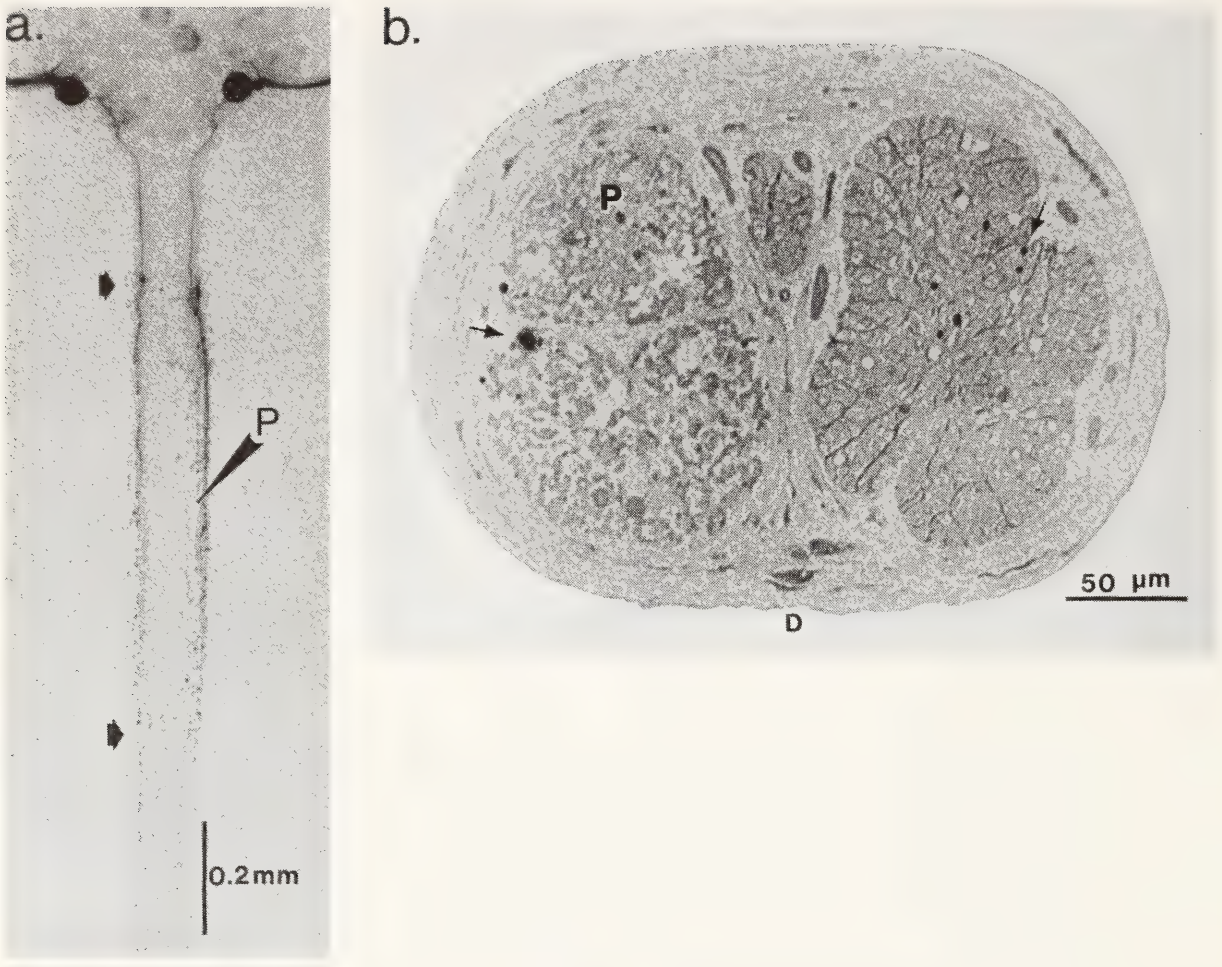


Fig. 7. Axons whose ensheathing glial cell has been killed can grow after crushing. (a) The connectives have been crushed in two places (arrows) and the glial cell of one lateral connective injected with protease (P) in the region between the two crushes. One week later, one sensory neuron on each side of the anterior ganglion was injected with HRP and stained to determine the extent of axon regeneration. Both the axon surrounded by normal glial cell (on left), and the axon whose ensheathing glial cell was injected with protease (on right), have sprouted extensively and grown beyond the crush toward the next ganglion. (b) A cross section between the two crushes of a preparation like that of (a) shows that the protease-injected glial cell has been killed. HRP-stained axonal sprouts (arrows) are present in both the normal lateral connective (on right) and the lateral connective whose glial cell has been killed (on left, denoted P).

terneurons, and S-cells, we have now shown that the site of selective excitation (a rectifying electrical junction which passes current in only one direction from the touch cell) is between the touch cell and the coupling interneuron. Thus in some respects the coupling interneuron would seem to be a functional extension of the S-cell. Electron microscopy has now shown that the coupling interneuron cannot be a simple cable extension of the S-cell, for the coupling interneuron makes and receives typical chemical synapses with an assortment of other cells (Fig. 8). Such chemical synapses would be capable of modulating the electrical synaptic transmission between touch cells and S-cells, in addition to reducing transmission by a phenomenon called branch-point failure (*Year Book 78*), and can thus provide the additional role of a cellular switch for such interneurons in the nervous system.



Fig. 8. In addition to having electrical synapses, detected physiologically, the coupling interneuron (C.I.) is presynaptic (arrow) and postsynaptic (arrowhead) at typical chemical synapses made with other, unidentified neurons in the ganglion. The coupling interneuron was injected with horseradish peroxidase and its process sectioned in the region of the ganglion between touch and S-cells.

CELL SURFACE AND SECRETORY GLYCOPROTEINS OF SKELETAL MUSCLE

R. Rotundo, J. M. Gardner, E. K. Bayne, E. Wakshull, M. J. Anderson, and D. M. Fambrough, with the technical assistance of D. Somerville

Research in our laboratory has focused on the metabolism of acetylcholine receptors and acetylcholinesterases in skeletal muscle. There are specific, sensitive methods for measuring the quantity and the cellular location of each of these large glycoproteins. In order to extend our studies to other muscle glycoproteins, we have invested our efforts in the making of cell lines that secrete single antibody species (monoclonal antibodies) targeted to individual muscle glycoproteins. The antibodies made by these cell lines are now being used in various ways to help answer some questions related to muscle glycoproteins: Are those glycoproteins that are part of the plasma membrane and those secreted from the muscle cells transported to the cell surface in a common transport vehicle? Do the cell surface glycoproteins have a common turnover rate? What is the fate or function of the secreted glycoproteins? Which of the secreted glycoproteins from muscle tissue are synthesized by the muscle fibers, and which by myoblasts, fibro-

blasts, and other types of cells? In addition to their value in approaching the above problems, the antibodies have proven useful in studying problems related to muscle differentiation.

In this report we present some recent data on acetylcholinesterase metabolism and its relation to acetylcholine receptor metabolism. We also describe a procedure for obtaining pure muscle fiber cell cultures, one which allows us to determine the contribution of these cells to the total secretory products of developing skeletal muscle and to define the secretion kinetics for these cells. Our studies on muscle extracellular matrix proteins, involving antibodies specific for individual components of the matrix, are briefly described. Finally, we describe two membrane antigens which should be important in studies of myogenesis.

Metabolism of Chick Embryo Muscle Acetylcholinesterase

The enzyme acetylcholinesterase (AChE) is responsible for terminating the action of the neurotransmitter acetylcholine at the neuromuscular junction. In muscle cells this enzyme exists as a family of molecular forms located within the cells and on the plasma membrane. In the vicinity of the synapses, AChE is associated with a specialized extracellular material referred to as the basal lamina. In cultured chick embryo muscle cells AChE exists as both membrane-bound molecules with sedimentation coefficients of 7.1S and 11.5S, and a secreted AChE form with a sedimentation coefficient of 7.1S (*Year Book 77*, *78*).

In order to study more accurately the degradation of the plasma membrane-bound AChE, we have employed a procedure enabling us to selectively label the enzyme molecules located on the plasma membrane (see *Year Book 78*). By selectively blocking the surface AChE with a specific, reversible inhibitor BW284c51, treating the cells with unlabeled DFP which irreversibly binds to the active site of the enzyme, and then removing the BW284c51 and treating the cells with tritiated DFP (^{3}H-DFP), we can follow the metabolism of the ^{3}H-DFP–labeled AChE molecules. As shown in Fig. 9, the degradation of cell surface AChE exhibits first-order decay kinetics with a half-life of about 50 hours. Under the same experimental conditions, in the presence of both labeled and unlabeled DFP, the half-life of the acetylcholine receptor is 19 hours. These experiments indicate that the muscle cells are capable of independently regulating the turnover rates of two cell-surface molecules. The mechanism(s) for the selective recognition, regulation, and internalization of cell surface components by specific cell types is unknown and is currently being investigated in this laboratory.

The kinetics of appearance of newly synthesized AChE molecules on the plasma membrane are illustrated in Fig. 10. By using DFP to inhibit all the muscle cell–associated AChE, we can subsequently track the appearance of newly synthesized AChE molecules in the plasma membrane with the cell surface AChE assay (*Year Book 77*). Following DFP treatment, there is a two-hour time lag before new AChE molecules appear on the plasma membrane. This latency period is similar to that observed for both the acetylcholine receptor and the secreted AChE molecules. Newly synthesized AChE molecules appear on the muscle cell surface at the rate of approximately 2–3% of the total cell surface AChE per hour. With the rate of appearance slightly exceeding the degradation rate for this particular molecular species, the net result should be the accumulation of enzyme on the cell surface. This is consistent with our earlier findings of increased enzyme accumulation during development of chick embryo muscle cells in culture.

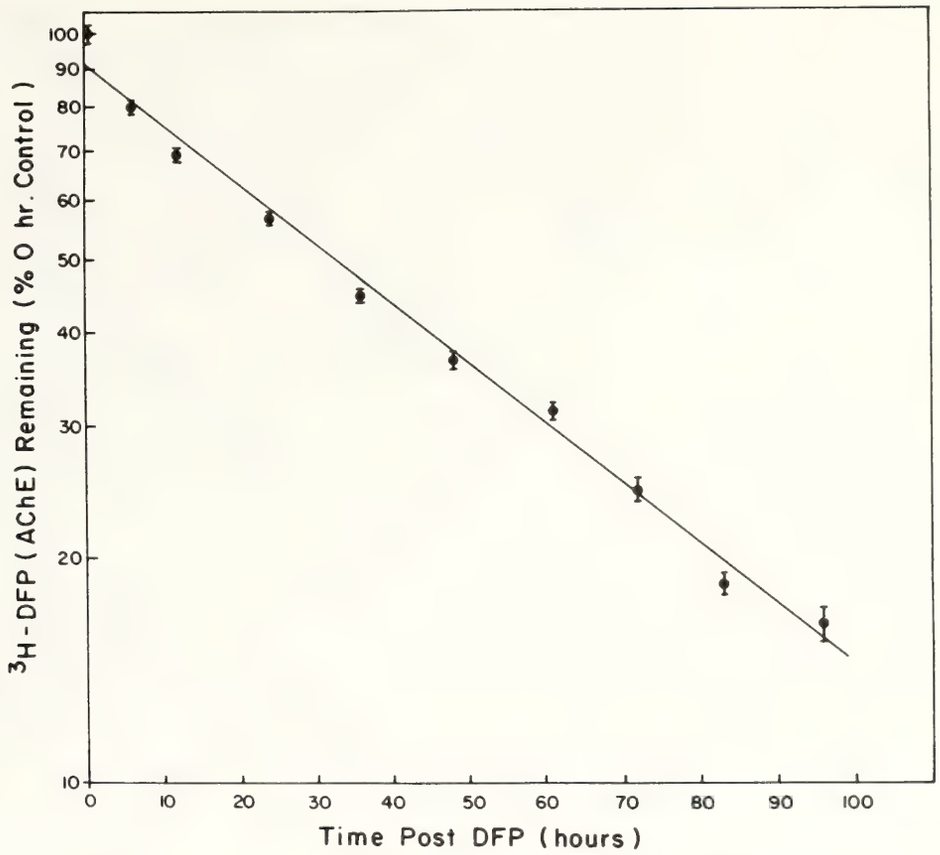


Fig. 9. Degradation of cell surface AChE. Cultured muscle cells were incubated for 10 minutes at room temperature in 10^{-3} M BW284c51, a reversible inhibitor of AChE that does not penetrate the cells. The unprotected, intracellular AChE was then irreversibly inhibited with unlabeled DFP. After extensive washing to remove both inhibitors, the remaining cell surface AChE was labeled using ^{3}H-DFP. Groups of four cultures were then extracted at timed intervals and the remaining cell-associated label counted. Each point is the mean ± SEM of four cultures. The half-life of cell surface AChE, calculated by linear regression analysis of this and similar experiments, is 50 hours.

This year we have continued our study of the relationship between the transport of the acetylcholine receptor, an integral membrane protein, and the secreted acetylcholinesterase molecules. Our previous data showed that these two molecules are transported at the same rate from their sites of synthesis to the plasma membrane (*Year Book 77, 78*). Furthermore, the transport processes were affected in a similar manner by inhibitors of protein synthesis, uncouplers of oxidative phosophorylation, and temperature. We have continued these studies, using a variety of compounds known to disrupt secretory processes. In each case we find that the transport and externalization of ACh receptors and secreted AChE are affected to the same extent. We interpret this inability to dissociate the transport of representative integral membrane and secreted proteins as suggestive evidence that these two classes of macromolecules are transported in unison from their sites of synthesis to the plasma membrane.

Our current views on the metabolism of the multiple molecular forms of acetylcholinesterase in cultured chick embryo muscle cells are summarized in Fig. 11. The 11.5S and 7.1S AChE molecular forms are synthesized at the relative rates of 3% and 17% of the total cell-associated AChE per hour, respectively. They are transported, probably in unison, to the plasma membrane over a 2–3 hour time interval. Thereafter their fates are vastly

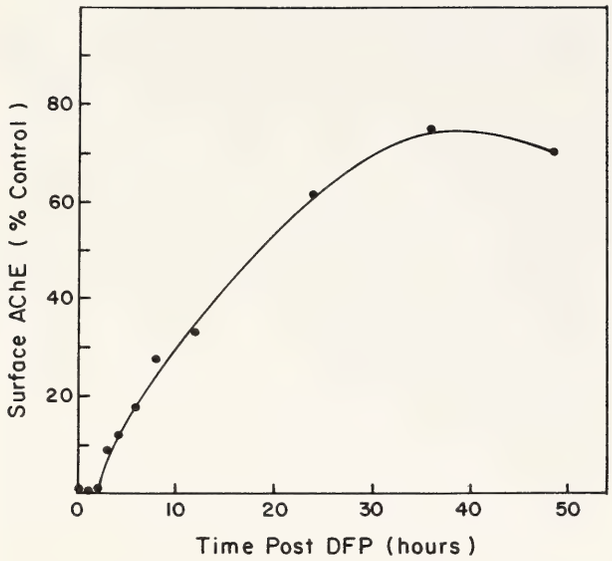


Fig. 10. Accumulation of newly synthesized AChE on the plasma membrane. Muscle cultures were treated with DFP to irreversibly inactivate all the cell-associated AChE. At the appropriate times, muscle cultures were assayed for cell surface AChE using a sensitive radiometric assay (*Year Book 77*). Each point is the mean of four cultures. Following a two-hour lag period, the newly synthesized AChE molecules accumulate on the plasma membrane at the rate of about 2–3% of total cell surface enzyme per hour.

different. One form of the 7.1S AChE is rapidly secreted into the culture medium. Another form of the 7.1S AChE molecule, and the 11.5S molecule, remain associated with the plasma membrane for a median time interval of approximately 50 hours.

Preparation of Pure Muscle Cultures and Analysis of Secretion Products

Our studies of protein secretion by muscle have been facilitated by the development of a method for preparing cell cultures which are highly enriched for muscle fibers (or myotubes). It has proven possible to obtain nearly pure cultures of embryonic chick myotubes by exposing primary muscle cultures simultaneously to a monoclonal antibody which recognizes dividing cells and to guinea pig complement. The resulting complement-mediated lysis of the target cells leaves differentiated muscle cells as the viable elements in the culture (Fig. 12). To quantify the complement-induced cytotoxicity, well-differentiated chick muscle cultures were treated for varying times with the antibody plus guinea pig complement. Controls in which antibody secreted by MOPC P3X63 myeloma cells was substituted for the specific antibody were run in parallel. At appropriate times, duplicate experimental and control cultures were rinsed

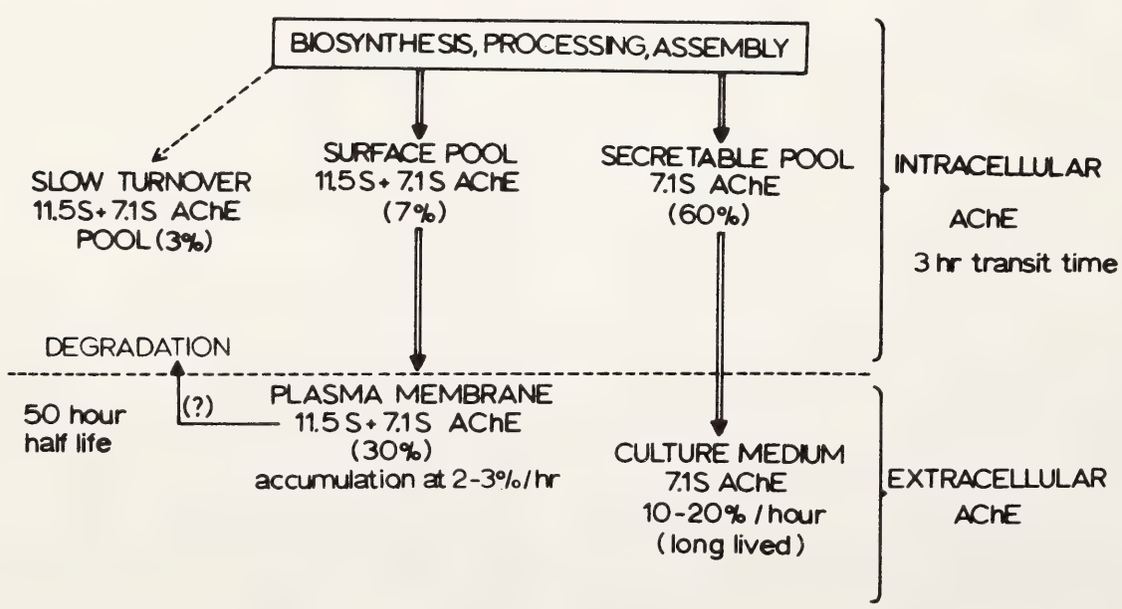


Fig. 11. Summary of our current understanding of the metabolism of the cell surface and secreted acetylcholinesterase molecular forms in cultured chick embryo muscle cells.

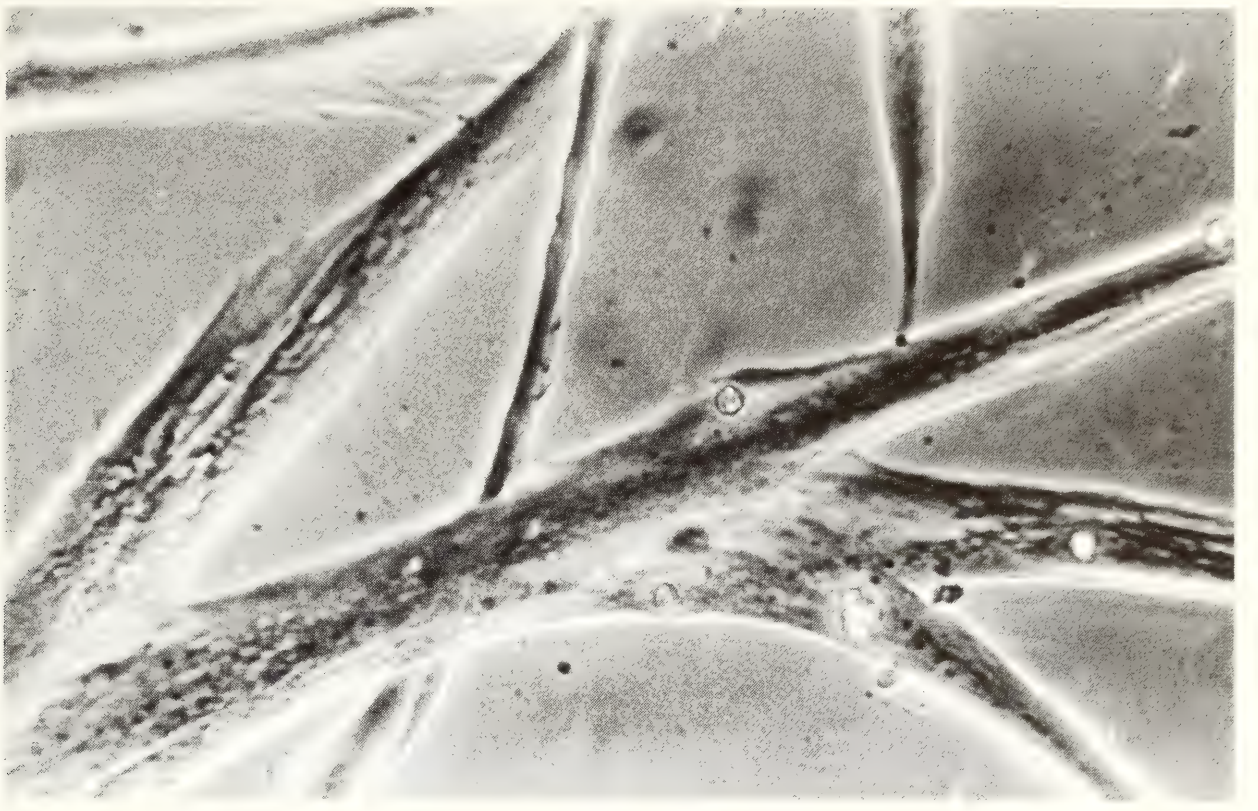


Fig. 12. Phase contrast micrograph of primary chick breast muscle culture after the deep-six procedure.

briefly with culture medium and incubated for 10 minutes with trypan blue diluted in culture medium to a final concentration of 0.05%. Following trypan blue staining (of killed cells), the cultures were rinsed with saline solution and fixed in glutaraldehyde. Random fields were then scored for viable vs. nonviable mononucleated cells and for the number of nuclei in viable vs. nonviable myotubes (Table 1). Less than 5% of the original population of mononucleated cells remained viable by the end of the experimental exposure to antibody plus complement, while no killing of myotubes occurred. (That myotubes are susceptible to complement-mediated lysis and that the affected myotubes do stain with trypan blue was demonstrated using other monoclonal antibodies which bind to myotube surfaces.) Of the total viable nuclei present at the end of antibody-plus-complement treatment,

TABLE 1. Time Course of Complement-Mediated Lysis of Mononucleate Cells by Number 6 Hybridoma IgM*

	% of Total Viable Nuclei Present in Multinucleated Myotubes	
Length of Treatment (minutes)	IgM Number 6-Treated Cultures	MOPC 21-Treated Cultures
0	53	53
15	84	52
30	90	56
45	93	49
60	93	55
120	96	51
180	97	40
300	97	43

*Myogenic cell cultures were treated with 1 μg/ml purified antibody together with 20% guinea pig complement in complete medium at 37°C. At the indicated times cultures were stained with trypan blue to reveal dead cells and then fixed and analyzed. As a control, purified MOPC 21 protein (from P3X63 myeloma) was substituted for number 6 antibody.

97% were in multinucleated cells. Some of the viable mononucleate cells morphologically resemble myogenic cells which have differentiated into muscle without having fused with other myoblasts.

Thus the method is effective for removing fibroblasts from muscle cultures. In the past, drugs such as cytosine arabinoside and fluorodeoxyuridine have been used for this purpose. These drugs, however, exert effects on all cells within the culture. The antibody method obviates such problems. We are currently using this method to prepare cultures for experiments assessing the contribution of muscle and fibroblasts in the synthesis of secretory glycoproteins and in the assembly of extracellular matrix. The method also seems useful in preparing pure neuron cultures from chick spinal cord. Since the cell line producing the useful antibody for this procedure was arbitrarily assigned the number 6, we affectionately refer to the procedure as the "deep-six" procedure.

Experiments have been performed in which pure myotube cultures have been labeled continuously with ^{35}S-methionine, and aliquots of the medium were removed at various times. Analysis of the labeled proteins in the medium (myotube secretory proteins) by SDS polyacrylamide gel electrophoresis and fluorography indicate that secreted proteins appear in the medium with linear kinetics after a 2–3 hour lag period. This agrees with our previous observations of a 2–3 hour intracellular transit period for secretory acetylcholinesterase and for integral membrane acetylcholine receptors and acetylcholinesterase. All the secretory components showed similar kinetics of secretion. An example of the profile of seceted products from pure myogenic cultures labeled with either ^{35}S-methionine or ^{3}H-proline is shown in Fig. 13. One is immediately struck by the large variety of secretory products from these cells, which are not usually thought of as secretory cells. What are the functions of the secretory proteins? The proline-rich components of the secretory proteins include a family of collagenase-sensitive polypeptides, which are all recognized by one of our monoclonal antibodies (number 9) and also a doublet of polypeptides which are fibronectins (recognized by our antifibronectin monoclonal antibody B3). These and at least several of the other secretory proteins become part of the complex extracellular matrix of muscle tissue. We will discuss this topic later in this report.

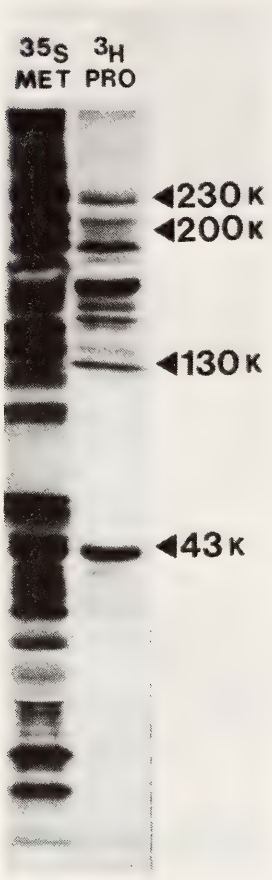


Fig. 13. SDS polyacrylamide gel electrophoretic patterns of chick skeletal muscle-fiber secretory proteins metabolically labeled with ^{35}S-methionine and ^{3}H-proline. The proline-rich components include a fibronectin doublet with apparent molecular weights around 230,000 daltons and several collagenous peptides in the molecular weight range from 150,000 to 200,000 daltons. Some approximate molecular weights, based upon the electrophoretic migration of standards, are indicated at right.

Various secretory products from the cultured muscle cells become bound to cells and to the collagenous substratum on which the cells grow and differentiate. This phenomenon has proven useful in determining the class of exposed antigen to which each of our monoclonal antibodies is directed. Some of the monoclonal antibodies bind exclusively to cell surfaces and presumably recognize integral membrane proteins. Many other monoclonal antibodies bind to the cultures at sites on or under the cells and also to sites remote from cells. Each of these monoclonal antibodies seems to be targeted to a secretory protein. One case of this targeting was illustrated in *Year Book 78*. A simple proof that each antibody is targeted to a different antigen is the fact that each antibody binds with a unique distribution on substratum and cells. Each of the monoclonal antibodies also recognizes a component of the extracellular matrix in the muscle tissue of adult chickens. Again, the distributions of the antigens are different from each other and provide some clues as to the molecular identity of the antigens. Differences in (1) distance from the muscle fiber plasmalemma, (2) morphological appearance, and (3) uniformity of distribution around myofibers are noted when the binding of different antibodies is examined via immunofluorescence (Fig. 14). Even at this limited level of resolution, the distributions lead to some tentative conclusions. Antibody number 33 seems to recognize a noncollagenous component

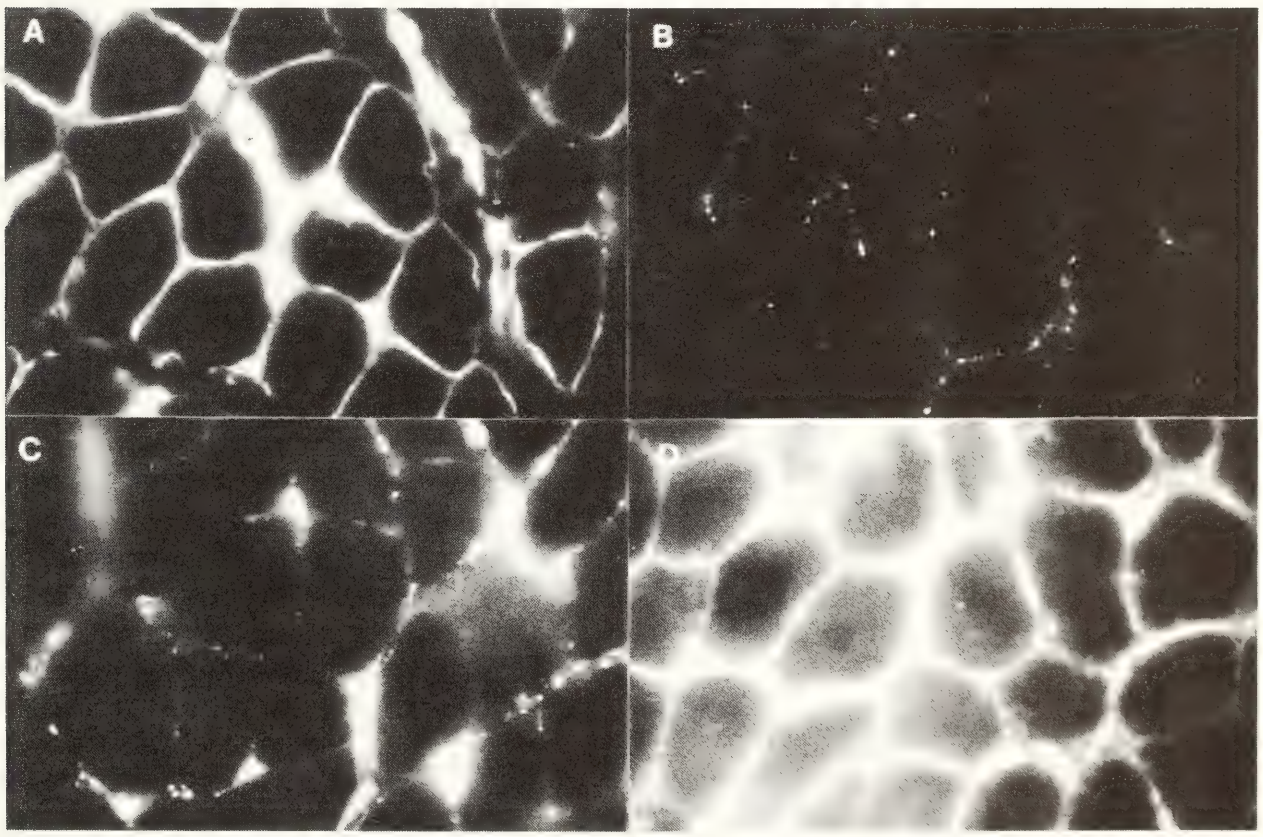


Fig. 14. Immunofluorescent staining of adult chicken skeletal muscle cross sections with monoclonal antibodies to different components of the extracellular matrix. This series demonstrates the different arrangements of some of these antigens. (A) Staining of a presumed basal lamina component with hybridoma 33 IgG. (B) Hybridoma 3 antibody staining, possible of strands of collagen fibrils surrounding each muscle fiber. (C) Staining of fibronectin with hybridoma B3 IgG. (D) Staining of the extracellular matrix with hybridoma 15 IgG. A highly stained neuromuscular junction (*) is indicated in panel (A).

of the basal lamina, and this component is concentrated in the synaptic clefts of neuromuscular junctions. Two other antibodies may recognize different populations of collagen, perhaps different collagen types. Fibronectin does not seem to be a major component of the basement membrane, but rather is distributed in a manner suggesting association with interstitial collagen cables and capillaries. Another antibody (number 15) recognizes a more diffusely distributed component of extracellular matrix whose identity cannot yet be guessed. All in all, these antibodies give us a view of the extracellular matrix of skeletal muscle as a very complex, ordered structure. Some components of this matrix do not even have names. Heretofore there has been no evidence as to which components are manufactured by which cells or how the components interact to form the matrix structure. Cell culture and the antibody technique provide sufficient tools to allow study of these matters in depth.

Control of Muscle Cell Surface Structure during Development

The motor end plate of the adult skeletal muscle fiber shows striking morphological and chemical differences when compared with the remainder of the cell surface. For example, acetylcholinesterase and the acetylcholine receptor, two functional elements of the synaptic apparatus, exist at high local concentrations within the end plate but are virtually absent from adjacent portions of the muscle fiber. Each of these chemical specializations appears to arise in response to a poorly understood "inductive" action of the motor neuron during synaptogenesis. Over the past decade considerable information has been obtained about the manner in which innervation controls both the metabolism and distribution of the acetylcholine receptor, an integral membrane protein which is contained within the sarcolemma. This effort has been possible because of the discovery of snake toxins, which bind specifically and virtually irreversibly to the nicotinic acetylcholine receptor. It nevertheless remains unclear how the control of receptor distribution is related to neural regulation of other synaptic markers. It is known, for example, that the developing nerve can induce an accumulation of mobile acetylcholine receptors adjacent to its site of contact with the muscle cell. It is not known, however, whether this effect is brought about directly by a change in the properties of individual receptor molecules, or indirectly as a result of changes in the chemical composition of the muscle cell surface at the site of nerve-muscle contact. In order to approach this problem, it will be necessary to compare changes in receptor distribution with corresponding changes in the distribution of other markers during the development of the neuromuscular junction.

To achieve this goal we are exploiting recent advances in immunochemical technology pioneered by Kohler and Milstein. As illustrated above, these techniques permit the generation of monospecific immunoglobulins which can be used as markers to identify and examine the distribution of antigenic determinants localized within the synaptic apparatus. The potential of such an immunological approach can be illustrated by recent experimental observations obtained using conventional polyclonal rabbit antisera directed against acetylcholinesterase and a large collagen-binding protein isolated from the marine elasmobranch *Torpedo californica*. These antisera cross-react with immune determinants present at neuromuscular junctions which develop in cultures of nerve and muscle cells from the African toad *Xenopus laevis*. Moreover, immunocytochemical techniques allow the distribution of these antigens to be compared with the

corresponding distribution of acetylcholine receptors on the same muscle cells. Such a comparison reveals that chemical specializations in the distribution of acetylcholine receptors, which occur even in the absence of innervation, are associated with analogous accumulations of both immunological markers. On the basis of this observation it is reasonable to assume that there are related mechanisms which produce local sites of elaborate chemical specialization on the muscle surface, and that these mechanisms are at least partially independent of interaction with a developing nerve fiber. We anticipate that further studies of the chemical organization of these specialized regions, and of the manner in which the muscle cell surface is modified by nerve-muscle interaction, will reveal fundamental mechanisms involved in the differentiation of synapses.

Some Other Interesting Monoclonal Antibodies

Several different monoclonal antibodies, when assayed for binding on chick muscle cultures, bind only to the surfaces of myogenic cells (and not to fibroblasts). This conclusion, based on autoradiographic and immunofluorescence data, was confirmed by assays of tertiary fibroblast cultures: The antibodies exhibited no binding above the nonspecific binding of control monoclonal antibodies. Surprisingly, however, the antibodies that are myogenic cell specific, as judged from muscle-culture binding, actually do bind specifically to some other cell types.

Hybridoma line 24 secretes an immunoglobulin which recognizes an antigen present on neural as well as muscle tissue. When antibody binding to cultures of dissociated cells from chick spinal cord was assessed by autoradiography, a striking pattern emerged—nerve networks outlined by silver grains. Neuronal cell bodies as well as processes were heavily labeled, while cells with flattened morphologies remained unlabeled (Fig. 15a). During myogenesis in vitro, the antigen is present at early myoblast stages as well as on myotubes (Fig. 15b, c). In frozen sections of adult chicken muscle, the antigen recognized by number 24 antibody appears localized in sarcolemma and possibly t-tubule system of muscle fibers. The antigen is also seen associated with nerve processes, including axonal membrane under the myelin sheaths, and is more prevalent on nerves than muscle.

Hybridoma C3/1 produces an antibody which recognizes an antigen present on dividing myoblasts, which decreases during muscle differentiation. When adult muscle is examined by indirect immunofluorescence, no detectable antigen is seen associated with muscle fiber plasmalemma. In preparations of muscle fibers teased from adult tissue, however, we do find fluorescence associated with a population of mononucleated cells which, at the light microscope level, appear to be muscle satellite cells. These cells are thought to be the equivalent of myoblasts and to be responsible for the regenerative capacity of skeletal muscle following muscle damage. We expect that the C3/1 monoclonal antibody will allow us to explore this matter in some depth. We are currently in the process of determining the binding sites for C3/1 antibody at the electron microscope level, since only at this level can satellite cells be identified unequivocally. Oddly, the antigen recognized by C3/1 antibody also occurs on a population of non-neuronal cells in tissue-cultured chick spinal cord and at high levels in the Schwann cell wrappings of peripheral nerves.

A perennial question is whether the antigens defined by our monoclonal antibodies are proteinaceous. We are carrying out a systematic analysis of the nature of the antigens, including

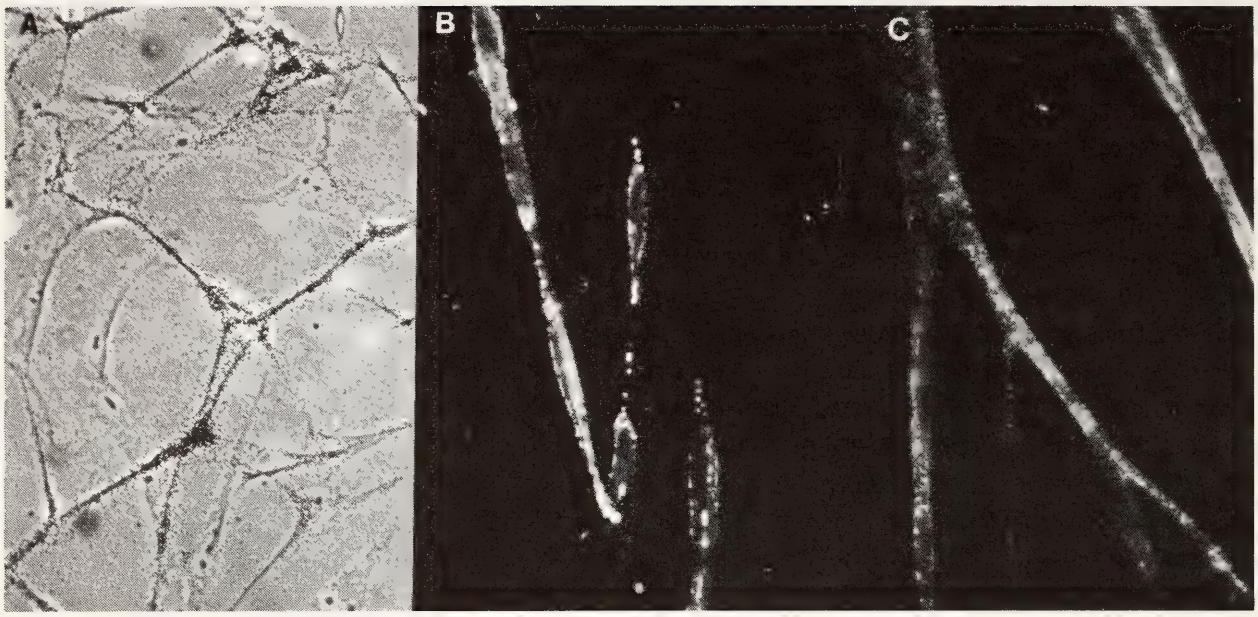


Fig. 15. Distribution of target antigen for hybridoma 24 IgG on nerve and myogenic cell cultures. (A) Autoradiograph showing silver grains over neuronal cell bodies and processes in chick spinal cord tissue culture exposed to number 24 antibody and then to iodinated rabbit antimouse antibody. (B and C) Immunofluorescence staining of myoblasts (B) and myotubes (C) with number 24 IgG followed by fluoresceinated rabbit antimouse antibody.

studies of the sensitivity of the antigens to protein-denaturing conditions, protease treatments, and chemical modifications. To date, all tests suggest that all the antigens are proteinaceous. Many of the antigens are sensitive to trypsin. Several have been purified by immunoprecipitation or identified by antibody binding after electrophoretic transfer of proteins from SDS gels to cellulose nitrate to diazotized paper.

ORGANIZATION, DYNAMICS, AND METABOLISM OF CELL SURFACE LIPIDS

D. Hoekstra, O. C. Martin, J. W. Nichols, A. J. Schroit, D. K. Struck, and R. E. Pagano

This past year we have continued our studies on cell surface lipids. Our approach is based on technology developed in this laboratory for the introduction of chemically defined and appropriately tagged lipid molecules into the cell surface from an exogenous source, phospholipid vesicles. Once these molecules are integrated into the plasma membrane bilayer of cells, we seek to follow their dynamics and metabolism (see *Year Book 78*). This year we have emphasized the use of fluorescence methods to trace the fate of exogenous lipids once they become cell associated. Such an approach permits direct measurements on the localization of vesicle constituents to be carried out routinely on living cells and represents, for many applications, a considerable improvement over earlier approaches that relied on isotopically labeled compounds.

In this report, Nichols presents some fundamental data on the physical properties of the fluorescent lipids used in

many of our recent studies. This data suggests that certain kinds of lipids can equilibrate between membranes in the absence of direct membrane contact. Struck describes a novel assay employing fluorescence energy transfer to examine both vesicle-vesicle and vesicle-cell interactions. In the latter case, we can now unequivocally discriminate fusion from adsorption—this is fundamental in determining whether or not exogenous lipids are properly integrated into the plasma membrane bilayer or are simply cell-associated as adherent vesicles. Pagano and Martin report on their efforts to examine the topology of membrane fusion events. In the case of vesicle-cell fusion, topology of membrane lipids is apparently conserved. Finally, Schroit presents his latest progress on the capping of fluorescent lipids in the lymphocyte plasma membrane. His latest findings suggest that the capping of exogenously introduced lipids is not restricted to haptenated lipids used in earlier studies, but also occurs with fluorescently tagged phospholipids.

Kinetics of Phospholipid Transfer between Vesicles

J. W. Nichols

Previous studies from this laboratory and others have shown that phospholipids are readily transferred between essentially any combination of cells, lipoproteins, and vesicles. To gain insight into the mechanism of these transfer processes, we have studied a similar transfer process in a simple model system. Specifically, we have investigated the kinetics of transfer of the fluorescently tagged phospholipid, 1-acyl-2-(N-4-nitrobenzo, -2-oxa-1,3-diazole)-aminolauric phosphatidylcholine (C_{12}-NBD-PC), into unlabeled acceptor vesicles. Vesicles prepared from phospholipids containing greater than 50% C_{12}-NBD-PC are more than 97% self-quenched. When these vesicles are mixed with acceptor vesicles composed of unlabeled phospholipids, the C_{12}-NBD-PC molecules immediately begin transferring to the acceptor vesicles, where they are no longer quenched. As shown in Fig. 16, this results in a significant increase in fluorescence. We have used this simple technique to measure the rate of C_{12}-NBD-PC transfer between two vesicle populations.

There are basically two simple mechanisms for phospholipid transfer between vesicles. Either phospholipids are transferred upon collision of two vesicles or they are transferred by the diffusion of free monomers in equilibrium with molecules in the bilayer. A model based on the collision-mediated process would predict that the initial rate of transfer upon mixing would increase exponentially as both acceptor and donor vesicle concentrations were increased linearly. Since our results do not confirm this prediction, we have eliminated vesicle collision as the mechanism for C_{12}-NBD-PC transfer.

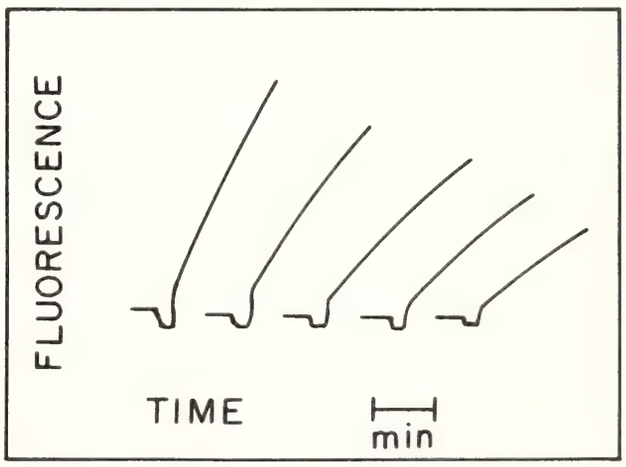


Fig. 16. A series of initial transfer rate measurements. Donor vesicles consisting of 100% C_{12}-NBD-PC in 1.9 ml of 150 mM NaCl–10 mM Hepes, pH 7.4, were equilibrated at 49°C in an Aminco Bowman Spectrophotofluorometer. Transfer was initiated by the addition of 100% dimyristoyl phosphatidylcholine (DMPC) acceptor vesicles. The cuvette was stirred and fluorescence was recorded. The final concentration of DMPC was 8.8×10^{-5} M; the final concentrations of C_{12}-NBD-PC were varied, from left to right 1.87, 1.25, 0.94, 0.75, and 0.63×10^{-6} M.

In an effort to gain a fuller understanding of diffusion-mediated transfer, we have adapted a kinetic model, which predicts the initial rate of transfer as a function of the donor and acceptor vesicle concentrations, and rate constants, which describe the likelihood a given phospholipid will enter or leave a given vesicle population. With the dequenching technique we have been able to test the kinetics of phospholipid transfer in the most rigorous fashion to date and have confirmed that our adapted kinetic model accurately describes diffusion-mediated phospholipid transfer. As a result we conclude the following: The rate at which a phospholipid enters or leaves a bilayer from free solution depends both on its structure and the composition of the vesicle. Prior to these measurements, it has been commonly assumed that the "on" and "off" rates for phospholipids entering and leaving vesicles were solely a function of the phospholipid structure and independent of vesicle composition. These results provide new guidelines for the development of testable hypotheses for the mechanism of phospholipid transfer in biologically relevant lipid structures.

In the coming year we plan to apply the insights gained from this work to understanding the mechanism of phospholipid transfer between cells and vesicles and between cells and lipoproteins.

Assay of Membrane Interactions Using Fluorescence Energy Transfer

D. K. Struck

One approach to demonstrate the fusion of unilamellar lipid vesicles and cultured cells is to follow the mixing of lipids present in the vesicle bilayer with those present in cellular membranes. Such lipid mixing would be expected if vesicle-cell interaction did, indeed, involve the merging of the vesicle lipid bilayer with the plasma membrane of a cell, and if lipid molecules were free to diffuse in the plane of the newly formed membrane. Preliminary experiments have indicated that this type of lipid mixing can be measured by fluorescence energy transfer. This technique relies upon the interactions occurring between two fluorophores if the emission band of one overlaps the excitation band of the second and the two probes are in close physical proximity. When these conditions are met, the energy absorbed by the first fluorophore, the energy donor, can be transferred to the second fluorophore, the energy acceptor, which will then fluoresce as though it had been excited directly by the incident light. Accordingly, the fluorescence yield from the energy donor will be reduced, since a fraction of the energy it had absorbed is transferred to the energy acceptor. Since the efficiency of fluorescence energy transfer between two given fluorophores primarily depends on their average separation, changes in this efficiency can be used to measure lipid mixing during membrane fusion.

In the system we have developed, NBD is the energy donor and rhodamine is the energy acceptor. These two fluorophores are coupled to the free amino group of phosphatidylethanolamine (PE) to give fluorescent phospholipid analogs (NBD-PE and rhodamine-PE), which can be incorporated into a vesicle bilayer. When both analogs are present in the same bilayer at appropriate concentrations, efficient energy transfer between NBD-PE and rhodamine-PE is observed. Thus, excitation of the NBD fluorophore gives rise to fluorescence at wavelengths characteristic for rhodamine, while the fluorescence yield from NBD is much lower than that observed in the absence of the energy acceptor. If the two fluorescent lipids are diluted with respect to one another (that is, if the ratio of fluorescent lipid to total lipid decreases for bilayers containing the fluorescent de-

rivatives) by fusion with a second membrane there is a reduction in the efficiency of energy transfer, since the average separation between the two fluorophores has increased. This reduction in energy transfer results in an increase in fluorescence at 530 nm from NBD and a decrease in fluorescence at 586 nm from rhodamine when the sample is excited at 470 nm, the excitation maximum for NBD.

The fact that fluorescence energy transfer can be used to measure membrane fusion was demonstrated using calcium-induced fusion of phosphatidylserine vesicles as a model system. In these experiments, NBD-PE and rhodamine-PE were incorporated into phosphatidylserine vesicles, and this preparation was mixed with an excess of pure phosphatidylserine vesicles. Upon the addition of calcium to this mixture, there is a rapid increase in light-scattering from the sample, reflecting both the vesicle-vesicle fusion and vesicle-vesicle aggregation occurring in the system (Fig. 17). In control experiments, the same phosphatidylserine vesicles containing both fluorescent lipids were mixed with an excess of pure phosphatidylcholine vesicles that do not undergo calcium-induced fusion. When calcium is added to this mixture, there is an increase in light-scattering owing to the aggregation/fusion of the phosphatidylserine vesicles with each other (Fig. 17). However, there is little change in the fluorescence yield at 530 nm, since all of the phosphatidylserine vesicles present contain both NBD-PE and rhodamine-PE. Thus, fusion between these vesicles does not result in a dilution of the fluorescent lipids with respect to one another so that the efficiency of energy transfer remains the same.

The magnitude of the spectral changes occurring during calcium-induced fusion of phosphatidylserine/NBD-PE/rhodamine-PE vesicles with phosphatidylserine vesicles is illustrated in Fig. 18. Before the addition of calcium,

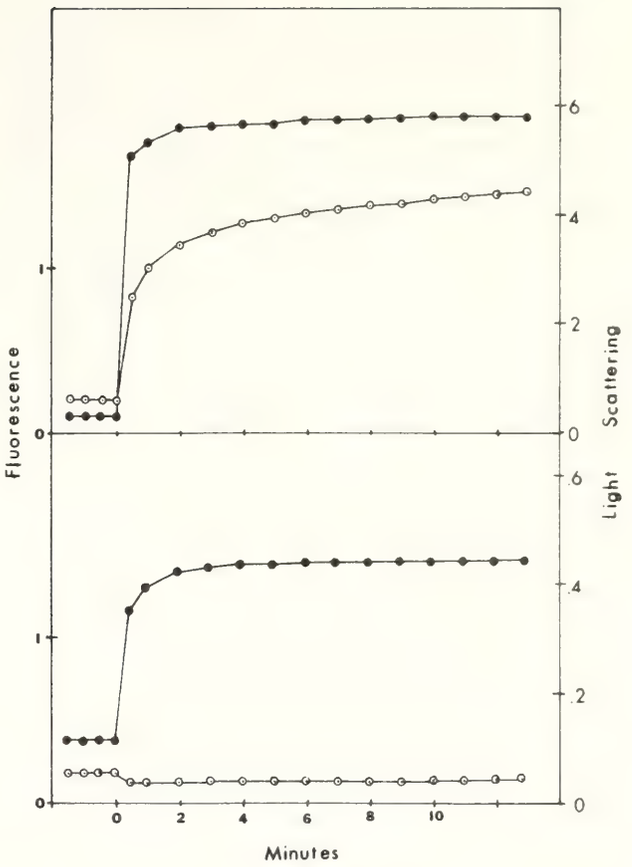


Fig. 17. Rate of fusion between two populations of unilamellar vesicles. Upper panel: phosphatidylserine/NBD-PE/rhodamine-PE vesicles were incubated with pure phosphatidylserine vesicles. Lower panel: phosphatidylserine/NBD-PE/rhodamine-PE vesicles were incubated with pure phosphatidylcholine vesicles. At zero time, calcium was added and either light scattering at 400 nm (● — ●) or fluorescence at 530 nm (o — o) was followed with time. Samples were excited at 470 nm for fluorescence measurements.

there is an increase in the emission peak at 530 nm and a decrease in the emission peak at 586 nm. These changes reflect the reduction in energy transfer caused by the dilution of the fluorescent lipids with respect to each other and are consistent with the mixing of membrane phases that should occur during fusion between the two vesicle populations.

While fluorescence energy transfer can be used to study vesicle-vesicle interactions, this technique is particularly well suited for investigating the mechanisms of vesicle-cell interaction, since the problem introduced by the

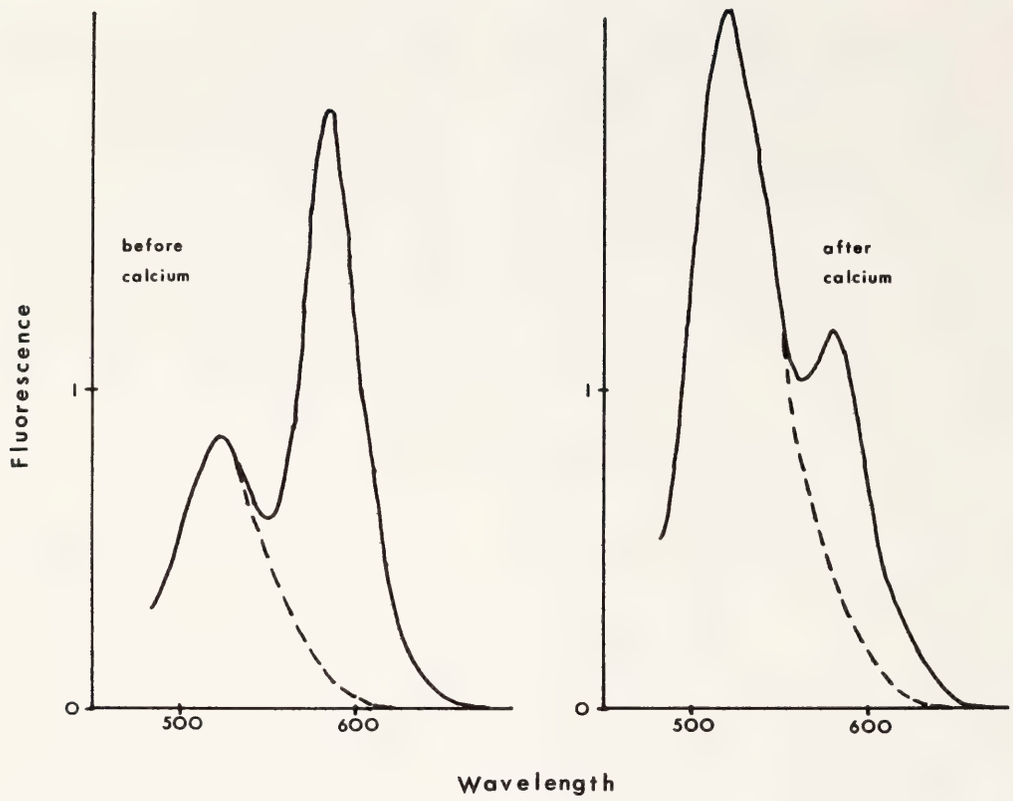


Fig. 18. Reduction in energy transfer due to membrane fusion. Emission spectra were obtained using a mixture of phsophatidylserine/NBD—PE/rhodamine—PE and pure phosphatidylserine vesicles in the presence and absence of calcium. Samples were excited at 470 nm.

small amounts of vesicle lipid transferred to cells can be overcome by the high sensitivity of fluorescent measurements (pmole of fluorophore per ml can be detected). Fluorescence energy transfer provides, in theory, a method by which vesicle-cell fusion and vesicle-cell adsorption/endocytosis can be distinguished. Fluorescent lipids introduced into cells by fusion should be free to mix with lipids present in the plasma membrane of the recipient cells so that they become diluted to the extent that energy transfer is eliminated. However, if cellular uptake of fluorescent lipid is due to the adsorption or endocytosis of intact vesicles, there should be no reduction in energy transfer. Currently, we are exploring the possibility of using fluorescence energy transfer to investigate the mechanisms of vesicle-cell interaction.

Topology of Membrane Fusion

R. E. Pagano and O. C. Martin

We are attempting to look at the topology of fusion of artificial lipid vesicles with the cell surface in order to gain further insight into the molecular details of membrane fusion processes in general. Our strategy is first to generate small unilamellar vesicles (250–500 Å in diameter) in which a particular lipid is restricted to the inner or outer leaflet of the vesicle bilayer, and then to examine the orientation of that lipid in the plasma membrane bilayer after vesicle-cell fusion. If membrane topology is conserved, lipids initially present in the outer leaflet of the vesicle bilayer should reside in the external leaflet of the plasma membrane bilayer

following fusion, while lipids initially present in the inner leaflet of the vesicle should be delivered to the cytoplasmic side of the plasma membrane. The orientation of vesicle-derived lipids in the cell surface could be determined in the case of isotopically labeled phosphatidylethanolamine (PE) molecules by using an impermeable amino reactive reagent that would react only with externally, but not internally, disposed amino groups at the cell surface. An alternative strategy employing vesicles with an asymmetric distribution of fluorescent lipids might also prove useful, since fluorescent lipids delivered to each of the two leaflets of the plasma membrane might be processed very differently by the cell and thereby give rise to very different staining patterns.

This year we developed a routine procedure for generating asymmetric vesicles in which a fluorescent lipid is restricted primarily to the inner or outer leaflet of a vesicle bilayer. We found that when small unilamellar vesicles formed from dioleoyl phosphatidylcholine and 5–20 mol % NBD-PC (or NBD-PE) are incubated with an appropriate acceptor membrane, there is a rapid, spontaneous net transfer of the NBD-lipid to the acceptor. A variety of acceptor membranes have been used in these experiments—the most useful to date have been large (~ 1,000 Å diameter) unilamellar vesicles formed from a phosphatidylcholine containing brominated fatty acid side chains. The large difference in density of the donor and acceptor membranes permits a rapid and complete separation of the two populations of vesicles from one another by ultracentrifugation. Incubation of donor and acceptor membranes can be repeated several times with a fresh excess of acceptors. About 45–55% of the original fluorescent lipid is lost from the donor vesicles during such an exchange. The amount of NBD-lipid remaining in the outer leaflet of the vesicle bilayer was assessed by (1) the ability of antibodies to bind to (trinitrophenylated) NBD-PE and (2) by the ability of the remaining NBD-lipid (an energy donor) to exchange into a population of vesicles containing rhodamine-labeled PE (an energy acceptor and a nonexchangeable lipid) and subsequently exhibit fluorescence energy transfer (see Struck, this Report). Both methods indicate that the vesicles are highly asymmetric, with ~ 80–100% of the NBD-lipid originally present in the outer leaflet of the vesicle bilayer having been removed by exchange. Outer leaflet labeled vesicles can be prepared by the exchange of NBD-PC (or NBD-PE) from large unilamellar donor vesicles to small unilamellar acceptor vesicles.

In preliminary experiments, V79 fibroblasts were incubated for 30 minutes at 37 °C with vesicles in which the fluorescent lipid was either uniformly distributed across the vesicle bilayer or restricted to the inner leaflet of the vesicle. Cell-associated fluorescent NBD-PC derived from uniformly labeled vesicles is located both in the plasma membrane and in intracellular membranes, whereas with asymmetric vesicles the cell-associated NBD-PC is localized in intracellular membranes but not in the plasma membrane (Fig. 19). This finding is consistent with the fusion of vesicles with cells, and suggests that during fusion, lipid molecules residing in the inner leaflet of the vesicles are delivered to the inner leaflet of the cell plasma membrane where they are then rapidly transferred to intracellular membranes, possibly by a spontaneous exchange process. The difference in uptake of asymmetric vs. uniformly labeled vesicles is only obtained when vesicle-cell incubations are carried out at low vesicle concentrations (< 1–5 μgm lipid/ml). At higher concentrations, ring staining similar to that seen in Fig. 19b is seen for *both* uniform and asymmetric vesicles. This might be explained by the fact that at

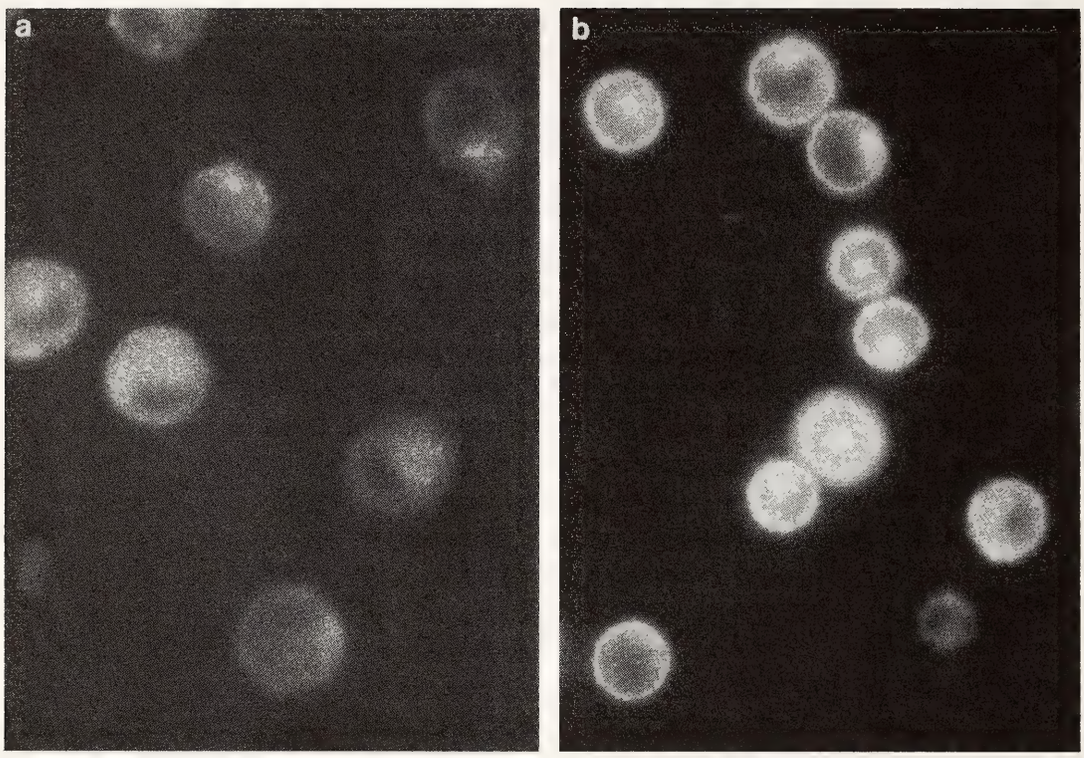


Fig. 19. Fluorescence micrographs of V79 fibroblasts incubated for 30 min at 37 °C with phosphatidylcholine vesicles containing NBD-PC in which the fluorescent lipid in the vesicle was (a) restricted to the inner leaflet, or (b) present on both leaflets of the vesicle bilayer.

high vesicle concentrations vesicle-cell adsorption predominates over fusion. Experiments using fluorescence energy transfer to examine the concentration dependence of adsorption vs. fusion are in progress.

Lipid Capping in Lymphocytes

A. J. Schroit

We have previously shown it possible to integrate haptenated phospholipids into the plasma membrane of Chinese hamster fibroblasts and lymphocytes by transfer of the lipid from small unilamellar vesicles (liposomes). We have also shown that the incorporated phospholipid, N-2,4,6 trinitrobenzyldioleoylphosphatidylethanolamine (Tnp-DOPE), spontaneously caps in lymphocytes (*Year Book 78*) and undergoes an antibody-mediated redistribution in the presence of divalent anti-hapten antibodies in fibroblasts (*Year Book 77*).

This year these studies have been extended to other phospholipid analogs, in particular to lipids that do not contain the Tnp hapten, in order to determine whether this group may have been responsible for the capping phenomena in lymphocytes. In order to follow the fate of exogenously supplied lipids in the lymphocyte membrane we have prepared phospholipid vesicles containing 5% 1-acyl-2-(N-4-nitrobenzo-2-oxa-1,3-diazole)-aminocaproyl phosphatidylcholine (NBD-PC), a fluorescent phospholipid analog, and 95% dioleoylphosphatidylcholine (DOPC).

When DOPC vesicles containing NBD-PC are incubated with EL-4 lymphoma cells at 2 °C, a bright peripheral ring of fluorescence is seen when the cells are examined under the fluorescence microscope (Fig. 20a). The ring of fluorescence is stable and persists for

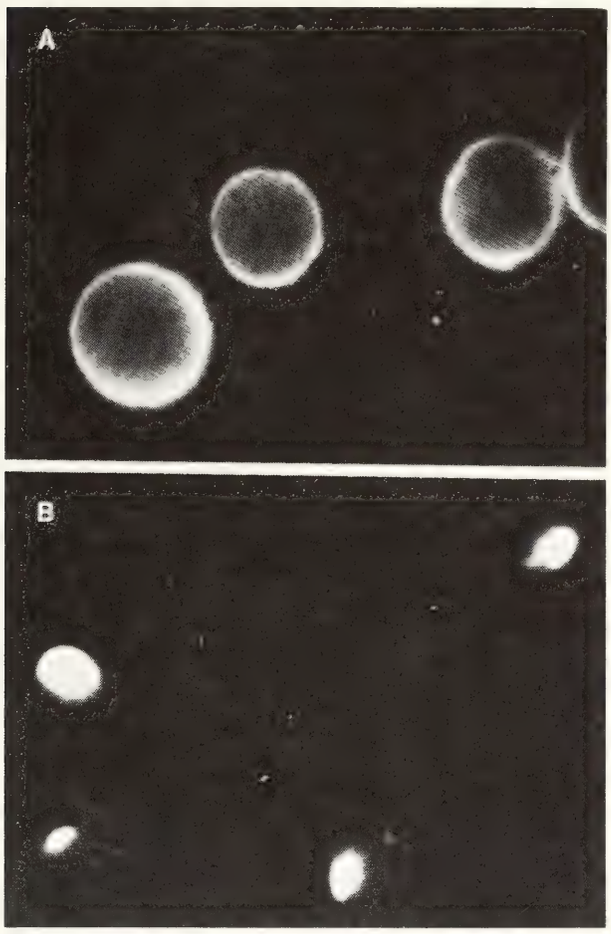


Fig. 20. Redistribution of NBD-PC in EL-4 cells. Cells were treated with NBD-PC containing vesicles for 60 min at 2°C. The cells were then (A) washed and photographed immediately, or (B) after a 20-min incubation at 37°C.

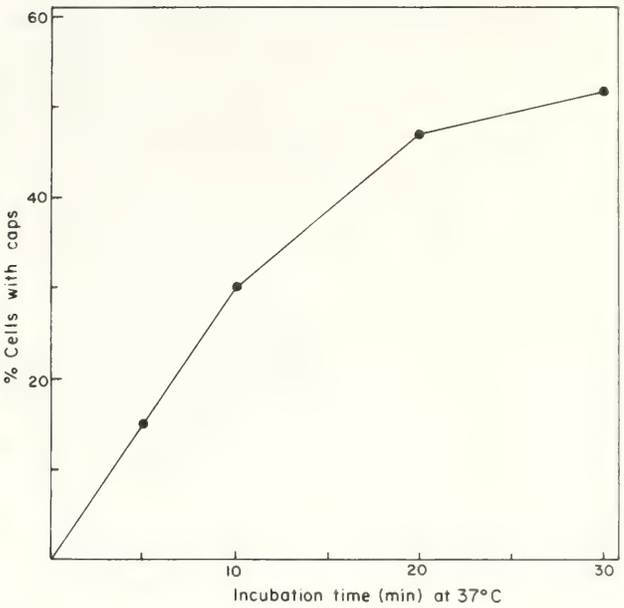


Fig. 21. Capping of NBD-PC in EL-4 cells. Cells treated with vesicles containing NBD-PC at 2°C were washed and subsequently incubated at 37°C for various periods. Percentage of capped cells was determined by counting ≥ 300 cells per point.

TABLE 2. Inhibition of NBD-PC Cap Formation by Various Drugs*

Treatment	% Caps
Control	52
2°C	0
NaN_3 (0.2%)	7
Cytochalasin B (10 μg/ml)	5
Colchicine (10^{-4} M)	53
Cytochalasin B (10 μg/ml) + Colchicine (10^{-4} M)	4

*Cells were labeled with NBD-PC containing vesicles at 2°C for 60 min. The cells were washed, suspended in the drugs for 5 min at 2°C, and then transferred to 37°C for 30 min. The cells were then chilled and scored.

several hours as long as the cells are maintained at 2°C. However, upon warming the cells to 37°C, the fluorescent ring was observed to slowly reorganize and finally form a cap at one pole of the cell surface (Fig. 20b). Approximately 50% of the cells exhibited fluorescent caps after 25-min incubation at 37°C, as shown by the kinetic studies in Figure 21. The capping of NBD-PC is inhibited by low temperature, sodium azide, and cytochalasin B (Table 2). Colchicine had no effect and the combination of cytochalasin B plus colchicine had no greater effect than cytochalasine B alone.

Several experiments were carried out to exclude the possibility that the NBD-PC caps were not artifacts arising from adherent vesicles. In the first experiment, fluorescence photobleaching recovery measurements were carried out on cells immediately following vesicle treatment. Using this technique, it was found that ~80% of the fluorescent lipid was initially mobile in the plane of the EL-4 plasma membrane with diffusion coefficients of ~ 4–6 × 10^{-9} cm^2/sec (Table 3). This result strongly suggests that the NBD-

TABLE 3. Diffusion of NBD-PC in EL-4 Cells*

First Bleach		Re-Bleach	
Diffusing Fraction	D ($cm^2/sec \times 10^9$)	Diffusing Fraction	D ($cm^2/sec \times 10^9$)
0.76 ±0.06	4.93 ±0.98	0.83 ±0.05	5.65 ±1.84

*Cells were labeled with NBD-PC containing vesicles at 2°C for 60 min. The cells were then washed, and fluorescence photobleaching recovery analysis was immediately carried out at 20°C. Values shown represent means ± SD.

PC associated with the EL-4 surface is able to rapidly diffuse immediately following vesicle-cell incubation. Based on previous experiments, we assume that if the NBD-PE were associated with the cell surface in the form of adherent vesicles, either there would be no recovery of fluorescence after photobleaching or the apparent diffusion coefficient would be considerably smaller than that observed.

Additional evidence against the association of intact vesicles with the EL-4 cell surface comes from the following experiment. Vesicles containing *both* NBD-PC and Tnp-DOPE were incubated with cells for 60 minutes at 2°C. The cells were then washed and treated with anti-Tnp IgG and TMR anti-IgG. As can be seen in Fig. 22, virtually all of the Tnp-DOPE was capped during the 5-min incubation period whereas the majority of the NBD-PC remained uniformly distributed on the cell surface. Further incubation of the cells at 37°C results in the capping of the NBD-PC as well. The finding that both lipid markers behave independently in the EL-4 plasma membrane indicates that the vesicles cannot be simply adhering to the cell surface since, if this were the case, one would expect both markers to simultaneously co-cap. This experiment also demonstrates that antibody-induced lipid capping is rapid compared to capping in the absence of antibody, and con-

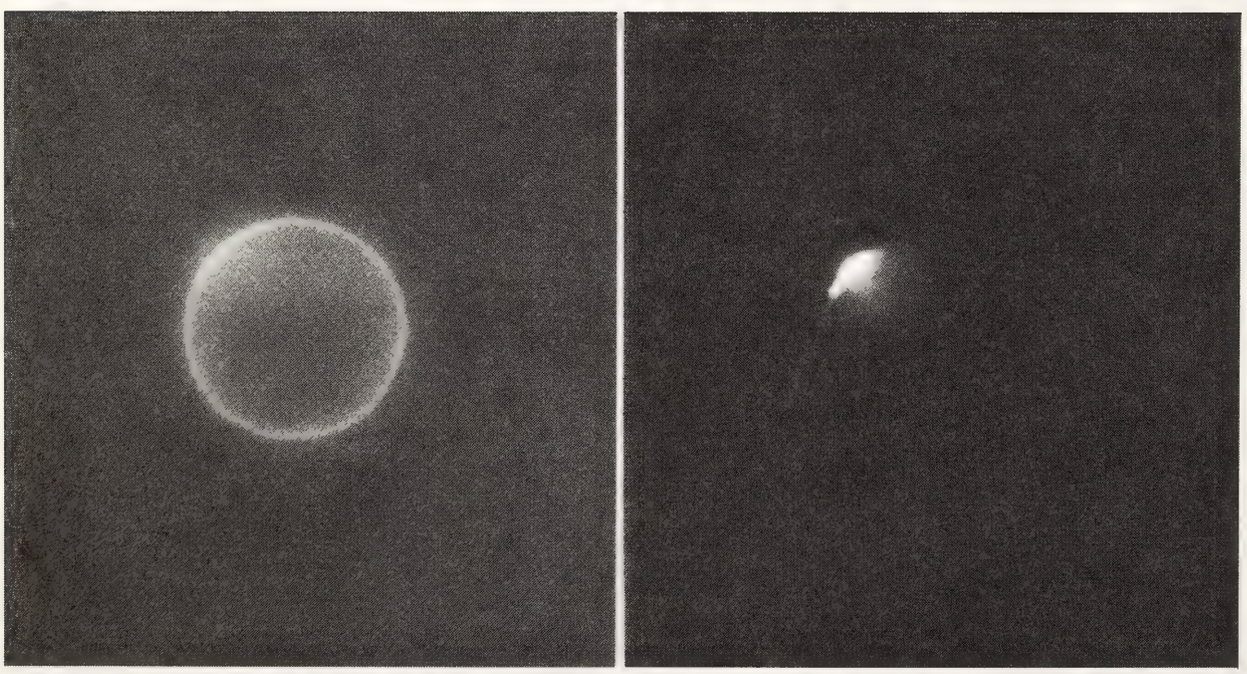


Fig. 22. Independent distribution of NBD-PC and Tnp-DOPE in EL-4 cells. Cells were treated with vesicles containing NBD-PC and Tnp-DOPE at 2°C. The cells were then washed, treated with anti-Tnp IgG at 2°C, and incubated at 37°C for 5 min. The cells were then chilled and stained with TMR anti-IgG at 2°C. (Left) NBD-PC, (right) TMR anti-IgG fluorescence of the same cell.

firms our observations on rapid and slow capping reported in *Year Book 78.*

It should be noted that detailed studies on the mechanism of vesicle-cell interactions at 2 °C have not been carried out on this system. Thus, while vesicle-cell exchange may be occurring in this system, other modes of vesicle association are also possible. In any event, it is clear from the data reported here, namely the fluorescence photobleaching recovery analysis and the independent behavior of Tnp-DOPE and NBD-PC at the cell surface, that these lipids cannot be present as adherent vesicles.

It is difficult to see just how a lipid molecule can be capped by the cells, as cross-linking does not appear to be required for this process. Furthermore, the sensitivity of the process to cytochalasin B suggests that microfilaments may play a role in this process. This result is surprising, since there is no known association between plasma membrane phospholipids and cytoskeletal structures. The molecular basis for the capping of NBD-PC is not yet known, and experiments are currently in progress to investigate several possibilities, including the lipid flow model of Bretscher.

GENETIC SPECIFICATION OF CELLULAR MORPHOLOGY

S. Ward, T. Roberts, D. Burke, G. Nelson, Y. Argon, B. Nathans, and E. Hogan

Our laboratory is trying to learn how the morphology of a cell is specified genetically. We would like to know how many gene products are directly involved in determining cell shape, how these gene products are localized to specific parts of the cell, and how the developmental sequence of morphogenesis is determined. Our approach to this problem is a genetic one: isolate a large number of mutants which affect the morphogenesis of a single cell type and analyze them anatomically and biochemically to learn about the normal function of the mutated gene. The cell that we have chosen to study is the sperm of the nematode *C. elegans (Year Book 77, 78).*

This year we have determined the sequence of morphogenetic events that generate the normal sperm by taking advantage of in vitro conditions for development and the discovery that the final steps of spermiogenesis could be triggered in vitro with the ionophore monensin. By analyzing the development of morphological defects in mutant sperm, we have shown that the individual events of morphogenesis proceed independently of one another. Study of the rearrangements of lectin receptors and membrane lipids during in vitro morphogenesis and during spermatozoan crawling has provided evidence for directed flow of membranes which could be the mechanism of spermatozoa movement. Improved methods for worm culture and sperm isolation have increased the yield and purity of sperm available for biochemical analysis. This has enabled us to find a small amount of actin in the sperm.

The Ionophore Monensin Triggers Spermiogenesis in vitro

G. A. Nelson and S. Ward

We reported in *Year Book 78* that the ionophore monensin, which transports monovalent ions into cells, will cause the activation of sessile spermatids to motile spermatozoa. By examining cells during the process of activation, we have been able to describe the sequence of morphogenetic events that generate mature spermatozoa. These are shown by scanning electron micro-

scopy and transmission electron microscopy in Figs. 23 and 24. About two minutes after exposure to submicromolar concentration of monensin, spermatids begin to rotate. At this time SEM examination shows that the microvilli which dot the spermatid surface have begun to coalesce and rearrange to one side of the cell. During this rearrangement, membranous organelles fuse with the plasma membrane at the back end of the cell where all the cytoplasmic organelles accumulate. Three to five minutes after exposure to monensin the pseudopod begins to form from the region where microvilli accumulate, and within 1–20 seconds it extends to its full length. Movements in the pseudopod are detectable as soon as it begins to extend.

This sequence of morphogenetic events in vitro corresponds precisely to that described from examination of in vivo intermediates. The time required for pseudopod extension is the same in vitro as in vivo. The motility of monensin-activated spermatozoa is indistinguishable from that of normally activated spermatozoa. Therefore we are confident that the in vitro activation faithfully mimics the in vivo process. We suspect that monensin acts by causing an influx of sodium ions into the cell, an event normally triggered by a male accesory gland secretion. Sperm of two mutants, *fer-5* and *fer-15*, fail to respond to either the natural trigger for activation or monensin.

The Development of Wild-Type and Mutant Sperm

S. Ward, G. A. Nelson, and Y. Argon

Our understanding of the normal process of sperm morphogenesis, based on scanning and transmission electron microscopy, is diagrammed in Figure 25. The primary spermatocyte buds off the central core of the testes while in pachytene of meiosis I (Fig. 25a, b). Some spermatocytes continue devel-

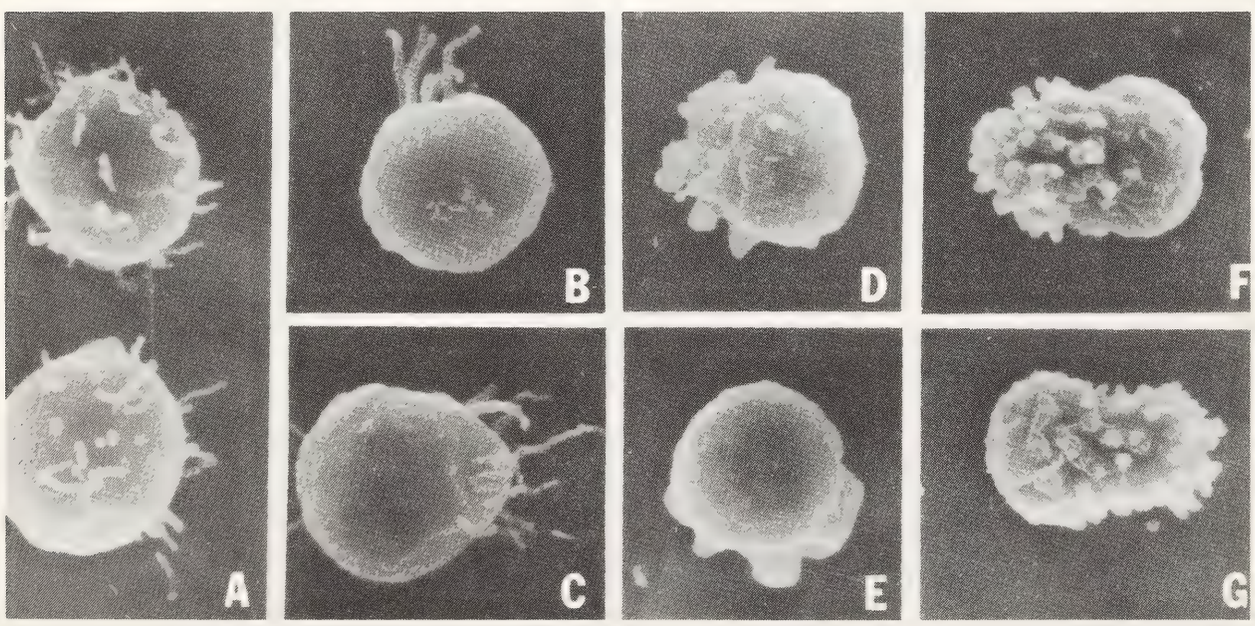


Fig. 23. Scanning electron micrographs of wild-type sperm fixed at various times after monensin treatment. (A) Two spermatids fixed immediately after dissection into sperm medium with 5×10^{-7} M ionophore are dotted by numerous microvilli. (B–E) Sperm fixed 4 min after ionophore activation. In (B) and (C), microvilli are clustered at one pole of the cell. In (D) and (E), microvilli have been cleared from the cell surface, and pseudopodia have begun to extend from the cell bodies. (F and G) Sperm fixed 12 min after monensin treatment display large pseudopodia covered by numerous pseudopodial projections. Magnification 6000×.

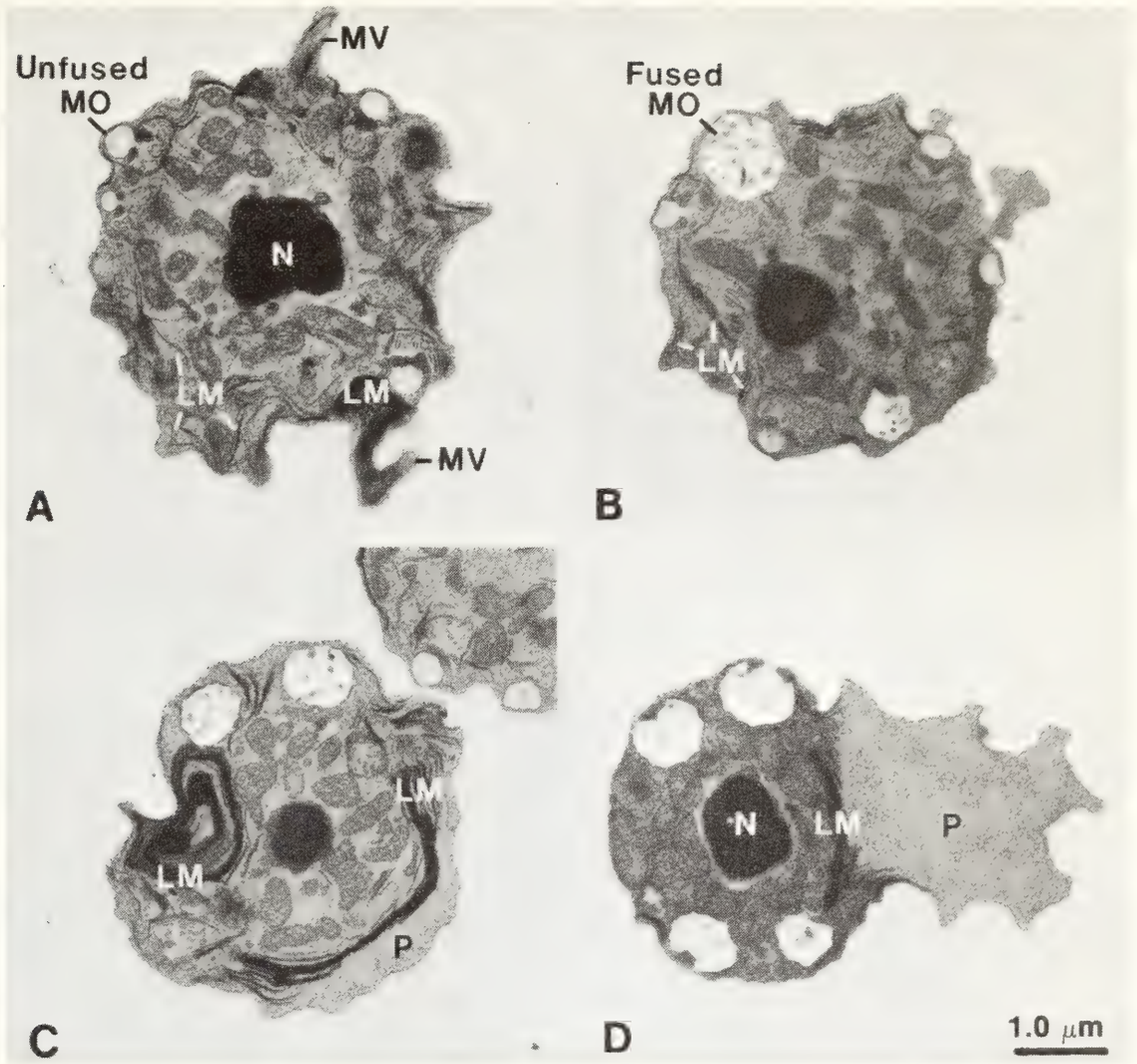


Fig. 24. Transmission electron micrographs of monensin-treated spermatids in the process of activation. (A) 2 min; (B and C) 6 min; (D) 9 min. (MO) Membranous organelle; (MV) microvillus; (LM) laminar membrane; (N) nucleus; (P) pseudopod. Note in (B) that MO fusion has preceded pseudopod formation. The opaque appearance of the laminar membranes is due to preferential binding of lead ions during staining. Magnification 14,000×; bar = 1 μm.

opment in vitro and the successive stages of development have been followed both in vitro and in vivo. The nucleus of the spermatocyte divides with a conventional spindle of microtubules and the two diploid nuclei segregate (Fig. 25c). Cytokinesis is often incomplete at this division, so both secondary spermatocytes remain joined by a cytoplasmic bridge. The nuclei divide again without chromatin decondensation and segregate to the corners of the cell without aid of a spindle (Fig. 25d). As these nuclei separate, the cytoplasm of the secondary spermatocytes begins to segregate. Ribosomes, endoplasmic reticulum, and Golgi complexes accumulate in the center; mitochondria and other organelles segregate to the periphery with the nuclei. The most prominent organelles in the sperm are the membranous organelles (MO) surrounding fibrous bodies. These arise from the Golgi complex in spermatogonia and early spermatocytes as a complex membrane enveloping a paracrystalline fibrous bundle. They grow as the sperm matures until they occupy 35% of the spermatid's volume. Some micro-

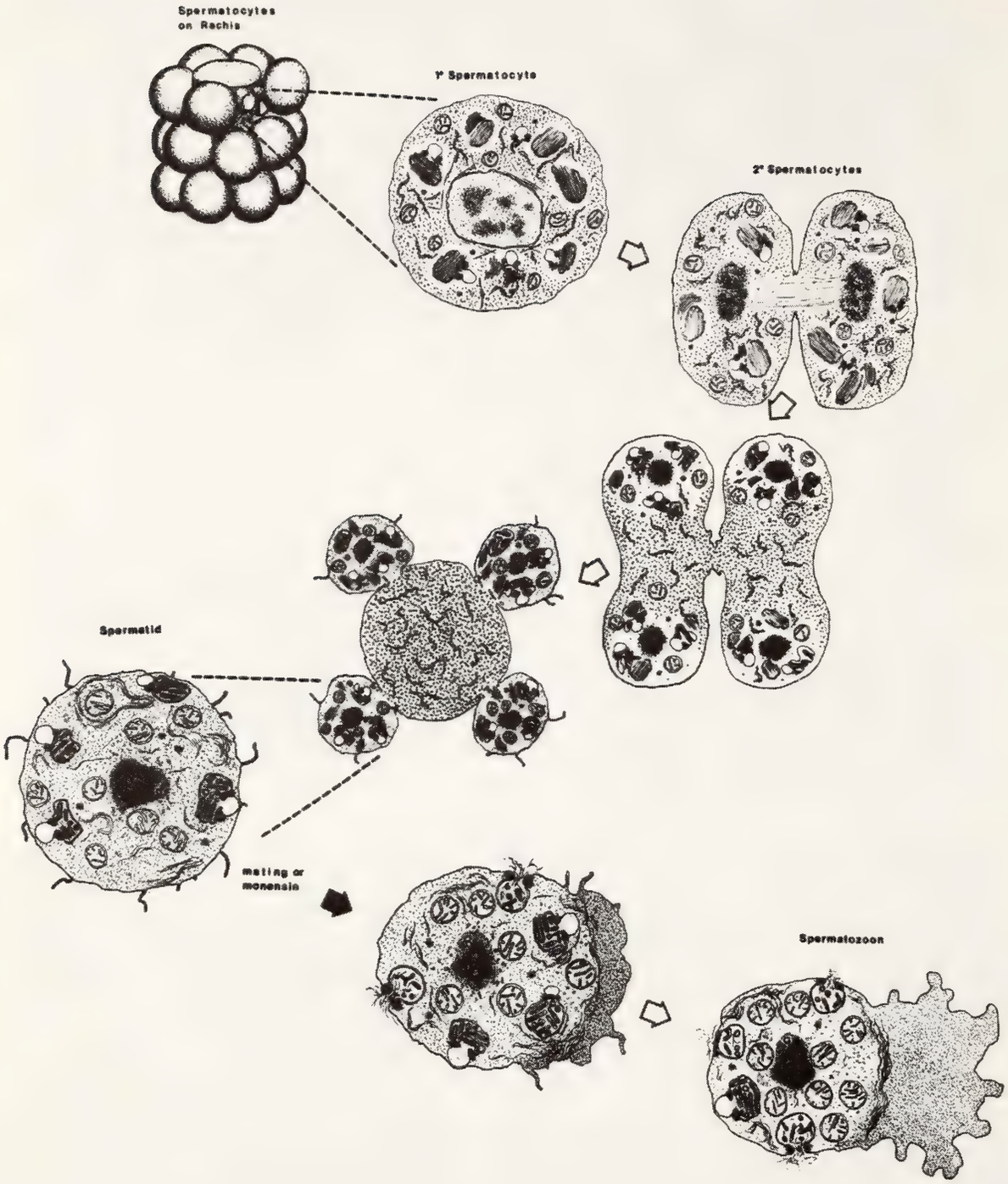


Fig. 25. Summary of sperm development. See text for explanation.

tubules are found associated with these complexes and may participate in their movement during development.

The spermatid forms around the haploid nucleus and separates from the central region of ribosomes and membranes by budding, leaving behind a residual body (Fig. 25e). Membranes form between the spermatid and residual body by fusion of cytoplasmic vesicles. As this budding proceeds, the spermatid nucleus completes its maturation by fully condensing its chromatin and forming an RNA-containing perinuclear halo which includes the sperm's centriole. While the nucleus completes its maturation the MO membrane separates from the fibrous body

and folds into a compact structure which then accumulates against the cell membrane. The fibrous body dissociates and apparently distributes its fibers to the cytoplasm in amorphous form. Microvilli form on the surface of the spermatid just before it buds. After budding, the spermatid continues some maturation and then arrests its development awaiting the final trigger to mature to a spermatozoon (Fig. 25f), as described in the previous report (Fig. 25g, h).

Our description of sperm morphogenesis subdivides the whole process into events and structures we recognize as separate in the electron microscope. Such subdivision is essential if we hope to reduce the apparent complexity of morphogenesis to an understandable level; but the biological problem is to understand the relation between individual events and to learn how the genes controlling morphogenesis subdivide the process. The development of morphological defects in five *fer* mutants suggests a striking answer. Most individual events appear to be causally and genetically independent of each other. The strict sequence of morphogenetic events occurring in wild-type does not arise because each step depends on previous steps. For example, MO fusion does not occur in *fer-1* mutant sperm, yet the pseudopod forms. MO fusion does occur in *fer-2* mutant sperm, yet the pseudopod does not form in most of the sperm (*Year Book 78*). Therefore pseudopod formation and MO fusion are independent morphogenetic events. In *fer-2*, *fer-3*, and *fer-4* mutant sperm the perinuclear halo is aberrant, yet in all of these MO fusion occurs and, in *fer-3*, the pseudopod is usually normal. In *fer-5* mutant sperm, the MO membrane pulls away from the fibrous bundles, yet these bundles fail to dissociate and remain clustered in the cytoplasm. Thus these two events are separately controlled.

The small set of mutants analyzed so far suggests that one of the principles of genetic control of virus assembly applies to cells as well—the principle of subassembly. Thus the morphogenesis of a cell is like the construction of a prefabricated house: Parts already assembled are joined together rather than built all at once from individual gene products. The problem of genetic control of cell morphogenesis can then be separated into the genetic control of individual organelle construction and the genetic control of organelle movements and interactions.

Actin in Sperm

S. Ward, E. Hogan, and T. Roberts

In order to pursue the biochemical analysis of mutant and wild-type sperm, we have improved culture conditions for worm growth by increasing aeration and preventing contamination and have improved the methods for isolation of sperm from males. We now routinely obtain 10^8 sperm from a 200-ml culture of worms, and larger cultures can be grown if desired. Our previous studies showed that although present in all other amoeboid cells, actin was not a major sperm component (*Year Book 78*). With more material available for assay and more sensitive methods for identifying proteins after gel fractionation, we now find that the sperm do have a protein with the same molecular weight (42,000) and isoelectric point (pI=5.6) as worm muscle actin. Quantitation of gels of sperm proteins show that this presumed actin is only 0.02% of the sperm's total protein, thus explaining why we had difficulty detecting it previously. Indirect immunofluorescent staining of spermatozoa showed that this actin is located in the sperm pseudopods. No microfilaments have been found there so this actin is apparently in a nonfilamentous form. We do not know how the actin participates in cell motility, if it participates at all.

Membrane Mobility in Nematode Sperm

T. Roberts and S. Ward

When a *C. elegans* spermatid differentiates into a spermatozoon, it acquires distinct morphological asymmetry (see above; *Year Book 77, 78*). The pseudopod is covered by numerous projections which appear to move centripetally from the tip of the pseudopod to its junction with the cell body and then disappear. In contrast, the surface of the cell body appears immobile. Thus the morphogenesis of the spermatozoon creates an asymmetry in behavior of plasma membrane components. Because the acquisition of this asymmetry can be triggered in vitro, we can answer several questions about the behavior of membrane components during differentiation: Where does the pseudopodal membrane come from? Does the apparent movement of the pseudopodial projections reflect actual membrane flow? Does membrane movement occur only on the pseudopod and not on the cell body?

To answer the first of these questions, we exposed spermatids to rhodamine-conjugated wheat germ agglutinin (RITC-WGA) or soybean agglutinin (RITC-SBA), washed away all unbound lectin, and activated the cells with monensin. A ring of fluorescence was observed on spermatids (Fig. 26a), indicating that lectin was bound to the plasma membrane and excluded from the cytoplasm. When these cells first formed pseudopods, the ring of fluorescence encircled both the pseudopod and the cell body (Fig. 26a). This shows that the pseudopod membrane derives, at least in part, from the plasma membrane of the spermatid. About one minute after pseudopod formation the distribution of lectin receptors changed dramatically; the cell body remained stained while the fluorescence on the pseudopod decreased markedly (Fig. 26b). This asymmetric pattern was observed with both lectins tested, but was more striking using RITC-SBA (compare Fig. 26b and Fig. 26c).

Better resolution and quantitative analysis of the redistribution of lectin

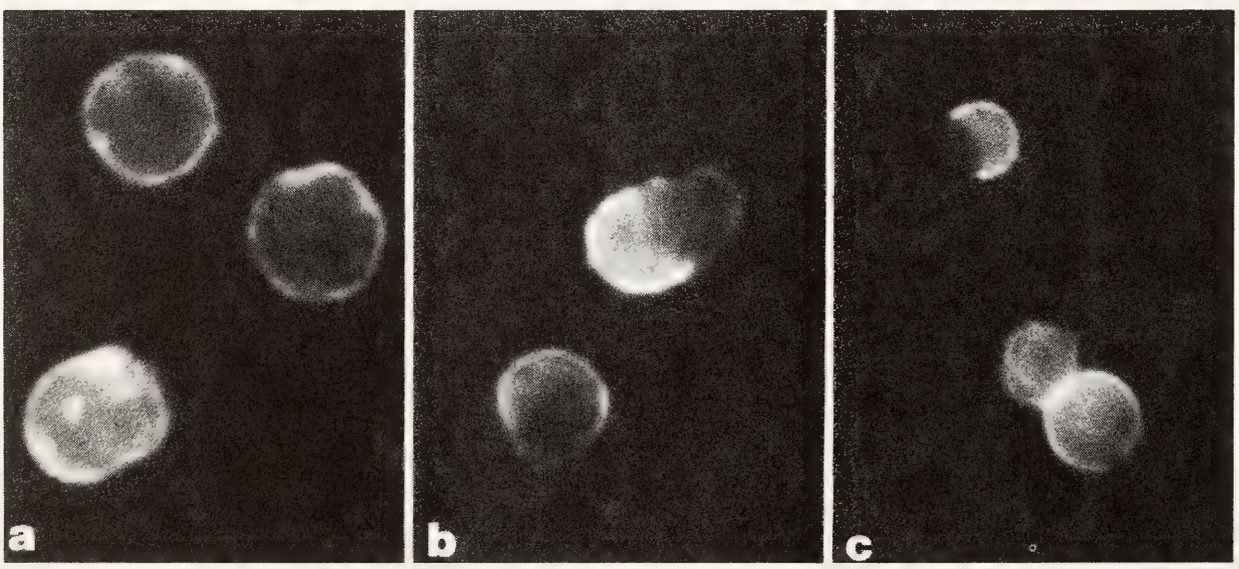


Fig. 26. Spermatids and spermatozoa stained with rhodamine-conjugated lectins. Nearly spherical cells are spermatids, others are spermatozoa. (a) Cells stained with RITC-WGA. The spermatozoon formed a pseudopod five seconds before being photographed. (b) Spermatozoon stained with RITC-WGA and photographed 60 seconds after forming a pseudopod. (c) Two spermatids (lower right) and a spermatozoon stained with RITC-SBA.

receptors during morphogenesis have been obtained by incubating spermatids with biotinylated lectin followed by ferritin-conjugated avidin. Thus, by taking advantage of the high affinity binding between biotin and avidin we are able to indirectly label membrane lectin receptors with electron-dense ferritin molecules. After monensin activation, cells were fixed and processed for electron microscopy. Cells fixed just after pseudopod formation had nearly equal densities of ferritin grains on their cell body and pseudopod (the ferritin density on spermatids and on the cell body of spermatozoa was also the same). Clearance of lectin receptors from the pseudopods began at the tips of the projections and proceeded until nearly all ferritin was removed from the surface of the pseudopod. Concomitantly, ferritin density increased at the junction between the cell body and the pseudopod. As lectin receptors were cleared from the pseudopod, the density of ferritin on the cell body remained stable. We did not observe any ferritin within the cytoplasm or within any internal membranes.

We repeated this experiment using a fluorescent phospholipid analogue instead of lectins as the probe. This probe has two advantages over lectins. First, we are able to assess the behavior of a different class of membrane components—lipids rather than glycoproteins. Second, the lipid inserts directly into the membrane thus eliminating the possibility of receptor cross-linkage and ligand-induced redistribution that might be encountered with lectins. To label the cells, we incubated spermatids on ice with lipid vesicles comprising 1-acyl-2-(N-4-nitrobenzo-2-oxa-1,3-diazole) and aminocaproylphosphatidylcholine (NBD-PC). Under these conditions, the vesicles fuse with the plasma membrane (see Pagano *et al., Year Book 78*), resulting in spermatids that exhibit a uniform ring of fluorescence. Following monensin treatment, the fluorescent probe revealed that just after pseudopod formation the cell's entire surface membrane was uniformly labeled and that over the next 1–2 minutes the intensity of fluorescence in the pseudopod membrane diminished, resulting in an asymmetrically stained spermatozoon. During this time the cell body membrane retained its fluorescence. Two observations indicate that the fluorescent lipid is cleared from the surface of the pseudopod by membrane mobility rather than cytoplasmic uptake. First, the cell body membrane remains labeled as the intensity of fluorescence on the pseudopod diminishes. Second, we only observed cytoplasmic fluorescence more than 15 minutes after the establishment of asymmetric membrane staining. Therefore, we observed the same pattern and timing of membrane redistribution with a lipid probe, which inserts directly into the membrane, as with lectins. In both cases, redistribution began only after pseudopod formation and involved selectively removing the probe from the surface of the pseudopod without altering the distribution on the cell body. These results reveal the behavior of the surface membrane during morphogenesis.

Does membrane mobility continue on mature spermatozoa? To answer this question, we exposed spermatozoa to positively charged polystyrene spheres. These 0.5-μm beads bound to both the cell body and the pseudopod but behaved very differently on these two parts of the cell. Microspheres attaching to the pseudopod were immediately transported toward the cell body and stopped moving when they reached the base of the pseudopod (Fig. 27). The beads invariably accumulated at the junction of the pseudopod and cell body, and never moved further onto the cell body or back onto the pseudopod. Microspheres attaching to the cell body never moved at all. Therefore, the movement of polystyrene beads exactly mimics the movement of pseudopodal projections both in speed

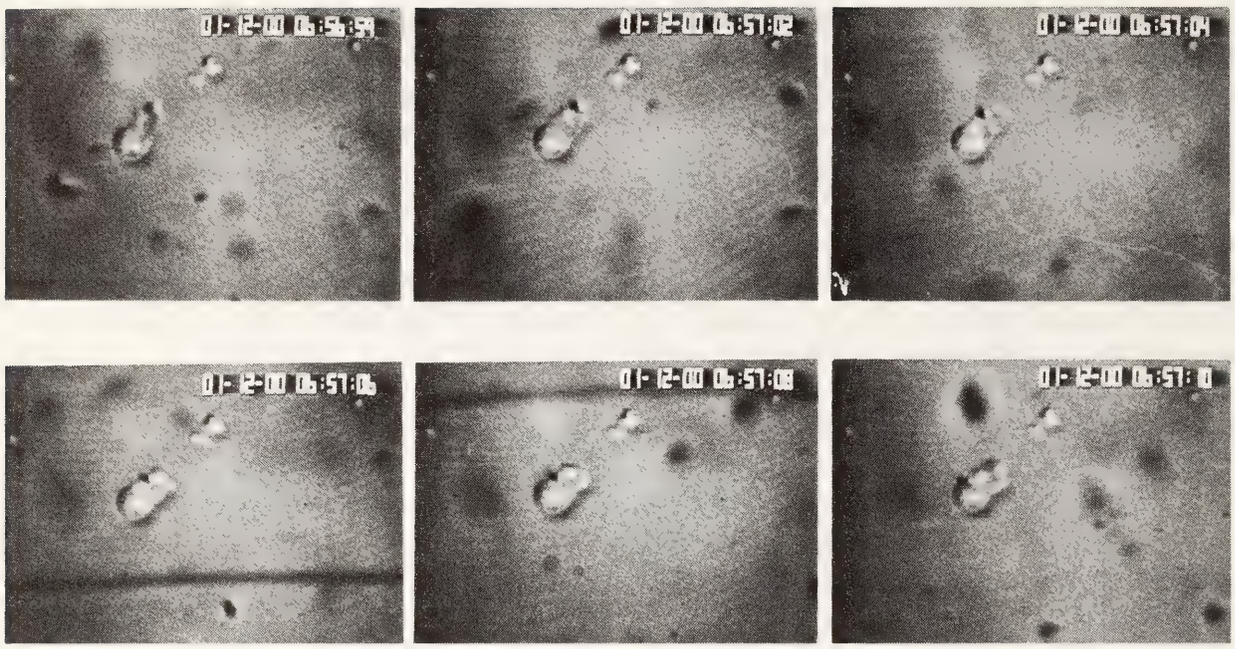


Fig. 27. Sequence showing the movement of a positively charged polystyrene microsphere on the pseudopod of a spermatozoan. First frame taken as the head attached to the cell; last frame taken when the head stopped moving. Elapsed time = 11 seconds.

and direction of movement and in restriction of movement to the pseudopod.

Results with all of our probes indicate that membrane movement is unidirectional from the tip of the pseudopod toward its base. If this is so, new membrane must be inserted into the surface of the pseudopod and this insertion must be coupled to membrane uptake.

We have used lectins to detect insertion of new pseudopodal membrane. Spermatids were incubated in unlabeled WGA, thus blocking all WGA receptors. After washing, monensin treatment, and pseudopod formation, the cells were pulsed for 30 seconds with RITC-WGA to detect newly inserted WGA receptors. Very faint fluorescence was observed on spermatids as well as on the cell body and proximal portion of pseudopods of spermatozoa. Significantly, bright areas of fluorescence, presumably indicating new lectin receptors appearing during insertion of new membrane, were localized in a single discrete portion of the cell—at the tip of the pseudopod (Fig. 28).

If new membrane is inserted at the tip of the pseudopod, flows over the surface, and fails to move onto the cell body, what is its fate? We suspect that cytoplasmic structures known as laminar membranes (*Year Book 78*) may serve as a "sink" for taking up the mobile pseudopodal membrane. These laminar membranes are distributed throughout the cytoplasm of spermatids; however, during differentiation they localize in the cytoplasm at the junction between the cell body and the pseudopod. Thus, these membranes lie just underneath the portion of the surface membrane where we observed accumulation of microspheres and lectin-bound ferritin grains. While we have not detected connections between these membranes and the plasma membrane, one line of evidence suggests that membrane initially on the surface of the cell can be detected in the laminar membranes. Spermatozoa were treated with horseradish peroxi-

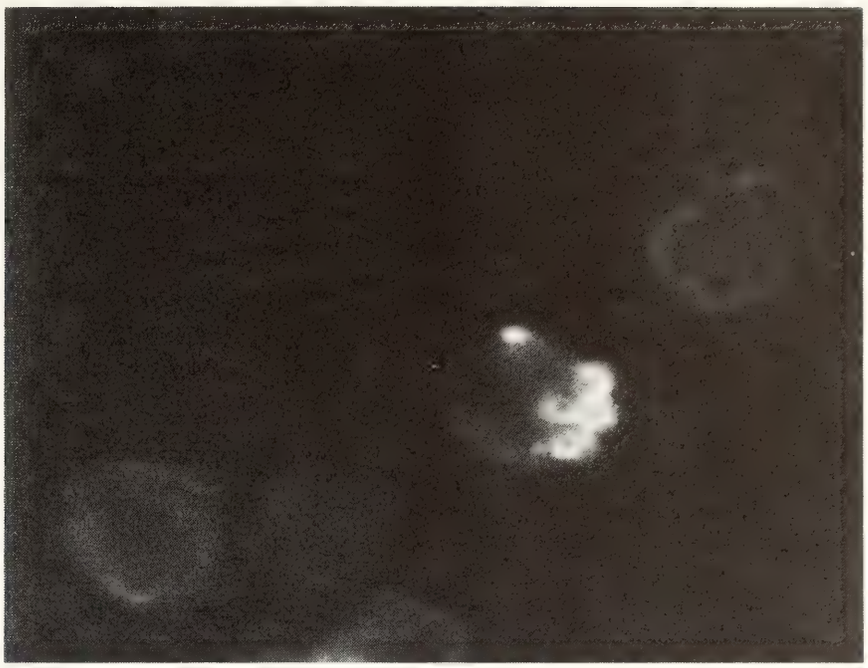


Fig. 28. Cells pulse-labeled with RITC-WGA. (See text for explanation of procedure.) Bright area at the tip of the pseudopod of the spermatozoon indicates the region bearing newly inserted WGA receptors. Other cells in the field are spermatids.

dase (HRP), washed, and fixed. After sectioning for transmission EM and appropriate histochemical techniques, the HRP reaction product was detected over the entire surface of the cell as well as on the laminar membranes. The reaction product was not seen on any membrane-bound cytoplasmic organelles; this condition serves as an internal control, indicating that HRP did not reach the laminar membranes via general uptake into the cell. Rather, these results suggest that membrane initially on the surface of the cell is somehow transported to the cytoplasmic laminar membranes. This supports our hypothesis that the laminar membranes function as the sink for pseudopodal membrane flow.

In summary, the morphological asymmetry of *C. elegans* spermatozoa is accomplished by asymmetric mobility of the surface membrane. This mobility, which includes both lipid and glycoprotein membrane components, involves insertion of membrane at the tip of the pseudopod, unidirectional, centripetal movement restricted to the surface of the pseudopod, and apparent uptake into cytoplasmic laminar membrane located at the cell body-pseudopod junction.

EXPRESSION OF ANTIBODY VARIABLE AND CONSTANT REGIONS DURING THE IMMUNE RESPONSE

P. Gearhart and N. Nivera

A unique feature of the immune response to an antigen is the production of many different antibody molecules which all bind specifically to the antigen. Antibodies are composed of a pair of heavy (H) and light (L) polypeptide chains, and each chain consists of a variable (V) region and a constant (C) region. Both the V region of the H chain (V_H) and the V region of the L chain (V_L) combine to form the site which reacts with antigen. The induction of an antibody response results from the selection and triggering by antigen of B lymphocytes bearing immunoglobulin receptors. An activated B cell produces a clone of cells which secretes antibody with one V_H region and one V_L region. A knowledge of the structural diversity of V regions binding to an antigen is essential in order to understand the genetic basis of diversity, the developmental control of antibodies during ontogeny, and the regulation of lymphocyte stimulation during an immune response. We have focused on determining the diversity in amino acid sequences of antibodies from BALB/c mice that bind to phosphorylcholine (PC), for the following reasons. First, the antibody response is relatively restricted, and variability in V_H and V_L regions could be analyzed more easily than it could in a heterogeneous population of antibodies. Second, since approximately half of the anti-PC antibodies possess a V-region marker called an idiotype in common with the T15 myeloma protein, antibodies with and without this idiotype could be selected and the diversity in each pool could be analyzed. Third, the amino acid sequences for several myeloma proteins that bind PC are known and can provide a basis of comparison for sequences of normal antibodies. The NH_2-terminal amino acid sequences of anti-PC antibodies have revealed much diversity in a group of antibodies that were originally thought to be homogeneous. These findings suggest that the antibody response is extremely diverse in an inbred strain and emphasize the importance of understanding how B cells can generate a vast array of different antibody-combining sites from germline genetic information.

In addition to the large number of V regions, the murine H-chain locus has several genes which code for C regions (C_H). One V_H region can be expressed together with different C_H regions to form antibodies with different immunoglobulin classes, e.g., IgM, IgD, IgG, IgA, and IgE. The mechanisms by which B cells differentiate and mature into antibody-secreting cells include a novel feature, namely, a switching of the expression of immunoglobulin classes. Although daughter cells of B lymphocytes can be observed to express different classes in vitro, it is not known how versatile a single cell or a proliferating line of cells within a clone can be in expressing different classes simultaneously or sequentially. In this report, we have analyzed immunoglobulin class expression during intraclonal differentiation by assaying the daughter cells that are derived from individual B cells. Using staining techniques to identify IgM, IgG1, and IgA antibodies in the cytoplasm of cells, we have sought to determine (1) if cells contain one or two H-chain classes, (2) if a cell line can switch expression of classes twice, and (3) if there must be a stepwise sequence of expression of IgM followed by IgG1 followed by IgA within a clone of cells. Assuming that the gene coding for the IgA C_H region is the last gene in the

gene cluster coding for H-chain classes, we have proposed a model of successive, but not necessarily stepwise, switching of immunoglobulin classes within B-cell lines, leading to the eventual accumulation of cells expressing IgA.

Diversity in the V Regions of Anti-PC Antibodies

Anti-PC antibodies were generated by immunizing BALB/c mice with PC and fusing the spleen cells with SP2/0-Ag 14 tumor cells to produce hybridoma cells. Hybridoma cells secreting anti-PC antibodies were also obtained from J. Hurwitz, Johns Hopkins University, and J. Davie, Washington University. Hybridoma cells were grown as ascites in mice, and antibody in the ascites fluids was purified on a PC-Sepharose column and eluted with PC. The NH_2-terminal amino acid sequences of H and L chains were determined by Nelson Johnson and Leroy Hood, California Institute of Technology. Antibody V_H regions with the same sequence or differing by one to three amino acids over the first 27 residues are classified as members of a single group. As seen in Fig. 29, the sequences of all 16 anti-PC hybridoma V_H regions and five myeloma V_H regions belong to one group. Ten of the hybridoma H chains show no differences when compared to T15, five H chains (G5, G6, G9, G10, and G16) differ by one single-base substitution, and one H chain (G14) has five one-base and one two-base changes. The substitutions in the proteins can either be within or without the first hypervariable region, which is involved in the antigen-combining site. The only amino acid identical in all the PC-binding hybridoma and myeloma pro-

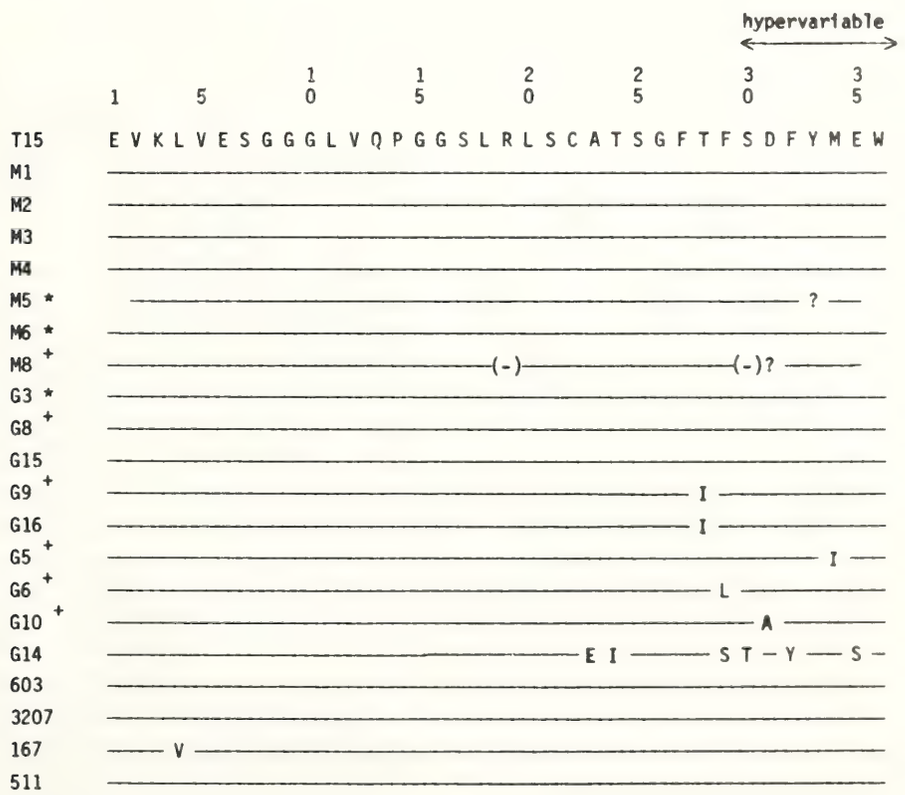


Fig. 29. V_H region sequences of anti-PC antibodies. M1 through G16 proteins are produced by BALB/c hybridoma cells. The sequences of T15, 603, 3207, 167, and 511 myeloma proteins have been published elsewhere. Asterisks mark antibodies derived from a single mouse; crosses mark antibodies derived from a separate mouse. All other antibodies were derived from individual mice.

teins is tyrosine at residue 33, which has been shown to be in direct contact with PC. The sequences of V_L regions of anti-PC myeloma proteins belong to three groups: the T15 group, 603 group, and 167 group. The groups differ by 45–60% from each other over the first 37 residues and by only one to a few residues within a group. It can be seen in Fig. 30 that the 16 hybridoma sequences fall into these three groups. Substitutions from the prototype sequence are found within and without the first hypervariable region. Whole antibody molecules were then examined to determine how the variability in V_H and V_L region sequences affected idiotypic determinants and affinity for PC. The data in Table 4 indicate that anti-PC antibodies are found with the μ, $\gamma 1$, and $\gamma 3$ C_H regions, and with and without the T15 idiotype. The results show three important findings.

(1) Antibodies with the same idiotype are not homogeneous. M1, M2, and M5 antibodies, which have the T15 idiotype, have identical V_H and V_L NH_2-terminal sequences, but G3, G9, and G16 antibodies, which also have the T15 idiotype, have different V_H and V_L region sequences from T15. The frequency of B cells that produce antibody with the T15 idiotype has been estimated at one per 75,000 B cells; this pool must now be considered to contain at least three types of B cells. Although heterologous anti-T15 antisera cannot distinguish between these antibodies, it is possible that monoclonal anti-idiotype antibodies or autologous anti-idiotype antibodies generated by the mouse itself may discriminate among the populations.

(2) Combinatorial pairing of H and L chains forms new binding sites. Because both the H and L chains form the

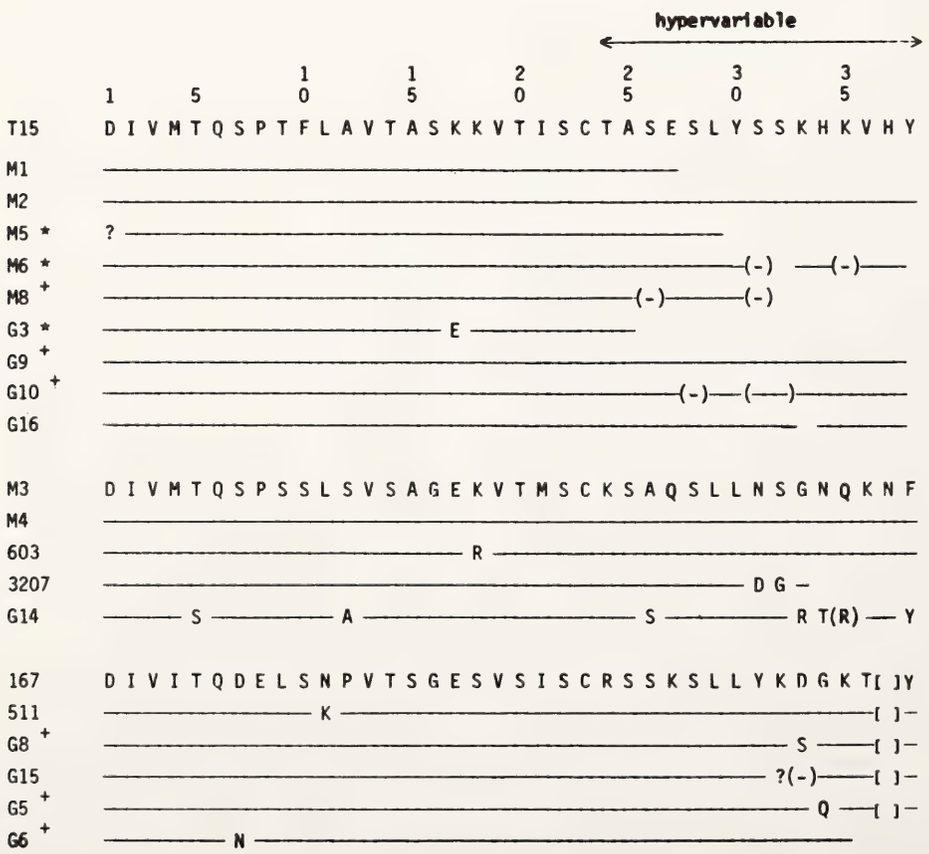


Fig. 30. V_L region sequences of anti-PC antibodies. The prototype sequence is shown for the T15 group, the 603 group, and the 167 group. Asterisks and crosses, same as Fig. 29.

TABLE 4. C_H Region, Idiotype, and Affinity of BALB/c Anti-PC Antibodies

Antibodies	C_H Region	T15 Idiotype	$K_a \times 10^5\ M^{-1}$ for PC 25°C
T15-V_H group and T15-V_L group			
M1	μ	+	...
M2	μ	+	3.5
M5	μ	+	2.4
M6	μ	−	...
M8	μ	−	3.2
G3	γ^3	+	1.3
G9	γ^3	+	...
G16	γ^3	+	...
G10	γ^1	−	4.4
T15	α	+	4.3
T15-V_H group and 603-V_L group			
M3	μ	−	0.34
M4	μ	−	...
G14	γ^1	−	0.13
3207	α	−	2.5
T15-V_H group and 167-V_L group			
G5	γ^3	−	0.25
G8	γ^3	−	...
G6	γ^1	−	1.8
G15	γ^1	−	1.0
167	α	−	1.9

antibody-combining site, it has been predicted that animals could form new combining sites by pairing different H and L chains. An example of combinatorial pairing of H and L chains is found in M2 and M3 proteins. The H chains of M2 and M3 have been completely sequenced and their V_H regions are found to be identical, although the antibody molecules contain entirely different L chains. The mixing of L chains with a single H chain by M2 and M3 has created binding sites with different affinities for PC (Table 4). Nevertheless, the contribution of combinatorial pairing to antibody diversity must be considered with caution, since there is no current evidence that it generates binding sites for diverse antigens.

(3) IgG antibodies are more diverse than IgM antibodies. Eight out of nine IgG proteins differed from the prototype T15-V_H sequence, the T15-V_L sequence, the 603-V_L sequence, or the 167-V_L sequence. However, all of the seven IgM proteins were identical to the prototype sequences. The difference in V-region diversity between IgM and IgG antibodies may be explained if the IgM hybridoma antibodies were derived from nonimmune B cells, and the IgG hybridoma antibodies were derived from immune B cells. Since immune B cells persist longer than nonimmune B cells, they may be under more selective pressures by antigen, T cells, or anti-idiotype than nonimmune cells. The role of antigen in selection is not clear, since there is no evidence in Table 4 that the IgG antibodies have been selected on the basis of higher affinity for antigen than IgM antibodies. However, it is possible that the IgG antibodies may have a higher affinity for a larger determinant containing PC than for the hapten itself.

Successive Switching of Heavy Chain Classes Expressed with the Cell Lines of a B-Cell Clone

In collaboration with Julia Hurwitz and John Cebra at the Johns Hopkins University, we have examined the sequence of H-chain class expression by proliferating cell lines within a clone by directly staining for immunoglobulin in the cytoplasm of clonal daughter cells. B-cell differentiation and maturation into antibody-secreting cells was studied in vitro by using splenic fragment cultures that permit clonal growth. All of the clones selected for analysis originally secreted IgM as well as other immunoglobulin classes, as determined by radioimmunoassay of culture fluids. The results of cell staining (Table 5) showed (1) at least 25% of the cells contained more than one H-chain class, indicating that cells can switch expression of classes during clonal expansion, (2) some cells contained both IgM and IgA without detectable IgG1, and some cells contained

TABLE 5. Cytoplasmic Staining of Cells from Clones Secreting Anti-PC Antibody*

	No. of Cells (% of Total)	
	Day 7	Day 12
Clones stained for IgM and IgA		
IgM	17 (24)	27 (22)
IgA	12 (17)	31 (25)
IgM and IgA	18 (26)	16 (13)
Neither	23 (33)	49 (40)
Clones stained for IgG1 and IgA		
IgG1	24 (24)	49 (22)
IgA	13 (13)	60 (26)
IgG1 and IgA	18 (18)	77 (34)
Neither	45 (45)	41 (18)

*Only cells that contained cytoplasmic anti-PC antibody were examined for isotype staining. Those cells staining for neither IgM nor IgA may contain IgG1, and those cells staining for neither IgG1 nor IgA may contain IgM. None of the clones secreted IgG2 or IgG3. IgE was not examined.

both IgM and IgG1 without detectable IgA (data not shown), suggesting that cells can switch from IgM directly to IgG1 or IgA, and (3) some cells contained both IgG1 and IgA, indicating that cell lines can undergo two successive switches from IgM to the IgG1 and IgA classes. A hypothetical model of H-chain class expression by a clone of cells derived from an antigen-stimulated B cell is presented in Fig. 31. A cell line within the clone is defined as the direct descendant of a precursor cell, so that by the fifth division there would be 16 cell lines with the clone. Cells may express two H-chain classes by containing long-lived mRNA and/or immunoglobulin protein from a previous V_H-C_H arrangement, and mRNA and protein from a current V_H-C_H arrangement.

The model predicts that at most points in time the clone would contain cells expressing a variety of immunoglobulin classes. The data in Table 5 show that the expression of different classes in the cytoplasm of cells is not synchronous; for example, at a given time point, some cells contained IgM, some cells contained IgA, some cells contained both IgM and IgA, and some cells contained neither IgM nor IgA. The nonsequential expression of secreted IgM, IgG1, and IgA antibodies by the clonal progeny of antigen-stimulated B cells as detected by radioimmunoassay of culture fluids has also been reported. If the switching events occur asynchronously within various cell lines of the clone, the temporal heterogeneity with respect

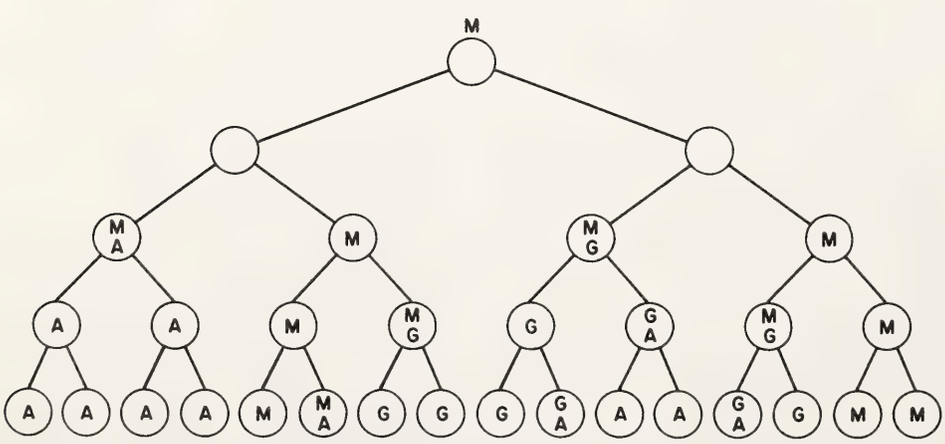


Fig. 31. Model of isotype switching with a clone. The first cell represents a B cell bearing membrane IgM and probably IgD; the daughter cells contain cytoplasmic IgM, IgG1, or IgA. The clone may divide at least 6–8 times. The cell products of the first few divisions are not known, nor is the proportion of clonal progeny maturing to antibody-secreting cells.

to class expression by the clone as a whole is expected.

Using myeloma cells, Honjo *et al.* (*Proc. Nat. Acad. Sci. USA, 75*, 2140, 1978) obtained experimental evidence that the expression of an H-chain class is accompanied by the irreversible deletion of the C_H genes proximal to the array of V_H genes. Their results suggest that the C_H gene order is μ, $\gamma 3$, $\gamma 1$, $\gamma 2b$, $\gamma 2a$, and α. We propose that H-chain switching can occur within a B-cell line any number of times until the potential to express IgA, the presumed last C_H gene, is achieved. The accumulation of B cells committed to IgA synthesis would require successive, vectorial but not necessarily stepwise, irreversible switches of C_H genes within a B-cell line. One reason why all clones do not secrete only IgA at later time points after stimulation may be that cells stop dividing in vitro before they have all switched to IgA. The model of successive switching within a B-cell line leading to the accumulation of cells committed to IgA expression may also occur in vivo among antigen-sensitive memory B cells in an environment that favors cell division without terminal maturation to plasma cells. We have postulated previously that the reason why mucosal follicles such as Peyer's patches contain an abundance of B cells committed to IgA synthesis is because the cells are specific for environmental antigens found in the gut. Constant stimulation by antigen would cause the B cells to divide repeatedly and switch H chains successively until the terminal C_H gene is expressed. The present report provides evidence consistent with such a conclusion, but the direct role of antigen in this process remains to be established.

MOLECULAR STUDIES ON THE CONTROLLING ELEMENTS OF MAIZE

N. Fedoroff, S. McCormick, and J. Mauvais

Controlling elements in maize are transposable genetic units capable of altering a gene's pattern of expression in development. The alteration is consequent on integration of the transposable element (or a cognate recognition sequence) in or near the gene. Transposable elements are known to effect changes of several kinds in the developmental profile of gene expression. They can displace or restrict the timing of gene expression, change its tissue specificity, or impose an alien spatial pattern of gene expression within a tissue type. Virtually all of the information presently available on controlling elements is genetic. The reader is referred to successive Year Books beginning with *Year Book 45* (1946) for Dr. Barbara McClintock's extensive work on controlling elements. We wish to explore the molecular biology of controlling elements and their relationship to gene sequences. We hope that this work will eventually lead to insights into the organization of eukaryotic genetic loci, especially those portions that are involved in developmental programming.

Controlling elements (or their cognate recognition sequences) are known to have become associated with a number of different genes. Such genes are designated "mutable" genes or alleles of a gene. The most intensively studied of these are several genes in the anthocyanin and starch biosynthetic pathways. These genes are especially favorable for analysis because they are expressed in the endosperm of the kernel. Endosperm tissue is triploid, but has the same genetic constitution as the

embryo. Each endosperm therefore displays the result of a separate mating event, vastly facilitating genetic analysis and the selection and propagation of mutants. By far the largest and most absorbing array of transposable element-altered phenotypes is associated with genes in the anthocyanin pigment biosynthetic pathway. In the kernel, this pathway is expressed in the single layer of cells, termed the aleurone, which comprises the endosperm surface. Pigment expression is easily visualized, and controlling element mutants are known which affect the level, distribution, and timing of gene expression in development. Controlling element-responsive alleles of several genes in the starch biosynthetic pathway have also been identified. These are the Sh (sucrose synthetase), Sh2 (ADP-glucose pyrophosphorylase), Bt (enzymatic activity unknown), and Waxy (starch glucosyl transferase) loci. In general, controlling element alleles of these starch biosynthetic loci are less favorable for genetic analysis of the interactions between genes and controlling elements because changes in the expression of such genes are not as sensitively mirrored in the phenotype as is the case for genes in the pigment biosynthesis pathway. Completely recessive sh, sh2, and bt mutants have collapsed kernels due to their inability to convert sugar to starch. Alleles responsive to controlling elements display a phenotype intermediate between the dominant and the recessive, but subtle differences in timing and level of gene expression are difficult or impossible to detect. Since such subtle differences are likely to be informative, controlling element alleles of genes in the anthocyanin pigment pathway are preferable for molecular analysis over alleles of genes in the starch biosynthetic pathways. Unfortunately, the immediate accessibility to molecular studies of such genes appears to be inversely proportional to their potential interest, since they appear to encode proteins that are made in very small amounts.

This year we have done a variety of exploratory studies, both biochemical and genetic, to determine the feasibility of various approaches to molecular studies on controlling elements. The loci we have chosen to work on are described briefly below. Of the controlling element systems that have been studied in some detail, we are particularly interested in the Suppressor-mutator system (Spm). However, Spm has not been isolated in conjunction with any of the loci likely to be most immediately accessible for molecular analysis. The strategies we are pursuing to make this system accessible are discussed.

Anthocyanin Pigment Pathway

A1 locus. The A1 locus encodes an enzyme in the anthocyanin pigment pathway. Many Spm-controlled alleles are available, including alleles that have Spm integrated very near the locus and one in which the locus appears to reflect directly the activity phase of Spm. This is probably the most intensively studied Spm-controlled locus. A large variety of alleles is already available and more can be generated easily. Alleles controlled by the Activator-Dissociation (Ac-Ds) system are also known, although none appear to have Ac at the locus. The enzymatic activity of the A1 locus has not been identified. The A1 locus is on chromosome 3 and is tightly linked (0.1–0.2% recombination) to the Sh2 locus.

Bronze (Bz) locus. Many Ac-controlled alleles are known, including at least two that have Ac at the locus. No Spm-controlled alleles have so far been identified. The Bz locus encodes what appears to be the last enzyme in the anthocyanin pigment pathway. It is a glucosyl transferase which glycosylates the anthocyanin molecule, thereby stabilizing it. The Bz locus is

on chromosome 9 and at a distance of 2 recombination units from the Sh locus.

Starch Biosynthesis

Shrunken (Sh) locus. Three or four Ac-controlled alleles have been identified; none has Ac at the locus. No Spm-controlled alleles have been identified. The Sh locus is on chromosome 9 and encodes one of the most abundant soluble endosperm proteins, sucrose synthetase.

Shrunken 2 (Sh2) locus. One Ac-controlled allele of the Sh2 locus is known; no Spm-controlled loci have been identified. The Sh2 locus is extremely close to the A1 locus on chromosome 3 and encodes an ADP-glucose pyrophosphorylase.

Waxy (Wx) locus. Both Spm- and Ac-controlled alleles are known, including one having Ac at the locus. The Waxy locus appears to encode a starch granule-bound UDPG-starch glucosyl transferase which is necessary for amylose synthesis. The level of Wx gene expression can be roughly visualized in kernels having colorless or nearly colorless pericarp and aleurone layers, since amylose-containing kernels or kernel sectors have a glassy appearance, while those having only amylopectin are rather opaque and dull. The starch composition is also readily assayed by a simple iodine staining procedure. The Wx locus is on chromosome 9, 28 recombination units from the Bz locus.

The results of our studies on the loci described above appear in the following sections.

A1 Locus

The A1 locus is especially attractive because of the enormous variety of Spm-controlled alleles that exist. Dr. McClintock has kindly supplied many of these alleles, and they were expanded last summer at the Brookhaven National Laboratory. We wish to have these alleles in both homozygous and heterozygous form for eventual molecular analysis. This work was continued in last winter's Florida crop and the current crop at the University of Missouri (Drs. Coe and Neuffer).

The A1 locus appears to encode an enzyme that functions late in the anthocyanin pigment pathway, probably to convert the flavanonol intermediate to a flavenol (Styles *et al.*, *Can. J. Genet. Cytol.*, *19*, 289, 1977). Since the enzymatic function of the protein encoded by this locus has not yet been established, we attempted to identify the protein directly in aleurone tissue. This was done by comparing the proteins being synthesized at about 30 days after pollination in aleurone tissue having and lacking A1 function. We were encouraged to attempt such a direct identification by our observation that the enzyme encoded by the Bz locus, also in the anthocyanin biosynthetic pathway, comprises approximately 0.3% of aleurone protein at maturity in normal tissue. In order to minimize the problem of background genetic heterogeneity at unidentified loci, we compared the proteins present in adjacent sectors from single kernels in which the A1 locus was undergoing somatic reversion from the a1 to the A1 phenotype, giving colorless and colored sectors on each kernel. We labeled aleurone tissue from such kernels with [^{3}H]-leucine and were able to obtain several microcuries of radioactive protein from single tissue sectors comprising 10–20% of the aleurone layer. We have compared the proteins in more than 30 pairs of labeled aleurone sectors on two-dimensional gels. We have not been able to identify a consistent difference between the patterns of radioactive proteins given by a pair of sectors derived from a single kernel. Our subsequent experience with the Bronze locus suggests that the likeliest explanations for our failure to identify

the A1-encoded protein by this method is that the cell clones in which somatic mutations have occurred to restore A1 gene function make a small fraction of the amount of A1 gene product synthesized in a normal A1 strain.

Our present strategy is to approach isolation of the A1 locus indirectly. The two approaches we are pursuing are (1) to isolate a controlling element sequence in conjunction with a more readily accessible locus and use that sequence to identify the A1 locus in a strain containing the controlling element at the A1 locus and (2) to isolate the nearby Sh2 locus, which may well be within chromosome "walking" distance of the A1 locus. Toward the first objective, we have obtained several strains from Dr. McClintock in which the A1 locus is associated with either the Activator-Dissociation (Ac-Ds) or Spm controlling element system. These are being expanded in appropriate form for analysis at the molecular level. Toward the second objective, Dr. Sheila McCormick is currently engaged in purifying an ADP-glucose pyrophosphorylase, part of which is believed to be encoded by the Sh2 locus (Smith *et al.*, *Maize Genet. Coop. Newsletter*, *52*, 105, 1978). We have obtained a strain from Dr. Oliver Nelson (University of Wisconsin) in which the Sh2 locus is associated with the Ac-Ds controlling element system. This strain should facilitate the identification of the polypeptide encoded by the Sh2 locus.

Assuming that one of these approaches is successful in isolating the A1 locus, it will become necessary to verify its identity. Since the gene product has not been identified, this will have to be done indirectly. There are enough controlling element alleles of the A1 locus so that it should be possible to verify its identity by establishing a correlation between genetic and molecular alterations of the locus. Another, somewhat more innovative solution to this problem may be the development of direct DNA-mediated transformation of tissue culture cells. Dr. McCormick has made substantial progress in culturing the strains that would be required for such experiments and in identifying conditions which permit anthocyanin expression in cultured tissue (McCormick, see below). We are encouraged in attempting to develop such a nonselective, visually scorable transformation system by the recent observation that cultured plant cells can be transformed at a very high efficiency by the Agrobacterium plasmid that causes grown gall tumors (Giles, personal communication).

Finally, we are employing some of the controlling element strains of the A1 locus in genetic experiments whose objective is to isolate Spm at a locus that is biochemically more accessible than the A1 locus. We have selected the Sh, Sh2, and Bz loci for this purpose and are continuing to look for new mutable alleles. Drs. McCormick and Coe are also involved in this effort. We have so far examined more than 200,000 kernels and have identified several possible new mutable alleles. These must now be analyzed genetically over the next few seasons. In an effort to make such experiments more efficient, we have developed a genetic means of identifying cultures showing high rates of Spm transposition or early transposition events. These are being used as starting material in present efforts to identify new Spm-controlled alleles. Over the past six months, we have had two room-sized growth chambers installed and are presently growing our first experimental crop. These growth chambers will greatly facilitate the analysis of rare mutants. They will increase the mutants' chances of survival, since these plants will not be subject to the environmental hazards of survival in the field. They will also speed up genetic analysis because we will be able to grow at least three crops per year (and possibly four) indoors.

Bronze Locus

The Bronze locus encodes a flavonoid: UDPG glucosyl transferase, and was, until recently, the only enzyme in the anthocyanin pigment pathway whose activity had been identified. (H. Dooner has recently done some studies on the C2 locus, which appears to encode a highly unstable flavanone synthetase.) The Bz locus is attractive for our studies because the enzymatic activity is known and because of its proximity to the Sh locus, which encodes an extremely abundant protein. We have developed a purification scheme for the glucosyl transferase, prepared several hundred micrograms of the protein, and raised rabbit anti-glucosyl transferase antiserum. These studies are summarized below.

The major difficulty that we encountered in purifying the glucosyl transferase, which survives to kernel maturity and can be obtained from mature, dry seed, is that the enzyme experiences a precipitous drop in stability as it approaches purity. Crude and partially purified preparations of the enzyme are remarkably stable: We have kept several such preparations at −20 °C in 50% glycerol without detectable loss of activity for more than a year. However, our most highly purified preparations lose half of their activity within a day under the same storage conditions. Our present purification scheme includes chromatography on DEAE-cellulose, CM-cellulose, Affigel blue, and hydroxylapatite (HAP).

A homogenate is prepared from powdered dry kernels in the presence of a small amount of ion exchange resin to adsorb the anthocyanin pigments. The homogenate is subjected to centrifugation to remove starch and cell debris, dialyzed, applied to DEAE-cellulose, and eluted with an NaCl gradient. The enzyme elutes from DEAE-cellulose at roughly 0.15 M NaCl, approximately 20-fold purified with respect to the starting material (Fig. 32, lane a). The glucosyl transferase has an isoelectric point between pH 5 and pH 6. The low isoelectric point is exploited in the next purification step, in which the partially purified enzyme is adjusted to pH 5 and passed through CM-cellulose at a salt concentration which permits adsorption of most of the proteins present in the preparation, but not the glucosyl transferase. The enzyme emerges 20- to 40-fold purified (Fig. 32, lane b). The CM-cellulose-purified enzyme is then applied to the affinity resin Affigel blue at neutral pH. Under these conditions, only the glucosyl transferase and one or two other proteins adsorb to the column and these can be eluted with 0.2–0.4 M NaCl (Fig. 32, lane c). Finally, the glucosyl transfer-

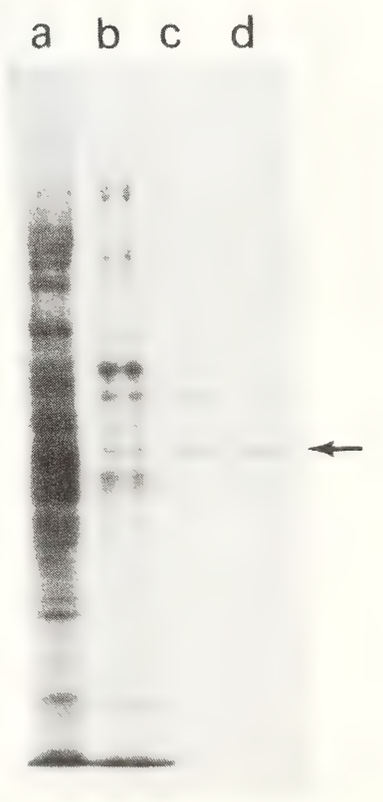


Fig. 32. SDS-polyacrylamide gel electrophoretic analysis of proteins present in preparations of glucosyl transferase at various steps in the purification scheme. Lanes (a) to (d) represent the proteins present after chromatography on DEAE cellulose, CM-cellulose, Affigel blue, and hydroxylapatite, respectively. The arrow marks the position of the glucosyl transferase polypeptide.

ase can be separated from the remaining contaminants on HAP at very low phosphate buffer concentrations (Fig. 32, lane d). At this final stage of purification, we generally observe two slightly separable peaks of glucosyl transferase activity on HAP and we have found two major polypeptides on examining the enzyme preparations by 2-dimensional gel electrophoresis. The two polypeptides appear to be of the same molecular weight and, since they are immediately adjacent to each other, probably differ by a single charge. Both HAP glucosyl transferase activity peaks show proteins of identical size; we have not yet determined whether there is a correlation between the charge difference observed on isoelectric focusing and the difference in HAP elution properties.

Purified glucosyl transferase preparations containing both HAP peaks were used to raise antiserum. Despite continuing efforts over many months, we have not been able to obtain antiserum of very high titer. (H. Dooner had a similar experience with partially purified glucosyl transferase.) This suggests that the protein is a poor antigen. The titer of the antiserum that we currently have is such that we can precipitate about 1–2 μg of the glucosyl transferase per 100 μl of antiserum. This titer is sufficient for some, but not all, of the experiments we wish to do. It will, for example, be quite adequate for establishing whether or not we have isolated either a genomic or a cDNA clone containing some or all of the coding sequence. However, we had hoped to be able to analyze directly the size and charge of the glucosyl transferase made in a number of mutable bronze strains. This is of interest in view of Hugo Dooner and Oliver Nelson's observation that the glucosyl transferase in some of these strains has an altered heat stability, suggesting a primary structural change from the original form consequent on integration of a controlling element sequence at the locus (Dooner *et al.*, *Proc. Nat. Acad. Sci. USA*, *74*, 5623, 1977). We have invested some effort in trying to identify the glucosyl transferase protein in labeled protein preparations from immature aleurone tissue and have encountered substantial difficulties. Knowing the specific activity of the purified glucosyl transferase, we estimate that it comprises at least 0.3% of the protein in mature aleurone tissue. Were it that abundant in immature tissue, we should have been able to identify it by examining labeled proteins from Bz and bz aleurone tissue sectors of bronze mutable strains by two-dimensional gel electrophoresis, since we also know the size and charge of the protein. We were not, however, able to identify the protein in in vivo-labeled material. Upon closer examination, it became apparent that part of the reason for this is that a relatively small amount of enzyme is sufficient to give the normal phenotype. This was established by doing direct enzymatic assays on protein extracts from pigmented aleurone sectors appearing on ears having a mutable bronze locus. Thus tissue sectors having a normal pigment intensity varied between virtually undetectable and moderate levels of glucosyl transferase activity, but these never approached the levels observed in genetically "wild-type" tissue having the corresponding dose of Bz genes. We then turned to the immunological analysis of labeled extracts from normal and mutant strains to increase the sensitivity of our detection. Although these experiments have not been completed, it appears likely from the results obtained so far that the rate of glucosyl transferase synthesis is at least an order of magnitude lower than we had anticipated from its final representation in mature tissue. This probably means that its high concentration in the mature aleurone is at least partly attributable to the fact that it is more stable than other proteins, surviving degradation during tissue dehydration.

We intend to pursue these studies somewhat further, using mRNA purified from immature aleurone. As will be seen in subsequent sections, maize mRNAs are readily translated in a rabbit reticulocyte cell-free protein-synthesizing system. One can obtain proteins labeled to much higher specific activities for immunologic analysis than can be prepared by in vivo labeling. We will attempt to estimate the concentration of glucosyl transferase mRNA by this means before proceeding further with cloning.

Given the low rate of glucosyl transferase synthesis, it is probable that the most efficient means of cloning the corresponding mRNA is to synthesize a primer oligonucleotide that will permit selective synthesis of the cDNA to the glucosyl transferase mRNA. This necessitates partial sequencing of the protein. A collaborative effort to sequence the protein and synthesize the appropriate oligonucleotide is currently being developed. In addition, the Bz locus may be accessible by the indirect means described for the A1 locus, using the nearby Sh locus. Some time ago, McClintock derived a number of interesting strains from one in which Ds (of the Ac-Ds system) was located distal to the Sh locus on chromosome 9, but had no obvious effect on the expression of a gene. From this strain, she derived others which behaved as though they were unidirectional deletions extending away from Ds, either toward the more distal C locus or toward the more proximal Sh and Bz loci. This strain gave rise to the mutable shrunken strains that McClintock studied, as well as to the mutable bronze strain. The mutable bronze derived from this strain, designated *Ds sh bz^{m4}* by McClintock, behaves as though it were deleted for the Sh locus, based on the depression in recombination value between sh and bz^{m4}. McClintock reports that she saw no recombinants. More recently, Dooner believes he has obtained such recombinants at a very low frequency. These observations suggest that there is either a deletion or some type of rearrangement in this strain. We will shortly be able to determine whether the Sh locus is there in whole or in part and whether its flanking sequences are altered. Depending on the outcome of these experiments, this strain may prove quite useful in identifying and isolating the Bronze locus, since it may well have all or a portion of the Sh locus in immediate juxtaposition with the Bz locus.

Shrunken Locus

Of the loci considered here, the Shrunken locus is undoubtedly the most immediately accessible to molecular analysis. It encodes sucrose synthetase, an enzyme in the starch biosynthetic pathway (Choury *et al.*, *Biochem. Genet.*, *14*, 1041, 1976). This enzyme is one of the most abundant endosperm proteins. The enzyme is easily purified and highly antigenic. Figure 33 shows an analysis of the enzyme preparation at various stages of purification. Lane a (Fig. 33) shows a crude homogenate of immature endosperm. The sucrose synthetase appears as a prominent band comprising several percent of the total protein. Purification of the crude homogenate by chromatography on Affigel blue effects a substantial enrichment (Fig. 33, lane b). Repetition of the chromatography step yields virtually pure sucrose synthetase (Fig. 33, lane c). High titer antiserum was readily obtained using purified synthetase. When total poly A$^+$ mRNA purified from immature kernels is translated in a cell-free rabbit reticulocyte protein-synthesizing system, a protein band having the electrophoretic mobility of sucrose synthetase is apparent, and it is precipitated by antiserum prepared against sucrose synthetase (Fig. 33). Although it appears from Fig. 33 that sucrose synthetase is one of the most abundant endosperm

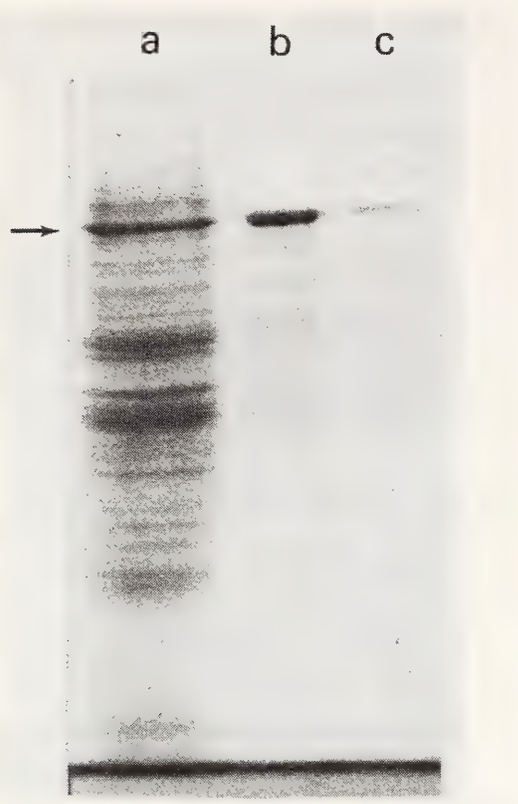


Fig. 33. SDS-polyacrylamide gel electrophoretic analysis of proteins present in preparations of sucrose synthetase at various steps in the purification scheme. Lane (a) shows the total soluble proteins of immature endosperm, while lanes (b) and (c) show the polypeptides present after one and two cycles of purification on an Affigel blue column, respectively. The arrow marks the position of the sucrose synthetase polypeptide.

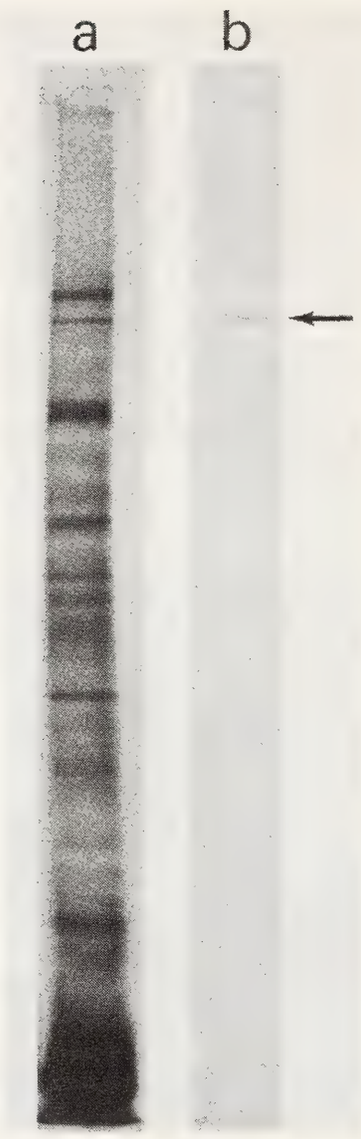


Fig. 34. SDS-polyacrylamide gel electrophoretic analysis of [S^{35}]-methionine-labeled proteins synthesized in a rabbit reticulocyte cell-free protein synthesizing system from total maize endosperm poly A^+ mRNA. Lane (a) shows the total array of proteins synthesized from maize endosperm mRNA. Lane (b) shows the single polypeptide precipitated from the mixture shown in lane (a) by antisucrose synthetase antiserum. The arrow marks the position of sucrose synthetase.

proteins, that is because only soluble proteins are extracted under the conditions employed for isolating the enzyme. The water-insoluble zeins are substantially more abundant, and this is evident in Fig. 34, which is a fluorogram of the proteins translated from total endosperm mRNA. The small polypeptides migrating near the bottom of the gel are the zeins. The mRNAs encoding zeins are the most abundant endosperm mRNAs, comprising as much as one third of the total mRNA. Fractionation of the mRNAs on a sucrose gradient was therefore employed to enrich for the sucrose synthetase mRNA. The sucrose synthetase polypeptide has a molecular weight of approximately 88,000 and is encoded by a relatively large mRNA. This is apparent in Fig. 35, which shows the proteins synthesized by the mRNAs present in successive fractions from a sucrose gradient. Under the conditions employed, the sucrose synthetase mRNA activity is most abundant in fractions 4 and 5 of the sucrose gradient, while the zein mRNA activity is most abundant in

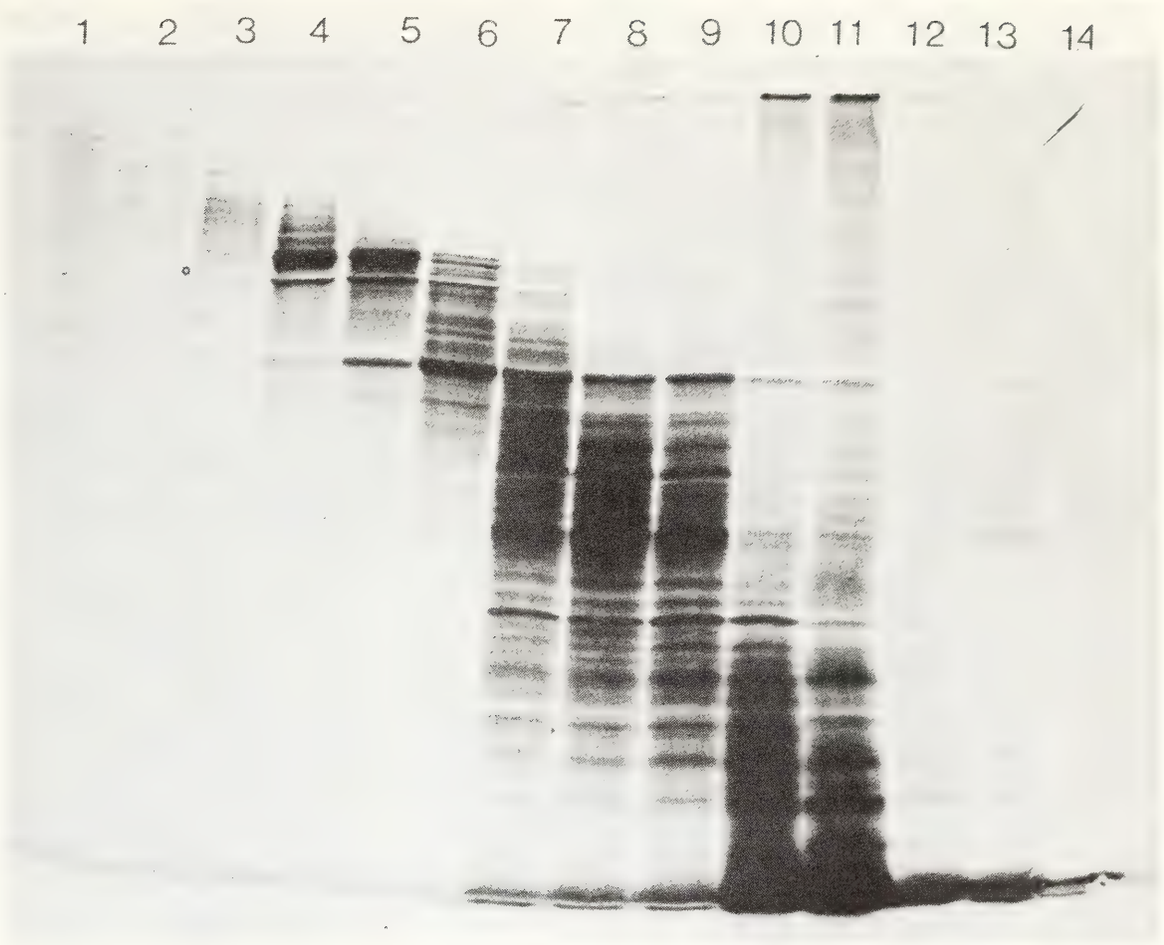


Fig. 35. SDS-polyacrylamide gel electrophoretic analysis of proteins synthesized in a rabbit reticulocyte translation system by successive mRNA fractions from a sucrose gradient. The direction of sedimentation was from right to left. Maize 25S rRNA sedimented in fraction (3). The RNA in each fraction of the gradient was recovered separately, an aliquot was translated in vitro in the presence of [S^{35}]-methionine, and the labeled proteins were analyzed on an SDS-polyacrylamide gel. A small open circle adjacent to lane (3) marks the position of sucrose synthetase.

fractions 10 and 11. From these and other experiments, we estimate that the sucrose synthetase mRNA is 3,000–35,000 nucleotides long.

We have prepared double-stranded cDNA from RNA preparations enriched for sucrose synthetase mRNA and cloned it at the PstI site of the *E. coli* plasmid pBR322. Enrichment for sucrose synthetase mRNA was achieved on preparative sucrose gradients similar to that shown in Fig. 35. Fractions having the highest concentration of sucrose synthetase mRNA were incubated with AMV reverse transcriptase, an oligo dT primer, and nucleotide triphosphates (Wahli *et al.*, *Devel. Biol.*, *67*, 371, 1978). The resulting distribution of cDNA is shown in Fig. 36, lane b. The top end of the distribution is between 3,000 and 4,000 nucleotides in length, indicative of full-length copies of the mRNAs. Lane a of Fig. 36 shows the distribution on an alkaline agarose gel of DNA fragments obtained after removal of the mRNA template and synthesis of the complementary strand. The complementary strands were subsequently separated by digestion with nuclease S1 and prepared for cloning by addition of oligo dC tails, followed by fractionation on a sucrose gradient. The oligo dC-tailed cDNA was annealed to oligo dG-tailed, PstI-cut pBR322 and used to transform *E. coli* HB101. More than 3,000

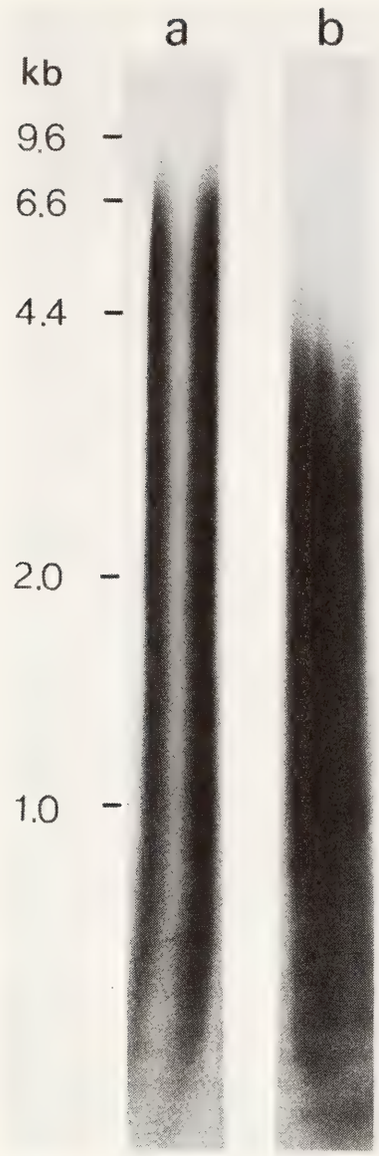


Fig. 36. Electrophoretic analysis of [P^{32}]-labeled cDNA on an alkaline agarose gel. Fractions of mRNA enriched for sucrose synthetase were transcribed using AMV reverse transcriptase. The cDNA prepared to the mRNA is analyzed in lane (b). Lane (a) shows the distribution of DNA fragments obtained upon removal of the RNA template and synthesis of the complementary strand.

transformants have been obtained and these are presently being screened for inserts homologous to sucrose synthetase mRNA.

Sucrose synthetase cDNA clones will be used to analyze restriction enzyme digests from a variety of maize strains, ranging from the normal Sh strains, to bz^{m4} (discussed above), and including two strains which may be deleted for both the Sh and the Bz locus (derived by Mottinger). Decisions about which DNAs will be cloned will be made on the basis of the results of these experiments. We have developed a procedure for obtaining DNA of which 70–80% is in the size range from λ DNA (50 kb) to T4 phage DNA (170 kb) from mature embryos. Briefly, the embryos are dissected from mature seeds, then frozen and powdered in liquid nitrogen. Nuclei are isolated and lysed, and the DNA is spun to equilibrium in a CsCl-ethidium bromide gradient. Contaminating polysaccharides, which account for most of the difficulty in working with plant DNAs, band well away from the DNA under these conditions. The DNA is generally recovered and banded on a second CsCl gradient. DNA for analysis by hybridization of cDNA clones to restriction enzyme-digested, fractionated DNA (Southern blots) has been prepared from normal (wild-type), shrunken mutable, and bronze mutable strains.

Only a few mutable alleles are known for the Sh locus and these have Ds but not Ac at the locus. The Sh locus, which promises to be the first of the mutable loci to be isolated, is valuable primarily as a "molecular handle" on controlling element sequences, although it is likely that information on the organization of Ds and its relationship to the coding sequence of the Sh locus will also emerge from studies on the mutable shrunken strains. We hope that our studies on the mutable Sh alleles will allow us to develop probes for other loci (especially the Bz and A1 loci) with which Ds is known to be associated.

Shrunken 2 Locus

The Sh2 locus was mentioned earlier in connection with the nearby A1 locus. It is presently believed that the Sh2 and the Bt2 loci each contribute polypeptides to the endosperm ADP-glucose pyrophosphorylase activity. Although there exists an Ac-controlled

mutable allele of this locus, derived by Oliver Nelson some years ago, we view this locus as valuable primarily because of its proximity to the A1 locus discussed above. Dr. McCormick is presently purifying the enzyme, which appears to consist of two polypeptides somewhat larger than the sucrose synthetase monomer. A cloned copy of its mRNA may well be among the cDNA clones we already have, and we will be able to screen for it when we have obtained antiserum to the purified protein. We are also attempting to isolate new Spm-controlled Sh2 mutable alleles and currently have several possible candidates awaiting genetic analysis.

Waxy Locus

The Waxy locus encodes a starch granule-bound enzyme which transfers glucose from UDPG to starch in the synthesis of amylose (Nelson *et al.*, *Biochem. Biophys. Res. Commun.*, *9*, 297, 1962). It is the only locus in the starch biosynthetic pathway for which an Spm-controlled allele is available. Since little progress has been made in solubilizing the enzyme, it appears worthwhile to attempt to identify the protein directly. We plan to purify starch particles and examine the proteins associated with them by two-dimensional gel electrophoresis. To aid in identifying the protein, we have constructed a number of strains having mutable Waxy alleles, with or without the cognate controlling element. If this protein is reasonably abundant, as are the other starch-synthesizing enzymes, we may be able to identify it without having to solubilize it by correlating its presence or absence with the genetic composition of the strain.

Maize Tissue Culture

S. McCormick

Maize tissue culture is technically difficult. Only a few inbred strains of sweet corns have been successfully cultured as friable callus and suspension cultures. The standard maize tissue culture media contain the synthetic auxin 2,4-dichlorophenoxyacetic acid (2,4-D) as the hormone source. Callus initiated from our genetic stocks on such media grew slowly, gave a compact, rooty morphology, and died within four months. Work done by Roger Hangarter (Michigan State University) suggested that indole acetic acid–amino acid conjugates, which are naturally occurring bound forms of auxin, might be a superior auxin source. He showed that certain conjugates could promote rapid callus growth and suppress organogenesis in both tobacco and tomato test systems. Other amino acid conjugates had different effects. Some allowed shoot formation but suppressed root formation, while others did not promote callus growth at all. It is believed that these differences are due to different rates of release of indole acetic acid (IAA) from the conjugated form.

Maize callus was initiated from mesocotyl sections of 14-day-old seedlings on 50-micromolar IAA-alanine medium and maintained on the same medium by subculturing every three weeks. Callus grown on IAA-alanine differed strikingly in morphology from that grown on 2,4-D. The callus was white and friable and grew rapidly, showing a 2–3-fold fresh weight increase in three weeks. Some of these cultures have now been maintained for more than 18 months.

Suspension cultures have been initiated in liquid medium of the same composition and have been maintained through weekly subcultures for periods up to three months. There are approximately 2.5×10^5 cells/ml in a suspension culture three days after subculture, and the cells are in clumps of 1–20 cells. We have not yet found conditions that will allow continued growth of suspension cells upon plating in soft agar.

Several of our original callus lines were genetically competent to express anthocyanin, and both the callus and suspension cultures derived from the callus initially showed purple pigment in some cells. However, upon further subculture, pigmentation was greatly reduced or lost. This may result from the fact that rapidly growing cells often do not express differentiated traits, such as anthocyanin synthesis. We have found that growth on IAA conjugates of leucine, valine, and phenylalanine all give a more rooty morphology than the IAA-alanine controls, but allow anthocyanin expression. However, the callus dies on these conjugates after a few subcultures. Callus grown on conjugates that permit pigment expression can be rescued by transfer to IAA-alanine. The original morphology is regained and growth resumes. Thus by sequential transfers it is possible to manipulate the morphological characteristics and the anthocyanin expression of these cultures. Experiments still in progress suggest that callus grown on IAA-aspartate may display both the desired growth characteristics and pigment expression.

STUDIES ON THE THYMIDINE KINASE GENE OF HERPES SIMPLEX VIRUS

S. L. McKnight, E. R. Gavis, and R. C. Kingsbury

We are ultimately interested in determining which sequences within, and adjacent to, the Herpes Simplex Virus (HSV) thymidine kinase (tk) gene are involved in its proper expression. In order to obtain information of this sort, we have adopted an approach that is best described as in vitro genetics. Several essential components are required to study a gene system in vitro. First, one must be able to isolate and fully characterize the structure of the gene. Once characterized, the gene can be mutated in vitro by a variety of methods. Most importantly, however, a sensitive and straightforward assay system must be available to test how specific mutations affect expression of the gene.

In last year's Report (*Year Book 78*) we described the isolation and molecular cloning of the HSV thymidine kinase gene. We showed that a recombinant plasmid harboring a copy of the tk gene, termed pHSV-106, is fully capable of transfecting cultured tk^- mouse cells to the tk^+ phenotype. During the past year we have concentrated our studies on two aspects of the tk gene system. First, we have resolved the nucleotide sequence and derived a messenger RNA map of the tk gene. Second, we have demonstrated that the tk gene is expressed in the form of enzymatically functional protein when pHSV-106 DNA is microinjected into *Xenopus laevis* oocyte nuclei. The latter finding has been used to established an assay for testing the functional capacities of mutated isolates of the HSV thymidine kinase gene.

Microinjected Frog Oocytes Will Express the HSV tk Gene

To test whether the HSV tk gene could be expressed in frog oocytes, we microinjected pHSV-106 DNA into oocyte nuclei, allowed the oocytes to incubate for 24 hours, then assayed a homogenate fraction of the injected oocytes for tk enzyme activity. Table 6 shows the results of an experiment in which we compared the tk activity of oocytes injected with pHSV-106 with that of both uninjected oocytes and

TABLE 6A. Thymidine Kinase Enzyme Activity Assays on Oocyte Extracts*

Source of Extract	tk Activity Units × 10^2 per ml	Stimulation tk Activity
Uninjected oocytes	0.05	. . .
pBR-322-injected oocytes	0.06	Not detected
pHSV-106-injected oocytes	8.82	176.4×

TABLE 6B. Immunological Neutralization of tk Enzyme Activity

Source of Extract	tk Activity Units × 10^{-2} per ml		
	PBS	non-immune IgG	anti-tk IgG
Uninjected oocytes	0.041	0.021	0.038
X. laevis liver	0.720	0.450	0.600
pHSV-106-injected oocytes	3.330	3.680	0.550

*For each oocyte injection experiment, 50 mature oocytes were injected with 50 nl of a 0.2 mg/ml solution of supercoiled plasmid DNA. The injected oocytes were incubated for 24 hours, homogenized and centrifuged at 100,000 × *g* for one hour. Thymidine kinase enzyme assays were carried out using the high-speed supernatant fraction. For immunological neutralization assays, samples were pre-incubated with 20 μg IgG (either non-immune or anti-tk) for one hour at 37 °C and 12 hours at 4 °C prior to tk enzyme assays.

oocytes injected with pBR-322. Fortuitously, *Xenopus laevis* oocytes exhibit an exceedingly low level of tk activity. As Table 6 shows, the level of tk activity is not increased when oocytes are injected with pBR-322. When oocytes are injected with pHSV-106, however, a dramatic increase in tk activity is observed. The level of tk enzyme induction resulting from injection of pHSV-106 DNA usually ranges from 100- to 200-fold greater than the background level of uninjected oocytes.

Two types of experiments have been undertaken to show that the additional enzyme observed in oocytes microinjected with pHSV-106 is HSV tk. First, we used an antibody preparation from rabbits immunized with purified HSV tk to immunoprecipitate HSV tk protein from oocytes injected with pHSV-106. The antibody was kindly provided by Drs. Saul Silverstein and Adele El Karah of Columbia University. We found that the immunoprecipitation procedure specifically neutralizes the tk activity of oocytes injected with the tk gene. That is, immunoprecipitation with a non-immune antibody preparation does not result in a substantial reduction in the tk activity of pHSV-106-injected oocytes. Furthermore, the antibody directed against HSV tk protein does not reduce the tk enzyme activity level endogenous to *Xenopus laevis*. The results of these experiments are included in Table 6.

We have also used the immunoprecipitation procedure to analyze, by SDS gel electrophoresis, proteins that are synthesized in microinjected oocytes. Figure 37 shows an autoradiogram of a polyacrylamide gel that was used to separate proteins synthesized in oocyte samples co-injected with plasmid DNA and ^{35}S-methionine. The autoradiogram compares proteins synthesized in oocytes injected with pBR-322 with proteins made in pHSV-106-injected oocytes. Although no distinct differences were observed when whole extracts of two samples were separated by electrophoresis, we were able to show that when a homogenate from pHSV-106-injected oocytes is immunoprecipitated with the anti-tk immunoglobulin preparation, a single band of radioactivity is observed at a position corresponding to roughly 40,000 daltons. The position of this band corresponds quite well with the reported size of tk protein synthesized in HSV-infected cells (Cremer *et al.*, *Nucl. Acids Res.*, *5*, 2333, 1980). Since the band is not observed in samples immunoprecipitated from oocytes injected with pBR-322, and since non-immune

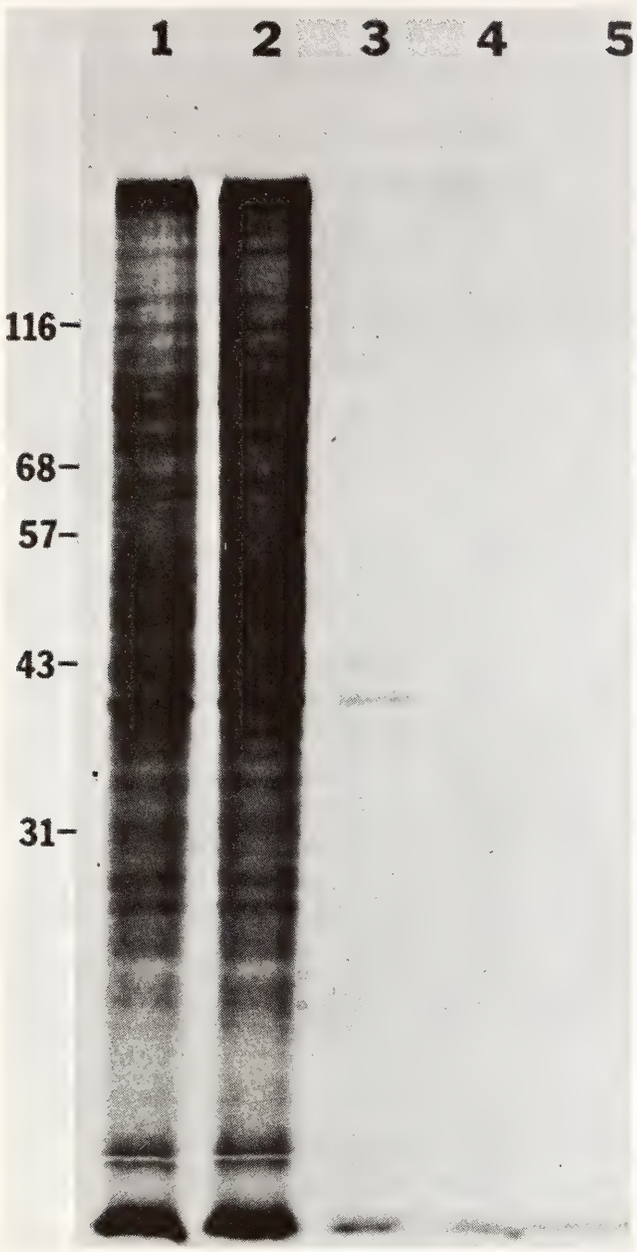


Fig. 37. An autoradiographic exposure of a 10% SDS-polyacrylamide gel used to separate proteins synthesized in microinjected frog oocytes. Batches of 100 oocytes were injected with ^{35}S-methionine and either pHSV-106 or pBR-322. After a 24-hour incubation interval, the oocytes were homogenized in phosphate-buffered saline and centrifuged at 100,000 × *g*. Lanes (1) and (2) show the proteins synthesized by oocytes injected with pBR-322 and pHSV-106, respectively. Lane (3) was loaded with proteins immunoprecipitated by anti-tk IgG from oocytes injected with pHSV-106. A single protein band, exhibiting an apparent molecular weight of roughly 40,000 daltons, is observed in Lane (3). Lane (4) was loaded with proteins immunoprecipitated by non-immune IgG from oocytes injected with pHSV-106. Lane (5) was loaded with proteins immunoprecipitated by anit-tk IgG from oocytes injected with pBR-322. Numbers to the left of the figure mark the positions of molecular weight marker proteins.

antibody does not precipitate the protein from pHSV-106–injected oocyte extracts, we conclude that the 40,000–dalton band is authentic tk protein.

With the help of Dr. William Summers of the Yale University Medical School we have performed a second set of experiments that confirm the identity of HSV tk enzyme synthesized by frog oocytes. It is known that HSV tk can utilize deoxycytidine as a substrate for phosphorylation, but that cellular tk cannot (Cooper, *Proc. Nat. Acad. Sci. USA*, *70*, 3788, 1973). William Summers developed a specific assay for HSV tk using ^{125}Iododeoxycytidine. This assay can be carried out either in vivo or in vitro, and can monitor HSV tk activity in a background of cellular tk activity. When we used the ^{125}IdC assay on extracts prepared from microinjected oocytes, we found that extracts prepared from pHSV-106–injected oocytes exhibit a substantial kinase activity, while preparations of pBR-322–injected or uninjected oocytes show little or no capacity to phosphorylate iododeoxycytidine (data not shown). These results, in concert with the immunological data considered previously, show that the HSV tk gene can be expressed in microinjected oocytes.

Construction and Analysis of Deletion Mutants of the HSV tk Gene

We have used the oocyte assay to test the functional capacities of mutated variants of the tk gene. Two systematic sets of deletion mutants of the tk gene were constructed in vitro according to the procedure developed by Shigeru Sakonju (*Year Book 78*). One set of mutants sequentially delete segments of the tk insert in pHSV-106 progressing from the BamHI site proximal to the unique HindIII site of the plasmid. These mutants are termed 5′ deletion mutants, as they remove DNA sequences from, and into, the tk

gene in a direction consistent with the polarity of transcription (Smiley *et al.*, *Virology, 102*, 83, 1980). The other set of mutants sequentially delete segments of the tk insert progressing from the BamHI site proximal to the unique SalI site of the plasmid. This second set of deletion mutants progressively delete segments of the tk gene in a direction opposing the known polarity of the tk gene transcription. Figure 38 shows a restriction map of the 3.4-kb tk insert in pHSV-106 and diagrams the approximate end points of 15 deletion mutants that were chosen for analysis.

Purified plasmid DNA of each deletion mutant was injected into frog oocytes in order to correlate the physical map of each mutant with its capacity to stimulate tk enzyme synthesis in oocytes. The results of these experiments are shown in Table 7. The 5′ deletion mutants can be classified in three groups according to the response they elicit when introduced into oocytes. The first class, of which Δ5′ −0.20 is the sole member, includes mutants that stimulate tk synthesis to the same level as the parental isolate, pHSV-106. We assume that the sequences missing from Δ5′−0.20 are not important for tk gene expression in oocytes. The second class, which includes Δ5′−0.67 and Δ5′−0.72, is characterized by deletion isolates that reproducibly show a detectable induction of tk enzyme activity when injected into oocytes. The level of enzyme activ-

TABLE 7. Oocyte Injection Assays of tk Deletion Mutants*

Deletion Isolate	Stimulation of tk Activity above Oocyte Background
Δ5′−0.20	224×
Δ5′−0.67	12.9×
Δ5′−0.72	3.3×
Δ5′−1.01	nd
Δ5′−1.19	nd
Δ5′−1.24	nd
Δ5′−1.34	nd
Δ3′−0.21	63×
Δ3′−0.57	86×
Δ3′−0.77	71×
Δ3′−1.13	60×
Δ3′−1.32	78×
Δ3′−1.60	nd
Δ3′−1.94	nd

*The plasmid DNA of each deletion mutant was microinjected into 50 oocytes. In order to standardize the assays, all 5′ (or 3′) deletion mutants were tested using oocytes prepared from the same female frog. Twenty-four hours after injection, the oocytes were prepared for thymidine kinase enzyme assays.

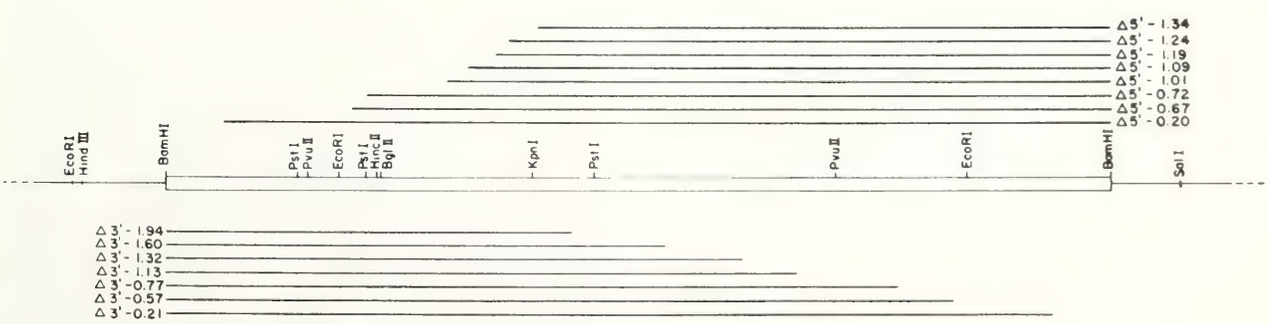


Fig. 38. A restriction enzyme map of the Herpes Simplex Virus tk DNA inserted in pHSV-106. The inserted segment is bounded by BamHI restriction enzyme sites. The solid lines above the restriction map diagram the DNA sequences remaining within each of eight 5′ deletion mutants. The nomenclature for 5′ deletion mutants is derived from the amount of DNA in kilobase pairs that was deleted from the leftward BamHI site. For example, Δ5′−1.34 is missing 1.34 kb (1,340 base pairs) from the leftward BamHI site of pHSV-106. The solid lines below the restriction map diagram the sequences remaining within each 3′ deletion mutant. The nomenclature for 3′ deletion mutants describes the amount of DNA missing from the rightward BamHI site of pHSV-106. All deletion mutant end points are terminated with a synthetic HindIII linker molecule.

ity produced in oocytes injected with this second class of mutants is, however, greatly reduced as compared with the parental isolate, pHSV-106. The third class of deletion mutants consists of those that fail to direct a detectable induction in tk activity in the oocyte injection assay. As Table 7 shows, the 3′ deletion mutants fall into only two classes. One class includes mutants that function as well as the parental plasmid; mutants of the other class fail to direct any detectable increase in tk activity in microinjected oocytes.

We interpret these data in the following way. The Class I mutants appear not to have lost DNA sequences integral to tk gene expression. The Class II mutants have lost sequences required for a "wild-type"response in microinjected oocytes, but maintain a limited ability to produce tk enzyme. This class of mutants may reflect those that have lost regulatory sequences involved in the production of functional tk mRNA but probably maintain the entire protein-coding sequence of the tk gene. The Class III mutants are interpreted as having lost DNA sequences integral to the production of functional tk polypeptide. While these interpretations may not be entirely correct, the data generated by these experiments provide a basis for initiating structural studies of the tk gene. For example, we expect that a functional boundary of the tk gene occurs somewhere between the 3′ deletion mutants Δ3′−1.32 and Δ3′−1.60. Similarly, one might expect that the DNA sequences in the vicinity surrounding the 5′ mutants Δ5′−0.67 and Δ5′−0.72 might harbor a functional boundary of the HSV tk gene.

Structural Studies of the HSV tk Gene

We have resolved the nucleotide sequence of most of the HSV tk gene cloned in pHSV-106 by the chemical method of DNA sequencing (Maxam *et al., Proc. Nat. Acad. Sci. USA, 74,* 56, 1977). Figure 39 shows the nucleotide sequence of the noncoding strand of the tk gene. The precise end points of each of the deletion mutants mentioned in the preceding section were identified by DNA sequencing and are pointed out in Fig. 39. Additionally, restriction endonuclease recognition sites corresponding to those in Fig. 38 are indicated in the sequence shown in Fig. 39.

We have mapped the positions on the sequence corresponding to the 5′ and 3′ termini of tk mRNA using a modification of the S_1 mapping procedure (Berk *et al., Cell, 12,* 721, 1977). To map the 3′ terminus of tk mRNA we isolated a single-stranded, coding strand, DNA fragment that extends from the Hae III site at nucleotide 1,254 to the Hae III site at nucleotide 1,593. This 339-nucleotide molecule was expected to encompass the sequence complementary to the 3′ terminus of tk mRNA because it spans most of the region between deletion mutants Δ3′−1.32 and Δ3′−1.60. The DNA fragment was uniquely labeled at its 3′ terminus with α^{32}P-CTP and terminal transferase then hybridized to poly-A$^+$ RNA prepared from HSV-infected cells. The hybridized material was exposed to exonuclease S_1, which removes the unhybridized single-stranded DNA and the poly-A tail of the mRNA, leaving an RNA/DNA hybrid duplex that should map the distance from the Hae III site at nucleotide 1,254 to the position at which the poly-A tail is added onto the tk mRNA. As the autoradiogram in Fig. 40 shows, the size of the protected fragment is approximately 255 pb. Thus, the 3′ terminus of tk mRNA, excluding the poly-A tail, maps to a position between nucleotides 1,505 and 1,510.

A similar approach was used to map the 5′ terminus of tk mRNA. We knew from mRNA-sizing experiments that the tk mRNA message is approximately 1,300 ribonucleotides in length not including the poly-A tail (data not

Fig. 39. The DNA sequence of the HSV thymidine kinase gene. The noncoding strand of the DNA sequence is displayed progressing from the PvuII restriction enzyme recognition site to the end point of deletion mutant Δ3′−1.13. The sequence was resolved using the chemical methods of sequencing (Maxam *et al., Proc. Nat. Acad. Sci. USA, 74,* 56, 1977). The adenosine residue that occurs 77 base pairs to the right of the Eco RI site, designated as nucleotide 201, is believed to be complementary to the 5′ terminus of tk mRNA (see text and Fig. 41). Restriction enzyme recognition sites are underlined and the end points of deletion mutants are indicated by arrows.

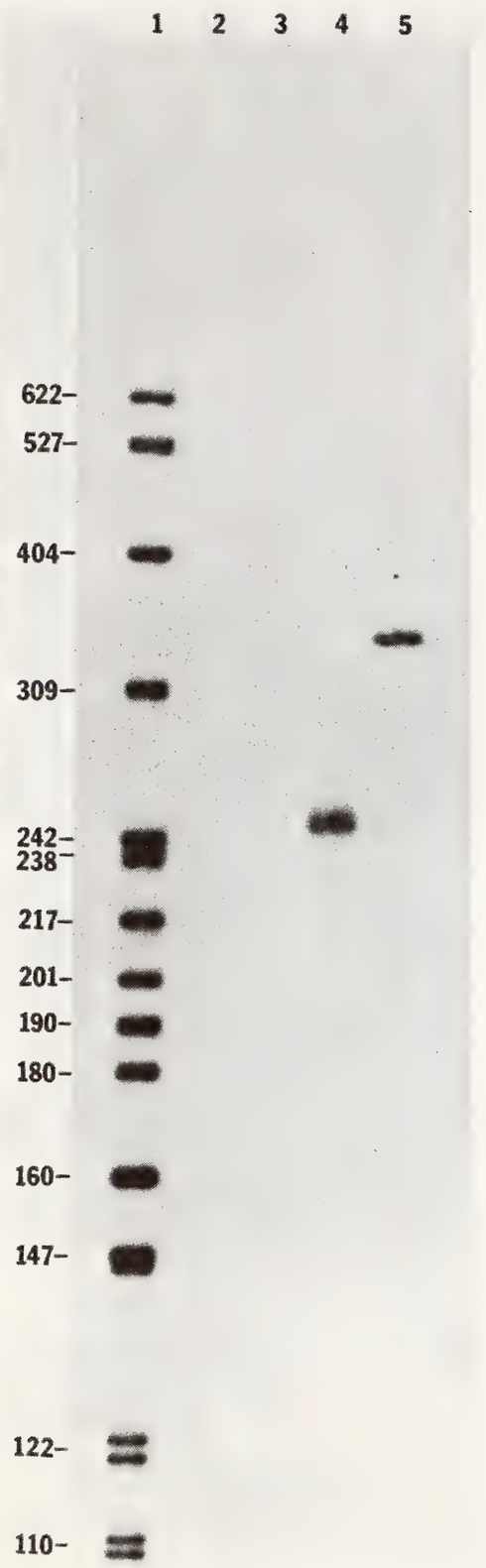


Fig. 40. In order to map the 3′ terminus of tk mRNA, a single-stranded probe DNA molecule extending from the HaeIII site at nucleotide 1,254 to the HaeIII site at 1,593 (see Fig. 39) was isolated and labeled at its 3′ terminus with ^{32}P. The 339-nucleotide probe was hybridized to mRNA prepared from cultured cells infected with HSVI. RNA/DNA hybrid molecules were digested with exonuclease S_1 which removes any single-stranded DNA and RNA from the hybrids, and electrophoresed on an 8% polyacrylamide sequencing gel. This autoradiographic exposure of the gel was used to map the 3′ terminus of tk mRNA. ^{32}P-labeled marker DNA fragments were loaded in Lane (1). The numbers adjacent to the marker DNA bands indicate the size of each marker fragment in nucleotides. Probe DNA digested with S_1 was loaded in Lane (2). Lane (3) was loaded with probe DNA that had been hybridized to mRNA before exposure to S_1. Lane (4) was loaded with intact probe DNA.

shown). As Fig. 39 shows, the 5′ deletion mutants Δ5′−0.67 and Δ5′−0.72 map in a region about 1,250–1,350 bp from the putative 3′ terminus of the tk gene identified in the preceding section. As mentioned previously, these two deletion mutants substantially reduce the capacity of the tk gene to direct tk enzyme accumulation in microinjected oocytes. From those observations we predicted that the 5′ terminus of the tk gene might map in the 131-bp sequence bounded on the 5′ side by the EcoRI site at nucleotide 121 and on the 3′ side by the Bgl II site at nucleotide 252. We isolated the coding DNA strand of this fragment, labeled it with ^{32}P at the terminal (5′) nucleotide of the Bgl II site, and hybridized it to mRNA prepared from HSV-infected cells. The hybrids were digested with S_1 and electrophoresed on a DNA sequencing gel. The autoradiogram displayed in Fig. 41 shows that about 60 nucleotides of the probe DNA were protected from S_1 digestion by the tk mRNA. We conclude from these data that the 5′ terminus of the most abundant tk mRNA found in HSV-infected cells maps to adenosine residue 201 (see Fig. 39).

From these structural studies, we conclude that tk mRNA is slightly larger than 1,300 ribonucleotides if measured from the 5′ terminus to the poly-A addition site. We also predict that the tk polypeptide is translated starting at an AUG codon found at nu-

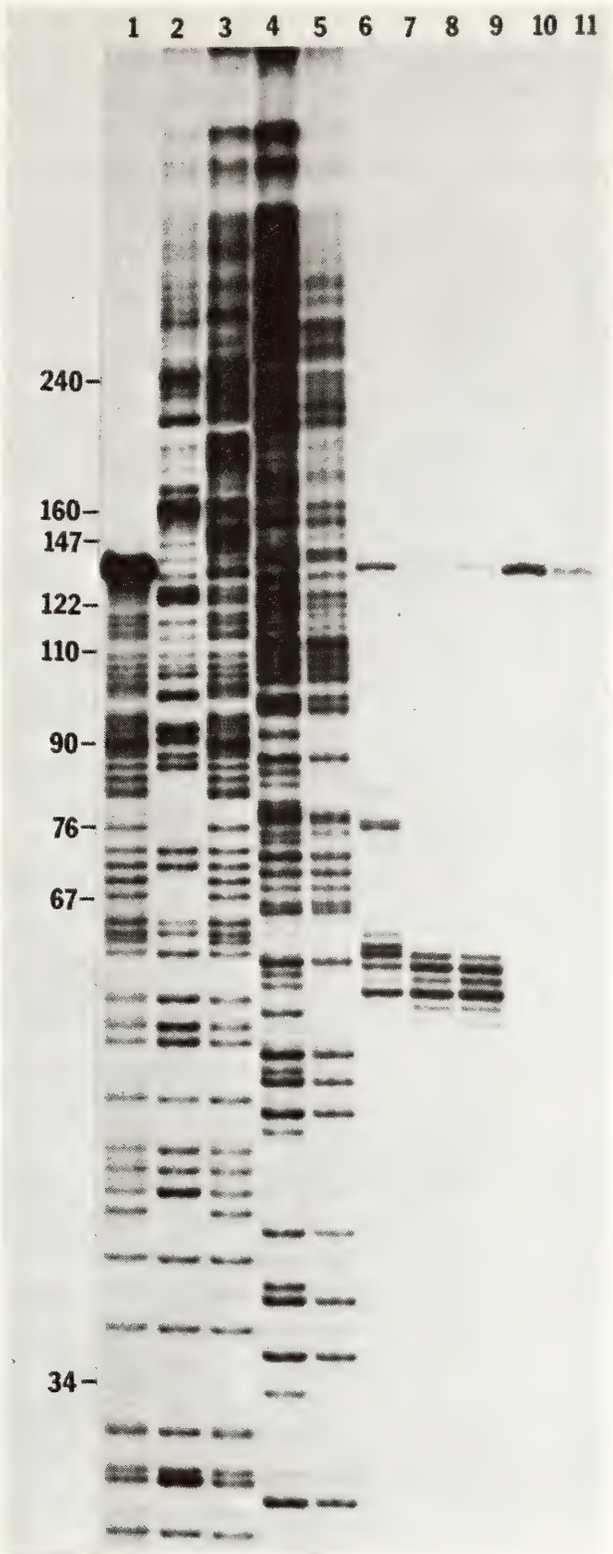


Fig. 41. The 5′ terminus of tk mRNA was mapped using a single-stranded probe DNA that extends from the EcoRI site at nucleotide 121 to the BglII site at nucleotide 252 (see Fig. 39). The DNA fragment was labeled at its 5′ terminus with ^{32}P, hybridized to mRNA prepared from HSVI-infected cells, digested with Exonuclease S_1, then electrophoresed on a 20% polyacrylamide sequencing gel. This autoradiogram of the gel was used to map the 5′ terminus of tk mRNA. The numbers to the left designate the positions of molecular weight marker DNA fragments. Probe DNA modified with pyridinium formate and cleaved with piperidine (sequence reaction "A") was loaded into Lane (1). Lanes (2–5) were loaded with sequenced DNA fragments (G, A, T, and C, respectively) that were prepared from a DNA fragment labeled at the BglII site and extending to the leftward BamHI site of pHSV-106. Lanes (6–8) were loaded with the BglII–EcoRI probe that had been digested with 1, 10, and 50 units of S_1, respectively, after hybridization to mRNA prepared from HSV-infected cells. Lane (9) was loaded with intact probe DNA, and Lane (10) was loaded with probe DNA digested with one unit of S_1 without having been hybridized to mRNA.

cleotide 111. This prediction assumes that tk translation starts at the first methionine codon "downstream" from the 5′ terminus of the mRNA. Finally, we point out that the tk gene of Herpes Virus does not appear to be interrupted by an intervening DNA sequence. This conclusion rests on the basis of mRNA mapping data showing that roughly 1,300 bp of single-stranded tk probe DNA is fully protected from S_1 digestion by tk mRNA.

INITIATION AND TERMINATION SIGNALS OF *Xenopus* RIBOSOMAL DNA

Mapping the Transcription Initiation and Termination Signals of *Xenopus laevis* Ribosomal DNA

B. Sollner-Webb, A. Bakken, G. Morgan,* S. Busby,† and R. H. Reeder†*

We earlier reported the location of the in vivo transcriptional initiation and termination sites of *Xenopus laevis* ribosomal DNA (rDNA) and the nucleotide sequence of the surrounding DNA region (*Year Book 78*). We have now begun to map the location of the nucleotides that constitute the transcription initiation signal and have obtained information concerning the specificity of the termination signals.

In order to map these transcription signals, a transcription assay is required. The assay we have chosen involves injection of rDNA-containing plasmids into an oocyte nucleus and examination of the resultant transcription complexes by electron microscopy, as first described by Trendelenburg (*Nature, 276,* 292, 1978). We first confirmed the following results of Trendelenburg and Gurdon: (1) when pXlr101, a plasmid containing an entire rDNA repeat, is injected into a *Xenopus laevis* oocyte, transcription units of the same length as those of endogenous rDNA genes are seen on recombinant DNA molecules, and (2) only a very small fraction of the injected DNA is observed in these structures. This suggests that the added genes initiate and terminate "properly," but that a factor necessary for initiation functions to only a limited extent with this added DNA.

The very low yield of transcription units observed when rDNA is injected into *Xenopus* oocyte nuclei makes this assay rather unsatisfactory for routine plasmid screening. We thus decided to inject these genes into *Triturus* oocyte nuclei, where endogenous rRNA genes spread more completely for electron microscopy than they do in *Xenopus* oocyte nuclei. As hoped, a far greater fraction of the rDNA that is injected into *Triturus* oocytes supports formation of transcription units. As with the *Xenopus* oocyte injections, a gradient of fiber lengths suggests that there is one initiation site per rDNA repeat. In this case, however, termination appears not to work reproducibly when pXlr101A is injected. Some of the resultant transcription units are the expected length but most are longer, as if the polymerase reads through the end of the gene. The question of termination will be discussed below. First, we will examine initiation in the *Triturus* oocyte injection system.

We have begun to map the nucleotide sequences necessary for transcriptional initiation in the *Triturus* oocytes by injecting successively more limited regions of cloned *Xenopus* rDNA. First, we observed that a plasmid containing from 1150 nucleotides before to 2250 nucleotides after the in vivo initiation site supports transcription, while control plasmids lacking this region of the rDNA do not. From the left-hand side the closest we have approached this initiation control region is 316 nucleotides before the in vivo initiation site; plasmid pE5, which contains from 316 nucleotides before to 1300 nucleotides after the in vivo initiation site, supports transcription in this system. From the right-hand side, the closest we have approached this control region is 115 nucleotides after the in vivo initiation site; plasmid pXlr14C, which contains from 1150 nucleotides before to 115 nucleotides

*Dept. of Zoology, University of Washington, Seattle.

†Hutchinson Cancer Research Center, Seattle.

after the in vivo initiation site, supports transcription. Finer mapping is currently in progress. However, the present data suggest that the transcription initiation control region for *Xenopus laevis* rDNA is located between 316 nucleotides before and 115 nucleotides after the in vivo transcription initiation site. That is, we have tentatively mapped this control sequence to a region comprising 3% of the rDNA repeat length.

In the rDNA spacer there are regions ("Bam islands") with >90% sequence homology to the region from 127 nucleotides before to 4 nucleotides after the in vivo initiation site, and it has been suggested that these regions are necessary in order to achieve full polymerase loading onto the rRNA genes. Since pE5 appears to support production of fully loaded transcription units, we can say that in this injection system the Bam islands are not required for polymerase loading onto the rRNA genes.

As noted above, *Xenopus* rDNA injected into *Triturus* usually does not terminate transcription "properly." In many cases, there appears to be no recognized termination signal on the plasmid; rather, transcription proceeds for multiple circuits, since plasmids covered with very long fibers are observed. In this system a long string of T residues apparently is not sufficient to specify termination, since pXlr14C, which was made by AT tailing such that ~50 T residues are joined onto the noncoding strand 115 nucleotides after the in vivo transcription initiation site, still supports the production of long transcription units.

Transcription termination may, however, be examined using *Xenopus* rDNA in the homologous *Xenopus laevis* oocyte injection system. As noted above, when the entire rDNA repeat excised with Hind III and inserted clockwise into the Hind III site of the tetracycline resistance gene of pMB9 or pBR322 (plasmids pXlr101 or pXlr101A, respectively) is injected into *Xenopus* oocytes, a transcription unit of the in vivo length is observed, suggesting that transcription terminates at the in vivo site. In fact, the in vivo termination site resides within the Hind III recognition sequence, at the start of a T_4 cluster. In pXlr101 and pXlr101A the vector contributes one additional T to the Hind III recognition sequence (AAGCTT) to form a T_3 cluster. This sequence apparently is sufficient for termination. However, pXlr101B, which has the same HindIII cut rDNA repeat as pXlr101A but is inserted into pBR322 in the opposite orientation, does not terminate transcription faithfully at this site. In this orientation the vector contributes an A-residue adjacent to the HindIII site at the end of the rDNA gene. There are only two T-residues, which apparently are insufficient for termination. Thus, unless oligonucleotides beyond the T_n cluster are involved in specifying termination, we can tentatively conclude that a T_3 at the end of the HindIII site is sufficient to specify faithful termination, but a T_2 is not. In pXlr101B there are numerous T_4 and T_5 clusters contributed by pBR322 within a few hundred base pairs beyond the Hind III site, yet these do not cause termination in a large fraction of the transcription unit; this suggests that nucleotides other than the T residues of the termination site are important in specifying the termination signal, Finally, we noted that transcription of pXlr101B never proceeds for multiple circuits of the plasmid, but rather appears to stop just prior to the initiation site on the plasmid, if not before. DNA sequence analysis of this region of the rDNA had demonstrated an oligonucleotide, approximately 230 nucleotides before the in vivo initiation site, having many characteristics usually attributed to a termination signal (*Year Book 78*). We suggested that this region may act as a "fail-safe" termination signal to prevent transcripts—occasionally seen in

the "nontranscribed spacer" in vivo—from proceeding into the transcription initiation site. Possibly the termination observed near the initiation site in pXlr101B results from such a fail-safe termination signal. Further analysis will allow the nucleotide sequences constituting the initiation and termination signals to be more precisely delimited.

The *Xenopus laevis* Ribosomal DNA Transcription Termination Signal is Correctly Read by RNA Polymerase III

B. Sollner-Webb and D. Bogenhagen

We earlier mapped the in vivo transcription termination site of *X. laevis* ribosomal DNA (rDNA) and sequenced the surrounding DNA region (*Year Book 78*). Transcription terminates within the lone HindIII recognition sequence of the rDNA repeat at the start of a T_4 cluster. The presence of this T_4 oligonucleotide suggests a similarity between this region of the rDNA and transcriptional termination signals of genes that are transcribed by RNA polymerase III and by *E. coli* RNA polymerase.

We wanted to test whether the termination site of rDNA that is transcribed in vivo by RNA polymerase I would serve to terminate transcription by another class of RNA polymerase. A fragment of rDNA containing the termination site was recombined with that part of a 5S RNA gene containing the signal for RNA polymerase III initiation. This hybrid "gene" was cloned in pBR322. The resultant plasmid contains the site where RNA polymerase I normally terminates transcription ~260 nucleotides downstream from the site where RNA polymerase III initiates synthesis. Transcription of this plasmid was examined in the in vitro system routinely used to assay RNA polymerase III transcription (Birkenmeier *et al., Year Book 77*). The resultant RNA was sized on gels and found to be ~260 nucleotides long, the length expected if RNA polymerase III terminated synthesis at the normal RNA polymerase I termination site.

A second, related plasmid was constructed, which contains the rDNA region from ~30 nucleotides before to ~200 nucleotides after the rDNA termination site joined to the same RNA polymerase III initiation fragment used above. This second construction serves two purposes. First, it allows us to test whether any extensive intragenic regions preceding the rDNA Hind III site are necessary for transcription termination. Second, if transcription termination still occurs, the predicted 133-nucleotide RNA product will be small enough to size accurately by gel electrophoresis. When this plasmid was transcribed in vitro and the resultant RNA sized, the transcript was seen to be ~133 nucleotides in length.

We conclude that in vitro transcription by RNA polymerase III terminates efficiently at the nucleotide sequence that encodes the termination of transcription by RNA polymerase I in vivo. From the results with the second plasmid, it appears that the termination coding sequence does not extend more than 30 nucleotides before the rDNA termination site. Whether sequences other than the T_4 oligonucleotides are involved in specifying this termination awaits further examination. This "interchangeable termination signal" may represent either evolutionary relatedness of RNA polymerase I and III or perhaps the recognition site of a termination-specific factor common to both polymerases.

THE STRUCTURE AND EXPRESSION OF *Drosophila* CHORION GENES

A. Spradling with the technical assistance of L. Pedersen

The development of multicellular organisms proceeds in an orderly and highly integrated manner despite the occurrence of substantial environmental or experimental perturbations. These observations have led to the idea that the zygote contains a relatively stable "developmental program" presumably consisting of stored information and mechanisms for its activation at the appropriate time and place. Ultimately, our studies are based on the assumption that an understanding of how individual genes are controlled will shed light on at least some of the mechanisms of developmental programming. Consequently we have concentrated our efforts on an interesting and experimentally favorable system for studying gene regulation—the ovary of the fruitfly *Drosophila melanogaster*. At present we are particularly interested in understanding events that control the expression of the structural genes for the eggshell proteins during the terminal stages of oogenesis.

In *Drosophila* an oogonial cell is capable of maturing into an egg in less than a week. The production of the outer two layers of the egg-shell, the endochorion and exochorion, requires only five hours and is particularly favorable for study. Since these layers consist primarily of five or six major structural proteins which are synthesized by the 1,000 follicle cells of an egg chamber, very high rates of synthesis are required. Furthermore, each protein is produced for only part of the five-hour period, during which time its messenger RNA is abundant in the follicle cells. At least two specific patterns of synthesis consisting of different subgroups of the major proteins occur sequentially. The follicle cells thus provide an extreme example of temporal gene regulation.

Two basic mechanisms have been described previously which allow unusually high rates of production by a cell of a particular gene product. Genes may be present in multiple copies in the germline but be expressed in only certain cells. The oocyte-specific 5S multigene families of *Xenopus* studied by Brown and his colleagues (see *Year Book 69* and subsequent Year Books) provide such an example. The large amounts of rRNA which are required during oogenesis in *Xenopus* are produced in a different way. Instead of maintaining the large number of rRNA genes which would be required in the germ line, extra rounds of replication of these genes occur in oocytes (see Brown and Dawid, *Year Book 67*).

In collaboration with Dr. Anthony Mahowald of Indiana University and Dr. Gail Waring of Marquette University, we have previously characterized some of the major chorion proteins and their genes (Table 8). Although the genes are clustered at two chromosomal sites, only single copies of each one appear to be present in the genome of the embryo. However, by using cDNA clones complementary to chorion messenger RNAs, we have shown that the

TABLE 8. Properties of Major Chorion Protein Genes of *Drosophila melanogaster*

Protein	mRNA Size (kb)	Cytogenetic Locus	Time of Expression
c38	1.4	7F1-2	stage 12-13
c36	1.2	7F1-2	stage 12-13
c18	.8	66D15	stage 13-14
c15*	.7	66D15	stage 13-14

*The association of c15 with this chorion gene is uncertain.

second type of mechanism, gene amplification, is involved in the rapid synthesis of the eggshell proteins by follicle cells. Egg chambers just prior to and during the period of choriogenesis contain a 12-fold to 30-fold higher concentration of genes for major chorion proteins than egg chambers at earlier stages or in other tissues.

Mechanism of Chorion Gene Amplification

The mechanism by which extra copies of the chorion genes are synthesized has been studied using several approaches. Of particular interest is the question whether the amplified genes are present as extrachromosomal molecules, as in the case of amplified rDNA genes in *Xenopus* and other organisms. In *Xenopus* the different rDNA genes of the germline do not contribute equally to the amplified DNA (Wellauer *et al., J. Mol. Biol., 105,* 497, 1976). The situation appears to be somewhat different in the case of the chorion genes. Females heterozygous for electrophoretic variants of the chorion proteins c36 or c38 express both forms equally in their ovaries. We have taken advantage of the existence of a BamHI site in the c38 gene which is polymorphic between two strains to demonstrate directly that approximately equal amounts of the two allelic forms of the gene are amplified in the ovaries of heterozygotes. It remains to be shown that both alleles are amplified within a single follicle cell. However, flies that are heterozygous for a chorion gene deficiency or for a defective chorion gene do not produce eggshells which are detectably mosaic. Thus if amplification does occur by the production of extrachromosomal molecules, it is likely that both homologues contribute equally in their production.

Direct attempts to separate the amplified genes from the remainder of the ovarian DNA have not been successful. The amplified sequences have nearly the same buoyant density as the main band in neutral CsCl gradients. They do not separate from the bulk of the DNA in CsCl-EtBr gradients. The sequences detected by hybridization with a chorion gene probe were found to sediment heterogeneously with high molecular weight DNA in sucrose gradients.

The size of the amplified DNA has been investigated by selecting segments of chromosomal DNA containing the chorion genes and their surrounding sequences from "libraries" of cloned genomic fragments. So far we have obtained a collection of six overlapping clones centered on the chorion gene clusters of both the X and third chromosomes. These clones define a DNA sequence of about 60 kb at both sites (see Fig. 42). By hybridizing labeled fragments of these DNAs to restriction digests of egg chamber DNA, it has been determined that a large contiguous region of chromosomal DNA, which includes the chorion sequences, is amplified on both chromosomes. The exact lengths of the amplified regions have yet to be determined, but they contain at least 60 kb of DNA.

The restriction fragments complementary to sequences at the ends of the amplified regions are of particular interest. If amplification occurs by an extrachromosomal mechanism, the restriction fragments at the ends of the molecules should differ in amplified, compared to nonamplified, DNA. If a different mechanism is involved, study of the fragment pattern and relative amounts of end fragments would be expected to provide information about its nature.

Effect of Mutations on Chorion Gene Amplification and Expression

The mechanisms by which mutations alter gene expression in eukaryotic organisms are not as well understood as they are in prokaryotes. This is par-

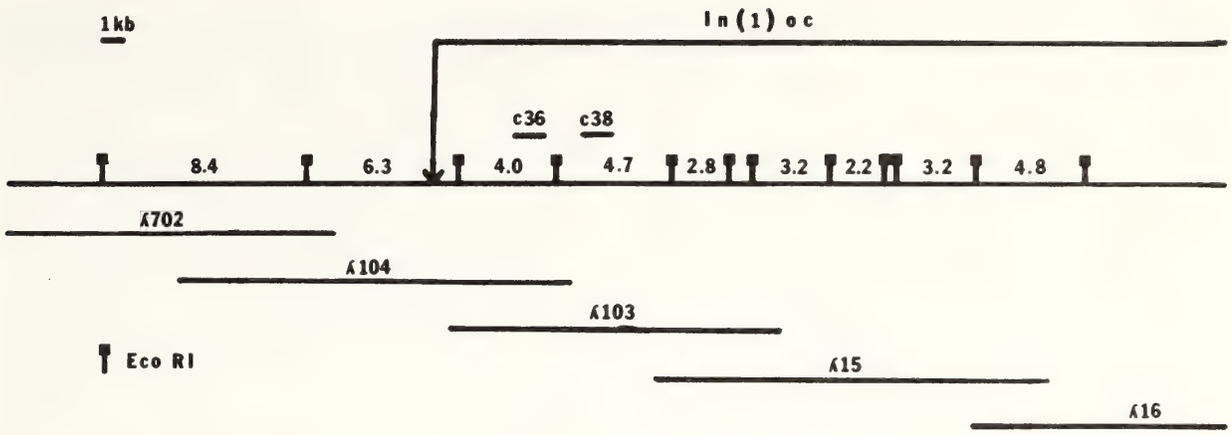


Fig. 42. Map of the chromosomal region containing the c36 and c38 chorion genes. Cloned segments of *Drosophila* genomic DNA were used to construct a restriction map of DNA from part of the 7F region of the X chromosome. The position of the c36 and c38 chorion genes were determined by hybridization with cDNA clones. The approximate site of the *ocelliless* inversion breakpoint is indicated. Approximate distances between sites of EcoRI cleavage (vertical lines) are given in kilobases.

ticularly true in the case of chromosome aberrations, such as those induced by x rays. Studies correlating the cytogenetic location of chromosome breakpoints with the induced phenotype in *Drosophila* have provided strong evidence that chromosome breakage and rejoining can have effects on genes located at a large distance from the breakpoint itself (for example, see Demerec, *J. Genet. Suppl., 1941,* 99, 1939). Such mutations have been called position effects. Lewis (*Adv. Genet., 3,* 73, 1950) distinguished two types of position effects. Variegated position effects result from the expression of a normally active gene only in certain developing clones within a tissue. This type of instability is often seen when the gene in question resides near a heterochromatic region following rearrangement. In contrast, wholly euchromatic chromosome rearrangements are believed to sometimes result in a stable reduction in the expression of very closely linked genes. The molecular mechanisms underlying either type of altered gene control are unknown, but it is interesting to speculate that mechanisms involved in some aspects of developmental programming may require the continuity of certain chromosomal regions to function normally.

The selection and analysis of mutations altering the patterns of chorion gene expression provide an approach to understanding chorion gene control. In the coming year we plan to select a series of such mutations following mutagenesis with x rays. Currently, Mary Ellen Digan and Anthony Mahowald of Indiana University and George LeFevre of California State University have provided us with strains carrying mutations in genes in the 7F region of the X chromosome. Our studies have concentrated on a single mutation, *ocelliless* (*oc*), which maps at 7F and which causes homozygous females to produce reduced amounts of both the c36 and c38 chorion proteins in ovarian tissue. Such females are sterile and produce mature oocytes with morphologically abnormal chorions. The heads of such females also show a complete lack of the ocelli and a deranged pattern of bristles in the surrounding region. A combination of genetic and biochemical studies have recently clarified the mechanisms underlying these defects. They suggest that *ocelliless* is an example of a "stable" type of position effect which acts by interfering with

amplification in the 7F chorion gene region.

Figure 43A shows that when a probe specific for the c36 gene was hybridized *in situ* to polytene chromosomes from a larva homozygous for *oc,* a surprising result was obtained. c36 complementary sequences were not located at identical positions on the two homologues but were displaced by a small interval. Figure 43B demonstrates that this displacement is the result of a small inversion in the *ocelliless* homologue with breakpoints at approximately 7F1-2 and 8A1-2.

Complementation studies of *ocelliless* and *JA101,* an EMS-induced lethal mutation isolated by G. LeFevre, also suggested a multisite origin for the defects shown by *oc* homozygotes. *oc/JA101* heterozygotes show effects on the head of the fly typical of *ocelliless* but are fertile because the *JA101* chromosome produces normal amounts of both c36 and c38. An EMS-induced female sterile mutation isolated by M. E. Digan, *cor-36,* complemented *JA101* for both the head phenotype and sterility, although *cor-36* homozygotes fail to accumulate detectable c36. The simplest explanation is that the inversion causes effects on two separate genes: the *JA101* (or true *ocelliless*) gene associated possibly with the proximal breakpoint, and the c36 and c38 chorion genes associated with the distal breakpoint.

To learn more about how inversion might result in the underproduction of products from two closely linked genes, the breakpoint was localized relative to the restriction map defined by the genomic clones. Figure 44 demonstrates that when a probe complementary to the λ104 genomic clone is hybridized *in situ* to polytene chromosomes from *ocelliless,* labeling is observed at both ends of the inverted region. The same probe labels only a single site on wild-type chromosomes. This indicates that the inversion breakpoint is located within the 16 kb of

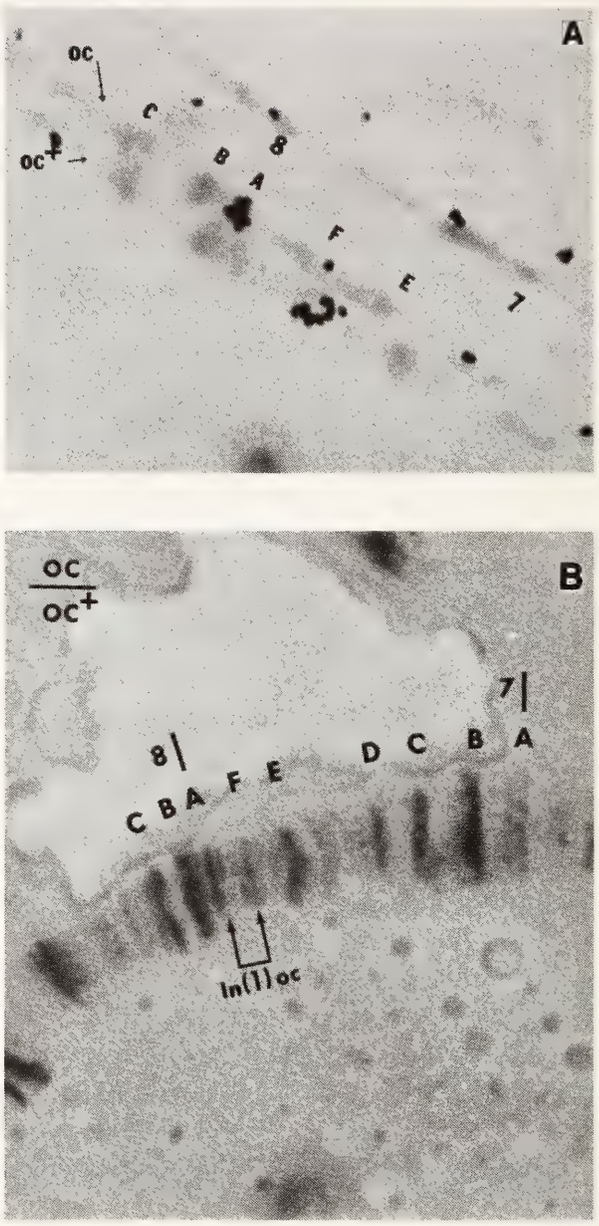


Fig. 43. (A) In situ hybridization of c36 sequences to polytene chromosomes from oc/oc^+ heterozygotes. ^{3}H-RNA transcripts complementary to a c36 cDNA clone were hybridized in situ to salivary gland chromosomes from larvae heterozygous for *ocelliless.* Grains were observed at the normal position near 7F1-2 on one homologue, but on the *ocelliless* homologue their position was close to 8A1-2. (B) Salivary gland chromosome from oc/oc^+ showing the presence of a small inversion in the *ocelliless* homologue. Lactic acetic orcein stain was used.

Drosophila DNA contained in this clone. The position of the breakpoint was further localized by comparing the restriction fragments complementary to λ104 in wild-type and *ocelliless* DNA. Only one small region was found

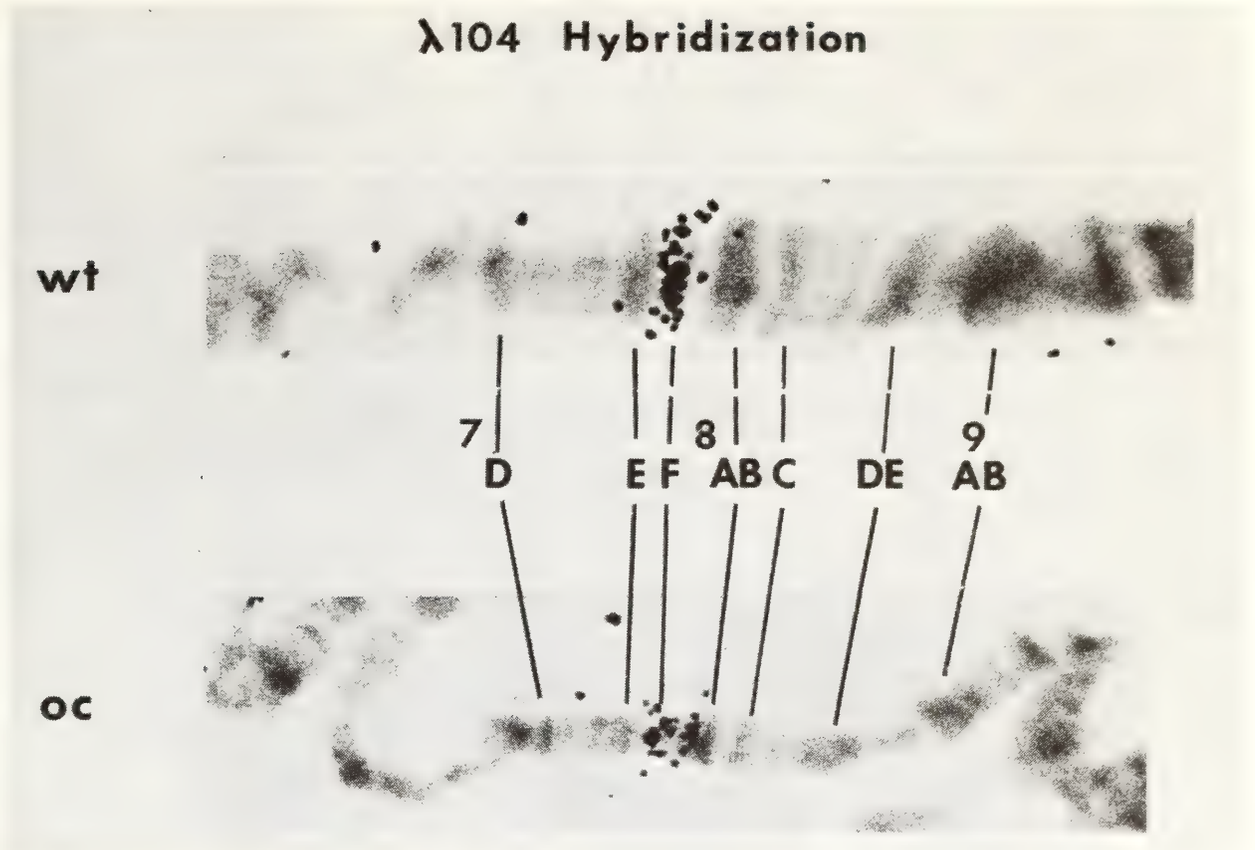


Fig. 44. Demonstration that the *In(1)oc* breakpoint is contained in the sequences cloned in λ104. ^{3}H-RNA complementary to λ104 DNA was hybridized in situ to polytene chromosomes from wild-type (wt) or *ocelliless* (oc) larval salivary glands. One band at 7F1-2 was labeled in the wild type, but bands at both 7F1-2 and 8A1-2 were labeled in *ocelliless* chromosomes.

where extensive differences exist; it was located 2–3 kb from the c36 gene (see Fig. 42). Since c36 is known to be included within the inverted region (Fig. 43A), this allows orientation of the restriction map relative to the X chromosome (c38 must be proximal).

These studies indicated that an inversion whose breakpoint is located at least 2 kb from the structural sequences of a gene can alter the level of its expression. We have shown previously that c36 and c38 sequences are amplified 3–4-fold less in *ocelliless* than in wild-type females. Thus part or all of the reduced production of c36 and c38 could result from the effects of the inversion on the replication of the chorion gene region.

Figure 45 shows the results of hybridizing ^{32}P-labeled λ104 DNA to Eco RI digests of wild-type and *ocelliless* DNA from preamplification (stages 1–8) and postamplification (stages 10–14) egg chambers. In wild-type DNA, EcoRI fragments of 8.4, 6.3, and 4.0 kb are labeled (see also Fig. 42). The intensity of all these fragments is greater with DNA from late-stage egg chambers owing to uniform amplification of this region. A different result is obtained in the case of *ocelliless* egg chambers, however. Four EcoRI fragments are labeled, a 4.0-kb fragment containing the c36 gene, a 7.7-kb fragment which corresponds to the wild-type 8.4-kb fragment, and two end fragments of 2.1 kb and 5.9 kb which contain the sequences of the 6.3-kb fragment proximal and distal respectively to the inversion breakpoint. When the relative intensities of these bands are compared in egg-chamber DNA before and after amplification

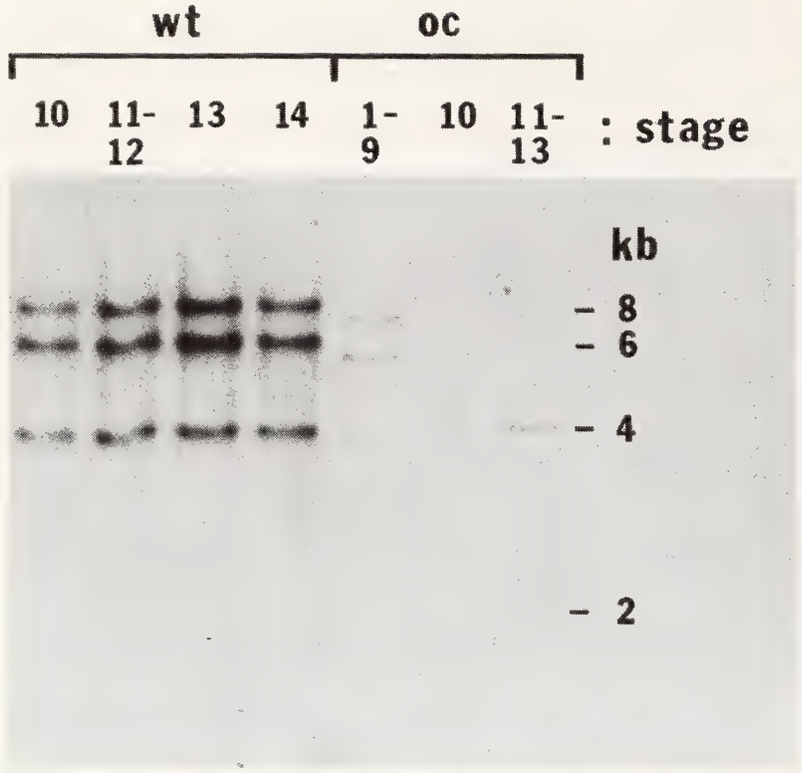


Fig. 45. Amplification of DNA sequences complementary to λ104 in wild-type and *ocelliless* egg chambers. ^{32}P-labeled λ104 DNA was hybridized to gel transfers of EcoRI-digested RNA purified from wild-type and *ocelliless* egg chambers. Each lane contains the DNA from approximately ten egg chambers of the indicated developmental stages. The molecular weight in kilobases of the indicated bands was determined relative to marker fragments of known size present in parallel lanes of the gel.

has occurred, it can be seen that the intensity of only the 4.0-kb and 2.1-kb bands has increased (Fig. 45). This indicates that amplification of sequences included within the inverted region is still observed in late-stage *ocelliless* egg chambers, although the magnitude of the increase is considerably less than in the wild type. However, DNA sequences distal to the breakpoint (the 5.9-kb and 7.7-kb framents), which are normally amplified at a level about the same as the proximal sequences, do not undergo any detectable extra replication in the presence of the inversion.

These results argue that amplification is dependent on a cis-acting chromosomal element, possibly an origin of DNA replication, which is included within the inversion. The large separation of the distal sequences from this element in the inverted chromosome may explain their failure to replicate normally. We are currently investigating whether sequences in the 8A region which are brought into close proximity of this chromosomal element undergo amplification only in DNA from *ocelliless* egg chambers.

The effects of the *ocelliless* inversion show that interruption of the continuity of a chromosomal region can alter its replication properties. We are interested in the possibility that disturbances of DNA replication may be involved in other cases of position effects resulting from chromosome rearrangements.

THE DUAL 5S GENE SYSTEM IN *Xenopus*

D. D. Brown, D. Bogenhagen, E. Jordan, H. Pelham, R. Peterson, S. Sakonju, H. Shin, and M. Wormington

In previous Annual Reports we described the structures and complete sequences of individual repeating units of five multigene families of 5S DNA isolated from two species of *Xenopus*. These descriptive experiments were complemented by the development of an assay system in which cloned 5S RNA genes are faithfully transcribed into RNA (*Year Book 77*). This has made possible two kinds of experiments —the alteration of 5S DNA to delimit regions that control its expression, and the fractionation of cell extracts to identify those molecules responsible for the accurate initiation and termination of transcription. In *Year Book 78* we reported the surprising finding that accurate initiation of transcription of a 5S RNA gene is controlled by a region within the gene. This contrasts with the location of promoter sites in prokaryotic DNA that are known to flank the 5′ end of structural genes. David Engelke and Robert Roeder of Washington University (Engelke *et al.*, *Cell, 19*, 717, 1980) isolated from *Xenopus* ovaries a protein required for accurate transcription of the 5S RNA gene. They made the interesting observation that this protein binds to the center of the gene—the same region that we had demonstrated controlled accurate transcription of the gene. In this report, we describe two new findings related to this transcription factor. First, protein binding studies carried out by Sakonju in collaboration with Roeder's group confirm the importance of the interior control region. Deletions that have lost part of this region no longer bind the transcription factor. Second, Pelham has proven that the transcription factor is identical to an abundant protein known to be complexed with 5S RNA in early oocytes. This 7S particle accumulates in early oogenesis prior to ribosome synthesis (Picard *et al.*, *Proc. Nat. Acad. Sci. USA, 76*, 241, 1979). Therefore the protein has two functions: it turns on the 5S RNA genes in oogenesis and then complexes with the gene product, 5S RNA. This may be the first true "differentiation factor" to be identified, since the active synthesis of this protein could activate specifically the 5S RNA genes in immature oocytes.

M. Wormington has devised a quantitative assay that compares the rates of transcription of different kinds of 5S RNA genes and deletions of 5S DNA. By competing one kind of 5S RNA gene against another, the "relative strength" of the control region in a mutated gene can be assessed. This has resulted in two important findings. First, deletions upstream from the control region reduce the ability of a 5S RNA gene to compete for the transcription of a wild-type 5S RNA gene. This means that these regions influence 5S RNA gene transcription. Second, one family of oocyte-specific 5S RNA genes is transcribed as efficiently as somatic genes but competes with them very weakly. We believe that the analysis of this difference may be the first step in understanding how the oocyte-specific genes are shut off in somatic cells.

D. Bogenhagen reports an analysis of the transcription termination site of 5S RNA gene. This was accomplished by careful deletion and rearrangement of the gene near its 3′ end. Four T's on the noncoding strand are required but are not sufficient for accurate termination. They may need to be flanked by one GC-residue on either side.

Initial experiments are reported by Shin and Peterson on the fractionation

of components in cell extracts required for accurate transcription of 5S DNA, transfer RNA genes (tDNA), and the VA gene from adenovirus. Different cell extracts that have widely varying activities for transcribing these three kinds of genes can be used to complement each other as an assay system for the purification of transcription factors.

A Transcription Factor Binds to the Control Region of 5S DNA

S. Sakonju and D. D. Brown in collaboration with D. Engelke and R. G. Roeder**

In *Year Book 78*, we reported the identification of a region within the 5S RNA gene that directs specific initiation of transcription. *X. borealis* somatic 5S DNA with deletions from the 5′ or 3′ side of the gene was constructed in vitro, cloned, and tested for the ability to initiate 5S RNA transcription in an oocyte nuclear extract. We found that the 5S RNA gene can be deleted to gene residue +50 (+1 being the first nucleotide of the 5S RNA gene) from the 5′ side or to +83 from the 3′ side without losing its ability to support specific initiation of transcription. We have since shown that the gene region from +41 to +87 by itself contains sufficient information to direct specific transcription initiation. Therefore, the information that is essential for initiation of transcription resides within the 5S RNA gene in the region between residues +50 to +83 as defined by our "in vitro" genetic analysis. (For a full account, see Sakonju *et al.*, *Cell*, *19*, 13, 1980; Bogenhagen *et al.*, *Cell*, *19*, 27, 1980).

Our findings were soon followed by a report from the laboratory of Dr. R. Roeder of Washington University telling of the isolation of a 5S RNA specific transcription factor (Engelke *et al.*, *Cell*, *19*, 717, 1980). They showed that the purified protein factor, with an apparent molecular weight of 37,000, interacts specifically with the region between +45 to +97 of the 5S RNA gene. The almost identical location of the control region delimited by us, and the binding region of the protein determined by Engelke *et al.*, makes it likely that the protein they purified is an initiation factor for 5S RNA transcription. In order to strengthen this correlation, we have examined the interaction of the transcription factor with various 5S DNA deletion mutants using the technique of "footprinting" (developed by Galas and Schmitz, *Nucl. Acids Res.*, *5*, 3157, 1978). The work was done in collaboration with Dr. Roeder and his colleagues, who provided the purified protein.

DNA fragments from various deletion mutants were labeled with ^{32}P on one terminus and purified from polyacrylamide gels. Each of the DNA fragments was incubated with the purified protein in a binding buffer identical to that used for the transcription reaction. Following the binding reaction, DNase I was added to the reaction mixture for a brief period, and the resultant partially cleaved DNA fragments were electrophoresed on acrylamide gels containing 7M urea. Figure 46 shows the result of such an experiment using DNA fragments prepared from various 3′ deletion mutants. The fragments are labeled at a Hind III site located 50 base pairs upstream from the 5′ end of the gene. In each fragment the complete or deleted 5S RNA gene is joined at its 3′ site to pBR322. The comparison of the DNase-digested fragments in the presence and in the absence of the protein shows a region where the radioactive bands are absent for XbsΔ3′+124 and +97. This indicates that the protein has bound to the DNA and protected the region from DNase I digestion. Residues +45 to +97 are protected as reported by Engelke *et al.* There are also sites of en-

*Washington University, St. Louis.

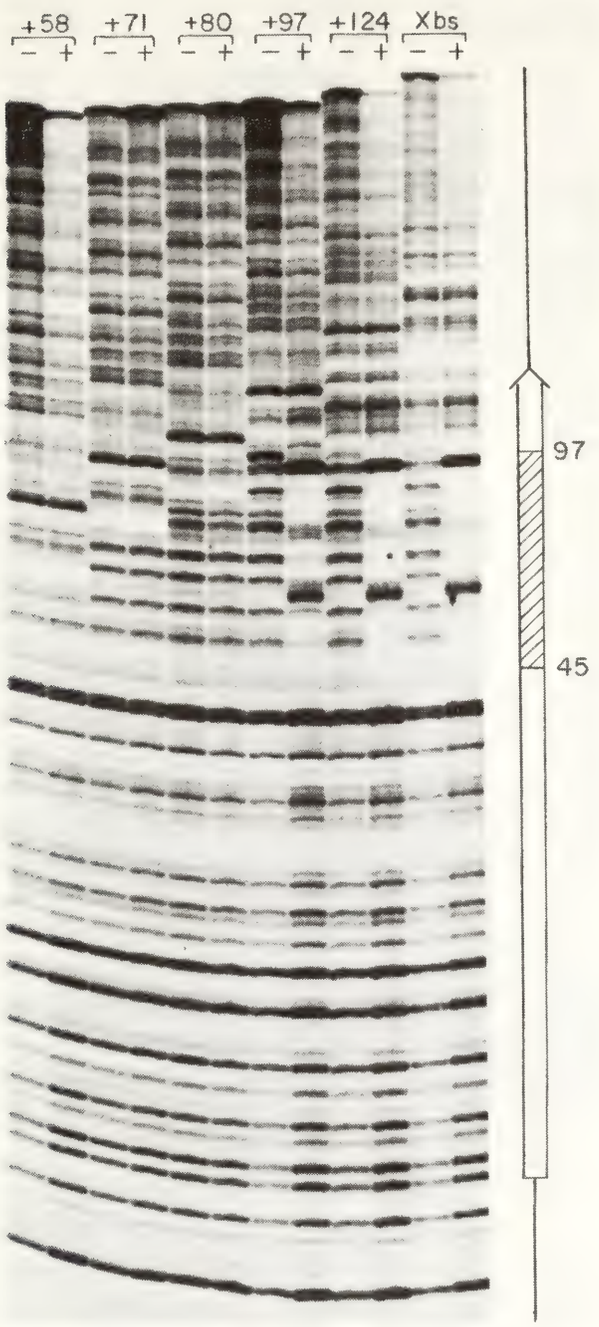


Fig. 46. Footprint analyses of several 3′-deleted 5S DNA with or without the purified transcription factor. The region corresponding to 5S RNA gene is shown schematically on the right. The cross-hatched area between residues +45 and +97 represents the transcription factor binding site. The transcription factor is present in plus lanes and absent in minus lanes. The numbers above each lane refer to the extent of each deletion.

hanced cleavage by DNase I at the locations previously reported. Hence we find that those 3′ deletion mutants that retain the ability to initiate transcription are also capable of binding the transcription factor. In contrast, the cleavage patterns are identical in the presence and absence of the factor when the DNA fragments from +58, +75, and +80 deletion mutants are used. These deletion mutants do not direct transcription initiation. Therefore, the lack of ability to initiate transcription in a mutant DNA is accompanied by the loss of binding to the transcription factor.

Similar conclusions can be drawn from the "footprint" experiments using DNA fragments from 5′ deletion mutants, three of which are shown in Fig. 47. The DNA fragments from the 5′ deletion mutants that retain the ability to initiate transcription show the region, extending from +45 to +97, protected by the factor. There are no enhanced cleavage sites within the protected region, indicating that the binding of the protein is asymmetric with respect to each strand of DNA (DNA fragments from the 3′ deletion mutants are labeled on the noncoding strand while those from the 5′ deletion mutants are labeled on the coding strand). The DNA fragment from the +64 deletion mutant cannot initiate transcription, yet it remains partially protected between residues +65 and +97 (see Fig. 47). We did not observe any protection of the DNA fragment from the +77 deletion mutant, which also does not initiate transcription (not shown).

Thus deletion of the control sequence from the 3′ end (i.e. +80 to +97) leads to a complete loss of factor binding for the entire control region. On the other hand, the deletion of the 5′ end of the control region (+45 to +65) does not lead to the loss of binding to the remainder of the control region. These observations suggest that the dominant recognition sequence for the binding of the factor resides near the 3′ end of the binding region, and that binding there is a prerequisite for binding to the 5′ part of the region. However, when the 5′ end of the control re-

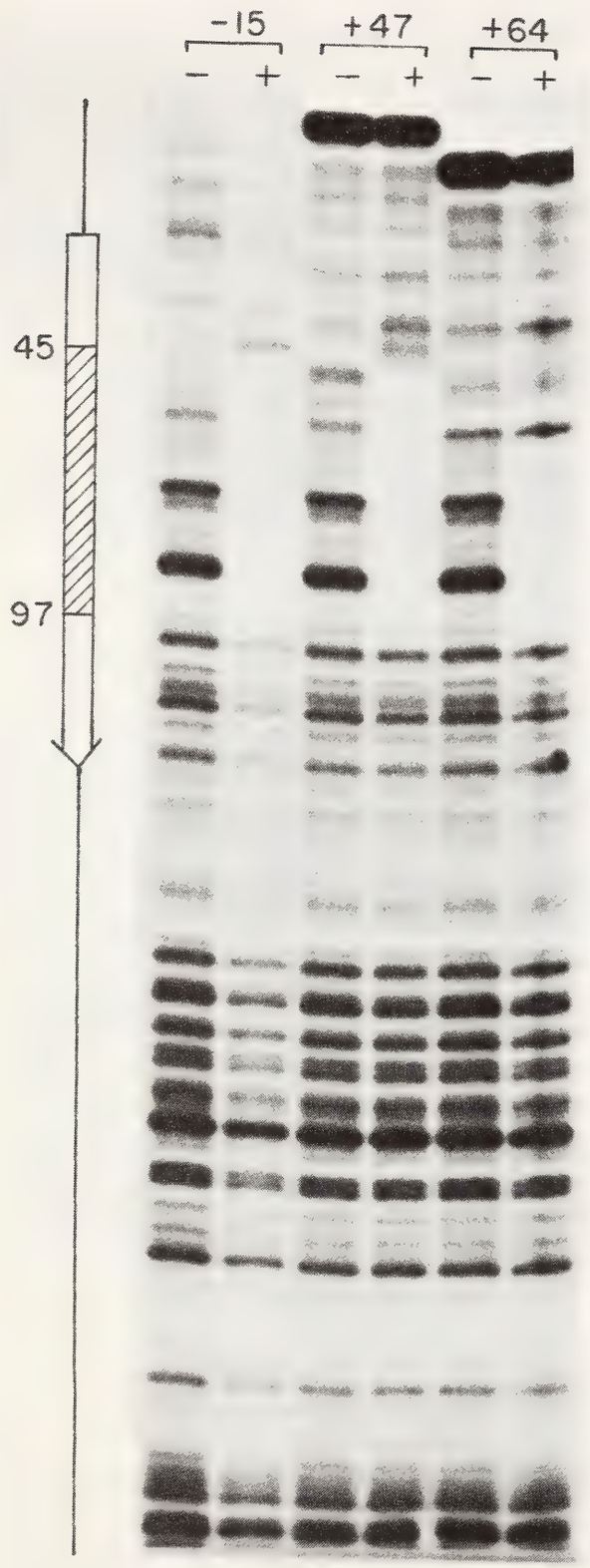


Fig. 47. Footprint analyses of several 5′-deleted 5S DNAs with or without the purified transcription factor. The 5S RNA gene and the binding region are shown schematically on the left. The numbers above the lanes refer to the extent of each deletion.

gion is missing, binding of the protein does not lead to transcription initiation.

The above conclusions are drawn from the qualitative results of the "footprint" experiments. We have yet to address ourselves to quantitative questions regarding the binding of the factor to various deletion mutants.

Finally, to confirm the report that the transcription factor is specific for 5S RNA transcription, we did "footprint" experiments with DNA fragments containing *Drosophila melanogaster* $tRNA^{arg}$ gene and the VA_1 gene of adenovirus 2. Both of these genes are transcribed in the oocyte nuclear extract. Using the same condition as the 5S DNA experiments (including the protein and DNA concentrations), we did not observe binding of the factor to the gene sequences or to the flanking regions. Thus it appears that the transcription factor is indeed specific for 5S RNA transcription.

The 5S DNA Transcription Factor is the Same Protein that Complexes 5S RNA in Oocytes

H. Pelham and D. D. Brown

During our investigations of the factors that determine the rate of 5S RNA synthesis in vivo, we considered the possibility that free 5S RNA might inhibit its own synthesis in vivo. This could effectively couple the rates of transcription of the 5S RNA genes and ribosome assembly. To test this idea, we investigated the effect of 5S RNA on transcription of cloned 5S DNA in the oocyte nuclear extract. 5S RNA (at 5–40 μg/ml) inhibits its own synthesis without inhibiting transcription of tRNA or adenovirus VA RNA genes. Specific inhibition was not observed when tRNA (from *Xenopus* or *E. coli*) was added to the transcription system.

Further studies showed a number of interesting characteristics of the inhi-

bition by 5S RNA. The only DNA sequence required for the effect is the previously defined intragenic control region. Residues 41–87 of the gene had been subcloned by D. Bogenhagen and shown to direct specific initiation of transcription. Termination occurs at multiple sites within the plasmid DNA, yielding heterogeneous products which are larger than 5S RNA. Figure 48 shows that synthesis of all these products was inhibited by 5S RNA, while transcription of plasmid DNA and of a cloned tRNA gene added as an internal control was unaffected.

The inhibition could be overcome by raising DNA concentration, suggesting that 5S RNA competes with 5S DNA for some factor required for transcription. Furthermore, inhibition was only observed when the RNA was added to the cell-free system at the same time as (or before) the DNA. If the DNA was preincubated with the nuclear extract for 30 minutes, the subsequent addition of 5S RNA had little effect for 40 minutes or more; thereafter the transcription rate fell slowly.

As the simplest explanation of these results, we predicted the existence of a transcription factor which would be able to interact either with the control region of 5S DNA or with 5S RNA, but not with both simultaneously. In fact, workers in Roeder's laboratory (Engelke *et al.*, *Cell*, *19*, 717, 1980) had already isolated a protein from *Xenopus* ovaries that was required for 5S RNA synthesis and could bind to the control region, but there was no reported evidence that this protein could interact with 5S RNA.

One protein that is known to bind 5S RNA is found in large quantities in the cytoplasm of immature oocytes. These cells begin to accumulate 5S RNA and transfer RNA 1–2 months prior to the synthesis of 18S and 28S rRNA. The stored 5S RNA is then incorporated into ribosomes together with the newly-made rRNAs. This uncoupling of 5S RNA synthesis from ribosome as-



Fig. 48. Autoradiogram of (^{32}P) RNA synthesized in vitro in the absence (a, c) or presence (b, d) of 20 μg/ml 5S RNA. All incubations contained cloned *Drosophila* arginine tDNA and, in addition, a cloned fragment consisting of either residues 41–87 of the Xbs 5S RNA gene (a,b), or pBR-322 (c,d). Arrow indicates the position of migration of 5S RNA.

sembly is apparently a device to compensate for the 20-fold numerical excess of amplified rRNA genes over 5S RNA genes at this stage.

About 70% of the 5S RNA in immature oocytes is found in a 7S complex that contains one molecule each of 5S RNA and a protein whose reported molecular weight is about 40,000 (Picard *et al.*, *Proc. Nat. Acad. Sci. USA*, *76*, 241, 1979). This protein is very abundant—it constitutes up to 15% of the soluble protein in the cells. The rest of the 5S RNA is in a 42S particle which also contains tRNA and two proteins; the smaller of these proteins also has a molecular weight of about 40,000. We compared the protein in the 7S particle to the one in the 42S particle and to the transcription factor isolated (and kindly donated) by Engelke and others in Roeder's laboratory. The proteins were labeled with (^{14}C) iodoacetate and subjected to partial proteolysis with chymotrypsin. The peptide maps of the 42S and 7S proteins were quite different, but the protein from the 7S particle appeared to be identical to the transcription factor. We therefore tested the ability of intact 7S particles and the protein purified from them to bind 5S DNA. This was accomplished by the "footprinting" method that has been described previously. Figure 49 shows the result of such an experiment, using DNA labeled at the 5′ end of the coding strand. When intact 7S particles were mixed with this DNA, no specific binding was detected. However, when the particles were treated with pancreatic RNase before addition to the DNA, the released protein protected residues 45–96 of the 5S RNA gene from DNase. RNase alone did not affect the DNase digestion pattern. Similar results were obtained with 5S DNA labeled on the noncoding strand, but no binding to a *Drosophila* arginine tRNA gene (tDNA) could be detected. 42S particles, either with or without RNase treatment, did not protect any specific region of 5S DNA or tDNA.

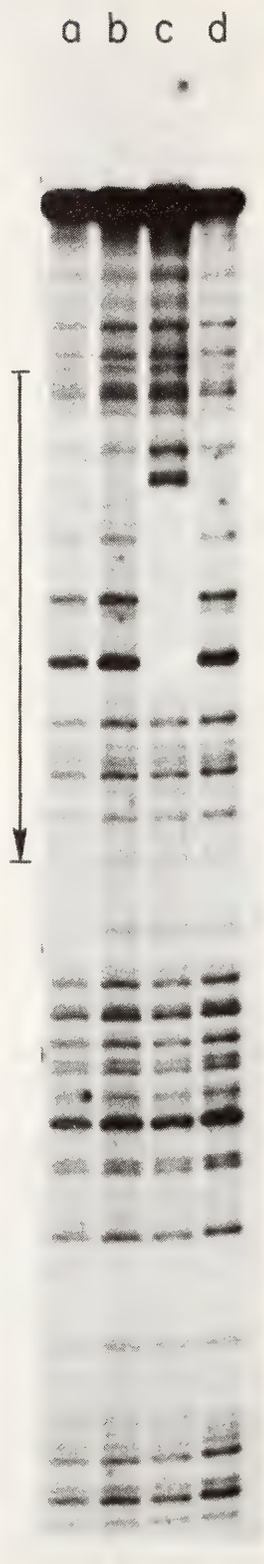


Fig. 49. Footprinting of 5S DNA. A kinase-labeled DNA fragment was incubated with no further additions (a), with 7S particles (b), with 7S particles and RNase (c), or with RNase alone (d). The mixtures were then treated briefly with DNase, and the DNA was extracted and run on a sequencing gel. The arrow indicates the region corresponding to the 5S RNA gene and its direction of transcription.

To purify the protein from the 7S particles, we made use of the observation that the particle, but not the protein, binds tightly to a DEAE-cellulose column. The protein was eluted from the column in 7M urea, leaving the RNA bound. With appropriate manipulation, the protein obtained was at least 95% pure, and after dialysis to remove the urea it had the same DNA-binding activity as RNase-treated 7S particles. This activity could be abolished by preincubation of the protein with 5S RNA, whereas preincubation with the same amount of *E. coli* tRNA had no effect. Thus the protein can bind either 5S RNA or 5S DNA, but not both at once. We were also able to demonstrate enhancement of 5S DNA transcription by adding the purified protein to the *Xenopus* nuclear extract. At saturating DNA levels, addition of as little as 0.5 μg/ml of the protein significantly stimulated transcription of 5S DNA, and at higher levels fourfold stimulation was readily obtained. Under these conditions, tRNA synthesis was either unaffected or inhibited.

The existence of a protein which can bind specifically either to 5S DNA or to 5S RNA and its activity as a transcription factor are sufficient to explain the inhibition of 5S RNA synthesis in vitro by added 5S RNA. The presence of large amounts of this protein in immature oocytes can also account both for the very high rate of synthesis and the subsequent storage of 5S RNA in these cells. We do not yet know, however, whether this same protein is involved in 5S RNA synthesis in somatic cells or whether the rate of 5S RNA synthesis in somatic cells is controlled by feedback inhibition. We are attempting to answer these questions using antisera raised against the purified protein and cell-free systems derived from somatic cells.

Quantitation of in Vitro Transcription by "Competition" of 5S RNA Genes

M. Wormington and E. Jordan

Transcription of deletion mutants derived from pXbs1 has identified a region from residues +50 to +83 within the gene that qualitatively directs accurate initiation of 5S RNA (*Year Book 78*). In order to quantitatively measure the contribution of this control region, as well as any influence of the adjacent flanking sequences, to the efficient transcription of pXbs1, we have designed a "competition" assay. This assay measures the ability of increasing amounts of an altered 5S DNA to interact with factors required for transcription of pXbs1, thereby inhibiting or "competing" transcription of a fixed concentration of this standard gene. The amount of competitor DNA required to compete pXbs1 transcription 50% is an index of its competitive strength. A gene that interacts efficiently with factors utilized by pXbs1 should compete at a lower DNA concentration than a deleted gene that interacts poorly with these factors.

To distinguish the RNA products of both the competitor and the standard templates, it was necessary to use a modified Xbs gene, the "+20 maxigene" (*Year Book 78*), which encodes an RNA that migrates slower than normal 5S RNA during electrophoresis in 7M urea polyacrylamide gels. The +20 maxigene was tested for its ability to compete transcription of unaltered pXbs1. pXbs1 was chosen as the "wild-type" gene because of its efficient transcription in vitro and since it was the original cloned fragment used to generate 5S DNA deletions (*Year Book 78*). Under appropriate reaction conditions, a 2:1 ratio of +20 maxigene DNA to pXbs1 competed transcription of the latter by 50%. The reverse competition revealed that pXbs1 competed 50% of maxigene transcription at the

same DNA concentration under identical conditions, indicating that these two genes were equivalent by this assay. This enabled us to use the +20 maxigene as standard against which 5′ and 3′ deletions of pXbs1 could be tested.

Deletion of the 5′ flanking sequences of pXbs1 to within 18 residues preceding the initiation site had no effect on competition strength (Fig. 50). Further deletion to 11 base pairs from the start site lowered the competitive strength by 50%. Deletion to this point included loss of a highly conserved A_4G sequence from residues −17 to −12 present in all *Xenopus* 5S DNAs (*Year Book 77*). Complete removal of the 5′ flanking sequence further reduced competitive strength to only 40% of that seen by the intact gene.

The 5′ flanking sequences of pXbs1, therefore, appear to exert a major influence on the interaction of this gene with factors required for its efficient transcription. Competition strength decreased further in a gradual manner as 5′ deletions progressed into the gene. Surprisingly, deletions extending into the control region to +60 still weakly competed transcription of the standard 5S RNA gene even though this extensive deletion abolishes specific transcription initiation. Deletions beyond that point competed as poorly as did the vector DNA, pBR322. That deletions of the 5′ end of the control region can still compete may be explained by the observation that these fragments still bind the transcription factor (see Fig. 47).

In contrast to the progressive loss of competition strength upon deletion of 5′ sequences, deletions from the 3′ end showed an abrupt decline in competition at +87 and a complete loss of competitive strength at +83. While previous studies defined the region from +50 to +83 as necessary and sufficient to direct accurate initiation, these

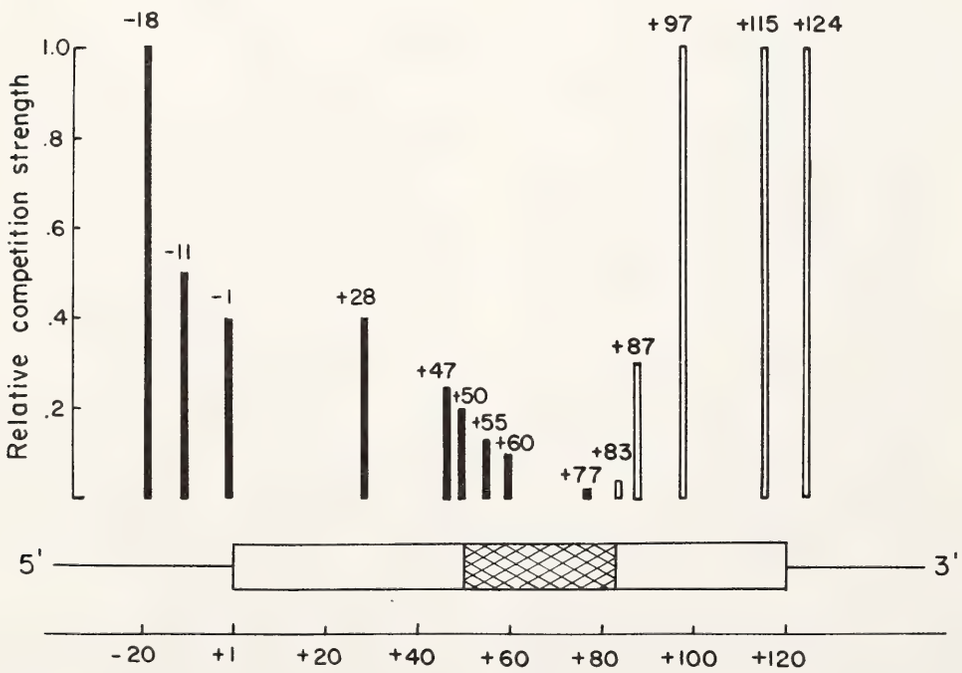


Fig. 50. Summary of competition strengths of 5′ and 3′ deletions of pXbs1. The 5S RNA gene is represented as a block, and the cross-hatched region contains sequences required for accurate initiation of 5S RNA synthesis. 5′ deletions are denoted as solid lines, while 3′ deletions are shown as open bars. Competition strength is measured as the amount of DNA required to compete 5S RNA synthesis of 5 μg/ml of "+20 maxigene" by 50%. A competition strength of 1.0 represents 50% competition of maxigene transcription by 10 μg/ml of pXbs1. A deletion mutant with a competition of 0.5 requires 20 μg/ml of DNA to compete 50%.

quantitative measurements have revealed the importance of sequences beyond the 3′ border of this region to approximately residue 90. This analysis of 3′ deletion mutants shows that their ability to compete is dependent on only one region—the intragenic control region. Since these 3′ deletion mutants contain a normal 5′ flanking region and normal initiation site, it appears that these 5′ regions exert an influence in the competition assay only when the intragenic control region is intact.

As described elsewhere, a single protein required for specific transcription of 5S DNA has been shown to interact with sequences within the intragenic control region. Binding of this factor is, perhaps, a prerequisite for the interaction of other putative factors, including RNA polymerase III, with 5′ flanking sequences near the initiation site. In addition, competition experiments revealed that the adenovirus VA gene and a *Xenopus* tRNA gene, although transcribed by RNA polymerase III, compete poorly against pXbs1. These genes have been shown qualitatively to have no interaction with the 5S DNA transcription factor previously described.

Deletions that lowered competition strength were also shown to decrease the rate of transcription in essentially the same pattern. Deletion of the entire 5′ flanking sequence reduced the number of 5S RNA molecules synthesized per gene per hour from 15 to 9, again indicating the importance of these sequences in transcription of somatic 5S DNA.

Since the competition assay measures the relative contributions of different regions of a single somatic 5S DNA, it was of interest to determine if this assay could reveal quantitative differences in strength between single genes of oocyte-specific 5S DNA (Xlo and Xlt) relative to pXbs1. A single intact Xlt gene competed transcription of a somatic 5S RNA gene only one fourth as well as did somatic genes themselves (Table 9). Removal of the 5′ flanking sequence of this gene to within nine base pairs of the start site caused only a minor decrease in competition strength. A single Xlo gene containing only 11 residues of 5′ flanking sequence had a competitive strength of 0.25, equivalent to that of the complete Xlt gene. Surprisingly, the Xlo "pseudogene" had the same competitive strength as the Xlo gene. These quantitative measurements of lowered competitive strength of Xlo and Xlt relative to Xls and Xbs are the first differences detected in vitro in the transcription strengths of these kinds of genes. It is noteworthy that these differences were observed in an extract prepared from oocytes in which the oocyte-type genes are expressed. It remains to be seen if the reduced ability of Xlo and Xlt to compete Xbs reflects a quantitative decrease in their ability to bind to the same factors as Xbs or if factors are present that are specific to somatic 5S DNA but are not recognized by Xlo and Xlt 5S DNAs. The comparatively small contribution of the 5′ flanking sequence of Xlt relative to Xbs is suggestive of differences in interactions involving these regions. It is also of interest to note that four of the six base changes that distinguish oocyte from somatic 5S RNA occur within the intragenic control region, possibly influencing the binding of at

TABLE 9. Relative Competition Strengths of 5S RNA Genes

Gene	Competition Strength*
Xbs	1.00
Xls	1.00
Xlt	0.25
XltΔ5′−9	0.20
XloΔ5′−11	0.25
Xlo "pseudogene"	0.25

*Competition strength is the amount of DNA required to compete 50% of "maxigene" 5S RNA synthesis relative to the same level of competition by 10 μg/ml of pXbsl.

least one factor required for both oocyte and somatic 5S DNA transcription in vitro.

Partial Purification of a Factor for 5S DNA Transcription

H. S. Shin

Accurate in vitro transcription of *Xenopus* 5S RNA genes involves RNA polymerase III, the 5S specific transcription factor described above, and other components that at present are poorly characterized. The 5S specific transcription factor was isolated recently from *Xenopus* oocytes and was shown to consist of a 37,000-dalton polypeptide. Interestingly, unfertilized *Xenopus* eggs cannot synthesize 5S RNA, and the absence of this factor alone accounts for the inability of unfertilized egg extracts to support 5S RNA gene transcription (Engelke *et al.*, *Cell*, *19*, 717, 1980). My goal was to isolate a component required for 5S RNA gene transcription from unfertilized eggs.

A complementation assay to detect this component in unfertilized egg extracts was developed. In this assay, an extract was prepared by the method of Weil *et al.* (*J. Biol. Chem.*, *254*, 6163, 1979) from a tissue culture line of the mouse P815 tumor. This tumor extract had considerable RNA polymerase activity but was incapable of supporting accurate transcription of 5S RNA genes. However, the extract from unfertilized *Xenopus* eggs complemented the P815 extract for the transcription of 5S genes and also the *Drosophila* $tRNA^{arg}$ gene, as shown in Fig. 51. The accuracy of 5S RNA gene transcription was verified by RNA fingerprint analysis.

The factor in unfertilized eggs that can complement the P815 extract for 5S transcription has an approximate molecular weight of 120,000 daltons as estimated by gel filtration on a Sepha-

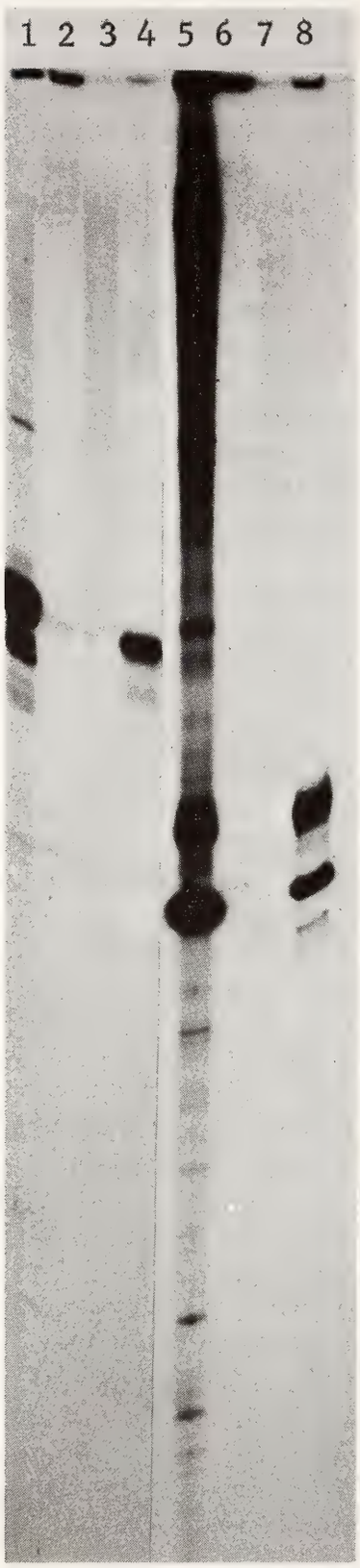


Fig. 51. The transcription assay was performed and the products were analyzed by electrophoresis as described by Birkenmeier *et al.* (*Cell*, *15*, 1077, 1979), except that the transcription reaction was carried out at 30°C in a Tris-buffered solution (Ng, *Proc. Nat. Acad. Sci. USA*, *76*, 136, 1979). Autoradiograms of transcription products of the *Xenopus* 5S RNA genes are shown in lanes (1–4) and those of the

dex G-200 column, and has an isoelectric point of 6.1. Its activity was lost upon heating at 80 °C for 10 minutes. The physicochemical properties of this factor and its presence in unfertilized eggs indicate that this factor is different from RNA polymerase III, the 5S specific transcription factor, and the nucleosome assembly factor described by Laskey *et al.* (*Nature, 275,* 416, 1978) A large-scale purification of this new factor is planned. Unfertilized eggs are a good source of this component because of the ease in obtaining large amounts of material, the high titer of the component, and its stability in the extracts.

In Vitro Transcription with Extracts from Tissue Culture Cells

R. Peterson

Extracts from the nuclei (germinal vesicles) of *Xenopus* oocytes accurately transcribe 5S RNA genes in vitro (*Year Book 77*). Oocytes transcribe both oocyte and somatic 5S RNA genes in vivo, and the extract derived from oocytes also transcribes the oocyte and somatic 5S RNA genes in vitro. We have made extracts from *X. laevis* tissue culture cells that accurately transcribe 5S RNA genes in vitro but at a much lower efficiency than the germinal vesicle supernate. This extract, derived from somatic cells, also transcribes both somatic and oocyte 5S RNA genes.

Extracts that accurately transcribe 5S DNA and tDNA have been prepared from KB cells. The KB cell line is derived from a human carcinoma, and the cells can be grown easily in suspension culture. In this extract, tRNA genes are transcribed more efficiently than 5S RNA genes, whereas 5S RNA genes are transcribed more efficiently than tRNA genes in the germinal vesicle extract. The transcription of tDNA by the germinal vesicle extract is stimulated greatly by the addition of small amounts of KB cell extract. The final activity of the mixture of these two extracts on cloned tRNA genes is greater than the sum of the individual extracts. The KB cell extract has been fractionated on a DEAE-cellulose ion-exchange column and assayed for stimulation of tRNA gene transcription in the GV supernate. The stimulatory activity can be separated partially from RNA polymerase III activity on this column indicating that factors from the KB cell extract are responsible for the increased tRNA gene transcription. The KB cell extract appears to be a good source of material for identification of a transcription factor specific for tRNA genes.

Drosophila $tRNA^{arg}$ gene are shown in lanes (5–8). All reactions were carried out in a final volume of 10 μl and the DNA concentration was 15 μg/ml. The cell extracts added to the reaction mixtures were as follows: lanes (1) and (5), 3 μl of germinal vesicle extract; lanes (2) and (6), 3 μl of P815 extract; lanes (3) and (7), 1 μl of unfertilized egg extract; and lanes (4) and (8), 3 μl of P815 extract plus 1 μl of unfertilized egg extract.

Nucleotide Sequences Required for Termination of 5S RNA Synthesis

D. Bogenhagen

In this report, we describe altered 5S DNAs designed to elucidate the DNA sequences required for accurate termination of transcription. Termination of 5S RNA synthesis occurs within clusters of four or more T residues in the noncoding DNA strand. Our experiments have been designed to test the influence on transcription termination of several sorts of DNA sequence signals surrounding this T cluster. These putative termination signals are suggested by analogy to known prokaryotic termination sites and include the following: (1) sequence homology in the 3′ spacer region following the T cluster;

(2) dyad symmetry in the sequence preceding the T cluster; and (3) high GC content in the sequence preceding the T cluster.

Our previous construction of 3′ deletion mutants of *Xenopus borealis* somatic (Xbs) 5S DNA produced two deletion mutants, designated pXbsΔ3′ +124 and pXbsΔ3′+115 whose deletion endpoints (four bases after the gene and five bases before the end of the gene, respectively) bracket the cluster of four T residues (118 to 122). Both plasmids support accurate initiation of transcription, but only transcripts of the longer plasmid containing the T cluster terminate properly. These results indicate that the 3′ spacer spacer region deleted in both plasmids is not required for termination, but that the additional nine bp containing the T cluster, which are deleted in pXbsΔ3′+115, are required for termination.

To test the role of intragenic sequences we constructed 5′ deletions of the Xbs 5S RNA gene approaching the T cluster from within the gene. These putative terminator fragments were then rejoined to 3′ deletions that contained 5′ proximal gene fragments capable of directing transcription initiation. Figure 52 shows the construction of two such recombinant genes with the first 97 bp of the gene joined to either the last 44 or the last 15 residues of the gene. Only the longer of these two terminal fragments contains the dyad symmetry identified by the sequence analysis of Korn and Brown (*Cell, 15*, 1145, 1978) as a possible termination signal by analogy to known pro-

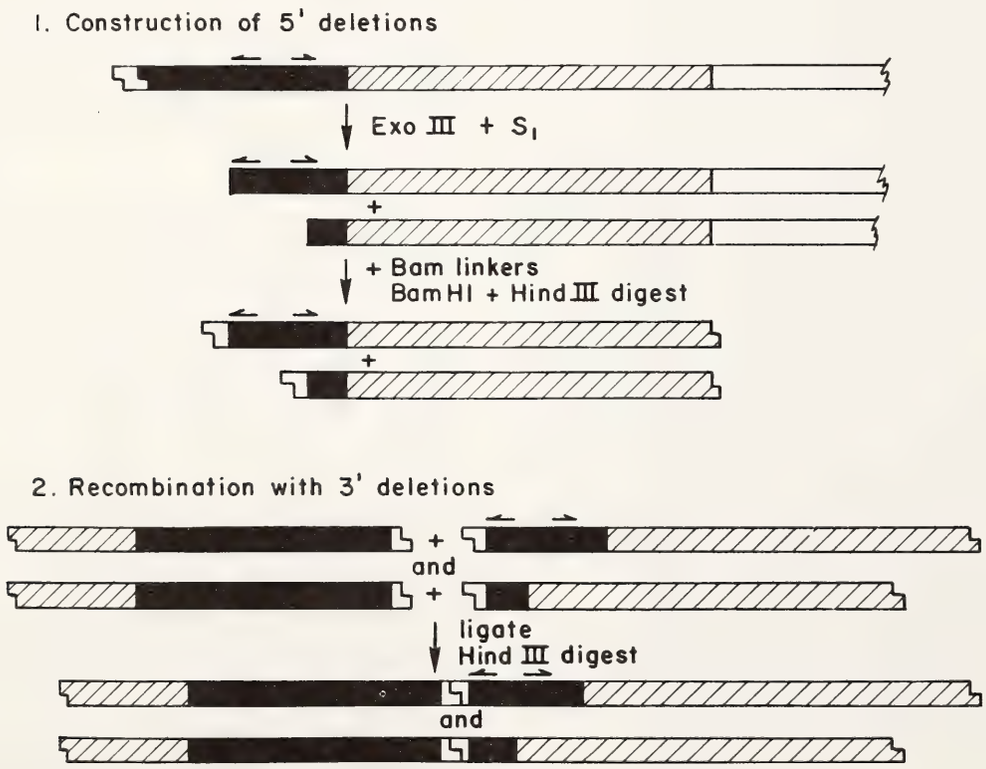


Fig. 52. (1) Construction of Xbs 5S RNA genes to test the role of dyad symmetry in transcription termination. The 3′ portion of the 5S RNA genes (black) containing a region of dyad symmetry (← →) is shown flanked by 3′ spacer DNA (cross-hatched) and pBR322 plasmid DNA (unshaded). Deletions were performed as indicated, following methods described in *Year Book 78*. Two of these 5′ deletions, designated pXbsΔ5′+77 and Δ5′+105 were found respectively to contain or lack the region of dyad symmetry, as shown. These putative terminator fragments were rejoined, as shown in (2), to a 3′-deleted fragment of the pXbs1 gene capable of transcription initiation but not termination.

karyotic termination signals. Figure 53 shows the transcripts of several plasmids containing "initiator" fragments of different lengths joined to either of these two terminators. Since transcription termination occurs faithfully for all of these plasmids, we conclude that this particular dyad symmetry is not an important termination signal. However, the use of a synthetic decanucleotide BamHI linker (CCGGATCCGG) to join these initiator and terminator fragments introduced an additional dyad symmetry in the sequence preceding the T cluster. This dyad symmetry has been removed by joining the initiator and terminator fragments using the Hpa II restriction sites (CCGG) in the linker, and transcription termination still occurs normally.

These experiments show that signals for initiation and termination of transcription are clearly separable, since the RNAs produced vary in length from 94 to 169 nucleotides. In other experiments we have constructed recombinant 5S RNA genes containing as few as three nucleotides of the normal sequence preceding the T cluster. Again, the majority of transcripts terminate normally. However, a slightly larger fraction of transcripts now read through the primary T cluster and terminate at a second T cluster eight nucleotides downstream. When the primary T cluster is partially or entirely deleted, the secondary T cluster serves as an efficient termination site. These experiments suggest that no extensive regions at the 3′ end of the 5S RNA gene are required for termination. All of our constructions have left the T cluster surrounded by GC-rich sequences. We have not yet directly tested whether this surrounding GC-richness is absolutely required. However, we know of cases in which clusters of four T residues surrounded by AT-rich sequences do not terminate transcription efficiently (e.g., in the Xlo 5S RNA gene). We must presume



Fig. 53. Autoradiogram of a gel electrophoretic analysis of transcripts of recombinant 5S RNA genes. The construction of recombinant 5S RNA genes is given in the text and the legend of Fig. 52. Left lane, control showing 120 nucleotide transcripts of Xbs201. Next four lanes, transcripts of four plasmids with 5′ "initiator" fragments containing the first +83, 87, 97, and 115 nucleotides of the 5S RNA gene, respectively, linked to the longer "terminator" fragment containing the last 44 nucleotides of the genes. Last four lanes, transcripts of four plasmids similar to those whose transcripts are shown in second through fifth lanes except that the "terminator" fragment used contains only the last 15 nucleotides of the gene.

that the GC-rich flanking sequences are important to termination until this can be directly tested with a site-specific mutagenic approach.

Abundance and Chromosomal Arrangement of Three 5S DNA Multigene Families in *X. laevis*

R. Peterson

Part of characterizing the 5S DNA multigene families is determination of the number of copies of the repeating units and the arrangement of these repeating units in clusters on the chromosomes. The major oocyte 5S RNA gene family from *X. laevis* (Xlo) has been shown to have about 20,000 copies, which are located at the telomeres of most of the chromosomes. We have now determined the approximate sizes of the *X. laevis* somatic (Xls) and *X. laevis* trace (Xlt) 5S RNA gene families and have learned something about their chromosomal arrangement.

To distinguish between the different families of 5S DNA, fragments of DNA from the spacer regions of Xls and Xlt 5S DNAs were cloned in plasmids. These cloned spacer fragments were shown to be specific probes for their respective 5S DNA families. When radioactive spacer fragments were used as hybridization probes, they did not cross-hybridize with the other 5S DNA families nor did they hybridize to other repetitive DNA families. These radioactively labeled spacer fragments were used in solution hybridization kinetic experiments to determine the relative size of the three 5S DNA families of *X. laevis*. In this experiment, the rate at which a particular gene family hybridizes is a function of the number of copies of repeats in that gene family. The number of repeating units in the three multigene families was found to be about 20,000, 1,300, and 400 copies, respectively, for Xlo, Xlt, and Xls 5S DNA.

Xlo 5S DNA had been located on most of the chromosomes by hybridization *in situ* to *X. laevis* chromosomes (Pardue *et al.*, *Chromosoma*, *42*, 191, 1973). Attempts to locate the Xls and Xlt 5S DNAs by this method were not successful, owing to the small size of these gene families and their apparent distribution on several chromosomes. An estimate of the chromosomal distribution of these 5S DNAs was determined by examining the segregation of Xlt and Xls 5S DNA in hybrid frogs. F_1 crosses between *X. laevis* and *X. borealis* were backcrossed against *X. borealis* (see *Year Book 72*). DNAs from these backcrossed frogs were analyzed for the presence of Xls and Xlt 5S DNA. Xls and Xlt 5S DNAs were found in 25/27 and in 29/29 of the progeny, respectively. Assuming that these hybrid frogs are diploid, this analysis indicates that both Xls and Xlt 5S DNA are located on more than one chromosome. The data fit three or four chromosomes for Xls 5S DNA and at least four chromosomes for Xlt 5S DNA.

To determine the size of the clusters of Xls and Xlt 5S DNA, high-molecular-weight *X. laevis* DNA was digested with various restriction endonucleases which do not cut within 5S DNA. The DNA fragments were separated on dilute agarose gels (0.2%), transferred to nitrocellulose, and hybridized with 5S DNA probes. The Xls 5S DNA was found on DNA fragments from about 65,000 to 80,000 bp in size, and Xlt was found on fragments about 50,000 to 60,000 bp in size. The sizes of these clusters is consistent with the presence of these 5S DNAs on a few but not all of the 18 *Xenopus* chromosomes.

THE COLLECTION OF HUMAN EMBRYOS

Ronan O'Rahilly

The embryological collections, both human and comparative, are housed at the University of California, Davis. All inquiries, as well as requests for permission for publication, should be addressed to Professor R. O'Rahilly, Carnegie Laboratories of Embryology, University of California, Davis, California 95616.

Placentology

A significant and beautifully produced book appeared during the year, namely an account of the anatomy, physiology, radiology, and clinical aspects of placental vasculature and circulation, by Elizabeth M. Ramsey and Martin W. Donner. The brief text provides an overall view of current opinion, as well as a summary of the authors' own studies. An important feature is the inclusion of more than 100 illustrations, including superb photographs of Carnegie material and attractive and helpful drawings by Ranice W. Crosby. At the beginning of the book, a list of acknowledgements includes the names of the technical staff of the Carnegie Department of Embryology, "well known to the many investigators who have come to work in Baltimore" over the years.

Developmental Stages in Human Embryos

The revision of stages 10 to 23 and the tabulation of the timing and sequence of developmental events in staged human embryos are being pursued, and an account of vertebral development has been published recently by O'Rahilly and Meyer. Moreover, detailed studies of the skull and vertebral column at stage 23 by Müller and O'Rahilly are awaiting publication. Further work on the embryonic vertebral column is being planned with Dr. David B. Meyer (Wayne State University), and Dr. Daniel R. Benson (Department of Orthopaedic Surgery, Sacramento), is studing the normal and abnormal fetal column.

The computerized catalogue of Carnegie specimens established by Dr. Alexander Barry now includes the collections of the California Primate Research Center (Davis), the University of Washington, the University of Alabama, the University of Michigan, and the Blechschmidt Collection.

Development of the Nervous System

The project on the developmental neurobiology of primates has been furthered by a study of the very early nervous system in staged insectivore and primate embryos, which is awaiting publication. In addition, O'Rahilly and Müller have begun a reinvestigation of stage 8 in the human. In this important stage, the first indication of the nervous system is observed. This year, John S. Popko successfully presented for a Master of Science degree, a thesis on the early development of the eye in the lesser mouse lemur (*Microcebus murinus*).

Collaboration with Professor W. Woźniak (Poznań) continues, and light and electron microscopic studies of neural cells in the spinal ganglia of human embryos and early fetuses have been published. A related investigation of the developing spinal cord is in press. A study of the cranial parasympathetic ganglia in staged human embryos has been started.

Professor Jean Bossy (Nîmes Section, University of Montpellier) stud-

ied the collection of staged embryos, and an article on the development of olfactory and related structures is in preparation.

Visitors

Visitors who studied the collection included Dr. Rolf Baur (Basel), Dr. Jean Bossy (Nîmes), Drs. Bent G. and Reneé Laya Böving (Detroit), Dr. Mary E. Desmond (Villanova, Pennsylvania), Dr. Virginia E. Diewert (Vancouver), Dr. Hans Elias (San Francisco), Dr. Grover M. Hutchins (Baltimore), Dr. David B. Meyer (Detroit), Dr. G. William Moore (Baltimore), and Dr. Witold Woźniak (Poznań).

STAFF ACTIVITIES

During the year Staff Members participated as chairpersons and speakers at the following conferences: Gordon Conferences on Immunochemistry and Immunobiology, Developmental Biology, Fertilization, and Nucleic Acid; Plant Biology Workshop; 39th Symposium of the Society of Developmental Biology; 14th Harden Conference; University of Texas Health Science Center National Symposium; 13th FEBS Meeting, Symposium on Cell Fusion; Joint Immunology Meeting; 1979 National Drosophila Meeting; Symposium on Drug Receptors and their Effectors, Ciba Foundation and Middlesex Hospital; Couteaux Symposium: Annual Meeting of the Society for Neuroscience; Winter Brain Research Conference; American Society of Biological Chemists (Plenary Lecture); Molecular Basis of Cell-Cell Interaction; DNA Protein Interactions in Transcription, Replication and Repair; Annual Meeting of the Helen Hay Whitney Foundation; National Conference on Diabetes; Symposium on Biological Development; Symposium on Developmental Genetics; New York Society of Electron Microscopists Symposium on Gene Expression.

Lectures were given at Johns Hopkins University, National Institutes of Health, University of North Carolina, University of Connecticut Health Science Center, Medical College of Virginia, Purdue University, California Institute of Technology, University of California at Los Angeles, University of Virginia, Albert Einstein College of Medicine, University of Pennsylvania, State University of New York Medical School at Syracuse, Indiana University, Massachusetts Institute of Technology, Yale University, Rockefeller University, Michigan State University, Princeton University, Cold Spring Harbor Laboratories, Harvard Medical School, Wayne State University, Washington University Medical School, University of Missouri, University of Pennsylvania, Salk Institute, University of Kansas Society of Neuroscience Chapter, University of Maryland School of Medicine, Columbia University College of Physicians and Surgeons, University of Alberta, MRC Molecular Biology Laboratory, Worcester Foundation, Scripps Research Institute, University of California at Berkeley, Brown University, Stanford University Medical School, University of California at San Diego, McGill University, Walter and Eliza Hall Institute of Medical Research, Melbourne, Australia, CSIRO (Division of Plant Industry), Canberra, Australia, Wistar Institute, Institute for Cancer Research.

Members of the Staff served on the National Science Foundation Developmental Biology Panel; Science Advisory Committee, Office of Technology Assessment—Congress of the United States; National Institutes of Health Recombinant DNA Advisory

Committee; 1979–1980 Cole Award Selection Committee—Biophysical Society; the Editorial Board of Developmental Biology. Even though the Editor of Developmental Biology has moved to the National Institutes of Health, the office remains in this Department and is ably run by Deborah Bowers. Additional consulting activities include memberships on the visiting committees of the Roche Institute of Molecular Biology (chairman); the Biology (chairman) and Biochemistry and Molecular Biology Departments of Harvard University; the Centre de Génétique Moléculaire of the CNRS, Gif-sur-Yvette; and the Board of Scientific Counselors of the National Institute of Child Health and Development.

Seminars

The Department offers at least two seminars each week, one of them usually presented by a scientist from outside the Department. This year, 25 invited speakers from the Baltimore scientific community lectured. The third annual Mini-Symposium was entitled "Genes, Receptors, and Cells in the Immune Response;" The four principal speakers were Lee Hood, California Institute of Technology, Robert Perry, Institute for Cancer Research, Ellen Vitetta, University of Texas, and William Paul, National Institutes of Health. In addition to this Symposium, the following visitors spoke: A. Nienhius, T. Reese, and D. Nebert, from the National Institutes of Health; S. Zigmond, and M. Ryoji, the University of Pennsylvania; M. Shander, Wistar Institute; S. Treistman, Bryn Mawr College; L. Laimons, University of Chicago; T. Silhavy, Frederick Cancer Research Institute; M. Kielian, Rockefeller University; L. Sealy, University of Iowa; R. Britten, M. Davis, and E. Davidson, California Institute of Technology; M. Sinesky, Eleanor Roosevelt Institute; M. Geftner Massachusetts Institute of Technology; F. Ausubel, Harvard University; D. Chaleff, Cornell University; M. Imada, University of Colorado Medical School; K. Vaca, University of Connecticut; B. Dryden, University of Alberta; S. Hauschka, University of Washington—Seattle; C. Gabel, University of Washington; C. Bassett, University of Georgia; J. Rothman, Stanford University; N. Proudfoot, L. Korn, and D. Melton, MRC Unit, Cambridge, England; B. Kass, and K.-W. Yau, University of Cambridge, England; C. Kafiani, Institute of Molecular Biology, USSR; D. Smith, Cornell University.

BIBLIOGRAPHY

Beyer, A. L., O. L. Miller, Jr., and S. L. McKnight, Ribonucleoprotein structure in nascent hnRNA is non-random and sequence dependent. *Cell, 20,* 75–84, 1980.

Birkenmeier, E. H., see Brown, D. D., and Korn, L. J.

Bogenhagen, D. F., S. Sakonju, and D. D. Brown, A control region in the center of the 5S RNA gene directs specific initiation of transcription: II. The 3′ border of the region. *Cell, 19,* 27–35, 1980.

Bogenhagen, D. F., see Sakonju, S.

Brown, D. D., Oocytes and the beginning of development in amphibia. *Differentiation, 13,* 21–22, 1979.

Brown, D. D., L. J. Korn, E. H. Birkenmeier, R. Peterson, and S. Sakonju, The *in vitro* transcription of *Xenopus* 5S DNA. In *Eukaryotic Gene Regulation*, R. Axel, T. Maniatis and C. F. Fox, eds., Academic Press, Inc., New York, pp. 511–519, 1979.

Brown, D. D., see Bogenhagen, D. F., Korn, L. J., Peterson, R. C., and Sakonju, S.

Carrel, S., see Ward, S.

Cebra, J., C. Crandall, P. Gearhart, S. Robertson, J. Tseng, and P. Watson, Cellular events concerned with the initiation, expression and control of the mucosal immune response. In *The Immunology of Breast Milk,* D. Dayton, ed., Raven Press, New York, pp. 1–16, 1979.

Craig, E., see Spradling, A. C.

Crandall, C., see Cebra, J.

Digan, M. E., A. C. Spradling, G. L. Waring, and A. P. Mahowald, The genetic analysis of chorion morphogenesis in *Drosophila melanogaster.* In *Eukaryotic Gene Regulation,* R. Axel, T. Maniatis and C. F. Fox, eds., Academic Press, New York, pp. 171–181, 1979.

Digan, M. E., see Spradling, A. C.

Doering, J. L., see Peterson, R. C.

Donner, M. W., see Ramsey, E. M.

Fambrough, D. M., see Linden, D. C., and Rotundo, R. L.

Gardner, E., see Olszewska, B., and O'Rahilly, R.

Gardner, J. M., see Linden, D. C.

Gearhart, P., see Cebra, J., and Phillips, R.

Korn, L. J., E. H. Birkenmeier, and D. D. Brown, Transcription initiation of *Xenopus* 5S ribosomal RNA genes *in vitro. Nucl. Acids Res.,* 7, 947–958. 1979.

Korn, L. J., see Brown, D. D.

Linden, D. C., J. M. Gardner, and D. M. Fambrough, Some observations on denervation supersensitivity in skeletal muscle. In *Advances in Pharmacology and Therapeutics,* Vol. 1, J. Jacob, eds., Pergamon Press, New York, pp. 91–97, 1978.

McKnight, S. L., and O. L. Miller, Jr., Post-replicative non-ribosomal transcription units in *D. melanogaster* embryos. *Cell, 17,* 551–563, 1979.

McKnight, S. L., see Beyer, A. L.

Mahowald, A. P., see Digan, M. E.

Mahowald, A. P., see Spradling, A. C.

Meyer, D. B., see O'Rahilly, R.

Miller, O. L., Jr., see Beyer, A. L., and McKnight, S. L.

Müller, F., see O'Rahilly, R.

Muller, K. J., and S. A. Scott, Correct axonal regeneration after target cell removal in the central nervous system of the leech. *Science, 206,* 87–89, 1979.

Muller, K. J., and S. A. Scott, Removal of the synaptic target permits terminal sprouting of a mature intact axon. *Nature, 283,* 89–90, 1980.

Nelson, G. A., and S. Ward, Vesicle fusion, pseudopod extension and amoeboid motility are induced in nematode spermatids by the ionophore monensin. *Cell, 19,* 457–464, 1980.

Olszewka, B., W. Woźniak, E. Gardner, and R. O'Rahilly, Types of neural cells in the spinal ganglia of human embryos and early fetuses. *Mikrosk. Anat. Forsch., 93,* 1182–1199, 1980.

O'Rahilly, R., Early human development and the chief sources of information on staged human embryos. *Eur. J. Obstet. Gynecol. Reproduct. Biol., 9,* 273–280, 1979.

O'Rahilly, R., and E. Gardner, The initial development of the human brain. *Acta Anat., 104,* 123–133, 1979.

O'Rahilly, R., and D. B. Meyer, The timing and sequence of events in the development of the human vertebral column during the embryonic period proper. *Anat. Embryol., 157,* 167–176, 1979.

O'Rahilly, R., and F. Müller, The early development of the nervous system in staged insectivore and primate embryos. *Anat. Rec., 196,* 243A, 144A, 1980.

O'Rahilly, R., see Olszewska, B., and Woźniak, W.

Pagano, R. E., D. K. Struck, and A. J. Schroit, Introduction of phospholipids into mammalian cells via lipid vesicles. In *Liposomes and Immunobiology,* National Symposium, B. H. Tom and H. R. Six, eds., Elsevier-North Holland, in press, 1980.

Pagano, R. E., see Struck, D. K.

Peterson, R. C., J. L. Doering, and D. D. Brown, Characterization of two *Xenopus* somatic 5S DNAs and one minor oocyte-specific 5S DNA. *Cell, 20,* 131–141, 1980.

Peterson, R. C., see Brown, D. D.

Phillips, R., and P. Gearhart, Biased summary: ontogeny and differentiation of B cells. In *B Lymphocytes in the Immune Response,* M. Cooper, D. Mosier, I. Scher, and E. Vitetta, eds., Elsevier North-Holland, New York, pp. 107–112, 1979.

Popko, J. S., The early development of the eye in the lesser mouse lemur (*Microcebus murinus*). M. S. Thesis, University of California, Davis, 1979.

Ramsey, E. M., and M. W. Donner, *Placental Vasculature and Circulation,* G. Thieme, Stuttgart, 1980.

Robertson, S., see Cebra, J.

Rotundo, R. L., and D. M. Fambrough, Molecular forms of chicken embryo acetylcholinesterase *in vitro* and *in vivo*: Isolation and Characterization. *J. Biol. Chem.*, 254, 4790–4799, 1979.

Sakonju, S., D. F. Bogenhagen, and D. D. Brown, A control region in the center of the 5S RNA gene directs specific initiation of transcription: I. The 5′ border of the region. *Cell, 19,* 13–25, 1980.

Sakonju, S., see Bogenhagen, D. F., and Brown, D. D.

Schroit, A. J., see Pagano, R. E.

Scott, M., see Spradling, A. C.

Scott, S. A., see Muller, K. J.

Spradling, A. C., M. E. Digan, A. P. Mahowald, M. Scott, and E. Craig, Two clusters of major chorion genes in *Drosophila melanogaster. Cell, 19,* 905–914.

Spradling, A. C., and A. P. Mahowald, Amplification of chorion genes during oogenesis in *Drosophila melanogaster. Proc. Nat. Acad. Sci. USA, 77,* 1096–1100, 1980.

Spradling, A. C., see Digan, M. E.

Struck, D. K., and R. E. Pagano, Insertion of fluorescent phospholipids into the plasma membrane of mammalian cell. *J. Biol. Chem., 255,* 5404–5410, 1980.

Struck, D. K., see Pagano, R. E.

Tseng, J., see Cebra, J.

Ward, S., and J. S. Carrel, Fertilization and sperm competition in the nematode *Caenorhabditis elegans. Develop. Biol., 73,* 304–321, 1979.

Ward, S., see Nelson, G. A.

Waring, G. L., see Digan, M. E.

Watson, P., see Cebra, J.

Woźniak, W., and R. O'Rahilly, The times of appearance and the developmental sequence of the cranial parasympathetic ganglia in staged human embryos. *Anat. Rec., 196,* 255A–256A, 1980.

Woźniak, W., see Olszewska, B.

PERSONNEL

Year Ended June 30, 1980

(Including those whose services ended during the year)

Research Staff

Donald D. Brown, Director
Douglas M. Fambrough
Nina V. Fedoroff
Kenneth J. Muller
Richard E. Pagano
Allan Spradling
Samuel Ward

Staff Associate

Patricia Gearhart

Research Associates (Extramural)

Bent Böving, Detroit, Michigan
Igor B. Dawid, Bethesda, Maryland
Robert L. DeHaan, Atlanta, Georgia
Arthur T. Hertig, Boston, Massachusetts
Irwin R. Konigsberg, Charlottesville, Virginia
Ronan O'Rahilly, Davis, California
Elizabeth M. Ramsey, Washington, D.C.
Ronald H. Reeder, Seattle, Washington
Yoshiaki Suzuki, Okazaki City, Japan

Postdoctoral Fellows and Grant-Supported Associates

M. John Anderson, Research Associate, Muscular Dystrophy (Fambrough)
Ellen Bayne, Fellow of Carnegie Institution of Washington
Daniel Bogenhagen, Fellow of Helen Hay Whitney Foundation
Ellen Elliott, Fellow, Multiple Sclerosis Grant
Dick Hoekstra, Fellow of the Carnegie Institution of Washington
Sheila McCormick, Fellow of the National Institutes of Health
Steven McKnight, Fellow of Helen Hay Whitney Foundation
Wylie Nichols, Research Associate, National Institutes of Health Grant (Pagano)
Hugh Pelham, Research Associate, National Institutes of Health Grant (Brown)
Ronald Peterson, Fellow of Helen Hay Whitney Foundation
Thomas Roberts, Fellow of the National Insitutes of Health
Richard Rotundo, Fellow of Muscular Dystrophy Association of America, Inc.
Alan Schroit, Research Associate, National Institutes of Health Grant (Pagano)
Sheryl Scott,[1] Fellow of the National Institutes of Health and the Carnegie Institution of Washington
Mavis Shure, Fellow of Damon Runyon–Walter Winchell Cancer Fund
Barbara Sollner-Webb,[2] Fellow of the National Institutes of Health
Douglas Struck, Fellow of the American Cancer Society
Eric Wakshull, Fellow of Muscular Dystrophy Association of America, Inc.
Susan Wessler, Postdoctoral Associate of the National Science Foundation (Fedoroff)

Students

Yair Argon,[3] Harvard University (graduate student)
Dan Burke, National Research Council of Canada (graduate student)
John M. Gardner, Johns Hopkins University (graduate student)
Elizabeth Gavis, Cornell University (undergraduate)
Gregory A. Nelson,[4] Harvard University (graduate student)
Shigeru Sakonju, Johns Hopkins University (graduate student)

[1]To September 30, 1979
[2]To November 30, 1979
[3]To November 15, 1979
[4]To September 30, 1979

Heidi Schaeffer,[5] University of Edinburgh, Scotland (undergraduate)

Visiting Investigators and Extramural Collaborators

A. Bakken, Seattle, Washington
S. Busby, Seattle, Washington
J. Cebra, Baltimore, Maryland
E. H. Coe, St. Louis, Missouri
C. Emerson, Charlottesville, Virginia
S. Emerson, Charlottesville, Virginia
D. Engelke, St. Louis, Missouri
L. Hood, Pasadena, California
N. Johnson, Pasadena, California
E. Macagno, New York, New York
B. McClintock, Cold Spring Harbor, New York
G. Morgan, Seattle, Washington
M. G. Neuffer, St. Louis, Missouri
R. H. Reeder, Seattle, Washington
R. G. Roeder, St. Louis, Missouri
H. Shin, Baltimore, Maryland
D. Weisblat, Berkeley, California

Clerical and Technical Staff

James H. Blackwell, Custodian
Paul Blackwell, Custodian (part-time)
Patricia Chase, Laboratory Helper
William H. Duncan, Senior Technician
Ernestine V. Flemmings, Laboratory Helper
Richard D. Grill, Photographer
Virginia Hicks, Laboratory Helper
Mary E. Hogan, Technician
Joyce Irwin,[6] Secretary (part-time)
John E. Jones, Custodian
Eddie Jordan, Senior Technician
Robert Kingsbury, Technician
Catherine R. Lane, Librarian (part-time)
Alice H. Mabin, Laboratory Helper
Thomas F. Malooly, Business Manager
Ona Martin, Technician
Jeffrey Mauvais, Technician
Clinton E. Miller,[7] Technician
Thomas F. Miller, Custodian
Ben Nathans, Technician
Nadine Nivera, Technician
Joyce Patterson,[8] Laboratory Helper
John Pazdernik, Building Engineer
Leslie Pedersen, Technician
Betty Lou Phebus, Bookkeeper/Clerk
Susan D. Satchell, Secretary
Patricia Schmidt, Secretary
Ginny Selby,[9] Secretary (part-time)
Audrey Sheppard, Laboratory Helper
Bessie Smith,[10] Laboratory Helper
Delores Somerville, Senior Technician
Barbara Thomas, Technician
Joe Vokroy, Machinist
John Wiser,[11] Machinist

[5]From June 26, 1979 to August 31, 1979
[6]To May 6, 1980
[7]To August 1, 1980
[8]To March 24, 1980
[9]To November 30, 1979
[10]To December 31, 1979
[11]To July 31, 1979

Department of Plant Biology

Stanford, California

Winslow R. Briggs

Director

Carnegie Institution of Washington Year Book 79, 1979–1980

Contents

Introduction (Briggs) 105

Ancient repeated sequences in the pea and mung bean genomes (Murray, Peters, and Thompson) 112

Evolutionary sequence divergence in families of repeated DNA (Preisler and Thompson) 114

Observing patterns of gene expression at the RNA level: the greening response in *Pisum* (Jorgensen and Thompson) 116

Cloned repeated sequence elements for the study of DNA sequence evolution in higher plants (Cuellar and Thompson) 119

Studies on higher plant chloroplast and mitochondrial DNA (Palmer and Thompson) 120

Blue light stimulates a local electrical current efflux in the alga *Vaucheria sessilis* (Blatt and Weisenseel) . 123

Influence of light on growth of etiolated oat seedlings (Mandoli and Briggs) 126

Reverse reciprocity failure of phytochrome-mediated responses in light-grown corn (Gorton and Briggs) 128

Partial purification and characterization of a blue-light-sensitive cytochrome-flavin complex from corn membranes (Leong and Briggs) . . 131

Solubilization of a photoactive, membrane-associated flavin-cytochrome complex from corn (Leong, Caubergs, and Briggs) 134

The effect of σ-aminolevulinic acid on red-light-induced leaf unrolling (Sundqvist and Briggs) 136

Binding of cations to phytochrome (Sundqvist and Briggs) 138

Seasonal changes in high temperature acclimation of desert winter annuals (Seemann, Berry, and Downton) 141

Thermal stability of photosynthesis in desert plants (Downton, Seemann, and Berry) 143

Photosynthetic capacity of desert winter annuals measured *in situ* (Seemann, Field, and Berry) . . . 146

The changes in thylakoid acyl lipid composition of *Nerium oleander* accompanying acclimation to high temperature (Roberts and Berry) 147

Response and adaptation to water stress in *Nerium oleander* (Björkman, Downton, and Mooney) . . . 150

Interaction between light intensity and chilling temperatures on inhibition of photosynthesis in chilling-sensitive plants (Powles, Berry, and Björkman) 157

Photosynthetic performance of isolated leaf cells from sun and shade plants (Harvey) 160

Chromosome numbers in Australian species of *Atriplex* (Nobs) 164

A laboratory-constructed sensitive difference spectrophotometer for the ultraviolet, visible, and far-red region of the spectrum (Melis and Hart) 170

Stoichiometry of system I and system II reaction centers in photosynthetic membranes (Melis and Brown) 172

Fluorescence spectroscopy of intermittent-light and daylight-grown pea and wheat chloroplasts (Brown) 176

A comparative study of phase transition temperatures determined for chloroplast thylakoid membranes and for liposomes prepared from phospholipids extracted from photosynthetic membranes of higher plants (Fork, van Ginkel, and Harvey) 179

The effect of aging in vitro of spinach chloroplasts on the phase transition temperatures of thylakoid membranes (van Ginkel and Fork) 184

A comparative study of the photosynthetic unit sizes in sun and shade plants (Malkin and Fork) 187

Chlorophyll *a* fluorescence transients from sun and shade plants (Fork and Govindjee) 189

Chlorophyll *a* fluorescence transient as an indicator of the water potential of leaves (Govindjee, Downton, Fork, and Armond) 191

Effects of dessication on the excitation energy distribution between the two photosystems in the red alga *Porphyra perforata* (Öquist and Fork) 193

Comparison of photosomes with and without a manganese-containing protein (Govindjee, Fork, Wydrzynski, Spector, and Winget) . . . 198

Photosynthesis bibliographic file update—June 1980 (Brown) . . . 200

Bibliography 200

Speeches 202

Personnel 205

INTRODUCTION

That part of biology commonly called molecular biology had its origins and explosive development in studies of procaryotic organisms. Techniques and understanding reached a high level of sophistication well before eucaryotic cells became useful as experimental systems. The relative simplicity of the procaryotic genome, the rapidity with which procaryotic cells could reproduce themselves, the development of a technology permitting highly quantitative investigations, and the influx of very bright students who might formerly have gone into chemistry, physics, or mathematics, all contributed to this extraordinary development. As experiments with eucaryotes became feasible, it was natural that animal cells would immediately become the material of choice. Given the efforts and financial support of the biomedical establishment, studies in animal biology soon flourished. Many of the important pioneering findings were made by Carnegie scientists, both at the Department of Terrestrial Magnetism and the Department of Embryology. A glance at the current Annual Report of the Department of Embryology will be more than sufficient to indicate the great strength and continuing pioneering by Carnegie in this field.

By contrast, plant molecular biology has been late and slow to develop. The agricultural establishment did not provide the kind of support given by the biomedical establishment to animal molecular biology. Thus, limitations in dollars for plant research led a majority of the bright students to greener pastures. Only very recently have we seen the beginnings of an effective and creative relationship between agriculture and the plant molecular biology field; even today the number of scientists doing plant molecular biology is so small that virtually all of them can attend a single Gordon conference!

An obvious consequence is that plant biologists are forced to cover ground already well worn by their "animal" counterparts. The last five Annual Reports from the Department of Plant Biology show that William Thompson and his students and associates have played an important role in the catching-up process. Much of their time had to be devoted to learning how to handle plant nucleic acids—how to obtain them in uncontaminated form, how to clone them, how to cope with the very large repeated sequence fractions frequently encountered. Meanwhile, they made substantial progress both on evolutionary problems and on problems of genome organization and temporal expression. The first articles in this Report attest to their progress.

Plant Molecular Biology

Murray, Peters, and Thompson have continued their investigations into the organization of pea and mung bean genomes; they have found, surprisingly, that if the criteria for reassociation of single-stranded DNA are somewhat relaxed, virtually all the DNA from peas can form duplexes, including almost all of that normally classified as single copy. Both reassociation and melting (thermal dissociation) techniques clearly indicate that the DNA actually expressed in messenger RNA is indeed single copy. There is however a much larger class of DNA which behaves as though it were single copy under normal reassociation conditions but in fact is distantly diverged repeated sequences, and Murray and colleagues have coined the term "fossil repeats" to describe it. Mung bean, in

contrast, contains much less DNA in this fraction. Most of the mung bean DNA that appears as single copy under normal reassociation criteria behaves as single copy under the relaxed criteria as well.

Preisler and Thompson have also investigated the reassociation behavior of the repeated fractions from pea and mung bean and, as with the single copy fractions, they find significant differences between these two plants. The evidence shows that in peas, amplification of regions of the genome followed by divergence followed by reamplification of the diverged regions must have occurred during the evolution of pea DNA, leading to considerable heterogeneity within many of the families of repeated sequences present. In mung bean, however, there is no evidence for the reamplification events, and the families of repeated sequences are quite homogeneous. Both of these studies contribute to our knowledge of evolutionary processes that affect genome organization.

In their report last year of the successful cloning of plant DNA, Cuellar, Selker, Jorgensen, and Thompson described considerable progress in developing and characterizing cDNA clones and in using them to follow developmental changes in the RNA sequences found in greening pea seedlings. These workers have also developed techniques to permit them to make accurate measurements of the concentrations of large numbers of different RNA sequences. Thus the hope of following in detail transcriptional changes during development is now much closer to reality. Meanwhile, Cuellar and Thompson are successfully using cloning techniques to study genome fine structure and organization at the level of single repeated-sequence families.

Finally, Palmer and Thompson have made dramatic progress in their studies both of chloroplast and of mitochondrial DNA in plants. In addition to determining the relative amounts of chloroplast (5–15%) and mitochondrial (1–2%) DNA in the total genome, they have shown homology of 60% or greater between chloroplast DNAs from plants as distantly related as corn and spinach, with the homologies between the mitochondrial DNAs being much lower (as low as 27%). The mitochondrial genomes show unexpectedly large kinetic complexity. To account for this complexity, they hypothesize that the mitochondrial genome may consist of a number of different circular molecules of different sizes, sharing little sequence homology. Finally, they have constructed complete clone banks of the chloroplast genomes from mung bean, pea, and spinach. These banks should provide powerful tools for the study of a wide range of problems related to chloroplast molecular biology.

Photomorphogenesis

Work in my own laboratory has continued to focus on photosensitive molecules, both phytochrome (sensitive to radiation at the red end of the spectrum) and blue light photoreceptors. As in the past, studies have been both physiological, with intact seedlings, and biochemical, on isolated and purified subcellular fractions. Mandoli has now obtained detailed characterization of the responses of dark-grown oat seedlings to light. Surprisingly, these seedlings are extraordinarily sensitive. Their growth pattern is significantly changed when they receive an amount of light equivalent to one second of full moonlight. In order to do the experiments at all, Mandoli had to develop techniques for handling the plants in complete darkness, since even dim green "safelights" would transform enough phytochrome in a few minutes to yield a substantial response. Both coleoptiles and mesocotyls showed not one but two distinct responses, one almost four orders of magnitude more sensitive than the other. For the less

sensitive response, Mandoli* showed that irradiation of the node between coleoptile and mesocotyl was most effective in obtaining responses from either organ, although growth of tissues at some distance from the node is what was affected.

Gorton has continued her investigations on the effect of phytochrome state at the end of the day on the growth pattern and anthocyanin synthesis in corn seedlings. Reciprocity tests indicate that short and high-fluence-rate light pulses are far more effective than longer and lower-fluence-rate pulses, though the total energy in both cases is the same. This failure of reciprocity is anomalous in two ways. First, the responses are to small doses of light, and such low irradiance responses normally obey the reciprocity law; second, the reciprocity failure for high irradiance responses is normally in the opposite direction: long and low-fluence-rate irradiations are the most effective, rather than the least effective. There is at present no simple model to account for these anomalies.

In another series of physiological studies, Sundqvist discovered that σ-aminolevulinic acid, a precursor for pyrrole synthesis, would promote the unrolling response of dark-grown barley leaves when present in low concentrations, but would inhibit unrolling at millimolar concentrations. Since red light is known to promote unrolling, a process reversible by far-red, it seemed possible that the compound might be acting in some way through its role as a precursor for the phytochrome chromophore. However, the unrolling process clearly could escape from far-red reversibility after red light much more quickly than from inhibition by σ-aminolevulinic acid. Thus the effect of the acid must be on some step in the reaction chain beyond phytochrome. In studies with highly purified phytochrome, Sundqvist initiated studies on the influence of divalent cations on phytochrome photochemistry. Although the results are preliminary, they suggest that cations may be effective probes in investigating the molecular changes that occur on phytochrome photoconversion.

Blatt, who spent over a year on a Fulbright fellowship in Wolfgang Haupt's laboratory in Erlangen, West Germany, collaborated with Weisenseel in measuring currents around a filament of the alga *Vaucheria sessilis* illuminated with a microbeam of blue light. As reported last year, chloroplasts aggregate in such an illuminated region probably because of disruption of the actin cables along which they are moving. These cables break down and form a reticulum under the influence of blue light. Blatt and Weisenseel found that there was a well-defined efflux of positive charges (or influx of negative charges) confined to the illuminated region of the cell. The process had the same kinetics, the same wavelength discrimination, and the same relative sensitivity as the reticulation and aggregation phenomena, suggesting that these phenomena are all closely related. Though the point is not entirely settled, it seems likely that the light-induced current is a reflection of an efflux of protons. Since actin aggregation is sharply pH-dependent, a small local change in pH within the cell could lead directly to the reticulation phenomenon. Though this suggestion remains an hypothesis, Blatt has uncovered another important facet of a rapid response to blue light in this organism.

Leong has made substantial prog-

*This year for the first time, we are unable to publish individual reports on all of the research carried out at the Department of Plant Biology during the year. This restriction comes from two sources: a physical limitation on the number of pages which we can publish, and an increase in the number of reportable projects—some of them very substantial—brought to fruition in the past months. The Director has done his best to summarize those projects omitted, and has identified these in the text by asterisks.

ress in the isolation and purification of a blue light photoreceptor complex from corn. Following work initiated by Goldsmith and Caubergs (and reported in *Year Book 78*), he succeeded in separating completely the membrane fraction containing the light-sensitive complex, which contains both a cytochrome and a flavin, from other cytochrome-containing fractions, and in showing that the photoactivity co-purified with activity of a putative marker for the plasma membrane. With Caubergs, he also succeeded in solubilizing the photoactivity from the purified membrane fraction, using a mild detergent. As the photoactivity was virtually unchanged by solubilization, it seems likely that both flavin and cytochrome are on the same protein. Room temperature spectra for this cytochrome clearly distinguished it from the other well-known extramitochondrial cytochrome, cytochrome b_5 of the endoplasmic reticulum; low-temperature spectra taken in collaboration with Richard Vierstra* of Michigan State University revealed this distinction even more dramatically.

Finally, Sundqvist* took advantage of our computerized spectrophotometers to make analyses of a curious form of protochlorophyll found in the inner seed coats of *Cyclanthera explodens*. He obtained both absorption and fluorescence data to complete the spectral characterization work he started in Sweden before coming to Plant Biology.

Physiological Ecology

The plants of Death Valley and the Arizona desert continue to provide valuable subjects for studies of acclimation to high temperature. Seemann, Berry, and Downton have followed acclimation of photosynthesis through a Death Valley growing season for a group of annual species, and they found that all these species increase their tolerance to high temperature as the cool weather accompanying the winter rains is replaced by the intense summer heat. Desert perennials showed the same flexibility as those winter annuals investigated. By contrast, a group of summer annuals growing in the Arizona desert where the rains come in summer, not winter, showed a significantly lower capacity to acclimate. Though all the summer annuals were tolerant of high temperatures, they had a more limited capacity for adjustment than the other groups of species investigated. The range of high-temperature acclimation observed over a growing season for plants in the field was matched very well by plants grown in laboratory cabinets, where temperature alone was varied. Thus the range of adjustment found in the field is probably a response to changes in temperature during the season, and this physiological change in the capacity to tolerate high temperatures may enable the plants to extend their growing season into the hotter parts of the year. In another part of the study, the three workers found that the photosynthetic rates of eight desert winter annuals were on the average 40% higher than those for a wide range of agricultural and native species from very diverse environments. There is clearly something special about these desert plants.

Roberts and Berry have continued monitoring membrane changes occurring in mature leaves of the shrub *Nerium oleander* when it is shifted from a cool to a hot regime. There are several dramatic changes in the lipid species found in the chloroplast membranes, some of them clearly apparent after a single day at the high-temperature regime. There is a general decline in unsaturated and an increase in saturated fatty acids, as might be expected from work on other systems. Surprisingly, the abundances of specific fatty acids change in opposite directions in the galactolipids and the phospholipids. The control mechanisms for these changes

are completely unknown and clearly merit further study.

During the past few years, the physiological ecology group has concentrated their studies of acclimation almost exclusively on a single factor—temperature. Great efforts were expended to make certain that water was not limiting, and that saturating levels of CO_2 were available when appropriate so that the intrinsic responses of the system to temperature changes could be isolated and studied. Interest also focused (although not exclusively) on the upper end of the temperature range. This year, the group presents reports dealing with two other factors, carbon dioxide enrichment and water stress, as well as a report on the phenomenon of chilling sensitivity.

With strong evidence for a significant increase in carbon dioxide in the atmosphere as a consequence of the burning of fossil fuel and deforestation, it is essential to determine the long-term effects of the higher carbon dioxide partial pressures on photosynthesis. Björkman, Downton, and Pike* have investigated the effect of CO_2 enrichment lasting weeks or months on several C_3 and C_4 plants. Not surprisingly there was very little effect on the C_4 plants, since a distinctive feature of C_4 photosynthesis is that it concentrates carbon dioxide for fixation by ribulose bisphosphate carboxylase. However, CO_2 enrichment produced strong increases both in light-limited and light-saturated photosynthetic rates and significant enhancement in dry-matter production of C_3 plants. Perhaps the most impressive consequence of enrichment on both C_3 and C_4 plants was a dramatic increase in the water-use efficiency (carbon dioxide fixed per unit of water lost through transpiration). Though other aspects of a CO_2-enriched atmosphere may not necessarily be beneficial, the effects reported here could have a positive impact on agricultural productivity.

Björkman, Downton, and Mooney have also initiated studies of the effect of water stress on *Nerium oleander.* The shrub is highly tolerant to water stress, and regulates its water status solely through stomatal opening and closing. Contrary to expectations, there was no osmotic adjustment in response to a gradually imposed water stress. There is a reduction in intrinsic photosynthetic capacity, a response expected on the basis of previous studies here and elsewhere, and it could be accounted for entirely by a decrease in the capacity for photosynthetic electron transport and photophosphorylation in the stressed plants. These studies mark the onset of a new program of investigation of interaction of stress factors on photosynthetic systems.

Powles, Berry, and Björkman have obtained some provocative results from studies on the interactions between light and temperature in chilling-sensitive plants. Such plants (beans and tomatoes are well-known examples) are simply unable to tolerate temperatures below 10 °C or so, and have a lower limit for growth well above freezing. The results clearly establish that exposure of leaves of these plants to temperatures below 10 °C in normal air and high light intensity produces damage to the photosynthetic apparatus. Such damage does not occur if the oxygen tension is lowered or if the light intensity is reduced. While details of the mechanism of injury remain to be resolved, the results could have agricultural implications.

Some years ago, Björkman showed that there were significant biochemical differences between sun and shade leaves related to their different photosynthetic capacities at light saturation. There are also anatomical differences between such leaves, however, which some workers suggest could account for part or all of the photosynthetic superiority of sun leaves. Harvey has compared the photosynthetic capacities of sun and shade leaves in two ways: measurements of photosyn-

thesis by intact leaves, and measurements of photosynthesis by isolated intact leaf cells, which are obtained by enzymatic maceration. Since the differences in photosynthetic capacity between sun and shade leaves persist in the macerated cells, biochemical and/or cytological differences between the leaves must largely account for these differences.

Finally Nobs, who has just returned from a sabbatical in Australia, reports the results of his extensive cytological investigations of the chromosome numbers of a majority of the Australian species of *Atriplex*. *Atriplex* has been used throughout the world for ecological studies, and some species are used to desalinate over-irrigated soils. However, information on the chromosome numbers—essential for any hybridization program—was almost completely lacking. Nobs' study goes a long way to rectify this lack.

Photosynthesis

The past year has been a highly productive one for the photosynthesis group as well. Melis and Brown, using a specially designed spectrophotometer built in our own shops, were able for the first time to obtain quantitative information on the relative numbers of reaction centers in each of the two photosystems of photosynthesis. Contrary to expectation, the ratio of the two was not unity, and when chloroplast membranes were appropriately fractionated, it was possible to obtain fractions differentially enriched for one of the two systems; this result clearly indicates some spatial differentiation within the chloroplast and is consistent with other studies. Finally, the ratio does not remain constant for a given plant but changes during development. These studies have uncovered an unexpected and important aspect of chloroplast organization which should have a substantial effect on the course of a number of research efforts both here and elsewhere.

Brown has continued her extensive studies on chlorophyll fluorescence by investigating chloroplasts from plants grown under intermittent light. It is known that such plants fail to form any significant amount of chlorophyll *b*. In comparison with normal green plants, intermittent-light plants showed two major anomalies: (1) there was a much greater amount of shorter wavelength fluorescence, and (2) the remaining long-wavelength fluorescence was shifted 10 nm to shorter wavelengths. There were also differences in the fluorescence excitation spectra not entirely related to the lack of chlorophyll *b* in the treated plants. The intermittent-light-grown plants should provide very useful material in future investigations of the organization of chloroplast pigments and photosystems.

Fork continues to play a unique catalytic role in work with visiting researchers. Most of these visitors were here only briefly, but the collaboration was in each case fruitful. Fork, van Ginkel, and Harvey studied phase transitions of chloroplast lipids, using either chlorophyll as an intrinsic probe with native thylakoid membranes and chlorophyll *a*, or *trans*-parinaric acid as a probe added to liposomes from extracted thylakoid phospholipids. The results showed that the phase transitions occurred over a broad temperature range. Sharp phase transitions could only be obtained with liposomes made from single phospholipids. In a related study, van Ginkel and Fork used similar techniques to show that the phase transition behavior of the thylakoid membranes changes significantly if the chloroplasts are allowed to age a few hours, even if they are kept on ice, and that these changes are reflected in the behavior of liposomes made from the extracted phospholipids. The results dictate caution in performing experiments where more

than minimal chloroplast aging can occur.

Malkin and Fork used the fluorescence technique they developed two years ago to make determinations of the size of the photosynthetic units—expressed as total number of chlorophyll molecules per photosystem II reaction center—for a number of different sun and shade plants. All the sun plants yielded values between 220 and 540, and all the shade plants yielded values from 630 to 940. Fork and Govindjee also measured the time of appearance of a transient peak in chlorophyll *a* fluorescence in most of the same plants, and found a general inverse correlation between time of appearance of the peak and photosynthetic unit size. The technique should be adaptable to nondestructive field estimates of photosynthetic unit size if this inverse relationship holds up in other plants.

In studies complementary to those of the physiological ecology group, Fork and his associates have used fluorescence to study the effects of water stress both in *Nerium oleander* and in an intertidal alga *Porphyra perforata*. In the oleander studies, they again concentrated on a fluorescence transient, studying the effect of water potential on the ratio of maximum to minimum fluorescence in the transient. There was an excellent correlation between decrease in water potential and decrease in this ratio. Again, the method should be readily adaptable to field measurements providing a rapid, simple, and nondestructive indicator for water-stress effects.

Öquist and Fork used fluorescence at low temperature to study the effects of dessication on the photosynthetic apparatus of *Porphyra*. Like any intertidal alga, this species is exposed to air drying during low tide, and must somehow avoid photodynamic damage when this drying occurs during periods of high light intensity. The studies showed that dessication led to a loss of photosystem II emission with a concomitant increase in photosystem I fluorescence. These changes are rapidly reversed on rehydration. Öquist and Fork hypothesize that photosystem I may be far better suited to dissipating excitation energy as heat than is photosystem II, and that the change in energy distribution between the two photosystems may provide a possible mechanism to avoid photodynamic damage.

Last year, Berry and his colleagues reported on the rise in fluorescence which provided indication of the onset of thermal damage in heat-treated leaves; this year Fork, Downton, and Berry* have obtained fluorescence emission spectra before and at various times during heating of isolated chloroplasts. Surprisingly, there were only relatively small changes in the fluorescence emission characteristics of the chloroplasts, and there was no specific evidence for any dissociation of light-harvesting pigments from photosystem II even at temperatures as high as 67 °C. Such a dissociation has been proposed on the basis of fluorescence studies with intact leaves of other plants, and it is unclear whether the difference in results is attributable to species differences, differences in technique, or both.

Finally, Fork collaborated with workers from the University of Illinois and the University of Cincinnati to study the behavior of extracted thylakoids incorporated into liposomes and a recently characterized manganese-containing protein thought to play an important role in oxygen evolution in photosynthesis. The liposomes showed normal oxygen evolution (including normal charge accumulation in experiments with multiple flashes), normal variable fluorescence, and a normal carotenoid absorbance change at 515 nm on illumination as long as the manganese-containing protein was present. In the absence of the protein, there was no oxygen evolution, no variable

fluorescence, and evidence only for carotenoid photobleaching. The results clearly strengthen the hypothesis that the protein indeed functions on the electron donor side of photosystem II.

This introduction would be incomplete without mention of instrumentation developments during the past year. Melis and Hart designed and built a spectrophotometer, which has the capability of measuring very small absorbance changes in the ultraviolet (a difficult measurement because of the extremely high background absorption of any biological materials below 400 nm). It was only because of such instrumentation that Melis and Brown could make the direct measurements of photosystem II reaction center concentrations mentioned above. Field* (a Stanford graduate student) and Berry have designed and built a compact portable system for measuring carbon dioxide and water exchange away from the laboratory; the apparatus allows far greater flexibility for certain types of field work than the effective but cumbersome mobile laboratory, with no sacrifice in accuracy. Indeed, Seemann, Downton, and Berry made substantial use of this equipment in their studies of Death Valley annuals, mentioned above.

The reader may have noticed some perhaps unobjective enthusiasm in the above paragraphs. It simply underscores my conviction that the Department of Plant Biology is in excellent health and is continuing to do fine science.

Winslow R. Briggs

ANCIENT REPEATED SEQUENCES IN THE PEA AND MUNG BEAN GENOMES

Michael G. Murray, Debra L. Peters, and William F. Thompson

We reported last year that striking differences exist between the sequence organization patterns in pea and mung bean nuclear DNA. While a large portion of the mung bean genome is composed of single copy DNA sequences longer than 6700 nucleotides, pea DNA contains no clearly detectable single copy DNA longer than about 1000 nucleotides. In fact, the modal length of single copy sequences in pea DNA could be shown to be on the order of 300–400 nucleotides. Repetitive sequences of this length have been recognized in many genomes, but single copy sequences are usually thought to be much longer.

The short length of single copy regions in the pea genome is consistent with the "gradual divergence hypothesis" presented two years ago (Thompson, *Year Book 77,* 310–316). Short single copy sequences could originate from short, interspersed repetitive sequences when mutational divergence proceeds to the point at which members of the same family no longer recognize one another under normal in vitro conditions. If this hypothesis is correct, we would expect at least some of the sequences that react with single copy kinetics under normal conditions (about 25° below the T_m of native DNA) to behave as repetitive when the reassociation temperature is reduced and more divergent sequence combinations are allowed to form stable hybrids. Work carried out during the past year indicates that a surprisingly large fraction of the "single copy" DNA in the pea genome is composed of such diverged repeats. In contrast, coding sequences represented in messenger RNA continue to behave as "true" single copy sequences even at the lower reassociation criterion, as

does most of the single copy DNA in the mung bean genome.

The term "single copy" is still largely an operational definition, since the fraction of the genome that consists of recognizably repetitive elements can be shown to be a function of the reassociation criterion. For the purposes of discussion we will use the following operational definitions. The term "single copy" refers to sequences that reassociate at standard criterion (T_m −25 °C) with kinetics consistent with their existence in only one or two copies per haploid genome. "Repetitive" sequences are represented many times per haploid genome, with members of each family able to reassociate with one another at T_m −25 °C. "Fossil repeats" are sequences which reassociate with single copy kinetics at standard criterion but which form mismatched duplexes and can show repetitive kinetics at a more permissive criterion (here about T_m −35 °C). These sequences are thought to be members of repeat families created by ancient amplification events which have now accumulated so much mutational sequence divergence that they can no longer reassociate with each other at T_m −25 °C. Finally we define "true single copy" sequences as those which show single copy kinetics even at a permissive criterion and which do not form mismatched duplexes. We emphasize that these definitions are still arbitrary and that no clear-cut divisions may actually exist. Even "true" single copy DNA might be shown to have been derived from repetitive sequences if we could extend our analysis to much lower experimental criteria.

Only about 30% of the pea genome reassociates with single copy kinetics at T_m −25 °C, and sequence interspersion effects reduce this value to about 19% when assays are carried out with 300-nucleotide DNA fragments (Murray *et al.*, 1978; *Year Book 77*, 316–323). To determine whether a significant fraction of the single copy sequences in the pea genome fall into the above classification of fossil repeats, the reassociation kinetics of a tracer enriched in single copy DNA were followed at standard and permissive criterion. Complete details of these experiments are published elsewhere (Murray *et al.*, 1980). The single copy tracer was prepared by successive reassociation and hydroxylapatite fractionation at C_0t 300 and C_0t 1000. The material remaining single stranded was mixed with fresh unlabeled 300-nucleotide pea DNA and again reassociated to C_0t 1000 to remove any residual repeats that may have failed to form hydroxylapatite-bindable duplexes during the first two reassociations. When reassociation of the resulting tracer was examined at standard criterion in the presence of excess unlabeled pea DNA, about 60% reacted with the predicted single copy kinetics. However, under permissive conditions the presumptive single copy component reassociated about 18 times faster than expected. No more than about 8% of the low-criterion reaction could be described using the predicted single copy rate constant. This fraction of the tracer corresponds to between 1 and 2% of the total pea genome. Examination of thermal stability profiles indicated an average mismatch of about 9% for "single copy" duplexes formed at standard criterion and about 14% for the slowest component at permissive criterion. The profiles upon which this statement is based were obtained by taking the difference between separate profiles at high and low C_0t values; thus in each case they reflect the melting behavior of only the most slowly reassociating duplexes. We conclude that virtually all the sequences in the pea genome that would normally be classified single copy actually fit the above definition for fossil repeats.

We reported last year that in peas, as in most other organisms, the bulk of the mRNAs are single copy transcripts (Peters *et al.*, *Year Book 78*, 208–212).

Additional experiments have confirmed that most sequences represented in a cDNA preparation from polysomal poly (A)+ mRNA show true single copy behavior; i.e., the cDNA reassociates with single copy kinetics at both standard and permissive criteria, and little mismatch is detected at either temperature. We did find that about 10% of the cDNA reaction could be fit with a repetitive component at both criteria, and there was a small amount of mismatched material after reaction at the permissive criterion. It seems likely that a small fraction of the mRNAs in peas represents repetitive multigene families. However, most mRNA sequences are transcribed from true single copy DNA.

The fact that virtually all the cDNA shows true single copy behavior while no more than 1–2% of the total DNA does so indicates that coding sequences represent a very small fraction of the pea genome. It was therefore of interest to determine whether true single copy sequences constitute a more readily measurable fraction of the mung bean genome, a genome some nine times smaller that that of the pea (Murray *et al.,* 1979; *Year Book 78,* 204–207). Essentially all the single copy tracer from mung bean followed single copy kinetics at standard criterion. The reaction at low criterion could also be described with a single second-order component. Although the average reassociation rate was about twice that at standard criterion, the kinetics were close enough to those at standard criterion so that it was not necessary to postulate a substantial fraction of fossil repeats on the basis of kinetic data alone. Evidence for some fossil repeats was obtained from thermal stability profiles for reassociated mung bean single copy tracer duplexes. While the modal melting temperatures were identical at both criteria (about 2 °C below that for native DNA), the profiles were asymmetrical. A low-stability shoulder was evident in duplexes formed at the permissive criterion, lowering the T_m to 6 °C below native DNA. However, in sharp contrast to pea DNA, fossil repeats do not make up more than about 30% of the total mung bean single copy fraction.

References

Murray, M. G., R. E. Cuellar, and W. F. Thompson, *Biochemistry, 17,* 5781–5790, 1978.

Murray, M. G., J. D. Palmer, R. E. Cuellar, and W. F. Thompson, *Biochemistry, 18,* 5259–5266, 1979.

Murray, M. G., D. L. Peters, and W. F. Thompson, *J. Mol. Evol.,* in press, 1980.

EVOLUTIONARY SEQUENCE DIVERGENCE IN FAMILIES OF REPEATED DNA

Richard S. Preisler and William F. Thompson

From an evolutionary viewpoint, the high proportion of repetitive DNA and "fossil" repeats in the pea genome relative to that in mung beans (Murray *et al.,* this Report) suggests that the formation of repetitive DNA by sequence amplification has been much more frequent in the evolutionary history of peas. One consequence of frequent amplification might be that members of preexisting repetitive families would often be reamplified to produce new subsets of repeats within a larger family. If secondary amplification events involve members of older families whose members have accumulated base substitutions and are no longer identical, we would expect the sequences in each new subfamily to be more similar to each other than to other subfamilies or other members of the original family.

Most conventional techniques do not distinguish such *heterogeneous* fam-

ilies from *homogeneous* families evolving in the absence of secondary amplification. As we discussed previously (Preisler and Thompson, *Year Book 77*, 323–330), the reassociation kinetic assay used by Bendich and Anderson (1977) in an attempt to make this distinction cannot be applied when wide variation in size (copy number) exists among the families in a given genome. At that time we attributed some of the "anomalous" reassociation behavior seen for mung bean leaf DNA to the presence of chloroplast genomes reassociating along with the repetitive nuclear DNA. While subsequent experiments have confirmed the presence of large amounts of chloroplast DNA in preparations made from leaves, we have also observed very similar reassociation behavior in mung bean nuclear DNA preparations containing only trace amounts of chloroplast sequences. Just as in the case of total DNA, the average reassociation rate for nuclear repeats increases under more stringent conditions, a result contrary to predictions of the Bendich and Anderson model for either homogeneous or heterogeneous families. We believe that newer, less diverged families of repeats tend to be present in higher copy numbers in mung bean DNA, a situation which invalidates one of the crucial assumptions of the kinetic assay (Preisler, 1980).

To avoid this and other problems in the kinetic analysis, we have developed an assay which distinguishes heterogeneous and homogeneous families by comparing thermal denaturation (melting) profiles for repetitive DNA after reassociation under high-criterion and low-criterion conditions. In heterogeneous families, reassociation at a low criterion should permit the formation of many duplexes between members of different subfamilies. These hybrids would contain more mismatched base pairs, and thus have lower thermal stabilities than those formed between members of a single subfamily. At a high reassociation criterion, however, formation of mismatched duplexes would be inhibited, and duplex formation *within* subfamilies would be favored over reassociation *between* subfamilies. Thus at the high criterion we would expect heterogeneous families to form more high-stability duplexes than would be produced by low-criterion reassociation. Experiments with model mixtures of normal and partially deaminated *E. coli* DNA supported these assumptions. In contrast, homogeneous families should not show such an increase in high-stability duplexes, since they lack the subfamily structure that is the basis for altering the duplex distribution.

Results of these experiments will be reported in detail elsewhere. In brief, however, a comparison of melting data for repeats reassociated to equivalent C_0t values at high and low temperatures provided strong evidence that many families in the pea genome are heterogeneous, while homogeneous families predominate in mung bean DNA. Attempts to fractionate pea DNA by thermal stability in order to enrich for groups of sequences showing homogeneous behavior were unsuccessful; clear evidence of heterogeneity was obtained in all cases. We conclude that the pea genome has probably evolved by an extensive series of amplification events often involving secondary amplification within preexisting repetitive families.

Our data for pea DNA are consistent with other evidence indicating that secondary amplification has occurred in at least some repetitive families in the wheat and rye genomes (reviewed by Flavell, 1980), but go beyond previous data in indicating that heterogeneity is a prominent feature of the entire repetitive fraction. The homogeneity we find in mung bean DNA represents yet one more striking difference between the patterns of sequence organization in these two legume species. We believe that the

most likely interpretation of this and most other differences between these two genomes is that the pea genome has been subject to a high rate of sequence amplification during its evolution, while the rate in the mung bean genome has been much lower. In this respect, the mung bean genome may be more similar to those of many higher animals than it is to higher plants with haploid DNA amounts in excess of 1–2 picograms. A general model designed to explain differences in sequence organization largely in terms of amplification or turnover (amplification plus deletion) rates has been discussed briefly by Thompson and Murray (1980) and will be presented in detail elsewhere (Murray *et al.*, 1980).

References

Bendich, A. J. and R. S. Anderson, *Biochemistry, 16,* 4655–4663, 1977.

Flavell, R. B., *Annu. Rev. Plant Physiol.,* in press, 1980.

Murray, M. G., D. L. Peters, and W. F. Thompson, *J. Mol. Evol.*, in press, 1980.

Preisler, R. S., Ph.D. thesis, Stanford University, 1980.

Thompson, W. F. and M. G. Murray, in *The Plant Genome,* D. R. Davies and D. A. Hopwood, eds., pp. 31–45, The John Innes Charity, Norwich, England, 1980.

OBSERVING PATTERNS OF GENE EXPRESSION AT THE RNA LEVEL: THE GREENING RESPONSE IN *Pisum*

Richard A. Jorgensen and William F. Thompson

Last year (*Year Book 78,* 212–214), we reported the isolation and preliminary characterization of 50 molecular clones of pea leaf cDNAs (synthetic DNA molecules complementary to polyadenylated messenger RNA [polyA mRNA] molecules). Using these clones as probes, we were able to demonstrate substantial tissue-specific differences in levels of polyA mRNA for RNA sequences homologous to 30 of the clones. This experiment (known as a colony hybridization assay) involved making highly radioactive cDNAs from both leaf and bud mRNAs and then determining the relative degree of hybridization of these two populations of cDNA with individual cloned cDNAs from leaves. This year's report presents a more detailed characterization of these clones and then discusses how these clones are being used to develop techniques for making more quantitative and rapid physiological measurements of RNA abundance levels in developing tissues.

Further characterization of the 50 cDNA clones described last year has led to the following conclusions and qualifications. (1) Several of the cDNA clones are unstable, in that deletions and/or rearrangements of the cloned sequences occur at an unusually high frequency. The practical result of this instability is that 12 of the clones are unusable or have been lost from the collection. The remaining clones are relatively stable as long as selection for the tetracycline resistance marker is maintained. An exception has been the occasional appearance of very short deletions (<5–30 base pairs in length) within the cDNA segments of roughly one third of the clones. (2) Each of the seven clones displaying greater abundance in bud RNA than leaf RNA is homologous to ribosomal RNA (rRNA). Since rRNA is expected to be present in polyA mRNA preparations only as a contaminant, the tissue-specific response attributed to these seven clones is artifactual, being instead the result of higher levels of rRNA contamination in the bud than in the leaf RNA preparations. (3) The cDNA inserts of three clones were found to be too short for efficient

hybridization to homologous sequences and so are of limited usefulness. (4) The remaining 29 clones fall into 14 independent groups by tests for sequence cross homology in colony hybridization assays. Table 1 shows the number of clones composing each of the 14 groups and the length of the cDNA insert in each clone (with a standard reference clone for each group). (Note: multiple homologous clones are not necessarily the products of independent mRNA molecules, since all 50 clones were isolated from the same transformation culture.)

The remainder of this report will discuss an experimental approach designed for making quantitative and rapid physiological measurements of the abundance levels of RNA sequences present in greening pea seedlings. The method we are using to measure relative concentrations of individual RNA sequences is a modification of a filter hybridization procedure developed by Kafatos *et al.*, 1979. In brief, nitrocellulose filter-bound DNA representing a single molecularly cloned sequence is allowed to hybridize to homologous sequences in a radioactively labeled RNA population, as in a colony hybridization assay. In the current procedure we are using purified plasmid DNA rather than crude bac-

TABLE 1. Hybridization Characteristics of cDNA Clones

Cross-Homology Group	# of Clones	Reference Clone			Hybridization to RNA†			
					End Label‡		cDNA Label§	
		Name	Insert Size (basepairs)	Hybridization to poly A*	Etiolated Bud	Mature Leaf	Etiolated Bud	Mature Leaf
F	2	pEA2	700	+	<1	<1	<0.1	<0.1
H	2	pEA4	300	−	<1	<1	<0.1	<0.1
B	1	pEA5	570	−	1	2	<0.1	1.6
K	1	pEA9	500	−	<1	<1	<0.1	<0.1
L	1	pEA13	300	−	<1	<1	<0.1	<0.1
E	3	pEA14	1,000‖	+	2	2	1.6	1.6
I	1	pEA22	230	−	1	1	<0.1	<0.1
A	3	pEA28	500	+	4	8	1.6	3.2
D	4	pEA25	350	+	<1	1	<0.1	<0.1
G	3	pEA30	200	−	<1	<1	<0.1	<0.1
M	2	pEA35	500	−	64	64	0.4	0.2
P	1	pEA41	250	+	<1	<1	0.4	0.8
N	2	pEA46	325	−	<1	<1	<0.1	0.4
J	3	pEA47	300	−	<1	1	<0.1	0.2
nuclear rRNA	7	pEA17	1,800	−	16,384	8,192	25.1	1.6
chloroplast rRNA		p11.5	11,500	n.t.	512	6,384	1.6	0.8

*Determined by colony hybridization assay using labeled poly-dA as probe.

†Determined as described in the text. Numbers are estimates based on visual comparison of autoradiographic band intensity with standards differing in multiples of two. Thus all numbers reported here are multiples of two.

‡Labeling procedure outlined in text. Number estimates are standardized to the number 1 which is taken as a signal twofold greater than background.

§Labeling procedure outlined in text. Number estimates are standardized to 0.1, which is taken as a signal twofold greater than background. Results are roughly comparable (within fourfold) between end-labeled and cDNA-labeled experiments, having been normalized for total RNA concentration in the hybridization reaction.

‖Rearrangement between insert and vector sequences indicates that 1,000bp is not a correct measure of the length of the cloned segment in this case.

terial lysates, and we bind the DNA to the filters in the shape of a rectangular band ($\sim 1 \times 8$ mm) rather than in a circular spot, as done by Kafatos *et al.* or as *in situ* lysates as in the colony hybridization. Using purified DNA rather than crude *in situ* lysates gives an increase in sensitivity of two or more orders of magnitude. Measurement of the amount of hybridization (which is proportional to the concentration of homologous sequences in the labeled population) is done by autoradiography. Loading DNA onto filters in bands allows simple and quantitative analysis of autoradiographic responses by densitometric scanning. To simplify data collection and analysis further, we plan to record such data in computer files. Such a capability should permit experimental investigation of large numbers of cloned sequences and RNA populations.

To illustrate the technique, we have carried out some preliminary experiments with the 14 cDNA clones (Table 1), an rRNA clone (pEA17, Table 1), and clones of 11 of the 12 PstI restriction fragments of the pea chloroplast genome (see Palmer and Thompson, this Report). The RNA populations analyzed were "total RNA" preparations isolated by a modification of the procedure of Glisin *et al.*, 1974. Total RNA preparations represent a minimally biased population, in that each RNA species in the preparation is expected to be present at essentially the same relative concentration as in the living tissue. Radioactive labeling of the RNAs was done in vitro, either by enzymatic 5′-phosphorylation of limited alkaline hydrolysates to introduce a relatively nonspecific label of high specific activity ($>2 \times 10^7$ dpm/μg) or by synthesis of radioactive cDNA by reverse transcription with oligo-dT primers in order to label specifically only the polyadenylated fraction of the RNA preparation. Comparison of results obtained with the two labeling procedures allows one to measure the fraction of all RNA sequences homologous to the filter-bound probe that are polyadenylated.

Results of some recent filter hybridization experiments with total RNA populations derived from etiolated buds and mature leaves are presented in Table 1. Some preliminary conclusions from these data are the following: rRNA encoded by the nuclear genome does not appear to change in abundance (within experimental error) in etiolated buds versus mature leaves; however, chloroplast-encoded rRNA increases its autoradiographic response 30-fold during development of buds into leaves. As would be expected, we find that less than 0.1–0.01% (i.e., essentially not any) of these rRNAs are polyadenylated.

The most abundant nonribosomal RNA sequence observed is sequence M, whose response is less than 1% of the rRNA response. The abundance of sequence M does not change nor is the sequence polyadenylated in these developing tissues. In contrast, sequences E and A, whose responses are from 10-fold to 30-fold lower than that of sequence M, are substantially polyadenylated but are not developmentally changing in abundance in these tissues. A fourth sequence (B), which is in the same abundance range as E and A, shows striking developmental regulation of polyadenylated RNA species homologous to it, while the total RNA sequences homologous to B are equally expressed in both tissues. This observation suggests a movement of sequences from a precursor fraction into a polyadenylated fraction. It is not possible to state conclusively that sequences A, B, or E encode polypeptides, though it seems a good possibility.

Autoradiographic responses from the remaining sequences in Table 1 are near or at background levels. However, we have detected RNA sequences

homologous to nearly all these sequences in a purified polysomal polyA mRNA preparation. rRNA constitutes roughly 99% of the RNA in total RNA preparations, so we expect that its removal should increase the sensitivity of the filter hybridization by nearly 100-fold. This technique should allow us to detect RNA sequences homologous to most cDNA clones, as in the case of the purified polyA mRNA preparation. Thus, current work is directed toward isolating genomic clones of the nuclear and chloroplast rRNA genes to provide a source of rDNA sequences that can be used to remove rRNA specifically from total RNA preparations.

In summary, we have used molecularly cloned sequences from the pea genome to monitor developmental and physiological changes in RNA sequences in greening pea seedlings. Further refinements of the technique should allow the accurate measurement of RNA concentrations of large numbers (100–1000) of different sequences as a function of developmental stage and should result in the description of patterns of gene expression at the RNA level. We note also the possibility for comparing such patterns among genetic variants (i.e., ecotypes and mutants) of *Pisum* in order to assess the relationship between these physiological parameters and the genetic diversity of the genus.

References

Glisin, V., R. Crkvenjakov, and C. Byus, *Biochemistry, 13,* 2633–2637, 1974.

Kafatos, F. C., C. W. Jones, and A. Efstratiadis, *Nucl. Acids Res., 7,* 1541–1552, 1979.

CLONED REPEATED SEQUENCE ELEMENTS FOR THE STUDY OF DNA SEQUENCE EVOLUTION IN HIGHER PLANTS

Richard E. Cuellar and William F. Thompson

For the past several years the pea and mung bean genomes have been studied with conventional methods, such as solution hybridization and kinetic analysis. Those studies made it clear that both genomes are extremely complex and difficult to characterize further than is illustrated in the accompanying articles. For more detailed analysis of the structure and evolution of these genomes, we have constructed banks of cloned restriction fragments containing representatives of repeated DNA families. Such discrete cloned sequences now allow the study of fine structure and organization at the level of the individual repeated-sequence family.

Clones containing repetitive DNA were selected by screening a large number of recombinants by the "colony hybridization" method of Grunstein and Hogness (1975). We have used those colonies which gave a positive hybridization signal when exposed to ^{32}P-labeled cRNA synthesized from a repeated sequence fraction of pea and/or mung bean DNA.

About 30 independent pea DNA clones have been surveyed by hybridization to "Southern blots" (Southern, 1975) of restricted DNA fragments electrophoretically separated on agarose gels and then transferred to nitrocellulose filters. A radioactive copy of a cloned DNA is then hybridized to the filter-bound fragments. Among the clones so far examined are examples of tandemly repeated sequences, including some that exhibit sequence divergence. The divergence is evidenced by "ladders" formed when

hybridization is carried out with blots of *Eco*RI-digested DNA, indicating base substitution, deletion, or possibly methylation, within the *Eco*RI recognition sequence of some members of the tandem array. Other families do not appear to be tandemly arranged by this assay. These occur in restriction fragments covering a very broad size range and thus, presumably, in many different sequence environments at different locations in the genome. It is clear that many of the clones contain several different repeated sequence elements on a single fragment, as would be predicted from the permuted repeat pattern we envisioned in earlier analyses (Murray *et al., Year Book 77,* 316–332). Cloned pea DNA fragments longer than 1000 nucleotides invariably display such heterogeneity; some 20% of all the pea fragments cloned, including some of the clones we are currently analyzing, were shown to hybridize with a probe from mung bean repetitive DNA.

In order to simplify the analysis of complex fragments, we have used a modification of the Southern blotting method. After hybridization with a cloned probe, the filters can be cut into several strips and thermal stability analysis carried out by exposing different strips to various denaturing conditions of increasing stringency prior to autoradiography.

Some of the fragments being studied in detail are pPs 18 (an 8-kb fragment containing at least four and probably more different repeated sequence elements, at least one of which is also represented in mung bean DNA), pPs 21, 42, and 84 (a set of independent clones which apparently share an element or elements which yield strikingly similar patterns in Southern blot hybridizations, in combination with other elements which appear to be entirely different), and pPs 25 (which represents a tandemly repeated family undergoing sequence divergence).

Further analysis of cloned repeat sequences will lead to a better understanding of the processes underlying DNA sequence evolution in higher organisms. Of particular interest is the mechanism by which repeated sequence elements are transposed throughout the genome. Primary sequence determination of fragments, such as those represented in pPs 21, 42, and 84, should indicate whether or not there are recognizable homologies at the junction regions of repeated sequence elements.

References

Grunstein, M. and D. Hogness, *Proc. Nat. Acad. Sci. USA., 72,* 3961–3965, 1975.

Southern, E. M., *J. Molec. Biol., 98,* 503–517, 1975.

STUDIES ON HIGHER PLANT CHLOROPLAST AND MITOCHONDRIAL DNA

Jeffrey D. Palmer and William F. Thompson

Last year, we reported initial measurements of the amount of chloroplast DNA in mung bean and pea tissues (*Year Book 78,* 226–231). We are currently extending these measurements with the same techniques to include several other species of plants, and we plan to study a wide range of tissues and developmental stages. The primary finding from an extensive study of tobacco leaves is that the percentage of chloroplast DNA is quite constant at about 5% in leaves ranging in length from 1.5 to 30 cm. This is in sharp contrast to a recent report that up to two thirds of the DNA in very large tobacco leaves is chloroplast DNA (Jope *et al.*, 1978).

Most of the legumes, cereals, and chenopods surveyed contain between 5% and 15% chloroplast DNA in green leaves (Table 2). The highest value yet measured is 30% for the runner bean. Etiolated leaves contain as much or even more chloroplast DNA than do green leaves.

Mitochondrial DNA has been prepared from a number of higher plants and used as a probe to quantitate levels of mitochondrial DNA in various species and tissues. We find much less mitochondrial DNA, generally only 1–2%, than chloroplast DNA in both green and etiolated tissues (Table 2).

A most surprising finding in the course of calibrating the mitochondrial DNA reassociation reaction is that the kinetic complexity of mitochrondrial DNA from corn, mung bean, and spinach is between 300 and 500 kilobases (kb)—from two to four times the complexity of the chloroplast genome. These reassociation reactions were monitored by hydroxylapatite chromatography; we are now performing optical reassociations in order to confirm the above findings and to determine more precisely the complexity of the mitochondrial genome. Our present estimates of kinetic complexity are 3–6 times higher than all previous measurements (Wells and Birnstiel, 1969; Kolodner and Tewari, 1972; Vedel and Quetier, 1974). While there is no obvious explanation for so large a discrepancy, we note that the high kinetic complexities we measure are consistent with the very complex mitochondrial restriction patterns that we and others (e.g., Quetier and Vedel, 1977; Pring *et al.*, 1980) observe. To reconcile the large kinetic and restriction complexities of mitochondrial DNA with the failure to find a single mitochondrial DNA molecule long enough to accommodate this information (Kolodner and Tewari, 1972; Vedel and Quetier, 1974; Quetier and Vedel, 1977; Synenki *et al.*, 1978) and the occurrence of a variety of mitochondrial DNA circle sizes in soybean (Synenki *et al.*, 1978), corn (V. Walbot, personal communication), and tobacco (R. Dale, personal communication), we suggest that the higher plant mitochondrial genome is distributed over a number of molecules, ap-

TABLE 2. Percentage of Chloroplast and Mitochondrial DNA in Higher Plant Tissues

		Tissue							
		Green Leaves		Etiolated Leaves		Etiolated hypocotyl		Roots	
Probe DNA	Driver DNA	%Ct DNA	%Mt DNA	%Ct DNA	%Mt DNA	%Ct DNA	%Mt DNA	%Ct DNA	%Mt DNA
Mung Bean	Mung Bean	17.3	2.0	20.3	2.4	2.3	1.5	2.0	...
	Soy Bean	10.9	1.6	14.2	1.0	3.1	1.2	1.3	1.4
	Broad Bean	3.2	0.5	...	...	...	...	0.2	0.1
	Runner Bean	31.6	2.6	...	...	...	...	...	...
Corn	Corn	14.1	1.7	11.5	2.3	...	...	...	...
	Wheat	4.7	0.3	...	...	...	...	...	...
	Barley	7.3	0.6	...	...	...	...	...	...
	Oats	4.8	0.6	...	...	...	...	...	...
Spinach	Spinach	15.7	2.3	...	...	...	...	...	...
	Atriplex hortensis	12.4	1.1	...	...	...	...	...	...
	A. sabulosa	4.3	3.8	...	...	...	...	...	...
	A. fruticulosa	2.6	1.4	...	...	...	...	...	...
Tobacco	*Nicotinana tabacum*	5.0 ± 3.0	2.0 ± 1.0	green leaves 1.5–21 cm long					
	N. excelsior	5.0 ± 3.0	2.0 ± 1.0						

parently circular and differing in size, which have little or no sequence homology with each other.

We have also used the hydroxylapatite assay to measure the extent of sequence homology between chloroplast and mitochondrial DNA from spinach and the corresponding organelle genomes of five other higher plants. The highest chloroplast DNA homologies are found for *Atriplex sabulosa* (89%), a member of the same family as spinach, and tobacco (79%). Corn, mung bean, and pea all show about 60% homology with spinach chloroplast DNA. These homology values are higher than those obtained by Lamppa and Bendich (1977) in experiments with a pea chloroplast DNA probe. We believe the differences between the two sets of data probably reflect differences in the evolution of the spinach and pea chloroplast genomes. For example, they may reflect deletion events associated with the rearrangements leading to their quite different organization (Kolodner and Tewari, 1979). The mitochondrial genomes are significantly more diverged than the corresponding chloroplast genomes. We find only 27–45% homology between spinach mitochondrial DNA and that from mung bean, pea, corn, tobacco, and *Atriplex sabulosa*. Reciprocal cross-reaction experiments with labeled corn, mung bean, and tobacco chloroplast and mitochondrial DNAs confirm the generality of the conclusion that higher plant chloroplast DNA shows much more sequence conservation than does higher plant mitochondrial DNA.

To provide tools for high-resolution analysis of many aspects of chloroplast molecular biology, we have constructed complete clone banks of the mung bean, pea, and spinach chloroplast genomes. With a single exception, each of the chloroplast PstI restriction fragments has been cloned into plasmid pBR322. pBR322 derivatives containing the largest mung bean and spinach fragments (34 kb and 54 kb) are extremely unstable and rapidly delete parts of the inserted chloroplast sequence. However, it should be emphasized that the cloning of chloroplast DNA does not pose the more general deletion problems encountered in cloning plant nuclear DNA, and does not require the use of a rec A^- host strain to insure plasmid stability (see Cuellar *et al., Year Book 78,* 215–217). Clones containing mung bean and spinach XhoI fragments covering the 34-kb and 54-kb PstI regions have been identified by Grunstein colony hybridization of Xho I banks constructed in plasmid pACYC177. The only Pst I fragment that we have been unable to clone (after a search of several thousand recombinant colonies) is a pea chloroplast fragment of 12.5 kb. Perhaps expression of this fragment is lethal to *E. coli*; alternatively a specific sequence of the fragment may promote recombination within the pBR322 genome, which destroys plasmid-mediated resistance to tetracycline.

The chloroplast clones are being used in Southern blot experiments to probe for the presence of chloroplast DNA sequences in plant nuclear DNA. They will also be used as tools to map patterns of sequence homologies and sequence rearrangements in these and other higher plant chloroplast genomes, and will provide a basis for the construction of detailed transcriptional maps of chloroplast DNA.

References

Jope, C. A., A. Hirai, and S. G. Wildman, *J. Cell Biol., 79,* 631–636, 1978.

Kolodner, R., and K. K. Tewari, *Proc. Nat. Acad. Sci. U.S.A., 69,* 1830–1834, 1972.

Kolodner, R., and K. K. Tewari, *Proc. Nat., Acad. Sci. U.S.A., 76,* 41–45, 1979.

Lamppa, G. K., and A. J. Bendich, *Plant Physiol., 63,* 660–668, 1979.

Pring, D. R., C. S. Levings, and M. F. Conde, in *The Plant Genome,* 111–120, D. R. Davies and D. A. Heywood, eds., John Innes Charity, 1978.

Quetier, F., and F. Vedel, *Nature, 268,* 365–368, 1977.
Synenki, R. W., C. W. Levings III, and D. M. Shah, *Plant Physiol., 61,* 460–464, 1978.
Vedel, F., and F. Quetier, *Biochim. Biophys. Acta, 340,* 374–387, 1974.
Wells, R., and M. Birstiel, *Biochem. J., 112,* 777–786, 1969.

BLUE LIGHT STIMULATES A LOCAL ELECTRICAL CURRENT EFFLUX IN THE ALGA *Vaucheria sessilis*

*Michael R. Blatt and Manfred Weisenseel**

Stimulation of plant cells by light gives rise to a diversity of motive responses, many of which are accompanied by ionic fluxes, electrical currents, and changes in transmembrane electrical potentials (Jaffe and Nucitelli, 1977; Nultsch and Häder, 1979). The chronology of events leading to photomovement and the rapidity with which the concomitant electrical phenomena follow the initial light stimulus support the view that the early events of photosensory transduction take place at the plant cell membrane.

In the siphonaceous alga *Vaucheria sessilis,* light-induced organelle aggregation is accompanied by a destabilization of longitudinally oriented cytoplasmic fibers and the formation of a cortical fiber reticulum in the light (Blatt and Briggs, 1980). Cortical fiber reticulation precedes organelle aggregation, and shows a wavelength dependence similar to that of aggregation. The cortical fibers are composed, at least in part, of filamentous actin, a mechanical component in cytoplasmic streaming of the dark-adapted alga (Blatt *et al.,* 1980). These and other observations indicate that fiber reticulation is causally related to organelle aggregation in *Vaucheria.* Since in many cases actin filament stability is highly sensitive to small changes in pH and calcium concentration, local transmembrane ionic fluxes may in turn act to destabilize the longitudinally oriented fibers, disrupt normal cytoplasmic streaming, and eventually lead to organelle aggregation in the light.

Extracellular electrical current measurements were made using a vibrating reed electrode (Nucitelli and Jaffe, 1974). Dark-adapted filaments of *Vaucheria,* supported in a bathing medium containing 0.01 mM KCl, 0.1 mM NaCl, 0.01 mM $CaCl_2$, and 0.3 mM Tris, pH 7.5, were irradiated locally with light from a single, crown glass optical fiber (Blatt and Briggs, *Year Book 77,* 278–281) at a distance of 100 μm. Interference filters (DAL series 454, 473, 543, 579, and 668; Schott, Mainz), in conjunction with glass cutoff filters (Schott), were used to select discrete wavelengths of light for actinic irradiation. Broadband blue light was filtered with a Schott Blue Glass filter (BG 12, 4 mm). The actinic beam was attenuated with neutral density filters (Schott). Fluence rate calibrations were performed as described previously (Blatt and Briggs, 1980). Light from the microscope lamp filtered with an AL554 (Schott) interference filter and a KG1 (Schott) heat filter provided safe background lighting during manipulation of the electrode.

Current measurements were made by comparing the field strength registered with the electrode, or probe, in a "site" position to that measured at a reference position far removed from any electrical sources or sinks. A typical electrical current recording from *Vaucheria* and schematic repre-

*Botanisches Institut, Erlangen, 8520 Erlangen, West Germany.

sentations of the arrangement of alga, the optical fiber used for point irradiation, and probe are shown in Fig. 1. The reference position was 500 μm distant both from the algal filament and the optical fiber. In the "site" position the probe was located with its center of vibration 40 μm from the cell surface. The probe vibrated perpendicular to the central axis of the cell (as shown) in the plane described by the central axes of the cell and optical fiber.

As shown in Fig. 1, point irradiation with blue light gives rise to a current efflux relative to the "dark" current level as measured at the "site" position. Although not always the case, in the current recording shown an absolute current efflux was measured. Invariably, when the light is turned off the current decays rapidly to preirradiation levels with a half-time of 1–3 minutes.

As in the case for aggregation, wavelengths of light longer than 530 nm were found to be ineffective in eliciting an electrical response. For blue light, both the net current efflux above the dark current level, $I_{hv,net}$

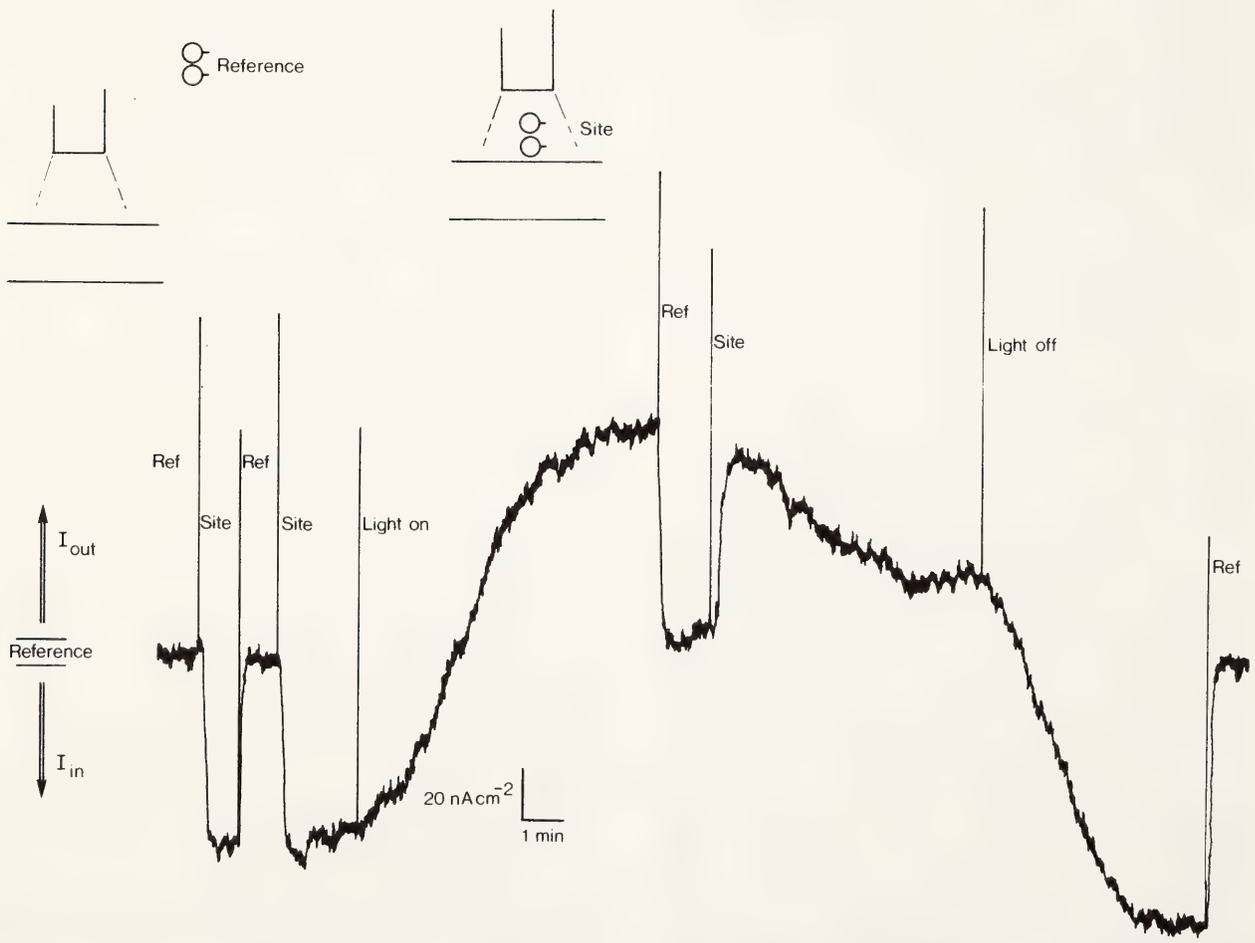


Fig. 1. A typical current recording from a single filament of *Vaucheria sessilis*. Schematic representations of the orientation of the alga, optical fiber used for irradiation, and probe in reference and "site" positions are shown above. A length of the algal filament is pictured horizontally with the optical fiber irradiating the alga from above. The probe is depicted as a "blurred" double image, much as it appears under the microscope, indicating the axis of vibration. In the recording, vertical lines mark the points in time when the probe was moved from reference to "site" position or vice versa, and when the actinic light was turned on or off. These event markers are labeled accordingly. A pen position below the reference level corresponds to an influx of current into the cell, while a current record in "site" position above that of reference indicates a current efflux. Light at 473 nm was used to stimulate the response. The fluence rate at the alga was 10 W m^{-2}.

and the current rise velocity, dI_{hv}/dt, were proportional to the logarithm of the actinic fluence rate. In Fig. 1 the light-induced current efflux begins to rise within 5 seconds of the onset of irradiation (473 nm). At this wavelength and fluence rate, organelle aggregation begins after a lag of 15–20 sec (Blatt and Briggs, 1980). Similar results were obtained at other fluence rates and with 454 nm or broadband blue light.

Both organelle aggregation and cortical fiber reticulation are strictly limited to the irradiated region of the algal filament (Blatt and Briggs, 1980). The electrical current profiles of algae point-irradiated with 473 nm light indicate that the blue-light-induced current efflux from *Vaucheria* is also localized in the light. Absolute current effluxes were measured in a raster pattern at points along each alga once the light-induced current reached its peak value. Measurements were performed with the probe vibrating both perpendicular to and parallel to the major cell axis. The results of each experiment were used to create a current vector diagram, such as is shown in Fig. 2. Fig. 3 is an idealized summary of six such experiments.

These observations point to a similarity between aggregation and reticulation on the one hand, and light-induced current efflux on the other. All three photoresponses are limited to the irradiated region of the alga and are first observed after short lag periods. A temporal ordering of the photoresponses, based on their order of appearance, is consistent with the hypothesis that a light-induced ionic flux results in reticulation, which in turn leads to aggregation (see also Blatt and Briggs, 1980). Finally, all three photoresponses exhibit comparable light-dependent properties. Investigations are now in progress to identify the ionic species responsible for this current efflux and its bearing on organelle aggregation in *Vaucheria*.

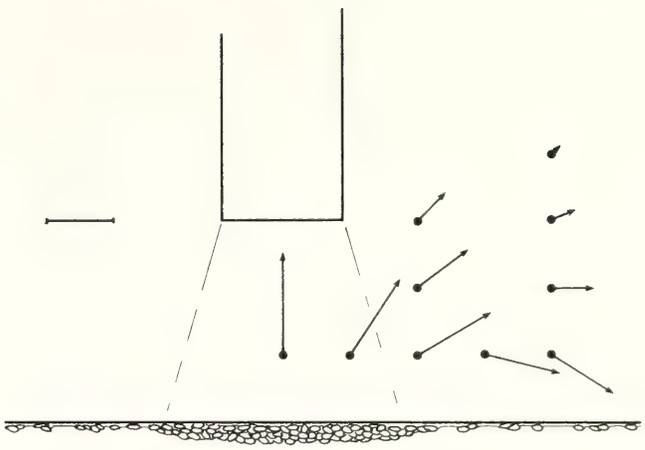


Fig. 2. A current vector diagram used in mapping the current profile of the light-induced current efflux from *Vaucheria*. The alga and optical fiber are positioned as depicted in Fig. 1. Filled circles (●) mark the sites where the probe was positioned, both perpendicular and parallel to the cell major axis, for current measurements. Vectors at each point indicate the magnitude and direction of the current recorded at that position. Light at 473 nm with a fluence rate of 10 W m^{-2} at the alga was used to stimulate the photoresponse. Scale: 33 μm or 100 nA cm^{-2}.

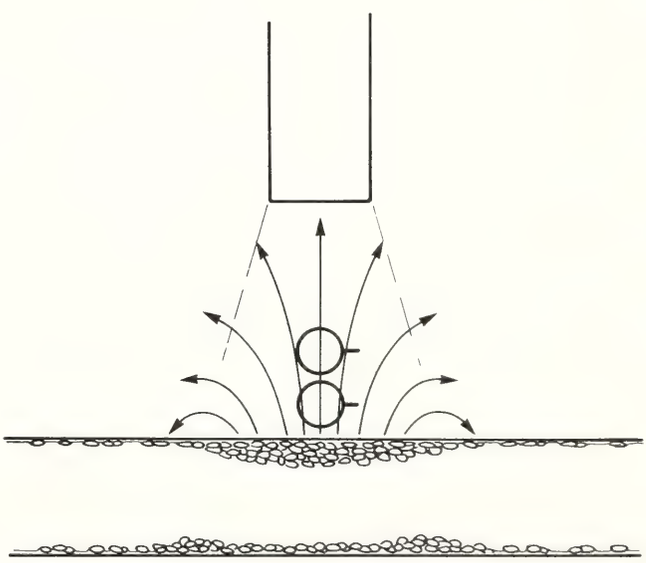


Fig. 3. A schematic summary of the current efflux from a *Vaucheria* filament under blue light irradiation from an optical fiber. Alga, probe, and optical fiber are depicted as in Fig. 1. The arrows reflect the flow of current during point irradiation.

References

Blatt, M., and W. Briggs, *Planta, 147,* 355–362, 1980.

Blatt, M., N. Wessells, and W. Briggs, *Planta, 147,* 363–375, 1980.

Jaffe, L., and R. Nucitelli, *Annu. Rev. Biophys. Bioenerg., 6,* 445–476, 1977.

Nucitelli, R., and L. Jaffe, *J. Cell Biol., 63,* 614–628, 1974.

Nultsch, W., and D.-P. Häder, *Photochem. and Photobiol., 29,* 423–437, 1979.

INFLUENCE OF LIGHT ON GROWTH OF ETIOLATED OAT SEEDLINGS

Dina F. Mandoli and Winslow R. Briggs

Etiolated oat (*Avena sativa* L.) seedlings react to light by increasing the growth rate of the coleoptile and decreasing that of the mesocotyl (Beyer, 1927). In both tissues the overall reaction is triphasic; the first two responses, to low irradiance, are dependent on the fluence alone, and the last, to high irradiance, depends on both fluence and the duration of the light exposure (Blaauw *et al.,* 1968). Vanderhoef *et al.* (1979) have shown that corn mesocotyls also display at least two of these responses (see *Year Book 78,* 140–144). This report deals only with the two low-irradiance responses of oat.

In the past, photomorphogenesis of etiolated *Avena* seedlings has been studied predominantly in the mesocotyls. Few experiments for the coleoptile have been reported because the variables affecting its growth and responses to light were previously unknown (e.g., Mer, 1953). Unfortunately, most of the work reported in the literature must be completely reevaluated or in many cases discarded, since it has been shown that *Avena* is sensitive to all known "safe" lights (Blaauw *et al.,* 1968; *Year Book 78,* 140–144). Uncontrolled "safe" light conditions have been shown to be the major variable in most previous reports (*Year Book 78,* 140–144). The experiments summarized here describe some aspects of the photobiological processes that regulate morphogenesis in oats.

Large numbers of uniform seedlings (40–50) were obtained using the protocol reported last year (*Year Book 78,* 140–144). Computerized measurements of mean organ length yielded standard errors between 1.5 and 3.5%. Irradiation from above for each group of seedlings has been automated with a custom-built, multiple-gate timing system equipped with a "programmable" laser-type shutter. Fluence rates were varied with neutral density filters (Bausch and Lomb) and calibrated scattering agents (e.g., opal glass). Fluence rates were measured either with a Licor quantum flux radiometer or with an Eppley eight-junction thermopile in conjunction with a Keithley 150B microvoltmeter that had been previously calibrated against a standard lamp (National Bureau of Standards). All fluences too low to measure with either instrument were calculated from the lamp output, distance from the source, duration of exposure, and density of the filters and scattering agents used. An incandescent source (300 W) in conjunction with two heat filters and either Rohm and Haas red (2444) or far-red (RFR) plexiglas provided broadband red and far-red light. When far-red light fluences greater than 300 nmol cm^{-2} were required, a similar source with a 650-W bulb was used (Quail and Briggs, 1978). Gold fluorescent bulbs with one layer each of Rohm and Haas green (2092) and blue (2424) plexiglas provided green light (Schiff, 1972).

The first response (R1) of seedlings to light (both coleoptile stimulation and mesocotyl inhibition) resulted in roughly 50% of the overall low irradiance reaction (Fig. 4). Note that both mesocotyl and coleoptile responses were described by one curve (Fig. 4). Response 1 had a threshold at 10^{-14} mol cm^{-2} and became saturated at 3.0×10^{-12} mol cm^{-2} of red light (Table 3). Reciprocity for R1 was valid from 1 to 600 s; the same dose given over a longer period of time resulted in a greater response of both the coleoptile and the mesocotyl. Response 1 was not far-red reversible (see Blaauw *et al.*, 1968; Blaauw and Blaauw-Jansen, 1975).

The second response (R2), again in both coleoptiles and mesocotyls, resulted in completion of (100%) the low-irradiance responses (Fig. 4). Response 2 had a threshold at 10^{-10} mol cm^{-2} and became saturated with 3.0×10^{-7} mol cm^{-2} of red light (Table 3). This response was reversible by far-red light and showed reciprocity failure only when the fluence was delivered over a period of time longer than 10^4 s.

TABLE 3. Low-Irradiance Photoresponses* of Etiolated *Avena* Seedlings

	Response 1	Response 2
Percentage Response	55%	100%
Threshold (mol cm^{-2})	10^{-14}	10^{-10}
Saturation (mol cm^{-2})	3.0×10^{-12}	3.0×10^{-7}
Reciprocity Validity	1-600 s	1-10,000 s
R/FR Reversibility	No	Yes
Percentage Pfr Required:		
Threshold	0.01%	2.24%
Saturation	0.37%	87.10%

*Coleoptile stimulation and mesocotyl inhibition in etiolated *Avena sativa* (cv. Lodi) seedlings.

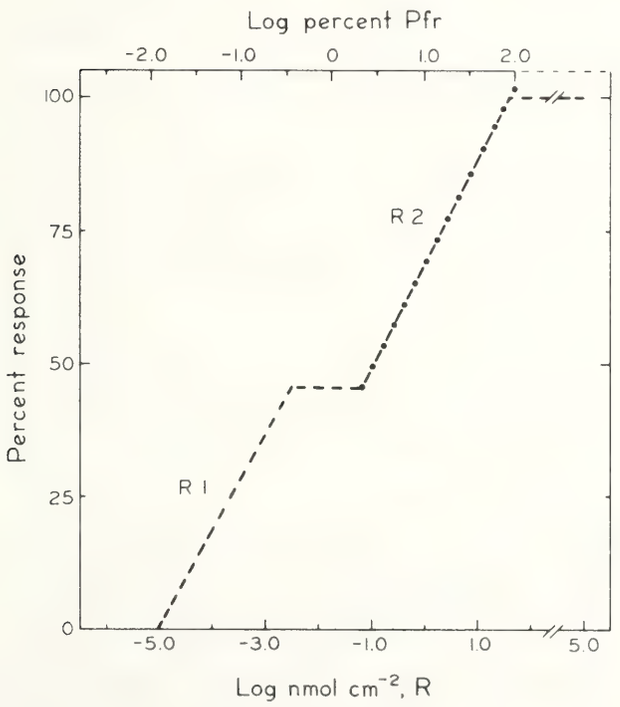


Fig. 4. Regression lines for mesocotyl and coleoptile responses R1 and R2, red light (- - -) normalized to the percentage of the total response obtained. One line describes both curves. The linear regression ($r^2 = 0.97$) for mesocotyl data from Loercher (1966) and for coleoptile data from Hopkins and Hillman (1965), which compare percentage response (R2) with the percentage of photoconvertible Pfr, have also been reproduced here (. . .). We have assumed that threshold and saturation for percentage R2 in their experiments and ours are the same.

Mesocotyl and coleoptile dose-response curves for green and far-red light had the same shape as those for red light, indicating that the same photoreceptor was involved in the responses seen at all three wavelengths. Threshold and saturation occurred with doses of green light 10-fold and of far-red 1000-fold higher than those needed with red light. These values are predictable on the basis of the photoefficiency of phytochrome conversion (Pratt and Briggs, 1966). This result and the fact that R2 is red/far-red reversible leads us to conclude that phytochrome is the photoreceptor for these responses.

Loercher (1966) has measured the photostationary state of phytochrome in *Avena* and correlated the percentage Pfr with the in vivo mesocotyl response. Hopkins and Hillman (1965) have performed similar measurements on excised *Avena* coleoptiles. When percentage responses from both

groups are plotted as a function of the log percent photoconvertible Pfr, the data fall on a single straight line ($y = 34.87x + 34.04$, $r^2 = 0.97$). Threshold and saturation values for their responses have been normalized to those obtained in our experiments and replotted with the regression lines for both our mesocotyl and coleoptile data (Fig. 4). From this figure we can obtain values of the percentage Pfr required for threshold and saturation of R1 and R2 (Table 3). The estimates of the percentage Pfr required to elicit R1 assume that we are dealing with a single molecular species of phytochrome.

To summarize, reproducible light-induced coleoptile stimulation and mesocotyl suppression in etiolated *Avena sativa* have been obtained. The magnitude of the responses described here are 2–3 times greater than those published elsewhere, largely because green "safe" lights have not been used. Both of the responses summarized in this report are compatible with the action of the photomorphogenic pigment phytochrome. The first response is induced by 0.01% Pfr and saturated with about 0.37% of the phytochrome in the Pfr form. The first response is 10,000 times less sensitive to red light than is R1 but is still induced by little more than 2.0% Pfr (Fig. 4; Table 3).

Further work on this system will attempt to localize the major sites of photoreception and relate the observed phytochrome-mediated changes in growth rate to changes in rates of cell division and cell elongation.

References

Beyer, A., *Ber. Deut. Bot. Ges., 45,* 179–187, 1927.

Blaauw, O. H., G. Blaauw-Jansen, and W. J. van Leeuwen, *Planta, 82,* 87–104, 1968.

Blaauw, O. H., and G. Blaauw-Jansen, *Z. Pflanzenphysiol., 76,* 333–338, 1975.

Hopkins, G. W., and W. S. Hillman, *Planta, 65,* 157–166, 1965.

Loercher, L., *Plant Physiol., 11,* 932–936, 1966.

Mer, C. L., *Ann. Bot., 17,* 569–578, 1953.

Pratt, L., and W. R. Briggs, *Plant Physiol., 41,* 467–474, 1966.

Quail, P. H., and W. R. Briggs, *Plant Physiol., 62,* 773–778, 1978.

Schiff, J. A., in *Methods in Enzymol., 24* (B), 321–322, A. San Pietro, ed., Academic Press, N.Y., 1972.

Vanderhoef, L., P. H. Quail, and W. R. Briggs, *Plant Physiol., 63,* 1062–1067, 1979.

REVERSE RECIPROCITY FAILURE OF PHYTOCHROME-MEDIATED RESPONSES IN LIGHT-GROWN CORN

Holly L. Gorton and Winslow R. Briggs

We have described several red (R) reversible responses of white-light-grown corn seedlings to end-of-day far-red (FR) irradiations (*Year Book 78*, 134–137; 1980). These include stimulation of coleoptile and mesocotyl elongation and inhibition of anthocyanin accumulation in the coleoptile. Here we report that these responses do not obey the Bunson-Roscoe reciprocity law. The failure occurs over a range of seconds and in the opposite direction from that normally observed in etiolated plants where long dim irradiations are more effective than shorter ones of the same total energy. We have termed our observation "reverse reciprocity failure" to emphasize this difference.

Growth and irradiation conditions have been described elsewhere (Gorton and Briggs, 1980). The reciprocity law was tested for FR "induction" and R "reversal" of the three responses by varying duration and intensity of end-of-day irradiations inversely, always maintaining the same subsaturating total dose. Intensity was varied by changing the distance between the lights and the plants and also by using large neutral-density filters made from

several layers of Whatmann chromatography paper.

Both induction of the three responses by end-of-day FR and reversal by subsequent R showed dramatic reverse reciprocity failure. Although only the anthocyanin data is shown here (Figs. 5,6), the mesocotyl and coleoptile elongation responses showed the same type of reciprocity failure over the same time period. In all cases, short intense irradiations were more effective than long, dim ones. Reciprocity failure was very rapid; 25-s FR irradiations were significantly more effective than 100-s irradiations of the same total energy. Similarly, 8-s R irradiations were more effective than 30-s irradiations. Raven and Shropshire (1975) have observed reverse reciprocity failure for chlorophyll formation in pea seedlings "de-etiolated" by a saturating dose of R, but only for irradiations longer than about 15 min.

This rapid, reverse reciprocity failure is difficult to explain on the basis of standard phytochrome dogma. The FR-reciprocity failure cannot be caused by a high-irradiance response taking over at long irradiation times, in contrast, for example, to a response in mustard (Lange *et al.*, 1971; Mohr *et al.*, 1971). An FR high-irradiance response should act in the same direction

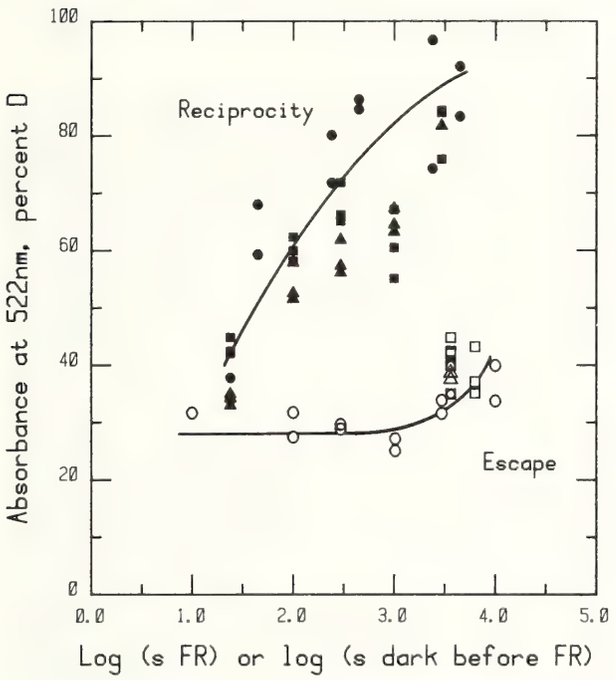


Fig. 5. Reciprocity (closed symbols) and escape (open symbols) tests for the anthocyanin response to end-of-day FR irradiations. For the reciprocity test, the duration of FR irradiations was varied from 25 s to 75 min. The same total dose (160 nmol cm^{-2}) was maintained by changing intensity. To check for escape from FR reversibility, dark periods of different lengths were given between the end of the white light period and the beginning of the maximally effective FR dose shown on the reciprocity curve (25 s). Again, all points represent plants receiving light treatments of the same total energy (160 nmol cm^{-2}). Different symbols represent different experiments; replicate measurements are shown at each time point for each experiment. Data are plotted as percentage of a dark control (D) which received no end-of-day irradiation. Anthocyanin assay methods have been described elsewhere (Gorton and Briggs, 1980).

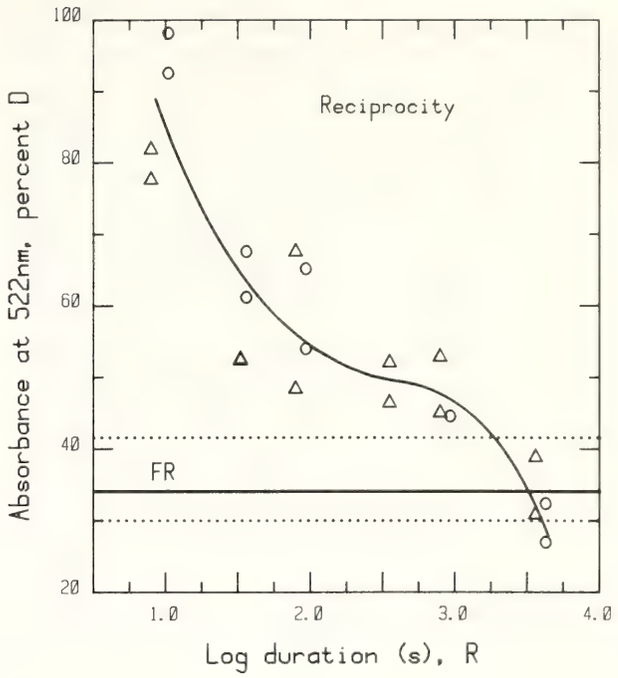


Fig. 6. Reciprocity test for R reversal of the decrease in anthocyanin content of coleoptiles by end-of-day FR. R irradiations (8 s to 70 min) of the same total energy (10 nmol cm^{-2}) were given immediately after a FR dose of 250 nmol cm^{-2} given over 46 s. Data for replicate samples from each of two experiments are plotted as percentage of the dark control. The amount of anthocyanin present in coleoptiles from plants exposed to end-of-day FR alone is indicated by the solid horizontal line (FR). The range of values from the two experiments is represented by the dotted lines.

as the R seen during the white light period, causing *increased* anthocyanin synthesis. However, we have shown previously that the effectiveness of end-of-day FR irradiations at *reducing* anthocyanin synthesis improves with longer irradiation times, if the intensity is held constant (Gorton and Briggs, 1980).

We thought it possible that the reciprocity failure might be caused by "escape from reversibility." For instance, in the case of the FR failure, it might be necessary to administer the FR dose within a certain time period after the end of the daily white light period. Similarly, the R might be necessary soon after the FR dose to be effective at reversing it. These possibilities were tested by examining the effect of dark periods of varied duration given either between the end of the 8-h white light period and the effective (25 s, intense) FR dose (Fig. 6), or between an effective FR dose given immediately after the white light and the effective (8 s, intense) R dose (Fig. 7). FR-reciprocity failure cannot be explained by escape, because a short intense irradiation given after 1 h of darkness is just as effective at reducing the anthocyanin levels as it is if given immediately after the end of the white light period (Fig. 5). Also, although there is about 50% escape from R reversibility over the course of an hour (Fig. 7), escape cannot fully explain the 100% R-reciprocity failure during this time (Fig. 6). The mesocotyl and coleoptile elongation responses were similar to the anthocyanin response in this regard (data not shown).

Another possible cause of the reciprocity failure might be differences in photoconversion or in the total amount of phytochrome (Ptot) under the different illumination conditions. Several experiments indicate that this possibility is unlikely. First, we have measured Pfr/Ptot and Ptot spectrophotometrically in 1-cm tips (coleoptile plus primary leaf) of four-day etiolated corn

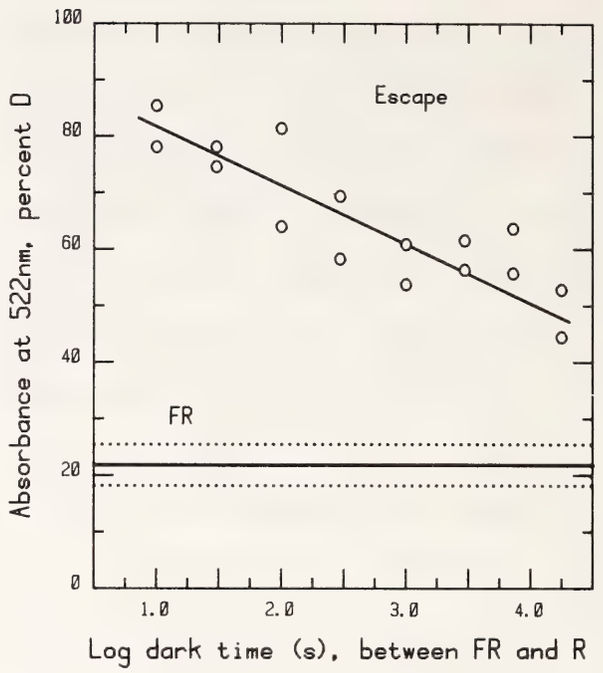


Fig. 7. Test for escape from reversibility of the effects of end-of-day FR on the anthocyanin content of coleoptiles by R. Experimental design was the same as for Fig. 6 except plants were left in the dark for varying amounts of time between FR and R. The R dose was 10 nmol cm^{-2} delivered over 8 s. Data for plants which received end-of-day FR alone is expressed as in Fig. 6.

seedlings. There were no differences in the extent of photoconversion or in Ptot after exposure to the extreme FR-reciprocity doses (25 s at 6.6 nmol cm^{-2} s^{-1} and 1 h at 4.4 $\times$ 10^{-2} nmol cm^{-2} s^{-1}). Thus far we have been unable to make these measurements reliably on light-grown corn treated with the chlorosis-inducing herbicide Sandoz 9789 because of the extremely small amount of phytochrome present.

If there is no difference in photoconversion or Ptot after the different reciprocity doses and if Pfr is the controlling factor in these responses, we must postulate that a long, low-intensity FR exposure in some way causes increased sensitivity to Pfr relative to a short intense irradiation of the same total energy. Similarly, a long dim R exposure would have to cause decreased sensitivity to Pfr. This possibility has been tested for FR by giving two irra-

diations of the same total energy but different duration sequentially, and seeing if the effectiveness of the combination is altered by the order in which the irradiations are given. Results to date show no effect of changing the order of irradiation. A changing sensitivity to Pfr is therefore unlikely.

The reciprocity failure indicates that the reactions are strongly intensity dependent. The rate of pigment cycling may play an important role.

References

Gorton, H. L., and W. R. Briggs, *Plant Physiol.*, in press, 1980.

Lange, H., W. Shropshire, and H. Mohr, *Plant Physiol.*, *47*, 649–655, 1971.

Mohr, H., I. Bienger, and H. Lange, *Nature*, *230*, 56–58, 1971.

Raven, C. W., and W. Shropshire, *Photochem. and Photobiol.*, *21*, 423–429, 1975.

PARTIAL PURIFICATION AND CHARACTERIZATION OF A BLUE-LIGHT-SENSITIVE CYTOCHROME-FLAVIN COMPLEX FROM CORN MEMBRANES

Ta-Yan Leong and Winslow R. Briggs

Blue light causes reduction of a *b*-type cytochrome present in a particulate fraction obtained by differential centrifugation of homogenates of corn coleoptile and *Neurospora* mycelium (Brain *et al.*, 1977). The reaction presumably involves a flavin moiety which when excited by blue light reduces specifically the *b*-type cytochrome. Given the optimized conditions to obtain stable and reproducible reduction in corn coleoptile preparations (Goldsmith *et al.*, 1980), we have worked out a procedure to purify the membrane fraction and characterize the photoreaction.

The extent of blue-light-inducible reduction of *b*-cytochrome in the 21,000 × *g* pellet (21KP) is related to the intensity of blue light. The reciprocal of the absorbance change when plotted against the reciprocal of the light intensity yields a straight line, and the intercept gives the maximum possible reduction of the *b*-type cytochrome. Irrespective of the endogenous photoreceptor, or exogenously added riboflavin and methylene blue as photosensitizers, the double-reciprocal plots all intercept the *Y*-axis at the same point (Leong *et al.*, this Report), suggesting that the same *b*-type cytochrome is being specifically reduced.

Taking advantage of the fact that sucrose and Renografin have different properties with regard to density, osmotic behavior, and viscosity, we could purify the 21KP first on sucrose gradients (25–45% w/w) to separate endoplasmic reticulum from the blue-light-sensitive cytochrome-flavin complex; the complex could then be separated from mitochondria and other contaminants on Renografin, as was the case with metrizamide gradients (see Hertel *et al.*, 1980).

Assays for enzyme markers have shown that the blue-light-sensitive cytochrome-flavin complex is virtually free from endoplasmic recticulum (NADH-cytochrome *c* reductase), golgi particles (glucan synthetase I), and mitochondria (cytochrome *c* oxidase) as shown in Fig. 8. Furthermore, in the Renografin gradient, the blue-light-sensitive cytochrome-flavin complex is shown to coincide with the peak of glucan synthetase II activity (Fig. 9), which is suggested to be a marker for plasma membrane in higher plants (Ray, 1977; see Quail, 1979, for evaluation of membrane markers). In *Neurospora*, the blue-light-sensitive cytochrome-flavin complex has been indicated to be associated with plasma membrane (Brain *et al.*, 1977). It seems

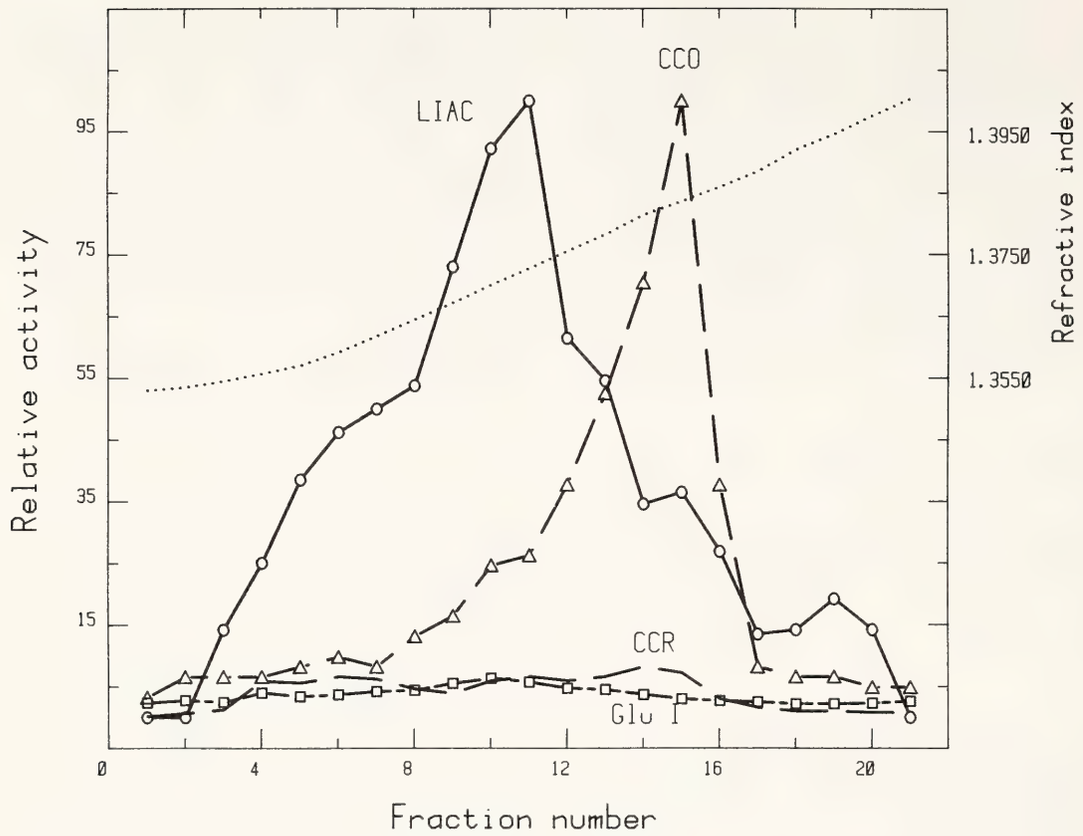


Fig. 8. Purification of the blue-light-sensitive flavin-cytochrome complex. The resuspended 21KP was layered on a sucrose gradient (25–45%, w/w) and centrifuged at 75,000 × *g* for 16 h. Fractions corresponding to densities from 1.3937 to 1.4071 were pooled, pelleted, resuspended, and applied onto a Renografin gradient (15–61% Renografin-76, v/v) and centrifuged at 75,000 × *g* for 60 min. Fractions (1.7 ml) were collected and assayed for activities: CCO: cyt. *c* oxidase; CCR: cyt. *c* reductase; LIAC: light-induced absorbance change; Glu I: Glucan synthetase I. For glucan synthetase, assay fractions were repelleted and resuspended in buffer free of Renografin.

plausible that the blue-light-sensitive cytochrome-flavin complex is probably associated with plasma membrane in corn coleoptiles as well.

Light-minus-dark and dithionite reduced-minus-oxidized difference spectra of "plasma membrane," purified on sucrose and then Renografin gradients, have been recorded from 400 to 500 nm and from 500 to 600 nm and compared. In crude 21KP preparations, it has been reported that the blue light-minus-dark difference spectra obtained either with endogenous photoreceptor, exogenously added riboflavin, or methylene blue as photosensitizers, are different from dithionite reduced-minus-oxidized difference spectra (Britz *et al.*, 1979, Goldsmith *et al.*, 1980). Indications are that dithionite reduces all the cytochrome present, whereas blue light would reduce specifically one *b*-type cytochrome among all the cytochromes present.

In the present study, the blue light-minus-dark and dithionite reduced-minus-oxidized spectra are shown to have difference bands with identical peak wavelength (Fig. 10), 427 nm for the Soret band and 557 nm for the alpha band (Fig. 11). This result indicates that the blue-light-sensitive cytochrome is the only cytochrome present in significant amount in the purified membrane fraction. Furthermore, it supports conclusions from the enzyme marker assays that the purified "plasma membrane" is not contaminated by other cytochrome-containing particulates, since cytochromes from other or-

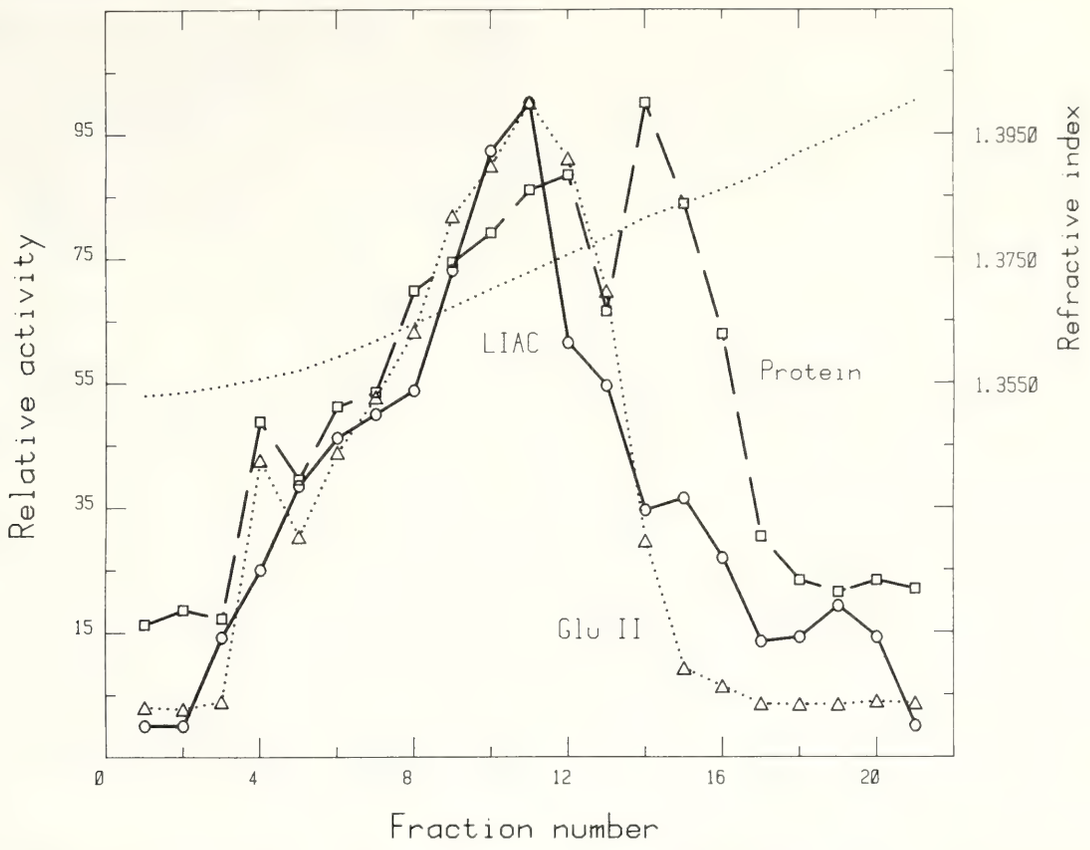


Fig. 9. From same gradient as Fig. 8. Glu II: glucan synthetase II; LIAC: light-induced absorbance change.

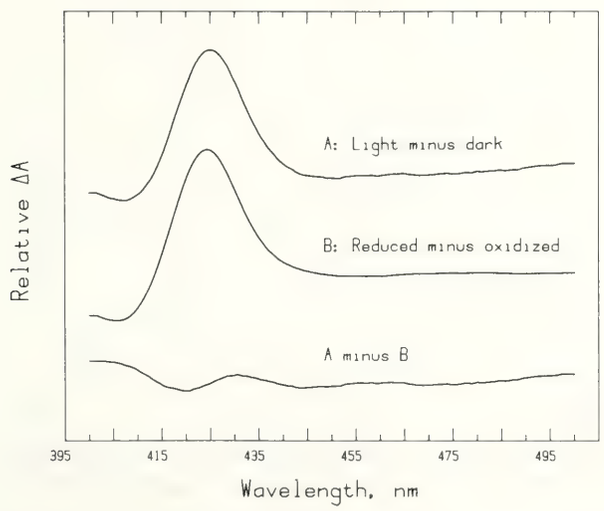


Fig. 10. Comparison of difference spectra between 400 and 500 nm induced in the Renografin gradient-purified "plasma membrane" from corn coleoptile by actinic light or by dithionite. The sample contained 2.8 mg/ml protein, 20 mM EDTA, 1 mg/ml β-D-glucose, 1 mM KCN and 1 mg/ml glucose oxidase. Ten difference spectra were averaged for the light-minus-dark spectrum. A saturating amount of dithionite was then added to one cuvette, and ten difference spectra were recorded and averaged.

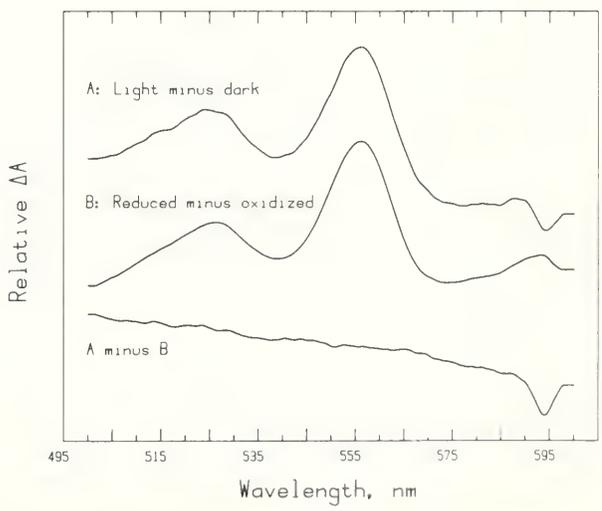


Fig. 11. Same as Fig. 10, but between 500 and 600 nm.

ganelles are not detected in the difference spectra.

Isolation and further purification of the blue light photoreceptor from this "plasma membrane" fraction is in progress.

References

Brain, R. D., J. A. Freeberg, C. V. Weiss, and W. R. Briggs, *Plant Physiol., 59*, 948-957, 1977.

Britz, S. J., E. Schrott, S. Widell, and W. R. Briggs, *Photochem. and Photobiol., 29*, 359-365, 1979.

Goldsmith, M. H. M., R. J. Caubergs, and W. R. Briggs, *Plant Physiol.*, in press, 1980.

Hertel, R., A. J. Jesaitis, U. Dohrmann, and W. R. Briggs, *Planta, 147*, 312-319, 1980.

Quail, P., *Annu. Rev. Plant Physiol., 30*, 425-484, 1979.

Ray, P. M., *Plant Physiol., 59*, 594-599, 1977.

SOLUBILIZATION OF A PHOTOACTIVE, MEMBRANE-ASSOCIATED FLAVIN-CYTOCHROME COMPLEX FROM CORN

Ta-Yan Leong, Roland J. Caubergs, and Winslow R. Briggs

This laboratory has previously reported the existence of a blue-light-sensitive cytochrome-flavin complex in both *Neurospora* mycelium and corn coleoptiles (Brain *et al.*, 1977). Although the nature of the photoreceptor for this photoreaction is still unknown, studies with inhibitors have indicated that a flavin is involved in the photoreduction of the *b*-type cytochrome (Caubergs *et al.*, *Year Book 77*, 356-357). This assumption has been supported by experiments using exogenously added flavin as a photosensitizer, showing that exogenously added flavins would enhance the photoreduction (Goldsmith *et al.*, *Year Book 78*, 118-121).

Subsequent efforts from this laboratory have optimized conditions for stable and reproducible photoreactions in membrane fractions prepared from higher plants (Goldsmith *et al.*, 1980), and it becomes possible to do kinetic studies even with a crude particulate fraction.

The 21,000 × *g* pellet (21KP) was obtained after differential centrifugation of corn coleoptile homogenate obtained as described elsewhere (Goldsmith *et al.*, 1980) and collected through a 32% sucrose cushion. The amount of blue-light-inducible change in absorbance at 428 nm with respect to absorbance at 410 nm, $\Delta(A_{428} - A_{410})$, was recorded at different light intensities. When the reciprocal of $\Delta(A_{428} - A_{410})$ is plotted against the reciprocal of light intensity, a straight line is obtained, with an intercept on the *Y*-axis (Fig. 12), indicating the maximum possible amount of absorbance change at light saturation, designated ΔA_{max}.

Triton X-100 was able to solubilize the flavin-cytochrome complex with-

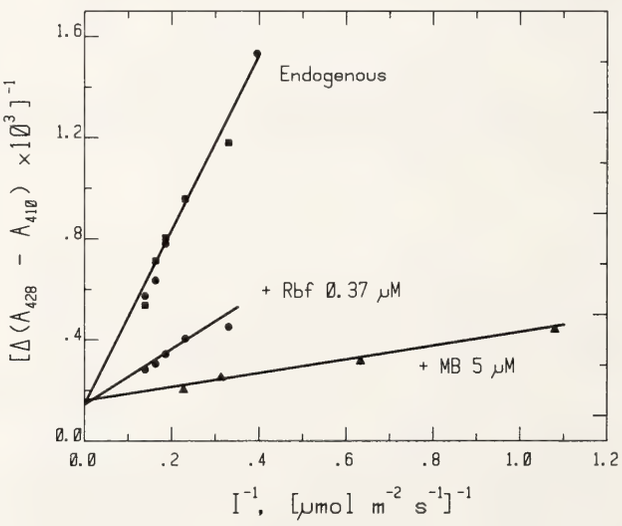


Fig. 12. Double-reciprocal plot of blue-light-induced absorbance change as a function of light intensity for the endogenous membrane-bound photoreceptor and exogenously added riboflavin (Rbf) and methylene blue (MB) as photosensitizers. To 500 μl of resuspended 21KP (3.8 mg protein), EDTA, glucose, KCN, and glucose oxidase were added (Goldsmith *et al.*, 1980). The mixture was irradiated with 2-min pulses of different light intensities to give the curve for endogenous photoreceptor. Riboflavin (0.37 μM) or methylene blue (5 μM) were added and the mixture irradiated to give the double-reciprocal plots.

out significantly altering the photoactivity. A concentration of 0.1% Triton X-100 was sufficient to extract the flavin-cytochrome complex. Double-reciprocal plots of $\Delta(A_{428} - A_{410})$ against light intensity for even a 1% Triton X-100 extract gives a very similar straight line, shown in Fig. 13. The ΔA_{max} obtained with the 1% Triton X-100 solution is identical to that obtained with the endogenous photoreceptor, suggesting that Triton X-100 has solubilized the flavin-cytochrome complex but has not altered the kinetics to any significant extent. This result also suggests that the flavin and cytochrome moieties may be on the same protein, as is the case for cytochrome b_2 from yeast (Lemberg and Barrett, 1973). The flavin must be tightly bound to this protein, as it has survived the Triton X-100 treatment without loss of photosensitizing capacity.

Dr. Richard D. Vierstra, of Michigan State University, did extensive spectral studies on our Triton-solubilized fraction. The light-minus-dark spectrum for the cytochrome-flavin complex at liquid nitrogen temperature is shown in Fig. 14. Lack of alpha bands other than the single sharp peak near 555 nm indicates the absence either of mitochondrial cytochromes or of cytochrome b_5 from the endoplasmic reticulum.

Since the low concentration (0.1%) of Triton X-100 has totally solubilized the flavin-cytochrome complex together with only a small portion of the membrane, this solubilization represents an advance in our efforts to purify the photoreceptor.

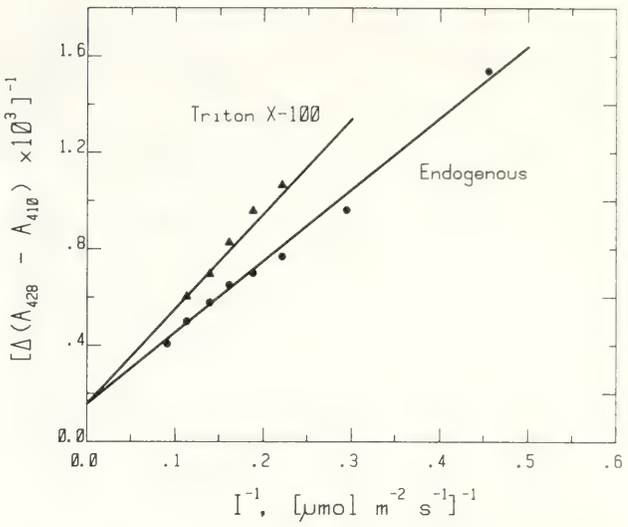


Fig. 13. Double-reciprocal plot of blue-light-induced absorbance change, as a function of light intensity for the endogenous membrane-bound photoreceptor and a 1% Triton X-100 extract. The endogenous curve was obtained as in Fig. 12. Triton X-100 was added to a final concentration of 1% and the mixture centrifuged to give a clear supernatant, which was used to give the double-reciprocal plot for the Triton X-100 extract.

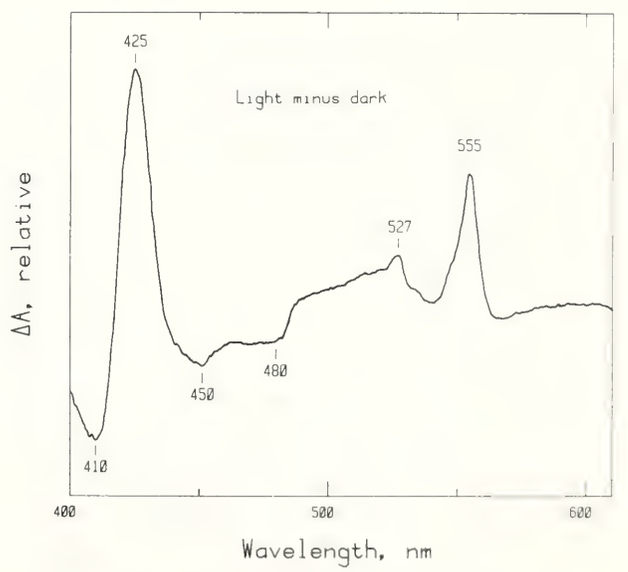


Fig. 14. Light-minus-dark difference spectrum of Triton-solubilized photoactivity from Renografin-purified photosensitive membrane fraction from corn. Alpha-band difference peak at 555 nm actually 0.03 OD in height. Under the conditions used to obtain photoreduction, about 25% of the cytochrome became photoreduced. Sample at liquid nitrogen temperature.

References

Brain, R. D., J. A. Freeberg, C. V. Weiss, and W. R. Briggs, *Plant Physiol.*, *59*, 948–952, 1977.

Goldsmith, M. H. M., R. J. Caubergs, and W. R. Briggs, *Plant Physiol.*, in press, 1980.

Lemberg, R., and J. Barrett, *Cytochromes*, 1–580, Academic Press, London, 1973.

THE EFFECT OF σ-AMINOLEVULINIC ACID ON RED-LIGHT-INDUCED LEAF UNROLLING

Christer Sundqvist and Winslow R. Briggs

Leaf unrolling has been found to be a phytochrome-controlled reaction (Virgin, 1962). The unrolling is a result of an increased cell expansion of the inner mesophyll layer (Burström, 1942). The red light irradiation triggers a short-lived increase in the amount of gibberellic acid (GA). Short pulses (2 h) of exogenously supplied GA can also stimulate the unrolling in absence of light (Loveys and Wareing, 1971). Inhibitors of RNA and protein synthesis prevent both light- and GA-induced unrolling, indicating a need for macromolecular biosynthesis. During a study of the effect of σ-aminolevulinic acid (ALA) on porphyrin biosynthesis, it was found that this substance influenced the leaf unrolling process. In this report, the effect of ALA is compared with the effect of hormones and other keto acids and amino acids on leaf unrolling.

Barley seedlings (*Hordeum vulgar* L. cv Klages) were grown at 28 °C in darkness for six days in closed plastic containers on a layer of Kimpack moistened with tap water. Leaf sections 2 cm long, cut 1 cm from the tip of the first leaf, were used in all unrolling experiments. For the coleoptile section, growth test coleoptile sections 7.4 mm long were cut 3 mm below the tip of three-day-old barley seedlings.

The leaf or coleoptile sections were floated on different solutions in small (5-cm) plastic Petri dishes. During the incubation time, the pH of the solution was kept at 6.5 with 0.035 M phosphate buffer. The red and far-red light sources have been described earlier (Gorton and Briggs, *Year Book 78*, 134–137). The light intensity at the level of the leaves was 1.2 nM cm^{-2} s^{-1} red light and 4.3 nM cm^{-2} s^{-1} far-red light. The irradiation time was 10 min of red light unless otherwise noted. The leaf width was measured 24 h after the red irradiation by photocopying and measuring the images with a computerized digitizer. Data points were collected from 40–60 individual leaf sections.

Floating the leaf sections on ALA solutions after a red light irradiation influenced the leaf unrolling (Fig. 15). At a concentration near 0.1 mM, a slight stimulation was found (solid curve). Above 1 mM, the stimulation was replaced by an inhibition. With a shorter treatment time with ALA (6 h), a slight stimulation could still be found but the inhibition was less evident. Even at the highest concentration used (20 mM) approximately 20% unrolling occurred. (100% unrolling is the difference in width between the buffer control [3.20 mm] and the dark-grown [1.77 mm] leaf.) When the leaves were pretreated with ALA (10 mM) for 5 h before the red light irradiation, only 7% unrolling occurred. On the other hand, if the ALA treatment (10 mM) lasted for only 1–3 h, a stimulation of

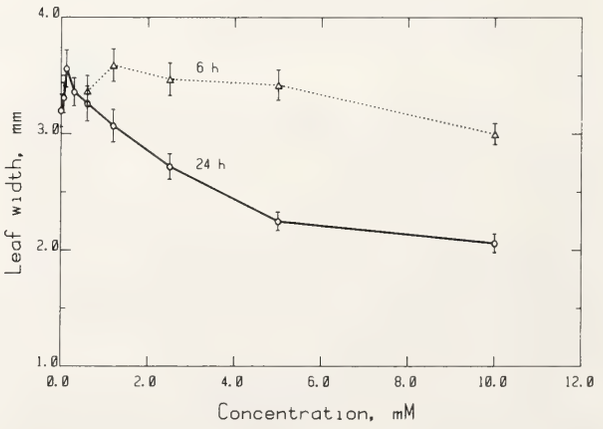


Fig. 15. Unrolling of barley leaf sections in ALA solutions of different concentrations. The leaves were irradiated 10 min with red light and then floated on ALA solutions for 6 or 24 h. The leaf widths were measured 24 h after irradiation. The leaves treated for 6 h on ALA were floated on buffer for the remaining 18 h.

the unrolling took place (Fig. 16). With a longer treatment time than 3 h, the inhibitory effect soon became prevailing. At a lower concentration (2.5 mM) neither the stimulation nor the inhibition is as evident (Fig. 16).

The inhibitory effect could be an unspecific toxic effect at the high concentration used. It is known that several amino acids inhibit growth in the concentration range used (Wilson and Bell, 1978). Therefore the effects of several other amino acids and keto acids were compared to that of ALA on leaf unrolling and coleoptile section growth. As shown in Table 4, no other substance tested showed the same pronounced inhibition of leaf unrolling without also affecting the coleoptile growth significantly.

The red light irradiation transforms the phytochrome to the Pfr form, which presumably triggers the release of hormones (GA) that stimulate the leaf unrolling. The effect of ALA could be at the phytochrome level, the hormone level, or the cell-expansion level. The effect of red light on the leaf unrolling could be reversed by far-red light. Escape from far-red reversibility took place rather rapidly. With a time delay of only 1 h between the red and far-red light, only 50% of the red-induced unrolling was reversed (Fig. 17). In the same way, when the ALA treatment was delayed after the red light irradiation an escape from the ALA-induced inhibition took place. In this case, 50% inhibition of the unrolling was still obtained after 4 h. Thus it seems likely that the ALA influences the control of the leaf unrolling in a step beyond the photoconversion

TABLE 4. The Effect of Some Chemicals on Leaf Unrolling and Coleoptile Section Growth*

Chemical 2×10^{-2} M	% Inhibition of Leaf Unrolling	% Inhibition of Coleoptile Growth
Aminolevulinic acid	83	1
Levulinic acid	62	42
Ketoglutaric acid	+21	+19
Ketoadipic acid	83	35
Ketovaleric acid	77	55
Phenylalanine	28	8
Methionine	55	+4
Cysteine	100	58

*The values are given in % of the unrolling of leaf segments floated on buffer or growth of coleoptile segments floated on buffer. Promotion indicated by plus signs.

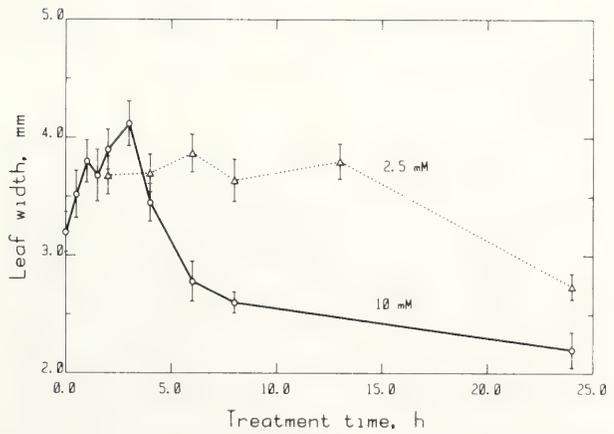


Fig. 16. Unrolling of barley leaf segments after floating on ALA solutions for different times. All leaf segments were irradiated with 10 min red light, floated on 10 mM ALA (o——o) or 2.5 mM (Δ ···· Δ) ALA for the time denoted by the abscissa and then transferred to buffer and measured 24 h after red light irradiation.

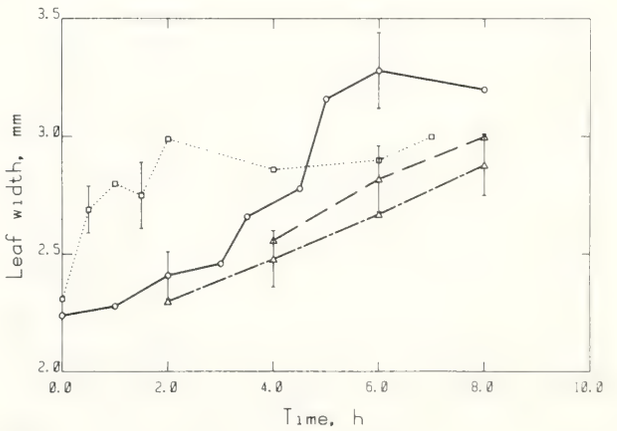


Fig. 17. Escape from inhibition of red-light-induced leaf unrolling. All leaves were irradiated with 10 min red light and the leaf width measured after 24 h. Leaves were given far-red light (□·····□) or ALA (o——o) at time denoted by the abscissa. Leaves were given 1 h (Δ-·-·-Δ) or 3 h (Δ- - - Δ) darkness before 15 min far-red light and then ALA as denoted by the abscissa.

of phytochrome. However, when the leaves are given both far-red (after 1 or 3 h) and ALA, the escape from inhibition is still further delayed. Kinetin 10^{-5} M was found to reverse the inhibitory effect of ALA partially. At a concentration of 2.5 mM ALA, the inhibition was decreased from 30% to 10% by kinetin. When GA was added together with ALA, the inhibition at 10^{-5} M GA and 5 mM ALA decreased from 70% to 20%.

The occurrence of both stimulation and inhibition of leaf unrolling during the treatment with ALA suggests that this substance is not simply acting as a toxic metabolite when in excess of what is needed for porphyrin formation. The metabolic step(s) affected is probably located between the phytochrome system and the hormonal regulation of the leaf unrolling. The evidence for this hypothesis is that the escape from far-red reversibility is much faster than the escape from ALA inhibition. Furthermore the hormones GA and kinetin can partially overcome the ALA-induced inhibition. No effect of ALA was found on the cell expansion itself, as manifested by the coleoptile section test.

References

Burström, H., *Bot. Notiser, 7*, 351–362, 1942.
Loveys, B. R., and P. F. Wareing, *Planta, 98*, 117–127, 1971.
Virgin, H. I., *Physiol. Plant., 15*, 380–389, 1962.
Wilson, M. F., and E. A. Bell, *Phytochemistry, 17*, 403–406, 1978.

BINDING OF CATIONS TO PHYTOCHROME

Christer Sundqvist and Winslow R. Briggs

Purification of oat phytochrome with monospecific antibodies immobilized on CNBr-activated Sepharose was described previously (Quail and Briggs, *Year Book 78*, 126–128). The same column has been used repeatedly this year to purify a total of about 200 mg phytochrome. Some of this phytochrome, eluted with $MgCl_2$, has been used for a study of the interaction between phytochrome and metal ions.

Several different cations of transition metals have been found to cause a spectral alteration of phytochrome, e.g., Cu^{2+}, Zn^{2+}, and Co^{2+} (Pratt and Cundiff, 1975). The effect observed is a very low absorption of phytochrome in both red and far-red spectral regions after red irradiation in the presence of the cation. Phytochrome in the P_r form seems to be unaffected. The addition of EDTA causes a regeneration of the normal spectral properties, but these are fully restored only after phototransformation of the phytochrome with far-red light. The effect of transition cations on phytochrome has also been studied by Lisansky and Galston (1974) and interpreted as irreversible loss of photoreversibility of the phytochrome molecule. The spectral alteration obtained in the presence of Zn^{2+} is shown in Fig. 18. In the presence of 0.5 mM Zn^{2+}, approximately 0.1 A is lost in absorbance at 730 nm when the concentration of phytochrome is 0.6 mg/ml.

During a prolonged exposure of the phytochrome to Zn^{2+}, photoreversibility decreases slowly with time, as shown in Fig. 19. Some of the photoreversibility can be regained if EDTA is added. However, the capacity to recover photoreversibility is also rapidly lost with time, and after 4 h in room temperature is entirely gone. On the contrary, if a sample of phytochrome has been exposed to Zn^{2+} and then receives EDTA, it becomes stabilized by EDTA and no further decrease in photoreversibility is detected. The molecular basis for the cation-induced change

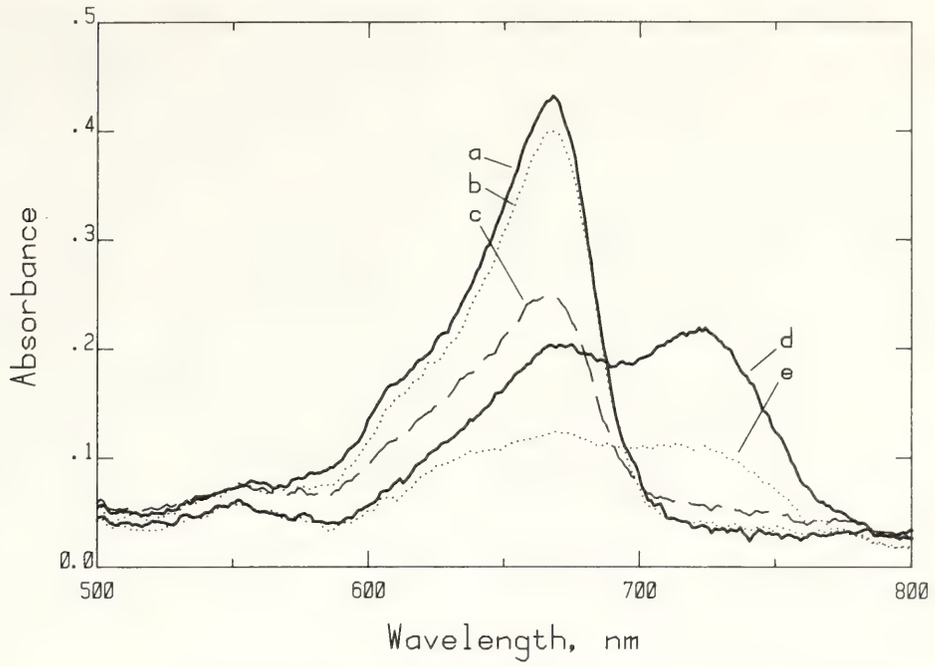


Fig. 18. Absorption spectra of oat phytochrome in the presence of 0.5 mM $ZnCl_2$. The phytochrome was in 5 mM histidine buffer pH 7.4 before addition of $ZnCl_2$ (a and d); (a) after saturating far-red light (40 s 12.1 nE cm^{-2} s^{-1}) and (d) after saturating red light (40 s 4.8 nE cm^{-2} s^{-1}). Spectra (b, c, and e) after addition of $ZnCl_2$; (b) after saturating far-red light; (e) after saturating red light; (c) after another saturating far-red light irradiation. Phytochrome 0.6 mg/ml, absorbance ratio (A665/A280) 0.81.

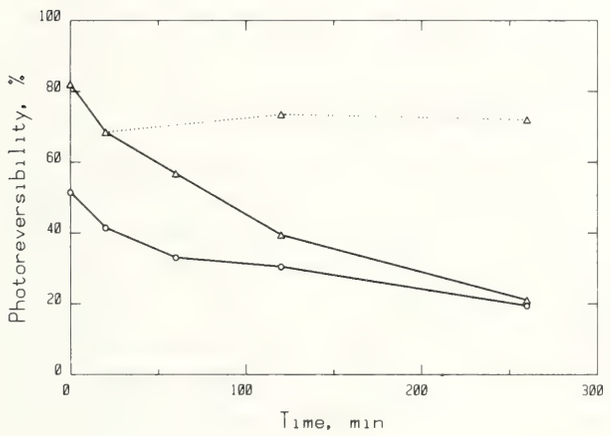


Fig. 19. The effect of $ZnCl_2$ on the photoreversibility of phytochrome. Photoreversibility was measured as a change in optical density between 730 nm and 700 nm with a Ratiospect R-2 spectrophotometer (Agricultural Specialty Company, Inc.) and is shown as percentage of the value for phytochrome in buffer solution at the start of the experiment. This value for phytochrome in buffer only did not change by more than five percent during the experiment. A set of five samples with phytochrome (0.06 mg/ml) were made 0.13 mM with $ZnCl_2$ at time zero, and then used to determine the percentage photoreversibility left after different times at 20°C indicated by the abscissa (o —— o). After this determination the samples were made 6.3 mM with EDTA, and the photoreversibility was determined again (Δ —— Δ). The sample given EDTA at 20 min was measured also after 120 and 260 min (Δ ····· Δ).

in absorbance of the P_{fr} form of the pigment is unknown. The addition of cations to P_r seems to have very little or no effect on the spectral properties of this form. A question raised is whether or not phototransformation has to take place before the cation can bind to the phytochrome molecule. To answer this question, it was necessary to use a method by which the metal-protein binding could be detected in a way other than the spectral alteration of the P_{fr} form.

The fluorescence of lanthanides and especially terbium (Tb^{3+}) has commonly been used to study the binding of metals to proteins (Leavis *et al.*, 1980; Sherry *et al.*, 1978). Tb^{3+} fluorescence can increase 1,000-fold when this metal binds to a protein and the binding site is in close proximity to an

amino acid residue with absorption near 280 nm. The absorption of Tb^{3+} is comparatively low in this region, and the Tb^{3+} fluorescence is increased by energy transfer if an excitation wavelength is used at which the amino acid residue absorbs. The main absorption band of Tb^{3+} is at 352 nm, with strong fluorescence bands at 492 nm, 545 nm, and 580 nm.

Figure 20 shows the fluorescence increase at 545 nm when Tb^{3+} successively is added to a phytochrome solution (0.2 mg/ml). There is approximately an eightfold increase in fluorescence at 545 nm when Tb^{3+} is added to the phytochrome-containing solution. By contrast, there is only a small increase when it is added to the histidine buffer without phytochrome. An addition of EDTA to the sample rapidly reduces the fluorescence. The excitation wavelength used was 250 nm. The measurements were made with the phytochrome in the P_r form as verified by absorption measurements of the sample before and after the fluorescence measurements. However, no difference was evident if the measurement was made with the phytochrome in the P_{fr} form.

If Zn^{2+} (0.1 mM or 0.05 mM) were added to the phytochrome solution before the addition of Tb^{3+}, the fluorescence increase was much smaller. The addition of Mg^{2+} (0.1 mM) had no effect on the fluorescence from added Tb^{3+}.

From the competition between Tb^{3+}

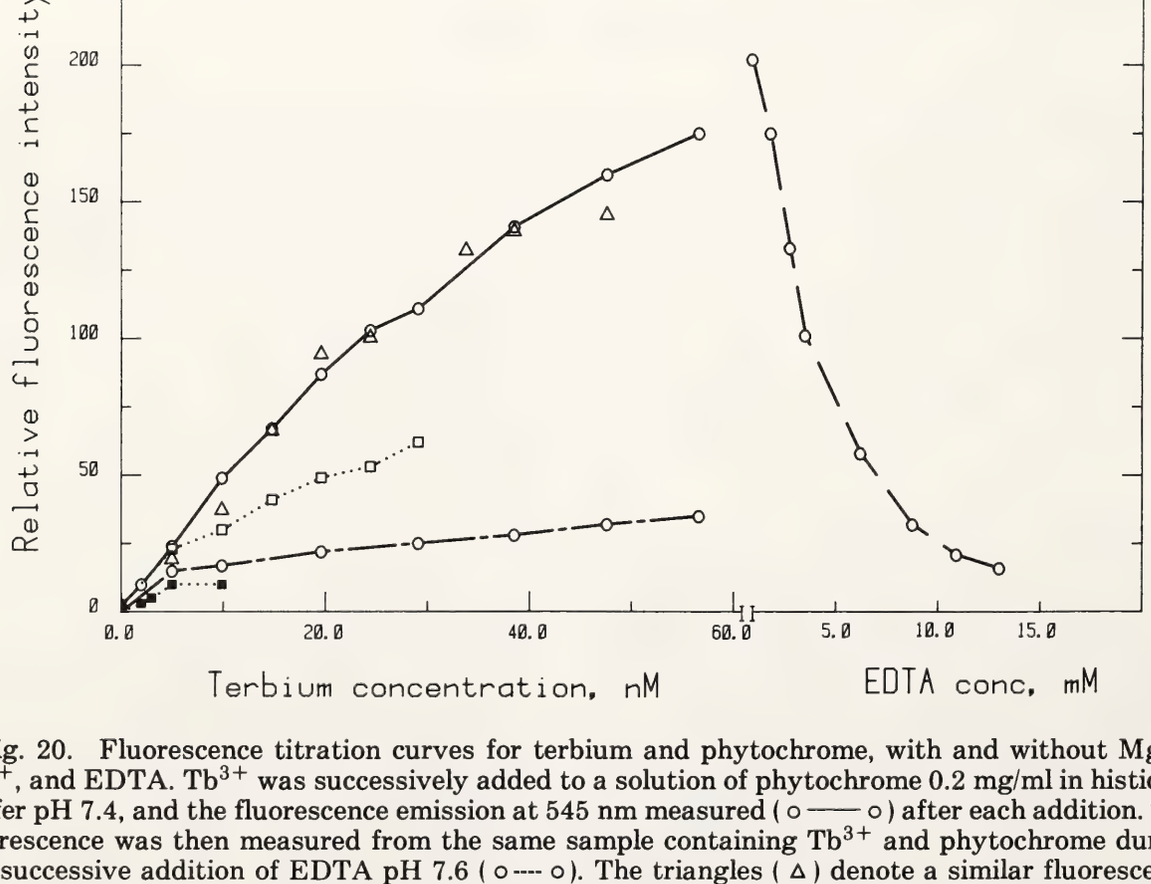


Fig. 20. Fluorescence titration curves for terbium and phytochrome, with and without Mg^{2+}, Zn^{2+}, and EDTA. Tb^{3+} was successively added to a solution of phytochrome 0.2 mg/ml in histidine buffer pH 7.4, and the fluorescence emission at 545 nm measured (o —— o) after each addition. The fluorescence was then measured from the same sample containing Tb^{3+} and phytochrome during the successive addition of EDTA pH 7.6 (o---- o). The triangles (△) denote a similar fluorescence titration experiment but the phytochrome solution also contained 0.1 mM Mg^{2+} before the addition of Tb^{3+}. Similar samples without Mg^{2+} but containing 0.1 mM Zn^{2+} (■ · · · · ■) and 0.5 mM Zn^{2+} (□ · · · · □) are also illustrated. An excitation wavelength of 250 nm was used, the excitation slit was 24 nm, and the emission slit was 10 nm. The experiment was performed at 20 °C. The fluorescence from Tb^{3+} in histidine buffer without any phytochrome (o —-— o) is also shown.

and Zn^{2+} on the fluorescence of Tb^{3+}, and from the effect of EDTA to decrease the fluorescence from Tb^{3+} and to restore the photoreversibility of phytochrome spectrally denatured by Zn^{2+}, it can be concluded that these two cations may bind to the phytochrome molecule in similar ways. As the binding of Tb^{3+} can take place to the P_r form, it is possible that the binding of Zn^{2+} also takes place to P_r even if this binding does not cause spectral changes. The bound cation can then inhibit the formation of spectrally normal P_{fr} after phototransformation in some yet unknown way.

References

Leavis, P. C., B. Nagy, S. S. Lehrer, H. Bialkowska, and J. Gergely, *Arch. Biochem. Biophys., 200*, 17–21, 1980.

Lisansky, S. G., and A. W. Galston, *Plant Physiol., 53*, 352–359, 1974.

Pratt, L. H., and S. C. Cundiff, *Photochem. and Photobiol., 21*, 91–97, 1975.

Sherry, A. D., S. Au-young, and G. L. Cottam, *Arch. Biochem. Biophys., 189*, 277–282, 1978.

SEASONAL CHANGES IN HIGH-TEMPERATURE ACCLIMATION OF DESERT WINTER ANNUALS

Jeffrey R. Seemann, Joseph A. Berry, and W. J. S. Downton

We have previously reported (*Year Book 78,* 157–162) that desert winter annuals possess the capacity to alter components of the photosynthetic apparatus in response to increasing leaf temperature so as to increase both the temperature optimum and thermal stability of the CO_2 fixation process. In this study we have followed the extent and seasonal dynamics of this acclimation process under natural conditions in Death Valley, California, with the objective of obtaining a clearer understanding of the environmental stimuli and plant processes that bring about acclimation to high temperature.

Temperature-dependent changes in whole leaf chlorophyll fluorescence levels were used as an indicator of the thermal tolerance limits of the photosynthetic apparatus. Our earlier work (*Year Book 78,* 157–162) has demonstrated that the temperature at which the F_0 chlorophyll fluorescence level begins to rise sharply (the "fluorescence-rise temperature") is closely correlated with the temperature at which CO_2 fixation (as measured by gas exchange) falls dramatically because of high-temperature-induced irreversible damage to the photosynthetic capacity of the leaf.

The thermal stability of plants growing under natural conditions in Death Valley was assessed (1) soon after germination, (2) during midseason, and (3) at the end of the growing season. The fluorescence-rise temperature of separate samples from five representative species are plotted in Fig. 21. It is clear that there is an upward trend in the apparent tolerance of each of these species to high temperature as the season progressed. These patterns were quite consistent among all species measured. (Comparable data for six other annual species is not shown.) Although the winter and spring rainfall pattern produced multiple germination pulses of annuals in Death Valley during 1980, this study concentrated principally on the major population of plants that germinated after the initial rainfall in January.

The apparent thermal tolerance limit increased 6–9 °C over the course of the season for every species examined. The environmental temperature, as indicated by the maximum air temperatures recorded at the weather station in

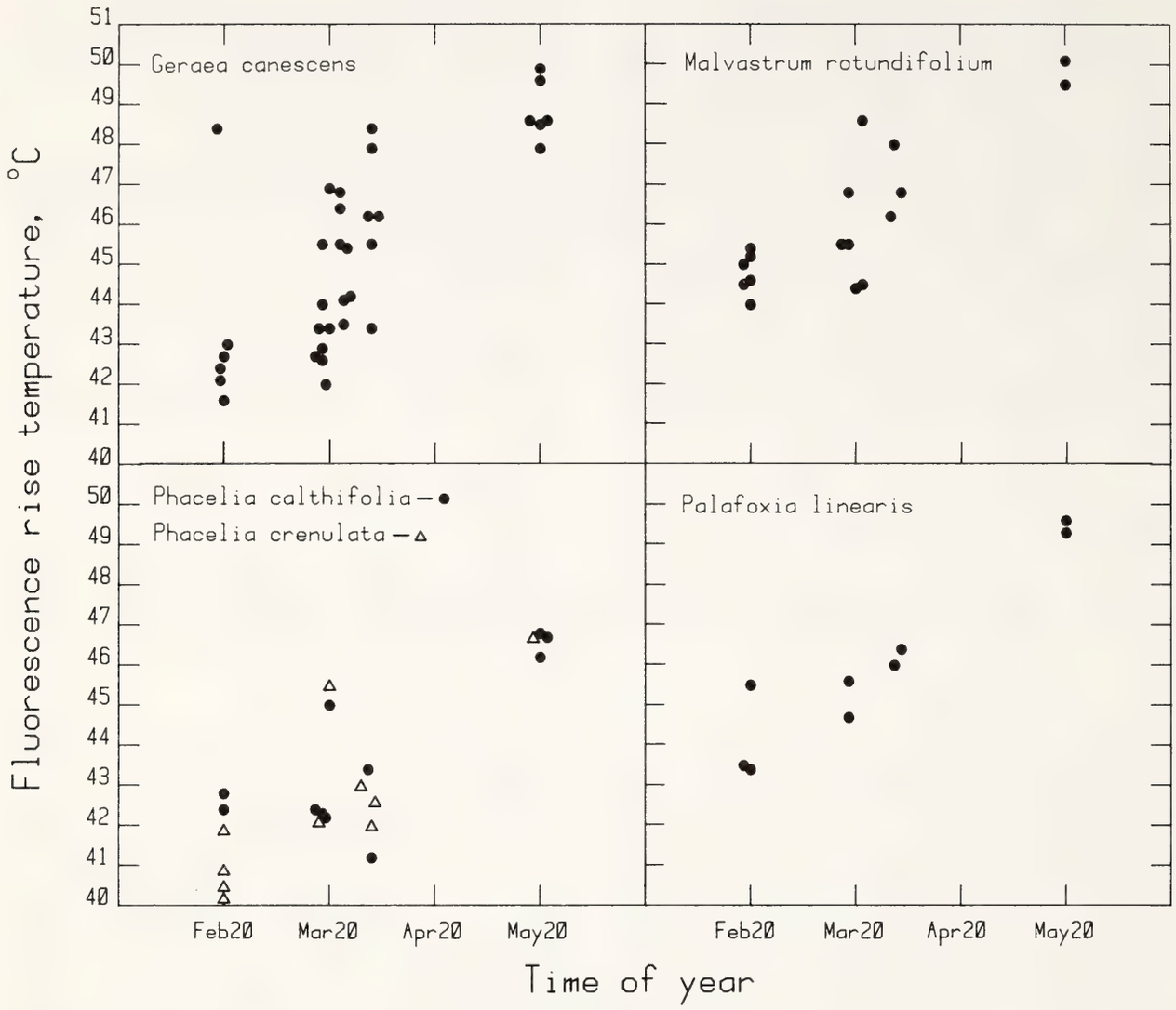


Fig. 21. Changes in the thermal tolerance of desert winter annuals during the 1980 growing season. Plotted is the fluorescence rise temperature (breakpoint) vs. the date of the determination. Samples were taken from plants growing under natural conditions in Death Valley, California, and fluorescence determinations were made on the same day, as described previously (*Year Book 78,* 157-162).

Furnace Creek, increased about 12 °C over this period. The mean daily maxima for the 14 days preceding the early- and late-season measurements were 22.9 ± 2.8 °C and 35.0 ± 4.4 °C, respectively, and the highest recorded temperature of the preceding 14 days was 28.3° and 41.7 °C, respectively. The physiological adjustments of these plants, which increased their tolerance to high temperature, are thus strongly correlated with the increase in environmental temperature.

It should be emphasized that air temperature in the field gives only a rough estimate of how the leaf temperature changed during the season. There are also changes in other factors such as leaf size, leaf position, plant water status, humidity, and radiation load, which affect the leaf temperature. We reported last year (*Year Book 78,* 157-162) that plants of *Geraea canescens* at different water status were apparently acclimated to different thermal regimes. Drought-stressed plants had about 5 °C higher tolerance despite the fact that these plants experienced nearly identical atmospheric conditions. This result sug-

gests that the considerable variability in thermal stabilities seen during midseason (see Fig. 21; also *Year Book 78,* 157–162) is the result of site-to-site differences in water availability and resultant differences in leaf cooling capacity via evapotranspiration.

This type of indirect effect of plant water status on thermal stability is consistent with at least one proposed mechanism for this acclimation response. Raison and Berry (*Year Book, 78,* 149–152) and Roberts and Berry (this Report) suggest that changes in thermal tolerance induced by high temperature are associated with changes in the physical properties and composition of chloroplast membranes. Santarius and Müller (1979) argue, however, that changes in chloroplast lipid composition did not account for a small (3 °C) change in the thermal tolerance of spinach plants exposed to high temperature. The prediction that lipid properties of desert annuals change with growth temperature needs to be tested.

Downton *et al.* (this Report) showed that the range of acclimation to high temperature that could be induced in laboratory studies where only growth temperature was manipulated, was as large as that observed in the field, where both temperature and water status may change. In other studies (data not shown), possible effects of leaf and plant age were explored and shown to be small. However, a strong correlation between increased heat tolerance and decreased leaf water potential was observed (data not shown). A direct effect of water potential should not be discounted since Armond and Hess (*Year Book 78,* 168–171) demonstrated that the aqueous medium in which chloroplast membranes are suspended may have an effect in addition to that attributed to lipid changes on thermal tolerance. Santarius (1973) showed that the heat resistance of certain chloroplast membrane-associated processes depended upon the concentration and molecular properties of sugars included in the chloroplast suspending medium, and our unpublished results confirm this observation. It therefore seems entirely possible that solute changes associated with the osmotic adjustment of these plants to water stress could also result in changes in the thermal tolerance of the membranes, and studies will continue to examine this possibility.

References

Santarius, K. A., *Planta, 113,* 105–114, 1973.
Santarius, K. A., and M. Müller, *Planta, 146,* 529–538, 1979.

THERMAL STABILITY OF PHOTOSYNTHESIS IN DESERT PLANTS

W. J. S. Downton, Jeffrey R. Seemann, and Joseph A. Berry

Studies of the heat tolerance of photosynthetic components of desert winter annuals (Seemann *et al.*, this Report; *Year Book 78,* 157–162) have been extended to include other groups of desert plants. These field studies have been supplemented with experiments with controlled growth chambers to examine the heat tolerance and acclimation responses of these plants grown in specified thermal regimes.

Field studies (which utilized the fluorescence-rise temperature procedure to assay for heat tolerance of leaves, Seemann *et al.*, this Report) were conducted during April and August 1979. Some results of the April study in the Death Valley region were presented last year (*Year Book 78,* 157–162). The summer study included the Death Valley region, the eastern Mojave Desert of California, and the Sonoran

Desert of Arizona. Data collected in these surveys will be presented here in summary form, as the mean and standard deviation of groupings of species of similar life forms.

A group of leafy perennials sampled in Death Valley (see the legend of Fig. 22 for lists of species sampled) increased in heat tolerance by an average of about 3 degrees over the summer (47.5 ± 1.6 °C in April vs. 50.7 ± 1.4 °C in August). The different ephemeral floras present at these times also had different tolerance to heat (44.8 ± 2.1 °C for winter annuals in April and 47.5 ± 1.5 °C for summer annuals in August). These increases in heat tolerance are probably related to the increase in environmental temperature (see also Seemann *et al.*, this Report). The ephemeral species were in general less tolerant of heat than the leafy perennials at the same times of the year, and samples taken from perennial

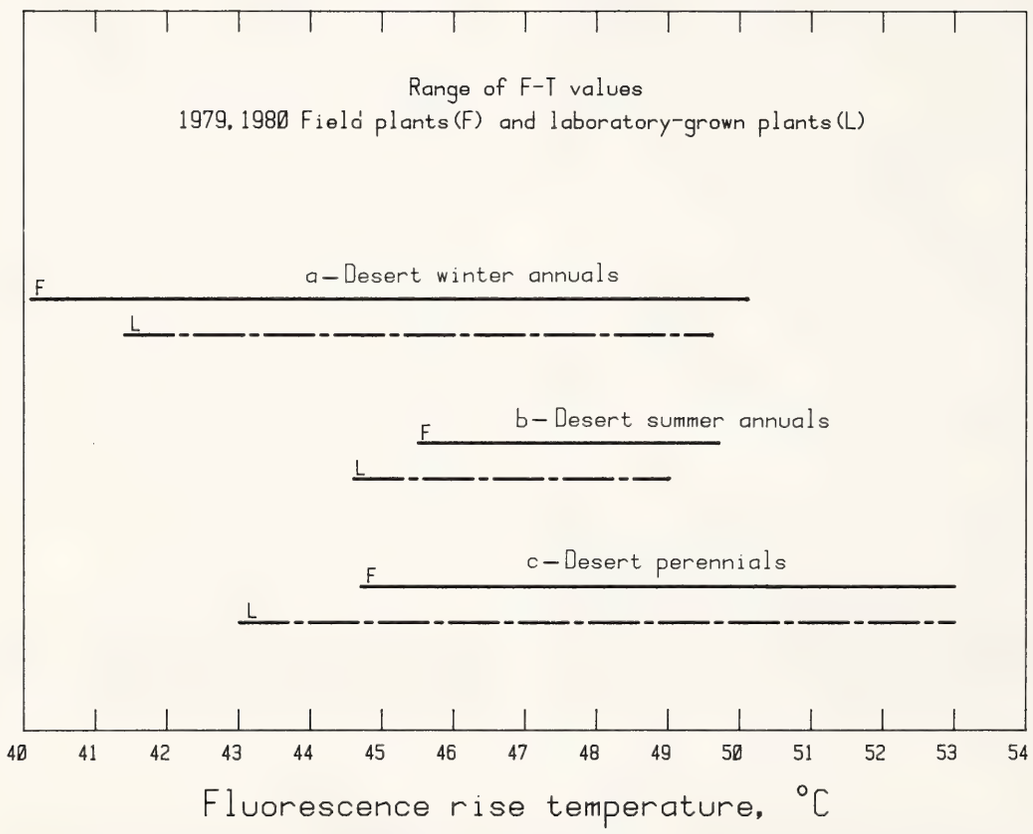


Fig. 22. A comparison of the capacity for thermal acclimation observed in the field (F) and in controlled-temperature studies (L) for three groups of plants. (a) desert winter annuals; field study species—*Abronia villosa, Camissonia brevipes, C. claviformis, Geraea canescens, Gilia latiflora, Malvastrum rotundifolium, Mohavea breviflora, Palafoxia linearis, Phacelia calthifolia, P. crenulata* (field studies were conducted in Death Valley); laboratory study species—*Camissonia brevipes, Geraea canescens, Nicotiana trigonophylla, Phacelia crenulata, Plantago insularis, Stanleya pinnata.* (b) desert summer annuals: field study species—*Allionia incarnata, Amaranthus palmeri, Atriplex elegans, Bouteloua barbata, Curcurbita palmata, Datura meteloides, Digitaria sanguinalis, Eriogonum deflexum, Panicum hirticaule, Pectis papposa, Portulaca oleracea, Proboscidea parviflora, Tidestromia lanuginosa, Trianthema portulacastrum* (field studies were conducted in southern Arizona during Sept. 1979); laboratory study species—*Amaranthus palmeri, Atriplex elegans, Digitaria sanguinalis, Gossypium hirsutum, Pectis papposa, Portulaca oleracea.* (c) desert perennials: field study species—*Atriplex hymenelytra, Allenrolfea occidentalis, Boerhaavia annulata, Distichlis spicata, Larrea divaricata, Nerium oleander, Sporobolus airoides, Suaeda torreyana, Tamarix aphylla, Tidestromia oblongifolia* (field data was obtained during spring and late summer, 1979–1980, in Death Valley); laboratory study species—*Atriplex lentiformis, Boerhaavia coccinea, Larrea divaricata, Nerium oleander.* (Some data for lab perennials taken from Armond *et al.*, 1978; Pearcy *et al.*, 1977; and Raison and Berry, *Year Book 78*, 149–152.)

succulents during August were the most tolerant (54.7 ± 2.7 °C). These forms of plants differ in their heat balance such that, given the same environment, they should have different tissue temperatures. Differential effects of microclimatic zones and physiological activity were also evident. For example, perennial species sampled during August from wet sites, or from around springs, were less heat tolerant than the same species sampled in adjacent desert areas. Agricultural species growing in summer in the Imperial Valley had heat tolerances (from 48° to 51 °C) similar to those found for native summer-active species.

Representatives of the spring- and summer-active ephemeral floras were grown in controlled environments. The species and growth conditions compare directly with the survey of Pike and Berry (1980; *Year Book 78,* 163–168), which examined the lipid-phase separation temperatures of these two groups of plants. Consistent with their findings of a higher phase-separation temperature of lipids from the warm-season than from the cool-season plants, the heat tolerances differed (46.0 ± 1.2° and 41.3 ± 0.9 °C for the warm-season and cool-season plants, respectively) when these species were grown in a common temperature (28°/21 °C, day/night). The difference in heat tolerance (5 °C) was not as large, however, as the difference in lipid phase-separation temperatures (10 °C).

In other studies, desert plants were grown at a range of controlled temperatures. Growth at lower temperatures (20°/15° or 28°/21 °C day/night) did not cause progressively lower heat tolerance of the plants studied. Induction of the acclimation response occurred at growth temperatures above some critical threshold temperature. Plants grown at temperatures below this threshold appeared to have a fairly constant minimum heat tolerance which may be genetically specified. Within each group (Fig. 22a–c) there was very good agreement between the acclimation of those plants induced in the laboratory by 40° to 43°/32 °C day/night growth temperature and the range of heat tolerance observed in the field collections. This result indicates that much of the variation between plants of these groups of species in the field could be attributed to direct effects of leaf temperature on the acclimation mechanism of the plants (as previously suggested, *Year Book 78,* 157–162). It is also noteworthy that the summer annual species have a lower capacity for acclimation (4.5 °C) than either the winter annuals (8.5 °C) or the perennials (10 °C). The greater range of temperatures likely to occur during the growth seasons of these latter groups is obvious, and the capacity of these plants to acclimate to heat as the season changes may be more significant to the success of these species than it would be for the summer annual species.

References

Armond, P. A., U. Schreiber, and O. Björkman, *Plant Physiol., 61,* 411–415, 1978.

Pike, C. S., and J. A. Berry, *Plant Physiol.,* in press, 1980.

PHOTOSYNTHETIC CAPACITY OF DESERT WINTER ANNUALS MEASURED *IN SITU*

Jeffrey R. Seemann, Christopher Field, and Joseph A. Berry*

Since the report of Mooney *et al.* (1976) of the exceptionally high photosynthetic rate of an individual of *Camissonia claviformis* growing in Death Valley, it has been hypothesized that desert winter annuals may possess photosynthetic properties which may serve as an adaptation to a potentially limited growing season. Although such high rates of carbon fixation (approaching 60 μmoles CO_2 m^{-2} s^{-1}) have been duplicated for this species and *C. brevipes* under optimal laboratory growth conditions (Seemann, unpublished; Longstreth *et al.*, 1980), there has been no systematic examination of the *in situ* photosynthetic characteristics of desert winter annual species to test this hypothesis.

Using a field-portable gas exchange system (Field and Berry, in preparation), we measured the photosynthetic rates of eight species of desert winter annuals in Death Valley during late March 1980 (see Table 5 for details). The results of these photosynthesis measurements (Table 5) indicate that although rates of CO_2 fixation under natural field conditions may be somewhat lower than those of plants grown under optimal conditions, these rates ($\bar{x} = 34.9 \pm 5.5$ μmoles m^{-2} s^{-1}) are nonetheless significantly higher ($\sim$40%) than values from the literature compiled by Björkman (1980) for a wide range of high-light-grown agricultural and native C_3 species from diverse environments. Rates of photosynthesis for desert winter annuals are on the average more than 50% above those reported for early successional winter and summer annuals of eastern deciduous forest areas (Bazazz, 1979). The two *Camissonia* species possess the highest photosynthetic capacities of these desert annuals. These rates of CO_2 fixation are among the highest ever reported for plants (C_3 or C_4) measured in the field, although the rates are not as high as those for plants that develop under optimal conditions. The very high

TABLE 5. Rates of Photosynthesis, Desert Annuals, Death Valley, March–April 1980*

Species	Ps Rate (μmol cm^{-2} s^{-1})	Conductance (mm s^{-1})
Camissonia claviformis	43.4	29.3
Camissonia claviformis	42.9	26.9
Camissonia claviformis	40.3	25.1
Camissonia claviformis	38.5	21.8
Camissonia claviformis	36.5	23.5
Camissonia claviformis	34.6	13.3
Camissonia claviformis	32.8	23.6
Camissonia claviformis	30.0	18.1
Camissonia brevipes	41.5	15.8
Camissonia brevipes	40.8	19.4
Camissonia brevipes	37.5	19.3
Camissonia brevipes	27.7	19.6
Abronia villosa	35.5	15.9
Atrichoseris platyphylla	24.6	11.4
Geraea canescens	30.8	15.7
Malvastrum rotundifolium	35.5	19.7
Malvastrum rotundifolium	31.1	21.4
Phacelia calthifolia	31.4	14.8
Phacelia crenulata	28.2	9.4

*Rate of photosynthesis of single attached leaves of desert winter annuals growing under natural conditions in Death Valley, California. All measurements were made at 20°C. Ambient CO_2 concentrations ranged from 330 to 350 ppm, and the air contained 21% O_2. The water vapor deficit ranged from 1.0 to 1.5 KPa. Light fluence rate was 1700–2000 μmol m^{-2} s^{-1}. Each value is the mean of at least three calculations made after the leaf had attained steady-state photosynthesis, and replicate points for several species are for separate plants. The measurements were made during March 19 to April 1, 1980.

*Department of Biological Sciences, Stanford University, California.

photosynthetic rates of this group of plants accounts in part for the capacity of these species to complete their entire life cycle successfully in a period as short as six weeks, for example, when germination occurs late in the season (Beatley, 1967).

References

Bazazz, F. A., *Annu. Rev. Ecol. Syst., 10,* 351–371, 1979.
Beatley, J. A., *Ecology, 48,* 745–750, 1967.
Björkman, O., In *Encyclopedia of Plant Physiol. New Series, Physiol. Plant Ecol.,* Vol. A, in press, 1980.
Longstreth, D. J., T. L. Harsock, and P. S. Nobel, *Physiol. Plant., 48,* 494–498, 1980.
Mooney, H. A., J. Ehleringer, and J. A. Berry, *Science, 194,* 322–324, 1976.

THE CHANGES IN THYLAKOID ACYL LIPID COMPOSITION OF *Nerium oleander* ACCOMPANYING ACCLIMATION TO HIGH TEMPERATURE

Justin K. M. Roberts and Joseph A. Berry

Previous work has established that acclimation of photosynthesis in *Nerium oleander,* which occurs when fully developed leaves are transferred from 20 °C to 45 °C, involves an increased thermostability of thylakoid-membrane-associated reactions and corresponding changes in properties of the lipids of the chloroplast membrane. In particular, the capacities for noncyclic photophosphorylation and photosystem II–driven electron transport reactions to tolerate high temperatures are greatly increased after acclimation (*Year Book 77,* 262–276; *Year Book 78,* 145–148). There is also a change of approximately 10 °C in the temperature at which chlorophyll fluorescence (from intact leaves) increases with heating (*Year Book 78,* 149–152; see also Seemann *et al.,* this Report). This increase in fluorescence is attributed to thermal denaturation of proteins of the photochemical apparatus in the chloroplast membranes (*Year Book 78,* 153–157), and the change in apparent thermal stability of these proteins with acclimation is correlated with a change in the properties of the lipids of the chloroplast membrane. A kinetic correlation was found between changes in the fluorescence-rise temperature and changes in lipid fluidity during acclimation. Furthermore the changes in lipid fluidity that occurred with acclimation of leaves to a new growth temperature exactly compensated for the normal tendency of fluidity to increase with temperature, and the fluidity of lipids from plants acclimated to different temperatures, when measured at the corresponding breakpoint temperatures, was constant (*Year Book 78,* 149–152.) It seemed most likely that this compensation of lipid properties would be based upon environmentally induced changes in the chemical composition of the lipids incorporated into the chloroplast membranes at different temperatures. It was therefore of interest to examine the chemical composition of the thylakoid lipids with respect to acclimation in *N. oleander.*

Methods

Cloned *N. oleander* plants were grown, and thylakoid lipids extracted and separated as described (*Year Book 77,* 262–276). The acetone fraction obtained by silicic acid column chromatography was separated by one-dimensional TLC on silica gel G plates (20 × 20 cm) into monogalactosyl diglyceride (MGDG), digalactosyl diglyceride (DGDG), and sulphoglycosyl diglyceride (SL), with chloroform/metha-

nol/acetic acid/water (170:25:25:4, v/v) as solvent. The methanol fraction was separated by two-dimensional silica gel TLC into phosphatidyl inositol (PI), phosphatidyl choline (PC), phosphatidyl ethanolamine (PE), and phosphatidyl glycerol (PG), with the above solvent (second dimension) and chloroform/methanol/ammonium hydroxide (65:30:4).

Individual lipids, visualized using dichlorofluoroscein, were hydrolyzed in NaOH/MeOH, methylated with BF_3 as catalyst, and the fatty acid methyl esters separated by gas-liquid chromatography (GLC). Heptadecanoic acid (17:0) was used as an internal standard to determine the relative amounts of each lipid. GLC peak areas were determined by triangulation. Results are expressed as percentages of total peak area.

Results

The lipid species present in the thylakoid membranes of *N. oleander* (Table 6) are similar to those of *Spinacae oleracea* (Lichtenthaler and Park, 1963; Nishahara *et al.*, 1980), and we detected no significant differences in the relative abundance of these lipid species with acclimation. The fatty acid composition of the total saponifiable lipids changed significantly with acclimation, however. Most notable was a decline in 18:3 and corresponding increases in 16:0, 18:0, and 18:1. These changes in the total acyl composition are the sum of multiple changes in the composition of the individual lipid species. To some extent these counteract one another, and as a result several significant changes are not reflected in the data for total composition.

Thus, 18:2 content of galactolipids goes up dramatically (about 10%) during acclimation, while in phospholipids it goes down (10–25%); and 18:3 levels fall significantly in the galactolipids + SL, whereas in the phospholipids they remain practically unchanged. Many other differences can be seen upon careful examination of the data. Their significance is not clear at this time, but the differences clearly indicate that at least those mechanisms that control the fatty acid composition of the galactolipids are to a large extent distinct from those controlling that of the phospholipids. Very few details of these mechanisms are currently known.

Changes similar in direction to those seen two weeks after transfer are apparent after only one day at 45 °C. However, it is clear also that MGDG and PC change very quickly (more than half the total change in one day). Thus the lipids found at initial points in lipid metabolism—for example those species labeled first when radioactive CO_2 is fed to a leaf (namely PC for phospholipids and galactolipids; Slack and Roughan, 1975)—have the most rapid response to temperature.

Previous studies (*Year Book 78*, 147–152) indicated that acclimation (at the level of changes in fluidity and chlorophyll fluorescence vs. temperature) was about half complete after 24 h. The data do not show a linear relationship between the change in physical properties and changes in fatty acid composition. There are two possibilities: either there is not a linear relationship between fluidity and composition, or individual lipid species may have disproportionate effects on the overall fluidity—for example the changes in composition of the most abundant lipid species, MGDG, is more than half complete in one day.

Acknowledgement

Use of the Varian 3700 gas chromatograph in Professor P. M. Ray's laboratory (Dept. Biological Sciences, Stanford University) is gratefully acknowledged. This research was partially supported by NSF Grant DEB 78-10727.

TABLE 6. Changes in the Acyl Fatty Acid Composition of Chloroplast Membrane Lipids of *Nerium oleander**

Lipid Species		Fatty Acids†, % of Total					
		16:0	16:1	18:0	18:1	18:2	18:3
Total	control	15.2 ± 1.5	<1.0	2.2 ± 0.4	5.8 ± 1.1	12.4 ± 1.3	64.7 ± 1.4
(100%)	1 day	16.6 ± 1.5	<1.0	2.8 ± 0.3	7.8 ± 0.4	12.5 ± 1.0	60.3 ± 1.5
	14 day	19.0 ± 1.7	<1.0	4.2 ± 0.7	11.1 ± 0.8	15.1 ± 1.3	50.4 ± 2.1
monogalactosyldiglyceride	control	1.7 ± 0.9	<0.5	0.5 ± 0.1	1.1 ± 0.3	3.2 ± 0.7	93.6 ± 0.9
(51%)	1 day	3.0 ± 0.4	<0.5	0.8 ± 0.1	2.5 ± 0.4	7.9 ± 0.8	85.5 ± 1.0
	14 day	3.0 ± 0.6	<0.5	0.9 ± 0.2	4.9 ± 0.5	14.5 ± 1.8	76.6 ± 1.9
digalactosyldiglyceride	control	14.9 ± 1.3	<0.5	3.8 ± 0.6	2.1 ± 0.3	2.6 ± 0.7	76.6 ± 2.1
(30%)	1 day	17.4 ± 1.0	<0.5	4.7 ± 0.4	2.5 ± 0.6	4.5 ± 0.3	70.9 ± 1.5
	14 day	20.4 ± 1.6	<0.5	7.8 ± 0.4	6.3 ± 1.6	13.5 ± 1.9	52.0 ± 2.3
sulphoglycosyldiglyceride	control	37.7 ± 2.9	<0.5	3.1 ± 0.5	12.2 ± 2.7	7.0 ± 0.9	40.0 ± 3.3
(7%)	1 day	41.9 ± 1.8	<0.5	3.2 ± 0.4	14.4 ± 1.2	8.2 ± 1.3	32.3 ± 1.7
	14 day	46.5 ± 2.4	<0.5	4.6 ± 0.8	18.2 ± 2.0	9.7 ± 1.4	20.4 ± 2.6
phosphatidylglycerol	control	27.6 ± 1.9	18.1 ± 3.4	1.7 ± 0.4	33.2 ± 3.3	12.9 ± 2.7	6.6 ± 1.3
(6%)	1 day	38.5 ± 2.4	15.8 ± 0.6	2.6 ± 0.5	29.8 ± 1.6	8.8 ± 1.0	4.6 ± 0.6
	14 day	43.5 ± 2.5	10.2 ± 1.0	2.5 ± 0.7	39.6 ± 0.9	3.1 ± 0.7	1.3 ± 0.2
phosphatidylethanolamine	control	16.5 ± 2.5	<0.5	2.4 ± 0.7	7.4 ± 2.0	57.8 ± 3.4	15.9 ± 2.9
(3%)	1 day	22.2 ± 1.3	<0.5	3.0 ± 0.2	11.2 ± 1.5	46.2 ± 1.9	17.5 ± 0.7
	14 day	20.0 ± 3.1	<0.5	3.6 ± 0.9	21.1 ± 2.1	36.0 ± 3.7	19.1 ± 2.4
phosphatidylcholine	control	16.2 ± 2.2	<0.5	3.1 ± 0.5	11.5 ± 1.9	49.5 ± 2.2	19.6 ± 4.5
(1.8%)	1 day	24.5 ± 2.9	<0.5	5.2 ± 0.3	22.2 ± 1.4	30.1 ± 0.9	18.2 ± 2.3
	14 day	27.8 ± 5.5	<0.5	5.1 ± 0.5	29.4 ± 3.2	20.0 ± 3.6	17.9 ± 1.3
phosphatidylinositol	control	42.5 ± 1.9	<0.5	3.3 ± 0.3	6.8 ± 2.9	26.5 ± 3.3	20.7 ± 3.5
(1.2%)	1 day	46.9 ± 0.3	<0.5	3.4 ± 0.4	9.9 ± 0.9	21.7 ± 0.8	18.2 ± 0.4
	14 day	44.8 ± 3.5	<0.5	3.5 ± 1.0	13.4 ± 0.7	17.2 ± 2.2	21.1 ± 3.2

*Upon acclimation of fully expanded leaves from a 20 °/15 °C (day/night) growth regime to a 45 °/32 °C (day/night) growth regime. Values for the controls (leaves harvested before transfer of plants) and samples harvested one day and two weeks (or more) after transfer from cool to hot conditions are shown. The mean percentage of the total fatty acid content of each lipid class and the standard deviation from that mean is given. (Each horizontal line should total 100%.) At least four plants were analyzed separately for each time point.

†Fatty acid chain length: number of double bonds.

References

Lichtenthalen, H. K., and R. B. Park, *Nature, 198,* 1070–1072, 1963.

Nishahara, M., K. Yohota, and M. Kito, *Biochim. Biophys. Acta, 617,* 12–19, 1980.

Slack, C. R., and T. G. Roughan, *Biochem. J., 152,* 217–228, 1975.

RESPONSE AND ADAPTATION TO WATER STRESS IN *Nerium oleander*

*Olle Björkman, W. J. S. Downton, and Harold A. Mooney**

Much of our previous work on photosynthetic response and adaptation to ecologically contrasting environments has employed a "single factor" approach. That is, the responses of photosynthesis to a certain component of the physical environment, such as irradiance, temperature, water or nutrient status, have been studied one at a time, while attempting to minimize the influence of other variables. This is a necessary first approach to gaining insight into the physical, physiological, and biochemical mechanisms of adaptation. However, natural environments, including those that show striking contrasts with respect to one component factor (e.g., temperature) inevitably also differ in other, often covarying factors. For example, in desert habitats such as Death Valley, peak temperatures are reached at the time of year when the water supply is at a minimum and the irradiance and the atmospheric drought are maximal.

To understand adaptation to a particular type of natural habitat it is therefore necessary to have information both on the response to each major component factor and on the interactive effects of these factors. We plan to investigate in the same plant species, the nature of inhibitory effects on the photosynthetic system, the effects of major stress factors such as extremes of temperature, excessive irradiance, and low plant water status, and the interactions of these stress factors in aggravating or alleviating injury to or modifying the response of the photosynthetic apparatus.

For this purpose we have initiated exploratory work with *Nerium oleander.* This species is unusually well suited for studies that must combine work at the level of the whole plant, single leaf, isolated chloroplasts, and enzymes, and we have much valuable information on its photosynthetic characteristics. However, we had no information on the water relations of *N. oleander,* and exploratory studies presented here were made to provide necessary background information for our future work.

Nerium oleander, originally native to arid regions of Southwest Asia and Northwest Africa, is commonly found planted along roads in the arid regions of the southwestern United States. It is perhaps the most common exotic species planted in areas of human activity in the Death Valley National Monument where, when supplied with adequate water, it remains active throughout the year.

For our preliminary work on the drought tolerance of *N. oleander* we took advantage of the occurrence in Death Valley of plant stands which had been left unwatered for long periods of time. In more extreme cases, the leaves showed obvious signs of advanced desiccation, having a dull grayish-green appearance and an abnormal inclination. Measurement of leaf water potential (ψ_w) with a psychrometric technique revealed that in some individuals ψ_w was as low as

*Department of Biological Sciences, Stanford University, California.

−7 MPa (−70 bar). Measurements of osmotic potential (ψ_s) on the same samples confirmed that the leaves had no turgor pressure. Irrigation of such highly water-stressed plants resulted in a rapid increase in ψ_w, reaching −1.4 MPa (−14 bar) within six hours, a value typical for plants that had been kept well watered. At the same time, the leaves with few exceptions regained positive turgor, the normal gloss, healthy dark green color, and inclination found in well-watered plants. No visible signs of permanent injury could be detected in these leaves. Subsequent controlled drought experiments at Stanford confirmed that *N. oleander* leaves have a remarkable ability to recover from severe water stress, showing no loss of chlorophyll or protein or irreversible damage to their photosynthetic structures.

Osmotic adjustment. There is considerable evidence that continued function of cellular processes at low water potentials depend on the presence of a positive pressure (turgor, T). Since $T = \psi_w - \psi_s$, it follows that in order to maintain a positive value of T at low water potentials, ψ_s must decrease to at least the same extent as the decrease in ψ_w. Water loss associated with declining water potential inevitably results in a passive increase in solute concentration and hence a decline in ψ_s. This decline in ψ_s is by itself insufficient to maintain a positive turgor pressure at low water potentials, but an active increase in solute content (= osmotic adjustment) could effect a sufficiently large decrease in ψ_s to counterbalance the effect on T of a decline in ψ_w. There is also experimental evidence that osmotic adjustment does indeed occur in response to a gradually imposed water stress in certain drought-tolerant plants (see Osmond *et al.*, 1980). Mooney *et al.* (*Year Book 76*, 328–335) suggested that osmotic adjustment may be responsible for the greatly increased tolerance to inhibition of the quantum yield of photosynthesis at low leaf water potentials in *Larrea divaricata* growing in Death Valley over that of *Larrea* plants grown under ample water supply at the laboratory.

To determine the extent to which *N. oleander* plants are capable of osmotic adjustment, plants were grown in the Stanford laboratory under a series of watering regimes. To facilitate the control of soil drying rates, 18-liter containers were used. Additional studies were made on established plants in the field. The water potentials of the plants grown under the various water regimes were monitored periodically throughout the period of the experiments (June through September, 1979). Since the presence of laticifers in *N. oleander* leaves precludes the use of pressure chamber techniques, all measurements were made psychrometrically on leaf discs at 30.0 °C, with a series of Wescor Model C-52 thermocouple psychrometers equipped with appropriate electronic circuitry. Determinations of osmotic potentials were made on the same discs used for the water potential measurements following breakage of the cell walls by freezing and thawing. Determinations of relative water content (RWC) were made by weighing a number of leaf disc samples before and after equilibration with water-saturated air and after drying at 90 °C to constant weight. RWC is defined as:

$$\text{RWC} = \frac{\text{initial weight} - \text{dry weight}}{\text{saturated weight} - \text{dry weight}} \times 100\,(\%).$$

Table 7 shows values for ψ_w and ψ_s before and 4–6 hours after watering of *N. oleander* shrubs grown under a wide range of water regimes. The water potential prior to watering ranged from −0.93 to −3.2 MPa for container plants grown under ample and restricted water supply, respectively, to −6.7 MPa for severely water-stressed plants growing in the field in Death Valley. Within a few hours after rewatering there were only small differences in water potential

TABLE 7. Water and Osmotic Relations of *Nerium oleander* Leaves 4–6 Hours after Watering of Plants Grown under Different Water Regimes

Growing Conditions	Before Watering	After Watering	
	ψ_w, MPa	ψ_w, MPa	ψ_s, MPa
*Container plants**			
Ample water supply #1	−0.93	−0.90	−1.51
Restricted water supply #2	−2.62	−1.06	−1.61
Restricted water supply #3	−3.20	−1.20	−1.53
Field Plant, Death Valley	−6.70	−1.40	−1.73

*Eight-week-old plants, grown in the Stanford garden in 18-liter containers under ample water supply, were subjected to the different treatments for six weeks before these measurements were made in September 1979. One set of plants (#1) received continued daily watering; a second (#2) and a third (#3) received 2 liters of water per plant every three and four days, respectively. The latter treatments resulted in a gradual decline in ψ_w over the six-week period.

between the different plants. Moreover, the osmotic potentials of the leaves were not markedly different, suggesting that no pronounced osmotic adjustment had occurred in response to a declining water potential during growth.

Further evidence confirmed that the *N. oleander* plants do not increase their solute content in response to a gradually imposed water stress. Figure 23 shows the osmotic potential as a function of relative water content in leaves of three different groups of container-grown plants. The data points for all three groups closely follow the curve depicting the decrease in osmotic potential that would result from passive water loss alone. The data points for plants grown under the intermediate water supply (treatment #2) which show considerable diurnal changes in ψ_s also fell close to the predicted curve, indicating that there was no significant diurnal changes in ψ_s attributable to an active change in solute content. Finally, as shown it Table 8, both container-grown and field-grown plants subjected to different water regimes and having widely differing water status showed no significant differences in osmotic potential following equilibration of leaf discs with water-saturated air.

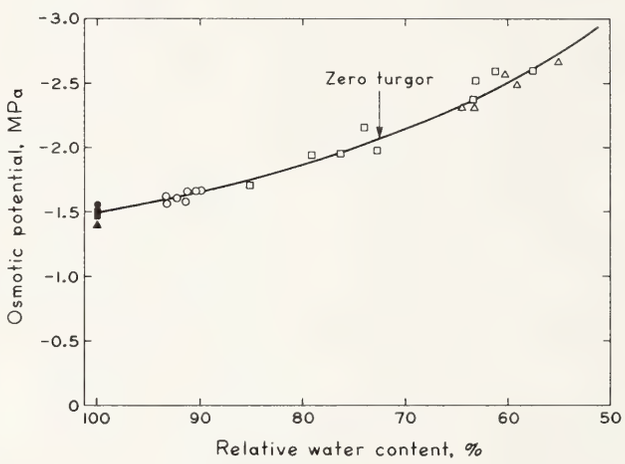


Fig. 23. Effect of growing *Nerium oleander* under different water regimes on the relationship between osmotic potential (ψ_s) and the relative water content (RWC) of the leaves. The solid line shows the calculated relationship between ψ_s and RWC, assuming that changes in ψ_s are caused by passive water loss alone. Open circles, squares, and triangles depict values for plants grown under water regimes #1, #2, and #3, respectively (see Table 7). The range of values within each treatment is caused by diurnal changes in ψ_s and RWC. The diurnal range of ψ_w was from −0.7 to −1.0 MPa for treatment #1, from −1.3 to −2.9 MPa for treatment #2, and from −2.6 to −3.1 MPa for treatment #3. Closed symbols represent values for ψ_s following equilibration of leaf discs with water-saturated air. The arrow indicates the point at which $\psi_w = \psi_s$.

Response of stomatal conductance and photosynthesis to long-term water stress. Figure 24 shows the daily course of leaf water potential and conductance (C_s) to the diffusive loss of water vapor from the leaves of plants growing under the three different water regimes. The

TABLE 8. Effect of Growing *N. oleander* under Different Levels of Water Supply on Water and Osmotic Relations of the Leaves Before and After Equilibration of Leaf Discs with Water-Saturated Air

Treatment	Before Equilibration			After Equilibration		
	ψ_w MPa	ψ_s MPa	RWC %	ψ_w MPa	ψ_s MPa	RWC %
*Container plants**						
Ample water supply #1	−0.92	−1.58	91.5	−3.1	−1.48	100
Restricted water supply #2	−2.69	−2.38	63.7	−3.2	−1.45	100
Restricted water supply #3	−3.07	−2.65	54.9	−3.0	−1.37	100
Field plants†						
Irrigated shrub	−0.53	−1.85	87.6	−3.0	−1.42	100
Unirrigated shrub #1	−1.95	−2.23	64.9	−3.2	−1.16	100
Unirrigated shrub #2	−2.97	−2.68	. . .	−3.3	−1.17	100

*Conditions were as in Table 7.

†These plants had been established in the field at Stanford for at least one year before measurements were made in September 1979. For one shrub, irrigation was continued at weekly intervals throughout the summer; for the others irrigation was discontinued in May 1979.

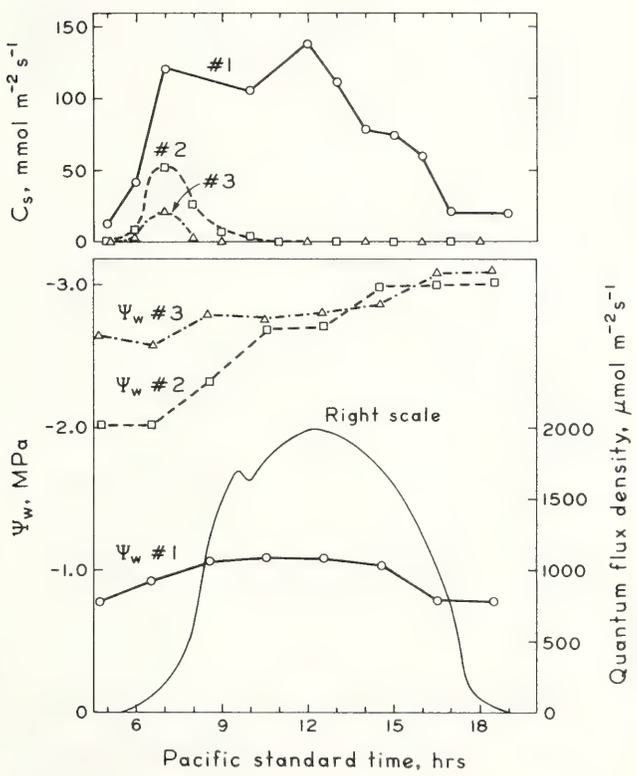


Fig. 24. Effect of growing *N. oleander* at different levels of water supply on the diurnal course of leaf conductance to water vapor exchange (C_s) and leaf water potential (ψ_w). Treatments (#1, #2, #3) were as described in Table 7. The solid line in lower part of the figure depicts the daily course of solar radiation (quantum flux density).

data shown here represent the last day in the cycle before the plants receive a limited amount of water in treatments #2 and #3. In the plant growing under ample water supply, stomata start to open very early in the morning, and C_s remains high throughout the day. Leaf water potential shows a small decline until noon, and in late afternoon returns to its morning value. In the plants growing under restricted water supply #2, partial stomatal opening occurs when there is sufficient light to drive photosynthesis, but the conductance declines again soon after the leaf water potential starts to fall, and after eleven o'clock PST stomata remain closed (C_s < 0.5 nmol m^{-2} s^{-1}) for the remainder of the day. The plants grown under treatment #3 show an even more extreme response, with stomata staying partially open for only a very brief period in the early morning. Calculations based on the daily course of C_s and the water vapor pressure difference between the leaf and the ambient air show that the daily water loss by transpiration of the plants grown under treatment #2 was about 4%, and that of plants under treatment #3 only about 1%, of the water loss by the plant grown

under ample water supply. These and other similar experiments (not shown) demonstrate that stomata exert a very close control of gas exchange in *N. oleander* plants subjected to water stress.

A comparison of the stomatal conductances and photosynthetic rates of plants grown under different water regimes is shown in Table 9. These gas exchange measurements were conducted under controlled conditions in the laboratory. As expected, C_s declined with decreasing ψ_w and there was a parallel decline in photosynthetic rate. The lower photosynthetic rate in the water-stressed plants is in part attributable to the lower intercellular CO_2 pressure resulting from the decrease in C_s. However, comparisons with the photosynthetic rate of unstressed plants at the same intercellular CO_2 pressure as those found in the stressed plants indicate that the reduction in photosynthetic rate in the stressed plants is considerably greater than can be accounted for by differences in C_s.

The results shown in Fig. 25 provide evidence that the reduction in intrinsic photosynthetic capacity found in the plants growing under water stress depends not only on the current but also on the past water status. In this experiment the rate of photosynthesis as a function of intercellular CO_2 pressure was determined on a plant grown under water stress treatment #3 following addition of ample water, permitting the leaf water potential to increase to the value found in plants grown under ample water supply. Evidently, the intrinsic photosynthetic

TABLE 9. Effect of Growing *N. oleander* under Different Levels of Water Stress on Light-Saturated Photosynthetic Rate and Stomatal Conductance

	Treatment*		
	#1	#2a	#2b
ψ_w, MPa	−0.71	−1.35	−1.78
Leaf conductance,† mmol H_2O m^{-2} s^{-1}	208	82	41
Photosynthetic rate,† μmol CO_2 m^{-2} s^{-1}	22.0	10.9	5.8
Intercellular pressure,† μbar	179	123	110
Expected photosynthetic rate,‡ μmol CO_2 m^{-2} s^{-1}	22.0	15.2	12.5

*Treatments were as described in Table 7. Columns 2a and 2b denote two different plants grown under treatment #2.

†Leaf conductance to water vapor exchange and photosynthetic rate were determined at 30°C, 330 μbar ambient CO_2 pressure, and a quantum flux density of 2000 μmol m^{-2} s^{-1}. Intercellular pressure (p_i) was calculated from the relationship $p_i = p_a - (P/C_s) \times 1.56$, where p_a is the intercellular CO_2 pressure, P the photosynthetic rate (in μmol CO_2 m^{-2} s^{-1}), C_s the leaf conductance (in mmol H_2O m^{-2} s^{-1}), and 1.56 the ratio of the diffusivity of water vapor to that of CO_2.

‡Photosynthetic rate at p_i calculated from the relationship between P and p_i for well-watered plants.

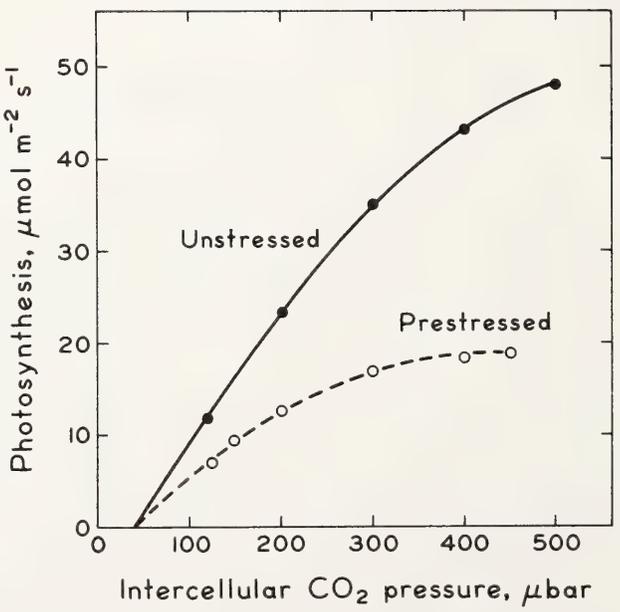


Fig. 25. Light-saturated photosynthetic rate as a function of intercellular pressure in leaves of *N. oleander*, grown under treatment #1 ("unstressed") and treatment #3 ("prestressed"). Measurements on the "prestressed" plants were made eight hours after rewatering (ψ_w = −3.3 MPa before rewatering). At the time of measurement, ψ_w was equal to −0.84 and −0.82 MPa for the "unstressed" and "prestressed" plants, respectively. Other conditions were as described in Table 9.

capacity remained considerably lower in the "prestressed" plant than in the "unstressed" plant even though at the time of these measurements the two plants had the same high water potentials. Preliminary experiments indicate that although recovery of intrinsic photosynthetic capacity in *N. oleander* plants grown under water stress commences almost immediately upon rehydration of the leaves, it would probably require several days for the photosynthetic capacity to approach that of unstressed plants.

Effect of water stress on leaf composition, RuP_2 carboxylase activity, and photosynthetic electron transport. Reduction in intrinsic photosynthetic capacity such as that found in *N. oleander* grown under water stress could a priori have several different causes. For example, prolonged water stress might slow down biosynthetic processes such as protein synthesis, leading to a reduction in the amount of photosynthetic enzymes and chlorophyll-protein complexes. Low water status could also cause an inactivation of certain component reactions of photosynthesis.

The data presented in Table 10 do not support the notion that the low intrinsic photosynthetic capacity of *N. oleander* plants after prolonged water stress is caused by a generally lower level of chloroplast constituents. There were only small differences among the different treatments in factors such as specific weight, chlorophyll, nitrogen, and soluble protein content. Likewise, the level of RuP_2 carboxylase, a potentially rate-limiting factor of photosynthesis, was little affected by water stress.

By contrast, the capacities for photosynthetic electron transport and photophosphorylation of chloroplasts isolated from water-stressed *N. oleander* plants were considerably lower than those of unstressed plants (Table 11). A substantial reduction in both of these chloroplast functions could be detected at $\psi_w = -2.28$ MPa, and it is possible that there was a significant reduction in electron transport capacity even at $\psi_w = -1.5$ MPa. The reduction became increasingly severe with decreased ψ_w, and at $\psi_w = -3.44$ the capacities of electron transport and photophosphorylation were only one third those determined for unstressed plants.

Conclusions and Discussion

These exploratory studies of the water relations of *N. oleander* confirm

TABLE 10. Effect of Growing *N. oleander* under Different Levels of Water Supply on Plant Characteristics

	Treatment*		
	#1	#2	#3
ψ_w, MPa	−0.62 to −0.77	−2.06 to −2.16	−3.25
Specific leaf dry weight, g m^{-2}	146	138	146
Chlorophyll $a + b$, mg m^{-2}	810	680	710
Nitrogen, g m^{-2}	4.11	. . .	4.10
Soluble protein, g m^{-2}	11.3	10.2	10.2
RuP_2 carboxylase,†			
μmol m^{-2} s^{-1}	170	163	146
μmol g^{-1} Chl s^{-1}	217	242	213
μmol g^{-1} soluble protein s^{-1}	15.6	16.1	14.3

*Treatments were as described in Table 7.
†RuP_2 carboxylase activity was assayed at 30 °C, according to Lorimer *et al.* (1977).

TABLE 11. Effect of Leaf Water Potential on the Activities of Light-Saturated Photosynthetic Electron Transport and Photophosphorylation by Isolated Chloroplasts*

Treatment†	ψ_w, MPa	Electron transport μmol g^{-1} Chl s^{-1}	Photophosphorylation μmol g^{-1} Chl s^{-1}
#1	−0.95	141 (100)‡	113 (100)
#2	−1.50	121 (86)	... ...
#2	−2.28	92 (65)	76 (67)
#2	−2.60	85 (60)	... ...
#3	−3.33	64 (45)	60 (53)
#3	−3.44	46 (33)	38 (33)

*Chloroplasts were prepared and whole-chain electron transport (H_2O → methylviologen) and photophosphorylation (ADP-dependent pH change) were determined at 30 °C, as described by Björkman *et al.* (*Year Book 77*, p. 269).

†Treatments were as described in Table 7.

‡Numbers in parenthesis denote percentages with respect to unstressed control.

that it is indeed highly tolerant of water stress. Contrary to expectations, no evidence for osmotic adjustment was obtained even under conditions that should be near maximal for inducing such a response. Although the lack of capability for osmotic adjustment obviously excludes the use of this species for studies of the adaptive role of osmotic adjustment, it has the advantage of removing one complication in studies of other aspects of water relations.

Stomatal regulation evidently exerts a major control of CO_2 and H_2O exchange in *N. oleander* grown under limited water supply, and such conditions render the stomata more responsive to environmental perturbations. In well-watered plants photosynthesis and transpiration follow the diurnal course of irradiance, and stomata exert a relatively small restriction on photosynthesis. With increasing water stress, gas exchange becomes restricted to shorter and shorter periods during the early part of the day. When stomata are closed no gas exchange can be detected (leaf conductance <0.5 mmol H_2O m^{-2} s^{-1} compared with ~ 400 mmol H_2O m^{-2} s^{-1} for fully open stomata). This type of response may be typical for plants native to arid habitats (see review by Osmond *et al.*, 1980). However, in *N. oleander* partial stomatal closure commences and complete closure occurs at relatively high water potentials in comparison with certain desert species such as *Larrea divaricata*, which in Death Valley appears to keep the stomata fully open at $\psi_w = -2.5$ MPa and maintains a relatively high stomatal conductance even at $\psi_w = -4.0$ MPa (Mooney *et al.*, *Year Book 76*, 328–355). This difference may at least in part be related to the absence of osmotic adjustment in *N. oleander*.

Although photosynthesis by *N. oleander* leaves under conditions of water stress is probably largely controlled by stomatal regulation, experiments show that even moderate levels of water stress cause a reduction in photosynthetic activity which cannot be accounted for by stomatal factors. This reduction in intrinsic photosynthetic capacity resembles the results obtained when plants grown under ample water supply were subjected to dehydration over periods ranging from less than one hour to several days. Such studies include those on sunflower (Boyer, 1971), *Simmondsia chinensis* (Collatz, 1977), and *Larrea divaricata* (Mooney *et al.*, *Year Book 76*, 328–335).

Growth of *N. oleander* under dif-

ferent levels of water supply had no marked effect on specific leaf weight or chlorophyll, nitrogen, soluble protein, or RuP_2 carboxylase levels, whereas the capacities of photosynthetic electron transport and photophosphorylation by isolated chloroplasts were greatly affected. The latter response resembles that observed in short-term leaf desiccation experiments by Boyer and co-workers (e.g., Keck and Boyer, 1974; Mohanty and Boyer, 1976), who found that the degree of inhibition at a given leaf water potential of intrinsic photosynthetic capacity of whole sunflower leaves was similar to the inactivation of electron transport and photophosphorylation of isolated chloroplasts. These results suggest that water stress, by some yet unknown mechanism, inactivates noncyclic electron transport and photophosphorylation; as a consequence, the overall photosynthetic activity is also reduced. The present results indicate that such an inactivation may also be responsible for the differences in intrinsic photosynthetic capacity of leaves of *N. oleander* grown under the different levels of water supply.

These exploratory studies indicate that *N. oleander* would provide a suitable experimental material for our planned investigations of interactions of different stress factors on the photosynthetic system. Studies on the relationship between the effects of irradiance and water status have now been initiated.

References

Boyer, J. S., *Plant Physiol., 48,* 523–536, 1971.
Collatz, G. J., *Planta, 134,* 127–132, 1977.
Keck, R. W., and J. S. Boyer, *Plant Physiol., 53,* 474–479, 1974.
Mohanty, P., and J. S. Boyer, *Plant Physiol., 57,* 704–709, 1976.
Osmond, C. B., O. Björkman, and D. J. Anderson, *Physiological Processes in Plant Ecology,* Springer, Berlin, Heidelberg, New York, 1980.

INTERACTION BETWEEN LIGHT INTENSITY AND CHILLING TEMPERATURES ON INHIBITION OF PHOTOSYNTHESIS IN CHILLING-SENSITIVE PLANTS

Stephen B. Powles, Joseph A. Berry, and Olle Björkman

It is well established that leaves of higher plants may be damaged if they are exposed to light intensities that far exceed their capacity to dissipate the absorbed light energy. One of the first signs of such damage is a reduction of the quantum yield of photosynthesis. The process is commonly called photoinhibition. Plants may suffer photoinhibition if illuminated in normal air at light intensities greatly exceeding that required to saturate photosynthesis (Björkman and Holmgren, 1963; Powles and Critchley, 1980) or if illuminated at moderate light intensities under conditions in which the photosynthetic carbon metabolism reactions are restricted by low CO_2 partial pressures (Powles and Critchley, 1980).

Exposure of so-called chilling-sensitive plants to low temperatures (0° to 12°C) is also known to result in damage to the photosynthetic apparatus (Levitt, 1980), and some studies indicate that this damage is aggravated by high light intensities (Taylor and Rowley, 1971). Since exposure to low temperatures is known to restrict the light-saturated photosynthetic capacity greatly, it seemed possible that chilling injury may, in part, be a result of photoinhibition and photooxidative reactions. The present study was undertaken to explore the interaction between light intensity and temperature on damage to the photosynthetic apparatus in chilling-sensitive plants.

Plants were grown from seed in the

department phytocells under 25°/20°C temperatures during the late spring months when light intensities regularly reached quantum fluxes of 2000 μmol quanta m^{-2} s^{-1}. CO_2 and H_2O vapor gas-exchange measurements were made on intact attached fully expanded leaf material from plants approximately 35 days from seeding. In each experiment the apparent quantum yield was determined by measuring the rates of CO_2 assimilation at a range of low light intensities. The light intensity was then increased to 2000 μmol quanta m^{-2} s^{-1}, and a constant CO_2 assimilation rate in air at 25°C was achieved. The required leaf temperature was then obtained by regulating the temperature of the leaf chamber. The exposure to the chilling temperature was for 3 h, during which the leaf was in normal air (330–340 μbar CO_2, 210 mbar O_2). Immediately after the treatment period, the light intensity was reduced to approximately 400 μmol quanta m^{-2} s^{-1} and the leaf temperature increased to 25°C. These conditions were maintained for 1 h, and the apparent quantum yield was then redetermined under the same conditions as those before the treatment.

The effect of a 3-h pretreatment of an intact attached bean leaflet (*Phaseolus vulgaris* L.; W. Hawkesbury Wonder) with a light intensity of 2000 μmol quanta m^{-2} s^{-1} (full sunlight) and a leaflet temperature of 6°C is shown in Fig. 26. The apparent quantum yield of the leaf was substantially inhibited following this treatment. When a similar experiment was conducted but at a very low light intensity (70 μmol quanta m^{-2} s^{-1}) there was no inhibition of the subsequent quantum yield (Fig. 27). It appears that the inhibition of the subsequent photosynthetic capacity is caused by the presence of light of high intensity throughout the period of exposure to a chilling temperature. Results similar to those shown in Figs. 26 and 27 have been obtained with intact attached leaves of the chill-

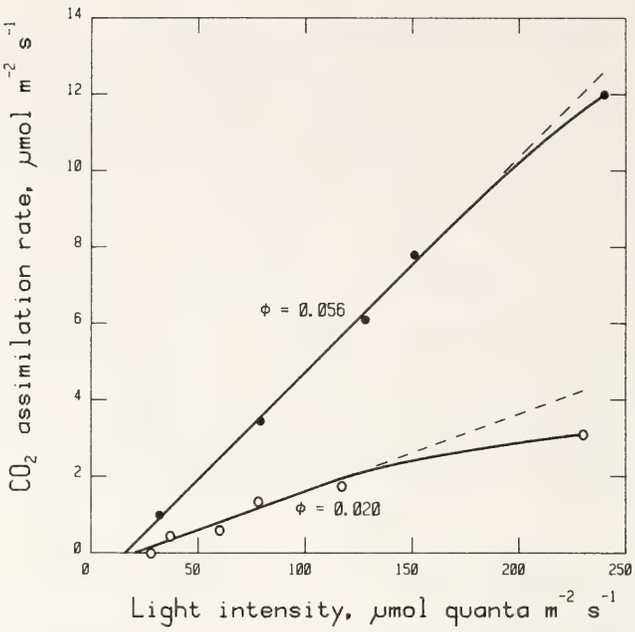


Fig. 26. Effect of a 3-h exposure to illumination at a light intensity of 2000 μmol quanta m^{-2} s^{-1} at a leaflet temperature of 6°C (normal air) on the apparent quantum yield of an intact attached bean leaflet. (●): before treatment; (○): after treatment. Measurements were made in 500 μbar CO_2, 10 mbar O_2, at 25°C.

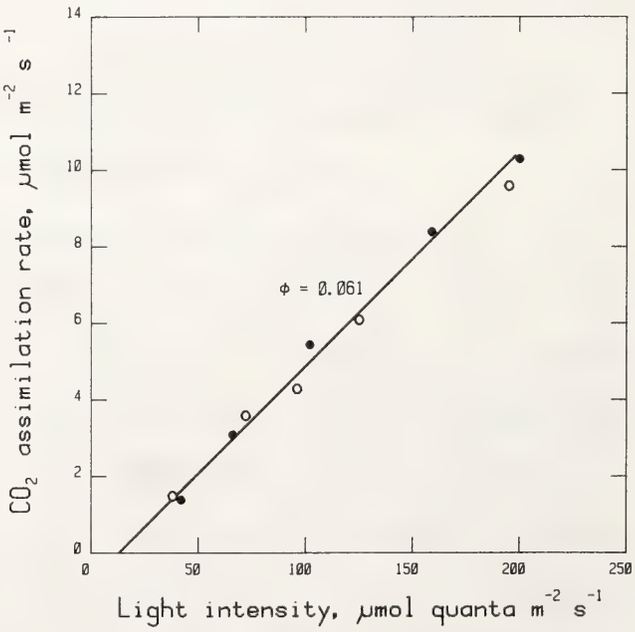


Fig. 27. Effect of a 3-h exposure to a leaflet temperature of 5.5°C (normal air) at a low light intensity (70 μmol quanta m^{-2} s^{-1}) on the apparent quantum yield of an intact attached bean leaflet. (●): before treatment; (○): after treatment.

ing-sensitive plants, *Gossypium hirstum* and *Xanthium strumarium.*

In all experiments the low-temperature treatments lead to a subsequent reduction in stomatal conductance, but this reduction does not account for the observed inhibition of apparent quantum yield. The inhibition observed in the experiments occurred without any bleaching of chlorophyll pigments and without any signs of visible injury to the treated leaf material. Treated leaves recovered their prior photosynthetic capacity over a period of 24–48 h if returned to the glasshouse (at 25 °C and moderate light intensities); the time course and characteristics of the recovery of photosynthesis require detailed investigation. The inhibition observed when the leaf material was treated in the presence of a high light intensity and at 6 °C in air (210 mbar O_2) was much less if only 10 mbar O_2 (1%) was present throughout the 3-h treatment period (330 μbar CO_2 in nitrogen plus 10 mbar O_2). This result suggests the involvement of photooxidative reactions in this inhibition phenomenon.

That the inhibition of the apparent quantum yield observed in Fig. 26 is a light-dependent process can also be seen from the experiments illustrated in Fig. 28. In these experiments the leaflets were subjected to a 3-h treatment at a leaflet temperature of 5.5 °C in air, and each experiment was conducted at a different light intensity. Leaflets illuminated at or below 620 μmol of quanta m^{-2} s^{-1} throughout the treatment period showed no inhibition of the subsequent apparent quantum yield, whereas when the treatment occurred at a higher light intensity the percentage inhibition of the quantum yield rose in proportion to the light intensity maintained throughout the treatment period.

The inhibition of the apparent quantum yield observed when intact attached bean leaflets were illuminated while at chilling temperatures is a

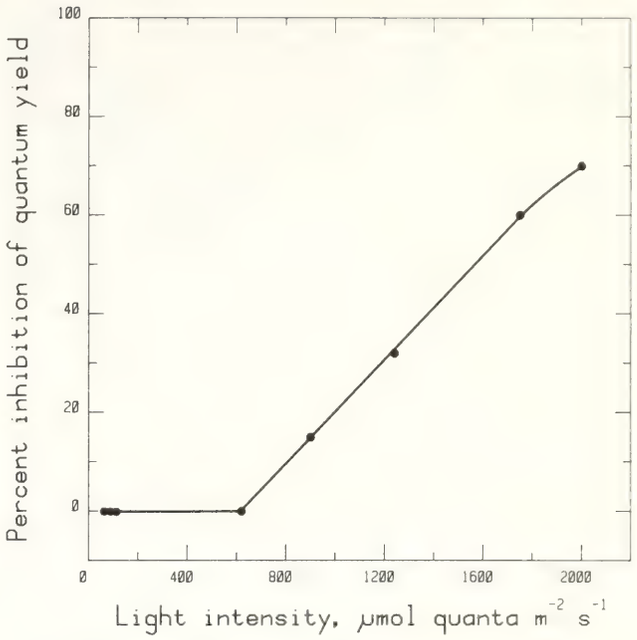


Fig. 28. Effect of the light intensity maintained throughout a 3-h exposure to a leaflet temperature of 5.5 °C (normal air) on inhibition of the apparent quantum yield. Reduction of the apparent quantum yield for each experiment was calculated from light response curves as shown in Fig. 26.

temperature-dependent phenomenon. Figure 29 illustrates the results of experiments in which intact bean leaflets were illuminated at 2000 μmol quanta m^{-2} s^{-1} for 3 h (in air) while the leaflet temperature was held constant. No inhibition of the subsequent apparent quantum yield occurred if the treatment was at a leaflet temperature of 11.5 °C or higher. At leaflet temperatures less than 11.5 °C inhibition did occur, and treatment at the lowest leaflet temperature (5 °C) led to the greatest inhibition of the quantum yield.

These results establish that exposure of intact leaves of chilling-sensitive plants to chilling temperatures in normal air leads to a light-dependent inhibition of subsequent photosynthetic capacity. This inhibition did not occur unless the low-temperature treatment was accompanied by a moderate-to-high light intensity. These experiments are in agreement with reports by Taylor and Rowley (1971)

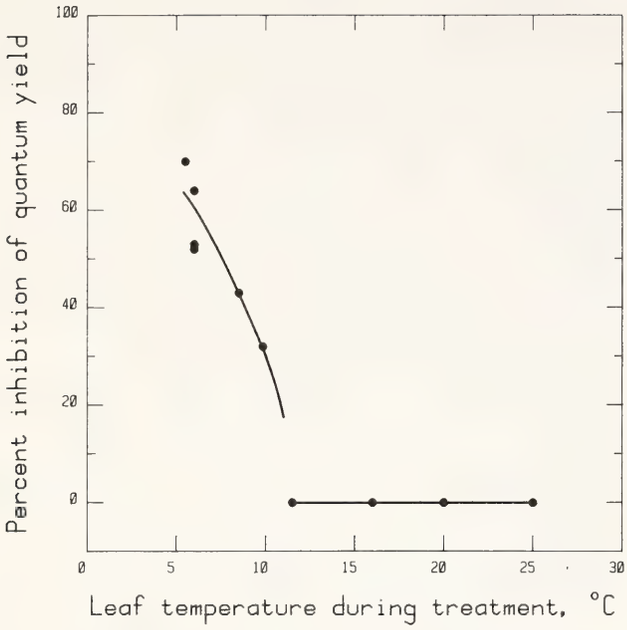


Fig. 29. Effect of the leaflet temperature maintained throughout a 3-h exposure to a light intensity of 2000 μmol m^{-2} s^{-1} (normal air) on inhibition of the apparent quantum yield. Percentage inhibition was calculated as in Figure 28.

and Lasley *et al.* (1979) that light is involved in the expression of chilling injury. Figures 28 and 29 provide quantitative data related to this light-chilling temperature interaction. The observations that the inhibition is lessened at low O_2 partial pressures suggests that photooxidative reactions are involved. Further experiments are required to assess the role of O_2 in the expression of this phenomenon. Studies employing isolated chloroplasts and protoplasts from leaves of chilling-sensitive species subject in vivo and in vitro to illumination at chilling temperatures may be useful in assessing the chloroplast reactions inhibited following treatment and the molecular mechanism involved in the expression of this phenomenon. Of particular relevance is consideration of the degree to which photoinhibitory and photooxidative reactions are involved.

Additional studies of the chilling-temperature–light interaction are being conducted with species that do not exhibit chilling injury at temperatures between 0° and 12°C. The similarities and differences between these two groups of plants in terms of their ability to maintain substantial rates of photosynthesis at low temperatures and their tolerance to high light intensities remain to be assessed.

References

Björkman, O., and P. Holmgren, *Physiol. Plant., 16,* 889–914, 1963.

Lasley, S. E., M. P. Garber, and C. F. Hodges, *HortScience, 104,* 447–480, 1979.

Levitt, J., *Responses of Plants to Environmental Stresses.* Vol. 1, Academic Press, 1980.

Powles, S. B., and C. Critchley, *Plant Physiol., 65,* 1181–1187, 1980.

Taylor, A. O., and J. A. Rowley, *Plant Physiol., 47,* 713–718, 1971.

PHOTOSYNTHETIC PERFORMANCE OF ISOLATED LEAF CELLS FROM SUN AND SHADE PLANTS

Geoffrey W. Harvey

Leaves developed in shaded microclimates have much lower photosynthetic capacities than those developed in full sunlight. There is convincing evidence for biochemical disparities between sun and shade leaves (Björkman, 1968; Björkman *et al.,* 1973). However, microscopic examination demonstrates that there are also anatomical differences between such leaves. Internal mesophyll surface area exposed to the intercellular air spaces is much greater in thicker sun leaves (Nobel *et al.,* 1975; Nobel, 1976). Nobel suggests the resultant decrease in mesophyll resistance accounts for the superiority of sun leaf photosynthetic capacity.

Techniques for enzymatic macera-

tion of leaves and isolation of viable cells have improved in recent years (Rehfeld and Jensen, 1973; Collatz and Badger, *Year Book 77,* 245–247). The methodology allows dissolution of anatomical integrity and isolation of photosynthetically active leaf cells. Techniques of cell isolation have been applied to the resolution of the relative contributions of biochemical and anatomical differences to the photosynthetic capacity of sun-developed and shade-developed leaves. The light-response characteristics of isolated cells from the sun-adapted plant *Atriplex triangularis (Atriplex patula)* and the shade-adapted plant *Asarum caudatum* have been compared. Light-response characteristics of isolated cells from *Atriplex* leaves acclimated to different quantum doses were compared.

Materials and Methods

Atriplex triangularis was grown in phytocell A (Björkman *et al., Year Book 72,* 393–403) with a 30 °C day and 20 °C night temperature (thermoperiod 16–8 h) at 70% relative humidity. Illumination was entirely solar. Individual plants were placed in covered cages with neutral-density screening of varying thicknesses. Cages provided average quantum doses of 4450, 1450, and 600 μmol cm^{-2} day^{-1}. The different treatments will be referred to as high, intermediate, and low quantum dose, respectively. *Asarum caudatum* leaves were collected from a population growing in a deeply shaded area near the Carnegie laboratory.

Carbon dioxide gas exchange measurements were performed as outlined earlier by Ehlringer and Björkman (1978). Leaves of *Atriplex* and *Asarum* were enzymatically macerated and cells were isolated using a slight modification of the technique reported by Collatz and Badger (*Year Book 77,* 245–247). Sodium ascorbate (5 mM) was incorporated into all but the assay and final storage buffers. Storage and assay buffers contained 5 mM $MgCl_2$. Cells could be stored for up to 48 h under light at 4 °C without significant loss of photosynthetic activity.

Bicarbonate-dependent oxygen evolution was measured in a 2-ml sample of assay buffer containing 30 μg chlorophyll as isolated cell suspension and made 15 mM in $NaHCO_3$ (970 μM CO_2) to initiate the reaction. Oxygen exchange was measured with a Rank oxygen electrode (Rank Brothers, Bottisham, Cambridge, England).

Absolute methanol was used for extraction and estimation of chlorophyll. The equations of Holden (1965), based upon the extinction coefficients determined by McKinney (1941), were used for calculation of chlorophyll content.

Results

Asarum caudatum (wild ginger) flourishes in densely shaded areas under stands of coastal redwood (*Sequoia sempervirens*). The photosynthetic light response characteristics of *Asarum* leaves are similar to the redwood shade species studied by Björkman (1968) (Fig. 30). By contrast, and as expected, the light-response behavior of *Atriplex* leaves is similar to that previously reported for this species by Björkman (1973) and for other sun plants (Björkman, 1968).

Photosynthetic rates of isolated cells are roughly one third those of intact leaves on a chlorophyll basis. However, the light-response curves of isolated cells parallel the analogous curves developed by measuring CO_2 uptake of intact leaves (Fig. 31). *Asarum* has a lower light compensation point than *Atriplex* because of lower dark respiration and becomes light saturated at lower light intensities. Light-saturated photosynthetic capacity is modest in *Asarum* compared to *Atriplex.*

Comparison of sun and shade plant cells suggests that cytological and biochemical peculiarities of the cells themselves underlie the very different

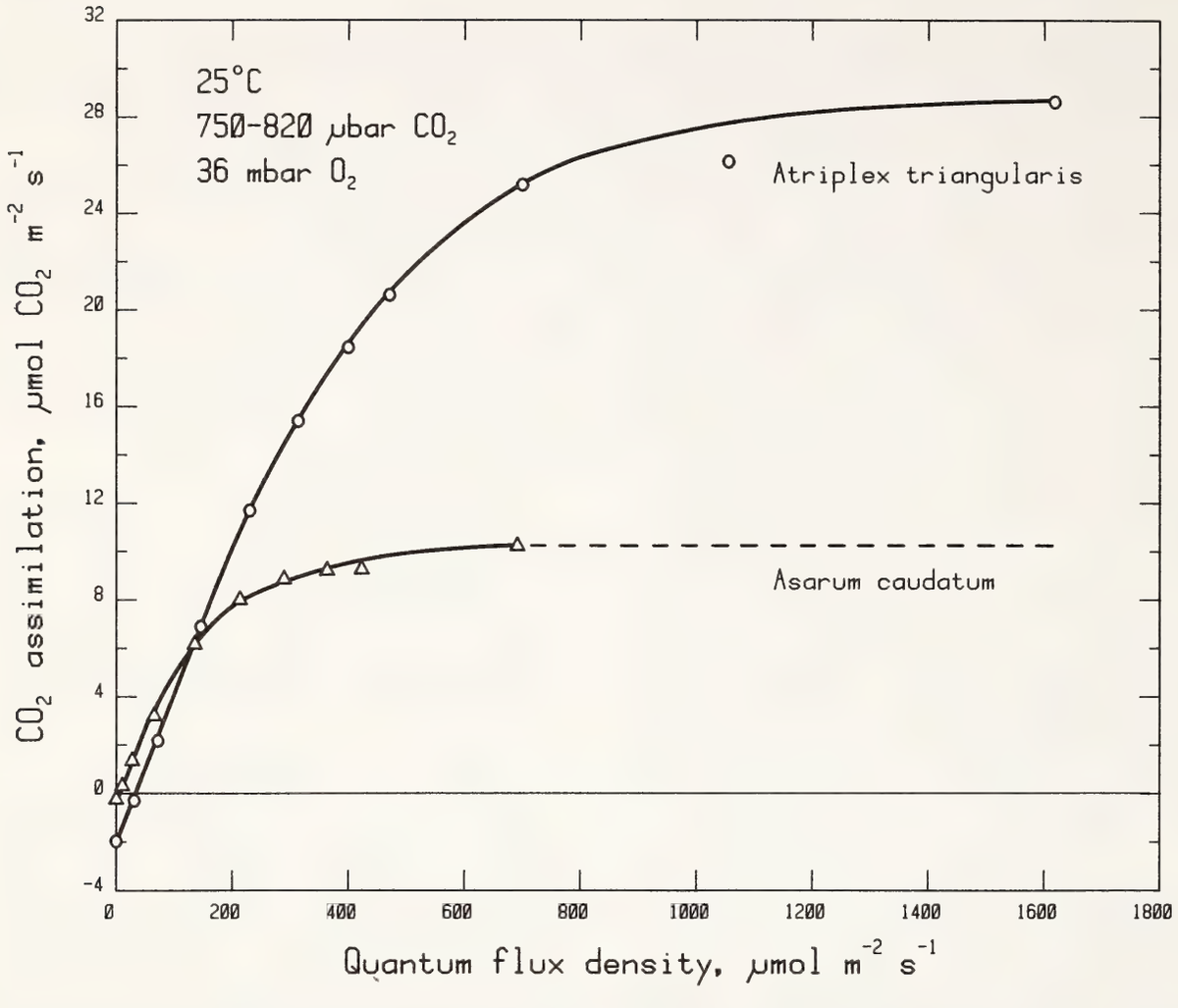


Fig. 30. Photosynthetic light response curves of intact leaves of the sun plant *Atriplex triangularis* and the shade plant *Asarum caudatum*. Photosynthetic rate was measured as carbon dioxide uptake.

photosynthetic capacities. A test of this hypothesis was made by applying the same approach to the sun plant *Atriplex triangularis (Atriplex patula)* grown with differing quantum doses. Björkman and co-workers (*Year Book 71,* 115–135) conclusively demonstrated that *Atriplex* leaves acclimated to light environments of low quantum dose assume the light-response character of shade leaves. Light-response curves of leaf cells developed under conditions of high, intermediate, and low quantum dose (Fig. 32) are very similar to the carbon dioxide exchange curves for intact leaves reported earlier (Björkman *et al., Year Book 71,* 115–135). One minor difference is apparent. Essentially no differences in light compensation point was found for isolated leaf cells. In other respects the curves are similar, indicating that the biochemical and cytological features of the cells dictate the leaves' photosynthetic capacity.

Discussion

The character of the light-response curves of *Asarum* and *Atriplex* is conserved in the leaf cells even though leaf anatomy has been destroyed. However, the possibility of species-dependent differences in damage related to cell isolation in *Asarum* and *Atriplex* cells must be discounted if the conclusions are valid. The most convenient method

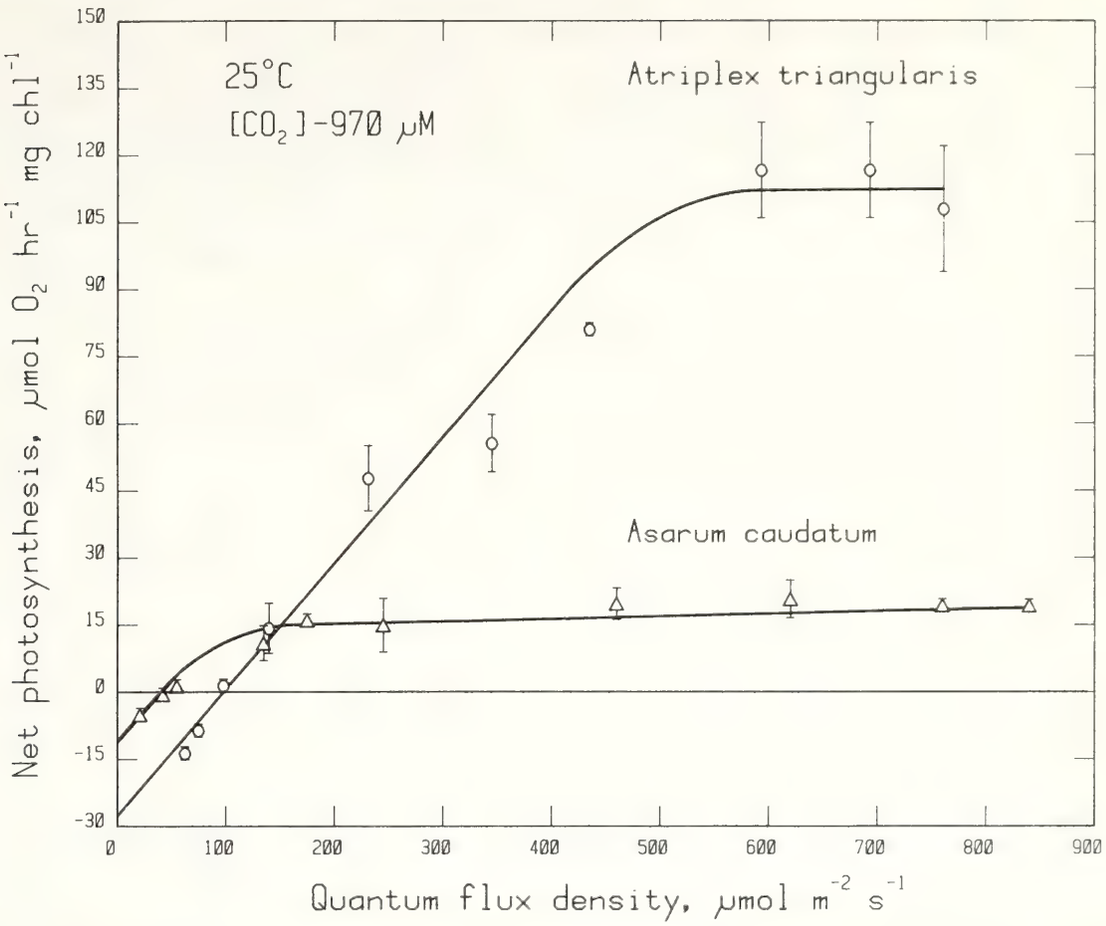


Fig. 31. Photosynthetic light response curves of isolated leaf cells from the sun plant *Atriplex triangularis* and the shade plant *Asarum caudatum.* Photosynthesis is measured as bicarbonate-dependent oxygen evolution. Techniques of plant culture and photosynthetic assay are detailed in the methods. Error bars represent standard deviation. Oxygen concentration was 4–6%.

of eliminating this possibility was to study a single species grown under conditions of varying quantum dose. When leaf anatomy is abolished by maceration, the isolated leaf cells retain light-response curves very similar to those developed by measuring carbon dioxide exchange of the intact leaves (Björkman *et al., Year Book 71,* 115–135). The *Atriplex* light-response curves derived from isolated cells do not have different light compensation points, in contrast to the curves from intact leaves (Björkman *et al., Year Book 71,* 115–135). The lack of distinct compensation points is explained by two differences. Cell suspensions with identical chlorophyll content have uniform absorptivity, while leaves developed with different quantum doses vary in thickness and absorptivity (Björkman *et al., Year Book 71,* 115–135). The slightly elevated respiratory rates of isolated leaf cells shift the light compensation points to higher quantum flux.

The results demonstrate that differences in internal cell surface area can account for little of the difference in photosynthetic capacity of sun and shade leaves of *Atriplex* and *Asarum.* Since isolated intact leaf cells exhibit nearly the same light-response characteristics of the intact leaf, biochemical and cytological differences between these sun and shade leaves must account for the majority of their disparate photosynthetic capacities.

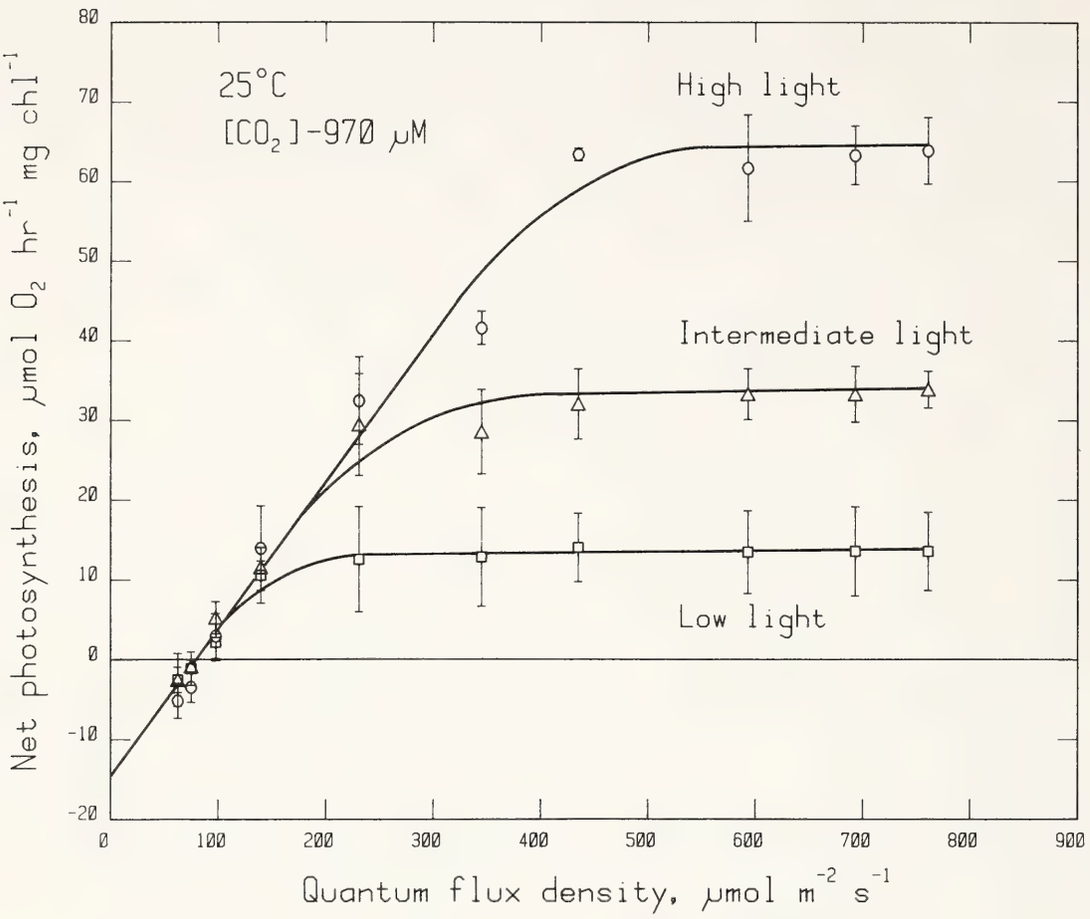


Fig. 32. Photosynthetic light response curves of isolated leaf cells from *Atriplex triangularis* grown under conditions of high, intermediate, and low quantum doses as outlined in the methods. Photosynthesis is measured as bicarbonate-dependent oxygen evolution. Error bars represent standard deviation. Oxygen concentration was 4–6%.

References

Björkman, O., *Physiol. Plant., 21,* 1–10, 1968.

Björkman, O., in *Photophysiology,* Vol. 8, 1–63, A. Geise, ed., Academic Press, New York, 1973.

Ehlringer, J. R., and O. Björkman, *Plant Physiol., 62,* 185–190, 1978.

Holden, M., in *Chemistry and Biochemistry of Plant Pigments,* 461–488, T. W. Goodwin, ed., Academic Press, New York, 1965.

McKinney, G., *J. Biol. Chem., 140,* 312–315, 1941.

Nobel, P. S., L. J. Zaragoza, and W. K. Smith, *Plant Physiol., 55,* 1067–1070, 1975.

Nobel, P. S., *Plant Physiol., 58,* 218–223, 1976.

Rehfeld, R. W., and R. G. Jensen, *Plant Physiol., 52,* 1973.

CHROMOSOME NUMBERS IN AUSTRALIAN SPECIES OF *Atriplex*

Malcolm A. Nobs

During the preparation of the manuscript for *Physiological Processes in Plant Ecology: Toward a Synthesis with* Atriplex (C. B. Osmond, Olle Björkman, and D. J. Anderson, 1980), it became evident that the cytogenetics are reasonably well known for many Eurasian and North American members of the *Atriplex* genus, but chromosome counts were available for only four of the species found in Australia. Since Australia, with more than 50 en-

demic species, is a major center of diversity for the genus, knowledge of the cytogenetics of the Australian taxa is essential to gaining an understanding of evolutionary relationships of the genus. During the past year a concentrated effort has been made to acquire such information.

Most of the plant material used in the present study was obtained from this author's extensive field collections; other material was obtained from experimental cultures of the Western Australia Department of Agriculture and from cultures growing in King's Park Botanical Garden, Perth, or the National Botanical Garden, Canberra. All species were identified by this author. The identifications were kindly verified by Dr. Hj. Eichler, Director of Herbarium Australiense, C.S.I.R.O., Canberra. Vouchers of each taxon for which chromosome counts were made will be deposited with the Dudley Herbarium of the California Academy of Sciences, San Francisco, Herbarium Australiense, C.S.I.R.O., Canberra, and the National Herbarium of Western Australia, Perth.

Chromosome counts with two exceptions were made on acetocarmine squash preparations of pollen mother cells previously fixed in acetic acid/ethanol. These cells were either fixed in the field or from cultures raised from seed in the greenhouses at the Research School of Biological Sciences, Australian National University, Canberra.

Chromosome counts for a total of 127 populations of 40 *Atriplex* species are shown in Table 12. Twenty-nine species (82 populations) are annuals or herbaceous perennials, of which two species (8 populations) are almost certainly northern hemisphere introductions, and the remainder endemic to Australia. Eleven species (45 populations) are woody perennials, all endemic. As also illustrated in Fig. 33, the chromosome complement in Australian *Atriplex* ranges from diploid to octoploid. No aneuploidy or deviation from the base number $n = 9II$ was found. With the exception of polyploid interspecific hybrids (discussed below), meiosis was completely regular in all cases.

All 27 endemic herbaceous species examined in this study (about two thirds of the Australian herbaceous *Atriplex*) were monoecious and diploid. The consistent diploidy of these Australian species contrasts strikingly with North American and Eurasian annual species, in which polyploidy is frequent. Apparently, there exist strong zygotic barriers to gene exchange between the Australian herbaceous species, for usually from three to eight such species grow intermixed in the same locale with overlapping flowering times, yet there was no evidence of hybrid individuals.

Although the woody perennials compose only about 20% of the total number of species endemic to Australia, many are very widely distributed and constitute a major element in the vast chenopod range lands of semiarid shrub-steppe vegetation of Australia. Like their North American counterparts, all of these woody perennial species are predominantly dioecious, although all species occasionally bear both male and female flowers in the same inflorescence.

Chromosome counts were obtained for all of the woody perennial species with the exception of *A. humile* F. Muell. Unfortunately, counts for only a single population each of *A. hymenetheca* and *A. hypoleuca* could be obtained. The chromosome numbers among the woody perennial species ranged from diploid to octoploid. *A. stipitata*, which was sampled throughout its wide range of distribution, was diploid without exception. *A. bunburyana* and *A. cinerea* were uniformly hexaploid and *A. nummularia*, *A. incrassata*, and *A. rhagoidiodes* were uniformly octaploid. The widely distributed and the most polymorphic

TABLE 12. Chromosome Numbers in Australian *Atriplex*

Species	Culture No.	Source	S. Lat.	E. Long.	Chromosome No., *n*
Annuals and Herbaceous Perennials					
A. acutibractea Anderson	1608	Port Augusta, S.A.	32° 30′	137° 46′	9^{II}
	1542 (C28)	Cunderdin, W.A.	31° 37′	117° 14′	9^{II}
	M666 (C29)	Cocklebiddy, W.A.	32° 02′	126° 06′	9^{II}
	1689	13 km W. of Lake Hart, S.A.	31° 10′	136° 10′	9^{II}
	M678 (C42)	Eyre Highway, S.A.	...	...	9^{II}
A. angulata Benth.	1517	25 km S. of Fowlers Gap, N.S.W.	31° 50′	141° 40′	9^{II}
	1519	Bijerkerno, N.S.W.	31° 25′	141° 40′	9^{II}
	1611	10 km N. of Quorn, S.A.	32° 13′	138° 08′	9^{II}
	1675	Evelyn Downs, S.A.	28° 12′	134° 29′	9^{II}
A. conduplicata F. Muell.	1515	30 km NE. of Penarie, N.S.W.	34° 15′	143° 49′	9^{II}
	1612	10 km N. of Quorn, S.A.	32° 13′	138° 08′	9^{II}
A. eardleyae Aellen (*A. campanulata* Benth.)	1522 (20)	Fowlers Gap, N.S.W.	31° 05′	141° 42′	9^{II}
	1571	Southern Cross, W.A.	31° 14′	119° 19′	9^{II}
	1594	8 km SE. of Port Pirie, S.A.	33° 14′	138° 07′	9^{II}
	1609	10 km NE. of Port Augusta, S.A.	32° 28′	137° 50′	9^{II}
	1631	Marree, S.A.	29° 39′	138° 04′	9^{II}
A. eichleri Aellen	1624	Lyndhurst, S.A.	30° 17′	138° 21′	9^{II}
	1633	Marree, S.A.	29° 39′	138° 04′	9^{II}
A. elachophylla F. Muell.	1650	Kulgera, N.T.	25° 50′	133° 18′	9^{II}
	1656	Alice Springs, N.T.	23° 42′	133° 52′	9^{II}
	1662	Alice Springs, N.T.	23° 42′	133° 52′	9^{II}
	1682	Coober Pedy, S.A.	29° 01′	134° 45′	9^{II}
A. fissivalvis F. Muell.	1526	Fowlers Gap, N.S.W.	31° 05′	141° 04′	9^{II}
A. holocarpa F. Muell.	1521	25 km S. of Bijerkerno, N.S.W.	31° 25′	144° 40′	9^{II}
	1623	Lyndhurst, S.A.	30° 17′	138° 21′	9^{II}
A. inflata F. Muell.	1508 (C14)	Hay, N.S.W.	34° 30′	144° 51′	9^{II}
	1572	Southern Cross, W.A.	31° 14′	119° 19′	9^{II}
	1718	Stephens Creek, N.S.W.	31° 50′	141° 31′	9^{II}
A. intermedia Anderson	1518	25 km S. of Bijerkerno, N.S.W.	31° 25′	144° 40′	9^{II}
	1680	57 km S. of Mt. Barry Stn. S.A.	28° 41′	134° 52′	9^{II}
A. kochiana Maiden	1641	65 km N. of Williams Ck., S.A.	28° 34′	135° 44′	9^{II}
A. leptocarpa F. Muell.	1501	40 km E. of Hay, N.S.W.	34° 30′	145° 16′	9^{II}
	1502	40 km E. of Hay, N.S.W.	34° 30′	145° 16′	9^{II}
	1714	50 km W. of Hillston, N.S.W.	33° 21′	145° 08′	9^{II}
A. limbata Benth.	1516 (C26)	Broken Hill, N.S.W.	31° 58′	141° 27′	9^{II}
	1626	Mt. Lyndhurst Stn., S.A.	30° 11′	138° 43′	9^{II}
	1651	Kulgera, N.T.	25° 50′	133° 18′	9^{II}
	1654	Alice Springs, N.T.	33° 42′	133° 52′	9^{II}
	1657	Alice Springs, N.T.	33° 42′	133° 52′	9^{II}
A. lindleyi Moq.	1531 (C17)	Broken Hill, N.S.W.	31° 58′	141° 27′	9^{II}
	1706	18 km NW. of Swan Hill, Vic.	35° 12′	143° 22′	9^{II}
	M.513 (C40)	Pingrup, W.A.	33° 32′	118° 30′	9^{II}
A. lobativalvis F. Muell.	1661	S. of Sewerage Farm, Alice Springs, N.T.	32° 42′	133° 52′	9^{II}
A. macropterocarpa (Aellen) Hj. Eichler	1618	36 km S. of Leigh Creek, S.A.	30° 46′	138° 20′	9^{II}
	1627	Mt. Lyndhurst Stn., S.A.	30° 11′	138° 43′	9^{II}
	1635	Bopeechee, S.A.	29° 36′	137° 23′	9^{II}
	1678	38 km S. of Mt. Barry Stn., S.A.	28° 30′	135° 00′	9^{II}
A. morrissii Anderson	1625	Lyndhurst, S.A.	30° 17′	138° 21′	9^{II}
A. pseudocampanulata Aellen	1503	50 km E. of Hay, N.S.W.	34° 30′	145° 26′	9^{II}
	1511 (C14)	10 km SW. of Oxley, N.S.W.	34° 12′	144° 06′	9^{II}

TABLE 12. Continued.

Species	Culture No.	Source	S. Lat.	E. Long.	Chromosome No., *n*
A. pumilio R. Br.	1573	Southern Cross, W.A.	31° 14′	119° 19′	9^{II}
	1701	Murrayville, Vic.	35° 16′	141° 11′	9^{II}
A. quadrivalvata Diels. var *sessilifolia* (Ising) Ising	1667	Wintinna, S.A.	27° 37′	133° 53′	9^{II}
	1676	Evelyn Downs, S.A.	28° 12′	134° 29′	9^{II}
A. quinii F. Muell.	1684	45 km S. of Coober Pedy, S.A.	29° 19′	134° 45′	9^{II}
	1674	22 km NW. of Evelyn Downs, S.A.	28° 01′	134° 29′	9^{II}
A. semibaccata R. Br.	1539	Meckering, W.A.	31° 37′	117° 01′	9^{II}
	1700	Murrayville, Vic.	35° 16′	141° 11′	9^{II}
A. semilunaris Aellen	M.838 (C48)	Winchester, W.A.	29° 46′	115° 56′	9^{II}
	1576	Southern Cross, W.A.	31° 14′	119° 19′	9^{II}
A. spongiosa F. Muell.	1521	Bijerkerno, N.S.W.	31° 25′	141° 40′	9^{II}
	1544 (C52)	Ejanding, W.A.	31° 01′	117° 06′	9^{II}
	1634	Bopeechee, S.A.	29° 36′	137° 23′	9^{II}
A. suberecta Verdoorn	1504 (C24)	Hay, N.S.W.	34° 30′	144° 51′	9^{II}
	1530 (C25)	Broken Hill, N.S.W.	31° 58′	141° 27′	9^{II}
	1570	Southern Cross, W.A.	31° 14′	119° 19′	9^{II}
	1699	Murrayville, Vic.	35° 16′	141° 11′	9^{II}
A. turbinata (Anderson) Aellen	1620	Lyndhurst, S.A.	30° 17′	138° 21′	9^{II}
	1644	Mt. Dutton, S.A.	27° 48′	135° 41′	9^{II}
	1673	San Marino, S.A.	28° 01′	134° 29′	9^{II}
	1629B	Marree, S.A.	29° 39′	138° 04′	9^{II}
A. velutinella F. Muell.	1617	36 km S. of Leigh Creek, S.A.	30° 46′	138° 20′	9^{II}
	1622	Lyndhurst, S.A.	30° 17′	138° 21′	9^{II}
	1690	Lake Hart, S.A.	31° 13′	136° 24′	9^{II}
Northern Hemisphere Introductions					
A. triangularus Willd.	1536	Swan River, Perth, W.A.	31° 57′	115° 51′	9^{II}
	1560	Fremantle, W.A.	32° 03′	115° 44′	9^{II}
	1579	Tooradin, Vic.	38° 13′	145° 23′	9^{II}
	1584	Pt. Wilson Bird Sanctuary, Vic.	38° 12′	145° 23′	9^{II}
	1585	Pt. Wilson Bird Sanctuary, Vic.	38° 12′	145° 23′	9^{II}
	1592	Lake Colac, Vic.	38° 21′	143° 35′	9^{II}
	1711	Durras, N.S.W.	35° 40′	150° 18′	9^{II}
A. australasica Moq. (*A. patula* L.)	1713	Oakley Beach, N.S.W.	35° 41′	150° 18′	18^{II}
Woody Perennials					
A. bunburyana F. Muell.	1549	9 km E. of Ejanding, W.A.	30° 57′	117° 23′	27^{II}
	1551	Wallambin Lake, W.A.	30° 59′	117° 35′	27^{II}
A. cinerea Poir.	1534	Kiola Beach, N.S.W.	35° 33′	150° 23′	27^{II}
	1583	Mordialloc, Vic.	38° 03′	145° 05′	27^{II}
	1586	Avalon Beach, Vic.	38° 06′	144° 29′	27^{II}
	1590	Avalon Salt Marsh, Vic.	38° 06′	144° 29′	27^{II}
	1593	8 Mile Creek, S.A.	38° 04′	140° 39′	27^{II}
A. hymenotheca Moq.	1538	Meckering, W.A.	31° 37′	117° 01′	9^{II}
A. hypoleuca Nees.	1537	Swan River, Perth	31° 57′	115° 51′	9^{II}
A. incrassata F. Muell.	1628	Mt. Lyndhurst Stn., S.A.	30° 12′	138° 43′	36^{II}
	1647	8 km SW. of Oodnadatta, S.A.	27° 38′	135° 35′	36^{II}
	1629	Marree, S.A.	29° 39′	138° 04′	36^{II}
A. nummularia Lindl.	1500	National Bot. Gardens, Herbarium, A.C.T.	(#752193, planted)		36^{II}
	1512	4 km S. of Oxley, N.S.W.	34° 15′	144° 04′	36^{II}
	1529	Broken Hill, N.S.W.	31° 58′	141° 27′	36^{II}
	1546	Ejanding, W.A.	31° 01′	117° 06′	36^{II}
	1653	Alice Springs, N.T.	23° 42′	133° 52′	36^{II}

TABLE 12. Continued.

Species	Culture No.	Source	S. Lat.	E. Long.	Chromosome No., *n*
A. paludosa R. Br.	1559	King's Park, Perth, W.A.	(604 72, planted)		27^{II}
	1563	Lake Jilakin, W.A.	32° 40′	118° 22′	36^{II}
	1564	W. Busselton, W.A.	33° 39′	115° 20′	27^{II}
A. paludosa R. Br. (Ctd.)	1565 (M530)	Three Springs, W.A.	29° 32′	115° 46′	36^{II}
	1543 (M464)	65 km N. of Kingston, S.A.	36° 04′	139° 35′	27^{II}
	1566 (M464)	65 km N. of Kingston, S.A.	36° 04′	139° 35′	27^{II}
	1578 A & B	Tooradin, Vic.	38° 13′	145° 23′	27^{II}
	1580	Sewerton Hotel, Tooradin, Vic.	38° 13′	145° 23′	27^{II}
	1581	Warneet Boat Yard, Vic.	38° 14′	145° 19′	27^{II}
	1587	Avalon Salt Marsh, Vic.	38° 06′	144° 29′	27^{II}
	1596	4 km W. of Nectar Brook, S.A.	32° 42′	137° 52′	27^{II}
	1606	4 km W. of Nectar Brook, S.A.	32° 42′	137° 52′	27^{II}
A. rhagodioides F. Muell.	1545	Ejanding, W.A.	31° 01′	117° 06′	36^{II}
	1557 (M411)	Edah Station, W.A.	28° 16′	117° 09′	36^{II}
A. stipitata Benth.	1528	Broken Hill, N.S.W.	31° 58′	141° 27′	9^{II}
	1541	3 km W. of Cunderdin, W.A.	31° 37′	117° 14′	9^{II}
	1550	9 km E. of Ejanding, W.A.	30° 57′	117° 23′	9^{II}
	1574	Southern Cross, W.A.	31° 14′	119° 19′	9^{II}
	1593B	8 km SE. of Port Pirie, S.A.	31° 14′	138° 07′	9^{II}
A. vesicaria Heward ex Benth., Bladderless	1602	4 km W. of Nectar Brook, S.A.	32° 42′	137° 52′	9^{II}
	1705	20 km W. of Nowingi, Vic.	34° 37′	142° 00′	27^{II}
A. vesicaria Heward ex Benth., Small Bladder	1509	Newmarket Stn., N.S.W.	34° 28′	144° 24′	18^{II}
	1520	Bijerkerno, N.S.W.	31° 25′	141° 40′	9^{II}
	1524	Fowlers Gap, N.S.W.	31° 05′	141° 42′	9^{II}
	1704	4 km W. of Nectar Brook, S.A.	32° 42′	137° 52′	27^{II}
A. vesicaria Heward ex Benth., (Ctd.) Large Bladder	1523	Fowlers Gap, N.S.W.	31° 05′	141° 42′	18^{II}
	1575	Southern Cross, W.A.	31° 14′	119° 19′	9^{II}
	1613	4 km W. of Nectar Brook, S.A.	32° 42′	137° 52′	27^{II}

species, *A. paludosa* and *A. vesicaria*, show varying ploidy levels. *A. paludosa* has both hexaploid and octoploid forms. *A. vesicaria* can be diploid, tetraploid, or hexaploid, but there was no apparent correlation between chromosome number and morphological type, nor with geographical distribution. In two localities, Nectar Brook, South Australia, and Fowlers Gap, New South Wales, two levels of ploidy are present in overlapping populations.

The barriers to gene interchange which appear to be present in the herbaceous diploids are not evident where two of the woody dioecious polyploids grow together. Two such populations were studied. The first was in a strand bordering the Avalon Salt Marsh south of Melbourne, Victoria. Here *A. cinerea* and *A. paludosa*, both hexaploids, grow in close proximity, the former on the drier dikes and the latter in the salt marsh. In the area between these two extremes, a hybrid swarm of 24 plants was studied. Seven of these plants were morphologically intermediate in every respect and appeared to be F_1 hybrids. They had highly irregular meiosis with 8–10 univalents, highly variable pollen size, and 54–57% aborted pollen. The remaining plants intergraded into both parents. In these plants the aborted pollen comprised only 20%. A similar hybrid swarm was observed on a road fill at Ejanding,

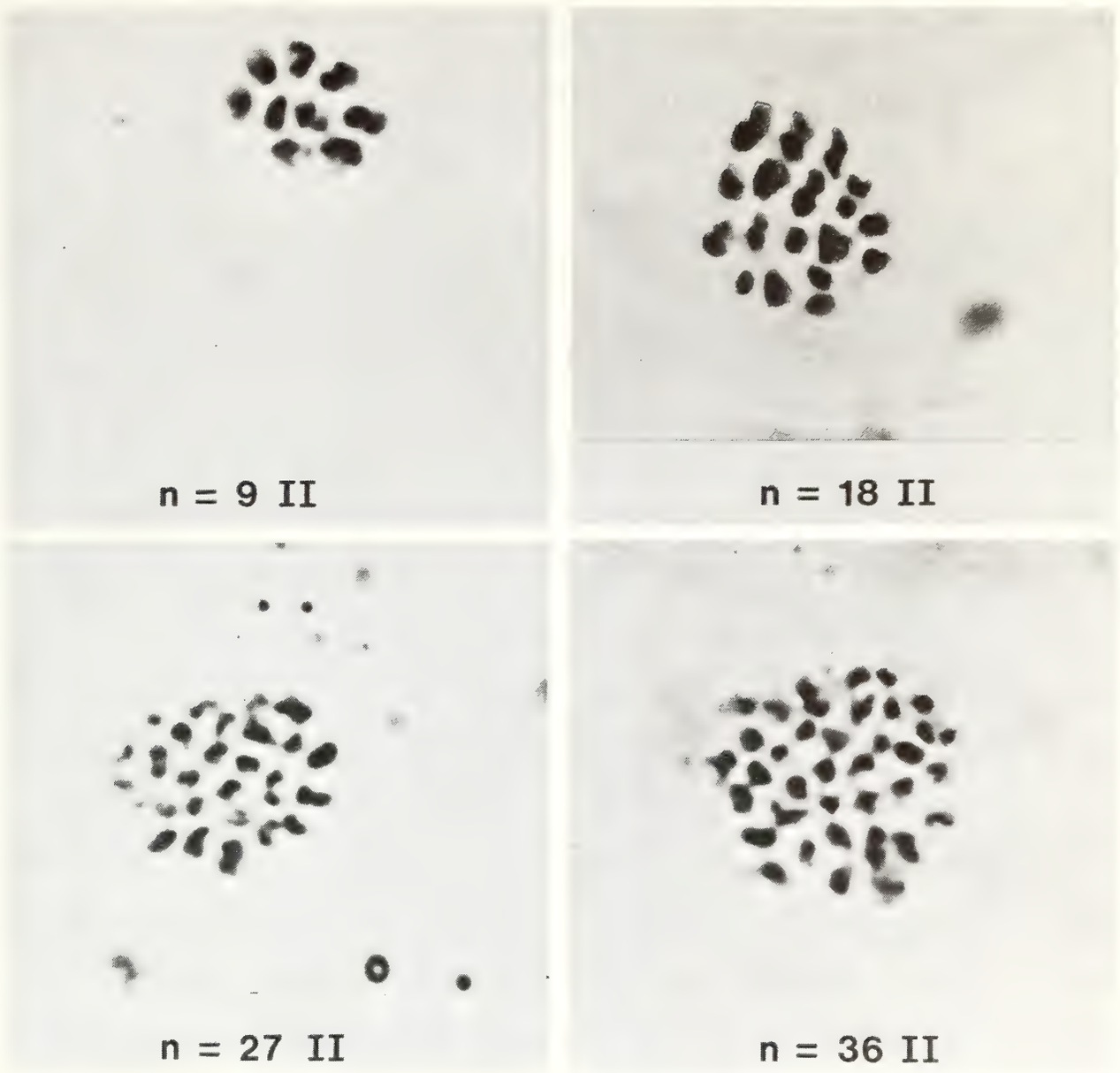


Fig. 33. Meiotic chromosomes of Australian *Atriplex*. Upper left, *A. angulata* 1519; upper right, *A. vesicaria* 1523; lower left, *A. cinerea 1534;* lower right, *A. nummularia* 1500.

Western Australia, where *A. nummularia* and *A. rhagodioides*, both octoploid species, were growing together. The F_1-like plants had highly irregular meiosis, up to 60% of the pollen had aborted, and their morphology was completely intermediate between the two species. A characteristic of the putative hybrids both between *A. cinerea* and *A. paludosa* and between *A. nummularia* and *A. rhagodiodes* is that, unlike the parental species which were dioecious, the hybrids were monoecious. The hybrids also appeared more vigorous than the parental species.

Extensive seed collections of Australian species of *Atriplex* have been brought to the laboratory for future studies of cytogenetic characteristics in the genus.

A LABORATORY-CONSTRUCTED SENSITIVE DIFFERENCE SPECTROPHOTOMETER FOR THE ULTRAVIOLET, VISIBLE, AND FAR-RED REGION OF THE SPECTRUM

Anastasios Melis and Richard W. Hart

A split-beam difference spectrophotometer was constructed, which can measure small absorbance changes (on the order of 10^{-4}) in the wavelength region between 200 and 850 nm. Such absorbance changes commonly take place upon illumination of photosynthetic material and are indicative of changes in the oxidation-reduction state of photosynthetic electron transfer intermediates (see next article). The principle of such "split-beam" type apparatus has been applied earlier by Duysens (1952) and Amesz (1964).

The apparatus is divided into two main parts: optical and electronic.

Optical Part (Fig. 34). There are two compartments in optical alignment. The main compartment contained the sample cuvette and the auxiliary compartment contained the beam splitter (BS). Each compartment has several optical windows on which glass filters and lenses can be mounted. A measuring photomultiplier tube (PM_m) was attached on the main compartment in the direction of the optical path of the measuring beam. A reference photomultiplier (PM_r) was attached on the auxiliary compartment at 90° to the direction of the measuring beam path. The measuring light source (ML) was a 150-W Hanovia 901C-11 Xenon lamp for work in the ultraviolet or a 150-W Sylvania DNF Tungsten lamp for work in the visible and far-red.

The light of the measuring source was modulated at a frequency of 1 kHz by a mechanical light chopper (Princeton Applied Research, Model 125A) and passed through a Bausch and Lomb 33086-45-01 monochromator (f/4.4, 500

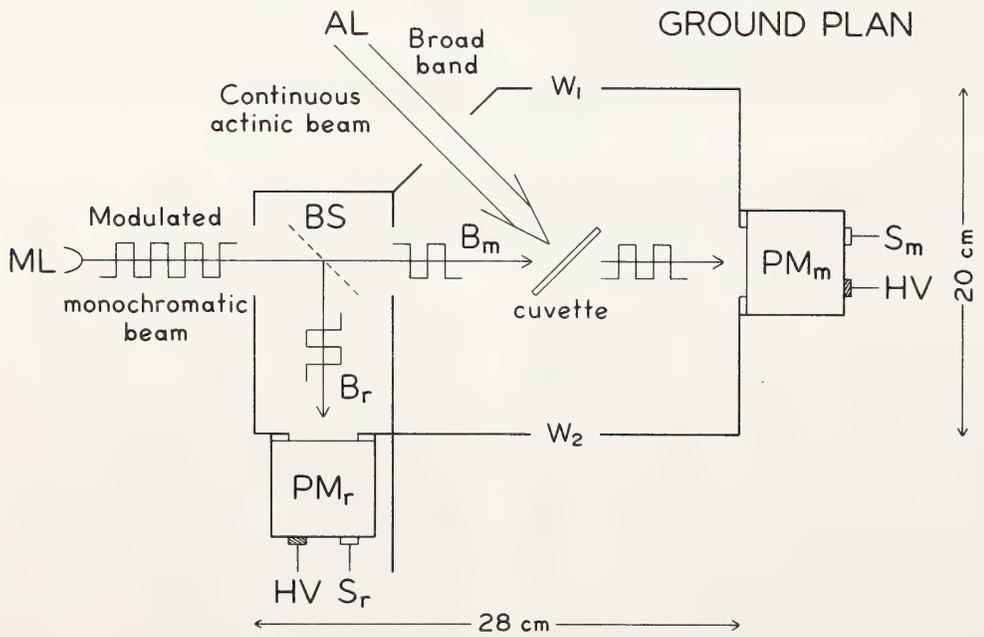


Fig. 34. Schematic diagram of the optical part of the split-beam spectrophotometer. It consists of two metallic boxes in optical alignment with each other. ML and AL are the measuring and actinic light sources, respectively. BS, beam splitter. B_m and B_r, the measuring and reference beams resolved by the beam splitter. PM_m and PM_r, measuring and reference photomultiplier tubes. W_1 and W_2, optical windows. HV, high voltage. S_m and S_r, measuring and reference signals.

nm focal length, 1200 grooves/nm grating). The resulting modulated monochromatic beam entered the auxiliary compartment and was split into two beams, measuring (B_m) and reference (B_r; $B_r = 0.1\ B_m$), one of which (B_r) was deflected by 90° in the direction of the PM_r. The measuring beam (B_m) passed through the chloroplast-containing cuvette, and the transmitted light was measured by the PM_m.

Actinic light (AL) was provided by a 500-W Sylvania CZX projector lamp and entered the cuvette compartment from a side window either at 45° or 90° to the measuring beam. The quality of the actinic beam was determined by broadband glass filters. The actinic beam was turned on and off by an electronic shutter (Vincent Associates 225LOA3X5, response time about 1 ms). The sample was contained either in a quartz cuvette 4 cm high and 4 cm wide, with a 0.1-cm pathlength, or a quartz cuvette 4 cm high and 1 cm wide, with a 1-cm pathlength.

Electronic Part (Fig. 35). The amplitude of the measuring (S_m) and reference (S_r) signals from the output of the photomultiplier tubes (Hamamatsu R562) was equalized by appropriately adjusting the high voltage (HV) applied to their respective cathodes. The two signals were fed to the differential input of an AC amplifier (Princeton Applied Research 128A). The resulting zero-amplitude signal was fed to a band-pass AC amplifier (PAR 98, half-band width approximately 200 Hz) tuned to a frequency of 1 kHz and subsequently passed through the phase-sensitive detector (PSD) of the lock-in amplifier (PAR 128A). The phase-sensitive detector operated in phase with the reference oscillator, the signal of which was derived either internally (PAR 99) or externally from the mechanical light chopper. Actinic illumination of the sample caused the oxidation or reduction of specific electron transport compounds in the chloroplasts and, consequently, a small change ΔT in the transmission of the measuring light through the cuvette. Such changes of transmission were converted to small changes in the modulated signal amplitude (ΔS_m) at the measuring photomultiplier tube and

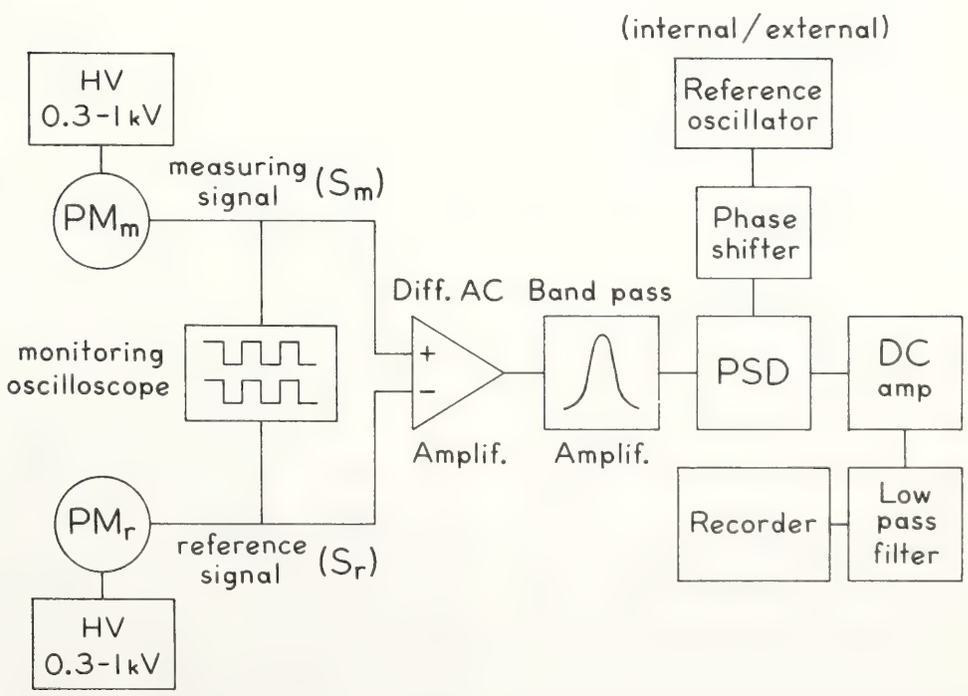


Fig. 35. Block diagram of the electronics of the split-beam difference spectrophotometer.

were finally rectified at the phase-sensitive detector to a DC signal. A DC amplifier (Hewlett-Packard 2470A), connected in series to the lock-in amplifier system, amplified the resulting DC signals by a factor continuously variable from 1 to 3,500. The output of the DC amplifier was connected to a system of low-pass electronic filters (introducing a time constant of 5–500 ms) and monitored on a chart recorder (E&K model 785) or storage oscilloscope (Tektronix 5103N).

Modulation of the monochromatic measuring beam in combination with the lock-in amplifier system helped to eliminate actinic light (DC) artifacts originating from light leaks through the filters in the ultraviolet and fluorescence in the red region of the spectrum. Under our experimental conditions, the noncoherent rejection achieved by the lock-in amplifier system was approximately 1×10^{-3}.

In the wavelength regions where the signal could be separated from light artifacts by optical filters only, it was possible to remove the modulator of the measuring beam and bypass the AC amplifier system. In such a continuous measuring beam operation, the time response of the apparatus could be reduced to as low as 100 ns.

The high sensitivity and high stability of the apparatus allowed the registration of very small absorbance changes initiated by the actinic illumination. With a chloroplast suspension having an apparent absorption of 0.8 at 325 nm, the sensitivity of the apparatus was approximately 2×10^{-5} ΔA (with a time constant of 100 ms). Under experimental conditions the stability of the apparatus was determined by the physical properties of the sample particles, i.e., the rate of chloroplast settling in the cuvette. With nonsettling samples, the stability of the apparatus was measured as a deflection of the recorder pen (drift) and found to be of the order of 10^{-7} ΔA per second.

References

Amesz, J., Ph.D. Thesis, University of Leiden, 1964.

Duysens, L. N. M., Ph.D. Thesis, University of Utrecht, 1952.

STOICHIOMETRY OF SYSTEM I AND SYSTEM II REACTION CENTERS IN PHOTOSYNTHETIC MEMBRANES

Anastasios Melis and Jeanette S. Brown

Photosynthesis in green plants involves the absorption and transfer of excitation energy to the photochemical reaction centers, RCI and RCII. These centers are specialized chlorophyll *a* molecules connected in series to each other by intermediate electron transfer carriers. Their main function is to sustain, through the utilization of light energy, the energetically uphill flow of electrons from dissociated H_2O molecules to $NADP^+$. It has generally been assumed that the ratio of RCII to RCI is unity, but several recent observations indicated a variable ratio in some photosynthetic membranes. The first indication came from chloroplast fractionation studies in which the relative activity of PSII to PSI was greater in grana thylakoids and much less in stroma membranes (Brown, 1973). From measurements of light-induced absorption changes, Haehnel (1976) found that only about 75% of RCI is coupled to RCII via linear electron transport in spinach chloroplasts. Kawamura *et al.* (1979) found considerable variation (from 0.25 to 1) in the ratio of RCII (determined by O_2-flash yield) to RCI (absorbance change of

P700) in several blue-green algae grown under different light intensities. Melis and Thielen (1980) reported that mutations can also alter the ratio of the two reaction centers.

A major problem in determining the ratio of RCII to RCI has been the difficulty in measuring RCII quantitatively. RCI (P700) can be measured readily by the light-induced absorption change at 700 nm, and its concentration calculated from the known extinction coefficient (Hiyama and Ke, 1972). The amount of RCII (P680) can be measured quantitatively only by equipment having a fast time response (~ 100 MHz). Such measurements are further complicated by overlapping absorption changes and a low signal-to-noise ratio. It has been shown that the primary electron acceptor of RCII is a specialized quinone molecule (Q) that has a characteristic, light-induced absorption difference spectrum in the ultraviolet region (van Gorkom, 1974). Figure 36 shows this difference spectrum measured in spinach chloroplasts with the apparatus described in a previous section of this report (Melis & Hart). With the logical assumption that one molecule of Q is reduced for every RCII chlorophyll that is oxidized, the concentration of RCII can be estimated from the light-induced absorption change at 325 nm and the previously determined extinction coefficient of Q (van Gorkom, 1974).

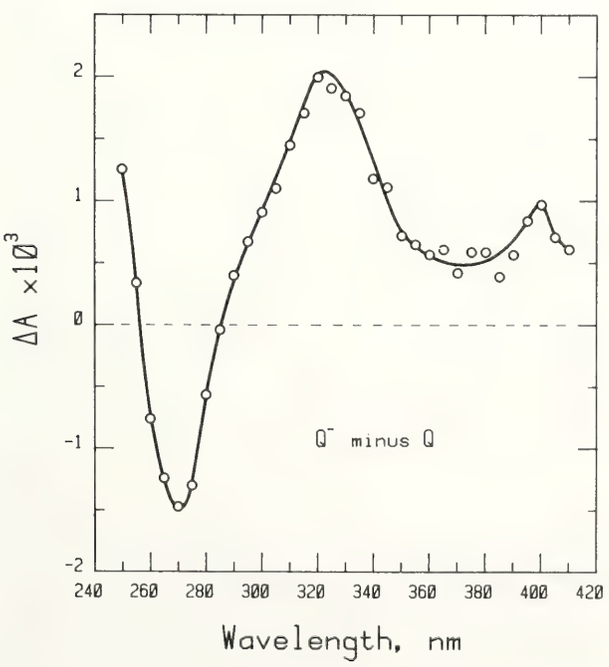


Fig. 36. The photoreduced-minus-oxidized difference spectrum of the primary electron acceptor (Q) of PSII.

Thus we can now measure the concentrations of both kinds of reaction centers with the same apparatus and aliquots of the same plant material. An advantage of measuring Q rather than some other manifestation of Photosystem II activity such as O_2 evolution or dye reduction is that the latter are usually subject to partial inactivation by the treatment or isolation procedure.

Results

The concentrations of Q, P700, and plastoquinone (PQ) and the Chl *a/b* ratio measured in a variety of photosynthetic membranes are shown in Table 13. Chloroplasts from spinach purchased from a local market were broken in a French pressure cell and fractionated by differential centrifugation according to Sane *et al.* (1970). Each value for the spinach fractions represents an average of four separate experiments. Table 13 shows that grana fractions of spinach are enriched in PSII (RCII/RCI = 3.4), while stroma membranes contain primarily PSI (RCII/RCI = 0.4). The sum of both Q and P700 recovered in the fractions was found equal to the amount detected in the whole chloroplasts on a chlorophyll basis. Therefore, it can be concluded that reaction centers of PSII or PSI were not deactivated by the fractionation procedure. Table 13 also shows that developing chloroplasts have a higher RCII/RCI than mature ones isolated from the same species, and that the membranes of a blue-green alga had an RCII/RCI of 0.4, a value similar to that found with the spinach stroma thylakoids.

TABLE 13. Photosystem I (P700) and II (Q) Reaction Centers (RC) and Plastoquinone (PQ) on a Chlorophyll Basis in Photosynthetic Membranes

Material	Chl *a/b*	Chl *a* + *b*	P700 (μmol)	Q	RCII / RCI	Chl/PQ	
						Photo	Chemical
Spinach chloroplasts	2.71	100	0.19	0.38	2.0	32	19
French-press homogenate	2.66	100	0.18	0.39	2.2	50	32
Fractions							
10 K (grana)	2.34	70	0.10	0.35	3.4	80	32
40 K	2.99	23	0.05	0.07	1.3	1125	28
160 K (stroma)	3.68	7	0.03	0.01	0.4	∞	27
Sum of fractions	...	100	0.18	0.43	...	...	...
Pea chloroplasts							
mature	2.50	100	0.19	0.15	0.8	...	...
developing	>8	100	0.30	0.98	3.3	...	...
Blue-green alga	...	100	0.75	0.32	0.4	...	...

An additional line of evidence to be considered here concerns the presence of a pool of plastoquinone (PQ) molecules in the chloroplasts that can be reduced by PSII and oxidized by PSI (Stiehl and Witt, 1968; Amesz, 1973). After adding gramicidin to spinach chloroplasts to prevent light-scattering changes, we measured the light-minus-dark absorption difference spectrum of plastoquinone (Fig. 37). The spectrum has been corrected for changes caused by the simultaneous reduction of Q.

The total amount of photoreducible PQ was estimated from the absorption change at 263 nm in spinach chloroplasts, a French-press homogenate, and three centrifugal fractions. In separate experiments we also measured the total amount of PQ by a chemical method (Bishop and Wong, 1974) in each of these fractions. The ratios of chlorophyll to photoreducible and total PQ are shown in Table 13.

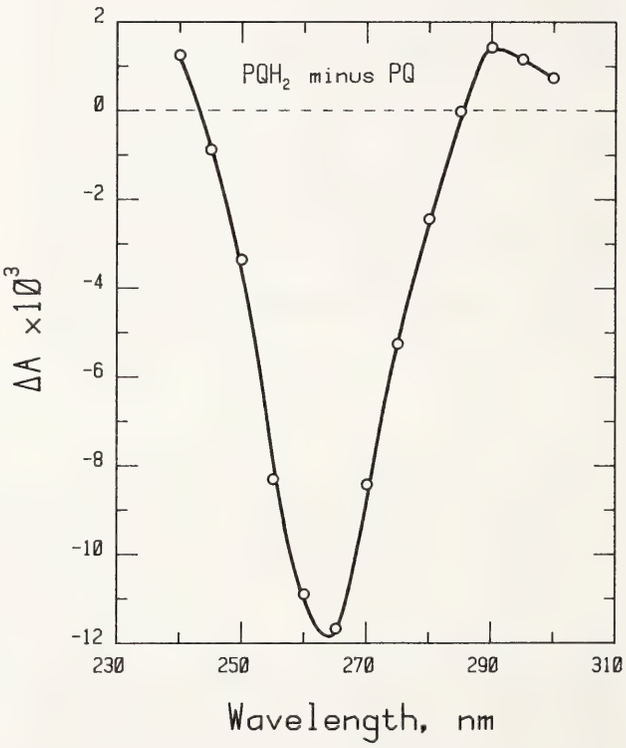


Fig. 37. The light-induced difference spectrum of plastohydroquinone-minus-plastoquinone in chloroplasts.

It is known that up to 50% of the PQ in chloroplasts may reside in the plastoglobuli (Bailey and Whyborn, 1963), and the remainder are bound to the chloroplast membranes. Our results showed that only a part of the total PQ can be photoreduced in the intact chloroplasts. This part was approximately equal to the total membrane-bound PQ that was measured chemically. (See Chl/PQ: chemical, in Table 13.) After French-press treatment of the chloroplasts and differential centrifugation of the fragments, the amount of photoreducible PQ decreased drastically, in-

dicating detachment of PQ from the electron transport chain. The distribution of PQ in spinach chloroplast fractions suggests that most of the PQ pool resides in the grana. The PQ found in the stroma membranes may participate in a diffusion path for the transfer of electrons from a granum to an adjacent stroma thylakoid, as suggested by Sane *et al.* (1970).

The function of PQ as an electron carrier between PSII and PSI is well known (Amesz, 1973). In the spinach grana membranes, we measured a ratio of PSII:PQ:PSI to be approximately 5:(35–40):2. Apparently these values can vary in different plants or in the same plant grown under different conditions. Our results imply that linear electron transfer from H_2O to $NADP^+$ in the grana is accomplished by the cooperation of several, but not stoichiometrically equal, PSII and PSI units associated with the same electron transfer chain. The rates of electron flow through each photoreaction center will be determined by the number of antenna pigment molecules servicing each center, or in other words their effective absorption cross section.

A term often used in the current literature is that of the "photosynthetic unit" (PSU). As originally coined by Gaffron and Wohl (1936), it had a functional validity in referring to the number of chlorophyll molecules cooperating in the absorption of light for the evolution of one O_2 molecule (Emerson and Arnold, 1932). Later the assumption has often been made that the PSU could be defined by the ratio of chlorophyll to RCI or RCII. Our results show that the latter is not a meaningful definition because it is not stated how many chlorophylls are connected to each particular reaction center, and it is further complicated by the uneven amounts of RCII and RCI in a chloroplast sample. As a functionally meaningful concept we propose the term "photochemical unit" (PCU), defining the number of antenna chlorophyll molecules that transfer their excitation energy to a specific reaction center. It is implicit in the definition that the PCU of System II may be different from that of System I and ought to be measured separately.

This work is discussed more fully elsewhere (Melis and Brown, 1980).

References

Amesz, J., *Biochim. Biophys. Acta, 301,* 35–51, 1973.

Bailey, J. L., and A. G. Whyborn, *Biochim. Biophys. Acta, 78,* 163–174, 1963.

Bishop, N. I., and J. Wong, *Ber. Deut. Bot. Ges., 87,* 359–371, 1974.

Brown, J. S., *Current Topics in Photophysiology, VIII,* 97–111, A. C. Giese, ed., Academic Press, New York, 1973.

Emerson, R., and W. Arnold, *J. Gen. Physiol., 16,* 191–205, 1932.

Gaffron, H., and K. Wohl, *Naturwissenschaften, 24,* 81–90, 1936.

Haehnel, W., *Biochim. Biophys. Acta, 423,* 499–509, 1976.

Hiyama, T., and B. Ke, *Biochim. Biophys. Acta, 267,* 160–171, 1972.

Kawamura, M., M. Mimuro, and Y. Fujita, *Plant Cell Physiol., 20,* 697–705, 1979.

Melis, A., and A. P. G. M. Thielen, *Biochim. Biophys. Acta, 589,* 275–285, 1980.

Melis, A., and J. S. Brown, *Proc. Nat. Acad. Sci.,* in press, 1980.

Sane, P. V., D. F. Goodchild, and R. B. Park, *Biochim. Biophys. Acta, 216,* 162–178, 1970.

Stiehl, H. H., and H. T. Witt, *Z. Naturforsch. 23b,* 220–224, 1968.

van Gorkom, H. J., *Biochim. Biophys. Acta, 347,* 439–442, 1974.

FLUORESCENCE SPECTROSCOPY OF INTERMITTENT-LIGHT AND DAYLIGHT-GROWN PEA AND WHEAT CHLOROPLASTS

Jeanette S. Brown

A basic problem in photosynthesis research is to understand the state and primary function of chlorophyll in plant membranes. An approach to this problem is to examine absorption and fluorescence spectra of chlorophyll bound in chloroplast membrane fragments and protein complexes; such measurements have been carried out in this Department for many years. Although our Perkin-Elmer Spectrofluorometer was interphased with a computer over two years ago, a new computer has greatly increased the capability of collecting and manipulating fluorescence spectra. Soon the Cary absorption spectrophotometer will be connected to the same system, making it much easier to compare absorption and fluorescence spectra directly.

We reported a procedure to correct fluorescence excitation spectra between 400 and 500 nm for artifacts caused by the Xenon lamp emission and other characteristics of the equipment (*Year Book 76*, p. 211). This procedure involves the division of an experimental spectrum by an excitation spectrum for Rhodamine B measured at the same excitation slit-width. A series of Rhodamine curves measured at several slit widths are stored in the computer for this purpose. Recently we have calibrated the phototube and optical system of the instrument for emission spectra as well. We first measured the response to the emission of a standard lamp between 640 and 760 nm. This measured response curve was corrected mathematically for the known standard lamp emission and stored. Experimental emission spectra can be divided by this correction curve to give spectra free of instrumental artifacts.

In addition to improved instrumentation, the examination of new or different plant material frequently provides valuable information. Over ten years ago Argyroudi-Akoyunoglou and Akoyunoglou (1970) observed that when etiolated bean plants were exposed to cycles of 2 min light and 98 min darkness, only Chl *a* was formed for the first 20–40 cycles; gradually some Chl *b* accumulated, but the ratio of Chl *a/b* remained high unless the plants were exposed to continuous light. Argyroudi-Akoyunoglou and Akoyunoglou (1979) have continued to investigate various properties of these intermittent-light-grown (ImL) plants, and a number of workers have utilized this material for fluorescence studies (including Strasser and Butler, 1977a,b; Davis *et al.*, 1976; Mullet *et al.*, 1980a,b). Strasser and Butler (1977a) measured some excitation spectra of ImL-grown bean leaves, but the other authors used isolated chloroplasts and measured only emission spectra. Therefore, we decided to compare both excitation and emission spectra of ImL- and daylight-grown wheat and pea chloroplasts.

Plants were germinated and grown at room temperature in a chamber in which an incandescent lamp provided an average light intensity of 25 μE m^{-2} s^{-1} at ground level for 15 min out of every 2 h. Wheat leaves were harvested when they were 7–9 cm tall (about 7 days), and peas when they had 3–6 expanded leaves (10–12 days). Chloroplasts were prepared by blending the cut leaves in 0.4 M sucrose, 5 mM $MgCl_2$, 10 mM KCl, and 50 mM Tricine, pH 7.6, for 15 sec, followed by differential centrifugation. These chloroplasts are more fragile than those from plants grown under normal illumination, and after differential centrifugation, a less dense fraction could be obtained in

which the ratio of photosystem I reaction centers (P700) per chlorophyll was 20–40% higher than in the membrane fragments sedimented at lower speed. Thus a partial separation of the photosystems from these ImL plastids is possible without prior French press or detergent treatment. For comparison, chloroplasts were also prepared from both species grown under daylight in a glass-house or in the chamber under continuous illumination.

For fluorescence measurements, a strip of Whatman #2 filter paper 0.5 cm wide was moistened with the chloroplast suspension and placed in the dewar, which was filled with liquid N_2 and set in the spectrofluorometer compartment. To avoid artifacts caused by reabsorption, the chloroplast suspensions were diluted to the point where further dilution did not change the shape of the spectra.

Emission spectra of ImL- and daylight-grown chloroplasts from both wheat and pea leaves are shown in Fig. 38. Two striking differences in both species are the increase in the amount of shorter wavelength (686-nm) relative to longer wavelength emission, and the blueshift of the longer wavelength maximum (740–730 nm) of the ImL compared to daylight-grown plants. Spectra of chloroplasts from plants grown in continuous light were very similar to those of daylight-grown plants.

Excitation spectra (400–500 nm) for emission at 686 nm are shown in Fig. 39 and (600–700 nm) for emission at 740 nm in Fig. 40. As expected, the ImL plants that had little or no Chl *b* did not show excitation bands in the 470 or 650 nm regions where Chl *b* absorbs maximally. Certain carotenoids are able to transfer excitation energy in vivo to Chl *a* and evidence for this transfer can be seen by effective excitation in the spectral region between 460 and 490 nm of the daylight-grown plants. The ImL-grown plants may either lack these carotenoids (in addition

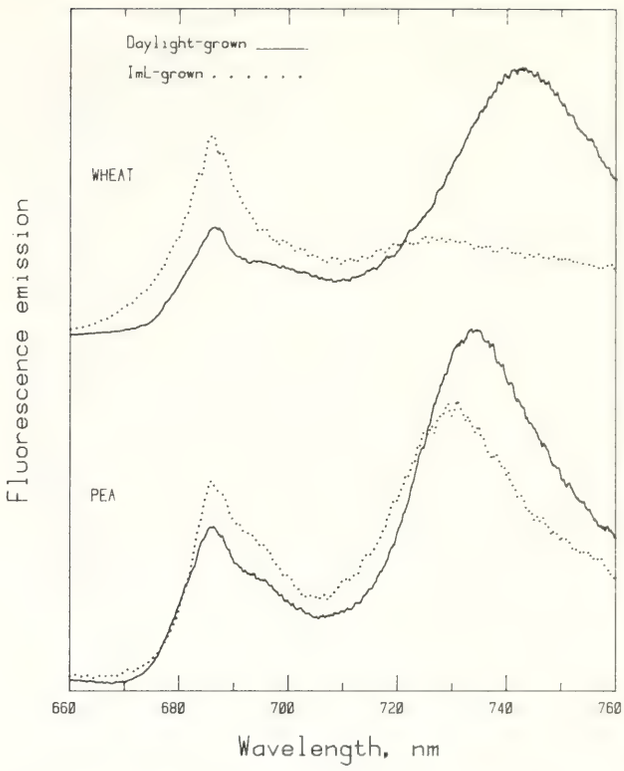


Fig. 38. Fluorescence emission spectra of chloroplasts from wheat and pea leaves grown under ImL or daylight. Slit width = 3 nm. Excitation at 440 nm, slit width = 6 nm. Measured at −196 °C.

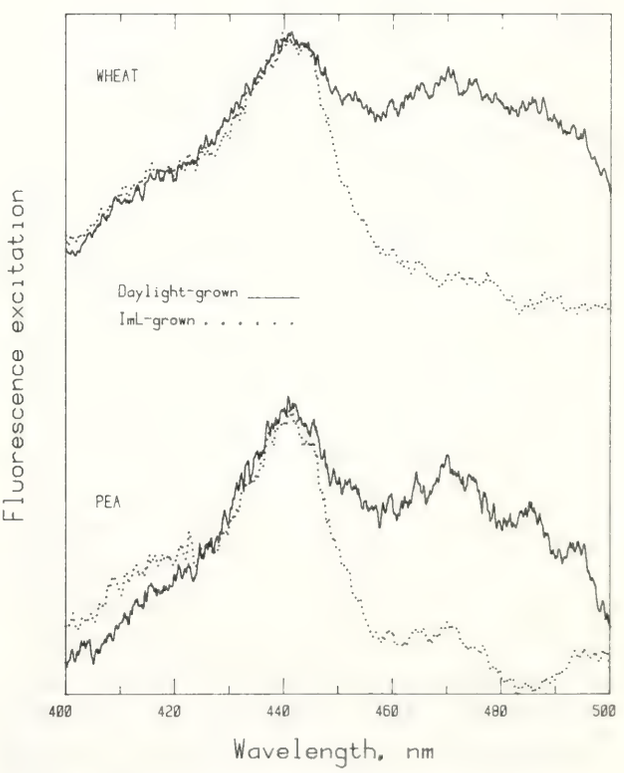


Fig. 39. Fluorescence excitation spectra of chloroplasts from wheat and pea leaves grown under ImL or daylight, slit width = 4 nm. Emission at 686 nm, slit width = 5 nm, −196 °C.

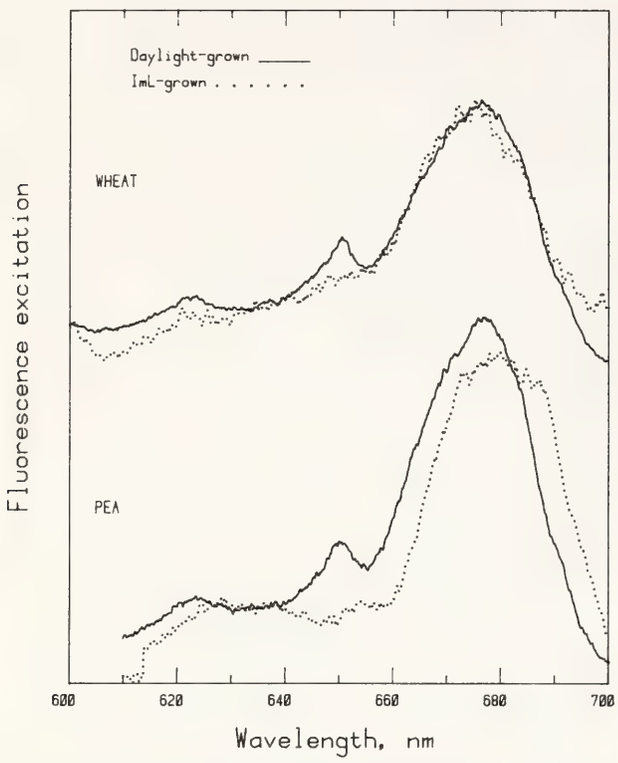


Fig. 40. Same as Fig. 39 except for emission at 740 nm. Slit width = 8 nm.

to chlorophyll *b*) or if present these are not organized in the membrane in such a way as to allow for energy transfer. Excitation spectra (400–500 nm) were also measured for emission at 740 nm (not shown) and were similar to those for emission at 686 nm for all plastids except for relatively greater excitation near 450 nm. This greater excitation by 450 nm for the longer wavelength emission bands of chloroplast particles or Chl-protein complexes was observed earlier (*Year Book 76*, p. 209), but the source of it has not yet been identified.

The excitation of 740-nm emission was considerably greater near 690 nm in ImL-grown than in daylight-grown pea chloroplasts (Fig. 40). The absorption spectra (not shown) measured near −185 °C showed similar differences between the two samples; both spectra indicating that the ImL-grown pea chloroplasts were enriched in a form of Chl *a* absorbing near 685 nm. This form was not evident in ImL-grown wheat (Fig. 40).

The emission spectra of Fig. 38 are nearly identical to corresponding spectra of chloroplasts from ImL-grown and control peas (Davis *et al.*, 1976) and a viridis-k mutant and wild-type barley (Nielsen *et al.*, 1979). In each case the emission maximum at 686 nm is relatively higher, and the long wavelength maximum is shifted from about 740 to 730 nm in spectra of ImL-grown or mutant chloroplasts compared to light-grown or wild-type. On the other hand, spectra obtained in vivo from flashed bean leaves (Strasser and Butler, 1977a), which like the ImL and viridus mutant lack the Chl *ab*-antenna complex, show a sharp emission maximum at 694 nm. The ratio of this maximum to the 730-nm band varied from 0.7 to 3.9 in leaves from different plants grown under identical conditions (Strasser and Butler, 1977b). The optical properties of leaves are such that nearly all of the fluorescence emitted within the chlorophyll absorption band (660–690 nm) is reabsorbed. This reabsorption artifact may account for the apparent difference in intensity of the 686-nm and 694-nm bands between chloroplasts and leaves as well as the different ratios of short-to-long wavelength emission in greening leaves. Even the addition of some Chl *ab*-protein into chloroplast thylakoids may enhance the reabsorption artifact and cause some of the apparent differences between ImL-grown and daylight-grown plants seen in Fig. 38.

An excellent study of the Chl-proteins of PSI and their fluorescence emission by Mullet *et al.*, (1980a,b) has very recently appeared. These workers conclude that native PSI in fully develped plastids contains polypeptides of 22,500–24,500 daltons which function to bind 40–45 chlorophyll molecules including those that fluoresce at 736 nm. The ImL-grown plants and certain mutants do not contain these polypeptides or their associated chlorophylls, thus providing a possible explanation for the decrease and shift of the emission from about 740 to 730 nm.

Some preliminary measurements of the numbers of reaction centers (see Melis and Brown, this Report) in plants grown in daylight or in the continuous light of the chamber suggest that the spectral quality of the light may influence these numbers. Thus far the shapes of the excitation and emission spectra appear to be far more dependent upon the amount and kind of antenna pigment than upon the concentration of either reaction center. However, the ability to manipulate the proportions of both antenna and reaction center chlorophyll in the same species by the light conditions during greening should provide excellent material for further spectroscopic studies.

References

Argyroudi-Akoyunoglou, J. H., and G. Akoyunoglou, *Plant Physiol., 46,* 247–249, 1970.

Argyroudi-Akoyunoglou, J. H., and G. Akoyunoglou, *FEBS Lett., 104,* 78–84, 1979.

Davis, D. J., P. A. Armond, E. L. Gross, and C. J. Arntzen, *Arch. Biochem. Biophys., 175,* 64–70, 1976.

Mullet, J. E., J. J. Burke, and C. J. Arntzen, *Plant Physiol., 65,* 814–822, 1980a.

Mullet, J. E., J. J. Burke, and C. J. Arntzen, *Plant Physiol., 65,* 823–827, 1980b.

Nielsen, N. C., R. M. Smillie, K. W. Henningsen, D. von Wettstein, and C. S. French, *Plant Physiol., 63,* 174–182, 1979.

Strasser, R. J., and W. L. Butler, *Biochim. Biophys. Acta., 462,* 295–306, 1977a.

Strasser, R. J., and W. L. Butler, *Biochim. Biophys. Acta., 462,* 307–316, 1977b.

A COMPARATIVE STUDY OF PHASE TRANSITION TEMPERATURES DETERMINED FOR CHLOROPLAST THYLAKOID MEMBRANES AND FOR LIPOSOMES PREPARED FROM PHOSPHOLIPIDS EXTRACTED FROM PHOTOSYNTHETIC MEMBRANES OF HIGHER PLANTS

David C. Fork, Gijs van Ginkel, and Geoffrey Harvey

The physical phase of the lipids that make up the thylakoid membranes plays an important role in photosynthetic function. Our studies over the last several years (*Year Book 74*, 766–776; *75*, 465–472; *76*, 220–235; *77*, 283–291; *78*, 196–199) have shown that as temperature is lowered there are abrupt decreases of a number of photosynthetic reactions at temperatures corresponding to the beginning of lipid solidification (phase transition or phase separation temperatures). These effects were found to be reversible. Normal activity is regained when increasing temperatures allow the lipids of the thylakoid membranes to regain their former liquid-crystalline state.

In this study we measured lipid phase transitions of intact thylakoid membranes isolated from a variety of plants. For these measurements we used native chlorophyll *a* (Chl *a*) as an intrinsic fluorescent probe (*Year Book 74*, 766–776). Phospholipids were also extracted from the thylakoid lamellae of these plants, usually purified further by thin layer chromatography, converted into Chl-containing liposomes, and examined for their phase transition temperatures. For some preparations of phospholipid vesicles we compared the results obtained when the fluorescent probe *trans*-parinaric acid (9,11,13,15-octadecatetraenoic acid, all *trans*; *trans*-PnA; Sklar *et al.*, 1975) was substituted for Chl *a*.

Leaves of corn (Bonanza), tomato (Ace), and bell pepper were collected from plants growing in fields of the Webb Ranch, Palo Alto, California. Water hyacinth was grown in a greenhouse in 30-cm-diameter and 20-cm-deep plastic tubs containing nutrient solution. *Mimulus cardinalis* (scarlet monkey flower) was collected at an alti-

tude of 400 m on Priest's Grade in the foothills of the Sierra Nevada.

Chloroplasts were prepared in 20 mM Tricine buffer (pH 8.0), 0.4 M sucrose, 3 mM $MgCl_2$, washed once and resuspended in a solution containing 0.2 M sucrose, 50 mM Tricine (pH 8.0), 3 mM KCl, 3 mM $MgCl_2$ and 5 mg/ml BSA.

Fluorescence of Chl *a* versus temperature curves were measured, as described previously (*Year Book 74*, 766–776), either at 685 nm for intact thylakoid membranes (to which 40 μM DCMU was added) or at 675 nm for liposomes. Purified lipids such as dimyristoyl phosphatidyl choline (DMPC), and distearoyl phosphatidyl choline (DSPC) were purchased from Sigma Chemical Co. and used without further purification.

To prepare the phospholipids that are associated with the photosynthetic lamellae, the total lipid was extracted from chloroplasts according to the method of Williams and Merrilees (1970) and fractionated by column chromatography on silicic acid. The phospholipid fraction was further purified by preparative thin layer chromatography on a stationary phase of 0.5-mm silica gel G and with a solvent system containing chloroform-methanol-7 N NH_4OH (65:30:4 v/v/v). Phospholipid regions were visualized by developing a narrow strip at the plate edge in an iodine vapor bath. The iodine-free areas of phospholipid distribution were scraped off, and the phospholipids eluted with chloroform-methanol (2:1 v/v). Liposomes were prepared by adding purified Chl *a* dissolved in chloroform to a chloroform-methanol solution of the phospholipid in the ratio of 1 Chl *a* to 400 phospholipid (w/w). This solution was dried under N_2, suspended in 0.1 M Tris buffer (pH 7.8) and 5 mM EDTA, and sonicated in a bath-type sonicator (Bransonic-32) for 2–3 minutes to form vesicles.

When used, the probe *trans*-parinaric acid was incorporated into the liposomes at the ratio of 1 to 570 phospholipid (w/w), and fluorescence was measured as described previously (*Year Book 78*, 163–168).

Figure 41 compares the results obtained from chloroplasts with those obtained from liposomes prepared from chloroplast phospholipids. A general agreement can be seen between the temperatures of the phase transition in both types of preparation. In corn chloroplasts, for example, (Fig. 41A) phase transition temperatures are seen at 16° and 19°C upon decreasing and increasing the temperature, respectively. The phospholipids from corn also showed a phase transition at 16°C upon decreasing the temperature. A broad shoulder with no distinct break point was seen with increasing temperatures. Like corn, the chilling-sensitive pepper showed phase transitions of the chloroplast preparation near 13° and 16°C with decrease and increase of temperature. In addition, a broad shoulder was seen in the pepper chloroplast phospholipid preparation around −20°C. The phospholipid preparation made from pepper chloroplasts showed peaks at 12° and 16°C and, in addition, had a small maximum near −21°C.

Tomato chloroplasts showed peaks at 9° and 13°C depending on the direction of the temperature change. The tomato phospholipid preparation, like the chloroplast preparation, showed a peak near 9°C during temperature decrease. In addition, another peak was seen at −27°C. This low-temperature peak was not evident in the chloroplast preparation. A similar situation was seen in *Mimulus*, where the chloroplast preparation showed a very broad maximum centered at 0° and 25°C upon decreasing and increasing the temperature. The *Mimulus* phospholipid preparation showed indistinct shoulders near these two temperatures and, in addition, at −27° and −23°C when the temperature was respectively decreased and increased.

We were not able to obtain chloro-

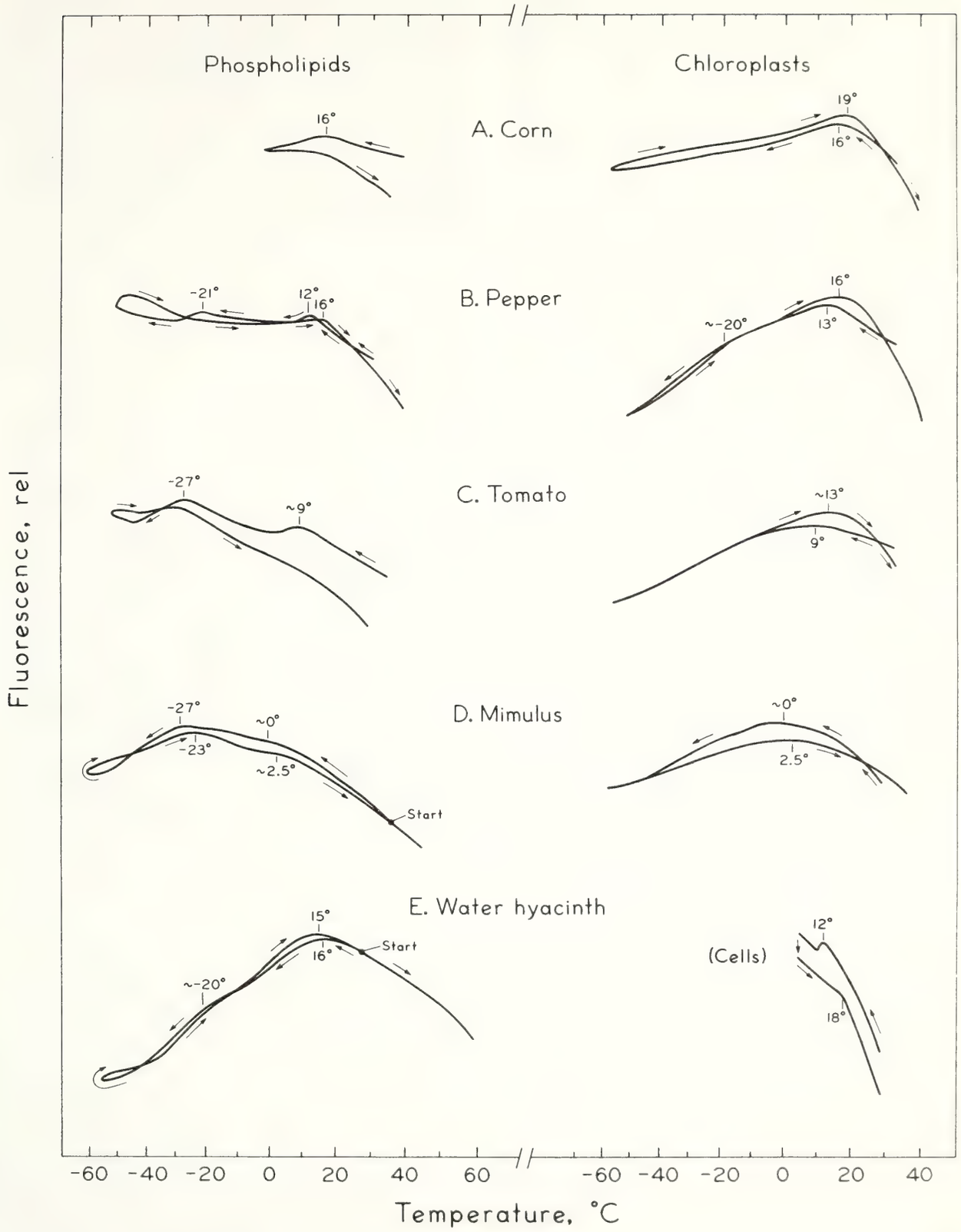


Fig. 41. Phase transition temperatures in higher plant chloroplasts and in liposomes prepared from phospholipids extracted from the chloroplasts measured; chlorophyll *a* is used as the fluorescent probe, as described in the text. Arrows indicate the direction of the temperature change.

plast preparations from water hyacinth that showed any structure in the temperature versus fluorescence curves. Other plants sometimes also gave difficulties in this regard. This may be due to the release of certain substances (e.g., phospholipases) that degrade the thylakoid membrane structure and prevent observation in vivo of the lipid phase transitions.

We were able to use whole cells isolated from water hyacinth by a maceration technique (*Year Book 77*, 245–247) that showed peaks at 12° and 18°C upon temperature decrease and increase, respectively. These two peaks were also seen in the curve obtained with water hyacinth phospholipid vesicles which, in addition, showed a low-temperature shoulder around −20°C.

These results show that in general there is a good agreement between the phase transition temperatures of intact thylakoid membrane lipids and the purified phospholipid fraction extracted from these thylakoids. Corn, pepper, tomato, and hyacinth plants, which are chilling sensitive, all had phase transitions in the temperature range from 9° to 19°C. In our previous measurements with tomato (*Year Book 74*, 766–776) we did not find a phase transition temperature above 0°C. As noted previously, it is sometimes difficult to see phase transitions in intact membranes from certain plants, since chloroplast preparation may release substances deleterious to the thylakoid membrane. Also, as is discussed elsewhere (van Ginkel and Fork, this Report) aging of chloroplasts can decrease the temperature at which phase transitions are seen. Unfortunately, we have so far been unsuccessful in attempts to see phase transitions in vivo in intact leaves.

The maxima seen above 0°C in these temperature versus fluorescence curves indicate the beginning of the phase separation state when the temperature is lowered. These state changes have in some cases been correlated with changes in biochemical processes of crop plants (Lyons *et al.*, 1979). Our studies (*Year Book 76*, 220–235) of the 515-nm change in tomato and in bean have shown that the thylakoid membranes become leaky to ions when the temperature is lowered below about 10° and 15°C, respectively. Many of the preparations shown in Fig. 41 have a second peak or a shoulder appearing at sub-zero temperatures in addition to the phase transitions seen as peaks at temperatures above 0°C. Further studies will be needed to understand the sub-zero phase transitions seen in most of these preparations.

It is clear from these results that phase transitions occur over a broad temperature range both for the intact thylakoids and for the extracted chloroplast phospholipids. Most of the phospholipid preparations used in these experiments contained at least three and sometimes five different kinds of phospholipids. As is well known and will be seen in Fig. 42, only vesicles containing a single species of phospholipid show sharply defined phase transition temperatures.

We wanted to see if the results obtained with the fluorescent probe

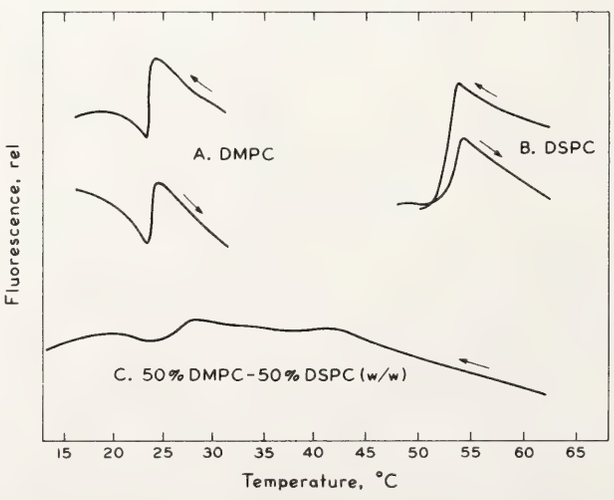


Fig. 42. Phase transitions detected with Chl *a* as a fluorescent probe in liposomes containing dimyristoyl phosphatidyl choline (A) or distearoyl phosphatidyl choline (B) or a 50/50 mixture (C) of each of these phospholipids. See text for details of the measurements.

trans-PnA would agree with the results obtained with Chl *a* as the fluorescent probe. *Trans*-PnA has been shown to partition preferentially into solid-phase phospholipids. The fluorescence intensity and polarization of this probe added to lipid vesicles can be used to determine phase transition temperatures, and the polarization ratio to provide information on the fluidity of the preparation (Sklar *et al.*, 1979).

We compared the results using *trans*-PnA and Chl *a* as fluorescent probes using liposomes containing only one species of a pure phospholipid (DMPC or DSPC) and liposomes containing a 50/50 mixture of these two phospholipids.

Figures 42 and 43 show that similar results were obtained using either of these fluorescent probes. With Chl *a* the phase transition temperature occurred near 23°C for DMPC when either Chl *a* or *trans*-PnA were used as fluorescent probes. For DSPC the phase transition was found to be near 53°C with Chl *a* as the probe (Fig. 42B). These values agree with earlier results with Chl *a* as a probe (Lee, 1975), *trans*-PnA as a probe (Sklar *et al.*, 1975), and with other measurements using calorimetric or ESR spin label techniques (see Jacobs *et al.*, 1977).

Mixtures of equal amounts of these two lipids produced a very broad fluorescence-versus-temperature diagram that had indistinct features (Foster and Yguerabide, 1979) compared to curves seen for the individual lipids (Figs. 42C, 43B). This buffering of the very sharp phase behavior of individual phospholipids after mixing together different species of phospholipids is reflected in similar broad phase transition curves of the complex plant phospholipid preparations (Figs. 41 and 43C) which, as mentioned earlier, are mixtures of at least three different species of phospholipids.

Table 14 gives the results obtained measuring phase transitions of chloro-

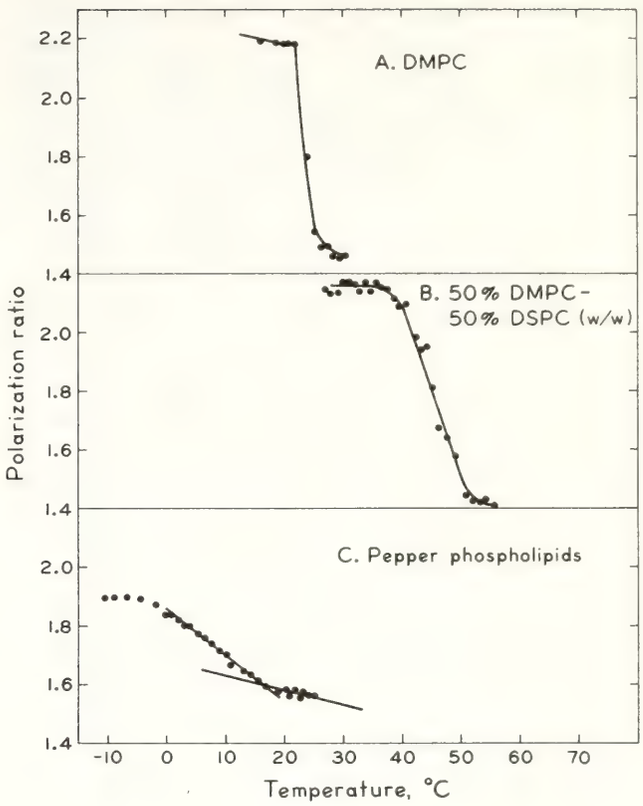


Fig. 43. Phase transitions detected with *trans*-parinaric acid fluorescence polarization measured in liposomes containing dimyristoyl phosphatidyl choline (A) or a 50/50 mixture of dimyristoyl phosphatidyl choline and distearoyl phosphatidyl choline (B). In (C) the phase behavior of liposomes made from purified phospholipids extracted from pepper chloroplasts was measured. The value of the fluorescence emission with the polarizer parallel divided by fluorescence with the polarizer perpendicular was used as the polarization ratio.

TABLE 14. Phase Transition Temperatures for Chloroplast Phospholipid Preparations with Different Fluorescent Probes

	Temperature of Phase Transition, °C	
Plant	Trans-Parinaric Acid*	Chlorophyll *a*†
Tomato	9–11	9
Corn	12	16
Pepper	16–17	12–16
Water hyacinth	18	15–16
Cyanidium caldarium	18–19	18–19

*Values determined from fluorescence polarization.

†Values determined from fluorescence at 675 nm.

plast phospholipid preparations with *trans*-PnA and Chl *a* as fluorescent probes. Except for corn, very nearly the same temperatures for phase separation were obtained with either fluorescent probe. Unfortunately, fluorescent probes such as *trans*-PnA cannot be used to determine the phase transition behavior of the intact thylakoid membrane lipids. In our earlier work on the phase transition temperatures of thylakoid membrane fragments of the blue-green alga *Anacystis nidulans* (Murata and Fork, 1975), we also found that exogeneous fluorescent probes such as ANS (8 anilinonaphthalene-1-sulfonate) or NPN (*N*-phenyl-1-naphthylamine) did not work well, presumably because the fluorescence emitted by the probe was efficiently transferred to Chl *a*, and/or carotenoids. As was demonstrated in these and other studies, Chl *a*, unlike *trans*-PnA, can be used to reveal the phase transition behavior of the intact thylakoid membrane lipids, since Chl *a* is an endogeneous fluorescent component of photosynthetic material.

References

Colbow, K., *Biochim. Biophys. Acta, 318*, 4–9, 1973.

Foster, M. C., and J. Yguerabide, *J. Membr. Biol., 45*, 147–166, 1979.

Jacobs, R. E., B. S. Hudson, and H. C. Andersen, *Biochem., 16*, 4349–4359, 1977.

Lee, A. G., *Biochim. Biophys. Acta, 413*, 11–23, 1975.

Lyons, L. M., J. K. Raison, and P. L. Steponkus in *Low Temperature Stress in Crop Plants. The Role of the Membrane*, 1–24, J. M. Lyons, D. Graham, and J. K. Raison, eds., Academic Press, New York, 1979.

Murata, N., and D. C. Fork, *Plant Physiol., 56*, 508–517, 1975.

Sklar, L. A., B. S. Hudson, and R. D. Simoni, *Proc. Nat. Acad. Sci. USA, 72*, 1649–1653, 1975.

Sklar, L. A., G. P. Miljanich, and E. A. Dratz, *Biochem., 18*, 1707–1716, 1979.

Williams, J. P., and P. A. Merrilees, *Lipids, 5*, 367–370, 1970.

THE EFFECT OF AGING IN VITRO OF SPINACH CHLOROPLASTS ON THE PHASE TRANSITION TEMPERATURES OF THYLAKOID MEMBRANES

Gijs van Ginkel and David C. Fork

Our earlier studies with spinach chloroplasts suggested that phase transition temperatures occurred in the range of −20° to −31 °C depending upon whether cations were absent or present. Results of studies of certain photosynthetic reactions in spinach chloroplasts have suggested phase transitions of −9 °C (Inoué, 1978) and −35 °C (Cox, 1975).

In the course of these studies using chlorophyll *a* as an endogenous and intrinsic fluorescent probe (Colbow, 1973; Murata and Fork, 1977; Lee, 1975a,b), we found that aging of spinach chloroplasts lowered their phase transition temperatures.

Spinach chloroplasts were isolated in a medium containing 600 mM sucrose, 30 mM phosphate buffer (pH 7.2), and 5 mM $MgCl_2$. They were used immediately after isolation or frozen in liquid nitrogen. Chlorophyll *a* fluorescence as a function of temperature was measured in chloroplasts to which 40 μM DCMU was added to suppress fluorescence transients (*Year Book 74*, 766–776). Ethylene glycol (60%) was added to protect samples from freezing.

We also wanted to know the phase transition temperatures of the phospholipids of thylakoid membranes, since these lipids might function as structural lipids. To isolate the phospholipids, the total lipid of chloroplasts was extracted (Williams and Merrilees,

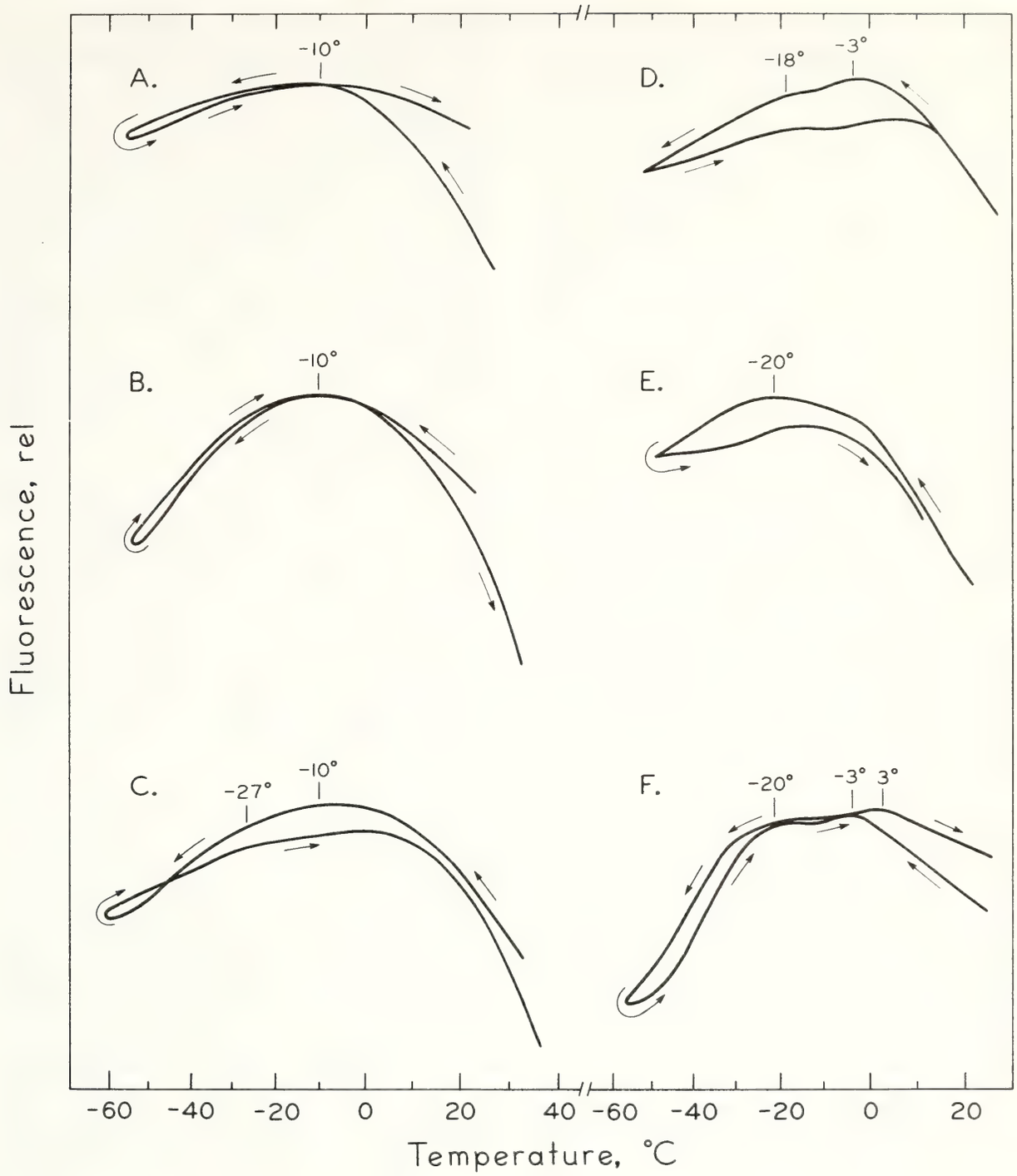


Fig. 44. Temperature dependence of chlorophyll *a* fluorescence in spinach chloroplasts and in vesicles made from phospholipids extracted from spinach chloroplasts. Arrows indicate the direction of the temperature change. (A) Chloroplasts measured immediately after isolation in the medium described in the text; ethylene glycol, 60%; BSA, 5.0 mg/ml. (B) Chloroplasts measured immediately after isolation in 0.35 M NaCl plus other additions described in (A). (C) Chloroplasts measured after thawing from liquid nitrogen and prepared in 400 mM sucrose; 1.5 mM $MgCl_2$; 10 mM phosphate buffer, pH 7.2, and ethylene glycol and BSA (~ 0.5 mg/ml). (D) Chloroplasts from (C) after storage for 7 h in the dark on ice. (E) Chloroplasts from (C) after storage for 24 h in the dark on ice. (F) Vesicles made from chloroplast phospholipids and 0.1 M Tris, pH 7.2; 5 mM EDTA; 60% ethylene glycol.

1970) and fractionated by column chromatography on silicic acid. The methanol fraction eluted from the column contained crude phospholipids. A known amount of these phospholipids were dried under N_2 and suspended in 0.1 M Tris buffer (pH 7.2) and 5 mM EDTA, shaken with glass beads, and sonicated for 2–3 minutes in a bath-type sonicator at 20 °C to form vesicles. These phospholipids contained a trace of chlorophyll *a*, so none had to be added for the measurements of phase transition.

Figure 44A shows a phase transition at −10 °C for spinach chloroplasts measured immediately after isolation in sucrose buffer containing BSA as a protective agent. The same result was obtained when NaCl replaced sucrose in the isolation buffer (Fig. 44B). Chloroplasts freshly thawed from liquid nitrogen that were prepared in sucrose buffer containing only a trace of BSA had a phase transition temperature near −10 °C and the suggestion of a broad shoulder near −27 °C (Fig. 44C).

Aging chloroplasts on ice for seven hours accentuated the shoulder at −18 °C and shifted the main peak to −3 °C (Fig. 44D). After 24 h of aging, almost all the phase transition had shifted to −20 °C, as shown in Fig. 44E. Vesicles prepared from phospholipids isolated from freshly isolated spinach chloroplasts showed phase transition temperatures around −3 °C and −20 °C (Fig. 44F) near those seen in chloroplasts that had aged somewhat (compare with Fig. 44D).

It is well known that chloroplasts isolated from green leaves of higher plants are unstable and gradually lose their photochemical activity even when stored at 0 °C (Wasserman and Fleischer, 1968; van Ginkel, 1977; Wintermans *et al.*, 1969; Constantopoulos and Kenyon, 1968). When we used chloroplasts immediately after thawing from liquid nitrogen, they gave results like those mentioned above for freshly prepared chloroplasts, although the low-temperature shoulder became just visible even in this preparation.

Hoshina *et al.* (1975) found that aging of spinach chloroplasts in the dark caused decomposition of the endogenous monogalactolipid and phosphatidyl choline releasing free fatty acids and lysolecithin.

Thus it appears that the decrease of the phase transition temperature is produced by aging-induced alterations of the thylakoid membranes. It is therefore important to use carefully defined preparations when studying phase transitions and related changes in physiological activities in isolated chloroplasts.

References

Colbow, K., *Biochim. Biophys. Acta, 318*, 4–9, 1973.

Constantopoulos, G., and C. N. Kenyon, *Plant Physiol., 43*, 531–536, 1968.

Cox, R. P., *Eur. J. Biochem., 55*, 625–631, 1975.

Hoshina, S., T. Kaji, and K. Nishida, *Plant Cell Physiol., 16*, 465–474, 1975.

Inoué, H., *Plant Cell Physiol., 19*, 355–363, 1978.

Lee, A. G., *Biochem., 14*, 4397–4402, 1975a.

Lee, A. G., *Biochim. Biophys. Acta, 413*, 11–23, 1975b.

Murata, N., and D. C. Fork, *Plant Cell Physiol., 18*, 1265–1271, 1977.

van Ginkel, G., *Acta Bot. Neer., 26*, 303–311, 1977.

Wasserman, A. R., and S. Fleischer, *Biochim. Biophys. Acta, 153*, 154–169, 1968.

Williams, J. P., and P. A. Merrilees, *Lipids, 5*, 367–370, 1970.

Wintermans, J. F. G. M., P. J. Helmsing, B. J. J. Polman, J. van Ginsbergen, and J. Collard, *Biochim. Biophys. Acta, 189*, 95–105, 1969.

A COMPARATIVE STUDY OF THE PHOTOSYNTHETIC UNIT SIZES IN SUN AND SHADE PLANTS

Shmuel Malkin and David C. Fork

Plants are adapted to live in extremely shaded habitats as well as in the direct sun of open fields. Usually plants adapted to one habitat will not survive in the opposite environment. One idea to explain the differences between shade and sun plants is that shade plants have larger ratios of antenna chlorophyll to reaction centers (photosynthetic unit size or PSU) than do sun plants.

However, Boardman and Björkman (Boardman, 1977; *Year Book 71*, 107–135; Björkman, 1973) have stated that the ratios of chlorophyll to reaction centers did not vary significantly between the sun and shade plants. They considered that the main difference between sun and shade plants was that sun plants developed more electron transport enzymes and enzymatic activity associated with CO_2 fixation per chlorophyll than did shade plants.

We have reevaluated this question by measuring photosynthetic unit sizes in leaves by making measurements of fluorescence induction coupled with computer analysis of the data (*Year Book 78*, 199–201). This technique allowed us to obtain quickly and precisely the values for the initial slope, the normalized area above the fluorescence induction curve (induction time), and tables showing the relation between partial areas as a function of the fluorescence.

Leaves of shade plants were collected from plants growing in a redwood forest near Woodside, California, as well as from plants growing in the open fields of the Carnegie Institution, and vacuum-infiltrated with DCMU (2×10^{-5} M). Green (550 nm) actinic light having uniform intensity across a spot diameter of 25 mm was used to illuminate the upper surface of the horizontally placed leaf. Fluorescence at 685 nm was detected with a photomultiplier (EMI 9558B) placed above the sample and at an angle of 60° with the vertical.

The fluorescence signal was stored and displayed on a Nicolet 1010 signal averager and also was sent into a computer (Hewlett-Packard 1000F). The computer signal was digitized into 1024 points at specified time intervals. A group of the last points was averaged to obtain the maximum fluorescence level (F_{max}). To find the initial level of fluorescence attained immediately after illumination (F_0) a procedure was used whereby the computer used the exciting light as a reference and sensed the exact time at which the shutter was half opened. This point was fixed as time zero. The extrapolation of the fluorescence time curve for the first points when the shutter was fully opened to time zero gave the required F_0 and also served as a "corrected" fluorescence curve for the uncertainty period of the shutter opening time (*Year Book 78*, 199–201). This correction was small compared to the induction times of the leaves, since the shutter opening time was of the order of 3 ms.

Computer analysis was done so as to limit the induction time to a reasonable range during which only the main increase phase of the fluorescence was completed. This limitation was important, since in some cases additional, very slowly increasing or decreasing phases of small amplitudes were observed following the main fluorescence rise.

Although the above-mentioned fluorescence changes were of small amplitude, they could add or subtract significant area and change the induction time artificially. To eliminate the effect of these slow phases completely, the fluorescence curves were run with dif-

ferent termination times and the area was plotted as a function of the termination time. Back extrapolation from the values obtained at large termination times gave a value close to the correct one, as could be proved by a simple mathematical analysis. Criteria were developed for the full time scale to be used in each experiment, optimized to obtain the correct result.

The fluorescence curve measured in the presence of DCMU gives information on the concentration of reaction centers. The concentration of reaction centers, n, per chlorophyll can be obtained from the formula (*Year Book 77*, 237–240)

$$n/\text{chl} = [1 - (F_0/F_{\max})] \times 0.5 \times 2300 \times \epsilon_i \times I \times \bar{t},$$

where $1 - F_0/F_{\max}$ is the maximum quantum yield of excitation trapping when all of the reaction centers are open. The value 0.5 is a tentative factor for the fraction of the light that is distributed to PS II. Conversion of decadic to natural logarithms and expressing volume in cubic centimeters produced the factor 2300. The extinction coefficient (ϵ_i) at the wavelength of the actinic light is for chlorophyll in its in vivo environment. We have used a tentative average value of 8000 M^{-1} cm^{-1} at 500 nm. This value is not known precisely because of spectroscopic artifacts that tend to distort it. We estimated this value previously by measuring the absorption spectrum of chloroplast suspensions placed in an integrating sphere. I is the incident light intensity and $\bar{t}$ is the average induction time and is given by the area above the induction curve when $F_{\max} - F_0$ is normalized to unity.

The value of $\bar{t}$ was corrected for light attenuation effects in the leaf by division by the factor $[1 + (\epsilon_i/\epsilon_f) \cos \Theta]$ where ϵ_f is the extinction coefficient for the fluorescent light (685 nm) and Θ is the average angle between the direc-

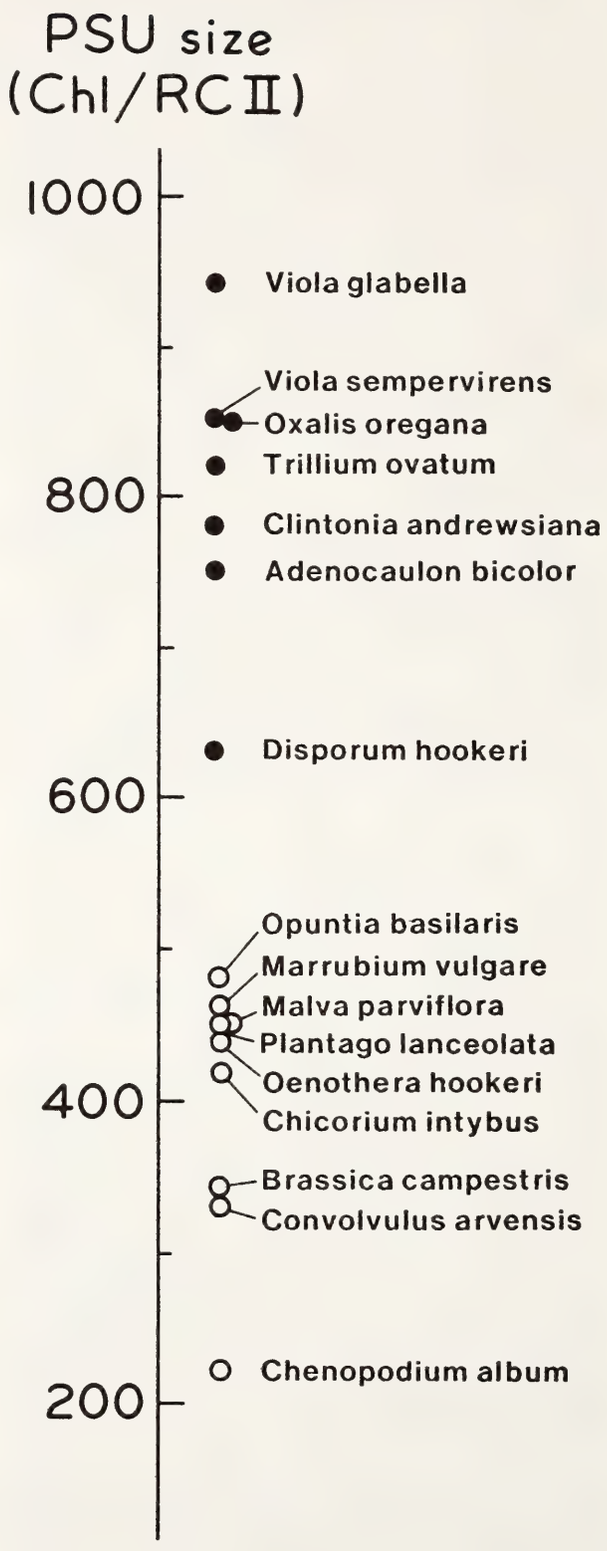


Fig. 45. Photosynthetic unit sizes (chlorophyll/reaction center of PS II) for a variety of sun plants (open circles) and shade plants (closed circles).

tion of the fluorescent light in the leaf, as viewed by the photomultiplier, and a line normal to the leaf surface. This correction factor for our case was small (around 7%).

Figure 45 shows the results of photosynthetic unit determinations made on eight sun and seven shade plants. Sun plants gave ratios of chlorophyll per reaction centers ranging from 220–540. The shade plants had photosynthetic unit sizes ranging from 630 to 940. Thus the range of all possible photosynthetic unit sizes is divided into two more or less separate regions: low values for all sun plants examined and high values for all shade plants tested.

It is an interesting question whether the photosynthetic unit is a characteristic of the genotype and cannot vary much when a plant is acclimated to an environment other than its natural one. Björkman *et al.* (*Year Book 71*, 115–135) found relatively little variation of the PSU sizes when *Atriplex patula* was grown under different light intensities, but other electron transport components did vary.

It is possible that changes in photosynthetic unit size may involve early evolutionary adaptation to changes in light level in the environment. It may now be possible to define the degree of adaptation of a sun or a shade plant according to the photosynthetic unit concept.

References

Boardman, N. K., *Annu. Rev. Plant Physiol., 28*, 355–377, 1977.

Björkman, O. in *Photophysiology,* Vol. 8, 1–63, A. C. Giese, ed., Academic Press, New York, 1973.

CHLOROPHYLL *a* FLUORESCENCE TRANSIENTS FROM SUN AND SHADE PLANTS

David C. Fork and Govindjee

Chlorophyll *a* fluorescence induction has been used in photosynthesis research to obtain information on the excitation energy transfer, heterogeneity of electron acceptors, size of the electron acceptor pool(s) of photosystem II (PS II), the electron flow on the electron donor or the acceptor side of PS II, etc. (see Papageorgiou, 1975; Lavorel and Etienne, 1977). Malkin and Fork (this Report) have obtained information on the size of the photosynthetic unit in DCMU-infiltrated leaves from sun and shade plants. The size of the photosynthetic unit (PSU), defined as the ratio of the number of bulk chlorophyll molecules (Chl) to the number of Q (the electron acceptor of PS II) molecules, in all the shade plants was about twice that in the sun plants. In this report we present comparative measurements on the chlorophyll *a* fluorescence induction of untreated leaves from several sun and shade plants. It is shown here that the time of the appearance of the peak *P* (see Papageorgiou, 1975) in the fluorescence induction (the Kautsky phenomenon) of untreated plants can be taken as a semiquantitative monitor of the size of the photosynthetic unit. In shade plants, this time ranges from 500 to 900 ms whereas the size of the PSU ranges from 600 to 1000 Chl per Q (this Report). In sun plants, however, this time ranges from 1500 to 3500 ms whereas PSU ranges from 200 to 500. The plants used in this study were chosen from those used by Malkin and Fork to measure photosynthetic unit size (this Report). The chlorophyll *a* fluorescence transient of 685 nm from the front surface of leaves was measured by excitation with saturating green light (540 nm).

Figure 46 shows representative tran-

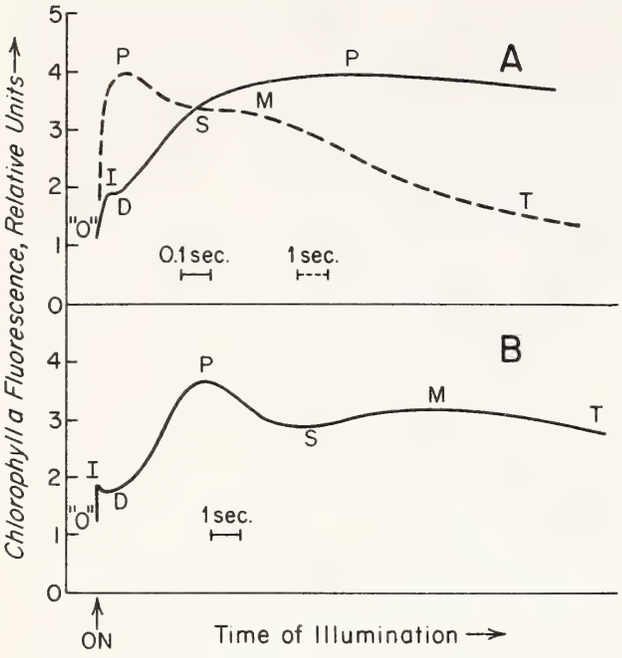


Fig. 46. Time course of chlorophyll *a* fluorescence on two time scales (20 s and 500 ms full scale) for a leaf from (A) a shade plant *Viola sempervirens* and (B) from a sun plant *Convolvulus arvensis*. For explanation of the transient points (OIDPSMT), see Papageorgiou (1975).

TABLE 15. Time of Appearance of Peak *P* in Fluorescence Induction, and Photosynthetic Size of Sun and Shade Plants

	Time of Appearance of Peak *P* ms	Photosynthetic Unit Size*
A. Shade Plants		
Viola glabella	1000	940
Viola sempervirens	900	850
Oxalis oregana	600	848
Clintonia andrewsiana	800	780
Adenocaulon bicolor	900	750
Disporum hookeri	750	630
Average	825	800
B. Sun Plants		
Opuntia basilaris	3000	480
Marrubium vulgare	2000	460
Plantago lanceolata	1500	450
Oenothera hookeri	1500	440
Brassica campestris	2000	340
Convolvulus arvensis	3500	330
Chenopodium album	3000	220
Average	2400	390

*From Malkin and Fork, this Report.

sients for two leaves selected from a shade plant (*Viola sempervirens*) and a sun plant (*Convolvulus arvensis*). The time of the appearance of the peak *P* is ~900 ms in *Viola* and 3500 ms in *Convolvulus*. Table 15 shows a compilation of the time of peak *P* in the untreated leaves including the size of the photosynthetic unit calculated from DCMU-treated leaves of the same plants (taken from the data of Malkin and Fork, this Report). An average of 800 Chl/Q corresponds to a time of peak of about 825 ms in shade plants, and an average of about 400 Chl/Q corresponds to a time of peak of about 2400 ms. An overall agreement between the two measurements in the two groups of plants is observed although no quantitative correlations were observed in individual species, as the two measurements were not made on identical leaves. A general inverse correlation between the time of the appearance of the peak *P* and the size of the photosynthetic unit is, however, clear. This work extends the usefulness of fluorescence measurements to ascertain the physiological status of higher plants.

References

Lavorel, J., and A. L. Etienne, in *Primary Processes of Photosynthesis*, 203–269, J. Barber ed., Elsevier Publishers, Amsterdam, 1977.

Papageorgiou, G., in *Bioenergetics of Photosynthesis*, 319–371, Govindjee, ed., Academic Press, New York, 1975.

CHLOROPHYLL *a* FLUORESCENCE TRANSIENT AS AN INDICATOR OF WATER POTENTIAL OF LEAVES

Govindjee, W. J. S. Downton, David C. Fork, and Paul A. Armond

Water stress leads to several changes in the photosynthetic apparatus of green plants (Boyer, 1976). Low water potential has been observed to cause a decrease in the quantum yield of O_2 evolution in chloroplasts and leaves from sunflower plants (Mohanty and Boyer, 1976), a decrease in the ability of the coupling factor, isolated from spinach leaves, to bind fluorescent nucleotides (ϵ-ATP, ϵ-ADP) (Younis *et al.*, 1979), and a decrease in the ratio of the maximum (*P* level) to the minimum (*O* level) fluorescence in the red alga *Porphyra sanjuanensis* (Wiltens *et al.*, 1978). In this report, we show that the "*P*" to "*O*" ratio in the leaves of *Nerium oleander* decreased when intact plants grown in soil were water stressed (water potential of leaves decreasing from −8 to −39 bar). Furthermore, this change was reversed when the plants were rewatered. A similar relationship between water potential and the *P/O* ratio was also observed in the leaves from *Atriplex triangularis* and *Tolmiea menziesii*. These data indicate that water stress inhibits the electron donation side of the photosystem II (PS II).

N. oleander plants were grown in 4- or 18-l pots outdoors for seven months and were about 1 m in height when used. Mean daily temperatures during the period of water stress studies were 27° max/5° min. Paired leaves were detached—one leaf was used for chlorophyll *a* fluorescence transient measurements after a 10-min dark adaptation, and the other leaf was used for water potential measurements also after a 10-min period. Water potential was measured in Wescor C52 psychrometers (Wescor, Inc., Logan, Utah), and

TABLE 16. Ratio of Maximum (*P*) to Minimum (*O*) Chlorophyll *a* Fluorescence Intensity as a Function of Water Potential of *Nerium oleander* Leaves

Conditions	Water potential, ψ_w, bar	*P/O*
1. Grown in 4-l pot; plant watered daily; sample time: 12:30 p.m.	−8.3	4.3
2. Grown in 18-l pot; watered daily; 3:00 p.m.	−8.7	3.1
3. Same as #2; a different plant	−9.9	2.8
4. Grown in 4-l pot; water stressed by the addition of only small quantities of water (~⅓ of control plant requirement) over the preceding 4 days; 2:30 p.m.	−14.6	2.6
5. Same as #4; a different plant; 11:30 a.m.	−16.2	2.7
6. Grown in 18-l pot; plant received no water for the preceding 4 days; 4:00 p.m.	−17.6	2.8
7. Grown in 4-l pot; water restricted (to ~¼ of the control plant requirement) for the preceding 3 days; 1:30 p.m.	−20.5	2.5
8. Leaf of #7 left for one hour for dehydration in room light	(est. −25*)	1.8
9. Grown in 4-l pot; plant received no water for the preceding 5 days; 1:30 p.m.	−39.2	1.1
10. #9 watered—allowed to recover for 18 hours; 11:00 a.m.	−9.9	2.5

*More negative than −20.5 (est. −25).

chlorophyll *a* fluorescence with the instrument described previously (Malkin, Fork, and Armond, *Year Book 77*, 237-240). Front surface fluorescence was monitored from the lower surface of the leaves at 685 nm and was excited by green light (550 nm).

Table 16 and Fig. 47 show the relationship between water potentials and the *P/O* ratios of *N. oleander* and other leaves under different conditions. The inset in Fig. 47 shows the fluorescence transient at several water potentials in *N. oleander* leaves. It is clear that *P/O* decreases from a high value of ~4.0 in well-watered *Nerium* plants ($\Psi_w = -8$ bar) to a low value of 1.1 in a severely stressed plant ($\Psi_w = -39$ bar). *Nerium* plants having a water potential of −39 bar could be recovered to a large extent by rewatering (compare #10 with #9, Table 16). Figure 47 shows a plot of *P/O* as a function of water potential in leaves of *N. oleander, A. triangularis* and *T. menziesii*. In *A. triangularis* and *T. menziesii*, different water potentials were obtained either by picking leaves at different times of the day or by dehydration of fresh leaves. Low-water-potential leaves were rehydrated by rewatering the intact plant or by simply placing the leaf in water. This recovery was not possible if the leaves were "crisp" dry (water potential substantially lower than −40 bar). In all cases examined, the *P/O* decreases as the wa-

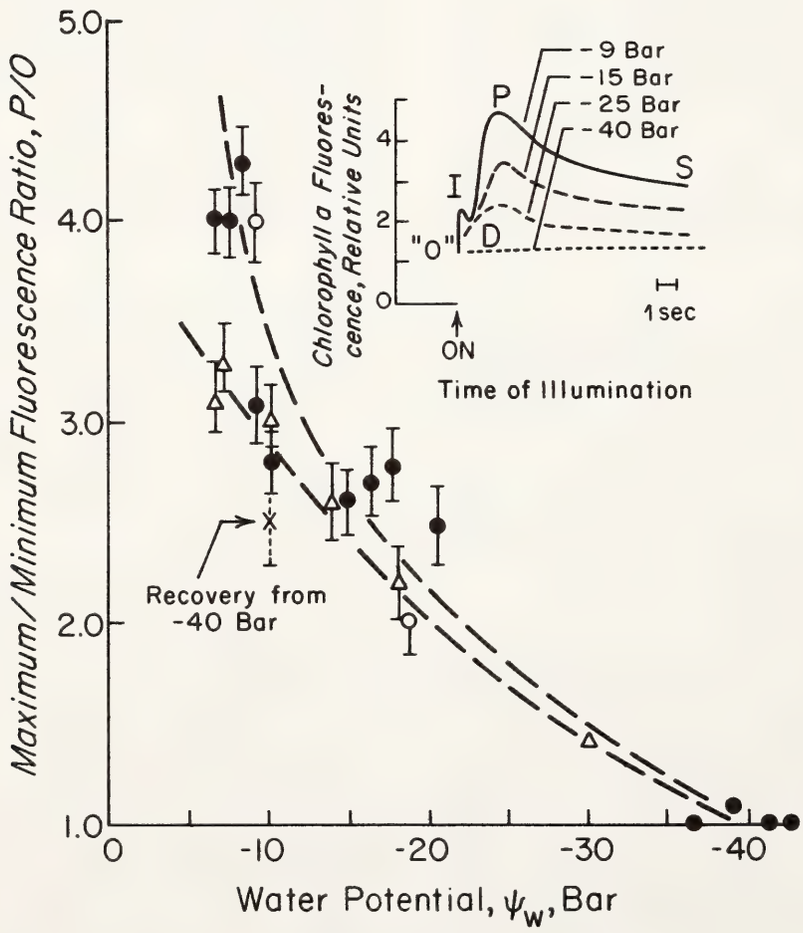


Fig. 47. A plot of the ratio of *P* (maximum) to *O* (minimum) chlorophyll *a* fluorescence as a function of the water potential of the leaves from *Nerium oleander* (●), *Atriplex triangularis* (△), and *Tolmiea menziesii* (○). × indicates recovered *N. oleander* leaf. Vertical bars indicate errors in measurement of *P/O* ratio. Inset: chlorophyll *a* fluorescence transient in four different *Nerium oleander* leaves at different water potentials. The meaning of the various points on the chlorophyll *a* fluorescence transient, referred to as O, I, D, P, and S, are described elsewhere (see Papageorgiou, 1975).

ter potential is decreased. Thus, the *P/O* ratio serves as a qualitative indicator of the leaf water potential.

A decrease in *P/O* ratio is equivalent to a decrease in the variable (*P* minus *O*) fluorescence. If the electron donation from the donor (water) side of PS II is inhibited, Q (the stable electron acceptor of PS II) cannot be reduced. Since chlorophyll *a* fluorescence is low when Q is in the oxidized state and is high when Q is in the reduced state (Duysens and Sweers, 1963), chlorophyll *a* fluorescence remains low, i.e., *P/O* is low when the block is on the water side of PS II. These results emphasize that water stress blocks electron flow on the water side of PS II. P. Mohanty and J. Boyer (personal communication) have recently observed that the *P/O* ratio is diminished in chloroplasts isolated from dehydrated sunflower leaves, also indicating a block on the electron donation side of PS II. Other studies in this Report deal with the effects of water stress on energy distribution between the two photosystems of photosynthesis.

References

Boyer, J. S., in *Water Deficits and Plant Growth*, Vol. 4, 153–190, T. T. Kozlowski, ed., Academic Press, N. Y., 1976.

Duysens, L. N. M., and H. E. Sweers, in *Studies in Microalgae and Photosynthetic Bacteria*, 353–372, Japanese Society of Plant Physiologists, ed., Tokyo, 1963.

Mohanty, P., and J. S. Boyer, *Plant Physiol., 57*, 704–709, 1976.

Papageorgiou, G., in *Bioenergetics of Photosynthesis*, 319–371, Govindjee, ed., Academic Press, N. Y., 1975.

Wiltens, J., U. Schreiber, and W. Vidaver, *Can. J. Bot., 56*, 2787–2794, 1978.

Younis, J. M., J. S. Boyer, and Govindjee, *Biochim. Biophys. Acta, 548*, 328–340, 1979.

EFFECTS OF DESICCATION ON THE EXCITATION ENERGY DISTRIBUTION BETWEEN THE TWO PHOTOSYSTEMS IN THE RED ALGA *Porphyra perforata*

Gunnar Öquist and David C. Fork

The most desiccation-tolerant plants are found among algae, lichens, and mosses (Levitt, 1972). Some species can tolerate very severe desiccation, often in combination with exposure to high light intensities and temperatures, and still recover their physiological activities upon rehydration. In order to increase our basic understanding of how drying affects photosynthesis on the membrane level and how dry desiccation-tolerant plants avoid photodynamic damage in strong light, we have used fluorescence techniques to study how desiccation of the red alga *Porphyra perforata* affects the energy distribution from the phycobilins to the two photosystems.

As *Porphyra* has a broad, flat thallus only one cell layer in thickness, its optical properties are very good for spectroscopic work. The alga lives in the upper intertidal zone and it loses its photosynthetic activity as it undergoes desiccation at low tide (Wiltens *et al.*, 1978). However, it still shows photochemical activity of photosystem I (PS I) in the dry state, and rewetting of dry *Porphyra* causes a rapid activation of electron transport (*Year Book 72*, 384–388). We show in this work that desiccation of *Porphyra* causes a loss of photosystem II (PS II) emission at −196 °C and an increased energy transfer from the phycobilins to PS I. Such a desiccation-controlled change of energy distribution has earlier been suggested for the lichen *Cladonia impexa* (Sigfridsson and Öquist, 1980) and it may be a part of the mechanism by which desiccation-tolerant plants avoid photodynamic damage when

photosynthesis becomes inhibited as a consequence of drying.

The red alga *Porphyra perforata* was collected weekly at Bean Hollow near Pigeon Point (north of Santa Cruz, California) and stored in sea water at 13 °C (photoperiod 12 h; 8 μmol quanta m^{-2} s^{-1}). The effects of desiccation on fluorescence emission spectra, excitation spectra, and fluorescence kinetics were studied with a microprocessor-based spectrofluorometer described earlier (*Year Book 78*, 196–199). Measurements were performed both at 20 ° and −196 °C, and samples of algae were dried in darkness for 2 h in an air stream at 20 °C, unless mentioned otherwise. Emission and excitation spectra were corrected against spectra obtained with a standard lamp and rhodamine B, respectively. The slits of the monochromator were set to pass a half band of 1.6 and 3.2 nm for emission and excitation spectra, respectively.

When exciting *Porphyra* with green light (543 nm; absorbed by phycoerythrin) at −196 °C, three main fluorescence emission bands were observed: F688, F697, and F742. Both F688 and F697 are characteristics of PS II, and their excitation spectra show that they both are primarily sensitized by light absorbed by the phycobilins. The fluorescence band F742, which originates from PS I, is primarily sensitized by light absorbed by chlorophyll *a*. However, the phycobilins become an increasingly important antenna even for F742 as the reaction center traps of PS II become closed at −196 °C, and the spillover of excitation energy from PS II to PS I increases (Butler, 1978).

The absorbance of *Porphyra* is affected by desiccation. If *Porphyra* is allowed to shrink during desiccation its absorbance increases about three times, as compared with a wet control. However, if the alga is kept stretched or if it is kept pressed to a glass surface, no increase of absorbance or other absorbance change is observed upon drying. In our comparisons of the fluorescence properties of dry and wet *Porphyra* we have used samples with similar absorbance. This matching was achieved by comparing the fluorescence of one layer of dry, nonstretched *Porphyra* with the fluorescence of three layers of wet *Porphyra*; or one layer of dry, stretched *Porphyra* was used for comparison with one layer of wet *Porphyra*.

The effects of desiccation on the −196 °C emission spectrum of dark-adapted *Porphyra* were studied using excitation either of chlorophyll *a* (433 nm) or of phycoerythrin (543 nm). Chlorophyll *a* excitation revealed that desiccation of *Porphyra* induced both a lowering of the fluorescence yield (2.6 times) and a 10-nm shift to shorter wavelengths of the far-red emission peak (Fig. 48). The shape and yield of these chlorophyll *a*-sensitized emission spectra were not affected by the state of the reaction centers of PS II; i.e., the results of Fig. 48 were obtained both when the spectra were recorded before or after closing of PS II traps, either by a 10-min treatment with strong green light at −196 °C or by freezing an algal sample in strong white light (2100 μmol quanta m^{-2} s^{-1}). Phycoerythrin excitation revealed that a phycobilin emission peak at 647 nm, and the PS II emission bands F688 and F697 almost disappeared as a result of desiccation (Fig. 49). Furthermore, the phycoerythrin-sensitized emission spectrum (excitation wavelength 543 nm) was the same for *Porphyra* dried either in the dark or light or after exposure to strong green light at −196 °C. This result shows that light treatment could not affect the state of reaction center traps of PS II in dry *Porphyra*. However, for wet *Porphyra* the phycoerythrin-sensitized emission spectrum was affected by the state of the PS II traps (Fig. 49, compare F_0 and F_{max} spectra). The fluorescence yields at 688, 697, and 742 nm were about two times higher when the PS II traps were closed (F_{max} spectrum; traps closed at

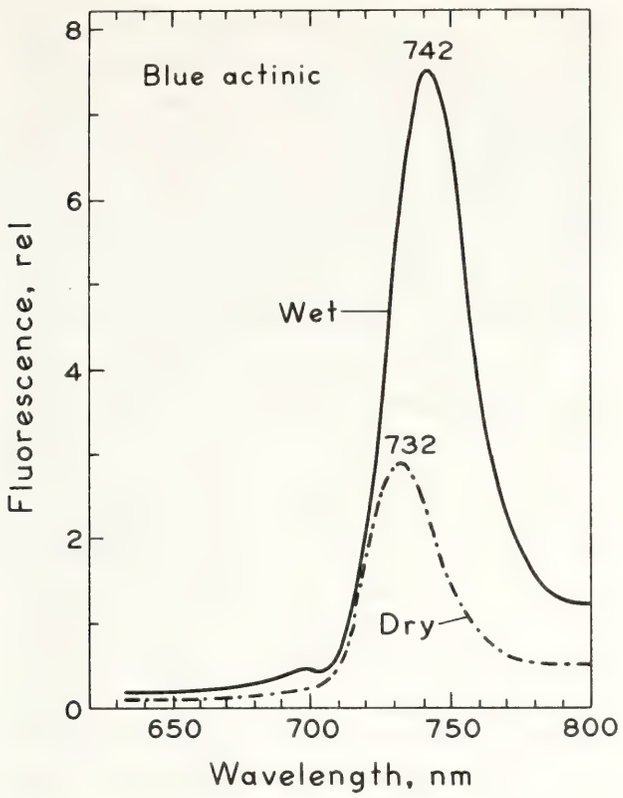


Fig. 48. Low-temperature (−196 °C) fluorescence emission spectra of wet (——) and desiccated (·-·-·-) *Porphyra perforata*. The fluorescence was sensitized by chlorophyll *a* excitation (Balzers 433, half band width 12 nm; Corning glass filter 5-60; Balzers Calflex C). Three layers of wet, dark-adapted *Porphyra* and one layer of dark-dried, nonstretched *Porphyra* were used in Figs. 48–51 in order to give the two samples equivalent absorption properties.

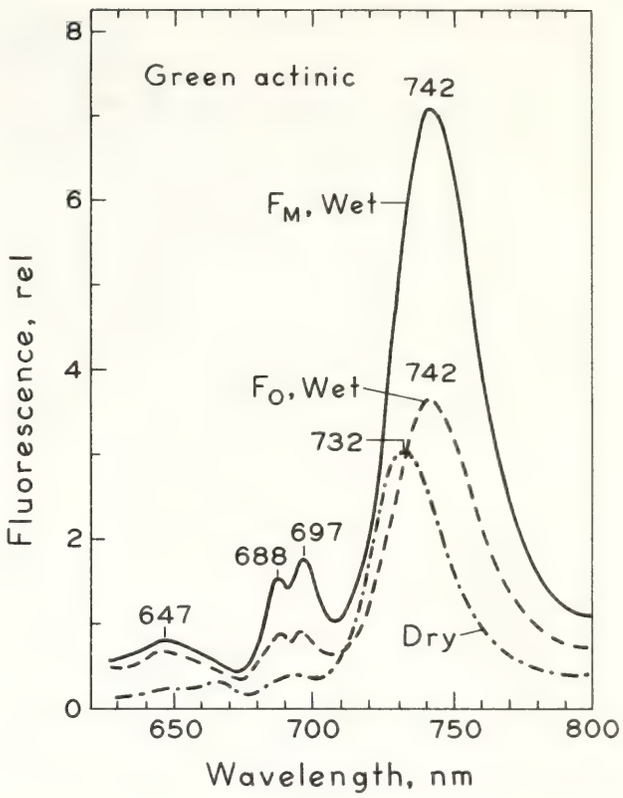


Fig. 49. Low-temperature (−196 °C) fluorescence emission spectra of wet (- - -, F_0; ——, F_{max}) and desiccated (·-·-·-) *Porphyra perforata*. The fluorescence was sensitized by phycoerythrin excitation (Balzers 543, half band width 9 nm; Corning glass filter 4-96; Balzers Calflex C). The F_0 spectrum was obtained when the PS II reaction centers were all open and F_{max} when they were all closed.

−196 °C by strong green light or by freezing the sample in strong white light of 2100 μmol quanta m^{-2} s^{-1}) compared to the yields when the traps were open (F_0 spectrum; dark-adapted samples were frozen and the excitation light was weak enough to avoid any significant trap closure during the emission spectrum measurement).

The shape of these emission spectra are dependent both on the fluorescence yield of emitting chlorophyll *a* forms and on energy transfer between antennae. In order to illustrate how desiccation of *Porphyra* affects the energy transfer from the phycobilins to the two photosystems, we have replotted the phycoerythrin-sensitized emission spectrum of dry *Porphyra* after correcting for the desiccation-induced decrease of fluorescence yield of the far-red emitting chlorophyll *a* forms (correction factor of 2.65 obtained from Fig. 48). The result is shown in Fig. 50. When the spectrum of dry *Porphyra* is compared with the F_0 spectrum of the wet control, it is obvious that the decrease of the two PS II emission bands F688 and F697 upon drying is accompanied by a 2.1 times increase of the height of the far-red emission band: the energy transfer from phycoerythrin to PS I has increased with the same factor as a result of drying. However, as the traps of PS II become closed in the wet sample, the energy transfer from phycoerythrin to PS I also increases by spillover, and the height of the far-red emission peak of wet *Porphyra* is just

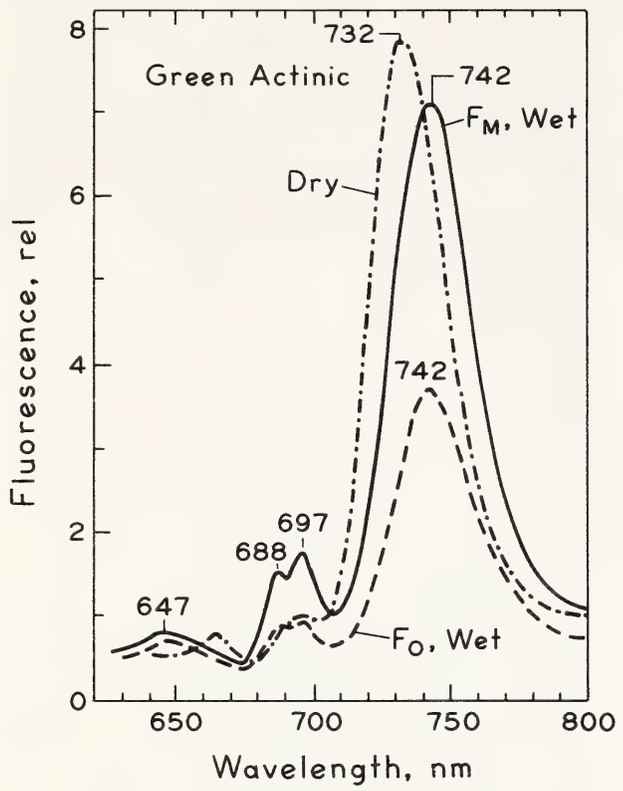


Fig. 50. Low-temperature (−196 °C) fluorescence emission spectra of wet (- - -, F_0; ——, F_{max}) and desiccated (·-·-·-) *Porphyra perforata* after the spectrum of dry *Porphyra* had been corrected for the decrease of the intrinsic fluorescence yield (Fig. 48) of the far-red-emitting chlorophyll *a* form(s). Excitation as in Fig. 49.

slightly lower than that of dry *Porphyra*. The slightly lower height of the far-red emission peak of wet (F_{max}) than of dry *Porphyra*, and the well-developed F688 and F697 PS II bands of wet *Porphyra*, may be because wet samples have a less complete spillover of excitation energy from PS II to PS I than dry samples.

By studying the time course of the fluorescence increase at 730 nm at −196 °C as the PS II reaction centers became closed in green light, we found a 107% increase of fluorescence yield in wet samples but only a 22% increase of fluorescence yield in dry samples. This result again shows that light exposure of dry *Porphyra* does not affect PS II very much. By using the F_0 and F_{max} values from these experiments on fluorescence kinetics, we calculated the ratios $F_{0\ dry}/F_{0\ wet} = 1.9$ and $F_{max\ dry}/F_{max\ wet} = 1.2$ (after correction for the desiccation-controlled decrease of the intrinsic fluorescence yield of PS I upon chlorophyll *a* excitation at 433 nm). These values are in close agreement with the data of Fig. 50.

From the results presented above we expected that the excitation spectrum for the far-red emission peak would show a higher phycoerythrin/chlorophyll efficiency ratio in dry compared to dark-adapted wet samples. Such a relationship was indeed found (Fig. 51; spectrum of dry vs. F_0 spectrum of wet sample). Closure of PS II reaction center traps in wet *Porphyra* again showed that the efficiency of phycoerythrin to sensitize far-red emission increased relative to chlorophyll. However, the increase was still less than that caused by desiccation.

Even at 20 °C *Porphyra* has a far-red emission peak or shoulder near 730 nm,

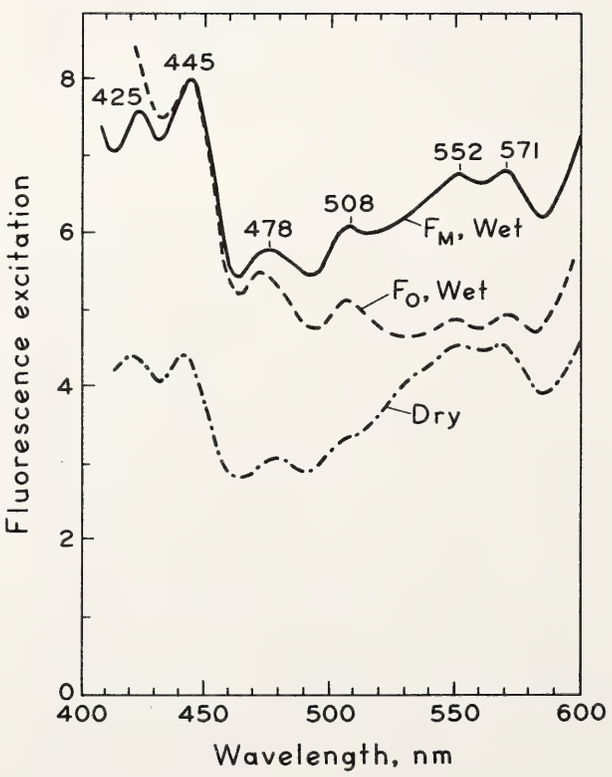


Fig. 51. Low-temperature (−196 °C) fluorescence excitation spectra for 730-nm emission in wet (- - -, F_0; ——, F_{max}) and desiccated (·-·-·-) *Porphyra perforata*.

which is sensitized by chlorophyll *a* and phycobilin absorption, whereas the main emission peak at 686 nm is sensitized only by phycobilin absorption. We have therefore concluded that *Porphyra*, unlike other plants, has measurable far-red emission from PS I even at room temperatures. The room-temperature fluorescence yield of this far-red-emitting chlorophyll form(s) increases during desiccation, which is opposite to our observation at −196 °C shown in Fig. 48. However, by taking this change into consideration we have by the above-mentioned fluorescence methods found that desiccation of *Porphyra* even at 20 °C causes an increased energy transfer from phycoerythrin to PS I.

The same increase of energy transfer from phycoerythrin to PS I was obtained irrespective of drying in darkness or strong light (incandescent light of 2100 μmol quanta m^{-2} s^{-1} or direct sunlight) as long as the samples were allowed to shrink during desiccation. However, if shrinkage was prevented by stretching the alga on a glass surface during desiccation, the observed increase in energy transfer from phycoerythrin to PS I became less pronounced, especially if the algae were dried in darkness.

Assuming that about 50% (or slightly less) of the excitation energy absorbed by the phycobilins is transferred to PS I when the PS II traps of wet samples are all open (Butler, 1978), we interpret the desiccation-induced doubling of F_0 fluorescence at 730 nm (Fig. 50) as showing that essentially all excitation energy absorbed by the phycobilins is transferred to PS I in dry *Porphyra*. We assume that desiccation increases the probability of energy spillover from PS II to PS I, thereby decreasing the probability of PS II trap closure or emission. (Phycoerythrin-sensitized PS II trap closure becomes very inefficient at the same time that the PS II emission bands, F688 and F697, almost disappear.)

The desiccation-controlled increase in spillover may be related to an increased proximity between chlorophyll *a* antennae of the two photosystems when the alga shrinks during drying. Furthermore, the short waveshift of the far-red emission peak upon drying may be a sign of closer energy coupling between PS II and PS I.

We hypothesize that the outlined change of energy distribution is an active process by which desiccation-tolerant plants can avoid photodynamic damage to PS II when photosynthesis becomes inhibited as a result of drying. The close proximity between β-carotene and the far-red-absorbing and far-red-emitting chlorophyll *a* forms of PS I might be the ultimate energy sink where excess excitation energy is transformed into heat (Öquist *et al.*, 1980). The fact that PS I is in a more hydrophilic environment than PS II also makes PS I better equipped to transform excitation energy to heat than PS II.

References

Butler, W. L., *Annu. Rev. Plant Physiol., 29*, 345–378, 1978.

Levitt, J., *Responses of Plants to Environmental Stresses*, Academic Press, New York, 1972.

Öquist, G., G. Samuelsson, and N. I. Bishop, *Physiol. Plant.*, 1980, in press.

Sigfridsson, B., and G. Öquist, *Physiol. Plant., 49*, 329–335, 1980.

Wiltens, J., U. Schreiber, and W. Vidaver, *Can. J. Bot., 56*, 2787–2794, 1978.

COMPARISON OF PHOTOSOMES WITH AND WITHOUT A MANGANESE-CONTAINING PROTEIN

Govindjee, David C. Fork, T. Wydrzynski, M. Spector,† and G. D. Winget†*

The mechanism of oxygen evolution in green plants is not well understood. Despite experimental evidence that there is a "charge accumulator" that accumulates four positive charges before O_2 is released from water and that manganese may play a key role in O_2 evolution (see a review by Radmer and Cheniae, 1977), little is known about the chemical intermediates involved in water splitting. Spector and Winget (1980) have recently purified a 65,000-dalton manganese-containing protein from spinach. They combined this protein with preformed liposomes containing cholate-extracted thylakoids, and they observed restoration up to 85% of the original O_2 evolution activity.

We report here several characteristics of liposomes containing the cholate-extracted thylakoids (to be referred to as depleted photosomes) and of liposomes containing the cholate-extracted thylakoids and the manganese protein (to be referred to as complete photosomes). The complete photosomes showed a normal chlorophyll *a* fluorescence transient, a normal pattern of O_2 evolution per flash in a series of flashes, almost normal steady-state O_2 evolution rates, and a normal 515-nm absorption change. In contrast, the depleted photosomes showed no variable chlorophyll *a* fluorescence, no O_2 evolution in either continuous light or with light flashes, and an unusual light-induced absorption decrease in the carotenoid region. We interpret our results to indicate that the depleted photosomes lack electron flow on the donor side of photosystem II (PS II), whereas complete photosomes catalyze PS II electron transport from water. Whether the restoration of O_2 evolution to the depleted photosomes is due solely to the addition of a specifically required manganese-containing protein (redox enzyme), or rather due to the reestablishment of electron flow by some indirect changes in the physical characteristics of depleted photosomes brought about by the addition of the manganese protein, cannot be answered from our present experiments.

The depleted and complete photosomes were prepared at the University of Cincinnati by two of us (M. S. and G. D. W.), as described by Spector and Winget (1980), and were mailed by air freight in dry ice (−80 °C) to Stanford, California, where the experiments were done. The stock preparations contained 2.1 mg lipid (asolectin) : 4 mg total protein : 1 mg chlorophyll. Samples were thawed before use, and were diluted to a chlorophyll concentration of 4 μg/ml for fluorescence and absorption measurements, and to ~20 μg/ml for O_2 measurements.

Steady-State O_2 Evolution Rates. Figure 52 (solid line) shows a trace of O_2 evolution in continuous saturating white light for complete photosomes suspended in 10 mM phosphate buffer and 2 mM $MgCl_2$ (pH 7.2); the rate of O_2 evolution in the samples used in this study was 160 μmol O_2/mg Chl/h with 2 mM ferricyanide as an electron acceptor. The depleted photosomes, on the other hand, showed no O_2 evolution (dashed curve, Fig. 52).

O_2 Evolution in Flashing Light. Figure 53 shows O_2/flash in a series of light flashes (duration, 0.6 μs; time between flashes, one second) for complete (●) and depleted (×) photosomes.

*Department of Botany, University of Illinois, Urbana 61801

†Biological Sciences Department, University of Cincinnati, Ohio 45221

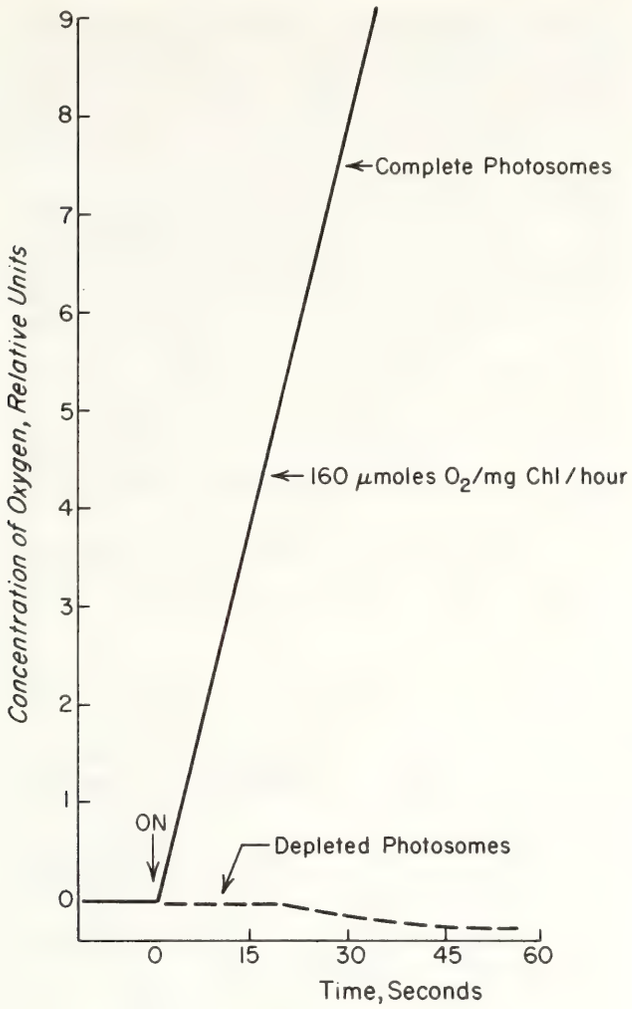


Fig. 52. O_2 evolution as a function of time of illumination in complete photosomes measured by a concentration electrode (solid line). The trace for depleted photosomes shows the absence of O_2 evolution (dashed line). Electron acceptor, 2 mM ferricyanide; calculated rate of O_2 evolution in complete photosomes was 160 μmol/mg Chl/h in the absence of an added uncoupler of photophosphorylation.

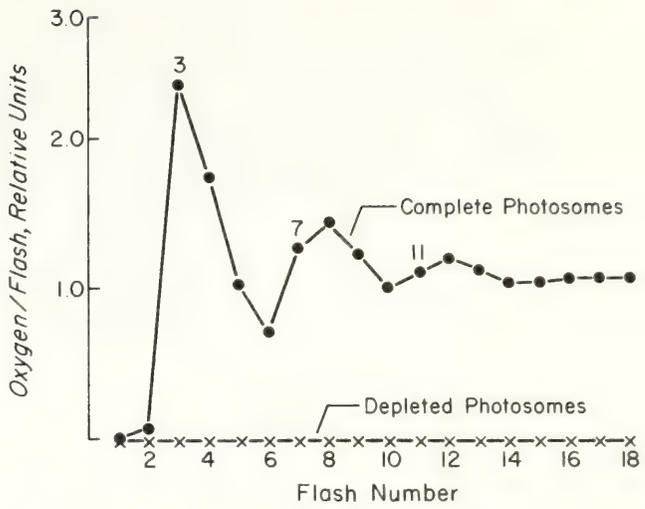


Fig. 53. O_2 evolution per flash as a function of flash number in a series of flashes in complete photosomes (●) and depleted photosomes (×). Note the absence of O_2 evolution in depleted photosomes. The complete photosomes show results similar to chloroplasts.

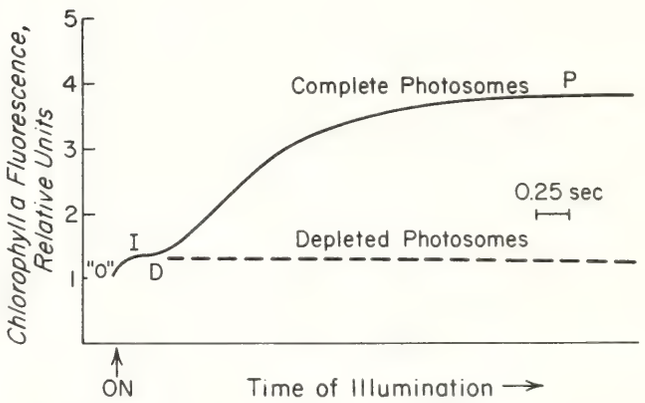


Fig. 54. Chlorophyll *a* fluorescence transients in complete (solid line) and depleted (dashed line) photosomes. For definition and meaning of symbols O, I, D, and P, see Papageorgiou (1975). Note the absence of variable fluorescence (D to P rise) in depleted photosomes. Complete photosomes show results similar to chloroplasts.

There was absolutely no O_2 evolution in the depleted photosomes, and an almost normal flash pattern in complete photosomes.

Chlorophyll a Fluorescence Transient. Figure 54 shows that the complete photosomes have the usual fluorescence transient (OIDP; see Papageorgiou, 1975). The depleted photosomes have no variable fluorescence. This suggests that electron donation is absent in these preparations as they give results identical to those obtained with heat-treated chloroplasts.

515-nm Absorption Change. Figure 55 shows that the complete photosomes have a light-induced absorbance increase at 515 nm just as chloroplasts have. However, depleted photosomes show only an absorbance decrease at 515 nm. A difference spectrum of this decrease suggests that carotenoids are bleached by the light in these preparations (data not shown).

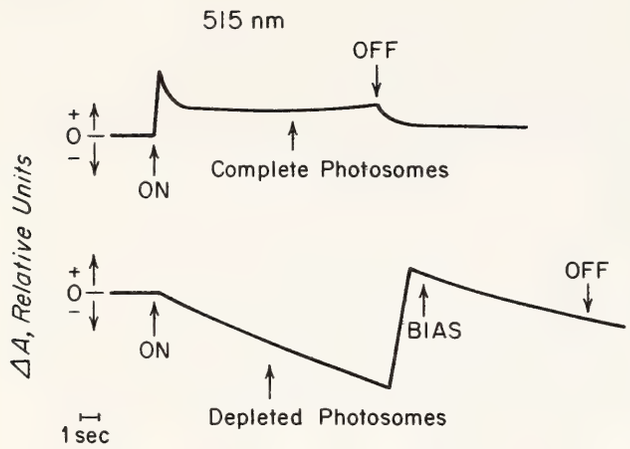


Fig. 55. Light-induced absorbance changes at 515 nm in complete photosomes (upper curve) and in depleted photosomes (lower curve). Note the absence of absorbance increase in depleted photosomes; instead, a large absorbance decrease is observed. Complete photosomes show results similar to chloroplasts.

Absorption spectra, emission spectra, and action spectra of chlorophyll *a* fluorescence of both complete and depleted photosomes are approximately the same (data not shown), suggesting that there are no significant changes in the excitation energy transfer or in the pigment content and composition after the mild cholate-treatment, as used by Spector and Winget (1980).

In conclusion, depleted photosomes behave as if a component on the electron donor side of photosystem II has been removed, whereas the complete photosomes behave as if this component has been replaced. This indicates that the 65,000-dalton manganese protein is involved in electron transport on the donor side of PS II.

Govindjee acknowledges financial support from NSF Grant 11657.

References

Papageorgiou, G., in *Bioenergetics of Photosynthesis*, 319–371, Govindjee ed., Academic Press, N.Y., 1975.

Radmer, R. and G. Cheniae, in *Primary Processes of Photosynthesis*, 303–348, J. Barber, ed., Elsevier, Holland, 1977.

Spector, M., and G. D. Winget, *Proc. Nat. Acad. Sci. U.S.A. 77*, 957–959, 1980.

PHOTOSYNTHESIS BIBLIOGRAPHIC FILE UPDATE—JUNE 1980

Jeanette S. Brown

The computer-based bibliographic information retrieval file described in *Year Book 72*, p. 407, *Year Book 75*, p. 479, and *Year Book 78*, p. 202 has increased by over 2000 records since last year to a current total of 11,200. Unfortunately, my suggestion to try searching the file from your own library terminal connected to the computer network was premature. However, the Research Libraries Group at Stanford University now is hoping to have the necessary documentation ready by the end of this calendar year. When this information is available, we shall notify those of you working in photosynthesis. My original offer to provide printouts of individual categories at cost will remain in effect.

BIBLIOGRAPHY

Anderson, D. J., *see* Osmond, C. B.

680 Armond, P. A., O. Björkman, and L. A. Staehelin, Dissociation of supramolecular complexes in chloroplast membranes: a manifestation of heat damage to the photosynthetic apparatus. *Biochim. Biophys. Acta, Biomembranes Section*, in press, 1980.

Armond, P. A., *see* Raison, J. K.

700 Badger, M. R., Properties of RuP_2 carboxylase from *Anabaena variabilis*, *Arch. Biochem. Biophys.*, in press, 1980.

699 Badger, M. R., A. Kaplan, and J. A. Berry, Inorganic carbon pool of *Clamydomonas reinhardtii, Plant Physiol.,* in press, 1980.

Badger, M. R., *see* Canvin, D. T.; Kaplan, A.

692 Belford, H. S., W. F. Thompson, and D. B. Stein, DNA hybridization techniques for the study of plant evolution. In *Phytochemistry and Angiosperm Phylogeny,* D. A. Young and D. S. Seigler, eds., Phytochemical Society Symposium, Praeger Scientific, New York, in press, 1980.

Belford, H. S., *see* Thompson, W. F.

673 Berry, J. A., and O. Björkman, Photosynthetic response and adaptation to temperature in higher plants, *Annu. Rev. Plant Physiol., 31,* 491–543, 1980.

Berry, J. A., *see* Badger, M. R.; Canvin, D. T.; Farquhar, G. D.; Kaplan, A.; Pike, C. S.; Raison, J. K.; Seemann, J. R.

691 Björkman, O., The response of photosynthesis to temperature. In *Plants and Their Atmospheric Environment,* Proceedings British Ecological Society, in press, 1980.

Björkman, O., *see* Armond, P. A.; Berry, J. A.; Kaplan, A.; Mooney, H. A.; Osmond, C. B.

Blatt, M. R., *see* Briggs, W. R.

696 Briggs, W. R., A blue light photoreceptor system in higher plants and fungi. In *Photoreceptors and Plant Development,* J. A. De Greef, ed., University of Antwerpen, in press, 1980.

681 Briggs, W. R., and R. Blatt, Blue light responses in the siphonaceous alga *Vaucheria.* In *The Blue Light Syndrome,* 261–268, H. Senger, ed., Springer, Berlin, Heidelberg, New York, 1980.

Briggs, W. R., *see* Britz, S. J.; Goldsmith, M. H. M.; Gorton, H. L.; Hertel, R. A.; Quail, P. H.; Senger, H.; Song, P.-S.; Widell, S.

675 Britz, S. J., and W. R. Briggs, Rhythmic chloroplast migration in the green alga *Ulva:* dissection of movement mechanism by differential inhibitor effects, *Eur. J. Cell Biol.,* in press, 1980.

Britz, S. J., *see* Widell, S.

684 Brown, J. S., Absorption and fluorescence spectra of chlorophyll proteins isolated from *Euglena gracilis, Biochim. Biophys. Acta, 591,* 9–21, 1980.

Brown, J. S., *see* Melis, A.

Caemmerer von, S., *see* Farquhar, G. D.

686 Canvin, D. T., J. A. Berry, M. R. Badger, H. Fock, and C. B. Osmond, Oxygen exchange in leaves in the light, *Plant Physiol., 66,* 302–309, 1980.

Caubergs, R. J., *see* Goldsmith, M. H. M.

Cuellar, R. E., *see* Thompson, W. F.

Dohrmann, V., *see* Hertel, R. A.

Downton, W. J. S., *see* Seemann, J. R.

703 Farquhar, G. D., S. von Caemmerer, and J. A. Berry, A biochemical model of photosynthetic CO_2 assimilation in leaves of C_3 species, *Planta, 149,* 78–90, 1980.

Fock, H., *see* Canvin, D. J.

Fork, D. C., *see* Hiyama, T.

Fugate, R. D., *see* Song, P.-S.

662 Goldsmith, M. H. R., R. J. Caubergs, and W. R. Briggs, Light-inducible cytochrome reduction in membrane preparations from corn coleoptiles. I. Stabilization and spectral characteristics of the reaction, *Plant Physiol.,* in press, 1980.

695 Gorton, H. L., and W. R. Briggs, Phytochrome responses to end-of-day irradiation in light-grown corn in the presence and absence of Sandoz 9789, *Plant Physiol.,* in press, 1980.

687 Harvey, G., Seasonal alteration of photosynthetic unit sizes in three herb layer components of a deciduous forest community, *Amer. J. Bot., 67,* 293–299, 1980.

693 Hertel, R. A., A. J. Jesaitis, U. Dohrmann, and W. R. Briggs, *In vitro* binding of riboflavin to subcellular particles from maize coleoptiles and *Cucurbita* hypocotyls, *Planta, 147,* 312–319, 1980.

661 Hiyama, T., and D. C. Fork, Kinetic identification of component Y as P430: A primary electron acceptor of photosystem I, *Arch. Biochim. Biophys., 199,* 488–496, 1980.

Jesaitis, A. J., *see* Hertel, R. A.

623 Kaplan, A., and O. Björkman, Ratio of CO_2 uptake to O_2 evolution during photosynthesis in higher plants, *Pflanzenphysiol., 96,* 185–188, 1980.

682 Kaplan, A., M. R. Badger, and J. A. Berry, Photosynthesis and the intracellular inorganic carbon pool in the blue-green alga *Anabaena variabilis:* response to external CO_2 concentration, *Planta,* in press, 1980.

Kaplan, A., *see* Badger, M. R.

701 Melis, A., and J. S. Brown, The stoichiometry of System I and II reaction centers in different photosynthetic members, *Proc. Nat. Acad. Sci., 77,* 4712–4716, 1980.

698 Mooney, H. A., O. Björkman, A. E. Hall, E. Medina, and P. B. Tomlinson, The study of physiological ecology of tropical plants—current status and needs, *BioScience, 30,* 22–26, 1980.

702 Murray, M. G., D. L. Peters and W. F. Thompson, Ancient repeated sequences in the pea and mung bean genomes and implications for genome evolution, *J. Mol. Evol.,* in press, 1980.

Murray, M. G., *see* Thompson, W. F.

Osmond, C. B., O. Björkman, and D. J. Anderson, *Physiological Processes in Plant Ecology: Toward a synthesis with* Atriplex, Springer, Berlin, Heidelberg, New York, 1980, 502 pp.

Osmond, C. B., *see* Canvin, D. T.

Peters, D. L., *see* Murray, M. G.

674 Pike, C. S., and J. A. Berry, Membrane phospholipid phase separation in plants adapted to or acclimated to different thermal regimes, *Plant Physiol., 66,* 238–241, 1980.

Pike, C. S., *see* Raison, J. K.

690 Quail, P. H., and W. R. Briggs, Irradiation-enhanced phytochrome pelletability: mixing experiments, *Plant Physiol.,* in press, 1980.

651 Raison, J. K., J. A. Berry, P. Armond, and C. S. Pike, Membrane properties in relation to the adaptation of plants to high and low temperature stress. In *Adaptations of Plants to Water and High Temperature Stress,* 261–273, Wiley-Interscience, 1980.

697 Seemann, J. R., J. A. Berry, and W. J. S. Downton, Studies of the physiological ecology of desert annual plants in Death Valley National Monument. In *Proceedings of AIBS-NPS 2nd Annual Conference on Research in National Parks,* in press, 1980.

706 Senger, H., and W. R. Briggs, The blue light receptor(s); Primary reactions and subsequent metabolic changes. In *Photochemical and Photobiological Reviews,* K. Smith, ed., Vol. 6, Plenum Press, New York, in press, 1980.

637 Song, P.-S., R. D. Fugate, and W. R. Briggs, Flavin as a photoreceptor for phototropic transduction: Fluorescence studies of model and corn coleoptile system. In *6th Flavin Symposium Proceedings,* 443–453, I. Yagi, T. Yamano, eds., University Park Press, Baltimore, 1978.

Staehelin, L. A., *see* Armond, P. A.

Stein, D. B., *see* Belford, H. S.

671 Thompson, W. F., M. G. Murray, and R. E. Cuellar, Contrasting patterns of DNA sequence organization in plants. In *Genome Organization and Expression in Plants,* 1–15, C. J. Leaver, ed., Plenum Press, New York, 1980.

685 Thompson, W. F., and M. G. Murray, Sequence organization in pea and mung bean DNA and a model for genome evolution. In *The Plant Genome,* 31–45, D. R. Davies and D. A. Hopwood, eds., John Innes Charity, Norwich, England, 1980.

659 Thompson, W. F., M. G. Murray, H. S. Belford, and R. E. Cuellar, Patterns of DNA sequence repetition and interspersion in higher plants. In *Genetic Improvement of Crops,* I. Rubenstein, R. L. Phillips, C. E. Green, and B. G. Gegenbach, eds., University of Minnesota Press, Minneapolis, in press, 1980.

658 Thompson, W. F., and M. G. Murray, The nuclear genome: structure and function, In *Biochemistry of Plants, 6,* A. Marcus, ed., Academic Press, New York, in press, 1980.

Thompson, W. F., *see* Belford, H. S.; Murray, M. G.

625 Widell, S., S. J. Britz, and W. R. Briggs, Characterization of the red light-induced reduction of a particle-associated *b*-type cytochrome from corn in the presence of methylene blue, *Photochem. Photobiol.,* in press, 1980.

SPEECHES

Armond, Paul A., Temperature-induced alterations of photosynthetic membrane structure and function, Pfizer Central Research, Groton, Connecticut, July 2, 1979.

Badger, Murray A., *see* Berry, Joseph A.

Belford, Heather, William F. Thompson, and Diana B. Stein, Use of DNA hybridization techniques in the study of plant evolution, Phytochemical Section, Botanical Society of America, Annual Meeting, Stillwater, Oklahoma, August 15, 1979.

Berry, Joseph A., and Murray A. Badger, Measurement of [^{18}O] oxygen uptake during photosynthesis by intact leaves of C_3 and C_4 plants at controlled CO_2 concentration, American Society of Plant Physiologists Meeting, Ohio State University, Columbus, July 30–August 4, 1979.

Berry, Joseph A., Mechanisms of adaptation of plants to high temperature, University of California at Davis, Department of Vegetable Crops, October 31, 1979.

Berry, Joseph A., Adaptation of higher plants to contrasting temperatures, Michigan State University, Plant Research Laboratory, East Lansing, November 15, 1979.

Berry, Joseph A., The Fixation and metabolism of oxygen in photorespiration, Michigan State University, Plant Research Laboratory, East Lansing, November 15, 1979.

Berry, Joseph A., Adaptations and acclimation of higher plants to contrasting temperatures, Photosynthesis Research Conference, Asilomar, California, December 14–16, 1979.

Berry, J. A., *see* Pike, C. S.

Berry, J. A., *see* Raison, J.; Björkman, O.

Björkman, Olle, Photosynthetic adaptation to contrasting temperature regimes, Department of Biology, University of Utah, Salt Lake City, October 25, 1979.

Björkman, Olle, Photosynthetic adaptation in desert plants, Department of Botany, Brigham Young University, Provo, Utah, October 26, 1979.

Björkman, Olle, Response and adaptation of photosynthesis to high temperature stress, College of Agricultural Environmental Sciences, University of California, Davis, November 28, 1979.

Björkman, Olle, Adaptation of plants to extremes of irradiance, Department of Biological Sciences, Stanford University, California, May 12, 1980.

Björkman, O., *see* Raison, J.

Blatt, Michael, R., Current events in *Vaucheria*, NATO-ASI School on Photomovement of micro-organisms, Pisa, Italy, September 2–14, 1979.

Blatt, Michael R., A chronology of events leading to chloroplast aggregation in *Vaucheria*, Botanisches Institüt, University of Erlangen, Erlangen, West Germany, November 27, 1979.

Blatt, Michael R., Electrical currents coupled to chloroplast aggregation in *Vaucheria*, Department of Botany, University of Wisconsin, Madison, December 22, 1979.

Blatt, Michael R., Shocking observations from a blue-light-irradiated alga, Stanford-Carnegie Plant Sciences Seminars, Carnegie Institution, Stanford, California, January 10, 1980.

Blatt, M. R., *see* Briggs, W. R.

Briggs, Winslow R., and Michael R. Blatt, Blue light responses in the siphonaceous alga *Vaucheria*, International Conference on the effect of blue light on plants and microorganisms, *The Blue Light Syndrome*, Marburg, West Germany, July 16, 1979.

Briggs, Winslow R., Blue light photoreception in higher plants, Annual European Symposium on Photomorphogenesis, *Photoreceptors and Plant Development*, Antwerpen, Belgium, July 22–28, 1979.

Briggs, Winslow R., The early consequences of blue light excitation in the higher plants and fungi, Hopkins Marine Station, Pacific Grove, California, January 17, 1980.

Briggs, Winslow R., A blue light photoreceptor system from plants and fungi, Botany Department, University of Wisconsin, Madison, February 28, 1980.

Briggs, Winslow R., Characterization of a blue light photoreceptor system from plants and fungi, Department of Biology, University of California at San Diego, La Jolla, March 5, 1980.

Briggs, Winslow R., Blue light photoreception in plants and fungi, Department of Biology, California State University at Northridge, Los Angeles, April 9, 1980.

Briggs, Winslow R., Perception and transduction of blue light signals by plants and fungi, Department of Biology, University of California at Los Angeles, April 10, 1980.

Briggs, W. R., *see* Caubergs, R.; Gorton, H.; Leong, T.-Y.; Mandoli, D.; Quail, P. H.

Brown, Jeanette S., Spectroscopy of chlorophyll-protein complexes, California Photosynthesis Conference/Asilomar, Asilomar, California, December 15, 1979.

Brown, Jeanette S., Absorption and fluorescence of chlorophyll *in vivo*, Gordon Research Conference, Santa Barbara, California, February 6, 1980.

Caubergs, Roland, The blue light photoreception in corn coleoptiles, International Conference of the Effect of Blue Light on Plants and Microorganisms, *The Blue Light Syndrome*, Marburg, West Germany, July 18, 1979.

Caubergs, Roland, Blue-light-induced absorbance changes in membrane preparations from corn coleoptiles, Annual European Symposium on Photomorphogenesis, *Photoreceptors and Plant Development*, Antwerpen, Belgium, July 27, 1979.

Cuellar, Richard E., Molecular cloning of cDNA and genomic DNA fragments and practical applications, SYVA Corporation, Palo Alto, California, April 16, 1980.

Cuellar, Richard E., Perspectives of a minority graduate student in science, MESA (Mathematics, Engineering, and Science Achievement) Awards Ceremony, Oakland, California, May 17, 1980.

Cuellar, Richard E., Comparison of five strains of *E. coli* for the cloning of plant DNA, NATO-FEBS Conference on Plant Genome Organization and Expression, University of Edinburgh, United Kingdom, June 11, 1979.

Cuellar, Richard E., Cloned fragments of pea DNA containing assays of repetitive sequence elements, Gordon Research Conference on Plant Molecular Biology, Proctor Academy, Andover, New Hampshire, June 11, 1980.

Cuellar, R. E., *see* Thompson, W. F.

Downton, W. J. S., Thermal stability of photosynthesis in desert ecosystems, Stanford-Carnegie Plant Sciences Seminars, Carnegie Institution, Stanford, California, October 3, 1979.

Fork, David C., Temperature control of photosynthesis, Department of Biological Sciences, Stanford University, California, May 7, 1980.

Fork, D. C., *see* Govindjee; Hiyama, T.; Malkin, S.

French, C. Stacy, Fads, facts, and progress in photosynthesis research: 1900–1970. Photosynthesis Research Conference, Asilomar, Pacific Grove, California, December 14, 1979.

Gorton, Holly L., and Winslow R. Briggs, Phytochrome responses in light-grown corn seedlings in the presence and absence of Sandoz, Annual European Symposium on Photomorphogenesis, *Photoreceptors and Plant Development*, Antwerpen, Belgium, July 28, 1970.

Govindjee, David C. Fork, Thomas Wydrzynski, Mark Spector, and G. Douglas Winget, Studies of photosomes with and without an M-protein, Gordon Research Conference, Santa Barbara, California, February 5, 1980.

Harvey, Geoffrey W., The adaptation and acclimation of plants to shading: A view of subcellular alterations, Department of Biology, University of Alaska, Anchorage, December 18, 1979.

Hiyama, Tetsuo, and David C. Fork, Kinetic identification of component X as P430: A primary electron acceptor of photosystem I, American Society of Plant Physiologists, Columbus, Ohio, August 1, 1979.

Jorgensen, Richard A., The molecular genetics of *Pisum sativum*, Department of Biology, University of Oregon, Eugene, April 10, 1980.

Jorgensen, Richard A., The molecular genetics of *Pisum sativum*, Department of Genetics, University of Alberta, Edmonton, Canada, April 17, 1980.

Jorgensen, Richard A., The molecular genetics of *Pisum sativum*, Monsanto Company, St. Louis, Missouri, May 5, 1980.

Leong, Ta-Yan, The role of protein synthesis in the photosynthesis circadian rhythm in *Acetabularia*, Stanford-Carnegie Plant Science Seminars, Carnegie Institution, Stanford, California, December 5, 1979.

Leong, Ta-Yan, and Winslow R. Briggs, Purification and characterization of particulate system showing a blue-light-induced reduction of a *b*-type cytochrome, Gordon Research Conference, Sensory Transduction of Microorganisms, Santa Barbara, California, January 7–11, 1980.

Leong, Ta-Yan, Purification and characterization of particulate system showing blue-light-induced reduction of a *b*-type cytochrome, Biology Department, University of California, Santa Cruz, February 8, 1980.

Levitt, Jacob, Plant responses to environmental stress, Agricultural College/USDA, North Carolina State University, Raleigh, October 17, 1979.

Levitt, Jacob, Stress resistance and the principle of complementarity, University of Mexico, Mexico City, February 6, 1980.

Malkin, Shmuel, and David C. Fork, Photosynthetic unit sizes in sun and shade plants, Gordon Research Conference, Santa Barbara, California, February 6, 1980.

Mandoli, Dina F., and Winslow R. Briggs, Photobiology of oat mesocotyl and coleoptile, American Society for Photobiology, Asilomar, California, June 26, 1979.

Mandoli, Dina F., Algal photomovement, Department of Biological Sciences, Stanford University, California, May 5, 1980.

Mandoli, Dina F., Phytochrome controls of two photomorphogenic events in oats, Stanford-Carnegie Plant Sciences Seminars, Carnegie Institution, Stanford, California, June 11, 1980.

Melis, Anastasios, Stoichiometry and unit size of PSI and PSII as related to the chloroplast ultrastructure, California Photosynthesis Conference/Asilomar, Asilomar, California, December 15, 1979.

Melis, Anastasios, The stoichiometry of PSII and PSI reaction centers in different photosynthetic membrane preparations, Gordon Research Conference, Santa Barbara, California, February 6, 1980.

Melis, Anastasios, Stoichiometry of PSII and PSI reaction centers in different photosynthetic membrane preparations, Botany Department, University of California, Berkeley, March 2, 1980.

Murray, Michael G., and William F. Thompson, Diverged repetitive sequences in "single copy DNA," NATO-FEBS Conference on Plant Genome Organization and Expression, University of Edinburgh, United Kingdom, June 11, 1979.

Murray, Michael G., Contrasting patterns of DNA sequence organization in peas and mung beans, Pfizer Central Research, Groton, Connecticut, February 29, 1980.

Murray, Michael G., and William F. Thompson, Studies on the organization of coding sequences in the pea nuclear genome, Gordon Conference on Plant Molecular Biology, Andover, New Hampshire, June 9–13, 1980.

Nobs, Malcolm, Evolution in Australian *Atriplex*, Ecological Workshop, Research School of Biological Sciences, Australian National University, Canberra City, March 17, 1980.

Öquist, Gunnar, Effects of frost hardening and winter stress on photosynthesis of pine, Stanford-Carnegie Plant Sciences Seminars, Carnegie Institution, Stanford University, California, February 20, 1980.

Pike, Carl S., and Joseph A. Berry, Lipid phase separation temperature in warm and cool climate plants, American Society of Plant Physiologists, Ohio State University, Columbus, July 30–August 4, 1979.

Powles, Steven B., The role of CO_2 assimilation and photorespiratory carbon cycling in the avoidance of photoinhibition in leaves of C_3 and C_4 plants: A gas exchange analysis, Stanford-Carnegie Plant Sciences Seminars, Carnegie Institution, Stanford, California, February 6, 1980.

Preisler, Richard S., Studies of evolutionary sequence divergence in repeated DNA of peas and mung beans, Stanford-Carnegie Plant Sciences Seminars, Carnegie Institution, Stanford, California, February 27, 1980.

Quail, Peter H., and Winslow R. Briggs, Irradiation-enhanced phytochrome pelletability—filtration and mixing experiments with *Avena*, Annual European Symposium on Photomorphogenesis, *Photoreceptors and Plant Development*, Antwerpen, Belgium, July 22–28, 1979.

Quail, Peter H., Phytochrome: the first five minutes from Pfr formation, Annual European Symposium on Photomorphogenesis, *Photoreceptors and Plant Development*, Antwerpen, Belgium, July 25, 1979.

Raison, John, Joseph A. Berry, and Olle Björkman, Changes in chloroplast lipid fluidity during acclimation of plants to high- and low-growth temperatures, American Society of Plant Physiologists, Ohio State University, Columbus, July 30–August 4, 1979.

Seemann, Jeffrey R., Studies of the physiological ecology of desert annual plants in Death Valley National Monument, AIBS-NPS, San Francisco, California, November 28, 1979.

Spector, Mark, *see* Govindjee.

Stein, D., *see* Belford, H.

Sundqvist, Christer, Ultrastructural appearance of protochlorophyll-containing plastids from the inner seed coat of *Curcurbita pepo* and *Cyclanthera explodens*, Stanford-Carnegie Plant Sciences Seminars, Carnegie Institution, Stanford, California, October 24, 1979.

Sundqvist, Christer, Ultrastructural appearance of the plastids in the inner seed coat of *Cucurbita* and *Cyclanthera*, Botany Department, University of California, Davis, January 24, 1980.

Thompson, William F., Michael G. Murray, and Richard E. Cuellar, Contrasting patterns of DNA sequence organization in plants, NATO-FEBS Workshop on Genome Organization and Expression in Plants, University of Edinburgh, United Kingdom, July 12, 1979.

Thompson, William F., and Michael Murray, Sequence organization in pea and mung-bean DNA and a model for genome evolution, John Innes Institute, Norwich, England, September 11, 1979.

Thompson, William F., What can we learn from DNA sequence organization patterns? Botany Department, University of California, Davis, October 11, 1979.

Thompson, William F., Comparison of the pea and mung bean genomes (and a model for genome evolution), Lake Arrowhead Genetics Conference, Lake Arrowhead, California, February 2, 1980.

Thompson, William F., A model for genome evolution, Biology Department, Oregon State University, Corvallis, May 28, 1980.

Thompson, William F., Heterogeneous families, fossil repeats, and evolutionary turnover in complex genomes, Gordon Conference, Andover, New Hampshire, June 9–13, 1980.

Thompson, W. F., *see* Belford, H.; Cuellar, R. E.; Murray, M. G.

van Ginkel, Gijsbert, and John Raison, O_2- and OH-formation in systems containing chlorophyll, American Society of Plant Physiologists Annual Meeting, Ohio State University, Columbus, August, 1979.

Winget, G. Douglas, *see* Govindjee.

Wydrzynski, Thomas, *see* Govindjee.

PERSONNEL

Research Staff

Joseph A. Berry
Olle Björkman
Winslow R. Briggs, Director
Jeanette S. Brown
David C. Fork
C. Stacy French, Director Emeritus
William M. Hiesey, Emeritus
Malcolm A. Nobs
William F. Thompson

Research Associate

Michael G. Murray

Postdoctoral Fellows

Richard A. Jorgensen, National Science Foundation Fellowship, University of Wisconsin, Madison, WI[1]
Jacob Levitt, Senior Fellow, University of Minnesota, Minneapolis, MN
Stephen B. Powles, CSIRO, Canberra, Australia
Thomas D. Sharkey, Australian National University, Canberra, Australia[2]

[1]To November 15, 1979
[2]To March 27, 1980

Carnegie Institution of Washington Postdoctoral Fellows

Paul A. Armond[3]
W. J. S. Downton, Senior Fellow, CSIRO, Adelaide, Australia[4]
Govindjee, Visiting Investigator, University of Illinois-Urbana, Urbana, IL[5]
Geoffrey W. Harvey
George E. Hoch, Senior Fellow, University of Rochester, NY
Richard A. Jorgensen
Ta-Yan Leong
Shmuel Malkin, Senior Fellow, Weizmann Institute of Science, Israel[6]
Anastasios Melis
Gunnar Öquist, Senior Fellow, University of Umeå, Sweden
Peter H. Quail, Senior Fellow[7]
Christer Sundqvist[8]
Gijsbert van Ginkel[8]

Graduate Students

Michael R. Blatt, Stanford University, CA
Richard E. Cuellar, Stanford University, CA
Holly L. Gorton, Stanford University, CA
Dina F. Mandoli, Stanford University, CA
Jeffrey D. Palmer, Stanford University, CA
Richard S. Preisler, Stanford University, CA
Jeffrey R. Seemann, Stanford University, CA
Celia M. Smith, Stanford University, CA
William E. Williams, Stanford University, CA

Clerical and Technical Staff

Peter A. Angwin, Laboratory Technician
Benny Catanzaro, Electronic Technician[9]
Dorothy Ruth Fischer, Administrative Assistant–Accountant
Glenn A. Ford, Laboratory Manager
Edward G. Gausden, Technician[10]
Steven M. Graff, Laboratory Technician
Richard W. Hart, Mechanical Engineer
Einar Ingebretsen, Electronic Technician
Fred Lakin, Technical Illustrator
David W. Lendrum, Technician
Nancy E. Malich, Laboratory Technician[11]
Frank Nicholson, Senior Technician
Debra Peters, Laboratory Technician
Norma J. Powell, Typist
Pedro Pulido, Technician
Patricia Sullivan, Laboratory Technician[12]
Rudolph Warren, Technician
Aida Wells, Department Secretary

[3]To August 31, 1979
[4]To December 15, 1979
[5]To August 31, 1979
[6]To July 31, 1979
[7]To August 31, 1979
[8]To June 30, 1980
[9]To March 7, 1980
[10]To March 31, 1980
[11]To August 10, 1979
[12]To September 30, 1979

Developmental Biology Research Group

Pasadena, California
and Kerckhoff Marine Laboratory,
Corona Del Mar, California

Roy J. Britten
Senior Research Fellow

Eric H. Davidson
Professor, California Institute of Technology

Carnegie Institution of Washington Year Book 79, 1979–1980

Contents

Introduction 211
Single Copy DNA Polymorphism of Sea Urchins in the Genus Strongylocentrotus 212
Analysis of Sequence Polymorphism in Regions Surrounding Structural Genes 212
Human Single Copy DNA Polymorphism 213
Sequence Organization around a Structural Gene in Sea Urchin DNA 213
Isolation of Insulin-Like DNA Sequences from the Sea Urchin 214
DNA Rearrangements around Homologous Structural Genes in Two Sea Urchins 214
Evolution of Sea Urchin DNA Coding Sequences 215
Repetitive Sequences of the Sea Urchin Genome 215
Nucleotide Sequence Analysis of the Fine Structure of Repetitive DNA 216
Isolation and Characterization of a Gene Battery 216
Cycles of Oogenesis in Wild and Laboratory-Maintained Sea Urchins 217
Sea Urchin Egg Poly(A)$^+$ RNAs contain Transcripts of Repeated DNA Sequences 217
Nature and Fate of Repetitive Sequence Transcripts in the Sea Urchin Egg 217
Repetitive Sequence Transcripts in *Xenopus* Egg RNA 218
Complexity of RNA in Developing Oocytes of *Drosophila* 218
Electron Microscope Visualization of Transcription in Echinoderm Oocytes 219
RNA Synthesis in the Fertilized Mouse Egg 219
Synthesis of Vitelline Layer Proteins of Sea Urchin Eggs 220
Limited Complexity of RNA in Micromeres of 16-Cell Sea Urchin Embryos 220
Messenger RNA Prevalence in Sea Urchin Embryos Measured with Cloned cDNAs 221
Regulation of mRNA Prevalence in the Sea Urchin Embryo 221
Patterns of Expression of mRNA Sequences of Sea Urchin Embryos 222
Rates of Accumulation and Turnover of Individual Messenger RNAs 222
Turnover Rates of Structural Gene Transcripts in Nuclear RNAs 223
Staff 223
Publications 223

INTRODUCTION

The Developmental Biology Research Group continues to focus on four areas of molecular biology: the sequence organization of the genome, the evolution and variation of the DNA and its sequence organization, the regulation of gene expression, and the modulation of genetic activity during embryonic development. Again this year, only short abstracts are included and the report is essentially identical to that in the annual report of the Biology Division of the California Institute of Technology. Perhaps the most striking observations reported this year relate to repetitive sequence transcripts which are present in stored poly $(A)^+$ RNA in the mature sea urchin egg. These moderately large RNA molecules (3–10 kb) are presumptive maternal messenger RNA, and include the sequences of the vast majority of the structural genes known to be expressed in sea urchin tissues. Most of these RNA molecules include transcripts of short repeats, and most or all of the different structural genes transcripts are covalently linked to repeat transcripts. Each family of repeats studied is found only in a set of a few different sizes of transcripts. The sets of transcripts are different for the plus and minus strands of each family of repeats. This indicates that the two complements of a family of repeats in egg maternal mRNA are each produced by specific individual events of asymmetric transcription. The RNAs can form repetitive duplexes and, in vitro, at least form complex branched structures. These complementary relationships among the maternal RNA molecules may have significance for the regulation of their future processing and expression in early development. In another and very suggestive project, a set of genes (battery?) were identified, all of which contain a member of one family of repeats which appears in the 3′ untranslated region of the mRNA transcript.

The work described in the following research reports has also been supported by:

American Cancer Society
American Cancer Society, California Division
Biomedical Research Support Grant (NIH)
Charles B. Corser Fund for Biological Research
March of Dimes
National Institutes of Health, USPHS
National Science Foundation
Veterans Administration
Weizmann Fellowship

SINGLE COPY DNA POLYMORPHISM OF SEA URCHINS IN THE GENUS STRONGYLOCENTROTUS

John W. Grula, Terrence J. Hall, John Hunt, Terrence Giugni, and Roy J. Britten*

Since the first observation of a large amount (4%) of single copy DNA sequence polymorphism in the sea urchin, *Strongylocentrotus purpuratus* (Britten, Cetta, and Davidson, 1978), we have been interested in determining the generality of this variation among other species. Therefore, the single copy DNA polymorphism of two related sea urchins, *S. drobachiensis* and *S. franciscanus,* has been measured. Both exhibit a slightly smaller degree of sequence polymorphism than *S. purpuratus* (2% and 3% for *S. drobachiensis* and *S. franciscanus,* respectively). Additional measurements indicate that there are no length differences in the duplexes formed with DNA from the same or an unrelated individual. This suggests that the observed polymorphism in these species is mainly attributable to randomly distributed base substitutions and not DNA rearrangements. Studies utilizing cloned DNA are now in progress to determine the relative importance of these alternative processes in generating intraspecific single copy DNA variation.

*University of Hawaii, Honolulu.

Reference

Britten, R. J., A. Cetta, and E. H. Davidson. (1978) *Cell 15:* 1175–1186.

ANALYSIS OF SEQUENCE POLYMORPHISM IN REGIONS SURROUNDING STRUCTURAL GENES

John W. Grula, John W. Roberts, Terry L. Thomas, Laurence A. Lasky, Eric H. Davidson, and Roy J. Britten

Thermal stability measurements have demonstrated about 4% single copy DNA sequence polymorphism in the sea urchin *Strongylocentrotus purpuratus.* There is evidence that this is the average of differences in sequence ranging from less than 1% to more than 10%. Restriction endonuclease digestion has been used to investigate the sequence polymorphism in regions surrounding several structural genes expressed in *S. purpuratus* gastrula cDNA. When a single copy labeled probe is incubated with a blot of a restriction digest of an individual DNA, one or two bands usually appear on an autoradiograph. The variation of the band positions for several individuals allows an estimate of the number of "alleles" or restriction site variants for each enzyme. One cDNA plasmid probe (SpG19) gave the same band for all eight individual DNA Eco RI digests. Plasmid SpG30 also gave only one allele with Eco RI, and two alleles were detected with Hind III. Thus, these two genes appear to occur in regions with little polymorphism. Plasmid SpG6 showed four alleles with Eco RI, four with Bam HI, and two with Hind III, and is in a somewhat more polymorphic region. Another structural gene region (Sp88) has been examined in considerable detail, as described elsewhere in this Report. Among eight individual DNAs, it shows eight alleles with Eco RI, six with Hae III, three with Pst, and eight with Hind III. Thus, this region is the most polymorphic so far studied by this technique. Calculation suggests that it may be in a region showing about 4% polymorphism, while SpG6 is in a region showing about 2%. The restriction analyses are consistent with single copy DNA polymorphism measured by thermal stability and show different degrees of polymorphism adjacent to different genes.

HUMAN SINGLE COPY DNA POLYMORPHISM

Terrence J. Hall, Terrence Giugni, Michael Cummings, and Roy J. Britten*

Human single copy DNA polymorphism has recently been examined. DNA was isolated from a single individual. Two different ^{3}H-DNA tracers were prepared by in vitro labeling of a human fibroblast culture or by nick translation of sperm DNA and isolation of the single copy DNA. The tracers were reacted with DNAs from the same individual, from an unrelated individual, and a mixture of DNA obtained from more than 20 individuals. The thermal stability reduction for the interindividual duplexes compared to controls indicate that there is approximately 1% base substitution in human single copy DNA. This observation for total single copy is consistent with the data of Jeffreys (1979) concerning the degree of base substitution within an intervening sequence of β-globin DNA.

*Illinois Institute for the Study of Developmental Disabilities, Chicago.

Reference

Jeffreys, A. J. (1979) *Cell 18:* 1–10.

SEQUENCE ORGANIZATION AROUND A STRUCTURAL GENE IN SEA URCHIN DNA

Terry L. Thomas, Nelson L. Smith, and Eric H. Davidson

We have cloned a sea urchin genomic DNA fragment, Sp88, that contains a single copy sequence coding for rare mRNAs. The number of Sp88 mRNA transcripts per embryo changes drastically during sea urchin development (Lev *et al.*, 1980). In addition, four distinct size classes of Sp88 RNA transcripts have been found in early sea urchin embryos (Lee *et al.*, 1980). At least three species are localized on polysomes of the 16-cell embryo; however, by the gastrula stage the predominant RNA species is approximately six kilobases (kb) in length and is represented almost exclusively in the nuclear RNA.

Sp88 has a complex sequence organization with several nonrepetitive DNA sequence elements interspersed with different repetitive sequence elements. However, all the Sp88 sequences are located 3′ to the coding region. We have recently isolated longer DNA sequences containing the Sp88 structural gene. This was accomplished by screening bacteriophage λ libraries, containing approximately 15 kb sea urchin DNA inserts, with labeled DNA probes made from the codogenic region of Sp88. One of these λ recombinants, λ-16, contains approximately 12 kb of genomic DNA 5′ to the original Sp88 coding region. With λ-16, we are examining the longer range sequence organization surrounding the Sp88 codogenic sequence, i.e., we wish to define with respect to the coding region the location of repetitive sequence elements and other codogenic and noncodogenic single copy DNA sequences. Additionally, λ-16 is being used to investigate the interesting and probably complex relationship between the primary transcripts of Sp88 and its respective mRNAs. This will allow us to determine whether the multiple polyadenylated transcripts seen in the 16-cell embryo are processing intermediates or whether they are different mRNAs that overlap at their 3′ termini.

References

Lee, A. S., T. L. Thomas, Z. Lev, R. J. Britten, and E. H. Davidson. (1980) *Proc. Nat. Acad. Sci. USA.* In press.

Lev, Z., T. L. Thomas, A. S. Lee, R. C. Angerer, R. J. Britten, and E. H. Davidson. (1980) *Devel. Biol. 76:* 322–340.

ISOLATION OF INSULIN-LIKE DNA SEQUENCES FROM THE SEA URCHIN

Terry L. Thomas, Argiris Efstratiadis, and Eric H. Davidson*

The importance of insulin and other peptide hormones in vertebrate physiology is well documented. Interestingly, there are a number of examples of insulin-like activities in invertebrates, including the starfish, an echinoderm. We have isolated three different insulin-like DNA sequences from sea urchin DNA by screening our *Strongylocentrotus purpuratus* bacteriophage λ libraries with a cloned rat insulin cDNA probe. This clone was constructed by Villa-Komaroff *et al.* (1978). Filter hybridization experiments suggest about 70% homology between these sea urchin λ recombinants and the rat preproinsulin gene. These homologies are being confirmed by direct DNA sequencing.

Our interest in these sea urchin DNA clones is directed at the genome organization surrounding the DNA sequences homologous to the insulin gene, and the expression of these sequences both in nuclear RNA and mRNA in embryonic and adult tissues. Preliminary RNA/DNA hybridization experiments with one of the insulin-like sequences show that this DNA sequence is represented at a very low level in both pluteus and intestine total RNA. We will also compare the DNA sequence of these insulin-like recombinants with the already determined DNA sequences of insulin structural genes of other species.

*Harvard University School of Medicine, Boston, Massachusetts.

Reference

Villa-Komaroff, L., A. Efstratiadis, S. Broome, P. Lomedico, R. Tizard, S. P. Naber, W. L. Chick, and W. Gilbert. (1978) *Proc. Nat. Acad. Sci. USA 75:* 3727–3731.

DNA REARRANGEMENTS AROUND HOMOLOGOUS STRUCTURAL GENES IN TWO SEA URCHINS

John W. Roberts, John W. Grula, Eric H. Davidson, Roy J. Britten, and Laurence A. Lasky

Little is known about the nature of DNA sequence changes which underlie evolutionary change on the phenotypic level. However, it is clear that the genome shows great evolutionary plasticity. The number of members of families of repeated sequences change rapidly in evolution. When probes representing particular repeat families are reassociated with "Southern blots" of DNA restriction digests, bands are observed representing multiple precise copies as well as wide distributions of fragment sizes representing interspersed short repeats. When the DNA from the related sea urchins *Strongylocentrotus purpuratus* and *S. franciscanus* are compared, particular repeat families show several different bands in each species. This implies that a number of different events of multiplication have occurred in this repeat family in both genomes. The interspersed repeats also show large contrasts in quantity between the two species. Thus, many events of multiplication, insertion, and deletion have occurred, and more than one mechanism is probably involved.

To explore these DNA rearrangements, we have started comparing large (15–20 kb) pieces of DNA containing homologous structural genes that have been isolated from the recombinant λ phage libraries of two sea urchins, *S. purpuratus* and *S. franciscanus.* Two plasmid cDNA clones made from *S.*

purpuratus gastrula poly(A)$^+$ RNA have been used to screen the libraries of each species. Lambda recombinants containing an insert homologous to a prevalent poly(A)$^+$ RNA have been purified from each library. The λ recombinants from each species sharing this structural gene region will be compared directly by electron microscope analysis of heteroduplexes and by restriction enzyme analysis. We will measure rearrangement events, reiteration frequency, and relatedness of regions near each structural gene in both species.

EVOLUTION OF SEA URCHIN DNA CODING SEQUENCES

Terrence J. Hall, Laurence A. Lasky, and Roy J. Britten

The thermal stabilities were measured for heteroduplexes formed by the reassociation of total DNA from five different sea urchin species with cDNA prepared from *Strongylocentrotus purpuratus* gastrula poly(A)$^+$ cytoplasmic RNA. The results indicate that the sequences represented in the *S. purpuratus* gastrula cDNA are conserved to a greater extent than that of total single copy DNA. (Estimates from this laboratory indicate that gastrula cDNA sequences represent less than 1% of the single copy DNA complexity.) The gastrula cDNA tracer was reacted with total DNA from *S. purpuratus, S. drobachiensis, S. franciscanus, Lytechinus pictus,* and *Tripneustes gratilla.* The heteroduplexes were isolated and melted in the chaotropic solvent, tetraethyl ammonium chloride (2.4M). The lengths of duplexes were determined after digestion with S1 nuclease, and corrections were made for the effect of length on thermal stability. The temperature at which 50% of the cDNA tracer remained as duplex was compared to previous measurements for the same set of species with total single copy DNA tracers. The results indicate that the evolutionary rate of change for these coding sequences is between one half and two thirds of that for the average single copy DNA sequence.

REPETITIVE SEQUENCES OF THE SEA URCHIN GENOME

David M. Anderson, Richard H. Scheller, Linda B. McAllister, and Steven W. Trabert

Three repetitive sequence families from the sea urchin genome were studied, each defined by homology with a specific cloned probe from one to a few hundred nucleotide pairs (nt) long. Recombinant λ sea urchin DNA libraries were screened with these probes, and individual recombinants were selected which include genomic members of these families. Restriction mapping, gel blot, and kinetic analyses were carried out to determine the organization of each repeat family. Sequence elements belonging to the first of the three repeat families were found to be embedded in longer repeat sequences. These repeat sequences frequently occur in small clusters. Members of the second repeat family are also found in a long repetitive sequence environment, but these repeats usually occur singly in any given region of the DNA. The se-

quences of the third repeat are only 200–300 nt long, and are generally terminated by single copy DNA, though a few examples were found associated with other repeats. These three repeat sequence families constitute sets of homologous sequence elements which relate distant regions of the DNA.

NUCLEOTIDE SEQUENCE ANALYSIS OF THE FINE STRUCTURE OF REPETITIVE DNA

James W. Posakony and Eric H. Davidson

As part of our investigations into the nature of repetitive sequence families in the sea urchin genome, we have been studying the fine structure of repeated DNA by nucleotide sequence analysis. We would like to answer several important questions: What are the main features of the internal organization of repetitive sequences? What, if any, sequence relationships exist between different repeat families at a fine level? What are the structural relationships between individual members of a repetitive sequence family?

We have determined the nucleotide sequences of several cloned repeat elements, representing both different repetitive families and different members of the same family. Our analysis of these data (1) indicates that repeats are generally complex sequences belonging to distinct families, (2) reveals the existence of significant internal structural organization in at least some repeat elements, and (3) demonstrates a striking non-colinearity of different members of the same repetitive family, indicative of fine-scale sequence rearrangement.

ISOLATION AND CHARACTERIZATION OF A GENE BATTERY

Richard H. Scheller, David M. Anderson, Linda B. McAllister, and Eric H. Davidson

The gastrula cDNA clone SpG2 contains 700 nucleotides of sea urchin DNA. This clone was cleaved into three 200–300 nucleotide fragments (band 1, band 2, and band 3), and these were used individually to screen a λ library of the sea urchin genome. Band 1 was found complementary to six distinct regions of the genome. Band 3, located on the 3′ end of the cDNA, was found to be reiterated about 100 times per haploid genome. Electron microscope heteroduplexing and R-loop experiments revealed that the band 1 clones contain an 1800-nucleotide coding region and two small divergent intervening sequences. Hybridization selection with band 1 followed by translation in a rabbit reticulocyte lysate system resulted in the synthesis of a 40,000-dalton protein.

The band 3 clones (i.e., those that hybridize to band 3 but not band 1) contain transcribed regions flanking the band 3 repetitive element. Blots of these clones with randomly and oligo-(dT)-initiated oocyte poly(A)$^+$ cDNA show that the repetitive element is usually on the 3′ end of the transcript. We have, therefore, a set of diverse messenger RNAs with a common 3′ repetitive element, and we present this as a

structural definition of a gene battery. While the sequence organization is quite striking, the function of this repetitive family is to date unknown. We are currently engaged in DNA sequencing and RNA blotting experiments directed at understanding the function of this 3′ repetitive sequence family.

CYCLES OF OOGENESIS IN WILD AND LABORATORY-MAINTAINED SEA URCHINS

Patrick S. Leahy and Eric H. Davidson

The reproductive state of female sea urchins from representative wild populations and in laboratory culture has been monitored every 2–3 months for several years. Data are based on counts of the numbers of previtellogenic, vitellogenic, and mature oocytes in disaggregated ovaries, and on average egg yields when the animals spawned artifically after KCl injection. As reported in previous investigations, fecundity of intertidal sea urchins is sharply seasonal. Two peaks of fertility per year were noted, and in the summer months virtually none of the animals contain any large vitellogenic oocytes or mature eggs. In contrast, a certain number of the female sea urchins living at depths of 50–70 feet in a kelp bed were found to contain mature oocytes all through the year. These urchins can be collected and maintained under laboratory conditions, and will continue to show a useful asynchrony in egg production.

SEA URCHIN EGG POLY(A)$^+$ RNAs CONTAIN TRANSCRIPTS OF REPEATED DNA SEQUENCES

Frank Costantini and Eric H. Davidson

The sea urchin genome includes over 100,000 short repetitive sequence elements interspersed with the single copy DNA regions. Earlier experiments showed that the genomic repeats belong to several thousand distinct sequence families, which in general share little or no homology. Though the biological role of these sequences is unknown, almost all of the diverse repeat families are represented in unfertilized egg RNA. Using cloned fragments of repeated and single copy sea urchin DNA to analyze egg poly(A)$^+$ RNA, we found that half the mass and most of the maternal mRNA sequences are covalently associated with transcripts of short repetitive sequences. Only a restricted group of the diverse genomic repeat families is significantly represented. The maternal messages fall into several hundred sets, each containing transcripts from a different repeat family.

NATURE AND FATE OF REPETITIVE SEQUENCE TRANSCRIPTS IN THE SEA URCHIN EGG

James W. Posakony and Eric H. Davidson

Previous studies in this laboratory demonstrated that the majority of the repetitive sequence families in the sea urchin genome are represented in the RNA of the unfertilized egg, and that both strands of each repeat are repre-

sented approximately equally. Furthermore, it was shown that most of the different single copy maternal mRNA sequences in the egg are covalently associated with repetitive sequence transcripts.

We are interested in the fate of the egg repeat-containing transcripts after fertilization. For example, how are they localized with respect to the nuclei and cytoplasm of the early cleavage-stage embryo? Are they subjected to RNA processing steps? Do any of them become associated immediately with ribosomes for translation?

As a basis for approaching these questions, we have investigated the nature of the repetitive sequence transcripts in the polyadenylated fraction of egg RNA. Using cloned DNA probes, we have found that the four repeat families studied so far are represented by multiple large (3–10 kb) transcripts, and that the transcripts complementary to the individual strands of each repeat are of distinct sizes.

REPETITIVE SEQUENCE TRANSCRIPTS IN *Xenopus* EGG RNA

Margaret E. Chamberlin and Eric H. Davidson

Repetitive sequences in mature oocytes of the sea urchin have been extensively studied in this laboratory (Costantini *et al.*, 1978). We wish to observe and compare various characteristics of repetitive sequence transcripts in the oocytes of another organism, *Xenopus laevis*.

In preliminary experiments we self-annealed poly(A)$^+$ RNA from *Xenopus* stage six (mature) oocytes to repetitive RNA Cots and visualized it in the electron microscope. A great deal of duplex is observed, indicating transcripts of repetitive sequence in the poly(A)$^+$ DNA. In order to further characterize these transcripts, we have constructed clones of genomic repeats. We accomplished this by subcloning HaeIII digests of random clones from a Charon 4 whole genome library of *X. laevis*. The HaeIII fragments were annealed with an excess of the appropriate decamer and ligated into the Bam site of pBR322 or the EcoRI site of pBR325. These plasmids were used to transform *E. coli* strain HB101. We will use the subclones containing repeats to determine their expression, prevalence, and other properties in the *Xenopus* oocyte. It will be of interest to compare our findings with what is already known about repeated DNA transcripts in sea urchin eggs.

Reference

Costantini, F. D., R. H. Scheller, R. J. Britten, and E. H. Davidson. (1978) *Cell 15:* 173–187.

COMPLEXITY OF RNA IN DEVELOPING OOCYTES OF *Drosophila*

Barbara R. Hough-Evans, Marcelo Jacobs-Lorena, and Eric H. Davidson*

Mass separation of *Drosophila* egg chambers into several size classes was accomplished by means of a column of nylon nets of graduated mesh size, and RNA was extracted from each egg chamber of each size class. We measured the complexity of the RNAs by

*Case Western Reserve University School of Medicine, Cleveland, Ohio.

hybridizing them with labeled single copy *Drosophila* DNA. Egg chamber RNAs from all stages of oogenesis, including early pre-vitellogenesis, contained single copy DNA transcripts equal in complexity to the RNA of the mature *Drosophila* egg.

ELECTRON MICROSCOPE VISUALIZATION OF TRANSCRIPTION IN ECHINODERM OOCYTES

Barbara R. Hough-Evans, Oscar L. Miller, Jr., and Eric H. Davidson

We have used a special technique (Miller and Beatty, 1969) to spread out chromatin from sea urchin oocytes for electron microscope observations. We found closely packed gradients of ribosomal RNA transcripts, separated by typical nontranscribed spacer regions. Although oocytes of several size classes were examined, from early vitellogenic (40-micron-diameter) to late, nearly mature oocytes, we did not find nonribosomal transcripts in similar arrays, although gradients of more widely spaced transcripts were seen. Thus, typical lampbrush chromosome arrangements of long transcripts such as have been observed in frog oocyte chromatin appear to be absent from sea urchin oocytes. A comparative study using oocytes of a starfish (in which typical lampbrush chromosomes have been observed with light microscopy) has been initiated.

Reference

Miller, O. L., Jr., and B. R. Beatty. (1969) *Science 164:* 955–957.

RNA SYNTHESIS IN THE FERTILIZED MOUSE EGG

Lajos Pikó, and Kerry B. Clegg**

Previous studies have shown that the mouse egg inherits a substantial amount of stored RNA but that new embryo-derived RNAs are synthesized at least from the two-cell stage onward. Whether the pronuclei of the one-cell fertilized egg are active in RNA synthesis has not been determined owing, in part, to the low permeability of the egg to most labeled precursors.

We have investigated RNA synthesis in the mouse egg after labeling with [^{3}H] adenosine which is taken up about 100 times more efficiently than uridine. Total RNA was extracted by an SDS-proteinase K-phenol procedure, and the labeled products were analyzed by LiCl precipitation, binding to poly(U) sepharose, electrophoresis in polyacrylamide gels, and enzymatic digestion. The specific activity of the ATP pool was monitored. The following main results were obtained: (1) Transfer RNA is heavily labeled at the −CCA terminal, but some new synthesis of transfer RNA also takes place. (2) The synthesis of ribosomal RNA is either absent or occurs at a rate of less than 0.5% that in 816-cell embryos (on a per cell basis). (3) Heterogeneous nuclear RNA is synthesized at an equilibrium level of about 0.5 pg per egg. (4) A substantial amount (about 0.25 pg over 5 hr) of poly(A) tracts are added to previously nonpolyadenylated, stored RNA. (5) On the basis of internally localized [^{3}H] adenosine label, new synthesis of poly(A)-containing RNA also occurs at a low rate. (6) Newly

*Veterans Administration Medical Center, Sepulveda, California.

polyadenylated RNA and newly synthesized poly(A)-containing RNA are associated with polysomes. These data indicate that the fertilized mouse egg synthesizes several types of RNA with the notable exception of ribosomal RNA. Cytoplasmic polyadenylation is significant and may represent recruitment of stored maternal messenger RNA.

SYNTHESIS OF VITELLINE LAYER PROTEINS OF SEA URCHIN EGGS

Boning Gao, Barbara R. Hough-Evans, and Eric H. Davidson

What is the concentration of mRNA coding for vitelline layer (VL) proteins during development of sea urchin oocytes? What is the length of time needed to accumulate the steady state amount of a given VL protein in the mature egg? In order to try to answer these questions, we first isolated VL proteins from mature sea urchin eggs, separated them on two-dimensional acrylamide gels, and stained the second-dimension gel to characterize the VL proteins. About 30 different proteins have been identified in this way.

We then dissected developing oocytes of different sizes out of sea urchin ovaries, and separated 40-μ, 50-μ, 60-μ and 70-μ (diameter) oocytes (the mature eggs are ~70–80 μ in diameter). The oocytes were incubated with [^{35}S] methionine to label newly synthesized proteins. Labeled samples were analyzed together with carrier vitelline layer proteins. If the VL proteins (and their mRNAs) are prevalent, some of the newly-labeled proteins will coincide with carrier VL proteins on two-dimensional gels. In experiments to date, these coincident spots have not been seen, and we conclude tentatively that the vitelline layer proteins are synthesized by a set of rare mRNAs.

LIMITED COMPLEXITY OF RNA IN MICROMERES OF 16-CELL SEA URCHIN EMBRYOS

Susan G. Ernst and Eric H. Davidson

Sea urchin eggs divide into cells equal in size until the fourth division. This unequal division produces a 16-cell embryo with three distinguishable cell types. Micromeres, the smallest of the cells, give rise to the cells that form the primary mesenchyme and produce the embryo skeleton later in development.

We examined the RNA of micromeres isolated from 16-cell embryos, and found that, in contrast to the cytoplasm of the cells in the rest of the embryo, micromere cytoplasm contains few, if any, complex maternal RNA species not represented in the polysomes. Both polysomal and cytoplasmic RNAs contain about 75% of the sequence complexity of maternal mRNA. Total 16-cell embryo cytoplasmic RNA includes all the sequence complexity of maternal mRNA, although the polysomal mRNA complexity again amounts to only 75% of the maternal 37 million nucleotides of diverse sequence.

It appears that the differences that determine the micromere pattern of differentiation occur subsequent to the 16-cell stage, and do not result from localization of very complex sets of maternal RNA sequences.

MESSENGER RNA PREVALENCE IN SEA URCHIN EMBRYOS MEASURED WITH CLONED cDNAs

Laurence A. Lasky, Ze'ev Lev, Ji-hou Xin, and Eric H. Davidson

Measurements of mRNA prevalence during sea urchin development were made by reacting cDNA clone colonies with labeled cDNA transcribed from unfertilized egg and embryo poly(A)$^+$ RNAs. The number of cytoplasmic transcripts per embryo complementary to three cDNA clones was determined independently by titration with poly(A)$^+$ RNA in solution, and the amount of cDNA bound to these clones in colony hybridization was shown to be proportional to the concentration of the respective poly(A)$^+$ RNAs in the embryo cytoplasm. Using these clones as standards for comparison, we found that at the gastrula stage, the most prevalent mRNA species occur at about 10^6 molecules per embryo. If all cells were equivalent, this would be a few hundred molecules per cell. By pluteus stage, the prevalence of some sequences has increased more than tenfold. Most, though not all, sequences prevalent in later embryos are also present in the maternal RNA of the unfertilized egg. For most poly(A)$^+$ RNA sequences, the prevalence levels determined during oogenesis are maintained throughout early development, while a minority of sequences display sharp stage-specific changes.

REGULATION OF mRNA PREVALENCE IN THE SEA URCHIN EMBRYO

Ze'ev Lev, Laurence A. Lasky, Gordon P. Moore, and Eric H. Davidson

Three cDNA clones, SpG10, SpG6, and SpG30, have been selected from a gastrula cDNA clone library on the basis of very different hybridization signals with ^{32}P-labeled gastrula cDNA. The approximate cytoplasmic prevalence of these clones has been determined using a variety of methods including colony hybridization (see this Report, p. 000), RNA-DNA titration, and labeling kinetics. These experiments have demonstrated the following average cytoplasmic prevalence levels: SpG10, 4 copies/cell; SpG6, 20 copies/cell; SpG30, 200 copies/cell. Thus, these clones represent poly(A)$^+$ mRNA sequences which vary in cytoplasmic concentration by almost two orders of magnitude.

We have isolated large genomic clones (10–20 kb in length), which contain the SpG30 and SpG6 cDNA sequences, from a λ phage–sea urchin genome library. We are now isolating the genomic clones containing SpG10. These clones are being mapped using a variety of restriction enzymes and the Southern blotting technique, with the appropriate cDNA clones as ^{32}P-labeled probes.

Future experiments will revolve around determining the nature of the factors which establish the cytoplasmic concentrations of these three mRNA sequences. Detailed transcription mapping using both S1 nuclease protection and electron microscope technology will allow us to measure the extent of the transcribed regions in these clones. Subsequent experiments will deal with the genomic sequence organization surrounding these transcribed regions. Finally, it is hoped that these clones will be amenable to transcription analysis using either oocyte injection, or in vitro transcription with sea urchin egg lysates, or more purified RNA polymerase II systems.

PATTERNS OF EXPRESSION OF mRNA SEQUENCES OF SEA URCHIN EMBRYOS

Ji-hou Xin, Laurence A. Lasky, and Eric H. Davidson

Libraries of cDNA clones have been constructed by the cloning of cDNA–cytoplasmic poly(A)$^+$ RNA hybrids of sea urchin gastrula and pluteus stage embryos. Hybridization of cDNA clone libraries with cDNA transcribed from the poly(A)$^+$ RNA of unfertilized eggs and of gastrula and pluteus stage embryos has been used to describe the distribution of mRNA prevalence classes in these embryos. The results show that for most abundant poly(A)$^+$ RNA sequences, the prevalence level is maintained throughout all embryo stages. In addition, some genes are expressed in a stage-specific manner, although they are in the minority (see this Report, p. 221).

It would be interesting to know whether these prevalent sequences are also expressed in adult tissues. We are therefore screening the cDNA libraries with intestine, coelomocyte, and other adult tissue cDNAs. Thus, it may be possible to find some cDNA clones specific for the embryo. The embryo-specific clones will be further characterized with respect to their presence and state in adult tissue hnRNA. It is hoped that in this way the mechanisms which control the expression of these sequences specifically in the early embryo will be elucidated.

RATES OF ACCUMULATION AND TURNOVER OF INDIVIDUAL MESSENGER RNAs

Jay W. Ellison, James Moore, and Eric H. Davidson

In order to learn about the relative contribution of factors which affect the prevalence of mRNA species, we have measured both the rates of transport of transcripts to the ctyoplasm and the half-lives of individual mRNAs. Sea urchin embryos were labeled with [^{3}H] guanosine during the blastula-gastrula stages of development (26–44 hours after fertilization). Cytoplasmic poly(A)$^+$ RNA was prepared at various times after addition of label. These ^{3}H-RNA samples were incubated with filters containing an excess of a given cDNA plasmid. The rate of incorporation of radioactivity into an individual poly(A)$^+$ RNA species could be obtained from the cpm bound to the filters. By measuring the ^{3}H-GTP specific activity we can convert the hybridization data to units of mass, and we thus derive: (1) molecules per minute per cell transported to the cytoplasm, and (2) half-life of the mRNA species. A number of cDNA clones representing RNAs of different prevalence in gastrula embryos have been analyzed in this way. The data obtained thus far indicate that more prevalent RNAs have both a greater rate of transport and a longer half-life than the rarer RNAs. Transcripts present at 1–5 copies per cell have half-lives similar to that of the total poly(A)$^+$ RNA (2–3 hr), while the more abundant species are more stable ($t_{1/2} \geq 12$ hr).

TURNOVER RATES OF STRUCTURAL GENE TRANSCRIPTS IN NUCLEAR RNAs

Carlos V. Cabrera and Eric H. Davidson

The purpose of this study is to test a proposition (Davidson and Britten, 1979) which was developed upon recent findings of the ubiquitous representation of nuclear RNAs (nRNAs) in distinct tissues of the adult sea urchin and in embryonic stages.

Our experimental approach makes use of a cDNA library made from poly(A)$^+$ RNA at the gastrula stage (Lasky *et al.*, 1980). An excess of individual cDNA clones differing in prevalence in the cytoplasm is being hybridized to nRNAs labeled with [^{3}H] guanosine at different times. The rate constants for synthesis and degradation of the individual nRNA molecules are then calculated, taking in account the specific activity of the endogenous GTP pool as a function of the labeling time.

Similar data have been obtained for the cytoplasmic RNA (Ellison *et al.*, above). Therefore, a comparative study should provide evidence as to which one of either the rate of transcription or the fraction of precursor RNAs that are processed and exported to the cytoplasm is the primary factor in determining the prevalence of cytoplasmic RNAs.

References

Davidson, E. H., and R. J. Britten. (1979). *Science 204:* 1052–1059.

Ellison, J. W., R. J. Britten, and E. H. Davidson. (1980). In preparation.

Lasky, L. A., Z. Lev, J.-H. Xin, R. J. Britten, and E. H. Davidson. (1980) *Proc. Nat. Acad. Sci. USA.* In press.

STAFF

Senior Research Associate: Roy J. Britten

Professor: Eric H. Davidson

Visiting Associates: Lajos Pikó, Oscar L. Miller, Ji-hou Xin

Senior Research Fellows: David M. Anderson, Susan G. Ernst, Barbara R. Hough-Evans, John W. Roberts, Terry L. Thomas

Weizmann Research Fellow: Ze'ev Lev

Research Fellows: Carlos V. Cabrera, John W. Grula, Terrence J. Hall, Laurence A. Lasky, Gordon P. Moore, Richard H. Scheller

Graduate Students: Frank Costantini, Jay W. Ellison, Boning Gao, James W. Posakony

Research Staff: Maria Alonso, Alison E. Blake, Margaret E. Chamberlin, Geoffrey J. Graham, Patrick S. Leahy, Yara Lewin, Michael Lusby, Jean Mueller, Jane Rigg, Nelson L. Smith, Steven W. Trabert

Laboratory Staff: Fargo Balliett, Steven T. Eckmann, Joseph A. Garcia, Jr., Terrence Giugni, Linda B. McAllister, George Pauls

PUBLICATIONS

Anderson, D. M., R. H. Scheller, J. W. Posakony, L. B. McAllister, S. W. Trabert, R. J. Britten, and E. H. Davidson. (1980) Repetitive sequences of the sea urchin genome. 1. Distribution of members of specific repetitive families. Submitted for publication.

Britten, R. J., T. J. Hall, Z. Lev, G. P. Moore, A. S. Lee, T. L. Thomas, and E. H. Davidson. (1979) Examples of evolution and expression in the sea urchin genome, In: *Eucaryotic Gene Regulation, ICN-UCLA Syposium on Molecular and Cellular Biology, Vol. 14*, R. Axel, T. Maniatis and C. F. Fox (eds.), pp. 219–227, Academic Press, New York.

Costantini, F. D., R. J. Britten, and E. H. Davidson. (1980) Message sequences and short repetitive sequences are interspersed in sea urchin egg poly(A)$^+$ RNAs. *Nature 287,* 111–117.

Ernst, S. G., B. R. Hough-Evans, R. J. Britten, and E. H. Davidson. (1980) Limited complexity of the RNA in micromeres of 16-cell sea urchin embryos. *Devel. Biol.* In press.

Hall, T. J., J. W. Grula, E. H. Davidson, and R. J. Britten. (1980) Evolution of sea urchin non-repetitive DNA. *J. Molec. Evol.* In press.

Hough-Evans, B. R., M. Jacobs-Lorena, M. R. Cummings, R. J. Britten, and E. H. Davidson. (1980) Complexity of RNA in eggs of *Drosophila melanogaster* and *Musca domestica. Genetics.* In press.

Jacobs-Lorena, M., B. R. Hough-Evans, R. J. Britten, and E. H. Davidson. (1980) Complexity of RNA in developing oocytes of *Drosophila melanogaster. Devel. Biol. 76:* 509–513.

Lasky, L. A., Z. Lev, J.-H. Xin, R. J. Britten, and E. H. Davidson. (1980) Messenger RNA prevalence in sea urchin embryos measured with cloned cDNAs. *Proc. Nat. Acad. Sci. USA.* In press.

Lee, A. S., T. L. Thomas, Z. Lev, R. J. Britten, and E. H. Davidson. (1980) Four sizes of transcript produced by a single sea urchin gene expressed in early embryos. *Proc. Nat. Acad. Sci. USA.* In press.

Lev, Z., T. L. Thomas, A. S. Lee, R. C. Angerer, R. J. Britten, and E. H. Davidson. (1980) Developmental expression of two cloned sequences coding for rare sea urchin embryo messages. *Devel. Biol. 76:* 322–340.

Moore, G. P., F. D. Costantini, J. W. Posakony, E. H. Davidson, and R. J. Britten. (1980) Evolutionary conservation of repetitive sequence expression in sea urchin egg RNAs. *Science 208:* 1046–1048.

Geophysical Laboratory

Washington, District of Columbia

Hatten S. Yoder, Jr.

Director

Contents

Director's Commentary and Review . . . 229

Experimental and Field Petrology 247
Experimental modeling of convection in layered intrusions (Irvine) 247
Convection and mixing in layered liquids (Irvine) 251
Observations on layering in the Skaergaard intrusion (Irvine) 257
Heat and mass transfer in magma generation: a progress report of an experimental study (Yoder) 263
Changes with pressure of degree of partial melting and K_2O content of liquids in the system Mg_2SiO_4-$KAlSiO_4$-SiO_2 (Kushiro) 267
Melting relations of an alkali-olivine basalt to 30 kbar, and their bearing on the origin of alkali basalt magmas (Takahashi) 271
High-pressure phase equilibria of a high-magnesia basalt: implications for the origin of mid-ocean ridge basalts (Elthon and Scarfe) 277
Experimental studies of magnetite in calc-alkaline rocks (Osborn and Rawson) 281
The complementary abyssal basalt glasses of Juan de Fuca and the "Galápagos Spreading Center" (Chayes) 285
Basalts and basanites (Chayes) 287
A world data base for igneous petrology (Chayes) 288
An effect of closure correlation on classification by ranges (Chayes) . . 289

Ultramafic Nodules, Kimberlite, and Carbonatite 290
Rates of dissolution of upper mantle minerals in an alkali-olivine basalt melt at high pressures (Scarfe, Takahashi, and Yoder) 290
Discrete nodules from the kimberlites of East Griqualand, southern Africa (Boyd and Nixon) 296
Ilmenite nodules and associated sulfides in kimberlite from Yakutia, U.S.S.R. (Boctor and Boyd) 302
Distribution of rare earth elements in perovskite from Oka carbonatite, Quebec (Boctor and Yoder) 304

Structure and Properties of Liquids and Glasses 307
Shear wave velocity in partially molten peridotite at high pressures (Murase and Fukuyama) 307
Anionic constitution of 1-atm silicate melts: implications for the structure of igneous melts (Virgo, Mysen, and Kushiro) 310
Relations between anionic structure and viscosity of silicate melts—a Raman spectroscopic study (Mysen, Virgo, and Scarfe) 312
The structural role of titanium in silicate melts (Mysen, Ryerson, and Virgo) . 313
The structural role of phosphorus in silicate melts (Mysen, Ryerson, and Virgo) 314
Viscosity-temperature relationships at 1 atm in the system diopside-anorthite (Scarfe, Cronin, Wenzel, and Kauffman) 315
Viscosity of lavas from the Level Mountain volcanic center, northern British Columbia (Scarfe and Hamilton) 318
Solubility mechanisms of water in silicate melts at high pressure and temperature (Mysen, Virgo, Scarfe, and Harrison) 320
Raman study of K_2CO_3-$MgCO_3$ glasses (Sharma and Simons) 322
Influence of melt structure on crystal-liquid trace-element partitioning (Mysen and Virgo) 326

Isotope and Element Partitioning 328
Oxygen isotope fractionation during regional metamorphism (Rumble) . . 328
Mg-Fe^{2+} partitioning between olivine and ferrian ulvospinel (Rawson and Irvine) 332
Partitioning of nickel between pyrrhotite and magnetite (Boctor and Mysen) . 337

Mineral-Solution Equilibria 340
Solubility constants of rock-forming minerals (Frantz, Popp, and Boctor) . 340
Mineral-solution equilibria in the system Mn_3O_4-H_2-H_2O-HCl (Boctor and Frantz) 345

Planetary Gases at High Pressures . . . 348
Crystal structures and compression of Ar, Ne, and CH_4 at 20 °C to 90 kbar (Hazen, Mao, Finger, and Bell) . . . 348
Phase transitions in methane under high pressures at room temperature—a Raman spectral study (Sharma, Mao, and Bell) 351
Acoustic velocity and refractive index of fluid hydrogen and deuterium at high pressures (Brody, Shimizu, Mao, Bell, and Bassett) 355

Raman measurements of deuterium in the pressure range 8–537 kbar at room temperature (Sharma, Mao, and Bell) 358

Spectral Mineralogy 364
Crystal structure of forsterite at 40 kbar (Hazen and Finger) 364
Raman evidence for a new high-pressure, room-temperature polymorph of TiO_2 (Mammone and Sharma) . . . 367
Pressure and temperature dependence of the Raman spectra of rutile-structure oxides (Mammone and Sharma) . . . 369
High-pressure experiments on the iron oxide wüstite ($Fe_{1-x}O$) (Zou, Mao, Bell, and Virgo) 374
Composition–lattice parameter relationship of the magnesiowüstite solid solution series (Simons) 376
Evidence for a localized 4*f*-shell breakdown in praseodymium under pressure (Mao, Hazen, Bell, and Wittig) 380

Biogeochemistry 384
The organic matter in Mississippi Valley–type deposits (Gize and Hoering) 384
Tracing food webs with stable hydrogen isotopes (Estep and Dabrowski) . . 388
The uptake and incorporation of the hydrogen from water into the organic matter of plants (Estep and Hoering) 391
The colloidal organic matter in waters of the Chesapeake Bay and Patuxent River (Sigleo, Hoering, and Hare) . . 394
Selective absorption of branched hydrocarbons by a synthetic polymorph of silica (Hoering) 399
Organic geochemical studies in Spitsbergen with a field-portable, high-performance liquid chromatograph (Hare and Miller) . . 403

New Techniques 406
High-temperature, diamond-anvil pressure cell for single-crystal studies (Hazen and Finger) 406
Design and operation of a diamond-window, high-pressure cell for the study of single-crystal samples loaded cryogenically (Mao and Bell) . 409
Experiment for *in situ* high-pressure, light-scattering measurements (Mao and Bell) 411
Infrared spectra of methanol and ethanol at high pressure (Mammone and Sharma) 415

Staff Activities 418
Petrologists' Club 418
Washington Crystal Colloquium 418
Seminar Series 418
Lectures and Symposia 419
Field Work 423

Bibliography 423

Personnel 425

DIRECTOR'S COMMENTARY AND REVIEW

The pursuit of scientific problems is an exciting, unpredictable adventure. Opportunities for basic research remain almost unlimited in spite of recent major advances and, indeed, are often created by such advances. The staff continue to uncover and delineate new areas for expanded effort. The key appears to be in asking significant and fundamental questions and in having courage to try unconventional approaches. The continued growth of geology as a science seems assured as nations become more responsive, within economic constraints, to the complex problems of natural resources and hazards.

One sponsor recently remarked that the Geophysical Laboratory is a mix of the best of both industrial, applied-research laboratories and university-based, basic-research laboratories. But how can a group be relevant to today's societal needs and still provide fundamental advances in knowledge for the future? The simple truth is that today's basic research *is* the relevant applied research of tomorrow. Because of the long lead time for the development of new ideas and directions, the Laboratory must focus on the principles that will provide the tools to solve those practical problems of the future.

Consider the Laboratory's basic research in the light of the potential nonfuel mineral shortages that may confront this nation after the year 2000. Studies of the fluid dynamics of magma bear on the accumulations of chromite, ilmenite, magnetite, and sulfides in layered intrusions that yield chromium, titanium, vanadium, nickel, copper, and platinum. Measurements of the solubilities of minerals contribute to an understanding of the selective transport of elements that concentrate into economically valuable deposits. Studies of the flow of fluids and permeability in metamorphic rocks help define the processes that result in element transport and concentration. Characterization of the organic substances in ore deposits illuminates their role in the concentration of such elements as uranium, lead, and zinc. Studies on the partitioning of elements between crystalline, liquid, and gas phases also contribute to understanding the aggregation of groups of elements. The investigation of ultramafic nodules from kimberlites outlines the conditions under which diamonds have formed and the role of mantle rocks as sources of ore minerals. The world data base for igneous petrology, continuously being expanded, provides empirical constraints on the identity and abundance of elements found in each rock type. In short, practically every endeavor at the Geophysical Laboratory can be perceived as contributing to an understanding of the principles whereby elements are accumulated in ore deposits. Although the staff members are largely motivated to perform these studies by other considerations, the fact is they are indirectly making a significant contribution to the future solution of the world's mineral resource problems. Similar applications of the work of the Laboratory—also dissociated from the staff's immediate interests—provide principles for other earth-related problems. It is this breadth of application that makes the study of principles of lasting value. And it is this realization that probably accounts for the recent increase in external support of the Laboratory.

Brief discussions of the past year's studies follow. The complementary and supplementary nature of the studies, not always discernible in such brief reports, enhances the merit of all. Because of space limitations, not all the studies mentioned are described in detail in the main body of the Report. Ar-

ticles described only in this introduction are here marked with an asterisk; more extended discussions of these studies will be available in open file at the Laboratory until publication of next year's Annual Report. Further, those results that will appear in full in appropriate journals before the publication of this Report have not been included: these titles appear in the Bibliography.

Experimental and Field Petrology

With the growth of the fields of fluid dynamics and heat transport in physics and mechanical engineering, convection and mixing in magmas have captured the attention of many petrologists. *Irvine* has been conducting scaled room-temperature experiments on convection and the structure of density currents, aimed at understanding the origin of layering in igneous intrusions. *Yoder*, on the other hand, has been preparing scaled experiments at high temperatures on heat transfer and convection, aimed at understanding the generation of large volumes of relatively homogeneous magmas.

Irvine describes the apparatus and methods, and outlines theory by which experiments can be scaled in terms of size, liquid viscosity, and cooling rate to simulate thermal convection in intrusions. He presents some of his initial results, illustrating patterns of convection in fluids stratified in density and composition. Marginal convection cells within fluid layers typically develop width-to-height ratios between 10:1 and 15:1 even though all of the flow funnels through a thermal boundary zone that, when scaled to magmatic conditions, is only about a meter thick. The flow in the boundary layer is turbulent; therefore, the process is effective in mixing the liquid in the convection cell. In a column of liquid layers, liquid is also passed down the thermal boundary zone from layer to layer. Irvine notes that the mixing of distinctly different magmatic liquids by this process could affect crystallization relations and thus might account for some of the lithological stratification that is seen both in the marginal zones and along the floors of layered ultramafic-gabbroic intrusions.

In addition to the above experimental studies, *Irvine* describes and illustrates some of the layering structures, including fragmental layers, redeposited layers, unconformities, and macrorhythmic layering, of the kinds he observed during field studies of the Skaergaard, Greenland, intrusion. All of these structures involve the thin (10–30 cm), rhythmically repeated, modally graded (from melanocratic to leucocratic upward) layers that are a classic feature of the intrusion, and Irvine's observations provide strong support for the case that these layers were deposited from magmatic density currents. The macrorhythmic layering is very different, however, and, rather remarkably, its distinctive features have not previously been emphasized even though it is prominent and extensively developed. It is typically defined by an alternation of light and dark layers several meters thick evidently paired in units, with the leucocratic layer at the bottom. Irvine suggests that this layering may have developed by *in situ* crystallization.

The generation of these magmatic liquids at the site of origin is the subject of *Yoder's* experiments now in progress. After some preliminary runs with the cooperation of Mysen on the generation of liquids in a pressure gradient, he has turned to the classical mode of generation of liquids in a temperature gradient—the hot-plate mode of heating. The many factors that influence the transfer of heat from a hot source through a partially molten layer are outlined. His goals are to measure quantitatively the rate of advancement of the melt front (the Stefan boundary) for both rhyolitelike and basaltlike melting behavior, to evaluate the effec-

tive thermal conductivity of the liquid + crystal region and the influence of crystal bridging, to ascertain the critical parameters for the onset of Rayleigh convection, and to characterize the Bénard convection cells, thermal stratification, and the evolution of potential individual convecting layers in the porous medium. These factors may contribute to an understanding of the processes that result in the generation of large volumes of relatively homogeneous magmas as well as the rate of magma production and mode of aggregation.

Kushiro has found that the amount of liquid formed near the beginning of melting of peridotitic compositions decreases with increasing pressure whereas the K_2O content of the liquid, a critical component of alkaline magmas, increases. Reversed experiments in the system Mg_2SiO_4-$KAlSiO_4$-SiO_2 at high temperatures and pressures show that the isobaric invariant point on the forsterite-enstatite liquidus boundary shift away from SiO_2 with increasing pressure. The K_2O content of the liquid increases from 12.8 wt % at 1 bar to 20.8 wt % at 30 kbar. Although the K_2O content of the liquids exceeds that of average basalts, these results support in principle the view that tholeiitic basalts have formed by relatively large degrees of partial melting at shallow depths, whereas alkali basalts have formed by small amounts of melting at relatively deep levels in the upper mantle.

The phase relationships of an alkali-olivine basalt (containing 3.4 wt % normative nepheline component) from Oki-Dogo Island, Japan, were studied to 30 kbar by *Takahashi*. The basalt contains large amounts of mantle-derived xenoliths, and its bulk chemical composition is considered to be compatible with mantle olivines on the basis of the olivine/liquid distribution coefficients for Ni, Fe, and Mg. At 14 kbar and 1275 °C, olivine, orthopyroxene, and clinopyroxene crystallize from the basalt liquid within a narrow temperature interval (~10 °C). He notes that the pseudoinvariant point, olivine + orthopyroxene + clinopyroxene + spinel + liquid, lies on the silica-deficient side of the critical plane plagioclase-diopside-forsterite in natural rock systems at 14 kbar. These relationships have led Takahashi to conclude that the alkali-olivine basalt magmas, which commonly contain spinel lherzolite xenoliths, are separated at intermediate pressures (~10–20 kbar).

In order to investigate current models for the genesis of mid-ocean ridge basalts, the phase relationships of a high-magnesia basalt (NT-23) from the Tortuga ophiolite complex, Chile, were determined at pressures up to 30 kbar by *Elthon* and *Scarfe*. At 25 kbar and 1480 °C, a liquid of the NT-23 composition was found to be saturated with olivine, orthopyroxene, clinopyroxene, and garnet. This result indicates that NT-23 may be a primary magma generated by invariant melting at a pressure of 25 kbar or greater. Even though the compositions of most mid-ocean ridge basalts cluster near the 1-bar cotectics, these compositions indicate that the primary magmas from which the basalts have been derived are similar to NT-23. It is possible, according to Elthon and Scarfe, to generate the observed array of primitive and evolved mid-ocean ridge basalts from NT-23 by low-pressure fractionation coupled with magma mixing.

Prior to their eruption, the basaltic andesites of Parícutin, Mexico, and Santorini, Greece, were apparently crystallizing at a depth of 35–50 km, at approximately 1200 °C, and at an oxygen fugacity greater than that of the Ni-NiO buffer. The H_2O content of the magmas was 1–2%. These are conclusions of *Osborn* and *Rawson* from experimental studies at 1 and 10 kbar total pressure of rock specimens from those volcanoes. In the experimental runs of rock specimens containing 2% H_2O, the TiO_2 content of magnetite co-

existing at near-liquidus temperatures with pyroxene, plagioclase, and olivine is much greater at 10 kbar than at 1 kbar, and serves as an indicator of the depth at which magnetite crystals formed in the magma. The findings are consistent with the concept that calc-alkaline volcanic rock series form principally as a result of fractional crystallization of oxygen-buffered, basaltic magma in which magnetite is a precipitating phase.

**Todd, Keith,* and *Irvine* have continued their study of the platinum-rich zone (J-M Reef) in the layered rocks of the Stillwater Complex in Montana. New analytical data have confirmed the presence of a discontinuity in the Fe content of olivine at the stratigraphic level of the reef; and the S and Cu contents of the rocks increase slightly, both at this level and at a slightly lower horizon where there is a distinct change in the general lithology of the layered rocks. These features support a previous suggestion that the J-M Reef formed in association with a major change in the composition of the crystallizing magma. A survey has also been made of the minerals that contain the platinum-group elements. Principal among these minerals are tellurides and sulfides with minor amounts of metal alloys, arsenides, antimonides, and bismuthinides.

In the course of a study of the general problem of rock classification by composition ranges, *Chayes* has recently noted that the distribution of several essential constituents in published analyses of abyssal basalt glasses from the "Galápagos Spreading Center" are conspicuously bimodal and that the central frequency minima in them coincide almost exactly with the frequency maxima of the sharply unimodal basalt glasses of the Juan de Fuca ridge. The glass samples of both suites, mostly unaltered selvages of basalt pillows, are almost devoid of phenocrysts and so were probably extruded as liquids. Although hundreds of specimens have been collected in dredge hauls from each area, the number of identifiable sample sites is very small in each. For this reason there is as yet insufficient knowledge of the field geology and areal distribution of these basalt glasses to evaluate the unusual compositional clustering.

**Chayes* points out that application of the modal classification of igneous rocks proposed by the Commission on Systematics of the International Union of Geological Sciences requires more information than is usually available for volcanic rocks. For most such rocks quantitative modes are not obtained and for many they are unobtainable. He proposes a normative analogue of the Commission's classification, for use on basic lavas when modal information is lacking. The classification parameters of the analogue are calculated directly from the bulk chemical analysis of the rock. From extended application of the scheme to the data of his file of published analyses of Cenozoic volcanic rocks, he concludes that, except for certain highly undersaturated salic volcanic rocks, it will usually yield the same result as the Commission's classification when the latter is applicable.

*Meteorites are a source of minerals formed at high pressures through shock. The pressures are greater than those deduced to date in specimens of rocks believed to have come from depth in the mantle. *Boctor, Mao,* and *Bell* have found that the high-pressure mineral majorite, which occurs in black veins in the Tenham chondrite, is not isochemical with the orthopyroxene in the matrix of this meteorite. Majorite contains small, but significant, amounts of Al_2O_3, Na_2O, CaO, and Cr_2O_3. Its occurrence in association with clinobronzite, ringwoodite, β phase, and diaplectic plagioclase glass is believed by Boctor, Mao, and Bell to be suggestive of large gradients in

pressure (from 100 to >300 kbar) over distances of a few micrometers during impact metamorphism.

*The main silicate minerals in the Cachari meteorite, a eucrite, are pyroxene and plagioclase. The host pyroxene is a low-Ca variety containing exsolution lamellae of high-Ca pyroxene and is more iron rich than pyroxene from cumulate eucrites and some lunar rocks. It commonly shows deformation lamellae similar to those described from pyroxenes in shocked lunar and terrestrial rocks. The plagioclase is anorthitic and shows incipient melting and partial transformation to diaplectic glass. Another indication of shock metamorphism in this meteorite is the presence of veinlets of mafic glass of inhomogeneous composition. The meteorite was metamorphosed, according to *Boctor, Bell,* and *Mao,* by high-velocity impact at a minimum peak pressure of 75 kbar to a pressure greater than 500 kbar.

Ultramafic Nodules, Kimberlite, and Carbonatite

Ultramafic nodules are of exceptional importance as samples of the deep (<250 km) mantle and they serve to define the local geothermal gradient (Boyd, 1973). They are presumed to have been ripped off the conduit walls and evidently were commonly brought up so rapidly that there was insufficient time for their digestion by the host magma. In order to determine the effects that differential dissolution rates have on partial melting and disintegration of mantle xenoliths during transport by alkali basalt magma, the dissolution of mantle minerals in alkali basalt melt was studied at pressures between 12.5 and 20 kbar and at temperatures between 1325° and 1400°C by *Scarfe, Takahashi,* and *Yoder.* Spheres of natural minerals were observed to dissolve with varying rates in the order garnet > clinopyroxene > spinel > orthopyroxene >> olivine in experimental run times between 10 and 100 min. This sequence correlates inversely with the magnitude of the enthalpy of fusion of the minerals, and it is also in agreement with the sequence of melting commonly observed at the surface contact between mantle xenoliths and their host basalt. The investigators emphasize that the size of the nodules requires rapid transport to the surface in fluid magma, during which time only minor digestion was possible.

*There is a continuing need for the characterization of the minerals in nodules, which seem to have a surprising range of rock types. *Boyd* has found that abundant apple-green megacrysts of diopside from the Kimberley pipes are commonly intensely deformed and intergrown with (metasomatic?) ilmenite and phlogopite. The apple-green diopside megacrysts differ from discrete nodules of diopside primarily in being more calcic, and they are never associated with garnet or enstatite. Boyd suggests that they may have originated by disaggregation of pegmatitic bodies in the rigid low-temperature (<1100°C) lithosphere through which the kimberlites were erupted.

Discrete pyroxene and garnet nodules in the East Griqualand kimberlites of southern Africa were found by *Boyd* and *Nixon* to be similar to those from other areas in minor element content but richer in magnesia and with a more restricted range of equilibration temperature. The East Griqualand xenoliths include rare varieties that appear to be cumulates of discrete nodules and discrete enstatites that have inclusions of both diopside and garnet. The rarity of cumulates of discrete nodules and the scarcity of olivine megacrysts might be explained by an eruptive model in which infiltration of volatiles and metasomatism produce small degrees of partial melting. It is hypothesized by Boyd and Nixon that defor-

mation immediately prior to eruption results in recrystallization of coarse olivine as microphenocrysts in the kimberlites.

Ilmenite nodules in kimberlite from Yakutia, U.S.S.R., have MgO and Fe_2O_3 contents within the ranges reported for other kimberlites. According to *Boctor* and *Boyd*, the Yakutia nodules are distinguished from ilmenite nodules in other kimberlites by the presence of large, polymineralic sulfide globules. The sulfide was trapped as an immiscible liquid by the crystallizing ilmenite and later crystallized to a Cu- and Ni-bearing monosulfide solid solution at about 1100 °C. Pentlandite and chalcopyrite, exsolved from the monosulfide, occurred on cooling, and the present sulfide assemblage may have equilibrated at temperatures below 575 °C.

*An alnoite from Malaita, Solomon Islands, contains a suite of nodules similar to those from kimberlites. Of particular interest to *Boctor, Boyd*, and *Nixon* was the unusually low rare earth content relative to that characteristic of kimberlite and carbonatite. The light-rare-earth enrichment of the mineral perovskite is a reflection of the light-rare-earth enrichment found in whole rock alnoites and suggests that perovskite is the main REE-bearing phase in these rocks.

In contrast to the above study, *Boctor* and *Yoder* have found that the rare earths in a carbonatite from Oka, Quebec, were not contained mainly within a single phase. Although the perovskite from Oka was relatively rich in the light-rare-earth elements and in niobium, the isomorphous substitution of Ti by Nb in Oka perovskite is more extensive than in perovskite from kimberlites and other alkaline rocks. Niobium is more abundant in carbonate melts than in silicate melts, probably because it forms stable carbonate complexes. Although experimental investigations of REE partitioning show that those elements favor carbonate melts relative to silicate melts, the total REE content in perovskite from Oka is, however, lower than that of perovskite from some kimberlites and alkaline igneous rocks. This observation is related to the presence of pyrochlore, which tends to be more enriched in REE relative to perovskite.

Structure and Properties of Liquids and Glasses

The determination of phase diagrams has been one of the major efforts of the Geophysical Laboratory. Historically, emphasis was given liquidus phases and the sequence of crystallization of major rock-forming minerals. Properties of synthetic crystals were carefully measured to correlate with those of similar crystals found in rocks. Because the equilibria established depend as much on the properties of the liquid as on those of crystals, a major effort is now being made to characterize fully the structure of magmas from which crystals grow. Knowledge of the structure and properties of liquids is useful in defining seismic zones of the earth, dimensions of magma chambers, processes of segregation of magma from its host, rate of ascent of magma, explosive characteristics of volatile-bearing magmas, and complex partitioning of elements between liquid, crystal, and gas phases.

The compressional wave velocity (V_p) in partially molten peridotite has been measured at 5 and 10 kbar by *Murase* and *Fukuyama*. It was found at 5 kbar that a 5% decrease in V_p, as observed for the earth's low-velocity zone (LVZ), is the result of about 7–9 vol % melting. The effect of melt concentration on shear wave velocity (V_s), which is more sensitive than V_p, was also studied through the melting range of a peridotite. At 5 kbar the relationship between normalized V_p and the degree of melting does not coincide with that of normalized V_s. At 10 kbar, however,

both relationships almost coincide in the low-degree-of-melting region, and they may be much closer to each other even at higher pressures. If the relationship at 10 kbar is applicable to the mantle, a 5%decrease in V_p and V_s observed for the LVZ implies a smaller amount of melting, about 2–3 vol %, under anhydrous conditions.

Raman spectroscopy has been used by *Virgo, Mysen*, and *Kushiro* to delineate the structural variations of silicate melts ranging in composition from orthosilicate to tectosilicate. Regardless of the type of metal cation or cations present, the equilibria between the anionic structural units vary according to the ratio of nonbridging oxygens to silicons. For example, when the ratio is 0.05 to 1.0, which is the range for most igneous rocks, the following equilibrium obtains between the structural units:

$$\underset{\text{sheets}}{Si_2O_5^{2-}} = \underset{\text{chains}}{SiO_3^{2-}} + \underset{\text{frameworks}}{SiO_2}.$$

Aluminum may substitute randomly for silicon in each structural unit, whereas all the cations that have tetrahedral coordination (Ti^{4+}, P^{5+}, and Fe^{3+}) tend to form separate structural units in the silicate melts. On this basis, it is possible to predict the viscous behavior of magma, variations of trace element partition coefficients between magma and a given mineral, redox equilibria of iron, and solution mechanisms of volatiles in magma.

Mysen, Virgo, and *Scarfe* integrated structural information with rheological properties from a range of silicate melt systems. They have found that the compositional regions between ortho- and tectosilicate compositions within which anionic structural units of the melts are the same coincide with well-defined ranges of activation energies of viscous flow of the melt. Mysen, Virgo, and Scarfe observe a close correlation between the ratio of nonbridging oxygens per tetrahedral cation and the viscosity of the silicate melts in all binary joins studied.

*It has been suggested that aluminum may occur in both tetrahedral and octahedral coordination in silicate melts, in which case the melts would be expected to show substantially different physical properties. *Virgo* and *Mysen* have used Raman spectroscopy to assess the bulk compositional controls of the structural role of Al^{3+}. Whenever monovalent or divalent metal cations are available for local charge balance of Al^{3+} in tetrahedral coordination, Al^{3+} will always substitute for Si^{4+} in tetrahedral coordination. They suggest that the more even distribution of Al between units in calcic systems than in sodic systems may be the explanation for the lower viscosity of the melts in the former systems.

*An understanding of the variables that affect redox equilibria of iron is necessary to determine the influence of iron on crystal-liquid equilibria. It is well known that such redox equilibria depend on the bulk compositions of silicate melts. *Mysen* and *Virgo* used Mössbauer spectroscopy in combination with Raman spectroscopy to determine which structural variables may relate to variations of redox ratios of iron. They have found that in metal oxide-silicate joins with a constant amount of iron oxide added to the melt, the Fe^{3+}/Fe^{2+} increased linearly with increasing ratio of nonbridging oxygens to silicon of the melt. This relationship holds within the compositional ranges where only the proportions of anionic structural units change as a function of bulk composition. Apparently when new anionic structural units formed in the melt, there was a rapid change of Fe^{3+}/Fe^{2+}. It appears that redox ratios of iron in silicate melts may be calculated at given f_{O_2}, temperature, and pressure only when the melt structure is known.

In order to determine the structural role of TiO_2 in silicate melts, *Mysen, Ryerson*, and *Virgo* used Raman spec-

troscopy to ascertain the influence of TiO_2 on the structure of melts both with and without nonbridging oxygens. In all cases they have found that titanate complexes, analogous to the silicate complexes already present, were formed. There is no evidence for mixing of Ti^{4+} and Si^{4+}. In melts with nonbridging oxygens, this observation implies that new bridging oxygens were formed. In melts with no nonbridging oxygens (e.g., aluminosilicate melts of feldspar compositions), the number of bridging oxygens is not affected. These data provide structural support, therefore, for the conclusions based on phase equilibria, which indicate that solution of TiO_2 in silicate melts enhances their polymerization.

Even though P_2O_5 is a minor oxide in most magmas, phosphorus has attracted considerable attention because solution of even 1 wt % or less P_2O_5 in silicate melt significantly affects crystal-liquid equilibria. *Mysen, Ryerson,* and *Virgo* used Raman spectroscopy to determine the solution mechanisms of P_2O_5 in melts with and without nonbridging oxygens. In depolymerized melts, P^{5+} is dissolved predominantly to form separate phosphate chains with no mixing with Si^{4+}. The silicate portion of the melt becomes more polymerized as a result of this solution. In fully polymerized aluminosilicate melts, phosphorus is dissolved to form three-dimensional aluminum phosphate complexes. Results to date suggest that phosphorus appears to be a network former in depolymerized melts such as basalt, but in more acidic melts (e.g., andesite to granite), solution of P^{5+} may cause the network to be broken up, thus enhancing stability fields of depolymerized minerals, lower crystal-liquid partition coefficients, and lower melt viscosity.

Although in the past much emphasis has been placed on the phase relationships of the classic system albite-anorthite-diopside, less attention has been paid to other important properties such as the viscosity and density variations of the melts. Thus, in conjunction with a study of the structure of melts in the ternary system, a systematic study of the viscosity-temperature relationships was initiated by *Scarfe, D. Cronin,*† *J. Wenzel,*† and *D. Kauffman.*† At constant temperature there is a systematic decrease in viscosities from anorthite to diopside; however, because of the temperature effect, viscosities increase along the liquidus, reaching a maximum at the eutectic composition. Results have been fitted to both Arrhenius and Fulcher equations, and calculated activation energies for viscous flow appear to show a plateau between 40 and 58 wt % diopside. This plateau may correspond to the region where significant structural changes take place in the melt.

*Melts of sodium melilite composition ($NaCaAlSi_2O_7$), alkali olivine basalt, and olivine nephelinite have been investigated by *Scarfe.* All three compositions exhibit a negative pressure dependence of viscosity. Between 1 bar and 15 kbar at 1400°–1450°C, the respective percentage decreases in viscosity are 59, 57, and 17 for sodium melilite, alkali olivine basalt, and olivine nephelinite, which have ratios of nonbridging oxygens to tetrahedral cations of 0.83, 0.70, and 1.17, respectively. These results are generally consistent, within experimental uncertainty, with a theoretical model relating viscosity and the ratio of nonbridging model oxygens to tetrahedral cations. Viscosity decreases with increasing pressure for melts whose ratio is less than 1. Conversely, silica-deficient, subaluminous melts with a ratio greater than 1 show an increase in viscosity with increasing pressure.

The viscosities of alkali basalt, hawaiite, and comendite melts, three magma types represented at Level

†Center for Materials Science, National Bureau of Standards, Washington, D. C.

Mountain, northern British Columbia, have been measured at 1 bar between 1200° and 1450°C by *Scarfe* and *T. S. Hamilton.*‡ At any temperature above the liquidus, the comendite has a much higher viscosity than hawaiite or alkali basalt. These differences can be explained by the differences in composition and degree of polymerization of the three types of melt. On the basis of ascent rates required to counteract sinking of entrained nodules in alkali basalt or hawaiite magma, it is estimated that ascent rates are ~1 km/hr, provided the melt has not undergone significant crystallization. These values are an order of magnitude faster than rates estimated from data for Hawaiian tholeiites (Eaton and Murata, 1960).

Mysen, Virgo, Scarfe, and *Harrison* have found that with up to 5 wt % H_2O in solution, water is dissolved in $NaAlSi_2O_6$ and $NaAlSi_3O_8$ melts by forming OH bonds with Si^{4+}. Additional OH^- is also locally charge balanced with Na^+. Aluminum is not bonded to OH groups; instead, an amount of Al^{3+} equivalent to the amount of Na^+ required to stabilize OH^- is no longer in tetrahedral coordination. According to Mysen, Virgo, Scarfe, and Harrison, the strong influence of H_2O on the physical and chemical properties of silicate melts results from the formation of new *anhydrous* structural units with nonbridging oxygens in the melts.

**Mysen* and *Virgo* used Raman spectroscopy to study solution mechanisms of H_2O in a melt of sodium melilite composition ($NaCaAlSi_2O_7$) in order to assess how water would affect aluminous melts with a significant number of nonbridging oxygens per tetrahedral cation. The solution of water in most, if not all, natural magma compositions affects the melt structure similarly. The effects become less pronounced the more depolymerized the melt.

*The same investigators also used Raman spectroscopy to deduce the solubility mechanism of CO_2 in melts of $NaAlSi_3O_8$ and $CaAl_2Si_2O_8$ composition. They have found that carbonate complexes and nonbridging oxygens are formed. An amount of Al^{3+} equivalent to the amount of metal cation required to stabilize CO_3^{2-} anions has apparently become a network modifier; thus depolymerization of the melt results. Consequently, phase equilibria and physical properties of such melts would be affected similarly by both CO_2 and H_2O.

Sharma and *Simons* investigated the Raman spectra of carbonate glasses of $2K_2CO_3 \cdot 3MgCO_3$, $K_2CO_3 \cdot MgCO_3$, and $CaCO_3 \cdot 19K_2MgCO_3$ compositions to elucidate the effect of disorder on the internal modes of CO_3^{2-} ions. On the basis of observed large splitting of the doubly degenerate antisymmetric stretching (ν_3) mode of CO_3^{2-} ions in these simple carbonate glasses (*Year Book 78*, 532–542), they have proposed that the splitting may be indicative of the presence of CO_3^{2-} ions at two or more distinct sites in the CO_3-bearing silicate glasses.

*Boron oxide plays a key role in both glasses and ceramics of high technological importance, yet its role in glass structure is not clearly defined. *Sharma, Simons,* and *Mammone* carried out a correlative study of the density, refractive index, and structure of B_2O_3 glasses, synthesized by quenching B_2O_3 melt from 1200°C in the pressure range 0.001–40 kbar. Both density (ρ) and refractive index (n) of B_2O_3 glass quenched at 40 kbar show large increases (ρ increases by 22.5% and n by 3.7%) relative to the density and refractive index of the glass at 1 bar (ρ = 1.78 g/cm^3, n = 1.475). With increasing pressure the boroxyl rings, which are major constituents of B_2O_3 glass at 1 bar, break up to form a more closely packed network of BO_3 triangles. The

‡Alberta Research Council, Edmonton, Canada.

increase in the fraction of BO_3 triangles in the random network relative to the fraction of BO_3 in the boroxyl rings with increasing pressure may account for the observed increase in density and refractive index of B_2O_3 glasses.

Inasmuch as changes in melt composition result in structural changes of the melt, *Mysen* and *Virgo* integrated Raman spectroscopic studies of melt structure with determination of crystal-liquid, trace-element partition coefficients. At constant temperature and pressure with a mineral of constant composition, variations of the Ni and REE crystal-liquid, trace-element partition coefficients are linearly correlated with the ratio of nonbridging oxygens per tetrahedral cation in the melt. With knowledge of the solution mechanisms of other elements in silicate melts, the influence of solution of their oxides in melts on the partition coefficients may be calculated at constant temperature. On the basis of such considerations, Mysen and Virgo conclude that even though addition of a small percentage by weight of a minor oxide to a magma will result in discernible effects on crystal-liquid partition coefficients, these effects are generally petrologically insignificant. Only when all oxide concentration changes are considered in total will crystal-liquid, trace-element partition coefficients be affected significantly by the liquid bulk composition.

Isotope and Element Partitioning

Rumble has constructed a mathematical model for computing the effects of metamorphism on the oxygen isotope composition of rocks and minerals. From the model it is possible to predict the changes in isotope composition that occur as a consequence of devolatization reactions, infiltration of hydrothermal solutions, and combined devolatization and infiltration. Provision is made for a number of factors that control isotope fractionation including temperature, proportions of H_2O and CO_2 in metamorphic fluids, changing amounts of reactant and product minerals during the course of reactions, and rock porosity. He concludes that Rayleigh distillation is not an efficacious mechanism for fractionating oxygen isotopes because of limitations imposed by the reaction stoichiometry of dehydration and decarbonation reactions. In these reactions, only a fraction of the total oxygen in a rock is released as CO_2 or H_2O; therefore, only a small amount of oxygen can be involved in the Rayleigh distillation process. Thus, where metamorphism has resulted in large changes in oxygen isotope composition of rocks and minerals, the isotopic changes must record the infiltration of hydrothermal solutions through rocks during metamorphism. Analyses of some fossiliferous calc-silicate rocks depleted by 10–12‰ in $\delta^{18}O$ suggest to Rumble that volumes of fluid from four to six times greater than that of the rocks flowed through the rocks during metamorphism.

The partitioning of Mg and Fe^{2+} between olivine and chromite spinel solid solutions in ultramafic and mafic rocks is highly variable and has proved to be useful for geothermometry. The temperature effect depends, however, on the overall composition of the spinel phase, which may also involve complex substitutions of Fe^{3+}, Al, Cr, Ti, V, and other elements. *Rawson* and *Irvine* have investigated the effect of Ti on Mg-Fe^{2+} partitioning between olivine and ferrian ulvospinel at 1 bar. No direct temperature effect was detected for these phases, but the data show strong evidence of nonideality in the mineral solid solutions, and those relationships should be useful for refining the olivine-chromite geothermometer.

*In order to study the pressure effect on the olivine-liquid distribution coefficients for divalent cations, two

series of high-pressure experiments have been made by *Takahashi.* On the join $MgFeSiO_4$-$K_2O \cdot 4SiO_2$, partitionings of Co^{2+}, Fe^{2+}, Mn^{2+}, and Mg^{2+} were studied at 1340 °C and 10, 15, and 20 kbar, with graphite capsules. Because 1 bar and 15 kbar liquidi for olivine intersect at about 1340 °C, the composition of the liquid coexisting with olivine is constant within the pressure range studied. No systematic pressure effect on the distribution coefficients has been observed. The partitioning of Ni^{2+} and Mg^{2+} was studied with another technique involving a capsule made of olivine for an alkali-olivine basalt and a picrite composition. The experiments were made along the liquidi of the rocks in the pressure ranges where they coexist with olivine, so that the compositions of the melts at different pressures are nearly identical. No systematic pressure effect on the distribution coefficient has been detected at least up to 15 kbar for the basalt and to 25 kbar for the picrite. These conclusions are important because distribution coefficients, calibrated as a function of liquid composition at 1 bar, may be applied to the geochemical modeling of igneous processes in the deep crust or upper mantle.

*That liquids with a high MgO content might be parental magmas for mid-ocean ridge basalts has seemed doubtful because, as end products of 20–30% olivine fractionation, they would have much lower Ni contents than actually observed (100–300 ppm). The $D_{Ni}^{Ol/Liq}$ values (3–8) measured in natural high-MgO basalts are much lower than the $D_{Ni}^{Ol/Liq}$ (12–20) measured in the more common basalts with 7–10% MgO. With the D_{Ni} values measured in high-MgO basalts, *Elthon* estimates that the Ni contents of primary magmas parental to the common mid-ocean ridge basalts contain 600–700 ppm Ni. With those D_{Ni} values and the effects of magma mixing taken into account, the Ni abundances in such basalts are nearly identical with the *calculated* abundances that would occur in basalts derived from a high-MgO primary magma. When $D_{Ni}^{Ol/Liq}$ values deemed appropriate by Elthon are used, the Ni content of mid-ocean ridge basalts is not an obstacle to their derivation from a high-MgO primary magma.

The partitioning of Ni between pyrrhotite and magnetite at 1000 °C was studied by *Boctor* and *Mysen* using solid buffers of quartz-fayalite-magnetite and wüstite-magnetite, to which either pyrrhotite or Ag + Ag_2S was added to control the f_{S_2}. The results indicate that regardless of the buffer or Ni concentration the partitioning of Ni favors pyrrhotite relative to magnetite. It has been suggested that the separation of sulfide and oxide phases from mafic and ultramafic magmas depletes the melts of Ni and other transition metals. In the view of Boctor and Mysen, however, in the presence of a sulfide phase, magnetite has a minor effect in depleting mafic magmas of Ni.

*Two types of coefficients (K_D, distribution coefficient for two elements; D, single-element distribution coefficient) are commonly used to describe crystal/liquid element partitioning. As a rule, D shows large variations as a function of temperature, pressure, and liquid compositions whereas K_D tends to be relatively constant. *Takahashi* and *Irvine* have found that the changing values of D can be calculated with reasonable accuracy from a given general set of constant K_D values when only the liquid composition is known. Calculated D values for olivine/liquid MgO, FeO, MnO, and NiO partitioning were compared with those obtained experimentally. As an application of their theory to other crystal/liquid equilibria, clinopyroxene/liquid rare earth element partitionings (D_{REE}) were evaluated. They suspect that the D_{REE} value depends most significantly on the CaO content of liquid.

Mineral-Solution Equilibria

The transport of elements in solution is critical to many of the processes of ore formation, metasomatism, alteration, and diagenesis. Characterizing the aqueous fluid in equilibrium with a mineral assemblage requires knowledge of mineral solubility. During the past several years, *Frantz, Popp,* and *Boctor* have determined the free-energy differences between aqueous salts and hydrogen chloride. These salts include $MgCl_2$, $CaCl_2$, $FeCl_2$, and NaCl. Data for NaCl were obtained this year and are described below. On the basis of these free-energy values and the published free-energy data for minerals, these investigators have calculated the solubility constants for 69 different mineral components at temperatures between 400° and 600°C and pressures of 1 and 2 kbar. These constants will be useful to petrologists in computing the composition of supercritical fluids in equilibrium with metamorphic mineral assemblages and in estimating the relative fluxes of elements involved in intergranular diffusion.

*The composition of chloride-bearing fluids in equilibrium at 1 kbar with the mineral assemblages low albite—andalusite—quartz has been determined by *Popp* and *Frantz* at temperatures between 500° and 650°C. Using the Ag + AgCl buffering technique, they determined the concentrations of sodium and associated hydrogen chloride in equilibrium with these minerals. The sodium was found to exist primarily as associated NaCl. These data were then used to compute the free-energy difference between associated NaCl and HCl and the equilibrium constant for the exchange reaction between low albite, microcline, NaCl, and KCl. Their computed constants agree well with experimentally determined values given in the literature.

Mineral-solution equilibria in the system Mn_3O_4-HCl-H_2-H_2O were also studied with the rapid-quench, hydrothermal technique and the Ag + AgCl buffer methods of Frantz and Eugster (1973) and Frantz and Popp (1979) in the temperature range 725°–500°C at 1 and 2 kbar. Variations of the molalities of Mn and associated HCl° at temperature and pressure were used by *Boctor* and *Frantz* to identify the predominant Mn species in the fluid in equilibrium with hausmannite. The associated $MnCl_2$° seem to be the predominant Mn species in the temperature range of the experiments. The present data and the data of Boctor *et al.* (1980) suggest that both Fe and Mn are transported as associated $MnCl_2$° and $FeCl_2$° in convecting hydrothermal systems associated with mid-oceanic ridges prior to their oxidation and deposition as hydroxides on the ridge crests.

*Whereas the above studies were concerned with dilute solutions, *Simons* and *Sharma* have confirmed, with Raman spectra, the common experience that the presence of trace amounts of water can markedly increase reaction rates in glass. They observed that trace amounts of water affect the physical properties of B_2O_3 glass and increase the rate of crystallization in B_2O_3 and sodium disilicate glasses. In K_2CO_3-$MgCO_3$ glasses, the diffusion of hydrogen through a $Pt_{95}Au_5$ capsule at high pressures and temperatures results in the formation of a complex crystalline bicarbonate along with crystalline $K_2Mg(CO_3)_2$. Because properties such as density, refractive index, and viscosity are sensitive to structural changes, special precautions must be taken to eliminate the effects of hydrogen diffusion in the preparation of anhydrous samples.

Planetary Gases at High Pressures

The dramatic discoveries resulting from observations made from the space probes have led to much interest in new ranges of physicochemical conditions and materials. The characteriza-

tion of those materials has required some novel techniques. Materials such as argon, neon, and methane, which are gases under room conditions, crystallize at very high pressure. *Hazen, Mao, Finger,* and *Bell* have found that each of these gases crystallizes in the cubic closest-packing structure at high pressure and that each forms *single* crystals within the gasketed sample chamber of a diamond-anvil, high-pressure cell at room temperature. Measurements of the cubic unit-cell volume vs. pressure with single-crystal, x-ray diffraction techniques reveal that these crystals are among the most compressible solids ever observed. As pressure is varied, the solids recrystallize to new single crystals in new orientations with little or no strain. These "gases" may thus be excellent hydrostatic pressure media, and at the same time their pressure-sensitive, unit-cell dimensions may provide a precise pressure calibration. Furthermore, pressure-volume data on methane, ammonia, and other fluids will constrain models now being proposed for the structures of Jovian planets.

The Raman spectra of methane (CH_4) measured as a function of pressure in the diamond-window, high-pressure cell by *Sharma, Mao,* and *Bell* indicate that two phase changes, one at 50 kbar, the other at 118 kbar, occur at 25 °C. These data may also be useful in interpreting properties of the interiors of the major gaseous planets.

In a joint study with *E. M. Brody*† and *H. Shimizu*†, *Mao* and *Bell* have undertaken pioneering studies of Brillouin scattering in fluid and crystalline hydrogen and deuterium. The scattering process is a Doppler frequency shift of a laser beam as it is Bragg-reflected from a thermal phonon in hydrogen and deuterium. The laser beam passes through the diamond windows of the pressure cell used in these experiments and is scattered by the sample. Analysis of the scattered radiation is made through a Fabry-Perot interferometer. The resulting values of phonon velocity are used to calculate the elastic moduli as a function of pressure. The data on hydrogen and deuterium obtained in this study compare well with ultrasonic data at low pressure. These techniques may prove useful in obtaining elastic moduli for minerals under deep mantle conditions.

The Raman spectrum of D_2 was determined by *Sharma, Mao,* and *Bell* to 550 kbar at 25 °C. The frequency of the Raman shift of D_2 increased with pressure, much like that of H_2, but the change in sign of the frequency shift vs. pressure curve was delayed until the pressure was close to 300 kbar, apparently from an isotopic effect. The inference is that H_2 will probably change to the atomic (metallic) state at a lower pressure than D_2.

*The classic reaction between H_2 and D_2 to yield HD was studied for the first time in the solid state at room temperature and high pressure. The metal gasket of the diamond-window, high-pressure cell containing the sample tended to catalyze the reaction, according to *Bell, Mao,* and *Sharma.* The reaction rate was greatly increased as a function of pressure (to 160 kbar).

Spectral Mineralogy

Most geological projects begin in the field, where specimens are collected that may contribute to an understanding of the processes that led to their formation. The conditions of formation are deduced from carefully determined properties of the constituent minerals. The deductions are based on the accurate characterization and calibration of analogous end-member minerals through laboratory experimentation. One of the principal requirements of any experimental research project is, therefore, to characterize fully not only starting materials, but also products. These properties are then compared with

†Institute of Optics, University of Rochester.

those determined on natural minerals for estimating the conditions last experienced by the rock. The more complex the mineral and its assemblage, the more information that can be recorded about its formation. For this reason a major focus of the Geophysical Laboratory is the characterization of minerals with all appropriate techniques at the greatest level of refinement. One of the first steps in characterization is an accurate determination of the crystal structure, because most properties must eventually be interpreted in terms of interatomic forces.

Crystal structures of minerals under nonambient conditions may be used to understand the nature of interatomic forces as well as specific structural instabilities that might lead to phase transitions. *Hazen* and *Finger* have been active in the development of techniques for the collection of data on crystal structures at high temperature and pressure. Dramatic improvement in procedures for the determination of high-pressure structures at room temperature is illustrated by their report on the structure of forsterite at 40 kbar. Errors have been reduced significantly, compared with a similar study five years ago. As a result, it is now possible to observe that the M1 octahedral Mg site has a significantly greater compressibility than the M2 site. This difference in site compressibility may influence cation-site distributions in olivines formed at high pressure.

*Cation ordering in silicate minerals is especially important in characterizing the paragenesis of host rocks. As part of an ongoing study of cation-site preferences in rock-forming silicates, *Hazen, Finger,* and *Velde* have determined the crystal structure of a silica-rich trioctahedral mica of unusual composition from a melilite-bearing eruptive rock. This mica, which has excess alkalies ($\Sigma Na + K > 1$), is the first known layer silicate with octahedral sodium. In spite of the complexity of the octahedral layer composition, which includes Mg, Fe, Na, Li, Ca, Mn, Ti, and vacancies, there is no evidence of cation ordering between the two distinct octahedral sites. The site energies of M1 and M2 in trioctahedral micas must, therefore, be nearly equal.

The effect of pressure on the Raman spectrum of TiO_2-II compressed to 372 kbar has been studied by *Mammone* and *Sharma.* A reversible phase transition in the 200–300 kbar range was observed. This new phase, designated TiO_2-III, may be the same phase previously observed in shock-wave experiments.

The effect of temperature and hydrostatic pressure on the Raman spectrum of rutile-type dioxides (TiO_2, GeO_2, SnO_2) was investigated by *Mammone* and *Sharma.* These materials serve as analogues for stishovite in the earth's interior. The temperature and pressure results were combined with bulk modulus and thermal expansion data to evaluate the volume and temperature contributions to the isobaric temperature dependence of the Raman frequencies. Large anharmonicities were observed in TiO_2 that were attributed to hybridization of the oxygen *p* states with the *d* states of the Ti ion. In contrast the *p*-electron bonding that is present in GeO_2 gives rise to much smaller anharmonicities. A low degree of anharmonicity, therefore, would also be expected in stishovite.

Wüstite is believed to be a dominant mineral species at high pressures in the earth's mantle. *Zou, Mao, Bell,* and *Virgo* have discovered a high-pressure phase change in wüstite by analysis of x-ray diffraction and ^{57}Fe Mössbauer data. Cubic and paramagnetic at 1 bar, wüstite becomes antiferromagnetic at approximately 120 kbar, at which pressure it has a distorted rhombohedral structure. At 400 kbar wüstite is magnetic and markedly rhombohedral. These properties would not have been predicted from low-pressure data and may be important in formulating equations of state of the earth's mantle.

Simons has determined the composition–lattice parameter relationship of both the pure end-member wüstite and magnesiowüstite solid solution series. Because no direct determination of the composition of magnesiowüstite under ultrahigh pressure is possible, wet-chemical analyses were performed on samples prepared at 1 bar. Simons demonstrated that with decreasing Fe content the Fe^{3+}/Fe decreases at a greater rate but is always > 0 for the smallest Fe concentrations. The lattice parameter for wüstite decreases with pressure, and he supposed that in comparison with the data obtained at 1 bar the Fe^{3+}/Fe increases accordingly. Because this supposition should be valid for the entire magnesiowüstite series, magnesiowüstite probably would have lost Fe, as metallic iron and the composition of the magnesiowüstite would have shifted toward Mg-richer compositions during its descent to the core of the earth. Owing to differences in density, the metallic iron would tend to sink faster toward the core and the assemblage magnesiowüstite–metallic iron would have thus unmixed. An iteration of the process proposed by Mao *et al.* (*Year Book 78,* 621–625) is believed by Simons to have resulted in a strongly iron-depleted magnesiowüstite in the lower mantle.

*The equation of state of CaO at high pressure has been previously calculated from shock-wave and static x-ray experiments (Jeanloz *et al., Year Book 78,* 627–630). These calculations indicated a possible transition of CaO from the *B*1 (sodium chloride type) to the *B*2 (cesium chloride type) structure between 0.6 and 0.7 Mbar. New static x-ray experiments from 1 bar to 700 kbar by *Mammone, Mao,* and *Bell* confirm these equation-of-state calculations. The *B*1-*B*2 transition was observed at pressures near 700 kbar. The density of the *B*2 phase of CaO is similar to that of the bulk mantle; calcium, therefore, may be a significant component of the earth's interior.

Mao, Hazen, and *Bell,* in a joint effort with *J. Wittig,*† have studied the physical properties of metallic praseodymium at high pressure for the purpose of analyzing an earlier observation of an abrupt change in electronic structure. The electronic change was accompanied by a volume change of approximately 19% and is much too large to be accounted for by simple close-packed distortions. They suspect that there has been a breakdown locally of the 4*f* electron shell. Such behavior provides a major new effect for interpreting changes in properties of the mantle.

*In conjunction with *M. Madon*‡ and *J. P. Poirier,*‡ *Bell* and *Mao* have studied crystals of $MgSiO_3$ with the perovskite structure by transmission electron microscopy (TEM). The crystals were small (0.1–0.5 μm), but excellent TEM photomicrographs were obtained, showing well-developed crystal edges and pseudotetragonal symmetry. The present experimental evidence suggests that silicate perovskite may be a dominant mineral in the earth's mantle.

Biogeochemistry

One of the fastest growing and most exciting areas of earth science today is biogeochemistry. It combines a vast array of new techniques from biology and chemistry for application to the broad paleontological, anthropological, stratigraphic, and major economic aspects of geology. The present results clearly demonstrate a positive feedback to the parent sciences. The unusually innovative studies described below illustrate the leadership and pioneering qualities of the biogeochemical group at the Geophysical Laboratory.

Several major factors in the genesis of Mississippi Valley–type lead-zinc deposits remain enigmatic, including the source of the metals, the complexes involved in the ore-forming solutions,

†Thomas B. Watson Laboratory.
‡University of Paris VI.

and the precipitation mechanism. A ubiquitous association of organic matter with the ore has been described frequently, and forms the basis of current work, which is an investigation of the organic matter in the host rock of the Wisconsin district. *Gize* and *Hoering* have shown that most of the organic material is indigenous to the host rock and was derived from algae and bacteria. Comparison between samples affected and unaffected by ore deposition reveals an increase at the ore body of low-molecular-weight saturated hydrocarbons and fatty acids. There is also an eightfold increase in the nickel-vanadyl ratio of a porphyrin at the ore body. More extensive sampling is needed, however, to generalize these results to the district. The maturity of the organic matter shows a remarkably low temperature history for the area since the Ordovician, supporting the derivation of the ore-forming solutions from a sedimentary basin, rather than from a magmatic source.

Variations in the ratios of stable hydrogen isotopes may aid in tracing food webs of marine and terrestrial life. *Estep* and *Dabrowski* have investigated the relationship of the isotope content of organically bonded hydrogen of an animal with the isotope content of its food source, in a simple natural population of snails and their possible algal food sources. *Littorina obstusata,* northern Atlantic intertidal snails that feed almost exclusively on the brown alga *Fucus vesiculosus,* have D/H identical with that of this alga and unlike that of the other algae available to the snails. In this natural population and in laboratory-reared mice, the D/H of the food source, not the water, determines for the most part the D/H of the organically bonded hydrogen in animals. Because of variations in the D/H of plants due to either metabolism or environmental influence, the D/H of organically bonded hydrogen in an animal's tissue may indicate the presence of a particular plant in its diet. The method, therefore, may be useful in the investigation of environmental or migratory phenomena and may even be applicable to the study of the organic matter in fossil bones, shells, and teeth.

Estep and *Hoering* have used high-precision, stable-isotope-ratio, mass spectrometry to identify some of the key reactions in plant metabolism that fractionate the hydrogen isotopes. A pool of intracellular, organically bound hydrogen generated during photosynthesis provides the hydrogen available for cellular biosynthesis. Stable hydrogen isotope fractionation is governed by this form of bound hydrogen. Hydrogen metabolism in biosynthesis and dark reactions is linked to that in light via the pools of photosynthetically generated reductant. Consequently, additional fractionation occurs during the biosynthesis of proteins and lipids. Hydrogen in the water of the growth medium was not incorporated immediately into organically bonded hydrogen. This lag in the uptake of hydrogen from water indicates that in actively photosynthesizing cells, a pool of excess reductant is available for cellular hydrogen metabolism. The complex network of chemical reactions linking the hydrogen in water to the organically bonded hydrogen is a problem uniquely accessible to measurement of isotope fractionation. Isotope fractionation is indicative of rate-limiting reactions or branching points; hence the enzymes at these critical points that control isotope fractionation also serve to regulate hydrogen metabolism in the plant cell.

Colloidal and particulate-sized material in the Chesapeake Bay and Patuxent River was collected and analyzed by *Sigleo, Hoering,* and *Hare* to document changes in natural organic material associated with chlorination of estuarine waters by power plants. The major challenge, however, proved to be the characterization of aquatic organic matter, a complex mixture of decompo-

sition and resynthesis products. The final results, including detailed amino acid analyses, indicate that this material consists primarily of proteinaceous-carbohydrate polymers derived from *in situ* aquatic microorganisms. Colloidal aquatic material, composed mainly of two classes of compounds, is of unusual significance because both proteinaceous material and carbohydrates contain numerous active functional groups with capacities to bind and transport trace metals and toxic organic substances.

Molecular sieves are valuable media for selectively absorbing organic matter with narrow ranges of molecular sizes and shapes. Complex mixtures isolated from sedimentary rocks can be simplified prior to analysis by gas chromatography–mass spectrometry. *Hoering* has evaluated the newly available silicalite, a synthetic polymorph of silica with a pore structure suitable for accommodating 2-methyl (iso) and 3-methyl (anteiso) hydrocarbons. Such hydrocarbons are potential indicators of the input from bacteria and higher plant waxes into sedimentary organic matter. By chaining together a series of chromatographic and molecular sieving techniques, a wide molecular-weight range of iso- and anteiso-hydrocarbons could be isolated and identified. The Green River shale, a sediment of lacustrine origin, contained these hydrocarbons with greater than 26 carbon atoms, indicating an input from plant waxes. Two crude oils from marine rocks also contained these high-molecular-weight compounds. The three materials examined by Hoering have about 50 ppm iso- and anteiso-hydrocarbons in the range from 14 to 30 carbon atoms.

In remote areas such as the high Arctic it is frequently advantageous to obtain geochemical information in the field rather than wait for sample processing at the home laboratory. A field-portable amino acid analyzer was built at the Geophysical Laboratory by *Hare* and *Miller* and used in Spitsbergen for stratigraphic correlation and relative age dating of fossil marine molluscs from interglacial and postglacial sediments. It was possible with a simplified sample procedure to process and analyze a sample in less than 30 min. Shells of increasing age yield progressively greater proportions of free amino acids as well as increased amounts of racemization. Information on the composition of the amino acids in the fossil shells proved useful in correlation of interglacial and postglacial stratigraphic units and also helped clarify some puzzling relationships suggested by radiocarbon dates obtained earlier. Holocene and Pleistocene mollusc shell fragments were readily differentiated by amino acid ratios into several distinct age groups. Shell samples from a stratigraphic layer, previously dated by ^{14}C at around 14,000 years on a composite sample of shell fragments, were shown by amino acids to be a mixture of Holocene (10,000 years) and older Pleistocene (>35,000 years) reworked fragments.

New Techniques

The study of crystal structures at the temperature and pressures of formation is critical to an understanding of the relationships between structure, thermochemical properties, and stability of minerals. In addition, these structure studies under nonambient conditions may be used to deduce the nature of interatomic forces as a result of the differential expansion and compression of bonds with changing temperature and pressure. *Hazen* and *Finger* have completed the first single-crystal x-ray structural analysis of a mineral held at simultaneous high temperature and pressure (300 °C at 30 kbar, on calcium fluoride). They describe the construction of a simple and inexpensive, heated diamond-anvil cell, which is easily adapted to x-ray diffractometry and photography. Maximum

conditions of 450°C and 40 kbar have been sustained; thus, conditions within much of the earth's crust may now be duplicated in single-crystal, x-ray experiments.

A new design of the diamond-window, high-pressure apparatus was made for a study of single crystals of solidified gases. *Mao* and *Bell* have modified the apparatus, originally designed by W. Bassett, for the purpose of cryogenic filling of fluids. This new device has been used successfully in obtaining single-crystal, x-ray diffraction data in precession space. For example, high-quality, single-crystal data were obtained on solidified argon and other gases *in situ* at high pressure after short exposure times (see Hazen, Mao, Finger, and Bell, this Report). *Mao* and *Bell* have also made an improved design of the diamond-window, high-pressure cell that contains apertures for 20 nonredundant scattering directions. In studies of Brillouin scattering, it is desirable to measure simultaneously several orientations of longitudinal and transverse acoustic wave velocity in order to define the elastic moduli for a single crystal under pressure. In some instances it is possible to measure the acoustic velocity in certain directions and utilize other apertures in combination to obtain the refractive index of the pressurized crystal. The multiple apertures of this cell result in measurements of the Raman spectra of a pressurized sample free of fluorescent interference originating in the diamonds. Furthermore, the dependence of Raman spectra of a pressurized sample on scattering direction can be determined. This modified design takes into account refraction of light at the interfaces.

*The electrical resistance of geological materials ranges over several orders of magnitude, and a range of methods is required for its measurement. In the design of techniques for measuring resistance of conductors and semiconductors at high pressure, *Mao* and *Bell* have used microcircuitry for the diamond-window, high-pressure cell to correct problems caused by metallic leads. The resistance measurements in this new design are obtained from the voltage drop across the sample, and thus the contribution of the lead wires is eliminated. It should now be possible to study the electrical properties of metals at the highest pressures available (1.7 Mbar), equivalent to those at the earth's core-mantle boundary.

Infrared transmission spectra of methanol and ethanol have been measured at elevated pressures (77 kbar) and room temperature in the diamond-anvil cell by *Mammone* and *Sharma* in conjunction with a previous Raman study. Methanol crystallizes in the α-structure ($P2_1$ symmetry) at high pressures. The vibrational spectra for ethanol were interpreted in terms of the monoclinic (Pc; $X = 4$) low-temperature structure. These alcohols are of technological interest as hydrostatic media at high pressures. Their infrared absorption is very intense; therefore, the 4:1 methanol:ethanol mixture is not useful as a pressure-transmitting medium for mid-infrared (4000–400 cm^{-1}) spectroscopic experiments.

Hatten S. Yoder, Jr.

References

Boctor, N. Z., R. K. Popp, and J. D. Frantz, Mineral-solution equilibria—IV. Solubilities and the thermodynamic properties of $FeCl_2°$ in the system Fe_2O_3-H_2-H_2O-HCl, *Geochim. Cosmochim. Acta*, in press, 1980.

Boyd, F. R., A pyroxene geothermometer, *Geochim. Cosmochim. Acta, 37,* 2533–2546, 1973.

Eaton, J. P., and J. K. Murata, How volcanoes grow, *Science, 132,* 925–938, 1960.

Frantz, J. D., and H. P. Eugster, Acid-base buffers: use of Ag + AgCl in the experimental control of solution equilibria at elevated pressures and temperatures, *Amer. J. Sci., 267,* 268–286, 1973.

Frantz, J. D., and R. K. Popp, Mineral solution equilibria—I. An experimental study of complexing and thermodynamic properties of aqueous $MgCl_2$ in the system MgO-SiO_2-H_2O-HCl, *Geochim. Cosmochim. Acta, 43,* 1223–1239, 1979.

EXPERIMENTAL AND FIELD PETROLOGY

Experimental Modeling of Convection in Layered Intrusions*

T. N. Irvine

This report describes some first steps in the development of equipment, techniques, and scaling theory for low-temperature experimental simulation of convection processes in layered intrusions. The next report describes some first results. To date, particular attention has been given to bodies of liquid stratified in composition and density.

Experimental Methods

The experiments have been made mainly with two small Plexiglas tanks fitted with independent compartments along the bottom and side edges and in their lids. Cooled or cooled and heated water are circulated through the marginal compartments to produce the differential temperature conditions necessary to cause thermal convection of the liquid contained in the main chamber. One tank is rectangular, with an inner chamber about 32 cm deep, 40 cm wide, and 6.5 cm thick from front to back. The other has the same thickness, but its walls are inclined inward at 40°, so the inner chamber tapers from about 65 cm at the top to 30 cm at the bottom through a depth of 15 cm. The circulated water comes from temperature-controlled refrigerated baths; its temperature is measured with thermocouples where it enters and leaves each marginal compartment. Temperatures within the tank are measured with thermocouples inserted through ports in the lids.

In a typical experiment, the inner chamber of the tank is filled with salt or salt-sugar solutions, the densities of which have been measured with a hydrometer. A column of liquid layers decreasing in density upward is produced either by slowly injecting successively denser liquids through a funnel extending to the bottom of the column or by carefully pouring successively less dense solutions onto a porous pad floating on the top. If a gradient of composition and density is required, the Oster (1965) two-bucket technique of tank-filling is employed. Combinations of salt and sugar solutions are used to produce double-diffusive convection (Turner and Chen, 1974; see below).

The liquid layers are tinted with dye to distinguish them, and their convection is observed by the shadowgraph method. For the latter, the tank is back-lit with the slide projector, and the image of the liquids is viewed on translucent paper taped to the front. Sharp boundaries between solutions differing in refractive index then resemble Becke lines, a feature that is especially prominent if there is double-diffusive convection. Circulation patterns are observed by introducing streaks and blobs of dyed solutions having as nearly as possible the same densities as the liquids in the tank. The motions are photographed with a movie camera or a 35-mm camera equipped with motor drive, and are timed by a digital clock visible in the photographs.

Scaling Considerations

Summary derivations of some scaling equations, expressed in terms of model ratios, appear in Table 1; representative numerical examples are given in Table 2. The key equation is that defining the model ratio of length in terms of the ratio for kinematic viscosity (= viscosity/density). This relationship determines the size of the

*Research supported by National Science Foundation grant EAR7911188.

TABLE 1. Scaling Equations for the Model Experiments

Model ratios:
(= value in model/value in original)
Length, l_r
Mass, m_r
Density, $\rho_r = m_r l_r^{-3}$*
Time, t_r
Velocity, $v_r = l_r t_r^{-1}$*
Gravitational acceleration, g_r
Viscosity, $\eta_r = m_r l_r^{-1} t_r^{-1}$*
Kinematic viscosity, $\nu_r = \eta_r \rho_r^{-1}$
Temperature difference, ΔT_r
Thermal expansion, α_r
Thermal conductivity, K_r
Thermal diffusivity, κ_r
Heat flux, J_r

Mechanical scaling:
Because $g_r = 1$, $t_r = l_r^{1/2}$*
Hence, $\eta_r = m_r l_r^{-3/2} = \rho_r l_r^{3/2}$
Thus, $l_r = (\eta_r/\rho_r)^{2/3} = \nu_r^{2/3}$
$t_r = \nu^{1/3}$, and $v_r = \nu^{1/3}$

Thermal scaling:
Prandtl number ratio:
$Pr_r = \nu_r \kappa_r^{-1} = 1$
Hence, $\nu_r = \kappa_r$
Grashof number ratio:

$$Gr_r = \frac{g_r \alpha_r \Delta T_r l_r^3}{\nu_r^2} = 1$$

Hence, $\Delta T_r = \alpha_r^{-1}$
Nusselt number ratio:

$$Nu_r = \frac{J_r l_r}{K_r \Delta T_r} = 1$$

Hence, $J_r = K_r \alpha_r^{-1} \nu_r^{-2/3}$

* Relationships from Hubbert (1937).

experimental tank necessary to model an intrusion—or in more realistic terms, the size of the *part* of an intrusion that can be examined in an experimental tank.

The latter statement is more appropriate because the size-viscosity relationship is demanding. For example, with an aqueous solution ($\eta = 0.01$ poise; $\rho = 1.0$–1.1 g cm^{-3}) for the experimental liquid, if the magma were an ultrabasic-basic liquid ($\rho = 2.7$–2.8 g cm^{-3}) with a viscosity of 100 poises, then 1 cm in the tank would be equivalent to only 2.4 m; and even for a magma viscosity of 1000 poises, it would correspond to only 11 m. Thus, to model an intrusion 5–10 km in diameter and 1–2 km deep would require a tank the size of a swimming pool. It is interesting conceptually that a swimming pool of water compares with an intrusion of magma; but to translate this observation into an experiment is economically formidable!

With the present tanks, therefore (or even a planned tank several times larger), only very local phenomena in an intrusion can be examined *quantitatively*—effects, for example, that might occur near an external contact or in the interior along boundaries between liquid layers. This limitation, however, does not necessarily pertain to qualitative observations, like those on the evolution and decay of convection cells described in the next report. And even certain quantitative measurements, when expressed as dimensionless ratios, may be sufficiently independent of size to be applied to large intrusions.

The mechanical scaling also places severe limits on the time period of an intrusion's history that can be "observed" experimentally (because the time ratio is the square root of the length ratio). Thus, in the above model of an ultrabasic-basic magma, an hour in the experiment is equivalent to 4 hr in the intrusion at a magma viscosity of 100 poises, and to 15 hr at 1000 poises. Obviously, to simulate any extended part of an intrusion history lasting thousands of years is out of the question.

What one can do, at least in principle, is "tune in" on the intrusion at selected times and examine rates of convection and the effect of short-term events (such as the addition of fresh magma) that might occur at those times. This approach is possible through the "thermal scaling."

The behavior of a fluid undergoing free thermal convection theoretically depends on certain dimensionless ratios, the most important of which are

TABLE 2. Examples of Some Scaling Calculations*

	I			II			III		
	Original	Model	Ratio	Original	Model	Ratio	Original	Model	Ratio
Scaling Parameters									
ρ, g cm^{-3}	2.70	1.10	0.407	2.70	1.1	0.407	2.70	1.00	0.370
η, poises	30	2.23	0.074	300	22.3	0.074	30	0.01	0.0003
ν, cm^2 s^{-1}	11.1	2.03	0.183	111.1	20.3	0.183	11.1	0.01	0.0009
c, cal g^{-1} °C^{-1}	0.26	1.00	3.842	0.26	1.0	3.842	0.26	1.00	3.842
K, cal cm^{-2} s^{-1}	0.005	0.0014	0.286	0.005	0.0014	0.286	0.005	0.0014	0.286
κ, cm^2 s^{-1}	0.007	0.0013	0.183	0.007	0.0013	0.183	0.007	0.0014	0.201
α, °C^{-1}	5×10^{-5}	0.00021	4.140	5×10^{-5}	0.00021	4.140	5×10^{-5}	0.00021	4.140
l, cm	3.1	1.0	0.322	3.1	1.0	0.322	107	1.0	0.009
t, hr	1.8	1.0	0.568	1.8	1.0	0.568	10.3	1.0	0.096
ΔT, °C	4.1	1.0	0.242	4.1	1.0	0.242	4.1	1.0	0.241
Pr	1560	1560	1.000	15,600	15,600	1.000	1560	7.0	0.0013
Cooling Conditions									
T_L, °C	1200	...	...	1200	...	...	1325	...	...
αcum, m yr$^{-1/2}$	16	...	...	16	...	...	24	...	...
1. t_e, yr	0.1	...	...	0.1	...	...	0.1	...	...
J, cal cm^{-2}s^{-1}	1.9×10^{-2}	4.1×10^{-3}	0.215	1.9×10^{-2}	4.1×10^{-3}	0.215	2.8×10^{-2}	9.4×10^{-4}	0.033
ΔT_w, °C†	...	...	6.2	...	...	6.2	...	...	1.44
2. t_e, yr	1.0	...	...	1.0	...	...	1.0	...	...
J, cal cm^{-2}s^{-1}	5.9×10^{-3}	1.3×10^{-3}	0.215	5.9×10^{-3}	1.3×10^{-3}	0.215	9.0×10^{-3}	3.0×10^{-4}	0.033
ΔT_w, °C†	...	...	2.0	...	...	2.0	...	...	0.46

* Symbols: c, heat capacity; T_L, liquid temperature; others as in Table 1 or text.
† Per 0.25 inch thickness of Plexiglas.

known as the Prandtl, Grashof, and Nusselt numbers (e.g., see Shaw, 1974; Tritton, 1977). Another commonly used ratio, the Rayleigh number, is the product of the Prandtl and Grashof numbers. Ideally in a scaled experiment, these ratios should have model ratios of unity. The thermal scaling in Table 1 outlines one way in which this condition can be achieved. To use the equations, the heat fluxes that would be expected through the intrusion's roof and walls are calculated for the time of interest after the magma was emplaced. Then, by comparing these values with the model ratio, estimates are made of the heat fluxes required through the Plexiglas roof and walls of the main chamber of the experimental tank.

Heat-flux values for the intrusion can be conveniently estimated through mathematical cooling models for layered intrusions developed by Irvine (1970). These models were devised for layered sills, and heat flux was not specifically tabulated. However, values graphed for a parameter α_{CUM}, described as a layered series "accumulation-rate index," relate directly to the heat flux through the top contact of the main body of liquid in the sill. For present purposes, this heat flux could equally pertain to vertical or inclined walls adjoining the magma. In practice, α_{CUM} can be converted into a "heat-flux index" (denoted ϕ_J) simply by multiplying it by 3.739×10^{-4}. The heat flux through the contact, in cal cm^{-2} sec^{-1}, is then $J_o = \phi_J t_e^{-1/2}$, where t_e is the time after emplacement in years. The steady-state temperature gradients that must then be maintained through the Plexiglas roof and walls of the experimental tank are then given by $\Delta T_w / \Delta X_w = J_m K_w^{-1}$, where ΔX_w and K_w are the thickness and thermal conductivity of the Plexiglas walls, and $J_m = J_r J_o$.

Implementation

The general experience in scale-model experimentation is that not all significant parameters can be rigor-

ously scaled at the same time, at least not to the desired conditions.

The principal limitations relating to the present scaling are well illustrated by the numerical examples in Table 2, where the original liquids could be ultrabasic-basic magmas, and the model liquids are either water (in III) or water plus additives to increase its viscosity. In I and II, all scaling constraints are satisfied; in III, the requirement of a unit ratio for the Prandtl (and Rayleigh) number has been relaxed.

An experimental limitation arises because the need to observe the convection has priority over the need to insulate the tank. Before the scaling equations were developed, it was thought that this limitation would relate to large temperature differences, but as it turns out, the problem is just the opposite. Except for very short "times after emplacement" (t_e), the amount of cooling that must be imposed on the tank is too small to be controlled accurately. In terms of primary emplacement, only very hot, fluid magmas can be modeled for t_e as great as 1 year. Otherwise, the models are appropriate only where t_e either is not a factor or pertains to secondary movements of magma into new temperature environments.

The other major limitation relates to the Prandtl number constraint. This requires an increase in the viscosity of the model liquid over that of water and leads to results like those for examples I and II, where the equivalent of 1 cm in the tank is reduced to only 3 cm in the intrusion and the equivalent of an hour of experiment is only 1.8 original hours. Such conditions are useful for examining very local effects like convection at contacts between liquid layers,* but the possibility of modeling a sizeable body of liquid is clearly excluded.

To model large-scale convection, a low-viscosity model liquid like water is required, but with a thermal conductivity much lower than water. None is available, so one must resort to other methods. If the problem concerns *vertical* heat and mass transfer between liquid layers, then it may be possible, as described in the following report, to use chemically driven convection as a surrogate for thermal convection. But if cooling through a wall is involved, there seems no alternative but to abandon the constraint on the Prandtl number, as in III. In such case, the Nusselt number scaling equation in Table 1 is no longer strictly applicable, because in terms of the scaling, heat is removed from the liquid more rapidly than the liquid motion can respond to its removal. Consequently, the thermal boundary layer becomes too thick, the buoyancy forces become too large, and the convection becomes too strong.

This effect can be compensated by reducing the cooling rate to accord with a model ratio of thermal conductivity corresponding to a unit Prandtl number ratio. The Prandtl number ratio is defined, $Pr_r = \nu_r \kappa_r^{-1}$, where $\kappa_r = K_r \rho_r^{-1} c_r^{-1}$; thus, by substitution and rearrangement, $K_r = \rho_r c_r \nu_r Pr_r^{-1}$. Therefore, if Pr_r is assumed to be unity, even though in fact it is much smaller, K_r (and hence J_r), will be proportionately reduced. But this adjustment pertains only to the walls where the cooling is controlled. As the cooled liquid convects into the tank, it will still gain heat from its surroundings more rapidly than it ideally should. In some circumstances, however, this effect may serve to approximate the production of heat of crystallization in supercooled magma.

*Note that I and II are identical except that the liquids have different viscosities. Contacts between liquid layers of different viscosity can, therefore, be modeled with some rigor.

References

Hubbert, M. K., Theory of scale models as applied to the study of geologic structures, *Geol. Soc. Amer. Bull., 40*, 1459–1520, 1937.

Irvine, T. N., Heat transfer during solidification of layered intrusions. I. Sheets and sills, *Can. J. Earth Sci.*, *7*, 1031–1061, 1970.
Oster, G., Density gradients, *Sci. Amer.*, *213*, 70–76, 1965.
Shaw, H. R., Diffusion of H_2O in granitic liquids: Part I. Experimental data; Part II. Mass transfer in magma chambers, *Carnegie Inst. Wash. Publ. 634*, 139–170, 1974.
Tritton, D. J., *Physical Fluid Dynamics*, Van Nostrand Reinhold Company, New York, 1977.
Turner, J. S., and C. F. Chen, Two-dimensional effects in double-diffusive convection, *J. Fluid Mech.*, *63*, 577–593, 1974.

Convection and Mixing in Layered Liquids*

T. N. Irvine

Major inroads into the understanding of layered intrusions are the recent realizations that the magmatic liquid can become stratified through density variations relating to even very small differences in composition and that this stratification can be a dominant control on convection systems and mechanisms of crystallization (Turner and Gustafson, 1978; Chen and Turner, 1980; Turner, 1980; McBirney and Noyes, 1979; Irvine, 1980a,b; Sparks *et al.*, 1980; Huppert and Sparks, 1980). This report summarizes a variety of pertinent experimental observations on convection in density-stratified liquids, and mechanisms of liquid mixing are illustrated.

In the experiments, aqueous salt and salt-sugar solutions substitute for ultrabasic-basic magmas, as described in the foregoing report. A principal objective has been to define the ways that the magma might circulate from the roof and walls of the intrusion chamber, where most of the heat is eventually removed, to the floor, where (typically) most of the rocks have formed from the bottom up. Indications are that, despite the importance of magmatic current transport and the deposition of crystals in producing imposing layering structures, the majority of the crystals in the layered rocks have probably formed at or near the places where they are observed (Irvine, 1980a,b). A fundamental problem then is to define how the liquid is supercooled and transferred to these sites.

*Research supported by National Science Foundation grant EAR7911188.

Effects of Heat Transfer Between Liquid Layers

The process of double-diffusive convection (Fig. 1) is especially important to heat and mass transfer between liquid layers. The mechanism depends on a contrast in diffusivities—either between thermal and chemical diffusivity or between the diffusivities of two chemical components (see Turner, 1973). In aqueous salt-sugar solutions, salt diffuses faster, in this respect, like heat when thermal diffusivity is involved. But an increase in salt concentration increases the solution density, an effect opposite to that of an increase in heat. Thus, in discussions of the salt-sugar system, salt is sometimes referred to as "negative heat."

On this basis, the solution arrangement of salt-over-sugar for the diffusive case (Fig. 1) compares with a magmatic arrangement of a relatively cool, low-density magma floating on hotter but denser liquid. Magnesian basalt over picritic tholeiite is an example evident in the Muskox intrusion (Irvine, 1980b). A major question, however, is whether the experimental process is a realistic model.

A partial answer comes from the Prandtl and Schmidt numbers. The Prandtl number effectively compares the diffusivity of momentum and vorticity during motion with the diffusivity of heat, and the Schmidt number is the analogous comparison with the diffusivity of a chemical component. Schmidt numbers for the salt-sugar system (Sc = kinematic viscosity/chemical diffusivity = ν/D = 600–2000) that are of the same order of

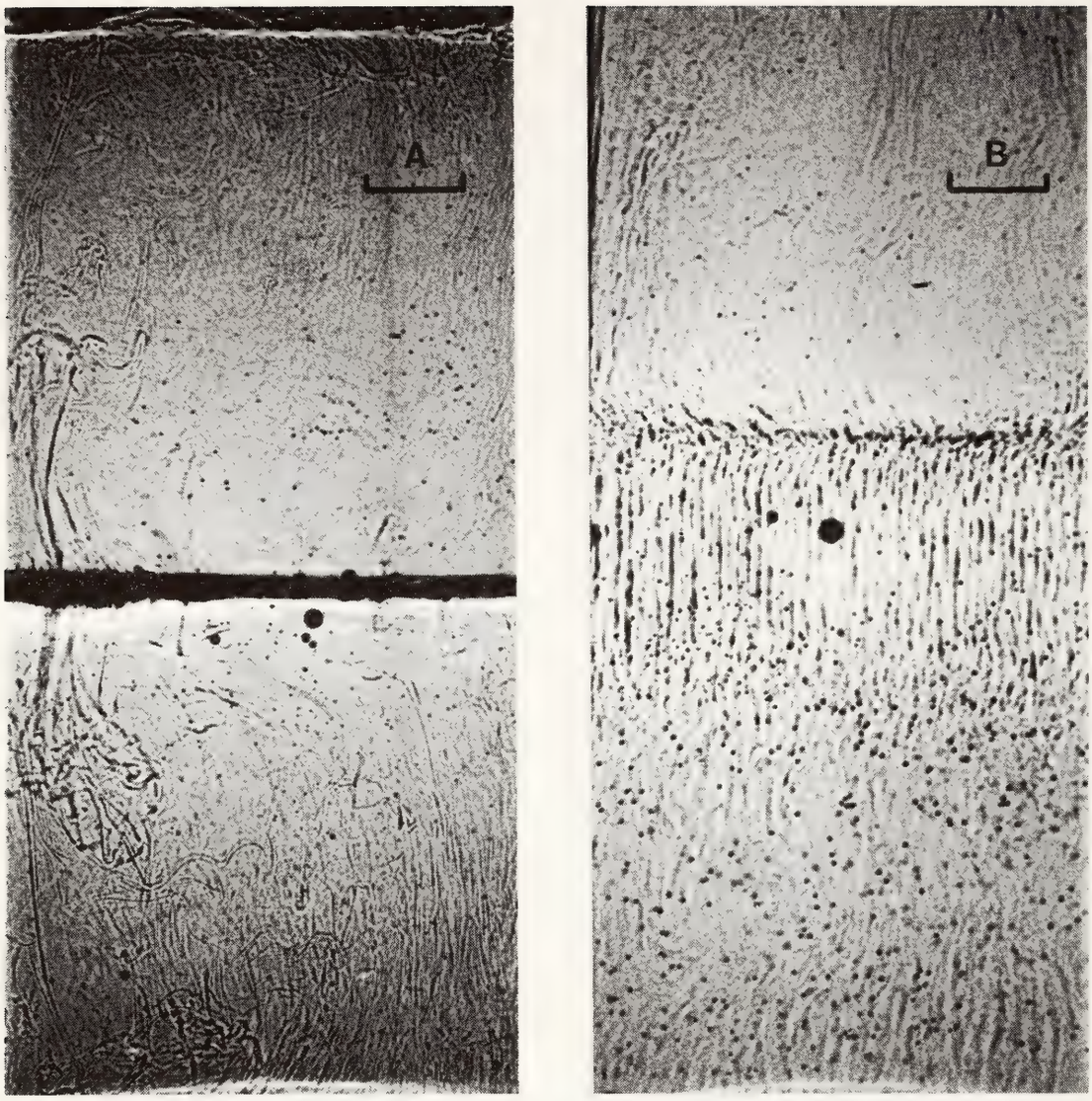


Fig. 1. Double-diffusive convection in stratified systems of aqueous salt and sugar solutions, viewed by the shadowgraph method. (A) The "diffusive case," at an interface between salt solution above and sugar solution below (see also Turner, 1973). Salt diffuses downward through the interface more rapidly than the sugar diffuses upward; consequently, gravitationally unstable fringes of salt-enriched and salt-depleted liquids respectively develop along the bottom and top surfaces of the interface. Thin plumes of these liquids then break out of the fringes and stream vertically into the layers below and above, mixing into them and causing turbulent convection. These streamers migrate irregularly back and forth, sweeping the interface. If food dye is added to one of the layers, it mixes through the layer in minutes, but it appears only slowly in the other layer (over several hours), presumably because the dye molecule is large and diffuses slowly. It is evident, therefore, that the interface is essentially stagnant and that the transfer of salt and sugar through it is almost entirely by vertical diffusion. (B) The "finger case," between sugar-rich solution above and salt-rich solution below (see also Shirtcliffe and Turner, 1970; Linden, 1973). The convecting layers above and below the zone of tubular fingers are characterized by streamers, as in (A), but the motion is initially much more violent and it dies out sooner. The fingers are visible because they are alternately different in composition and refractive index. If food dye is added to either of the convecting layers, it mixes through the layer and is soon seen migrating through the finger zone. In less than an hour, the other layer is equally colored. Thus, there is mass transfer through the fingers, upward in some, downward in others. This transfer is driven by differential *horizontal* diffusion of salt and sugar between the fingers. The bottom and top ends of the fingers are where the densities of the descending and ascending solutions finally are sufficiently raised or lowered that they can break out into the convecting layers.

The above types of convection occur because the differential transfer of salt and sugar by diffusion tends to *increase* the density contrast between the liquid layers. Eventually, however, the salt concentration gradient becomes relatively so reduced that the density effect of the transfer is no longer appreciable. The convection then ceases, the interfaces disappear, and the diffusion continues only at a much reduced rate.

magnitude as Prandtl numbers for ultrabasic-basic magmas (Pr = kinematic viscosity/thermal diffusivity = ν/κ = 500–5000). Thus, the plumes, or "streamers," of salt-enriched and depleted solutions released from the experimental diffusive interface (Fig. 1A) should separate and disperse in much the same way as thermal streamers from a magmatic interface, even though (on the basis of size scaling according to viscosity differences; see foregoing report) the latter might be 2–3 orders of magnitude larger.

It is also possible with the chemical system to model differences in temperature between the magmatic liquid layers by considering the chemical equivalents of the coefficient of thermal expansion (α) and the Rayleigh number. In terms of density (ρ), α equals $-\rho^{-1}(d\rho/dT)$, and the chemical equivalent is $\beta = \rho^{-1}(d\rho/dS)$, where S is concentration. Rayleigh numbers, Ra and Rs, are separately defined for the fast- and slow-diffusing components in each system (see Turner, 1973, p. 254). For the magma, $Ra_o = g\alpha_o\Delta T_o l_o^3/(\nu_o\kappa_o)$, and $Rs_o = g\beta_o\Delta S_o l_o^3/(\nu_o\kappa_o)$, where g is gravitational acceleration, l is length, and the o subscript identifies the igneous system. For the model system, if salt is 1 and sugar is 2, $Ra_m = g\beta_1\Delta S_1 l_m^3/(\nu_m D_1)$, and $Rs_m = g\beta_2\Delta S_2 l_m^3/(\nu_m D_1)$, where the m subscript distinguishes physical properties.

The model scaling is based on unit ratios for the Rayleigh numbers, but because salt is "negative heat," $Ra_r = Ra_m/Ra_o = -1$. Given that $l_r = l_m/l_o = (\nu_m/\nu_o)^{2/3} = \nu_r^{2/3}$ (see foregoing report), substitution and rearrangement leads to

$$\Delta T_o = -\beta_1\Delta S_1\kappa_o\nu_r/(\alpha_o D_1).$$

If the slow components both diffuse upward, $Rs_r = Rs_m/Rs_o = 1$, and hence,

$$\Delta S_o = \beta_2\Delta S_2\kappa_o\nu_r/(\beta_o D_1).$$

These equations should be most reliable when the Prandtl and Schmidt numbers are the same and when the two systems have the same diffusivity ratios for the fast and slow components (see Turner, 1973, pp. 254–257). The second condition cannot be met because the sugar diffusion is proportionately much faster than chemical diffusion in silicate melts. The calculated ΔT_o and ΔS_o will not be reliable, therefore, but it may eventually be possible to correct at least ΔT_o empirically by adjusting concentrations. For the moment, however, some typical numerical values for the diffusive case are $\alpha_o = 5 \times 10^{-5}(°C)^{-1}$; $\beta_1 = 0.007(\text{wt }\%)^{-1}$; $\beta_2 = 0.004$ (wt %)$^{-1}$; $\kappa_o = 0.0071$ cm^2 s^{-1}; $D_1 = 1.5 \times 10^{-5}$ cm^2 s^{-1}; $D_2 = 0.5 \times 10^{-5}$ cm^2 s^{-1}; $l_r = 0.0009$; $\Delta S_1 = -2$ wt %; and $\Delta S_2 = 7$ wt % (Δ = lower layer–upper layer). Accordingly, $\Delta T = 119°C$ and $\Delta S_o = 6.7$ wt %, results that compare with the contrasts of temperature and MgO concentration between basaltic and picritic liquids. The potential value of this approach is that it can be used to model large-scale thermal exchange between magma layers, something that cannot be done with a heat system (see foregoing report). Such modeling is important because it may reveal effects that would not be anticipated in a purely theoretical analysis of the problem.

Whether the finger case of double-diffusive convection (Fig. 1B) occurs in magmas is less certain, but in principle it could develop when relatively hot magma floats on a compositionally different, cooler liquid that is denser only because it is cooler. (An appropriate combination of liquids might be olivine tholeiite over iron-enriched basalt.) Then as the lower layer is warmed from above, a zone of fingers could develop along the interface and drive convective mixing both above and below. This possibility might develop during emplacement of new magma into an intrusion, and it could also obtain in any

cooling convection cell with regular or intermittent circulation. On the basis of scaling from the salt-sugar system in accordance with viscosity differences, thermal fingers for ultrabasic-basic magmas might be expected to be 10–20 cm in diameter and perhaps as much as a meter long.

Effects of External Cooling

If a series of salt-sugar layers in the diffusive arrangement is cooled from the top, the stagnant interfaces between them begin to thicken in succession from the top down and may reach 2–3 times their room-temperature thicknesses. This effect presumably results because diffusivities decrease, and viscosity increases, with decreasing temperature. Cooling from the top also affects the layers between the diffusive and finger interfaces by organizing the convecting streamers into Bénard cells (see Fig. 2A). The height of these cells is the thickness of the layer in which they occur, and their widths are of comparable size. When well developed, the Bénard cells tend to occur one above the other in successive layers.

If, however, the liquid layer has a stable density gradient (owing to a composition gradient), it tends to remain stagnant when cooled from the top. Zones of fingers are particularly notable in this respect. They have strong density gradients and so, despite their fragile appearance, withstand intense shearing by convection above and below. Streaks of dye injected through these zones can be seen almost motionless in the fingers long after the dye in the convecting layers has been dispersed.

The most striking effect of cooling

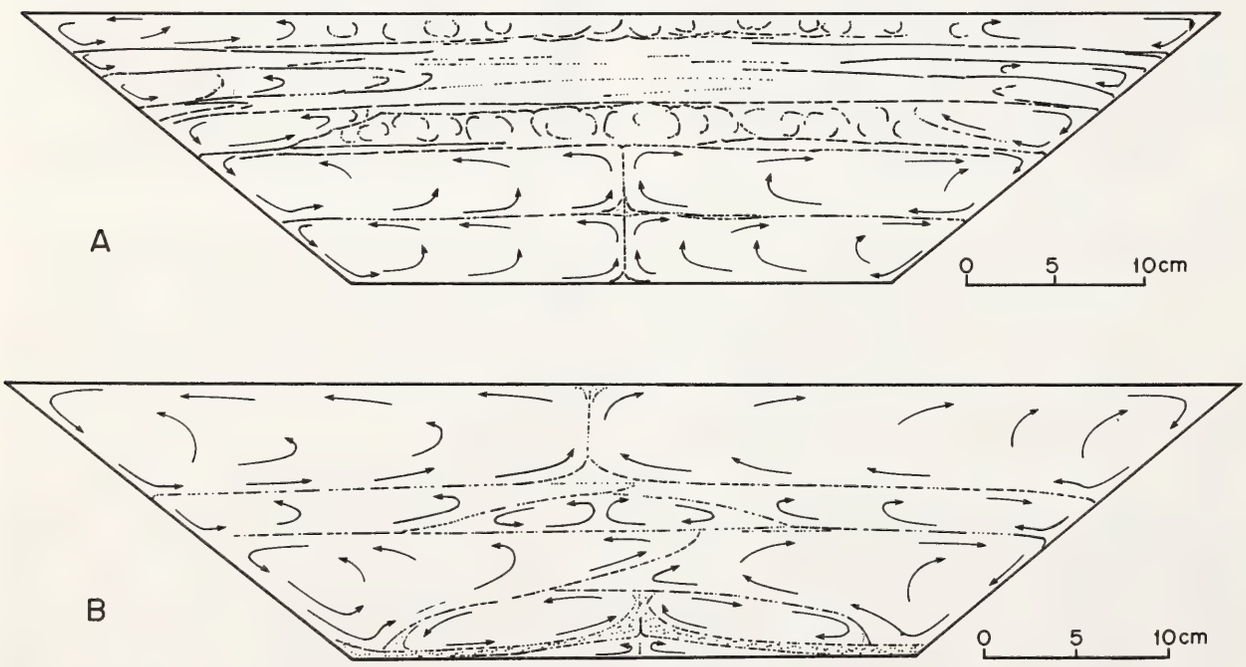


Fig. 2. Convection patterns in stratified salt-sugar solutions cooled gently along the top and sides while the bottom of the tank was left at room temperature. In (A), the initial liquid column graded from sugar-rich at the bottom to salt-rich at the top, but it spontaneously separated into a series of layers separated by diffusive interfaces. When these layers were cooled from the top, the convection of the type illustrated in Fig. 1A became organized into more regular Bénard cells. With cooling at the sides, wall convection cells developed and grew inward, including the streamers and gradually replacing the Bénard cells. In (B), the liquid column initially graded from salt-rich at the bottom to sugar-rich at the top, and it developed fingers throughout with no visible layering. The differential cooling overturned the composition gradient in thin wall cells that gradually grew and merged to the stage illustrated here.

the side of a density-stratified liquid column is the formation of thin, laterally extensive convection cells in which the circulation is down at the wall and into the tank, returning at the top of the cell (Figs. 2 and 3). These cells are here termed "wall cells." If the liquid has a smooth density gradient initially, with no visible layers, the wall cells appear at regular vertical intervals and grow slowly into the tank, occasionally merging, until they become layering. If the liquid column is layered from the start, then the wall cells develop within the layers; they grow most rapidly where there are streamers, but they will also replace Bénard cells. To the limited extent that the author has studied the wall cells, they appear to develop until their aspect ratios of width to height are about 15:1. When they grow together from opposite sides

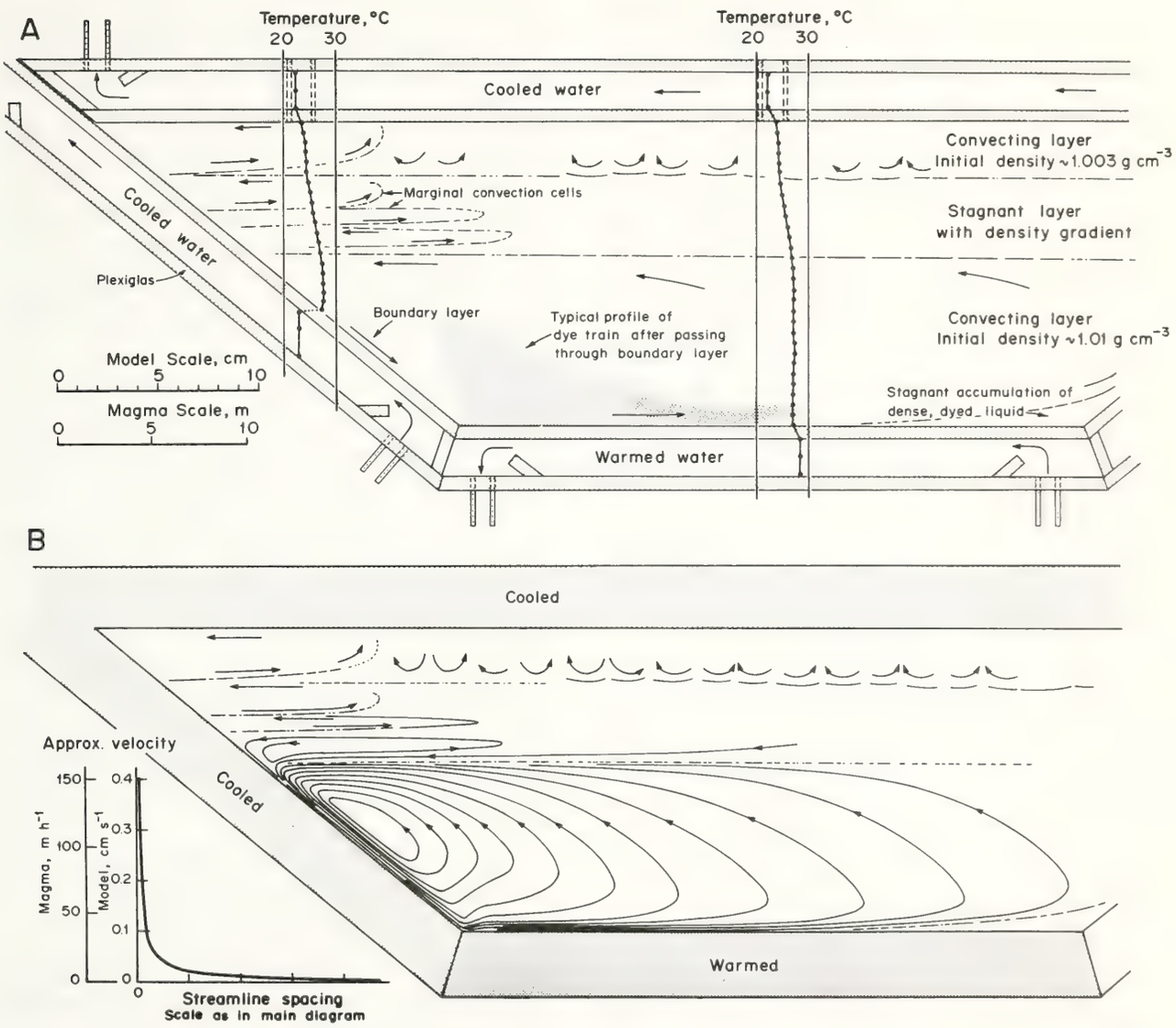


Fig. 3. Experiment in which the liquid column initially comprised three layers of salt water with densities as indicated in (A). The top of the tank and the left side were cooled by the same circulating water; the bottom was slightly heated, and the right side was at room temperature. The scaling is for magma with a temperature of 1325°C and a viscosity of 30 poises. The heat flux through the left footwall is scaled for a few days after emplacement. The top liquid layer is undergoing Bénard convection. The intermediate layer is mostly stagnant because of its density gradient, but it has three small wall cells. The bottom layer is essentially one large wall cell. (A) shows the configuration of a train of dye after it has passed through the thermal boundary layer. (B) shows a generalized flow pattern for the large cell.

of a tank, they join compatibly along a zone of ascending flow. From layer to layer, however, the flow is in opposite directions, and so the interface is constantly under shear.

A particularly important feature of wall cells, illustrated in Fig. 3B, is that they are driven by the downward flow of liquid through only a very thin thermal boundary layer along the cooled wall. In terms of the magma scale in the diagram, the large cell is about 10 m high and 60 m wide, but the boundary layer is only about a meter thick (cf. Shaw, 1974). The indicated flow pattern is sufficiently close to steady state that the streamlines are also pathlines; hence, it is additionally evident that (1) all the liquid in the cell must eventually funnel through the boundary layer, (2) the liquid entering the boundary layer at any instant has origins in all parts of the cell, and (3) some liquid is also entrained from the overlying liquid layer. The average scaled magma velocity for the thermal boundary layer is about 60–70 m hr^{-1}, and as judged by the behavior of dye trains, the flow is marginally turbulent, an observation that accords with the Grashof number.* The model is for a time only a few days after the magma was emplaced, but because Gr increases as l^3, turbulence may be expected in larger wall cells at much later times. It would appear, therefore, that igneous thermal boundary layers should be important sites of magma mixing, both within liquid layers and between them.

A last feature of note in Fig. 3B is that, after the cooled liquid leaves the thermal boundary layer, it tends to flow directly out along the bottom of the cell so that a fraction of it can reach the far end. On this basis, magmatic wall cells with aspect ratios of 10:1 or 15:1 would need be only a few hundred meters thick to transport cooled liquid far into the interior of an intrusion.

*For an inclined wall, $Gr = g\ \alpha\Delta T l^3 \sin\theta/\nu^2$, where l is the boundary layer length, and θ is the dip angle. Substitution of the experimental values for Fig. 3 gives, $Gr = 980 \times 0.000207 \times 1 \times (13)^3 \times \sin[40°/(0.01)^2] = 2.86 \times 10^6$. Turbulence is expected at $Gr > 10^6$ (Tritton, 1977).

References

Chen, C. F., and J. S. Turner, Crystallization in a double-diffusive system, *J. Geophys. Res.*, *85*, 2573–2593, 1980.

Huppert, H. E., and R. S. J. Sparks, Restrictions on the compositions of mid-ocean ridge basalts: a fluid dynamical investigation, *Nature*, in press, 1980.

Irvine, T. N., Magmatic density currents and cumulus processes, *Amer. J. Sci.*, *280A*, 1–58, 1980a.

Irvine, T. N., Infiltration metasomatism, adcumulus growth, and double-diffusive fractional crystallization in the Muskox intrusion and other layered intrusions, in *Physics of Magmatic Processes*, R. B. Hargraves, ed., Princeton University Press, in press, 1980b.

Linden, P. F., On the structure of salt fingers, *Deep-Sea Res.*, *20*, 325–340, 1973.

McBirney, A. R., and R. M. Noyes, Crystallization and layering of the Skaergaard intrusion, *J. Petrology*, *20*, 487–554, 1979.

Shaw, H. R., Diffusion of H_2O in granitic liquids: I. Experimental data; II. Mass transfer in magma chambers, *Carnegie Inst. Wash. Publ. 634*, 139–170, 1974.

Shirtcliffe, T. G. L., and J. S. Turner, Observation of the cell structure of salt fingers, *J. Fluid Mech.*, *41*, 707–719, 1970.

Sparks, R. S. J., P. C. Meyer, and H. Sigurdsson, Density variations amongst mid-ocean ridge basalts: implications for magma mixing and the scarcity of primitive lavas, *Earth Planet. Sci. Lett.*, *46*, 419–430, 1980.

Tritton, D. J., *Physical Fluid Dynamics*, Van Nostrand Reinhold, New York, 1977.

Turner, J. S., *Buoyancy Effects in Fluids*, Cambridge University Press, England, 1973.

Turner, J. S., Differentiation and layering in magma chambers—a fluid dynamical model, *Nature*, in press, 1980.

Turner, J. S., and L. B. Gustafsson, The flow of hot saline solutions from vents in the sea floor—some implications for exhalative massive sulfide and other ore deposits, *Econ. Geol.*, *73*, 1082–1100, 1978.

Observations on Layering in the Skaergaard Intrusion*

T. N. Irvine

Field studies of the Skaergaard intrusion were continued on a six-week expedition from July to September, 1979. The author's efforts were mainly concentrated on extending the mapping of the trough banding reported in *Year Book 77* (pp. 725–732), but some time was devoted to documenting other kinds of layering structures. In a paper based on previous observations (and in galley proof by the time the expedition began; Irvine, 1980), the author had proposed a current-deposition origin for the rhythmically repeated, modally graded layers that are a familiar feature of Skaergaard geology (see Wager and Brown, 1967). The additional field time provided further opportunity to evaluate this mechanism and to examine other possibilities and problems raised in the paper. The fundamental question, which stems from the observation that the cumulus plagioclase in the layered rocks should have floated in the Skaergaard magma (Bottinga and Weill, 1970; Campbell *et al.*, 1977; McBirney and Noyes, 1979), is whether the layers could have formed by current deposition or had to develop by *in situ* crystallization. Some of the documented structures are described below with comments on their significance.

Fragmental Layers

Many of the Skaergaard layering structures are associated with angular-to-subangular cognate xenoliths of leucocratic (anorthositic) gabbro, apparently derived from the upper border group of the intrusion (cf. Wager and Brown, 1967). These bodies range from fragments a few centimeters in length to blocks more than 100 m on a side. They are most abundant in the middle zone (MZ) of the layered series but can be found at all levels from the bottom part of lower zone (LZa) to the lower part of upper zone (UZa). In most places, they either occur individually or are jumbled together, but locally, fragments and slabs from a few centimeters to 6 m in length are distributed in well-defined layers. Mapped sections of two such layers are shown in Fig. 4; in each case, the total exposed length of the layer is about twice that illustrated.

The two illustrated layers occur in the lower part of MZ near the east side of Kramers Island, where they are interstratified with numerous, non-fragmental, modally graded layers, 10–30 cm thick. The fragmental layers have slight concentrations of mafic minerals along their bottom contacts, but, as seen in Fig. 4, the slabs and fragments within them are poorly sorted, both vertically and horizontally. The one known exception to this generalization is that the fragments in layer B decrease rapidly in size where the layer tapers out to the northwest. Followed further in this direction, the layer eventually becomes a normal graded layer. In both layers A and B, the matrix between the fragments is indistinguishable from the gabbroic cumulates that form the other layers in the same vicinity.

Layer A attracted attention initially because the slabs within it show a distinct imbrication, such as might indicate current transport and deposition (by a current moving to the southeast, or to the left in Fig. 4). The mapping shows, however, that the layer underlies a large anorthositic block, and on this basis the imbrication now appears more probably to be an effect of differential compaction beneath the block. There seems no question, however, but that the fragments in both layers A and B were spread by a process of current flow, because the

*Research supported by National Science Foundation grant EAR7911188.

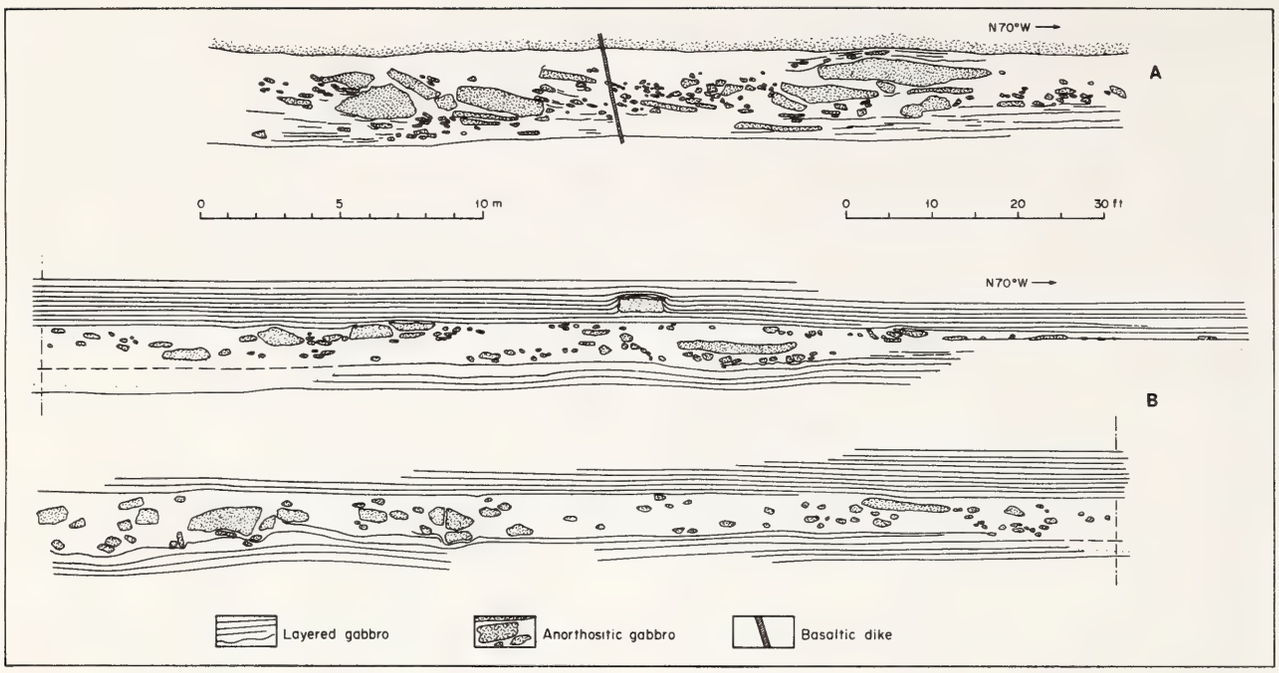


Fig. 4. Two fragmental layers in the middle zone of the Skaergaard layered series. Layer B is shown in two parts divided at the vertical dash-dot line. Note the contrast between the relations of the fragments in layer B and those of the individual block that dropped onto the layers above it. The tendency of the layering to be smoothed over the fragments is common to both cases, however.

layers are well-defined and regular in thickness and clearly are not just local piles of debris. It also seems clear that the plagioclase-bearing matrix around the fragments was carried along with them and, therefore, was probably derived from some relatively distant part of the intrusion. The implication is that plagioclase was indeed transported down to and spread across the cumulate floor by magmatic currents—and remained there, even though it should have floated.

Redeposited Layers

Some of the more convincing evidence of current deposition of layers in the Duke Island ultramafic complex is represented in structures involving local erosion and redeposition of layered cumulates in response to impact of blocks at low angles of incidence (see Irvine, 1974, Plate 27). Until the 1979 expedition, such structures had not been found in the Skaergaard intrusion. A more concerted search, however, revealed several excellent examples, one of which is illustrated in Fig. 5. From the mapped relations it is apparent that part of the feldspathic layer denoted *a* was scraped up by the main block as the latter was introduced from the right (i.e., from the west).* The disturbed material was then swept to the left and redeposited as layer *a'* above another part of *a*. Asymmetric, flamelike convolutions in the deformed and redeposited layers indicate transport to the left, as do similar convolutions in layers above the block.

Note also that, in the process of redeposition, the materials in layers *a'* were probably inverted horizontally (and vertically) by virtue of momentum transfer. Thus, the part of layer *a* that was first impacted by the block on the right (when the block had maximum

*Figures 5 and 6 are maps, but by virtue of the inclinations of the layering and the outcrop surface, they can both effectively be read as sections. In each case, the layering has been tilted about 15° since it was formed (see Wager and Brown, 1967, pp. 18–19).

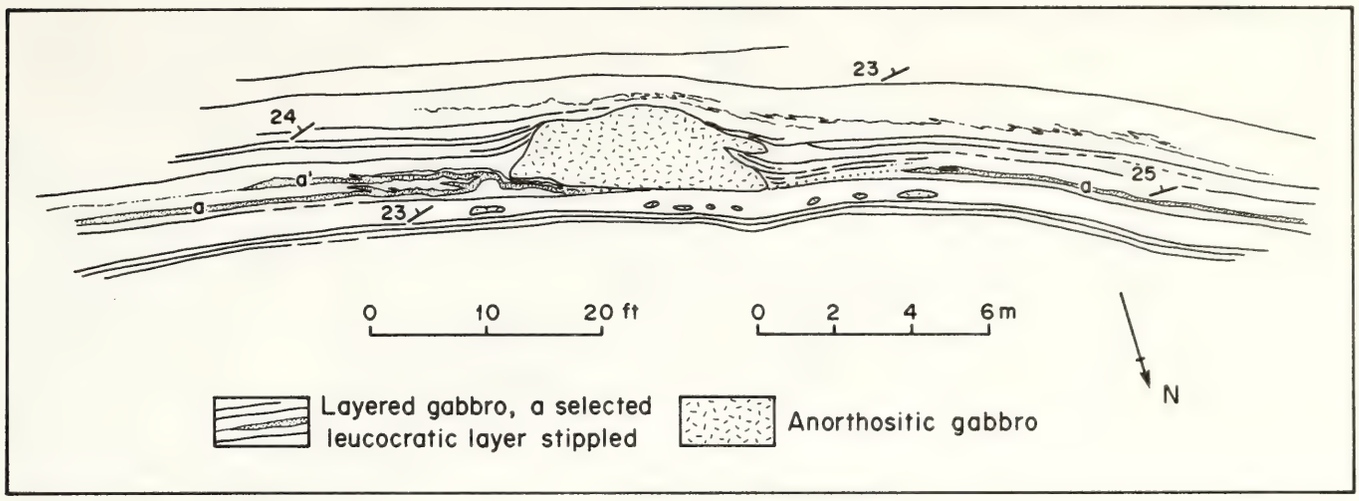


Fig. 5. Redeposited layer in middle zone, east side of Kramers Island.

velocity) presumably now forms the distal part of *a'* on the left; from there, *a'* can be traced back into the original layer where the block finally stopped.

Unconformities

A possibility that was suggested (Irvine, 1980) for the origin of density currents in the Skaergaard magma is that they formed through slumping of loosely consolidated cumulates, especially from aprons deposited around the edges of the layered series at the base of the inward-dipping walls formed by the marginal border group. The "cross-bedded belt" defined by Wager and Brown (1967) appears to represent such a source region. It features countless unconformities, and it fringes the layered series as marginal facies through a stratigraphic interval of about 1500 m. There is some question, however, as to whether enough material was eroded from any of the unconformities to yield density currents large enough to form the graded layers observed in the interior of the intrusion. Time was not available for extensive mapping of the cross-bedded belt, but a small area at its inner edge in which there appeared to be an appreciable unconformity was selected for documentation. Part of the unconformity is shown in Fig. 6; brief additional observations indicated that it extends for roughly an equivalent distance to the south (i.e., to the upper right in the diagram) and probably has the form of a broad eroded channel. On the basis of the attitudes of the layers and differences in elevation, it is estimated that *at least* a 25-m thickness of the layering beneath the unconformity has been truncated between points *a* and *b* along its surface. Moreover, the uncertainty in this estimate is such that the truncation could be as much as 35 m.

One example does not prove that such deep erosion is common, but it should be noted that the map area was chosen after only a brief search, and that the extent of the truncation is much larger than was initially anticipated and did not become apparent until the mapping was well along.

Another feature of note is the melanocratic layers immediately above the unconformity. Similar layers have been found along two unconformities in the mapped areas of trough bands, and the association suggests preferential deposition of the dense mafic minerals by strong currents funneled into the erosion channels. The presence of several small unconformities in the axis of the structure in Fig. 6 (above the melanocratic layers) also suggests funneling of currents.

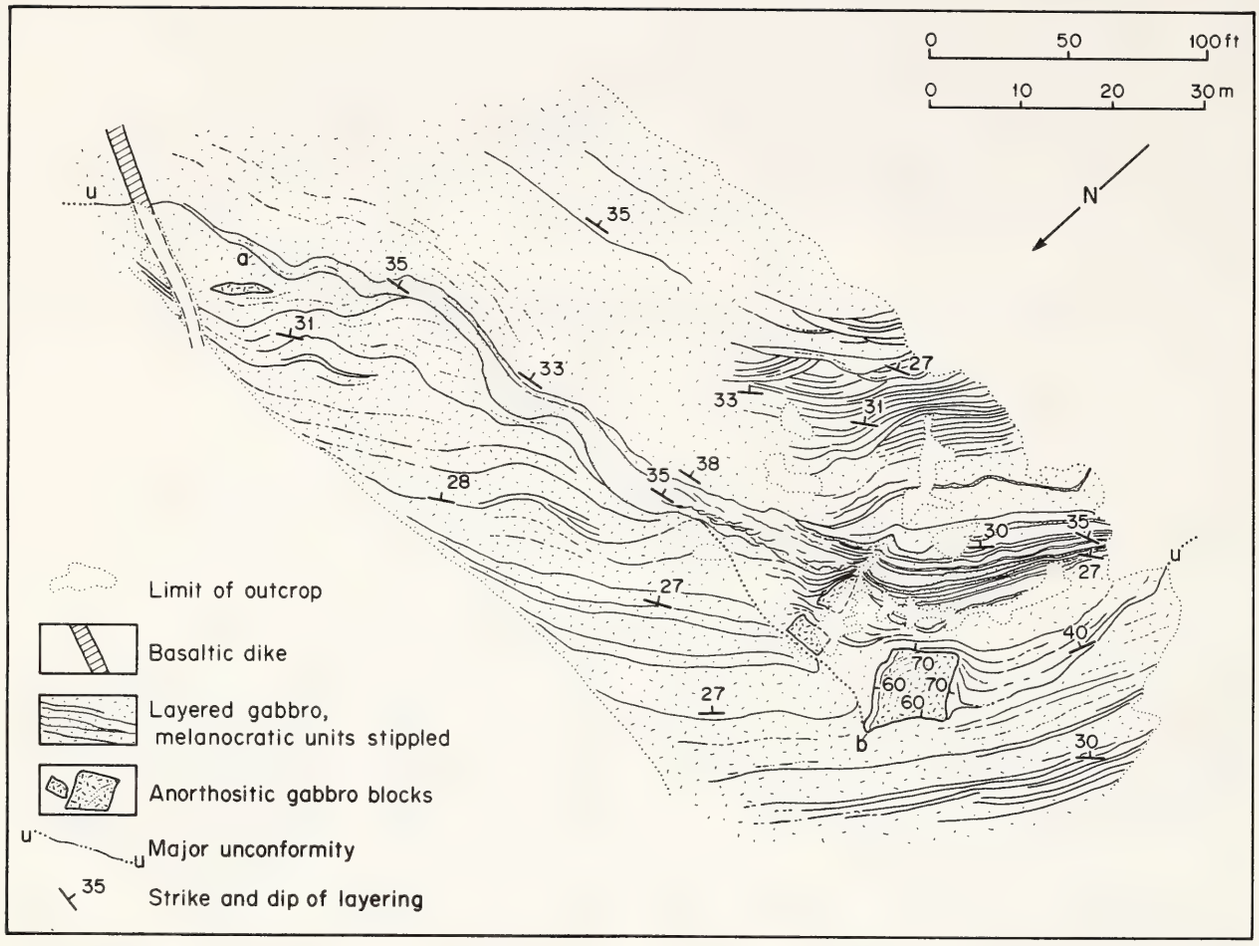


Fig. 6. Unconformity in lower zone (LZa) near Uttentals Sund below Uttentals Plateau.

Macrorhythmic Layering

A problem that was of particular concern in the paper on density currents (Irvine, 1980) pertained to some exceptionally extensive, thick layers that were known to be well developed in the high mountains (Gabbro Peak and Wager Peak) in the center of the intrusion. From the information available prior to the 1979 field work, these layers were thought to be essentially similar to the thin graded layers; thus, given that they were much larger, very large density currents had to be invoked to explain their origin. This information, however, proved misleading.* During the recent expedition, the thick layering was studied closely on Pukugaqryggen Peak, and it was found to be very different from the common rhythmic layering.

A stratigraphic section of some of the thick layering is shown in Fig. 7. Typically, it is defined by an alternation of light and dark, uniform strata, 4–7 m thick. The cumulus mineralogy of the contrasting layers appears to be the same, and their contacts are commonly gradational; the only obvious difference between them is in their content of plagioclase. Thin, modally graded layers are commonly developed

*Although the thick layering had been illustrated in photographs by Wager and Deer (1939, Plate 6), Wager and Brown (1967, Plate IV) and McBirney and Noyes (1979, Plate 8), it had never been described in detail. In fact, only recently was it realized that the thick layering is the same as the "zebra banding" of Wager and Brown (1967, p. 74), which they described in only two sentences and illustrated in a photograph without a scale.

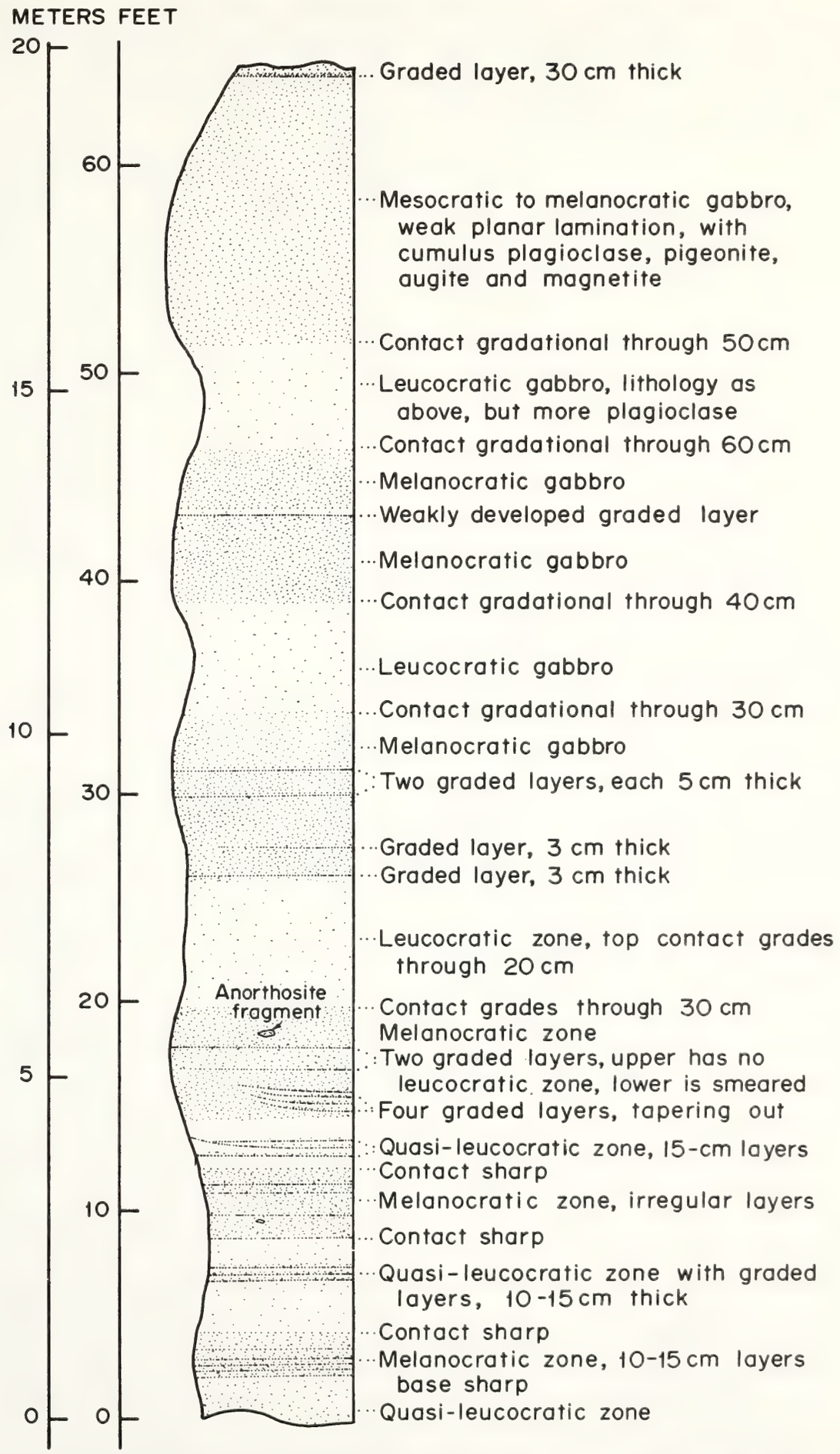


Fig. 7. Macrorhythmic layering in middle zone on the lower west side of Pukugaqryggen.

within the thick layers, but their distribution is erratic, and they are much less extensive. Although they apparently formed concurrently with the thick layering, they are almost certainly of fundamentally different origin.

It would seem that the thick, light-and-dark layers should be paired into units, but in most cases it is not obvious which is the lower member. The layering, however, is especially well developed just below the three prominent stratification units that comprise the Triple Group, and it appears to have similar extent (about 4 km^2; see Wager and Brown, 1967, Plate IV and p. 74). The impression, therefore, is that the postulated units are essentially miniature versions of the same phenomenon. The Triple Group units are about 20 m thick, and each consists of a plagioclase-rich zone beneath a more melanocratic zone (see Maaloe, 1978). It is probable, therefore, that the layer units considered here also are plagioclase-rich at the bottom and darker at the top.

Given that the thin, modally graded layers of the Skaergaard intrusion are the essential component of "rhythmic layering" in its type locality (Wager and Deer, 1939), the thicker layering (including the Triple Group) would seem appropriately called "macrorhythmic layering."† With regard to the question of current deposition vs. *in situ* crystallization, it is noted that although the Skaergaard macrorhythmic layering is best developed in MZ, it is also extensively developed (although much less prominent) in LZ, especially in LZb. Volumetrically, it makes up much more of the layered series than the modally graded layers, even though the latter have received much more attention. The relations described above strongly support the case that modally graded layers are density current deposits, but, as emphasized elsewhere (Irvine, 1980), this does not mean the entire layered series was formed in the same way. The present observations suggest that if *in situ* crystallization was important in the Skaergaard layered series, the evidence is more likely to be found in the macrorhythmic layering than in the thin graded layers.

†The author shares the view expressed by Wager and Brown (1967, p. 74) that this layering is probably different in origin from the layered units of the Rhum intrusion, to which they gave the name "macrorhythmic units," but he considers their use of this latter term unfortunate. The Rhum units more closely resemble the "cyclic units" of the Stillwater and Muskox intrusions and are better referred to by that name, following the recent practice of Dunham and Wadsworth (1978). The Triple Group units could then be type "macrorhythmic units."

References

Bottinga, Y., and D. F. Weill, Densities of liquid silicate systems calculated from partial molar volumes of oxide components, *Amer. J. Sci.*, *269*, 169–182, 1970.

Campbell, I. H., J. H. Dixon, and P. L. Roeder, Crystal buoyancy in basaltic liquids and other experiments with a centrifuge furnace, (abstract), *Eos*, *58*, 527, 1977.

Dunham, A. C., and W. J. Wadsworth, Cryptic variation in the Rhum layered intrusion, *Mineral. Mag.*, *42*, 347–356, 1978.

Irvine, T. N., Petrology of the Duke Island ultramafic complex, southeastern Alaska, *Geol. Soc. Amer. Mem.*, *138*, 1974.

Irvine, T. N., Magmatic density currents and cumulus processes, *Amer. J. Sci.*, *280A*, 1–58, 1980.

Maaloe, S., The origin of rhythmic layering, *Mineral. Mag.*, *42*, 337–346, 1978.

McBirney, A. R., and R. H. Noyes, Crystallization and layering of the Skaergaard intrusion, *J. Petrology*, *20*, 487–554, 1979.

Wager, L. R., and G. M. Brown, *Layered Igneous Rocks*, Oliver and Boyd, Ltd., Edinburgh, 1967.

Wager, L. R., and W. A. Deer, Geological investigations in East Greenland. III, The petrology of the Skaergaard intrusion, Kangerdluqssuaq, East Greenland, *Medd. Groenl.*, *105*, No. 4, 1939 (reissued 1962).

Heat and Mass Transfer in Magma Generation: A Progress Report of an Experimental Study

H. S. Yoder, Jr.

One of the major problems in igneous petrology is defining the thermal processes by which large volumes of relatively homogeneous magma are generated from crystalline crust or mantle. Two extremes of the many possible models for the formation of liquid (Yoder, 1978) involve an *internal* heat source arising from adiabatic decompression (e.g., diapiric rise) and heat transfer from an *external* hot source (hot-plate conduction). Although relatively invariant physicochemical conditions of formation may account for homogeneity of magma in general, the separation of liquids over a range of conditions during diapiric rise or hot-plate type melting probably yields liquids of continuously varying composition. Because magma is generated in gradients of pressure, temperature, and composition, some internal mechanism (e.g., convection) would seem to be required to homogenize large volumes of magma, such as the Columbia River basalts (200,000 km^3). The eruption of these large volumes took place within the short period of 1–3 m. y. for the Columbia River basalts, so that the rate of production, or aggregation, or both, become significant factors. The purpose of the present study is to obtain quantitative information on (1) rates of magma production, (2) thermal properties of magma in the crystal + liquid region, and (3) internal mechanisms for liquid homogenization.

The partial melting of a rock is a complex thermal process, and has not been successfully modeled mathematically where convective mixing is involved. Consider the events in an undepleted (undepleted in basaltic constituents, for example) planar slab of finite thickness, at the appropriate temperature of the geotherm, suddenly heated from below by a hotter refractory body emplaced by a tectonic event. The refractory body may be sufficiently large and sustain processes that maintain a high temperature at the contact, or its temperature may gradually decrease from heat losses. In either case the temperature in the undepleted body is presumed to reach eventually the beginning of melting by thermal conduction. The sequence of events that follows, especially the advancement of the melting front, depends considerably on the physicochemical relations of the melting body. If the assemblage of minerals, *all* of which take part in the melting, melts in a eutectic-like fashion, the rate of melting will be different than if the melting is over a range of temperatures. For examples, a rhyolite of minimum melting compositions will transform from an all-crystalline condition to an all-liquid condition at an almost constant temperature, whereas a basalt will melt over a range of temperatures of about 250 °C at 1 atm. The enthalpy of melting for rhyolite, therefore, will be required at a fixed temperature, whereas that for the melting of basalt will be absorbed over a range of temperatures and will depend on the change with temperature of the degree of melting and proportion of phases involved. This principle may be appreciated by examining a plot of enthalpy (H) vs. composition (Fig. 8B) deduced for the simple binary system sodium disilicate (SD)—nepheline (Ne) (Fig. 8A). At the eutectic composition R the ratio of the sensible heat to the latent heat (the Stefan number, St) is essentially zero:

$$St = C_p \Delta T / \Delta H,$$

where C_p is the specific heat; ΔT, the change in temperature; and ΔH, the change in enthalpy. On the other hand, for composition B, the Stefan number is about 5.6. The heat transfer process

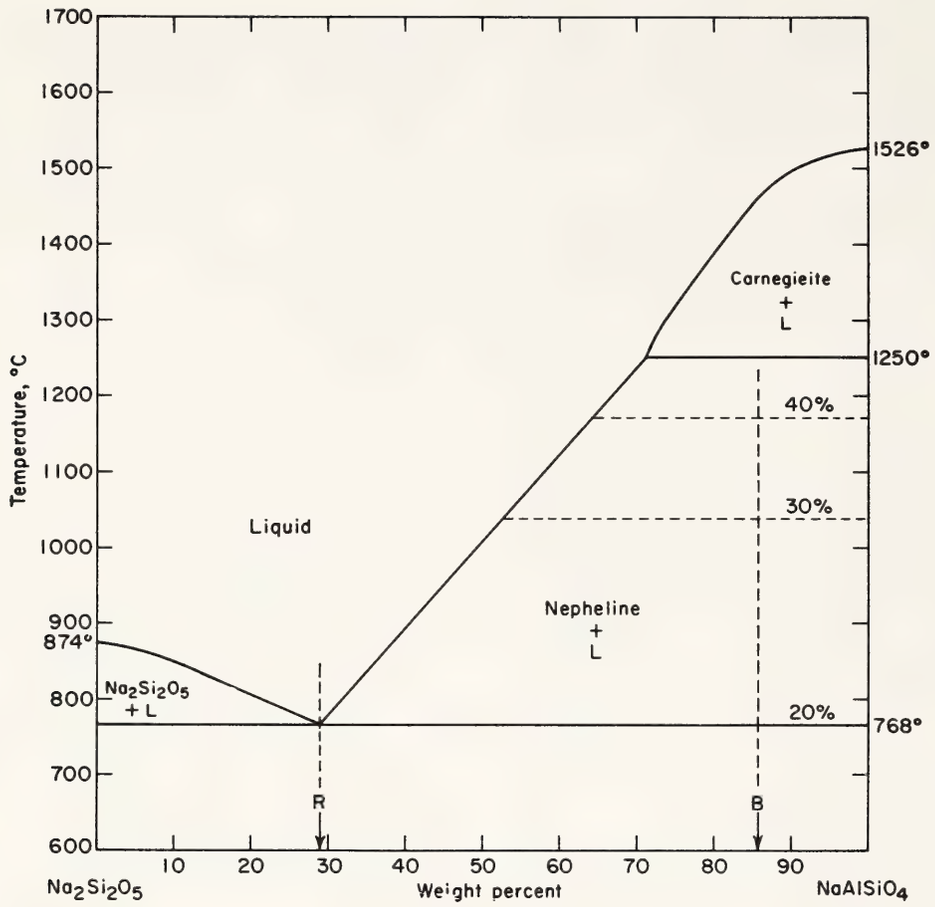


Fig. 8A. Phase diagram for $Na_2Si_2O_5$-$NaAlSiO_4$ (Tilley, 1933). The melting behavior of composition *R* is believed to be analogous to that of rhyolite, and the melting behavior of composition *B* is believed to be analogous to that of basalt. The temperatures for degrees of melting of 20%, 30%, and 40% (by wt) of composition *B* are indicated by horizontal dashed lines.

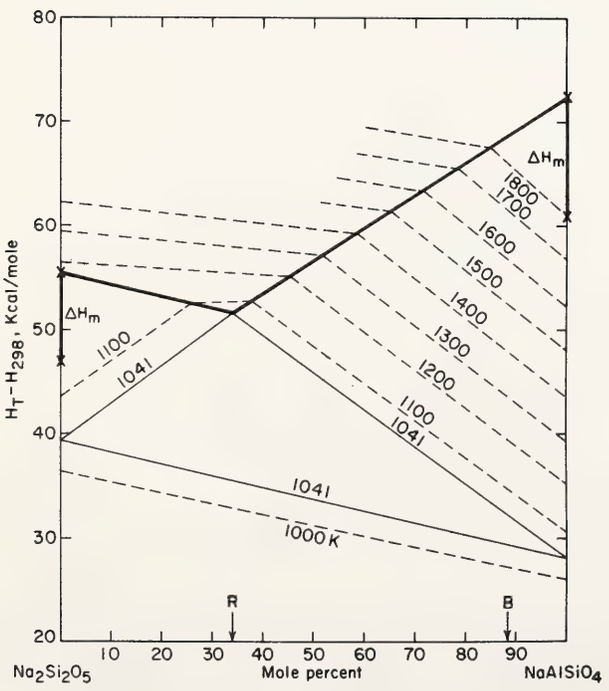


Fig. 8B. Estimate of change of enthalpy of melting with composition in the system $Na_2Si_2O_5$-$NaAlSiO_4$.

in rhyolite appears to be controlled mainly by the latent heat consumption, and that in basalt, mainly by the sensible heat consumption. That is to say, advancement of the melting front will be much slower in compositions with eutectic-like (or minimum-like) melting compared with that in compositions with a large melting interval.

As liquid is generated, the increase in volume imposes a stress on the crystalline material. The initial volume changes for the eutectic composition *R* of SD-Ne (Fig. 8A) is about 4.3%, for example, whereas that for the composition *B*, $SD_{14.2}$ $Ne_{86.8}$ (by weight), is about 0.9% for the 20% liquid produced at the eutectic temperature. The thermal stress due to expansion on melting may be relieved in nature by extension of the slab either vertically or horizon-

tally.* Because of the thermomechanical coupling, there may be an effect on the chemical relations if the stress is not relieved. The volume (and density) of each phase is a function of temperature and pressure, and it will be seen below that the temperature dependence induces other processes.

The generation of liquid also affects the thermal conductivity of the partially melted layer. In the simple binary system in Fig. 8A, it may be presumed that the thermal conductivity for composition R may be expected to change to that of the liquid. On the other hand, the thermal conductivity of the crystal + liquid assemblage of composition B will be a combination of the property of each phase. As pointed out by Woodside and Messmer (1961), the conduction of heat in an assemblage of two phases may be in "series," "parallel," or a combination of both, and a geometric mean may best describe the effective thermal conductivity, k_e, of the assemblage. That is, for the simple binary system, the thermal conductivity for composition B in the crystal + liquid region will be

$$k_e = k_{\mathrm{Ne}}{}^{x}\, k_{\mathrm{Liq}}{}^{1-x},$$

where x is the volume concentration of the crystalline phase. The thermal conductivity of each phase is a function of temperature; unfortunately it is uncertain whether k_e in the crystal + liquid region increases or decreases with temperature.

If the temperature contrast or the heat flux at the base of the slab is adequate, the surface marking the upper boundary of the partially molten region between the refractory heat source and the all-crystalline, undepleted slab, called the Stefan boundary,† will advance upward. The advancement of the Stefan boundary induces other processes. Because the hottest, least-dense liquid is adjacent to the heating surface at the base, and the coolest, most-dense liquid is at the Stefan boundary, convection may result. The conditions marking the onset of convection in the liquid + crystal region depend on several factors, especially the temperature contrast and the thickness of the melt layer. For examples, high thermal conductivity enhances stagnation, whereas large expansion coefficients, high permeability, and increasing thickness of the liquid-bearing layer facilitate convection. The critical factors are characterized by the dimensionless Rayleigh number, Ra, which is the ratio of the buoyancy forces to the dissipative forces of viscous drag and heat diffusion:

$$Ra = \frac{\alpha p g d \Delta T}{\kappa_m \nu},$$

where α is the coefficient of volume expansion (deg^{-1}); p, the permeability of the partially melted layer (cm^2)‡; g, the gravitational acceleration ($\mathrm{cm\ sec}^{-2}$); d, the thickness of the partially melted layer (cm); ΔT, the temperature difference across the layer of thickness d

*It is assumed that there is no porosity in the deep crust or mantle. In laboratory experiments the initial porosity of the specimen may accommodate some of the expansion. After melting, the space occupied by the liquid (i.e., the degree of melting) is considered to be the porosity.

†Named after Stefan, who first studied a problem involving the transfer of heat through a material undergoing a phase change (e.g., the melting of a layer of ice; Stefan, 1889).

‡Permeability is defined from the empirical relations of Darcy's law wherein the buoyancy force ($\rho g \alpha \Delta T d$) is substituted for the pressure gradient. The permeability of the crystalline host to the liquid is dependent on the form of the crystal-bridging network. On the basis of electrical conductivity studies (Murase *et al., Year Book 76,* 416–419), rocks undergoing partial melting are permeable at the very onset of melting. Grain-boundary wetting is apparently adequate to establish interconnecting pathways. In nature and in the laboratory, the crystals undergo continuous recrystallization, especially in the presence of a liquid, so that the tortuosity of the pathways will also likely be changing continuously.

(deg); κ_m, the mean thermal diffusivity ($cm^2\ sec^{-1}$); ν, the kinematic viscosity ($cm^2\ sec^{-1}$). The critical value of Ra at which convection may occur is approximately 40 ($= 4\pi^2$)§ for a partially melted (liquid-saturated) layer (Lapwood, 1948) in which the viscosity is constant. Because viscosity decreases with increasing temperature toward the bottom of the layer (Kassoy and Zebib, 1975), the Rayleigh number, and hence the potential for instability, will be greater. It is noted that the proportion of liquid relative to crystals increases toward the bottom.

With convection there is an increase in heat transfer, and the thickness of the layer of partial melting will increase more rapidly. Free, natural convection will initially be laminar. Cells similar to those described by Bénard (1901) may be initiated. The diameter of the Bénard cells is presumed to be about equal to the thickness of the layer. At large temperature contrasts, turbulence may set in and an even greater transfer of heat would be expected. It is likely that the Stefan surface itself will no longer remain planar with the variations of heat transfer imposed by convection.

Because of the temperature gradient there will also be a gradient in composition (see phase diagram, Fig. 8A), and it is possible for double-diffusive convection (Turner and Chen, 1974) to take place. The number of stratifications in which the Bénard cells operate is expected to decrease with time in the liquid-saturated media. Whereas conduction will initially be the principal mode of heat transfer, convection will become the dominant mechanism as the partial melt layer thickens. With the resulting increased heat transfer, the temperature difference between the top and bottom of the layer will be reduced, and convection will eventually diminish. The efficiency of the convective mixing process, a value yet to be determined, may be adequate to account for the relative homogeneity of large volumes of magma.

Because no general analytical method is known that will provide an exact solution for the rate of heat transfer in a convecting system, an experimental approach is being attempted. In brief, measurements will be made of the heat flux into and out of a simple binary composition, and of the temperature at various fixed points throughout the sample as a function of time with different contrasts of temperature between the top and bottom of the sample, with various degrees of partial melting, and with associated changes in liquid composition under both transient and equilibrium conditions. The experiments should yield the following information bearing on the rate of magma production, thermal properties of magma, and one possible homogenization process:

1. Rate of advancement of the Stefan surface with varying temperature contrasts for compositions having a rhyolite-like or a basalt-like melting behavior.

2. An evaluation of the influence of crystal bridging on heat transfer and a measure of the effective thermal conductivity of the liquid + crystal region.

3. The parameters important to the onset of convection in a partially melted (liquid-saturated) medium, including a possible evaluation of the "thickness" parameter d.

4. The character of the Bénard convection cells, thermal stratification, and the evolution of potential double-diffusive convection in a body of circular planform.

The experiment will serve as a primitive model for which there is some prospect for mathematical analysis.

§In contrast, the theoretical value of the critical Rayleigh number for free convection in a viscous fluid between horizontal plates heated from below is 1,709 (Jeffreys, 1928).

References

Bénard, H., Les tourbillons cellulaires dans une nappe liquide propageant de la chaleur par convection, en régime permanent (1st thèse), 88 pp., Gauthier-Villars, Paris, 1901.

Jeffreys, H., Some cases of instability in fluid motion, *Proc. Roy. Soc. London, Ser. A, 118,* 195–208, 1928.

Kassoy, D. R., and A. Zebib, Variable viscosity effects on the onset of convection in porous media, *Phys. Fluids, 18,* 1649–1651, 1975.

Lapwood, E. R., Convection of a fluid in a porous medium, *Cambridge Phil. Soc. Proc., 44,* 508–521, 1948.

Stefan, J., Ueber die theorie der Eisbildung ins besondere ueber die Eisbildung im Polarmeere, *S.-B. Wien. Akad. Mat. Natur., 98,* 965–983, 1889.

Tilley, C. E., The ternary system Na_2SiO_3-$Na_2Si_2O_5$-$NaAlSiO_4$, *Mineral. Petrol. Mitt., 43,* 406–421, 1933.

Turner, J. S., and C. F. Chen, Two-dimensional effects in double-diffusive convection, *J. Fluid Mech., 63,* 577–592, 1974.

Woodside, W., and J. H. Messmer, Thermal conductivity of porous media, *J. Appl. Phys., 32,* 1699–1706, 1961.

Yoder, H. S., Jr., Basic magma generation and aggregation, *Bull. Volcanol., 41,* 301–316, 1978.

Changes with Pressure of Degree of Partial Melting and K_2O Content of Liquids in the System Mg_2SiO_4-$KAlSiO_4$-SiO_2

I. Kushiro

The compositions of magmas change significantly with the degree of partial melting. In the present study on the melting relations in the system Mg_2SiO_4-$KAlSiO_4$-SiO_2, it is demonstrated that the amount of liquid formed at or near the beginning of melting of peridotitic mixtures decreases with increasing pressure and the K_2O content in the liquid increases. Similar changes occur in the systems Mg_2SiO_4-$NaAlSiO_4$-SiO_2 and Mg_2SiO_4-SiO_2-H_2O and are significant for understanding the origin of magmas formed in the upper mantle.

Six compositions in the system Mg_2SiO_4-$KAlSiO_4$-SiO_2 have been studied in the pressure range 14–31 kbar and in the temperature range 1360°–1600°C with a solid-media, high-pressure apparatus and graphite capsules. Because the compositions of the liquids coexisting with forsterite and enstatite are related to magmas formed in the peridotitic upper mantle, the liquidus boundary between forsterite and enstatite has been determined in the above pressure range.

Figure 9 shows the liquidus boundary between forsterite and enstatite solid solution (hereafter referred to as enstatite) at 15, 25, and 30 kbar. The liquidus boundary at 1 atm between forsterite and protoenstatite, shown for comparison, was determined by Schairer (1954). The position of the boundary was determined by making runs on each mixture and estimating the pressure at which the changeover of the liquidus phase from forsterite to enstatite takes place. An example is shown in Fig. 10 for the mixture $MgSiO_3$ 29, $KAlSi_3O_8$ 71 wt %. For this composition, the liquidus phase is forsterite at 15 kbar and enstatite above 16 kbar. Reversals were made to confirm the stable assemblages; the forsterite + liquid assemblage was obtained from the enstatite + glass starting material at 14.5 kbar, and the enstatite + liquid assemblage was obtained from the forsterite + glass starting material at 17.5 kbar. These results indicate that the forsterite-enstatite liquidus boundary passes the composition $En_{29}Or_{71}$ at 15.5 kbar. The boundary at 15 kbar is therefore located slightly to the silica side of this composition. The forsterite-enstatite liquidus boundary on the join Mg_2SiO_4-SiO_2 has been determined by Chen and Presnall (1975) up to 25 kbar, and the phase relations on the join $KAlSiO_4$-SiO_2 have been determined by Lindsley (*Year Book 65*) at pressures to 40 kbar. Their data were taken into account when the boundaries near these joins were drawn; however, the exact position of the isobaric invariant

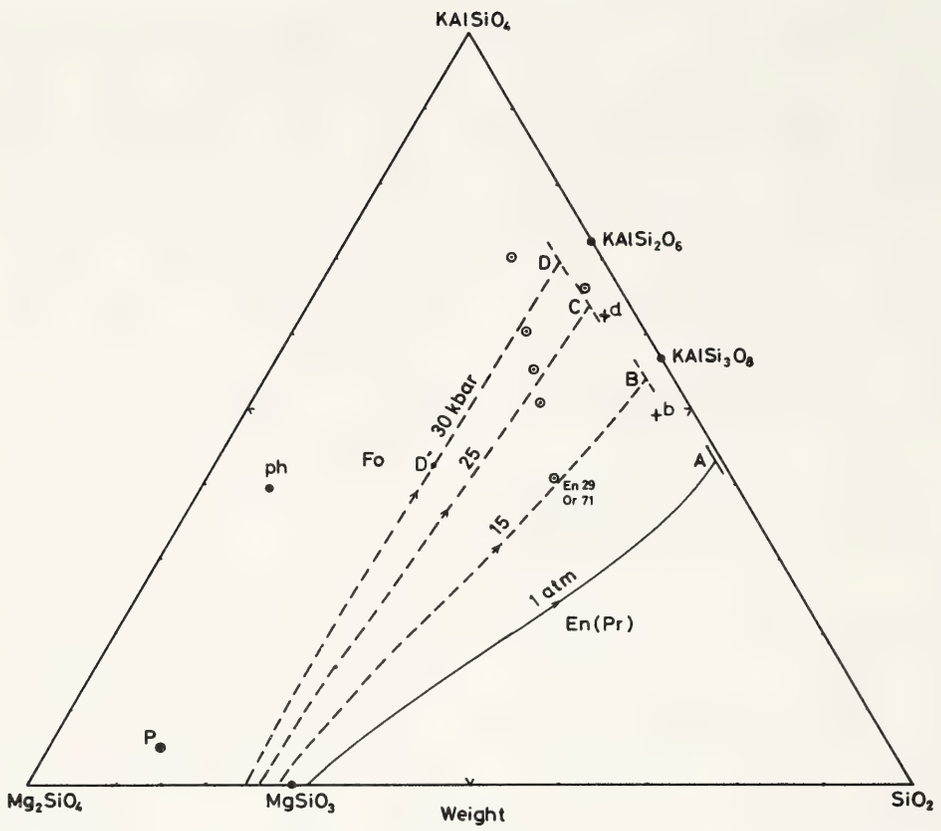


Fig. 9. Shift of the forsterite (Fo)-enstatite (En) liquidus boundary with pressure. Dashed lines indicate the boundary at 15, 25, and 30 kbar determined in the present study. Solid line indicates the forsterite-protoenstatite liquidus boundary at 1 atm determined by Schairer (1954). Symbols: *P*, peridotitic mixture (forsterite 51.7, enstatite 39.6, and sanidine 8.7 wt %, or Mg_2SiO_4 80, $KAlSiO_4$ 5, SiO_2 15 wt %); ph, phlogopite composition; open circles, compositions of starting materials; *b* and *d*, compositions of liquids coexisting with forsterite, enstatite, and phlogopite at 15 and 30 kbar, respectively, determined by Modreski and Boettcher (1973). The amounts of liquid formed by melting of *P* at piercing points *A*, *B*, *C*, and *D* are 12.8, 9.3, 7.9, and 7.1 wt %, respectively.

point* where forsterite, enstatite, and sanidine or leucite coexist with liquid has not been determined.

The liquidus boundary between forsterite and enstatite (or protoenstatite at low pressures) shifts away from silica with increasing pressure (Fig. 9). In consequence, the isobaric invariant point or the lowest temperature point of the forsterite-enstatite liquidus boundary shifts away from the SiO_2

*Strictly speaking, this point is not an isobaric invariant point but is a piercing point because enstatite crystallizing in this system contains Al_2O_3 as a solid solution, its composition does not lie on the plane Mg_2SiO_4-$KAlSiO_4$-SiO_2, and the compositions of liquids coexisting with this enstatite are slightly off this plane.

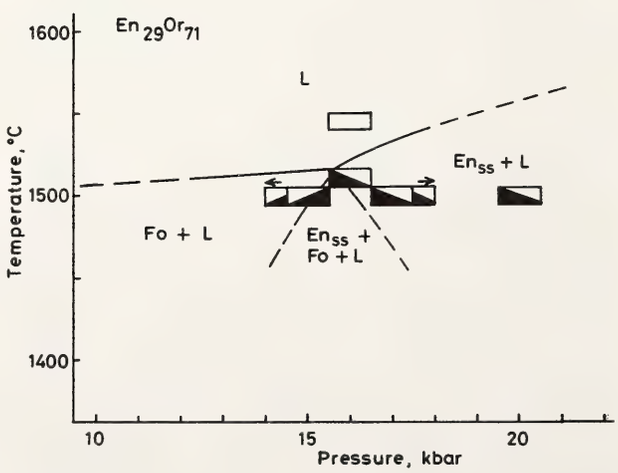


Fig. 10. Runs made on the mixture En ($MgSO_3$) 20, Or ($KAlSi_3O_8$) 71 wt %. Arrows indicate "reverse runs."

apex nearly parallel to the join KAl SiO_4-SiO_2.†

Partial melting of mixture *P* (Mg_2SiO_4 80, $KAlSiO_4$ 5, SiO_2 15 wt %, equivalent to forsterite 51.7, enstatite 39.6, and sanidine 8.7 wt %) produces liquids *A*, *B*, *C*, and *D* at 1 atm, 15, 25, and 30 kbar, respectively (Fig. 9). The amounts of liquid produced at these points are about 11.6, 9.3, 7.9, and 7.1 wt %, respectively. Hence, the degree of melting of this peridotitic mixture at the piercing point (near the beginning of melting) decreases with increasing pressure. The K_2O content of the liquid increases from 12.8 wt % at 1 atm to 20.8% at 30 kbar.

Similar changes in liquid composition, under hydrous conditions where phlogopite is present during partial melting, have been observed by Modreski and Boettcher (1973). They found that liquids coexisting with forsterite, enstatite, and phlogopite become K_2O-rich and silica-poor with increasing pressure (e.g., 14.4 wt % K_2O and 65.6% SiO_2 at 15 kbar, and 18.3% K_2O and 58.8% SiO_2 at 30 kbar; *b* and *d*, respectively, in Fig. 9). The amount of liquid at the beginning of melting, however, was not determined.

These results and those obtained by Kushiro (1968) for the system Mg_2SiO_4-$NaAlSiO_4$-SiO_2 suggest that at lower pressures larger amounts of liquids containing smaller amounts of K_2O and Na_2O are produced by partial melting of peridotitic materials. Large amounts of liquids can also be produced at high pressures if the temperature is high; for example, at 30 kbar, 11.6% liquid (the same as that at the piercing point at 1 atm) is produced in the system Mg_2SiO_4-$KAlSiO_4$-SiO_2 if the temperature is raised to point *D'* in Fig. 9.

The solubility of K_2O and Na_2O or $KAlO_2$ and $NaAlO_2$ in the liquids coexisting with forsterite and enstatite increases with increasing pressure at least to 30 kbar. The solubility of H_2O in such liquids also increases with increasing pressure at least to 20 kbar (Kushiro *et al.*, 1968; Eggler, *Year Book 72*), as shown in Fig. 11. The amount of H_2O-saturated liquids formed by partial melting of a peridotitic material with fixed H_2O content, therefore, must decrease with increasing pressure. For example, a peridotitic mixture *P'* (H_2O 1, $MgSiO_3$ 99 wt %, which consists of enstatite and small amounts of forsterite and vapor near the solidus) produces 9.1 wt % liquid at the beginning of melting (*A'*) at 10 kbar, whereas at 20 kbar only 4.6% li-

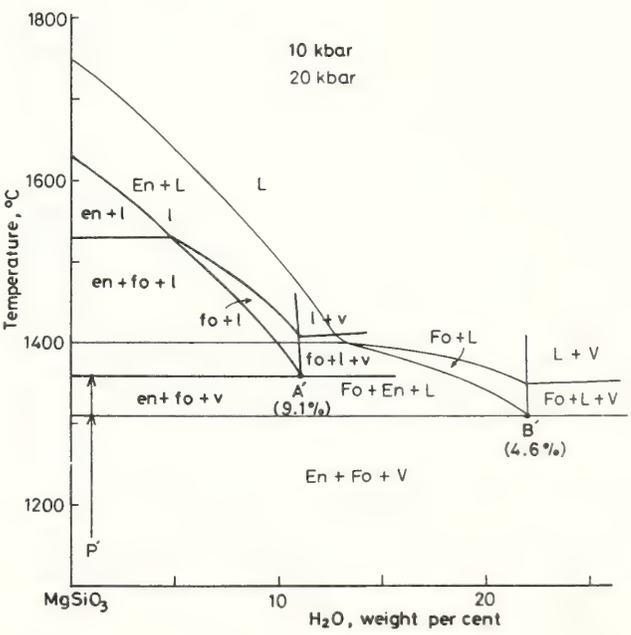


Fig. 11. Phase-equilibrium relations on the join $MgSiO_3$-H_2O at 10 kbar (thick lines with lower case letters) and 20 kbar (thin lines with upper case letters) determined by Kushiro *et al.* (1968) and Eggler (*Year Book 72*), respectively. The amounts of liquid formed by melting of *P'* (H_2O 1, $MgSiO_3$ 99 wt %, or enstatite + forsterite + vapor) at the beginning of melting *A'* (10 kbar) and *B'* (20 kbar), where enstatite, forsterite, and vapor coexist with liquid, are 9.1 and 4.6 wt %, respectively.

†Recently, Wendlandt and Eggler (1980) published a more detailed study on the system Mg_2SiO_4-$KAlSiO_4$-SiO_2 and also showed that liquids coexisting with forsterite, enstatite, and sanidine (or leucite at low pressure) become enriched in K_2O and depleted in silica with increasing pressure.

quid is produced (B') as shown in Fig. 11.

Clinopyroxene containing significant amounts of Na_2O may be present during partial melting. In this case the melting relations are different from those shown in the system Mg_2SiO_4-$NaAlSiO_4$-SiO_2, and the change in the amount of liquid and its Na_2O content may be smaller than shown for this system.

The results of the present and previous experiments indicate that the degree of partial melting of peridotitic materials can be smaller at higher pressures. When partial melting occurs at relatively deep levels in the upper mantle, the *initial melt* is enriched in K_2O, H_2O, and probably other "incompatible elements," and the amount of the melt will be small. Alkali basalt and kimberlite magmas probably represent such liquids. Many geochemists (e.g., Gast, 1968) have suggested that alkali basalts are products of a small degree of partial melting. On the other hand, if partial melting of peridotitic materials occurs at relatively shallow levels, the degree of melting cannot be small compared with that at deep levels and, therefore, the liquids will contain relatively small amounts of K_2O, H_2O, and other incompatible elements. Tholeiitic basalt magmas, especially mid-oceanic ridge basalt magmas are depleted in K_2O and other incompatible elements, and probably represent liquids formed by a relatively large degree of partial melting. This may be caused by formation at relatively shallow levels, and the degree of melting is relatively large, even near the beginning of melting.

The K_2O content in Quaternary volcanic rocks (e.g., basalts) in island arcs and active continental margins increases gradually from the trench side to the continental side. If the site of magma generation gradually deepens toward a continent, as suggested by Kuno (1959) for example, the observed K_2O variation may be explained by these experiments.

The shift of the forsterite-enstatite liquidus boundary with pressure is greater in the system Mg_2SiO_4-$KAlSiO_4$-SiO_2 (Fig. 9) than in the systems Mg_2SiO_4-$NaAlSiO_4$-SiO_2, Mg_2SiO_4-$Ca_{0.5}AlSiO_4$, and $Mg_{0.5}AlSiO_4$-SiO_2. Figure 12 shows the shift of the forsterite-enstatite liquidus boundary with pressure in these four systems. Each line indicates the shift of a point at 0.2 mol of each component (e.g., $KAlSiO_4$) on the forsterite-enstatite liquidus boundary. It is demonstrated that the degree of the shift from 1 atm to 30 kbar is largest for $KAlSiO_4$ and decreases in the order $NaAlSiO_4$, $Ca_{0.5}AlSiO_4$, and $Mg_{0.5}AlSiO_4$. The shift of the forsterite-enstatite liquidus boundary away from SiO_2 with increasing pressure is explained by the decrease of the molar volume from the forsterite + liquid assemblage to the enstatite + liquid assemblage with the same crystal-liquid ratio (Kushiro, 1980). The degree of the shift of the boundary would be related to the value of ΔV (volume difference between the above two assemblages). It is expected that the value of ΔV is largest in the system Mg_2SiO_4-$KAlSiO_4$-SiO_2 and decreases in the order mentioned above. The compressibility of liquid coexisting with forsterite and enstatite in the above four systems, therefore, would probably decrease in the same order.

References

Chen, C.-H., and D. Presnall, The system Mg_2SiO_4-SiO_2 at pressures up to 25 kilobars, *Amer. Mineral., 60,* 398–406, 1975.

Gast, P. W., Trace element fractionation and the origin of tholeiitic and alkaline magma types, *Geochim. Cosmochim. Acta, 32,* 1057–1086, 1968.

Kuno, H., Origin of Cenozoic petrographic provinces of Japan and surrounding areas, *Bull. Volcanol., 20,* 37–76, 1959.

Kushiro, I., Compositions of magmas formed by partial zone melting of the earth's upper mantle, *J. Geophys. Res., 73,* 619–637, 1968.

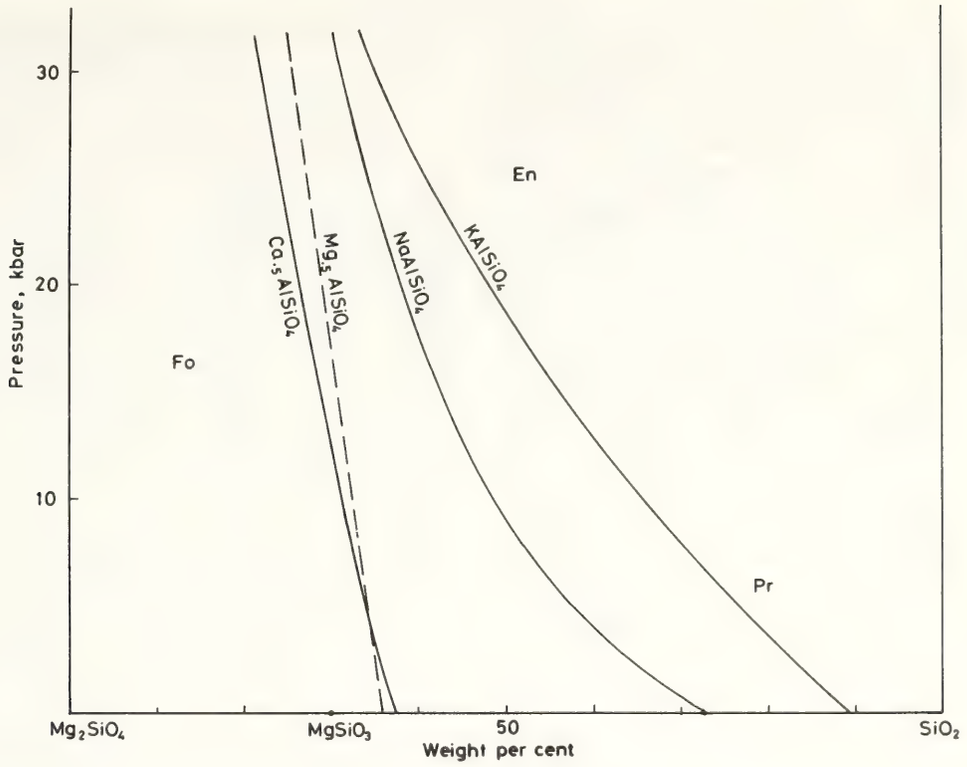


Fig. 12. Shift of the forsterite (Fo)-enstatite (En) liquidus boundary with pressure in the systems Mg_2SiO_4-$KAlSiO_4$-SiO_2, Mg_2SiO_4-$NaAlSiO_4$-SiO_2, Mg_2SiO_4-$Ca_{0.5}AlSiO_4$-SiO_2, and $Mg_{0.5}AlSiO_4$-SiO_2. Each line indicates the shift of a point at 0.2 mole of each component on the Fo-En liquidus boundary, projected onto the join Mg_2SiO_4-SiO_2 from the apex of each component.

Kushiro, I., Viscosity, density, and structure of melts at high pressures and their petrological applications, in *Physics of Magmatic Processes,* Princeton University Press, in press, 1980.

Kushiro, I., H. S. Yoder, Jr., and M. Nishikawa, Effect of water on the melting of enstatite, *Geol. Soc. Amer. Bull., 79,* 1685–1692, 1968.

Modreski, P. J., and A. L. Boettcher, Phase relationships of phlogopite in the system K_2O-MgO-CaO-Al_2O_3-SiO_2-H_2O to 35 kilobars: a better model for micas in the interior of the earth, *Amer. J. Sci., 273,* 385–414, 1973.

Schairer, J. F., The system K_2O-MgO-Al_2O_3-SiO_2: I. Results of quenching experiments on four joins in the tetrahedron cordierite-forsterite-leucite-silica and on the join cordierite-mullite-potash feldspar, *J. Amer. Ceram. Soc., 37,* 501–533, 1954.

Wendlandt, R. F., and D. H. Eggler, The origins of potassic magmas: 1. Melting relations in the systems $KAlSiO_4$-Mg_2SiO_4-SiO_2 and $KAlSiO_4$-MgO-SiO_2-CO_2 to 30 kilobars, *Amer. J. Sci., 280,* 385–420, 1980.

Melting Relations of an Alkali-Olivine Basalt to 30 kbar, and Their Bearing on the Origin of Alkali Basalt Magmas

E. Takahashi

Basalt magmas may be produced in the upper mantle by the partial melting of peridotite. If a basalt represents a primitive upper mantle melt, then the melt should in all likelihood coexist with olivine and orthopyroxene at the pressure of its formation (O'Hara, 1968; Yoder, 1976). If the basalt represents an incipient melt and the source rock was a lherzolite (Yoder, 1976), then the melt should also be saturated with clinopyroxene and some aluminous phase (garnet, spinel, or plagioclase) at the pressure where it last equilibrated with the mantle source. Such multiple saturation has been found for abyssal tholeiites at about 8

kbar (Kushiro, 1973; Fujii and Kushiro, *Year Book 76,* 461–465) and for a tholeiite picrite at about 25 kbar (Elthon and Scarfe, this Report). This report describes the melting relations of a primitive alkali-olivine basalt, which is shown to coexist with olivine, orthopyroxene, and clinopyroxene at about 14 kbar and 1275 °C. It is suggested that this basaltic magma, prior to eruption, equilibrated last with upper mantle peridotite under about these conditions.

The basalt used in the present study was collected from a Pliocene lava flow (KRB) on Oki-Dogo Island in the Japan Sea. The rock is fresh and consists of microphenocrysts of olivine, augite, and plagioclase, and groundmass of olivine, augite, plagioclase, magnetite, ilmenite, and apatite. Abundant xenolithic fragments (up to 30 cm in diameter) are present in the flow, variously consisting of spinel lherzolite, layered peridotite, and pyroxenite cumulates, pyroxene granulite, and gabbro. The petrology of the xenoliths has been described (Takahashi, 1978a), and a more detailed description is in preparation. Given the presence of the large, mantle-derived xenoliths, the ascent of the magma from the upper mantle was probably very rapid (Kushiro *et al.,* 1976), and so separation of crystallized phenocrysts has probably not occurred. The bulk rock chemical composition of the basalt (Table 3), therefore, is believed to represent the composition of liquid separated in the upper mantle. The composition of the olivine that would coexist with such a liquid, as calculated by means of olivine-liquid distribution coefficients [K_D(Fe/Mg) = 0.30, K_D(Ni/Mg) = 2.3; for details, see Takahashi, 1978b, composition KRB], is Fo_{88} with 0.33 wt % NiO. The composition of the olivine microphenocryst (more than 10 vol %) is Fe-rich (Fo_{75-80}), but that of olivine crystallized in a 1-atm liquidus experiment (1220 °C, 10^{-8} f_{O_2}) was the same as predicted. Furthermore, the predicted composition is within the compositional range of olivine in the spinel lherzolite xenoliths from Oki-Dogo Island (Fo = 86–90 mole %, NiO = 0.33–0.40 wt %).

TABLE 3. Composition of Basalt Starting Material KRB

Oxide, wt %		CIPW Norm	
SiO_2	47.47	Or	10.04
TiO_2	2.43	Ab	24.94
Al_2O_3	17.15	An	25.46
Fe_2O_3	2.26	Ne	3.40
FeO	7.22	Cpx	8.22
MnO	0.15	Ol	18.47
MgO	8.76	Mt	3.29
CaO	8.03	Il	4.64
Na_2O	3.67	Ap	1.54
K_2O	1.69		
P_2O_5	0.66		
H_2O^+	0.61		
H_2O^-	0.22		
Total	100.32		
Ni, ppm	205		

Experimental

High-pressure experiments were made with a solid-media, high-pressure apparatus (Boyd and England, 1960). The piston-out technique was employed with a −4% friction correction. The basalt was powdered to grain sizes ≲ 10 μm. The charges, which weighed about 30 mg, were melted in graphite capsules to avoid Fe loss to the container. The furnace parts, including the charge and the Pyrex glass sleeve, were dried for 30 sec with a gas torch immediately prior to the melting experiment. One-atmosphere experiments were made with a thyristor-regulated, silicon-carbide quenching furnace at Tokyo University. Oxygen fugacities were controlled by CO_2-H_2 gas mixtures. Run durations ranged from 2 hr on the liquidus to 48 hr at temperatures more than 100 °C below the liquidus. Replicate runs of 15–20 hr were made for liquidus experiments between 12 and 15 kbar. The phases were identified micro-

scopically and analyzed with an electron microprobe.

Results

A preliminary *P-T* diagram of the melting relations of basalt KRB is presented in Fig. 13. The basalt has olivine on the liquidus to about 14 kbar, and then clinopyroxene to about 30 kbar. Orthopyroxene appears to be a liquidus phase together with clinopyroxene in a narrow interval between about 14 and 15 kbar. A four-phase assemblage, olivine + orthopyroxene + clinopyroxene + liquid, was found in three experiments in the range 13.5–14 kbar, 1250°–1270°C. This assemblage has also been confirmed by replicate experiments of longer duration (15–20 hr) and with basalt melt as a starting material instead of rock powder. Quench crystals of clinopyroxene were found in runs above 25 kbar but not below. Overall, the melting relations of basalt KRB are consistent with results obtained for a synthetic rock composition simulating alkali-olivine basalt (slightly poorer in normative nepheline and richer in normative olivine) by Green and Ringwood (1967).

Compositions of the olivine, orthopyroxene, clinopyroxene, and liquid coexisting experimentally at 1270°C and 14 kbar are listed in Table 4. Because of the low oxygen fugacity imposed by the graphite capsule (in the wüstite stability field; Thompson and Kushiro, *Year Book 71,* 615–616), essentially all the iron in the melt is divalent. The compositions of the crystalline phases, therefore, are slightly less magnesian than those calculated from the MgO-FeO ratio of the original rock. The clinopyroxenes formed with orthopyroxene at temperatures above 1250°C at 14 kbar are pigeonite (Table 4); those formed at lower temperatures at 14 kbar and under all other pressure-temperature conditions are augite (Table

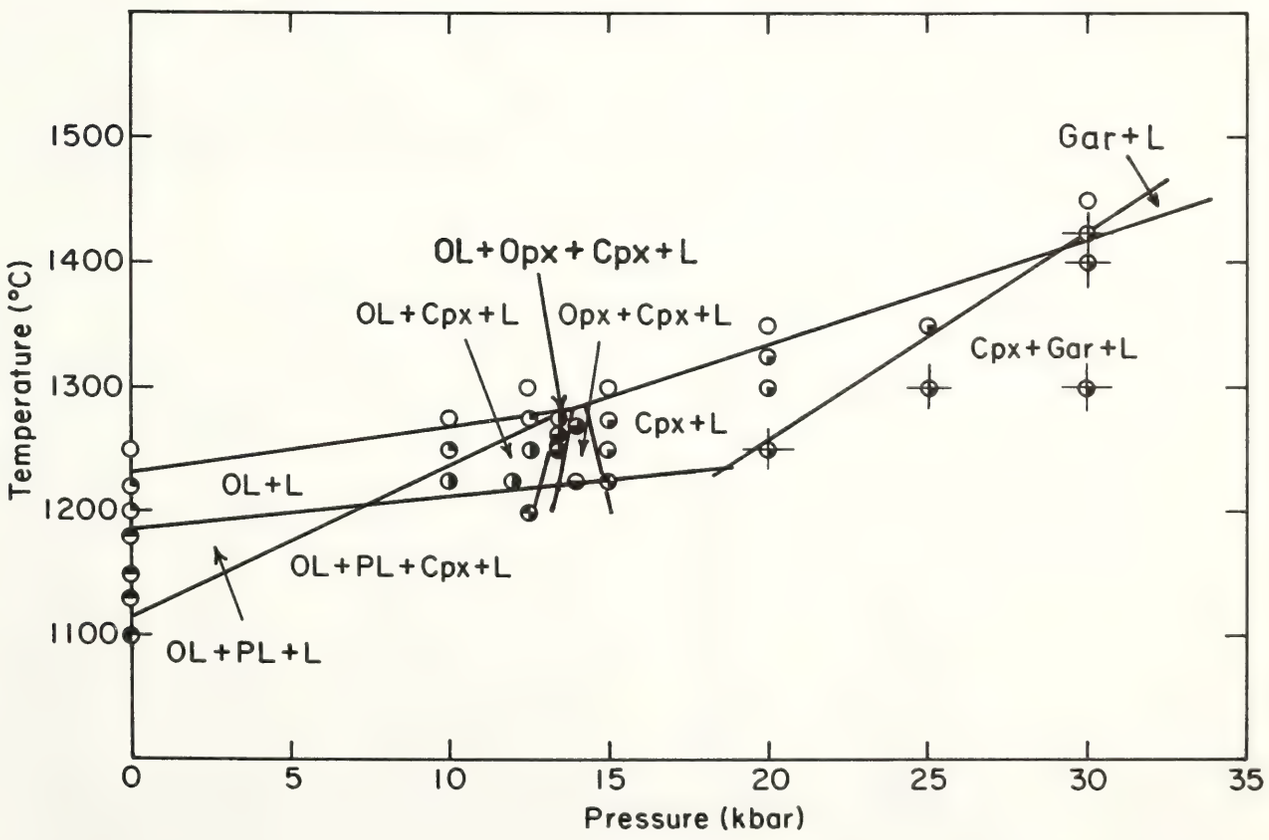


Fig. 13. Preliminary melting relations of an alkali-olivine basalt (KRB). The basalt melt coexists with olivine, orthopyroxene, and clinopyroxene in a narrow range, 13.5–14 kbar, 1250°-1270°C.

TABLE 4. Composition of Coexisting Phases in Experiment with Graphite Capsule (14 kbar, 1270 °C, 4 hr)

	Liquid	Olivine	Orthopyroxene	Clinopyroxene (Pigeonite)
SiO_2	49.57	39.89	55.71	53.67
Al_2O_3	16.31	0.24	3.47	4.48
TiO_2	2.28	0.07	0.35	0.48
FeO	8.76	14.59	9.10	8.77
MnO	0.13	0.18	0.18	0.21
MgO	8.13	45.28	30.42	25.72
CaO	7.52	0.28	2.18	5.43
Na_2O	3.80	0.05	0.17	0.41
K_2O	1.80	0.00	0.00	0.00
Cr_2O_3	0.03	0.04	0.24	0.33
Total	98.33	100.62	101.82	99.50
Mg/(Mg + Fe)		0.847	0.850	0.840
Ca/(Ca + Mg + Fe)		. . .	0.042	0.113
Mg/(Ca + Mg + Fe)		. . .	0.820	0.745

5). At any pressure, the Wo, Al_2O_3, and Na_2O contents of the clinopyroxenes were lower at liquidus temperatures than at lower temperatures. On the liquidus, the Na_2O content increased from 0.4 wt % at 14 kbar to 1.6 wt % at 30 kbar. In the replicate experiments noted above (with basalt melt as a starting material), pigeonite coexisted with orthopyroxene and olivine at 14 kbar, 1270 °C.

In order to confirm multiple saturation of the melt with olivine + orthopyroxene + clinopyroxene, a time study was made at 14 kbar and 1275 °C with powdered spinel lherzolite (OKD-13) as a capsule material. The spinel lherzolite (OKD-13) is a xenolith collected from a volcanic neck adjacent to the lava flow KRB. The rock capsules are similar to those used in nickel partitioning experiments (Takahashi, 1980),

TABLE 5. Some Clinopyroxene Compositions

	12.5 kbar 1200 °C	13.5 kbar 1250 °C	15 kbar 1275 °C	15 kbar 1225 °C	20 kbar 1300 °C	30 kbar 1425 °C
SiO_2	48.87	51.55	51.13	49.27	50.58	51.37
Al_2O_3	9.52	6.74	7.73	10.53	9.28	9.62
TiO_2	2.69	0.82	0.84	1.63	0.96	0.73
FeO	9.34	8.23	8.95	9.66	8.64	7.36
MnO	0.21	0.14	0.18	0.09	0.18	0.14
MgO	15.91	21.55	21.87	16.98	18.89	17.16
CaO	12.66	9.65	8.97	10.86	11.17	12.47
Na_2O	0.90	0.69	0.68	1.14	0.91	1.64
K_2O	0.02	0.00	0.02	0.01	0.02	0.03
Cr_2O_3	0.26	0.21	0.30	0.12	0.28	0.23
NiO	0.00	0.09	0.03	0.00	0.06	0.05
Total	100.38	99.67	100.70	100.29	100.97	100.80
Ca/(Ca + Mg + Fe)	0.30	0.21	0.19	0.26	0.25	0.30
Mg/(Ca + Mg + Fe)	0.53	0.65	0.66	0.56	0.59	0.57

except that they are contained in graphite rather than Pt. The same experimental technique has been used by Stolper (1980) for high-pressure melting experiments on an abyssal tholeiite. In these runs, it was clear that the basalt melt was in contact with all of the phases olivine, orthopyroxene, and clinopyroxene along its wall, but no spinel crystals were found either along the melt-peridotite boundaries or within the melt. Analyses of the melts showed only slight variations (cf. Tables 6 and 4) as a function of run duration (30 min to 48 hr). The above fact is considered to be evidence that the melt is saturated with olivine + orthopyroxene + clinopyroxene under the pressure and temperature conditions, because the chemical composition of a melt trapped in the peridotite capsules will change significantly at the expense of crystalline phases when the melt is not saturated with them (Stolper, 1980; Takahashi, 1980). Indeed, compositions of olivine, orthopyroxene, and clinopyroxene in contact with the basalt melt (Table 6) are nearly identical with those crystallized in the graphite capsule except that the clinopyroxene is much more calcic (cf. Table 4).

Discussion

On the basis of the experiments, the alkali-olivine basalt KRB could have coexisted with olivine, orthopyroxene, and clinopyroxene at about 14 kbar. In the system CaO-MgO-Al_2O_3-SiO_2 (CMAS), the isobaric invariant point, olivine + orthopyroxene + clinopyroxene + spinel + liquid, is situated in the Di-An-Fo-En tetrahedron at pressures from 7 to at least 20 kbar (Presnall *et al.*, 1978, 1979). Nepheline-normative liquids, therefore, by virtue of lying on the silica-deficient side of the critical plane An-Di-Fo, cannot coexist with orthopyroxene below 20 kbar. In the natural rocks containing other components, however, the pseudoinvariant point olivine + orthopyroxene + clinopyroxene + spinel + liquid evidently becomes nepheline normative at some pressure between 10 and 20 kbar (Kushiro, *Year Book 71*, 357–362; Kushiro, 1973; Presnall *et al.*, 1978; Mysen and Kushiro, 1977), and the present results suggest that it is actually on the silica-poor side of the critical plane Pl-Di-Fo at 14 kbar. The appearance of pigeonite in the experiments with graphite containers at 13.5–14

TABLE 6. Composition of Coexisting Phases in Experiment with Peridotite Capsule (14 kbar, 1275 °C, 22 hr)

	Liquid	Olivine	Orthopyroxene	Clinopyroxene
SiO_2	49.94	39.72	53.33	49.54
Al_2O_3	16.82	0.16	5.98	8.16
TiO_2	2.29	0.04	0.52	1.13
FeO	7.50	13.36	8.57	5.66
MnO	0.14	0.18	0.18	0.16
MgO	7.87	46.28	29.18	17.84
CaO	7.92	0.31	2.40	15.00
Na_2O	4.25	0.05	0.20	0.80
K_2O	1.82	0.00	0.01	0.01
NiO	...	0.36	0.07	0.08
Cr_2O_3	0.06	...	...	...
Total	98.61	100.46	100.44	98.38
Mg/(Mg + Fe)		0.861	0.859	0.849
Ca/(Ca + Mg + Fe)		...	0.048	0.339
Mg/(Ca + Mg + Fe)		...	0.818	0.562

kbar and 1250°–1270°C is accounted for according to the argument of Eggler (1978) that pigeonite has a small liquidus volume close to the pseudoinvariant point at high pressures. Because the composition of the melt (KRB) is situated very close to the pseudoinvariant point at 14 kbar, it may crystallize either pigeonite or augite owing to a very small change in composition (cf. Tables 4 and 6). Pigeonite was also observed near the solidus of peridotite 1611 at 20 kbar and 1450°-1500°C (Mysen and Kushiro, 1977).

Two principal origins have been proposed for alkali-olivine basalt magmas: fractional crystallization of tholeiitic magmas at high pressures (Yoder and Tilley, 1962; Green and Ringwood, 1967) and small degrees of partial melting of lherzolite at high pressures (Gast, 1968; O'Hara, 1968; Kushiro, 1973). The melting relations of basalt KRB suggest that the melt last equilibrated with the upper mantle lherzolite at about 14 kbar, provided that the effects of H_2O and CO_2 on the melting relations are insignificant. The basalt KRB may have been generated as a partial melt at that depth or may have been produced at a greater depth but rose, maintaining chemical equilibrium with the upper mantle lherzolite. The fact that alkali-olivine basalts commonly host spinel lherzolite xenoliths (e.g., Forbes and Kuno, 1967) but rarely transport garnet lherzolite xenoliths is consistent with the hypothesis that they form in the stability region of spinel lherzolite, that is, between about 10 and about 25 kbar.

References

Boyd, F. R., and J. L. England, Apparatus for phase-equilibrium measurements at pressures to 50 kilobars and temperatures up to 1750°C, *J. Geophys. Res., 65,* 741–748, 1960.

Eggler, D. H., The effect of CO_2 upon partial melting of peridotite in the system Na_2O-CaO-Al_2O_3-MgO-SiO_2-CO_2 to 35 kb, with an analysis of melting in a peridotite-H_2O-CO_2 system, *Amer. J. Sci., 278,* 305–343, 1978.

Forbes, R. B., and H. Kuno, Peridotite inclusions and basaltic host rocks, in *Ultramafic and Related Rocks,* P. J. Wyllie, ed., John Wiley and Sons, Inc., New York, pp. 328–336, 1967.

Gast, P. W., Trace element fractionation and the origin of tholeiite and alkaline magma types, *Geochim. Cosmochim. Acta, 32,* 1057–1086, 1968.

Green, D. H., and A. E. Ringwood, The genesis of basaltic magmas, *Contrib. Mineral. Petrol., 15,* 103–190, 1967.

Kushiro, I., Origin of some magmas in oceanic and circum-oceanic regions, *Tectonophysics, 17,* 211–222, 1973.

Kushiro, I., H. S. Yoder, Jr., and B. O. Mysen, Viscosities of basalt and andesite melts at high pressures, *J. Geophys. Res., 81,* 6351–6356, 1976.

Mysen, B. O., and I. Kushiro, Compositional variations of coexisting phases with degree of melting of peridotite in the upper mantle, *Amer. Mineral., 62,* 843–865, 1977.

O'Hara, M. J., The bearing of phase equilibria in synthetic and natural systems on the origin and evolution of basic and ultrabasic rocks, *Earth Sci. Rev., 4,* 69–133, 1968.

Presnall, D. C., S. A. Dixon, J. R. Dixon, T. H. O'Donnell, N. J. Brenner, R. L. Schrock, and D. W. Dycus, Liquidus phase relations on the join diopside-forsterite-anorthite from 1 atm to 20 kbar: their bearing on the generation and crystallization of basaltic magma, *Contrib. Mineral. Petrol., 66,* 203–220, 1978.

Presnall, D. C., J. R. Dixon, T. H. O'Donnell, and S. A. Dixon, Generation of mid-ocean ridge tholeiites, *J. Petrology, 20,* 3–35, 1979.

Stolper, E., A phase diagram for mid-ocean ridge basalts (abstract), *EOS, 61,* 405, 1980.

Takahashi, E., Petrologic model of the crust and upper mantle of the Japanese island arcs, *Bull. Volcanol., 41,* 529–547, 1978a.

Takahashi, E., Partitioning of N^{2+}, Co^{2+}, Fe^{2+}, Mn^{2+}, and Mg^{2+} between olivine and silicate melts: compositional dependence of partition coefficient, *Geochim. Cosmochim. Acta, 42,* 1829–1844, 1978b.

Takahashi, E., Olivine/liquid nickel partitioning at high pressures: experiments with an olivine capsule (abstract), *EOS, 61,* 397, 1980.

Yoder, H. S., Jr., *Generation of Basaltic Magma,* National Academy of Sciences, Washington, D.C., 1976.

Yoder, H. S., Jr., and C. E. Tilley, Origin of basalt magmas: an experimental study of natural and synthetic rock systems, *J. Petrology, 3,* 342–532, 1962.

High-Pressure Phase Equilibria of a High-Magnesia Basalt: Implications for the Origin of Mid-Ocean Ridge Basalts

D. Elthon and C. M. Scarfe*

Several models for the origin of mid-ocean ridge basalts are being actively debated. Presnall *et al.* (1979) proposed that mid-ocean ridge basalts are generated at low pressures ($\lesssim$10 kbar) and that they are primary magmas or have undergone only minor fractionation prior to eruption. Alternatively, O'Hara (1968) has proposed that mid-ocean ridge basalts are the end products of extensive low-pressure fractionation and are derived from picritic magmas produced at 25–30 kbar. The major difficulty in deciding which of these two general models is more nearly correct is the uncertainty in estimating the pressure at which primary magmas are separated from the suboceanic mantle.

On the basis of comparisons between the composition and petrology of ophiolites and the oceanic crust, it has been proposed that NT-23, a high-MgO basalt from the Tortuga ophiolite complex, Chile, is similar to primary magmas generated in the present-day, suboceanic mantle (Elthon, 1979). The melting relations of NT-23 described in this report indicate that it has olivine, orthopyroxene, clinopyroxene, and garnet on the liquidus at 25 kbar, and consequently NT-23 may be a primary magma generated by invariant melting of a garnet peridotite at pressures $\geq$25 kbar. These results support O'Hara's (1968) proposal that primary mid-ocean ridge basalts are generated at 25–30 kbar and are picritic in composition.

*Work carried out under a cooperative predoctoral fellowship program of the Geophysical Laboratory and Lamont-Doherty Geological Observatory of Columbia University.

Experimental Methods

The high-pressure experiments were carried out in a solid-media, high-pressure apparatus with a 1/2-inch diameter furnace assembly (Boyd and England, 1960). The piston-out technique was used with a -4% correction for friction. The starting materials were placed in graphite containers that were sealed inside 3-mm-O.D. platinum capsules. A Pyrex glass sleeve around the heating element inhibited water access to the sample region and minimized hydrogen diffusion into the capsule. The graphite containers prevented iron loss to the platinum capsule and maintained a relatively low f_{O_2} at the graphite-CO-CO_2 buffer. Runs were 1 hr in duration. The observation that no change occurred in the phase equilibria between experiments 1 and 10 hr in duration at 25 kbar and 1470°C was taken to indicate that equilibrium was achieved in the shorter runs. All phase identifications have been verified with the electron microprobe.

Results

At 25 kbar, olivine, orthopyroxene, clinopyroxene, and garnet crystallize within 10°C of the liquidus (Fig. 14). At pressures > 25 kbar, clinopyroxene is the liquidus phase, whereas at pressures < 25 kbar, olivine is the liquidus phase and is followed by spinel, clinopyroxene, and eventually orthopyroxene during crystallization. The coexistence of olivine, orthopyroxene, clinopyroxene, and either garnet, spinel, or plagioclase with the silicate liquid defines an isobaric upper mantle pseudoinvariant point. The compositions of the liquid (quenched to glass) coexisting with these four phase assemblages at various pressures are given in Table 7. These glass compositions are used to constrain the locations of pseudoinvariant points shown in Fig. 15. Because graphite capsules were used in

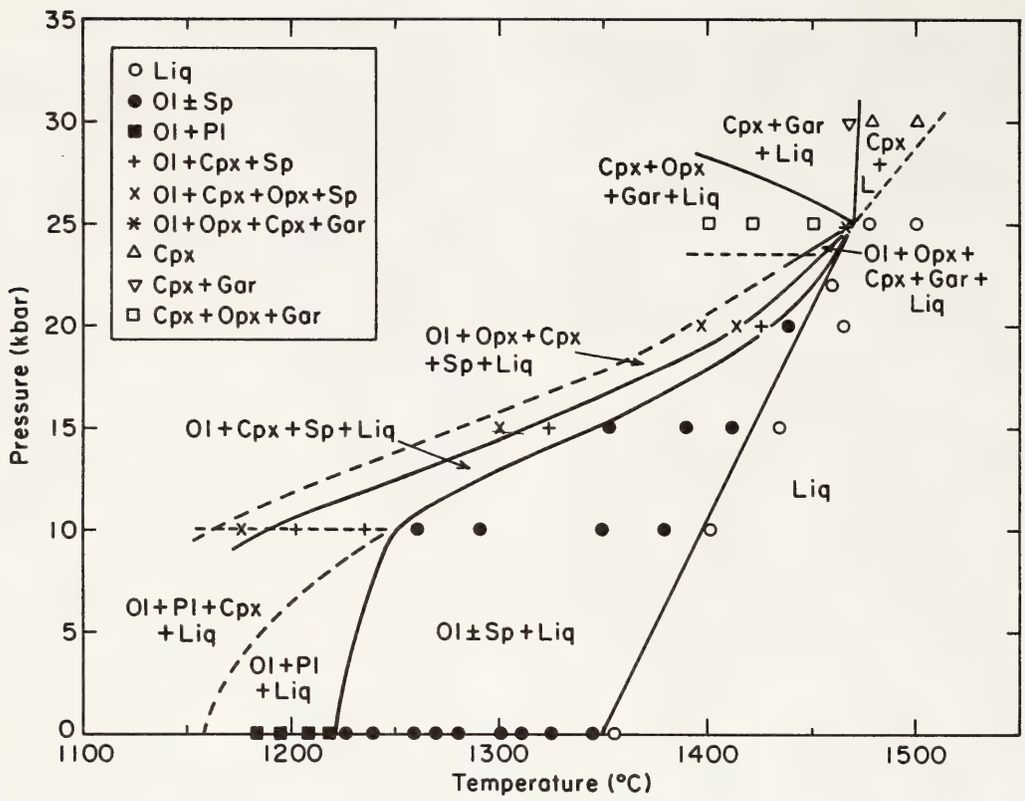


Fig. 14. Phase diagram for high-MgO basalt NT-23.

these experiments, a minor amount of CO_2 may be dissolved in the melt at high pressure (e.g., Green *et al.*, 1979). The amount of CO_2 in the melt is presumed to be small because the electron microprobe analyses of the glasses sum to near 100% (see Table 7).

Discussion

In order to evaluate the origin of mid-ocean ridge basalts, the upper mantle pseudoinvariant points, indicating the composition of the liquid in equilibrium with olivine, orthopy-

TABLE 7. Bulk Composition of NT-23 and Composition of Glasses at the Four Pseudoinvariant Points

	NT-23	25 kbar	20 kbar	15 kbar	10 kbar
SiO_2	47.25	47.35	47.93	47.99	47.99
TiO_2	0.79	0.93	0.92	1.29	1.53
Al_2O_3	13.64	13.88	14.62	16.20	18.90
Cr_2O_3	0.20	0.19	0.25	0.07	0.06
MnO	0.14	0.22	0.10	0.11	0.18
FeO	9.77	9.83	8.40	9.37	10.12
MgO	17.61	17.07	15.22	12.38	8.56
CaO	9.58	10.86	12.25	11.65	10.38
Na_2O	0.89	0.86	0.46	0.78	2.13
K_2O	0.06	0.00	0.00	0.02	0.05
Total	99.93	101.21	100.15	99.86	99.90
Solid phases coexisting with liquids		Ol Opx Cpx Gar	Ol Opx Cpx Sp	Ol Opx Cpx Sp	Ol Opx Cpx Sp

roxene, clinopyroxene, and either garnet, spinel, or plagioclase at 25, 20, 15, and 10 kbar, are projected onto the olivine-An_{70}-quartz plane in the CMAS system (Fig. 15). Also projected onto this plane are basalts from the FAMOUS area (Bryan and Moore, 1977) and other suites of mid-ocean ridge basalts (Frey *et al.*, 1974; Blanchard *et al.*, 1976; Melson *et al.*, 1976). Basalts that project near the upper mantle pseudoinvariant points and that potentially represent primary magmas are the Svartenhuk (SV) and Baffin Island (BI) picrites (Clarke, 1970), NT-23, the Gorgona Island (G) komatiite (Gansser *et al.*, 1979), and a few basalts that lie near the 10-kbar pseudoinvariant point. Almost all mid-ocean ridge basalts cluster near the 1 atm olivine + plagioclase ± clinopyroxene cotectics in the CMAS system, and this result indicates that their compositions have been modified by low-pressure fractionation.

Previous high-pressure phase-equilibrium studies have demonstrated that *primitive* mid-ocean ridge basalts (e.g., FAMOUS basalt 527-1-1, Bender *et al.*, 1978; DSDP basalt 3-18-7-1, Green *et al.*, 1979) projecting at the silica-poor end of the basalt cluster (Fig. 15) do not have orthopyroxene as a liquidus phase at any pressure,

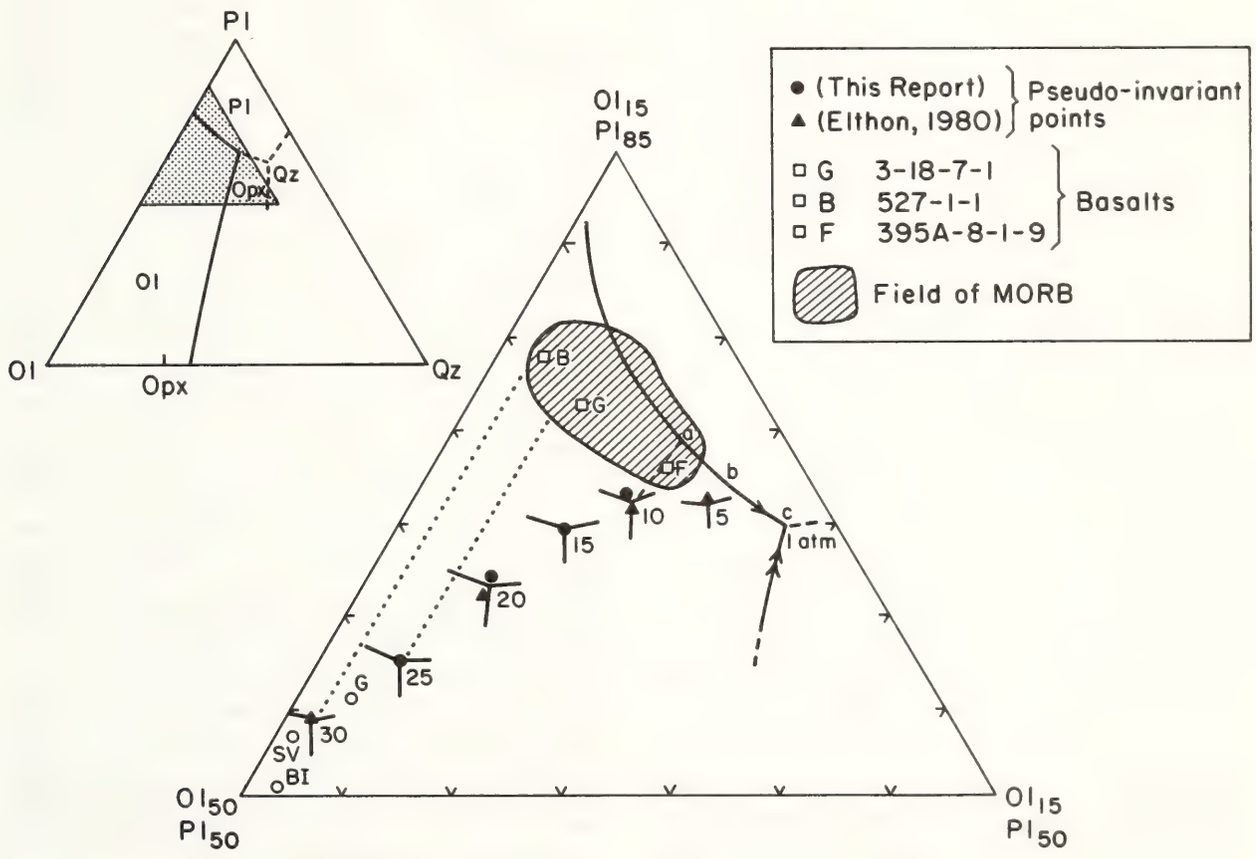


Fig. 15. The An_{70}-Ol-Qz plane in the CMAS system, showing positions of pseudoinvariant points at several pressures. Two sets of pseudoinvariant points are shown; circles represent the liquid compositions in Table 7, whereas the triangles have been deduced from the high-pressure phase equilibria of other basalts. Basalt 3-18-7-1 is a primitive mid-ocean ridge basalt (from the N. Atlantic Ocean) that has been studied experimentally by Green *et al.* (1979). Basalt 527-1-1 is the most primitive sample recovered from the project FAMOUS area of the Atlantic Ocean and has been investigated experimentally by Bender *et al.* (1978). The melting relationships of olivine tholeiite 395A-8-1-9 from the Mid-Atlantic Ridge has been studied by Fujii and Kushiro (*Year Book 76*, 461–465). The 1 atm olivine + clinopyroxene + plagioclase + liquid pseudounivariant curve that includes *a-b-c* is from Walker *et al.* (1979). For other details see text.

whereas *evolved* mid-ocean ridge basalts (Kushiro, 1973; Fujii and Kushiro, *Year Book 76,* 461–465) at the silica-rich end of the basalt cluster (Fig. 15) may be multiply saturated with olivine, clinopyroxene, orthopyroxene, and plagioclase at 7.5–8 kbar. This latter feature is thought to be a consequence of the upper mantle pseudoinvariant points lying near the evolved end of the basalt cluster at 5–10 kbar, whereas at higher pressures, the pseudoinvariant points are significantly displaced from the main cluster of mid-ocean ridge basalts (Fig. 15).

A primary magma generated at $\lesssim 10$ kbar, as proposed by Presnall *et al.* (1979), will undergo olivine fractionation followed by olivine + plagioclase, olivine + plagioclase + clinopyroxene, and finally olivine + plagioclase + clinopyroxene + orthopyroxene as the liquid composition changes from the 10-kbar pseudoinvariant point to *a, b,* and *c* (Fig. 15). Even with open-system fractionation (O'Hara, 1977) in which the crustal magma chamber is periodically refilled with an aliquot of primary magma, periodic injection of the primary magma generated at 10 kbar into the fractionating magma chamber (*a-b-c*) will produce basaltic compositions that project to the silica-rich (right-hand) side of the olivine subtraction line drawn from the 10-kbar pseudoinvariant point. Similarly, fractionation within the mantle will produce basalts lying further to the silica-rich side of this olivine subtraction line because combinations of the fractionating phases (Ol, Opx, Cpx, Gar, Sp) lie to the silica-poor side of the pseudoinvariant point. The majority of mid-ocean ridge basalts (>80%) lie significantly to the silica-poor side of the olivine subtraction line drawn from the 10-kbar pseudoinvariant point, and cannot be produced from primary magmas generated at these low pressures.

Even though some mid-ocean ridge basalts project near the 10-kbar pseudoinvariant point and could have been derived by melting at 10 kbar or less, the main controversy in the discussion of whether mid-ocean ridge basalts are primary melts or the end product of extensive fractionation centers on the origin of the comparatively rare olivine-phyric basalts, such as FAMOUS basalt 527-1-1. These basalts have phenocrysts of Fo_{87} and low incompatible-element (e.g., Zr, Ti, Y) abundances, and have not equilibrated to the low-pressure olivine + plagioclase ± clinopyroxene cotectics. In order to generate these comparatively primitive mid-ocean ridge basalts lying at the silica-poor end of the basalt cluster, melting in the mantle must occur at substantially higher pressures than suggested by Presnall *et al.* (1979). The experimental results in Fig. 14 indicate that NT-23 is either a primary melt generated at 25 kbar or the end product of a primary melt that has been generated at higher (>25 kbar) pressures but has subsequently equilibrated to the 25-kbar pseudoinvariant point. Regardless of which interpretation for the origin of NT-23 is preferred, the compositions of primitive basalts such as 527-1-1 suggest that they have been derived by ~25% olivine fractionation from a high-MgO basalt magma whose final pressure of equilibration with the mantle is 25–30 kbar (Fig. 15). Open-system fractionation, in which pulses of this high-MgO basalt are periodically injected into the base of the crustal magma chamber, will generate complex mixing-fractionation cycles that result in a spectrum of mid-ocean ridge basalt compositions that cluster near the 1-atm olivine + plagioclase ± clinopyroxene cotectics (O'Hara, 1977; Elthon, 1980).

These results are in agreement with previous experimental studies on oceanic basalts (e.g., Kushiro, 1973; Fujii and Kushiro, *Year Book 76,* 461–465; Bender *et al.,* 1978; Green *et al.,* 1979), which indicate that the orthopyroxene volume lies close to the silica-rich end of the basalt cluster at ~7.5 kbar but

is significantly displaced from the silica-poor end at higher pressures. As a consequence, melting at 25–30 kbar is required in order to generate primary high-MgO melts that will fractionate to mid-ocean ridge basalts such as 527-1-1 by open- or closed-system fractionation processes.

References

Bender, J. F., F. N. Hodges, and A. E. Bence, Petrogenesis of basalts from the project FAMOUS area: experimental study from 0 to 15 kbars, *Earth Planet. Sci. Lett., 41,* 277–302, 1978.

Blanchard, D. P., J. M. Rhodes, M. A. Dungan, K. V. Rodgers, C. H. Donaldson, J. C. Brannon, J. W. Jacobs, and E. K. Gibson, The chemistry and petrology of basalts from Leg 37 of the Deep Sea Drilling Project, *J. Geophys. Res., 81,* 4231–4246, 1976.

Boyd, F. R., and J. L. England, Apparatus for phase equilibrium measurements at pressures up to 50 kilobars and temperatures up to 1750°C, *J. Geophys. Res., 65,* 741–748, 1960.

Bryan, W. B., and J. G. Moore, Compositional variation of young basalts in the Mid-Atlantic Ridge rift valley near 36°49'N., *Geol. Soc. Amer. Bull., 88,* 556–570, 1977.

Clarke, D. B., Tertiary basalts from Baffin Bay: possible primary magma from the mantle, *Contrib. Mineral. Petrol., 25,* 203–224, 1970.

Elthon, D., High magnesia liquids as the parental magma for ocean floor basalts, *Nature, 278,* 514–518, 1979.

Elthon, D., The petrology of the Tortuga ophiolite complex, Chile: implications for igneous and metamorphic processes at oceanic ridges, unpublished Ph.D. thesis, Columbia University, 1980.

Frey, F. A., W. B. Bryan, and G. Thompson, Atlantic Ocean floor: geochemistry and petrology of basalts from Legs 2 and 3 of the Deep Sea Drilling Project, *J. Geophys. Res., 79,* 5507–5527, 1974.

Gansser, A., V. J. Dietrich, and W. E. Cameron, Paleogene komatiites from Gorgona Island, *Nature, 278,* 545–546, 1979.

Green, D. H., W. O. Hibberson, and A. L. Jaques, Petrogenesis of mid-ocean ridge basalts, in *The Earth: Its Origin, Structure, and Evolution,* M. W. McElhinney, ed., Academic Press, New York, pp. 265–299, 1979.

Kushiro, I., Origin of some magmas in oceanic and circumoceanic regions, *Tectonophysics, 17,* 211–222, 1973.

Melson, W. G., T. L. Vallier, T. L. Wright, G. Byerly, and J. Nelen, Chemical diversity of abyssal volcanic glass erupted along Pacific, Atlantic, and Indian Ocean seafloor spreading centers, in *The Geophysics of the Pacific Ocean Basin, Geophys. Monogr. Amer. Geophys. Union, 19,* 351–367, 1976.

O'Hara, M. J., Are ocean floor basalts primary magmas? *Nature, 220,* 683–686, 1968.

O'Hara, M. J., Geochemical evolution during fractional crystallization of a periodically refilled magma chamber, *Nature, 266,* 503–507, 1977.

Presnall, D. C., J. R. Dixon, T. H. O'Donnell, and S. A. Dixon, Generation of mid-ocean ridge tholeiites, *J. Petrology, 20,* 3–35, 1979.

Walker, D., T. Shibata, and S. E. DeLong, Abyssal tholeiites from the Oceanographer Fracture Zone, *Contrib. Mineral. Petrol., 70,* 111–125, 1979.

Experimental Studies of Magnetite in Calc-Alkaline Rocks

E. F. Osborn and S. A. Rawson

In the formation of subalkaline volcanic rock series by fractional crystallization, the presence or absence of magnetite as a precipitating phase is of critical importance in determining compositional trends of the magma (Osborn, 1959, 1979). This conclusion has been based principally on an examination of the influence of oxygen partial pressure on fractional crystallization paths in the model system Mg_2SiO_4-FeO-Fe_2O_3-SiO_2 and further substantiated by results of studies of the systems Mg_2SiO_4-FeO-Fe_2O_3-$CaAl_2Si_2O_8$-SiO_2 (Roeder and Osborn, 1966) and Mg_2SiO_4-FeO-Fe_2O_3-$NaAlSi_3O_8$-$CaAl_2Si_2O_8$-SiO_2 (Eggler and Osborn, 1980). To learn more about the role of magnetite in volcanic rock suites, studies have been made of the composition of magnetite as it occurs in the rocks, and of synthetic magnetite formed experimentally in these same rock compositions, in equilibrium with liquid in sealed capsules at total pressures of 1 and 10 kbar (Osborn *et al., Year Book 78,* 475–481). Five rock suites were used in the experimental studies: calc-alkaline suites from Parícutin, Cascades, and Santorini, consisting of basalts and basaltic andesites; and tholeiite suites from the Galápagos

TABLE 8. Results of Experiments on Magnetite in Calc-Alkaline Rocks

Rock Specimen*	Run No.	Composition of Magnetite†						H_2O, wt %	*P*, kbar	*T*, °C	Time, hr	Capsule Composition	Material in Outer Capsule	Phases Present‡
		TiO_2	Al_2O_3	Cr_2O_3	Fe_2O_3	FeO	MgO							
P-51W19		11	2.4	4.6	39	39	2.1							
	25							2	10	1175	8	Ag-Pd§	NiO	mt + ol + gl
	22	8.2	5.1	0.2	44	31	3.9	2	10	1300	1	Pt-Au‖	NiO	mt + pl + cpx + opx + gl
										1150	7			
	24	10.1	3.8	0.1	40	32	4.1	2	10	1150	8	Ag-Pd	NiO	mt + pl + cpx + gl
	23	6.6	4.2	0.5	48	30	3.4	4	10	1300	1	Pt-Au	NiO	mt + cpx + gl
										1150	7			
	26							2	10	1150	8	Ag-Pd	Ni + NiO + H_2O	gl
	27	4.6¶						2	1	1110	8	Ag-Pd	Ni + NiO + H_2O	mt + pl + px + gl
P-55478		7	2.9	14	36	32	3.2							
	26							2	10	1175	8	Ag-Pd	NiO	mt + ol + pl + px + gl
	24	6.5	5.5	0.1	47	31	3.5	2	10	1300	1	Pt-Au	NiO	mt + pl + cpx + opx + gl
										1150	7			
	25	**						2	10	1150	8	Ag-Pd	NiO	mt + pl + px + gl
	27							2	10	1150	8	Ag-Pd	Ni + NiO + H_2O	ol + gl
	28	1.7	7.8	1.2	56	20	8.6	2	1	1110	8	Ag-Pd	Ni + NiO + H_2O	mt + pl + px + gl
S-85		14	2.6	0.1	34	44	0.6							
	20							2	10	1175	8	Ag-Pd	NiO	mt + cpx + gl
	19	7.5	4.0	0.02	48	34	3.5	2	10	1150	8	Ag-Pd	NiO	mt + cpx + pl + gl
	21							2	10	1150	8	Ag-Pd	Ni + NiO + H_2O	gl
	22	1.6¶						2	1	1110	8	Ag-Pd	Ni + NiO + H_2O	mt + pl + gl

* Specimen P-51W19, erupted from Paricutin in March 1943 and assumed to have essentially the same composition as a specimen erupted at the same time and listed as No. 2 by Wilcox (1954, p. 294, Table 2). Specimen P-55478, erupted from Paricutin in March 1944; analysis listed in *Year Book 65* (264, Table 5). Specimen S-85 from Santorini; analysis listed in Nicholls (1971, p. 83, Table 3, No. 9).

† Composition determined by electron microprobe.

‡ Abbreviations: mt, magnetite; ol, olivine; pl, plagioclase; opx, Ca-poor pyroxene; cpx, Ca-rich pyroxene; px, pyroxene not analyzed; gl, glass.

§ Composition of Ag-Pd capsules used was 50Ag-50Pd.

‖ Composition of Pt-Au capsules used was 95Pt-5Au.

¶ Magnetite crystals too small for quantitative analysis. Figure for TiO_2 is qualitative estimate.

** Magnetite too small for microprobe analysis.

Islands and Iceland, each consisting of a series of compositions ranging from olivine tholeiite and tholeiite through ferrobasalt and icelandite to siliceous trachyte. Principal findings reported by Osborn *et al. (Year Book 78)* were: (1) Magnetite in the rocks is titaniferous, is generally lower in TiO_2 in the calc-alkaline than in the tholeiitic rocks, and ranges in TiO_2 content from a low of 7% for magnetite in one of the Paricutin specimens to a high of 25% for the magnetite in both a Galápagos and an Iceland specimen. (2) In the experimental runs at 1 kbar total pressure, magnetite is a liquidus or near-liquidus phase in all these basalt and basaltic andesite compositions, and the TiO_2 content of the magnetite is very low, generally about 1% for the calc-alkaline compositions and about 3% for the tholeiitic compositions. (3) In the experimental runs at 10 kbar, in which samples of the calc-alkaline rocks were used, magnetite is not a liquidus or a near-liquidus phase, occurring 30° to 40° below the liquidus temperature, and its composition, with only one exception, is almost identical with that at 1 kbar. In marked contrast, magnetite in the Galápagos and Iceland specimens is a liquidus phase at 10 kbar, and the TiO_2 content is high, ranging from 10% to 18%—values intermediate between the TiO_2 content of the magnetite at 1 kbar and that of the natural magnetite (Osborn *et al., Year Book 78,* 477, Table 4).

These results point to the conclusion that, for the Galápagos and Iceland rocks, the TiO_2 content of the magnetite is related to the pressure at which the magnetite composition equilibrated with the liquid, being higher the higher the pressure. Magnetite is perceived as having formed in the Galápagos and Iceland tholeiitic magmas at a pressure greater than 10 kbar. For the calc-alkaline rocks, however, some factor in addition to pressure seems to be involved to account for the low TiO_2 content of magnetite in the 10-kbar runs and for the absence of magnetite as a near-liquidus phase at a pressure of 10 kbar. This factor is believed to be water content. Whereas the Galápagos and Iceland tholeiitic magmas are presumed to have been essentially dry, the water content of the calc-alkaline magmas may have been great enough that liquidus phase relations at 10 kbar are significantly different from those of the dry rock compositions.

To learn the effect of H_2O on the phase relations and composition of magnetite in the calc-alkaline rocks, studies have been in progress in which additions of 2% and 4% H_2O have been made for runs at 10 kbar and 1 kbar. The charge, consisting of the powdered rock with H_2O added, was contained in a sealed capsule of either 50Ag-50Pd or 95Pt-5Au, inside an outer sealed Pt capsule containing either NiO or Ni + NiO + H_2O. In examinations of the material in the outer capsule after the runs, no Ni was found where NiO alone was originally present, and all three phases were present with the NNO buffer. The oxygen-fugacity (f_{O_2}) of the charges during the runs was therefore approximately at or higher than that of the NNO buffer. Runs were made in the gas-media, high-pressure apparatus of Yoder (1950), in which the furnace assembly and sample capsules are fully immersed in water-pumped, purified argon.

Results obtained for three specimens of basaltic andesite used in the previous studies (Osborn *et al., Year Book 78,* 475–481), two from Paricutin and one from Santorini, are summarized in Table 8. The 10-kbar runs at 1150°C were made by approaching this temperature from both lower and higher temperatures. In the latter case, the charge was first held for 1 hr at 1300°C to produce a homogeneous liquid, and then the temperature was lowered for a 7-hr run at 1150°. From the data for P-51W19, it will be seen that the composition of magnetite and phase relations are similar for both temperature

schedules and for 2% and 4% H_2O, except that plagioclase is present as a phase at 2% H_2O and absent at 4% H_2O.

The TiO_2 content of the magnetite is of particular interest. It will be noted (Table 8) that for P-55478, the TiO_2 content of the natural magnetite and that of the synthetic magnetite from the 10-kbar run are very similar (7% and 6.5%, respectively), whereas the TiO_2 content of synthetic magnetite from the 1-kbar run is only 1.7%. For P-51W19 and S-85, the TiO_2 content of magnetite from the 10-kbar runs is lower than that of the natural magnetite, but is actually greater than that for P-55478, ranging from 6.6% to 10.1%, and again is considerably higher than the value from the 1-kbar runs. The results, therefore, where H_2O is a component added to the dry calc-alkaline rock specimens, are similar to those for the Galápagos and Iceland tholeiites without a water addition, i.e., the TiO_2 content of the magnetite phase is much higher at 10 kbar than at 1 kbar, approaching the TiO_2 content of the natural magnetite in the rock specimens. Additionally, magnetite was found to be a liquidus or near-liquidus phase for the calc-alkaline specimens in the runs at 10 kbar with H_2O present.

Conclusions that can be drawn from these findings, applicable to basaltic andesites erupted at Parícutin and Santorini, are as follows: (1) Water was present to a small but significant extent in the calc-alkaline magmas at the time of formation of the magnetite and the megaphenocrysts now in the rocks. This conclusion follows from the data for runs at 10 kbar and 2% H_2O, in which magnetite has a high content of TiO_2 and is a near-liquidus phase along with crystals of silicates. These compositional and phase relations are similar to those for natural magnetite in the rock specimens, but are unlike those for synthetic magnetite in runs at 10 kbar with no H_2O present. The water content was not greater than about 2%, inasmuch as plagioclase is a megaphenocryst in the rocks and is present as a near-liquidus phase in experimental runs at 10 kbar and 1150°C with 2% H_2O present, but is absent at 4% H_2O. The microphenocrysts present in the rocks formed as the magma, in approaching the surface, lost water. (2) The pressure at the time of formation of magnetite and the megaphenocrysts was in the range 10–15 kbar, as indicated by the TiO_2 content of the magnetite. (3) With a water content of 1–2% and a pressure of 10 kbar, the magma would have been at a temperature of approximately 1200°C on the basis of the data of Table 8. From temperature measurements at the volcano, Zies (1946) estimated that the temperature of the Parícutin magma on eruption was also approximately 1200°C. (4) The f_{O_2} of the magma was greater than that of the NNO buffer. Evidence for this is along two lines. First, no Ni formed by partial reduction of NiO for any of the runs where NiO alone was initially present in the outer capsule; this result indicates that the f_{O_2} of the charge was at least as high as that of the NNO buffer. Second, when NNO buffer was used, liquidus temperatures were lower than with only NiO in the outer capsule; hence a higher f_{O_2} for the rock specimens than that of the NNO buffer is indicated, inasmuch as it is usual for liquidus temperatures of phase assemblages in iron silicate systems to be lower at lower oxygen fugacities (e.g., Muan and Osborn [1956] and Hamilton *et al.* [1964]). The presence or absence of magnetite as a liquidus phase in basaltic magma is critically dependent on f_{O_2}, as shown by Hamilton *et al.* (1964, p. 36, fig. 6). That the f_{O_2} of the Paricutin basaltic andesite magma was greater than that of the NNO buffer may be an explanation of the fact that magnetite was found to be a liquidus phase in the present studies with only NiO in the outer envelope, but was not found to be a liquidus phase

in earlier studies of a Paricutin andesite where the lower oxygen fugacities of the NNO and QFM buffers were used (Eggler, 1972).

References

Eggler, D. H., Water-saturated and undersaturated melting relations in a Parícutin andesite and an estimate of water content in the natural magma, *Contrib. Mineral. Petrol., 34,* 261–271, 1972.

Eggler, D. H., and E. F. Osborn, Experimental studies of the system MgO-FeO-Fe_2O_3-$NaAlSi_3O_8$-$CaAl_2Si_2O_8$-SiO_2—a model for subalkaline magmas, *Amer. J. Sci.,* in press, 1980.

Hamilton, D. L., C. W. Burnham, and E. F. Osborn, The solubility of water and effects of oxygen fugacity and water content on crystallization in mafic magmas, *J. Petrology, 5,* 21–39, 1964.

Muan, A., and E. F. Osborn, Phase equilibria at liquidus temperatures in the system MgO-FeO-Fe_2O_3-SiO_2, *J. Amer. Ceram. Soc., 39,* 121–140, 1956.

Nicholls, I. A., Petrology of Santorini volcano, Cyclades, Greece, *J. Petrology, 12,* 67–119, 1971.

Osborn, E. F., Role of oxygen pressure in the crystallization and differentiation of basaltic magma, *Amer. J. Sci., 257,* 609–647, 1959.

Osborn, E. F., The reaction principle, in *The Evolution of the Igneous Rocks: Fiftieth Anniversary Perspectives,* H. S. Yoder, Jr., ed., Princeton University Press, pp. 133–169, 1979.

Roeder, P. L., and E. F. Osborn, Experimental data for the system MgO-FeO-Fe_2O_3-$CaAl_2Si_2O_8$-SiO_2 and their petrologic implications, *Amer. J. Sci., 264,* 428–480, 1966.

Wilcox, R. E., Petrology of Parícutin volcano, Mexico, *U.S. Geol. Surv. Bull., 965-C,* 281–353, 1954.

Yoder, H. S., Jr., High-low quartz inversion up to 10,000 bars, *Trans. Amer. Geophys. Union, 31,* 827–835, 1950.

Zies, E. G., Temperature measurements at Parícutin volcano, *Trans. Amer. Geophys. Union, 27,* 178–180, 1946.

The Complementary Abyssal Basalt Glasses of Juan de Fuca and the "Galápagos Spreading Center"

Felix Chayes

Byerly *et al.* (1975) have pointed out that the commonest rock specimens recovered from the ocean floors are pillow lavas on most of which there is a glassy outer selvage. They have argued cogently that "portions of the glassy rim often remain unaltered and . . . are the material most representative of the primary igneous chemistry." The recovery of extremely siliceous, nonbasaltic glasses in dredge hauls from the "Galápagos Spreading Center," first reported by Melson *et al.* (1975), is now well known, but several other interesting compositional anomalies in the dominantly basaltic glasses of this part of the ocean floor seem to have escaped attention.

Briefly, glasses collected there are often exceedingly rich in iron, and in the basaltic ones the sample distributions of Ca, Mg, Al, Ti, P, and Fe are markedly bimodal, the central frequency minimum in each falling near the maximum for other abyssal glass suites. These relations are summarized in Fig. 16, in which the upper half of each histogram shows the distribution of one of the essential components in 250 specimens of glass collected from the Galápagos Center, the lower half that of the same component in 250 glass specimens from the Juan de Fuca ridge in the northeastern Pacific. The scales are common for the upper and lower half of each diagram. The Juan de Fuca suite is used for comparison because the number of available analyses is the same as for the Galápagos suite and, except for iron, the mean values for Juan de Fuca are about like those for other abyssal glass suites. (Like most Pacific oceanic volcanic materials, the Juan de Fuca glasses are conspicuously richer in Fe than their Atlantic and Indian Ocean counterparts.)

The extreme peakedness of some of the Juan de Fuca sample distributions is perhaps partly attributable to sampling conditions. Of the 250 Juan de Fuca specimens for which analyses are available, 229 are from dredge hauls distant from each other by less than 0.5° of latitude and 1° of longitude,

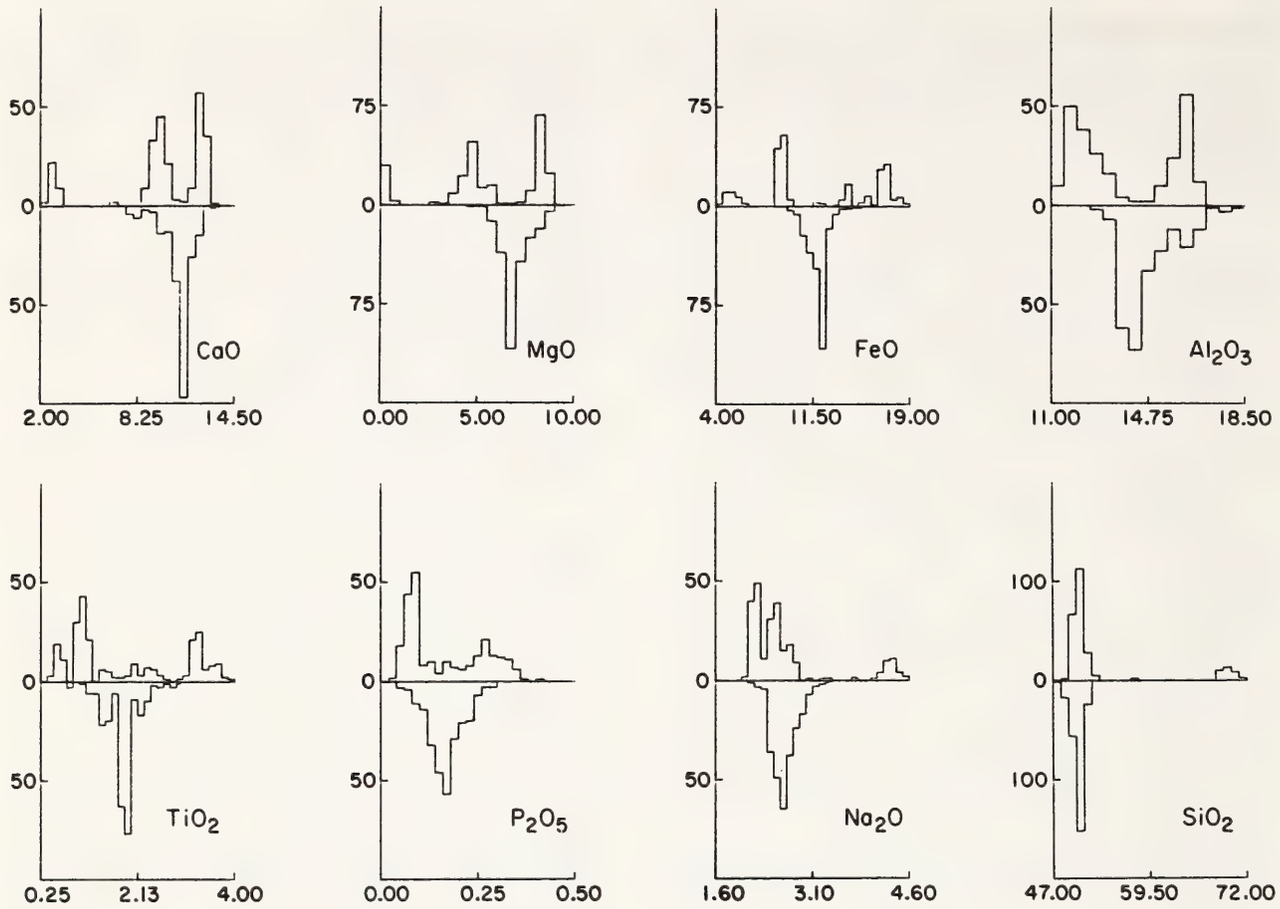


Fig. 16. Distributions of some essential components in specimens of abyssal glass from the "Galápagos Spreading Center" (upper half of each histogram) and Juan de Fuca ridge (lower half of each histogram). Data from Melson *et al.* (1975).

and 130 are from *one* of the hauls. The Galápagos sampling is also spotty, 205 of the 250 specimens having been found in just three dredge hauls; all the highly siliceous specimens occurred in one of these and all the exceedingly ferriferous glasses in another.

The sampling is thus inadequate to support far-reaching petrogenetic inference, but it is worth noting that in abyssal glasses collected to date from the Galápagos Center

1. Al varies inversely with Ca, Mg, Fe and Ti.

2. The basalt glasses richest in Fe are also richest in Ti.

3. The highly siliceous glasses are far too poor in alkalies and too rich in CaO to warrant their description as either rhyolite or pantellerite. They most nearly satisfy the definitions of siliceous dacite or rhyodacite, but are much richer in Fe and poorer in Mg, K, and Al than either. They are richer in Ti and Fe than most terrestrial glasses of similar Si content.

4. None of the Galápagos abyssal glasses is normatively feldspathoidal even if all Fe is considered bivalent for the purpose of the calculation. (The marked inverse variation of Fe and Al in the basalt glasses suggests that much of the Fe may be trivalent, but no data concerning the oxidation state of Fe in them appear to have been published.)

5. The sample distribution of SiO_2 in the Galápagos abyssal glasses is sharply bimodal; only three of the 250 analyses lie in the range $53 < SiO_2 <$

68 although there are 33 in which 68 < SiO_2 < 72 and 214 in which 48 < SiO_2 < 53.

6. The clearly bimodal distribution of CaO, MgO, Al_2O_3, TiO_2, and FeO in *basalt* glasses, however, is entirely lacking in the SiO_2 distribution. All the basalt glasses seem to have about the same SiO_2 content, and the SiO_2 distribution for basaltic Galápagos glasses is very like that for those of Juan de Fuca and other suites of abyssal glasses.

The data used here are from the catalogue published by Melson *et al.* (1975) but were made available to the writer in punched card form by W. B. Bryan. (A much larger composite file of holdings at Woods Hole and the Smithsonian Institution is now in preparation by Melson and Bryan.) The writer is grateful for NSF support of computations on which Fig. 16 is based.

References

Byerly, G., W. G. Melson, J. A. Nelen, and E. Jarosewich, Abyssal basaltic glasses as indicators of magma composition, *Mineral. Sci. Invest., 1974-1975, Smithson. Contrib. Earth Sci.*, No. 19, 22-30, 1975.

Melson, W. G., G. R. Byerly, J. A. Nelen, T. O'Hearn, T. L. Wright, and T. Vallier, A catalog of the major element chemistry of abyssal volcanic glasses, *Mineral. Sci. Invest., 1974-1975, Smithson. Contrib. Earth Sci.*, No. 19, 31-60, 1975.

Basalts and Basanites

Felix Chayes

The distributions of 8280 analyses of Cenozoic rocks called basalt, andesite, dacite, and basanite in the primary source references were plotted in Q'A'P'F', the suggested normative analogue (see above, p. 232) of the modal classification proposed by the IUGS Subcommittee on Systematics in Petrology. One of the major results of this exercise was the discovery that Cenozoic lavas described in the literature as basalt are often much more strongly undersaturated with respect to SiO_2 than is suggested by many text and reference definitions. Specifically, if the QAPF field boundaries proposed by the Commission (see, for instance, Streckeisen, 1976) are superposed directly on Q'A'P'F', nearly two thirds (64.3%) of the analyses plotting in the fields reserved for basanite and tephrite are of rocks described in the literature as basalt.

The Commission's position with regard to the distinction between basalt and basanite is compatible with that taken in most modern texts and references, and the great bulk of analyses used in the study reported here are of very recent vintage. Are the standard definitions unrealistic or does the replacement of QAPF by Q'A'P'F' introduce a major bias? The latter possibility must be carefully considered because if both sets of coordinates can in fact be determined they will in general differ.

Space does not permit a detailed examination of this question but the average compositions reported in Table 9 provide conclusive evidence that in this case the bias introduced by use of the normative analogue must be very small indeed. Cenozoic *ne*-nor-

TABLE 9. Average Compositions of *ne*-Normative Basalt and Basanite

	All		Filtered*	
	Basalt	Basanite	Basalt	Basanite
SiO_2	45.20	43.84	45.89	44.31
Al_2O_3	14.70	14.28	14.87	14.24
Fe_2O_3	4.33	4.51	2.78	3.12
FeO	7.29	7.16	8.66	8.75
MgO	8.19	8.70	8.48	9.30
CaO	10.17	10.70	10.11	10.53
Na_2O	3.47	3.55	3.38	3.44
K_2O	1.56	1.81	1.35	1.57
TiO_2	2.62	2.74	2.64	2.83
P_2O_5	0.64	0.65	0.58	0.61
Analyses	1673	516]	628]	151]

* Includes only analyses in which H_2O < 2.5, K_2O < 5.5, Na_2O < 5.5, Fe^3/Fe^2 < 1, lc = 0.

mative rocks called basanite and basalt are so similar in average composition that there is no reason to suppose their modes—if averages had modes in the sense required for classification by QAPF—could be very different.

In actual usage the relation between basalt and basanite seems to be hierarchical, not exclusive. In a realistic classification, basanite would be considered a variety of alkali basalt. The basanite-alkali basalt relation is in this respect very like the dacite-andesite relation, i.e., rocks that are called basanite (dacite) by some petrologists are called basalt (andesite) by most petrologists.

A full report of the work summarized here and in the file note referred to above has been submitted to the Commission. The data used in this work were drawn from data base RKOC76 by information system RKNFSYS; the writer is grateful for National Science Foundation support of the rather extensive computation this required.

Reference

Streckeisen, A., Classification of the common igneous rocks by means of their chemical composition, *Neues Jahrb. Mineral. Monatsh.*, 1–15, 1976.

A World Data Base for Igneous Petrology

Felix Chayes

Background information on this work and the project of the International Geological Correlation Program of which it is a part is given in *Year Book 78* (pp. 484–485 and associated bibliography). The work falls into four categories: (1) transfer of data from the world literature to coding sheets designed by the project, (2) movement of data from coding sheets to machine-readable form, (3) generation of a data base from the card image files accumulated in step 2, and (4) development of software for exploitation of the base, and of procedures for making it available to the scientific public.

During the report year the work of steps 1 and 2, above, was brought to a level at which it becomes practical to resume active work on 3 and necessary to start the detailed planning of 4.

The most difficult and time-consuming part of the entire operation is the work of step 1, which is done entirely by volunteers who accept responsibility for covering specific rock types, areas, or publications. More than 40 contributors, working either as individuals or as members of one of the national groups of the project, are now actively engaged in this work.

With a much improved version of the conversational program described in *Year Book 78*, the previously forbidding task of moving the data from coding sheets to machine-readable form has been reduced to manageable dimensions. More than 3500 specimen descriptions are now stored in card image files. Similar processing capability has been developed in the Turkish and Spanish centers of the project, a second U.S. facility is now active, and individual U.S. contributors are being encouraged to undertake this step for themselves. The systematic scan of major domestic literature by the U.S. group of the project is about a third complete. Many data collections for specific areas or rock types, domestic and foreign, have been received and processed.

The practical problem is to maintain a level of activity in step 2 sufficient to retain the interest and enthusiasm of those contributing to the work of step 1 while at the same time bringing steps 3 and 4 to a stage at which it will be possible to find a permanent, stably funded home for the entire project. As a result of progress made during the report year, this now seems entirely feasible.

An Effect of Closure Correlation on Classification by Ranges

Felix Chayes

Multiple ranges of compositional variables are often used in petrographic definition and classification. If distributions of the individual variables are known and their independence is assumed, the probability that a specimen will conform to a set of range specifications is readily computed. If the variables are compositional, however, they cannot be independent because they are members of a closed array, and in petrographic context their distributions will almost always be unknown. The effects of multiple range restrictions on petrographic data are nevertheless of considerable interest, both practically and in comparison with what would be anticipated for normal independent variables. An appraisal of the practical aspects of multiple range classification, with an example based on a large collection of analyses of abyssal basalt glasses, has been submitted for publication elsewhere. Here attention is centered on the theoretical problem.

In the simplest form of multiple range classification a specimen is to be rejected if the content of any variable in it is outside its specified acceptance range. If acceptance ranges are centered about the modes of unimodal variables, the fact that one variable in a particular specimen lies outside its specified acceptance range increases the probability that this will be true also of other correlated variables in the same specimen. By associating outliers with each other in this fashion, correlation tends to increase the number of acceptable specimens—i.e., those free of outliers—over what would be expected if the variables involved were independent.

Data used in the following example were drawn from a file of analyses of abyssal glasses made available to the writer by W. B. Bryan. In this file specimens are not identified by name, so a criterion proposed to the IUGS Commission on Systematics in Petrology, namely, that silica content not exceed 52.5%, was used to separate basaltic from other abyssal glasses. After exclusion of all analyses with more than 52.5% silica, and of a few extraordinarily ferriferous specimens from the "Galápagos Spreading Center," there remained 1584 analyses, almost every one of which would have been identified by almost any petrologist as that of a basalt. The major contributors to the variance of this array are SiO_2, Al_2O_3, Fe_2O_3, TiO_2, CaO, MgO, and Na_2O. The variances of K_2O and P_2O_5 are scarcely above the trace level and so cannot exert appreciable influence on closure effects between major components. For all combinations of $i \leq 7$ of the major components, the average frequencies of analyses rejected because at least one component lay outside the range

$$\bar{x}_k - s_k < X_k < \bar{x}_k + s_k$$

were found, where X_k denotes the value of component k in a specimen, $\bar{x}_k$ and s_k its sample mean and standard deviation, respectively. These average "rejection" frequencies are listed in the column headed $f(r)$ in Table 10. In the column headed $E(r)$ are listed the rejection frequencies expected for indepen-

TABLE 10. Expected and Observed Acceptance Frequencies*

i	$f(r)$	$E(r)$	d
1	479.3	502.8	−0.0467
2	747.0	845.9	−0.1169
3	915.4	1080.2	−0.1526
4	1030.8	1240.1	−0.1688
5	1115.8	1349.3	−0.1731
6	1179.7	1423.8	−0.1714
7	1230	1474.6	−0.1659

* See text for definitions of column captions.

dent normal variables with means and variances like those in the sample. The argument of the last column of the table is $d = [f(r) - E(r)]/E(r)$, the ratio of the difference between observed and expected rejection frequencies to the expected rejection frequency. In the current example, d is negative for all i. For $i = 1$, it is of course very small, but with increase in i it increases abruptly and then levels off at approximately $-1/6$; that is to say, for $i > 2$ about a sixth (on average, 0.1665) of the specimens that would be rejected if the variables were independently normal are in fact accepted.

It is certainly a startling coincidence that this average value of d is also the value of the correlation generated by closure of an open array of seven random variables homogeneous in mean and variance, the governing relation for such an i-variable array (see, for instance, Chayes, 1971) being that $\rho \cong -1/(i - 1)$. Although an array formed by closure of independent open variables homogeneous in mean and variance would itself be homogeneous in mean and variance, there are order-of-magnitude differences in each of these statistics in the actual closed array, as shown in Table 11.

TABLE 11. Means and Variances of Major Components in 1584 Specimens of Abyssal Basalt Glasses*

Component	Mean	Variance
SiO_2	50.55	0.6724
Al_2O_3	15.27	0.8836
TiO_2	1.48	0.1936
FeO†	10.28	1.8225
MgO	7.55	0.8836
CaO	11.52	0.8649
Na_2O	2.57	0.1764

* Raw data courtesy of W. B. Bryan.
†Total Fe as FeO.

Reference

Chayes, F., *Ratio Correlation, A Manual for Students of Petrology and Geochemistry*, University of Chicago Press, 1971.

ULTRAMAFIC NODULES, KIMBERLITE, AND CARBONATITE

Rates of Dissolution of Upper Mantle Minerals in an Alkali-Olivine Basalt Melt at High Pressures

C. M. Scarfe, E. Takahashi, and H. S. Yoder, Jr.

The evidence for an upper mantle of garnet peridotite composition has been extensively reviewed and discussed by Yoder (1976). The dominance of spinel and garnet lherzolites as xenoliths in alkali basalts and kimberlites has been considered important evidence (e.g., Kuno and Aoki, 1970). This viewpoint, however, has been challenged by Kutolin and co-workers on the basis of observations of melt phenomena in ultramafic xenoliths captured by basaltic magmas (Kutolin and Frolova, 1970) and from experimental dissolution studies of mantle minerals in "basalt" melt at 1 atm (Kutolin and Agafonov, 1978). They argued that because of differential dissolution rates, which favor the preservation of olivine at the expense of pyroxenes and garnet or spinel, the mantle sample preserved at the earth's surface may be underrepresented in eclogite and pyroxenites, a conclusion that could lead to a reevaluation of the composition of the upper mantle.

Because of the significance of this conclusion to petrological thought, it was considered important to test their observations on the rates of dissolution of mantle minerals at the high pressures believed to be close to the

pressure or depth of origin of alkali basalts.

Starting Materials and Experimental Methods

The mineralogy, chemistry, and phase relationships of the alkali basalt (KRB) from Oki-Dogo Island, Japan, have been described elsewhere (Takahashi, this Report). Liquid of KRB composition is multiply saturated with olivine, orthopyroxene, and clinopyroxene at 14 kbar and 1275 °C. This result indicates that this was the minimum pressure at which the basalt was last in equilibrium with the major minerals of the upper mantle.

Olivine, orthopyroxene, clinopyroxene, and spinel (Table 12) were separated from a spinel lherzolite xenolith from Boss Mountain, British Columbia (Littlejohn and Greenwood, 1974). Garnet from the Bultfontein Floors was kindly supplied by F. R. Boyd (Boyd and Nixon, 1978). Mineral spheres (0.05–0.10 cm in diameter) were made with the sphere-making device designed by Bond (1951). Spheres were placed in dried powder of KRB at the base of a graphite capsule 10 mm long and 5 mm in diameter.

High-pressure experiments were performed at 12.5, 14, and 20 kbar in a solid-media, high-pressure apparatus (Boyd and England, 1960) with a furnace assembly of 0.75-inch diameter incorporating a graphite heater with a 3° tapered inner wall, which reduces the temperature gradient along the sample to 10 °C (Kushiro, 1976). The piston-out technique was used with a −4% correction for friction. Pressure measurements have an uncertainty of ±1.0 kbar, and temperature measurements, made with Pt-Pt90Rh10 thermocouples, have an uncertainty of ±10 °C. Rapid approach to the desired experimental temperature was facilitated by a programmable controller (Hadidiacos, *Year Book 76*, 664–668), and quench rates were approximately 125 °/sec. Redox conditions during the experiments were within the wüstite field (Thompson and Kushiro, *Year Book 71*, 615–616).

At the termination of each run the charge was quenched and sectioned.

TABLE 12. Starting Materials for Dissolution Experiments

	1*	2	3	4	5	6
SiO_2	47.47	41.07	55.13	52.20	...	42.31
TiO_2	2.43	...	0.05	0.18	0.11	0.81
Al_2O_3	17.15	...	3.70	4.59	44.20	21.68
FeO†	9.25	8.42	5.57	2.49	11.42	10.44
MnO	0.15	0.15	0.14	0.09	0.24	0.38
MgO	8.76	50.09	33.38	16.49	18.91	19.40
CaO	8.03	0.08	0.90	20.92	...	4.75
Na_2O	3.67	...	0.07	1.02	...	0.12
NiO	...	0.39	0.10	...	0.27	...
Cr_2O_3	...	...	0.60	1.10	24.32	0.46
K_2O	1.69	...	...	...	...	...
P_2O_5	0.66	...	...	...	...	...
H_2O^+	0.61	...	...	...	...	...
Total	99.87	100.20	99.64	99.08	99.47	100.35

*1: Alkali olivine basalt, Oki-Dogo Island, Japan (KRB-3). 2: Olivine from xenolith, Boss Mountain, British Columbia (BC 1000). 3: Orthopyroxene (BC 1000). 4: Clinopyroxene (BC 1000). 5: Spinel (BC 1000). 6: Garnet megacryst from Bultfontein Floors.

†Total iron as FeO. Analysis 1 by wet chemistry; analyses 2–6, averages of at least five microprobe analyses.

Sphere diameters before and after each run were measured with a stage micrometer. Because of imperfect sphericity and because of the difficulty of ensuring exposure of the maximum diameter during grinding, a relative uncertainty of ±10% is associated with the measurement of the diameter (hence ±30% volume).

Experimental Results

The results of dissolution experiments are given in Fig. 17. Experiments were performed as a function of time close to the 14 kbar pseudoinvariant point and at pressures of 12.5 and 20 kbar. Temperatures were 40°–70°C above the liquidus (Takahashi, this Report). At 14 kbar, dissolution is faster for clinopyroxene than for olivine, orthopyroxene, and spinel. This differential dissolution behavior is repeated at pressures above and below the 14-kbar pseudoinvariant point where five phases, including garnet, were investigated. At 12.5 and 20 kbar the liquidus phase is, respectively, olivine and clinopyroxene (Takahashi, this Report). The time taken to completely dissolve ~0.05-cm-diameter spheres of clinopyroxene is 60–100 min at 1325°C and 14 kbar. Garnet dissolves rapidly because it is present as a disequilibrium phase at these pressures; however, the data in Fig. 17 suggest that the rate of dissolution decreases with pressure as the stability field of garnet is approached at high pressures. Because of the limited number of data points, the volume vs. time plots were drawn as straight lines as a first approximation (see, for example, discussion in Kretz, 1974).

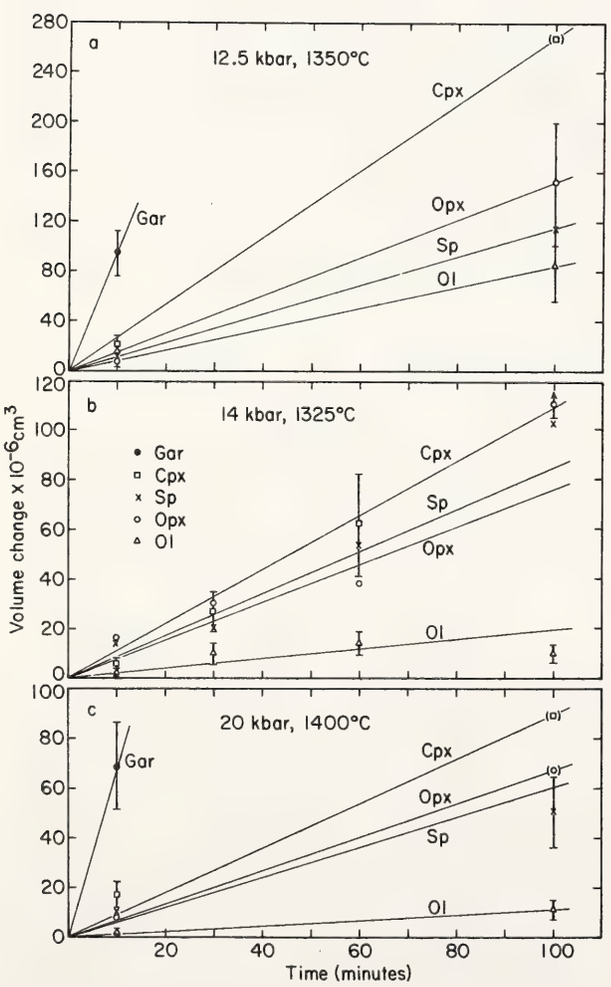


Fig. 17. Results of dissolution experiments at three pressures. Some error bars omitted for clarity. Bracketed data points represent complete dissolution of spheres.

The appearance of a typical charge is shown in Fig. 18. Spheres of olivine, orthopyroxene, clinopyroxene, spinel, and garnet are surrounded by a brown glass. Some fracturing of the charge has occurred during quenching, and a reaction rim consisting of fine-grained pyroxene and spinel is observed around garnet.

Compositional gradients in both glass and spheres were investigated by microprobe analysis. Compositional gradients were absent in the spheres, and only small gradients were present in the glass (Fig. 19). Compositional gradients are more extensive around clinopyroxene and garnet; the greatest changes, however, which occur within 30 μm of the contact, are due to overgrowth effects during quenching.

Discussion

At all three pressures investigated, olivine is the most resistant to dissolution, even though it is not the stable liquidus phase above 14 kbar. Con-



Fig. 18. Polished section of basalt glass containing mineral spheres. Clockwise from top left: garnet, spinel, olivine, and orthopyroxene, with clinopyroxene in the center (20 kbar, 1400°C, 10 min). Spheres ~0.05 cm diameter.

versely, clinopyroxene and garnet dissolve rather rapidly. In order to provide a more complete description of dissolution rates, however, these experiments should be extended to other temperatures, particularly at the 14-kbar pressure of the pseudoinvariant point. Nevertheless, it is believed that whereas temperature changes may modify the absolute rate of dissolution, relative rates of dissolution will remain unchanged (compare for example Figs. 17a and 17b).

In an attempt to understand the reasons for these differential dissolution rates, heat conduction theory was applied to the problem of the dissolution of mineral spheres in basalt melt. On the basis of the analogy of the melting of ice in water (e.g., Ingersol and Zobel, 1948), the temperature at the crystal-melt boundary is assumed to be lower than the average temperature of the melt. The temperature distribution within the crystal and melt is described by

$$\frac{\partial T}{\partial t} = \frac{K}{\rho C_p}\left(\frac{\partial^2 T}{\partial r^2} + \frac{2}{r}\frac{\partial T}{\partial r}\right), \qquad (1)$$

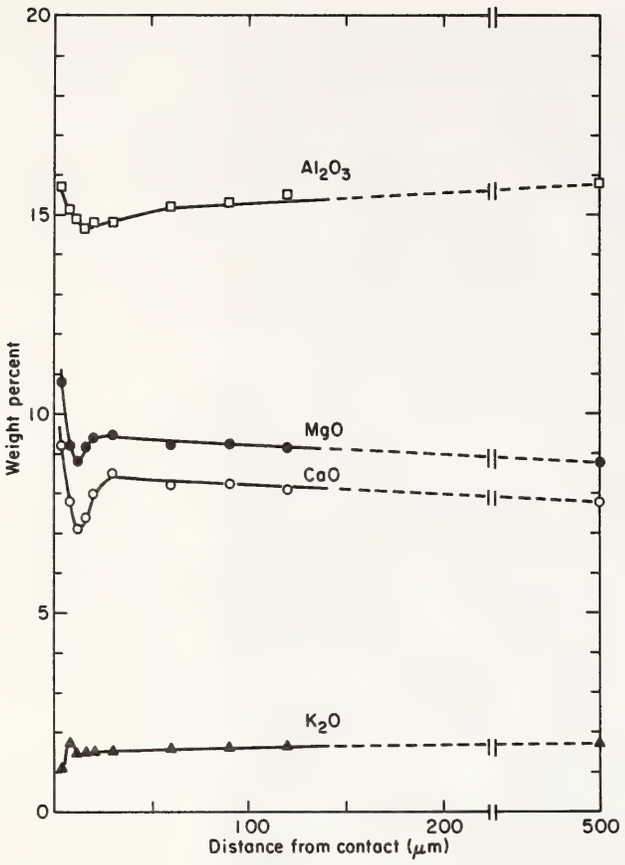


Fig. 19. Example of microprobe line traverse in glass surrounding clinopyroxene sphere (20 kbar, 1400°C, 10 min).

where T is the temperature (°C), t is the time (sec), r is the radial distance from the center of the sphere (cm), ρ is the density (g/cm^3), C_p is the specific heat (cal/g deg), and K is the thermal conductivity (cal/sec cm deg). Because the crystal is small (~0.05 cm in diameter) and has a large thermal diffusivity (~10^{-3} cm^2/sec; Kawada, 1966), the temperature distribution inside the crystal will be homogenized within a second (see also Carslaw and Jaeger, 1947, fig. 22). The equation of heat conservation at the crystal-melt boundary,

$$4\pi r^2 K\left[\left(\frac{dT}{dr}\right)_{\text{melt}} - \left(\frac{dT}{dr}\right)_{\text{crystal}}\right] = \Delta H \rho 4\pi r^2 \left(\frac{dr}{dt}\right)_{\text{boundary}}, \quad (2)$$

therefore, can be simplified to

$$\left(\frac{dr}{dt}\right)_{\text{boundary}} = \frac{K}{\Delta H \rho}\left(\frac{dT}{dr}\right)_{\text{melt}}, \quad (3)$$

where (dr/dt) is the radial velocity of dissolution of the crystal (cm/sec), and ΔH is the latent heat of fusion of the crystal (cal/g). The relative rates of dissolution should therefore be inversely proportional to the relative magnitudes of ΔH normalized by volume ($\Delta H \rho$ cal/cm^3),* provided that the temperature gradient in the melt surrounding each crystal is a constant. When ΔH values calculated from phase diagrams are used (Mg_2SiO_4, 930 cal/cm^3; $MgSiO_3$, 620 cal/cm^3; $CaMgSi_2O_6$, 520 cal/cm^3; Ghiorso and Carmichael, 1980), it can be seen that there is indeed an inverse correlation between ΔH of fusion and the results of dissolution experiments reported in this paper.

There is a similarity between the present results at high pressures and the conclusions of Kutolin and Agafonov (1978) at 1 atm. It is worth noting, however, that the composition of their "basaltic" melt contained 20% normative nepheline and actually classifies as a phonolite. It should also be remembered that at 1 atm olivine is most likely the stable liquidus phase and would therefore be expected to be more stable than the other phases in their experiments.

It is unlikely that dissolution rates reported here are applicable to partial melting of peridotite in the upper man-

*According to Weill *et al.* (1980), the enthalpy of mixing (ΔH_m) in the ternary system Di-An-Ab is approximately ±1.6 kcal/gfw. Because the enthalpies of fusion (ΔH_f) of the minerals discussed in this study (10–30 kcal/gfw) are much greater, the magnitude of the enthalpy of solution (ΔH) in Equation 3 can be approximated by the enthalpy of fusion. It is also noted that ΔH_f values are subject to large uncertainties because the results are from different measurement and estimation techniques (see discussion in Weill *et al.*, 1980; Ghiorso and Carmichael, 1980).

tle unless melting takes place on time scales comparable to those in the present experiments. The time scale of melting in the upper mantle, however, is more likely to be of the order of 10^5–10^6 yr (Yoder, 1978). On the other hand, the present results are applicable to dissolution phenomena that affect mantle xenoliths during transport to the surface in alkali basalt magma. The residence times for mantle xenoliths in alkali basalt melt are probably <50 hr (Kushiro *et al.*, 1976). Thus, evidence for dissolution in nodule suites transported to the surface should parallel the results reported here. This parallelism does seem to be the case—olivine is much more resistant to attack by the host magma than are pyroxenes, spinel, and garnet. It is commonly observed, however, that melting is confined to thin rinds on the exterior and does not extend to the interior of xenoliths (e. g., Wilshire and Binns, 1961; White, 1966; Kutolin and Frolova, 1970) except where decompression melting of phlogopite or amphibole occurs (e.g., Frey and Green, 1974; Frey and Prinz, 1978).* It is not obvious, therefore, that widespread dissolution and disintegration of pyroxenite and eclogite nodules has occurred to any appreciable extent during magma transport as suggested by Kutolin and co-workers (1970, 1978). The paucity of eclogite nodules is more likely due to the presumption that eclogite is uncommon in the mantle (Yoder, 1976).

References

Bond, W. L., Making small spheres, *Rev. Sci. Instrum., 22*, 344–345, 1951.

Boyd, F. R., and J. L. England, Apparatus for phase equilibrium measurements at pressures up to 50 kilobars and temperatures up to 1750°C, *J. Geophys. Res., 65*, 741–748, 1960.

Boyd, F. R., and P. H. Nixon, Ultramafic nodules from the Kimberley pipes, South Africa, *Geochim. Cosmochim. Acta, 42*, 1367–1382, 1978.

Carslaw, H. S., and J. C. Jaeger, *Conduction of Heat in Solids*, Clarendon Press, Oxford, England, 1947.

Frey, F. A., and D. H. Green, The mineralogy, geochemistry and origin of lherzolite inclusions in Victorian basanites, *Geochim. Cosmochim. Acta, 38*, 1023–1059, 1974.

Frey, F. A., and M. Prinz, Ultramafic inclusions from San Carlos, Arizona: petrologic and geochemical data bearing on their petrogenesis, *Earth Planet. Sci. Lett., 38*, 129–176, 1978.

Ghiorso, M. S., and I. S. E. Carmichael, A regular solution model for met-aluminous silicate liquids: applications to geothermometry, immiscibility, and the source regions of basic magmas, *Contrib. Mineral. Petrol., 71*, 323–342, 1980.

Ingersol, L. R., and O. J. Zobel, *Heat Conduction, with Engineering and Geological Applications*, McGraw-Hill Book Company, Inc., New York, 1948.

Kawada, K., Studies of the thermal state of the earth. The 17th paper: Variation of thermal conductivity of rocks, Pt. 2, *Bull. Earthquake Res. Inst. Tokyo Univ., 44*, 1071–1091, 1966.

Kretz, R., Some models for the rate of crystallization of garnet in metamorphic rocks, *Lithos, 7*, 123–131, 1974.

Kuno, H., and K. Aoki, Chemistry of ultramafic nodules and their bearing on the origin of basaltic magmas, *Phys. Earth Planet. Inter., 3*, 273–301, 1970.

Kushiro, I., Changes in viscosity and structure of melt of $NaAlSi_2O_6$ composition at high pressures, *J. Geophys. Res., 81*, 6347–6350, 1976.

Kushiro, I., H. S. Yoder, Jr., and B. O. Mysen, Viscosities of basalt and andesite melts at high pressures, *J. Geophys. Res., 81*, 6351–6356, 1976.

Kutolin, V. A., and L. V. Agafonov, On the upper mantle composition with reference to the relative stability of the ultrabasic nodules, *Geol. Geofiz. (Akad. Nauk USSR, Novosibirsk)*, No. 5, 3–13, 1978.

Kutolin, V. A., and V. M. Frolova, Petrology of ultrabasic inclusions from basalts of Minusa and Transbaikalian regions (Siberia, USSR), *Contrib. Mineral. Petrol., 29*, 163–179, 1970.

Littlejohn, A. L., and H. J. Greenwood, Lherzolite nodules in basalts from British Columbia, Canada, *Can. J. Earth Sci., 11*, 1288–1308, 1974.

Weill, D. F., R. Hon, and A. Navrotsky, The igneous system $CaMgSi_2O_6$-$CaAlSi_2O_8$-$NaAlSi_3O_8$: variations on a classic theme by Bowen, in *Physics of Magmatic Processes*, R. B. Hargraves, ed., Princeton University Press, in press, 1980.

*The thin rinds could represent what remains after the removal by abrasion of the more extensively melted outermost portion of the nodules. Removal of already formed liquid at the periphery would in fact show the rate of melting because of the reduction in heat transfer.

White, R. W., Ultramafic inclusions in basaltic rocks from Hawaii, *Contrib. Mineral. Petrol., 12*, 245–314, 1966.
Wilshire, H. G., and R. A. Binns, Basic and ultrabasic xenoliths from volcanic rocks of New South Wales, *J. Petrol., 2*, 185–208, 1961.
Yoder, H. S., Jr., *Generation of Basaltic Magma*, National Academy of Sciences, Washington, D.C., 1976.
Yoder, H. S., Jr., Basic magma generation and aggregation, *Bull. Volcanol., 41*, 301–316, 1978.

Discrete Nodules from the Kimberlites of East Griqualand, Southern Africa

F. R. Boyd and P. H. Nixon

Large single crystals of subcalcic diopside, enstatite, and garnet are common to many kimberlites in southern Africa (Nixon and Boyd, 1973) and other parts of the world (e.g., Eggler *et al.*, 1979). Host-inclusion relations have been used to establish that these megacrysts form cogenetic assemblages (e.g., Boyd and Nixon, 1975). Nevertheless, their compositional and morphological relations distinguish them from similar minerals in the peridotite xenoliths found in kimberlite pipes. What then is their origin?

The discrete nodules, as these megacrysts are called, may have been high-pressure phenocrysts in kimberlite magmas (Gurney *et al.*, 1979). Trace-element studies have led many authors to speculate that kimberlite magmas form by small (<5%) degrees of melting of garnet peridotite in the presence of volatiles (e.g., Frey *et al.*, 1977). Discrete nodules are less refractory than equivalent phases in the commonest types of garnet peridotite xenoliths. If these xenoliths are representative of the parent rocks for kimberlites, the kimberlite magmas must have been segregated and fractionated prior to crystallization of the discrete nodules (Eggler *et al.*, 1979). If such a process commonly preceded kimberlite eruption, it is puzzling that *cumulates* with the chemical characteristics of discrete nodules are so rare.

Another puzzle is that olivine megacrysts are seldom present in kimberlites in the abundances characteristic of peridotites and required by the phenocryst hypothesis. Much olivine is present in kimberlites, but it commonly forms microphenocrysts rather than megacrysts.

Compositional Relations

Diopside discrete nodules from East Griqualand have a restricted compositional range (Fig. 20). Greater variations in Ca content exhibited by discrete diopsides from northern Lesotho and the Kimberley pipes are due to large variations in equilibration temperature. Discrete diopsides from the East Griqualand kimberlites do not include specimens with equilibration temperatures as high as those from Kimberley and northern Lesotho. Furthermore, both the East Griqualand and Kimberley nodule suites lack diopsides that are intergrown with ilmenite (Fig. 20).

Features that particularly suggest that discrete nodules originated as phenocrysts are (1) they are more Fe-rich than comparable minerals in the residual, depleted peridotites and (2) they may show a considerable range in Mg/(Mg + Fe) (Boyd and Nixon, 1975). This latter characteristic is most easily seen in the ranges found for discrete garnet compositions (Fig. 21). On the average, discrete garnets from the kimberlites of East Griqualand have higher Mg/(Mg + Fe) and a more restricted compositional range than their counterparts from northern Lesotho if ilmenite-bearing specimens from the latter area are included.

Most discrete nodules (e. g., garnets, Fig. 22) contain more TiO_2 and less Cr_2O_3 than their counterparts in the high-temperature (>1100 °C) garnet lherzolites with which they are associated in depth of origin. Variations in

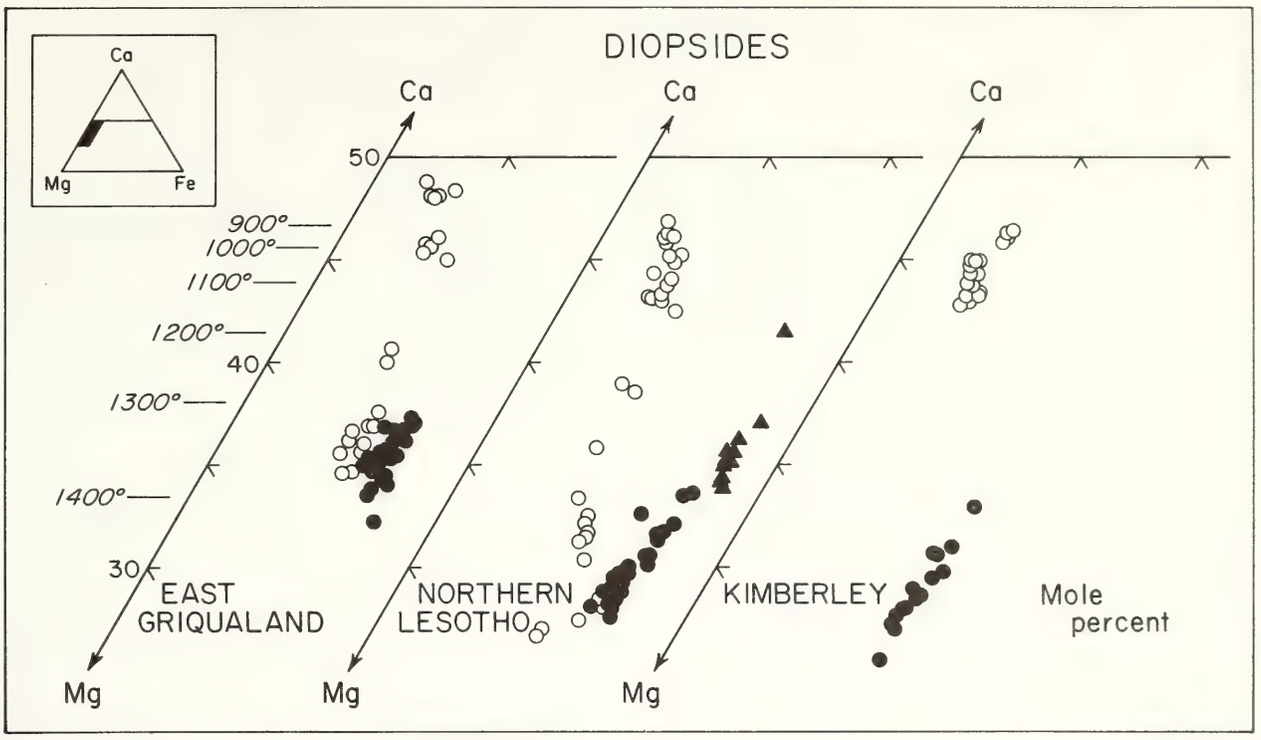


Fig. 20. Compositions of diopsides in lherzolites (open circles) and discrete nodules (solid circles) from kimberlites of three areas in southern Africa, plotted in a portion of the pyroxene quadrilateral. Solid triangles (northern Lesotho) are for intergrowths of diopside and ilmenite—predominantly lamellar. Data for diopsides from northern Lesotho are from Nixon and Boyd (1973) and Boyd and Nixon (1975). Data for diopsides from the Kimberley pipes are from Boyd and Nixon (1978).

TiO_2 are limited and virtually identical in discrete diopsides from East Griqualand and northern Lesotho (Fig. 23), but there is substantially more variation in Cr_2O_3 in the East Griqualand samples.

In Fig. 24, discrete diopsides from East Griqualand and northern Lesotho are compared on a plot of Ca/(Ca + Mg) vs. Na/(Al + Cr). Decreasing Ca/(Ca + Mg) in diopside in equilibrium with enstatite is a measure of increasing equilibration temperature. The diopsides from northern Lesotho define a trend transecting a 1:1 relation between Na and Al + Cr, with the higher temperature samples having Na < (Al + Cr), indicating a small Tschermak component. The lower-temperature specimens, including those intergrown with ilmenite, have Na > (Al + Cr), suggesting the presence of ferric iron. The discrete diopsides from East Griqualand cluster in a portion of the diagram (Fig. 24) where Na < < (Al + Cr), reflecting a large Tschermak component. This relationship is believed to reflect a much shallower depth of crystallization, as discussed below.

A polygranular enstatite pyroxenite with minor intergrown diopside and garnet from Abbotsford (Table 13, PHN 3025) and a similar specimen with minor intergrown garnet from Ramatseliso (Table 13, PHN 3076) may be the first cumulates of discrete nodules from kimberlites to be found in southern Africa. The compositions of all phases in these nodules are within the ranges established for discrete nodules. The grain size of the enstatite is 1–3 cm, but the nodules are small (3–6 cm) and the textural relations cannot be well seen.

Discrete nodules of pyroxene and garnet containing inclusions of one other phase have been found in a number of localities (Nixon and Boyd, 1973; Gurney *et al.*, 1979), but two unusual specimens from the Ramatseliso pipe

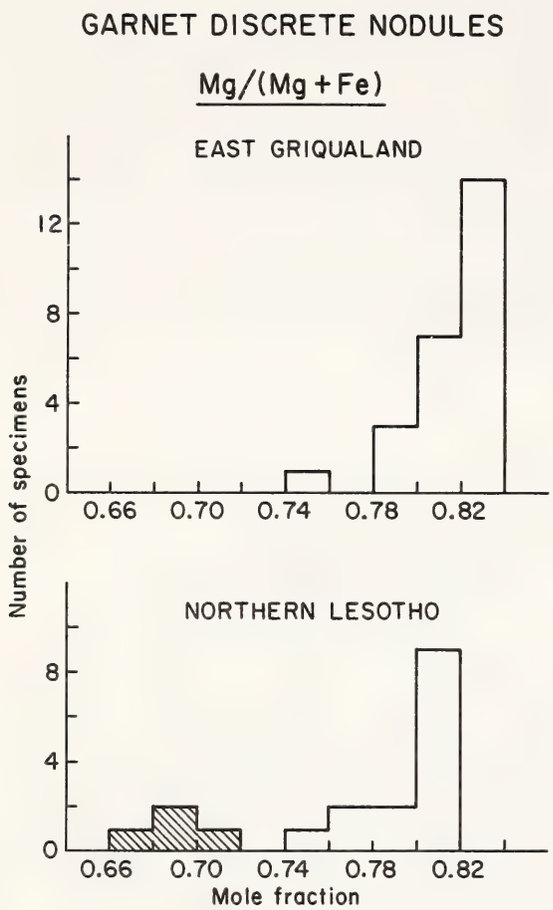


Fig. 21. Histograms for Mg/(Mg + Fe) in garnet discrete nodules from East Griqualand and northern Lesotho. Hatched portion in northern Lesotho diagram is for garnets intergrown with ilmenite.

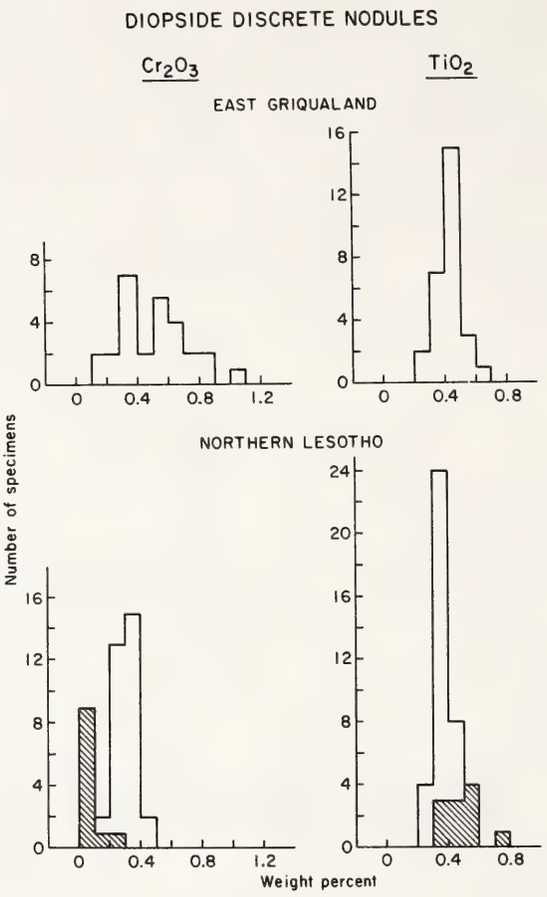


Fig. 23. Histograms for Cr_2O_3 and TiO_2 in diopside discrete nodules from East Griqualand, compared with those from the kimberlites of northern Lesotho. Hatched portions of the northern Lesotho diagrams are for diopsides from intergrowths with ilmenite.

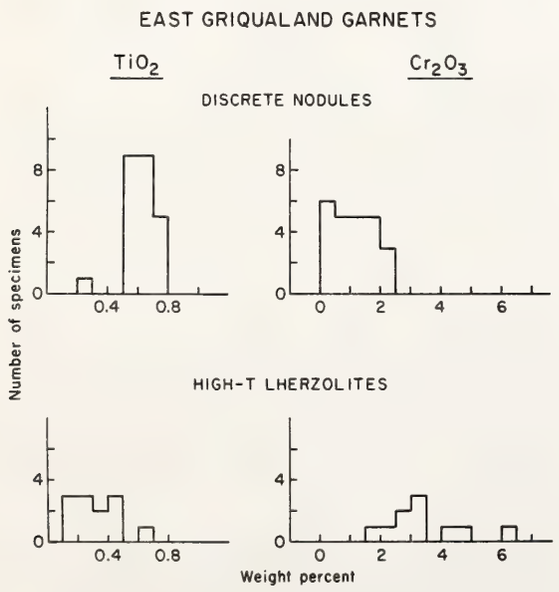


Fig. 22. Histograms for the TiO_2 and Cr_2O_3 contents of garnets in discrete nodules and in high-temperature (>1100°C) lherzolites from East Griqualand kimberlites.

in the East Griqualand group consist of coarse single crystals of enstatite with inclusions of both diopside and garnet (Table 14). Another enstatite discrete nodule from Zeekoegat contains an inclusion of diopside.

Estimates of the temperatures and depths of equilibration of these three xenocrysts have been made by the method developed for lherzolites (Boyd, 1973). Less precise estimates have also been made for single-phase discrete enstatites with the method outlined by Boyd and Nixon (1973). These estimates are compared with the temperature-depth field found for the lherzolites from East Griqualand (Boyd and Nixon, *Year Book 78*, 489, Fig. 19) in Fig. 25. The crystallization conditions of the

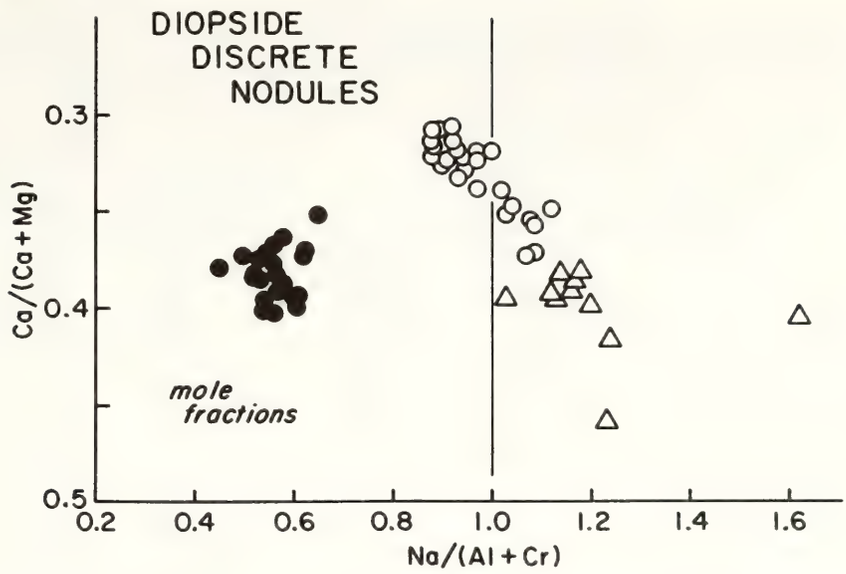


Fig. 24. A plot of Ca/(Ca + Mg) against Na/(Al + Cr) for diopside discrete nodules from East Griqualand (solid circles) and from northern Lesotho (open circles). The open triangles represent diopsides intergrown with ilmenite. If the assumption that these diopsides have equilibrated with enstatite is correct, decreasing Ca/(Ca + Mg) is equivalent to increasing equilibration temperature.

TABLE 13. Compositions of Minerals in Coarse Pyroxenites in which the Constituent Minerals Have Chemical Similarities to Discrete Nodules, wt %

	PHN 3025*			PHN 3076*	
	Enstatite	Diopside	Garnet	Enstatite	Garnet
SiO_2	55.6	54.5	42.3	54.9	41.5
TiO_2	0.26	0.45	0.60	0.30	0.65
Al_2O_3	2.29	3.31	22.1	2.40	21.9
Cr_2O_3	0.20	0.40	1.08	0.20	1.09
FeO†	6.86	4.34	7.86	6.75	8.00
MnO	0.13	0.12	0.25	0.15	0.23
MgO	32.3	19.1	21.2	32.3	20.7
CaO	1.50	16.5	4.40	1.50	5.07
Na_2O	0.25	1.31	0.07	0.20	0.05
Total	99.4	100.0	99.9	98.7	99.2
O =	6,000	6,000	12,000	6,000	12,000
Si	1,942	1,956	3,005	1,933	2,979
Ti	7	12	32	8	35
Al	94	140	1,850	100	1,854
Cr	6	11	61	6	62
Fe†	200	130	467	199	480
Mn	4	4	15	4	14
Mg	1,685	1,021	2,240	1,693	2,212
Ca	56	636	335	57	390
Na	17	91	10	14	7
Total	4,011	4,001	8,015	4,014	8,033
Ca/(Ca + Mg)	0.032	0.384	. . .	0.032	. . .
Mg/(Mg + Fe)	0.894	0.887	0.828	0.895	0.822

*PHN 3025: Pyroxenite nodule, Abbotsford, 6 cm in largest dimension, predominantly enstatite with minor intergrown diopside and garnet. Grain size of coarse enstatite is 1–3 cm. PHN 3076: Chip of pyroxenite, Ramatseliso, 2 cm long, with coarse enstatite crystals up to 1 cm and minor intergrown garnet.

†Total Fe as ferrous iron.

TABLE 14. Compositions of Phases in Enstatite Discrete Nodules That Have Inclusions of Diopside and Garnet, Ramatseliso, wt %

	PHN 1734*			PHN 3077*		
	Enstatite	Diopside	Garnet	Enstatite	Diopside	Garnet
SiO_2	55.8	53.8	42.6	55.2	54.5	42.8
TiO_2	0.29	0.41	0.57	0.22	0.41	0.62
Al_2O_3	2.48	3.52	21.8	2.39	3.39	21.4
Cr_2O_3	0.30	0.63	1.71	0.35	0.69	2.08
FeO†	6.71	4.42	7.53	6.79	4.35	7.30
MnO	0.13	0.12	0.26	0.13	0.12	0.23
MgO	32.7	18.9	21.3	32.8	19.4	21.2
CaO	1.55	16.2	5.18	1.58	15.3	5.02
Na_2O	0.24	1.26	<0.03	0.23	1.35	0.05
Total	100.2	99.3	101.0	99.7	99.5	100.7
O =	6,000	6,000	12,000	6,000	6,000	12,000
Si	1,934	1,948	3,000	1,927	1,961	3,017
Ti	8	11	30	6	11	33
Al	101	150	1,806	98	144	1,778
Cr	8	18	95	10	20	116
Fe†	195	134	444	198	131	431
Mn	4	4	16	4	4	14
Mg	1,689	1,019	2,237	1,705	1,040	2,231
Ca	58	629	391	59	590	380
Na	16	88	3	16	94	7
Total	4,013	4,001	8,022	4,023	3,995	8,007
Ca/(Ca + Mg)	0.033	0.382	. . .	0.033	0.362	. . .
Mg/(Mg + Fe)	0.897	0.884	0.835	0.896	0.888	0.838

*PHN 1734: Single crystal of enstatite (4 cm) with adhering hardebank. Multiple, irregularly shaped lenticles of diopside with sparser garnet. PHN 3077: Single crystal of enstatite (3 cm) with multiple, irregularly shaped diopside inclusions that are in optical continuity. A grain of garnet (1 cm) is partly included. Enstatite shows markedly undulate extinction.

†Total iron as ferrous iron.

enstatite megacrysts (and presumably of the other discrete nodules) overlap the temperatures and depths of equilibration of the high-temperature lherzolites. This relationship is the same as that found for northern Lesotho (Boyd and Nixon, 1975) and the Frank Smith Mine (Boyd, *Year Book 73*, 185).

The lherzolites and discrete nodules from the East Griqualand pipes have estimated depths of equilibration that are 40–50 km less than those of similar xenoliths and xenocrysts from the kimberlites of northern Lesotho (Fig. 25) and other localities within the Kaapvaal craton. Boyd and Nixon (*Year Book 78*, 488) suggested that these relations indicate that the kimberlites were erupted from a zone just beneath the lithosphere-asthenosphere boundary and that this boundary shelved from beneath the Kaapvaal craton toward the Indian Ocean.

Discussion

The coexistence of dry high-temperature lherzolites in the same temperature-depth range as magmas containing discrete nodules implies a pronounced localization of volatiles within the upper mantle prior to kimberlite eruption. This localization could have been caused by simple intrusion of volatile-rich magma into dry mantle. Alternatively, localized infiltration of vol-

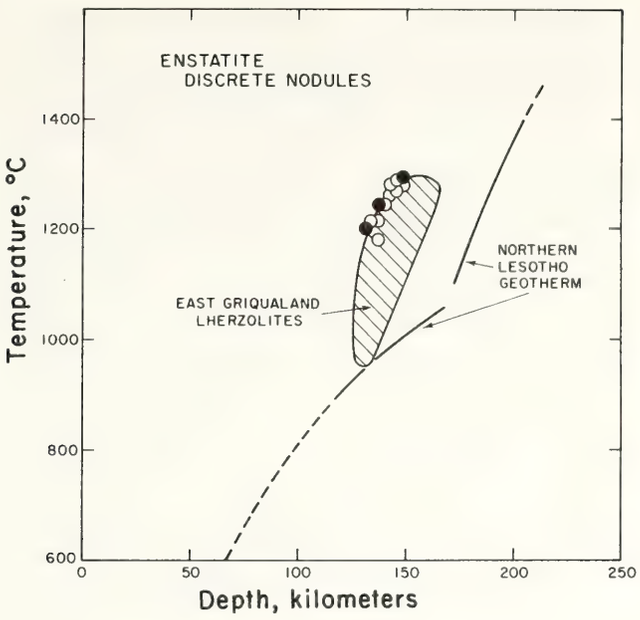


Fig. 25. Estimated temperatures and depths of origin for enstatite discrete nodules from East Griqualand, compared with the field found for the lherzolites (*Year Book 78*, 489, Fig. 19) and with the northern Lesotho geotherm (Boyd, 1973, Fig. 7a). Solid circles represent enstatite nodules with inclusions of diopside. Temperatures for enstatite nodules that do not contain diopside were estimated by the method of Boyd and Nixon (1973). Diopside-enstatite pairs from the East Griqualand lherzolites were used to calibrate the thermometer.

atiles from greater depth might have produced metasomatism and limited partial melting. That the discrete nodules are less refractory than the common depleted peridotites might possibly be due to metasomatism rather than segregation and fractionation of liquid. In such circumstances, the proportions of liquid need never have been large and the rarity of cumulates of discrete nodules is easily understood.

If the proportions of liquid were small at the onset of kimberlite eruption, then possibly the crystalline fraction (i.e., the discrete nodules) was subject to differential stress. Deformation under conditions of partial melting has been observed in laboratory experiments (Molen and Paterson, 1979), and enstatite discrete nodules that have been deformed have been found at the Frank Smith Mine (Pasteris *et al.*, 1979) and in East Griqualand (Table 14). Olivine recrystallizes first during subsolidus deformation of peridotite, with the result that coarse porphyroclasts of pyroxene and garnet are commonly found in a matrix of fine-grained, mosaic olivine. Thus it is possible that coarse olivine crystals originally accompanied the pyroxene and garnet discrete nodules in association with minor amounts of liquid, but that they were deformed during the early stages of eruption and recrystallized as abundant microphenocrysts in the kimberlite.

References

Boyd, F. R., A pyroxene geotherm, *Geochim. Cosmochim. Acta, 37*, 2533–2546, 1973.

Boyd, F. R., and P. H. Nixon, Origin of the ilmenite-silicate nodules in kimberlites from Lesotho and South Africa, in *Lesotho Kimberlites*, P. H. Nixon, ed., Lesotho National Development Corporation, Maseru, Lesotho, pp. 254–268, 1973.

Boyd, F. R., and P. H. Nixon, Origins of the ultramafic nodules from some kimberlites of northern Lesotho and the Monastery Mine, South Africa, *Phys. Chem. Earth, 9*, 431–454, 1975.

Boyd, F. R., and P. H. Nixon, Ultramafic nodules from the Kimberley pipes, South Africa, *Geochim. Cosmochim. Acta, 42*, 1367–1382, 1978.

Eggler, D. H., M. E. McCallum, and C. B. Smith, Megacryst assemblages in kimberlites from northern Colorado and southern Wyoming: petrology, geothermometry-barometry, and areal distribution, in *The Mantle Sample (Proc. 2d Int. Kimberlite Conf.*, Vol. 2) F. R. Boyd and H. O. A. Meyer, eds., American Geophysical Union, Washington, D.C., pp. 213–226, 1979.

Frey, F. A., J. Ferguson, and B. W. Chappell, Petrogenesis of South African and Australian kimberlitic suites, *Extended Abstracts, Second International Kimberlite Conference*, Santa Fe, New Mexico, 1977.

Gurney, J. J., W. R. O. Jakob, and J. B. Dawson, Megacrysts from the Monastery kimberlite pipe, South Africa, in *The Mantle Sample (Proc. 2d Int. Kimberlite Conf.*, Vol. 2), F. R. Boyd and H. O. A. Meyer, eds., American Geophysical Union, Washington, D.C., pp. 227–243, 1979.

Molen, I. van der, and M. S. Paterson, Experimental deformation of partially melted granite, *Contrib. Mineral. Petrol., 70*, 299–318, 1979.

Nixon, P. H., and F. R. Boyd, The discrete nodule association in kimberlites from northern Lesotho, in *Lesotho Kimberlites*, P. H. Nixon, ed., Lesotho National Development Corporation, Maseru, Lesotho, pp. 67–75, 1973.

Pasteris, J. D., F. R. Boyd, and P. H. Nixon, The ilmenite association at the Frank Smith Mine, RSA, in *The Mantle Sample (Proc. 2d Int. Kimberlite Conf.*, Vol. 2), F. R. Boyd and H. O. A. Meyer, eds., American Geophysical Union, Washington, D.C., pp. 265–278, 1979.

Ilmenite Nodules and Associated Sulfides in Kimberlite from Yakutia, U.S.S.R.

N. Z. Boctor and F. R. Boyd

Discrete ilmenite nodules are common in kimberlites and have been the subject of several investigations (e.g., Mitchell, 1977; Haggerty *et al.*, 1979; Pasteris *et al.*, 1979). Ilmenite nodules are commonly monomineralic, but symplectic intergrowths of ilmenite and pyroxene have also been found in some kimberlites. There is no general agreement on the origin of the ilmenite nodules. They are considered by some investigators as high-pressure phenocrysts that crystallized from the kimberlite magma (e.g., Mitchell, 1977). Sulfide minerals are rarely observed in discrete ilmenite nodules and, when present, occur as tiny spheres of pyrrhotite. In certain instances, the sulfides occur in later carbonate veinlets transecting the nodules.

During the study of discrete ilmenite nodules from an unknown diamond-bearing kimberlite pipe from Yakutia, U.S.S.R., large globules of polymineralic sulfides (0.5 to 2 mm) were found as inclusions in the ilmenite. The sulfide assemblage is similar in mineralogy and texture to sulfides formed by liquid immiscibility in eclogite nodules from kimberlites and suggests an equilibration temperature below 575 °C.

The ilmenite nodules are large, ranging in size from 0.6 to 2 cm. The nodules appear as single crystals and show no deformation, zoning, or reaction mantles. Their MgO and Cr_2O_3 contents (Table 15), though lower than those observed for some South African kimberlites, are still within the ranges reported by Haggerty (1975) and Mitchell (1977) for kimberlitic ilmenite. When the MgO contents of the ilmenite nodules are plotted against their Cr_2O_3 contents, they fall on the base of the parabolic curve of Haggerty (1975). The Fe_2O_3 of the ilmenite discrete nodules is similar to that of ilmenite from other kimberlites.

The sulfide globules are similar in mineralogy and texture. They are composed mainly of pyrrhotite with fine, closely spaced exsolution lamellae of

TABLE 15. Representative Electron Microprobe Analyses of Ilmenite Nodules from Yakutia Kimberlite, U.S.S.R.*

Oxide	1	2	3	4	5	6	7	8
SiO_2	0.11	<0.01	<0.01	<0.01	<0.01	<0.01	<0.01	<0.01
TiO_2	48.60	47.72	47.89	48.17	47.76	48.19	48.30	47.89
Al_2O_3	0.79	0.72	0.82	0.85	0.70	0.75	0.75	0.85
Cr_2O_3	0.11	0.12	0.18	0.16	0.17	0.14	0.16	0.19
Fe_2O_3	7.11	8.62	7.63	8.17	7.87	7.75	7.94	8.16
FeO	32.92	33.09	33.29	32.80	32.93	33.30	32.62	32.79
MnO	0.32	0.19	0.16	0.14	0.17	0.17	0.16	0.18
NiO	0.02	0.08	0.11	0.09	0.11	0.16	0.12	0.18
MgO	9.52	9.11	9.36	9.65	9.44	9.39	9.77	9.65
CaO	0.04	0.08	0.02	<0.01	<0.01	<0.01	0.03	0.02
Total	99.53	99.72	99.46	100.11	99.09	99.86	99.78	99.94

*In wt %.

pentlandite. Chalcopyrite forms discontinuous rims at the peripheries of some nodules and rarely occurs as fine exsolution lamellae in pyrrhotite. Because of the fine-grained nature of the intergrowths, it was not possible to analyze individual mineral phases, and bulk compositions obtained by defocused-beam electron microprobe analyses are given in Table 16.

The sulfide mineral assemblages observed in the ilmenite nodules are generally similar to those described from eclogite xenolith in kimberlite (Frick, 1973; Meyer and Boctor, 1975; Tsai *et al.*, 1979). They are particularly similar to the sulfides described by Vakhrushev and Sobolev (1973) from eclogite nodules from Yakutia kimberlites.

The bulk composition of the sulfide assemblage lies within the boundaries of the monosulfide solid solution in the quaternary system Cu-Fe-Ni-S. According to the phase relations in this system (Craig and Kullerud, 1969), a sulfide liquid of a composition similar to the bulk composition of the sulfide assemblage in the nodules would crystallize to a monosulfide solid solution (M_{ss}) at a temperature of 1100 °C. The effect of pressure on the phase relations in the Cu-Fe-Ni-S system is not known, but it is likely that the temperature will be higher than 1100 °C. On low-temperature equilibration, pentlandite and chalcopyrite would exsolve from the M_{ss} at a temperature below 575 °C (Craig and Kullerud, 1969). The upper stability limit of pentlandite is 610° ± 2 °C (Kullerud, 1963). The temperature of pentlandite exsolution, however, was found to be dependent on the metal-to-sulfur ratio in the M_{ss} (Naldret *et al.*, 1967) rather than on the Ni content of the M_{ss}. Pressure seems to drastically reduce the upper stability limit of pentlandite (Bell *et al.*, *Year Book 64*, 206–207). It is likely, therefore, that pentlandite actually exsolved at a much lower temperature than 575 °C.

The chalcopyrite rims at the peripheries of the sulfide globules described by Tsai *et al.* (1979) were interpreted as a product of crystallization from a Cu-rich liquid that coexisted with the M_{ss}, the composition of which lies within the Cu-Fe-Ni-S quaternary extension of the intermediate solid solution (I_{ss}) in the Cu-Fe-S system (Cabri, 1973; Barton, 1973). In the sulfide assemblage observed in ilmenite nodules from Yakutia, the amount of chalcopyrite on the margins of the sulfide globules is small and can be accounted for by exsolution from the original M_{ss}. The presence of lamellar intergrowths of chalcopyrite in pyrrhotite and the fact that chalcopyrite is always present in association with pyrrhotite and not as a discrete phase, seem to support a subsolidus formation of chalcopyrite by exsolution from the M_{ss} rather than by crystallization from a Cu-rich liquid. Because the crystal structures of pyrrhotite and chalcopy-

TABLE 16. Electron Microprobe Analyses of Sulfide Intergrowths in Ilmenite Nodules from Yakutia Kimberlite*

Element	1	2	3	4	5	6
Cu	1.57	1.82	0.89	2.33	3.45	0.67
Ni	9.75	5.39	5.27	5.77	4.20	2.51
Co	0.39	0.36	0.42	0.29	0.44	0.29
Fe	51.53	52.34	52.78	51.59	51.26	56.27
S	37.47	39.04	39.43	38.90	39.32	39.52
Total	100.72	98.94	98.79	98.88	98.32	99.25

*Defocused beam analyses of pyrrhotite-pentlandite-chalcopyrite intergrowths. Values in wt %.

rite are different, a high strain energy is induced by the nucleation of the exsolved phase. Because grain boundaries represent loci of minimum strain energy, migration of exsolved chalcopyrite to grain boundaries would decrease the strain energy of the system. Brett (1964) noted that chalcopyrite exsolved from bornite in the Cu-Fe-S system tends to migrate to grain boundaries regardless of the temperature or degree of supersaturation of chalcopyrite in the initial solid solution.

In conclusion, the precursor of the sulfide mineral assemblage in ilmenite nodules from Yakutia kimberlite was an immiscible sulfide liquid of a bulk composition falling in the M_{ss} field in the Cu-Fe-Ni-S system. The liquid was incorporated in the crystallizing ilmenite at temperatures higher than 1100 °C. Crystallization of the liquid to a M_{ss} and the equilibration of the latter at temperatures below 575 °C gave rise to the pyrrhotite-pentlandite-chalcopyrite assemblage observed in the nodules.

References

Barton, P. B., Jr., Solid solutions in the system Cu-Fe-S. Part I. The Cu-S and Cu-Fe-S joins, *Econ. Geol., 68*, 455–465, 1973.

Brett, P. R., Experimental data from the system Cu-Fe-S and their bearing on exsolution textures in ores, *Econ. Geol., 62*, 354–369, 1964.

Cabri, L. J., New data on phase relations in the Cu-Fe-S system, *Econ. Geol., 68*, 443–454, 1973.

Craig, J. R., and G. Kullerud, Phase relations in the Cu-Fe-Ni-S system and their application to magmatic ore deposits, *Econ. Geol. Monogr., 4*, 334–358, 1969.

Frick, C., The sulfides in griquaite and garnet peridotite xenolith in kimberlites, *Contrib. Mineral. Petrol., 39*, 1–16, 1973.

Haggerty, S. E., The chemistry and genesis of opaque minerals in kimberlites, *Phys. Chem. Earth, 9*, 295–308, 1975.

Haggerty, S. E., R. B. Hardie, III, and B. M. McMahon, The mineral chemistry of ilmenite nodule associations from the Monastery diatreme, in *The Mantle Sample (Proc. 2d Int. Kimberlite Conf.,* Vol. 2), F. R. Boyd and H. O. A. Meyer, eds., American Geophysical Union, pp. 249–256, 1979.

Kullerud, G., Thermal stability of pentlandite, *Can. Mineral., 7*, 353–366, 1963.

Meyer, H. O. A., and N. Z. Boctor, Sulfide oxide minerals in eclogite from Stockdale kimberlite, Kansas, *Contrib. Mineral. Petrol., 52*, 57–68, 1975.

Mitchell, R. H., Geochemistry of magnesian ilmenites from kimberlite in South Africa and Lesotho, *Lithos, 10*, 29–37, 1977.

Naldrett, A. J., J. R. Craig, and G. Kullerud, The central portion of the Fe-Ni-S system and its bearing on pentlandite exsolution in iron-nickel sulfide ores, *Econ. Geol., 62*, 826–847, 1967.

Pasteris, J. D., F. R. Boyd, and P. H. Nixon, The ilmenite association at the Frank Smith Mine, R.S.A., in *The Mantle Sample (Proc. 2d Int. Kimberlite Conf.*, Vol. 2), F. R. Boyd and H. O. A. Meyer, eds., American Geophysical Union, pp. 265–278, 1979.

Tsai, H. M., Y. N. Shieh, and H. O. A. Meyer, Mineralogy and S^{34}/S^{32} ratios of sulfides associated with kimberlite, xenolith and diamonds, in *The Mantle Sample (Proc. 2d Int. Kimberlite Conf.*, Vol. 2), F. R. Boyd and H. O. A. Meyer, eds., American Geophysical Union, pp. 87–103, 1979.

Vakhrushev, V. A., and N. V. Sobolev, Sulfidic formation in deep xenoliths from kimberlite pipes in Yakutia, *Int. Geol. Rev., 15*, 103–110, 1973.

Distribution of Rare Earth Elements in Perovskite from Oka Carbonatite, Quebec

N. Z. Boctor and H. S. Yoder, Jr.

Carbonatites are enriched in rare earth elements (REE) relative to associated alkaline rocks in igneous complexes (Haskin *et al.*, 1966; Cullers and Medaris, 1977). Perovskite, a common mineral in some carbonatites, is known to incorporate REE and other incompatible elements in its crystal structure. Perovskite also tends to concentrate the light rare earth elements (LREE) relative to the heavy lanthanides (HREE) (Boctor and Boyd, *Year Book 78*, 572–574; Borodin and Barinskii, 1960; Nagasawa *et al.*, 1980). Perovskite from nephelinites and melilite-bearing rocks, as well as that from kimberlite, is enriched in REE and

seems to be the main phase responsible for the concentration of REE in these rocks. Because of its capacity for LREE enrichment, perovskite, if abundant, may influence the whole-rock REE patterns observed in these rocks. In order to assess the role played by perovskite in the REE geochemistry of carbonatites, the distribution of REE in perovskite from the classical carbonatite occurrence at Oka, Quebec, was investigated. Perovskite in this carbonatite does not seem to be enriched in total REE or in LREE relative to perovskite from alkaline rocks, but is remarkably enriched in Nb relative to perovskite from these rocks. This observation may be attributed to the incorporation of a significant part of the LREE in pyrochlore, which is another major REE-bearing phase in Oka carbonatite.

The distribution of REE in perovskite from Oka carbonatite was determined by the electron microprobe. The technique described by Boctor and Boyd (1980) was used for analysis of perovskite, and data reduction was performed by the Magic IV computer program (Colby, 1971). It is clear from the electron microprobe data (see Table 17) that even though it shows the same trend of LREE enrichment observed in perovskite from kimberlite and other alkaline rocks, perovskite in Oka carbonatite has a lower total REE content than that observed in perovskite from some of these rocks (see Boctor and Boyd, *Year Book 78*, 572–574; Smith, 1970). Carbonate melts are enriched in REE relative to silicate melts, as suggested by experimental studies (Wendlandt and Harrison, 1979) and by study of the distribution of REE between carbonatites and cogenetic alkaline igneous rocks (Cullers and Medaris, 1977). Perovskite in carbonatite is, therefore, expected to be enriched in

TABLE 17. Representative Electron Microprobe Analyses of Perovskite from Oka Carbonatite*

Oxide	1	2	3	4	5	6†
SiO_2	0.09	0.09	0.07	0.09	0.07	0.09
TiO_2	36.20	35.56	34.98	35.72	36.72	2.49
FeO	4.88	4.85	4.91	4.88	4.41	1.73
MgO	0.46	0.59	0.58	0.54	0.55	0.16
CaO	35.43	35.98	35.43	35.14	34.79	17.23
Na_2O	0.98	0.94	1.14	1.02	1.08	5.44
Y_2O_3	n.d.‡	n.d.	n.d.	n.d.	n.d.	n.d.
La_2O_3	1.13	0.99	0.87	0.99	0.51	1.01
Ce_2O_3	2.19	2.12	2.36	2.22	2.34	6.03
Pr_2O_3	0.10	0.17	0.11	0.16	0.10	n.d.
Nd_2O_3	0.11	0.21	0.37	0.23	0.25	n.d.
Sm_2O_3	n.d.	n.d.	n.d.	n.d.	n.d.	n.d.
Eu_2O_3	0.09	0.03	0.01	0.04	n.d.	0.28
Gd_2O_3	n.d.	n.d.	n.d.	n.d.	n.d.	n.d.
Tb_2O_3	n.d.	n.d.	n.d.	n.d.	n.d.	n.d.
Dy_2O_3	n.d.	n.d.	n.d.	n.d.	n.d.	0.16
Ho_2O_3	0.41	0.55	0.68	0.55	0.64	1.16
Er_2O_3	0.06	0.04	0.09	0.03	0.07	0.02
Tm_2O_3	n.d.	n.d.	n.d.	n.d.	n.d.	n.d.
Yb_2O_3	n.d.	n.d.	n.d.	n.d.	n.d.	n.d.
Lu_2O_3	n.d.	n.d.	n.d.	n.d.	n.d.	n.d.
Nb_2O_5	16.79	17.63	17.78	17.39	17.02	62.86
Total	99.09	99.75	99.27	99.00	98.59	98.66

*Values in wt %.
†Pyrochlore analysis; F, Ta, and U were not analyzed.
‡n.d. = not detected.

REE relative to that from silicate rocks if REE partitioning between perovskite and carbonate and silicate melts is concentration dependent and if no other phases concentrating REE are present. In Oka carbonatite, perovskite coexists with pyrochlore and apatite. Pyrochlore is known to have high concentrations of LREE, particularly the lightest lanthanides. Apatite also tends to concentrate more LREE relative to HREE (Haskin *et al.*, 1966). Electron microprobe analysis of pyrochlore in Oka carbonatite (Table 17, analysis 6) shows that it is more enriched in REE, particularly the light lanthanides, than coexisting perovskite. Enrichment of REE in Oka pyrochlore has also been reported by Petruk and Owens (1975) and McMahon and Haggerty (1979). Pyrochlore is not known to occur in any of the alkaline rocks that coexist with carbonatite in alkaline rock complexes or in kimberlite. It is likely, therefore, that the crystallization of pyrochlore from the carbonate melt that formed Oka carbonatite and the higher capacity for concentrating REE of this mineral compared with perovskite are responsible for the observed depletion in the REE content of Oka perovskite relative to that from some alkaline rocks.

Another significant characteristic of perovskite from Oka carbonatite is its enrichment in Nb and Fe relative to perovskite from coexisting alkaline rocks and kimberlites. Nickel and McAdam (1962) reported a much higher Nb (43.90 wt % Nb_2O_5) and Fe (8.74 wt %) content in a purified commercial concentrate of perovskite from Oka than those reported in the present study. If the concentrate was not contaminated by pyrochlore, this result suggests a large variation in the Nb concentration in perovskite from one sample to another. The high concentration of Nb in the precursor carbonate melt from which pyrochlore and perovskite crystallized is consistent with the tendency of this element to form stable carbonate and hydroxyl complexes (e.g., Ringwood, 1955). The high volatile content of carbonatitic magma seems to support this conclusion.

The high iron content of perovskite in Oka carbonatite relative to that of perovskite in kimberlite is significant, as it provides an indication of the redox conditions prevailing during the crystallization of this mineral. Kimura and Muan (1971a, b) showed experimentally from a study of the CaO-TiO_2-FeO system that perovskite crystallizing under high f_{O_2} conditions incorporates a substantial amount of Fe as Fe_2O_3 in its structure by a coupled substitution of $2Fe^{3+}$ for $Ca^{2+} + Ti^{4+}$, whereas under strongly reducing conditions the amount of Fe as FeO that enters the perovskite structure is negligible. The high iron content of perovskite at Oka suggests that it possibly crystallized under more oxidizing conditions than perovskite in kimberlites. Although the f_{O_2} at which perovskite crystallized in Oka carbonatite is not known, it is interesting to note that a temperature of 710° ± 15°C and an f_{O_2} of $10^{-17.1 \pm 0.5}$ bar was reported by Friel and Ulmer (1974) for the final equilibration of the assemblage magnetite-perovskite-olivine in Oka carbonatite by intrinsic oxygen-fugacity measurements. This f_{O_2} is significantly higher than that reported by Mitchell (1973) at the final temperature of groundmass crystallization in kimberlites ($f_{O_2} = 10^{-20}$ bar at 650°C).

In conclusion, perovskite in Oka carbonatite is depleted in REE relative to that from some alkaline rocks and kimberlites. Such depletion is attributed to the crystallization of pyrochlore, which has a higher geochemical affinity to the LREE that usually tend to concentrate in perovskite. Unlike kimberlites, in which the crystallization of abundant REE-rich perovskite may influence the whole-rock REE pattern, the crystallization of perovskite from some carbonatites may have little effect on the whole-rock pattern because a sub-

stantial part of the total REE is incorporated in pyrochlore and possibly apatite. The Oka perovskite is highly enriched in iron and Nb relative to perovskite in kimberlites. The high Nb content is attributed to the tendency of this element to concentrate in carbonate melts during silicate-carbonate immiscibility because it forms stable carbonate complexes. The high concentration of iron in perovskite, however, suggests that it crystallized at a higher f_{O_2} than that prevailing during crystallization of kimberlitic perovskite.

References

Boctor, N. Z., and F. R. Boyd, Oxide minerals in the Liqhobong kimberlite, Lesotho, *Amer. Mineral.*, in press, 1980.

Borodin, L. S., and R. L. Barinskii, Rare earths in perovskites (knopites) from massifs of ultrabasic alkaline rocks, *Geochemistry*, No. 4, 343–350, 1960.

Colby, J. W., Magic IV, a computer program for quantitative electron microprobe analysis, Bell Telephone Laboratories, Allentown, Pennsylvania, 1971.

Cullers, R. L., and L. G. Medaris, Rare earth elements in carbonatites and cogenetic alkaline rocks: examples from Seabrook Lake and Callander Bay, Ontario, *Contrib. Mineral. Petrol., 65*, 143–153, 1977.

Friel, J. J., and G. C. Ulmer, Oxygen fugacity geothermometry of the Oka carbonatite, *Amer. Mineral., 59*, 314–318, 1974.

Haskin, L. A., F. A. Frey, M. A. Haskin, R. F. Schmitt, and R. H. Smith, Meteorite, solar and terrestrial abundances of rare earth distribution, *Phys. Chem. Earth, 7*, 167–321, 1966.

Kimura, S., and A. Muan, Phase relations in the system CaO-iron oxide-TiO_2 in air, *Amer. Mineral., 56*, 1332–1346, 1971a.

Kimura, S., and A. Muan, Phase relations in the system CaO-iron oxide-titanium oxide under strongly reducing conditions, *Amer. Mineral., 56*, 1347–1358, 1971b.

McMahon, B. M., and S. E. Haggerty, The Oka carbonatite complex: magnetite compositions and the related role of titanium in pyrochlore, in *The Mantle Sample (Proc. 2d Int. Kimberlite Conf.*, Vol. 2), F. R. Boyd and H. O. A. Meyer, eds., American Geophysical Union, pp. 382–392, 1979.

Mitchell, R. H., Composition of olivine, silica activity, and oxygen fugacity in kimberlites, *Lithos, 6*, 65–81, 1973.

Nagasawa, H., H. D. Schreiber, and R. V. Morris, Experimental mineral/liquid partition coefficients of the rare earth elements (REE), Sc and Sr for perovskite, spinel and melilite, *Earth Planet. Sci. Lett., 46*, 431–437, 1980.

Nickel, E. H., and R. C. McAdam, Niobian perovskite from Oka, Quebec; a new classification for minerals of the perovskite group, *Can. Mineral., 7*, 683–697, 1962.

Petruk, W., and D. Owens, Electron microprobe analyses for pyrochlore from Oka, Quebec, *Can. Mineral., 13*, 282–285, 1975.

Ringwood, A. E., The principles governing trace element behavior during magmatic crystallization. Part II. The role of complex formation, *Geochim. Cosmochim. Acta, 7*, 242–254, 1955.

Smith, A. L., Sphene, perovskite and coexisting Fe-Ti oxide minerals, *Am. Mineral., 55*, 264–269, 1970.

Wendlandt, R. F., and W. J. Harrison, Rare earth partitioning between immiscible carbonate and silicate liquids and CO_2 vapor: results and implications for the formation of light rare earth enriched rocks, *Contrib. Mineral. Petrol., 69*, 409–419, 1979.

STRUCTURE AND PROPERTIES OF LIQUIDS AND GLASSES

Shear Wave Velocity in Partially Molten Peridotite at High Pressures

T. Murase and H. Fukuyama

Direct measurements of the compressional wave velocity (V_p) in partially molten peridotite were made at high pressures for the first time last year (*Year Book 78*, 559–562). It was found that at 5 kbar, a 5% decrease in V_p, as observed for the low-velocity zone of the upper mantle (e.g., Nur, 1974), implies a maximum of 7–9 vol % melting. It was evident, however, that measurements were needed at higher pressures and that an investigation was required of the effect of melting on the shear wave velocity (V_s), which according to the Eshelby-Walsh theory

should be more sensitive to melting than V_p (Anderson and Spetzler, 1970). In the present studies V_s was measured at 5 and 10 kbar, and the degree of melting was measured as a function of temperature through the melting range of the peridotite at 10 kbar.

Experimental

The methods used here were virtually identical with those described previously for compressional wave velocity measurements (*Year Book 78*, 559–562), except that both the sample and the buffer rods were packed in a platinum container to ensure acoustical contact between the sample and the face of the rods.

The starting material was a spinel lherzolite inclusion (BCP) from a Cenozoic alkali basalt eruption in British Columbia collected by T. N. Irvine. The spinel lherzolite sample was ground to 100–500 μm and was dried and packed in the central part of a platinum container, 18.0 cm long, 1.0 cm in diameter, and 0.03 cm in wall thickness. The length of the sample was 2.0 cm. Platinum foils and mullite buffer rods, 1.0 cm in diameter and 7.7 cm long, were placed on both sides of the sample.

The container was sealed by welding so that argon gas would not have access to the sample during the measurements. Before the actual runs the sealed container was compressed at 5 kbar in a gas-media, high-pressure apparatus to avoid extensive deformation during the velocity measurements. Shear-mode lithium niobate transducers of 1 MHz natural frequency were glued with a cyanoacrylate adhesive to the ends of the container. A schematic diagram of the furnace is shown in Fig. 26.

All free space in and around the furnace assembly was filled with alundum powder to prevent convection of argon gas in response to the large temperature gradient between the even zone of high temperature where the peridotite melted and the ends of the furnace. The temperature variation over the 2-cm length of the sample was less than 5° at 1000°C and 5 kbar; the temperature around the transducer was below 100°C.

The velocity measurements were made in the gas-media, high-pressure apparatus designed by Yoder (1950). The method used for the measurements was a modified pulse transmission technique (Murase and McBirney, 1973). The delay time of the buffer rod assembly without a sample was measured at high temperature and elevated pressure after the velocity measurements had been made on the sample. The uncertainty in the velocity measurements, due mostly to uncertainty in determining the first arrival of the shear wave, was ±0.2 km/sec, or about 5%.

The degree of partial melting of the

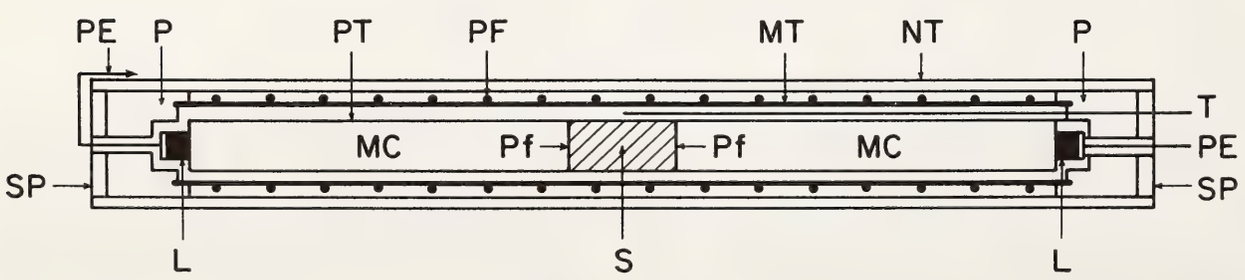


Fig. 26. Schematic diagram of furnace. S, sample; MC, mullite cylinder; MT, mullite tube; PF, platinum-wound furnace; NT, nickel tube; PE, platinum electrode; L, lithium niobate transducer; SP, stainless steel plate; P, pyrophyllite; Pf, platinum foil; T, thermocouple. Both sample and mullite cylinders are sealed by a platinum tube.

sample was measured independently by the β-track counting method of Mysen and Kushiro (1977), except for the data at 1290° and 1300°C at 10 kbar, which were obtained by modal point counting. Relative errors are less than 10% for the β-track counting and about 15% for the point counting.

The textural distribution of the melt at 10 kbar is similar to that observed previously at 5 kbar (*Year Book 78*, 559–562). There is more modification of its configuration by quench crystallization at 10 kbar (cf., Jacques and Green, 1979), but the general discussion given for 5 kbar is probably still valid qualitatively.

Results and Discussion

All the data that have been obtained on V_s, V_p, and degree of melting in the peridotite at 5 and 10 kbar are illustrated as functions of temperature in Fig. 27. In the solid peridotite, V_s decreases with increasing temperature at almost the same rate as it did in an olivine aggregate of zero porosity investigated by Birch (1969). Above 1150°C at 5 kbar the first arriving S wave of 0.6 MHz attenuated and disappeared into the noise of the oscilloscope, even though no melt was observed at that temperature. Consequently, the velocity of the 0.3-MHz wave that followed the first wave is shown between 1150°C and 1300°C. At 10 kbar the velocity of the first arriving 0.6-MHz S wave began to decrease with the onset of melting at 1200°C, and the wave disappeared above 1300°C. The velocities of the 0.3-MHz wave are, therefore, also used between 1300° and 1400°C.

The velocities of the 0.6-MHz S wave at 10 kbar and the P wave at 5 and 10 kbar are normalized to the velocity of the unmelted sample at its solidus temperature (1150°C at 5 kbar and 1200°C at 10 kbar). The relationship between the normalized velocity and the degree of melting is shown in Fig. 28. The relationship for the S wave at 5 kbar may decrease in the same way as at 10 kbar, and in an extreme case, it may decrease sharply along the ordinate, as shown in the figure by a dashed line, inasmuch as very little melt is present.

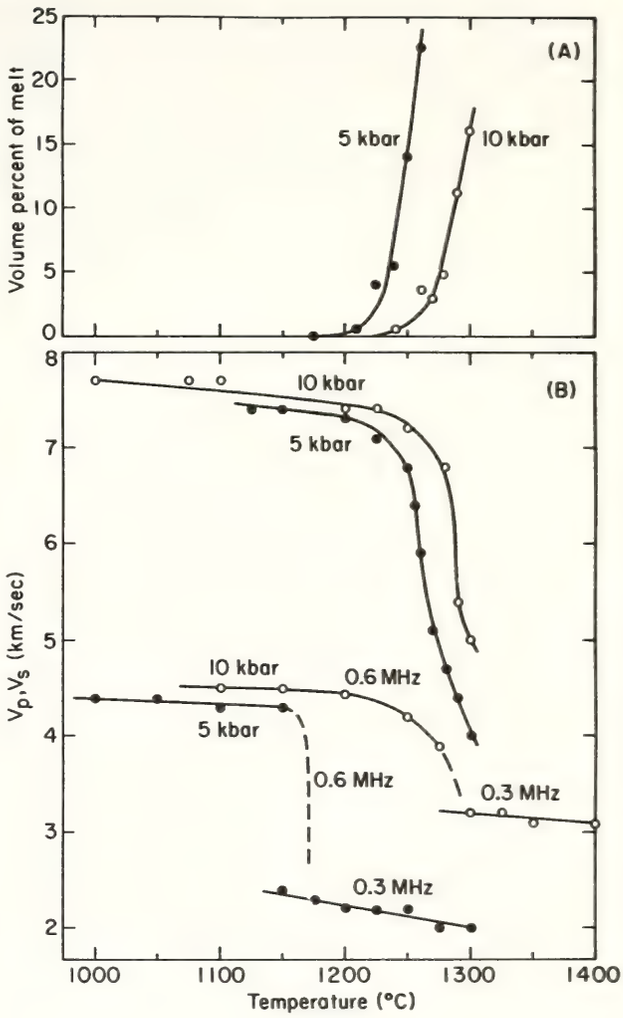


Fig. 27. (A) Shear and compressional wave velocities vs. temperature for spinel lherzolite at 5 kbar (solid circles) and 10 kbar (open circles). (B) Percentage of melt vs. temperature for spinel lherzolite inclusion (BCP) at 5 and 10 kbar. The data on compressional wave velocity and degree of melting at 5 kbar were obtained by Murase and Kushiro (*Year Book 78*).

The normalized velocities show an essentially linear decrease to about 10% melt. At 5 kbar the relationship between the normalized V_p and the degree of melting does not coincide with that of the normalized V_s. At 10 kbar, however, both relationships almost coincide in the region of low de-

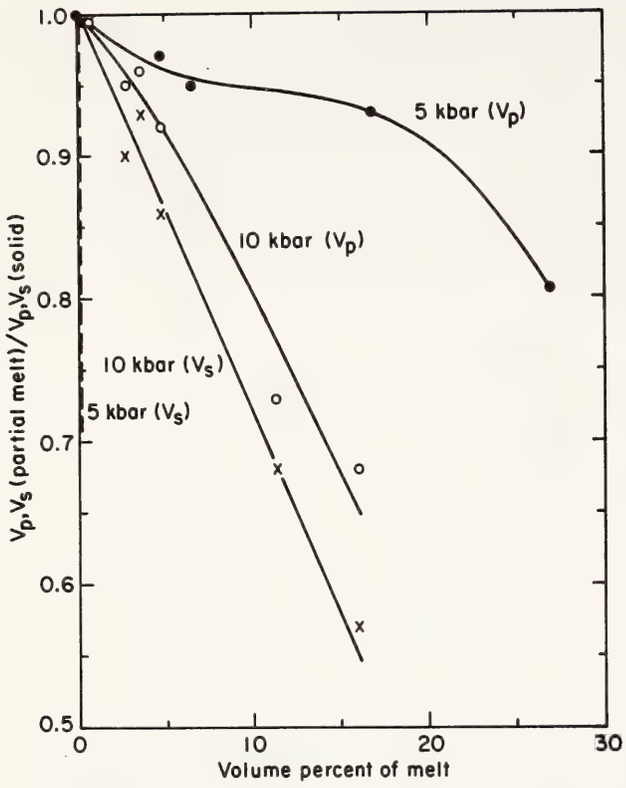


Fig. 28. Normalized shear and compressional wave velocities in partial melts vs. volume percentage of melt for spinel lherzolite at 5 kbar (dashed line and solid circles) and 10 kbar (crosses and open circles).

gree of melting, and they may draw much closer to each other at a higher pressure. Accordingly, the relationship may hold to several tens of kilobars in the region of low degree of melting. If the relationship at 10 kbar is applicable to the mantle, then a 5% decrease in V_p and V_s, as observed for the low-velocity zone, implies about 2–3 vol % melting under anhydrous conditions.

References

Anderson, D. L., and H. Spetzler, Partial melting and the low-velocity zone, *Phys. Earth Planet. Inter., 4,* 62–64, 1970.

Birch, F., Density and composition of the upper mantle: first approximation as an olivine layer, in "The Earth's Crust and Upper Mantle," P. J. Hart, ed., *Geophys. Monogr. Amer. Geophys. Union, 13,* 18–36, 1969.

Jacques, A. J., and D. H. Green, Determination of liquid compositions in high-pressure melting of peridotite, *Amer. Mineral., 64,* 1312–1321, 1979.

Murase, T., and A. R. McBirney, Properties of some common igneous rocks and their melts at high temperatures, *Geol. Soc. Amer. Bull., 84,* 3563–3592, 1973.

Mysen, B. O., and I. Kushiro, Compositional variations of coexisting phases with degree of melting of peridotite in the upper mantle, *Amer. Mineral., 62,* 843–865, 1977.

Nur, A., Tectonophysics: the study of relations between deformation and forces in the earth, in *Advances in Rock Mechanics,* Vol. 1, Part A, National Academy of Sciences, pp. 243–317, 1974.

Yoder, H. S., Jr., High-low quartz inversion up to 10,000 bars, *Trans. Amer. Geophys. Union, 31,* 827–835, 1950.

Anionic Constitution of 1-atm Silicate Melts: Implications for the Structure of Igneous Melts

D. Virgo, B. O. Mysen, and I. Kushiro

In order to understand crystal-melt equilibria as well as geophysically and petrologically important physical properties of magma, it is necessary to determine the structure of such melts. To build a comprehensive model of the structure of silicate melts, Virgo *et al.* (1980) combined their own Raman spectroscopic data with published vibrational spectroscopic data on binary, ternary, and more complex joins (Brawer and White, 1975, 1977; Furukawa and White, 1980; Verweij, 1979a, b; Sweet and White, 1969; Bell and Dean, 1972; Galeener and Lucovsky, 1976; Lucovsky, 1979a, b; Furukawa *et al.*, 1978).

Virgo *et al.* (1980) found that on all MO-SiO_2 and M_2O-SiO_2 joins (M = Li, Na, K, Mg, Ca, Sr, and Pb) a total of five different anionic structures occur. The joins between orthosilicate (NBO/Si* = 4) and the three-dimensional network (NBO/Si = 0) can be subdivided into three structural regions, within each of which three units are in equilibrium:

NBO/Si = 4–2.1:

$$Si_2O_7^{6-} = SiO_4^{4-} + SiO_3^{2-}; \quad (1)$$

*Nonbridging oxygen per silicon.

NBO/Si = 2.1–1.0:

$$3SiO_3^{2-} = SiO_4^{4-} + Si_2O_5^{2-}; \quad (2)$$

NBO/Si = 1.0–0.05:

$$Si_2O_5^{2-} = SiO_3^{2-} + SiO_2. \quad (3)$$

These ranges of NBO/Si are not significantly affected by the different metal cations.

Aluminum is mixed randomly with silicon in each structural unit provided that metal cations are present for local charge balance. Aluminum is a network modifier if there is not sufficient metal cation present for local charge balance (see also Mysen, Virgo, and Scarfe, this Report).

Ferric iron (charge balanced with alkali metals), titanium, and phosphorus are also network formers, but these cations occur in discrete structural units rather than in random mixtures with silicon. Spectroscopically, this difference is manifested in a continuous shift of characteristic stretch bands involving Si^{4+} and Al^{3+}, whereas in the other three cations, characteristic stretch vibrations for the individual tetrahedral cations are observed. The Si-O stretch vibrations in such systems are not affected unless coupled Al^{3+} is required to make new, aluminum-bearing, tetrahedral complexes.

On the basis of these considerations, Virgo *et al.* (1980) concluded that the anionic units in magmas can be calculated. All natural magmas more acidic than picrite or olivine basalt lie in the compositional field corresponding to Equation 3. The bulk NBO/*T* (nonbridging oxygen per tetrahedral cation) of these magmas differ, however, so that the proportions of the individual units will differ depending on the composition of the magma. For tholeiite, NBO/*T* = 0.6–0.8; for andesite, NBO/*T* is about 0.3; and for granite, NBO/*T* is equal to or less than 0.1.

With these data it is possible to predict the viscous behavior of the magma (Mysen, Scarfe, and Virgo, this Report), variations of trace-element partition coefficients between the magma and a given mineral (Mysen and Virgo, this Report), redox equilibria of iron (Mysen and Virgo, this Report), and solution mechanisms of volatiles in the magma (Mysen, Virgo, Scarfe, and Harrison, this Report; Mysen and Virgo, this Report).

References

Bell, R. J., and P. Dean, Localization of phonons in vitreous silica and related glasses, in *International Conference on the Physics of Noncrystalline Solids, 3rd, University of Sheffield, 1970,* R. W. Douglas and B. Ellis, eds., Wiley-Interscience, London, pp. 443–452, 1972.

Brawer, S. A., and W. B. White, Raman spectroscopic investigation of the structure of silicate glasses. I. The binary silicate glasses, *J. Chem. Phys., 63,* 2421–2432, 1975.

Brawer, S. A., and W. B. White, Raman spectroscopic investigation of the structure of silicate glasses. II. Soda-alkaline earth-alumina ternary and quaternary glasses, *J. Non-Cryst. Solids, 23,* 261–278, 1977.

Furukawa, T., and W. B. White, Raman spectroscopic investigation of the structure of silicate glasses. III. Alkali-silico-germanates, *J. Chem. Phys.,* in press, 1980.

Furukawa, T., S. A. Brawer, and W. B. White, The structure of lead silicate glasses determined by vibrational spectroscopy, *J. Mater. Sci., 13,* 268–282, 1978.

Galeener, F. L., and G. Lucovsky, Longitudinal optical vibrations in glasses; GeO_2 and SiO_2, *Phys. Rev. Lett., 37,* 1474–1478, 1976.

Lucovsky, G., Spectroscopic evidence for valence alternation pair defects in vitreous SiO_2, *Phil. Mag., 39,* 513–531, 1979a.

Lucovsky, G., Defect-controlled carrier transport in amorphous SiO_2, *Phil. Mag., 39,* 531–541, 1979b.

Sweet, J. R., and W. B. White, Study of sodium silicate glasses and liquids by infrared spectroscopy, *Phys. Chem. Glasses, 10,* 246–251, 1969.

Verweij, H., Raman study of the structure of alkali germano-silicate glasses. I. Sodium and potassium metagermano-silicate glasses, *J. Non-Cryst. Solids, 33,* 41–53, 1979a.

Verweij, H., Raman study of the structure of alkali germano-silicate glasses. II. Lithium, sodium and potassium digermano-silicate glasses, *J. Non-Cryst. Solids, 33,* 55–69, 1979b.

Virgo, D., B. O. Mysen, and I. Kushiro, Anionic constitution of silicate melts quenched at 1 atm from Raman spectroscopy: implications for the structure of igneous melts, *Science,* in press, 1980.

Relations Between Anionic Structure and Viscosity of Silicate Melts—a Raman Spectroscopic Study

B. O. Mysen, D. Virgo, and C. M. Scarfe

The viscosity of silicate melts is closely related to their anionic structure (Bockris *et al.*, 1956; Mackenzie, 1960; Bockris and Reddy, 1970). Mysen *et al.* (1980) studied a range of silicate melt compositions and attempted to relate the structural results to the viscous behavior of the melts.

The melt compositions were in the binary systems Na_2O-SiO_2, CaO-SiO_2, (Ca,Mg)O-SiO_2, and SiO_2-Al_2O_3. These compositions were chosen because it had been observed that the activation energy of viscous flow in such systems is systematically related to NBO/Si of the melt (Bockris and Reddy, 1970).

The anionic structure of the melts was determined with Raman spectroscopy. The samples were quenched melts of the appropriate compositions. All details of sample preparation and analysis are given in Mysen *et al.* (1980). The latter investigators found that melts on these joins can be subdivided structurally into three groups (see also Virgo and Mysen, this Report). With NBO/Si greater than 2, monomers (SiO_4^{4-}), dimers ($Si_2O_7^{6-}$), and chains ($Si_2O_6^{4-}$) coexist. With NBO/Si between about 2 and 1, chains, monomers, and sheets ($Si_2O_5^{2-}$) coexist. With NBO/Si less than about 1, chains, sheets, and three-dimensional network structures (SiO_2) coexist. These subdivisions do not depend significantly on the type of network-modifying cation.

Aluminum is only a network former when charge is balanced with other metal cations so that the local charge balance is 4. Aluminum is therefore a network former on the join $NaAlO_2$-SiO_2, for example.

On binary joins the absolute value of the viscosity decreases as a continuous function of increasing NBO/Si (Bockris *et al.*, 1956; Lacy, 1968). It is noted, however, that the activation energy of viscous flow (E_η), recalculated to kilocalories/silicon in the anionic structure, is independent of NBO/Si within each of the compositional ranges where a fixed set of anionic structures coexist. Inasmuch as the E_η primarily reflects the dissociation energy of cation-oxygen bonds, and is invariant as a function of NBO/Si, Mysen *et al.* (1980) concluded that the number of metal-oxygen bonds broken to generate the flow units is constant within each compositional range where E_η is constant. As the NBO/Si decreases with increasing metal/silicon within each range, this conclusion implies that the size of the flow unit decreases with increasing NBO/Si. With NBO/Si less than about 1, the flow unit most likely resembles a $3D$ structure. In the compositional range where NBO/Si lies between 1 and 2, the flow unit decreases in size and has an average NBO/Si of about 3 when the NBO/Si of the melt is equal to 2. For more depolymerized melts (NBO/Si greater than 2) the flow units may become monomers.

The E_η increases with increasing metal-cation size and with increasing valence of the metal cation(s). If T-O bonds (T = tetrahedrally coordinated cation) control the activation energy (Bockris and Reddy, 1970), the above conclusion implies that for fixed NBO/Si of the melt, the size of a flow unit increases as the metal-cation size or its valence increases. Alternatively, Mysen *et al.* (1980) suggested that the energy required to break metal-cation–oxygen bonds (about 20% of that of an Si-O bond; Tossell, 1980) also influences the value of the activation energy. As the number of oxygens in metal-oxygen cation polyhedra in the melt increases with increasing metal radius and with increasing charge, the activation energy of viscous flow will also increase in the same direction.

Mysen *et al.* (1980) concluded on the basis of these experiments that if

Na/K, Ca/Mg, or Ca/Na of a melt decreases (as a result of fractional crystallization, for example), the viscosity of the melt will decrease. They also concluded that with Fe^{3+} as a network former (see Mysen and Virgo, this Report) the viscosity of the melt will decrease as Fe^{3+}/Al^{3+} increases. The latter effect may be observed in peralkaline magmas.

References

Bockris, J. O'M., and A. K. N. Reddy, *Modern Electrochemistry,* Vol. 1, Plenum Press, New York, 1970.

Bockris, J. O'M., J. W. Tomlinson, and J. L. White, The structure of liquid silicates, *Trans. Faraday Soc., 52,* 299–311, 1956.

Lacy, E. D., Structure transition in alkali silicate glasses, *J. Amer. Ceram. Soc., 51,* 150–157, 1968.

Mackenzie, J. D., Structure of some inorganic glasses from high-temperature studies, in *Modern Aspects of the Vitreous State,* Vol. 1, J. D. Mackenzie, ed., Butterworths, Washington, D.C., pp. 188–218, 1960.

Mysen, B. O., D. Virgo, and C. M. Scarfe, Relations between the anionic structure and viscosity of silicate melts—a Raman spectroscopic study, *Amer. Mineral., 65,* 690–710, 1980.

Tossell, J. A., Calculation of bond distances and heats of formation of BeO, MgO, SiO_2, FeO and ZnO using the ionic model, *Amer. Mineral., 64,* 163–174, 1980.

The Structural Role of Titanium in Silicate Melts

B. O. Mysen, F. J. Ryerson, and D. Virgo

It has been suggested that titanium acts as a polymerizer of the network in silicate melts (Kushiro, 1975; Visser and Koster van Groos, 1979). Solution of TiO_2 in magmas may therefore affect crystal-liquid equilibria (Kushiro, 1975).

In order to determine the details of the titanium solution mechanisms in silicate melts relevant to petrogenic processes of igneous rocks, Mysen *et al.* (1980a) used Raman spectroscopy to study the effect on Ti^{4+} on the structure of both depolymerized (NBO/Si greater than 1) and fully polymerized (NBO/Si = 0) melts. The melt compositions were the same as those of Mysen, Ryerson, and Virgo (this Report).

Solution if TiO_2 in both $CaMgSi_2O_6$ (Di) and $NaSiO_3$ (NS) melts results in the appearance of three Ti-O stretch bands in addition to the Si-O stretch bands. With the exception of the $^{-}$O-Si(Ti)-O° stretch band near 1020 cm^{-1}, the other two Ti-O stretch bands (Ti-O^{2-}, 780 cm^{-1}, and $^{-}$O-Ti-O^{-}, 850 cm^{-1}) indicate that there is little or no effect of Si^{4+} on these vibrational modes. Furthermore, the three Si-O stretch bands (Si-O^{2-}, 870 cm^{-1}, $^{-}$O-Si-O^{-}, 970 cm^{-1}; and $^{-}$O-Si-O°, 1100 cm^{-1}) are pure Si-O vibrational modes. Mysen *et al.* (1980a) concluded, therefore, that TiO_2-bearing, depolymerized silicate melts exhibit two-mode behavior; that is, three silicate anionic units and three titanate anionic units coexist in equilibrium in the melts. The generalized expression for titanium solution in depolymerized melts is (Mysen *et al.,* 1980a)

$$Si_4O_9^{2-}\,(\text{melt}) + 4TiO_2 = Ti_4O_9^{2-}\,(\text{melt}) + 4SiO_2\,(\text{melt}). \quad (1)$$

According to the stoichiometry of Equation 1, NBO/Si decreases by 0.0031 unit per mol percent dissolved TiO_2.

In fully polymerized aluminosilicate melts, titanium plays the same structural role as silicon except that aluminum titanate complexes coexist in equilibrium with aluminum silicate complexes, all of which have a three-dimensional network structure (Mysen *et al.,* 1980a). In order to form the aluminum titanate complexes, the aluminum silicate complexes are less aluminous in Ti-bearing aluminum silicate melts than in the aluminum-free analogue (Mysen *et al.,* 1980a). Aside from the fact that Ti-O bonds probably are weaker than the corresponding Si-O bonds and may, therefore, affect physical properties of the melt (Mysen *et al.,*

1980b), no changes in NBO/T (T = tetrahedrally coordinated cation) are observed in these melts.

Inasmuch as the effect of Ti^{4+} on depolymerized melt structure is similar to that of P^{5+} (see Mysen, Ryerson, and Virgo, this Report), solution of TiO_2 and P_2O_5 in such melts will have similar effects on the melt structures, as also documented by experiment (Visser and Koster van Groos, 1979; Ryerson and Hess, 1980).

The viscosity of depolymerized melts probably is increased with increasing Ti content of the melt because of the lowering of NBO/T as TiO_2 is dissolved. In fully polymerized melts the solution of Ti results in dilution of the silicate and thus causes a lowering of the activity of silica in the melt. Consequently, one would expect that liquidus boundaries between minerals of different degrees of polymerization (e.g., plagioclase and pyroxene) would shift toward the silicate-rich portion of the system. This effect differs from that of P_2O_5 in similar melts (Mysen, Ryerson, and Virgo, this Report), where the formation of nonbridging oxygens results in an expansion of the liquidus field of the least polymerized phase.

References

Kushiro, I., On the nature of silicate melt and its significance in magma genesis: regularities in the shift of liquidus boundaries involving olivine, pyroxene and silica minerals, *Amer. J. Sci., 275,* 411–431, 1975.

Mysen, B. O., F. J. Ryerson, and D. Virgo, The influence of TiO_2 on the structure and derivative properties of silicate melts, *Amer. Mineral.,* in press, 1980a.

Mysen, B. O., D. Virgo, and C. M. Scarfe, Relations between the anionic structure and viscosity of silicate melts—a Raman spectroscopic study, *Amer. Mineral., 65,* 690–710, 1980b.

Ryerson, F. J., and P. C. Hess, The role of P_2O_5 in silicate melts, *Geochim. Cosmochim. Acta, 44,* 611–625, 1980.

Visser, W., and A. F. Koster van Groos, Effects of P_2O_5 and TiO_2 on the liquid-liquid equilibria in the system K_2O-FeO-Al_2O_3-SiO_2, *Amer. J. Sci., 279,* 970–988, 1979.

The Structural Role of Phosphorus in Silicate Melts

B. O. Mysen, F. J. Ryerson, and D. Virgo

Even though P_2O_5 is a minor oxide in most magmas, phosphorus has attracted considerable attention because solution of P^{5+} in silicate melts appears to result in significant polymerization of the melt. Such polymerization affects phase equilibria (Kushiro, 1975; Visser and Koster van Groos, 1979), crystal-liquid trace element partitioning (Watson, 1976; Ryerson and Hess, 1978), and rheological properties of the melt (Mysen *et al.,* 1980b).

In order to understand the structural role of P^{5+} in silicate melts, Mysen *et al.* (1980a) studied the structure of P_2O_5-bearing silicate melts using Raman spectroscopy. They used diopside (Di, $CaMgSi_2O_6$) and sodium metasilicate (NS, $NaSiO_3$) melt compositions as examples of melts with a significant number of NBO/Si (nonbridging oxygen per silicon) and albite (Ab, $NaAlSi_3O_8$) and anorthite (An, $CaAl_2Si_2O_8$) compositions as examples of fully polymerized melts.

The Raman spectra of phosphorous-bearing, depolymerized melts indicate that phosphate chains are formed and that the proportion of silicate chains relative to monomers and sheet structures according to Mysen *et al.* (1980a) decreases. (See Virgo and Mysen, this Report, for discussion of silicate melt structures.) This mechanism may be expressed with the equation

$$Si_4O_9^{2-}\,(\text{melt}) + P_2O_5 = 2PO_3^{-}\,(\text{melt}) + 4SiO_2\,(\text{melt}). \qquad (1)$$

In fully polymerized, aluminosilicate melts, aluminophosphate complexes are formed. This reaction is accompanied by increased Si content of the three-dimensional aluminosilicate complexes and the formation of an aluminosilicate complex containing nonbridging oxygen:

$$3AlSi_3O_8^- \text{ (melt)} + P_2O_5 = 2AlPO_4 \text{ (melt)} + 8SiO_2 \text{ (melt)} + AlSiO_5^{3-} \text{ (melt)}. \quad (2)$$

The solution mechanism indicated in Equation 1 is similar to that suggested by others (Ryerson and Hess, 1978; Visser and Koster van Groos, 1979) to explain the effect of P_2O_5 on liquid immiscibility (Watson, 1976), liquidus boundary shifts (Kushiro, 1975), and crystal-liquid trace element partitioning (Watson, 1976). The stoichiometry of Equation 2 indicates that fully polymerized silicate melts will, in fact, become depolymerized as P_2O_5 is dissolved. Consequently, crystal-liquid trace-element partition coefficients involving such melts may decrease as phosphorus is dissolved (see also Mysen and Virgo, this Report). Liquidus boundaries involving plagioclase and pyroxene, for example, will shift toward the silica-deficient side of systems such as basalt and andesite. Furthermore, Mysen *et al.* (1980a) concluded that the viscosity of melts such as those of andesite and granite composition will be substantially lowered as P_2O_5 is dissolved in the melt.

References

Kushiro, I., On the nature of silicate melt and its significance in magma genesis: regularities in the shift of liquidus boundaries involving olivine, pyroxene, and silica minerals, *Amer. J. Sci., 275,* 411–431, 1975.

Mysen, B. O., F. J. Ryerson, and D. Virgo, The structural role of phosphorus in silicate melts, *Amer. Mineral.,* in press, 1980a.

Mysen, B. O., D. Virgo, and C. M. Scarfe, Relations between the anionic structure and viscosity of silicate melts—a Raman spectroscopic study, *Amer. Mineral., 65,* 690–710, 1980b.

Ryerson, F. J., and P. C. Hess, The partitioning of trace elements between immiscible silicate melts (abstract), *Eos, 56,* 470, 1978.

Visser, W., and A. F. Koster van Groos, Effects of P_2O_5 and TiO_2 on the liquid-liquid equilibria in the system K_2O-FeO-Al_2O_3-SiO_2, *Amer. J. Sci., 279,* 970–988, 1979.

Watson, E. B., Two-liquid partition coefficients: experimental data and geochemical implications, *Contrib. Mineral. Petrol., 56,* 119–134, 1976.

Viscosity-Temperature Relationships at 1 atm in the System Diopside-Anorthite

C. M. Scarfe, D. Cronin, J. Wenzel,* and D. Kauffman**

Bowen (1915) selected the ternary system $CaMgSi_2O_6$ (Di)-$CaAl_2Si_2O_8$ (An)-$NaAlSi_3O_8$ (Ab) to illustrate the crystallization of haplobasaltic and haplodioritic magmas. Since that time, considerable attention has been given to the phase relationships (e.g., Osborn, 1942; Schairer and Yoder, 1960; Wyllie, 1963; Kushiro and Schairer, *Year Book 68,* 222–226; Kushiro, *Year Book 72,* 502–507) and more recently to the thermochemistry (e.g., Weill *et al.,* 1980) of this classic system. In contrast, much less attention has been paid to other petrologically important properties such as the viscosity and density of melts in the system. Thus, in conjunction with a study of the structure of melts by laser Raman spectroscopy, a study of the viscosity-temperature relationships in this system was initiated with facilities at the National Bureau of Standards, Washington, D.C. This report describes results for the join diopside-anorthite in the temperature range 1200°–1650°C.

Experimental Method

Starting mixtures were prepared in 650-g batches from reagent-grade oxides, carbonates, and purified quartz sand. Melts free from bubbles and crystals were obtained by melting at approximately 100°C above the liquidus temperature. Melts were made in platinum crucibles in an electrically heated furnace with SiC resistance elements, and were stirred for approximately 2 hr to assure homogeneity. The melts were then poured directly into a 10.5 × 5.5 cm diameter platinum crucible, which was used for the viscosity measure-

*Center for Materials Science, National Bureau of Standards, Washington, D.C.

ments. The homogeneity and composition of the quenched melts (glasses) were verified by microprobe analysis.

Viscosities were measured with a commercially available rotating spindle viscometer, which uses a platinum spindle 5 × 1.2 cm in diameter, with conical ends. The apparatus was calibrated with NBS standard glass SRM 711, for which the viscosity-temperature relationship is accurately known. The viscosities are accurate to ±5%, and the temperatures are accurate to ±2°C.

Results and Discussion

The results are shown in Fig. 29 for six compositions along the join diopside-anorthite. Viscosities were measured over a range of temperatures above the liquidus and in the supercooled liquid region until significant crystallization intervened and the measurements became time dependent. Viscosities for all compositions decrease with increasing temperature, and the curves are nearly parallel to each other. For each composition, the viscosities at the liquidus temperature and at 1600°C are given in Table 18. At constant temperature, there is a systematic decrease in viscosities from anorthite to diopside; however, because of the temperature effect viscosities at the liquidus increase away from both end-member melts to a maximum at the eutectic composition.

The present data are compared in Fig. 29 with some previous determinations. For all compositions the present results are lower than the measurements of Kozu and Kani (1935). Bottinga and Weill (1972), in a discussion

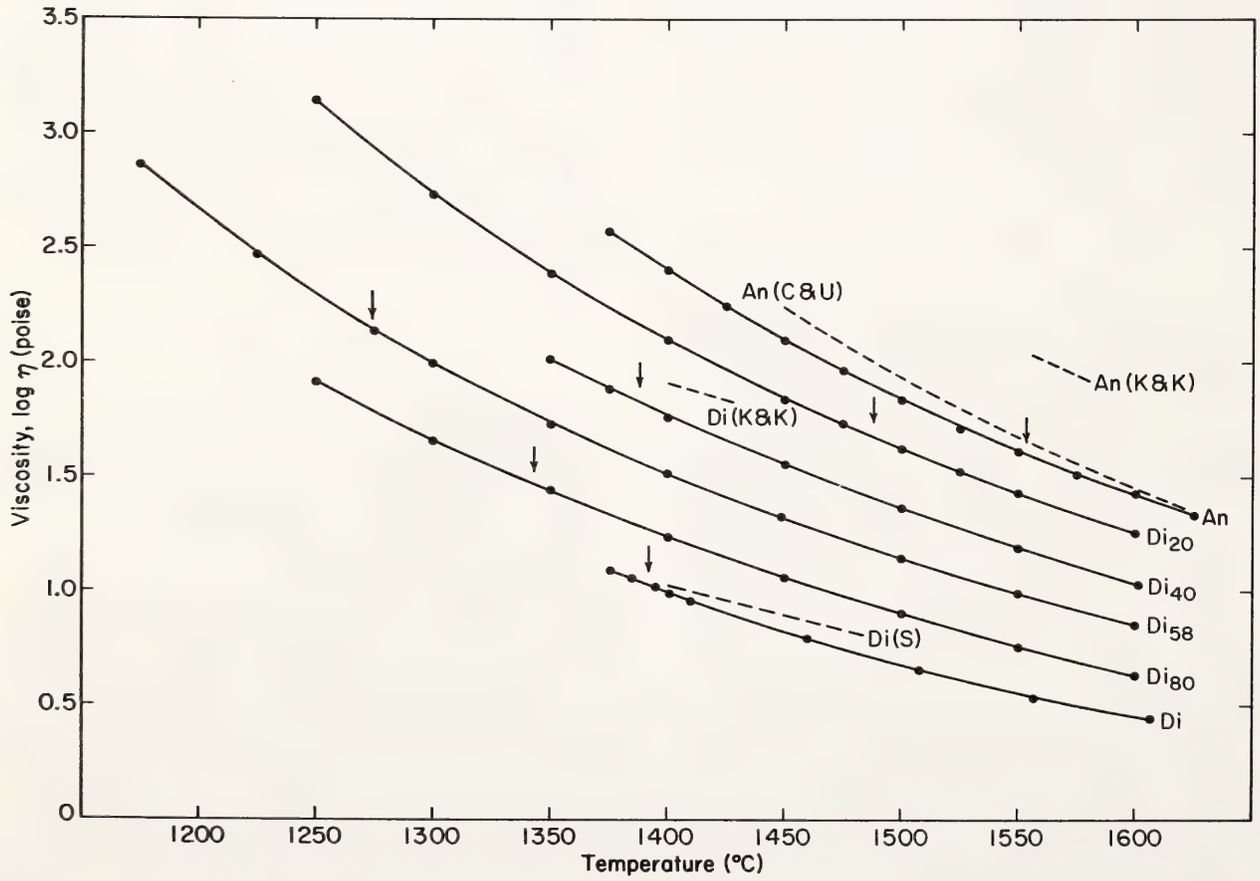


Fig. 29. Viscosity-temperature plot for compositions in the system diopside-anorthite. Dashed lines are previous determinations by Kozu and Kani (1935), Cukierman and Uhlmann (1973), and Scarfe (*Year Book 78*, 547-552). Arrows indicate liquidus temperatures.

TABLE 18. Compositions and Viscosities in the Diopside-Anorthite System

Diopside, wt %	Liquidus, °C	log η (T_l), poises	log η (1600°C), poises
100	1391.5	1.03	0.47
80	1343	1.46	0.64
58*	1274	2.14	0.85
40	1388	1.82	1.03
20	1488	1.67	1.25
0	1553	1.61	1.43

* Eutectic composition. Liquidus temperatures from phase diagram by Osborn (1942); see also Yoder (1976).

of their model for the viscosities of silicate melts, noted similar discrepancies between their calculations and the results of Kozu and Kani (1935). There is, however, agreement between the present results for diopside and data published by Scarfe (*Year Book 78*, 547–552). Results for anorthite are also in agreement with the work of Cukierman and Uhlmann (1973).

Viscosities above the liquidus have been fitted to an Arrhenius relationship of the form

$$\log \eta = \eta_0 + E_\eta/(2.3RT),$$

where η_0 is a constant, E_η the activation energy for viscous flow, R the gas constant, and T the absolute temperature. Activation energies range from 60 kcal mol^{-1} for anorthite to 39 kcal mol^{-1} for diopside (Table 19). Between the eutectic composition and 40 wt % diopside there seems to be a plateau in the activation energy for viscous flow. Viscosities over the entire range of melt and supercooled liquid temperatures were fitted by the method of least squares to the Fulcher (1925) equation

$$\log \eta = A + B/(T - T_0),$$

where T is the temperature in degrees centigrade, and A, B, and T_0 are constants (Table 19). The Fulcher equation reproduces the experimental data for each melt to better than 0.02 in log η throughout the temperature range measured.

Because the activation energy for viscous flow is a structure-sensitive parameter, the plateau in E_η between 40 and 58 wt % diopside may correspond to the region where significant structural changes take place in the melt. According to the model for the anionic structure of silicate melts (Mysen *et al.*, 1980), melts increasingly rich in anorthite will increase their degree of polymerization by elimination of SiO_4^{4-} monomers in favor of 3-*D* units. Mysen *et al.* (1980) showed that this type of structural change can be correlated with breaks in E_η vs. composition analogous to those observed here.

References

Bottinga, Y., and D. F. Weill, The viscosity of magmatic silicate liquids: a model for calculation, *Amer. J. Sci., 272*, 438–475, 1972.

TABLE 19. Arrhenius and Fulcher Equation Constants

Diopside, wt %	η_0	E_η	A	B	T_0
100	−4.137	39.2	−0.813	854.5	927.0
80	−4.615	44.9	−2.016	2841	526.8
58*	−5.281	52.3	−1.519	2203	672.4
40	−5.021	51.9	−1.965	3067	578.2
20	−5.472	57.6	−1.571	2483	722.7
0	−5.600	60.2	−1.476	2305	805.3

* Eutectic composition.

Bowen, N. L., The crystallization of haplobasaltic, haplodioritic and related magmas, *Amer. J. Sci., 40,* 161–185, 1915.

Cukierman, M., and D. R. Uhlmann, Viscosity of liquid anorthite, *J. Geophys. Res., 78,* 4920–4923, 1973.

Fulcher, G. S., Analysis of recent measurements of the viscosity of glasses, *Bull. Amer. Ceram. Soc., 8,* 339–355, 1925.

Kozu, S., and K. Kani, Viscosity measurements of the ternary system diopside-albite-anorthite at high temperatures, *Proc. Imp. Acad. Japan, 11,* 383–385, 1935.

Mysen, B. O., D. Virgo, and C. M. Scarfe, Relations between the anionic structure and viscosity of silicate melts—a Raman spectroscopic study, *Amer. Mineral., 65,* 690–710, 1980.

Osborn, E. F., The system $CaSiO_3$-diopside-anorthite, *Amer. J. Sci., 240,* 751–788, 1942.

Schairer, J. F., and H. S. Yoder, Jr., The nature of residual liquids from crystallization, with data on the system nepheline-diopside-silica, *Amer. J. Sci., 258A,* 273–283, 1960.

Weill, D. F., R. Hon, and A. Navrotsky, The igneous system $CaMgSi_2O_6$-$CaAl_2Si_2O_8$-$NaAlSi_3O_8$: variations on a classic theme by Bowen, in *Physics of Magmatic Processes,* R. B. Hargraves, ed., Princeton University Press, in press, 1980.

Wyllie, P. J., Effects of the changes in slope occurring on the liquidus and solidus paths in the system diopside-anorthite-albite, *Mineral. Soc. Amer. Spec. Pap., 1,* 204–212, 1963.

Yoder, H. S., Jr., *Generation of Basaltic Magma,* National Academy of Sciences, Washington, D.C., 1976.

Viscosity of Lavas from the Level Mountain Volcanic Center, Northern British Columbia

*C. M. Scarfe and T. S. Hamilton**

As part of a study of the petrology of alkaline volcanic rocks from Level Mountain, northern British Columbia (Hamilton and Scarfe, 1977; Hamilton, in preparation), viscosity measurements have been made on three representative lava types—an alkali basalt, a hawaiite, and a comendite. The measurements were made at 1 atm between 1200° and 1450°C. The data are significant to the ascent rate of the lavas and to the transport of mafic nodules included in them.

*Alberta Research Council, Edmonton, Canada.

Experimental Method

The starting materials were dried rock powders ground to pass 200 mesh. Chemical analyses and liquidus temperatures for the rocks, which are aphyric to fine grained and relatively free of phenocrysts, are given in Table 20.

Melts free from bubbles and crystals were fused from rock powder in a coal-gas/air furnace at 1400°–1600°C for 2 hr. Melts were prepared under reducing conditions, except for the hawaiite, which was prepared under both reducing and oxidizing conditions. The liquid was poured into a steel mold, the internal dimensions of which were iden-

TABLE 20. Chemical Analyses and Liquidus Temperatures of Rocks*

	1†	2	3
SiO_2	47.92	47.82	73.37
TiO_2	1.77	2.94	0.17
Al_2O_3	15.00	15.38	12.08
Fe_2O_3	4.22	2.42	1.84
FeO	7.42	10.73	2.11
MnO	0.14	0.18	0.10
MgO	10.61	5.99	0.07
CaO	7.80	9.06	0.18
Na_2O	1.57	3.81	5.79
K_2O	1.54	0.86	4.27
P_2O_5	...	0.58	0.01
H_2O^+	...	0.03	0.00
Total	97.99	99.80	99.99
NBO/T‡	0.86	0.75	0.06
T_l(°C)§	1275 ± 15	1270 ± 15	1215 ± 15

*Electron microprobe analyses of fused beads of rocks. FeO and H_2O by wet chemistry.

†1. Alkali basalt (PAP). 2. Hawaiite (8/25-50/6397). 3. Comendite (8/25-54/6345).

‡Number of nonbridging oxygens to tetrahedrally coordinated cations in the melt, as deduced from the chemical composition (Scarfe *et al., Year Book 78,* 547–552; Mysen *et al.,* 1980).

§Liquidus temperature measured under f_{O_2} conditions between the QFM and MW buffers (Hamilton, in preparation).

tical with the internal dimensions of the outer cylinder of a concentric-cylinder viscometer (Scarfe, 1977). Under run conditions the glass slug (~ 8 cm^3) filled the cavity between the inner and outer platinum cylinders of the viscometer. The torque transmitted to the inner cylinder by the silicate liquid was measured as an angular displacement and recorded by a light-spot deflection on a linear scale. Further details are given in Scarfe (1977). Viscosities are accurate to $\pm 5\%$, and temperatures to ± 5 °C. All experiments were conducted in air.

Results and Discussion

At any temperature above the liquidus, the comendite has a higher viscosity than the hawaiite and alkali basalt (Fig. 30). For example, at 1300 °C there is a difference of three orders of magnitude (10^2–10^5 poises) between the viscosities of comendite and hawaiite.

At temperatures above 1300 °C the data on all three rocks show a linear relationship between the logarithm of the viscosity and reciprocal temperature, in accord with the Arrhenius relationship

$$\log \eta = \eta_0 + E_\eta / 2.3RT,$$

where η_0 is a constant and E_η is the activation energy for viscous flow. Viscosities calculated by the Shaw (1972) method agree to within 0.2 log unit for comendite and hawaiite, and 0.4 log unit for alkali basalt (Fig. 30).

At temperatures below the liquidus, viscosities increase because of the presence of crystals, and Newtonian behavior no longer obtains (Shaw, 1969; Scarfe, 1973; Murase and McBirney, 1973). The oxidation state of the melt appears to have only marginal effect on the viscosities. Melts of hawaiite composition prepared under both oxidizing and reducing conditions show only small differences in viscosity.

The lower viscosity of the hawaiite and alkali basalt compared with that of the comendite may be explained as a function of melt composition and structure. Basic melts have a higher proportion of network-modifier cations and a less polymerized anionic melt structure (Scarfe, 1973, 1977; Scarfe *et al., Year Book 78,* 547–552; Mysen *et al.,* 1980). These differences are summarized by the structure-composition parameter NBO/*T,* which decreases from alkali basalt to comendite (Table 20). A further measure of the polymerization is the magnitude of the activation energy for viscous flow of these compositions: 98, 54, and 53 kcal mol^{-1} for comendite, hawaiite, and alkali basalt, respectively.

Because of the fine-grained to glassy nature of the rocks and because they contain few phenocrysts, it is assumed

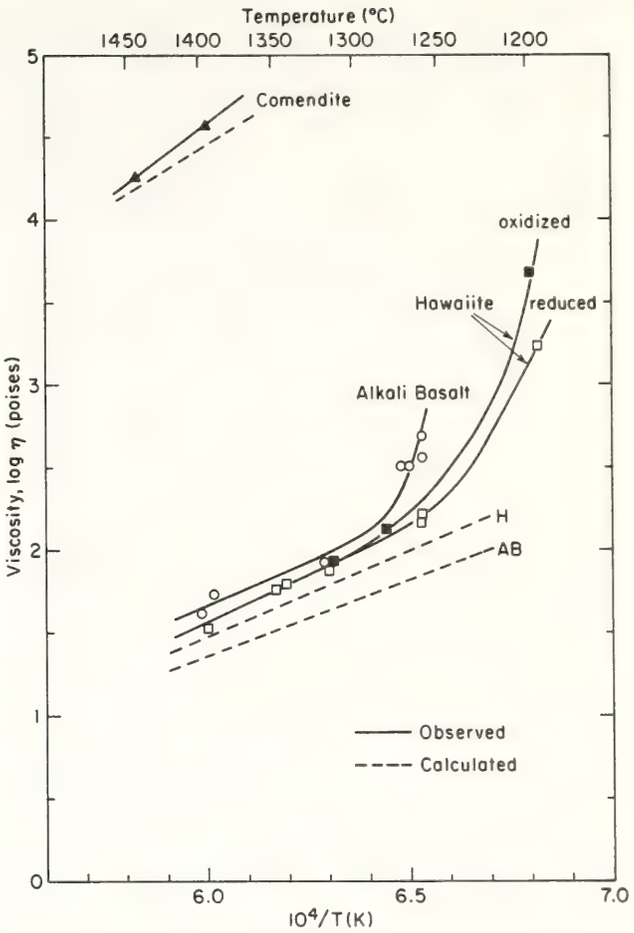


Fig. 30. Viscosity vs. reciprocal temperature for lavas from Level Mountain, northern British Columbia. H and AB refer to hawaiite and alkali basalt, respectively.

that the lavas extruded close to their liquidus temperatures. The viscosity of comendite at its liquidus temperature is about 10^6 poises. This viscosity is approximately four orders of magnitude higher than the viscosity of hawaiite and alkali basalt magmas at their eruptive temperatures. Volatiles dissolved in the comendite melt, however, particulary F and Cl (Macdonald *et al.*, 1974; Scarfe, 1977), may reduce viscosities considerably below 10^6 poises and may account for the apparent fluid nature of comendite flows in some locations on Level Mountain.

Ascent rates required to counteract sinking of mafic and ultramafic xenoliths entrained in the magmas can be estimated from Stokes' law and reasonable values for the change in melt viscosity and density at depth (Scarfe *et al., Year Book 78,* 547–552). When spinel lherzolite nodules ($\rho = 3.37$ g cm^{-3}, diameter = 5 cm) found in alkali basalts and troctolite nodules ($\rho = 3.13$ g cm^{-3}, diameter = 15 cm) found in hawaiites are used, minimum ascent rates of approximately 1 km/hr are obtained, provided that the melt has not undergone significant crystallization. These ascent rates are an order of magnitude faster than those estimated from data for Hawaiian tholeiites (Eaton and Murata, 1960).

The ascent velocity of a magma may also be calculated if it is assumed that the magma ascends along a conduit of diameter (d) as a consequence of the density contrast ($\Delta\rho$) between the melt and the country rock. The velocity of the ascending magma is described by

$$v = \frac{\Delta\rho g d^2}{12\eta}$$

where g is the gravitational constant and η is the melt viscosity (Takeuchi *et al.*, 1972). From this relationship it is clear that the rate of ascent of a given magma varies inversely as the magnitude of its viscosity. Thus, provided that the melts are free of volatiles and if reasonable conduit diameters are assumed, ascent rates for comendite are much slower than ascent rates for alkali basalt and hawaiite.

References

Eaton, J. P., and J. K. Murata, How volcanoes grow, *Science, 132,* 925–938, 1960.

Hamilton, T. S., and C. M. Scarfe, Preliminary report of the petrology of the Level Mountain volcanic center, northwestern British Columbia, *Geol. Surv. Can. Pap., 77-1A,* 429–434, 1977.

Macdonald, R., D. K. Bailey, and F. Barberi, Recommendations for further studies on the peralkalic oversaturated volcanic rocks, *Bull. Volcanol., 38,* 828–836, 1974.

Murase, T., and A. R. McBirney, Properties of some common igneous rocks and their melts at high temperatures, *Bull. Geol. Soc. Amer., 84,* 3563–3592, 1973.

Mysen, B. O., D. Virgo, and C. M. Scarfe, Relations between the anionic structure and viscosity of silicate melts—a Raman spectroscopic study, *Amer. Mineral., 65,* 690–710, 1980.

Scarfe, C. M., Viscosity of basic magmas at varying pressure, *Nature, 241,* 101–102, 1973.

Scarfe, C. M., Viscosity of a pantellerite melt at one atmosphere, *Can. Mineral., 15,* 185–189, 1977.

Shaw, H. R., Rheology of basalt in the melting range, *J. Petrology, 10,* 510–535, 1969.

Shaw, H. R., Viscosities of magmatic silicate liquids: an empirical method of prediction, *Amer. J. Sci., 272,* 870–893, 1972.

Takeuchi, H., N. Fujii, and M. Kikuchi, Mechanism of magma ascent (in Japanese), *Zishin, Ser. 2, 25,* 266–268, 1972.

Solubility Mechanisms of Water in Silicate Melts at High Pressure and Temperature

B. O. Mysen, D. Virgo, C. M. Scarfe, and W. J. Harrison

The solubility behavior of H_2O in silicate melts has been used to develop models of silicate melt structure (e.g., Burnham, 1974, 1975). Such models have subsequently been used to derive models for the petrogenetic histories of hydrous magmas. Mysen *et al.* (1980) concluded, however, that solubility mechanisms for H_2O in magma can be

determined directly by Raman spectroscopy of quenched liquids. After such data are available, the pronounced influence of water on crystal-liquid equilibria may be appreciated (see Mysen, 1977, for review).

Mysen *et al.* (1980) studied the role of H_2O in fully polymerized melts [$NaAlSi_2O_6$ (Jd) and $NaAlSi_3O_8$ (Ab)] and also in melts with NBO/Si (nonbridging oxygen per silicon) greater than zero. Melt compositions on the join Na_2O-SiO_2 were used as models for depolymerized silicate melts.

The Raman spectra of hydrous silicate melts show a broad, strong band near 3600 cm^{-1}, characteristic of OH groups in the melt (Stolen and Walrafen, 1976). There are no Raman bands attributable to molecular H_2O or hydrogen-metal bonds.

In the high-frequency envelope between 800 and 1200 cm^{-1}, stretch bands indicative of structural units with 0, 1, and 2 nonbridging oxygens occur in the melts. When H_2O is added to Ab and Jd melts, Si-OH symmetric stretch vibrations appear near 970 cm^{-1}, and an ^{-}O-Si(Al)-O^{-} stretch band is found near 860 cm^{-1}. An antisymmetric Si-O° stretch band near 1060 cm^{-1} is also observed.

It is concluded, therefore, that the solubility mechanism of water in fully polymerized melts results in depolymerization:

$$14NaAlSi_3O_8\,(\text{melt}) + 13H_2O\,(\text{vapor}) = 9Si_4O_7(OH)_2\,(\text{melt}) + 8Na^{+}\,(\text{melt}) + 8OH^{-}\,(\text{melt}) + 8Al^{3+}\,(\text{melt}) + 6NaAlSiO_6^{4-}\,(\text{melt}), \quad (1)$$

where, as Mysen *et al.* (1980) pointed out, not only did water produce anhydrous structural units with nonbridging oxygens, but some aluminum (equivalent to the amount of OH associated with Na) would no longer be a network former.

In melts on the join Na_2O-SiO_2-H_2O, the intensity of Raman bands indicative of nonbridging oxygen in the melt diminishes with increasing water content. This observation indicates that in melts with NBO/Si greater than 0, solution of H_2O at high pressure results in a decrease of NBO/Si, a suggestion also made by Uys and King (1963). Mysen *et al.* (1980) suggested the following solution mechanism for water in such melts:

$$6Si_2O_5^{2-}\,(\text{melt}) + 8H_2O\,(\text{vapor}) = 2Si_4O_7(OH)_2\,(\text{melt}) + 4SiO_2\,(\text{melt}) + 12OH^{-}\,(\text{melt}). \quad (2)$$

According to the stoichiometry of Equation 2, the NBO/Si *decreases* by 0.018 unit per mol % dissolved H_2O, whereas according to Equation 1, where water dissolves in fully polymerized melts, NBO/Si increases by 0.016 unit per mol % dissolved H_2O.

Albite and jadeite melts serve as models for andesitic and granitic melts. Mysen *et al.* (1980) concluded, on the basis of their experiments, that the increased NBO/Si of fully polymerized melts with water in solution helps explain why the melt viscosity decreases (viscosity decreases with increasing NBO/Si; Lacy, 1968) with increasing water content. The observation that the viscosity of hydrous, fully polymerized silicate melts does not decrease with increasing pressure (Kushiro, *Year Book 77,* 675–678) may also be appreciated in view of the increased NBO/Si (see Mysen *et al.,* this Report).

In view of the decrease of NBO/Si of depolymerized melts as H_2O is dissolved, Mysen *et al.* (1980) suggested that the viscosity of depolymerized melts such as those of komatiite and picrite composition may increase with increasing pressure because of the high NBO/Si of such melts. Addition of water to these melts may also result in an increase in their viscosity.

The liquidus boundaries between crystalline phases of different degrees of polymerization shift toward the silica-rich side of the system with increasing water content (see Kushiro, 1969,

1972). This shift is explained, according to Mysen *et al.* (1980), as a result of the increased NBO/Si of such melts.

References

Burnham, C. W., $NaAlSi_3O_8$-H_2O solutions: a thermodynamic model for hydrous magmas, *Bull. Soc. Fr. Mineral. Cristallogr., 97,* 223–230, 1974.

Burnham, C. W., Thermodynamics of melting in experimental silicate-volatile systems, *Geochim. Cosmochim. Acta, 39,* 1077–1084, 1975.

Kushiro, I., The system forsterite-diopside-silica with and without water at high pressures, *Amer. J. Sci., 267A,* 269–294, 1969.

Kushiro, I., Effect of water on the composition of magmas formed at high pressures, *J. Petrology, 13,* 311–334, 1972.

Lacy, E. D., Structure transition in alkali silicate glasses, *J. Amer. Ceram. Soc., 51,* 150–157, 1968.

Mysen, B. O., The solubility of H_2O and CO_2 in the predicted pressure and temperature range of magma genesis in the upper mantle, and some petrological and geophysical implications, *Rev. Geophys., 15,* 351–361, 1977.

Mysen, B. O., D. Virgo, W. J. Harrison, and C. M. Scarfe, Solubility mechanisms of H_2O in silicate melts at high pressures and temperatures: a Raman spectroscopic study, *Amer. Mineral.,* in press, 1980.

Stolen, R. H., and G. E. Walrafen, Water and its relation to broken bond defects in fused silica, *J. Chem. Phys., 64,* 2623–2631, 1976.

Uys, J. M., and T. B. King, The effect of basicity on the solubility of water in silicate melts, *Trans. Metall. Soc. AIME, 227,* 492–500, 1963.

Raman Study of K_2CO_3-$MgCO_3$ Glasses

S. K. Sharma and B. Simons

Carbonate has been detected in potassium silicate glasses (Verweij *et al.,* 1977) and in glasses of akermanite ($Ca_2MgSi_2O_7$), diopside ($CaMgSi_2O_6$, and sodium melilite ($CaNaAlSi_2O_7$) compositions, which were formed by quenching CO_2-saturated melts under pressure ($P \leq 25$ kbar) (Sharma *et al., Year Book 78,* 532–542). In the spectra of these carbonate-bearing silicate glasses, the Raman bands due to silicate species overlap with some of the bands of the CO_3^{2-} group and complicate the spectra. From these spectra it is difficult to evaluate the effect of disorder on the internal modes of carbonate ions and, consequently, structural information regarding the CO_3^{2-} ions. Knowledge of the effect of disorder on the internal modes of CO_3^{2-} ions in simple carbonate glasses may provide a better understanding of the structure of carbonate-bearing silicate melts. Raman spectra of glasses of $K_2CO_3 \cdot 3MgCO_3$, $K_2CO \cdot MgCO_3$, and $CaCO_3 \cdot 19K_2Mg(CO_3)_2$ compositions were therefore investigated.

Experimental

Reagent-grade K_2CO_3 and $CaCO_3$ were used. Natural magnesite rhombs from Brazil were the source of $MgCO_3$. The specific carbonate mixtures were kept at 110°C for 12 hr, and ~50-mg aliquots were sealed into $Pt_{95}Au_5$ capsules. Mixtures of $2K_2CO_3 \cdot 3MgCO_3$, $K_2CO_3 \cdot MgCO_3$ [$K_2Mg(CO_3)_2$], and $CaCO_3 \cdot 19K_2Mg(CO_3)_2$ were melted at 900°C and 1/2 kbar in a gas-media, high-pressure apparatus (Yoder, 1950) and then quenched rapidly under pressure. The melts of $K_2Mg(CO_3)_2$ and $CaCO_3 \cdot 19K_2Mg(CO_3)_2$ compositions quenched to clear, transparent glasses, whereas the melt of $2K_2CO_3 \cdot 3MgCO_3$ composition quenched to a brown glass (Datta *et al.,* 1964; Ragone *et al.,* 1966). Raman spectra were recorded with a Jobin-Yvon Raman spectrometer (Ramanor HG.2S). Details of the Raman apparatus are given elsewhere (Sharma, *Year Book 78,* 902–904).

Polarized spectra of the glass of $K_2CO_3 \cdot MgCO_3$ composition are shown in Fig. 31. Portions of the Raman spectra of carbonate glasses in the region of internal vibrational modes of the CO_3^{2-} ions are presented in Fig. 32. In glasses of $2K_2CO_3 \cdot 3MgCO_3$ and $CaCO_3 \cdot 19K_2Mg(CO_3)_2$ compositions it was not possible to measure the polarization characteristics of the bands because of the small sample size (<1 mm^3) and the

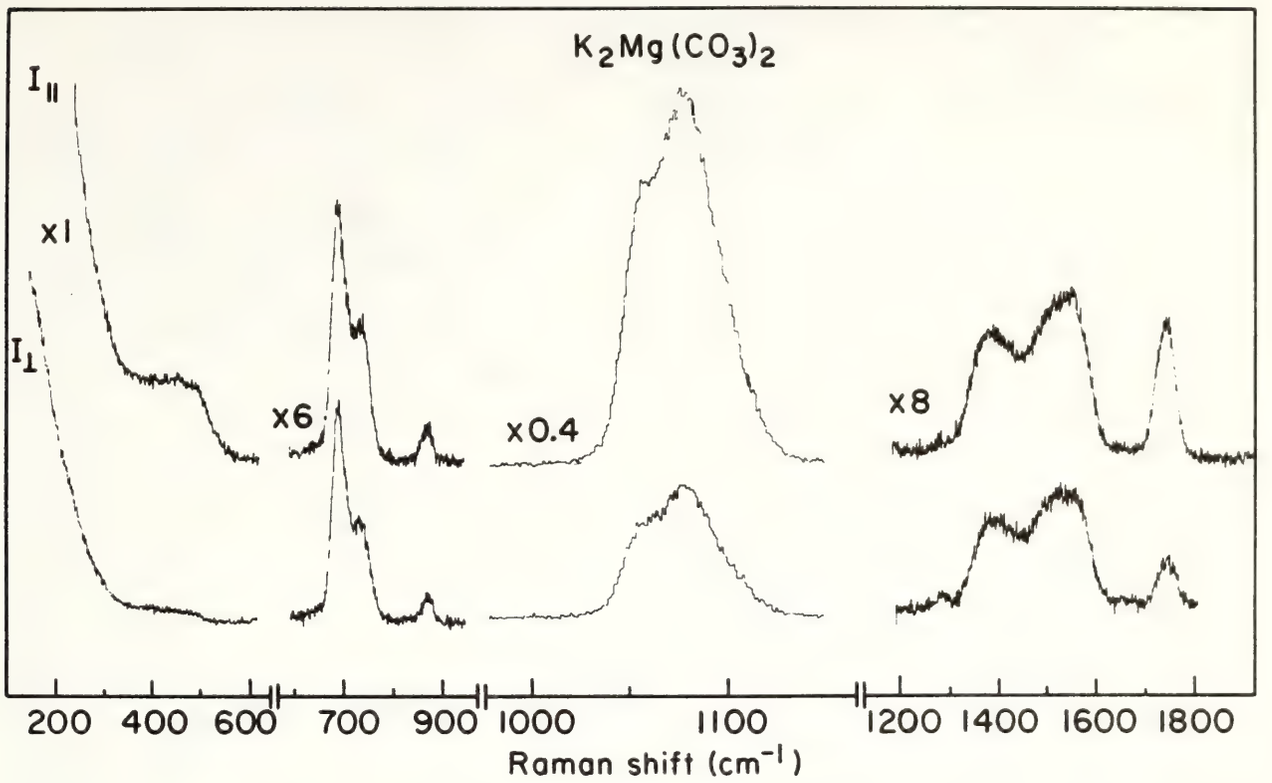


Fig. 31. Portions of Raman spectrum of glass of $K_2Mg(CO_3)_2$ composition. $I_{\parallel}$ and $I_{\perp}$, respectively, refer to the spectra recorded with the electric vector of scattered light parallel to and perpendicular to the electric vector of the laser beam. (Experimental: 488.0 nm excitation, 200 mW at the sample. Slit 10 cm^{-1}, except in 900-1100 cm^{-1} region where spectral slit width was 3 cm^{-1}.) The amplification factor refers to the values of amplification needed to record different portions of the spectra at a constant slit width of 10 cm^{-1}.

presence of strain. Positions and other spectral characteristics are given in Table 21.

Discussion

The symmetrical stretch ν_1 (A'_1) mode of a CO_3^{2-} ion is nondegenerate and appears in the 1000–1100 cm^{-1} region. The presence of at least three overlapping bands in this region of the spectra of $2K_2CO_3 \cdot 3MgCO_3$, $K_2Mg(CO_3)_2$, and $CaCO_3 \cdot 19K_2Mg(CO_3)_2$ glasses (Fig. 32) indicates the presence of carbonate ions at a minimum of three nonequivalent sites in these glasses.

The weak band at the 800–900 cm^{-1} region is an out-of-plane bending mode ν_2 (A''_2). This band is also a nondegenerate mode. In the spectra of glasses of $K_2CO_3 \cdot MgCO_3$ composition, there is no evidence for splitting of this band. If CO_3^{2-} ions are present at sites that have a three-fold axis of symmetry, the ν_2 mode is not allowed in the Raman spectrum. The presence of a single ν_2 band in the Raman spectra of glasses of $2K_2CO_3 \cdot 3MgCO_3$ and $K_2CO_3 \cdot MgCO_3$ compositions indicates that at least one of the sites in which CO_3^{2-} ions are present has lower symmetry (C_{2v} or C_s). In the spectrum of glass of $CaCO_3 \cdot 19K_2Mg(CO_3)_2$ composition the ν_2 band appears to split, and there is an additional band at ~822 cm^{-1}. The presence of three ν_2 bands in the spectrum of this glass is consistent with the hypothesis that in this glass carbonate ions are present at three nonequivalent sites; all these sites must have lower site symmetries (C_{2v} or C_s). Similar splitting of the ν_2 bands is observed in the infrared spectra of crys-

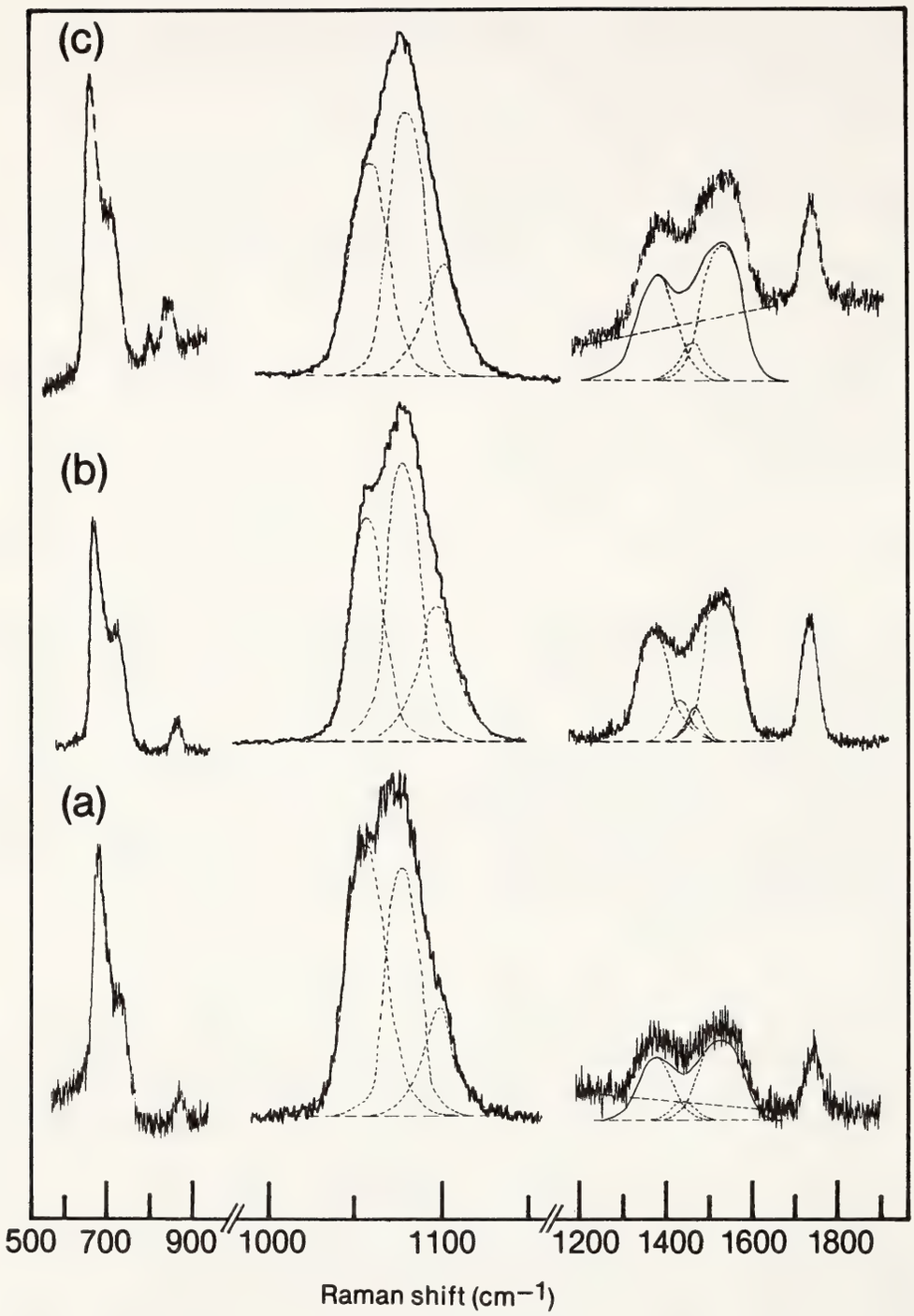


Fig. 32. Portions of the Raman spectra of carbonate glasses of (a) $2K_2CO_3 \cdot 3MgCO_3$, (b) $K_2CO_3 \cdot MgCO_3$ [$K_2Mg(CO_3)_2$], and (c) $CaCO_3 \cdot 19K_2Mg(CO_3)_2$ compositions. (Experimental: 488.0 nm excitation, 200 mW at the sample, except for sample (a) where 50 mW laser was used to avoid dissociation. Slit 10 cm^{-1}, except the 900-1100 cm^{-1} region where spectral slit width was 3 cm^{-1}.)

talline carbonates that are known to have CO_3^{2-} in two nonequivalent sites (White, 1974; Adler and Kerr, 1963).

The antisymmetric stretching mode, $\nu_3(E)$, of the CO_3^{2-} ion is a weak Raman scatterer. It appears as a very weak and broad envelope in the spectra of carbonate glasses (Fig. 32). A graphical analysis of these envelopes indicates that there are at least three overlapping bands. The ν_3 band is doubly degenerate, and splitting can occur if the carbonate ion (1) is present at a site without a three-fold axis and (2) com-

TABLE 21. Raman Frequencies (cm^{-1}) of Carbonate Glasses*

$2K_2CO_3 \cdot MgCO_3$	$K_2CO_3 \cdot MgCO_3$	$CaCO_3 \cdot 19K_2Mg(CO_3)_2$
~469 w, bd†	~456 w, bd, p	
688 m	684 m, dp	690 m
~730 (sh)	(ω = 48)	738 (sh)
	724 (sh), dp	
	(ω = 44)	
...	...	822 vw
...	...	854 w
865	872 w, p/dp	872 (sh)
	(ω = 30)	
1059 (sh)	~1058 (sh), p	~1062 (sh)
(ω = 25)	(ω = 21)	(ω = 26)
1078 s	1079 s, p	1080 s
(ω = 22)	(ω = 22)	(ω = 24)
~1098 (sh)	~1097 (sh)	~1104 (sh)
(ω = 20)	(ω = 26)	(ω = 24)
~1380 w, bd	~1376 w, bd, wp	~1390 w, bd
~1440 w, bd	~1432 w, bd	...
...	~1470 (sh)	~1470 (sh)
1528 w, bd	~1532 w, bd, wp	~1536 w, bd
1744 w	1744 w, p	1740 w

*Measurement accuracy is ± 10 cm^{-1} for weak and broad bands, ± 4 cm^{-1} for strong bands.
†Abbreviations: w, weak; m, medium; s, strong; sh, shoulder; bd, broad; p, polarized; dp, depolarized; wp, weakly polarized; ω, band width at half maximum height.

plexes covalently with cation. In aragonite, where CO_3^{2-} is in a site of lower symmetry, C_s, the bands in the ν_3 region are split by only 2 cm^{-1} (White, 1974; Nakamoto, 1978). Even in the spectra of calcite II and III at high pressures, the ν_3 band is split by only 26 cm^{-1} (Fong and Nicol, 1971).

Large splitting of the ν_3 modes has been observed in the infrared spectra of metallocarbonate complexes, where carbonate ions bonded covalently with a C_s symmetry (Nakamoto *et al.*, 1957; Fujita *et al.*, 1962). The possibility of covalent interaction of the CO_3^{2-} ion with Mg^{2+} and K^+ in these glasses can be ruled out because the low-frequency bands expected from such a complex are not observed in the spectra of all the glasses (Table 21). In the spectra of all three glasses the ν_3 modes show large splitting (Fig. 32, Table 21) and seem to be due to presence of CO_3^{2-} ions at nonequivalent sites in these glasses. The latter possibility should also be considered in interpreting spectra of carbonate-bearing silicate glasses.

The in-plane deformation mode $\nu_4(E)$ of the carbonate ion is doubly degenerate. In the Raman spectra of molten alkali metal carbonates no splitting of the ν_4 band was observed (Maroni and Cairns, 1970). The observed splitting of the ν_4 band at ~40 cm^{-1} is largely due to the presence of CO_3^{2-} ions in nonequivalent sites. The lower site symmetries of the CO_3^{2-} ions in these glasses may also contribute to the splitting of the ν_4 band. In the Raman spectra of K_2NO_3-$Mg(NO_3)_2$ (50-50; 55-45 mol %) (Furukawa *et al.*, 1978) the ν_1 band appears as a doublet and the ν_3 and ν_4 modes of nitrate ions show large splitting. The splitting of the ν_1 band was attributed to the presence of NO_3^- ions at two distinct sites.

In the Raman spectra of CO_3^{2-}-bear-

ing glasses of akermanite ($Ca_2MgSi_2O_7$) (Sharma, Hoering, and Yoder, *Year Book 78,* 537–542), diopside ($CaMgSi_2O_6$), and sodium melilite ($CaNaAlSi_2O_7$) (Sharma, *Year Book 78,* 532–537) compositions a large splitting (~ 90 cm^{-1}) of the ν_3 bands of CO_3^{2-} ions is observed. It has been suggested that the observed large splitting of the ν_3 bands in these silicate glasses may be due to covalent interaction of the CO_3^{2-} ion. No such splitting of the ν_3 band was observed in the Raman spectrum of carbonate-bearing potassium silicate glasses (Verweij *et al.,* 1977).

References

Adler, H. H., and P. F. Kerr, Infrared absorption frequency trend for anhydrous normal carbonates, *Amer. Mineral., 48,* 124–137, 1963.

Datta, R. K., D. M. Roy, S. P. Faile, and O. F. Tuttle, Glass formation in carbonate systems, *J. Amer. Ceram. Soc., 47,* 153, 1964.

Fong, F. Y., and M. Nicol, Raman spectrum of calcium carbonate at high pressures, *J. Chem. Phys., 54,* 579–585, 1971.

Fujita, J., A. E. Martell, and K. Nakamoto, Infrared spectra of metal chelate compounds. VIII. Infrared spectra of carbonate complexes, *J. Chem. Phys., 36,* 339–345, 1962.

Furukawa, T., S. A. Brawer, and W. B. White, Raman spectroscopic study of nitrate glasses, *J. Chem. Phys., 69,* 2639–2651, 1978.

Maroni, V. A., and E. J. Cairns, Raman spectra of fused carbonates, *J. Chem. Phys., 52,* 4915–4916, 1970.

Nakamoto, K., *Infrared and Raman Spectra of Inorganic and Coordination Compounds,* 3d ed., John Wiley and Sons, Inc., New York, 1978.

Nakamoto, K., J. Fujita, S. Tanaka, and M. Kobayashi, Infrared spectra of metallic complexes. IV. Comparison of infrared spectra of unidentate and bidentate metallic complexes, *J. Amer. Chem. Soc., 79,* 4904–4908, 1957.

Ragone, S. E., R. D. Datta, D. M. Roy, and O. F. Tuttle, The system potassium carbonate–magnesium carbonate, *J. Phys. Chem., 70,* 3360–3361, 1966.

Verweij, H., H. van den Boom, and R. E. Breemer, Raman scattering of carbonate ions dissolved in potassium silicate glasses, *J. Amer. Ceram. Soc., 60,* 529–534, 1977.

White, W. B., The carbonate minerals, in *The Infrared Spectra of Minerals,* V. C. Farmer, ed., Mineralogical Society, London, pp. 227–284, 1974.

Yoder, H. S., Jr., High-low quartz inversion up to 10,000 bars, *Trans. Amer. Geophys. Union, 31,* 827–835, 1950.

Influence of Melt Structure on Crystal-Liquid Trace-Element Partitioning

B. O. Mysen and D. Virgo

Trace-element partitioning is important in deducing the petrogenetic history of igneous rocks. It is therefore necessary to understand the mechanisms that control the changes of trace-element activity coefficients in the silicate melts. The processes of trace-element partitioning between minerals and silicate melt depend strongly on the bulk composition and thus on the structure of the melt (Watson, 1977; Hart and Davis, 1978; Irving, 1978). Mysen and Virgo (1980) used Raman spectral data on melt structures (Virgo *et al.*, 1980) in combination with determination of trace-element partition coefficients to study this relationship.

Nickel and rare earth element (REE) partition coefficients were determined along the 1500° and 1200°C isotherms in the respective systems $NaAlSi_3O_8$-$CaAl_2Si_2O_8$-Mg_2SiO_4 (AAF) (Schairer and Yoder, 1960) and $CaMgSi_2O_6$-$NaAlSiO_4$-SiO_2 (DNS) (Schairer and Yoder, *Year Book 65,* 204–209). In AAF, forsterite coexists with liquid of a broad compositional range, and in DNS, diopside coexists with liquid.

Mysen and Virgo (1980) found that Ni and REE partition coefficients are linear functions of NBO/T (nonbridging oxygen per tetrahedral cation) of the melt at constant temperature. They also found that the forsterite-liquid Mn-partitioning data of Watson (1977) obtained in the system AAF can be described with linear equations. The calculated relationships are

$$K_{Ni}^{fo\text{-}liq}\,(1500\,°C) = 19.16 - 15.65(NBO/T); \quad (1)$$

$$K_{Ce}^{\text{di-liq}}\,(1200\,^{\circ}\text{C}) = 0.140 - 0.118(\text{NBO}/T); \quad (2)$$

$$K_{Sm}^{\text{di-liq}}\,(1200\,^{\circ}\text{C}) = 0.962 - 1.510(\text{NBO}/T); \quad (3)$$

$$K_{Tm}^{\text{di-liq}}\,(1200\,^{\circ}\text{C}) = 0.686 - 1.140(\text{NBO}/T); \quad (4)$$

$$K_{Mn}^{\text{fo-liq}}\,(1350\,^{\circ}\text{C}) = 1.70 - 1.450(\text{NBO}/T); \quad (5)$$

$$K_{Mn}^{\text{fo-liq}}\,(1450\,^{\circ}\text{C}) = 1.34 - 0.880(\text{NBO}/T). \quad (6)$$

These equations are valid only within the calibrated compositional ranges. In the present case, these ranges correspond to the compositional range where the anionic structual units coexisting in the melt are chains, sheets, and three-dimensional network.

Inasmuch as the only variable in these systems is the structure of the melt, the changes of crystal-liquid partition coefficients are linearly correlated with the activity coefficients of the trace element in the melt. Mysen and Virgo (1980) concluded, therefore, that the activity coefficients of REE, Mn, and Ni in silicate magmas are linearly correlated with the NBO/T of the melt.

Mysen and Virgo (1980) summarized data on the solubility mechanisms of Al^{3+}, Fe^{3+}, P^{5+}, Ti^{4+}, Fe^{2+}, CO_2, and H_2O in silicate melts. From these data, they calculated changes in NBO/T as a function of the concentration of dissolved oxide. With such data it is possible to calculate changes in values of crystal-liquid partition coefficients as a function of composition of the silicate melt. For example, for H_2O dissolved in aluminosilicate melts, the diopside-liquid partition coefficient for cerium is

$$K_{Ce}^{\text{di-liq}}\,(1200\,^{\circ}\text{C}) = 0.13X_{H_2O}^{\text{mol}} + 0.118(\text{NBO}/T)^{\text{dry melt}}. \quad (7)$$

Similar equations may be derived for other oxides and other melt compositions.

Mysen and Virgo (1980) concluded that addition of a few wt % minor oxide to magma will result in discernible effects on crystal-liquid partition coefficients. Such variations, however, may not be petrologically significant. Only when changes of all oxide concentrations are considered and converted into variations in NBO/T will crystal-liquid trace element partition coefficients be significantly affected by the liquid composition.

References

Hart, S. R., and K. E. Davis, Nickel partitioning between olivine and silicate melt, *Earth Planet. Sci. Lett., 40*, 203–220, 1978.

Irving, A. J., A review of experimental studies of crystal/liquid trace element partitioning, *Geochim. Cosmochim. Acta, 42*, 743–771, 1978.

Mysen, B. O., and D. Virgo, Trace element partitioning and melt structure: an experimental study at 1 atm pressure, *Geochim. Cosmochim. Acta*, in press, 1980.

Schairer, J. F., and H. S. Yoder, Jr., The nature of residual liquids from crystallization, with data on the system nepheline-diopside, *Amer. J. Sci., 258A*, 273–283, 1960.

Virgo, D., B. O. Mysen, and I. Kushiro, Anionic constitution of 1-atmosphere silicate melts: implications for the structure of igneous melts, *Science, 208*, 1371–1373, 1980.

Watson, E. B., Partitioning of manganese between forsterite and silicate liquid, *Geochim. Cosmochim. Acta, 41*, 1363–1374, 1977.

ISOTOPE AND ELEMENT PARTITIONING

Oxygen Isotope Fractionation during Regional Metamorphism

Douglas Rumble III

Oxygen isotopic analysis has become an important tool for investigating the interaction of hydrothermal solutions and rocks in the earth's crust. Isotope geochemists have enjoyed their greatest successes to date in the study of near-surface processes such as epizonal contact metamorphism and epithermal ore deposition (Taylor, 1979). There is growing evidence that oxygen isotope methods are useful in deducing the nature of fluid-rock interaction during deep-seated processes such as regional metamorphism (see review by O'Neill, 1979). The purpose of this report is to discuss the problem of deducing mechanisms of fluid-rock interaction from measurements of the oxygen isotope composition of regionally metamorphosed rocks and minerals. Included in the discussion is an enumeration of the factors that control partitioning of oxygen isotopes between rock and fluid. The mechanisms of Rayleigh distillation during devolatization reactions and infiltration from an external reservoir are evaluated quantitatively with a numerical model developed especially for the purpose. A major conclusion of the study is that oxygen isotopic analysis is, indeed, a powerful tool for deducing the mechanisms of interaction between hydrothermal solutions and rocks during regional metamorphism of deeply buried rocks.

Method of Study

Rayleigh distillation is a process in which the products of a reaction are isolated from reactants immediately after formation. Such a process is likely to occur during metamorphism because the volatile products of metamorphic reactions are driven away from the reaction site by pressure gradients and buoyancy. Product H_2O and CO_2 do not remain, therefore, in isotopic equilibrium with the rocks from which they were released. Rayleigh distillation in a two-phase system is described by the following equation (Broecker and Oversby, 1971, p. 166):

$$\delta_{\text{initial}} - \delta_{\text{final}} = 1000(f^{\alpha-1} - 1), \quad (1)$$

where $\delta_{\text{initial}} - \delta_{\text{final}}$ gives the change in reactant composition, f is the fraction of unconverted reactant, and α is the partitioning of isotopes between product and reactant (symbols are explained in Table 22). Equation 1 is inadequate to deal with devolatization reactions, however, because it is valid only for constant α. Consideration of Equation 2 (below) shows that $\Delta_{\text{WR-FL}}$ ($\cong 1000 \ln \alpha$) would change in response to the changing proportions of minerals undergoing reaction at constant T, and constant δ_{FL}. Accordingly, a numerical scheme was devised to calculate the effects of Rayleigh distillation, taking into account all the factors influencing $\Delta_{\text{WR-FL}}$.

TABLE 22. Explanation of Symbols

$\delta_i = \{[(^{18}O/^{16}O)_i/(^{18}O/^{16}O)_s] - 1\} \times 1000$, where i refers to an unknown sample and s refers to a standard.

$\alpha_{i-j} = (^{18}O/^{16}O)_i/(^{18}O/^{16}O)_j$: the partitioning of ^{18}O and ^{16}O between phases i and j.

WR: whole rock. FL: fluid. f: fluid species. i: mineral. Q: quartz.

$\Delta_{\text{WR}-\text{FL}} = \delta_{\text{WR}} - \delta_{\text{FL}} \simeq 1000 \ln \alpha_{\text{WR}-\text{FL}}$
$\Delta_{\text{Q}-f} = \delta_{\text{quartz}} - \delta_f \simeq 1000 \ln \alpha_{\text{Q}-f}$
$\Delta_{\text{Q}-i} = \delta_{\text{quartz}} - \delta_i \simeq 1000 \ln \alpha_{\text{Q}-i}$

X_f: atomic fraction of oxygen in fluid species f relative to the total number of oxygen atoms in fluid.
X_i: atomic fraction of oxygen in mineral i relative to the total number of oxygen atoms in whole rock.

In the numerical model of this work, the principle of conservation of mass is used to compute the isotopic effects of devolatization reactions for very small increments of reaction progress. The calculations are reiterated with continually updated values so that what is finally obtained is the approximation of smooth curves by short, straight-line segments. The convergence of the computation scheme was checked by using smaller and smaller increments of reaction progress. Test calculations of Rayleigh distillation in a two-phase system (the evaporation of H_2O) show agreement of ± 0.1 ‰ for up to 70% completed reaction and of ± 0.5 ‰ for 90% completed reaction between the computer program of this study and the analytic form of Rayleigh's equation with constant α (see Equation 1).

Rayleigh distillation is but one of a number of mechanisms of fluid-rock interaction. Another mechanism of fluid-rock interaction is infiltration, a process whereby the minerals in rock exchange isotopes with fluid flowing through the rock. By this means a rock may come to be in isotopic equilibrium with an external reservoir. Such a process is likely to occur during metamorphism because the volatile species released by metamorphic reactions must pass through other rocks in order to reach the earth's surface. The numerical procedure described above was modified to compute the effects of infiltration either alone or combined with Rayleigh distillation. Test calculations of infiltration into a rock *not* undergoing devolatization give results in agreement with fluid-rock ratios computed with Taylor's (1977, p. 524) "open system," or "single-pass" model.

Whole Rock-Fluid Partitioning

The magnitude of isotope partitioning between whole rock and fluid is an important factor to be taken into account because it controls the effectiveness of isotope fractionation by Rayleigh distillation (as discussed below). The magnitude of whole rock–fluid partitioning, at equilibrium, is governed by (1) temperature, (2) identity and abundance of oxygen-bearing minerals in a rock, and (3) identity and abundance of oxygen-bearing species in fluid. These relationships, for quartzose rocks, are summarized in the following equation:

$$\Delta_{\text{WR-FL}} = \sum_f X_f \Delta_{Q-f} - \sum_i X_i \Delta_{Q-i}. \quad (2)$$

The values X_i are calculated from measured modal and chemical analyses of minerals in a rock. (Symbols are explained in Table 22.) The quantities X_f are computed from the chemical and species composition of fluid in a rock under study. The terms Δ_{Q-f} and Δ_{Q-i} are functions of temperature only.

It may be deduced from Equation 2 that the sign and magnitude of $\Delta_{\text{WR-FL}}$ are controlled by fluid composition, at constant T and constant δ_{WR}. An example of the dependence of $\Delta_{\text{WR-FL}}$ on fluid composition is given in Fig. 33, where it may be seen that $\Delta_{\text{WR-FL}}$ (rock assumed to consist entirely of quartz) changes from $+1.8$ for pure H_2O to -5.6 for pure CO_2 (cf. Ohmoto, 1972). These observations clearly demonstrate the necessity of estimating the proportions of H_2O and CO_2 in metamorphic fluids so that $\Delta_{\text{WR-FL}}$ can be computed accurately.

Mechanisms of Fluid-Rock Interaction

The mechanism of fluid-rock interaction is another important factor in controlling oxygen isotopic fractionation during metamorphism. An example of Rayleigh distillation is presented in Fig. 34A, where it may be seen that changes in δ values of minerals and whole rock are small, 1 ‰, and 3 ‰, respectively. The calculated results of Rayleigh distillation associated with a variety of other dehydration and combined dehydration-decarbonation reac-

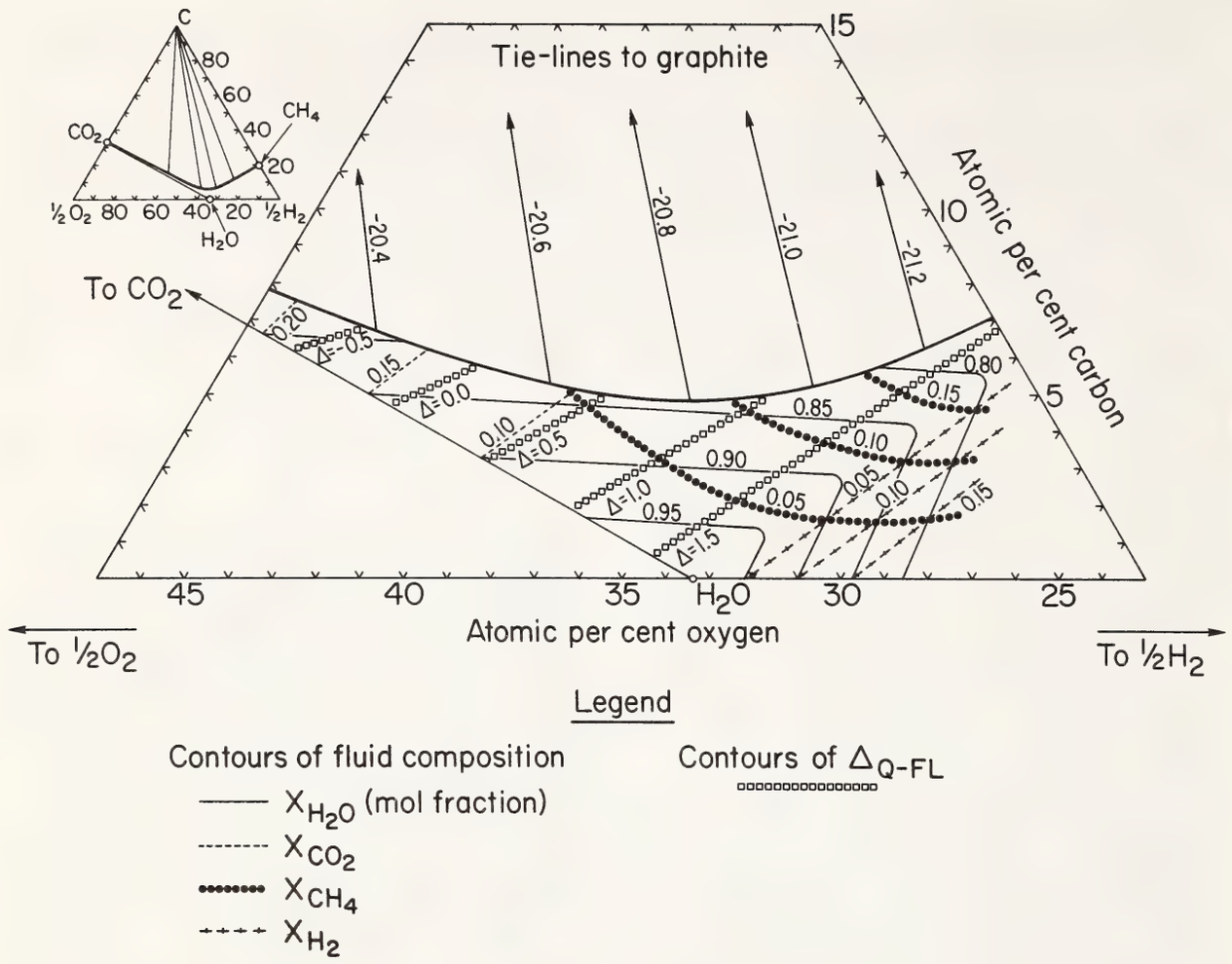


Fig. 33. Variation in Δ_{Q-FL} as a function of H_2O/CO_2 in fluid, at 600°C, 3.5 kbar. Tie lines to graphite are labeled with appropriate values of $\log_{10} fO_2$.

tions show as small or smaller changes in δ values. Fractionation of oxygen isotopes by Rayleigh distillation is small because the amount of oxygen released as H_2O or CO_2 is a small fraction of the total oxygen contained in a rock. The value of f in Equation 2 is limited by reaction stoichiometry to greater than 0.6. Rayleigh distillation during devolatization reactions, therefore, cannot be an efficacious mechanism for fractionating oxygen isotopes.

An example of combined Rayleigh distillation and infiltration is presented in Fig. 34B. At each increment of decarbonation a sufficient amount of H_2O is added to the rock to maintain fluid composition at equilibrium CO_2/H_2O. Reaction increments are chosen to be so small that the amount of fluid added to or removed from a rock does not exceed its porosity. This example might be referred to as "disequilibrium" infiltration because the infiltrating fluid is not, initially, in isotopic equilibrium with the rock being infiltrated. It may be seen that changes in δ values of minerals and whole rock are far larger for a given degree of reaction progress, than changes calculated for Rayleigh distillation (Fig. 34A). Rayleigh distillation is inherently limited in its effectiveness to fractionate oxygen isotopes because of the reaction stoichiometry of devolatization reactions. Fractionation by means of infiltration has no such limitation and may change oxygen isotopic compositions of rocks and minerals by 10–20 ‰.

Another example of combined Rayleigh distillation and infiltration is given in Fig. 35. In this case, the oxy-

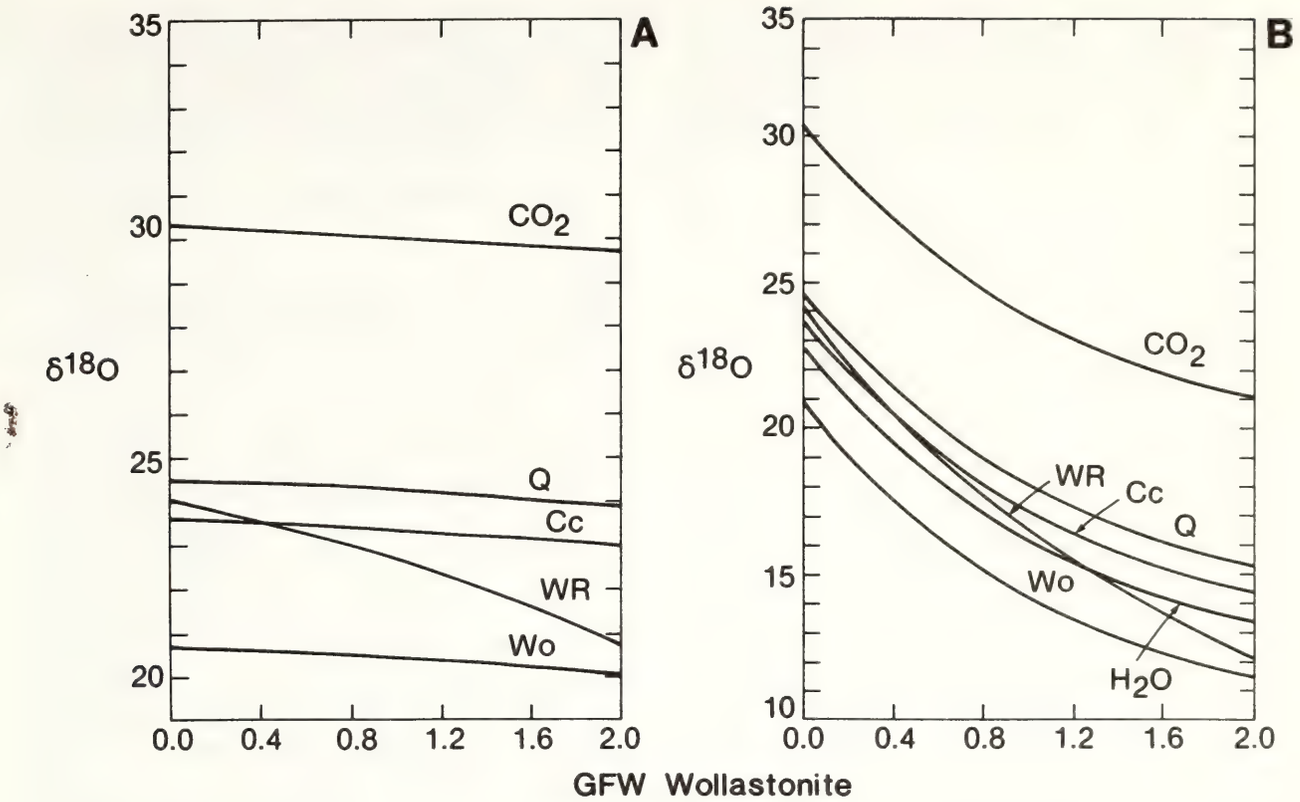


Fig. 34. Plots of $\delta^{18}O$ of minerals and whole rock vs. reaction progress, as measured by numbers of gram-formula-weight (gfw) units of wollastonite formed by the reaction Cc + Q = Wo + CO_2 at 600°C and 3.5 kbar. (A) shows computed changes in $\delta^{18}O$ for Rayleigh distillation alone. Fluid composition is pure CO_2. (B) gives calculated changes in $\delta^{18}O$ for a rock infiltrated by H_2O with $\delta^{18}O_{H_2O} = +12.5‰$. Fluid composition is maintained at equilibrium value of $X_{CO_2} = 0.09$ (mole fraction). For both (A) and (B), initial amounts of Cc and Q are 2.11 and 2.49 gfw, respectively, and initial $\delta_{WR} = +24.0‰$. Abbreviations: Cc, calcite; Q, quartz; Wo, wollastonite; and WR, whole rock.

gen isotope composition of added H_2O is stipulated to be whatever is in equilibrium with the minerals of the rock at a given stage of reaction progress. The effect of such fluid-rock interaction on the oxygen isotope composition of minerals and whole rock is even smaller than that of Rayleigh distillation alone.

Conclusions

The models described in this report emphasize the factors that must be considered when interpreting mechanisms and extent of fluid-rock interaction from oxygen isotope analyses of metamorphosed rocks and minerals. (1) Accurate geothermometry is required to estimate isotopic partitioning between minerals and fluid components. (2) The proportions of H_2O and CO_2 in fluid together with modal analysis of a rock and chemical analyses of its minerals are required to calculate $\Delta_{WR\text{-}FL}$. (3) Unambiguous evidence on the isotopic composition of rocks prior to metamorphism is needed to deduce mechanisms of fluid-rock interaction. Such evidence might be unmetamorphosed stratigraphic and sedimentologic equivalents of the rocks under study or metamorphosed rocks that contain recognizable fossils of marine invertebrates. (4) Finally, an accurate computational model of fluid-rock interaction must be used to test hypotheses against measured data.

A general conclusion emerges from this study. If large changes in a rock's oxygen isotopic composition (10‰ or more) are observed as a consequence of metamorphism, then it is a virtual certainty that the rock was infiltrated by

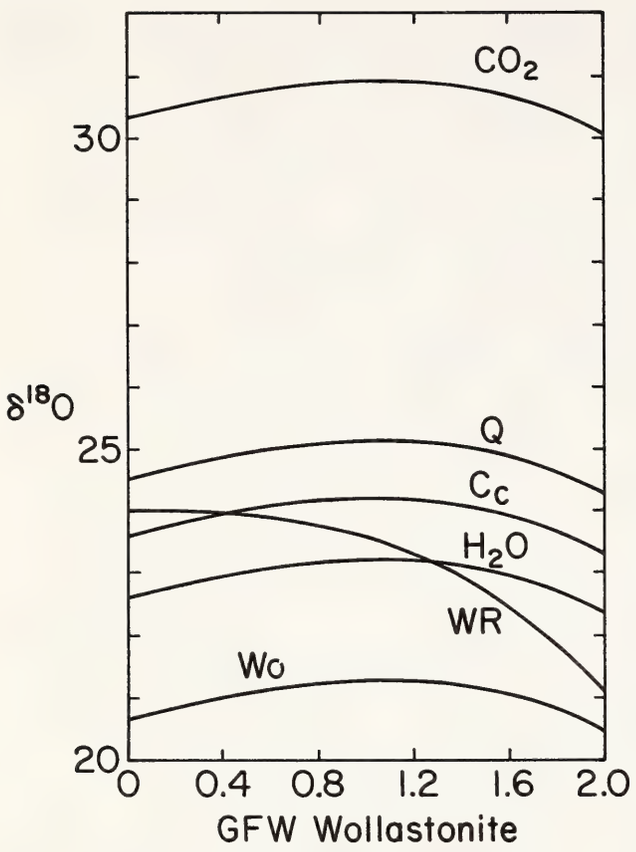


Fig. 35. Plot of $\delta^{18}O$ of minerals and whole rock vs. reaction progress for the reaction Cc + Q = Wo + CO_2 at 3.5 kbar and 600°C. Rock infiltrated by H_2O, in oxygen isotopic equilibrium with minerals in rock at given stage of reaction progress. Fluid composition is maintained at equilibrium value of X_{CO_2} = 0.09 (mole fraction). Initial amounts of minerals, initial $\delta^{18}O_{WR}$, and abbreviations, as in Fig. 34.

large amounts of fluid initially not in isotopic equilibrium with the rock. Calculated values of fluid/rock in the range of 2–4, by volume, have been obtained for metamorphosed, fossiliferous calc-silicate rocks.

References

Broecker, W. S., and V. M. Oversby, *Chemical Equilibria in the Earth*, McGraw-Hill Book Co., New York, 1971.

Ohmoto, H., Systematics of sulfur and carbon isotopes in hydrothermal ore deposits, *Econ. Geol., 67*, 551–578, 1972.

O'Neill, J. R., Stable isotope geochemistry, *Rev. Geophys. Space Phys., 17*, 839–850, 1979.

Taylor, H. P., Jr., Water/rock interactions and the origin of H_2O in granitic batholiths, *J. Geol. Soc. London, 133*, 509–558, 1977.

Taylor, H. P., Jr., Oxygen and hydrogen isotope relationships in hydrothermal mineral deposits, in *Geochemistry of Hydrothermal Ore Deposits*, 2d ed., H. L. Barnes, ed., John Wiley and Sons, Inc., New York, pp. 236–277, 1979.

Mg-Fe^{2+} Partitioning Between Olivine and Ferrian Ulvospinel

S. A. Rawson and T. N. Irvine

The partitioning of Mg and Fe^{2+} between olivine and spinel solid solutions in ultramafic and mafic igneous rocks is highly variable and, in principle, can be used for geothermometry, the pressure effect being small. The magnitude of the temperature effect depends, however, on the overall composition of the spinel phase, which may involve complex substitutions of Fe^{3+}, Al, Cr, Ti, V, and other elements. The thermodynamic basis of a geothermometer for the chromite spinels was set out by Irvine (1965), and Jackson (1969) provided a first calibration. Over the years, improvements have been made on both the theory and the calibration (Wood and Nichols, 1978; Evans and Frost, 1975; Medaris, 1975; Roeder *et al.*, 1979; Fabries, 1979; Engi, 1978). In none of these works, however, have the effects of Ti been considered, even though this element is known to be a significant constituent of most spinels in terrestrial igneous rocks, lunar rocks, and meteorites (cf. El Goresy *et al.*, 1976). In the present study, experimental data have been obtained on olivine–spinel composition–temperature relations in a system in which the essential components are MgO, FeO, Fe_2O_3, TiO_2, and SiO_2.

Theory

The following spinel end-member components are pertinent to the experimental study and will be referred to by the indicated symbols, based in part on the affiliated mineral names:

$Fe_2^{2+}TiO_4$: Ulvospinel, Us

$Fe^{2+}Fe_2^{3+}O_4$: Magnetite, Mt

Mg_2TiO_4: Magnesiotitanate, Ms

$MgFe_2^{3+}O_4$: Magnesioferrite, Mf.

Like other spinel components, Us and Ms have three cations and four oxygens, but they are distinctive in that they have two Mg^{2+} and Fe^{2+} ions per formula unit, rather than the more usual one. Accordingly, if N_i^{α} denotes the mole or cation fraction of constituent i in phase α, the total fraction of Ti end member is

$$Y_{Ti}^{sp} = (N_{Us}^{sp} + N_{Ms}^{sp})/(N_{Us}^{sp} + N_{Ms}^{sp} + N_{Mt}^{sp} + N_{Mf}^{sp}), \quad (1)$$

$$= 3N_{Ti}^{sp}/(3N_{Ti}^{sp} + 1.5\,N_{Fe^{3+}}^{sp}),$$

$$= 2N_{Ti}^{sp}/(2N_{Ti}^{sp} + N_{Fe^{3+}}^{sp}), \quad (1')$$

and similarly, the Fe^{3+} end-member fraction is

$$Y_{Fe^{3+}}^{sp} = N_{Fe^{3+}}^{sp}/(2N_{Ti}^{sp} + N_{Fe^{3+}}^{sp}). \quad (2)$$

Note that, by expanding the denominator in Equation 1, expressions similar to Equation 2 can be obtained for end members of Cr, Al, V^{3+}, and other trivalent elements.

The Mg-Fe^{2+} exchange between olivine and the Ti-Fe^{3+} spinels involves two main reactions:

$$0.5\,Fe_2^{2+}SiO_4 + 0.5\,Mg_2TiO_4 \rightleftharpoons 0.5\,Mg_2SiO_4 + 0.5\,Fe_2^{2+}TiO_4, \quad (a)$$

and

$$0.5\,Fe_2^{2+}SiO_4 + MgFe_2^{3+}O_4 \rightleftharpoons 0.5\,Mg_2SiO_4 + Fe^{2+}Fe_2^{3+}O_4. \quad (b)$$

By multiplying Reaction a by Y_{Ti}^{sp} and Reaction b by $Y_{Fe^{3+}}^{sp}$, and noting that $Y_{Ti}^{sp} + Y_{Fe^{3+}}^{sp} = 1$, the following joint exchange equation is obtained:

$$0.5\,Fe_2^{2+}SiO_4 + 0.5\,Y_{Ti}^{sp}\,Mg_2TiO_4 + Y_{Fe^{3+}}^{sp}\,MgFe_2^{3+}O_4 \rightleftharpoons 0.5\,Mg_2SiO_4 + 0.5\,Y_{Ti}^{sp}\,Fe_2^{2+}TiO_4 + Y_{Fe^{3+}}^{sp}\,Fe^{2+}Fe_2^{3+}O_4. \quad (c)$$

The equilibrium constant of Reaction c is

$$K_{(c)} = \frac{(a_{Fo}^{ol})^{0.5}\,(a_{Us}^{sp})^{0.5Y_{Ti}^{sp}}\,(a_{Mt}^{sp})^{Y_{Fe^{3+}}^{sp}}}{(a_{Fa}^{ol})^{0.5}\,(a_{Ms}^{sp})^{0.5Y_{Ti}^{sp}}\,(a_{Mt}^{sp})^{Y_{Fe^{3+}}^{sp}}}, \quad (3)$$

where a_i^{α} is the activity of i in α.

By means of the Temkin (1945) model, the activities may be related to the phase compositions by equations like the following three examples for the Mg components:

$$a_{Fo}^{ol} = \gamma_{Fo}^{ol}\,(N_{Mg}^{ol})^2\,(N_{Si}^{ol}),$$

$$a_{Us}^{sp} = \gamma_{Us}^{sp}\,(N_{Mg}^{sp})^2\,(N_{Ti}^{sp}), \text{ and}$$

$$a_{Mf}^{sp} = \gamma_{Mf}^{sp}\,(N_{Mg}^{sp})\,(N_{Fe^{3+}}^{sp})^2.$$

Substitution of these equations into Equation 3 yields

$$K_{(c)} = K'_{(c)}\,(X_{Mg}^{ol}/X_{Fe^{2+}}^{ol})/(X_{Mg}^{sp}/X_{Fe^{2+}}^{sp}), \quad (4)$$

where $X_{Mg}^{\alpha} = N_{Mg}^{\alpha}/(N_{Mg}^{\alpha} + N_{Fe}^{\alpha})$; $X_{Fe^{2+}}^{\alpha} = 1 - X_{Mg}^{\alpha}$; and $K'_{(c)}$ combines the γ activity coefficient terms and represents the joint departures of the two solid solutions from thermodynamic ideality. The last part of Equation 4 is the Mg-Fe^{2+} distribution coefficient, K_D. Thus,

$$K_{(c)} = K'_{(c)}\,K_D. \quad (5)$$

The equilibrium constant of a reaction can also be written

$$\ln K_{\text{Reaction}} = -\Delta G^\circ_{\text{Reaction}}/RT, \quad (6)$$

where $\Delta G^\circ_{\text{Reaction}}$ is the Gibbs free energy change when the reaction occurs between the mineral end members, R is the gas constant, and T is temperature. Hence,

$$\ln K'_{(c)} K_D = (-Y_{\text{Ti}}^{\text{sp}} \Delta G^\circ_{(a)} - Y_{\text{Fe}^{3+}}^{\text{sp}} \Delta G_{(b)})/RT. \quad (7)$$

Consider now a fourth reaction,

$$0.5\text{Mg}_2\text{TiO}_4 + \text{Fe}^{2+}\text{Fe}_2^{3+}\text{O}_4 \rightleftharpoons 0.5\text{Fe}_2^{2+}\text{TiO}_4 + \text{MgFe}_2^{3+}\text{O}_4. \quad (d)$$

It is seen that Reaction b = Reaction a − Reaction d; therefore Equation 7 can be rewritten

$$\ln K'_{(c)} K_D = (-\Delta G^\circ_{(a)} + Y_{\text{Fe}^{3+}}^{\text{sp}} \Delta G^\circ_{(d)})/RT. \quad (8)$$

Substitutions of Equation 6 and rearrangement then gives

$$\ln K_D = \ln K_{(a)} - \ln K'_{(c)} - Y_{\text{Fe}^{3+}}^{\text{sp}} \ln K_{(d)}. \quad (9)$$

Thus, compositional data on equilibrated olivine-spinel pairs covering a range of $Y_{\text{Fe}^{3+}}^{\text{sp}}$ and formed at a temperature at which both minerals were ideal solutions (i.e., $\ln K'_{(c)} = 0$) should define a straight line on a plot of $\ln K_D$ vs. $Y_{\text{Fe}^{3+}}^{\text{sp}}$. The ordinate intercept of the line at $Y_{\text{Fe}^{3+}}^{\text{sp}} = 0$ should be $\ln K_{(a)}$, its slope should be $-\ln K_{(d)}$, and its intercept at $Y_{\text{Fe}^{3+}}^{\text{sp}} = 1$ should be $\ln K_{(b)}$. If temperature changed, a new line might be defined; if one or both of the minerals are nonideal, then the line may be curved, and the relationship may also depend on the Mg-Fe^{2+} ratios of the solid solutions.

Experimental Methods

Olivine-spinel pairs were formed by way of 1-atm melting experiments in Pt-wound quenching furnaces controlled to within 1 °C by silicon-control rectifiers (Hadidiacos, *Year Book 78*, 679–682). Temperatures were measured with Pt-Pt90Rh10 thermocouples calibrated to ±1.5 °C against the melting points of Au (1062.6) and diopside (1391.5). Oxygen fugacities (f_{O_2}) were controlled by gas mixtures of CO and CO_2 (Nafziger *et al.*, 1971) and were accurate to 0.16 log unit when tested against the Fe-FeO and Ni-NiO buffers. The experimental charges were hung on the looped ends of short pieces of 0.004-inch-diameter Pt wire to minimize iron loss under reducing conditions (Presnall and Brenner, 1974).

Crystalline starting materials were Fo, Fa, Us, and Ms. They were combined with potassium tetrasilicate ($K_2O \cdot 4SiO_2$), which served as a flux to promote the recrystallization and Mg-Fe^{2+} exchange necessary to equilibrate the solid solutions. Factors in the choice of flux were (1) K is practically excluded from olivine and spinel, and (2) $K_2O \cdot 4SiO_2$ has a low melting temperature and its liquidus relations with Fo and Fa are well known (Roedder, 1951, 1952), a feature that was helpful in selecting starting compositions. Starting compositions were chosen to cover as large a range of Mg/Fe^{2+} as possible and to yield approximately 40% crystals and 60% melt (to facilitate equilibration). The temperatures investigated were 1067 °C (1340 K) and 1167 °C (1440 K); f_{O_2} values ranged from 10^{-6} to $10^{-12.5}$ at both temperatures. Phases were examined optically and were analyzed with the electron microprobe. Phase compositions were generally uniform after 22–30 hr; selective duplication in runs of 48–50 hr gave practically the same compositions.

Results

The run products typically featured equant olivine grains, 25–50 μm in size, and cubic spinel crystals, 1–20 μm on a

side, both set in K-rich glass. The spinel is a ferrian ulvospinel, but with increasing f_{O_2}, it approaches Mf. With decreasing f_{O_2}, ilmenite appears and eventually takes the place of the spinel. The proportions of FeO and Fe_2O_3 in the spinel have not been measured directly but have been calculated on the assumption that the phase is stoichiometric with 4 oxygens per 3 cations. This procedure generally improved the analytical totals and so would appear to yield reasonable results.

The plot of the analytical data in Fig. 36 shows that K_D varies substantially with the Mg-Fe^{2+} ratios of both phases and also with Fe^{3+}/Ti in the spinel. In the plot of ln K_D vs. $Y_{Fe^{3+}}^{sp}$ in Fig. 37, the same data are contoured for the Mg/Fe^{2+} of the olivine. The contours are consistent but are not well defined. The uncertainties indicated by the sizes of the plot-point boxes reflect only the analytical precision. There is almost certainly some scatter in the data owing to equilibration problems, and there is also some uncertainty relating to the method of calculating Fe^{3+}/ Fe^{2+} in the spinel. The fact that the data can be even approximately contoured, however, is a significant indication of nonideality in the mineral solid solutions. Nafziger and Muan (1967) reported positive deviations from ideality in olivine in the temperature range 1150°–1250°C, and Nafziger (1973) found negative deviations in the Mt-Mf spinels at these temperatures. It is highly probable that the Ti-bearing spinels investigated here are also nonideal, but unfortunately, as illustrated in Fig. 37, the available thermochemical data for ln $K_{(a)}$ and ln $K_{(b)}$ exhibit such large disparities that it is not yet possible to evaluate ln $K'_{(c)}$ and the activity coefficients.

The thermochemical data illustrated in Fig. 37 do, nevertheless, indicate appreciable temperature dependences for Reactions *a* and *b*. These dependences should be reflected by the intercepts of the olivine-composition contours with the ln K_D axes, but they are not yet significantly defined by the experimental data. The above theory and the experimental data should, however, be useful even at this stage for refining the olivine-chromite geothermometer with respect to the effect of titanium. Thus, the original equation for the geother-

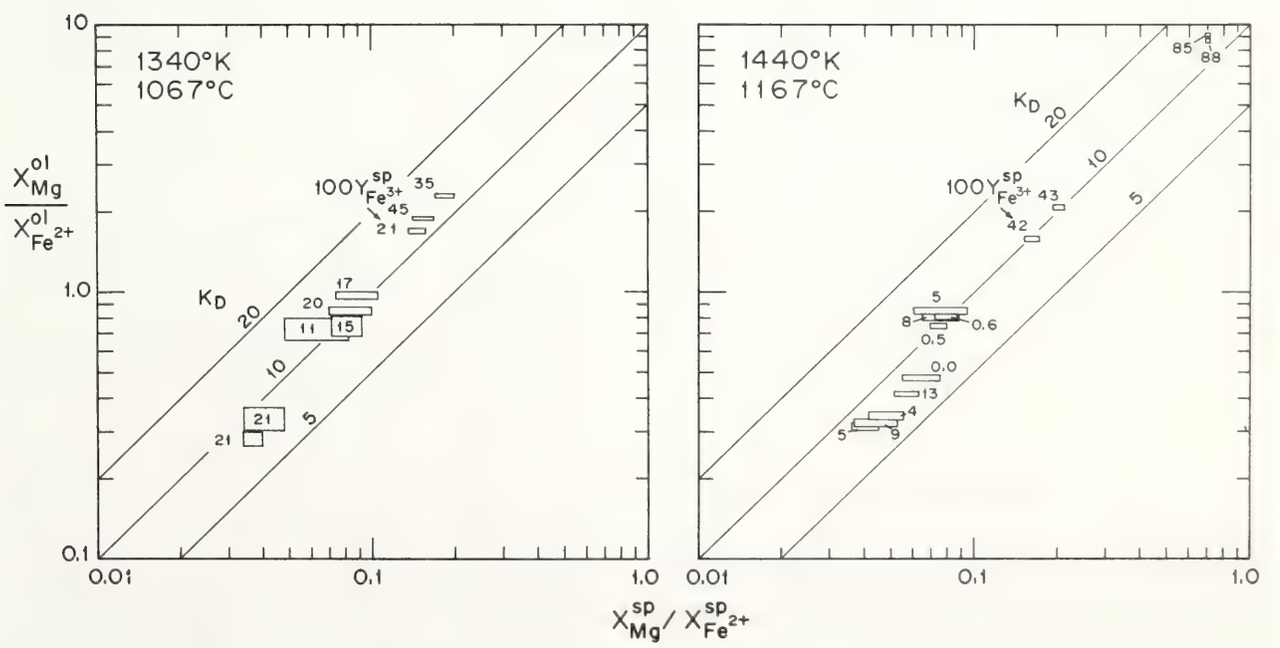


Fig. 36. Logarithmic plot of Mg/Fe^{2+} in olivine vs. Mg/Fe^{2+} in spinel at 1067° and 1167°C.

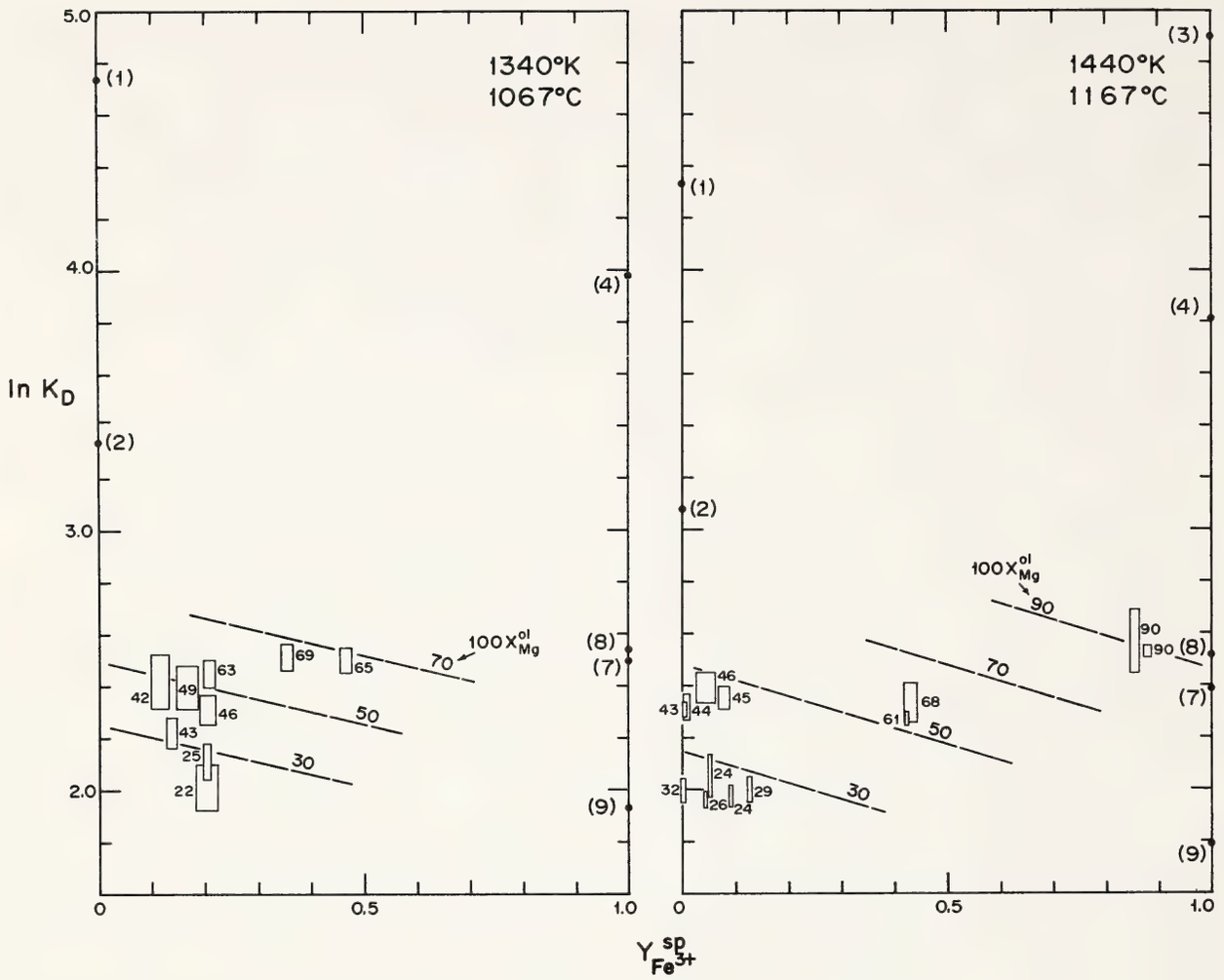


Fig. 37. Experimental data on a plot of ln K vs. $Y_{Fe^{3+}}^{sp}$. The forsterite contents of the olivine are indicated and tentatively contoured. Solid points with numerals in parentheses represent values of ln $K_{(a)}$ and ln $K_{(b)}$ for reactions (a) and (b) of the text, calculated from thermochemical data as follows: (1) olivine free energy from Robie and Waldbaum (1968), free energies for the spinel end members from Brezny and Muan (1969) and Johnson *et al.* (1971), and enthalpy and entropy data from Kelley (1960); (2) olivine free-energy data from Robie *et al.* (1978), Mg_2TiO_4 data from Stull and Prophet (1971), Fe_2TiO_4 data from Brezny and Muan (1969); (3) all data from Robie and Waldbaum (1968); (4) all data from Robie *et al.* (1978); (7), (8), and (9) values from data compiled by Roeder *et al.* (1979, Fig. 1) and plotted as curves identified by the same numbers.

mometer can be expanded to include Y_{Ti}^{sp}, and the ln K terms for Reactions a and b, above, can be assigned the experimental values of about 2.0–2.5 and 2.5–2.6, respectively.

References

Brezny, B., and A. Muan, Activity-composition relations of solid solutions and stabilities of Mg_2TiO_4, $MgTiO_3$, and $MgTi_2O_5$ at 1300°C as determined from equilibria in the system MgO-CoO-TiO_2 at 1300°C, *Thermochim. Acta, 2*, 107–119, 1969.

El Goresy, A., S. E. Haggerty, J. S. Huebner, D. H. Lindsley, and D. Rumble III, *Oxide Minerals, Mineral. Soc. Amer. Short Course Notes, 3*, 1976.

Engi, M., Mg-Fe exchange equilibria among Al-Cr spinel, olivine, orthopyroxene, and cordierite, Ph.D. thesis, Swiss Federal Institute of Technology, Zurich, 1978.

Evans, B. W., and B. R. Frost, Chrome-spinel in progressive metamorphism—a preliminary analysis, *Geochim. Cosmochim. Acta, 39*, 959–972, 1975.

Fabries, J., Spinel-olivine geothermometry in peridotites from ultramafic complexes, *Contrib. Mineral. Petrology, 69*, 329–336, 1979.

Irvine, T. N., Chromian spinel as a petrogenetic indicator, *Can. J. Earth Sci., 2*, 648–672, 1965.

Jackson, E. D., Chemical variation in coexisting chromite and olivine in the chromitite zones of the Stillwater Complex, *Econ. Geol. Monogr., 4*, 41–51, 1969.

Johnson, R. E., Woermann, and A. Muan, Equilibrium studies in the system MgO-"FeO"-TiO_2, *Amer. J. Sci., 271*, 278–292, 1971.

Kelley, K. K., Contributions to the data on theoretical metallurgy. XIII. High-temperature heat-content, heat-capacity, and entropy data for the elements and inorganic compounds, *U.S. Bur. Mines Bull., 534*, 1960.

Medaris, L. G., Coexisting spinel and silicates in alpine peridotites of the granulite facies, *Geochim. Cosmochim. Acta, 39*, 947–958, 1975.

Nafziger, R. H., High-temperature activity-composition relations of equilibrium spinels, olivines, and pyroxenes in the system Mg-Fe-Si-O, *Amer. Mineral., 58*, 457–465, 1973.

Nafziger, R. H., and A. Muan, Equilibrium phase compositions and thermodynamic properties of olivines and pyroxenes in the system MgO-"FeO"-SiO_2, *Amer. Mineral., 52*, 1364–1385, 1967.

Nafziger, R. H., G. C. Ulmer, and E. Woermann, Gaseous buffering for the control of oxygen fugacity at one atmosphere, in *Research Techniques for High Pressure and High Temperatures*, G. C. Ulmer, ed., Springer-Verlag, New York, pp. 9–41, 1971.

Presnall, D. C., and N. L. Brenner, A method for studying iron silicate liquids under reducing conditions with negligible iron loss, *Geochim. Cosmochim. Acta, 38*, 1785–1788, 1974.

Robie, R. A., and D. R. Waldbaum, Thermodynamic properties of minerals and related substances at 298.15°K (25.0°C) and one atmosphere (1.013 bars) pressure and at higher temperatures, *U.S. Geol. Surv. Bull., 1259*, 1968.

Robie, R. A., B. S. Hemingway, and J. R. Fisher, Thermodynamic properties of minerals and related substances at 298.15 K and 1 bar (10^5 pascals) pressure and at higher temperatures, *U.S. Geol. Surv. Bull., 1452*, 1978.

Roedder, E. W., The system K_2O-MgO-SiO_2—I, *Amer. J. Sci., 249*, 81–130, 1951.

Roedder, E. W., A reconnaissance of liquidus relations in the system $K_2O \cdot 2SiO_2$-FeO-SiO_2, *Amer. J. Sci., Bowen Vol.*, 435–456, 1952.

Roeder, P. L., I. H. Campbell, and H. E. Jamieson, A reevaluation of the olivine-spinel geothermometer, *Contrib. Mineral. Petrol., 68*, 325–334, 1979.

Stull, D. R., and H. Prophet, JANAF thermochemical tables, 2d ed., *Nat. Stand. Ref. Data Ser., Nat. Bur. Stand (U.S.), 37*, 1971.

Temkin, M., Mixtures of fused salts as ionic solutions, *Acta Physicochimica URSS, 20*, 411–416, 1945.

Wood, B. J., and J. Nichols, The thermodynamic properties of reciprocal solid solutions, *Contrib. Mineral. Petrol., 66*, 389–400, 1978.

Partitioning of Nickel between Pyrrhotite and Magnetite

N. Z. Boctor and B. O. Mysen

Iron-nickel sulfide ores that are commonly associated with mafic and ultramafic rocks are believed to be derived from an immiscible sulfide liquid that separated from its parent mafic and ultramafic magmas. Evidence of such sulfide liquid immiscibility has been demonstrated experimentally (Buchanan and Nolan, 1979; Helz, 1977; Rajamani and Naldrett, 1978) as well as from the study of basaltic flows (Czamanske and Moore, 1977; Skinner and Peck, 1969). Because nickel and other transition metals strongly favor sulfide melts relative to silicate melts ($D_{\text{silicate melt}}^{\text{Fe-rich sulfide melt}} = 250–300$, Mysen and Kushiro, *Year Book 75*, 478–484; Rajamani and Naldrett, 1978), Mysen and Popp (1980) suggested that the separation of a few tenths of a percent of immiscible sulfide melt during ascent of tholeiitic or andesitic magmas would lower the transition metal contents to the levels found in basaltic and andesitic rocks. Immiscible sulfide liquids from lava flows and from Sudbury-type Fe-Ni sulfide ores are usually associated with magnetite (Naldrett, 1969; Skinner and Peck, 1969). Naldrett (1969) suggested that a sulfide-oxide melt separates from mafic and ultramafic magmas and either undergoes gravity settling and crystallization as a nearly closed system to a mixture of pyrrhotite and magnetite or remains as dispersed droplets that continue to equilibrate with the crystallizing silicate melt. It is necessary, therefore, to study the partitioning of Ni between magnetite and iron monosulfide in order to evaluate whether the crystallization of magnetite in the presence of a sulfide phase would have any significant effect in lowering the Ni content of the parent magmas to the levels observed in igneous rocks.

The experiments were performed in

evacuated silica tubes at 1000°C. To avoid devitrification of the silica at this temperature, high-purity fused quartz tubes of 4–5 mm wall thickness and 4 mm I.D. were used in all experiments. The silica tubes were suspended vertically in a platinum furnace in which a continuous flow of nitrogen was passed during the experiments in order to minimize the devitrification effects. The runs were quenched by dropping the silica tubes into a beaker full of ice + water. Some devitrification effects were observed at the surface of the silica tubes on quenching; because of the large wall thickness, however, the charge was protected from any oxidation effects.

Nickel-bearing pyrrhotite was prepared by mixing appropriate amounts of $Fe_{1-x}S$ and $^{63}Ni_{1-x}S$ and annealing the mixtures in evacuated silica tubes at 900°–1000°C for two days. The temperature was later increased to 1150°C to melt the charge. The sulfide melt was kept at this temperature for one-half hour before it was quenched. Nickel-bearing magnetite was prepared by homogenizing Fe_3O_4 and $NiFe_2O_4$ of the desired proportions at 1000°C for one week. Attempts to synthesize Ni-bearing magnetite by reacting ^{63}Ni and Fe_2O_3 were unsuccessful owing to the formation of layers of wüstite around metallic nickel, which prevented it from further reaction with hematite. The homogeneity of all prepared Ni-bearing pyrrhotite and magnetite was checked by the electron microprobe.

The configuration of the buffers and charges in the experiments is shown in Fig. 38A, B. When pyrrhotite was used with QFM or WM buffers, its composition was chosen to be slightly different in metal-to-sulfur ratio from the pyrrhotite in the charge. At the termination of the experiments, the metal-to-sulfur ratios in pyrrhotite in both the buffer and charge were identical. This observation, as well as the reversal of the reaction, as demonstrated by the

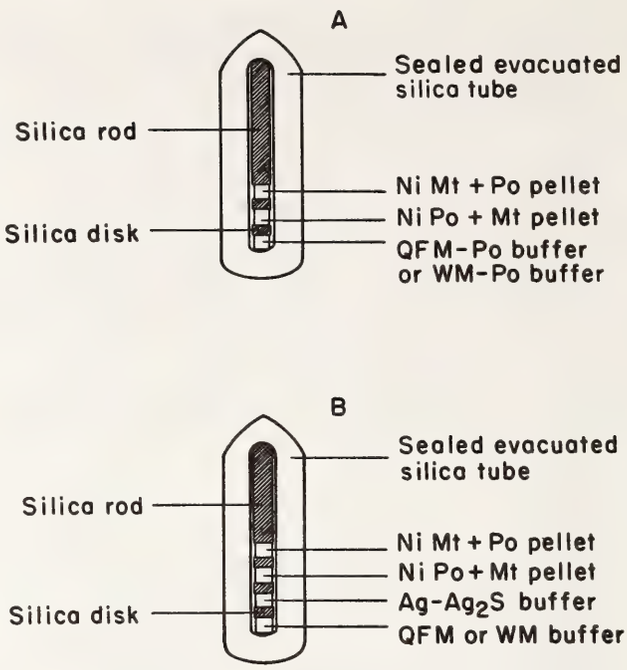


Fig. 38. Fused quartz tubes showing the configuration of buffers and charges in the experimental runs.

similarity of the Ni content of pyrrhotite and magnetite in experiments where the starting material was Ni-bearing pyrrhotite and Ni-free magnetite and vice versa, was considered a criterion for attainment of equilibrium in the experiments.

The duration of the experiments was 30 days at 1000°C. Attempts to extend the experiments to other temperatures were hampered by slow reaction rates at lower temperatures and by the melting of the charge at higher temperatures (1050°–1060°C), which resulted in the formation of a very fine graphic intergrowth of magnetite and pyrrhotite that was difficult to analyze.

The Ni concentration in charges where ^{63}Ni-bearing pyrrhotite was used was determined by the β-track method (Mysen and Seitz, 1975). In charges where Ni-bearing magnetite was used, the Ni concentrations were determined by the electron microprobe. The results of the two methods are comparable, although the standard deviations of the analyses of low Ni concentrations in magnetite are large.

The distribution coefficients of Ni between pyrrhotite and magnetite are shown in Table 23, and the wt % Ni in pyrrhotite is plotted as a function of the wt % Ni in magnetite in Fig. 39. From the experimental data, it is clear that in the f_{O_2}, f_{S_2}, and Ni concentration ranges of the present investigation, Ni partitioning favors pyrrhotite relative to magnetite regardless of the buffers or the activity of Ni. On the basis of the experimental results (Table 23), it is concluded that magnetite crystallizing from mafic and ultramafic magmas in association with iron monosulfide will play a minor role in depleting such magmas of Ni because this element strongly favors the sulfide phase relative to the oxide phase. Because magmas derived by partial melting of peridotite in the upper mantle are saturated with sulfur (Mysen and Popp, 1980), it is likely that the separation of an immiscible sulfide liquid would play the major role in decreasing the Ni content of such magmas to the levels observed in mafic rocks.

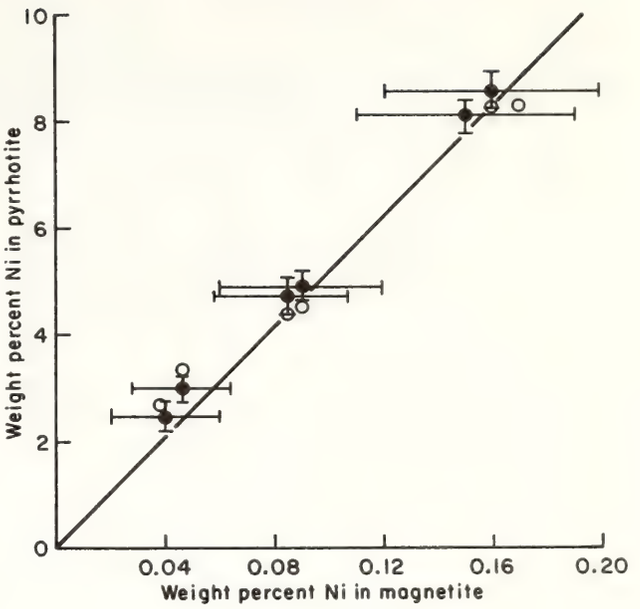


Fig. 39. A plot of wt % Ni in pyrrhotite vs. wt % Ni in magnetite. Open circles indicate concentrations determined by β-track mapping; size of symbol is equivalent to 1 standard deviation. Filled circles indicate concentrations determined by the electron microprobe; length of bar is equivalent to 1 standard deviation.

TABLE 23. Distribution Coefficients of Nickel Between Pyrrhotite and Magnetite

Sample No.*	Charge†	Buffer†	K_D^{Ni}‡
1*a*	NiPo + Mt	QFM − Po	18.3
1*b*	NiMt + Po	QFM − Po	26.8
2*a*	NiPo + Mt	QFM, Ag − Ag_2S	30.9
2*b*	NiMt + Po	QFM, Ag − Ag_2S	27.0
3*a*	NiPo + Mt	QFM − Po	24.6
3*b*	NiMt + Po	QFM − Po	22.3
4*a*	NiPo + Mt	WM − Po	22.7
4*b*	NiMt + Po	WM − Po	27.4
5*a*	NiPo + Mt	QFM, Ag − Ag_2S	22.7
5*b*	NiMt + Po	QFM, Ag − Ag_2S	24.5
6*a*	NiPo + Mt	WM, Ag − Ag_2S	19.8
6*b*	NiMt − Po	WM, Ag − Ag_2S	23.8
Average			24.2 ± 3.5

*In runs labeled *a*, Ni was determined by β-track mapping. In runs labeled *b*, Ni concentrations were determined by the electron microprobe.

†Symbols: Po, pyrrhotite; Mt, magnetite; QFM, quartz-fayalite-magnetite; WM, wüstite-magnetite.

‡$K_D^{Ni} = \left(\frac{X_{NiS}}{X_{FeS}}\right)_{Po} \div \left(\frac{X_{NiO \cdot Fe_2O_3}}{X_{FeO \cdot Fe_2O_3}}\right)_{Mt}$, where X is the mole fraction.

References

Buchanan, D. L., and J. Nolan, Solubility of sulfur and sulfide immiscibility in synthetic tholeittic melts and their relevance to Bushveld Complex rocks, *Can. Mineral., 17*, 483–494, 1979.

Czamanske, G. K., and J. Moore, Composition and phase chemistry of sulfide globules in basalt from the mid-Atlantic rift valley near 87° N Lat., *Geol. Soc. Amer. Bull., 88*, 587–599, 1977.

Helz, R. T., Determination of the *P-T* dependence of the first appearance of FeS-rich liquid in natural basalt to 20 kb (abstract), *Eos, 58*, 523, 1977.

Mysen, B. O., and R. K. Popp, Solubility of sulfur in $CaMgSi_2O_6$ and $NaAlSi_3O_8$ melts at high pressure and temperature with controlled fO_2 and fS_2, *Amer. J. Sci., 280*, 78–92, 1980.

Mysen, B. O., and M. G. Seitz, Trace element partitioning determined by beta-track mapping—an experimental study using carbon and samarium as examples, *J. Geophys. Res., 80*, 2627–2635, 1975.

Naldrett, A. J., A portion of the system Fe-S-O between 900 and 1080°C and its application to sulfide ore magmas, *J. Petrology, 10*, 171–201, 1969.

Rajamani, V., and A. J. Naldrett, Partitioning of Fe, Co, Ni, and Cu between sulfide liquid and basaltic melts and the composition of Ni-Cu sulfide deposits, *Econ. Geol., 73*, 82–94, 1978.

Skinner, B. J., and D. L. Peck, An immiscible sulfide melt from Hawaii, *Econ. Geol. Monogr., 4*, 310–322, 1969.

MINERAL-SOLUTION EQUILIBRIA

Solubility Constants of Rock-Forming Minerals

J. D. Frantz, R. K. Popp, and N. Z. Boctor

Prediction of mass transport along grain boundaries in hydrothermal rock systems requires knowledge of fluid compositions coexisting with the mineral assemblages. In the transport models describing infiltration and diffusion (Hofmann, 1972; Frantz and Mao, 1976, 1979), the fluxes of the elements depend directly on the *concentrations* or the *concentration gradients* of the aqueous species. Chemical potential gradients do not provide sufficient information. For this reason progress toward the interpretation of the genesis of nonisochemical rock bodies depends greatly upon knowledge of mineral-solution equilibria at elevated temperatures and pressures.

Calculation of the abundances of the most concentrated species is of primary importance because the fluxes of elements result mainly from the migration of these species. The addition of halogens to an aqueous solution has been shown to increase the solubility of most solid phases (Morey and Hesselgesser, 1951; Hemley, 1959). The common association of evaporite minerals with porphyry copper deposits, high chloride concentrations in geothermal brines, and the occurrence of halide crystals in fluid inclusions indicate the need for mineral-solution equilibrium data in chloride-bearing solutions.

To characterize fully the aqueous fluid in equilibrium with a mineral assemblage, mass-action constants for mineral solubility reactions must be obtained. Helgeson (1969) calculated the solubilities of many rock-forming minerals at temperatures up to 300°C. In light of recent experimental advances by Frantz, Popp, Boctor, and others, it is now possible to calculate mineral solubilities at even higher temperatures and pressures.

Frantz and Popp (1979) determined the equilibrium constant for the following reaction involving talc and quartz:

$$1/3Mg_3Si_4O_{10}(OH)_2 + 2HCl^\circ = MgCl_2^\circ + 4/3SiO_2 + 4/3H_2O.$$

Magnesium chloride was found to be predominantly associated above 500°C at 1000 and 2000 bars, and significant dissociation occurs at temperatures between 500° and 400°C. The difference

in free energy between associated magnesium chloride and hydrogen chloride [$G_f°$ ($MgCl_2$) − $2G_f°$ (HCl°)] was calculated as a function of temperature and pressure with published free-energy values for talc, quartz, and H_2O. In Part II of their study, Popp and Frantz (1979) determined the equilibrium constant for the reaction between wollastonite, quartz, and a supercritical chloride-bearing fluid:

$$CaSiO_3 + 2HCl° = CaCl_2° + SiO_2 + H_2O.$$

Associated $CaCl_2°$ was identified as the major calcium complex above 500°C, and the free-energy difference [$G_f°$ ($CaCl_2°$) − $2G_f°$ (HCl°)] was computed. Popp and Frantz (1980), studied the equilibrium between low-albite, andalusite, quartz, and fluid:

$$NaAlSi_3O_8 + HCl° = NaCl° + 1/2Al_2SiO_5 + 5/2SiO_2 + 1/2H_2O.$$

The free-energy differences [$G_f°$ (NaCl°) − $G_f°$ (HCl°)] were calculated for temperatures between 500° and 700°C at 1000 bars. Data of Montoya and Hemley (1975), Shade (1974), and Orville (1967) can be used to calculate these values at 2000 bars. Boctor, Popp, and Frantz (*Year Book 78*, 602–606) studied the reaction between hematite and chloride-bearing fluids:

$$Fe_2O_3 + 4HCl° + H_2 = 2FeCl_2° + 3H_2O.$$

They found that the predominant iron species from 400° to 600°C at 1000 and 2000 bars was associated $FeCl_2°$ and calculated the free-energy difference [$G_f°$ ($FeCl_2°$) − $2G_f°$ (HCl°)].

Standard-state free energies of formation [$G_f°$ (*i*)] refer to free energies of formation of the compounds at temperature and pressure from the elements at 25°C and 1 bar. For solids and gases such as H_2O, CO_2, and H_2, $G_f°$ (*i*) refers to the free energy of the pure compounds at temperature and pressure. With respect to aqueous solutes such as $MgCl_2°$ and HCl°, $G_f°$ (*i*) refers to hypothetical one-molal solutions at temperature and pressure. Free-energy differences between the complexes and HCl° were calculated rather than the free energies of the salts alone owing to the large uncertainty in the calculated free energy of HCl°. Calculation of the solubility constants of other minerals requires only the difference in free energy between the salt and HCl°.

The free-energy differences obtained in these studies are presented in Figs. 40 and 41. These data have been combined with the free-energy data in Helgeson *et al.* (1978) in order to compute the solubility constants of many of the major rock-forming minerals. The free energy of H_2O was obtained from Fisher and Zen (1971) and was adjusted to the standard state described above. The free energy of aqueous silica was obtained from Walther and Helgeson

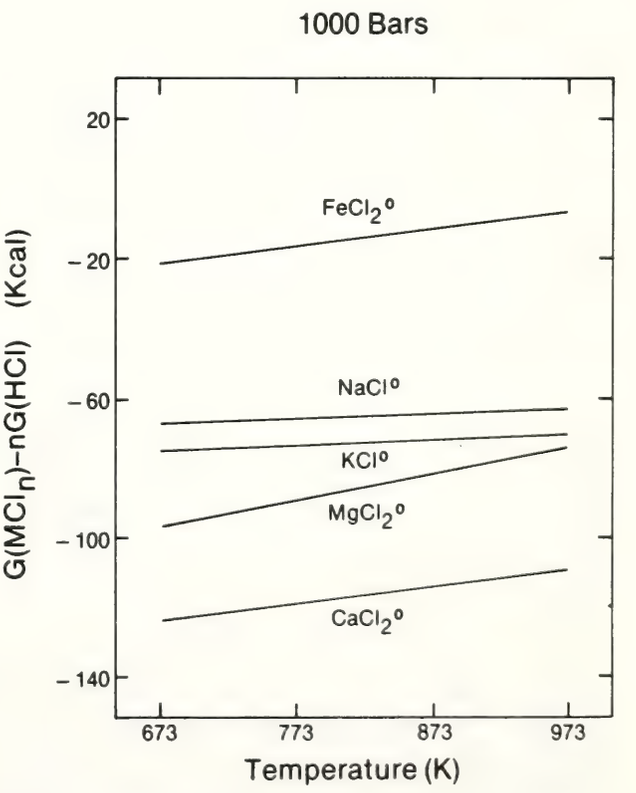


Fig. 40. Free-energy differences between aqueous metal chloride complexes and aqueous hydrogen chloride at 1000 bars and 400°-700°C.

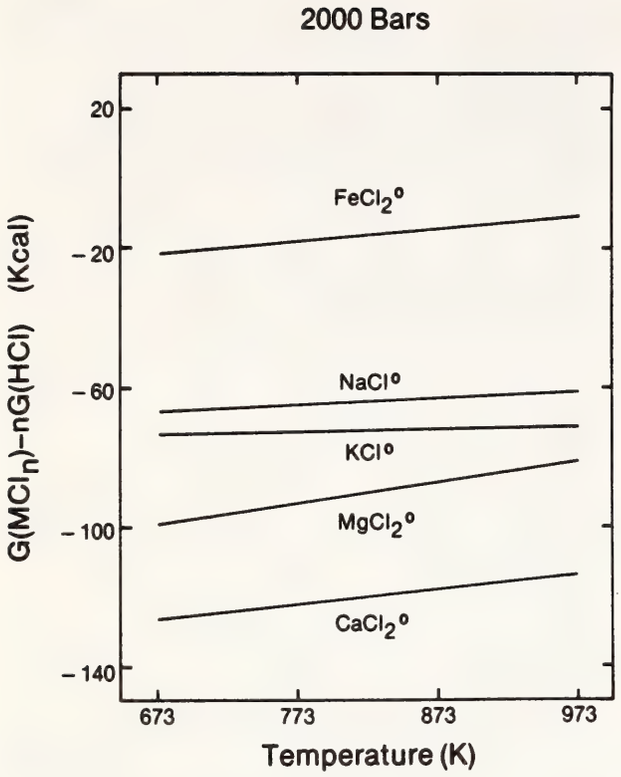


Fig. 41. Free-energy differences between aqueous metal chloride complexes and aqueous hydrogen chloride at 2000 bars and 400°-700°C.

(1977); the free energy of CO_2, from J. V. Walther (pers. comm.). Data for hydrogen are from Wicks and Block (1963). It should be emphasized that the standard state for H_2O, CO_2, and H_2 is the pure gas at temperature and pressure.

Linear equations representing the calculated solubility constants for temperatures between 400° and 600°C at 1000 and 2000 bars are presented in Table 24. The solubility reactions are written in terms of associated species. Accurate information concerning speciation and the free energy of aluminum in solution is lacking, and for this reason, the solubilities of all minerals containing aluminum are balanced with corundum (Al_2O_3). These data are thought to be accurate for total chloride concentrations ranging from 0.01 to 2.0 molal. At lower chloride concentrations, hydrolysis of the salts (especially the 2-1 electrolytes) is a distinct possibility.

TABLE 24. Solubility Constants of Mineral Components*

Mineral	Chemical Formula	Pressure, kbar	*A*	*B*
Oxides, Hydroxides, and Carbonates				
Hematite	$Fe_2O_3 + 4HCl° + H_2 = 2FeCl_2° + 3H_2O$	1.0	−15.580	20497.9
		2.0	−9.766	16917.6
Magnetite	$Fe_3O_4 + 6HCl° + H_2 = 3FeCl_2° + 4H_2O$	1.0	−25.218	30361.8
		2.0	−16.835	25124.1
Alpha Quartz	$SiO_2 + 2H_2O = H_4SiO_4$	1.0	−0.537	−657.0
		2.0	0.432	−1219.5
Spinel	$MgAl_2O_4 + 2HCl° = MgCl_2° + Al_2O_3 + H_2O$	1.0	−12.744	12050.3
		2.0	−9.581	10412.8
Periclase	$MgO + 2HCl° = MgCl_2° + H_2O$	1.0	−12.580	13308.7
		2.0	−9.411	11651.1
Boehmite	$AlO(OH) = 0.5Al_2O_3 + 0.5H_2O$	1.0	1.770	−1149.0
		2.0	1.585	−1049.8
Diaspore	$AlO(OH) = 0.5Al_2O_3 + 0.5H_2O$	1.0	2.457	−1614.0
		2.0	2.276	−1527.9
Gibbsite	$Al(OH)_3 = 0.5Al_2O_3 + 1.5H_2O$	1.0	5.001	−2647.0
		2.0	4.444	−2354.9
Brucite	$Mg(OH)_2 + 2HCl° = MgCl_2° + 2H_2O$	1.0	−9.527	10596.0
		2.0	−6.726	9135.6
Calcite	$CaCO_3 + 2HCl° = CaCl_2° + CO_2 + H_2O$	1.0	−2.877	4912.3
		2.0	−2.250	4827.2
Aragonite	$CaCO_3 + 2HCl° = CaCl_2° + CO_2 + H_2O$	1.0	−2.558	4814.3
		2.0	−1.931	4713.7
Dolomite	$CaMg(CO_3)_2 + 4HCl° = CaCl_2° + MgCl_2° + 2CO_2 + 2H_2O$	1.0	−10.248	12335.0
		2.0	−6.709	10524.0
Disord Dolomite	$CaMg(CO_3)_2 + 4HCl° = CaCl_2° + MgCl_2° + 2CO_2 + 2H_2O$	1.0	−10.584	12789.7
		2.0	−7.134	11043.9

TABLE 24. (*Continued*)

Mineral	Chemical Formula	Pressure, kbar	*A*	*B*
Ord Dolomite	$CaMg(CO_3)_2 + 4HCl^\circ = CaCl_2^\circ + MgCl_2^\circ + 2CO_2 + 2H_2O$	1.0	−10.150	12271.3
		2.0	−6.615	10463.2
Magnesite	$MgCO_3 + 2HCl^\circ = MgCl_2^\circ + CO_2 + H_2O$	1.0	−7.268	7771.8
		2.0	−4.452	6119.9
Orthosilicates and Ring Silicates				
Kyanite	$Al_2SiO_5 + 2H_2O = Al_2O_3 + H_4SiO_4$	1.0	−0.003	−1192.5
		2.0	1.006	−1797.5
Andalusite	$Al_2SiO_5 + 2H_2O = Al_2O_3 + H_4SiO_4$	1.0	−0.464	−943.2
		2.0	0.546	−1509.9
Sillimanite	$Al_2SiO_5 + 2H_2O = Al_2O_3 + H_4SiO_4$	1.0	−0.587	−825.5
		2.0	0.421	1398.3
Gehlenite	$Ca_2Al_2SiO_7 + 4HCl^\circ = 2CaCl_2^\circ + Al_2O_3 + H_4SiO_4$	1.0	−16.312	19174.6
		2.0	−13.550	18567.3
Grossular	$Ca_3Al_2Si_3O_{12} + 6HCl^\circ + 3H_2O = 3CaCl_2^\circ + Al_2O_3 + 3H_4SiO_4$	1.0	−20.147	20950.5
		2.0	−14.700	19171.1
Monticellite	$CaMgSiO_4 + 4HCl^\circ = CaCl_2^\circ + MgCl_2^\circ + H_4SiO_4$	1.0	−20.209	20028.9
		2.0	−15.261	17836.2
Merwinite	$Ca_3Mg(SiO_4)_2 + 8HCl^\circ = 3CaCl_2^\circ + MgCl_2^\circ + 2H_4SiO_4$	1.0	−36.297	40078.1
		2.0	−28.585	37215.9
Andradite	$Ca_3Fe_2Si_3O_{12} + 10HCl^\circ + H_2 = 3CaCl_2^\circ + 2FeCl_2^\circ + 3H_4SiO_4$	1.0	−35.946	42145.4
		2.0	−24.827	36880.4
Akermanite	$Ca_2MgSi_2O_7 + 6HCl^\circ + H_2O = 2CaCl_2^\circ + MgCl_2^\circ + 2H_4SiO_4$	1.0	−28.364	28943.2
		2.0	−21.784	26327.7
Fayalite	$Fe_2SiO_4 + 4HCl^\circ = 2FeCl_2^\circ + H_4SiO_4$	1.0	−17.386	18346.8
		2.0	−10.731	14111.2
Forsterite	$Mg_2SiO_4 + 4HCl^\circ = 2MgCl_2^\circ + H_4SiO_4$	1.0	−25.238	22381.6
		2.0	−18.104	18632.5
Cordierite	$Mg_2Al_4Si_5O_{18} + 4HCl^\circ + 8H_2O = 2MgCl_2^\circ + 2Al_2O_3 + 5H_4SiO_4$	1.0	−27.067	18495.4
		2.0	−16.767	13293.6
Hyd Cordierite	$Mg_2Al_4Si_5O_{18} \cdot H_2O + 4HCl^\circ + 7H_2O = 2MgCl_2^\circ + 2Al_2O_3 + 5H_4SiO_4 + 3H_2O$	1.0	−24.877	16661.3
		2.0	−14.949	11630.3
Clinozoisite	$Ca_2Al_3Si_3O_{12}(OH) + 4HCl^\circ + 3.5H_2O = 2CaCl_2^\circ + 1.5Al_2O_3 + 3H_4SiO_4$	1.0	−11.541	−4995.5
		2.0	−7.961	−6117.1
Zoisite	$Ca_2Al_3Si_3O_{12}(OH) + 4HCl^\circ + 3.5H_2O = 2CaCl_2^\circ + 1.5Al_2O_3 + 3H_4SiO_4$	1.0	−12.831	11139.7
		2.0	−8.666	9678.0
Lawsonite	$CaAl_2Si_2O_7(OH)_2 \cdot H_2O + 2HCl^\circ + H_2O = CaCl_2^\circ + Al_2O_3 + 2H_4SiO_4$	1.0	−1.226	2542.7
		2.0	1.183	1484.4
Ord Epidote	$Ca_2FeAl_2Si_3O_{12}(OH) + 6HCl^\circ + 2H_2O + 0.5H_2 = 2CaCl_2^\circ + FeCl_2^\circ + Al_2O_3 + 3H_4SiO_4$	1.0	−20.216	21120.9
		2.0	−13.161	17884.9
Epidote	$Ca_2FeAl_2Si_3O_{12}(OH) + 6HCl^\circ + 2H_2O + 0.5H_2 = 2CaCl_2^\circ + FeCl_2^\circ + Al_2O_3 + 3H_4SiO_4$	1.0	−22.489	22707.1
		2.0	−14.599	18865.3
Chain Silicates				
Wollastonite	$CaSiO_3 + 2HCl^\circ + H_2O = CaCl_2^\circ + H_4SiO_4$	1.0	−7.547	8287.4
		2.0	−5.773	7754.1
Ca-Al Pyroxene	$CaAl_2SiO_6 + 2HCl^\circ + H_2O = CaCl_2^\circ + Al_2O_3 + H_4SiO_4$	1.0	−8.252	8920.4
		2.0	−6.477	8375.9
Jadeite	$NaAlSi_2O_6 + HCl^\circ + 3.5H_2O = NaCl^\circ + 0.5Al_2O_3 + 2H_4SiO_4$	1.0	−3.181	3039.5
		2.0	−1.116	2178.6
Enstatite	$MgSiO_3 + 2HCl^\circ + H_2O = MgCl_2^\circ + H_4SiO_4$	1.0	−13.081	10844.0
		2.0	−8.863	8562.0
Ferrosilite	$FeSiO_3 + 2HCl^\circ + H_2O = FeCl_2^\circ + H_4SiO_4$	1.0	−8.579	8619.3
		2.0	−4.853	6278.9
Diopside	$CaMgSi_2O_6 + 4HCl^\circ + 2H_2O = CaCl_2^\circ + MgCl_2^\circ + 2H_4SiO_4$	1.0	−19.665	17347.3
		2.0	−13.929	14689.7
Hedenbergite	$CaFeSi_2O_6 + 4HCl^\circ + 2H_2O = CaCl_2^\circ + FeCl_2^\circ + 2H_4SiO_4$	1.0	−15.978	16344.2
		2.0	−10.480	13447.1
Anthophyllite	$Mg_7Si_8O_{22}(OH)_2 + 14HCl^\circ + 8H_2O = 7MgCl_2^\circ + 8H_4SiO_4$	1.0	−88.116	71232.6
		2.0	−57.865	54853.7
Tremolite	$Ca_2Mg_5Si_8O_{22}(OH)_2 + 14HCl^\circ + 8H_2O = 2CaCl_2^\circ + 5MgCl_2^\circ + 8H_4SiO_4$	1.0	−72.469	60074.7
		2.0	−48.681	48291.9
Pargasite	$NaCa_2Mg_4Al_3Si_6O_{22}(OH)_2 + 13HCl^\circ + 4.5H_2O = NaCl^\circ + 2CaCl_2^\circ + 4MgCl_2^\circ + 1.5Al_2O_3 + 6H_4SiO_4$	1.0	−68.760	60386.0
		2.0	−53.471	53613.0

TABLE 24. (*Continued*)

Mineral	Chemical Formula	Pressure, kbar	*A*	*B*
Framework Silicates				
Analcime	$NaAlSi_2O_6 \cdot H_2O + HCl° + 2.5H_2O = NaCl° + 0.5Al_2O_3 + 2H_4SiO_4$	1.0	−3.679	2620.4
		2.0	−1.934	2042.1
Dehyd Analcime	$NaAlSi_2O_6 + HCl° + 3.5H_2O = NaCl° + 0.5Al_2O_3 + 2H_4SiO_4$	1.0	−5.729	5017.3
		2.0	−5.130	6038.1
Albite	$NaAlSi_3O_8 + HCl° + 5.5H_2O = NaCl° + 0.5Al_2O_3 + 3H_4SiO_4$	1.0	−5.641	2636.6
		2.0	−2.567	1282.0
High Albite	$NaAlSi_3O_8 + HCl° + 5.5H_2O = NaCl° + 0.5Al_2O_3 + 3H_4SiO_4$	1.0	−5.951	3025.3
		2.0	−2.884	1676.9
Low Albite	$NaAlSi_3O_8 + HCl° + 5.5H_2O = NaCl° + 0.5Al_2O_3 + 3H_4SiO_4$	1.0	−5.232	2375.5
		2.0	−2.163	1024.0
Anorthite	$CaAl_2Si_2O_8 + 2HCl° + 3H_2O = CaCl_2° + Al_2O_3 + 2H_4SiO_4$	1.0	−9.014	6520.2
		2.0	−6.444	5624.8
K-Feldspar	$KAlSi_3O_8 + HCl° + 5.5H_2O = KCl° + 0.5Al_2O_3 + 3H_4SiO_4$	1.0	−6.569	2910.0
		2.0	−1.999	357.6
Microline	$KAlSi_3O_8 + HCl° + 5.5H_2O = KCl° + 0.5Al_2O_3 + 3H_4SiO_4$	1.0	−6.248	2685.5
		2.0	−1.586	98.3
Sanidine	$KAlSi_3O_8 + HCl° + 5.5H_2O = KCl° + 0.5Al_2O_3 + 3H_4SiO_4$	1.0	−6.895	3228.5
		2.0	−2.328	679.1
Wairakite	$CaAl_2Si_4O_{12} \cdot 2H_2O + 2HCl° + 5H_2O = CaCl_2° + Al_2O_3 + 4H_4SiO_4$	1.0	−8.949	4567.9
		2.0	−4.528	2557.5
Nepheline	$NaAlSiO_4 + HCl° + 1.5H_2O = NaCl° + 0.5Al_2O_3 + H_4SiO_4$	1.0	−4.146	4506.5
		2.0	−3.601	4685.4
Kalsilite	$KAlSiO_4 + HCl° + 1.5H_2O = KCl° + 0.5Al_2O_3 + H_4SiO_4$	1.0	−5.422	5064.5
		2.0	−1.724	2160.4
High Kalsilite	$KAlSiO_4 + HCl° + 1.5H_2O = KCl° + 0.5Al_2O_3 + H_4SiO_4$	1.0	−4.247	4050.4
		2.0	−4.271	3571.2
Sheet Silicates				
Laumontite	$CaAl_2Si_4O_{12} \cdot 4H_2O + 2HCl° + 3H_2O = CaCl_2° + Al_2O_3 + 4H_4SiO_4$	1.0	−1.086	167.3
		2.0	2.647	−1554.0
Kaolinite	$Al_2Si_2O_5(OH)_4 + 2H_2O = Al_2O_3 + 2H_4SiO_4$	1.0	6.531	−6448.0
		2.0	7.379	−6897.8
Pyrophyllite	$Al_2Si_4O_{10}(OH)_2 + 7H_2O = Al_2O_3 + 4H_4SiO_4$	1.0	4.271	−7214.9
		2.0	7.070	−8755.9
Chrysotile	$Mg_3Si_2O_5(OH)_4 + 6HCl° = 3MgCl_2° + 2H_4SiO_4 + H_2O$	1.0	−30.604	27658.8
		2.0	−20.249	22242.4
Talc	$Mg_3Si_4O_{10}(OH)_2 + 6HCl° + 4H_2O = 3MgCl_2° + 4H_4SiO_4$	1.0	−33.037	25870.6
		2.0	−20.727	19383.6
Phlogopite	$KMg_3AlSi_3O_{10}(OH)_2 + 7HCl° + 1.5H_2O = KCl° + 3MgCl_2° + 0.5Al_2O_3 + 3H_4SiO_4$	1.0	−38.419	32074.3
		2.0	−25.379	25199.4
Annite	$KFe_3AlSi_3O_{10}(OH)_2 + 7HCl° + 1.5H_2O = KCl° + 3FeCl_2° + 0.5Al_2O_3 + 3H_4SiO_4$	1.0	−29.153	29234.6
		2.0	−15.975	21012.7
Muscovite	$KAl_3Si_3O_{10}(OH)_2 + HCl° + 4.5H_2O = KCl° + 1.5Al_2O_3 + 3H_4SiO_4$	1.0	−2.256	914.7
		2.0	1.990	−3340.2
Paragonite	$NaAl_3Si_3O_{10}(OH)_2 + HCl° + 4.5H_2O = NaCl° + 1.5Al_2O_3 + 3H_4SiO_4$	1.0	−0.953	−1078.5
		2.0	1.789	−2296.8
14A-Chlorite	$Mg_5Al_2Si_3O_{10}(OH)_8 + 10HCl° = 5MgCl_2° + Al_2O_3 + 3H_4SiO_4 + 3H_2O$	1.0	−51.223	44314.8
		2.0	−34.469	35553.0
Sepiolite	$Mg_4Si_6O_{15}(OH)_2 \cdot 6H_2O + 8HCl° + H_2O = 4MgCl_2° + 6H_4SiO_4$	1.0	−26.344	27839.2
		2.0	−11.499	20090.8
Margarite	$CaAl_4Si_2O_{10}(OH)_2 + 2HCl° + 2H_2O = CaCl_2° + 2Al_2O_3 + 2H_4SiO_4$	1.0	−5.129	3520.9
		2.0	−2.467	2432.7
Prehnite	$Ca_2Al_2Si_3O_{10}(OH)_2 + 4HCl° + 3H_2O = 2CaCl_2° + Al_2O_3 + 3H_4SiO_4$	1.0	−12.682	11894.6
		2.0	−8.014	10086.0

*[$\log K = (A + B)/T$ K]

The distribution of the aqueous complexes in equilibrium with mineral assemblages can now be calculated with the data of Table 24. Calculation of solution compositions in equilibrium with mineral assemblages can be used to predict fluxes of elements between rocks not in chemical equilibrium. Qualitative predictions of relative fluxes can often be made by merely examining the differences in solution compositions between the two unaltered rocks. The actual reaction path producing metasomatic zoning is computed with mass-action equations describing mineral solubilities and solute ionization in conjunction with mass-balance equations such as Fick's law (Frantz and Mao, 1976; 1979). The data presented in this publication may aid petrologists in further understanding the conditions responsible for the formation of metasomatic reaction zones.

References

Fisher, J. R., and E.-A. Zen, Thermodynamic calculations from hydrothermal phase equilibrium data and free energy of H_2O, *Amer. J. Sci., 270,* 297–314, 1971.

Frantz, J. D., and H. K. Mao, Bimetasomatism resulting from intergranular diffusion—I. A theoretical model for monomineralic reaction zone sequences, *Amer. J. Sci., 276,* 817–840, 1976.

Frantz, J. D., and H. K. Mao, Bimetasomatism resulting from intergranular diffusion—II. Prediction of multimineralic zone sequences, *Amer. J. Sci., 279,* 302–323, 1979.

Frantz, J. D., and R. K. Popp, Mineral-solution equilibria—I. An experimental study of complexing and thermodynamic properties of aqueous $MgCl_2$ in the system MgO-SiO_2-H_2O-HCl, *Geochim. Cosmochim. Acta, 43,* 1223–1239, 1979.

Helgeson, H. C., Thermodynamics of hydrothermal systems at elevated temperatures and pressures, *Amer. J. Sci., 267,* 729–804, 1969.

Helgeson, H. C., J. M. Delany, H. W. Nesbitt, and D. K. Bird, Summary and critique of the thermodynamic properties of rock-forming minerals, *Amer. J. Sci., 278A,* 1–29, 1978.

Hemley, J. J., Some mineralogical equilibria in the system K_2O-Al_2O_3-SiO_2-H_2O, *Amer. J. Sci., 257,* 241–270, 1959.

Hofmann, A., Chromatographic theory of infiltration metasomatism and its application to feldspars, *Amer. J. Sci., 272,* 69–90, 1972.

Montoya, J. W., and J. J. Hemley, Activity relations and stabilities in alkali feldspar and mica alteration reactions, *Econ. Geol., 70,* 577–594, 1975.

Morey, G. W., and J. M. Hesselgesser, The solubility of some minerals in superheated steam at high pressures, *Econ. Geol., 46,* 821–835, 1951.

Orville, P. M., Unit cell parameters of the microcline-low albite and the sanidine-high albite solid solution series, *Amer. Mineral., 52,* 55–86, 1967.

Popp, R. K., and J. D. Frantz, Mineral-solution equilibria—II. An experimental study of mineral solubilities and the thermodynamic properties of aqueous $CaCl_2$ in the system CaO-SiO_2-H_2O-HCl, *Geochim. Cosmochim. Acta, 43,* 1777–1790, 1979.

Popp, R. K., and J. D. Frantz, Mineral-solution equilibria—III. The system Na_2O-Al_2O_3-SiO_2-H_2O-HCl, *Geochim. Cosmochim. Acta, 44,* 1029–1037, 1980.

Shade, J. W., Hydrolysis reactions in the SiO_2-excess portion of the system K_2O-Al_2O_3-SiO_2-H_2O in chloride fluids at magmatic conditions, *Econ. Geol., 69,* 218–228, 1974.

Walther, J. V., and H. C. Helgeson, Calculation of the thermodynamic properties of aqueous silica and the solubility of quartz and its polymorphs at high pressures and temperatures, *Amer. J. Sci., 277,* 767–816, 1977.

Wicks, C. E., and F. E. Block, Thermodynamic properties of sixty-five elements—their oxides, halides, carbides, and nitrides, *U.S. Bur. Mines Bull., 605,* 1963.

Mineral-Solution Equilibria in the System Mn_3O_4-H_2-H_2O-HCl

N. Z. Boctor and J. D. Frantz

Hausmannite occurs as a common mineral in veins of the so-called hypogene manganese oxide deposits. It also occurs in association with iron oxides in some Precambrian iron ores, for example in the Lake Superior region. Manganese oxides also occur in layered manganese ores that are believed by some investigators to be of volcanogenic origin. In addition, recent investigations of hydrothermal activity at mid-oceanic ridges have shown that manganese or ferromanganese mineralization occurs on the crests of some oceanic spreading centers. The Mn and

Fe in these deposits are believed to be leached from the oceanic crust by convecting sea water that penetrates through the crust to a depth of several kilometers. A study of the solubility of Mn in hydrothermal fluids, therefore, provides valuable information on the mass transport of Mn in different geological environments. The choice of chloride-bearing fluids is appropriate in view of its abundance in natural environments, as demonstrated by its presence in fluid inclusions, metal-bearing geothermal brines, and convecting hydrothermal systems associated with mid-oceanic ridges.

The solubility of hausmannite in supercritical chloride-bearing fluids was determined in the temperature range 500°–600°C at 2000 bars by using rapid-quench hydrothermal techniques and the Ag-AgCl methods of Frantz and Popp (1979). Total manganese and total chlorides in the inner and outer capsules were measured after quenching.

The variation of the molality of Mn and associated HCl in equilibrium with hausmannite provides the information needed to characterize the dominant ionic or molecular species of manganese in the fluid. The concentration of associated HCl was calculated from the total quench chlorides in the inner platinum capsules that were determined with colorimetric methods and from the dissociation constant of HCl (Frantz and Popp, 1979). In Fig. 42, the logarithm of the molalities of associated HCl° is plotted as a function of the logarithm of total manganese at 500° and 600°C at 2000 bars. The concentration of Mn in the fluid is much greater than that of total HCl, and, therefore, quench reactions involving HCl and the solids will have negligible effect on the concentration of total manganese.

The slopes of the lines in Fig. 42 help to determine the identity of the major complex in the fluid. If it is assumed that $MnCl_2°$ is the predominant species, the reaction involving hausmannite and the fluid can be written:

$$Mn_3O_4 + 6HCl° + H_2 = 3MnCl_2° + 4H_2O. \quad (1)$$

The equilibrium constant for this reaction is

$$K_1 = (a_{MnCl_2°})^3(a_{H_2O})^4/(a_{HCl°})^6(f_{H_2}). \quad (2)$$

The derivative of the logarithm of the molality of total manganese as a function of the logarithm of the molality of associated HCl° can be calculated (see Boctor *et al., Year Book 78,* 602–606):

$$\log m_{Mn_T}/\log m_{HCl°} = 2.7. \quad (3)$$

If Mn^{2+} or $MnCl^+$ were the dominant species, slopes of 1.0 or 2.0, respectively, would be expected. Comparison of these theoretical slopes to the slopes of the least-squares fits of the experimental data in which HCl was taken as a dependent variable (Fig. 42) indicates that $MnCl_2°$ was the dominant species under the temperature-pressure conditions of the experiments. The slopes for the 500° and 600°C data are 3.0 and 3.2. This conclusion is supported by the determination of Cl:Mn ratios in the outer capsules, which give values of $\simeq 2$.

A study of the solubility of hausmannite in chloride-bearing hydrothermal fluids has shown that $MnCl_2°$ is the predominant Mn species in equilibrium with hausmannite in the temperature range 500° to 600°C at 2000 bars. The data will be useful in accounting for the transport of Mn in the hydrothermal systems associated with mid-oceanic ridges. Manganese and iron leached from the oceanic crust by supercritical sea water will be transported as associated $MnCl_2°$ and $FeCl_2°$ complexes prior to their oxidation and deposition as hydroxides on oceanic ridge crests.

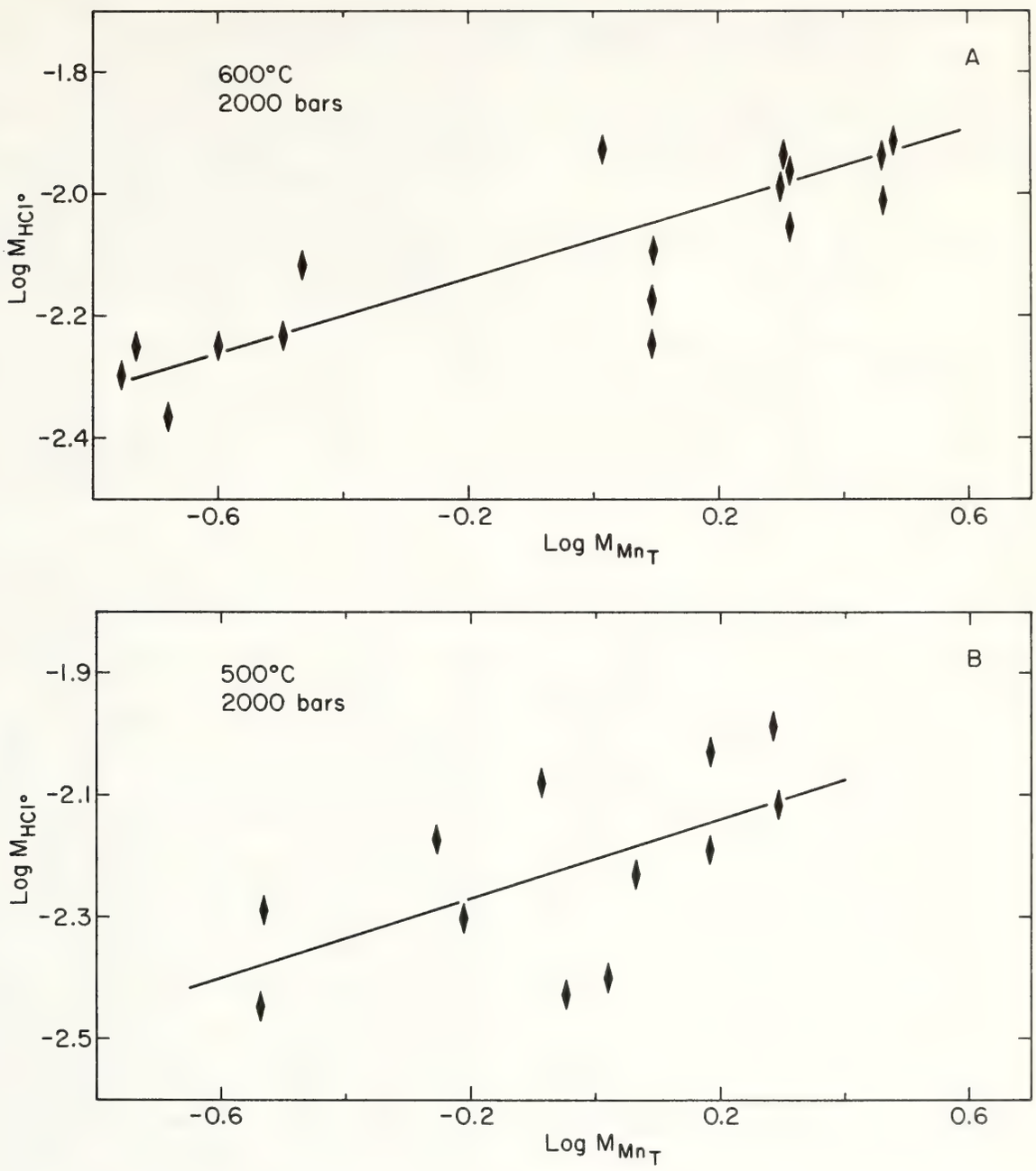


Fig. 42. Logarithm of the molality of associated HCl° as a function of the logarithm of the molality of total manganese in fluids from the unbuffered runs. The lines represent least-squares fits to the data.

Reference

Frantz, J. D., and R. K. Popp, Mineral-solution equilibria—I. An experimental study of complexing and thermodynamic properties of aqueous $MgCl_2$ in the system MgO-SiO_2-H_2O-HCl, *Geochim. Cosmochim. Acta*, *43*, 1223–1239, 1979.

PLANETARY GASES AT HIGH PRESSURES

Crystal Structures and Compression of Ar, Ne, and CH_4 at 20°C to 90 kbar

R. M. Hazen, H. K. Mao, L. W. Finger, and P. M. Bell

The diamond-anvil cell has been modified for use in the x-ray diffraction study of simple elements and compounds that are gases under ambient conditions. This report contains data on the structure, compression, and phase transitions of argon, neon, and methane at 20°C and pressures up to 90 kbar.

Single crystals of argon, neon, and methane were produced in separate experiments by immersing the cryogenic cell in liquified gas and pressurizing the cell to contain a sample, which is retained in the fluid state when the cell is removed to room temperature. Single crystals form above the freezing pressures, which are 11.5, 47.4, and 15.9 kbar for Ar, Ne, and CH_4, respectively. Fluorescence lines from a 10-μm ruby crystal, included in the sample chamber for pressure calibration, remained sharp under all conditions studied. Thus, no significant shear stress is maintained in the sample. The Ar, Ne, and CH_4 single crystals are much more compressible than ruby at least up to 90 kbar.

Crystals of all three materials were colorless and displayed no birefringence. X-ray diffraction photography and x-ray diffractometry were used to determine crystal symmetry and unit-cell dimensions of each sample at several pressures. All three materials crystallized in the cubic closest-packing (CCP) structure ($Fm3m$, $Z = 4$), on the basis of x-ray diffraction positions and intensities. The cubic cell edge is thus sufficient to define the molar volume and atomic positions. Values of unit-cell dimensions and volume changes from freezing (at 20°C) at several pressures are recorded in Table 25.

All three materials are extremely compressible, as illustrated in Fig. 43. Calculated volumes, bulk moduli, and derivatives of bulk moduli (at the pressure of freezing) are recorded in Table 26 for both second-order Murnaghan and second-order Birch-Murnaghan P-V equations of state (Murnaghan, 1967). These bulk moduli are among the smallest ever recorded for any solid.

A remarkable property was shown by all three materials when confined in the pressure cell. Any change of pressure greater than approximately 4 kbar recrystallized the sample to a new single crystal or small group of single crystals with one large individual. Rather than support the stress generated by a deforming gasket with changing pressure, the sample recrystallizes and thus conforms with the changing shape of the sample chamber. Furthermore, the new single crystal had preferred orientation with respect to the diamond faces. In more than half the runs a (220) CCP plane was parallel within $\pm 2°$ of arc to the randomly polished diamond anvil surface. Next in frequency of orientation was the (111) CCP plane, which is the plane of closest packing; and a third plane observed in four runs is (211). No orientation within 15° of the (100) plane was observed. These nonrandom crystallization directions probably occur as a result of the uniaxial stress associated with the diamond-anvil design and are not epitaxial on the diamond anvils, which are cut at a significant angle to crystallographic directions. The stability of single crystals in these solidified gases is evidence that the outer portions of the Jovian planets, which are largely composed of solidified CH_4, NH_3, and CO_2, may be coarsely crystalline.

TABLE 25. Unit-Cell Edge, Volume, and Compression at Several Pressures for Crystalline Argon, Neon, and Methane at 20 °C

Pressure, kbar	a, Å	V, Å^3	V/V_c*	Sequence No.
Argon				
12.8(6)	5.0868(20)	131.62(16)	1.000	14
14.2(3)	5.0724(5)	130.51(4)	0.992	1, 10
17.1(5)	4.9874(5)	124.06(4)	0.943	9
21.1(1)	4.9330(10)	120.04(7)	0.912	11
24.2(2)	4.90344(5)	117.897(4)	0.896	2
29.0(5)	4.83594(5)	113.095(4)	0.859	3
33.3(2)	4.7950(10)	110.25(7)	0.838	8
33.8(2)	4.7919(2)	110.033(14)	0.836	4
36.1(3)	4.7785(5)	109.11(4)	0.829	7
38.0(2)	4.7550(15)	107.51(10)	0.817	6
38.1(2)	4.7516(10)	107.28(7)	0.815	5
44.1(2)	4.714(8)	104.8(5)	0.796	16
47.7(1)	4.6834(20)	102.73(13)	0.781	13
50.0(3)	4.667(8)	101.6(5)	0.772	17
55.9(5)	4.6430(20)	100.09(13)	0.760	12
63.4(3)	4.603(8)	97.5(5)	0.741	18
67.8(4)	4.5930(20)	96.89(13)	0.736	14
71.2(1)	4.5830(20)	96.26(13)	0.731	15
81.7(6)	4.544(4)	93.82(25)	0.713	19
Neon				
47.5(4)	Crystals and liquid coexist			2, 6
48.3(5)	3.7860(20)	54.27(8)	1.000	3
58.4(4)	3.727(1)	51.77(4)	0.954	11
62.2(4)	3.7007(5)	50.68(2)	0.934	1
68.1(3)	3.684(3)	50.01(11)	0.921	12
72.0(3)	3.6614(10)	49.08(4)	0.904	5
72.3(5)	3.6499(10)	48.62(4)	0.896	4
77.1(4)	3.6424(20)	48.32(8)	0.890	7
80.1(3)	3.6361(10)	48.07(4)	0.886	10
87.7(4)	3.6101(20)	47.05(8)	0.867	8
87.9(5)	3.6007(30)	46.68(11)	0.860	9
Methane				
15.9(2)	Crystals and liquid coexist			
16.1(8)	5.4434(7)	161.29(8)	1.000	1
28.9(8)	5.3064(8)	149.42(8)	0.9264	2
39.5(8)	5.1963(6)	140.31(6)	0.8699	3
52.1(8)	5.0947(10)	132.24(11)	0.8199	4

* V_c is the unit-cell volume at melting (20 °C).

Phase Transition of Methane

Methane was observed to transform from a single crystal to an unidentified polycrystalline phase at approximately 50 kbar (see also Sharma *et al.*, this Report). Attempts to produce a single crystal of this second solid phase have not yet been successful. It should be noted, however, that extrapolation of the methane I (the CCP phase)/methane III phase boundary from low temperature to room temperature yields a transition pressure of approximately 50 kbar (Medina and Daniels, 1979), as illustrated in Fig. 44. It is possible, therefore, that the unidentified high-pressure form of CH_4 is methane III.

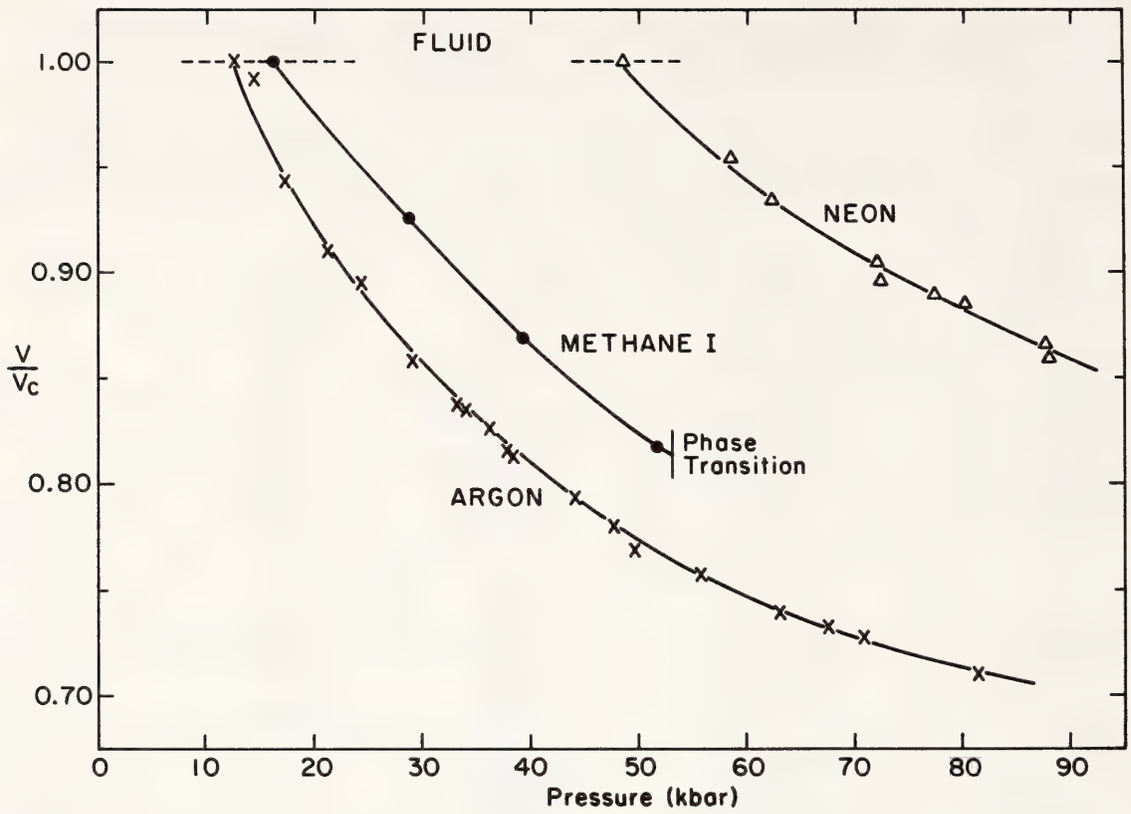


Fig. 43. Compression of crystalline argon, neon, and methane at 20°C. V/V_c is the ratio of unit-cell volume at high pressure to that of the solid at the pressure of melting at 20°C.

TABLE 26. Equation-of-State Parameters for Argon, Neon, and Methane at 20°C, Based on Changes from Freezing Pressures, P_f

Second-Order Murnaghan				Second-Order Birch-Murnaghan			
V_f	K_f	K'_f	K''_f	V_f	K_f	K'_f	K''_f
Argon							
148(5)	24(9)	6.7(5)	...				
146(9)	28(22)	6.3(20)	0.02(8)				
Neon							
54.8(9)	140(53)	7.3(25)	...	54.8(9)	139(57)	7.5(30)	...
55.0(15)	124(108)	9(11)	−0.1(6)				
Methane							
163.5(16)	111(10)	4	...	161.6(7)	150(15)	1.6(10)	...
161.7(8)	147(15)	1.9(9)	...				

No phase transitions were observed in either neon or argon up to 90 kbar.

Hydrostatic Pressure Media

Crystallized gases should prove valuable as simultaneous pressure media and internal pressure standards. To pressures of 90 kbar, and perhaps much higher, the ruby fluorescence lines are sharp, indicating nearly hydrostatic conditions. In experiments on helium and hydrogen (*Year Book 78*, 630–632), hydrostatic conditions at pressures to above 600 kbar were observed. These pressures are greater than the hydro-

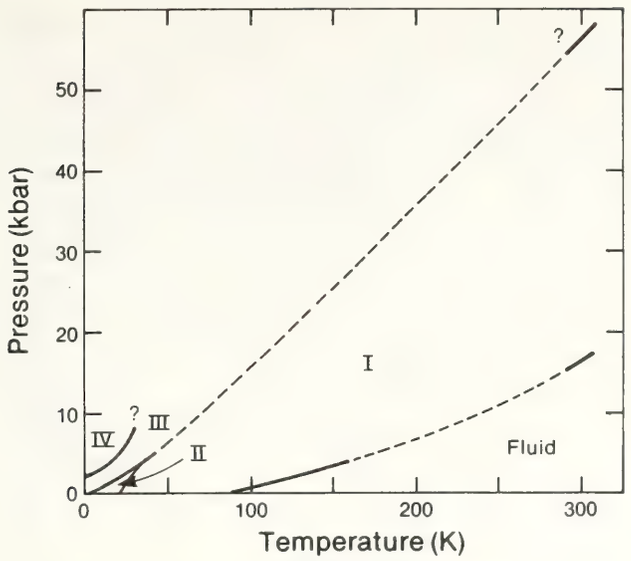


Fig. 44. Phase diagram for methane. Low-temperature data are from Medina and Daniels (1979). Room-temperature data are from this study.

static limits of pressure fluids that are liquid under ambient conditions.

Crystalline gases may also be used in pressure calibration, because they form single crystals around the sample under study. The unit-cell edge of the cubic "gas" is extremely sensitive to changes in pressure, with $\Delta a/a$ as much as 0.35%/kbar. An individual cell constant can be measured to one part in 20,000 with a four-circle diffractometer. The implied precision in pressure calibration, if the equation of state of the standard is known, is approximately ± 10 bar, which is at least an order of magnitude better than present diamond-anvil cell calibration techniques. The present design of the diamond-anvil cell has a maximum pressure range of about 90 kbar, at which pressure the beryllium-diamond supports fail. Argon is a strong x-ray scatterer and has sharp diffraction maxima from freezing at 11.5 kbar to above 80 kbar. Argon may thus prove to be the ideal hydrostatic medium-pressure standard for research with single-crystal diamond cells at very high pressures.

References

Medina, F. D., and W. B. Daniels, Raman spectrum of phase III of solid CH_4 in the lattice and intramolecular regions, *J. Chem. Phys., 70,* 2688–2694, 1979.

Murnaghan, F. D., *Finite Deformation of an Elastic Solid,* Dover Press, New York, 1967.

Phase Transitions in Methane under High Pressures at Room Temperature—A Raman Spectral Study

S. K. Sharma, H. K. Mao, and P. M. Bell

The phases of solid methane in the pressure range 16–187 kbar at room temperature have been investigated for the first time in the diamond-window, high-pressure cell by Raman spectroscopy. Previous studies of the phases of methane at low temperatures (4–150 K) had been limited to pressures below 10 kbar (Stevenson, 1957; Constantino and Daniels, 1975; Nijman and Trappeniers, 1977; Medina and Daniels, 1979).

Raman spectra of internal modes of CH_4 (99.97% pure) at room temperature and pressures between 16 and 51 kbar and between 118 and 187 kbar (ruby fluorescence pressure scale; Mao *et al.,* 1978) are shown in Figs. 45 and 46, respectively. The first-order phonon line of diamond at 1333 cm^{-1} obscures the antisymmetric C-H bending [$\nu_4(F)$] region of CH_4, but all other significant regions were accessible. The positions and spectral characteristics of the bands in the spectra of CH_4 at various pressures are summarized in Table 27. The pressure dependencies of the bands due to symmetric [$\nu_1(A_1)$] and antisymmetric [$\nu_3(F_2)$] C-H stretching vibration and the symmetric C-H bending vibration [$\nu_2(E)$] are plotted in Figs. 45 and 46.

The vibrational properties of CH_4 are well known (Dennison, 1940; Herzberg, 1945; Crawford *et al.,* 1952; Anderson and Savoie, 1965; Medina and Daniels,

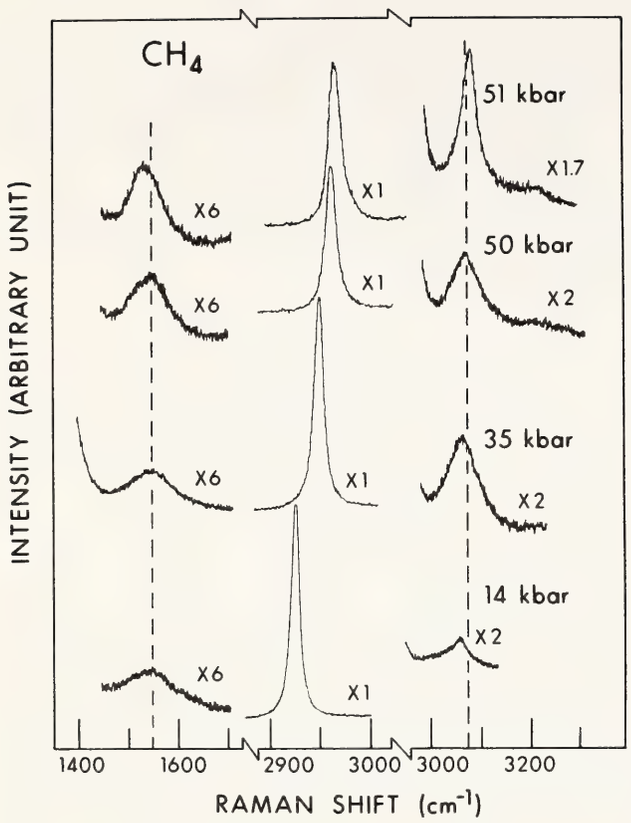


Fig. 45. Portions of Raman spectra of solid CH_4 at various pressures in the range 14–51 kbar at room temperature. Experimental: 488.0 nm Ar^+ laser, 300 mW at the sample. Spectral slit width was 12 cm^{-1} for the range 1400–1600 cm^{-1}, 4 cm^{-1} for the range 2900–3000 cm^{-1}, and 6 cm^{-1} for the range 3000–3200 cm^{-1}, except for the measurements at 14 kbar where the slit width for the 3000–3200 cm^{-1} regions was 4 cm^{-1}.

1979). For a free CH_4 molecule all normal modes are Raman active (symmetries: $A_1 + E + F_2 + F_2$), whereas only $\nu_3(F)$ and $\nu_4(F)$ modes are allowed in the infrared spectrum. The totally symmetric C-H stretching mode $\nu_1(A)$ of CH_4 gives the strongest Raman band, whereas the doubly degenerate C-H symmetric bending $\nu_2(E)$ mode and the triply degenerate $\nu_3(F)$ and $\nu_4(F)$ modes are weak in the Raman spectrum. Figures 45 and 46 illustrate the changes observed in the ν_1, ν_2, and ν_3 regions of the spectrum of CH_4 at the solid-solid phase transitions at 51 and ~118 kbar. Methane solidified at room temperature under high pressures (16–51 kbar) has the same structure (space group $Fm3m$ (O_h^5), $Z = 4$) as the low-temperature phase I of CH_4 (Hazen, Finger, Mao, and Bell, this Report). The relationship between two other high-pressure and room-temperature polymorphs of CH_4 and the low-temperature phases II, III, and IV of methane has not been established. Until determination of the two regions of the phase diagram has been completed, the intermediate (51–117 kbar) and the high-pressure phase (118–187 kbar) at room temperature are tentatively designated as phases V and VI, respectively (Table 27).

The transition from phase I to phase V is marked by an abrupt decrease in the half-width (ω) of the ν_3 band from 64 cm^{-1} in phase I at 50 kbar to 32 cm^{-1} in phase V at 51 kbar (Fig. 45, Table 27), and also by a decrease in the frequency of the ν_2 band from 1551 cm^{-1} (phase I) to 1536 cm^{-1} (phase V) (Table 27). The slopes of the ν_1 and ν_3 bands also change at this transition. The phase boundaries between phases I and V can also be observed visually under the microscope. On the basis of these observations, it is suggested that the change from phase I to V is associated with a first-order or nearly first-order phase transformation. This phase change is in contrast to the λ-type transitions observed in CH_4 at low temperatures (Colwell *et al.*, 1962, 1963; Press and Hüller, 1974).

With further increase of pressure on CH_4(V), all observed Raman bands shift toward higher frequency. The ν_3 mode in phase V is most pressure sensitive with a rate of shift of 1.3 cm^{-1}/kbar, and next is the ν_1 mode, which shifts at a rate of 0.95 cm^{-1}/kbar. The ν_2 band is least pressure sensitive ($\Delta\nu/\Delta P \approx 0.19$ cm^{-1}/kbar). At 118 kbar in the ν_1 stretching region of the spectrum, a weak shoulder at ~2991 cm^{-1} is observed. When the pressure is increased above 118 kbar, the intensity of the shoulder increases; at 187 kbar there are at least two weak shoulders and a strong band in the ν_1 region and

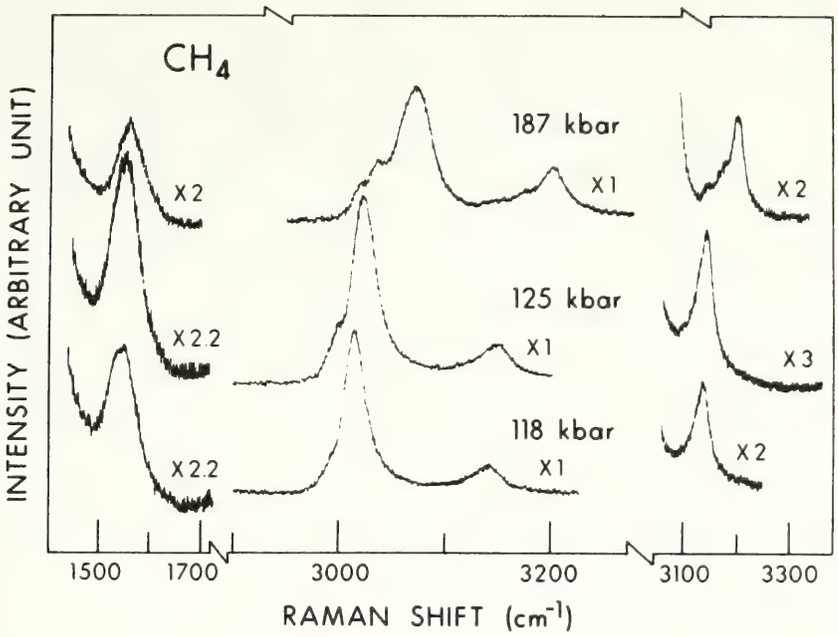


Fig. 46. Portions of Raman spectra of solid CH_4 at various pressures in the range 118–187 kbar at room temperature. Experimental: 488.0 nm Ar^+ laser, 300 mW at the sample. Spectral slit width was 12 cm^{-1} for the range 1400–1700 cm^{-1}, 4 cm^{-1} for the range 2900–3200 cm^{-1}, and 8 cm^{-1} for the range 3100–3300 cm^{-1}.

two very weak shoulders and a weak, broad band in the ν_3 region of the spectrum. It is clear that the V → VI transition is sluggish, and even at 187 kbar a small proportion of phase V may still exist. The frequency of the ν_2 band does not show any apparent discontinuity at the V → VI transition, whereas not only do both the ν_1 and the ν_3 band show shoulders on the low-frequency side but also the slopes of the main ν_1 and ν_2 bands show a small change; for example, $\Delta\nu/\Delta P$ for the ν_1 band changes from 0.95 cm^{-1}/kbar in phase V to 1.25 cm^{-1}/kbar in phase VI, and similarly $\Delta\nu/\Delta P$ for the ν_3 band changes from 1.3 cm^{-1}/kbar to 1.25 cm^{-1}/kbar. Under the optical microscope, no visual changes were observed at the V-VI transition. It is not clear, therefore, whether the V-VI transition is a first-order or a second-order transition. The presence of at least three $\nu_1(A_1)$ bands in the spectrum of phase VI, however, indicates that phase VI has more than two molecules in the unit cell and that these molecules may be present at distinct sites.

In the Raman spectra of all these phases no low-frequency bands were detected. The absence of well-defined lattice modes in the vibrational spectrum of phase I is due to its disordered structure (Crawford *et al.*, 1952; Anderson and Savoie, 1965; Savoie and Fournier, 1970). The absence of lattice modes in the spectra of phases V and VI probably indicates that phases V and VI are orientationally disordered or that these low-frequency bands are very weak as a result of anharmonic broadening of the 1-phonon transitions to the relatively high temperature of measurement. Additional studies of Raman spectra, structures, and phase boundaries of methane at high pressures and at temperatures between 80 and 280 K are needed for detailed interpretation of these observations.

References

Anderson, A., and R. Savoie, Raman spectra of crystalline CH_4 and CD_4, *J. Chem. Phys.*, *43*, 3468–3473, 1965.

Colwell, J. H., E. K. Gill, and J. A. Morrison,

TABLE 27. Raman Frequencies (cm^{-1}) of Methane at Various Pressures and Room Temperature

	P, kbar							
	0.001	14	35	50	51	118	125	187
Phase	Gas*	I	I	I	V	V + VI	V + VI	VI + (V)?
Assignment†								
$\nu_2(E)$	1526	~1540 vw, bd‡ ($\omega = 72$)	1542 vw, bd ($\omega = 72$)	1551 vw, bd ($\omega = 72$)	1536 vw, bd ($\omega = 72$)	1543 vw, bd ($\omega = 70$)	1544 vw, bd ($\omega = 72$)	1554 vw, bd ($\omega = 62$)
$\nu_4(F_2)$	1306.2	...§	...§	...§	...§	...§	...§	...§
$\nu_1(A_1)$	...	...	...	...	...	~2991 vw(sh)	~2996 w(sh)	~3020 w(sh)
	2914.2 s	2926 s ($\omega = 10$)	2949 s ($\omega = 10.5$)	2963 s ($\omega = 12$)	2966 s ($\omega = 14$)	~3035 w(sh) 3031 s ($\omega \approx 25$)	3020 s ($\omega \approx 26$)	3070 s ($\omega \approx 36$)
$\nu_3(F_2)$	...	...	...	...	...			~3139 vw(sh)
	3020.3 w	3058 w, bd ($\omega = 36$)	3066 w, bd ($\omega = 64$)	3074 w, bd ($\omega = 64$)	3086 w, bd ($\omega = 32$)	~3172 vw(sh) 3141 w, bd ($\omega = 32$)	3147 w, bd ($\omega \approx 40$)	3199 w, bd ($\omega \approx 31$)
	...	...	...	~3222 vw, bd	~3222 vw, bd	...	...	...

* From Herzberg (1945).

† Measurement accuracy is ± 4 cm^{-1} for weak and broad bands, ± 1 cm^{-1} for strong and sharp bands.

‡ Abbreviations: s, strong; w, weak; vw, very weak; m, medium; bd, broad; sh, shoulder.

§ Raman bands could not be measured because of low intensities and interference from very strong first-order (F_{2g}) Raman band of diamond at 1333 ± 1 cm^{-1}.

Second transition in solid CH_4, *J. Chem. Phys., 36,* 2223-2224, 1962.
Colwell, J. H., E. K. Gill, and J. A. Morrison, Thermodynamical properties of CH_4 and CD_4—interpretation of the properties of the solids, *J. Chem. Phys., 39,* 635-653, 1963.
Constantino, M. S., and W. B. Daniels, Dielectric constant of compressed solid methane at low temperature, *J. Chem. Phys., 62,* 764-770, 1975.
Crawford, M. F., H. L. Welsh, and J. H. Harrold, Rotational wings of Raman bands and free rotation in liquid oxygen, nitrogen and methane, *Can. J. Phys., 30,* 81-98, 1952.
Dennison, D. M., The infrared spectra of polyatomic molecules, part II, *Rev. Modern Phys., 12,* 175-214, 1940.
Herzberg, G., *Molecular Spectra and Molecular Structure,* Vol. 2, D. Van Nostrand Company, New York, 1945.
Mao, H. K., P. M. Bell, J. W. Shaner, and D. J. Steinberg, Specific volume measurements of Cu, Mo, Pd and Ag and calibration of the ruby R_1 fluorescence gauge from 0.06 to 1 Mbar, *J. Appl. Phys., 49,* 3276-3283, 1978.
Medina, F. D., and W. B. Daniels, Raman spectrum of phase III of solid CH_4 in the lattice and intermolecular regions, *J. Chem. Phys., 70,* 2688-2694, 1979.
Nijman, A. J., and N. J. Trappeniers, A NMR study of solid methane: the low-temperature phase transition, *Chem. Phys. Lett., 47,* 188-197, 1977.
Press, W., and A. Hüller, Phase transition in solid CD_4, in *Anharmonic Lattices, Structural Transitions, and Melting,* T. Riste, ed., Noordhoff International Publishing, Leiden, pp. 185-212, 1974.
Savoie, R., and R. P. Fournier, Far-infrared spectra of condensed methane and methane-d_4, *Chem. Phys. Lett., 7,* 1-3, 1970.
Stevenson, R., Solid methane—change in phase under pressure, *J. Chem. Phys., 27,* 656-658, 1957.

Acoustic Velocity and Refractive Index of Fluid Hydrogen and Deuterium at High Pressures

E. M. Brody, H. Shimizu,* H. K. Mao, P. M. Bell, and W. Bassett†*

High-pressure properties of molecular hydrogen and deuterium have been the subject of recent investigations in which ultrasonics and Raman scattering have been used. In none of these studies, however, has it been possible to ascertain directly the fundamental thermodynamic relation—the equation of state—between pressure and density, or volume, above 20 kbar. Such information is necessary, for example, for estimating the pressure at which a metallic state would be formed. Because the acoustic velocity is directly related to the isothermal partial derivative of the equation of state, $\partial V/\partial P|_T$, it serves as a sensitive check on the form this equation is chosen to have. In addition, the refractive index is related to the density by the Lorenz-Lorentz expression.

Brillouin scattering has been used to measure the acoustic velocities of fluid H_2 and D_2 at room temperature, 295 K (Fig. 47). The first measurements above 20 kbar and the only pressure-

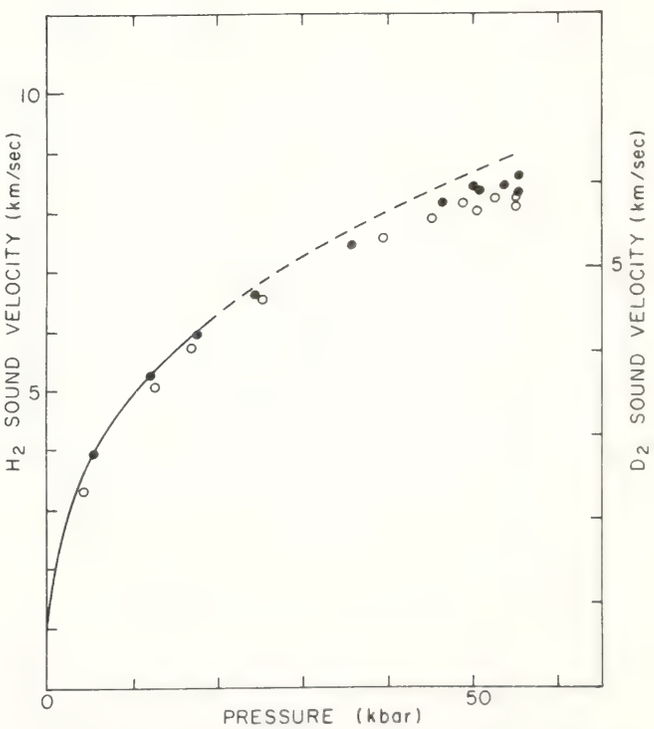


Fig. 47. Sound velocity of H_2 and D_2 with pressure. Solid circles, D_2; open circles, H_2. The vertical scale for H_2 sound velocity is $\sqrt{2} \times D_2$ sound-velocity scale. The solid curve below 2 kbar is due to Michels *et al.* (1963) and that above 2 kbar, to Liebenberg *et al.* (1979). The dashed line is an extrapolation of the equation of state given by Liebenberg *et al.*

*Institute of Optics, University of Rochester.
†Department of Geophysical Sciences, Cornell University.

dependent measurements of refractive index from 4 to 55 kbar, the solidification point (Fig. 48), have been made.

Experimental

A five-pass interferometric Brillouin spectrometer described previously by Dill and Brody (1976) was used. The $\lambda = 514.5$ nm Ar^+ laser line, single longitudinal mode, was used for excitation at power levels from 300 to 600 mW input. Owing to reflectivity losses at the diamond anvils, it is estimated that half of this power actually entered the sample volume. No variation of sound velocity with incident laser power was observed, a result indicative of insensitivity to sample heating. The signals were comparable in intensity to those from common liquids, and peaks with satisfactory signal-to-noise could be obtained in 5 min at the highest incident laser power.

The scattering geometry is that used in earlier studies (Dill and Brody, 1976) with the diamond cell. There is a 90° angle between the input beam entering the first diamond anvil and the scattered beam emerging from the second anvil (Fig. 49). For this geometry the Brillouin frequency shift, $\nu_s - \nu_l = \nu_1$, is related to the sound velocity U_s by the expression

$$U_s = \frac{\nu_1 \lambda_0}{\sqrt{2}}, \tag{1}$$

which is independent of refractive index of the medium. There is also a laser beam reflected from the second diamond anvil that serves as incident light, giving a back-scattered signal. In that case the Brillouin shift ν_2 is related to the sound velocity by the expression

$$U_s = \frac{\nu_2 \lambda_0}{2n}, \tag{2}$$

where n is the refractive index of the fluid. Both ν_1 and ν_2 can be detected simultaneously (Fig. 49). Because the fluid is acoustically isotropic, the sound velocity is the same in both Equations 1 and 2. The ratio of ν_1 to ν_2 therefore determines n, the refractive index. This technique results in a reproducibility of 0.5%, because it relies on a ratio of spectral shifts and is independent of the free spectral range of the interferometer.

The high-pressure cell is loaded with liquid at low temperatures, sealed, and then warmed to room temperature. The gases are high purity (99.999% pure), and the filling system is designed to trap any impurities. The material for the gasket, Incoloy 903, that contains the fluid between the two opposing anvils, was chosen for its resistance to reaction with H_2. Measurements were always begun from the solid phase, where chemical reaction with the gasket was not detected. A sequence of pressure measurements was completed in one day—from the solid, to low pres-

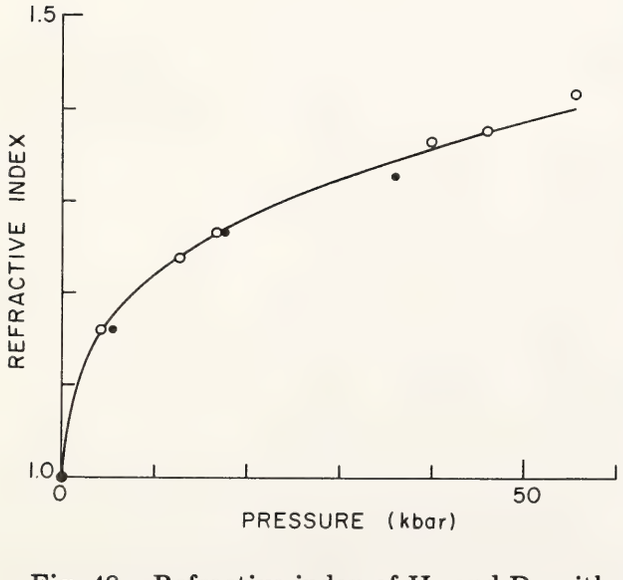


Fig. 48. Refractive index of H_2 and D_2 with pressure. Solid circles, D_2; open circles, H_2. The solid line is a fit to the Lorenz-Lorentz expression

$$\frac{n^2 - 1}{n^2 + 1} = \frac{4\pi}{3} \frac{N}{V} \alpha,$$

where N is Avogadro's number, V is calculated from the Liebenberg equation of state, and α (= 8.17×10^{-25} cm^3) is the molecular polarizability.

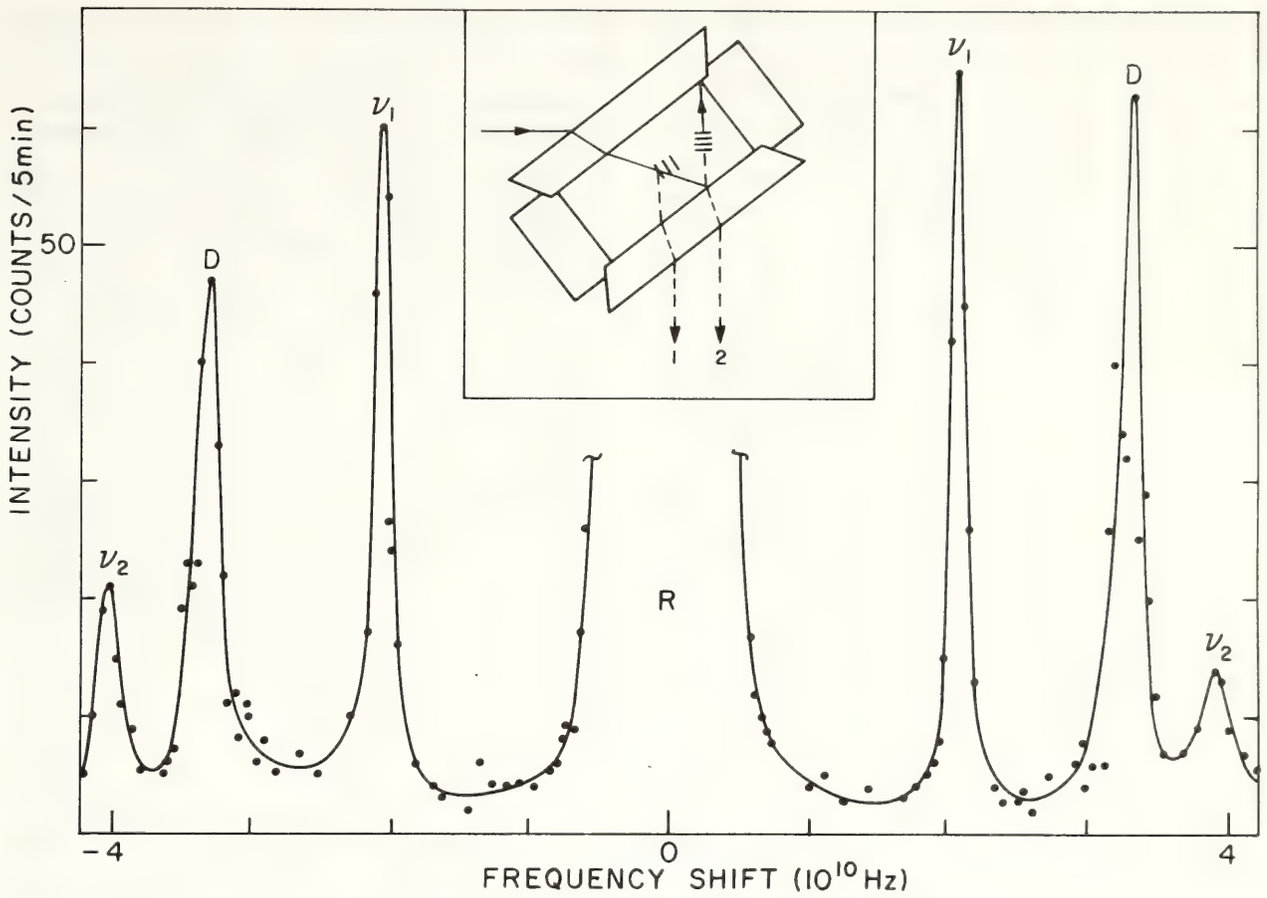


Fig. 49. Brillouin spectrum of H_2 at 39.5 kbar. λ_0 = 514.5 nm. Total accumulation time was 5 min. R is Rayleigh or elastically scattered light; ν_1 and ν_2 are Brillouin-shifted light from H_2; D is Brillouin-shifted light from the diamond anvils.

sures in the fluid, and then back to a solid. The reproducibility of the sound velocities at a pressure of 50 kbar was within the experimental reproducibility of 1% by comparison of the initial and final measurements of a sequence at the same pressure.

There was, however, some progressive contamination of the fluids with time, as noted by the fact that the sound velocity for H_2 decreased by 0.1 km/sec/day when left at the same pressure. The decrease of velocity in D_2 was slower. It is believed that the contamination effect is too small to account for the observation that sound velocities are systematically smaller than predicted by the equation of state. At 55 kbar, velocities of 8.04 to 8.22 km/sec were measured for H_2 (the variation is due to the hysteresis effect), whereas the equation of state gives a value of 8.93 km/sec.

Sound velocity (U) data show an excellent fit to a power law up to 50 kbar:

$$H_2,\ U_{H_2} = 2.25\ P^{0.317}, \qquad (3a)$$

and

$$D_2,\ U_{D_2} = 1.61\ P^{0.332}, \qquad (3b)$$

with P in kbar and U in km/sec.

The equations of state for H_2 given by Mills *et al.* (1977) and for D_2 given by Liebenberg *et al.* (1979) yield values on extrapolation for the velocities at 50 kbar that are only 5% and 2.5% higher than the measured values for H_2 and D_2, respectively. The ratio of the squares of the acoustic velocities is consistently less than 2: $(U_H/U_D)^2 \simeq 1.9$.

From 50 to 55 kbar the measured velocity increases relatively slowly with pressure, a feature not reproduced by

the equation of state. This phenomenon is a precursor to solidification but has not been seen when solidification occurred at lower temperatures and pressures. At 55 kbar there is a hysteresis effect in which sound velocities are higher by 2% to 3% when the pressure is increased to form the solid phase, compared with the values at the same pressure when the pressure had been decreased to form the fluid phase.

At high pressures, the refractive indices are comparable to values obtained for common liquids. At 45.6 kbar, for example, the refractive index of H_2 was found to be 1.374. To calculate the polarizability, the Lorenz-Lorentz relation was used:

$$\frac{n^2-1}{n^2+2}=\frac{4\pi}{3}\frac{N}{V}\alpha, \qquad (4)$$

where n is the refractive index; N, Avogadro's number; V, the molar volume; and α, the polarizability. If the previously mentioned equations of state were used to determine the molar volume at each pressure, it was found that $\alpha = 8.17 \pm 0.1 \times 10^{-25}$ cm^3 satisfied the observations (Fig. 48). The value of α is in agreement with that obtained from the measurements of n at 1 atm, $\alpha = 8.29 \times 10^{-25}$ cm^3. This result indicates that the polarizability is pressure insensitive up to solidification.

The density ρ can be calculated from the present data with the expression

$$\rho(P_B) - \rho(P_A) = \int_{P_A}^{P_B} \gamma/U^2\, dP, \qquad (5)$$

where $\gamma = C_p/C_v$ is the ratio of the specific heats at constant pressure and volume. With Equations 4 and 5 and constant $\bar{\gamma} = 1.07$ for H_2 and $\bar{\gamma} = 1.10$ for D_2 in the pressure range $P_A = 20$ kbar to $P_B = 50$ kbar, the density difference ρ (50 kbar) $-$ ρ (20 kbar) can be calculated with the Mills value at ρ (20 kbar). The values of molar volume at 50 kbar for H_2 are 8.30 cm^3 (this study), 8.70 cm^3 (Mills *et al.*, 1977); and for D_2, 8.42 cm^3 (this study), 8.55 cm^3 (Liebenberg *et al.*, 1979).

Calculation of the metallization pressure involves the following assumptions: (1) Equation 3 holds into the solid-phase region when a combination of velocities is used that would yield the bulk modulus; for example, for an acoustically isotopic cubic crystal the velocity in the solid is $U_s = (U_l^2 - 4.3\, U_t^2)^{1/2}$, where U_l and U_t are the longitudinal and transverse sound velocities; (2) $\bar{\gamma} = 1$; (3) the metallization density is 0.8 g/cm^3, a calculation made by Wigner and Huntington (1935). Under these assumptions Equation 3a yields a value of the metallization pressure in hydrogen of 1.5 Mbar.

References

Dill, J. G., and E. M. Brody, Brillouin scattering from isotropic metals, *Phys. Rev. B, 14,* 5218–5227, 1976.

Liebenberg, D. H., R. L. Mills, and J. C. Bronson, Equation of state for fluids at high densities—hydrogen isotope measurements and thermodynamic derivations, in *High-Pressure Science and Technology,* Vol. 1, K. D. Timmerhaus and M. S. Barber, eds., Plenum Publishing Corporation, New York, pp. 395–407, 1979.

Michels, A., W. de Graaff, and G. J. Wolkers, Thermodynamic properties of hydrogen and deuterium at temperatures between −175 °C and 150 °C and at pressures up to 2500 atmospheres, *Appl. Sci. Res., A12,* 9–32, 1963.

Mills, R. L., D. H. Liebenberg, J. C. Bronson, and L. C. Schmidt, Equation of state of fluid n-H_2 from *P-V-T* and sound velocity measurements to 20 kbar, *J. Chem. Phys., 66,* 3076–3084, 1977.

Wigner, E., and H. B. Huntington, On the possibility of a metallic modification of hydrogen, *J. Chem. Phys., 3,* 764–770, 1935.

Raman Measurements of Deuterium in the Pressure Range 8–537 kbar at Room Temperature

S. K. Sharma, H. K. Mao, and P. M. Bell

Recent methods for confining samples of hydrogen, helium, and other gases in the diamond-window, high-pressure cell (Mao and Bell, 1979, and

Year Book 78, 659–660; Besson and Pinceaux, 1979) have been used to study properties of these materials at very high pressure. In an earlier report (Sharma *et al.,* 1980, and *Year Book 78,* 645–649), measurements of rotational and vibrational Raman spectra of hydrogen over the pressure range from 0.02 to 630 kbar were presented. The results of the ultrahigh-pressure measurements on deuterium, one of the hydrogen isotopes, are reported here. The data on the heavier isotope of hydrogen under high pressures were obtained to evaluate the effect of pressure on molecular rotation and on the molecular bond of hydrogen. Measurements of the rotational and vibrational spectra of n-D_2 had previously been limited to pressures below 15 kbar with conventional apparatus (Stoicheff, 1957; Allin *et al.,* 1967; Vu *et al.,* 1975). Recently, Wijngaarden and Silvera (1980) reported Raman measurements on orthodeuterium in the low-frequency, lattice-vibration region (0–170 cm^{-1}) to 150 kbar at 5 K.

Experimental

The deuterium sample used in this study was 99.5% pure (Linde Corporation). The deuterium molecules of the sample at the start of the experiments were in the normal ratio of spin states (n-D_2), which is a 2:1 mixture of the ortho (o-D_2) and para (p-D_2) isomers at room temperature.

A modified diamond-window, high-pressure cell used in the present experiment and the techniques for loading the samples are described in detail elsewhere (Mao and Bell, 1979, and *Year Book 78,* 659–660). In these experiments, work-hardened stainless steel gaskets were used. Small ruby crystals (10–20 μm) were placed in the gasket aperture for pressure measurements (Mao *et al.,* 1978). The spectra were recorded with a Jobin-Yvon monochromator. The blue (488.0 nm) line of an Ar^+ laser was used for exciting Raman emulsions.

The experimental details for measurement of Raman spectra at high pressures have been described elsewhere (Sharma, *Year Book 78,* 660–665).

Results and Discussion

Raman spectra of n-D_2 in the region of molecular vibration and rotation at various pressures are shown in Figs. 50 and 51, respectively. The positions and other spectral characteristics of the bands in the spectra of fluid and solid deuterium are given in Table 28.

Above 8 kbar, resolution of many of the Q-branch lines of deuterium (Table 28) is lost, and only an intense D-D stretching band (Fig. 50) is observed. It can be seen from the relative intensities of the rotational lines (Fig. 51; Table 28) that the population of D_2 molecules at various pressures is at a maximum at the $J = 2$, $v = 0$ level,

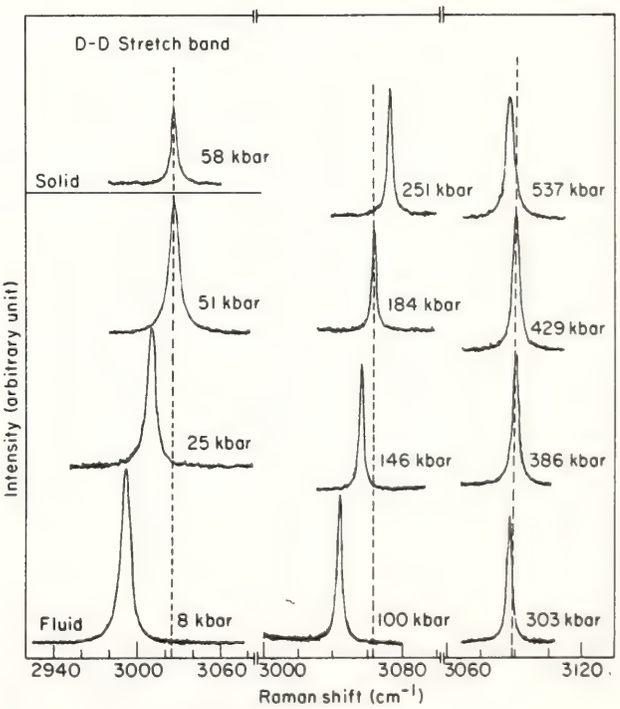


Fig. 50. The Q_1 (2) Raman active mode of $n-D_2$ at different pressures. Spectral slit width 3 cm^{-1} for fluid spectra and 2.5 cm^{-1} for spectra of solid $n-H_2$, 488.0 nm excitation, 400 mW at the sample.

TABLE 28. Frequencies (cm^{-1}) of Raman Bands of n-D_2 at Various Pressures and Room Temperature

	Rotational Bands						Vibrational Bands				
Pressure	$S_0(0)$	$S_0(1)$	$S_0(2)$	$S_0(3)$	$S_0(4)$	$S_0(5)$	$Q_1(0)$	$Q_1(1)$	$Q_1(2)$	$Q_1(3)$	$Q_1(4)$
1–2 bars*	179.056	297.521	414.655	529.907	642.807	...	2993.548	2991.446	2987.230	2980.877	2972.557
8 kbar†	180 m‡ ($\omega = 18$)	298 m ($\omega = 16$)	416 s ($\omega = 14$)	530 w ($\omega = 13$)	644 w ($\omega = 12$)	~751 vw	...§	...§	2993.05 ($\omega = 7.5$)	...§	...§
25 kbar	183 m ($\omega = 41$)	304 m ($\omega = 36$)	422 s ($\omega = 34$)	538 w ($\omega = 26$)	646 w ($\omega = 22$)	~758 vw	...§	...§	3007.5 ($\omega = 7.5$)	...§	...§
51 kbar	184 m ($\omega = 60$)	307 m ($\omega = 48$)	428 s ($\omega = 50$)	542 w ($\omega = 48$)	654 w ($\omega = 48$)	~762 vw	...§	...§	3026.5 ($\omega = 8.0$)	...§	...§
58 kbar	vw, bd	~300 w, bd	~428 s ($\omega = 72$)	~540 w ($\omega = 48$)	~654 w ($\omega = 48$)	... vw, bd	...§	...§	3025.5 ($\omega = 5$)	...§	...§
133 kbar	~190 w, sh	~300 vw, bd	~446 w ($\omega \approx 112$)	...§	...§	...§	...§	...§	3053.2 ($\omega = 3.2$)	...§	...§

* From Stoicheff (1957); the positions of rotational bands are within ± 0.02 cm^{-1}; those of Q-branch vibrational bands, within ± 0.05 cm^{-1}.
† Measurement accuracy ± 0.5 cm^{-1}.
‡ Abbreviations: w, weak; m, medium; s, strong; ω, full width at half maximum height; sh, shoulder.
§ Bands not observed (see text).

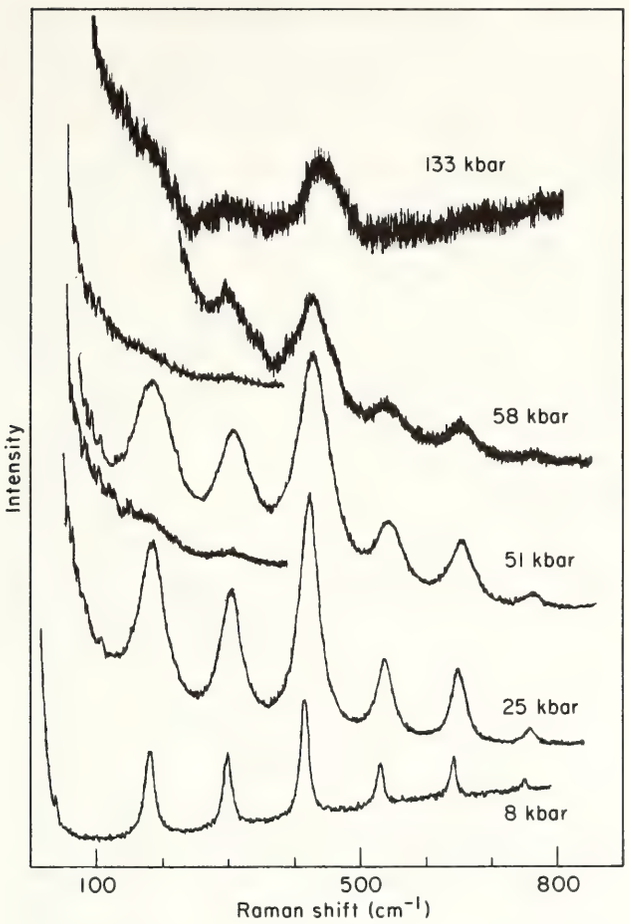


Fig. 51. Raman spectra of $n-D_2$ in the region of rotational modes at different pressures. 488.0 nm Ar^+ laser excitation, 200 mW at the sample. Spectral slit width 5 cm^{-1}. Where two traces are shown for a given pressure, the lower trace has an amplification of 0.1×.

where J and v are rotational and vibrational quantum numbers, respectively. The D-D stretch band will therefore be referred to as the $v[Q_1(2)]$ band. It should be emphasized, however, that the D-D stretch band is an envelope of all the bands in the Q branch, which have overlap due to pressure-induced broadening (May *et al.*, 1961). The width of this vibrational band increases significantly with pressure. When deuterium is fluid, the band broadens with increasing pressure to the solidification point (55 kbar at 22°C), where it suddenly becomes relatively sharp (Fig. 52). The decrease in the half-width (ω) of the $Q_1(2)$ band from 8 to 5 cm^{-1} (Fig. 50) is a result of reduction of collision-induced broadening in the solid and can be used as an indication of the transition. At the freezing pressure, the $v[Q_1(2)]$ also shows a small decrease (1 cm^{-1}) in frequency. In n-D_2 at low temperature, the frequencies of the $Q_1(0)$ and $Q_1(1)$ lines at the liquid-to-solid transition decreased by 2.53 and 2.1 cm^{-1}, respectively (Bhatnagar *et al.*, 1962). The observed small decrease in the frequency of the $Q_1(2)$ band at the freezing pressure indicates that repulsive forces are significant in the compressed solid at room temperature.

In solid deuterium, the $Q_1(2)$ band (Figs. 50 and 52) sharpens further with increasing pressure to about 184 kbar ($\omega = 3.03$), where it gradually broadens again, and the half-width increases rapidly above 300 kbar (Fig. 52). Figure 53 is a plot of the major shift of the $Q_1(2)$ band from 8 to 537 kbar. The following relationship is a polynomial least-squares fit to the observed data point in fluid deuterium:

$$\Delta v = 11.168 \times 10^{-1}P - 0.827 \times 10^{-3}P^2 \quad (P \leq 55 \text{ kbar}),$$

where Δv (cm^{-1}) is the frequency shift for the $Q_1(2)$ band and P (kbar) is the pressure in the fluid.

Figure 54 shows a plot of the frequency shift ratio of H_2 to D_2 as a function of pressure. This ratio would normally be related to the density difference, but the pressure shift evidently includes an isotopic effect. Instead of being constant, the data can be fit to the straight line:

$$\nu_{D_2}/\nu_{H_2} = 0.719 + 0.945 \times 10^{-5}P.$$

This function, calculated in combination with existing data for H_2, gives the frequency shift of solid D_2 as a function of pressure:

$$\Delta\nu_{D_2} = 10.2 + 0.600P - 0.164 \times 10^{-2}P_2 + 0.211 \times 10^{-5}P^3 - 0.116 \times 10^{-8}P^4.$$

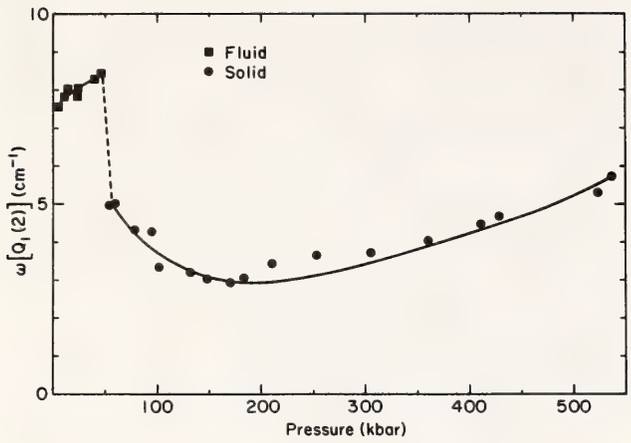


Fig. 52. Pressure dependence of the half-width (ω) of the Q_1 (2) band in $n-D_2$.

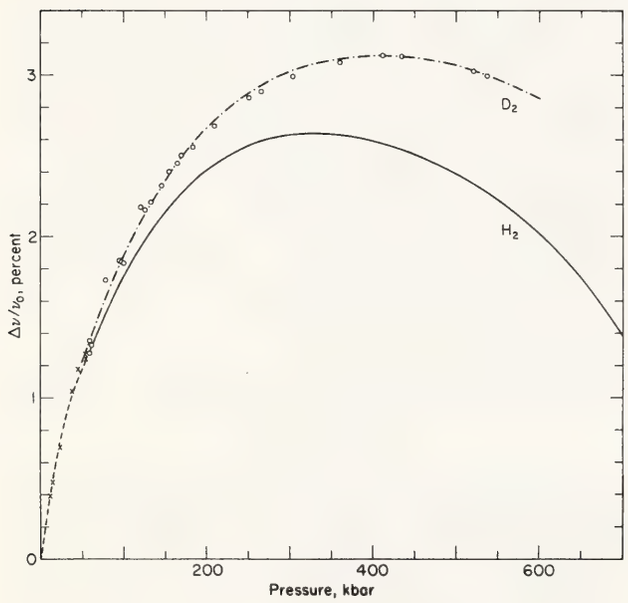


Fig. 53. The percentage of shift of $\Delta_\nu[Q_1\ (2)]$ as a function of pressure in $n-D_2$ in comparison with $n-H_2$ at room temperature (26° ± 4°C).

Initially the $Q_1(2)$ band shifts toward higher frequency, a result that can be attributed in a qualitative way to the predominance of the effect of intermolecular repulsive force over that of the attractive forces (May *et al.*, 1961). The rate of shift of the $Q_1(1)$ band decreases with increasing pressure, and the frequency reaches a maximum value of 3080.4 cm^{-1} at 400 kbar. When the pressure is increased above 400 kbar, the $Q_1(1)$ band frequency decreases from its maximum value of 3080.4

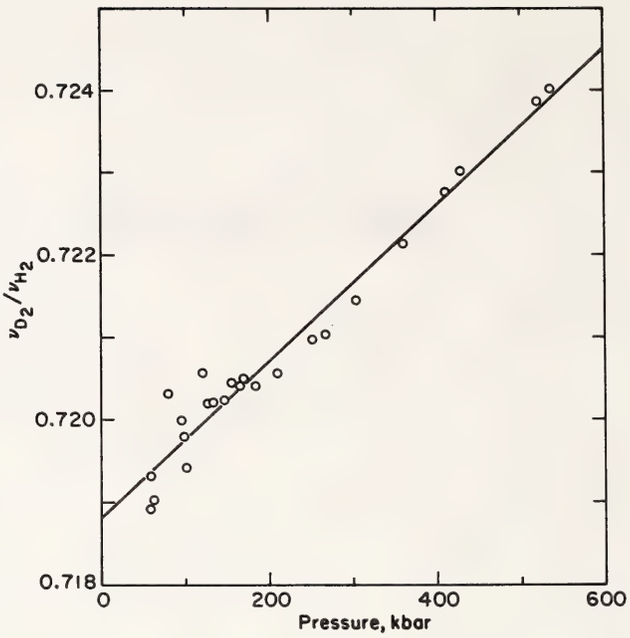


Fig. 54. Plot of ν_{H_2}/ν_{D_2} vs. pressure.

cm^{-1} at 400 kbar to 3076.7 cm^{-1} at 537 kbar, the maximum pressure used in the present experiment.

The increase in the frequency of the $Q_1(2)$ band is a direct response of deuterium to compression. This effect is observed in many polyatomic molecules (Whalley, 1975). The leveling off and then the decrease in frequency with pressure is an indication that the molecular bond is softening. These observed changes in the Raman spectra of deuterium under pressure are similar to those observed in the spectra of hydrogen (Sharma, Mao, and Bell, 1980, and *Year Book 78*, 645–649); however, there are some significant differences (see below). The observed pressure dependence of the shift of the $Q_1(2)$ band (Fig. 53) and the rapid increase in the half-width of this band (Fig. 52) in the range 300–527 kbar indicate that the intermolecular interactions and significant changes in the molecular bonds have already begun to occur.

In the spectrum of n-D_2 at 8 kbar, six rotational lines [$S_0(J)$ ($\Delta\nu = 0$; $\Delta J = \pm 2$; $J = 1, 2, 3, 4, 5$)] are observed (Fig. 51, Table 28). With increasing pressure

these lines show a small positive shift from their positions at 1 bar but are considerably broader (Fig. 51). The intensity of the Rayleigh tail also increases with increasing pressure and interferes with the rotational bands owing to collision broadening (Fig. 51) (Jammu *et al.*, 1960; Weber, 1973).

At the solidification pressure (55 kbar at 22°C), strong Rayleigh interference is observed (Fig. 51). No well-defined lattice mode was detected. The presence of a strong continuous background at low frequency may be caused by parasitic scattering from microscopic inhomogeneities in the solid sample or by anharmonic broadening of a 1-phonon transition due to the relatively high temperature of the measurement. Wijngaarden and Silvera (1980) have shown that at 79 K and 25.9 kbar the 1-phonon lattice modes of orthodeuterium appear as a weak, broad envelope, and are resolved only when the temperature is lowered to 5 K. High temperature and random distribution of o-D_2 and p=D_2 in the solid n-D_2 contribute to the broadening of the rotational bands (Van Kranendonk, 1959). Bhatnagar *et al.* (1962) showed that even at low temperature the presence of 20% p-D_2 causes serious broadening of the $S_0(0)$ line.

With increasing pressure on solid deuterium the rotational bands become very weak and diffuse (Fig. 51). Above 146 kbar it was not possible to detect even the $S_0(2)$ band. England *et al.* (1976) calculated from theory the effect of pressure on rotational motion of hydrogen isotopes. According to these calculations the rotation of D_2 molecules at 0 K is expected to cease at ~175 kbar. In the present study the low-frequency (50–1000 cm^{-1}) Raman spectra were featureless in the pressure range 150 to 537 kbar. The half-width of the $Q_1(2)$ band, however, decreased from 5 to 3 cm^{-1} at 184 kbar (Fig. 52). The observed decrease in the half-width could be due to progressive hindrance in the rotation of the molecules.

The changes observed in the Raman spectrum of n-D_2 over the pressure range 8–527 kbar closely resemble those observed in the spectra of n-H_2 (Sharma *et al.*, 1980, and *Year Book 78*, 645–649). There are, however, the following important differences: (1) In both fluid and solid phases, the D-D stretching band is narrower than the H-H stretching band at the corresponding pressures, and (2) The frequency ratio $\gamma_i (=\nu_D/\nu_H)$ increases gradually with increasing pressure in both fluid and solid phases.

The half-width (ω) of the $\nu_D[Q_1(2)]$ vibrational band in the fluid before freezing is only 8 cm^{-1}, compared with the half-width of 15 cm^{-1} observed for the $\nu_H[Q_1(1)]$ band. The half-width of this band in the solid deuterium is also smaller than the half-width of the ν_H band at the corresponding pressure. It appears that the heavy mass of the deuterium nuclei is probably responsible for the observed narrow width of the D-D stretching mode.

In the fluid phase of n-D_2 and n-H_2 ($8 \leq P \leq 51$ kbar) the average value of the ratio γ_i is 0.7190. In the solid state the average value of γ_i in the pressure range 58–528 kbar is estimated to be 0.7199. The average values of γ_i for high-pressure fluid and solid hydrogen isotopes increase by about 0.014% and 0.139%, respectively, with $\gamma_i = 0.7189$ at 1 bar.

More-exact data on the variation of the frequencies of H-H and D-D stretch bands with pressure will require higher spectral resolution; it is certain, however, that the ratio γ_i increases with increasing pressures. These changes in the value of γ_i are small but are significant because they imply either (1) a difference in the force constants of deuterium and hydrogen molecules or (2) a small difference in the compressibility of n-D_2 and n-H_2, or both.

Some very accurate measurements on the vibration-rotation spectra of $H^{35}Cl$ and $D^{35}Cl$ showed that the molecular force constants are invariant to

isotopic substitution (Rank *et al.*, 1962; Jones, 1971). The observed increase in the value of γ_i at very high pressures implies the likelihood of interaction of nuclear and electronic motion in solid deuterium and hydrogen. One possible interpretation based on the observations is that H_2 will change to the atomic (metallic) state at a lower pressure than D_2.

References

Allin, E. J., A. D. May, B. P. Stoicheff, J. C. Stryland, and H. L. Welsh, Spectroscopy research at the McLennan Physical Laboratories of the University of Toronto, *Appl. Optics, 6,* 1597–1608, 1967.

Besson, J. M., and J. P. Pinceaux, Melting of helium at room temperature and high pressure, *Science, 206,* 1073–1075, 1979.

Bhatnagar, S. S., E. J. Allin, and H. L. Welsh, The Raman spectra of liquid and solid H_2, D_2 and HD at high resolution, *Can. J. Chem., 40,* 9–23, 1962.

England, W., J. C. Raich, and R. D. Etters, Rotational motion under pressure in the solid molecular hydrogen, *J. Low Temp. Phys., 22,* 213–222, 1976.

Jammu, K. S., G. E. St. John, and H. L. Welsh, Pressure broadening of the rotational Raman lines of some simple gases, *Can. J. Phys., 44,* 797–814, 1960.

Jones, L. H., *Inorganic Vibrational Spectroscopy,* Vol. 1, Marcel Dekker, Inc., New York, pp. 50–51, 1971.

Mao, H. K., and P. M. Bell, Observations of hydrogen at room temperature (25 °C) and high pressure (to 500 kbar), *Science, 203,* 1004–1006, 1979.

Mao, H. K., P. M. Bell, J. W. Shaner, and D. J. Steinberg, Specific volume measurements of Cu, Mo, Pd and Ag and calibration of the ruby R_1 fluorescence gauge from 0.06 to 1 Mbar, *J. Appl. Phys., 49,* 3276–3283, 1978.

May, A. D., V. Degen, J. C. Stryland, and H. L. Welsh, The Raman effect in gaseous hydrogen at high pressures, *Can. J. Phys., 39,* 1769–1783, 1961.

Rank, D. H., D. P. Eastman, B. S. Rao, and T. A. Wiggins, Rotational and vibrational constants of the $H^{35}Cl$ and $D^{35}Cl$ molecules, *J. Opt. Soc. Amer., 52,* 1–7, 1962.

Sharma, S. K., H. K. Mao, and P. M. Bell, Raman measurements of hydrogen in the pressure range 0.2–630 kbar at room temperature, *Phys. Rev. Lett., 44,* 886–888, 1980.

Stoicheff, B. P., High resolution Raman spectroscopy of gases. IX. Spectra of H_2, HD and D_2, *Can. J. Phys., 35,* 730–741, 1957.

Van Kranendonk, J., Rotational and vibrational energy bands in solid hydrogen, *Physica, 25,* 1080–1094, 1959.

Vu, H., M. Jean-Louis, M. M. Thiery, D. Fabre, S. Avriller, and P. Khatibi, Infrared and Raman spectra of simple molecular solids up to 15 kbar at 4.2 K, in *Proceedings of the Fourth International Conference on High Pressure,* J. Osugi, ed., The Physico-chemical Society of Japan, Kyoto, pp. 348–353, 1975.

Weber, A., High resolution Raman studies of gases, in *The Raman Effect,* Vol. 2, A. Anderson, ed., Marcel Dekker, Inc., New York, pp. 543–757, 1973.

Wijngaarden, R. J., and I. F. Silvera, Raman spectrum of solid orthodeuterium to 150 kbar at 5 K, *Phys. Rev. Lett., 44,* 456–459, 1980.

Whalley, E., High-pressure Raman spectroscopy, in *Proceedings of the Fourth International Conference on High Pressure,* J. Osugi, ed., The Physico-chemical Society of Japan, Kyoto, pp. 37–43, 1975.

SPECTRAL MINERALOGY

Crystal Structure of Forsterite at 40 kbar

R. M. Hazen and L. W. Finger

The magnesian olivine, forsterite (Mg_2SiO_4), is a major component of rocks of the crust and upper mantle. As such, its physical properties and crystal structure as a function of temperature and pressure are of great interest. The first high-pressure crystal structure of any rock-forming silicate was determined on this mineral by Hazen (1976). Substantial changes in high-pressure x-ray diffraction techniques in the past several years have led to an improvement in the quality and analysis of these data. The crystal structure of forsterite at high pressure has thus been redetermined to test the validity of the original structure refinement of Hazen (1976) and to demonstrate the improvement in crystallographic procedures since that study.

The synthetic forsterite specimen, from the Crystal Products Division of Union Carbide Corporation, was the same as that employed in the previous investigation. A single crystal approximately 100 × 100 × 50 μm was mounted in a diamond-anvil x-ray cell (Merrill and Bassett, 1974) as modified by Hazen and Finger (*Year Book 76,* 655–656). A chip of ruby 10 μm in diameter was included in the mount for pressure calibration, and a 4:1 mixture of methanol:ethanol was employed as the hydrostatic pressure medium. Intensity data were collected on an automated four-circle diffractometer (Finger *et al., Year Book 72,* 694–699). All accessible reflections ($\sin\theta/\lambda < 0.7$) were collected, and measured intensities were corrected for specimen and pressure-cell absorption. A total of 473 reflections were observed ($I > 2\sigma_I$), yielding 104 symmetrically distinct *hkl*'s after data averaging. These data were refined with a model that employed isotropic temperature factors and an extinction coefficient. Weighted R of the converged refinement was 2.8% (4.4% unweighted). Refined structural parameters and unit-cell parameters for this 40-kbar forsterite determination, as well as the room-pressure and 40-kbar refinements of Hazen (1976) are recorded in Table 29. Selected interatomic distances and angles appear in Table 30 for these three structure determinations.

Comparison of forsterite refinements at 40 kbar from Hazen (1976) and this study demonstrates the improvement in high-pressure techniques in recent years. The weighted R has been reduced from 7.3% to 2.8% (9.6% to 4.4% unweighted), and the errors asso-

TABLE 29. Forsterite Positional Parameter, Isotropic Temperature Factors, Extinction Correction, and Unit-Cell Dimensions at 1 bar and 40 kbar

Unit-Cell Dimension	Site	Parameter	Hazen (1976)		This Study
			1 bar	40 kbar	40 kbar
a, Å			4.7535(4)	4.734(5)	4.7325(4)
b, Å			10.1943(5)	10.02(10)	10.1036(23)
c, Å			5.9807(4)	5.940(6)	5.9387(3)
V, Å^3			289.80(5)	281.8(5)	283.96(7)
	M1	*B*	0.26(1)	0.37(9)	0.54(8)
	M2	*x*	0.9915(2)	0.991(1)	0.9907(8)
		y	0.2774(1)	0.280(1)	0.2775(9)
		B	0.22(1)	0.52(10)	0.54(8)
	Si	*x*	0.4262(1)	0.426(1)	0.4264(6)
		y	0.0940(1)	0.093(1)	0.0940(8)
		B	0.08(1)	0.45(7)	0.44(8)
	O1	*x*	0.7657(3)	0.768(2)	0.7690(13)
		y	0.0913(2)	0.097(2)	0.0909(20)
		B	0.26(2)	0.1(2)	0.51(16)
	O2	*x*	0.2215(4)	0.220(2)	0.2200(14)
		y	0.4474(2)	0.444(2)	0.4447(18)
		B	0.24(2)	0.0(2)	0.63(15)
	O3	*x*	0.2777(2)	0.276(2)	0.2769(11)
		y	0.1628(1)	0.158(2)	0.1595(15)
		z	0.0331(2)	0.035(1)	0.0331(10)
		B	0.28(2)	0.4(1)	0.57(11)

TABLE 30. Forsterite Selected Interatomic Distances (Å) and Angles (°)

Parameter [Multiplicity]	Hazen (1976)		This Study
	1 bar	40 kbar	40 kbar
Silicon Tetrahedron			
Si-O1 [1]	1.615(3)	1.62(1)	1.622(7)
Si-O2 [1]	1.640(3)	1.66(2)	1.661(20)
Si-O3 [2]	1.633(2)	1.60(1)	1.612(9)
Mean Si-O	1.630	1.62	1.627
O1-Si-O2 [1]	114.1(3)	115.7(6)	113.6(10)
O1-Si-O3 [2]	115.6(2)	117.4(1.1)	116.5(5)
O2-Si-O3 [2]	102.7(2)	100.0(7)	100.9(6)
O3-Si-O3 [1]	104.6(3)	105.7(6)	106.1(8)
M1 Octahedron			
M1-O1 [2]	2.083(2)	2.08(1)	2.060(9)
M1-O2 [2]	2.074(2)	2.04(1)	2.067(6)
M1-O3 [2]	2.145(3)	2.07(2)	2.086(12)
Mean M1-O	2.101	2.06	2.071
O1-M1-O3 [2]	85.1(2)	84.5(6)	85.5(5)
O1-M1-O3 [2]	94.9(2)	95.5(6)	94.5(5)
O1-M1-O2 [2]	86.8(1)	86.7(4)	86.7(3)
O1-M1-O2 [2]	93.2(1)	93.3(4)	93.3(3)
O2-M1-O3 [2]	105.4(2)	105.2(7)	105.1(5)
O2-M1-O3 [2]	74.6(2)	74.8(7)	74.9(5)
M2 Octahedron			
M2-O1 [1]	2.166(3)	2.14(2)	2.157(20)
M2-O2 [1]	2.045(5)	2.04(2)	2.008(17)
M2-O3 [2]	2.208(4)	2.19(1)	2.217(11)
M2-O3 [2]	2.064(4)	2.08(1)	2.063(7)
Mean M2-O	2.126	2.12	2.121
O1-M2-O3 [2]	90.3(1)	90.9(6)	91.8(5)
O1-M2-O3 [2]	81.7(1)	80.2(6)	80.1(5)
O2-M2-O3 [2]	96.7(2)	96.2(6)	97.0(4)
O2-M2-O3 [2]	90.8(1)	91.6(7)	90.3(5)
O3-M2-O3 [1]	71.9(2)	70.1(6)	71.1(5)
O3-M2-O3 [2]	88.3(1)	89.6(4)	89.5(3)
O3-M2-O3 [1]	110.7(2)	109.9(6)	109.2(5)

ciated with structural parameters and interatomic distances and angles are also much lower. Among the modifications that have contributed to the increased precision are new procedures for crystal mounting, crystal centering, data collection, and absorption corrections (Finger and King, 1978; King and Finger, 1979). In addition, an extinction correction in the refinement of gem-quality crystals, not included in the 1976 study, is now recognized as obligatory.

In spite of the improved precision, the two 40-kbar structure refinements are in agreement. All unit-cell and refined structural parameters of the two high-pressure determinations match within two estimated standard deviations. Unit-cell dimensions of the present investigation are, however, an order of magnitude more precise than those of 1976, owing to the reflection-centering procedures of King and Finger (1979). Average axial compressibilities from 1 bar to 40 kbar are

1.10 ± 0.02, 2.22 ± 0.05, and $1.76 \pm 0.02 \times 10^{-4}$ kbar^{-1} for the *a*, *b*, and *c* axes, respectively. The axial compression ratios are $\Delta a/a:\Delta b/b:\Delta c/c = 1.000:2.018:1.600$, which are consistent with, but more precise than, those of the 1976 report.

Calculated bond distances and angles of the two 40-kbar refinements are also in agreement within two estimated standard deviations. As concluded in the earlier study, the silicon tetrahedron does not change significantly in size between 1 bar and 40 kbar. The tetrahedral bulk modulus, calculated from mean Si-O distances at 1 bar and 40 kbar, is greater than 3.0 Mbar. In the 1976 study, both M1 and M2 magnesium octahedral sites were observed to compress between 1 bar and 40 kbar, but the magnitude of bond-distance errors at 40 kbar did not result in a meaningful interpretation of the bond compressibilities. Within experimental error, both M1 and M2 were interpreted to have compressed the same amount. The redetermination of the 40-kbar structure is sufficiently more precise to demonstrate a difference in M1 and M2 compression. The mean M1-O distance decreases from 2.101 ± 0.003 to 2.071 ± 0.009 Å between 1 bar and 40 kbar; the calculated polyhedral bulk modulus of M1 is 1.0 ± 0.3 Mbar. The mean M2-O has a much smaller decrease, from 2.126 ± 0.004 to 2.120 ± 0.012 Å, over the same pressure range. The calculated bulk modulus of M2 is thus greater than 1.4 Mbar, and mean M2-O bond compression is significantly less than mean M1-O compression.

In summary, the conclusions of Hazen (1976) regarding the high-pressure structure response of forsterite are generally valid—the silicon tetrahedron compresses little, if at all, whereas Mg-O compression accounts for most of the structural changes in this olivine. The enhanced precision of current procedures, however, leads to the additional conclusion that M1 is significantly more compressible than M2.

References

Finger, L. W., and H. E. King, A revised method of operation of the single-crystal diamond cell and the refinement of the structure of NaCl at 32 kbar, *Amer. Mineral., 63,* 337–342, 1978.

Hazen, R. M., Effects of temperature and pressure on the crystal structure of forsterite, *Amer. Mineral., 61,* 1280–1293, 1976.

King, H. E., and L. W. Finger, Diffracted beam crystal centering and its applications to high-pressure crystallography, *J. Appl. Crystallogr., 12,* 374–378, 1979.

Merrill, L., and W. A. Bassett, Miniature diamond anvil pressure cell for x-ray diffraction studies, *Rev. Sci. Instrum., 45,* 290–294, 1974.

Raman Evidence for a New High-Pressure, Room-Temperature Polymorph of TiO_2

J. F. Mammone and S. K. Sharma*

Studies of phase transformations in rutile provide information on the possible phase transitions of stishovite, which may be an important component in the lower mantle. When rutile (TiO_2) was shock-loaded, a large volume discontinuity was observed at about 330 kbar, and the sample when recovered was found to be irreversibly transformed to the orthorhombic α-PbO_2 structure (McQueen *et al.*, 1967). The orthorhombic phase, TiO_2-II, is not believed to be the dense phase observed in the shock experiments because it is only 2.8% denser than rutile and, therefore, its presence would not account for the observed large volume discontinuity. Another modification of TiO_2 was observed by Liu (1978) in a diamond-anvil cell at 250 kbar in which the sample had been heated by a CW YAG laser. This new phase was not quenchable and also reverted to the

*Work carried out under a cooperative predoctoral fellowship program between the Geophysical Laboratory and the University of California, Los Angeles.

αPbO_2 form on release of pressure. Its structure could not be identified, but it may be the same dense phase observed in shock-wave experiments. In an attempt to characterize the high-pressure phase of TiO_2 the Raman spectra of TiO_2-II at extremely high pressures were measured.

The starting material was TiO_2-II synthesized from commercial anatase powder (Fisher Scientific Company) in a solid-media, high-pressure apparatus (Boyd and England, 1960). The anatase was sealed in a platinum capsule, held at a pressure of 40 kbar and a temperature of 400°C for three days, and then quenched under pressure. The structure of the synthetic TiO_2-II was verified by powder x-ray diffraction and contained a minor amount of rutile (~10%). The experimental details for measurement of Raman spectra at high pressures have been described elsewhere (Sharma, *Year Book 78,* 660–665). The pressure-transmitting medium was ice-VII.

The Raman spectra of TiO_2-II at several pressures are shown in Fig. 55,

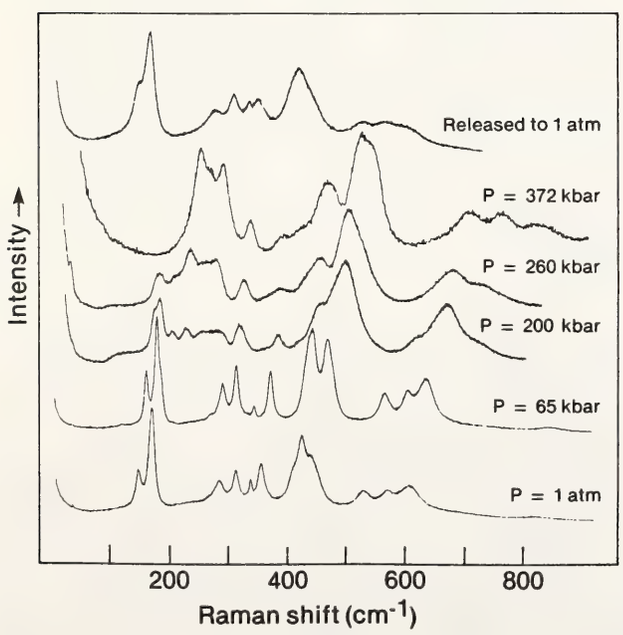


Fig. 55. Raman spectra of TiO_2-II at room temperature and various pressures (spectral slit width ~5 cm^{-1}).

and the frequencies are listed in Table 31. It is evident from the disappearance at extremely high pressures of the strongest band in TiO_2-II (172 cm^{-1} at 1 atm) that a phase change occurs. As the intensity of the 172 cm^{-1} band in TiO_2-II decreases with pressure, the intensity of a band envelope appearing in the 200–300 cm^{-1} region and assigned to the new phase, TiO_2-III, increases. This envelope contains at least three bands observed at 255, 269, and 294 cm^{-1} at 372 kbar. The band at 608 cm^{-1} in the spectrum at 1 atm is attributed to the minor amount of rutile present in the starting material, but upon application and release of pressure, this band disappears, reflecting the transformation of rutile to TiO_2-II (Fig. 55). The transformation is sluggish and occurs over a wide pressure range (Fig. 55). On release of pressure the sample completely reverts back to TiO_2-II. This result is consistent with the observations of McQueen *et al.* (1967) on shocked samples and those of Liu (1978) in a powder x-ray diffraction experiment at high pressure.

The major differences between the TiO_2-II and the TiO_2-III spectra involve low-frequency components. These observations suggest that the principal differences between TiO_2-II and TiO_2-III are secondary coordination and long-range structure and that primary Ti-O coordination is only slightly changed. Liu (1978) hypothesized that the high-pressure phase he observed may be related to the fluorite structure (Ti in 8-fold coordination), although there is no evidence supporting this view. The high-pressure phase observed in the present work is possibly the same phase observed by Liu (1978) and McQueen *et al.* (1967). *In situ,* powder x-ray diffraction experiments at high pressure are currently being performed to see if the new phase identified in the present work is the same as the one synthesized at high temperature and pressure by Liu (1978).

TABLE 31. Frequencies (cm^{-1}) of Raman Bands of TiO_2-II at Various Pressures and Room Temperature*

0.001 kbar	65 kbar	200 kbar	260 kbar	372 kbar	Pressure released
	128 w, bd	125 w, bd	111 w, bd		
150 s	163	178 sh			152 sh
172 vs	182 vs	186 s	187 m		171 vs
		206 w	212 m		
		229 w	239 m	255 s	
		258 w	265 m	269 s	
		284 w	283 m	294 s	
285 m	292 m				282 m
315 s	315 s	320 m	329 m	339 m	312 s
339 m	345 m				338 m
356 s	373 s	386 m	390 m	397 m	354 m
412 sh	437 sh	428 sh		432 sh	
426 vs	445 vs	455 sh	458 s	472 s	423 s
442 sh	469 s	500 vs	506 vs	528 vs	451 sh
				552 sh	
531 m	586 m	624 m			533 m
572 m	605 m				575 m
608 m	635 m	672 s	681 m	711 m	
			731 w	765 m	
				826 m	
819 w, bd	846 w, bd				

* Intensity estimates: vs, very strong; s, strong; m, medium; w, weak; sh, shoulder; bd, broad.

References

Boyd, F. R., and J. L. England, Apparatus for phase equilibrium measurements at pressures up to 50 kilobars and temperatures up to 1750°C, *J. Geophys. Res., 65,* 741–748, 1960.

Liu, L.-G., A fluorite isotype of SnO_2 and a new modification of TiO_2: implications for the earth's lower mantle, *Science, 199,* 422–425, 1978.

McQueen, R. G., J. C. Jamieson, and S. P. Marsh, Shock-wave compression and x-ray studies of titanium dioxide, *Science, 155,* 1401–1404, 1967.

Pressure and Temperature Dependence of the Raman Spectra of Rutile-Structure Oxides

J. F. Mammone and S. K. Sharma*

The synthesis of stishovite has stimulated much interest in the high-pressure behavior of rutile-type oxides. Rutile (TiO_2) itself has been studied particularly for its interesting dielectric, elastic, and optical properties. The effect of pressure on the Raman spectrum of TiO_2 has especially been the subject of considerable study (Nicol and Fong, 1971; Samara and Peercy, 1973; Mammone *et al.*, 1980). An effect of high pressure on both of these phases is the anomalous pressure dependence of the frequency of the B_{1_g} mode, in that it decreases with increasing pressure. In TiO_2 the interactions between the normal modes of vibration, which occur through the anharmonic terms in the lattice potential, play an important role in the lattice dynamics of the crystal. Raman scattering at high hydrostatic pressures is a useful tool to study the anharmonic effects as a function of relatively large volume changes. Coupled with Raman measurements at ambient pressure

*Work carried out under a cooperative predoctoral fellowship program between the Geophysical Laboratory and the University of California, Los Angeles.

and various temperatures, anharmonic self-energy contributions to the isobaric temperature dependence of the vibrational frequencies can be separated. These data provide a fundamental test of lattice-dynamical theories because it is difficult to model both the phonon dispersion and the mode Gruneisen parameters without a realistic description of both long- and short-range crystal forces. Thus, in an attempt to determine the magnitude and origin of the anharmonicity and to understand the effect of pressure and temperature on rutile-type oxides, the Raman spectra of TiO_2, GeO_2, and SnO_2 as a function of temperature and pressure have been studied.

Experimental

Synthetic TiO_2 crystals were obtained from the U.S. National Museum (USNM No. 136751). Ultra-pure SnO_2 powder was obtained from Alfa Products (Danvers, Massachusetts). Tetragonal GeO_2 was prepared from ultrapure hexagonal GeO_2 (Alfa Products) in a solid-media, high-pressure apparatus (Boyd and England, 1960). Hexagonal GeO_2 was sealed in a platinum capsule, held at a pressure of 15 kbar and a temperature of 1000 °C for 2 hr, and then quenched under pressure.

Experimental details for the measurement of Raman spectra at high pressures in the diamond-anvil cell have been described elsewhere (Sharma, *Year Book 78*, 660–665). Spectra at high temperatures were obtained from samples heated in a water-cooled resistance furnace equipped with entrance and exit ports for the exciting and scattered radiation, respectively. Temperatures in the furnace were recorded with a $Pt\text{-}Pt_{90}Rh_{10}$ thermocouple.

Results

The rutile structure is tetragonal with two molecules per unit cell and the space group D_{4h}^{14} ($P4/mnm$) (Wyckoff, 1963). The Raman-active modes, which have symmetries A_{1g}, B_{1g}, B_{2g}, and E_g, were studied in the present experiment.

The pressure dependence of the Raman spectra of TiO_2 to 89 kbar has been reported (Mammone and Sharma, *Year Book 78*, 636–640). In SnO_2 the pressure dependencies of the modes with symmetry A_{1g}, B_{2g}, and E_g were measured to 43 kbar. (The B_{1g} mode was too weak to be observed.) These three modes all behave normally in that they increase in frequency with increasing pressure. The slopes, however, are not in agreement with those obtained by Peercy and Morosin (1973), who studied the Raman spectrum of SnO_2 to only 4 kbar. Because of the greater range of pressure covered in the present experiment, one can calculate more reliable values for $(\partial\nu/\partial P)_T$. Typical Raman spectra for GeO_2 at 1 atm and high pressure are shown in Fig. 56. The frequencies of the A_{1g} and B_{2g} modes increase as a function of pressure, whereas the B_{1g} mode has a negative pressure dependence.

The temperature dependence of the frequencies of the A_{1g}, B_{1g}, and E_g modes in TiO_2 to 777 K have been plotted in Fig. 57. Results for the B_{1g} mode are consistent with measurements by Samara and Peercy (1973), who studied TiO_2 to 480 K. Their results do not agree with these data for $(\partial\nu/\partial T)_P$ and the A_{1g} mode, although the magnitude of the slope is relatively small so that only a small error is introduced in the subsequent calculations. The temperature dependence of the frequency of the E_g mode in TiO_2 is nonlinear and has a significant second derivative at 300 K that introduces a large error in any measurement of the slope. Thus, calculations for the E_g mode contain rela-

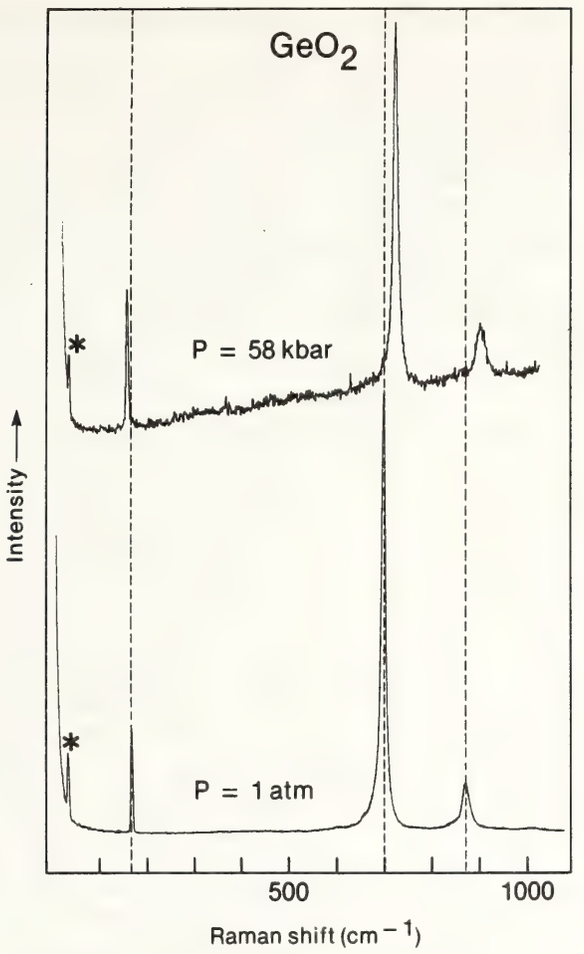


Fig. 56. Raman spectra of GeO_2 at 1 atm and under pressure. (Asterisk refers to plasma line.)

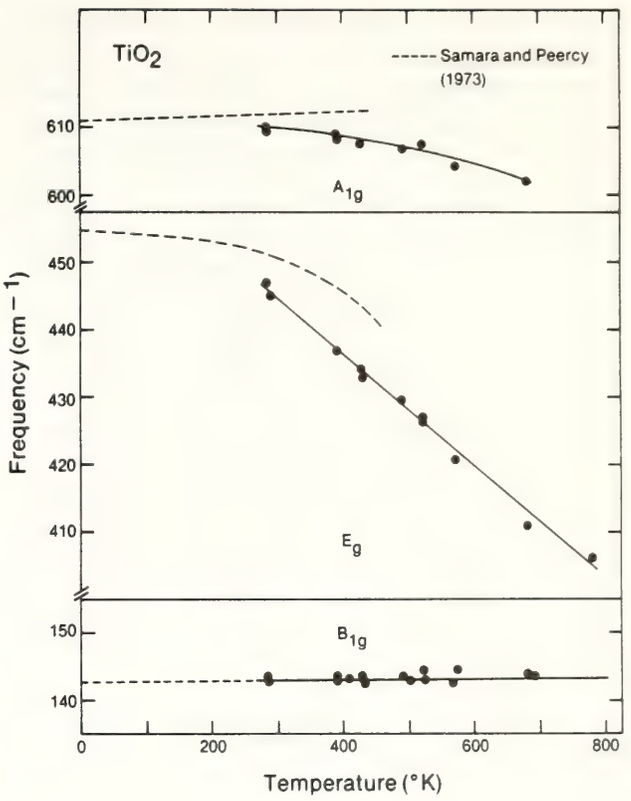


Fig. 57. Temperature dependence of the frequencies of the Raman-active modes in TiO_2, with symmetries A_{1g}, B_{1g}, and E_g.

tively large uncertainties. The data of Samara and Peercy (1973) for this mode are displaced about 3 cm^{-1} to higher frequencies relative to the data presented in this report and those of Porto *et al.* (1967), but the displacement does not affect the calculation of the slope. The temperature dependences of the frequencies of the A_{1_g}, B_{1_g}, and B_{2_g} modes in GeO_2 were measured to 1055 K with the frequency of the A_{1_g} and B_{2_g} modes decreasing and that of the B_{1_g} mode increasing with increasing temperature.

Discussion

If the phonon frequency is treated as a function of volume and temperature, then it is found with exact differentials (Peercy and Morosin, 1973) that

$$\left(\frac{\partial \ln \omega_i}{\partial T}\right)_P = \left(\frac{\partial \ln V}{\partial T}\right)_P \left(\frac{\partial \ln \omega_i}{\partial \ln V}\right)_T + \left(\frac{\partial \ln \omega_i}{\partial T}\right)_V \quad (1)$$

$$= -\beta K_T \left(\frac{\partial \ln \omega_i}{\partial P}\right)_T + \left(\frac{\partial \ln \omega_i}{\partial T}\right)_{V'} \quad (2)$$

where β refers to the volume thermal expansion coefficient $(\partial \ln V/\partial T)_P$, and K_T refers to the isothermal bulk modulus $(\partial P/\partial \ln V)_T$. Values of K_T and β for these compounds have been summarized in Table 32. The term on the left-hand side of Equation 2 and the first term on the right-hand side can be calculated from experimental data. The second term on the right-hand side may not be obtained directly from experiment, because the volume varies with temperature and is therefore calculated using Equation 2. Anharmonic contributions to the temperature-dependent phonon frequencies have been discussed in very complex calculations by Maradudin and Fein (1962) and

TABLE 32. Thermal Expansion and Bulk Modulus Data for Rutile-Structure Oxides

	$\beta(10^{-5}\,K^{-1})$	K_0, Mbar	K'_0
TiO_2	2.35 (ref. 1)*	2.2 (ref. 2)	6.84 (ref. 3)
GeO_2	2.027 (ref. 4)	2.65 (ref. 5)	6.16 (ref. 6)
SnO_2	1.17 (ref. 7)	2.03 (ref. 5)	
SiO_2		2.88 (ref. 8)	

*References: (1) Samara and Peercy, 1973; (2) Hazen and Finger, 1980; (3) Manghnani, 1969; (4) Rao *et al.*, 1968; (5) Liebermann, 1973; (6) Wang and Simmons, 1973; (7) Peercy and Morosin, 1973; (8) Olinger, 1976.

Cowley (1963). A qualitative evaluation of their origin has been made by Peercy and Morosin (1973). It has been shown that the first term on the right-hand side of Equation 2 represents the frequency shift due to thermal expansion (pure volume) and the second term represents multiphonon contributions due to cubic and quartic anharmonicities (pure temperature).

The data have been summarized and presented in Table 33. In GeO_2 and SnO_2, self-energy shifts are dominated by the pure-volume term due to thermal expansion. In TiO_2, the temperature dependence results about equally from thermal expansion and the pure-temperature term owing to higher order anharmonicities. In TiO_2, scattering due to multiphonon processes is even more intense than some first-order processes, whereas in GeO_2 and SnO_2 no scattering other than first order was observed. This observation is due to large anharmonicities present in the bonding in TiO_6 octahedra. In $SrTiO_3$, where Ti is also octahedrally coordinated, the multiphonon spectrum is also very strong (Nilsen and Skinner, 1969). The strong Raman spectrum from TiO_6 polyhedra is due to the unusual anisotropic polarizability of the oxide ion that arises from hybridization of the oxygen *p* states with the *d* states of the Ti ion (Migoni *et al.*, 1976). This interpretation can be contrasted to the *p*-electron bonding that is present in GeO_2 giving rise to much smaller anharmonicities. Little anharmonicity

TABLE 33. Logarithmic Pressure and Temperature Derivatives of the Frequencies of the Raman-Active Phonons for TiO_2, GeO_2, and SnO_2, and the Separation of the Isobaric Temperature Derivatives into Pure-Volume and Pure-Temperature Contributions at 298 K

Modes	ν, cm^{-1}	$\left(\frac{\partial \ln\omega_i}{\partial T}\right)_P = -\beta K_T\left(\frac{\partial \ln\omega_i}{\partial P}\right)_T + \left(\frac{\partial \ln\omega_i}{\partial T}\right)_V$				
TiO_2						
B_{1g}	143	0.4*	=	12.3	−	11.9
E_g	447	−13	=	−4.9	−	8.1
A_{1g}	612	−1.8	=	−3.0	+	1.2
B_{2g}	826	3	=	−4	+	7
GeO_2						
B_{1g}	170	2.6	=	5.7	−	3.1
A_{1g}	700	−3.1	=	−2.9	−	0.2
B_{2g}	873	−3.0	=	−2.7	−	0.3
SnO_2						
E_g	473	−1.8†	=	−1.7	−	0.1
A_{1g}	633	−4.3†	=	−2.0	−	2.3
B_{2g}	775	−4.4†	=	−1.7	−	2.7

*In units of $10^{-5}\,K^{-1}$.
†Peercy and Morosin, 1973.

would therefore be expected in stishovite.

Hazen and Finger (1980) have noted that TiO_2 does not conform to the inverse structural relationship, in that c/a increases with both increasing temperature and increasing pressure. GeO_2 exhibits normal behavior such that c/a increases with increasing pressure (Hazen and Finger, 1980) and decreases with increasing temperature (Rao *et al.*, 1968). The unusual expansion along the c axis in TiO_2 with increasing temperature is reflected by the large negative temperature dependence of the frequency of the E_g mode (Fig. 57; Table 33), which corresponds to vibrations of the oxygen ions parallel to the c axis. This self-energy shift is composed of significant contributions due to thermal expansion and higher-order anharmonicities (Table 33).

The B_{1_g} mode in these compounds exhibited anomalous temperature and pressure dependencies in that its frequency increased with temperature and decreased with pressure. From the softening of this mode with pressure, Nagel and O'Keeffe (1971) suggested that the high-pressure phase of TiO_2 has a $CaCl_2$-type structure. This idea seems logical because the atomic displacements associated with the B_{1_g} mode can lead to a transition to a $CaCl_2$-type structure as $\nu(B_{1_g}) \rightarrow 0$. No TiO_2, GeO_2, or SnO_2 polymorph with such a structure has been observed, and in SnO_2 and TiO_2 at high pressures a transition to the α-PbO_2 structure takes place (Liu, 1974; Mammone *et al.*, 1980). In addition, a study of the uniaxial-stress dependence of the first-order Raman spectrum of TiO_2 showed that there was no coupling between the B_{1_g} and A_{1_g} modes that would be indicative of a phase transition from rutile to $CaCl_2$-type structure (Merle *et al.*, 1980). The softening of the B_{1_g} mode, which corresponds to a rotation of oxygen atoms about the C_4 axis, is due to a stress-induced change in the bond-bending force constants; this change may be a consequence of the unusually short O-O nearest-neighbor distance. This behavior of the B_{1_g} mode is common to all three oxides, and it is therefore not a result of any unusual anharmonic interactions observed in TiO_2.

The difficulty in formulating an equation of state for oxides, including stishovite, lies in developing an adequate description for the potential of the oxide ion. Difluorides have been studied as analogs to stishovite (Jamieson, 1977), but their usefulness is limited to determining what structures are possible with RX_2 stoichiometry. Theoretical models that work well for halides often break down when applied to oxides. When two of the usual functional forms of the Gruneisen parameter (Dugdale-MacDonald; Slater) were used to calculate $\partial K/\partial P$ for GeO_2, the values differed by more than a factor of two when compared with experimental data (Wang and Simmons, 1973). To date, the most successful lattice dynamical model for rutile (TiO_2) was described by Traylor *et al.* (1971), who used a shell model to account for the polarizability of the oxygen ion. The case of stishovite is further complicated by preliminary data (Nicol *et al.*, 1980) suggesting that the structure of stishovite, while still containing silicon in 6-fold coordination, may not be isomorphous with rutile but can be assigned to some larger unit cell.

References

Boyd, F. R., and J. L. England, Apparatus for phase equilibrium measurements at pressures up to 50 kbar and temperatures up to 1750°C, *J. Geophys. Res.*, *65*, 741–748, 1960.

Cowley, R. A., The lattice dynamics of an anharmonic crystal, *Adv. Phys.*, *12*, 421–480, 1963.

Hazen, R. M., and L. W. Finger, Bulk moduli and high-pressure crystal structures of rutile-type compounds, *J. Phys. Chem. Solids*, in press, 1980.

Jamieson, J. C., Phase transitions in rutile-type structures, in *High Pressure Research: Applications in Geophysics*, M. H. Manghnani and

S. Akimoto, eds., Academic Press, New York, pp. 209–218, 1977.
Liebermann, R. C., Elastic properties of polycrystalline SnO_2 and GeO_2: comparison with stishovite and rutile data, *Phys. Earth Planet. Interiors, 7*, 461–465, 1973.
Liu, L.-G., Synthesis of a new high-pressure phase of tin dioxide and some geophysical implications, *Phys. Earth Planet. Interiors, 9*, 338–343, 1974.
Mammone, J. F., S. K. Sharma, and M. Nicol, Raman study of rutile (TiO_2) at high pressures, *Solid State Commun., 34*, 799–802, 1980.
Manghnani, M. H., Elastic constants of single-crystal rutile under pressures to 7.5 kilobars, *J. Geophys. Res., 74*, 4317–4328, 1969.
Maradudin, A. A., and A. E. Fein, Scattering of neutrons by an anharmonic crystal, *Phys. Rev., 128*, 2589–2608, 1962.
Merle, P., J. Pascual, J. Camassel, and H. Mathieu, Uniaxial-stress dependence of the first-order Raman spectrum of rutile. I. Experiments, *Phys. Rev. B, 21*, 1617–1626, 1980.
Migoni, R., H. Bilz, and D. Bauerle, Origin of Raman scattering and ferroelectricity in oxidic perovskites, *Phys. Rev. Lett., 37*, 1155–1158, 1976.
Nagel, L., and M. O'Keeffe, Pressure and stress induced polymorphism of compounds with the rutile structure, *Mater. Res. Bull., 6*, 1317–1320, 1971.
Nicol, M., J. M. Besson, and B. Velde, Raman spectra and the structure of stishovite, *Proceedings of the Seventh AIRPAT International High Pressure Conference, LeCreusot, France, 30 July–3 August, 1979*, Pergamon Press, Oxford, in press, 1980.
Nicol, M., and M. Y. Fong, Raman spectrum and polymorphism of titanium dioxide at high pressures, *J. Chem. Phys., 54*, 3167–3170, 1971.
Nilsen, W. G., and J. G. Skinner, Raman spectrum of strontium titanate, *J. Chem. Phys., 48*, 2240–2248, 1969.
Olinger, B., The compression of stishovite, *J. Geophys. Res., 81*, 5341–5343, 1976.
Peercy, P. S., and B. Morosin, Pressure and temperature dependencies of the Raman active phonons in SnO_2, *Phys. Rev. B, 7*, 2779–2786, 1973.
Porto, S. P. S., P. A. Fleury, and T. C. Damen, Raman spectra of TiO_2, MgF_2, ZnF_2, FeF_2, and MnF_2, *Phys. Rev., 154*, 522–536, 1967.
Rao, K. V. K., S. V. N. Naidu, and L. Iyengar, Thermal expansion of rutile-type GeO_2 by the x-ray method, *J. Amer. Ceram. Soc., 51*, 467–468, 1968.
Samara, G. A., and P. S. Peercy, Pressure and temperature dependence of the static dielectric constants and Raman spectra of TiO_2 (rutile), *Phys. Rev. B, 7*, 1131–1148, 1973.
Traylor, J. G., H. G. Smith, R. M. Nicklow, and M. K. Wilkinson, Lattice dynamics of rutile, *Phys. Rev. B, 3*, 3457–3472, 1971.
Wang, H., and G. Simmons, Elasticity of some mantle crystal structures. 2. Rutile GeO_2, *J. Geophys. Res., 78*, 1262–1273, 1973.
Wyckoff, R. W. G., *Crystal Structures*, 2d ed., John Wiley and Sons, New York, 1963.

High-Pressure Experiments on the Iron Oxide Wüstite ($Fe_{1-x}O$)

G. T. Zou, H. K. Mao, P. M. Bell, and D. Virgo

The ferrous iron oxide mineral wüstite ($Fe_{1-x}O$) plays a significant role in the mineralogy of the deep earth's mantle (see *Year Book 78*, 612–626). At 25 °C and 1 bar, wüstite is paramagnetic and crystallizes with the $B1$ (NaCl-type) structure. Below 198 K at 1 bar, however, wüstite becomes antiferromagnetic (Roth, 1960). With decreasing temperature, the structure gradually distorts from cubic symmetry by increasing elongation of the body diagonal (111). This structure is rhombohedral and has a value for c/a up to 1.2% larger than the equivalent cubic ratio, $\sqrt{6}$, at 90 K (Willis and Rooksby, 1953). Vaughan and Drickamer (1967) observed a broad magnetic absorption at large Doppler velocities in the Mössbauer spectra of wüstite that intensified slowly with pressure to 140 kbar at 25 °C. They interpreted the change as the increase of Néel temperature of the antiferromagnetic phase with increasing pressure. In the present study of wüstite to 700 kbar, a similar, major reversible phase change, possibly of the second-order type, was observed above approximately 50 kbar.

^{57}Fe-Mössbauer Data at Room Temperature (25 °C)

The sample was a synthetic $^{57}Fe_{0.947}O$ wüstite that was pressurized in the diamond-window, high-pres-

sure cell. The pressure medium was petroleum jelly. At pressures below ~50 kbar, the ^{57}Fe Mössbauer spectra are of iron oxide in a paramagnetic state, whereas at higher pressures, a broad, unresolved magnetic absorption similar to that observed by Vaughan and Drickamer (1967) appeared also in the spectra (increasingly with increasing pressure). At 180 kbar, the magnetic spectrum began to resolve into a six-peak hyperfine structure (Fig. 58). The resolution of this magnetic spectrum improved at higher pressure as the central paramagnetic peaks decreased in intensity. The spectra did not change qualitatively with further increase of pressure up to 700 kbar.

X-ray Diffraction at Room Temperature (25°C)

The x-ray diffraction lines (111) and (200), the two lines most diagnostic of rhombohedral distortions, are observed at 1 bar to have equal width. When a body diagonal (111) elongates and three others (111) contract, the (111) line in a cubic phase splits into two lines, (003) and (101), representing hexagonal symmetry. On the other hand, the cubic (200) becomes (102) of hexagonal symmetry and remains 3-fold degenerate without splitting.

Above 90 kbar, the (111) lines become broad, a result that is the first sign of splitting, whereas the (200) line remains sharp. The width of the (111) line continues to increase with pressure to 250 kbar and above, and eventually splits into two lines. The latter lines can be indexed as (003) and (101), consistent with hexagonal symmetry of the high-pressure phase. The calculated *c/a* of the hexagonal cell increases continuously to 2.603 at 389 kbar (Fig. 59), which deviates from the equivalent cubic value of 2.450 by as much as 6.2%. This distortion is much greater than the low-temperature distortion.

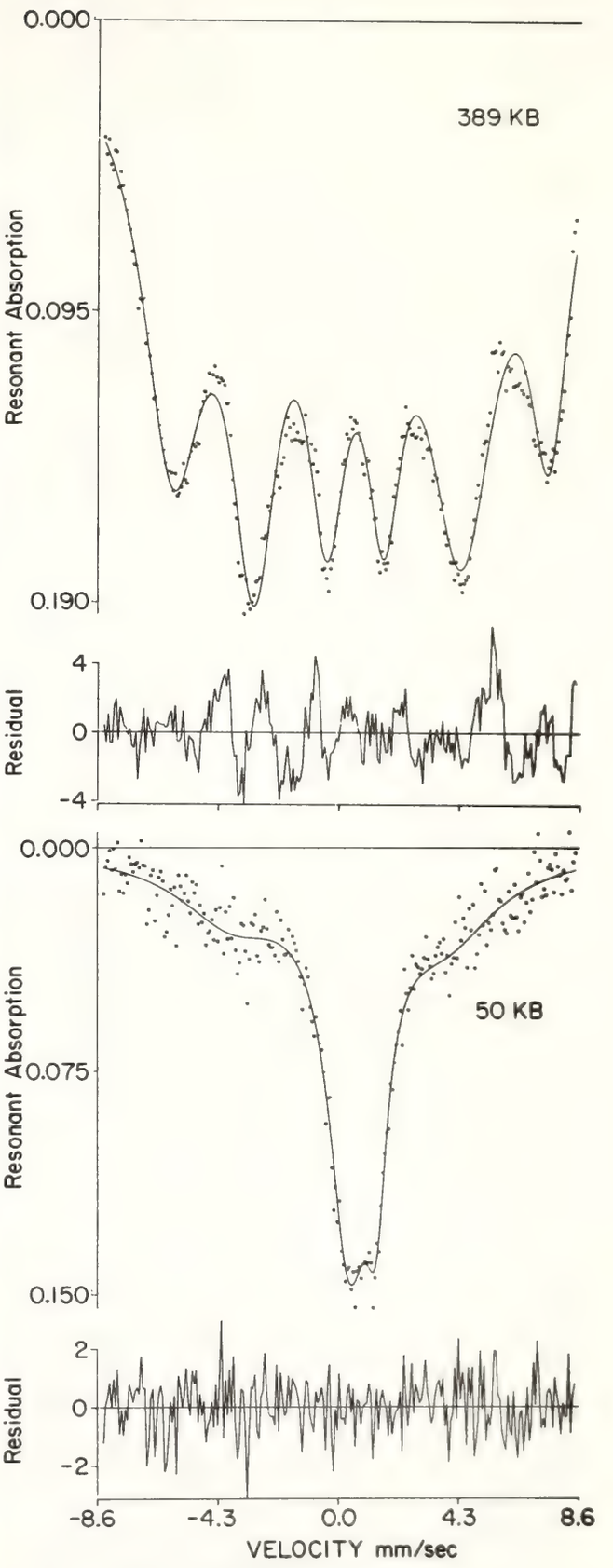


Fig. 58. ^{57}Fe-Mössbauer spectra of wüstite *in situ* at pressures of 389 kbar (upper) and 55 kbar (lower).

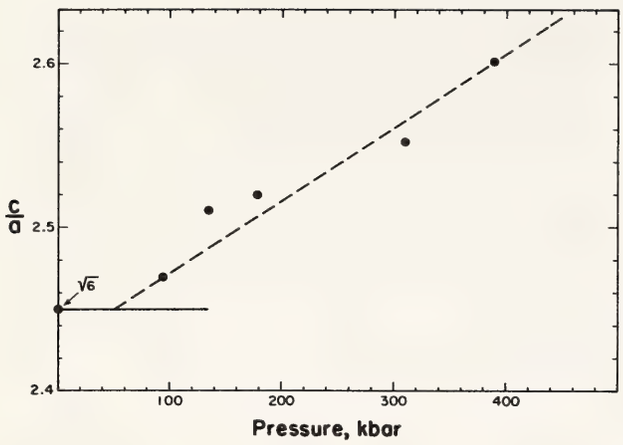


Fig. 59. The *c/a* of the hexagonal phase (distorted from cubic) of wüstite at high pressure.

Conclusion

Both ^{57}Fe-Mössbauer and x-ray diffraction data indicate the occurrence of a second-order phase transition in wüstite that occurs over a wide pressure interval. This transition is similar to one known to occur at low temperature but of greater magnitude. The transition pressure is approximately 50 kbar, but cannot be determined exactly. With increasing distortion, the volume becomes smaller than the extrapolated value of the cubic wüstite and becomes comparable with the value of a high-density phase observed in shock-wave experiments above 600 kbar (Jeanloz *et al.*, 1979; note that the shock pressure is a function of temperature). The structure of the new phase determined in the present study, however, is a rhombohedral distortion of the *B*1 cubic phase and is not the high-pressure *B*2 phase postulated by Jeanloz *et al.* (1979) from shock-wave data.

References

Jeanloz, R., T. J. Ahrens, and M. Somerville, FeO: equation of state to 2000 GPa (2 Mbar) (abstract), *Eos, 60*, 387, 1979.

Roth, W. L., Defect in the crystal and magnetic structures of ferrous oxide, *Acta Crystallogr., 13*, 140–149, 1960.

Vaughan, R. W., and H. G. Drickamer, High-pressure Mössbauer studies on α-Fe_2O_3, $FeTiO_3$ and FeO, *J. Chem. Phys., 47*, 1530–1536, 1967.

Willis, B. T., and H. P. Rooksby, Change of structure of ferrous oxide at low temperature, *Acta Crystallogr., 6*, 827–831, 1953.

Composition–Lattice Parameter Relationship of the Magnesiowüstite Solid Solution Series

Bruno Simons

Recently magnesiowüstite has been considered a major constituent phase in the earth's lower mantle (Mao and Bell, 1977). At pressures above 255 kbar, phases present in the system MgO-FeO-SiO_2 are perovskite [(Mg, Fe)SiO_3; pyroxene composition], stishovite (SiO_2), and magnesiowüstite [(Mg,Fe)O]. Iron is strongly partitioned in magnesiowüstite (Bell *et al., Year Book 78*, 618–621). The wüstite end member is known to be nonstoichiometric up to at least 60 kbar at 1200 °C (Simons and Seifert, *Year Book 78*, 625–626) and above 100 kbar at 1200 °–1600 °C (Liu, 1976). Simons and Seifert (*Year Book 78*, 625–626) considered it unlikely that stable wüstite becomes stoichiometric under any conditions of pressure and temperature. The nonstoichiometry is due to Fe^{3+} in the structure of wüstite, and Fe^{3+} (NaCl structure) might be present for any iron concentration in the magnesiowüstite structure at any pressure. Obviously the physical and chemical properties (i.e., density, compressibility, and magnetic structure) will be strongly influenced by the redox state of iron in magnesiowüstite. A careful examination of the composition of magnesiowüstite is thus of importance.

Chemical analysis of magnesiowüstite recovered from ultrahigh-pressure experiments was not possible in view of the extremely small size of the sample. An estimate of the composition can be made, however, by comparing

the lattice parameter observed at high pressures with the composition-lattice parameter relationship (CLP) obtained at 1 atm. In this study, a compilation of literature data on the CLP of wüstite and magnesiowüstite is presented and supplemented with new data. Magnesiowüstites have been synthesized and analyzed by x-ray powder diffraction and wet-chemical analysis. The data are used to discuss certain aspects of the differentiation process of the earth, as proposed by Mao *et al.* (*Year Book 78*, 621–625).

Experiments

Mixtures of MgO (Fisher M-51) and Fe_2O_3 (Fisher 1-116) have been homogenized in an agate mortar, for ½ hr under acetone, dried at 110°C for 24 hr, and fired at 1000°C for 24 hr. These samples were equilibrated in H_2/CO_2 gas mixtures at 1300°C in standard quenching furnaces under conditions where magnesiowüstites are in equilibrium with metallic iron. After each run the samples were rapidly quenched; the lower end of the furnace quench tube was cooled by liquid nitrogen.

These products have been inspected microscopically in reflected light and by x-ray powder diffraction with CuK_α radiation and with Si as an internal standard. Various samples have been chemically analyzed by methods similar to those described by Maxwell (1968).

Composition of Wüstite

Data on the CLP of wüstite have been reported by numerous authors (Fig. 60). Linear regression of these data in the range $Fe_{0.895}O$-$Fe_{0.955}O$ leads to the equation

$$a^\circ = 3.894 + 0.439X(\text{Å}), \quad r = 0.957, \qquad (1a)$$

where a° is the lattice parameter of wüstite; X, the mole fraction of Fe in wüstite; and r, the regression coefficient. When the data on high-pressure wüstite (Simons and Seifert, *Year Book 78*, 625–626) are included, the regression coefficient ($r = 0.964$) is increased.

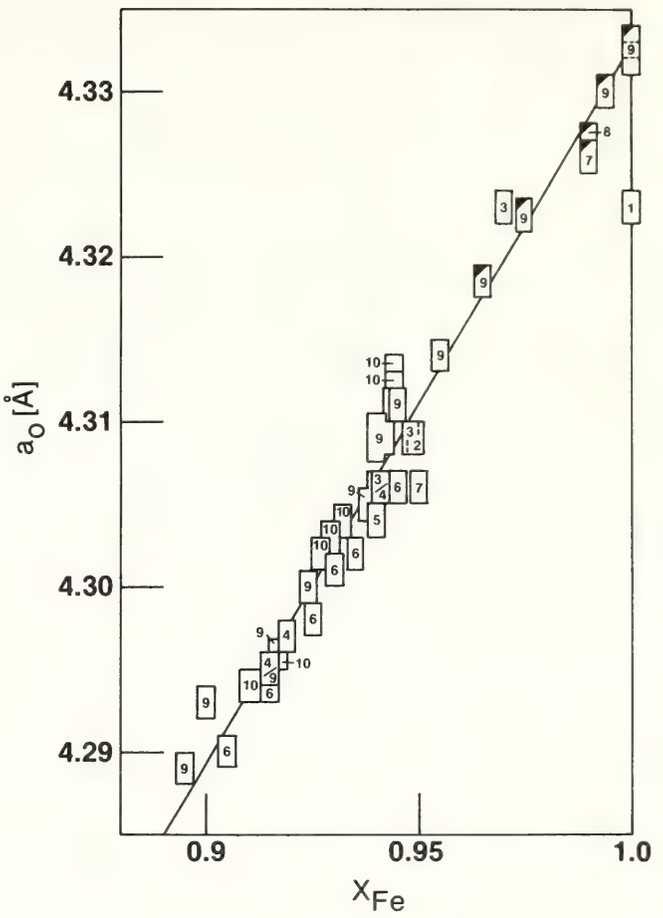


Fig. 60. Composition-lattice parameter relationship of wüstite. Size of symbol represents estimated uncertainty in composition and lattice parameter. Data shown by symbols with full triangular corners are estimates of composition by the authors cited below: 1, Katsura *et al.* (1967); 2, Rosenhauer *et al.* (*Year Book 75*, 513-515); 3, this study; 4, Shirane *et al.* (1962); 5, Roth (1960); 6, Foster and Welch (1956); 7, Greenwood and Howe (1972); 8, Hofmann (1959); 9, Hentschel (1970); 10, Jette and Foote (1933).

Hoffmann (1959), Hentschel (1970), and Greenwood and Howe (1972) reported lattice parameters of wüstites, prepared metastably below 570°C, that exceed those in the compositional range 0.875–0.955. The composition of these wüstites was estimated by the authors using their own data sets on the CLP for extrapolation in the range

of interest. Inclusion of these data in the linear regression leads to

$$a° = 3.900 + 0.433X(\text{Å}), \quad r = 0.988. \qquad (1b)$$

Equations 1a and 1b both result in a lattice parameter for stoichiometric wüstite of $a° = 4.333$ Å, which is in agreement with that reported by Hentschel (1970). The value reported by Katsura *et al.* (1967) ($a° = 4.323$ Å; $x = 1$) is too low and is not included in the linear regression, whereas the value reported by Simons and Seifert ($a° = 4.323$ Å; $x = 0.97$) (*Year Book 78*, 625–626) fits perfectly.

Composition of Magnesiowüstite

Data on the CLP have been presented by Rosenhauer *et al.* (*Year Book 75*, 513–515) and have been confirmed here (Fig. 61). Although the concentration of Fe^{3+} is very low, it is the most iron-poor [Fe/(Fe + Mg) = 0.2] of the compositions chosen for this study. Leider and Pipkorn (1968) demonstrated by Mössbauer spectroscopy of periclase (the Mg end member of the magnesiowüstite solid solution series) doped with 0.04 atomic % iron that Fe^{3+} is still present. The reported value of 15% Fe^{3+}, however, seems somewhat high and suggests that the Fe^{3+} content decreases linearly, whereas the Fe^{3+}/Fe remains unchanged. The results presented here show that the Fe^{3+} content decreases more rapidly than reported by Leider and Pipkorn. A simple equation is proposed for the present data with

$$X\text{Fe}^{3+} = a(X\text{Fe})^3,$$

where X is the mole fraction of Fe^{3+} and Fe in the magnesiowüstite solid solution series and a is a constant to which the analytical data are well fitted. The significance is that Fe^{3+}, and thus the associated vacancy concentration in the magnesiowüstite series as well, decreases rapidly with increasing Mg content, but is always nonzero for positive iron concentrations.

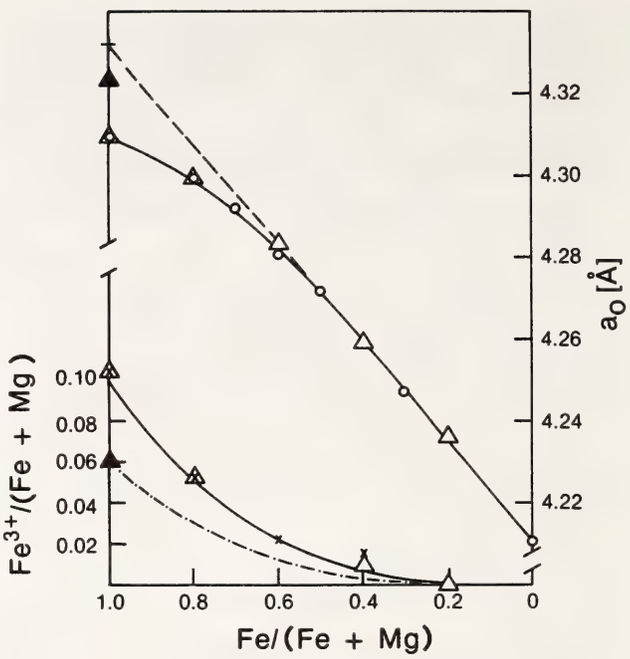


Fig. 61. Lattice parameters and composition of magnesiowüstite. Circles, after Nafziger and Muan (1967); crosses, after Rosenhauer *et al.* (*Year Book 75*, 513-515); triangles, this study; closed triangles, after Simons and Seifert (*Year Book 78*, 625-626); broken lines, estimated CLP for stoichiometric magnesiowüstite.

The minimum Fe^{3+} content for the magnesiowüstite solid solution series at high pressure is estimated (Fig. 61) on the basis of the above equation and the data on the composition of high-pressure wüstite (Simons and Seifert, *Year Book 78*, 625–626). No wüstite with a lattice constant higher than 4.323 Å has been reported at high pressures; thus the curve presented in Fig. 61 represents a lower limit for the Fe^{3+} content of the magnesiowüstite solid solution series. Note that the lattice parameter for wüstite prepared at pressures greater than 100 kbar was reported to be less than 4.323 Å (Liu, 1976).

The data on the lattice parameter reflect the exponential character of the curve for Fe^{3+} content. The most striking feature is that if the extrapolated value of 4.333 Å is taken for stoichio-

metric wüstite, Vegard's law fits the experimental values at low Fe^{3+} and high Mg contents. It might also be concluded that departure of the lattice constants of magnesiowüstite from Vegard's law is related to the Fe^{3+} concentration.

Conclusions

Wüstite, in equilibrium with metallic iron, becomes more iron rich with increasing pressure. This composition change is accompanied by a linear increase of the lattice parameter. Wüstite, nevertheless, does not become completely stoichiometric at pressures as high as 45 kbar despite the fact that the lattice constant approaches a constant value of 4.323 Å. At pressures above 100 kbar, the iron content of wüstite begins to decrease, since the reported lattice constants (Liu, 1976) are less than 4.323 Å and seem to decrease as a function of pressure. This behavior could be valid for the entire magnesiowüstite solid solution series because chemical analyses of magnesiowüstites prepared at 1 atm and 1300 °C indicate that for positive iron concentrations, XFe^{3+} is nonzero.

The data on the composition of magnesiowüstites reported here can be used to interpret an aspect of the differentiation process of the earth proposed by Mao *et al.* (*Year Book 78*, 621–625). As they outlined, for a bulk composition with $X_{Fe} \geq 0.2$ between olivine and pyroxene in the system $MgO\text{-}FeO\text{-}SiO_2$, iron will, at sufficient pressures and temperatures, be strongly partitioned to a magnesiowüstite of $X_{Fe} = 0.76$. If some arbitrary value of the constant a in Equation 3 is chosen, the Fe^{3+} content of a magnesiowüstite with $X_{Fe} = 0.76$ is given by A in Fig. 62. If, as they postulated, the magnesiowüstite is separated gravitationally, increased pressure will cause an enrichment of Fe^{3+} corresponding to the decrease of the lattice parameter with pressure (Liu, 1976). Thus the value of a in Equation 3 would increase. If, on the other hand, a new arbitrary value for a is chosen according to Equation 3, the resulting Fe^{3+} for the magnesiowüstites would be given by the upper line in Fig. 62. This result would suggest (step 1 in Fig. 62) that the Fe^{3+} content would remain unchanged, but that magnesiowüstite would lose iron. In this model, iron would move more rapidly toward the core owing to its higher density, whereas the iron-depleted magnesiowüstite could rise (step 2) and reequilibrate with the silicate layer (step 3) as proposed by Mao *et al.* (*Year Book 78*, 621–625). The process could be repeated several times (steps 1a–3a, etc.) with steady loss of iron to the core. Mao *et al.* suggested that because of the decrease in the difference in density for each cycle the process could cease. The above model for the compositional change of the magnesiowüstite, however, will be valid only if structural changes do not occur or if they affect the partitioning of iron between the oxide and the silicate only to a minor extent (see Zou *et al.*, this Report).

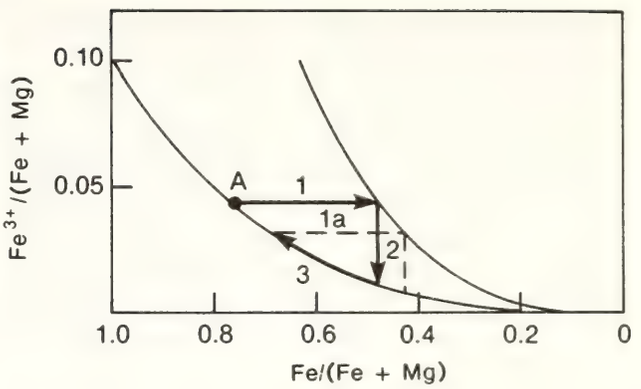


Fig. 62. Model of the change in composition of magnesiowüstite with pressure vs. depth within the earth. Lower curve, low pressure; upper curve, high pressure. Absolute values for $Fe^{3+}/(Fe + Mg)$ are arbitrary. A, 1, 2, etc., are explained in the text.

References

Foster, P. K., and A. J. E. Welch, Metal oxide solid solutions. Part I. Lattice constant and

phase relationships in ferrous oxide (wüstite) and in solid solutions of ferrous oxide and manganese oxide, *Trans. Faraday Soc., 52*, 1626–1635, 1956.

Greenwood, N. N., and A. T. Howe, Mössbauer studies of $Fe_{1-x}O$. Part II. Disproportionation between 300 and 700 K, *J. Chem. Soc. Dalton Trans.*, 116–121, 1972.

Hentschel, B., Stoichiometric FeO as metastable intermediate of the decomposition of wüstite at 225°C, *Z. Naturforsch. A, 25*, 1996–1997, 1970.

Hoffmann, A., Der Zerfallsmechanismus des Wüstits $Fe_{1-x}O$ unterhalb 570°C, *Z. Elektrochem., 63*, 207–213, 1959.

Jette, E. R., and F. Foote, An x-ray study of the wüstite (FeO) solid solutions, *J. Chem. Phys., 1*, 29–36, 1933.

Katsura, T. B., I. Iwasaki, and S. Kimura, High-pressure synthesis of the stoichiometric compound FeO, *J. Chem. Phys., 47*, 4559–4560, 1967.

Leider, H. R., and D. N. Pipkorn, Mössbauer effect in MgO:Fe^{+2}; low-temperature quadrupole splitting, *Phys. Rev., 165*, 494–500, 1968.

Liu, L., The high-pressure phases of $FeSiO_3$ with implications for Fe_2SiO_4 and FeO, *Earth Planet. Sci. Lett., 33*, 101–106, 1976.

Mao, H. K., and P. M. Bell, Disproportionation equilibrium in iron-bearing systems at pressures above 100 kbar with applications to chemistry of the earth's mantle, in *Energetics of Geological Processes*, S. K. Saxena and S. Bhattacharji, eds., Springer-Verlag, New York, pp. 236–249, 1977.

Maxwell, J. A., *Rock and Mineral Analysis*, Interscience Publishers, John Wiley and Sons, Inc., New York, 1968.

Nafziger, R. H., and A. Muan, Equilibrium phase compositions and thermodynamic properties of olivines and pyroxenes in the system MgO-"FeO"-SiO_2, *Amer. Mineral., 52*, 1364–1385, 1967.

Roth, W. L., Defects in the crystal and magnetic structures of ferrous oxide, *Acta Crystallogr., 13*, 140–149, 1960.

Shirane, G., D. E. Cox, and S. L. Ruby, Mössbauer study of isomer shift, quadrupole interaction and hyperfine field in several oxides containing Fe^{57}, *Phys. Rev., 125*, 1158–1165, 1962.

Evidence for a Localized 4*f*-Shell Breakdown in Praseodymium under Pressure

*H. K. Mao, R. M. Hazen, P. M. Bell, and J. Wittig**

At a pressure of approximately 200 kbar the rare earth metal praseodymium (Pr) undergoes a phase transition accompanied by features that are similar to those of the pressure-induced electronic transition in cerium. In the low-pressure phases, i.e. α-Ce and Pr III (the phase of Pr stable between 75 and 200 kbar), the resistance-temperature (R-T) curve characteristic is anomalous in comparison with simple metals. The temperature coefficient is extremely small between room temperature and 100 K. Below 50 K, however, the resistivity drops precipitously. In contrast, the R-T curve is not anomalous in either high-pressure phase (γ-Ce or Pr IV). Because of this similarity between Pr and Ce, it has been suggested that the Pr III–Pr IV transition may be analogous to the α-γ transition in Ce. The latter transition has been a long-standing enigma in metal physics because of the observed, but as yet unexplained, apparent shift of the level of the 4*f* electron of Ce with increasing pressure. The present study was undertaken to investigate the crystal structures and compressibilities of Pr III and Pr IV at high pressure in order to determine whether a similar volume collapse may occur at the Pr transition as in the α-γ transition in Ce.

The sample was reagent-grade praseodymium. The polycrystalline Pr sample, ruby powder, and a petroleum jelly pressure-transmitting medium were placed in the sample aperture of a full-hardened T301 stainless steel gasket and raised to high pressure in a diamond-window, high-pressure cell. Pressure was determined by observation of the calibrated shift of the R_1 fluorescent line (Mao *et al.*, 1978).

Debye-Scherrer x-ray diffraction patterns were obtained *in situ* at high pressure. No internal standard was used, but the film was corrected for camera radius and film shrinkage by comparison with standard patterns of copper, molybdenum, and silver obtained in the same experiment.

Debye-Scherrer x-ray diffraction photographs of Pr III contain as many as 20 lines with $\sin\theta/\lambda \leq 0.43$. Eight of

*Thomas B. Watson Laboratory.

these reflections, including the three most intense lines, correspond in position and intensity to the (111), (200), (220), (311), (222), and (400) reflections of a *fcc* structure with cubic axis, $a' \simeq 4.5$ Å. A well-separated doublet for the (111) reflection, as well as additional weaker lines, however, is evidence for a more complex structure closely related to *fcc* by lattice distortions.

The x-ray powder diffraction patterns were indexed for an orthorhombic phase. Unit-cell dimensions were calculated by least-squares procedures from all indexed data with the program LCLSQ (Burnham, *Year Book 61*, 132). A list of observed and calculated spacings appears in Table 34.

The Pr III orthorhombic unit cell is simply related to the *fcc* subcell: $a \approx b \approx \sqrt{2}\, a'$ and $c \approx 2\, a'$. The volume of the orthorhombic cell is four times that of the *fcc* subcell, and Z is thus assumed to be 16 atoms per unit cell. It should be noted that the crystal structure has not been refined, and fewer than 16 atoms per cell would obtain in a defect *fcc* structure. Such a vacancy-bearing structure is not likely at the high pressures of formation of Pr III, however. The relationship between the ideal *fcc* and orthorhombic Pr III is illustrated in Fig. 63. Actual atomic positions in Pr III are distorted from ideal positions, but the exact fractional coordinates could not be determined from the limited powder diffraction data.

No extinction criteria related to face- or body-centering operations obtain. The maximum possible space-group symmetry is $P2/m2/m2/m$, and site symmetry of the Pr atom is therefore reduced from $m3m$ in the ideal *fcc* structure to no greater than mmm in Pr III. If $Z = 16$, the volume per atom ranges from 24.1 to 21.5 Å^3/Pr between 144 and 212 kbar, as illustrated in Fig. 64.

Powder diffraction films of Pr IV above 210 kbar contained as many as 13 lines for which $\sin\theta/\lambda \leq 0.42$ (Table

TABLE 34. Calculated and Observed Powder Pattern for Pr III at 144 kbar*

h	k	l	d_{obs}	d_{calc}	I_{obs}, %	Equivalent *fcc* (hkl)
2	1	1	2.768	2.775	50	
2	0	2	2.663	2.664	60	111
0	2	2	2.624	2.632	100	
2	1	2	2.479	2.468	20	
2	2	0	2.282	2.288	10	200
2	1	3	2.110	2.113	20	
2	3	1	1.754	1.754	30	
1	3	3	1.698	1.695	10	
2	2	4	1.614	1.624	40	220
0	4	0		1.603		
2	3	3	1.549	1.546	40	
4	1	2	1.497	1.496	20	
2	4	0	1.442	1.439	10	
3	3	2		1.448		
2	4	2	1.374	1.374	70	311
0	4	4	1.311	1.316	30	222
2	2	6	1.278	1.276	20	
4	2	4	1.232	1.230	10	
3	4	3	1.190	1.189	10	
4	4	0	1.144	1.139	10	

*An additional line at $d = 2.87$ Å ($I = 30\%$) was not indexed.

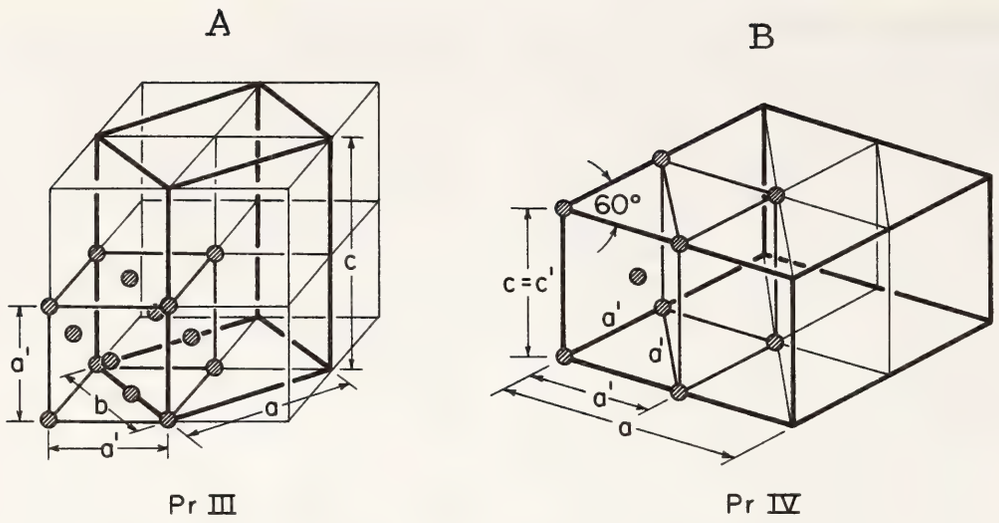


Fig. 63. (A) Relationship of orthorhombic Pr III to ideal *fcc*. (B) Relationship of hexagonal Pr IV to ideal *hcp*.

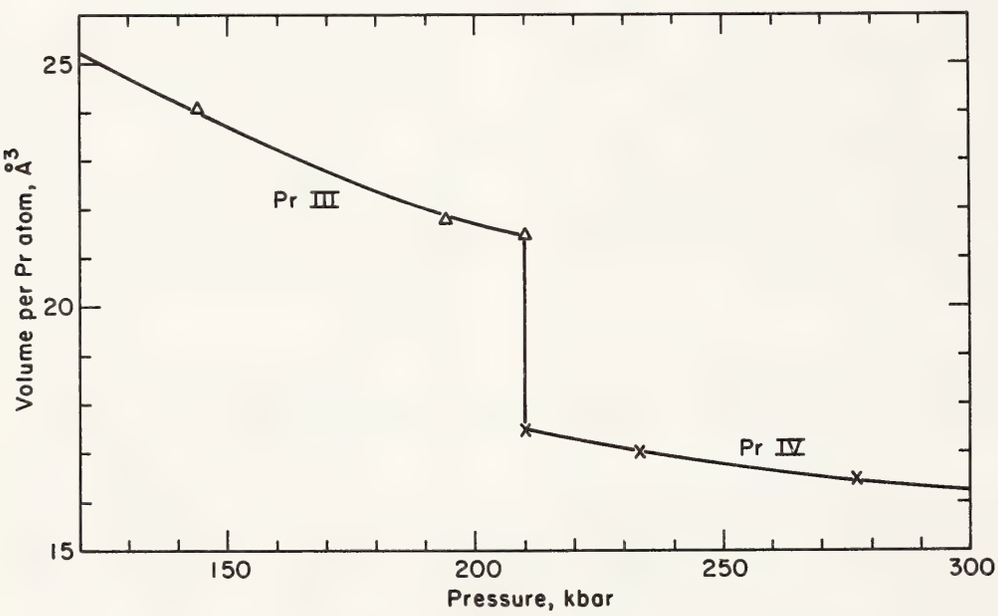


Fig. 64. Volume per Pr atom ($Å^3$) for four phases of praseodymium vs. pressure.

35). Four strong lines correspond in position and intensity to (002), (100), (102), and (110) reflections to an *hcp* structure with $a' \approx 2.8$ and $c' \approx 5.0$ Å. Additional reflections are an indication of a larger unit cell, probably a distorted *hcp* type.

The Hesse-Lipson procedure yielded a hexagonal unit cell, with axes simply related to the *hcp* subcell: $a \approx 2a'$ and $c \approx c'$. This Pr unit cell has four times the volume of the *hcp* subcell, or 8 atoms per unit cell, as illustrated in Fig. 63.

The space group of highest symmetry consistent with the observed unit cell and assumed distorted *hcp* atomic topology is trigonal, $P3m1$. The site symmetry of Pr atoms in Pr IV has been reduced from $6m2$ in ideal *hcp* to no greater than $3m$ or m in the trigonal phase. The nature of the distortions from closest packing could not be determined from the present intensity

TABLE 35. Calculated and Observed Powder Pattern for Pr IV at 233 kbar*

h	k	l	d_{obs}	d_{calc}	I_{obs}, %	Equivalent hcp
1	1	0	2.816	2.816	40	
0	0	2	2.482	2.481	50	002
2	0	0	2.431	2.438	100	100
1	0	2	2.209	2.211	80	
2	1	0	1.842	1.843	10	
2	0	2	1.738	1.739	70	102
3	0	1	1.550	1.545	5	
1	2	2	1.477	1.480	80	
2	2	0	1.406	1.408	40	110
2	2	1	1.354	1.354	30	
1	3	1	1.305	1.305	5	
1	0	4	1.203	1.202	50	

*An additional line at $d = 2.717$ Å ($I < 10\%$) could not be indexed.

data. The atomic volume if $Z = 8$ is less than 17.5 Å^3 per Pr, as illustrated in Fig. 64.

One unit-cell data point for Pr II, three for Pr III, and three for Pr IV at various pressures are recorded in Table 36 and illustrated in terms of volume per atom in Fig. 64. The volume vs. pressure data of Bridgman (1958) and one point on Pr II from Piermarini and Weir (1964) are also plotted. In the experiment at 212 kbar, Pr III and Pr IV coexist.

The primary objective in this study was to explore the Pr III–Pr IV transition at approximately 200 kbar, but x-ray diffraction measurements of Pr III at 144 kbar (run 9Pr6, Table 34) suggest that additional anomalous behavior may occur between 144 and 212 kbar, which merits further examination. For example, c/a for Pr III shown in Table 34 decreases significantly with increasing pressure, and this result indicates a continuous distortion of the unit cell from face-centered cubic. The c/a for Pr IV appears to be constant with increasing pressure to 277 kbar.

The results of this study are consistent with the tenet that the pressure-induced transition in Pr is due to a shift in its electronic structure. The volume change of 19% between Pr III and Pr IV is too large to be accounted for by a simple change in close-packed distortions. Thus, this high-pressure transition in Pr is analogous in its pressure-volume behavior to the α-γ transition in Ce.

TABLE 36. Unit-Cell Dimensions vs. Pressure for Pr II, III, and IV

Pressure, kbar	Phase	a, Å	b, Å	c, Å	c/a	V, Å^{-3}	V/atom, Å^{-1}
69.2	II	4.820(2)	...	...	...	112.0(1)	28.0
144(4)	III	6.530(11)	6.412(8)	9.221(19)	1.412(4)	386.2(7)	21.8
194(5)	III	6.344(11)	6.212(8)	8.852(18)	1.395(4)	348.8(6)	21.8
212(3)	III	6.31(5)	6.19(3)	8.81(7)	1.396(15)	343.9(22)	21.5
	IV	5.678(5)	...	5.017(6)	0.884(1)	140.1(3)	17.5
233(8)	IV	5.632(3)	...	4.962(5)	0.881(1)	136.3(2)	17.0
277(10)	IV	5.570(4)	...	4.912(s)	0.883(1)	132.2(2)	16.5

References

Bridgman, P. W., *The Physics of High Pressure*, G. Bell and Sons, Ltd., London, 1958.

Mao, H. K., P. M. Bell, J. W. Shaner, and D. J. Steinberg, Specific volume measurements of Cu, Mo, Pd, and Ag and calibration of the ruby R_1 fluorescence pressure gauge from 0.06 to 1 Mbar, *J. Appl. Phys., 49*, 3276–3283, 1978.

Piermarini, G., and C. Weir, Allotropy in some rare earth metals at high pressure, *Science, 144*, 69–71, 1964.

BIOGEOCHEMISTRY

The Organic Matter in Mississippi Valley-Type Deposits

A. P. Gize and T. C. Hoering*

Mississippi Valley–type lead-zinc deposits are major sources of these metals and have been worked for over 2000 years. Details of their genesis, however, including the source of the metals, the mode of their transport, and the precipitation mechanism, remain enigmatic (Ohle, 1980). A ubiquitous association of organic matter with the ore has been cited frequently, and it is this association that is being studied.

Mississippi Valley–type deposits are strata-bound, low-temperature (rarely as high as 200 °C) deposits, containing mainly galena, sphalerite, fluorite, and barite. Copper minerals are minor constituents of the ore. The host rocks are generally dolomitized carbonates but may also include sandstones and shales. The ore-forming fluids responsible for the Mississippi Valley–type deposits are believed to have been derived during the evolution of sedimentary basins, with the brines being expressed during sedimentary compaction. The evidence for this model comes from the proximity of the deposits to paleo-basins, the heavy sulfur isotope composition of the sulfides, the highly saline fluid inclusions, and the presence of petroleum-like material. The organic matter could be indigenous to the host rocks or, because petroleum is formed during the evolution of a sedimentary basin, it may have been introduced with the ore-forming solutions. The organic matter might have played an entirely passive role in the formation of the deposits or, as now seems more likely, it has been an active participant. If this latter case is true, then organic molecules could be involved during three stages of the formation of the deposits: (1) by initially concentrating the metals in the sedimentary basin (Macqueen, 1976), (2) by increasing metal solubility in the ore-forming solution by the formation of organo-metallic complexes (Barnes, 1979), and (3) by precipitating the ore (Barton, 1967). Hence a study of the organic matter associated with the ore is necessary for a further understanding of the genesis of these economically important deposits.

The initial part of the work has concentrated on the characterization of the organic material in the host rock of a stratigraphically and structurally simple deposit. The Wisconsin zinc-lead district fitted these criteria and has been well studied geologically (Heyl, 1970) and geochemically (McLimans, 1977). Samples were collected from the Shullsberg Mine, with the kind permission of the Eagle-Picher Mining Company, Inc. The epigenetic ores occur in a Middle Ordovician series of sandstones, dolomites, limestones, and shales, which represent widespread, shallow marine sediments deposited on a tectonically stable area.

The organic geochemistry of one limestone member (the Guttenberg, locally known as the "Oil"), which contains about 10 wt % organic carbon, was ex-

*Work carried out under a cooperative predoctoral fellowship program between the Geophysical Laboratory and The Pennsylvania State University.

amined at two localities. The first was adjacent to a major ore body, and the second was at a site unaffected by ore deposition. The objective of the extraction and analytical procedure, outlined in Fig. 65, was to determine the source of the organic matter, its thermal history, and whether it was indigenous to the host rocks or had been introduced by the ore-forming solutions.

Results

Gas chromatograms of the total saturated hydrocarbons from the two localities are shown in Fig. 66. Individual compounds were identified by mass spectrometry. The normal alkane distribution ranges from C_{14} to C_{27}, with a marked and unusual predominance of C_{15} and C_{17}. The iso- and anteiso-alkanes show a distribution from C_{16} to C_{20}, with iso-compounds predominating. The pristane-to-phytane ratio is about 2. Compounds in the low molecular weight region of the chromatograms (e.g., nC$_{14}$, nC$_{15}$, nC$_{16}$, pristane) are markedly increased at the ore body relative to the other locality.

The absence of high concentrations of long-chained compounds, especially in the range C_{25} to C_{33}, which would have been indicative of a contribution from terrestrial plants, is in agreement with the Ordovician age of the host rocks. Terrestrial plants did not evolve until the Devonian. The predominance of normal alkanes with an odd number

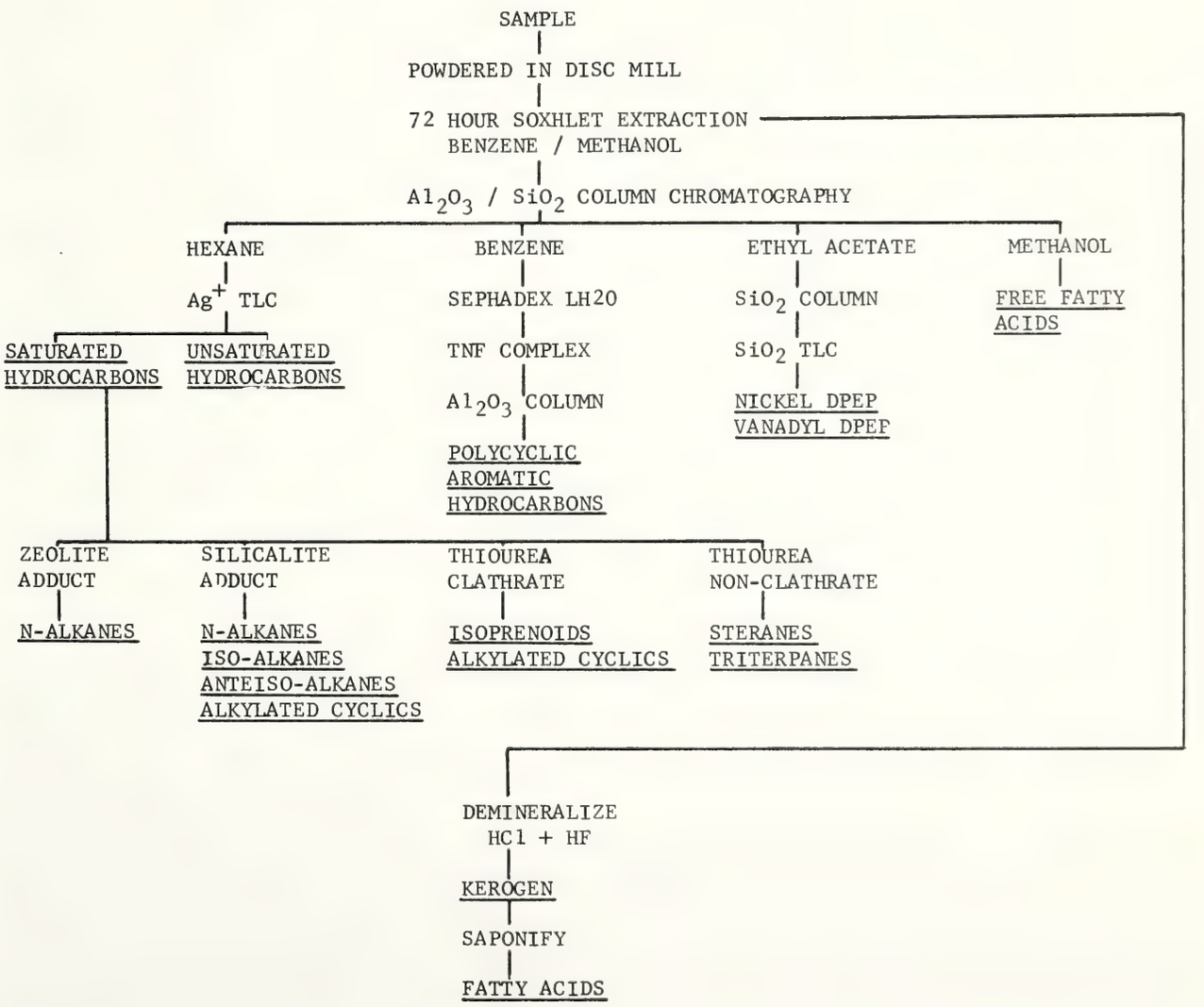


Fig. 65. Outline of extraction scheme.

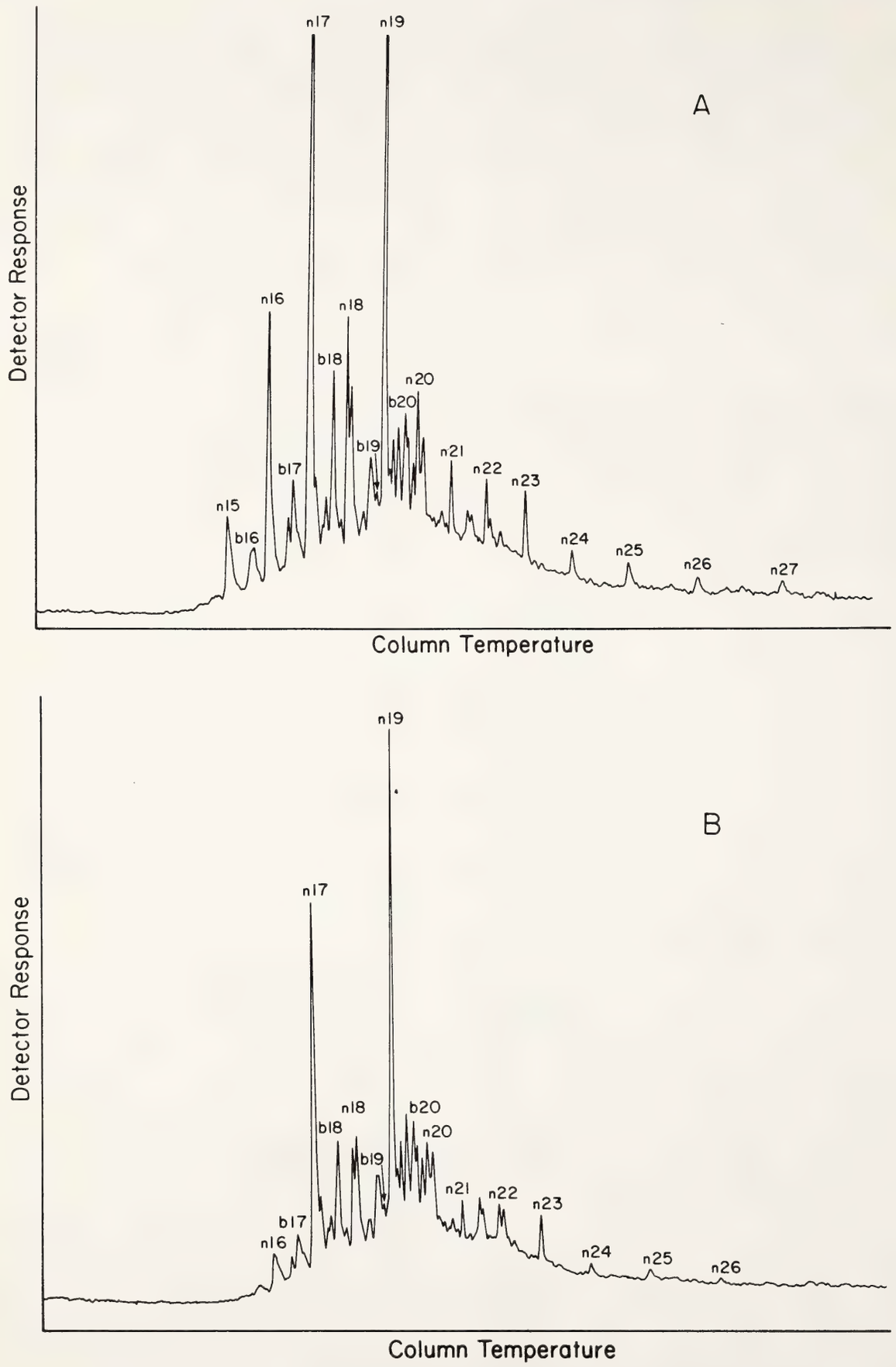


Fig. 66. Gas chromatogram of saturated hydrocarbons from the Guttenberg Formation. (A) At ore body, (B) away from ore body. A 100-ft by 0.020-inch I.D. support-coated open tubular column coated with OV-101 was used. The column temperature was programmed at a rate of 4 °C per minute. Peaks labeled with the prefix *n* are due to normal hydrocarbons with the carbon number indicated. The prefix *b* designates the branched, iso- and anteiso-hydrocarbons.

of carbon atoms is evidence that most of the saturated hydrocarbons are indigenous to the Guttenberg Formation. Petroleums of this age that have undergone migration contain normal alkanes with no preference of even or odd carbon numbers. Furthermore, the striking odd-carbon predominance occurs when a rock has had a low-temperature history. The organic matter has never been heated high enough to generate petroleum.

Other methods will be used to verify the conclusion that the hydrocarbons are indigenous to the Guttenberg Formation. They include measurements of stable carbon and hydrogen isotope ratios, optical activity, and the distribution of normal alkanes derived from indigenous kerogen by laboratory pyrolysis experiments. In addition, quantitative analysis of the hydrocarbons in the fluid inclusions in the ore will be made to evaluate the role of migrating organic fluids in the formation of these deposits.

The aromatic hydrocarbons were separated by gel permeation and alumina column chromatography (Giger and Blumer, 1974). Ultraviolet absorption spectra (250–450 nm) were obtained. Generally, the spectra were smooth envelopes owing to spectral overlap from numerous aromatic species. Differences in the amounts and distributions of aromatic hydrocarbons between the two localities are not readily noticeable.

The nickel and vanadyl porphyrins (as deoxophylloerythroetioporphyrin, DPEP) were isolated by column- and thin-layer-chromatography in the dark. These were quantified by using published values for the molar absorptivities of the Soret band (Hodgson *et al.*, 1968) and the major non-Soret band (Hodgson and Baker, 1967). At the ore deposit, the nickel and vanadyl DPEP concentrations were 98 $\mu g\ kg^{-1}$ and 6 $\mu g\ kg^{-1}$, respectively, whereas the sample away from the ore body contained 1.5 $\mu g\ kg^{-1}$ and 0.7 $\mu g\ kg^{-1}$. The salient point is the 8-fold increase in the nickel-to-vanadyl ratio at the ore body. Millerite (NiS) occurs paragenetically late at Wisconsin. Whether this increase in nickel DPEP is due to host rock heterogeneity, introduction of nickel DPEP or its precursor by the ore-forming solution, or complexation of nickel from the ore solution by DPEP indigenous to the host rock is not clear.

The bound fatty acid fraction, obtained by saponification of demineralized rock powders, contained a predominance of $nC_{16:0}$ (palmitic) and $nC_{18:0}$ (stearic) acids, as expected from a low-temperature assemblage of marine organic matter of algal derivation. A generic relationship between fatty acids and normal hydrocarbons is indicated. A decarboxylation (loss of CO_2 and gain of a hydrogen atom) of C_{16} and C_{18} fatty acids would yield the observed C_{15} and C_{17} normal hydrocarbons.

The kerogen (insoluble organic matter) obtained after demineralization of the rocks had a yellow color. This observation, combined with the unusual distribution of hydrocarbons and fatty acids plus the absence of an irresolvable mixture in the gas chromatograms due to thermodynamically favored branched isomers, indicates an unexpected and remarkably low temperature history for rocks of Ordovician age. The overall thermal maturity is only at the onset of catagenesis in a type-1 kerogen (i.e., a kerogen derived mainly from algae). The pseudo-activation energy derived by Connan (1974) from an empirical study of several oil basins was used to obtain an average temperature of 60°–70°C since the Ordovician for the Guttenberg Formation.

In summary, this work has shown that the organic matter in the Guttenberg limestone in the Wisconsin zinc-lead district is mainly indigenous and was derived from the degradation products of marine microorganisms. The remarkably low temperature history of the area has been demonstrated and

clearly negates the involvement of any postulated hidden magmatic sources in the formation of the deposit.

References

Barnes, H. L., Solubilities of ore minerals, in *Geochemistry of Hydrothermal Ore Deposits,* 2d ed., H. L. Barnes, ed., John Wiley and Sons, Inc., New York, pp. 404–460, 1979.

Barton, P. B., Possible role of organic matter in the precipitation of the Mississippi Valley ores, in *Genesis of Stratiform Lead-Zinc-Barite-Fluorite Deposits,* J. S. Brown, ed., *Econ. Geol. Monogr. 3,* 371–378, 1967.

Connan, J., Time-temperature relation in oil genesis, *Amer. Ass. Petrol. Geol. Bull., 58,* 2516–2521, 1974.

Giger, W., and M. Blumer, Polycyclic aromatic hydrocarbons in the environment: isolation and characterization by chromatography, visible, ultraviolet, and mass spectrometry, *Anal. Chem., 46,* 1663–1671, 1974.

Heyl, A. V., The Upper Mississippi Valley Base-Metal District, in *Ore Deposits in the United States 1933/1967,* Vol. 1, J. D. Ridge, ed., American Institute of Mining, Metallurgical, and Petroleum Engineers, New York, pp. 431–459, 1970.

Hodgson, G. W., and B. L. Baker, Spectra of selected geochemically significant porphyrins and chlorins, *Chem. Geol., 2,* 187–198, 1967.

Hodgson, G. W., B. Hitchon, T. Kazuo, B. L. Baker, and E. Peake, Geochemistry of porphyrins, chlorins, and polycyclic aromatics in soils, sediments, and sedimentary rocks, *Geochim. Cosmochim. Acta, 32,* 737–772, 1968.

Macqueen, R. W., Sediments, zinc and lead, Rocky Mountain belt, Canadian cordillera, *Geosci. Canada, 3,* 71–81, 1976.

McLimans, R. K., Geological, fluid-inclusion, and stable isotope studies of the Upper Mississippi Valley Zinc-Lead District, southwest Wisconsin, Ph.D. thesis, Department of Geological Sciences, The Pennsylvania State University, 1977.

Ohle, E. L., Some considerations in determining the origin of ore deposits of the Mississippi Valley type—Part 2, *Econ. Geol., 75,* 161–172, 1980.

Tracing Food Webs with Stable Hydrogen Isotopes

Marilyn F. Estep and Halina Dabrowski

Food web determinations may be used to predict biochemical energy fluxes in ecosystems where a number of different organisms are interacting. Tracing natural food webs, however, is a time-consuming task subject to many observational biases. For example, the foods in the stomachs of many animals are partially digested and only sometimes are identifiable, even by the most experienced workers. A relatively objective method for examining the abundance of plants or animals of different species in an animal's diet is based on the distinctive carbon isotope ratios of plants and the fact that there is little isotope discrimination between an animal and its food source (DeNiro and Epstein, 1978; Fry *et al.,* 1978). Variations in the ratios of stable hydrogen isotopes may aid in tracing food webs of marine and terrestrial life and result in the differentiation of species having similar carbon isotope ratios.

The organically bonded hydrogen of plant tissues is derived from the surrounding water and has a reproducibly lower concentration of the heavy hydrogen isotope than the water (Schiegl and Vogel, 1970; Epstein *et al.,* 1976; Estep and Hoering, 1980). Plants collected from the several ecosystems have characteristic fractionations of -90 to $-110‰$, but notable exceptions, such as certain micro- and macroalgae (i.e., *Ulva lactuca* and blue-green algae), exist. Furthermore, as the hydrogen isotope ratios of environmental waters vary with salinity, latitude, and altitude, the organically bonded hydrogen in plants of the same species growing in different localities will reflect the differences in hydrogen isotopic content of the environmental water (Epstein *et al.,* 1976). Because of variations in the hydrogen isotope ratios of plants, due to either metabolism or environmental influence, the hydrogen isotopic content of organically bonded hydrogen in an animal's tissue may indicate the presence of a particular plant in its diet or be useful in the investigation of environmental or migratory phenomena.

The hydrogen in animals is in the form of either water or organically bonded

hydrogen. Most plants and animals are 80% to 90% water derived from water ingested by the organisms (i.e., mammals) or water taken up from the environment by diffusion (i.e., plants, aquatic organisms). The organically bonded hydrogen isotopic content of an animal is dependent on the isotopic content of its food source. This relationship was defined by studying laboratory-reared mice (Estep and Hoering, *Year Book 77,* 891). In this study, an example is given of the relationship of a simple, natural population of snails and its possible algal food sources.

Identical species of snails and four species of algae were collected from three different tidal pools in Boothbay Harbor, Maine, by Drs. Wendy Harrison and Richard Wendlandt. The tidal pools were located 100–150 m apart at midtide level on a small harbor. The algal species were *Chondrus crispus* (Rhodophycophyta), *Fucus vesiculosus* (Phaeophycophyta), *Ulva lactuca* (Chlorophycophyta), and *Enteromorpha clathrata* (Chlorophycophyta). These algae were the dominant forms at this tidal level. The snails were of the species *Littorina obtusata* (Dr. J. Rosewater, Smithsonian Institution, personal communication) and were collected attached to *Fucus* or browsing on the rocks beneath this algal species. Water samples were also collected from these pools and the Atlantic Ocean. The snails and the algae were kept frozen at −70 °C for two months. The snails' tissue was separated from their shells. After freeze-drying the samples were placed in a vacuum oven at 60 °C over P_2O_5.

Six to ten milligrams of the dried sample were combusted in a platinum boat at 750 °C in an atmosphere of oxygen. The water from combustion was trapped with liquid nitrogen, converted to H_2, and analyzed by an isotope ratio mass spectrometer (Estep and Hoering, 1980). The results are reported in terms of δD, which is defined by the following equation:

$$\delta D = \left[\frac{\text{D/H sample}}{\text{D/H standard}} - 1\right] \times 10^3.$$

The hydrogen isotope standard was the Standard Mean Ocean Water (SMOW). This system for measuring hydrogen isotopes is routinely used on a variety of organic matter and typically yields results from triplicate analyses of these samples with a standard deviation of ±3‰.

The results of the hydrogen isotope analyses for ten samples of *Littorina obtusata* and ten samples of algae of four different species are given in Fig. 67 and Table 37. The average hydrogen isotope ratios for the snails from sites 1, 2, and 3 are identical, and this result indicates that they have the same diet. Furthermore, 80% of the individual δD values are within ±5 of the average. Of the four species of algae, only the hydrogen isotope ratio of *Fucus vesiculosus* shows any obvious relation to the δD of the snails. The δD of *Fucus* range from −102 to −116‰ or an average of −111‰, which compares with the average δD of −111 for the snails at the three sites. The δD of *Chondrus* is greater and that of *Ulva* and *Enteromorpha* is smaller than the δD of the snails.

A combination of *Chondrus* (δD = −92) and *Ulva* (δD = −173) in the snails' diet could account for the isotope ratio of the snails. *Littorina obtusata,* however, have been observed in nature and also in controlled laboratory experiments. They not only live and breed on *Fucus* but also consume *Fucus* as the primary source of their diet (Barkmann, 1956; Bakker, 1959).

The hydrogen isotope ratio of the food source, not the water, determines for the most part the hydrogen isotope ratio of the organically bonded hydrogen in animals. Although there is greater variation in the δD of the diet and of the animal tissue than is seen in $\delta^{13}C$ measurements, the expression "you are what you eat" applies to hy-

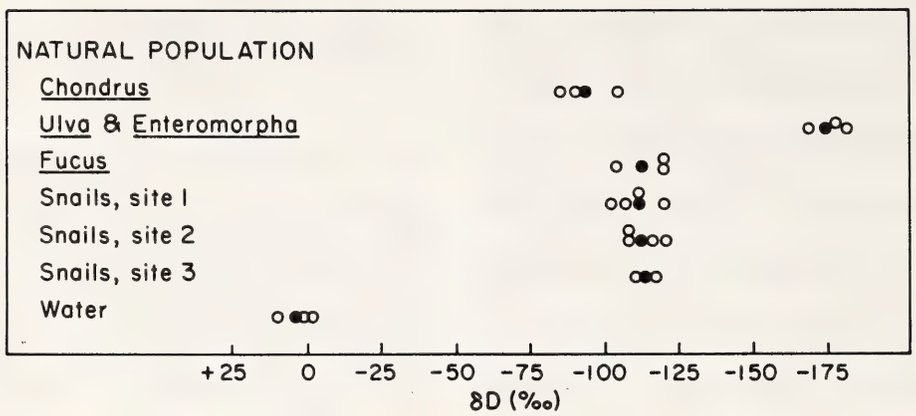


Fig. 67. Hydrogen isotope ratios of snails and their diet. Open circles indicate individual values. Closed circles indicate the average of individuals.

TABLE 37. Stable Hydrogen Isotope Ratios of Boothbay Harbor Samples

Classification/Species	δD* Site 1	δD* Site 2	δD* Site 3	Average δD
Plants: Algae				
Ulva lactuca	−180	−166		−173
Enteromorpha clathrata			−174	−174
Fucus vesiculosus	−116	−102	−116	−111
Chondrus crispus	−90	−103	−84	−92
Animals: Molluscs				
Littorina obtusata	−106(I)†	−116(C)	−111(C)	
	−119(C)	−106(C)	−113(C)	
	−101(I)	−115(I)		
	−109(I)	−107(I)		
Average δD (site)	−109	−111	−112	−111

*The δD of water at sites 1, 2, and 3, respectively, are +12, +2, and 0. The δD of Atlantic Ocean water at this area is +10.

†I, individual; C, composite.

drogen isotopes. Because of variations in the δD of the algae available to the snails, the diet of *Littorina* could be traced by isotopic methods. In this simple population and in laboratory-reared mice (Estep and Hoering, *Year Book 77,* 891), the conclusion from hydrogen isotope measurements is in agreement with direct observation.

References

Bakker, K., Feeding habits and zonation in some intertidal snails, *Arch. Neer. Zool., 13,* 230–257, 1959.

Barkmann, J. J., On the distribution and ecology of *Littorina obtusata* (L.) and its subspecific units, *Arch. Neer. Zool., 11,* 50–86, 1956.

DeNiro, M. J., and S. Epstein, Influence of diet on the distribution of carbon isotopes in animals, *Geochim. Cosmochim. Acta, 42,* 495–506, 1978.

Epstein, S., C. J. Yapp, and J. H. Hall, The determination of the D/H ratio of nonexchangeable hydrogen in cellulose extracted from aquatic and land plants, *Earth Planet. Sci. Lett., 30,* 241–251, 1976.

Estep, M. F., and T. C. Hoering, Biogeochemistry of the stable hydrogen isotopes, *Geochim. Cosmochim. Acta, 44,* 1197–1206, 1980.

Fry, B., A. Joern, and P. L. Parker, Grasshopper food web analysis: use of carbon isotope ratios

to examine feeding relationships among terrestrial herbivores, *Ecology, 59,* 498–506, 1978.
Schiegl, W. E., and J. C. Vogel, Deuterium content of organic matter, *Earth Planet. Sci. Lett., 7,* 307–313, 1970.

The Uptake and Incorporation of the Hydrogen from Water into the Organic Matter of Plants

Marilyn F. Estep and Thomas C. Hoering

Plants grown under controlled conditions show a reproducible and easily measurable discrimination (fractionation) of as much as 20% between the isotopes of hydrogen, deuterium (D) and protium (H) (Estep and Hoering, 1980; Ziegler *et al.,* 1976). Cultures of microalgae, natural populations of phytoplankton, macroalgae, mosses, and higher terrestrial plants all have lower concentrations of the heavy isotope of hydrogen (deuterium) than the environmental water.

Photosynthesis is the major process fractionating hydrogen isotopes in plants (Estep and Hoering, 1980). Additional fractionation of hydrogen isotopes occurs during biosynthesis. Fatty acids, hydrocarbons, sterols, and other lipids have much lower deuterium concentrations than the organically bonded hydrogen of the total organism (Hoering, 1977; Smith and Epstein, 1971). Because there are distinctive isotope fractionations in biochemical processes, and because differences of less than 1 ppm deuterium in the hydrogen isotopic content of organic matter can be measured by precision isotope ratio mass spectrometry, it is possible to conduct tracer experiments with hydrogen near the natural abundance level.

There is a class of biosynthetic problems involving the regulation of metabolism that is uniquely accessible to measurement of isotope fractionation. The hydrogen in the surrounding water is the ultimate source of all organically bonded hydrogen in autotrophically grown plant cells. The two are connected by a complex network of chemical reactions. Although a difference in reaction rates between hydrogen- and deuterium-containing compounds is possible in any of the individual steps, observable fractionation between major reactants and products will occur only when there is a distinctive isotope discrimination in a rate-determining step of the sequence or at a branching point in the flow of metabolites through the network of chemical reactions. Measurements of isotope fractionation can help locate such critical steps or biosynthetic branching points.

In order to understand further the biochemical reactions fractionating hydrogen isotopes in plants, with the goal of detecting critical steps, the hydrogen isotopic contents of different classes of compounds, carbohydrates, proteins, and lipids were determined. Second, the uptake of hydrogen from water into cellular organically bound hydrogen was studied by resuspending and growing algae in growth media water with a very slightly enriched deuterium content.

Experimental Methods

Axenic cultures of microalgae were obtained from Dr. Chase Van Baalen, Port Aransas Marine Laboratory, University of Texas. Algae were grown either in test-tube batch cultures in a thermostatically controlled water bath or in a glass, water-jacketed, growth chamber. The media used for growth and the exact culture conditions are given in detail in Estep and Hoering (1980). The algae were harvested by centrifugation, washed once with distilled water, and dried. During this procedure, the organically bonded hydrogen did not exchange with water (Estep and Hoering, 1980). The relative deuterium concentration of the water in the growth medium was the same before and after growth.

Proteins (and lipids) were separated

from the total organic matter of the coccoid, blue-green alga *Agmenellum quadruplicatum* strain PR-6, which was grown in the glass water-jacketed growth chamber and harvested daily. The cells were washed once with distilled water. A solution of 5% (w/v) trichloroacetic acid at 0° to 4°C extracted carbohydrates (Roberts *et al.*, 1955). Cellular lipids were extracted with an ethanol solution (75% v/v). A second solution of 5% trichloroacetic acid was added to the algal residue and was incubated at 100°C for 30 min. This solution extracted nucleic acids. The remainder was washed with 75% ethanol to remove residual trichloroacetic acid. The organic matter not extracted previously (a bright blue color) contained the bulk of the algal protein. Analyses of the amino acid content showed that this fraction was 90% to 99% protein. The trichloroacetic acid solutions, which contained the carbohydrate and nucleic acid fractions, were discarded, because the trichloroacetic acid (7.5 g in 150 ml) was difficult to remove from the algal fractions (10–20 mg) without possibly fractionating the hydrogen isotopes. The entire extraction procedure was also carried out with solutions spiked with deuterium. The added deuterium in the extracting solutions did not exchange with the cellular extracts (see Fig. 69, day 3).

Hydrogen isotope ratios were determined by combusting organic matter exactly as described by Estep and Dabrowski (this Report). The fractionation, ΔD, is equal to δD organic hydrogen–δD water.

Results

When the algae *Agmenellum, Anacystis nidulans* strain TX20, and *Chlorella sorokiniana* strain TX71105, grown photosynthetically, were suspended in mineral salts media with a slightly increased deuterium content, the new isotopic composition of the water was not displayed within 1–6 hr by the cellular organic hydrogen (Estep and Hoering, *Year Book 77,* 890; Figs. 68 and 69). Even after 2–3 days' growth, the cellular organic hydrogen was not in isotopic steady state with the new water in the growth media (Figs. 68 and 69). The dashed lines in Figs. 68 and 69 indicate theoretical δD values, calculated by a simple material-balance equation, for algae in isotopic equilibrium with the water in the growth medium. The failure to incorporate hydrogen rapidly from water into cellular-bound hydrogen indicates that hydrogen is metabolized into the cell via a pool of a bound complex, perhaps reduced nicotinamide adendine dinucleotide phosphate (NADPH), rather than as H_2O. In addition, the presence of luxury bound hydrogen, reducing power that is present in excess of the cell's immediate needs, in actively photosynthesizing cells is indicated. Only 16–33% of the hydrogen incorporated in algae growing in the heavier water was directly attributable to this isotopically heavier water.

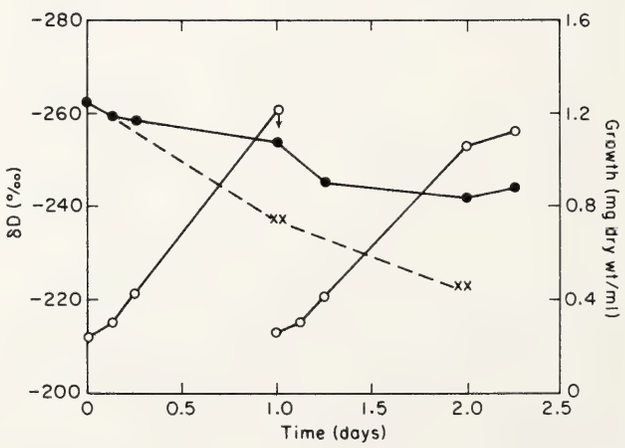


Fig. 68. Hydrogen isotope incorporation from water into organically bonded hydrogen in *Anacystis nidulans.* Closed circles, δD values with time. Dashed lines with crosses, theoretical δD values for algae in steady state with the isotopically heavier water. Open circles, growth of the algae as measured by mg dry wt/ml culture medium. The culture was diluted with fresh medium after 24 hr of growth. The δD of the water before the experiment was −52‰. At 0 hr, the δD of the water was −21; at 24 hr, the δD of the water was −2.

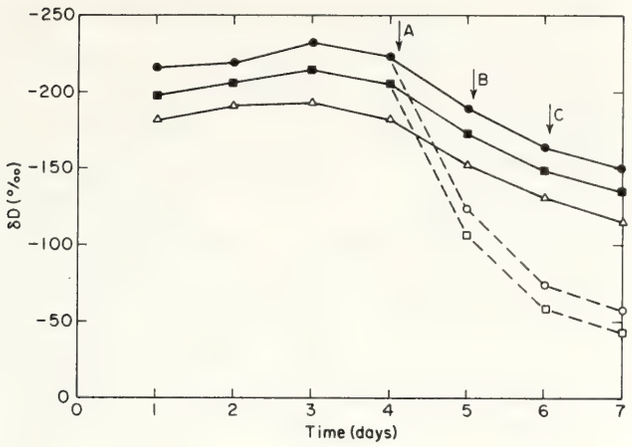


Fig. 69. Hydrogen isotope fractionation in whole algal cells and protein isolated from *Agmenellum quadruplicatum.* Closed circles, δD of protein. Closed squares, δD of whole algal cells. Dashed lines, theoretical δD values for algae in steady state with the isotopically heavier water. Open triangles, calculated δD values of algal cells minus protein. The δD of the water in the culture medium was −60‰ during days 1–4. The arrows indicate that during days 5–7, the δD of the water in the culture medium was changed to +65‰ (A), +103‰ (B), and +109‰ (C).

The hydrogen isotopic contents of individual classes of compounds are different. Cells of *Anacystis,* washed once with distilled water, were resuspended and incubated in a bicarbonate-carbonate buffer at pH 8.2 at 39 °C in the light for 24 hr (Fig. 70). The increase in dry weight is attributed to an increase in carbohydrate content, as this buffer without phosphate or nitrogen inhibits protein metabolism and cell division. By difference calculation, and by forcing algal cells to produce only carbohydrates, the hydrogen isotope fractionation between carbohydrates and water in the growth medium is approximately −100‰. This fractionation is calculated by the following equation, which is based on simple material balance:

(initial dry wt algae) (δD initial) + (dry wt carbohydrates) (δD carbohydrates) = (total dry wt algae + carbohydrates) (δD final).

Subsequently, the algae were transferred into the dark, inhibiting photosynthesis and promoting respiration. After 24 hr of darkness, the dry weight of the algal suspension had decreased to levels similar to those at the beginning of the experiment. The algae had metabolized the stored carbohydrates to CO_2 and water, in order to provide cell energy. In the case in which the δD of the buffer was the same as that of the growth medium, the δD of the algae after respiration was nearly identical with that of the initial algal cells. The hydrogen incorporated into carbohydrates during the period of light was eliminated during metabolism without isotope fractionation. This result indicates that dark respiration does not fractionate hydrogen isotopes. In the experiment in which the D content of the water was increased slightly, some recycling or exchange of hydrogen occurred.

Proteins and lipids isolated from *Agmenellum* have less deuterium than carbohydrates by approximately −30 to −50‰. Thus additional fractionation during the breakdown of glucose to form amino acids and fatty acids is indicated (Fig. 69). The hydrogen involved in the additional fractionation is related to the pool of bound hydro-

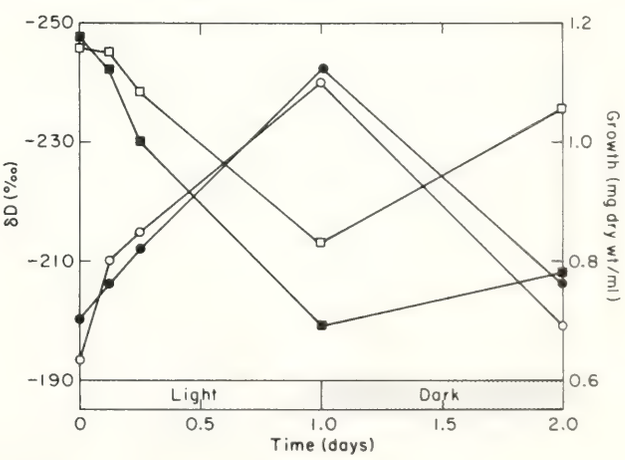


Fig. 70. Fixation of hydrogen into carbohydrates by *Anacystis nidulans* suspended in a bicarbonate-carbonate buffer. Dry wt: open circles, δD water = −66; closed circles, δD water = +9. δD values of the total algae through time: open squares, δD water = −66; closed squares, δD water = +9.

gen metabolized by the algal cells. Isolated proteins and lipids extracted from *Agmenellum* grown in heavy water had hydrogen isotope fractionations parallel to the whole organism fractionation rather than to the different isotope ratio of the water in the growth media. Hydrogen was incorporated into both the protein and lipid fraction and the carbohydrate fraction at a similar rate.

Conclusions

A pool of intracellular, organically bound hydrogen is responsible for providing the hydrogen available for cellular biosynthesis. This pool of hydrogen is generated in the light during photosynthesis and may reflect NADPH concentrations. It does not undergo isotope exchange with the water in the growth media. Stable hydrogen isotope fractionation in plants is governed by this form of bound hydrogen that is generated during photosynthesis. For example, red light activates hydrogen isotope fractionation and phosphoglyceric acid reduction (Estep, *Year Book 78,* 650). In this particular reducing reaction, hydrogen from photosynthetically produced NADPH is fixed into organic matter.

Hydrogen metabolism in biosynthesis and dark reactions is linked to that in the light via the pools of the reductants, NADPH or NADH, or both. Consequently, additional fractionation occurs during the biosynthesis of proteins and lipids. It was discovered that whereas the hydrogen from organic substances was immediately incorporated into the algal cells (Estep and Hoering, 1980), the hydrogen in the water of the growth medium was not. This lag in the incorporation of hydrogen from water indicates that in actively photosynthesizing cells, a pool of excess organically bound reductant is available for cellular hydrogen metabolism.

Precision stable isotope ratio mass spectrometry has been used to identify some of the key reactions in plant metabolism that fractionate the hydrogen isotopes. Isotope fractionation is indicative of rate-limiting reactions or branching points. Hence, the enzymes at these critical points that control isotope fractionation also serve to regulate hydrogen metabolism in the plant cell. The complex network of reactions between water and organically bonded hydrogen is regulated principally by photosynthesis, whereas secondary regulation occurs during glycolysis.

References

Estep, M. F., and T. C. Hoering, Biogeochemistry of the stable hydrogen isotopes, *Geochim. Cosmochim. Acta, 44,* 1197–1206, 1980.

Hoering, T. C., Stable isotopes of hydrogen in Precambrian organic matter, in *Chemical Evolution of the Early Precambrian,* C. Ponamperuma, ed., Academic Press, New York, pp. 81–85, 1977.

Roberts, R. B., P. H. Abelson, D. B. Cowie, E. T. Bolton, and R. J. Britten, *Studies of Biosynthesis of Escherichia coli,* Carnegie Inst. Wash. Publ. 607, 1955.

Smith, B. N., and S. Epstein, Biogeochemistry of the stable isotopes of hydrogen and carbon in salt marsh biota, *Plant Physiol., 46,* 129–139, 1971.

Ziegler, H., C. B. Osmond, W. Stichler, and P. Trimborn, Hydrogen isotope discrimination in higher plants: correlations with photosynthetic pathway and environment, *Planta, 128,* 85–92, 1976.

The Colloidal Organic Matter in Waters of the Chesapeake Bay and Patuxent River

A. C. Sigleo, T. C. Hoering and P. E. Hare*

The organic matter in river and estuarine water is not only an important part of the biological food web but also a precursor to the organic matter in sedimentary rocks. In sediments it provides the strongly reducing environ-

*Partial support from Department of Chemistry, University of Maryland, College Park, Maryland.

ment that is a primary control on sedimentary inorganic geochemistry. Aquatic organic matter is a dilute (approximately 3 ppm organic carbon in Chesapeake Bay) but complex mixture of polymeric molecules having a wide range in molecular weight that has been difficult to isolate and characterize. Detailed analysis of this important material is now possible owing to recent advances in organic geochemistry.

Techniques for characterizing colloidal-sized organic particles have been developed in this study on water samples collected from the Chesapeake Bay and Patuxent River of Maryland. This water system is ideal for the purpose because it provides an easily accessible variety of environments, including a salinity gradient varying from fresh water to nearly sea water.

There are two major potential sources for naturally occurring colloidal organic matter in fluvial and estuarine waters. The first is degradation products from *in situ* microorganisms such as phytoplankton and bacteria. The second is from terrestrial plants. The Patuxent River drains wooded and agricultural lands and could contain lignin derivatives or other compounds distinctive of land plants. Thus, it may be possible to monitor the transport of these compounds through the Chesapeake Bay.

Experimental Procedures

A procedure was developed for isolating dissolved and colloidal material from estuarine waters with the use of commercially available ultrafiltration equipment. Briefly, 20-liter samples are prefiltered through a 0.40-μm filter to remove suspended sediment and planktonic organisms (particulate fraction), concentrated and desalted by ultrafiltration (Amicon UM2 membrane, 1.2 nm nominal pore-size) under 50 psi N_2 pressure, and freeze-dried. Although ultrafiltration is slow, the advantage of it is that it requires no drastic pH changes that can significantly alter natural polymers.

The dried organic matter was characterized first by temperature-controlled, stepwise pyrolysis with a CDC model 100 solids pyrolyzer. A number of natural and synthetic polymers give characteristic pyrolysis products that can serve as "fingerprints." The volatile products were separated by gas chromatography with a 50 m by 0.25 mm I.D. glass capillary column coated with Carbowax 20M. The effluent of the column was analyzed by a DuPont model 491 mass spectrometer.

Some of the pyrolysis products were characteristic of proteinaceous material. Hence, amino acids analyses on aliquots of the same samples were made with ion exchange chromatography with *o*-phthalaldehyde fluorescent derivatives as described by Hare (1977).

Pyrolysis Results

Sequential, stepwise pyrolysis at 450°, 600°, and 750°C of the freeze-dried colloidal material produced a large number of products, as illustrated by the complex chromatograms in Fig. 71. The compounds identified are listed in Table 38. In addition to a series of low-molecular-weight alkanes, alkenes, and alcohols that elute in the initial peak, the primary pyrolysis products from the colloidal-sized material at the 450°C step are acetic acid, methyl furans, furaldehydes, furoic acid, furfuryl alcohol, and lactones. Such compounds are characteristic of carbohydrate thermal decomposition. Pyrroles, pyridines, acetamide, butyramide, indole, and other nitrogen-containing compounds become more prevalent and dominate the product yield at the 600°C pyrolysis step. These nitrogen compounds are typical pyrolyzates from proteins and smaller peptides.

The pyrolyzates from the particulate-sized material (>0.40 μm) are similar in composition to those of the colloidal

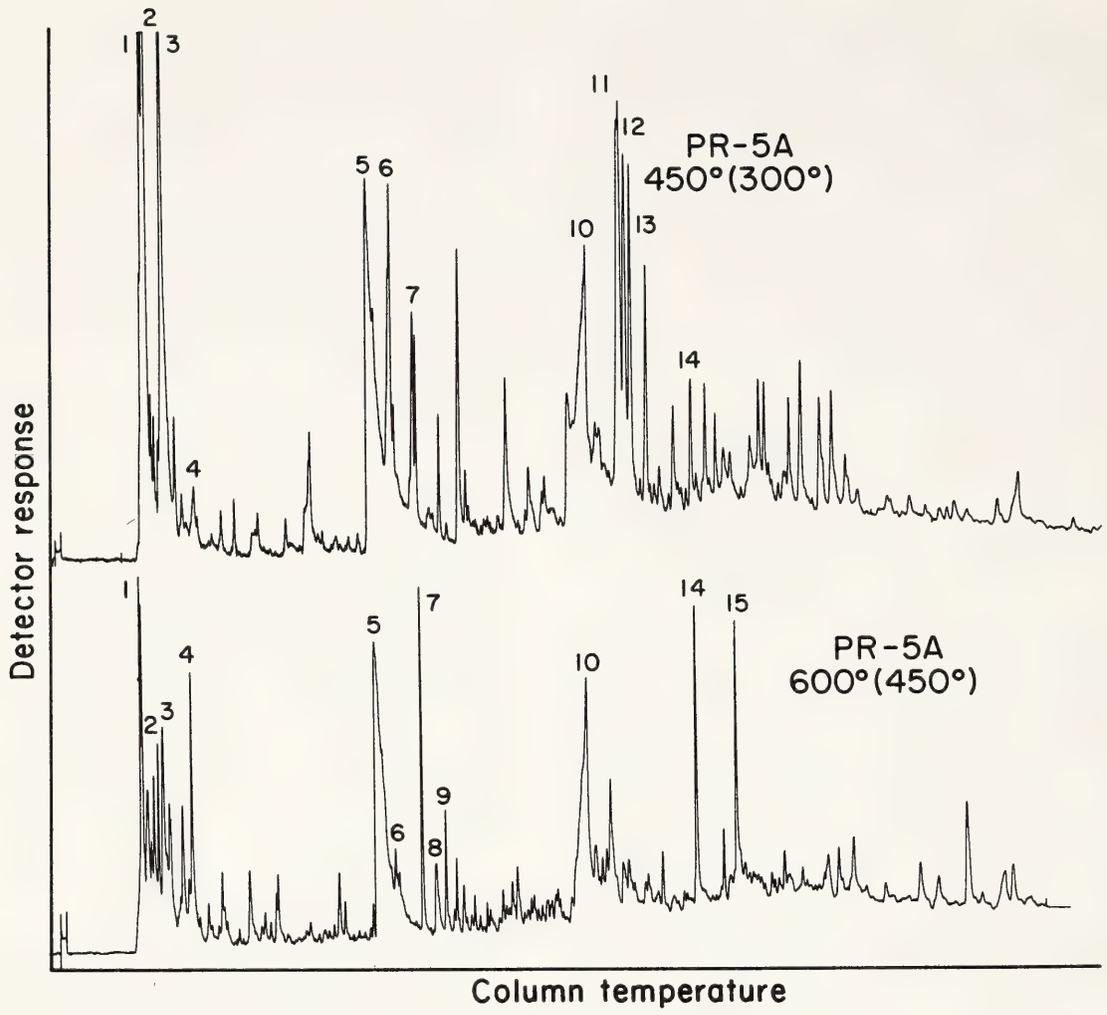


Fig. 71. Pyrograms of the colloidal fraction, Patuxent River water near Solomons Island, Maryland. The major peaks are (1) ethane, etc., (2) furan, (3) propanone, propanal, (4) benzene, (5) acetic acid, (6) methyl furaldehyde, (7) pyrrole, (8) 1-methyl pyrrole, (9) 2-methyl pyrrole, (10) acetamide, (11) dimethyl dioxane, (12) methyl heptanone, (13) furoic acid, (14) phenol, (15) cresol.

material, but the relative proportions of specific products are quite different (Fig. 72). In particular there is a comparatively minor product yield at 450 °C from the particulate fraction relative to the amount of material evolved from colloidal matter that reaches a maximum at that temperature. Although the products indicate that both colloidal and particulate polymers consist of a proteinaceous-carbohydrate matrix, the difference in product yield at the two temperatures suggests that the colloidal material is composed of smaller, more easily degraded polymers than the particulates. This reasoning is supported by scanning electron microscope examination of the two size fractions, which illustrates that the >0.40 μm material contains whole organisms (mainly centric diatoms), and the <0.40 μm fraction consists of a fine web-like polymer with some plankton fragments.

In addition to greater product yields at lower temperatures, the quantity of oxygen-containing compounds indicative of carbohydrates in the colloidal samples is far greater than the amount in particulate samples. There are two possible explanations for this result. The first is that the primary extracellular products of phytoplankton are glucans (small-molecular-weight polysaccarides), which readily accumulate in the water column. The second possibil-

TABLE 38. Pyrolysis Products Identified by Gas Chromatography–Mass Spectrometry*

CO_2†	Methyl cyclopentanone†
Ethene, ethane, propene, propane, etc.	Propionic acid†
Furan†	Hexanol† + hydrocarbon
Propanone, propanal†	Acetophenone or methylphenyl ketone
Benzene	Dimethyl pyrrole‡
Propadiene	Hydroquinone†
Butadiene	Acetamide‡
Toluene	Butyramide‡
Methyl propanol†	Dimethyl dioxane† or ethyl dioxane
Pyridine‡	Methyl heptanone†
Methyl pyridine‡	Furoic acid†
Styrene	Naphthalene§
Methyl styrene	Quinoline§‡
Dimethyl pyridine‡	Methylnaphthelene§
Indene	Methyl quinoline§
2-Furaldehyde†	Dimethyl quinoline§
Acetic acid†	Phenol
Methyl furaldehyde†	σ-Cresol
Pyrrole‡	ρ-Cresol
1-Methyl pyrrole‡	Xylenol or ethylphenol
2-Methyl pyrrole‡	Tolunitrile‡
Isobutyl formate†	Indole‡
Furfural alcohol†	Carbazole‡

*Compounds listed in order of elution.
†Compounds containing oxygen derived from carbohydrate degradation.
‡Compounds containing nitrogen derived from proteins.
§750°C pyrolyzates only.

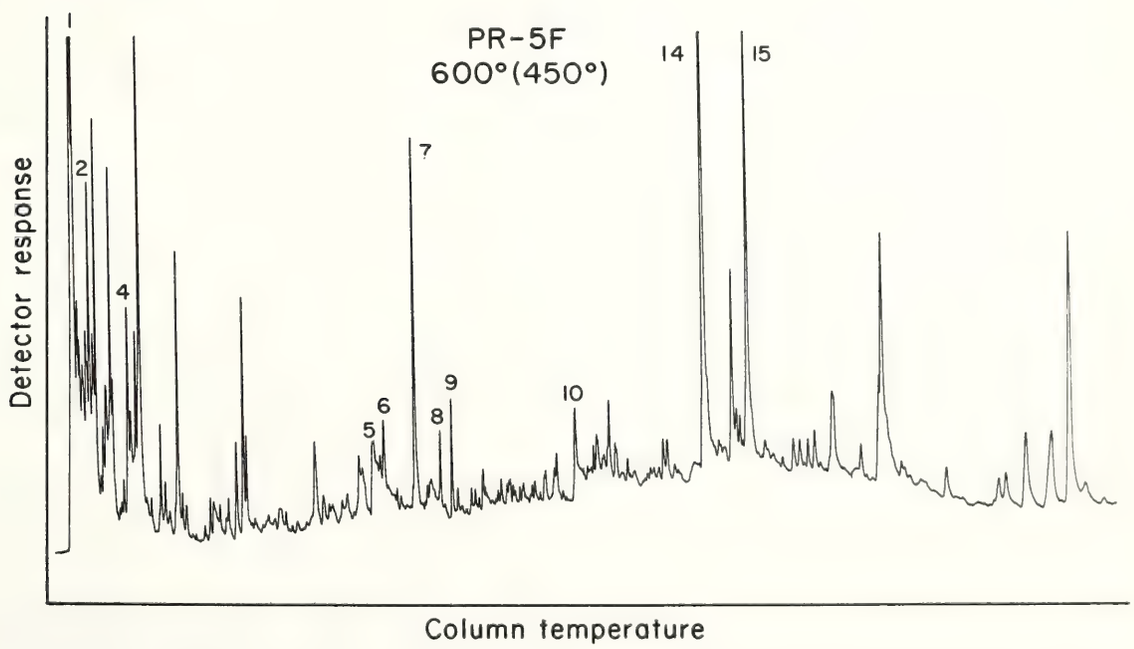


Fig. 72. Pyrogram of the particulate (>0.40 μm) fraction, Patuxent River water near Solomons Island, Maryland. The peak numbers are the same as in Fig. 71.

ity is that the carbohydrates are derived from partially hydrolyzed cellulose from the decay of terrestrial plants. Although it is not possible to distinguish the source from these analyses, it is worth nothing that carbohydrates are always present in high amounts in winter, summer, freshwater, or marine colloidal fractions. Furthermore they are not more abundant in the upriver samples, which would be expected from a terrestrial source. The relatively high concentrations of these compounds in the small-molecular-weight range in natural waters is most likely a function of their extreme solubility.

No lignin derivatives were identified in any of the samples analyzed. In order to determine the relative product yield, a pure lignin standard was pyrolyzed and chromatographed in the same manner as the samples. As may be observed in Fig. 73, the lignin derivatives (guaiacols) have a high product yield and would be easily detected even in trace quantities. The presence of lignin derivatives in sediments has been well documented (Hedges and Parker, 1976), and the absence of these compounds in the water column suggests that they are deposited rapidly.

The final major class of organic compounds, olefins and saturated hydrocarbons, derived from fatty acids, are present only in trace amounts. These results are consistent with the known composition of Chesapeake Bay phytoplankton, and the pyrolysis of an actual phytoplankton sample produced a suite of oxygen- and nitrogen-containing compounds identical with that of the particulate samples.

Amino Acid Results

In order to verify the pyrolysis data, which indicated that aquatic organic material consisted of a proteinaceous-carbohydrate polymer, the samples were analyzed for amino acid content. The results indicate a biological series of amino acids that are relatively intact. Although methionine is less abundant than expected in living organisms, it is easily oxidized and may have degraded during sample preparation. The absence of alloisoleucine, which increases with time in the geological

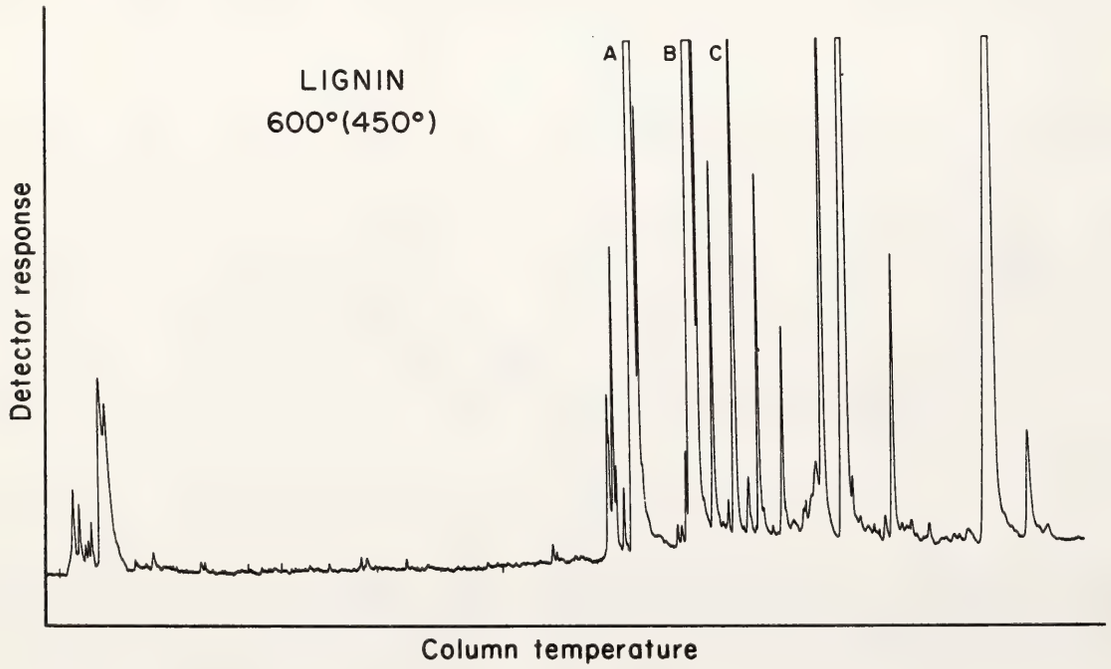


Fig. 73. Pyrogram of lignin. The major peaks diagnostic of lignin are (A) guaiacol (*o*-methoxyphenol), (B) methyl guaiacol, and (C) ethyl guaiacol.

record, indicates that the material is recent.

One method of comparing amino acid contents between samples is to compute amino acid residues per 1000 total amino acid residues. In this way, differences due to ash content are eliminated because the data are normalized to total amino acids. The results of these calculations (Fig. 74) for samples collected near Lower Marlboro, Maryland, indicate that winter colloidal material and summer colloidal and particulate samples have identical amino acid contents. In other words, the amino acids in all three sample types were derived from the same source, namely aquatic plankton and bacteria.

In summary, amino acid data support the conclusion from pyrolysis-gas chromatography-mass spectrometry analyses that *in situ* microorganisms are the primary source for the bulk of aquatic organic material. Furthermore, pyrolysis-GC-MS is a convenient technique for rapidly characterizing milligram samples of organic natural products. It is possible to differentiate the components in these heterogeneous polymeric materials and draw conclusions with regard to their source and history.

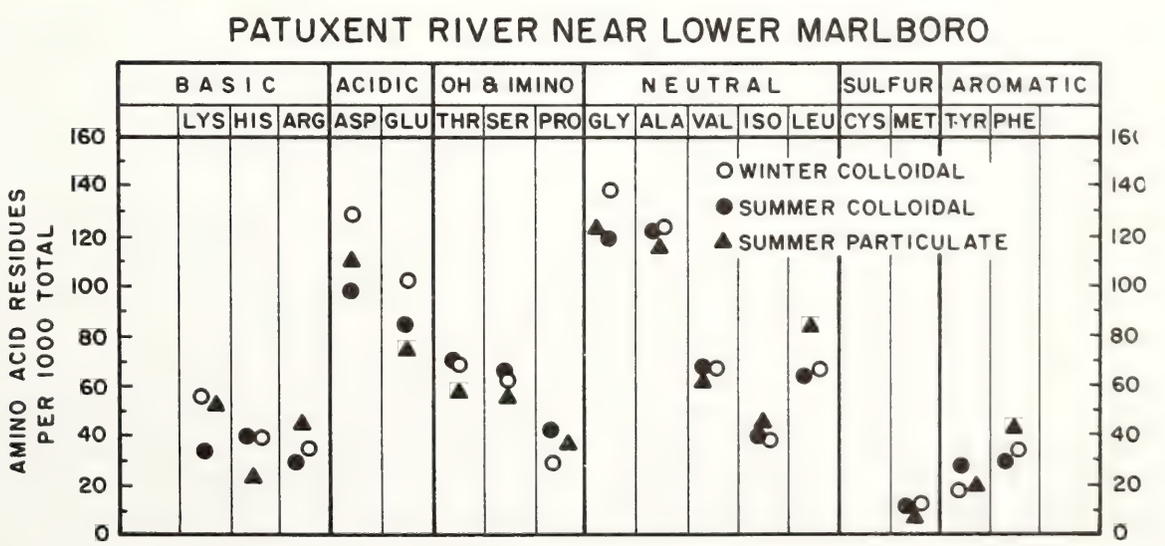


Fig. 74. Comparison of amino acid content of three samples from one station.

References

Hare, P. E., Subnanomole-range amino acid analysis, in *Methods in Enzymology, Vol. 47, Enzyme Structure, Part E,* C. H. W. Hirs and S. N. Timasheff, eds., Academic Press, New York, pp. 3-18, 1977.

Hedges, J. I., and P. L. Parker, Land-derived organic matter in surface sediments from the Gulf of Mexico, *Geochim. Cosmochim. Acta, 40,* 1019-1029, 1976.

Selective Absorption of Branched Hydrocarbons by a Synthetic Polymorph of Silica

Thomas C. Hoering

The molecular sieve Silicalite has been evaluated as a medium for selectively absorbing hydrocabron structural types. Silicalite is a proprietary name given to a new, synthetic polymorph of SiO_2 (Flanigen *et al.*, 1978). Among its many interesting features are channels of ellipsoidal cross section having axes of 5.1 and 5.7 Å units. The dimensions of these pores are slightly greater than those in the commonly used 5A molecular sieve, which is effective in selectively absorbing normal hydrocarbons, and are of the size needed to accommodate the bulkier 2-methyl (iso) and 3-methyl (anteiso) hydrocar-

bons. Molecular sieves and clathrating agents, such as synthetic zeolites, urea and thiourea crystals, and porous glasses and polymers, are useful for simplifying mixtures of organic compounds prior to analysis by gas chromatography and mass spectrometry.

The separation and identification of iso- and anteiso-hydrocarbons is the goal of this work. Such molecules have been described in crude oils, but have not been studied systematically because of the difficulty in isolating them. They are "molecular fossils" that reflect molecular structures in precursor living organisms (Tissot and Welte, 1978; Hunt, 1979). Lipids having mono-methyl branching at the 2 and 3 carbon atoms are minor components of most organisms, and branching at the 4, 5, and higher positions is rare, both in cells and in sedimentary organic matter. There are exceptions.

Iso- and anteiso-fatty acids, the precursors to hydrocarbons, are major constituents in a number of species of bacteria. These acids have carbon numbers ranging smoothly from about 14 to 20. The protective leaf waxes of many higher terrestrial plants contain methyl-branched hydrocarbons ranging from 27 to 33 carbon atoms, with those of odd number predominating (Polgar, 1971). Iso- and anteiso-hydrocarbons are potential tracers for the input of organic matter into sediments from these two different sources.

Pure, synthetic hydrocarbons are not readily available for evaluating the molecular sieve properties of silicalite; therefore, complex mixtures isolated from crude oils and a sediment extract were employed. Their sources were (1) the benzene-methanol extract of the Mahogany Ledge of the Eocene Green River shale, (2) a heavy, marine crude oil of Miocene age from the Los Angeles basin, and (3) a highly paraffinic, mature crude oil of Devonian age from the Bradford field of Pennsylvania.

The method developed in this study for isolating iso- and anteiso-hydrocarbons is shown in Table 39. The scheme links together several chromatographic and molecular-sieving techniques. The choice of the steps was governed by some general principles of separation science (Karger *et al.*, 1973). Processing of large amounts of material is possible in the first stages even though they yield only modest enrichments of the targeted compounds. As the separation proceeds and the product is concentrated, more specific methods with a higher resolution but a lower sample capacity are used to divide the sample into pure fractions. The gas chromatographic retention times and mass spectral fragmentation patterns of iso- and anteiso-hydrocarbons are characteristic, and combined gas chromatography–mass spectrometry was used to monitor the separation at each step.

The use of silica gel chromatography (step 1 of Table 39) and 5A molecular sieves (step 2) for isolating branched-cyclic hydrocarbons is well established (Murphy, 1969). Step 3 is new, and resulted in a major enrichment of the desired product. Two variations were used: batchwise absorption and molecular exclusion column chromatography. In the first, branched-cyclic hydrocarbons were dissolved in toluene and refluxed overnight with an excess of dried silicalite. The supernatent liquid was removed, and the solid was washed with hot toluene. The absorbed molecules were recovered by dissolving the silica in concentrated hydrofluoric acid and, after dilution, extracting them into pentane. Iso- and anteiso-hydrocarbons were completely absorbed and were major components of this fraction. Isoprenoid and polycyclic hydrocarbons were completely excluded. Some monocyclic and other acyclic hydrocarbons, however, followed the desired product. Both silicalite and urea selectively absorb hydrocarbons of a similar size and shape range, but the separations attainable with the first

TABLE 39. Flow Sheet for Separating Iso- and Anteiso-Hydrocarbons

Step	Material	Process	Typical Weight at Each Step
	Crude oil		10 grams
1	↓	Silica gel chromatography	
	Saturated hydrocarbons		3 grams
2	↓	5A molecular sieve absorption	
	Branched-cyclic hydrocarbons		2 grams
3	↓	Silicalite absorption	
	Mono-branched hydrocarbons		0.05 gram
4	↓ ↓ ↓	Gel permeation chromatography	
	$>C_{24}$ C_{24}-C_{20} $<C_{20}$		
	Iso- and anteiso-hydrocarbons		0.030 gram
5	↓ ↓ ↓ ↓ ↓ ↓ ↓ ↓ ↓ ↓ ↓ ↓ ↓	Preparative gas chromatography on a nonpolar substrate	
	Impure pairs of iso- and anteiso-hydrocarbons		Not determined
6	↓	Preparative gas chromatography on the polar substrate FFAP	
	Pairs of iso- and anteiso-hydrocarbons		0.001 to 0.002 gram of each pair

are better, as silicalite can be readily washed with organic solvents to remove loosely adhering material.

In order to improve the separation in step 3, a column of finely powdered silicalite, 240 mm long by 8 mm I.D., was prepared. The material was suspended in *n*-heptane, and a mixture of branched-cyclic hydrocarbons was injected. Most of the contaminants eluted rapidly with *n*-heptane, but the iso and anteiso compounds were retained. Continued elution removed them in a broad band, and only small amounts of monocyclic and other acyclic hydrocarbons were present. Minor amounts of normal hydrocarbons, incompletely removed in the preceding step of separation, remained on the column.

In the fourth step, gel permeation chromatography was explored as a means for isolating iso- and anteiso-hydrocarbons. A column of Sephadex-LH 20, expanded in 1/1 (V/V) benzene-methanol, was prepared. Hydrocarbons are eluted from this column in an order inverse to their molecular size, with the largest ones emerging first. Cyclic hydrocarbons, however, are retained more strongly than acyclic ones of corresponding molecular weights, and some separation and purification results. At this step the sample was fractionated into three parts containing iso- and anteiso-hydrocarbons: (1) with greater than 24 carbon atoms, (2) with 18–24, and (3) with less than 18.

At this stage, the enrichment of the desired products was a factor of at least 1000 above the crude starting material. The fifth step consisted of multiple, preparative gas chromatography on polar and nonpolar substrates. This method gives very specific separations, but was reserved as the final step be-

cause it is operable only on the milligram scale and necessarily divides the sample into many small fractions. Its success depends on the fact that monocyclic hydrocarbons are retained longer than acyclic ones of the same carbon number on the polar gas chromatographic substrate FFAP. Pairs of iso- and anteiso-hydrocarbons were isolated first, therefore, by preparative chromatography on the nonpolar substrate SE-30. Each of the fractions was then rechromatographed on an FFAP column. Although the procedure is tedious, excellent purification resulted. A gas chromatogram of one of the pairs of iso- and anteiso-hydrocarbons is given in Fig. 75. Even after the lengthy separation procedure, some contaminating acyclic material is still present. One to two milligrams of each of the pairs, covering a wide carbon-number range, was isolated.

The structural assignment of the hydrocarbons was proved by the use of the selected-ion-monitoring mode of the mass spectrometer data system. Isoalkanes (2-methyl) give a mass spectrometric fragmentation pattern having a major ion at a mass 43 less than the parent ion (loss of an isopropyl group). Anteiso alkanes (3-methyl) have a major fragment at 29 mass units less than the parent ion (loss of an ethyl group). Mass chromatograms of the individual pairs of products had the appropriate ion at the proper gas chromatographic retention time.

The 3-methyl hydrocarbons can exist as enantiomers (optical isomers). The number three carbon in the chain is substituted by four nonequivalent groups: a hydrogen, a methyl, an ethyl, and a long-chained alkyl group. A glass capillary column coated with the chiral substrate Chirasil-Val was used to attempt to resolve 3-methyl compounds by gas chromatography. This column effectively separates enantiomeric derivatives of amino acids, but no resolution of either synthetic hydrocarbons or the natural materials was observed.

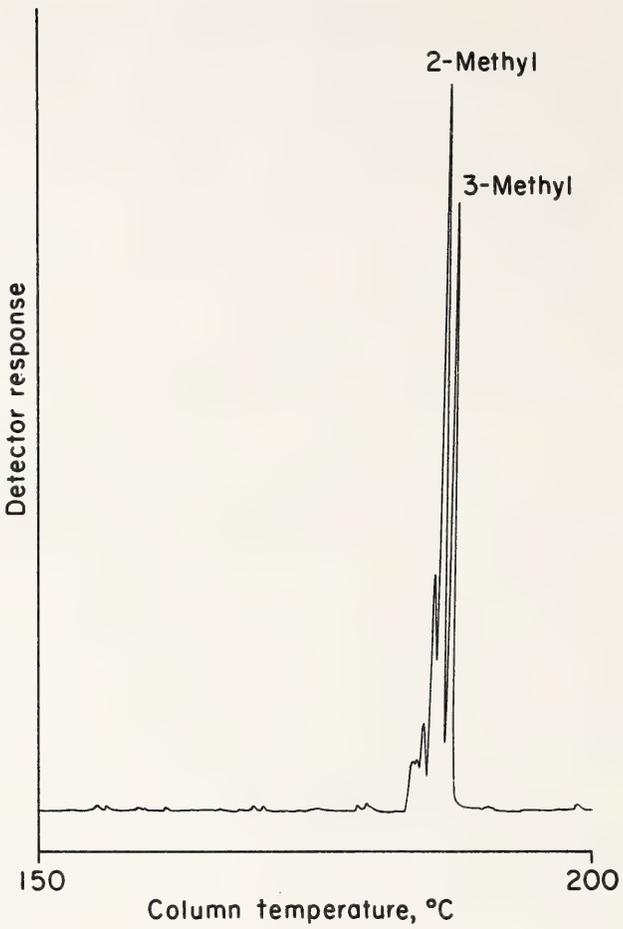


Fig. 75. Gas chromatogram of 2-methyl and 3-methyl octadecane in a Miocene crude oil from the Los Angeles basin. A 100-ft by 0.010-inch capillary column coated with OV-101 was used at 30 psi helium. The column temperature was programmed up from 150°C at a rate of 2.5° per minute. The impurities eluting before the 2-methyl isomer are due to di-branched, acyclic hydrocarbons.

The latter separation is expected to be difficult, and further progress will have to await the development of chiral phases that operate efficiently on hydrocarbon molecules.

Iso- and anteiso-hydrocarbons are minor constituents in the three widely differing geological samples examined in this study. They have a distribution of carbon numbers with no obvious even or odd preference. The 2-methyl isomer is more abundant than the 3-methyl. All three materials have hydrocarbons in the range 14 to 24 carbon atoms, perhaps indicating a bacterial source, but the Green River

shale has hydrocarbons up to 30 carbon atoms. A contribution from plant waxes is indicated in the latter case. This conclusion is consistent with the lacustrine origin of the Green River shale. Quantitative estimation is difficult, but the iso- and anteiso-hydrocarbons are of the order of 50 to 100 parts per million of the starting crude oils.

The potential of silicalite for separating branched hydrocarbons and the possibilities of using these organic molecules as tracers for bacterial and plant wax lipids have been demonstrated. The low abundance of these compounds and the difficulty of satisfactorily separating them by the present procedures, however, limit geochemical application. The development of an efficient, high-pressure liquid chromatographic column of silicalite, to be used as a molecular exclusion medium, may result in a more attractive method with the separation scaled down considerably in size.

References

Flanigen, E. M., J. M. Bennett, R. W. Grose, J. P. Cohen, R. L. Patton, R. M. Kirchner, and J. V. Smith, Silicalite, a new hydrophobic, crystalline, silica molecular sieve, *Nature, 271,* 512–517, 1978.

Hunt, J. M., *Petroleum Geochemistry,* W. H. Freeman and Co., San Francisco, 1979.

Karger, B. L., L. R. Snyder, and C. Horvath, *An Introduction to Separation Science,* John Wiley and Sons, Inc., New York, 1973.

Murphy, M. T. J., Analytical methods, in *Organic Geochemistry,* G. Eglinton and M. T. J. Murphy, eds., Springer Verlag, Berlin and Heidelberg, pp. 74–88, 1969.

Polgar, N., Natural alkyl-branched long-chain fatty acids, in *Topics in Lipid Chemistry, Vol. 2,* F. D. Gunstone, ed., Wiley-Interscience, New York, pp. 207–246, 1971.

Tissot, B. P., and D. H. Welte, *Petroleum Formation and Occurrence,* Springer Verlag, Berlin and Heidelberg, 1978.

Organic Geochemical Studies in Spitsbergen with a Field-Portable, High-Performance Liquid Chromatograph

*P. E. Hare and G. H. Miller**

The use of amino acid ratios in fossil mollusc shells has developed into a useful tool for stratigraphic correlation and relative age dating of fossils (Miller and Hare, 1980). Natural diagenesis of the shell matrix proteins yields free amino acids and results in the racemization of L amino acids into mixtures of both D and L isomers. In modern shells, the matrix proteins are intact and no significant levels of free amino acids are observed. In progressively older fossils, increasing amounts of free amino acids (relative to total amino acids) are observed as well as increasing ratios of D to L amino acids. In limited geographical areas where temperature effects are minimized, it is observed that the general level of free amino acids and the ratio of D-alloisoleucine to L-isoleucine is sufficient to distinguish the relative age of the fossil and hence the stratigraphic sequence of the deposit.

It is often desirable to obtain data on the relative age of fossils directly "on the spot" in the field. Contamination problems during storage and transportation to the laboratory are eliminated. (Frequently it is not possible to return later to an outcrop.) A most important factor in obtaining data directly in the field is the guidance such data can provide for day-to-day field operations.

In recent years amino acid analysis has become sensitive and rapid enough for use in the field at the time of sample collection. A prototype, field-portable, amino acid analyzer was constructed at the Geophysical Laboratory and tested during the 1979 field season of the University of East Anglia and the University of Colorado project in Spitsbergen.

*Institute of Arctic and Alpine Research, University of Colorado, Boulder, Colorado.

The field instrument was scaled down from the laboratory instrument described earlier (Hare, 1977) and the following commercially available components were used: (1) an Eldex minipump capable of 5000 psi operation, (2) an Aminco fluoromonitor, (3) a Valco injector valve, and (4) a Soltec battery-operated two-pen recorder. Buffer changes were made manually and *o*-phthalaldehyde reagent was used to detect the amino acids eluted from the 0.2 × 20 cm column of DC-4a cation-exchange resin. Column temperature was controlled by an RFL Industries model 70A controller. Typical operating parameters were column temperature, 60°C; flow rate, 12 ml/hr; pressure, 2000 psi. Total analysis time including sample preparation was under 30 min.

The measurement of free amino acids and the ratio of D-alloisoleucine to L-isoleucine can be obtained from a few milligrams of shell material. These measurements require no hydrolysis in 6N HCl (to yield total amino acids), and sample preparation is greatly simplified. An excess of shell material is mechanically cleaned and prepared for treatment. Solution of an aliquot of shell with enough 6N HCl to dissolve a known amount of $CaCO_3$, followed by dilution with H_2O, takes only a few minutes and requires no sample weighing. A micropipette is adequate for measuring volumes quickly and accurately.

The portable amino acid analyzer was set up in a trapper's small hut near Aavatsmarkbreen, a large outlet glacier 40 km south of Ny Aalesund on West Spitsbergen. A gasoline-powered generator supplied the electrical power needed. Extensive wave-eroded sections up to 30 m high have been described from this locality by Boulton (1979) and R. W. Feyling-Hanssen (unpublished manuscript). A range of nearshore and deeper water marine facies are present in the exposed sections, with molluscs present in most beds. A schematic representation of the stratigraphy is shown in Fig. 76. Available ^{14}C dates range between 9,000 and 15,000 YBP for the younger beach sequences to >40,000 YBP for the intermediate-age marine units (Boulton, 1979). The dates and elevations of samples from the younger beach sequence do not fit a simple glacio-isostatic recovery model and are substantially older than other late glacial dates from the archipelago. The shell ^{14}C dates in the 30,000–40,000 year range should probably be regarded as minimum estimates owing to problems of exchange with younger carbon. The site provided some specific problems that might be resolved by the amino acid method, aside from the possibility of stratigraphic correlation with other sites in Spitsbergen.

Analyses were carried out on the common marine pelecypod *Mya truncata*. To calibrate and establish a framework by which to interpret the amino acid results, paired valves of a modern and a known early Holocene *Mya* were analyzed. In both cases, no detectable alloisoleucine was present, but the levels of free amino acids were significantly higher in the early Holocene shells. *Mya* from deposits underlying the Holocene beach sequence yielded substantially higher levels of free amino acids and allo-iso ratios between 0.2 and 0.5 (see Fig. 76).

The early Holocene beach gravels in section 1 (unit 8) yielded only fragmented shells. These collections contained both highly abraded, thick shell fragments and relatively unabraded, generally thinner fragments. The mixture suggested the possibility that these collections contained populations of more than one age and that the resulting ^{14}C age was in fact a composite "age." To test this hypothesis, both abraded and unabraded fragments were analyzed. Because of the high sensitivity of the amino acid analyzer, it was necessary to take only a small portion of each fragment. The allo-iso ratio was

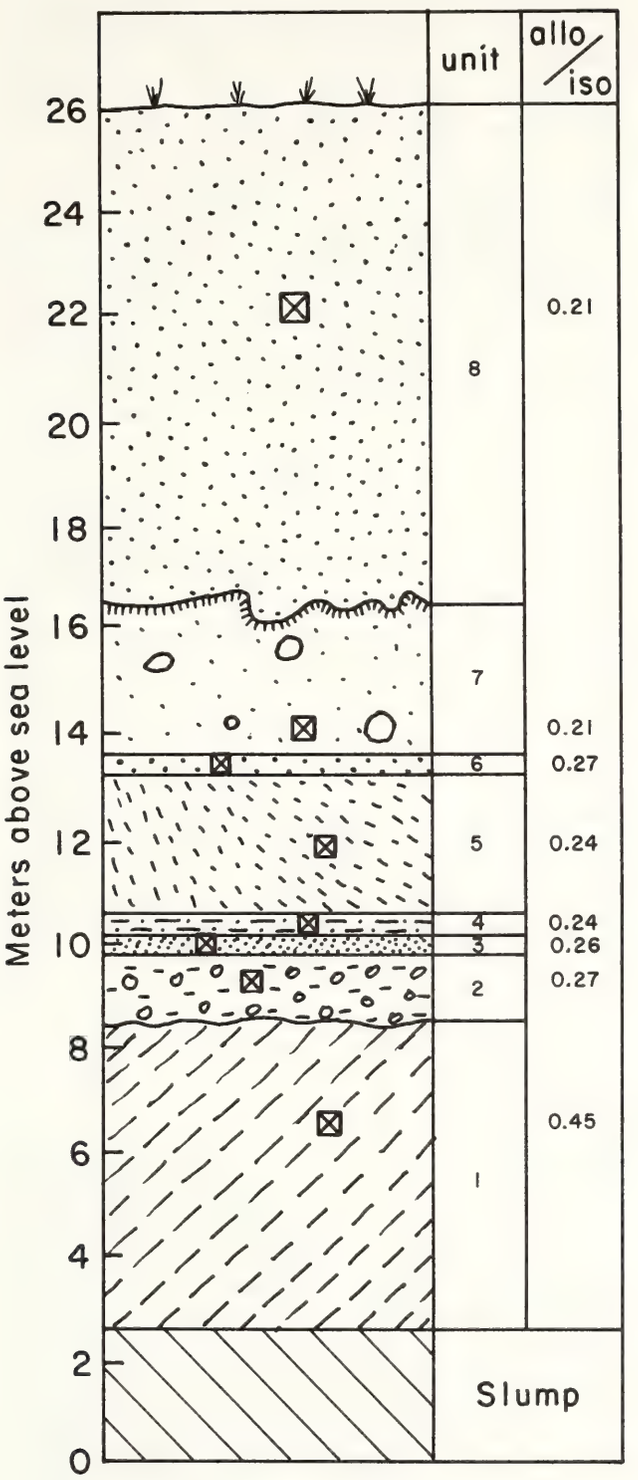


Fig. 76. Generalized stratigraphy at Aavatsmarkbreen, West Spitsbergen: Unit 1, massive, pebbly silt with erosional unconformity and possible paleosol at top; unit 2, blue-gray stoney, clayey silt, striated clasts, shell fragments; unit 3, stratified coarse sand, shell fragments; unit 4, sandy silt with shell fragments; unit 5, sorted fine sand, abundant whole shells; unit 6, silty gravel, angular shell fragments; unit 7, cobble-sand, abundant paired valves, cryoturbated soil at top; unit 8, gently dipping sand and gravel with interbedded sandy-silt lenses, shell fragments. Isoleucine epimerization ratios (allo-iso) in the free amino acids in *Mya* listed on right-hand side, as measured in the field. Unit 8 also has shells with no detectable alloisoleucine, indicative of its early age.

0.21 in an abraded shell, whereas an unabraded fragment yielded much lower levels of free amino acids and no detectable alloisoleucine. The anomalously old ^{14}C dates were obtained on fragments of diverse species from the same beds. The amino acid results strongly suggest that the ^{14}C measurements were made on a mixed population containing both early Holocene and much older (>35,000 YBP) shells. If the age of the shells is about 10,000 YBP, then a mixture of 30% to 50% "old" shells would yield apparent ages similar to those reported by Boulton (1979, Appendix 1). The early Holocene sea-level rise in this area transgressed across sediments known to be >30,000 years old, and the incorporation of older shells into the younger beaches is to be expected and has been observed elsewhere.

The pattern of amino acid ratios in section 1 is supported by the observed lithostratigraphic changes. A major depositional hiatus is indicated by the soil and extensive cryoturbation between units 7 and 8, and also is coincident with a marked increase in the degree of racemization. Ratios increase only slightly between units 7 and 2, indicating a relatively short depositional interval, whereas another major increase occurs across the boundary of units 1 and 2.

Samples from exposed sections 10–40 km south of Aavatsmarkbreen were also analyzed. The data suite (Table 40) suggests that at least four major depositional intervals are present along this portion of West Spitsbergen.

A collection of shells from Hermansøya, 40 km south of Aavatsmarkbreen, was initially interpreted to represent pre-Holocene deposition. Repeated amino acid analyses of the shells, however, indicated an early

TABLE 40. Amino Acid Chronozones for Quaternary Deposits in the Aavatsmarkbreen Area

Allo/Iso	Not detectable	0.21 to 0.27	0.38	0.43 to 0.45
Group	1	2	3	4
No. of measurements	8	14	1	2

Holocene age. More detailed investigations of the site at the end of the field season revealed stratigraphic complexities not previously noted in the earlier visit, and confirmed a Holocene age for the analyzed shells.

The portable amino acid analyzer can be used for obtaining independent chronologic information during field studies. Such data are particularly useful in directing attention to complexities in the lithostratigraphy of sampled sections and providing a local chronostratigraphic framework.

Further improvements in instrumentation have resulted in the construction of a more compact unit to be used for the coming field season. Other applications of a field-portable liquid chromatograph are feasible; for example, shipboard analysis of deep sea cores and water samples where contamination problems make it desirable to analyze the samples as soon as possible after collection.

References

Boulton, G. S., Glacial history of the Spitsbergen archipelago and the problem of a Barents Shelf ice sheet, *Boreas, 8,* 31–57, 1979.

Hare, P. E., Subnanomole-range amino acid analysis, in *Methods in Enzymology, Vol. 47, Enzyme Structure, Part E,* C. H. W. Hirs and S. N. Timasheff, eds., Academic Press, New York, pp. 3–18, 1977.

Miller, G. H., and P. E. Hare, Amino acid geochronology: integrity of the carbonate matrix and potential of molluscan fossils, in *Biogeochemistry of Amino Acids,* P. E. Hare, T. C. Hoering, and K. King, Jr., eds., John Wiley and Sons, Inc., New York, pp. 415–443, 1980.

NEW TECHNIQUES

High-Temperature, Diamond-Anvil Pressure Cell for Single-Crystal Studies

R. M. Hazen and L. W. Finger

Crystallographic studies under nonambient conditions are essential to an understanding of the solid state. A knowledge of atomic structures at high temperatures and pressures is especially crucial to realistic modeling of geological processes. Advances in high-temperature crystallography at room pressure and high-pressure crystallography at room temperature have been rapid and encouraging (Finger and Hazen, 1979). Simultaneous application of high temperature and pressure to a single crystal in an x-ray diffraction experiment, however, has proved to be more difficult.

Several experimental problems must be overcome in a high-temperature, high-pressure, single-crystal experiment. The crystal must remain in a fixed orientation with respect to the high-pressure cell, in order to maintain crystal alignment. The crystal must be in a hydrostatic environment to prevent crystal strain. The crystal must be heated as uniformly and to as high a temperature as possible without significant heating of the x-ray diffraction equipment. The cell must be easily adapted to standard, single-crystal, x-ray devices, including precession cameras and four-circle diffractometers. A procedure for calibrating both temperature and pressure of the sample is also essential. A simple and relatively inexpensive, high-temperature, diamond-anvil, high-pressure cell (here-

after referred to as the *PT* cell) that meets all the above criteria is described below.

Construction of the PT *Cell*

The following design is based on the widely used high-pressure, single-crystal x-ray cell of Merrill and Bassett (1974). The cell consists of five major components: triangular steel supports, boron carbide disks, pyrophyllite insulating rings, a resistance heater, and two gem-quality diamond anvils.

Triangular steel supports are identical with those used in the modified Merrill and Bassett cell described by Hazen and Finger (*Year Book 76,* 655–656). These two supports act as the framework that holds the diamonds rigidly together in proper alignment.

Disks of boron carbide are used in place of the beryllium disks in the room-temperature cell because of the softening of Be metal at temperatures above 100°C. Unlike the Be disks in room-temperature experiments, there are no holes in the center of the disks, and there is no optical access to the sample chamber. This restriction is necessitated because boron carbide is weakened by the presence of a hole.

Diamond anvils are identical with those used in the room-temperature device. Each diamond is approximately 10 points (1/10 carat) in weight, with an anvil face 0.5–1.0 mm in diameter. The greatest restriction on the temperature range of the diamond cell is the thermal instability of diamonds themselves. At approximately 700°C diamonds oxidize in air, and at temperatures as low as 800°C in an inert atmosphere they graphitize (H. K. Mao, personal communication).

A miniature resistance element is used to concentrate heat at the sample without excessive heating of the surrounding instrumentation. The heating element is a Pt-Pt10Rh thermocouple wire with the junction in the center of the winding. The furnace is operated in the manner described by Ohashi and Hadidiacos (*Year Book 75,* 828–829), in which power is applied to the winding during half of the cycle of the alternating current power source. The electromotive force of the thermocouple junction is sensed during the other half of the cycle and is thus used to control power to the furnace. Two pyrophyllite rings fit around the boron carbide disks and the heating element to add thermal insulation to the cell.

Several additional pieces are required for assembly of the *PT* cell. Two mica-sheet insulating washers fit into the circular wells of the triangular supports to provide additional thermal insulation. Three Allen cap screws are used to clamp the two halves of the cell together. Two Belleville spring washers are inserted next to each of the three screw heads. These washers are important in applying force to the diamonds. Without these washers, which are outside the triangular supports and thus cooler than other cell components, the three screws relax owing to heating at high temperature, and the pressure is reduced. A metal gasket is constructed from Inconel 750X (International Nickel Company) foil 250 μm thick. The gasket hole is approximately 300 μm in diameter.

Assembly of the PT *Cell*

The assembly of the *PT* cell is illustrated in Fig. 77. Each diamond is mounted with an epoxy-type cement at the center of a boron carbide disk. The disks with diamonds are placed inside the two insulating pyrophyllite rings, which are in turn placed in the circular wells of the triangular steel supports. Each half of the *PT* cell is then further insulated by applying Saureisen high-temperature cement to spaces around the pyrophyllite rings. The gasket is centered over the lower diamond and secured to it by a small dot of epoxy cement. The heater assembly is placed

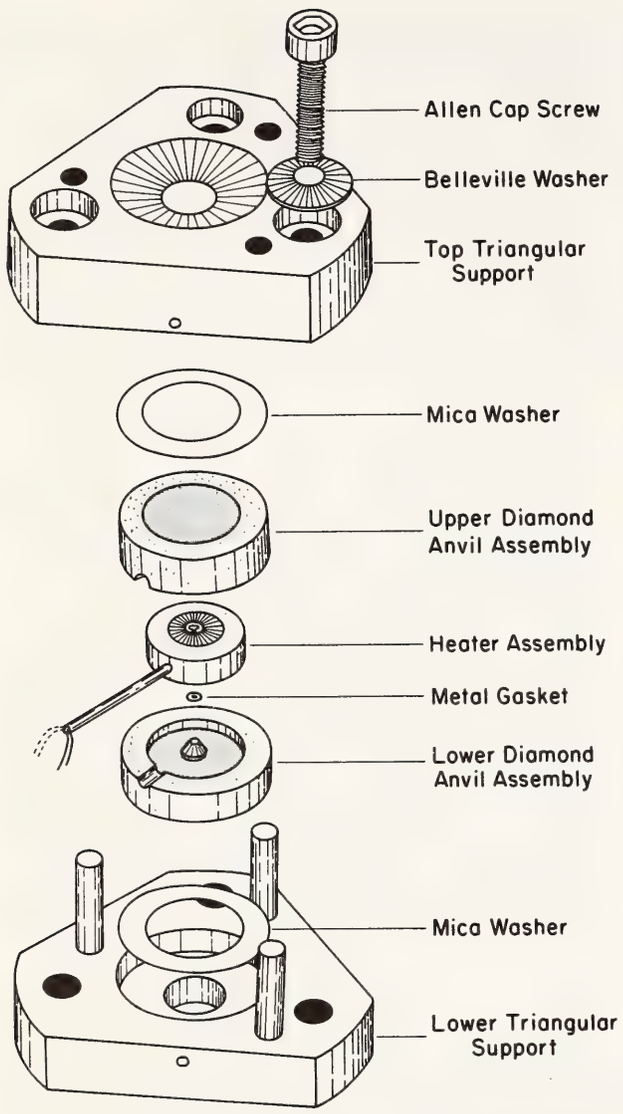


Fig. 77. Exploded view of the *PT* cell assembly. Pyrophyllite components are stippled.

around the diamond and gasket of the lower cell half and is fastened to the insulating pyrophyllite disk with Saureisen cement.

The single crystal is mounted in the center of the gasket, using a small amount of silicone vacuum grease as "glue." This grease keeps the crystal in a near-constant orientation with changes in temperature and pressure, yet does not cause crystal strain as observed in stronger glues such as epoxy-type cements. The gasket hole is filled with a pressure fluid such as index-of-refraction oil, and the two halves of the cell are closed together.

The fully assembled *PT* cell may be attached to a modified goniometer head and used on both single-crystal cameras and four-circle diffractometers. The goniometer cradle for the *PT* cell was constructed from fire-hardened pyrophyllite for thermal insulation.

Operation of the PT *Cell*

The *PT* cell is used in much the same way as the room-temperature device. The cell fits on a standard precession camera; only the beam stop needs to be modified to fit around the assembly. As in the cell with beryllium disks, MoK_α radiation should be used owing to high absorption of longer wavelengths. Major diffraction effects on x-ray films include diamond streaks, boron carbide powder rings, and sharp diffraction maxima from the single crystal under study.

Four-circle diffractometry procedures for the *PT* cell are much the same as those for the room-temperature cell. As in room-temperature diamond-cell experiments, the measured intensity data as well as the crystal itself must be corrected for absorption by boron carbide and diamond components of the cell.

The cell was calibrated for temperature against the expansion of NaCl, MgO, and CaF_2. All three calibrations agreed within ± 5 °C at temperatures to 450 °C, the highest temperature attempted. The temperature of subsequent experiments is set by presetting the feedback controller to the desired thermocouple electromotive force.

Pressure at high temperature is estimated by measuring the cubic cell edge of CaF_2. Calcium fluoride is an excellent x-ray scatterer and forms flat triangular (111) cleavage plates that remain parallel to one diamond face. This calibration crystal, which is mounted in each run, thus provides an internal standard. The equation of state of CaF_2 at high temperature and pressure

is not yet well known, but by reporting the cell edge of CaF_2 at a known temperature, a relative (semiquantitative) calibration is provided that may eventually be converted to a more precise pressure and temperature calibration when the effects of temperature on CaF_2 compression are known. The *PT* cell has achieved sustained temperatures up to 450 °C and pressures up to 40 kbar. Experiments on the crystal structures of minerals and *P-T-V* equations of state under these conditions are now in progress.

References

Finger, L. W., and R. M. Hazen, Response of oxygen-based structures to changes in pressure, temperature and composition, *Trans. Amer. Crystallogr. Assoc., 15,* 93–105, 1979.

Merrill, L., and W. A. Bassett, Miniature diamond anvil pressure cell for single crystal x-ray diffraction studies, *Rev. Sci. Instrum., 45,* 290–294, 1974.

Design and Operation of a Diamond-Window, High-Pressure Cell for the Study of Single-Crystal Samples Loaded Cryogenically

H. K. Mao and P. M. Bell

Modifications of the high-pressure, diamond-window cell are required for studies of single crystals of materials that normally exist as gases under ambient room temperatures and pressures. This type of sample can be loaded into the cell as a fluid at cryogenic temperatures and then pressurized at room temperature for study as single crystals by x-ray diffraction and infrared and Raman spectroscopy.

In addition to the intrinsic value of studying solidified gases at ambient temperature, their high compressibility in certain pressure ranges is a valuable property when they are employed as pressure-transmitting media for materials with low compressibility being studied at high pressure. Further, the calibrated compressibility and melting curves of solidified gases can be referenced for pressure calibration.

In this report, a modified high-pressure cell is described that is operable mechanically in the temperature range approximately 4–298 K (the pressurized sample can be heated independently from the cell itself to above 3000 K by a focused laser beam; see *Year Book 74,* 399–402).

The basic principles of this cell are almost the same as for the one described by Merrill and Bassett (1974), although the required modifications are rather extensive. Metallic parts of the cell shown in Fig. 78 (except parts 3, 5, 7, 9, 15) are made of maraging steel (Vascomax-50, Vanadium Corporation of America) because of its strength at cryogenic temperatures. The diamond anvils (parts 3) are cemented to Be disks with a very strong, low-temperature epoxy cement (Stycast-2850FT, Emerson and Cuming, Inc.). The Be disks are centered by set-screws (parts 6).

This cell has two circular end-plates (parts 1 and 2) guided into position by parts 10 and 11 as the lead screws (parts 12 are right-handed; parts 13 are left-handed) are advanced and the stainless steel Belleville springs (parts 15) are compressed. In Fig. 78, the relative position of the indicator grooves (14) on the screw heads is calibrated against sample pressure before the experiment, so the cell can be operated remotely in a liquid helium Dewar (see *Year Book 78,* 662).

The cell can be held on a standard goniometer head for mounting in an x-ray diffraction apparatus (see the notch at 16, Fig. 78). The diffracted beam exits from a 60° cone cut into an end-plate (Fig. 78, part 17).

Before an experiment can be run, the sample chamber of the gasket (Fig. 78, part 7) must be predrilled (diameter less than half the culet-free diameter) and positioned. At this stage in the procedure a few grains of fine ruby

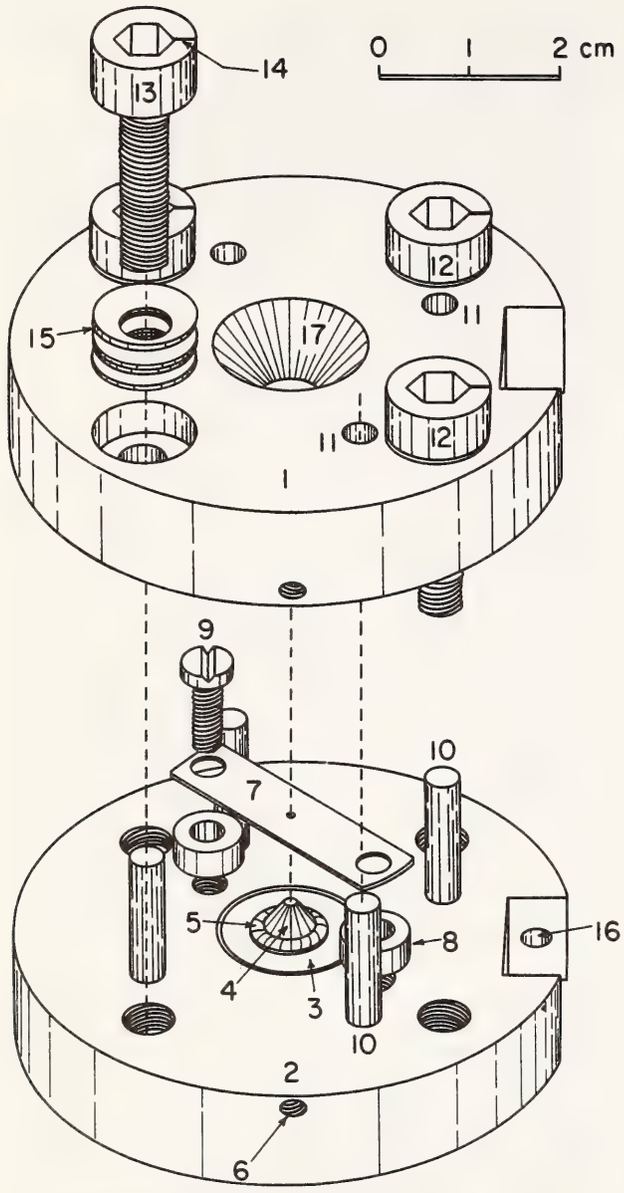


Fig. 78. Modified diamond-window, high-pressure cell for study of single crystals of solidified gases. Parts: 1, 2, end plates; 3, Be support disks; 4, diamond anvils; 5, epoxy cement; 6, set screws for adjusting part 5; 7, gasket; 8, spacers; 9, screw; 10, positioners; 11, hole for positioners; 12, 13, screws for raising sample pressure; 14, groove; 15, Belleville springs; 16, mounting notch.

powder are placed on the lower diamond culet face (with a sample crystal if the solidified gas is to be used as a pressure-transmitting medium). The end-plates (Fig. 78, parts 1 and 2) are positioned and adjusted to leave gaps of 0.2 mm between the diamond faces and the gasket piece (Fig. 78, part 7).

The cell is shown in Fig. 79, prepared for immersion in a cryogenic Dewar. Note that the cell has been placed in a metal cup (Fig. 79, part 4) and that a feeder tube (Fig. 79, part 6) has been positioned so gas can be pumped into the cell. Metal pieces (Fig. 79, parts 5) are constructed to fit empty spaces between parts 4 and the cell. Parts 7 in Fig. 79 are 2-m extensions for advancing the screws (Fig. 79, parts 8) from outside the Dewar.

The first step of an experiment is to flush the cell with the gas to be contained as the cell is lowered along the vertical temperature gradient in the Dewar. Thermocouples, not shown in Fig. 79 (see *Year Book 78*, 662), are used to indicate the temperature. The empty space in the cell is approximately 1 ml, which to be filled with liquified gas will require approximately one liter of the gas at STP. Usually the cell is overfilled by a factor of three (excess spills out and solidifies when it contacts liquid He at the base of the Dewar). Approximately three liters of liquid He is used for each filling.

When the cell is filled with liquified gas, the screws are rotated to prede-

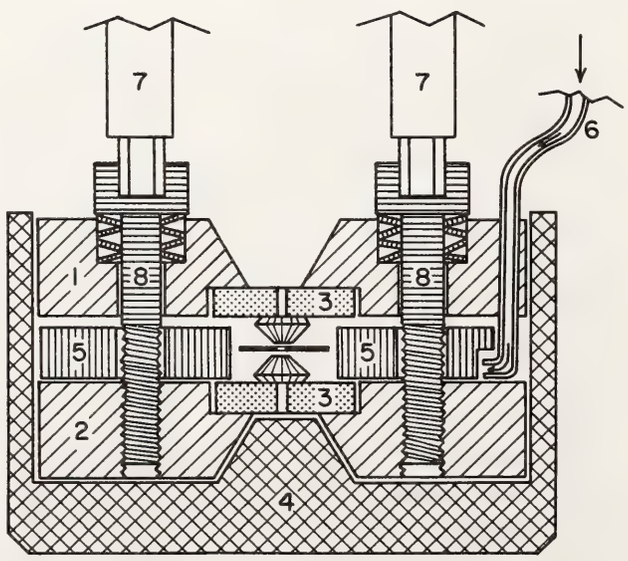


Fig. 79. Cross section of pressure cell ready for experiment. Parts: 1, 2, end plates; 3, Be supporting disks; 4, cup; 5, spacers; 6, gas tube; 7, extensions for rotating screws (8).

termined positions to seal the sample chamber and to raise the sample pressure to approximately 10 kbar. After the chamber is sealed the cell can be directly removed from the Dewar and warmed to room temperature with a hot-air blower. The pressure of the sample can then be adjusted and measured before it is mounted on x-ray diffraction or other spectral apparatus.

Reference

Merrill, L., and W. Bassett, Miniature diamond anvil pressure cell for single crystal x-ray diffraction studies, *Rev. Sci. Instrum., 45,* 290–294, 1974.

Experiment for *in situ* High-Pressure, Light-Scattering Measurements

H. K. Mao and P. M. Bell

Elastic properties of materials of geological and planetary interest can be obtained at high pressure by employing the direct relationship of Brillouin phonon scattering with acoustic velocity. Interferometric observations of Bragg-scattered photons are made of samples contained in a diamond-window, high-pressure cell (Whitfield *et al.,* 1976). This report is a description of an improved high-pressure cell designed for higher pressures and modified so that acoustic velocity can be measured independently from the index of refraction of an isotropic crystal under pressure. With this apparatus, one can study unoriented crystals grown in the cell and determine angular dependence of acoustical properties. The geometric relations needed to utilize the modified cell are derived herein for optically isotropic materials.

It was necessary to modify the pressure cell so that the incident and the scattered light beam directions could be specified. This requirement for experiments at high pressure can be met by designing in the pressure cell suitably located ports arranged to be consistent with crystal symmetry and with optical properties of the diamond windows. In addition to Brillouin scattering, the design may also be useful for measurements of Raman spectra of materials at high pressure in other than conventional directions (i.e., forward and backward; see Sharma, *Year Book 78,* 660–665) in the diamond cell to obtain the dependence of Raman spectra on scattering direction, and to minimize laser-induced fluorescent effects that originate in the diamonds.

Design of the special pressure cell is shown in Fig. 80. Special ports are positioned for transmitted and scattered light (see vector directions) that result in a total of eight independent directions.

Brillouin-Scattering Geometry

The Doppler shift of light, Bragg-scattered from a thermal phonon, is given by

$$\Delta\nu = (2nV\cos\beta)/\lambda, \text{ or} \qquad (1)$$

$$V = \lambda\Delta\nu/(2n\cos\beta), \qquad (2)$$

where n is the refractive index of the sample, V is the phonon velocity, λ is the laser wavelength, and 2β is the angle between the incident and scattered beams within the sample. Figure 81 shows a diagrammatic sketch of Brillouin-scattering geometry in the pressure cell (in principle, after Whitfield *et al.,* 1976). The parallelism of the horizontal surfaces of the diamonds is within two minutes of arc; thus their refractive effects cancel.

Acoustic Velocity Directions within the xy Plane

Figure 82 is a diagram of the paths and angles of the incident and scattered beams. It is apparent from the

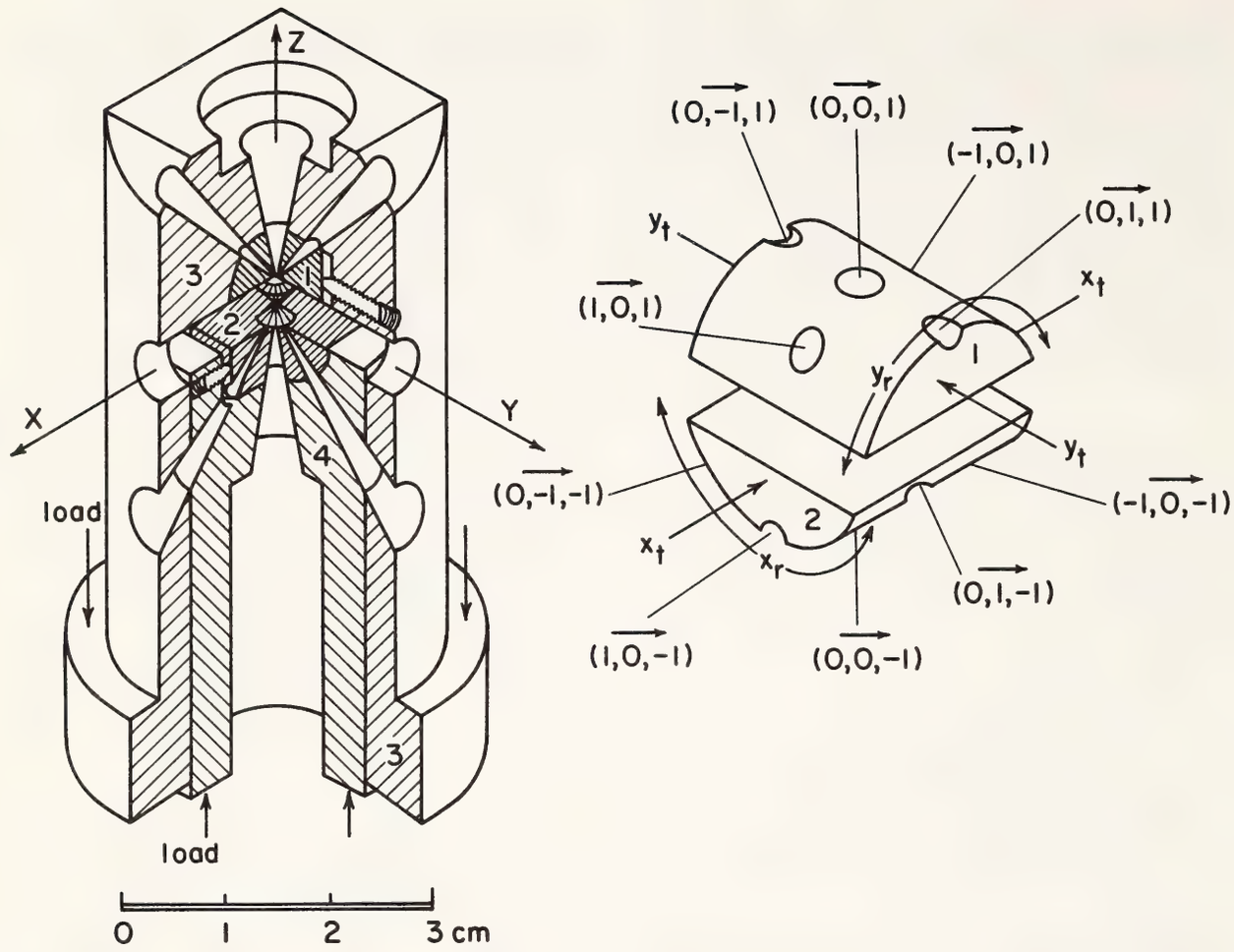


Fig. 80. Sectional view of the diamond-window, high-pressure cell with ports for use in light-scattering measurements. (Exploded view to the right shows the ports and their geometric direction indices in the tungsten carbide "rockers," parts 1 and 2.)

geometric relationships that for isotropic substances

$$\cos \alpha = \cos \psi \sin \Theta, \tag{3}$$

$$\cos \beta = \cos \psi \sin \Phi = \cos \alpha \sin \alpha / \sin \Theta, \tag{4}$$

and by combination of Snell's law,

$$\cos \beta = \cos \alpha / n, \tag{5}$$

with Equation 2,

$$V = \lambda \Delta \nu / (2 \cos \alpha). \tag{6}$$

$\vec{V}$ is the bisector of angle 2ψ, in the plane M. The advantages of this relation is evident in that V is determined simply by measuring $\Delta\nu$ independent of n. The relation is general for any α; however, in the present design the velocity in the $(\overrightarrow{1,0,0})$ direction of an oriented crystal in the cell (see Fig. 80) can be measured with apertures $(\overrightarrow{1,0,1})$ and $(\overrightarrow{1,0,-1})$, both in the xz plane. This set is equivalent to the directions used by Whitfield *et al.* (1976). In these instances, where $\psi = 0°$, $\alpha = \Theta = 45°$, the two velocity directions $(\overrightarrow{1,0,0})$ and $(\overrightarrow{0,1,0})$ can be determined by the following relationship:

$$V = \lambda \Delta \nu / \sqrt{2}. \tag{7}$$

For the veolcity directions $(\overrightarrow{1,1,0})$ and $(\overrightarrow{1,-1,0})$ (in the xy plane) the aperture pairs $(\overrightarrow{1,0,1})$ + $(\overrightarrow{0,1,-1})$ and $(\overrightarrow{1,0,1})$ + $(\overrightarrow{0,-1,-1})$ are utilized, where $\psi = 45°$, $\alpha = 60°$ and

$$V = \lambda \Delta \nu. \tag{8}$$

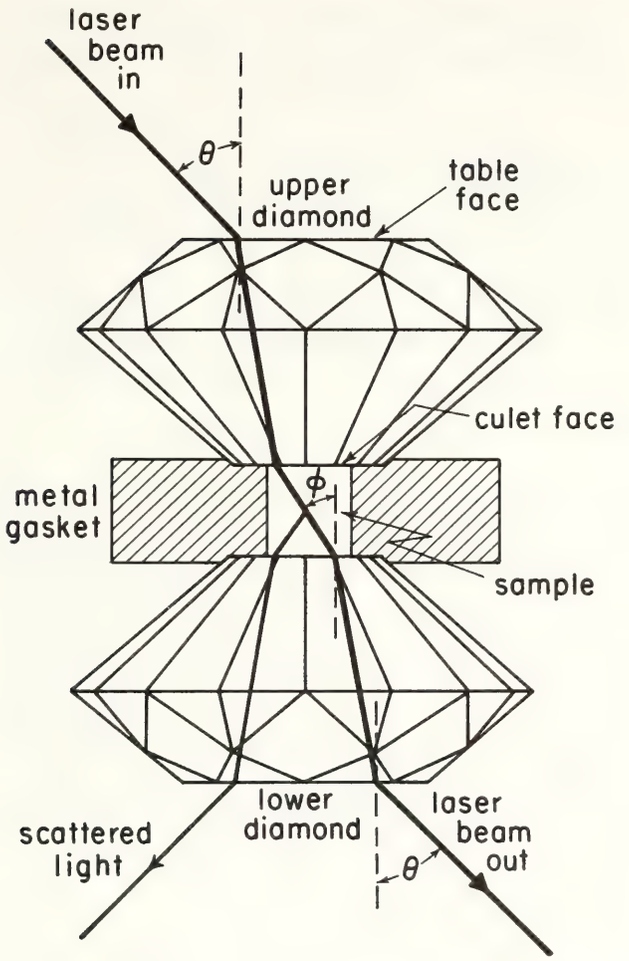


Fig. 81. View of incident light beam and photon-scattered light through a sample under pressure in the cell. Geometric relations between the incident laser beam, the cylindrical-shaped sample in the pressure cell, and the scattered beam for velocity direction V in the xy plane (see Fig. 80).

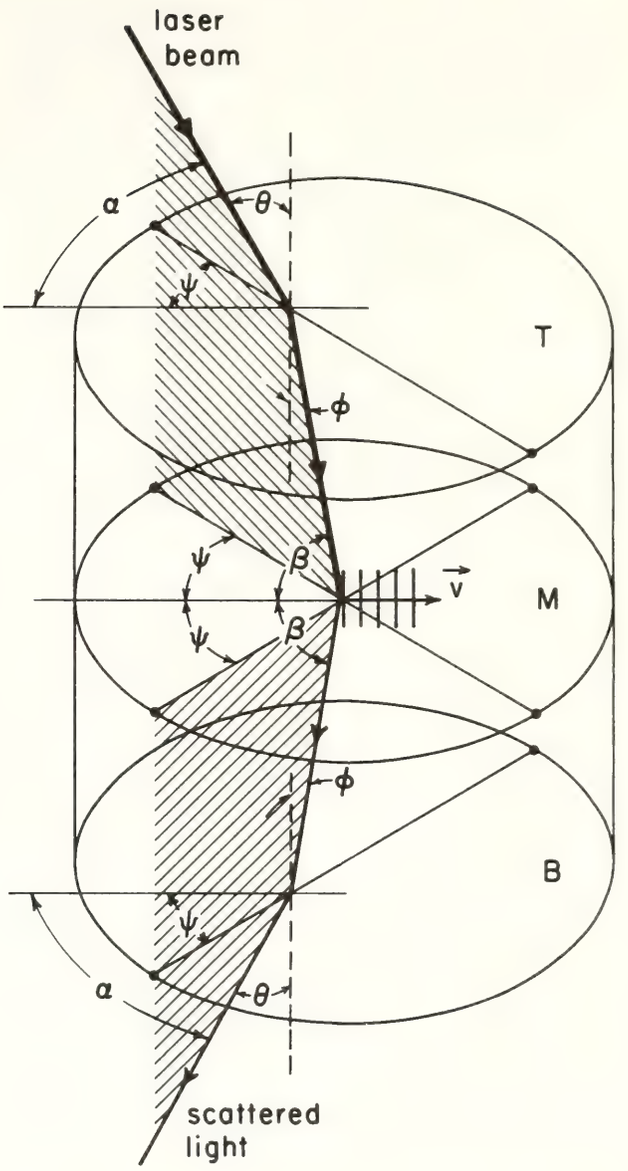


Fig. 82. Geometric relations between the incident laser beam, the cylindrical-shaped sample in the pressure cell, and the scattered beam for velocity direction V in the xy plane (see Fig. 80).

Acoustic Velocity Directions Out of the xy Plane

For velocity measurements out of the xy plane (i.e., out of the plane parallel with the diamond pressure faces) directions of the type shown in Fig. 83 are utilized. The geometric relations are

$$\sin \alpha = \cos \psi \sin \Theta \qquad (9)$$

$$\sin \beta = \cos \psi \sin \Phi. \qquad (10)$$

By combination of Snell's law,

$$\sin \beta = \sin \alpha / n \qquad (11)$$

$$\cos \beta = (n^2 - \sin^2 \alpha/n)^{1/2}, \qquad (12)$$

and Equation 2, the velocity is given by

$$V = 1/2\ \lambda \Delta\nu (n^2 - \sin^2 \alpha)^{-1/2}. \qquad (13)$$

The useful aperture combinations in the present design [those that do not have interference from the reflected laser beam; i.e., nonusable directions, such as $(\overrightarrow{1,0,1}) + (\overrightarrow{-1,0,1})$ or $(\overrightarrow{0,1,1}) + (\overrightarrow{0,-1,1})$] are $(\overrightarrow{1,0,1}) + (\overrightarrow{0,1,1})$, $(\overrightarrow{0,1,1}) + (\overrightarrow{-1,0,1})$, $(\overrightarrow{-1,0,1}) - (\overrightarrow{0,-1,1})$, for ve-

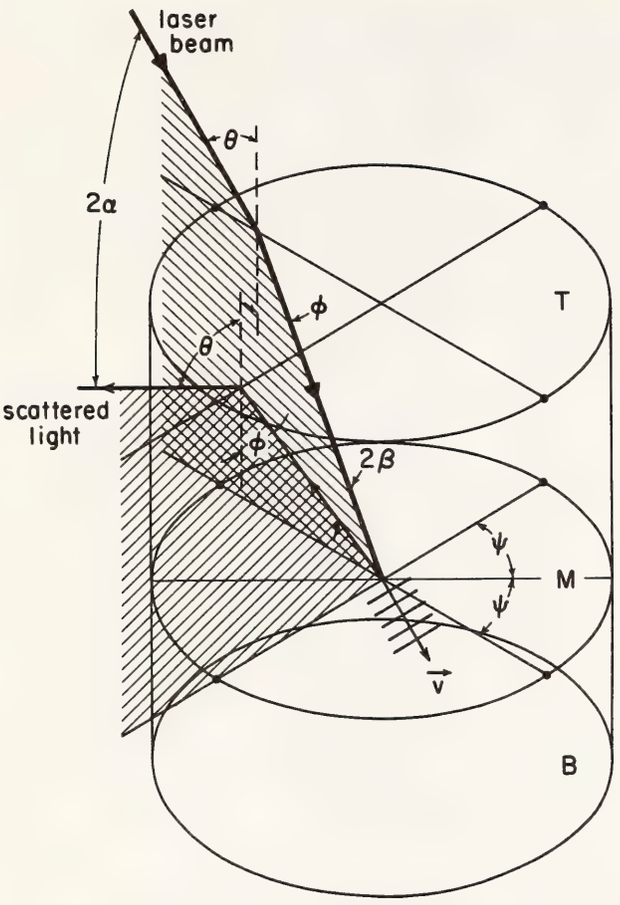


Fig. 83. Geometric relations of the incident laser beam, the scattered beam, the velocity direction out of the xy plane in a cylindrical sample in the pressure cell (see Fig. 80).

locity measurements in the directions $(\overrightarrow{1,1,K})$, $(\overrightarrow{-1,1,K})$, $(\overrightarrow{-1,-1,K})$ and $(\overrightarrow{1,-1,K})$, respectively, where

$$K = 2(2n^2 - 1)^{1/2}, \tag{14}$$

$\psi = \Theta = 45°$, and therefore $\alpha = 30°$. The equation for velocity is reduced to

$$V = \lambda\Delta\nu(4n^2 - 1)^{-1/2}. \tag{15}$$

If the index of refraction n can be determined to an accuracy of even 0.5% (i.e., by comparison with an internal standard; see, for example, Mao and Bell, 1976), there would be a negligible contribution to the error in V.

Axial Ports

There are additional directions that can be utilized by analysis of scattered light at the axial $(\overrightarrow{0,0,1})$ apertures. For forward directions,

$$\cos\beta = \sin\Phi/2 = 1 - \frac{(1 - \sin^2\Phi)^{1/2}}{2}$$
$$= \left[1 - \left(1 - \frac{(\sin^2\Theta/n^2)}{2}\right)^{1/2}\right]^{1/2}. \tag{16}$$

In the present design for these directions, $\Theta = 45°$, and thus Equation 16 is reduced to

$$V = \lambda\Delta\nu/[n(2 - (4n^2 - 2)^{1/2})]^{1/2}. \tag{17}$$

To visualize these geometric relations, note in Fig. 80 that, for example, the laser beam may be incident at each of the apertures $(\overrightarrow{1,0,-1})$, $(\overrightarrow{0,1,-1})$, $(\overrightarrow{-1,0,-1})$, and $(\overrightarrow{0,-1,-1})$. Corresponding to these, the scattered light analyzed at $(\overrightarrow{0,0,1})$ will yield acoustic velocities for the directions $(\overrightarrow{1,0,K})$, $(\overrightarrow{0,1,K})$, $(\overrightarrow{-1,0,K})$, and $(\overrightarrow{0,-1,K})$, respectively, where

$$K = (2n)^{1/2} - (2n^2 - 1)^{1/2}. \tag{18}$$

In back-reflection, $\Phi = 2\beta$, and thus

$$\cos\beta = \left[1 + \frac{(1 - (\sin^2\Theta)/n^2)^{1/2}}{2}\right]^{1/2}, \tag{19}$$

and

$$V = \lambda\Delta\nu/[n(2 + (4n^2 - 2)^{1/2})]^{1/2}. \tag{20}$$

Again with reference to Fig. 80, if the laser beam is incident at each aperture, $(\overrightarrow{1,0,1})$, $(\overrightarrow{0,1,1})$, $(\overrightarrow{-1,0,1})$, and $(\overrightarrow{0,-1,1})$, the scattered beam at $(\overrightarrow{0,0,1})$ will yield acoustic velocities corresponding to the direction $(\overrightarrow{1,0,K})$, $(\overrightarrow{0,1,K})$, $(\overrightarrow{-1,0,K})$, and $(\overrightarrow{0,-1,K})$, respectively, where

$$K = (2n)^{1/2} + (2n^2 - 1)^{1/2}. \tag{21}$$

This new pressure cell will be particularly useful for studying isotropic crystals, whose orientation cannot be determined a priori. Simultaneous determinations of velocity in several di-

rections would, in the case of cubic crystals, define unique orientation parameters and thus result in a complete set (two values) of elastic moduli.

For the special case of fluid samples, velocity is not directionally dependent; the velocity is measured in the directions shown in Fig. 82; the index of refraction can be determined with the relationship

$$n = 1/2[(\lambda\Delta\nu/V)^2 + 1]^{1/2}, \qquad (22)$$

for Doppler shifts measured with the direction shown in Fig. 83, where V is determined by Equation 15.

With known acoustic velocity the index of refraction can be measured. Values of index of refraction of a substance at high pressure can be used to calculate parameters such as the dielectric constant and the density.

References

Mao, H. K., and P. M. Bell, High-pressure physics: the 1-megabar mark on the ruby R_1 static pressure scale, *Science, 191,* 851–852, 1976.

Whitfield, C. H., E. M. Brady, and W. A. Bassett, Elastic moduli of NaCl by Brillouin scattering at high pressure in a diamond anvil cell, *Rev. Sci. Instrum., 47,* 942–947, 1976.

Infrared Spectra of Methanol and Ethanol at High Pressure

J. F. Mammone and S. K. Sharma*

The nature of the intermolecular forces in hydrogen-bonded systems, such as methanol and ethanol, is not only of fundamental theoretical interest (Pimentel and McClellan, 1960; Kollman and Allen, 1972) but has become important in high-pressure experiments, where a 4:1 methanol:ethanol mixture is widely used as a pressure-transmitting medium (Piermarini *et al.*, 1973). In this report the infrared spectra of the crystalline phases of these alcohols (at room temperature methanol freezes at 35.1 ± 1.0 kbar and ethanol freezes at 17.8 ± 1.0 kbar) have been measured at high pressure to supplement previous structural studies of methanol and ethanol with Raman spectroscopy (Mammone *et al.*, 1980).

Spectroscopic-grade methanol (Burdick and Jackson Laboratories Inc., Muskegon, Michigan) and absolute ethanol (U.S. Industrial Chemicals Company, New York) were used without further purification. The samples were compressed in a diamond-anvil cell designed by Mao and Bell (*Year Book 77,* 904–908). The liquids and a small ruby chip were contained in a hardened steel gasket, which was 0.3 mm in diameter and preindented from an original thickness of 0.075 mm. Pressures were calculated from the shift in the ruby R_1 fluorescence line (Mao *et al.*, 1978). Infrared absorption spectra were measured with a Nicolet 7199, Fourier-transform infrared spectrometer.

Transmission spectra of crystalline methanol are shown in Fig. 84, and the frequencies and other characteristics of the bands in methanol and ethanol are listed in Tables 41 and 42. The assignments of the internal modes of vibration presented in the tables are based on characteristic group frequencies (Colthup *et al.*, 1975). Absorption in the O-H stretching region in both alcohols was so intense that no bands in this region could be resolved, even with thin samples. To study strongly absorbing materials, infrared emission techniques must be employed. The strengthening of the hydrogen bonding in methanol with pressure is reflected by the 20 cm^{-1} shift in the frequency of the O-H out-of-plane bend at pressures above 23 kbar.

On the basis of Raman spectroscopic measurements (Mammone *et al.*, 1980) the structure of solid methanol at high

*Work carried out under a cooperative predoctoral fellowship program between the Geophysical Laboratory and the University of California, Los Angeles.

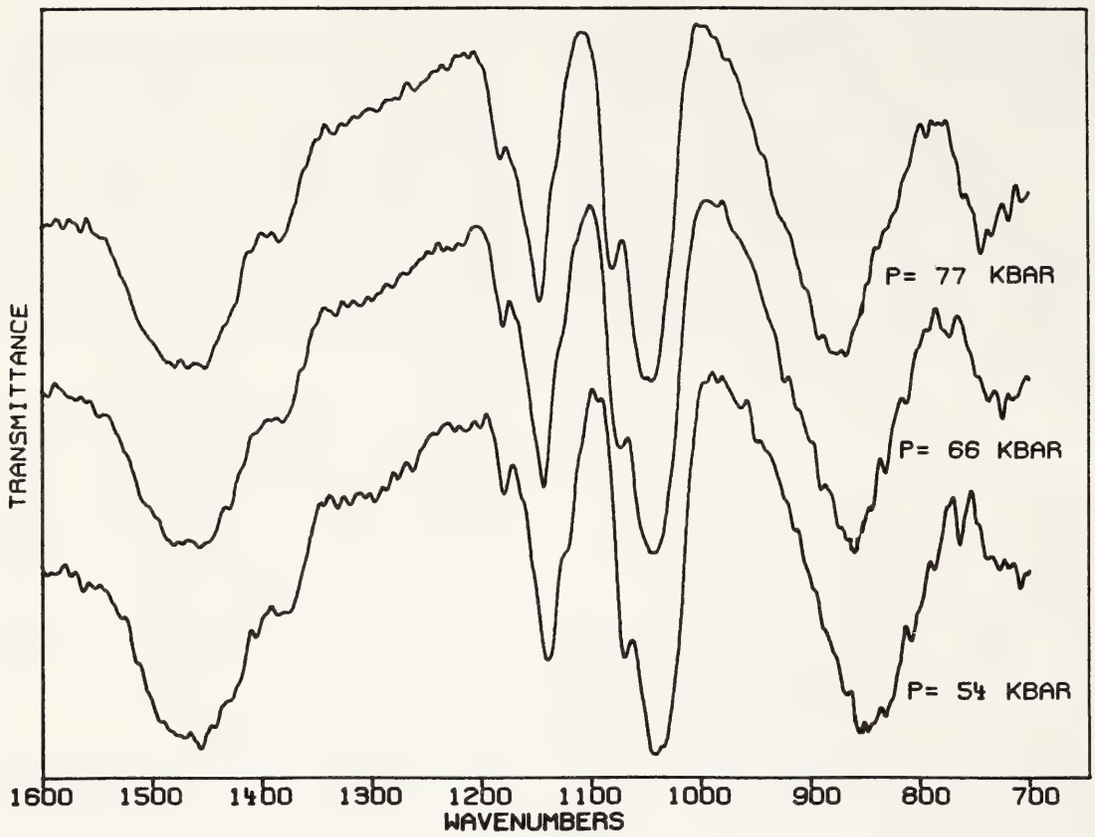


Fig. 84. Transmission spectra of crystalline methanol at various pressures (Oscillating noise is due to interference fringes from between the two diamond pressure faces).

pressure was assigned to the α-phase (space group $P2_1$ or $P2_1/m$; $Z = 2$). The crystal structure of methanol consists of hydrogen-bonded zigzag chains with two molecules per repeat unit, resembling the structure of polyethylene. The two space groups ($P2_1$ and $P2_1/m$) differ only in the position of the hydroxyl hydrogen atom, which is imprecisely determined by x-ray diffraction (Tauer and Lipscomb, 1952). In the space group $P2_1/m$ the hydroxyl hydrogen occupies a center of inversion, whereas in $P2_1$ it is displaced toward

TABLE 41. Infrared Frequencies (cm^{-1}) for Crystalline Methanol at Various Pressures*

54 kbar	66 kbar	77 kbar	Assignment
848 s	858 s	868 s	O—H out-of-plane bend
1040 vs 1071 sh	1043 vs 1073 sh	1045 vs 1080 sh	C—O stretch
1140 s 1178 sh	1142 s 1181 sh	1147 s 1182 sh	CH_3 rock
1377 sh	1378 sh	1383 sh	O—H in-plane bend
1463 vs	1465 vs	1464 vs	CH_3 bend

* Intensity estimates: vs, very strong; s, strong; sh, shoulder.

TABLE 42. Infrared Frequencies (cm^{-1}) for Crystalline Ethanol at Various Pressures*

30 kbar	55 kbar	76 kbar	Assignment
846 m 855 m	855 m	858 m	CH_2 rock
898 s 907 s	904 s 918 s	909 s 924 s	C—C stretch
1065 s	1085 s	1093 s	C—C stretch
1108 sh 1159 s	1118 sh 1167 s	1130 sh 1169 s	CH_3 rock
1272 m	1280 s	1286 s	CH_2 twist
1359 s	1359 s	1362 s	O—H in-plane bend
1384 s	1390 s	1398 s	CH_3 symmetric bend
1451 s 1476 s	1456 s 1489 s	1458 s 1497 s	CH_3 asymmetric bend
1495 s	1512 s	1523 s	CH_2 symmetric bend

* Intensity estimates: s, strong; m, medium; w, weak; sh, shoulder.

one of the oxygen atoms. For $P2_1/m$ symmetry, the mutual exclusion principle reduces the number of allowed bands in the vibrational spectrum from that permitted for the same number of molecules in a $P2_1$ structure and prohibits simultaneous infrared and Raman activity. The C-O stretching and CH_3 rocking modes were observed as doublets in both the infrared and Raman spectra, consistent with the $P2_1$ space group, whereas in the space group $P2_1/m$ only one component would be Raman-active and one infrared-active. The spectra for the α-phase at low temperature are also consistent with the space group $P2_1$ (Durig *et al.*, 1971).

The infrared spectra of ethanol (Table 42) agree with previous high-pressure experiments (Mikawa *et al.*, 1971). On the basis of infrared measurements, Jakobsen *et al.* (1967) concluded that only one polymorph for ethanol could be crystallized, regardless of whether the crystal was grown by lowering the temperature or increasing the pressure. Thus, the vibrational spectra of the high-pressure crystal can be interpreted in terms of the monoclinic crystal structure (Pc; $Z = 4$) determined by x-ray diffraction at 87 K (Jönsson, 1976). If ethanol is considered as an infinite hydrogen-bonded chain molecule (Tobin, 1955), each repeat unit also contains four molecules. There are $3n - 4 = 104$ ($n = 36$ atoms) optic modes, all of which are expected to be both Raman- and infrared-active because of the low symmetry; however, fewer bands were observed in the vibrational spectra. When the unit cell is large, long-range forces within the unit cell are insufficient to separate all the motions into discrete spectral bands.

The 4:1 methanol:ethanol mixture is useful in high-pressure Raman spectroscopic experiments because these alcohols have relatively low Raman-scattering cross sections. Their infrared absorption, however, is very intense owing to the change of the large dipole moment associated with the internal modes of vibration. The 4:1 mixture is, therefore, not useful as a pressure-transmitting medium for midinfrared (4000–400 cm^{-1}) spectroscopic experiments. The diamond-anvil cell, however, has been modified by Mao and Bell (*Year Book 78*, 659–660) for use with cryogenic liquids as pressure-transmitting media. Possibly an inert fluid such as argon would serve the purpose of providing a hydrostatic pressure medium for infrared absorption measurements.

References

Colthup, N. B., L. H. Daly, and S. E. Wiberly, *Introduction to Infrared and Raman Spectroscopy*, 2d ed., Academic Press, New York, 1975.

Durig, J. R., C. B. Pate, Y. S. Li, and D. J. Antion, Far-infrared and Raman spectra of solid methanol and methanol-d_4, *J. Chem. Phys., 54*, 4863–4870, 1971.

Jakobsen, R. J., J. W. Brasch, and Y. Mikawa, Hydrogen bonding in solid alcohols, *J. Mol. Struct., 1*, 309–321, 1967.

Jönsson, P. -G., Hydrogen bond studies. CXIII. The crystal structure of ethanol at 87 K, *Acta Crystallogr., B32*, 232–235, 1976.

Kollman, P. A., and L. C. Allen, Theory of the hydrogen bond, *Chem. Rev., 72*, 283–303, 1972.

Mammone, J. F., S. K. Sharma, and M. Nicol, Raman spectra of methanol and ethanol at pressures up to 100 kbar, *J. Phys. Chem.*, in press, 1980.

Mao, H. K., P. M. Bell, J. W. Shaner, and D. J. Steinberg, Specific volume measurements on Cu, Mo, Pd, and Ag and calibration of the ruby R_1 fluorescence pressure gauge from 0.06 to 1 Mbar, *J. Appl. Phys., 49*, 3276–3283, 1978.

Mikawa, Y., J. W. Brasch, and R. J. Jakobsen, Polarized infrared spectra of single crystals of ethyl alcohol, *Spectrochim. Acta, 27A*, 529–539, 1971.

Piermarini, G. J., S. Block, and J. D. Barnett, Hydrostatic limits in liquids and solids to 100 kbar, *J. Appl. Phys., 44*, 5377–5382, 1973.

Pimentel, G. C., and A. L. McClellan, *The Hydrogen Bond*, W. H. Freeman and Company, San Francisco, 1960.

Tauer, K. J., and W. N. Lipscomb, On the crystal structures, residual entropy and dielectric anomaly of methanol, *Acta Crystallogr., 5*, 606–612, 1952.

Tobin, M. C., Selection rules for normal modes of chain molecules, *J. Chem. Phys., 23*, 891–896, 1955.

STAFF ACTIVITIES

Petrologists' Club

Seven meetings were held during the 69th year of the Petrologists' Club, and the following lectures were presented:

"Effect of pressure on the shift of liquidus boundaries in silicate systems: systematics and interpretation," by Ikuo Kushiro (Geophysical Laboratory/University of Tokyo), October 9, 1979.

"Water and hornblende in some subduction zone magmas," by A. T. Anderson (University of Chicago), November 27, 1979.

"Geochemical studies of lower crustal nodules, Kilbourne Hole, New Mexico," by S. R. Hart (Massachusetts Institute of Technology), December 11, 1979.

"Submarine hot springs on the East Pacific Rise at 21°N," by H. D. Holland (Harvard University), January 15, 1980.

"High-pressure phase-equilibrium studies bearing on the origin of mid-ocean ridge basalts and Hawaiian basalts," by Dean Presnall (University of Texas at Dallas), February 19, 1980.

"Petrogenesis of some western Alpine peridotites," by W. G. Ernst (University of California, Los Angeles), April 1, 1980.

"Experimental petrology and plate tectonics," by P. J. Wyllie (University of Chicago), April 29, 1980.

Washington Crystal Colloquium

The Washington Crystal Colloquium, an informal group of crystallographers from the Washington area, met six times during the report year. The following lectures were presented:

"Application of derivative lattices to the indexing of powder patterns for modulated structures," by A. Santoro (National Bureau of Standards), October 26, 1979.

"Conformational characteristics of cyclic peptides," by Isabella Karle (Naval Research Laboratory), November 16, 1979.

"Three-dimensional structure of Rhizopus acid protease," by R. Bott (National Institutes of Health), December 14, 1979.

"Why least-squares . . ., and why not?" by E. Prince (National Bureau of Standards), January 18, 1980.

"Energy dispersive powder diffraction using the diamond-anvil pressure cell," by Floyd A. Mauer (National Bureau of Standards), February 22, 1980.

"Combined x-ray and neutron diffraction studies on Ribonuclease A," by Alex Wlodawer (National Institutes of Health and National Bureau of Standards), May 2, 1980.

Seminar Series

The seminar series met 12 times during the report year. The following lectures were presented:

"Geological and geochemical researches in China," by C. Wen-you (Institute of Geology, Academia Sinica) and T. Kwang-ze (Institute of Geochemistry, Academia Sinica), October 23, 1979.

"Petrologic computation," by R. LeMaitre (University of Melbourne), October 30, 1979.

"Reaction kinetics on hydrothermal systems: examples from carbonate systems," by A. Gaines (National Science Foundation), November 21, 1979.

"Fluid flow through rocks during metamorphism," by D. Rumble III (Geophysical Laboratory), November 30, 1979.

"Combined isotopic, chemical, and mineralogical studies of HAL (a Hebonite Allende inclusion)," by T. Lee (Department of Terrestrial Magnetism), December 6, 1979.

"The chemical petrology and stable

isotope geochemistry of some Adirondack rocks: evidence bearing on the nature of the fluid phase during metamorphism," by J. Valley (University of Michigan), December 13, 1979.

"The concentrations of H_2O, CO_2, S, and Cl during pre-eruption crystallization of mantle-derived magmas: new evidence from silicate melt inclusions," by D. Harris (U.S. Geological Survey, Reston), December 20, 1979.

"The biogeochemistry (both probable and fictitious) of the stable hydrogen and oxygen isotopes," by M. Estep (Geophysical Laboratory), January 11, 1980.

"Observations of hot springs on the East Pacific rise with ALVIN, deep-sea submersible," by J. Edmond (Massachusetts Institute of Technology), January 23, 1980.

"Madeira revisited: principal component and cluster analysis of Madeira lavas, based on 'essential constituents,'" by A. Possola (Yale University), March 13, 1980.

"Crystallization in a double-diffusive system," by C. F. Chen (Rutgers University), April 2, 1980.

"Light scattering at high pressure," by E. Brody (University of Rochester), April 24, 1980.

Lectures and Symposia

During the report year, staff members and fellows presented lectures and participated in symposia and other extracurricular activities, as follows:

Bell participated in the 7th International Conference on High Pressures held in LeCreusot, France, in July 1979. He lectured on "Earth and planetary interiors: direct experimental data" at the Department of Planetary Sciences, University of Arizona; on "Ultrahigh-pressure experiments and their application to the earth and planets" at NASA scientific colloquia at Goddard Space Flight Center in April 1980; and on "High-pressure studies in geophysics: A window on the deep interior of the earth" at the annual Carnegie Evening on May 8, 1980. Bell also addressed the Physics and Geoscience departments of the City University of New York (CUNY), Brooklyn, on November 26, 1979, and a symposium on shock-wave research at the annual meeting of the American Physical Society in Washington in April 1980. He was named the Associate Editor for News of *EOS*, a newsletter published by the American Geophysical Union; he is an associate editor of *Physics and Chemistry of Minerals;* and he is serving on the editorial board of *Science*, on the National Academy of Sciences' Solid State Sciences Committee, and on the Committee for Earth Sciences and Material Sciences of the National Research Council. He was elected Vice President of the Potomac Geophysical Society.

Boctor gave an invited paper on "Mineral-solution equilibria in the system Fe_2O_3-HCl-H_2-H_2O" at Michigan Technological University. At the 1979 fall meeting of the American Geophysical Union, he presented two papers: "Solubility of hematite in chloride-bearing hydrothermal fluids" with Frantz and Popp, and "Shock metamorphic features in Pampa del Infierno chondrite" with Bell, Mao, and Kullerud; at the 1980 spring meeting he presented a paper with Frantz on "Mineral-solution equilibria in the system Mn_3O_4-HCl-H_2-H_2O."

Boyd presented invited papers at the Diamond Conference and the Kimberlite Symposium held at Cambridge, England, in July 1979. He also gave a paper on "Conditions of origin of natural diamonds" at the George C. Kennedy 60th Birthday Symposium held at the University of California at Los Angeles in September.

Chayes currently serves in three capacities in the International Union of Geological Sciences. He is a member of its Committee on Storage, Automatic Processing and Retrieval of Geological Data, chairman of project 163 of its In-

ternational Geological Correlation Program, and a member of its Subcommission on Systematics in Petrology. In May he attended a meeting of the last group in Padua, Italy. Chayes is also an associate editor of the *American Mineralogist*, the *Bulletin of the Geological Society of America*, *Chemical Geology*, and the *Journal of Geology*.

Elthon lectured on "The compositions of primary mid-ocean ridge basalts" at the Lamont-Doherty Geological Observatory in December 1979, on "The origin of basalts from the Tortuga ophiolite complex, Chile" at the Woods Hole Oceanographic Institution in May 1980, and on "The compositions of primary mid-ocean ridge basalts and the evolution of basalts within crustal magma chambers" at the 1980 spring meeting of the American Geophysical Union.

Finger lectured at the Max Planck Institutes at Heidelberg and Stuttgart. He served as Secretary of the Mineralogical Society of America through October 1979, when he completed his second two-year term.

Frantz gave an invited lecture on "Electrical conductances of $MgCl_2$ and $CaCl_2$ at elevated temperatures and pressures" at the International Conference on the Properties of Steam at Munich, Germany, in September 1979. He also presented papers on "Mass transport models" and "Mineral solution equilibria" at the Department of Geology, Stanford University, in January 1980.

George held an appointment as Lecturer on the faculty of the Department of Earth and Planetary Sciences, Johns Hopkins University, in connection with a joint cooperative program with the University for the purpose of teaching a graduate course in the use of the electron microprobe at the Geophysical Laboratory.

Hare gave invited lectures at the Department of Chemistry, University of Maryland, in July 1979; at the National Cancer Institute, National Institutes of Health, and at the Eastern Analytical Symposium, New York City, in October 1979; at the Chemistry Department, Arizona State University, in November 1979; at the Geological Society of Washington, at the George Washington University Medical School, and at a symposium on chemical and nuclear dating methods at the American Chemical Society meeting at Houston in January 1980; and at the Institute of Arctic and Alpine Research, University of Colorado, in April 1980. He was appointed Adjunct Professor of the Department of Chemistry, University of Maryland, and gave a graduate seminar course there on "Biogeochemistry of amino acids" during the spring semester 1980.

Hazen gave invited lectures on "Publication as a measure of scientific growth" at the G. K. Gilbert symposium of the Geological Society of America at San Diego, "High-pressure crystal chemistry" at the University of Pennsylvania, and "Bibliometrics" at the Geological Society of Washington, in November 1979; on "Crystal structures at high temperatures and pressures" at a special conference on Chemistry of Complex Solids held at Castle Hot Springs, Arizona, in January 1980; and on "High-pressure crystal chemistry" at McMaster University, in May 1980. He served as MSA program chairman for the Geological Society of America annual meeting and as Secretary of the U.S. National Committee on the History of Geology.

Hoering lectured on "The geochemistry of organic substances" at the Department of Geochemistry and Mineralogy, Pennsylvania State University, in October 1979. He served on the American Institute of Biological Sciences' Planetary Biology Advisory Panel to NASA.

Irvine lectured on "Magmatic currents and convection in layered intrusions" at the Geological Survey of

Canada, Ottawa, and at Rutgers University. He spoke on "Convection in the Muskox intrusion" at a meeting on "Processes in Magma Chambers" sponsored by the Volcanic Studies Group of the Geological Society of London and held in Glasgow, Scotland, on May 15–16. He also lectured on "Layering and magmatic density currents in the Duke Island and Skaergaard intrusions" at Cambridge University, England. Irvine is serving as an Associate Editor for the *Canadian Journal of Earth Sciences* and for the *Journal of Geophysical Research.*

Lonker addressed the Geological Society of Washington on "Late Proterozoic uplift and cooling history in southeastern Ontario," and the American Geophysical Union on "Disequilibrium during metamorphism in high-grade pelites from the Frontenac Axis, Ontario, Canada" in May 1980.

Mao received the Annual Award of the Mineralogical Society of America in San Diego, November 6, for outstanding research at ultrahigh pressures. He spent the month of September in Peking and Kweiyang, People's Republic of China, visiting institutes of the Academia Sinica having research programs in earth sciences and physics. He found great interest among Chinese scientists now using diamond-anvil, high-pressure apparatus similar to that developed at the Geophysical Laboratory by Mao and Bell. Mao participated in the 7th International Conference on High Pressures held in LeCreusot, France, in July 1979.

Mysen gave invited lectures on "The structure of silicate melts and derivative properties" at Michigan State University in October 1979, "The influence of melt structure on crystal-liquid trace element partition coefficients" to an MSA symposium during the annual meeting of the Geological Society of America at San Diego in November 1979, "Petrogenesis of island arc andesites: Experimental constraints" at Rutgers University in March 1980, and "Relations between melt structure and physical properties" and "Experimental constraints on the petrogenesis of island arc andesites" at Harvard University in May 1980. He served as convenor of an MSA symposium on "Properties of silicate liquids" at the annual meeting of the GSA. Mysen was awarded the Reusch Medal of the Norwegian Geological Society for 1979 for studies on CO_2 solubility in silicate melts.

Osborn served as chairman of the Advisory Committee on Mining and Mineral Resources Research, advisory to the Secretary of the Interior; and as chairman of the ad hoc Committee on Geological Aspects of Industrial Waste Disposal, National Research Council (NRC). He served as a member of the following: ad hoc Committee on Abiogenic Methane, NRC; ad hoc Committee on Geology, NRC; Continental Scientific Drilling Committee, NRC; Panel on the Geochemistry of Fibrous Materials related to Health Risks, NRC; Materials Advisory Committee, Office of Technology Assessment, Congress of the United States; and Final Competitive Panel on Experimental Program to Stimulate Competitive Research, National Science Foundation. He presented testimony on Title III of the Surface Mining Control and Reclamation Act of 1977 before the Interior Subcommittee of the House Appropriations Committee. He presented an address entitled, "Dividing responsibilities in scientific research: Government, universities, and industry" at the Geological Society of America symposium on "Perspectives on government and science: Occasioned by the Centennial of the U. S. Geological Survey," San Diego, California, November 6, 1979.

Osborn also served on the Pennsylvania Research Corporation Board of Directors (Pennsylvania State University); the Geisinger Medical Center

Board of Directors, Danville, Pennsylvania; and the Board of Directors of the Institute for Medical Education and Research at Geisinger Medical Center.

Rumble gave invited lectures on "Fluid flow through rocks during metamorphism" at the Department of Earth and Planetary Sciences, Massachusetts Institute of Technology, the Department of Earth Sciences, Dartmouth College, and the Department of Geosciences, Pennsylvania State University; and on "Stable isotope fractionation during metamorphic devolatization reactions" at the Department of Chemistry, University of Maryland.

Scarfe addressed the Geological Society of America at its annual meeting in San Diego, the Lamont-Doherty Geological Observatory of Columbia University, and the Department of Chemistry, University of Maryland, on the viscosity of silicate melts.

Sharma presented two papers at the 7th International Conference on High Pressures in July 1979, at LeCreusot, France. He also lectured on Raman studies of solids at high pressures, and on structural studies of silicate melts and glasses by Raman spectroscopy at the University of Hawaii at Manoa, October 29–November 2, 1979, and at the University of California at Los Angeles, November 1979 and April 1980.

Van Valkenburg participated in the 7th International Conference on High Pressures held in LeCreusot, France, in July.

Virgo lectured on "Melt structure in multicomponent systems" at an MSA symposium on Properties of Silicate Melts at the Geological Society of America meeting in November 1979, and on "A structural study, using Raman spectroscopy, of the major anionic species in multicomponent silicate melts at 1 atm.; implications for their physical and chemical properties" as a delegate to the International Union of Geodesy and Geophysics meeting at Canberra, Australia, in December 1979.

Yoder was an invited speaker at the Nobel Symposium on "Chemistry and Geochemistry of Solutions at High Temperature and Pressure" held September 17–21 at Karlskoga, Sweden, the site of the Nobel chemical complex now operated by the Bofors Corporation. Yoder also served as a member of the Visiting Committee for the Institute of the Physics of the Globe, University of Paris VI, September 25–26. The Institute is directed by Prof. Claude Allègre, a frequent visitor to the departments in Washington. While in Paris, Yoder gave a lecture on "Experimental methods for measurement of transport properties of magma." Yoder gave two lectures at Iowa State University, and also visited the Department of Mechanical Engineering, University of Minnesota, to discuss problems of heat transfer in the melting of rocks. Seven days before the major eruption of St. Helens, Washington, he spoke at the Smithsonian Institution in connection with their Adult Course Program on laboratory experiments relating to "Explosive Volcanoes." He also visited the Oak Ridge National Laboratory, April 9–11, to speak on "Experimental methods for determination of transport properties of magmas." He delivered a commencement address on "Potential nonfuel mineral resource problems" at the Geology Department of the Virginia Polytechnic Institute and State University at Blacksburg, Virginia, on 7 June. He advised the Los Alamos Scientific Laboratory, New Mexico, in June in regard to a national mineral resource program for assessment and exploration.

Yoder was an invited guest of a panel on Geochemistry of Fibrous Materials Related to Health Risks. The meetings, sponsored by the U. S. National Committee for Geochemistry under the National Research Council, are

being held to investigate which, if any, of the minerals in the "asbestos" group are related to the diseases mesothelioma and lung cancer. Yoder also serves on the Nominating Committee of the National Academy of Sciences. *The Evolution of the Igneous Rocks: Fiftieth Anniversary Perspectives*, edited by Yoder, was officially published on 5 November 1979 and is already in the second printing. He is serving a second term as associate editor of the *American Journal of Science.*

Field Work

As part of two studies in connection with his work on fluid flow in metamorphism, D. Rumble examined rocks in the Mt. Moosilauke quadrangle of New Hampshire. In one study, the distribution of graphite through a granite pluton suggests pervasive infiltration of fluids through solidified rock during metamorphism. In the other, extensive isotopic disequilibrium between quartz veins, pegmatite, and wall rock indicates that flow was mostly confined to fractures.

T. N. Irvine participated in a six-week expedition to the Skaergaardcomplex, organized by A. R. McBirney, and in an excursion to the classic ultramafic complex of the Isle of Rhum, sponsored by the Volcanic Studies Group of the Geological Society of London. He also joined a Canadian Geological Survey party studying the Turnagain River ultramafic complex in British Columbia. Some of his work on Skaergaard layering is described in this Report.

F. R. Boyd collected xenoliths in the San Quentin volcanic field, Baja California, and P. E. Hare joined a University of Colorado expedition studying the stratigraphy of Spitsbergen, for a highly successful field test of his portable amino acid analyzer. D. Elthon was a member of a Woods Hole Oceanographic Institute cruise studying the Oceanographer Fracture Zone of the mid-Atlantic ridge. As a visiting investigator on the Johns Hopkins research vessel *Ridgley Warren*, M. Estep collected samples of Chesapeake Bay plankton for isotope analysis.

BIBLIOGRAPHY

Ahrens, T. J., *see* Jeanloz, R.

Bell, P. M., Ultra-high-pressure experimental mantle mineralogy, *Rev. Geophys. Space Phys., 17*, 788–791, 1979 (G.L. Paper 1779).

Bell, P. M., *see also* Jeanloz, R.; Mao, H. K.; Sharma, S. K.

Boyd, F. R., and R. V. Danchin, Lherzolites, eclogites, and megacrysts from some kimberlites of Angola, *Amer. J. Sci., 280A*, 528–549, 1980 (G.L. Paper 1784).

Chayes, F., Partitioning by discriminant analysis: a measure of consistency in the nomenclature and classification of volcanic rocks, in *The Evolution of the Igneous Rocks: Fiftieth Anniversary Perspectives*, H. S. Yoder, Jr., ed., Princeton University Press, pp. 521–532, 1979 (G.L. Paper 1795).

Chrenko, R. M., *see* Mao, H. K.

Danchin, R. V., *see* Boyd, F. R.

DeVries, R. C., *see* Mao, H. K.

Dunn, K. J., *see* Mao, H. K.

Eggler, D. H., and A. A. Kadik, The system $NaAlSi_3O_8$-H_2O-CO_2 to 20 kbar pressure: I. Compositional and thermodynamic relations of liquids and vapors coexisting with albite, *Amer. Mineral., 64*, 1036–1048, 1979 (G.L. Paper 1788).

Finger, L. W., and R. M. Hazen, Response of oxygen-based structures to changes in pressure, temperature and composition, *Trans. Amer. Crystallogr. Assoc., 15*, 93–105, 1979 (G.L. Paper 1785).

Finger, L. W., R. M. Hazen, and T. Yagi, Crystal structures and electron densities of nickel and iron silicate spinels at elevated temperature or pressure, *Amer. Mineral., 64*, 1002–1009, 1979 (G.L. Paper 1783).

Finger, L. W., *see also* Hazen, R. M.; King, H. E., Jr.

Frantz, J. D., and W. Marshall, Electrical conductances of aqueous calcium chloride and magnesium chloride solutions from 25 to 600°C at pressures up to 4,000 bars, in *Water and Steam; Their Properties and Current Industrial Applications*, J. Straub and K. Scheffler, eds., Pergamon Press, Oxford, 1980 (G.L. Paper 1781).

Frantz, J. D., and R. K. Popp, Mineral-solution equilibria—I. An experimental study of complexing and thermodynamic properties of aqueous $MgCl_2$ in the system MgO-SiO_2-H_2O-HCl, *Geochim. Cosmochim. Acta, 43*, 1223–1239, 1979 (G.L. Paper 1773).

Frantz, J. D., *see also* Popp, R. K.

Harrison, W. J., *see* Wendlandt, R. F.

Hazen, R. M., and L. W. Finger, Polyhedral tilting: a common type of pure displacive phase transition and its relationship to analcite at high pressure, *Phase Transitions, 1*, 1–22, 1979 (G.L. Paper 1774).

Hazen, R. M., and L. W. Finger, Linear compressibilities of $NaNO_2$ and $NaNO_3$, *J. Appl. Phys., 50*, 6826–6828, 1979 (G.L. Paper 1776).

Hazen, R. M., and L. W. Finger, Bulk modulus-volume relationship for cation-anion polyhedra, *J. Geophys. Res., 84*, 6723–6728, 1979 (G.L. Paper 1787).

Hazen, R. M., *see also* Finger, L. W.

Irvine, T. N., Rocks whose composition is determined by crystal accumulation and sorting, in *The Evolution of the Igneous Rocks: Fiftieth Anniversary Perspectives*, H. S. Yoder, Jr., ed., Princeton University Press, pp. 245–306, 1979 (G.L. Paper 1793).

Irvine, T. N., Magmatic density currents and cumulus processes, *Amer. J. Sci., 280A*, 1–58, 1980 (G.L. Paper 1780).

Jeanloz, R., T. J. Ahrens, H. K. Mao, and P. M. Bell, B1-B2 transition in calcium oxide from shock-wave and diamond-cell experiments, *Science, 206*, 829–830, 1979 (G.L. Paper 1799).

Kadik, A. A., *see* Eggler, D. H.

King, H. E., Jr., and L. W. Finger, Diffracted beam crystal centering and its application to high-pressure crystallography, *J. Appl. Crystallogr., 12*, 374–378, 1979 (G.L. Paper 1772).

Kushiro, I., Fractional crystallization of basaltic magma, in *The Evolution of the Igneous Rocks: Fiftieth Anniversary Perspectives*, H. S. Yoder, Jr., ed., Princeton University Press, pp. 171–203, 1979 (G.L. Paper 1792).

Kushiro, I., *see also* Sharma, S. K.; Virgo, D.

Mammone, J. F., S. K. Sharma, and M. Nicol, Raman study of rutile (TiO_2) at high pressures, *Solid State Commun., 34*, 799–802, 1980 (G.L. Paper 1812).

Mao, H. K., and P. M. Bell, Equations of state of MgO and Fe under static pressure conditions, *J. Geophys. Res., 84*, 4533–4536, 1979 (G.L. Paper 1759).

Mao, H. K., P. M. Bell, K. J. Dunn, R. M. Chrenko, and R. C. DeVries, Absolute pressure measurements and analysis of diamonds subjected to maximum static pressures of 1.3–1.7 Mbar, *Rev. Sci. Instrum., 50*, 1002–1009, 1979 (G.L. Paper 1771).

Mao, H. K., *see also* Jeanloz, R.; Sharma, S. K.

Marshall, W., *see* Frantz, J. D.

Mysen, B. O., Nickel partitioning between olivine and silicate melt: Henry's law revisited, *Amer. Mineral., 64*, 1107–1114, 1979 (G.L. Paper 1789).

Mysen, B. O., and R. K. Popp, Solubility of sulfur in $CaMgSi_2O_6$ and $NaAlSi_3O_8$ melts at high pressure and temperature with controlled f_{O_2} and f_{S_2}, *Amer. J. Sci., 280*, 78–92, 1980 (G.L. Paper 1786).

Mysen, B. O., *see also* Sharma, S. K.; Virgo, D.; Wendlandt, R. F.

Nicol, M., *see* Mammone, J. F.

Osborn, E. F., The reaction principle, in *The Evolution of the Igneous Rocks: Fiftieth Anniversary Perspectives*, H. S. Yoder, Jr., ed., Princeton University Press, pp. 133–169, 1979 (G.L. Paper 1791).

Popp, R. K., and J. D. Frantz, Mineral solution equilibria—II. An experimental study of mineral solubilities and the thermodynamic properties of aqueous $CaCl_2$ in the system CaO-SiO_2-H_2O-HCl, *Geochim. Cosmochim. Acta, 43*, 1777–1790, 1979 (G.L. Paper 1782).

Popp, R. K., J. D. Frantz, and G. L. Vogel, An electrode technique for measurement of chloride concentration in microsamples, *Amer. Mineral., 65*, 393–395, 1980 (G.L. Paper 1800).

Popp, R. K., *see also* Frantz, J. D.; Mysen, B. O.

Sharma, S. K., H. K. Mao, and P. M. Bell, Raman measurements of hydrogen in the pressure range 0.2–630 kbar at room temperature, *Phys. Rev. Lett., 44*, 886–888, 1980 (G.L. Paper 1801).

Sharma, S. K., D. Virgo, and I. Kushiro, Relationship between density, viscosity and structure of GeO_2 melts at low and high pressures, *J. Non-Cryst. Solids, 33*, 235–248, 1979 (G.L. Paper 1770).

Sharma, S. K., D. Virgo, and B. O. Mysen, Raman study of the coordination of aluminum in jadeite melts as a function of pressure, *Amer. Mineral., 64*, 779–787, 1979 (G.L. Paper 1775).

Sharma, S. K., *see also* Mammone, J. F.

Virgo, D., B. O. Mysen, and I. Kushiro, Anionic constitution of 1-atmosphere silicate melts: implications for the structure of igneous melts, *Science, 208*, 1371–1373, 1980 (G.L. Paper 1803).

Virgo, D., *see also* Sharma, S. K.

Vogel, G. L., *see* Popp, R. K.

Wendlandt, R. F., and W. J. Harrison, Rare earth partitioning between immiscible carbonate and silicate liquids and CO_2 vapor: results and implications for the formation of light rare earth-enriched rocks, *Contrib. Mineral. Petrol., 69*, 409–419, 1979 (G.L. Paper 1777).

Wendlandt, R. F., and B. O. Mysen, Melting phase relations of natural peridotite + CO_2 as a function of degree of partial melting at 15 and 30 kbar, *Amer. Mineral., 65*, 37–44, 1980 (G.L. Paper 1798).

Yagi, T., *see* Finger, L. W.

Yoder, H. S., Jr., Basic magma generation and aggregation, *Bull. Volcanol., 41*, 301–316, 1978 (G.L. Paper 1778).

Yoder, H. S., Jr., Melilite-bearing rocks and related lamprophyres, in *The Evolution of the Igneous Rocks: Fiftieth Anniversary Perspectives*, H. S. Yoder, Jr., ed., Princeton University Press, pp. 391–411, 1979 (G.L. Paper 1794).

Yoder, H. S., Jr., ed., *The Evolution of the Igneous Rocks: Fiftieth Anniversary Perspectives*, Princeton University Press, 1979 (G.L. Paper 1796).

Yoder, H. S., Jr., Experimental mineralogy: achievements and prospects, *Bull. Mineral., 103*, 5–26, 1980 (G.L. Paper 1797).

PERSONNEL

Scientific Staff

Director: H. S. Yoder, Jr., *Petrologist*

Emeritus Research Associate: E. G. Zies, *Chemist*

Emeritus Distinguished Professor, CIW: E. F. Osborn, *Petrologist*

Emeritus Isotope Geochemist: G. L. Davis

Systematic Petrologist: F. Chayes

Petrologists: F. R. Boyd, Jr., T. N. Irvine, I. Kushiro,[1] D. Rumble III

Physical Chemists: J. D. Frantz, T. C. Hoering

Geophysicists: P. M. Bell, H. K. Mao

Organic Geochemist: P. E. Hare

Crystallographer: L. W. Finger

Solid State Geochemist: D. Virgo

Geochemists: J. B. Brady,[2] B. O. Mysen

Experimental Mineralogist: R. M. Hazen

Biochemist: Marilyn L. F. Estep

Volcanologist: T. Murase[3]

Postdoctoral Research Associates: R. K. Popp, Virginia Polytechnic Institute and State University;[4] B. A. Simons, Rheinisch Westfälische Technische Hochschule Aachen, West Germany[5]

Postdoctoral Fellows: T. M. Benjamin, California Institute of Technology;[6] N. Z. Boctor, Purdue University; H. Fukuyama, University of Tokyo;[7] S. W. Lonker, Harvard University;[8] S. K. Sharma, Univer-

[1]Appointment from September 1 through October 31, 1979; on leave of absence at University of Tokyo from November 1, 1979.

[2]Appointment terminated August 31, 1979, to return to Department of Geology, Smith College, Northampton, Massachusetts.

[3]Temporary appointment through August 15, 1979, and from June 16, 1980.

[4]Appointment terminated August 31, 1979, to accept position as Assistant Professor, Department of Geology, Texas A. & M. University.

[5]Appointment terminated March 31, 1980, to accept position as Research Associate at the University of Kiel, West Germany.

[6]Appointment from January 1, 1980.

[7]Appointment terminated August 15, 1979, to accept position as Research Associate, Department of Chemistry, Arizona State University, Tempe.

[8]Appointment from September 1, 1979.

sity of Leicester, England;[9] E. Takahashi, University of Tokyo

Predoctoral Fellows: D. L. Elthon, Lamont-Doherty Geological Observatory, Columbia University;[10] A. P. Gize, Pennsylvania State University;[6] Wendy J. Harrison, University of Manchester, England;[11] R. H. Kingsley, University of Rhode Island;[12] J. F. Mammone, University of California at Los Angeles;[13] Shirley A. Rawson, University of Oregon[14]

Research Assistant (Graduate Student): A. M. G. Possolo, Yale University[15]

Fellowship Trainee: A. Rubin, Dartmouth College[16]

Executive High School Intern: Halina Dabrowski, Bethesda-Chevy Chase High School[17]

Summer Research Aide: Roshini Ponnamperuma, Sidwell Friends Upper School[18]

Guest Investigators: R. G. Anderson, Carleton University, Canada; J. Brandle, University of Madrid, Spain; Julia Carey, Virginia Polytechnic Institute and State University; J. M. Ferry, Arizona State University; E. Gil-Av, Weizmann Institute, Rehovot, Israel; R. Jeanloz, Harvard University; P. Karabinos, Johns Hopkins University; D. W. Keith, Johns-Manville Corporation; R. K. Kotra, University of Maryland; N. Kriausakul, University of Texas at Dallas; S. A. Margolis, National Bureau of Standards; B. McKinney, Johns Hopkins University; J. Myers, Johns Hopkins University; R. K. Popp, Texas A. & M. University; C. M. Scarfe, University of Alberta, Edmonton, Canada; Y. N. Shieh, Purdue University; Ann Sigleo, University of Maryland; E. Taylor, University of California, Riverside; S. R. Todd, Johns-Manville Corporation; C. Unan, Middle East Technical University, Ankara, Turkey; A. Van Valkenburg, U. S. Bureau of Mines (retired); J. Wittig, Thomas J. Watson (IBM) Research Laboratory; R. W. G. Wyckoff, University of Arizona; Kathy Zoon, National Institutes of Health; G. Zou, Jilin University, The People's Republic of China

[9]Appointment terminated April 30, 1980, to accept position as Geochemist/Spectroscopist at the Hawaii Institute of Geophysics, University of Hawaii.

[10]Appointment from October 1, 1979.

[11]Appointment terminated September 30, 1979, to accept position as National Research Council Research Associate at NASA Johnson Space Center, Houston, Texas.

[12]Appointment terminated October 31, 1979.

[13]Appointment terminated April 30, 1980, to accept position as Research Chemist, E. I. du Pont de Nemours and Co., Wilmington, Delaware.

[14]Appointment terminated December 31, 1979.

[15]Appointment from June 23, 1980.

[16]Appointment from April 1 through May 12, 1980.

[17]Appointment from September 10, 1979 through January 23, 1980.

[18]Appointment from July 1 through August 3, 1979.

Operating and Maintenance Staff

Executive Officer: A. D. Singer

Editor and Librarian: Dolores M. Petry

Stenographers: Marjorie E. Imlay, Mabel B. Mattingly

Typist-Accounting Clerk: Barbara B. Jones

Clerk and Technician: H. J. Lutz

Electronics Technicians: D. J. George, C. G. Hadidiacos

Shop Foreman and Instrument Maker: C. A. Batten

Laboratory Technician and Instrument Maker: G. E. Speicher

Instrument Makers: C. Brown, J. R. Pidgeon,[19] J. W. Schwartz[20]

Building Engineer: H. L. Moore

Custodian and Painter: M. Ferguson

Custodian and Thin-Section Technician: D. Ratliff, Jr.

Custodian and Mechanic: L. B. Patrick

[19]Appointment May 13–29, 1980.
[20]Retired June 30, 1980.

Department of Terrestrial Magnetism

Washington, District of Columbia

George W. Wetherill
Director

Contents

Introduction 433

Physics and Chemistry of the Earth . 447
Crust and upper mantle—geochemical studies 447
Gorgona komatiites: petrogenesis and relationship to other high-magnesium magmas . . 447
Oxygen and strontium isotopic composition of quaternary andesites from the Andes of SW Colombia 452
Oxygen isotopic composition of lower crustal xenoliths, Kilbourne Hole, New Mexico . 455
K, Rb, Sr, and Ba concentrations and Sr isotopic composition of plagioclase from submarine gabbros . . . 459
^{10}Be as a geochemical and geophysical probe 463
Esmeralda Bank: geochemistry of an active submarine volcano in the Mariana Island arc and its implications for magmagenesis in island arcs 465
Trace element geochemistry of Kohala volcano, Hawaii . . . 472
The role of subducted oceanic crust in mantle evolution . . 477
Rb-Sr whole-rock studies: Virginia Piedmont II 483
Incompatible element and $^{87}Sr/^{86}Sr$ composition of Mt. St. Helens ash 486
Crust and upper mantle—geophysical studies 486
Stress redistribution and slow earthquakes 486
Modeling of near-field straingrams recorded on Sacks-Evertson borehole strainmeters 491
Installation of a borehole strainmeter array in Iceland . . . 495
Preliminary velocity structure of Japanese islands and Philippine Sea from surface wave dispersion 498
Explosion seismology studies in southern Peru 505
Qs of the lower mantle—a body wave determination 508
On small-scale convection at the base of the mantle 512
Properties of geological materials . . 520
Diffusion of Ce, Sm, Eu, and Cs in dehydrated obsidian glass and melt 520
Oxide solution mechanisms in silicate melts 522

Earth, Planets, and Meteorites . . . 524
Reassessment of the "age of the Earth" 524
Inert gases on Venus 532
Isotopic anomalies in the early solar system 539
Meteorites from beyond Jupiter? . 543
Multiple cosmic ray exposure ages of meteorites 546
Brecciation chronology of three xenolithic chondrites using fission tracks 548
Variation of fission track densities on olivines from Murchison carbonaceous chondrite . . . 551
Occurrences and formation of tetrataenite, ordered FeNi, in meteorites 553

Stars and Galaxies 556
Neutral hydrogen shells in the Galaxy 556
Abundances of remote galactic halo subdwarfs 561
Blue stragglers 563
Systematic variations of dynamical properties along the Hubble spiral sequence . . . 566
The shape of 21-cm velocity profiles from spiral galaxies; correlations with luminosity and optical rotation curves . . 573

Instrumentation 578
Imaging detectors 578
Installation of the new 21-cm receiver at the Instituto Argentino de Radioastronomía 581

Bibliography 584

Personnel 586

INTRODUCTION

The work of this Department consists entirely of investigations of the sort commonly referred to as "basic research," a term which evokes different images in people's minds. To some, basic research appears to be a rather frivolous enterprise, directed toward supposedly silly goals such as "trying to find out why the grass is green." Scientists may inadvertently encourage this derogatory attitude when they describe their work as being paid to have fun, or give as their reason for investigating a problem " because it is there." A more serious version of this same concept is often given by description of the scientific venture in terms of humanistic values. This is expressed by the thought that the greatness of a civilization is best measured, not so much by its material wealth or even its survival, but rather by its contributions to art, music, and other creative works of the human mind: In the past great societies have freed certain gifted individuals from the burden of earning a living in practical tasks, thereby permitting them the freedom they needed to make great contributions to human culture.

A more commonly expressed view of basic research is one that is more likely to obtain support from those who pay taxes, write laws, and who view elitism with suspicion. This is that basic science is simply the forerunner of practical application, and therefore of demonstrable necessity to the economy and security of a modern nation. Even if the most basic science does not lead to important applications, when it does the reward is large enough to more than offset the poor guesses that didn't pay off. Successful oil companies drill many dry wells, and in the world outside of fairy tales, many frogs must be kissed to find a prince. From this point of view, it makes sense for agencies of the federal government with specific societal missions to identify those areas of basic research most likely to aid in achieving their immediate goals, and to award grants for research to find ways to reduce the time interval between a basic discovery and its practical application.

There is a third way of regarding basic research which is of comparable importance but is less often discussed. This derives from the importance not simply of obtaining and publishing scientific data but also of organizing scientific knowledge in such a way that it can be successfully transmitted to contemporaries and subsequent generations. Without this, the value of a scientific discovery would die with its discoverer, suffering a fate similar to that of the voice of a great singer who lived before the present electronic age. Without this, technological innovation would rest upon sterile empiricism. The principal genius of the scientific epoch that began in Europe a few centuries ago has been the close interaction between observation, experiment, and theory—the continuous effort to discover the underlying principles behind the chaos of empirical facts and the search for more empirical data with which to confront these syntheses. This striving for universal principles is not merely intellectually satisfying, it is necessary if scientific progress is to resemble a ladder more than a treadmill. Without this synthesis, there would be no way to discuss anything with more than a few experts, the teaching of courses would be impossible, and the wellspring of knowledge for future application would run dry. That this third concept of basic science

is distinct from those described earlier can be seen by considering the criteria one would use in selecting the best experimental or theoretical problems to investigate. They would be selected not because they were beautiful, elegant, amusing, or technologically promising, nor would the choice be entirely delegated to a selected individual, but choices would be made simply because in the best judgment of those concerned they were the most fundamental. Furthermore the investigations would not be considered satisfactorily completed until they were integrated into a common and communicable body of scientific knowledge, rather than simply being highly regarded by a small group of specialists.

All three concepts of basic research have merit and usefulness, and all three have been emphasized at various times within this Institution and Department. One of the earliest charges to the Institution was that "when the genius is discovered, provide him with the best equipment that can be obtained." The practical applications of this Department's work were emphasized by Andrew Carnegie in stating that its "worldwide mission is to ensure against shipwrecks," and by its later contributions to radar, nuclear fission, the electronic proximity fuze, and earthquake prediction.

The command to discover the genius is easier to write into the founding papers of an Institution than it is to actually carry out. It is fortunate that major scientific advances can be made by people of ordinary superior intelligence who, when they fall into some imaginary ninety-ninth percentile, share this position with more than two million other people in this country. It seems likely that the present antipathy toward elitism may be short-lived, and that it will be recognized that a large fraction of the progress of civilization can be attributed to the achievements of a minority of the population. But it is also true that the genuine elite is for the most part an unconscious one, characterized more by its members assuming unusual obligations rather than being singled out to receive special privileges. An "uncertainty principle" seems to exist, which requires that when individuals are identified as belonging to the elite, their membership is likely soon to expire.

Another article in its charter charges the Institution with the responsibility to avoid investigations that will be carried out by some other group anyway, and instead to preserve its limited resources for the unique contributions it can make. This tends to deemphasize the "conveyer belt" approach to basic research, which stresses evolution into practical application. It is less difficult for others to obtain financial support for research which can be justified by the expectation of rapid application, and federal and industrial funds are channeled in this direction.

Therefore, even though these three conceptions of basic research are by no means mutually exclusive, it is natural that the third of these, the one that emphasizes the search for fundamentals, continues to receive special emphasis in the work of this Department. For a somewhat different reason, a similar emphasis is preferred by most university scientists. In their case, the primary consideration is the close link between this concept of basic research and the teaching of courses and other aspects of the education of students. In any case, this convergence of emphasis has placed us in the same scientific community as scientists in the major research departments of the universities. In fact, this shared quest for fundamental knowledge is the true essence of "higher" education, transcending legal definitions that emphasize the rubrics of a catalog, courses, and a formal student body. From this larger point of view, we are all students and teachers, obtaining

new knowledge not only from published work of others, but from the world itself. These must be integrated into new syntheses, and transmitted to one another and to the larger scientific community of both the present and the future.

At the present time the need for unification is greatest in the borderlines between traditional specialities. Achieving this unification is a difficult challenge. Within the individual specialities, high standards of excellence and professional traditions, usages, and customs have been established, and those trained in these fields are naturally reluctant to tamper with them. One is particularly aware of this in our Department, where about 25 scientists from the fields of geochemistry, geophysics, geology, cosmochemistry, and astronomy are at least in physical contact with one another, unshielded by the insulation provided by larger groups and departmental administrations. Over the years our way of doing fundamental science has led to unique contributions. On the other hand, our way has not persuaded even some of our own astronomers that they should stop referring to almost all elements (including neon and sulfur) as metals. Cosmochemists have been known to refer to inert gas compositions that are found not in planets but only in meteorites, as "planetary." The need to invent not merely specialized, but even personal jargon and acronyms sometimes appears to be considered an essential duty of an independent scientist.

Maybe this doesn't matter, provided the individual contributions remain fundamental and of high quality. Nevertheless, it is my belief that we must also continue to strive to overcome these relatively trivial as well as other, deeper barriers to the integration of fundamental knowledge. Only in this way can we make full use of the opportunity we possess to accomplish something much more, and to provide those who remain here and those who leave to continue their work elsewhere, the inspiration and confidence needed to overcome the restraints of professional tradition, without sacrificing either personal rewards or the highest standards of science.

Selective Summary Of Current Research

The Earth's Crust and Mantle—General Context of the Work

One of the most active programs at DTM involves using the insights afforded by the plate tectonics synthesis, in an endeavor to understand in more detail the physical and chemical processes of the Earth's crust and mantle and their interaction. This theme occurs throughout most of our geochemical and seismological work. In order to make it easier to relate these studies to one another and to fundamental questions of each science, a brief discussion of current understanding of global tectonic processes will be given here.

It is now well established that the interior of the Earth is a giant heat engine. The radioactive decay of uranium, thorium, and potassium in the Earth's interior produce energy at a rate of 10^7 megawatts, coincidentally similar to the rate at which energy, primarily from fossil fuels, is consumed by human civilization. The energetic radiation emitted by natural radioactivity is stopped within a few centimeters of its mineral sources and is converted into heat. The accumulation of this heat causes the temperature of the rocks to rise. At high temperatures the strength of even solid rocks decreases enough to permit them to flow very slowly in much the same way that liquids flow. The force which drives the fluid flow of solid rocks is buoyancy. Because hot rocks have lower density than cool rocks, they flow upward toward the surface, where in a

somewhat complex way they lose their heat by conduction through a thin surface layer and subsequently radiate their heat from the surface of the Earth into space. After this loss of heat, the resulting cooler and denser rocks sink into the Earth's interior and displace the upward-moving hotter rocks. During this convective flow, buoyancy is also provided by the melting of rocks to form magmas, and by solid-state phase transitions as well.

The greatest convective activity occurs beneath the ocean basins. Large volumes of high-temperature rocks are rising beneath the worldwide system of mid-ocean ridges. As this material nears the surface the rocks partially melt, pouring out several cubic kilometers of volcanic lava onto the ocean floor annually. The lava then solidifies to form the basaltic crust of the ocean basins. The crust lies above a solid layer about 50 km thick, which represents the solid residue of this melt. This entire solid (crust plus residue) is termed the "lithosphere." The lithosphere drifts away in the form of plates in directions perpendicular to the ridge axes, and is replaced by fresh upwelling rock beneath the ridges. The solid plates of lithosphere glide along above a zone consisting of weaker, partially molten portions of the rock that ascended at the same time beneath the ridges (asthenosphere) but that didn't come near enough to the surface to completely solidify. As the uppermost mantle, consisting of lithosphere and asthenosphere, flows away from the ridge, the mantle material cools, and the solid lithosphere becomes thicker by solidification of the partially molten asthenosphere beneath it.

The Earth's surface contains about 13 of these moving plates, some of which are also fastened to the great continental masses whereas others are of purely oceanic nature. For geometrical reasons these plates do not move about freely, but interfere with the motion of each other along their lines of contact. At some of these contacts the plates slide with respect to one another along fault zones, illustrated by the San Andreas fault in California. In other cases their relative motion is permitted only as a consequence of subduction, whereby one of the plates yields its surface right-of-way to the other, plunges beneath it back into the Earth's interior, and thus constitutes a portion of the downward flow of the convective cycle. The surficial expression of the subducted plate is a seafloor trench.

When this subduction occurs at the junction of two oceanic plates, an arcuate chain of volcanic islands is found on the surface of the surviving plate, above the descending subducted plate (for example, the Marianas and the Aleutians). When the subduction occurs at the junction of an oceanic plate and a continental margin, a volcanic mountain chain is formed, as may be seen in the Andes.

In addition to the volcanic rocks of the mid-ocean ridge, and those associated with the island arcs and subduction zones, there are oceanic volcanic islands, for example, Hawaii, that appear to be unrelated to either of these sources.

Geochemical Studies of the Earth's Crust and Mantle

A major thrust of geochemical work at DTM and many other laboratories is to try to understand quantitatively the nature and origin of the lithospheric plates and the underlying mantle, the relationship of these to the various volcanic rocks and their sources, and what all of these things can tell us about properties and processes of the Earth's mantle. Several current investigations of this general kind will be discussed here.

In principle, the most straightforward way to study the oceanic plates would be to actually sample them by drilling a number of holes into them. In

practice, in spite of a very successful worldwide program of oceanic drilling, only the upper 300 meters of the oceanic crust are directly sampled in this way. However, there are rare occurrences where portions of oceanic crust have been elevated and preserved above sea level, and therefore become amenable to normal geological study. One such area is on Gorgona Island, off the Pacific coast of Colombia. Last year Echeverría described the occurrence on Gorgona of komatiite, a lava with a very high melting point and a very magnesium-rich composition, more characteristic of the Earth's mantle than the crust. The discovery was particularly noteworthy because all other well-established occurrences of komatiite were in rocks 2600 million years of age or older, and it was often surmised that such high-temperature lavas could have been produced only at an early time in Earth history when near-surface temperatures were probably higher. The discovery of very young komatiite at Gorgona not only showed this was not strictly true, but also afforded an opportunity to study in detail the occurrence of a geological phenomenon generally characteristic of an earlier stage in Earth history.

This opportunity has been pursued and the results described in this year's Report. It might have been supposed that the magnesium-rich composition of komatiite represented the parental material of the oceanic mantle which partially melted to form oceanic basalts. In a combined experimental and theoretical geochemical study, Echeverría and Hofmann show that this is not the case. The pattern of rare earth element concentrations shows that there is nothing primitive or primary about Gorgona komatiite. It is strongly depleted in the light rare earth elements and was probably formed by the partial melting of depleted oceanic mantle a considerable time after basaltic melts had already been extracted from it. These workers also show that the geochemical processes that produce komatiites, demonstrably lavas, are closely related to those that generate other relatively young rocks of high melting point which occur in Iceland and Spain, for which there has been disagreement about whether or not they were true melts, or rocks brought to the surface as solids. Their demonstrated relationship to komatiites thereby extends further the case for high-temperature melts late in Earth history.

More often, such direct sampling of a geologically observable section of oceanic crust is not possible, and it is necessary to make inferences concerning the oceanic crust and mantle from the thick sequences of volcanic rocks found on oceanic islands, in island arcs, and in mountain chains located above subducting slabs, such as the Andes.

The volcanic systems associated with subducted plates are of great geological importance because, among other things, they appear to represent a major, and quite possibly the dominant process whereby low-density, highly buoyant continental material is formed. It is this high buoyancy which permits continents to resist subduction and remain on the surface for billions of years, in contrast to oceanic crust which will survive for only about a hundred million years before it is destroyed by subduction. In order to understand how continents are formed, much attention has been given to trying to understand the source of the magma that erupts as lava from the Andean volcanoes above the subduction zone on the west coast of South America. Is the volcanic material derived by melting and upward migration of the oceanic crust after it is subducted? Or, does it primarily represent a recycling of continental material which is eroded from the continents onto the sea floor and subducted beneath the continent along with the oceanic plate, and which then undergoes melting and ascent back into the conti-

nental crust? In either case, to what extent is the ascending magma "contaminated" by assimilation of continental material as it migrates toward the surface?

For several years, James has devoted his attention to the use of the isotopic composition of oxygen and strontium in the Andean rocks to determine the extent to which they bear a "crustal signature" or appear to be pristine mantle material lacking a previous crustal history. Oxygen which has had a crustal history and consequently has been involved in processes of interaction with the atmosphere and surface water is characteristically enriched in the heavy oxygen isotope ^{18}O. This year, James reports the early results of a more extensive investigation on volcanic rocks from the central Andes. The enrichment in ^{18}O that is observed demonstrates the presence of a crustal component in these lavas, established either by assimilation of crustal material during ascent or by subduction of sediments of continental origin. Further investigation may distinguish between these two alternatives and permit more quantitative assignment of the relative importance of these various possible sources.

In another study, James and his collaborators Padovani and Hart at M.I.T. address the question of whether or not the isotopic composition of the oxygen in the lower continental crust also imposes a crustal signature upon a magma contaminated by the lower crust, or if the lower crust is indistinguishable from the mantle beneath it as a result of isotopic exchange with mantle rocks. In this work, the oxygen isotope composition was measured on rocks brought from a depth of 20–30 km in the lower crust by explosive volcanism. It was found that lower crustal rocks originally of sedimentary origin preserved their original crustal isotopic identity, despite long-term residence at near-melting temperatures in proximity to rocks of mantle origin that bear the characteristic mantle oxygen isotope signature. This persistence of oxygen isotope identity under these extreme conditions is thought to result from the extreme depletion of these rocks in water. Very dry rocks are characteristic of the lower crust, and therefore it appears likely that a crustal signature can be imposed on ascending magmas by either the upper or lower continental crust.

In the case of the volcanic island arcs, they are often far enough from a major source of eroded surface sediments that the contribution of these subducted and subsequently melted sediments to the lavas of the volcanic islands should be minor. This reduces the complexity of the problem of untangling the contribution of various sources to the volcanic rocks. However it is still necessary to distinguish the contribution of the downgoing plate, consisting of ocean ridge basalts and other solid rocks of the oceanic lithosphere, from the contribution of the wedge of oceanic upper mantle lying above the subducted plate.

The chemical and isotopic characteristics of igneous rocks produced at the ridge at the time they ascend as magmas is well-defined and uniform. However, during and after their eruption they interact extensively with seawater that percolates through the oceanic crust. The rocks are profoundly altered chemically, isotopically, and mineralogically by this interaction. It is necessary to understand the processes that take place in the course of this alteration, if one is to know the actual nature of the basalts of the oceanic crust at the time they are subducted, after transport across the ocean basins for tens of millions of years.

Ito reports the results of a geochemical study of the alteration of the deeper-seated equivalents (gabbros) of the volcanic rocks of the oceanic crust caused by their exchange with seawater. She makes use of the difference

in the isotopic composition of oxygen between the unaltered rocks and seawater to quantitatively calculate the volume of seawater with which a given volume of rock has exchanged. This result is then related to other chemical changes in the altered rocks. It is found that these rocks commonly react with volumes of seawater comparable to their own volumes. In the process, sodium is extracted from the seawater and incorporated into the minerals of the rock. At the same time, the minor and trace elements with a large ionic radii, potassium, rubidium, and barium, are partially lost to the seawater and also mineralogically redistributed within the rock. The concentration of strontium is not affected much by exchange with seawater, but the isotopic composition of the strontium changes slightly toward the composition of strontium in seawater. These effects seem to be understandable in terms of the known geochemical behavior of these elements.

Another study, also directed toward gathering the basic data needed to identify the contribution of the subducted slab to volcanic lavas, is described by Brown, Sacks, and Tera and their collaborators Klein and Middleton at the University of Pennsylvania. In this work it is planned to make use of the radioactive isotope ^{10}Be as a tracer to identify subducted material in volcanic rocks. ^{10}Be, produced in the atmosphere by cosmic rays, settles in oceanic sediments, which form the uppermost portion of the subducted plate. Techniques have been developed to use the University of Pennsylvania tandem Van de Graaff accelerator as an extremely sensitive mass spectrometer capable of measuring ^{10}Be even if its isotopic abundance is as small as 10^{-13}. If the subducted oceanic crust contributes a major portion of the trace elements to the volcanic rocks on a time scale comparable to or shorter than the 1.5-million-year half-life of ^{10}Be, then this isotope should be detected in the erupted lavas. ^{10}Be has already been identified in natural materials, including oceanic sediments, by this group. Extraction of beryllium from volcanic rocks is now underway.

Stern and his co-worker Bibee at Oregon State University report measurements of strontium and neodymium isotopic composition, and trace element concentrations in the volcanic rocks from the Mariana island arc. From these data they infer that the subducted slab of oceanic lithosphere is not the dominant source of these lavas. Instead, they present evidence to show that their source must be the only alternative, partial melt from the wedge of oceanic upper mantle lying above the subduction. If the wedge were the source, then one might expect, at least naively, that these rocks would resemble the mid-ocean ridge basalts, insofar as the wedge represents oceanic crust and upper mantle transported from the ridge, from which the ridge basalts were also formed by earlier partial melting. However, Stern and Bibee demonstrate differences between these arc basalts and those from the ridge, suggesting that the origin of the wedge is more complex. The arc basalts resemble the rocks of the oceanic islands, such as Hawaii, often believed to be the result of mantle plumes or "hot spots," unrelated to the ridge-to-trench migration cycle, and it is possible that similar material has been added to the wedge.

In the last of these experimental investigations, Feigenson and Hofmann report a study of trace elements and strontium isotopic compositions in rocks from one of the oceanic islands of Hawaii, a site of present-day volcanic activity. They found that the geochemical variations in these rocks can be entirely understood in terms of various degrees of partial melting of a homogeneous mantle source, situated at a depth probably somewhat deeper than the immediate source of ocean

ridge basalts. As is the case for other oceanic island basalts, the $^{87}Sr/^{86}Sr$ ratio is characteristically higher (0.7036) than that found for the ridge basalts (0.7027). This indicates their derivation from a mantle source which is different from that of the ridge basalts, one less depleted in the large-ion elements.

Finally, Hofmann and White describe a theoretical model which attempts to explain as many of these phenomena as possible in a single framework. Their basic idea is that the heterogeneities in the mantle responsible for the difference between ocean ridge and oceanic island volcanic rocks result from the subduction of oceanic crust, enriched in large-ion elements such as uranium, thorium, rubidium, and neodymium. Such crustal material becomes more dense above pressures corresponding to depths of about 40 km because of the conversion of lower density feldspar to garnet with higher density. It is proposed that this garnet-rich rock sinks into the mantle, perhaps all the way to the core-mantle boundary, maintaining its integrity. The resulting layer of former oceanic crust will be relatively rich in the heat-producing elements uranium, thorium, and potassium. After hundreds of millions of years, this material will heat itself sufficiently to lower its density and viscosity enough to permit it to rise to near the surface as a mantle plume, producing oceanic island basalts by partial melting of the hot plume near the surface as the melting point decreases at lower pressure. Ridge basalts are derived by partial melting of more homogeneous upper mantle sources. These basalts are extracted from this material to form the oceanic crust. In accordance with the Hofmann-White model, this material is not returned to the source, which therefore becomes progressively depleted in large-ion elements that are concentrated in basalt. These authors describe how, at least qualitatively, this model explains a number of geochemical and geological phenomena, including the observed decoupling of oceanic island volcanism from sea-floor spreading; the observed enrichment (relative to the bulk earth) of the uranium/lead ratios of the source of oceanic basalts, which is paradoxically opposite to that found for rubidium/strontium and neodymium/samarium; as well as the episodic character of terrestrial igneous and tectonic history.

Whether or not this theory remains viable depends upon further qualitative and quantitative comparison with a wide spectrum of data and more detailed modeling to learn if the physical processes assumed are realistic. For example, as discussed above, the conclusion of Stern and Bibee that island arc basalts are derived from the same source as those of the oceanic islands would require that this deep-mantle source dominate the large-ion trace element content of the oceanic upper mantle by the time it is subducted at the trenches. This does not agree with the most common view regarding the relative importance of the ridge and oceanic island sources, but nevertheless could well be true.

Geophysical Studies of the Earth's Crust and Mantle

The motion of the lithospheric plates places the rocks of the crust and mantle under stress. The most familiar way in which this stress is relieved is by rock fracture associated with earthquakes. Extension of the seismic frequency response to zero hertz by the use of Sacks-Evertson strainmeters shows that normal high-frequency earthquakes are not the only way seismic energy can be released. It appears that earthquakes occur which cause fault motions so slow that accelerations remain low, and the usual severe damage associated with a nor-

mal earthquake of the same magnitude does not result.

This year Sacks, Suyehiro, Linde, and Snoke discuss the first documented occurrence of a simultaneous normal earthquake and a nearby slow earthquake. This series of events took place in Japan in January 1978. The normal earthquake, of magnitude 7.0, took place at sea, and subsequent crustal deformation studies showed that similar fault motions occurred inland, but without large accelerations. The strainmeter data, presented in this report, confirm this observation, and show that the energy release was similar for both the normal and slow earthquakes. This extension of seismic data to very low frequencies is thus seen to be accompanied by the discovery of new phenomena. It is possible that episodic but gradual deformation of this kind may play a role in plate motion and other tectonic processes comparable to that of normal earthquakes.

In an accompanying article, the same authors describe a comparison between observed strainmeter data and theoretical modeling of the strain history following an earthquake. It is found that plausible rupture models can explain the observed "straingrams." When combined with higher-frequency seismic data, it seems likely that strainmeter data should provide more detailed knowledge of crustal processes that cause earthquakes.

Shiono, Sacks, and Linde describe the results of the use of seismic surface wave dispersion to study the nature of the upper mantle beneath the Japanese island arc and the Philippine Sea. Under Japan, it is found that low shear wave velocities extend all the way up to the base of the crust. When combined with previous attenuation data of Sacks and Okada, this suggests a relatively shallow zone of high temperature or partially melted rocks in the upper mantle beneath Japan, in contrast to the usual high-velocity lithosphere. More typical oceanic lithosphere-asthenosphere boundaries are found under the Philippine Sea.

In the foregoing summary, emphasis was placed on tectonic and associated geochemical phenomena in the crust and upper mantle. However, in some poorly understood way, it seems likely that convective motion also takes place in the lower mantle. In this connection, Lux and Sacks report a numerical investigation of the circumstances under which small-scale convection may occur near the core-mantle boundary. This convection was proposed earlier by Sacks, Snoke, and Beach to explain observed lateral variation in seismic transmission near the base of the mantle. These two-dimensional results indicate that when plausible physical parameters are used, stable small-scale convection may occur as a consequence of the strong dependence of viscosity on temperature. It is still possible that in the real three-dimensional situation, instabilities will occur which could penetrate upward and preclude stable small-scale convection at the base of the mantle.

The Earth and the Planets

Theoretical, observational, and experimental data about the origin of the Earth and solar system represent a principal interface between astronomy and earth science. On the one hand, our Sun probably formed as part of an ordinary star-forming episode, at which time a number of stars, some of one solar mass, formed within a dense interstellar molecular cloud. The attempt to understand such episodes is a central problem of stellar astronomy, and the history of star-forming processes in galaxies represents a major aspect of their evolution. On the other hand, this particular star-forming event established the initial conditions for the geological evolution of the Earth, Moon, and planets. Relics of these initial conditions are preserved in meteorites, on the Moon, and in a more in-

direct way on geologically evolved planets like the Earth.

In considering the origin of the Earth, one of the most important parameters is the time at which this event took place—"the age of the Earth". A good approximation to the value of this parameter was set at 4.55 billion years by Patterson in 1956; when corrected to the uranium-lead decay constants and other parameters in current use, this figure becomes 4.43 billion years. More recent calculations using newer data from the Earth and the Moon and a more sophisticated approach to the problem have also given 4.43 billion years. On the other hand, meteoritic data, using a consistent set of decay constants, give an age of 4.56 billion years. A number of workers have discussed the difference in these two values. Some authors assume that it is axiomatic that the Earth and meteorites must have an identical age, whereas some others at least appear to take the position that the "age of the Earth" is an essentially free parameter and has no necessary relation to plausible physical processes by which the Earth, Moon, and meteorites may have formed. When these simplistic points of view are abandoned and these processes are considered, it turns out that it is quite possible, and even probable, that about 100 million years was required to form the Earth from bodies similar in size to the parent bodies of the meteorites. However, the same physical processes which determine this time scale also determine the thermal history of the Earth, and indicate that the mean time of uranium-lead fractionation that accompanied the formation of the Earth's core corresponds to a shorter interval of 10–30 million years. The "age of the Earth" calculated from lead isotope data, probably actually dates this mean age of core formation. For this reason, an age of the Earth 100 million years later than the age indicated by meteorite data raises some difficulties for quantitative theories of planet formation.

In this Report, Tera presents data which strongly suggest that the actual time of core formation was in agreement with the theoretical expectation, namely about 4.54 billion years. These data are obtained from lead-bearing minerals more than 2.6 billion years of age. Tera discerns regularities in the lead isotope ratio from these ancient minerals and infers that for the first two billion years the mantle source of lead had a uranium-lead ratio about 15% lower than that usually accepted. Use of this value leads to a consistent result for both the age of the Earth and the value of this ratio, whereas other combinations are not consistent. It also appears likely that the source of lead minerals of this kind became more enriched in uranium and lead about 2.6 billion years ago. Use of younger samples which had experienced this more complex history leads to a younger, and probably incorrect, value for the age of the Earth.

Another example of the need to relate physical theories of solar system origin to geochemical data is discussed by Wetherill. In this case the geochemical data are the surprisingly high concentrations of the inert gases argon and neon found in the Venus atmosphere by U.S. and U.S.S.R. spacecraft in 1978. A theoretical investigation has been carried out to identify the constraints that these observations place on current theories of planet formation. It is found that within the framework of the major class of theories in which terrestrial planets form by the sweeping-up of smaller bodies, previous explanations of these results raise serious difficulties. An alternative hypothesis, that the excess gas results from the implantation of solar wind in the innermost edge of the protoplanetary disk, is quantitatively examined. It is found that the enhancement of solar wind activity required is

modest, and that a range of current dynamical models for the early stages of planet formation actually do lead to concentration of implanted gas in the region of Mercury and Venus. Whether or not the subsequent evolution of the swarm will preserve this concentration requires further theoretical work. Additional observational constraints may also be imposed by the heavier inert gases, krypton and xenon, when more certain atmospheric data for these elements become available.

During the same period of time 4.5 billion years ago that the terrestrial planets were forming, elsewhere in the solar system the parent bodies of the meteorites were formed. In many cases, the subsequent history of meteoritic matter has been so mild that details of these events in early solar system history are still preserved in the meteoritic record. Exploitation of this meteoritic record is an important aspect of current work at DTM, as well as in many other laboratories throughout the world. For example, Lee and Brown report on early stages of their work seeking further isotopic anomalies in meteorites; such anomalies indicate inhomogeneity in the mixing of material from various astrophysical sources, such as supernovae, in the formative solar system.

A serious limitation in the interpretation of meteoritic data is our present uncertainty regarding the relationship of meteorite samples studied in the laboratory to real astronomical bodies in the solar system. With the possible exception of a few rare meteorites, the only plausible sources are either asteroids or comets. It is likely that many, if not most, meteorites are fragments of the small asteroid-like Apollo objects, the orbits of which can intersect Earth's orbit. However, the possible sources of the Apollo objects themselves are limited to asteroids and comets.

The most common view is that essentially all meteorites are derived from the asteroid belt, either directly or indirectly via Apollo objects. However, as discussed by Wetherill and ReVelle in this Report, there is some observational evidence that meteoroids with physical properties similar to some meteorites are arriving on the Earth from beyond Jupiter, and thus at least for these objects a relation to comets is probable. In addition, there is still a problem of reconciling astronomical spectral data on asteroids with the most common types of meteorites. Therefore, while it is highly plausible to consider asteroids as prime candidates for meteorite sources, it is thought premature to regard these questions as settled.

The clearest evidence for an asteroidal origin of most meteorites is provided by data from brecciated (fragmentary) gas-rich meteorites, particulary those containing fragments that originally must have formed at different places (xenolithic chondrites). These meteorites exhibit, at least qualitatively, the characteristics of the surface material, or "regolith," of an atmosphere-free planet like the Moon. At least at first sight, it seems plausible to identify these meteorites with the analogous surfaces of asteroids. However, it is not clear whether or not it will prove possible to quantitatively explain meteoritic data in terms of the expected properties of an asteroidal regolith.

One reason for this difficulty stems from the fact that more or less similar breccia can be produced in several ways: by the accumulation of material during the original accretion of the meteorite parent bodies, during the course of a period of greatly enhanced collisional bombardment during the first several hundred million years of solar system history, or under the relatively well understood conditions that prevail in the present asteroid belt. It is plausible that effects from all

of these environments are present in different, or even in the same, meteorites.

Several investigations on these "regolithic" meteorites are being carried out at DTM, directed toward the goal of interpreting their brecciation history, and in particular trying to understand which phenomena should be related to early solar system events and which to more prosaic processes occurring on the surface of a modern asteroid.

Last year, Scott and Rajan, using metallographic data, showed that the xenolithic brecciated meteorites can be subdivided into two types: those that were first metamorphosed and cooled rapidly through 400 °C prior to brecciation and final compaction, and those that were first brecciated and compacted and then subsequently cooled very slowly through 400 °C. This year, Kothari and Rajan have extended this work by study of the fission tracks produced by the extinct radioisotope ^{244}Pu in phosphate mineral grains in some of these same meteorites. The work is directed toward understanding the time in solar system history at which these metamorphic cooling, brecciation, and compaction events took place.

One of these, Bhola, belongs to the group that was metamorphosed and cooled after brecciation. Kothari and Rajan find that ^{244}Pu (82 m.y. half-life) was still present in Bhola after the sequence of brecciation, metamorphism, and cooling. Quantitatively it is calulated that all of these events occurred prior to 4.01 billion years ago—relatively early in solar system history. Two other meteorites, Weston and Fayetteville, belong to the group that were brecciated and formed in a regolith subsequent to their early metamorphic history. These meteorites also contain phosphate grains which experienced an early irradiation by ^{244}Pu over a range of times that average about 4.25 billion years. However, in this case it is not clear whether the age represents the time of metamorphism or resulted from the subsequent history of brecciation, and further work is necessary to make this distinction.

In a related study, Scott, working with Clarke at the Smithsonian Institution, describes the occurrence of a new mineral "tetrataenite" that occurs in many meteorites, including the three discussed above. Scott and Clarke make use of the metallographic occurrence of this mineral to argue that diffusion of nickel in metal must be more rapid than previously believed. If this is the case, the metallographic cooling rates of meteorites based on the diffusion rate usually assumed will be too low. More rapid cooling would result in better agreement with meteorite ages of about 4.5 billion years, based on the time at which radiogenic ^{40}Ar was retained by the meteorite.

Stellar and Galactic Astronomy

While of great interest in their own right, in several ways the astronomical objects studied at DTM are also relevant to our work on solar system and Earth history. Many of the isotopic anomalies in the early solar system sought by Lee and Brown probably have their origin in supernova ejecta heterogeneously mixed into the solar system during its formation, possibly including material from a supernova which triggered the collapse of the interstellar molecular cloud that evolved into the Sun and other stars. The availability of material processed through a supernova is plausible. For example, neutral hydrogen shells in our Galaxy, described by Hu, are shown likely to represent a relic of similar supernova explosions.

Another connection between stellar and planetary science is the use of the abundance of naturally occurring and extinct radioisotopes, determined from meteorite data, to determine details of

the time scale for solar system formation and the relationship of this event to prior galactic history. These calculations involve assumptions about the rate of star and element formation in the Galaxy during its evolution.

Observational data concerning the earliest history of the Galaxy is provided by observations of its oldest stars. These are found far from the solar neighborhood, in the galactic halo, and in the distant globular clusters. Because of their great distance, it is difficult to carry out the high-resolution spectroscopic work needed to measure the chemical composition of these stars. Carney and his collaborator Peterson at Lockheed Research Laboratory in Palo Alto describe the results of an approach which avoids this problem. This involves measurements on members of this same halo population which happen to be at present near the Sun simply because the high eccentricity and inclination of their orbits in the Galaxy occasionally bring them close to the Sun. The three stars investigated have the common property that, relative to the Sun, their ratio of iron to hydrogen is depleted by a variable factor ranging from about 37 to more than 3000. Qualitatively, this would be expected for very old stars. The heavier elements, such as iron, are produced by nucleosynthesis in stars belonging to earlier generations of stars. Therefore the abundance of iron should increase as the Galaxy ages and as more and more stars go through stellar evolution and synthesize heavy elements from which new stars are formed. The surprising aspect of these observations is the variability of this depletion factor among stars of the remote galactic halo, which includes the most iron-deficient star ever observed. Another result is that the same star which is so deficient in iron has an aluminum-to-magnesium ratio quite similar to stars with a less extreme iron deficiency. This was unexpected, since at least some theories of heavy-element nucleosynthesis predict that neutron-rich isotopes such as ^{27}Al will be more abundant if the starting material is also neutron-rich, as is the case for stars containing a relatively high abundance of heavy elements.

The principal observational program at DTM is the measurement of the variation of galactic rotational velocities as a function of distance from the galactic center, for a large sample of galaxies of various types. This is a long-term project. It would be even longer were it not for the reduction in the time required to obtain spectra of the outer portions of a galaxy afforded by use of the Carnegie image tube.

Last year the rotation curves for a sample of 21 Hubble type Sc spiral galaxies were reported. This year the previous sample of large Sa and Sb spiral galaxies was extended to include lower luminosity objects, and a total of 50 rotation curves for the three galactic types have now been obtained.

Rotation curves for the entire sample are discussed by Rubin, Ford, Thonnard, and Burstein. In a complementary paper, Thonnard, Rubin, Ford, and M. S. Roberts (National Radio Astronomy Observatory) compare these results with 21-cm neutral hydrogen velocity data.

As discussed in previous Annual Reports, in a general way the rotation curves of all galaxies are similar to one another. In all cases, the rotational velocity first rises rapidly with increasing radial distance. In galaxies of low luminosity, the velocity is usually still increasing at the edge of the visible galaxy. In galaxies of high luminosity, spectra can be obtained at greater distances from the center. At these larger radii, the rise in velocity flattens out and is more or less constant out to the edge of the visible galaxy. Only rarely does the velocity decrease with distance, as would be expected if the outer portions of the galaxy revolved in Keplerian orbits about a concentrated central mass, as is the case for planets

of the solar system. These results show that the masses of galaxies are far from being concentrated near their center in spite of the central concentration of luminosity. A significant mass lies even beyond the limit of the optical image.

The newer data permit comparisons of rotation curves for different types of spiral galaxies. In spite of the general similarity, mentioned above, there are consistent differences between the various types. For example, the maximum rotational velocities decrease systematically from types Sa through Sc.

It is also found that the maximum rotational velocity of a galaxy increases with its total luminosity. This agrees with previous work wherein this correlation was used to determine galactic luminosity; distance to the galaxy can then be determined by comparing observed brightness with the intrinsic luminosity. However, the relationship between maximum velocity and Hubble type, noted above, requires that galactic type be taken into consideration in making use of this correlation.

A by-product of this investigation is a new relationship between rotation curves and luminosity which should also prove to be a very useful distance indicator. Again, even though roughly speaking all light curves are similar, there are systematic differences in detail. In high-luminosity galaxies, the velocity increases very sharply as one moves away from the galactic center. For galaxies of lower luminosity, the increase is more gradual. For galaxies of lowest luminosity, the maximum velocity is not reached before the edge of the optical image. It is expected that very distant and therefore faint galaxies of high luminosity will be identifiable by use of this relationship, and therefore it should prove to be a valuable cosmological distance indicator.

Comparison of the optical rotation curves with 21-cm data is still at an early stage. These radio frequency observations differ from the optical data in that they provide information on the rotation of the neutral hydrogen component of the galaxy, and also represent the integrated contribution of the entire galaxy, rather than a narrow strip along the major axis of the galaxy. Because of the low resolution of the 21-cm measurements, several times larger than the diameter of the galaxy, direct comparison of optical and 21-cm rotation data is not possible. However, it is possible to construct theoretical models of rotating galaxies that are consistent with galactic mass distributions obtained from optical rotation curves, now that these are available. Comparison of theoretical 21-cm profiles based on these models with observed 21-cm velocity profiles should then permit determination of the neutral hydrogen distribution as a function of Hubble type and luminosity. These comparisons will also permit understanding the extent to which asymmetries inferred from optical data, representing only a very limited portion of the galaxy, are actually large-scale phenomena. Preliminary results of this study suggest that this is the case.

George W. Wetherill

PHYSICS AND CHEMISTRY OF THE EARTH

CRUST AND UPPER MANTLE—GEOCHEMICAL STUDIES

Gorgona Komatiites: Petrogenesis and Relationship to Other High-Magnesium Magmas

Lina María Echeverría and A. W. Hofmann

The study of komatiitic volcanic rocks, initially reported on last year (Echeverría, 1979) has been continued. The Gorgona komatiites are unique in their young geological age and their virtually completely unaltered state of preservation. Because komatiites are undisputed ultramafic volcanic rocks representative of magnesium-rich silicate melts, they may be used in model calculations that elucidate possible origins of such melts, and they may be used as a basis for comparison with other mafic-ultramafic rocks that have been the subject of long-standing disputes as to whether they were ever true melts. Among the latter are picrites, that is, basalts with abundant olivine phenocrysts, and certain "mafic" layers in high-temperature peridotites. First, we show that the extreme light rare earth depletion of the Gorgona komatiites can be explained by a simple, two-stage melting process, and that it is therefore certainly misleading and probably incorrect to refer to these highly magnesian liquids as in any way particularly "primitive" or "primary." On the contrary, they appear to be the end product of a severe depletion process of the mantle, and as a result, they show rather extreme degrees of rare earth element fractionation. Second, we find that the most distinctive features of the chemistry of Gorgona komatiites are also observed in certain picrites and in mafic layers surrounded by peridotite.

REE Patterns of Gorgona Komatiites

Analyses of rare earth element (REE) abundances have been performed on eight samples of Gorgona komatiites, using isotope dilution mass spectrometry techniques. The chondrite-normalized REE plot thus obtained is shown on Fig. 1. With the exception of sample 47, which is lower in overall REE contents, the REE patterns constitute a very tight array. The patterns for all analyzed komatiites are nearly parallel and show the following characteristics: (1) extreme depletion in the light REE (LREE) relative to the heavy REE (HREE), with $(Ce/Sm)_N$ (chondrite-normalized ratio) ranging from 0.28 to 0.47, and averaging 0.38, and (2) negatively-sloped HREE patterns, with depleted Er and Yb relative to Dy.

These features result in asymmetric convex-upwards REE patterns, with a maximum at Dy or Gd. Because of the internal consistency of the REE patterns and the unaltered state of the rocks, it is clear that these patterns are original to the komatiitic melts rather than being the results of secondary processes.

Melt Model Calculations

Generation of komatiitic melts can be explained in terms of their REE patterns by means of a two-stage melting process. The mantle source region was assumed to be slightly depleted in the LREE relative to the HREE (Fig. 2A), as indicated by the Nd isotopic composition of the komatiites (Echeverría, 1980). Calculations were made using the simple batch-melting equation (Shaw, 1970) in two stages. The best-fit model is discussed here.

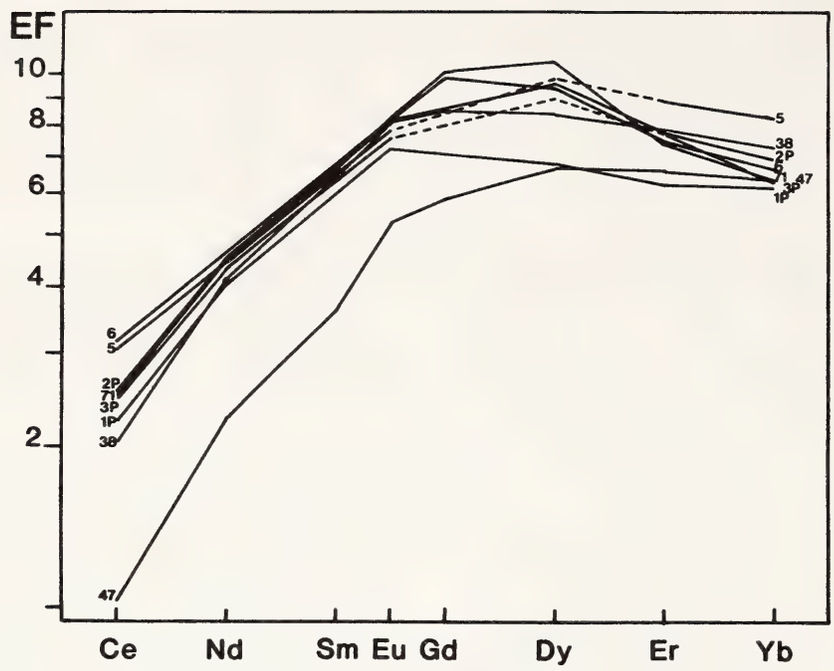


Fig. 1. Chondrite-normalized REE plot for komatiites from Gorgona island. EF: enrichment factor. Sample numbers shown with curves.

The phase proportions in the original mantle were assumed to be as follows: 60% olivine, 25% orthopyroxene, and 15% clinopyroxene. Partition coefficients used in the calculations appear on Table 1. Calculations made with garnet as a mantle constituent phase yielded first- and second-stage melts with positively sloped HREE patterns, even when garnet was present in amounts of the order of 5% or less. Thus, it is concluded that the komatiite melts cannot be generated by melting of a garnet-bearing mantle. Spinel, on the other hand, has little effect on the model calculations because it is a phase with very low and uniform partition coefficients for all the REE.

Upon 4% of melting of the original source mantle, in the proportions 5% olivine–35% orthopyroxene–60% clinopyroxene, a first-stage melt with the REE pattern shown on Fig. 2A is generated. This pattern is comparable with the REE pattern of some of the basalts associated with the komatiites on Gorgona Island (Fig. 2B).

Removal of the first-stage melt leaves behind a residual mantle consisting of 62% olivine, 25% orthopyroxene, and 14% clinopyroxene, and characterized by the REE pattern shown on Fig. 2C. With melting continuing in the same proportions, after an additional 8% of melting, a second-stage melt is generated with a REE pattern very close to that displayed by the Gorgona komatiites (compare Figs. 2B and 2C). The final residual mantle is severely depleted in the LREE relative to the HREE. The second-stage melt, on the other hand, shows a high degree of fractionation of the REE relative to the initial mantle. In this regard, the komatiite melts differ substantially from the mantle source, and rather than being "primary" are significantly "refined" melts.

Sr Isotopic Data

Additional Sr isotopic analyses performed on Gorgona komatiites (Table 2) substantiate the results reported previously (Echeverría, 1980), that the komatiite melts have been unaffected by alteration processes or continental contaminants. Thus, in terms of Sr iso-

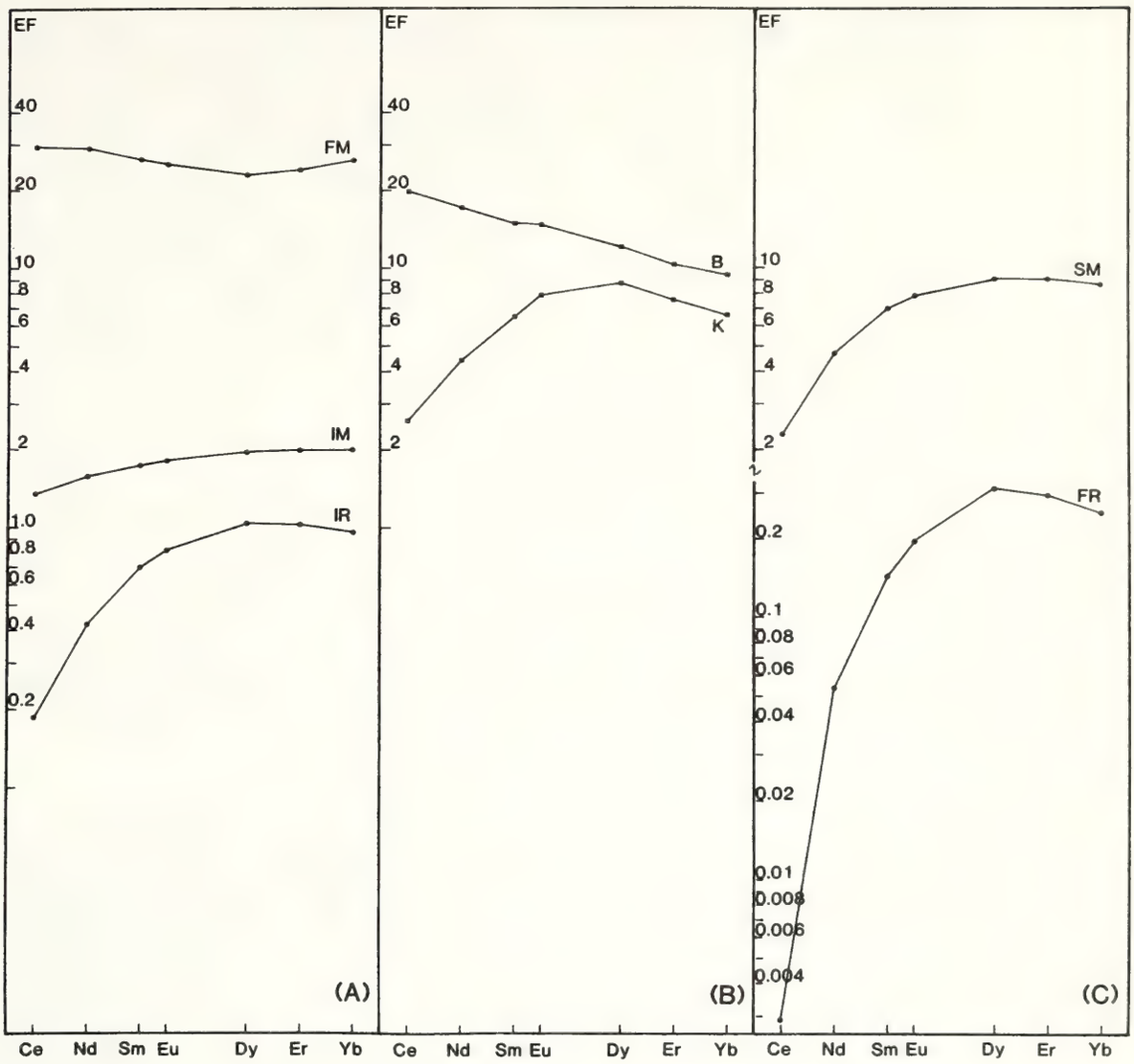


Fig. 2. (A) Chondrite-normalized REE plot for model calculations for komatiite melts. EF: enrichment factor. IM: initial mantle source; FM: first-stage melt after 4% melting of the initial mantle source; IR: residual mantle after extraction of first-stage melt. (B) Chondrite-normalized REE plot for average Gorgona komatiite, K, and associated basalt, B. (C) Chondrite-normalized REE plot for model calculations for komatiite melts. SM: second-stage melt after 8% additional melting; FR: residual mantle after extraction of second-stage melt.

topic data, the komatiites do bear the signature of their parental mantle source. $^{87}Sr/^{86}Sr$ values for the Gorgona komatiites range from 0.70274 to 0.70318, and are lower than values obtained for the Gorgona basalts, which range from 0.70324 to 0.70340 (Echeverría, 1980). An analogous bimodality has been also found for the Nd isotopes: $^{143}Nd/^{144}Nd$ ratios are higher for the komatiites than for the associated basalts (Echeverría, 1980).

Comparison with Picrites and "Mafic" Fusion Layers in Peridotites

The discovery of the Gorgona komatiites has provided unequivocal evidence that ultramafic lavas with MgO concentrations up to at least 22 wt % have been extruded in Phanerozoic time. This fact may help to resolve the long-standing controversy surrounding the origin and petrogenetic significance of Cenozoic picrites. Among the issues of this controversy

TABLE 1. Partition Coefficients Used in Melt Model Calculations

	Olivine-Orthopyroxene	Clinopyroxene
Ce	0.001	0.045
Nd	0.004	0.090
Sm	0.005	0.180
Eu	0.005	0.225
Dy	0.009	0.300
Er	0.009	0.275
Yb	0.010	0.225

TABLE 2. Sr Isotopic Composition of Gorgona Komatiites

Sample No.	$^{87}Sr/^{86}Sr$
1P	0.70307 ± 4
2P	0.70278 ± 4
3P	0.70295 ± 6
5	0.70305 ± 7
23B	0.70317 ± 6
71	0.70274 ± 4

are the questions (1) whether picrites represent the compositions of true melts or merely of melt-plus-olivine phenocrysts assemblages, and (2) whether picritic compositions (assuming they are true melts) are the more primitive (or parental) precursors of many or all tholeiitic basalts (Clarke and O'Hara, 1979).

Major Element Composition

Figure 3 shows a comparison of the major element concentrations of Gorgona komatiites, Reykjanes picrites, and "mafic" layers from the Ronda Massif. Major element compositions used here for the Reykjanes picrites and the Ronda fusion layers are respectively from Jakobsson *et al.* (1978) and Dickey (1970). The major problem with this kind of comparison is the uncertainty created by the effects of addition or removal of olivine. Typical Gorgona komatiites have an average of 18 wt % MgO and are reliably known to represent liquids (though not necessarily *parental* liquids). Consequently, we corrected all sets of data to remove the effect of olivine control in a manner identical to that described by Wright *et al.* (1975). In this way, all the data are normalized to an arbitrary MgO value of 18 wt % by adding or subtracting the appropriate amount of olivine Fo 90. The three suites of rocks show great similarity in composition in terms of major elements, SiO_2, Al_2O_3, and CaO. FeO^t (total iron expressed as FeO) is somewhat lower for the Reykjanes picrites, and considerably lower for the Ronda fusion layers, than for the Gorgona komatiites. The low values, together with the scatter displayed by the Ronda suite, may be the effect of contamination by reaction between the melt and the wall rock, as postulated by Dickey and Nicol (1979).

REE Composition

REE abundances of the Reykjanes picrites and the Ronda fusion layers have been presented by Zindler *et al.* (1979) and Suen (1978), respectively. The similarity between the REE patterns presented by these authors and those reported here is striking. In both cases, the overall abundance of REE is analogous to that of Gorgona komatiites, and the patterns are considerably depleted in LREE relative to HREE, producing convex-upwards patterns. Most of the samples of fusion layers reported by Suen (1978) display negatively sloped HREE patterns. The Reykjanes picrites, however, show from nearly flat to slightly positively sloped HREE patterns. The extreme depletion in LREE relative to HREE is of great significance when compared to the nearly flat or the slightly LREE-enriched patterns of the basalts associated with both the Gorgona komatiites and the Reykjanes picrites. The significance lies in that this depletion indicates that the high-Mg liquids were derived from more-depleted source materials than the associated basalts.

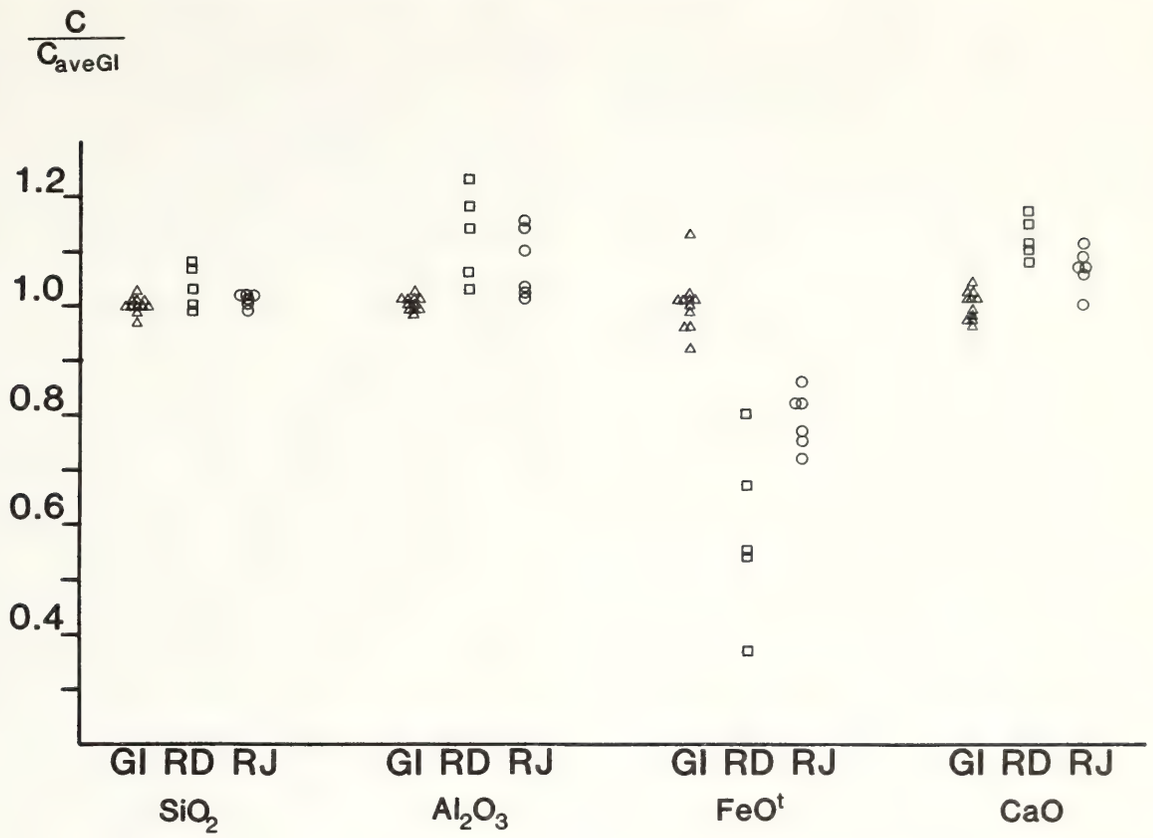


Fig. 3. Normalized concentration of SiO_2, Al_2O_3, FeO^t (total iron expressed as FeO), and CaO of Gorgona komatiites (GI, open triangles), fusion layers from the Ronda Massif (RD, open squares), and Reykjanes picrites (RJ, open circles), plotted relative to the average of the normalized Gorgona komatiites.

This conclusion is confirmed by the isotopic differences between picrites and basalts on the Reykjanes peninsula (Zindler *et al.*, 1979) and between komatiites and basalts on Gorgona Island (Echeverría, 1980). Therefore komatiites, picrites, and probably also the fusion layers in peridotites represent an important class of high-temperature melts, but they are not, at least in the cases studied, "primitive" precursors of ordinary basalts. More likely, they are the melt products of mantle sources that have been depleted by previous production of basalt. Because of the isotopic differences, this depletion must have occurred at an earlier time, and there is no direct genetic relationship between the present association of komatiites (or picrites) and basalts.

Conclusions

Komatiite melts are unusual liquids because of their very high Mg contents and the unusually high temperatures required to generate them. They are, however, not unique, because picrites and some fusion layers in peridotites are melts similar to komatiites both in terms of major elements and REE concentrations. Indeed, the main difference between them is one of texture, rather than composition.

Although the model calculations presented here are not necessarily unique, they do indicate that komatiites are neither melts parental to basalts nor "primitive," but rather are residual liquids produced by a two-stage process of melting of the mantle.

References

Clarke, D. B., and M. J. O'Hara, Nickel, and the existence of high-MgO liquids in nature, *Earth Planet. Sci. Lett., 44,* 153–158, 1979.

Dickey, J. S., Jr., Partial fusion products in Alpine-type peridotites: Serrania de la Ronda and other examples, *Mineral. Soc. Amer. Spec. Pap., 3,* 33–49, 1970.

Dickey, J. S., Jr., and Nicol, L. D., La historia petrológica del complejo ultramáfico de ronda, *Boletin Geologico y Minero de España, 92,* 175–183, 1979.

Echeverría, L. M., Tertiary komatiites of Gorgona Island, Colombia, *Carnegie Inst. Wash. Year Book 78,* 340–344, 1979.

Echeverría, L. M., Tertiary or Mesozoic komatiites from Gorgona Island, Colombia: field relations and geochemistry, *Contrib. Mineral. Petrol., 73,* 253–266, 1980.

Jakobsson, S. P., J. Jonsson, and F. Shido, Petrology of the Western Reykjanes Peninsula, Iceland, *J. Petrol., 19,* 669–705, 1978.

Shaw, D. M., Trace element fractionation during anatexis, *Geochim. Cosmochim. Acta, 34,* 237–243, 1970.

Suen, C. J., Geochemistry of peridotites and associated mafic rocks, Ronda ultramafic complex, Spain, unpublished Ph.D. Thesis, Mass. Inst. Tech., 283 pp., 1978.

Wright, T. L., D. A. Swanson, and W. A. Duffield, Chemical composition of Kilauea east-rift lava, 1968–1971, *J. Petrol., 16,* 110–133, 1975.

Zindler, A., S. R. Hart, F. A. Frey, and S. P. Jakobsson, Nd and Sr isotope ratios and rare earth element abundances in Reykjanes Peninsula basalts: evidence for mantle heterogeneity beneath Iceland, *Earth Planet. Sci. Lett., 45,* 249–262, 1979.

Oxygen and Strontium Isotopic Composition of Quaternary Andesites from The Andes of SW Colombia

David E. James

Introduction

Insight into mountain building processes gained from plate tectonics has provided the stimulus for a decade of broad-ranging studies aimed at understanding the nature and evolution of the Andean orogenic belt. With increased understanding has come keener appreciation that the Andean system is segmented into provinces with fundamentally different geologic and tectonic identities. There are three well-defined, active Andean volcanic provinces, generally termed northern, central, and southern, separated from one another by zones in which Quaternary volcanism is absent.

The northern Andes comprise part of a tectonic complex in which the Nazca, Cocos, Caribbean, and South American plates are in close dynamical interaction. The major geologic and tectonic features of interest in the area of study in southwestern Colombia are shown in Fig. 4. The Andean ranges converge in a narrow knot near the Colombia-Ecuador border and fan out northward as three major belts: (1) the Cordillera Oriental, comprising Precambrian and Paleozoic metamorphic rocks, (2) the Cordillera Central, the extension into Colombia of the active Andean volcanic arc, and (3) the Cordillera Occidental, comprising a mafic complex widely interpreted to be of oceanic origin (e.g., Case *et al.,* 1971). The work reported here represents the preliminary stages of a larger investigation into the nature and origin of Quaternary andesitic volcanic rocks of the Cordillera Central.

The late Cenozoic calc-alkaline volcanic rocks of the Andes vary widely in their isotopic and trace element compositions. Each of the three active Andean volcanic provinces seems to have its own distinctive geochemical "signature": the southern Andes are the least radiogenic, the northern Andes are slightly more radiogenic, and the central Andes are the most radiogenic and enriched in incompatible elements.

The origin of these variations in the composition of the lavas has been a major point of contention. At the heart of the controversy is the overriding question of whether the compositional variations observed are due to crustal contamination of a mantle-derived parent magma or instead are due to compositional variations of the source (or to a combination of both). In general, the

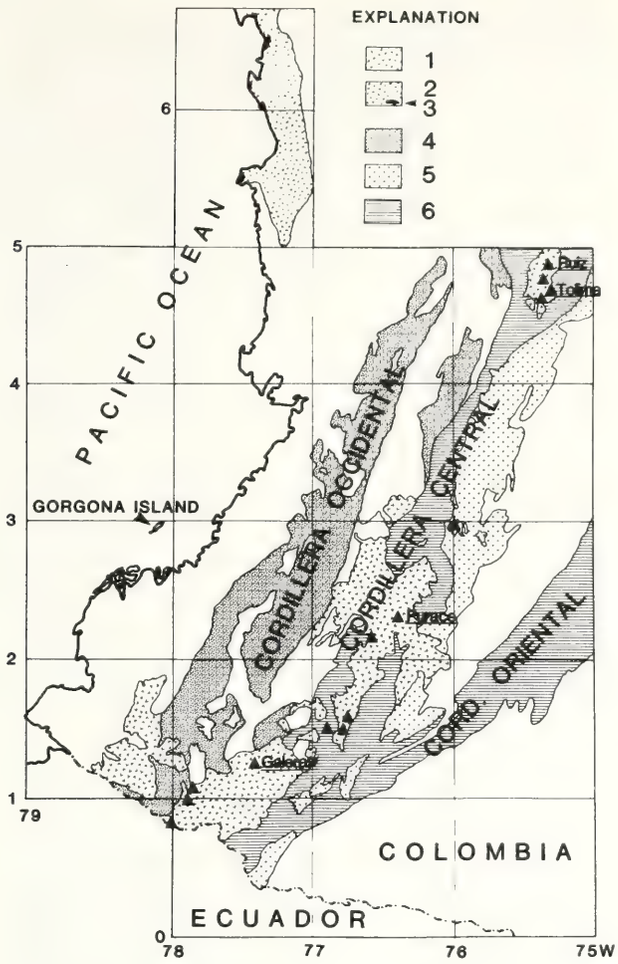


Fig. 4. Geologic sketch map of Andes of SW Colombia. Samples analysed for this paper are from volcanoes Galeras and Purace. 1 = Late Cenozoic calc-alkaline volcanic rocks; 2 = Tertiary mafic volcanic rocks (Serrania de Baudo); 3 = Tertiary ultramafic rocks (locales along coast); 4 = Mesozoic/Tertiary mafic rocks (Diabase Group); 5 = Mesozoic intrusive rocks; 6 = Precambrian/Paleozoic (?) metamorphic complex.

more radiogenic and alkali-enriched lavas are associated with regions of greater crustal thickness; accordingly, it has been suggested that crustal contamination is the principal cause of radiogenic isotope and trace element enrichment in the lavas (e.g., Klerkx *et al.*, 1977; Francis *et al.*, 1977; Briqueau and Lancelot, 1979).

Despite an apparently good correlation between crustal structure and lava compositions, studies in the central Andes reveal systematic isotopic and trace element variations which defy simple interpretation (James *et al.*, 1976; James, 1978a, 1980; Hawkesworth *et al.*, 1979; Tilton and Barreiro, 1980). In southern Peru, for example, andesitic rocks of the southernmost volcanic center (underlain by crust 50–60 km thick) have the lowest $^{87}Sr/^{86}Sr$ ratios (0.705–0.706) but the highest Rb/Sr ratios and alkali concentrations; andesites of the northernmost volcanic center (underlain by crust 40–50 km thick) have the highest $^{87}Sr/^{86}Sr$ ratios (0.707–0.708) but the lowest Rb/Sr ratios and alkali concentrations. All of the lavas of the regions are characterized by high Sr concentrations (550–1100 ppm), so that relatively large amounts of contaminant would be required to raise the $^{87}Sr/^{86}Sr$ ratios to values observed.

Analyses of O isotopes were undertaken at DTM as a direct means of evaluating crustal contamination. O isotopes can be used to assess possible crustal contamination of volcanic rocks (e.g., Magaritz *et al.*, 1978) because crustal material is generally enriched in ^{18}O (has higher $\delta^{18}O$) relative to mantle materials ($\delta^{18}O$ between +5.5 and 6.5‰). In the central Andes, measured $\delta^{18}O$ of about +7.2‰ in late Cenozoic lavas provides strong evidence that the magma contains a *small* crustal component which could have been acquired either in the subduction zone or in the continental crust (James, 1978a,b). The $\delta^{18}O$ values, however, are so low as to all but rule out crustal assimilation as the cause of the anomalously high $^{87}Sr/^{86}Sr$ ratios observed.

The purpose of this study of the calc-alkaline volcanic rocks of the northern Andes is to pursue the problem of Andean magmagenesis in a part of the Andes with distinctly different crustal structure from the central Andes, but where crustal contamination may plausibly remain a significant factor affecting volcanic compositions. (The crust beneath the Cordillera Central is old and about as thick [45 km] as that underlying some volcanoes in southern Peru and northern Chile whose lavas

exhibit anomalous isotopic compositions.)

Results and Discussion

Whole rock Sr and O isotopic ratios were measured on fresh Quaternary andesitic lavas from still-active volcanoes Galeras and Purace in southwestern Colombia. The data are summarized in Fig. 5 in the form of a plot of $^{87}Sr/^{86}Sr$ versus $\delta^{18}O$. The $^{87}Sr/^{86}Sr$ ratios are normalized to an assumed Eimer and Amend $SrCO_3$ standard of 0.70800. $\delta^{18}O$ values are normalized to an assumed CIT rose quartz standard value of $+8.45°/_{oo}$ (NBS #28 = $9.55°/_{oo}$).

The samples measured exhibit a very narrow range in $^{87}Sr/^{86}Sr$ ratios between 0.7040 and 0.7044. These ratios are close to or very slightly higher than typical $^{87}Sr/^{86}Sr$ ratios in volcanic rocks or purely oceanic island arcs and lie entirely within the range of $^{87}Sr/^{86}Sr$ ratios found for similar calc-alkaline volcanics from Ecuador (e.g., Hawkesworth *et al.*, 1979). In this regard, they are notably distinct from lavas of similar SiO_2 content in the central Andes, where $^{87}Sr/^{86}Sr$ ratios range from about 0.705 to 0.708.

Whole rock $\delta^{18}O$ values in Colombian lavas, however, are distinctly higher than $\delta^{18}O$ values measured in low $^{87}Sr/^{86}Sr$ rocks of oceanic island arcs (e.g., Matsuhisa, 1979; Magaritz *et al.*, 1978). The oxygen isotopic ratios in the Colombian lavas, in fact, are not significantly different from those measured in central Andean andesites (see James, 1978b). $\delta^{18}O$ values in central Andean andesites average $\sim 7.2°/_{oo}$, whereas those in Colombian andesites average $\sim 6.9°/_{oo}$. The high $\delta^{18}O$ values imply that the lavas have been modified by a crustal component, either in the subduction zone or in the underlying crust. The slight correlation of $\delta^{18}O$ with $^{87}Sr/^{86}Sr$ ratio (excluding GA1) is contrary to what was found for central Andean lavas, where there is no correlation over a much wider range in $^{87}Sr/^{86}Sr$ ratios, but further data will be necessary to determine whether the correlation is real or not. If the correlation holds up with additional data, it can be used to determine the source of the contamination and the composition of the end members. Studies by Hawkesworth *et al.* (1979) of Nd and Sr isotopes in Ecuadorian lavas suggest that some altered oceanic crust was involved in the petrogenesis of those lavas. On the other hand, the unusual ^{18}O enrichment in the Colombian lavas relative to enrichment in radiogenic strontium could point to upper crustal contamination by assimilation. The data presented here do not provide conclusive evidence for anything other than crustal contamination somewhere in the magma's history, either in the subduction zone or in transit through the crust.

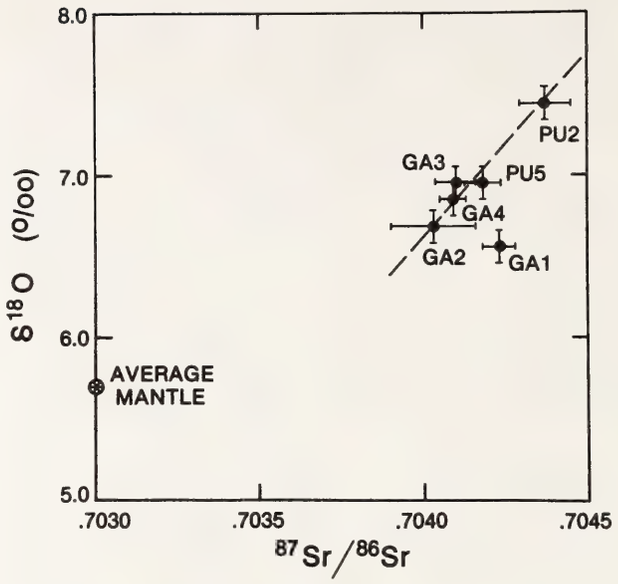


Fig. 5. Whole rock $\delta^{18}O$ versus $^{87}Sr/^{86}Sr$ in Quaternary andesitic rocks from Galeras (GA) and Purace (PU) volcanoes. Average trend, excluding GA1, is shown by dashed line.

References

Briqueau, L., and J. R. Lancelot, Rb-Sr systematics and crustal contamination models for calc-alkaline igneous rocks, *Earth Planet. Sci. Lett., 43,* 385–396, 1979.

Case, J. E., L. G. Duran S., Alfonso Lopez R., and W. R. Moore, Tectonic investigations in western Colombia and eastern Panama, *Geol. Soc. Amer. Bull., 82,* 2685–2712, 1971.

Francis, P. W., S. Moorbath, and R. S. Thorpe, Strontium isotope data for recent andesites in Ecuador and North Chile, *Earth Planet. Sci. Lett., 37,* 197–202, 1977.

Hawkesworth, C. J., M. J. Norry, J. C. Roddick, P. E. Baker, P. W. Francis, and R. S. Thorpe, $^{143}Nd/^{144}Nd$, $^{87}Sr/^{86}Sr$, and incompatible element variations in calc-alkaline andesites and plateau lavas from South America, *Earth Planet. Sci. Lett., 42,* 45–57, 1979.

James, D. E., C. Brooks, and A. Cuyubamba, Andean Cenozoic volcanism: magma genesis in the light of strontium isotopic composition and trace-element geochemistry, *Geol. Soc. Amer. Bull., 87,* 592–600, 1976.

James, D. E., Origin of high $^{87}Sr/^{86}Sr$ ratios in central Andean calc-alkaline lavas, *Short Papers of the Fourth International Conference on Geochronology, Cosmochronology, and Isotope Geology, Aspen, Colorado,* U.S. Geol. Surv., Open-File Report No. 78–701, 199–201, 1978a.

James, D. E., On the origin of the calc-alkaline volcanics of the central Andes: a revised interpretation, *Carnegie Inst. Wash. Year Book 77,* 562–590, 1978b.

James, D. E., Role of subducted continental material in the genesis of calc-alkaline volcanics of the central Andes, *Geol. Soc. Amer. Nazca Plate Mem.,* in press, 1980.

Klerkx, J., S. Deutsch, H. Pichler, and W. Zeil, Strontium isotopic composition and trace element data bearing on the origin of Cenozoic volcanic rocks of the central and southern Andes, *J. Volcanol. and Geotherm. Res., 2,* 49–71, 1977.

Magaritz, M., D. J. Whitford, and D. E. James, Oxygen isotopes and the origin of high $^{87}Sr/^{86}Sr$ andesites, *Earth Planet. Sci. Lett., 40,* 220–230, 1978.

Matsuhisa, Y., Oxygen isotopic compositions of volcanic rocks from the east Japan island arcs and their bearing on petrogenesis, *J. Volcanol. and Geotherm. Res., 5,* 271–296, 1979.

Tilton, G. R., and B. A. Barreiro, Origin of lead in Andean calc-alkaline lavas, southern Peru, *Science,* 1980, in press.

Oxygen Isotopic Composition of Lower Crustal Xenoliths, Kilbourne Hole, New Mexico

David E. James, Elaine R. Padovani, and Stanley R. Hart**

Introduction

It is well known that continental lavas vary widely in trace element and radiogenic isotopic composition (e.g., Brooks *et al.,* 1976, with references to other sources). The cause of that variability, however, is not known: It has been attributed by some to mantle heterogeneity (e.g., Brooks *et al.,* 1976; Wasserburg and De Paolo, 1979) and by others to crustal contamination (see Brooks *et al.,* 1976, for references) and could be a combination of both.

Oxygen isotope analysis provides one means of assessing the degree of crustal contamination of surface-reaching magmas. Crustal rocks which have interacted with the atmosphere and hydrosphere are typically much enriched in ^{18}O over rocks of purely mantle origin. Thus any magma of mantle origin which has been contaminated by such crustal rocks will exhibit ^{18}O enrichment (i.e., higher $\delta^{18}O$).

In general, *upper* crustal rocks are rich in ^{18}O. Accordingly, the case for or against upper crustal contamination of mantle-derived magma may readily be made on the basis of $\delta^{18}O$ measurements. It has not yet been demonstrated, however, that a similar statement can be made for *lower* crustal contamination. It has been argued, for example, that lower crustal rocks, either by virtue of their original oxygen isotopic composition or through exchange with a mantle-type reservoir, are similar in $\delta^{18}O$ to mantle materials. Results presented by Shieh and Schwarcz (1974) are interpreted by them to support the notion that scale oxygen exchange and homogenization (resulting in lower $\delta^{18}O$) are associated with high-grade metamorphism and migmatization in the lower crust. They suggest "that the fluid mobilisate present during anatexis acts as a carrier medium for oxygen transport, to permit oxygen isotopic exchange over large vertical and horizontal distances." If correct, this conclusion is an implicit statement that broad regions of continental lower crust may be characterized by homogeneous $\delta^{18}O$ values which do not differ significantly from those of mantle material.

*Department of Earth and Planetary Sciences, Massachusetts Institute of Technology, Cambridge.

In this report, we show that such massive oxygen exchange is *not* a general phenomenon, even in regions where anatectic melting has occurred. Our conclusion is based upon the study of lower crustal xenoliths carried to the surface in alkali basalt magma in Kilbourne Hole maar, New Mexico. Those lower crustal rocks have to a large degree preserved their original oxygen isotopic identity despite evidence of extensive lower crustal anatexis and the long-term persistence of near melting point temperatures (Padovani and Carter, 1977a).

Kilbourne Hole is situated in the Potrillo volcanic field and is part of the Rio Grande Rift system (see Fig. 6). The region is one of high heat flow (~ 2.4 heat flow units), implying a steep geothermal gradient and temperatures of about 800 ° to 1000 °C in the lower crust (see Fig. 7). Total crustal thickness is about 30 km, and the granulites included in this study come from the lower 10 km of the crust (as inferred from geobarometry; see Padovani and Carter, 1977a, with reference to other work). The xenoliths were apparently transported to the surface very rapidly (at velocities up to 90 kph) during explosive volcanism. As a result, although they do show evidence of rapid heating and some decompression melting, there appears to have been no chemical or isotopic reequilibration (Padovani and Carter, 1977b; Hart *et al.*, 1979).

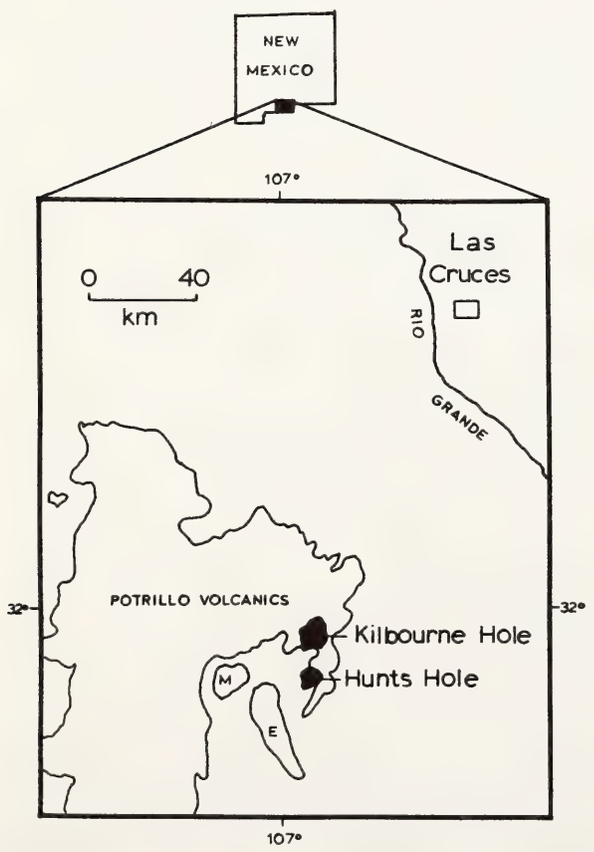


Fig. 6. Generalized geologic map showing location of Kilbourne Hole xenolith field. "M" denotes Mt. Riley; "E" denotes East Potrillo Mts. Based on U.S. Geological Survey Geologic Map of New Mexico (compiled by Carle H. Dane and George O. Bachman, 1965).

Analytical Techniques

O isotope analyses were performed using the method of BrF_5 dissolution and collection described by Clayton and Mayeda (1963). Mass spectrometer precision at the 1σ level is about ± 0.03‰, and estimated overall accuracy is better than ± 0.2‰. O isotope ratios are expressed relative to standard mean ocean water (SMOW) by the relationship

$$\delta^{18}O\ (‰) = \left[\frac{(^{18}O/^{16}O)_{sample} - (^{18}O/^{16}O)_{SMOW}}{(^{18}O/^{16}O)_{SMOW}}\right] \times 1000.$$

In practice, $\delta^{18}O$ values are normalized to an assumed CIT rose quartz standard value of +8.45‰ (M. Magaritz, oral communication). For that assumed value, NBS #28 white quartz has a measured $\delta^{18}O$ of 9.55‰.

Sr isotope ratios on whole rock samples were measured to an analytical precision of better than ± 0.0001 at the 95% confidence level. All ratios are normalized to $^{86}Sr/^{88}Sr = 0.1194$ and an Eimer and Amend standard $SrCO_3$ value of 0.70800.

Results

The lower crustal granulites studied are entirely anhydrous. They have been

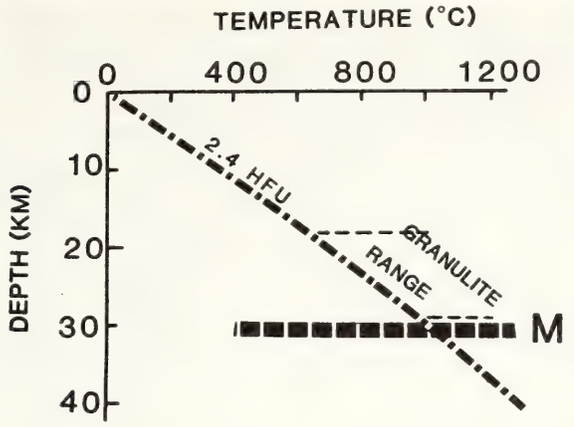


Fig. 7. Temperature-depth model for crust beneath Kilbourne Hole. M denotes Mohorovicic discontinuity. Depth range of granulites studied is indicated by dashed horizontal lines.

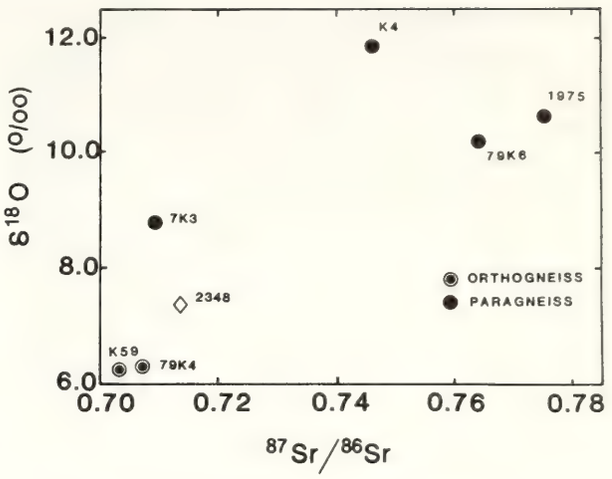


Fig. 8. Average $\delta^{18}O$ versus $^{87}Sr/^{86}Sr$ in garnet granulites (paragneiss) and mafic granulites (orthogneiss) studied. Sample 2348 is a composite orthogneiss and paragneiss sample.

classified by Padovani and Carter (1977a) into two major groups: garnet granulites, and mafic granulites. At least some of the garnet granulites have been interpreted to be the refractory residues of partial fusion of a pelitic rock, and they yield an age (probably for that melting event) of 1.7 b.y. (Hart *et al.*, 1979).

The garnet granulites are characterized by $\delta^{18}O$ values, which range from 8.8 to 11.8‰. The high $\delta^{18}O$ values are accompanied by high $^{87}Sr/^{86}Sr$ ratios (see Fig. 8 and Table 3) ranging from about 0.71 to 0.78. Both the oxygen and Sr isotopic ratios are near those typically found in metamorphosed pelitic rocks and indicate that the rocks have not undergone massive exchange with mantle-type material.

The mafic granulites include one two-pyroxene granulite (metagabbro) and a charnockite, both of which have been interpreted to be deep-seated intrusions of mantle-derived material. This interpretation is borne out by the oxygen and strontium isotopic results. $\delta^{18}O$ values for both samples are close to +6.3‰ and $^{87}Sr/^{86}Sr$ present-day ratios are correspondingly low, from 0.703 to 0.707 (Fig. 8). Both $\delta^{18}O$ and $^{87}Sr/^{86}Sr$ ratios are characteristic of mantle material.

Although there is no simple correla-

TABLE 3. Oxygen and Strontium Isotope Analyses of Lower Crustal Xenoliths, Kilbourne Hole, New Mexico

Sample No.	Subsample	$\delta^{18}O$	$^{87}Sr/^{86}Sr$*
Group 1 Garnet Granulites			
1975	1	10.75	. . .
1975	2	10.73	0.7753
1975	3	10.60	. . .
1975	4	10.49	. . .
79K6	2	10.20	. . .
79K6	3	10.12	0.7642
79K6	4	10.31	. . .
K4	. . .	11.84	0.7460
Group 2 Garnet Granulite			
7K3	1	8.89	. . .
7K3	2	8.82	. . .
7K3	3	8.90	0.7093
7K3	4	8.71	. . .
7K3	5	8.77	. . .
7K3	6	8.59	. . .
7K3	7	8.76	. . .
Mafic Granulites (including charnockite)			
K59	1	6.28	. . .
K59	2	6.17	0.7034
K59	3	6.36	. . .
79K4	1	6.57	. . .
79K4	2	6.14	. . .
79K4	3	6.25	0.7074
79K4	4	6.20	. . .
79K4	5	6.18	. . .

*Sr isotope data from Hart, Padovani, and Roden (1979). Tabulated ratios are whole-rock averages.

tion between high $\delta^{18}O$ and high $^{87}Sr/^{86}Sr$ ratios, the results shown in Fig. 8 clearly show that high $\delta^{18}O$ rocks are characterized by high $^{87}Sr/^{86}Sr$ ratios and low $\delta^{18}O$ rocks are characterized by low $^{87}Sr/^{86}Sr$ ratios, the difference lying in the original sedimentary origin of the high $\delta^{18}O$ granulites and the mantle origin of the low $\delta^{18}O$ granulites.

Discussion and Conclusions

Extreme conditions of temperature, anatexis, and intrusion should hasten isotopic exchange and equilibration between the various rock types in the lower crust and uppermost mantle. It is therefore significant that rocks of the deep crust beneath Kilbourne Hole, as represented by xenoliths carried to the surface, exhibit such wide variation in oxygen isotopic composition. The garnet granulites, all of which appear to be paragneisses, have $\delta^{18}O$ values which range from about 9 to 12‰ and are not markedly different from typical pelitic metasediments with $\delta^{18}O$ between 10 and 15‰. The mafic granulites, presumed to be metamorphosed mafic intrusive of mantle origin, have $\delta^{18}O$ values of about 6.25‰, well within the range of generally accepted mantle oxygen (Taylor, 1968). All the samples studied are in internal isotopic equilibrium.

The high $\delta^{18}O$ values in the felsic granulites and the large variation in oxygen isotopic composition between xenoliths demonstrate that the rocks of the lower crust beneath Kilbourne Hole have not undergone significant oxygen exchange. This result is contrary to the proposal by Shieh and Schwarcz (1974) that extensive oxygen isotopic exchange with some external reservoir of isotopically light oxygen is associated with migmatization in the lower crust. While such exchange may occur in some regions, it appears not to be a universal phenomenon. Indeed, unless a large external reservoir of water is available, it is difficult to conceive how even under conditions of extensive anatexis there can be sufficient oxygen exchange within broad regions of the lower crust to produce regional $\delta^{18}O$ near mantle values. In the anhydrous crust beneath Kilbourne Hole, such exchange apparently has not occurred despite periods of very high temperatures. We conclude, therefore, that oxygen isotopes may be used as reliable indicators of *lower* crustal contamination as well as of upper crustal contamination.

References

Brooks, C., D. E. James, and S. R. Hart, Ancient lithosphere: its role in young continental volcanism, *Science, 193,* 1086–1094, 1976.

Clayton, R. N., and T. Mayeda, The use of bromine pentafluoride in the extraction of oxygen from oxides and silicates for isotopic analysis, *Geochim. Cosmochim. Acta, 27,* 43–52, 1963.

Hart, S. R., E. R. Padovani, and M. K. Roden, Sr-isotopic relationships in lower crustal nodules from Kilbourne Hole, New Mexico, GSA Abstracts with Programs, *11,* no. 7, 439, 1979.

Padovani, E. R., and J. L. Carter, Aspects of the deep crustal evolution beneath south central New Mexico, in *The Earth's Crust,* pp. 19–55, J. G. Heacock, ed., AGU Monograph No. 20, 1977a.

Padovani, E. R., and J. L. Carter, Non-equilibrium partial fusion due to decompression and thermal effects in crustal xenoliths, in *Magma Genesis,* pp. 43–57, Henry J. B. Dick, ed., Proceedings of the Am. Geophys. Union Chapman Conference on Partial Melting in the Earth's Upper Mantle, State of Oregon, Dept. of Geology and Mineral Industries, Bulletin 96, 1977b.

Shieh, Y.-N., and H. P. Schwarcz, Oxygen isotope studies of granite and migmatite, Grenville province of Ontario, Canada, *Geochim. Cosmochim. Acta, 38,* 21–45, 1974.

Taylor, H. P., The oxygen isotope geochemistry of igneous rocks, *Contrib. Mineral. Petrol., 19,* 1–71, 1968.

Wasserburg, G. J., and D. J. DePaolo, Models of earth structure inferred from neodymium and strontium isotopic abundances, *Proc. Nat. Acad. Sci. U.S.A., 76,* No. 8, 3594–3598, 1979.

K, Rb, Sr, and Ba Concentrations and Sr Isotopic Composition of Plagioclase from Submarine Gabbros

Emi Ito

Interactions between oceanic crust and seawater result in a transfer of material and heat between the two reservoirs. The composition of seawater and oceanic crust and, by implication, the composition of material consumed in subduction zones are affected by the interactions. Our understanding of compositional changes occurring in oceanic crust comes largely from studies of basalts. The changes that take place in gabbroic rocks may not be similar to those of basalts either in their magnitude or in the direction of material transfer. Gabbros are coarser grained than basalts, are subjected to higher temperatures for longer times, and are likely to interact with lesser quantities of water.

We know from phase equilibria studies that some minerals will break down at shallower depths than others in subduction zones. The details of these breakdown processes are poorly understood, partly because the composition and mineralogy of subducted crust are poorly known. In particular, few studies have been done on the changes in mineral compositions of basalts and gabbros that take place during interaction with seawater.

In an attempt to better characterize the transfer of material during metamorphism of oceanic crust, concentrations of K, Rb, Sr, Ba, and the isotopic composition of Sr were analysed in 25 plagioclase samples from submarine gabbros. The same plagioclase samples and other minerals not included here were the subject of a previous study designed to provide more information about mineralogic changes in oceanic crust (Ito, 1979). Ito (1979) used a suite of gabbroic rocks collected from the rift valley wall of the Mid-Cayman Rise (Cayman Trough Project and Woods Hole Oceanographic Institution). Alteration temperatures and ratios of interacting seawater to rock were estimated on the basis of petrography, and mineral composition was determined by electron microprobe and oxygen isotopic analysis. The study showed that rock deformation played a key role in the metamorphism: The transformation of calcic plagioclase and pyroxene to sodic plagioclase and hornblende was more pronounced and prevalent in the fractured and granulated parts of the rock. Fractures provided access to seawater or seawater-derived fluid. The composition of amphibole (hornblende) and plagioclase (andesine-oligoclase) indicate metamorphism at temperatures above 500 °C (Liou *et al.*, 1974). Oxygen isotopic analyses of minerals indicate that pyroxene has preserved igneous isotopic ratios, but plagioclase and some amphibole have exchanged oxygen with a fluid whose isotopic composition was less than about 4‰. The hydrogen isotopic composition of amphibole indicates an exchange with a deuterium-rich fluid. For both oxygen and hydrogen, seawater has an appropriate isotopic composition. The volumetric water-to-rock ratios (W/R) were calculated for amphibole and plagioclase, assuming an exchange with unmodified seawater ($\delta^{18}O = 0.00‰$, $\delta D = 0.0‰$) at 500 °C in a closed system. The rocks show a wide range of W/R ratios, which are correlated with the degree of amphibolitization. Calculated W/R ratios for completely amphibolitized rocks are higher (≥ 1) than the ratios found for rocks with roughly equal amounts of amphibole and pyroxene. Rocks with little amphibole interacted with less water ($W/R < 0.5$). The W/R ratio calculated from plagioclase (O'Neil and Taylor, 1967) is consistent with the ratio calculated from amphibole (Suzuoki and Epstein, 1976). The calculated W/R ratio, however, depends heavily on the assumption

that exchange is with unmodified seawater at about 500 °C. The shift in oxygen isotopic composition is due to temperature-dependent fractionation, the exchange kinetics, the relative sizes of the oxygen reservoir (W/R), and, for plagioclase, its chemical composition.

Changes in Sr isotopic composition are independent of temperature fractionation but will depend on exchange kinetics, and the composition and size of the exchanging reservoirs. The determination of the concentration and the isotopic ratio of Sr in minerals in metagabbros may help reduce the ambiguities of W/R ratios constrained by oxygen isotopes. The exchange of Sr by a mineral with seawater ($^{87}Sr/^{86}Sr$ = 0.70909; Sr = 8.0 ppm) should be reflected in a higher isotopic ratio. Just as pyroxene preserves its igneous oxygen isotopic and chemical composition, it should also preserve its Sr isotopic composition, thus providing a reference ratio with which to compare the ratios of other minerals.

The effect of variable W/R ratios may also be measured in the concentration of elements such as K, Rb, and Ba. The partition coefficients of these three elements between the minerals contained in gabbros and the basaltic melt are much less than one (Philpotts and Schnetzler, 1970; Drake and Weill, 1975). During crystallization of a gabbro these elements are enriched in the residual liquid and may reside predominantly along the grain boundaries and near the outer surface of mineral grains. During subsequent metamorphism of plagioclase, increasing the proportion of albite, it is possible that these elements are incorporated into the plagioclase.

Results

The data are shown in Figs. 9 and 10. K, Rb, and Ba concentrations are plotted against An content of the plagioclase (Fig. 9). Two plagioclase samples from the same rock fragment but of differing chemical composition are connected by a tie line. The W/R ratio indicated for each point in Fig. 9 is based on calculations using the oxygen isotopic composition of the mineral, as described in the previous section. Although the concentrations of all three elements tend to increase with decreasing An content of the plagioclase, the correlation is strongest for Ba. Plagioclase that has interacted with less water (W/R $>$ 0.5) generally has a higher concentration of Ba and K for any given An content.

In Fig. 10, Sr concentrations in plagioclase are plotted against W/R ratio, but appear to be nearly independent of this ratio. On the other hand, Sr isotopic ratios show some increase with increasing W/R ratio, ranging from 0.70249 to 0.70291 (corrected to E & A = 0.70800) (see Fig. 10). Neither Sr concentrations nor isotopic ratios show any correlation with An content or oxygen isotopic composition.

Discussion

The data presented in Fig. 9 show that plagioclase which interacted with more seawater (W/R $\geq$ 0.5) has lost proportionately more K and Ba (365 ppm and 0.03 ppm, respectively, in seawater). This is not so evident for Rb, perhaps because its low concentration (averaging about 0.1 ppm) is approximately that of seawater. The relation between the elemental loss and W/R ratio suggest that: (1) much of K, Rb, and Ba in the gabbro resided along grain boundaries before metamorphism, and a large fraction of these elements were leached from the rock by seawater, (2) during metamorphism, some of this leachable intergranular material was incorporated in sodic plagioclase as it formed from calcic plagioclase interacting with seawater. The experiments by Mottl and Holland (1978) on the reactions of seawater with basalt in

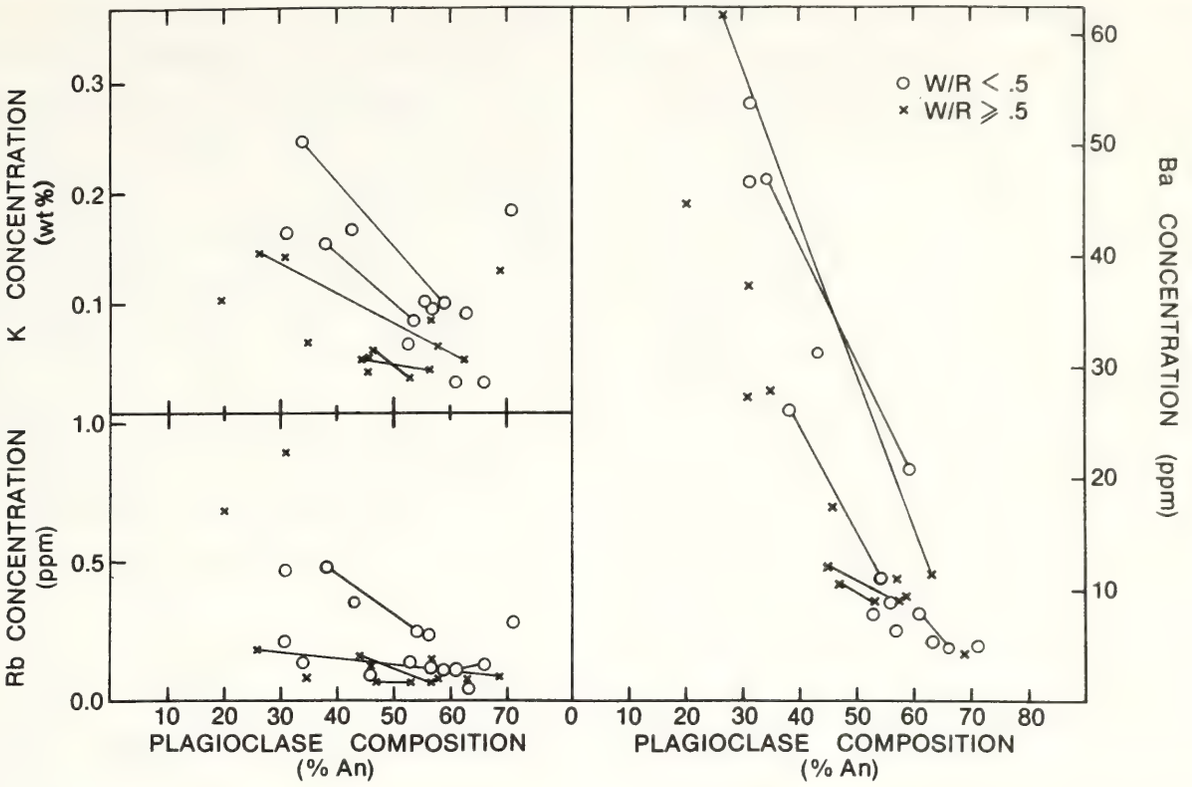


Fig. 9. K concentration (wt %), Rb and Ba concentrations (ppm), plotted against the average An content of each plagioclase sample. Two samples of differing An content from the same rock are connected by a tie line. Indicated W/R ratio for each sample was calculated from its oxygen isotopic composition (see text). The solid line shows calculated $^{87}Sr/^{86}Sr$ ratio of plagioclase assuming an exchange of Sr between plagioclase and seawater for each W/R ratio (see text).

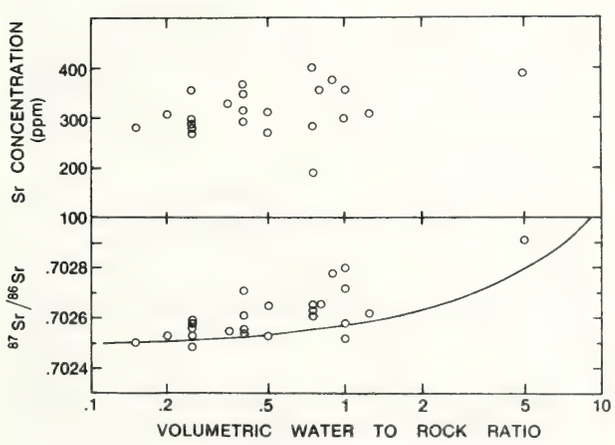


Fig. 10. Sr concentration (ppm) and isotopic ratio plotted against the calculated W/R ratio. Note that W/R ratio is on a log scale.

the temperature range 200°–500°C showed that K and Ba were leached from the basalt.

In contrast to K, Rb, and Ba, the partition coefficient of Sr between plagioclase and gabbroic melt is greater than one (Philpotts and Schnetzler, 1970; Drake and Weill, 1975). Crystallization of plagioclase will therefore result in lower Sr concentrations in the residual liquid and deplete Sr in late crystallizing plagioclase. If sodic plagioclase in the rocks formed as a late crystallizing phase rather than during metamorphism, its Sr concentration should be lower than for calcic plagioclase. The measured Sr concentrations do not show a statistically significant variation as a function of An content. The lack of correlation suggests that sodic plagioclase formed from more calcic plagioclase during metamorphism, just as was deduced from petrographic evidence. Humphris and Thompson (1978), in their study of metamorphosed submarine basalts, concluded that Sr is leached from basalt and suggested that it may follow the same chemistry as

Ca. Results reported here indicate that Sr is not lost from plagioclase grains which are free of alteration minerals. The results further suggest that plagioclase may gain Sr during the interaction with seawater, as evidenced by a weak correlation between the Sr concentration and isotopic ratio (Fig. 11).

The Sr isotopic data are consistent with an exchange of Sr between plagioclase and seawater. If plagioclase ($^{87}Sr/^{86}Sr \approx 0.70250$) exchanges Sr with its own volume of seawater, its isotopic ratio will increase to 0.70257; the ratio will increase to 0.70278 if the mineral exchanges with five times its volume of seawater. The calculated ratios, shown by a solid line in Fig. 10, are lower than most of the measured ratios. The discrepancies could be due to several factors. For example, the W/R ratios calculated from the oxygen isotopic ratios may be too small because the estimate of the temperature was too high and the estimate of the initial oxygen isotopic composition of water was too heavy. Alternatively, the additional increase in the Sr isotopic ratio could come from the direct gain of seawater Sr. The mechanism by which plagioclase gains Sr, however, is not known. Alteration of plagioclase to secondary minerals generally results in a decrease in Sr concentrations in the altered product. Petrographic or x-ray diffraction evidence for alteration minerals in these plagioclase samples is absent. On the other hand, oxygen isotopic evidence supports large-scale exchange with seawater. It is, then, possible that Sr partition coefficients between hot seawater and plagioclase which is undergoing albitization may allow for small increases in Sr concentration.

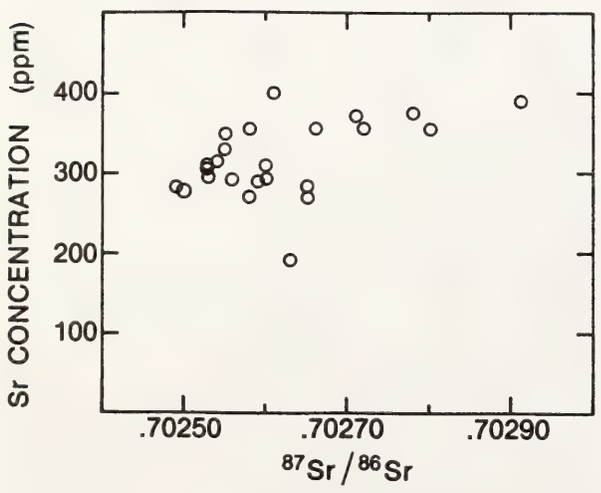


Fig. 11. Sr concentration (ppm) plotted against the isotopic ratio.

References

Drake, M. J., and D. F. Weill, Partition of Sr, Ba, Ca, Y, Eu^{2+}, Eu^{3+}, and other REE between plagioclase feldspar and magmatic liquid: an experimental study, *Geochim. Cosmochim. Acta, 39,* 689–712, 1975.

Humphris, S. E., and G. Thompson, Trace element mobility during hydrothermal alteration of oceanic basalts, *Geochim. Cosmochim. Acta, 42,* 127–136, 1978.

Ito, E., High-temperature metamorphism of plutonic rocks from the Mid-Cayman Rise: a petrographic and oxygen isotopic study, Ph.D. Thesis, University of Chicago, 1979.

Liou, J. G., S. Kuniyoshi, and K. Ito, Experimental studies of the phase relations between greenschist and amphibolite in a basaltic system, *Amer. J. Sci., 274,* 613–632, 1974.

Mottl, M. J., and H. D. Holland, Chemical exchange during hydrothermal alteration of basalt by seawater—I. Experimental results for major and minor components of seawater, *Geochim. Cosmochim. Acta, 42,* 1103–1115, 1978.

O'Neil, J. R., and M. P. Taylor, Jr., The oxygen isotope and cation exchange chemistry of feldspars, *Amer. Mineral., 52,* 1414–1437, 1967.

Philpotts, J. A., and C. C. Schnetzler, Phenocryst-matrix partition coefficients for K, Rb, Sr and Ba, with applications to anorthosite and basalt genesis, *Geochim. Cosmoschim. Acta, 34,* 307–322, 1970.

Suzuoki, T., and S. Epstein, Hydrogen isotope fractionation between OH-bearing minerals and water, *Geochim. Cosmochim. Acta, 40,* 1229–1240, 1976.

^{10}Be as a Geochemical and Geophysical Probe

L. Brown, J. Klein, R. Middleton,* I. S. Sacks, and F. Tera*

Since the realization has formed that the ocean floors are created at mid-ocean ridges and are subducted at the deep ocean trenches, investigators have turned much of their attention toward determining the fate of the descending rock and the effects that this movement produces. The locations of volcanoes in subduction zones show clear geographical relationships to the downgoing slabs, as delineated by the earthquake foci. While it is apparent that the volcanoes are a result of subduction, it is not known at present whether the magma is derived from the slab itself or is extruded from the overlying mantle by some emanation from the slab or from a combination of the two. Fig. 12 shows a section through a subduction zone that is more or less typical; it illustrates the spatial relationships of the mid-ocean ridge, the moving plate, the earthquake locations, the trench, and the volcanoes. We describe a technique that promises to shed light on this fundamental question.

It has been known for some years that ^{10}Be produced by cosmic rays in the upper atmosphere settles into the deep ocean sediments, where it is eventually carried down by the subducting plate. A layer of this mud is typically 100 m thick on arriving at the trench, having been laid down at about 0.01 mm/year. Apparently it is not for the most part scraped free of the lithospheric plate, as the existence of the trench itself suggests. The observation of ^{10}Be in lava from an island arc volcano would be direct evidence of the sedimentary origins of at least a fraction of the magma, since the production of this isotope in the Earth's crust

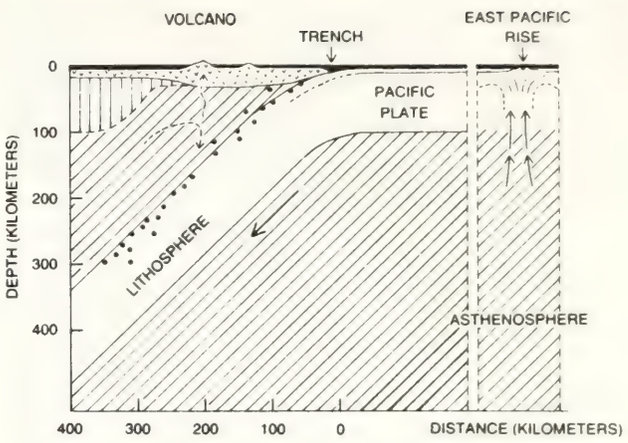


Fig. 12. Spatial relationship of a mid-ocean rise, lithospheric plate, deep ocean trench, and island arc volcano. The dots indicate the location of earthquakes that delineate the plate-mantle boundary.

and mantle by radioactivity or cosmic rays is negligible compared with the wide range of concentrations conjectured for volcano emissions.

Estimates of what might be observed begin by noting that the steady state accumulation of ^{10}Be on the ocean floor is about 3×10^{12} cm^{-2}, a number obtained by equating the number of atoms settling per unit time to the number undergoing radioactive decay. The decay, which has a half-life of 1.5 m.y., will have reduced the concentration by about a factor of ten by the time the material presumably passes beneath the volcanoes. The half-life of 1.5 m.y. is particularly suitable to our task because it is long enough to time the movement of the plates (about 50 km/m.y.) in their passage from trench to volcano (about 200 km) and is short enough to have decayed to negligible concentrations before it can be recycled in any significant amount. The concentration observed in the lava depends on the thickness of the rock with which this thin layer is mixed. If the lava comes from a mixture 100 m thick, a model seriously proposed (Marsh, 1979), then about 3×10^{12} cm^{-2} $\times$ 0.1×10^{-4} cm^{-1} $= 3 \times 10^{7}$ cm^{-3} can be expected. The natural isotope ^{9}Be is ubiquitous in rock at

*University of Pennsylvania, Philadelphia.

about 3×10^{17} cm^{-3}. The maximum $^{10}Be/^{9}Be$ ratio would thus be about 10^{-10}; if the dilution were into 10 km of rock rather than 100 m, the ratio would be 10^{-12}, easily obtainable with the technique described here.

Using a beam of atomic ions with energies greater than about 20 MeV, it is now possible to observe isotopic ratios as small as 10^{-13}, millions of times smaller than is possible with conventional mass spectrometers. This new technique (Muller, 1977) uses a cyclotron or tandem Van de Graaff machine as the mass spectrometer, exploiting two of their advantages. First, the beams of such accelerators have several orders of magnitude more current than conventional mass spectrometers; second, the ions of the low-intensity component have sufficient energy to allow the use of particle counter methods to ascertain the atomic number as well as the charge-to-mass ratio. Beryllium-10 has been observed in natural materials using accelerators: in ocean waters (Raisbeck *et al.*, 1979a), in ocean sediments (Raisbeck *et al.*, 1979b), in antarctic ice (Raisbeck *et al.*, 1978), and in manganese nodules (Turekian *et al.*, 1979). These determinations have been made with observational sensitivities that are inadequate for the needs of our problem, a consequence of the difficulties of producing beryllium beams. Recently the University of Pennsylvania tandem, equipped with a new form of ion source (Middleton, 1977), has yielded a $^{9}Be^{+4}$ beam of 0.1 μA, which was sustained for 21 h from a BeO loading of 0.7 mg Be. A loading spiked with ^{10}Be yielded the expected ratio; the background was 10^{-13}. A 0.1 μA beam of ^{9}Be will allow the observation of 190 atoms of ^{10}Be in 20 min, if a ratio of 10^{-12} exists.

To obtain tenths-of-milligram samples of beryllium from lava requires their extraction from hundreds of grams of rock, whereas in typical isotopic studies hundreds of milligrams are processed. This requirement essentially precludes the extraction of beryllium by the standard method of acetylacetone (Adam *et al.*, 1952), which requires large volumes of reagent, several adjustments of pH, and often the addition of carrier beryllium (Merril *et al.*, 1960). We have developed a method that utilizes the characteristics of beryllium to form the anion BeF_3^- in HF solutions and the cation Be^{+2} in HCl solutions, thereby

TABLE 4. ^{10}Be Concentrations in Various Natural Materials

Sample	Description	^{10}Be atoms/g
10176	Deep sea core taken at a depth greater than 76 and less than 90 cm into the mud of the Central Pacific Basin about 7200 km W of Panama. Coordinates are 9°31.5'N, 145°59.4'W, 5214 m depth.	36×10^8
482	Near continental core taken 120 m into the mud at the Tamayo transform fault, about 110 km S by E of the tip of Baja California. Coordinates are 22°47.2'N, 107°59.4'W, 2998 m depth.	3.2×10^8
San Pedro	Surface core from the San Pedro basin in the sea off southern California about 19 km SSW of the coast of Palos Verdes Hills. Coordinates are 33°35'N, 118°29'W, 913 m depth.	3.5×10^8
LA 1	Surface core from the Atchafalaya River just below Morgan City, Louisiana.	2.5×10^8
LA 4	Surface core from the Atchafalaya Bay.	1.9×10^8
LA 9	Surface core from the Gulf of Mexico taken about 56 km S of the bar of the Atchafalaya Bay.	2.3×10^8

allowing a relatively simple separation with ion exchange resins. The method has been used to extract beryllium from gram-sized quantities of muds, and provides yields of about 70%. Using it, we have observed ^{10}Be in muds from six locations that differ not only in their geometrical location but in the nature of their sedimentation processes. See Table 4 for a description of the samples and the ^{10}Be concentrations observed. The one deep-sea sediment, the only kind studied heretofore, is in excellent agreement with Raisbeck *et al.* (1979b). The others show lesser values, possibly resulting from the dilution by continental silt. We are continuing our studies of this isotope in various natural materials. These efforts are exploratory and sufficiently new to make further discussion of them out of place for the present. Having developed the methods of beryllium extraction for sediments, we have begun the extraction of beryllium from 450-g samples of volcanic lavas.

Acknowledgments

We are indebted to Dr. T. C. Hoering, Dr. Brian Lewis, and Mr. J. K. Cockran for providing us with the samples used in these studies.

References

Adam, J. A., E. Booth, and J. D. H. Strickland, Determination of microgram amounts of beryllium with acetylacetone, *Anal. Chim. Acta, 6,* 462–471, 1952.

Marsh, R. D., Island arc development: some observations, experiments and speculations, *J. Geology, 87,* 687–713, 1979.

Merril, J. R., M. Honda, and J. R. Arnold, Methods for separation and determination of beryllium in sediments and natural waters, *Anal. Chem., 23,* 1420–1426, 1960.

Middleton, R., A survey of negative ions from a cesium sputter source, *Nucl. Inst. Metho., 144,* 373–399, 1977.

Muller, Richard A., Radioisotope dating with a cyclotron, *Science, 196,* 489–494, 1977.

Raisbeck, G. M., F. Yiou, M. Fruenau, J. M. Loiseaux and M. Lieuvin, ^{10}Be concentration and residence time in the ocean surface layer, *Earth Planet. Sci. Lett., 43,* 237–240, 1979a.

Raisbeck, G. M., F. Yiou, M. Fruneau, J. M. Loiseaux, M. Lieuvin, J. C. Ravel, and J. D. Hays, A search in a marine sediment for ^{10}Be concentration variations during a geomagnetic field reversal, *Geophys. Res. Lett., 6,* 717–719, 1979b.

Raisbeck, G. M., F. Yiou, M. Fruneau, M. Lieuvin, and J. M. Loiseaux, Measurement of ^{10}Be in 1000 and 5000 year old antarctic ice, *Nature, 275,* 731–733, 1978.

Turekian, K. K., J. K. Cochran, S. Krishnaswami, W. A. Lanford, P. D. Parker, and K. A. Bauer, The measurement of ^{10}Be in manganese nodules using a tandem Van de Graaff accelerator, *Geophys. Res. Lett., 6,* 417–420, 1979.

Esmeralda Bank: Geochemistry of an Active Submarine Volcano in The Mariana Island Arc and Its Implications for Magmagenesis in Island Arcs

*R. J. Stern and L. D. Bibee**

The island arcs of the circum-Pacific "Ring of Fire" are intimately associated with those areas where it is thought the oceanic lithosphere is subducted and recycled into the mantle. Volcanoes in these regions owe their activity to some as yet poorly understood interaction between this subducted lithosphere and the superjacent mantle. Petrologic and geochemical investigations of the origin and nature of volcanic rocks from these regions promise to help us understand the nature of this interaction and to further illuminate related problems of magma generation, the composition of the upper mantle, and the evolution of the continents. Consequently, geochemists have been fascinated by problems of magmagenesis in and above the subduction zones. In the past, these investigations have concentrated in areas where the volcanoes are built on thickened, continental or proto-continental crust. In

*School of Oceanography, Oregon State University, Corvallis.

areas such as the Americas, Japan, New Zealand, or Indonesia, melts generated at depths of 50–150 km in the mantle must ascend through crustal materials which melt at relatively low temperatures. In these instances, the possibility that continental crust might be partially melted and contaminate rising magmas cannot be precluded. This makes it difficult to reconstruct with confidence the composition of the melt initially generated at greater depth. In contrast, island arcs built on oceanic crust have received less intensive study, largely because of lack of access. However, it is the volcanic rocks of these "intra-oceanic" island arcs that offer the best opportunity to understand first-generated or "primitive" melts, since the thinner and more refractory nature of oceanic crust is much less likely to partially melt and modify the chemistry of melts rising through it. For this reason, it is important to study the products of arc volcanoes built on oceanic crust.

Nearly all the intra-oceanic arcs are found in the western Pacific. Perhaps the most outstanding example of these is the discontinuous chain of volcanoes that extends south from Japan, through the Izu and Volcano Islands, to the Mariana Islands. Previous investigations of these and other arcs have concentrated on the subaerial volcanoes. Submarine volcanoes represent initial stages in the evolution of arc volcanoes but have scarcely been studied. We report here the results of geochemical and isotopic investigations of Esmeralda Bank, the southernmost known active volcano in the Mariana Arc (Fig. 13).

Esmeralda Bank is a submarine volcano whose summit reaches within 30 m of the ocean surface (Fig. 14). It is among the most active volcanoes in the Marianas, having erupted in 1944 and 1975. In 1978 the R/V *Thomas Washington* undertook a detailed survey of the volcano and made two

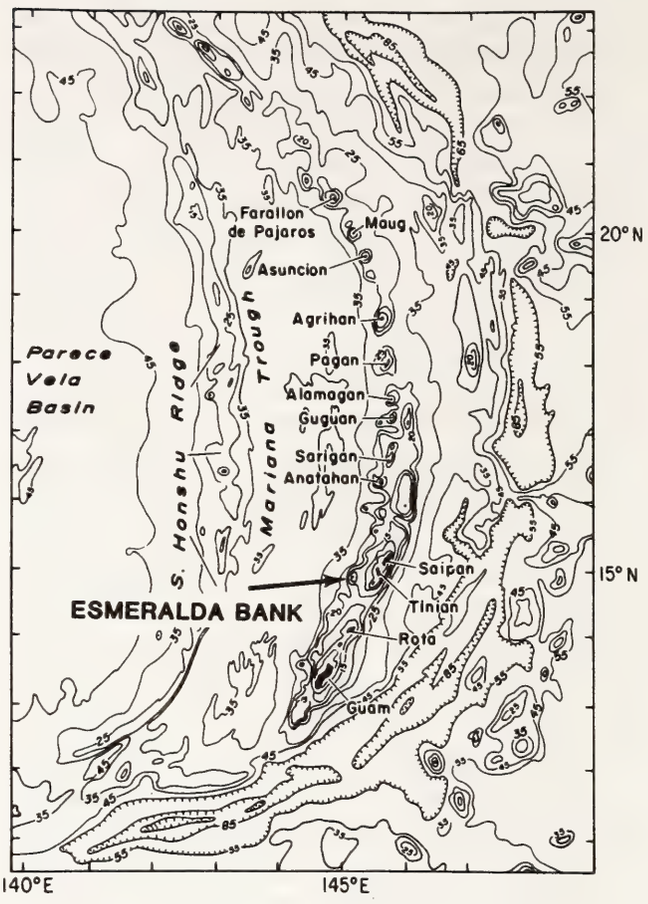


Fig. 13. Map showing the location of Esmeralda Bank in the Mariana Island Arc and bathymetry in the surrounding seas. Bathymetric contours are in hundreds of meters. Active volcanoes extend from Esmeralda Bank to north of Farallon de Pajaros. Map modified after that of Meijer, 1976.

dredges; one at 100–300 m depth from the wall of the central crater (M-45) and one at 800–1200 m depth from its flanks (M-46). Various lithologies were recovered from the crater: volcanic flows, breccias, glass, and gabbroic xenoliths. Fresh vesicular basalts were recovered from the flanks. Under the microscope, the basalts appear fresh and consist of $<5\%$ larger crystals of zoned labradorite, pyroxene, and olivine set in a matrix of clinopyroxene and plagioclase. The glassy samples consist of 20–30% crystals of labradorite and subordinate pyroxene and olivine set in a matrix of very fresh brown glass.

Four samples from the crater wall

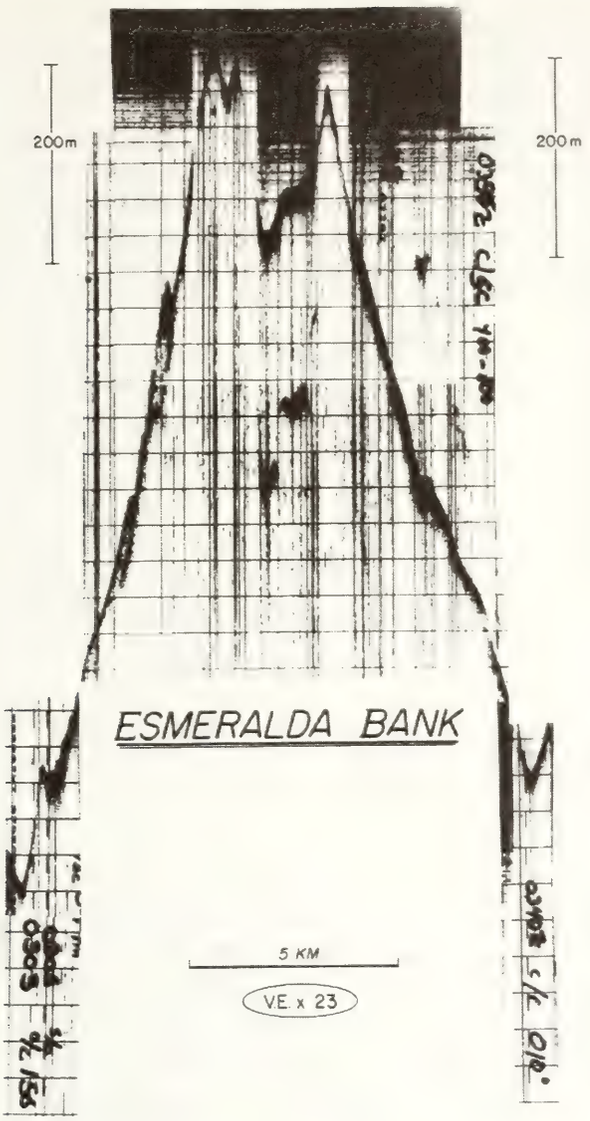


Fig. 14. 3.5-kHz seismic reflection profile crossing of Esmeralda Bank, approximately E-W. Note presence of central crater, 150–200 m deep and 2 km in diameter. Feature below central crater is a multiple reflection of crater floor. Note that the vertical dimension is exaggerated 23× relative to the horizontal dimension.

and six samples from the flank were analyzed for major oxides and selected trace elements. Mean abundances are listed in Table 5. These data show the volcanic rocks of Esmeralda Bank to be basalts of remarkable compositional uniformity. These basalts are similar to typical basalts of the Mariana Arc in their abundance of the "incompatible elements" K, Rb, and Ba. Mean values for the diagnostic ratios K/Rb = 488 and K/Ba = 28.8 are also similar to those of other Mariana Arc lavas (Chow *et al.*, 1980). However, concentrations of Ca, Al, and the transition elements Ti, Fe, and Mn are significantly lower and higher, respectively, than those of any other Mariana Arc lavas. Instead, concentrations of Ca, Al, Ti, Fe, and Mn in Esmeralda Bank basalts are more similar to those in basalts from the Mariana Trough, west of the arc, and other lavas east of the Mariana Trench, where magmagenesis is unrelated to subduction (compare Table 5 with D-19-2 from the Sorol Trough [Fornari *et al.*, 1979] and Dredge 1402 pillow basalts from the Pacific slope of the Mariana Trench [Dietrich *et al.*, 1978]).

The rare earth elements (REE) are especially useful for addressing problems of magmagenesis. The concentration of REE in melts is controlled by equilibrium between the melt and residual crystalline phases. This equilibrium is represented by partition coefficients between melt and solid ($D_i^{crystal/liquid}$), which reflect the relative abundance of an element "i" in the residual solid compared to its equilibrium melt. If one knows the phase and chemical composition of the source, the proportion of these phases contributing to the melt, and the pertinent distribution coefficients, it is possible to determine the fraction of melt produced. It is not generally possible to know these variables, but with reasonable assumptions the REE can be used to evaluate the plausibility of different petrogenetic schemes.

Four Esmeralda Bank basalts were analyzed for REE (Fig. 15). Relative to primitive chondritic meteorites, these samples are enriched in the light REE (18–23× chondrite). Negative Europium anomalies, indicative of significant plagioclase fractionation, are not observed. Data for the heavy REE, at 10.8–13.7× chondritic, does not allow for a significant amount of garnet to be present in the residium after melting. Distribution coefficients for heavy rare

TABLE 5. Mean Composition of Dredged Basalts, Esmeralda Bank

Major Oxides (wt %)†			Trace Elements (parts per million)‡		
	Mean	±1 Std. Dev.		Mean	±1 Std. Dev.
SiO_2	52.4	1.4	K	6892	891
TiO_2	1.29	0.10	Rb	14.13	1.75
Al_2O_3	15.1	1.1	Sr	350.7	37.9
FeO*	12.61	0.99	Cs	0.74	0.21
MnO	0.22	0.01	Ba	240.3	21.5
MgO	4.13	0.42	Ce	17.84	1.90
CaO	9.16	0.67	Nd	12.75	1.35
Na_2O	3.3	0.3	Sm	3.61	0.43
K_2O	0.92	0.08	Eu	1.30	0.12
P_2O_5	0.21	0.03	Gd	4.25	0.44
			Dy	4.44	0.51
			Er	2.81	0.36
			Yb	2.62	0.28
			Zr	89	7
			Ni	12	2

FeO = FeO + 0.9 Fe_2O_3.

†Major oxides determined by combined XRF (SiO_2, TiO_2, Al_2O_3, FeO*, CaO, K_2O, P_2O_5) and AA (MnO, MgO, Na_2O) techniques. Ten samples were analyzed for major oxides.

‡Trace elements were determined by isotope dilution on four samples, except for Zr and Ni which are for ten samples by XRF.

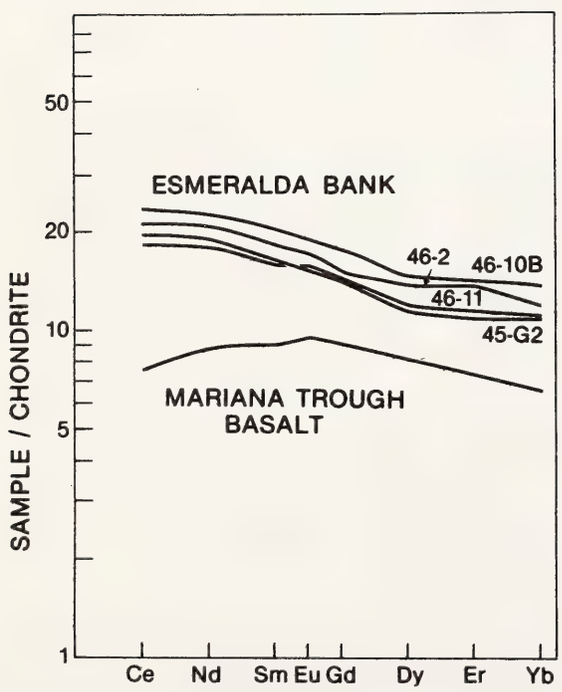


Fig. 15. Plot of rare earth elements in Esmeralda Bank basalts relative to those in chondritic meteorites. Note the Esmeralda Bank basalts are enriched in the light rare earths (Ce, Nd, Sm) relative to the heavy rare earths (Gd, Dy, Er, Yb). Also shown is a basalt from the Mariana Trough, west of the active arc (Stern, unpublished data). By comparison, this basalt is strongly depleted in light REE.

earths between garnet and equilibrium melts are in the range from 3 to 40 (Schnetzler and Philpotts, 1970; Shimizu and Kushiro, 1975; Arth, 1976). Melts generated from sources with 3-5× chondritic abundances of the heavy REE in equilibrium with significant (>10%) amounts of residual garnet should be severely depleted in heavy REE (Gill, 1974). Such heavy REE-depletion is not found for Esmeralda Bank basalts, suggesting that either (1) these were formed by melting at depths less than that required for garnet to be stable (<30-70 km; Ito and Kennedy, 1967), or (2) all the garnet was melted.

Unfortunately, petrogenetic inferences based on consideration of the abundances of the major and most trace elements alone are severely limited by many poorly understood or unknown processes which follow primary magmagenesis. Fractionation accompanying ascent and during residence in shallow crustal reservoirs is likely and may greatly modify the composition of the original melt. In order

to "see through" these secondary processes, it is necessary to rely on those chemical parameters that are least sensitive to post-generational fractionation. These include (1) ratios of the "incompatible elements" such as K/Rb and K/Ba, and (2) isotopic composition of the heavier elements, especially Sr, Nd, and Pb.

What can such data tell us about the source of melts in island arcs such as the Marianas? The problem of petrogenesis in intra-oceanic arcs concerns determination of the source: (1) subducted oceanic lithosphere, especially those components that melt at the lowest temperatures—sediments and basaltic crust; (2) the mantle wedge overlying the subducted lithosphere; or (3) some mixture of (1) and (2). Consideration of the expected isotopic composition of such materials can help place constraints on the nature of magmagenesis beneath arcs. For example, the Pacific seafloor east of the Mariana Trench consists of altered Mesozoic basaltic crust (Meijer, 1976) overlain by at least 300 m of Cretaceous-Tertiary chalks, up to 100 m of Cretaceous-Tertiary red clay, and a variable thickness of younger silty clay (Heezen *et al.*, 1973). The chalks and red clays should have $^{87}Sr/^{86}Sr$ similar to that of Mesozoic and younger seawater (0.7071–0.7091; Veizer and Compston, 1974). $^{143}Nd/^{144}Nd$ of these sediments is not known, but may be in the range 0.5122–0.5127 found for red clays, metalliferous sediments, and manganese nodules (O'Nions *et al.*, 1978; Piepgras *et al.*, 1979). The altered basaltic crust should be isotopically similar to oceanic crust of similar age exposed in Oman (McCulloch *et al.*, 1980). If such material were subducted and melted, the resultant liquids should have isotopic compositions characteristic of such sources. If the source lies in the mantle, we would expect the isotopic signature of such magmas to be similar to that of other, more clearly mantle-derived melts. If magmagenesis is a function of the interaction of the two sources, then resultant melts should reflect a mixing of their isotopic signatures.

Several Esmeralda Bank basalts were analyzed for $^{143}Nd/^{144}Nd$ and $^{87}Sr/^{86}Sr$, for the purpose of answering these questions. These data are listed in Table 6 and plotted in Fig. 16. Also plotted in Fig. 16 are fields occupied by mantle-derived basalts of Hawaii (O'Nions *et al.*, 1977), Galapágos (White and Hofmann, 1978), the Caroline Is. (Stern, unpublished data),

TABLE 6. K/Rb, K/Ba, and Isotopic Composition of Basalts from Esmeralda Bank, Mariana Arc*

Sample	K/Rb	K/Ba	$^{87}Sr/^{86}Sr$	$^{143}Nd/^{144}Nd$
Dredge 45:				
G-2	474	31.8	0.70342 ± 7	0.51293 ± 3
Dredge 46:				
2	517	31.9	0.70346 ± 6	0.51298 ± 3
10				
Flow Top	...	...	0.70346 ± 6	0.51301 ± 2
Flow Bottom	472	27.3	0.70348 ± 3	0.51304 ± 4
11	488	24.1	0.70346 ± 5	0.51305 ± 3
Subaerial Mariana Arc	367–617†	19–51†	0.7033–0.7035‡	0.51304–0.51310§

*$^{87}Sr/^{86}Sr$ data are normalized to $^{87}Sr/^{88}Sr = 0.1194$ and relative to E and A $SrCO_3 = 0.7080$. $^{143}Nd/^{144}Nd$ are normalized to $^{146}Nd/^{144}Nd$ of 0.7219 and relative to BCR-1 = 0.51271. Errors are $2\sigma_{\bar{x}}$.

†Chow *et al.*, 1980.

‡Stern, 1979.

§De Paolo and Wasserburg, 1977.

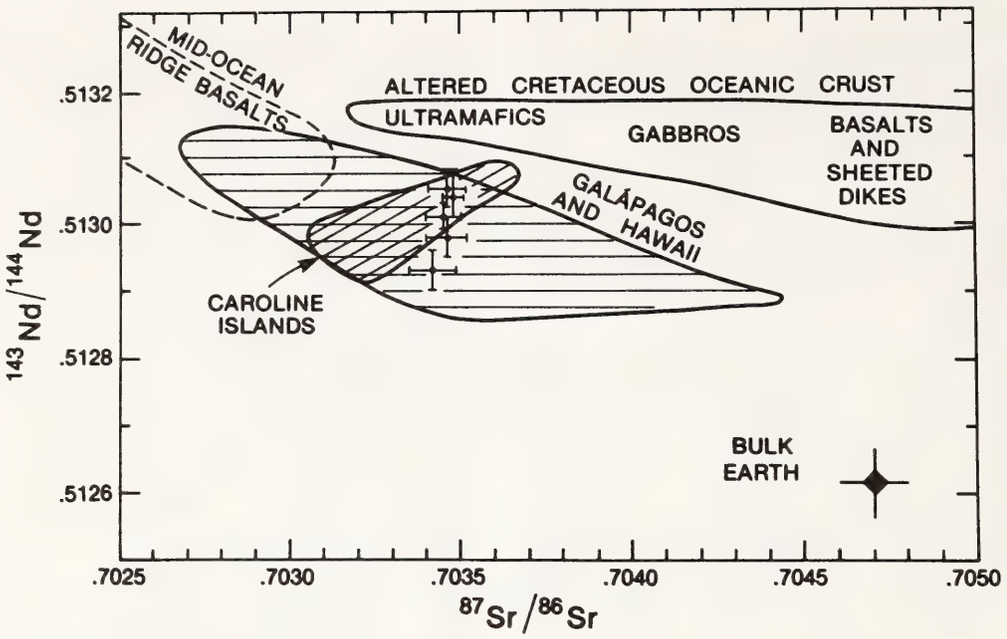


Fig. 16. Plot of $^{143}Nd/^{144}Nd$ vs. $^{87}Sr/^{86}Sr$ in Esmeralda Bank basalts. Esmeralda Bank basalts are shown with error bars. The field for the unequivocally mantle derived basalts of the mid-ocean ridges and some islands of the Pacific Basin (Hawaii, Galápagos, Carolines) are shown for comparison. Also shown is the field occupied by altered Cretaceous oceanic crust of the Samail Ophiolite, Oman (McCulloch *et al.*, 1980). This ophiolite may be representative of Pacific ocean floor now being subducted beneath the Mariana Arc. Pelagic and hemi-pelagic sediments such as those now being subducted beneath the Marianas would plot far to the lower right of the diagram. This diagram indicates the isotopic similarity of the sources of Esmeralda Bank basalts and Pacific intra-plate basalts, strongly suggesting these are derived from similar mantle sources. $^{87}Sr/^{86}Sr$ data normalized to E and A $SrCO_3$ = 0.70800. $^{143}Nd/^{144}Nd$ data normalized to BCR = 0.51271.

and mid-ocean ridge basalts. The field occupied by altered Cretaceous oceanic lithosphere exposed in Oman is also shown; fields occupied by chalks and clays are not shown, since these would plot far to the right, off Fig. 16.

Comparison of the combined Sr-Nd isotopic data for Esmeralda Bank basalts with the three plausible sources allows several conclusions to be made. First, it is clear that subducted pelagic sediments cannot be the primary source for these basalts; furthermore, mixing between fluids derived from such sediments and some other source must either be insignificant or not include Sr and Nd. Second, altered oceanic crust cannot be the primary source for these basalts. Contribution of fluids from the upper, more altered basaltic portion of the subducted crust must be minimal, although contributions from the less altered gabbroic and ultramafic lower crust cannot be precluded. However, since melting of oceanic lithosphere should involve altered basalt as the first melting fraction, it is likely that contributions from the lower crust and lithosphere would be accompanied by even greater additions from the upper crust. Finally, it is apparent that Esmeralda Bank basalts are isotopically similar to basalts erupted within the Pacific basin but away from the spreading centers and subduction zones. Consideration of K/Rb and K/Ba data underscores this similarity; K/Rb in Esmeralda Bank basalts (mean = 488 ± 21) compares with basalts from Kilauea, Hawaii (mean = 493 ± 13; Hofmann *et al.*, 1978) and the Caroline Is. (mean = 479 ± 29; Stern, unpublished data). K/Ba in Esmeralda Bank basalts

(mean = 28.8 ± 3.8) also is similar to that of Kilauea (mean = 35.7 ± 0.5) and the Carolines (mean = 24.3 ± 4.6).

It is also noteworthy that while $^{87}Sr/^{86}Sr$ in the Esmeralda Bank basalts is constant at 0.70346 with a maximum deviation of .006%, $^{143}Nd/^{144}Nd$ shows deviations of up to .014% from a mean value of 0.51300. Similar examples of relatively large variations in $^{143}Nd/^{144}Nd$ compared to $^{87}Sr/^{86}Sr$ are reported for volcanic rocks of Iceland (Zindler *et al.*, 1979) and the Scotia Arc (O'Nions *et al.*, 1978).

Esmeralda Bank basalts are indistinguishable in these critical elemental and isotopic ratios from the island basalts of the Pacific Basin. This allows for two possible modes of generation for Esmeralda Bank magmas: (1) melting of only the seamounts and islands in the lithosphere subducted beneath the Marianas, or (2) partial melting of a mantle source very similar to that responsible for the generation of the island basalts of the Pacific basin. It seems unlikely that melting in the subduction zone would affect only subducted seamounts and islands to the exclusion of sediments and altered seafloor; for this reason, the first possibility must be considered the less plausible. In contrast, melting of unmodified mantle similar to that melted in other oceanic tectonic environments is simple, consistent, and hence, appealing.

The conclusion that some intra-oceanic arc magmas are derived from melting of a mantle indistinguishable from that which produces intra-plate island basalts elsewhere in the Pacific provides a new constraint on the relative positions of more- and less-depleted mantle reservoirs. Subducted lithosphere lies at a depth of 100–150 km beneath Mariana volcanoes (Katsumata and Sykes, 1969). Due to the relatively cool and structurally intact nature of this slab, it seems unlikely that melts generated at greater depth could pass through it. Instead the presence of subducted lithosphere beneath these volcanoes acts as a lower limit beneath which melts cannot be derived. By this reasoning, the mantle source from which Esmeralda Bank melts were derived must lie within the upper 100–150 km of the mantle. Since this source is very similar in composition to the sources of the intra-plate island basalts, it is reasonable to infer that the relatively enriched mantle sources in the western Pacific must lie in part within the uppermost mantle, most likely in the asthenosphere. This interpretation agrees better with models placing undepleted mantle at shallower depths than depleted mantle (Tatsumoto, 1978) than with models calling for undepleted mantle to lie at greater depth (Schilling, 1973; Sun and Hanson, 1976). Studies are being undertaken to determine the sources of other recent volcanoes in the Izu-Volcano-Mariana Arc and to evaluate the promise of these results for further defining the nature and evolution of the upper mantle beneath the western Pacific.

References

Arth, J. G., Behavior of trace elements during magmatic processes—a summary of theoretical models and their applications, *J. Res. U.S. Geol. Surv., 4,* 41–47, 1976.

Chow, T. J., R. J. Stern, and T. H. Dixon, Absolute and relative abundances of K, Rb, Sr, and Ba in circum-Pacific island-arc magmas, with special reference to the Marianas, *Chem. Geol., 28,* 111–121, 1980.

DePaolo, D. J., and G. J. Wasserburg, The sources of island arcs as indicated by Nd and Sr isotopic studies, *Geophys. Res. Lett., 4,* 465–468, 1977.

Dietrich, V., R. Emmermann, R. Oberhänsli, and H. Puchelt, Geochemistry of basaltic and gabbroic rocks from the west Mariana Basin and the Mariana Trench, *Earth Planet. Sci. Lett., 39,* 127–144, 1978.

Fornari, D. J., J. K. Weissel, M. R. Perfit, and R. N. Anderson, Petrochemistry of the Sorol and Ayu Troughs: implications for crustal accretion at the northern and western boundaries of the Caroline Plate, *Earth Planet. Sci. Lett., 45,* 1–15, 1979.

Gill, J. B., Role of underthrust oceanic crust in the genesis of a Fijian calc-alkaline suite, *Contr. Mineral. Petrol., 43,* 29–45, 1974.

Heezen, B. C., I. D. MacGregor, H. P. Foreman, G. Forristall, H. Hekel, R. Heese, R. H. Hoskins, E. J. W. Jones, A. Kaneps, V. A. Krasheninnikov, H. Okada, and M. H. Rueff, the post Jurassic sedimentary sequence on the Pacific Plate: a kinematic interpretation of diachronous deposits, in *Initial Reports of the Deep Sea Drilling Project, 20,* pp. 725–738, Govt. Printing Office, Washington, D.C., 1973.

Hofmann, A. W., T. L. Wright, and M. Feigenson, Trace element and Sr isotope abundances in recent lavas from Kilauea, Hawaii, *Carnegie Inst. Wash. Year Book 77,* 590–596, 1978.

Ito, K., and G. C. Kennedy, Melting and phase relations in a natural peridotite to 40 kilobars, *Amer. J. Sci., 265,* 519–538, 1967.

Katsumata, M., and L. R. Sykes, Seismicity and tectonics of the western Pacific: Izu-Mariana-Caroline and Ryukyu-Taiwan Regions, *J. Geophys. Res., 74,* 5293–5948, 1969.

McCulloch, M. T., R. T. Gregory, G. J. Wasserburg, and H. P. Taylor, Jr., A neodymium, strontium, and oxygen isotopic study of the Cretaceous Samail Ophiolite and implications for the petrogenesis and seawater-hydrothermal alteration of oceanic crust, *Earth Planet. Sci. Lett., 46,* 201–211, 1980.

Meijer, A., Pb and Sr isotopic data bearing on the origin of volcanic rocks from the Mariana island-arc system, *Geol. Soc. Amer. Bull., 67,* 1358–1369, 1976.

O'Nions, R. K., P. J. Hamilton, and N. M. Evensen, Variations in $^{143}Nd/^{144}Nd$ and $^{87}Sr/^{86}Sr$ ratios in oceanic basalts, *Earth Planet. Sci. Lett., 34,* 13–22, 1977.

O'Nions, R. K., S. R. Carter, R. S. Cohen, N. M. Evensen, and P. S. Hamilton, Pb, Nd and Sr isotopes in oceanic ferromanganese deposits and ocean floor basalts, *Nature, 278,* 435–438, 1978.

Piepgras, D. J., G. J. Wasserburg, and E. J. Dasch, The isotopic composition of Nd in different ocean masses, *Earth Planet. Sci. Lett., 45,* 223–236, 1979.

Schilling, J. G., Iceland mantle plume: Geochemical study of the Reykjanes Ridge, *Nature, 242,* 565–571, 1973.

Schnetzler, C. C., and J. A. Philpotts, Partition coefficients of rare-earth elements between igneous matrix material and rock-forming mineral phenocrysts—II., *Geochim. Cosmochim. Acta, 34,* 331–340, 1970.

Shimizu, N., and I. Kushiro, The partitioning of rare earth elements between garnet and liquid at high pressure: preliminary experiments, *Geophys. Res. Lett., 2,* 413–416, 1975.

Stern, R. J., Strontium isotopes in island arcs and marginal basins from the circum-Pacific: regional variations and implications for magmagenesis, *Geol. Soc. Amer., Abstracts w. Progr., 524,* 1979.

Sun, S.-S., and G. N. Hanson, Evolution of the mantle: geochemical evidence from alkali basalt, *Geology, 3,* 297–302, 1976.

Tatsumoto, M., Isotopic composition of lead in oceanic basalt and its implication to mantle evolution, *Earth Planet. Sci. Lett., 38,* 63–87, 1978.

Veizer, J., and W. Compston, $^{87}Sr/^{86}Sr$ composition of seawater during the Phanerozoic, *Geochim. Cosmochim. Acta, 38,* 1461–1484, 1974.

White, W. M., and A. W. Hofmann, Geochemistry of the Galápagos Islands: implications for mantle dynamics and evolution, *Carnegie Inst. Wash. Year Book 77,* 596–606, 1978.

Zindler, A., S. R. Hart, F. A. Frey, and S. P. Jakobsson, Nd and Sr isotope ratios and rare earth element abundances in Reykjanes Peninsula basalts: evidence for mantle heterogeneity beneath Iceland, *Earth Planet. Sci. Lett., 45,* 249–262, 1979.

Trace Element Geochemistry of Kohala Volcano, Hawaii

M. D. Feigenson and A. W. Hofmann

Introduction

The study of oceanic basalts at DTM in recent years has proceeded with two general purposes: first, to map the large-scale isotopic and chemical heterogeneities in the suboceanic mantle and to relate these to large-scale tectonic features such as island chains and ocean ridges; second, to study in detail the constitution of the source material and the condition of melting. The latter purpose was initially achieved by studying a time sequence of samples from a single eruption on Kilauea volcano, Hawaii (Hofmann, Wright, and Feigenson, 1978; Hofmann and Wright, 1979). We demonstrated that the highly systematic variations in trace element abundances were produced by differences in the degree of melting and that the minerals garnet and clinopyroxene must be part of the solid residue in the mantle. These minerals have the effect of fractionating both the Rb/Sr and the Sm/Nd ratios in the source and in the

melt, and these fractionations will ultimately lead to isotopic variations in Sr and Nd and thus produce an isotopically heterogeneous mantle.

Our present work extends this study in three important aspects: (1) the choice of a different volcano (Kohala), (2) the systematic sampling of a much longer sequence of eruptions, and (3) the focus on the transition from the main, shield-building phase of tholeiitic volcanism to the late-stage, alkalic volcanism. In this way, we hope to establish whether our initial conclusions are essentially applicable to Hawaiian volcanism (and ultimately to oceanic-island volcanism in general). Our sampling method is much more detailed and systematic than is customary in trace element geochemical studies. By sampling flows in a stratigraphic sequence we obtain a much clearer understanding of the evolution of the melting process at the source of the volcano.

Sample Location

Kohala volcano on the island of Hawaii was chosen for the present study because of the presence of deep canyons on its northeastern side and the occurrence of numerous alkali basalt domes along its summit. Twenty-six samples from a stratigraphic section about 300 meters high were collected from the northeastern side of Kohala, although no samples were obtained in the upper 60 meters because of extensive weathering. On the southwestern flank, the greatly reduced rainfall has not carved canyons as deep as those to the north, but one gulch was found that exposed a section about 70 meters thick. This section is comprised of 16 thin-bedded flows, culminating in an alkali-basalt flow containing abundant peridotite and norite xenoliths. This sequence, projected down a 7° dip, occurs almost precisely at the same stratigraphic level as the weathered northeastern section. Together, the two exposures provide an excellent cross-section of the upper 300 meters of Kohala.

Geochemistry

Trace element data (corrected for olivine fractionation, as explained by Wright, *et al.,* 1975) for twenty specimens from Kohala are given in Table 7; included are ten analyses of $^{87}Sr/^{86}Sr$. They are listed from top to bottom in increasing stratigraphic position, or decreasing age of eruption. It is readily apparent that although the Sr isotopic composition of the samples does not change significantly, the trace element concentrations generally increase in the sequence. However, alkali concentrations from samples from the wet northeastern slope (and some from the southwest as well) are anomalously low, and may have been leached by rain water. This is supported by the extremely high and variable K/Rb ratios of samples with low K. Therefore, the discussion that follows rests principally on the variations of Sr, Ba, P, and the rare earth elements.

Figure 17 shows typical rare earth abundance patterns (normalized to chondritic) for this sequence of basalts. The fan-shaped patterns seen here are characteristic of oceanic island basalts; moreover, there is a general trend of increasing light rare earth enrichment with increasing stratigraphic height. Note, however, that there is some variation to the Yb contents of these lavas, in contrast to the nearly constant Yb found in the Mauna Ulu eruptions (Hofmann and Wright, 1979).

Figure 18 is a plot of Ce/Yb, Sm/Sr and $^{87}Sr/^{86}Sr$ vs. stratigraphic level. Several features of this diagram are noteworthy: (1) the constant Sr isotopic composition of the lavas indicates a homogeneous source; (2) the Ce/Yb ratio varies only slightly in the tholeiitic basalts (from about 2.6 to 3.0) and does not correlate precisely with stratigraphy, but the ratio gradually

TABLE 7. Trace Element Analyses from Kohala (Olivine Normalized)*

Elev. (meters)	K	Rb	Cs	Sr	Ba	Ce	Nd	Sm	Eu	Gd	Dy	Er	Yb	$^{87}Sr/^{86}Sr$
2	1390	0.60	0.006	326	89	28.9	27.7	24.6	24.0	20.8	14.6	11.4	9.7	...
28	1160	1.01	0.016	302	68	28.3	27.8	24.6	24.0	20.9	14.9	11.7	9.6	.70362
58	550	0.18	0.009	276	47	30.6	30.5	26.1	25.8	22.9	16.0	12.5	10.4	.70360
72	660	0.29	0.006	294	50	29.8	29.4	25.9	25.8	23.6	16.0	12.6	10.5	...
90	670	0.11	0.013	268	54	24.4	24.9	22.0	23.2	...	14.7	11.8	9.3	...
110	560	0.17	0.008	240	51	25.8	25.7	23.1	23.7	20.3	15.1	11.8	9.7	.70364
130	700	0.37	0.005	306	36	26.0	26.2	23.4	23.8	...	16.0	10.6	8.6	...
165	570	0.30	0.035	250	64	34.5	34.2	29.4	29.0	24.7	17.3	13.5	11.2	.70356
180	830	3.12	0.037	311	116	49.6	47.5	41.1	38.5	26.5	23.9	17.9	14.6	...
200	2140	0.91	0.005	363	105	40.0	39.9	33.6	32.4	29.1	18.5	14.8	11.8	...
215	2440	2.46	0.038	421	125	48.2	44.9	36.3	34.4	30.0	19.9	15.1	12.1	.70360
225	7740	10.89	0.054	514	261	70.9	62.9	47.1	42.9	37.3	23.0	17.5	13.8	...
228	1790	1.25	0.027	453	175	58.4	54.9	41.2	37.4	30.4	19.8	14.1	11.5	...
232	5320	11.33	0.126	479	194	56.4	48.9	37.4	34.9	28.5	18.9	14.0	11.6	.70364
238	1590	2.62	0.027	456	170	59.1	...	47.8	43.7	...	23.8	16.6	13.4	...
245	6050	12.97	0.133	403	179	56.5	50.1	38.3	35.4	28.9	19.3	14.4	11.8	.70362
255	8440	18.72	0.192	431	269	72.3	...	50.8	44.2	32.7	23.6	16.9	13.8	...
262	7050	6.64	0.120	551	364	84.4	73.9	53.5	47.5	37.8	27.9	20.4	16.9	.70365
268	6410	14.73	0.072	554	242	60.5	49.6	36.3	34.3	26.7	17.4	12.7	10.5	.70359
272	14640	33.45	0.150	1330	644	147	105	68.0	63.1	44.8	24.2	15.6	11.6	.70353

*All analyses are ppm except rare earths, which are chondrite normalized. Concentrations are by isotope dilution mass spectrometry. $^{87}Sr/^{86}Sr$ normalized to Eimer and Amend Standard $SrCO_3$ of 0.70800.

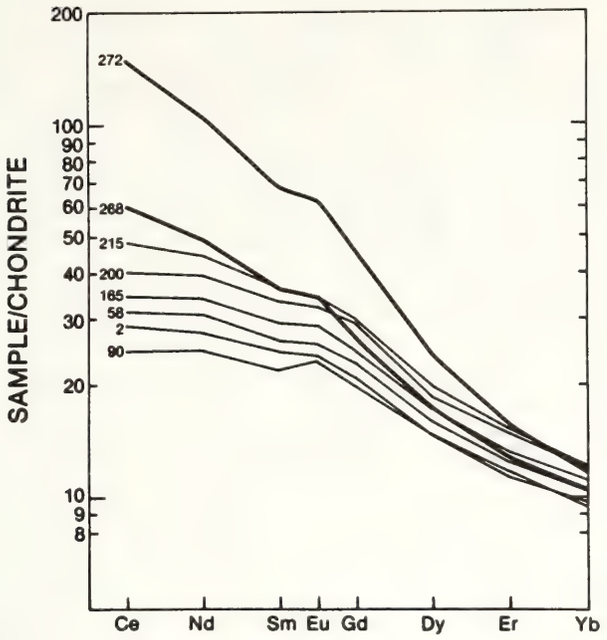


Fig. 17. Chondrite-normalized rare earth abundance patterns for Kohala basalts. Identification numbers are meters a.s.l. at Waipio Valley.

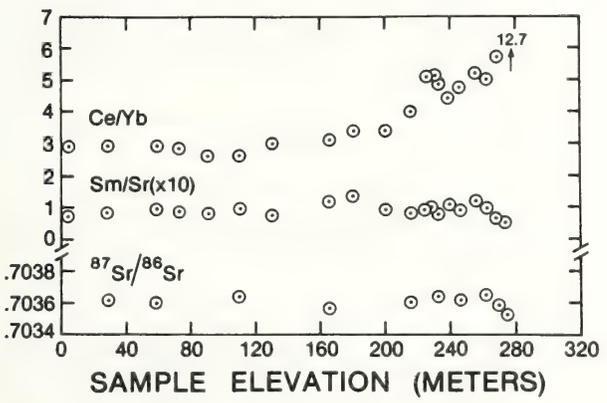


Fig. 18. Ce/Yb, Sm/Sr, and $^{84}Sr/^{86}Sr$ vs. stratigraphic level for Kohala basalts.

increases in the later flows; (3) the relatively smooth variation in Ce/Yb with height suggests a gradual change in melting conditions; and (4) the constant Sm/Sr ratio indicates that the partitioning behavior observed in the Mauna Ulu study is also operating in the production of basalts from Kohala.

Figure 19 shows several plots of selected trace element ratios vs. Ce concentration (normalized to chondritic). These types of diagrams have been proposed by Minster and Allègre (1978) and by Pankhurst (1977) to identify the mechanism responsible for the trace element abundance variations. Ratios of Ce/Nd and Ce/Yb against Ce plot as relatively tight linear arrays with positive slopes; such data sets are best produced through batch melting of a uniform source composition. Modification of magmas by fractional crystallization or zone refining tends to increase Ce, Nd, and Yb at the same time, resulting in horizontal trends, which is not the case for these lavas.

The other ratios plotted in Fig. 19 have different slopes depending on their bulk partition coefficients. The order of increasing coefficients is Ba < Ce ≈ P < Nd < Sm ≈ Sr < Yb. The graph of Ce/K vs. Ce shows the large scatter of points due to the weathering of alkalis, as discussed previously. Note that samples from the drier southwest side of Kohala plot uniformly low in Ce/K; this may represent the most likely (preweathering) Ce/K ratio.

These results show that a single source composition, partially melted to various degrees, can explain all the geochemical variation cited here. Quantitative modeling of the melting process requires that the trace element concentration be corrected for crystal fractionation effects. In the case of Kohala, the preliminary correction for olivine control (which was sufficient in the Mauna Ulu case) does not remove all the observed major element variations, and fractionation by other minerals, such as clinopyroxene, will have to be considered. However, several qualitative conclusions are possible: (1) the relatively small variation in Yb concentration over a wide range of Ce/Yb requires a residual phase with the partitioning properties of garnet, (2) the constancy of the Sr/Sm ratio, also observed in the Mauna Ulu study,

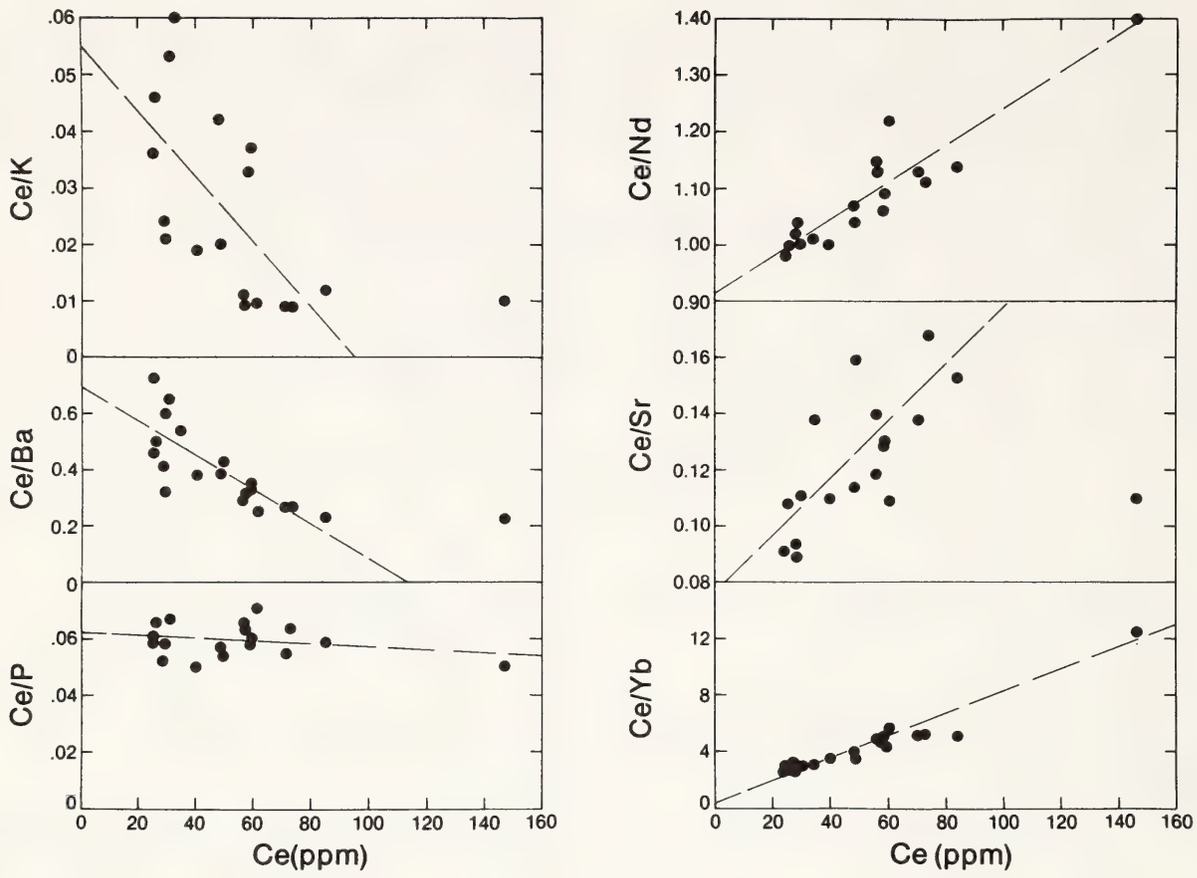


Fig. 19. Selected trace element ratios vs. Ce content; abundances have been corrected for olivine control. A better fit of the alkali basalt (Ce = 147 ppm) with the rest of the data occurs when clinopyroxene fractionation is also considered.

requires the presence of residual clinopyroxene in addition to garnet. The overall trend for the upper part of Kohala is a gradually decreasing degree of partial melting, including the transition from tholeiitic to alkalic basalts. Presumably, this decreasing extent of melting in the source region signals the end of magma production at a particular volcano.

Comparison with the systematic study by White (1979) on the FAMOUS basalts from the mid-Atlantic ridge indicates that a fundamental difference between the petrogenesis of tholeiites in the two environments is the presence of residual clinopyroxene only in the case of the mid-ocean ridge, and residual clinopyroxene plus garnet in case of the Hawaiian islands.

References

Hofmann, A. W., T. L. Wright, and M. Feigenson, Trace element and Sr isotope abundance in recent lavas from Kilauea, Hawaii, *Carnegie Inst. Wash. Year Book 77,* 590–596, 1978.

Hofmann, A. W., and T. L. Wright, Trace element fractionation and the nature of the residual phases during tholeiite production in Hawaii, *Carnegie Inst. Wash. Year Book 78,* 335–340, 1979.

Minster, J. F., and C. J. Allègre, Systematic use of trace elements in igneous processes, Part III. Inverse problem of batch melting in volcanic suites, *Contrib. Mineral. Petrol., 68,* 37–52, 1978.

Pankhurst, R. J., Open system crystal fractionation and incompatible element variation in basalts, *Nature, 268,* 36–38, 1977.

White, W. M., Geochemistry of basalts from the FAMOUS area: a reexamination, *Carnegie Inst. Wash. Year Book 78,* 325–331, 1979.

Wright, T. L., D. A. Swanson, and W. A. Duffield, Chemical compositions of Kilauea east-rift lava, 1968–1971, *J. Petrol., 16,* 110–133, 1975.

The Role of Subducted Oceanic Crust in Mantle Evolution

*A. W. Hofmann and W. M. White**

In this report, we propose what we believe to be a new model for the geochemical evolution of the Earth's mantle. The model emphasizes the importance of the geochemical properties and the heat production of the subducted oceanic crust, and it differs in this regard from previous interpretations, which emphasized the role of recycled *continental* crust (e.g., Armstrong, 1968), or the interplay of melt-depleted mantle with its undepleted counterpart (Allègre, 1969). In all these previous models, the oceanic crust was assumed to be rehomogenized with its complementary depleted residue, and its temporary existence could therefore be neglected for the purpose of developing whole-mantle evolution models. The only previous suggestions of a separate role for the oceanic crust are those of Ringwood (1975), who proposed that this crust sinks to the base of the mantle and is thereby irreversably lost from the convecting system, and of Anderson (1979), who proposed that the oceanic crust accumulates in the upper mantle (above 650 km depth) and is then recycled to form new oceanic crust.

In this report, we propose that the subducted oceanic crust accumulates at some level in the mantle, perhaps at its base. When the accumulated crust has locally reached a thickness of 100 km or more, its internal heat production raises its temperature by several hundred degrees over that of the ambient mantle, until it becomes unstable and rises diapirically to the surface. These diapirs are the plumes that give rise to oceanic-island volcanism as proposed by Morgan (1971, 1972). The plumes in turn trigger a new cycle of seafloor spreading, in which new oceanic crust is produced by passive upwelling and partial melting of upper-mantle material, again as proposed by Morgan. An attempt is made to show how this model may explain some of the baffling "geochemical paradoxes" which required various forms of special pleading for reconciliation of the observations with previous models.

Among these are (1) the longevity, localization, and quasi-stationary nature of oceanic island volcanism; (2) the occurrence of mantle isochrons yielding apparent ages of 1–2 b.y.; (3) the evidence that the U/Pb and U/Th ratios of oceanic island sources was higher than bulk earth values, while at the same time the Rb/Sr and the Nd/Sm ratios of these sources were lower than bulk earth values (e.g., Dupre and Allègre, 1980; Cohen *et al.*, 1980); (4) the evidence that these low Rb/Sr and Nd/Sm source ratios (which normally indicate differential loss of all four trace elements in the source) nevertheless yield magmas that have not only much higher Rb/Sr and Nd/Sm ratios but also much higher concentrations of these trace elements than could be expected from trace-element-depleted sources; and (5) the observation that continental igneous activity has been episodic rather than continuous, which implies that mantle convection was nonuniform in time.

The essential dynamical features of the model are sketched in Fig. 20. The sequence of processes starts arbitrarily 2 b.y. ago, a time of little or no significant igneous activity. The mantle is assumed to be stagnant, with a layer (probably of nonuniform thickness) of accumulated and subducted oceanic crust at its base. About 1.8 b.y. ago, this boundary layer becomes unstable owing to its now-elevated temperature, and it starts to form diapirs or plumes. These rise to the surface and trigger an episode of mantle convection with seafloor spreading and continental

*U.S. Geological Survey, Denver, Colorado.

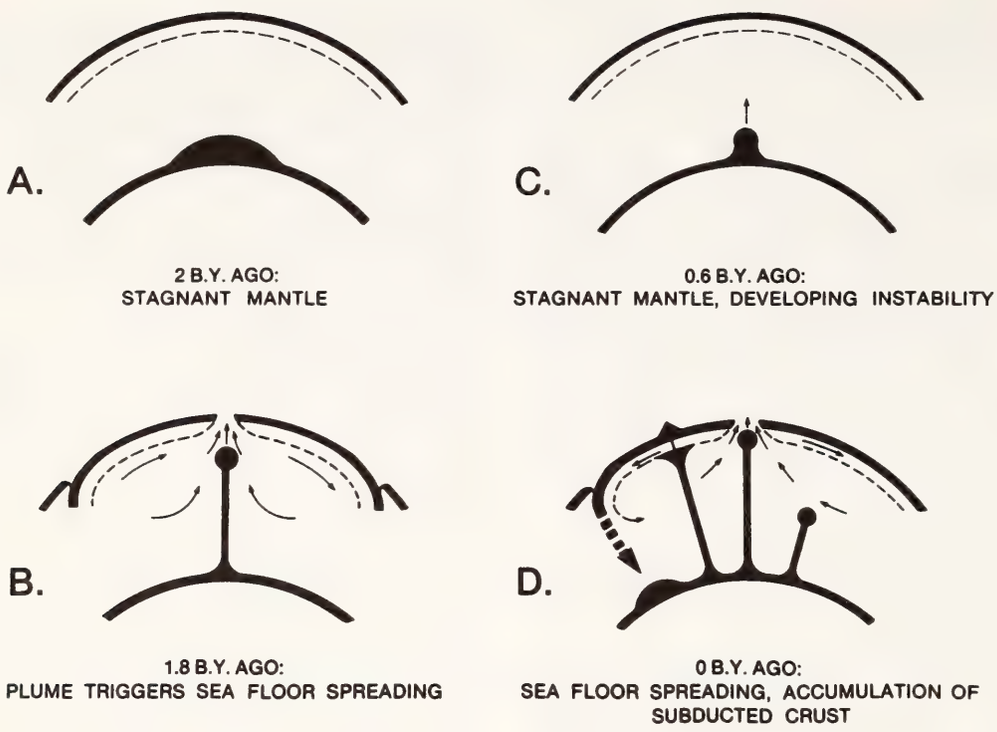


Fig. 20. Cartoon of different stages of mantle evolution. The oceanic crust, shown in solid black, is exaggerated for clarity. Continental regions are not shown.

igneous activity, which lasts until the hot boundary layer is exhausted and convection stops once again. During the period of convection, a new accumulation of oceanic crust has formed at the base of the mantle, and this will eventually trigger a new instability and thus give rise to a later cycle.

(*1*) *Heating and plume formation of the accumulated crust.* O'Nions *et al.* (1978) have shown that the Earth's present-day heat loss is much greater than the heat production of suboceanic mantle material. This means that either heat production and heat loss are not in balance or substantial quantities of heat-producing elements remain hidden in the mantle. The model of intermittent convection proposed here would lead to a disequilibrium between heat production and heat loss during most of the Earth's history.

Figure 21 shows the temperature profile of a stagnant medium that contains a heat-producing layer corresponding to the composition of ordinary oceanic crust. The temperature increase at the center of the layer (if heat is conducted to both sides) or at its base (if heat is reflected at its base) is about 650 °C after 1 b.y. and 1000 °C after 2 b.y. If the coefficient of expansion is $\alpha = 10^{-5}$ deg^{-1}, a density decrease of $\Delta\rho = 0.03$–0.05 g cm^{-3} will occur. Whitehead and Luther (1975) have shown how such a layer becomes unstable and forms rising plumes. They have also calculated ascent times for low-viscosity plumes through the mantle. For a mantle viscosity $\mu = 10^{22}$ poises and $\Delta\rho = 0.03$ g cm^{-3}, this ascent time is about 10^8 years.

The above discussion shows that accumulations of subducted oceanic crust provide the conditions suitable for plume formation and that the time scales for heating and ascent are appropriate. Whether such plumes are actually capable of triggering widespread convection in the upper mantle is a more speculative conjecture suggested by Morgan (1971, 1972) and tentatively adopted by us. In any

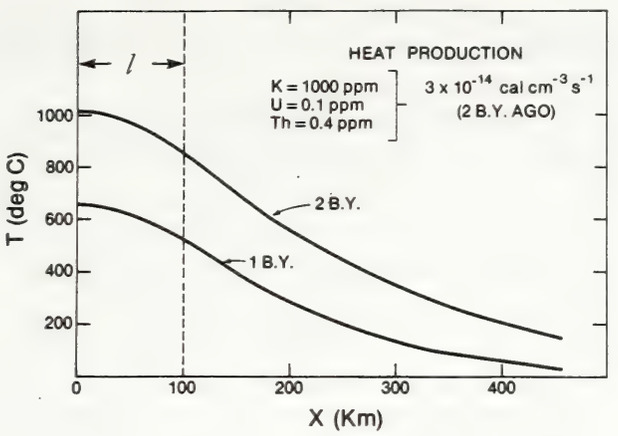


Fig. 21. Temperature profile in an infinite medium containing a heat-producing layer of 100-km half-thickness with zero initial temperature and no convection. The profiles also apply to a layer of 100-km total thickness, if no heat is conducted through the base, $x = 0$. The heat production is assumed constant and corresponds to the production rate in typical oceanic basalts at a time 2 b.y. ago.

TABLE 8. Model Ages of Mantle Sources of Island Groups*

Island Group	Pb-Pb Model Age (b.y.) (Secondary Isochron)	Author
Abyssal Tholeiites	1.76 ± 0.13	Tatsumoto (1978)
Hawaii	0.94 ± 0.21	Tatsumoto (1978)
Canary	1.80 ± 0.12	Sun (1980)
Iceland, Reykjanes R.	1.52	Sun *et al.* (1975) Sun and John (1975)
Galapagos	1.81 ± 0.12	White (1979)

*With well-defined linear correlations (= "secondary isochrons") on a $^{207}Pb/^{204}Pb$ versus $^{206}Pb/^{204}Pb$ diagram. Such model ages may represent events of U-Pb differentiation of the source, or they may be produced by binary mixing processes.

case, such plumes account very well for the quasi-stationary "hot spots" first recognized by Wilson (1963) and later reinterpreted by Morgan (1971).

(2) *Mantle isochrons.* Apparent isochron relations in the Rb-Sr and Pb-Pb isotope systems have been noted by many authors (e.g., Brooks *et al.*, 1976; Tatsumoto, 1978). The most prominent Pb-Pb isochrons are listed in Table 8, which shows that a number of island groups yield model ages of about 1.8 b.y. Brooks *et al.* (1976) pointed out that this value agrees with the worldwide apparent Rb-Sr isochron of recent oceanic tholeiites. It is well known that apparent isochrons can be produced by mixing processes, and therefore the existence of such mantle isochrons does not demonstrate that they date an important, mantle-wide event. On the other hand, an event of seafloor spreading and accumulation of the oceanic crust at about 1.8 b.y. such as we have postulated above, would certainly be a simple and plausible mechanism for generating such isochrons, whereas any explanation involving convective mixing requires a special explanation why the net result resembles a two-component rather than a multi-component mixture.

(3) *Source ratios of Rb/Sr, Sm/Nd, U/Pb and Th/U.* Figure 22 shows summarized and simplified isotopic data for oceanic basalts (e.g., DePaolo and Wasserburg, 1976; O'Nions *et al.*, 1977; Allègre *et al.*, 1979; Sun, 1980). The isotopic composition of Sr, Nd, and Pb of basalts from oceanic islands indicate that most of the sources of these basalts have been depleted in Rb, Nd, Pb, and Th relative to Sr, Sm, U, and U respectively. The depletion pattern produced by simple igneous processes would be Rb, Nd, and U relative to Sr, Sm, and Pb. Therefore, some additional mechanism is needed to reconcile the Sr and Nd isotopic data on the one hand with the Pb isotopic data on the other. The most popular way out of this dilemma is to postulate recycling of U, Th, and Pb from the upper continental crust into the mantle (Armstrong, 1968; O'Nions *et al.*, 1979; Evensen *et al.*, 1979). Pre-

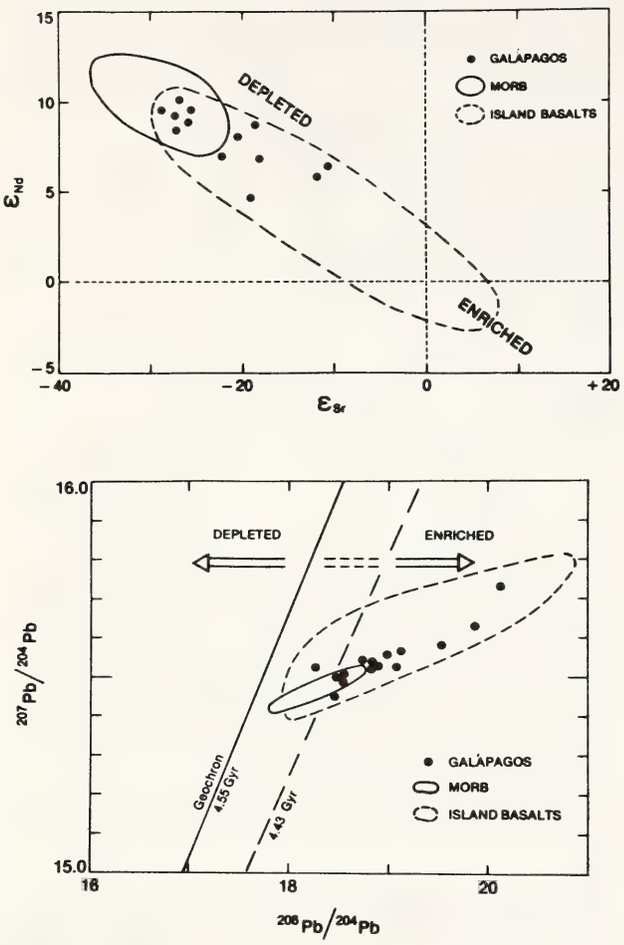


Fig. 22. Outlines of isotopic composition of oceanic basalts. The solid lines represent the fields of mid-ocean ridge basalts (MORB), the dashed lines show the oceanic island basalts. The solid dots are shown as examples from the Galápagos Islands and are taken from White and Hofmann (1978) and White (1979). The fields marked DEPLETED and ENRICHED indicate source regions with low and high ratios, respectively, of Rb/Sr, Nd/Sm, and U/Pb in relation to bulk-earth values (inferred from meteorite data). The inferred bulk-earth values are model dependent especially in the U-Pb system where the value depends strongly on the assumed age of the Earth. Nevertheless, even if the age of the Earth is as young as 4.43 b.y., most of the oceanic Pb data fall in the region of U/Pb enrichment, whereas most of the Nd and Sr data indicate Rb/Sr and Nd/Sm depletion of the source.

sumably, this would occur via subduction of sediments. We note, however, that at least pelagic sediments are not known to have particularly high U/Pb ratios. Furthermore, if the continental crust is recycled in this manner, then the vehicle for this process is the subducted *oceanic* crust, which is far more voluminous than the sediment cover.

We now consider whether there is a more efficient mechanism to create substantial volumes of material with high U/Pb and U/Th without significantly affecting the Rb/Sr and Nd/Sm ratios. In Table 9 we show estimates of the total fluxes of the relevant element through ocean water. The influx is given by the components dissolved in river water. The dissolved components may then be removed by precipitation in sediments or by hydrothermal low-temperature alteration of the oceanic crust. The figures in the last row are the percentage increases in concentration for the oceanic crust, with the assumption that *all* the dissolved components end up in the crust. Uranium is of special interest here because it is the only element that is removed from seawater primarily by hydrothermal interaction at the mid-ocean ridges (Edmond *et al.*, 1979). It appears inevitable, therefore, that the subducted oceanic crust is significantly enriched in uranium relative to Pb and Th. Also, if a substantial fraction of the dissolved Rb, Sr, and Pb is precipitated in nonsubducted sediments, as seems plausible, then uranium is the only element to be enriched significantly in the subducted oceanic crust. This material will then have the trace element ratios necessary to qualify as source material of oceanic islands. The Rb/Sr and Nd/Sm ratios of 1.8-b.y.-old oceanic crust would be lower than bulk earth values but not as low as present-day oceanic crust (because of progressive depletion of the upper mantle in Rb and Nd relative to Sr and Sm). On the other hand, the U/Pb and U/Th ratios would be increased over bulk earth values.

(*4*) Trace element concentrations in ocean island tholeiites are commonly several times higher than in ocean floor tholeiites. For example, light rare-earth (LRE) enrichment in Hawaiian

TABLE 9. Dissolved-Element Flux Through Ocean Water*

	U	Th	Pb	Rb	Sr	Nd
River influx (in 10^{10} g/yr)	1.9 (0.13)‡	0.03	...	3.2	59	...
Pelagic precipitation (10^{10} g/yr)	...	...	1.1	...	...	0.2–1.4
Net concentration increase of crust (in ppm)†	0.33 (0.13)‡	0.005	0.2	0.5	10	<0.24
Percentage concentration increase of crust (in % over fresh MORB)†	300 (20)‡	1	20	50	10	<2

*The upper two lines of data represent input estimates either from measurements of element concentrations in river waters or from estimates of prehistoric precipitation rates at the ocean bottom. The lower two lines are estimates of the bulk concentration increase of the oceanic crust if the entire influx is added to the oceanic crust of basaltic composition, produced at a rate of 18 km^3 per year. These are maximum estimates for most of the elements, especially Pb which is rapidly removed from solution by shallow-water organisms, and Sr which is coprecipitated with shallow-water carbonates. On the other hand, uranium is added to the oceanic crust by hydrothermal activity. Note, however, the U values based on the U concentration of Amazon river water only.

†Assuming the entire flux is added to the oceanic crust.

‡Based on the U concentration of Amazon river water only.

tholeiites is 20–50 times the chondritic value (see Feigenson and Hofmann, pp. 472–476, this Report). If undifferentiated mantle rock has twice-chondritic rare earth concentrations, the degree of melting required to form the tholeiites would be between 4 and 10 percent and associated alkali basalt with LRE enrichments of 100 and more would require degrees of 2 percent or less. These low melt fractions are widely believed to be unrealistic because of difficulties in extracting such a melt from the source rock. Our model provides a straightforward solution to this problem. Oceanic crust has commonly about ten-times-chondritic rare earth concentrations, and the corresponding melt fractions would be between 20 and 50 percent for tholeiites and 10 percent for alkali basalts. The specific case for typical Kilauea lavas (see Hofmann and Wright, 1979) is illustrated in Fig. 23. The source material used for the partial melting calculations is garnet pyroxenite of an overall basaltic composition and similar to garnet pyroxenite nodules from Hawaii (Beeson and Jackson, 1970).

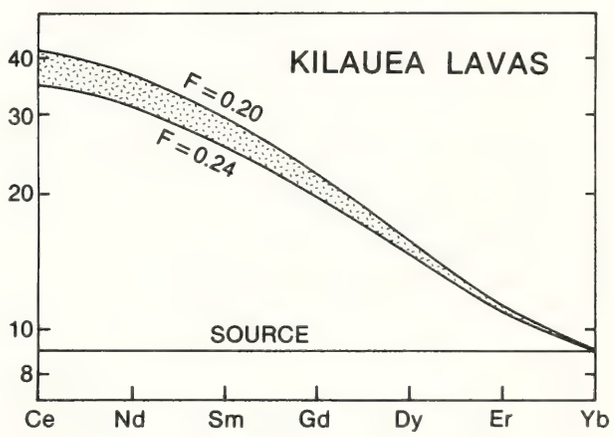


Fig. 23. Calculated rare earth concentrations using a simple batch-melting model from a garnet pyroxenite source with an initial REE pattern typical of ocean floor basalts. The calculated concentrations agree with the measured values of Hofmann and Wright (1979) for tholeiites from the Hawaiian volcano Kilauea. The light REE enrichment typical of ocean-island basalts is thereby explained in a straightforward manner with no need for metasomatic pre-enrichment of the source mantle and with degrees of partial melting (20–25%) widely believed to be "normal" for tholeiitic basalts.

(5) The episodic nature of continental igneous activity has been recognized by many geologists. Isotopic age determinations have given considerable

quantitative support (Gastil, 1960; Glickson, 1980, fig. 1), but a rigorous statistical treatment has never been published. If one accepts the reality of this episodicity together with the assumption that all magmatic activity is ultimately related to mantle convection, one almost inevitably reaches the conclusion that mantle convection is not a steady state process but has probably been intermittent. The major episodes of magmatic activity occurred 3.6, 2.7, 1.8, 1.0, and 0.5–0 b.y. ago. Mantle isochrons of modern oceanic island basalts indicate that they are derived from oceanic crust formed during the 1.8-b.y.-old episode of convection. If this is correct, the material accumulated during the intervening episode (1.0 b.y.) is not yet producing plumes. It appears, therefore, that the subducted crust accumulated during one convective episode need not be the one that triggers the next episode, because the heating time required is too long. An alternative possibility is that the apparent mantle isochrons are mixing lines between the accumulated crust and depleted mantle and that the apparent age of the isochrons is therefore biased.

In summary, we believe our model has merit because it apparently "solves" many of the more perplexing difficulties in reconciling geochemical observations with a geologically plausible history of mantle evolution. The model is further testable by future observations on the bulk alteration of the oceanic crust.

References

Allègre, C. J. Comportement des systems U-Th-Pb dans le manteau superieur et modele d'evolution de ce dernier au cours des temps geologiques, *Earth Planet. Sci. Lett., 5,* 261–269, 1969.

Allègre, C. J., D. Ben Othman, M. Polve, and R. Richard, The Nd-Sr isotopic correlation in mantle materials and geodynamic consequences, *Phys. Earth Planet. Interiors, 14,* 293–306, 1979.

Anderson, D. L., Chemical stratification of the mantle, *J. Geophys. Res., 84,* 6297–6298, 1979. 1979.

Armstrong, R. L., A model for Sr and Pb isotope evolution in a dynamic earth, *Rev. Geophys., 6,* 175–199, 1968.

Beeson, M. H., and E. D. Jackson, Origin of the garnet pyroxenite xenoliths at Salt Lake Crater, Oahua, *Mineral. Soc. Amer. Spec. Pap. 3,* 95–112, 1970.

Brooks, C., S. R. Hart, A. W. Hofmann, and D. E. James, Rb-Sr mantle isochrons from oceanic regions, *Earth Planet. Sci. Lett., 32,* 51–61, 1976.

Cohen, R. S., N. M. Evensen, P. J. Hamilton, R. K. O'Nions, U-Pb, Sm-Nd and Rb-Sr systematics of mid-ocean ridge basalt glasses, *Nature, 283,* 149–153, 1980.

DePaolo, D. J., and G. J. Wasserburg, Inferences about magma sources and mantle structure from variations of $^{143}Nd/^{144}Nd$, *Geophys. Res. Lett., 3,* 743–746, 1976.

Dupré, B., and C. J. Allègre, Pb-Sr-Nd isotopic correlation and the chemistry of the North Atlantic mantle, *Nature, 286,* 17–22, 1980.

Edmond, J. M., C. Measures, B. Magnum, B. Grant, F. R. Sclater, R. Collier, A. Hudson, L. I. Gordon, and T. B. Corliss, On the formation of metal-rich deposits at ridge crests, *Earth Planet. Sci. Lett., 46,* 19–30, 1979.

Evensen, N. M., P. J. Hamilton, and R. K. O'Nions, Lead isotopes, crustal evolution and mantle mixing: a model, *EOS, 60,* 406, 1979.

Gastil, G., The distribution of mineral dates in space and time, *Amer. J. Sci., 258,* 1–35, 1960.

Glickson, A. Y., Precambrian Sial-Sima relations: evidence for earth expansion, *Tectonophysics, 63,* 193–234, 1980.

Hofmann, A. W., and T. L. Wright, Trace element fractionation and the nature of the residual phases during tholeiitic production in Hawaii, *Carnegie Inst. Wash. Year Book 78,* 335–340, 1979.

Morgan, W. J., Convection plumes in the lower mantle, *Nature, 230,* 42–43, 1971.

Morgan, W. J., Plate motions and deep mantle convection, *Geol. Soc. Amer. Memoir, 132,* 7–22, 1972.

O'Nions, R. K., P. J. Hamilton, and N. M. Evensen, Variations in $^{143}Nd/^{144}Nd$ and $^{87}Sr/^{86}Sr$ ratios in oceanic basalts, *Earth Planet. Sci. Lett., 34,* 13–22, 1977.

O'Nions, R. K., N. M. Evensen, P. J. Hamilton, and S. R. Carter, Melting of the mantle past and present: isotope and trace element evidence, *Phil. Trans. Roy. Soc. Lond. A., 258,* 547–559, 1978.

O'Nions, R. K., N. M. Evensen, and P. J. Hamilton, Geochemical modeling of mantle differentiation and crustal growth, *J. Geophys. Res., 84,* 6091–6101, 1979.

Ringwood, A. E., *Composition and Petrology of the Earth's Mantle,* p. 539, McGraw-Hill, New York, 1975.

Sun, S.-S., and B. John, Lead and strontium isotopes in post-glacial basalts from Iceland, *Nature, 255,* 527–530, 1975.

Sun, S.-S., M. Tatsumoto, and J.-G. Schilling, Mantle mixing along the Reykjanes Ridge axis: lead isotopic evidence, *Science, 190,* 143–147, 1975.

Sun., S.-S., Lead isotopic study of young volcanic rocks from mid-ocean ridges, ocean islands and island arcs, *Phil. Trans. Roy. Soc. Lond.,* in press, 1980.

Tatsumoto, M., Isotopic composition of lead in oceanic basalt and its implication to mantle evolution, *Earth Planet. Sci. Lett., 38,* 63–87, 1978.

White, W. M., Pb isotope geochemistry of the Galápagos Islands, *Carnegie Inst. Wash. Year Book 78,* 331–335, 1979.

White, W. M., and A. W. Hofmann, Geochemistry of the Galápagos Islands: implications for mantle dynamics and evolution, *Carnegie Inst. Wash. Year Book 77,* 596–606, 1978.

Whitehead, J. A., Jr., and D. S. Luther, Dynamics of a laboratory diapir and plume models, *J. Geophys. Res., 80,* 705–717, 1975.

Wilson, J., A possible origin of the Hawaiian Islands, *Can. J. Phys., 41,* 863–870, 1963.

Rb-Sr Whole-Rock Studies: Virginia Piedmont II

*Douglas Mose**

The Appalachian Piedmont Province in Virginia consists of gently rolling hills bordered on the west by the Blue Ridge mountains and on the east by the relatively low-lying hills of the Atlantic Coastal Plain. Although unweathered rock exposures in the Piedmont are rare owing to a thick development of saprolite, major river valleys contain fresh outcrops. This paper is a report on rocks exposed along the Occoquan River valley in northern Virginia and the James River valley in central Virginia. Two of the rock units in these valleys have proven useful because they extend at least from northern Virginia (in the Quantico syncline) to south-central Virginia (in the Columbia and Arvonia synclines). These units are the Chopawamsic Formation and the Arvonia-Quantico Slate (Brown, 1970; Southwick *et al.,* 1971; Pavlides *et al.,* 1980; Pavlides, 1980).

The Chopawamsic Formation consists of metamorphosed mafic and felsic volcanic rocks and lesser amounts of metasedimentary rocks. The Chopawamsic and the related James Run Formation of eastern Maryland have both yielded zircons with U-Pb ages corresponding to Cambrian time (Higgins *et al.,* 1977). The contact between the Chopawamsic and the overlying Quantico Slate in northern Virginia is an unconformity, and Ordovician fossils have been found in the slate (Watson and Powell, 1911; Pavlides *et al.,* 1980). The Quantico Slate has been correlated with the Arvonia Slate in central Virginia (Pavlides, 1980). The Arvonia Slate also contains Ordovician fossils, and the slate unconformably overlies the Chopawamsic volcanics (Tillman, 1970; Brown, 1970; Higgins *et al.,* 1977; Brown, 1979).

In the Occoquan River area of northern Virginia, the Occoquan pluton (granite, granodiorite, tonalite, and quartz granitoid) is seen to have intruded the Chopawamsic Formation (Southwick *et al.,* 1971; Seiders *et al.,* 1975). Although there is no exposed contact between the Occoquan pluton and the Quantico Slate, a second pluton in the area called the Dale City pluton (quartz diorite and quartz monzonite) intruded the Chopawamsic Formation and is unconformably below the Quantico Slate (Pavlides *et al.,* 1980). In the James River area of central Virginia, the Columbia pluton (granite, granodiorite, and tonalite) is seen to have intruded the Chopawamsic Formation and is unconformably below the Arvonia Slate (Brown, 1970; Brown, 1979).

U-Pb data from the Occoquan pluton fall on a chord whose lower intercept is to the right of the origin on a concordia diagram, and whose upper intercept is at about 550 m.y. (Seiders *et al.,* 1975; Higgins *et al.,* 1977). However, as noted by Higgins (1976), point

*Department of Chemistry and Geology, George Mason University, Fairfax, Virginia.

no. 1 on Seiders' diagram is analytically poor and unusable. The remaining two data points yield a chord whose upper end does not intersect the concordia and whose lower end intersects at about 430 m.y. U-Pb data from the Dale City pluton yield a two-point chord whose upper end crosses the concordia at about 530 m.y., but one data point lies above the concordia curve and the lower end of the chord falls to the right of the origin (Seiders *et al.,* 1975; Higgins, 1976; Higgins *et al.,* 1977). U-Pb data from the Columbia pluton yield a two-point chord that is tangential to the concordia curve (Higgins *et al.,* 1977; Seiders, 1978). U-Pb data that yield chords whose upper ends do not intersect with the concordia or whose lower ends do not intersect with the concordia origin but fall to the right of the origin are thought to be characteristic of zircons that have inherited radiogenic lead, probably in the form of seed crystals (Higgins, 1976; Higgins *et al.,* 1977). Although Seiders (1978) notes that there is no analytical data in Higgins *et al.* (1977) which clearly reveal the presence of inherited radiogenic lead, and that no textural evidence for the inclusion of older zircon crystals is present in the zircons analyzed from the Occoquan and Dale City plutons, Zartman (1978) noted that in areas of older sialic basement (such as the Appalachians) younger plutonic rocks may contain zircon seed crystals derived from the basement and that zircon morphology studies do not always reveal this problem.

A Rb-Sr whole-rock study was made of the Occoquan, Dale City, and Columbia plutons to test the validity of the published ages of the Chopawamsic volcanics (U-Pb: about 550 m.y.) and the Arvonia-Quantico Slate (fossils: about 440–460 m.y.) and to determine how the Rb-Sr ages would compare with the available U-Pb "ages." The results are shown in Table 10 (copies of the isochrons, the sample locations, and the analytical data may be obtained upon request from the author; the technique used for the Rb-Sr analyses is described in Mose, 1979).

As discussed earlier, although U-Pb data from the plutons did not yield a clear resolution of their ages, their geologic setting and the age determinations for their host rock and cover rock show that the plutons were emplaced between about 550 m.y. ago and about 440–460 m.y. ago. The Rb-Sr ages agree with this interpretation. Furthermore, the initial $^{87}Sr/^{86}Sr$ ratios of the plutons is informative. Although the Rb-Sr data from the Dale City pluton are not sufficient to define an isochron, the data do not fall on the isochron for the nearby Occoquan pluton, indicating that the plutons are not comagmatic. It is therefore not correct to treat U-Pb data from both plutons simultaneously, as was done by Seiders *et al.* (1975). It is also true that early Paleozoic plutons in the southern Appalachians, in areas thought to be devoid of greatly older sialic rocks, generally have $(^{87}Sr/^{86}Sr)_o$ ratios of less than 0.706 (Fullagar, 1971). While the Dale City and Colum-

TABLE 10. Rb-Sr Age Determinations*

Rock Unit	Number of Samples	Age	Initial $^{87}Sr/^{86}Sr$
Columbia Pluton	5	454 ± 9 m.y.	0.7059 ± 0.0003
Dale City Pluton	2	500 (est.)	0.704 to 0.705
Occoquan Pluton	13	494 ± 14 m.y.	0.7118 ± 0.0004

*Errors given as 1σ.

bia plutons have $(^{87}Sr/^{86}Sr)_o$ ratios of 0.704–0.706, the Occoquan pluton has a relatively high ratio of about 0.712. It is therefore probable that the Occoquan incorporated country rock, some of which may have contributed xenocrystic zircons. It is likely that the Dale City and Columbia plutons also incorporated xenocrystic zircons, but the data are not sufficient to prove or disprove this possibility. The presence of xenocrystic zircons has also been proposed by Odom and Fullagar (1971) to explain a significant difference between Rb-Sr ages and U-Pb ages (Rankin *et al.*, 1969) for nearby Late Proterozoic plutonic rocks in the Blue Ridge Province.

At the present time, relatively few plutonic rocks in the southern Appalachians have been studied using both U-Pb and Rb-Sr radiometric techniques. This study of plutons in the Virginia Piedmont suggests that the Rb-Sr technique may be the more reliable technique, that more detailed U-Pb studies will show that Appalachian plutonic rocks often contain a mixed population of zircons (part derived from the host rocks) that produced chords whose interpretation is difficult, and that (as suggested by Higgins *et al.*, 1977) the U-Pb ages from polymetamorphic terranes such as the Appalachians should be used with caution.

References

Brown, W. R., Investigations of the sedimentary record in the Piedmont and Blue Ridge of Virginia, in *Studies of Appalachian Geology: Central and Southern*, pp. 335–349, Interscience Publishers, New York, 1970.

Brown, W. R., Field guide to the Arvonia-Schuyler district, in *Guides to Field Trips 1–3, Southeastern Section*, pp. 24–41, Geol. Soc. Amer. Annu. Mtg., Blacksburg, Virginia, 1979.

Fullagar, P. D., Age and origin of plutonic intrusions in the Piedmont of the southern Appalachians, *Bull. Geol. Soc. Amer., 82*, 2845–2862, 1971.

Higgins, M. W., Age, origin, regional relations, and nomenclature of the Glenarm Series, central Appalachian Piedmont, a reinterpretation: Reply, *Bull. Geol. Soc. Amer., 87*, 1523–1528, 1976.

Higgins, M. W., A. K. Sinha, R. E. Zarman, and W. S. Kirk, U-Pb zircon dates from the central Appalachian Piedmont: a possible case of inherited radiogenic lead, *Bull. Geol. Soc. Amer., 88*, 125–132, 1977.

Mose, D. G., Rb-Sr whole-rock studies: Virginia Piedmont, *Carnegie Inst. Wash. Year Book 78*, 345–346, 1979.

Odom, A. L., and P. D. Fullager, A major discordancy between U-Pb zircon ages and Rb-Sr whole-rock ages of late Precambrian granites in the Blue Ridge Province, *Geol. Soc. Amer., Abstracts w. Progr., 3*, 663, 1971.

Pavlides, L., J. Pojeta, M. Gordon, R. L. Parsley, and A. R. Bobyarchick, New evidence for the age of the Quantico Formation of Virginia, *Geology, 8*, 286–290, 1980.

Pavlides, L., Revised nomenclature and stratigraphic relationships of the Fredericksburg complex and the Quantico Formation of the Virginia Piedmont, *U.S. Geol. Surv. Prof. Paper 1146*, in press, 1980.

Rankin, D. W., T. W. Stern, J. C. Reed, and M. F. Newell, Zircon ages of felsic rocks in the upper Precambrian of the Blue Ridge, Appalachian Mountains, *Science, 166*, 741–744, 1969.

Seiders, V. M., R. B. Mixon, T. W. Stern, M. F. Newell, and C. B. Thomas, Age of plutonism and tectonism and a new minimum age limit on the Glenarm series in the northeast Virginia Piedmont near Occoquan, *Amer. J. Sci., 275*, 481–511, 1975.

Seiders, V. M., U-Pb zircon dates from the central Appalachian Piedmont: a possible case of inherited radiogenic lead: discussion, *Bull. Geol. Soc. Amer., 89*, 1115–1116, 1978.

Southwick, D. L., J. C. Reed, and R. B. Mixon, The Chopawamsic Formation: a new stratigraphic unit in the Piedmont of northeastern Virginia, *U.S. Geol. Surv. Bull., 1324-D*, D1–D11, 1971.

Tillman, C. G., Metamorphosed trilobites from Arvonia, Virginia, *Bull. Geol. Soc. Amer., 81*, 1189–1200, 1970.

Watson, T. L., and S. L. Powell, Fossil evidence of the age of the Virginia Piedmont slates, *Amer. J. Sci., 4th ser., 31*, 33–44, 1911.

Zartman, R. E., U-Pb zircon dates from the central Appalachian Piedmont: a possible case of inherited radiogenic lead: reply, *Bull. Geol. Soc. Amer., 89*, 1116–1117, 1978.

Incompatible Element and $^{87}Sr/^{86}Sr$ Composition of Mt. St. Helens Ash

R. J. Stern and Emi Ito

The catastrophic eruption of Mt. St. Helens on the morning of May 18, 1980 destroyed the north flank of the volcano, opened a crater 1.5 km wide, and produced a large quantity of volcanic ash. The ash is dacitic in composition (64–68% SiO_2; Christiansen, 1980). A sample of the ash was analyzed for incompatible elements (K, Rb, Sr, Cs, Ba) and $^{87}Sr/^{86}Sr$. The results are listed in Table 11. These show the ash to be similar to material produced by other circum-Pacific island arcs; K/Rb is slightly lower than that of the Mariana Arc while K/Ba is very similar (Chow *et al.*, 1980). $^{87}Sr/^{86}Sr$ is identical to the mean value of all circum-Pacific island arcs (0.7036; Stern, 1979).

TABLE 11. Composition of May 18, 1980, Mt. St. Helens Ash

K	1.33%	K/Rb	342
Rb	38.9 ppm	K/Ba	31.2
Sr	385.9	K/Cs	7824
Cs	1.7 ppm	Rb/Sr	0.1008
Ba	366.3 ppm	Rb/Ba	0.1062
		Ba/Sr	0.949
	$^{87}Sr/^{86}Sr$*	0.70359 ± 7	

*Strontium isotopic composition normalized to $^{86}Sr/^{88}Sr = 0.1194$, and E and A $SrCO_3$ = 0.70800.

References

Chow, T. J., R. J. Stern, and T. H. Dixon, Absolute and relative abundances of K, Rb, Sr, and Ba in circum-Pacific island-arc magmas, with special reference to the Marianas, *Chem. Geol., 28,* 111–121, 1980.

Christiansen, R. L., Volcanology, *Nature, 285,* 531–533, 1980.

Stern, R. J., Strontium isotopes in island arcs and marginal basins from the circum-Pacific: regional variations and implications for magmagenesis, *Geol. Soc. Amer., Abstracts w. Progr., 11,* 524, 1979.

CRUST AND UPPER MANTLE—GEOPHYSICAL STUDIES

Stress Redistribution and Slow Earthquakes

I. Selwyn Sacks, Shigeji Suyehiro, Alan T. Linde, and J. Arthur Snoke†*

Introduction

In *Year Book 76* (Sacks *et al.*, 1977, herein referred to as Paper 1), we reported the identification of slow earthquakes from recordings by Sacks-Evertson borehole strainmeters. The "slowquakes," which resemble normal earthquakes except for having longer time scales, provide a possible mechanism for stress redistribution which is rapid compared with gradual large-scale tectonic motion but slow in relation to the elastic changes following a normal earthquake.

In Paper 1, we reviewed indirect evidence for slowquakes and showed borehole strainmeter data, which we interpreted as direct observations of such events. Here, we review the basis for the statement that slowquakes and normal quakes are similar, and we present new data showing that our slowquake interpretation of the straingrams is confirmed by independent measurements of crustal deformation.

These data were recorded by a network of Sacks-Evertson borehole strainmeters installed along the seismically active Pacific coast of Honshu, south of Tokyo. These instruments have large dynamic range and high sensitivity from zero frequency to several hertz (Sacks *et al.*, 1971). Further description of the instrument is given elsewhere in this Report (Snoke *et al.*, pp. 491–495).

*Japanese Meteorological Agency, Tokyo.

†Department of Geological Sciences, Virginia Polytechnic Institute and State University, Blacksburg.

Normal and Slow Earthquake Straingrams: Observed and Synthetic

Figure 24 illustrates the similarity between the straingram for a slow earthquake and that for a normal earthquake (after low-pass filtering). We are not suggesting that the focal processes are similar; they are almost certain to be related to different physical properties of the medium. However, the general characteristics of the resulting waveforms differ only in their time scales—typically a factor of at least 10 to 100. We can therefore use the same synthetics programs to model both "slowquakes" and normal earthquakes. Our synthetics are obtained by calculating the response of a dilatometer installed at the free surface of a uniform, homogeneous, elastic halfspace to a double-couple point source (with a variable time history) located within the halfspace (see Snoke *et al.*, this Report).

Figure 25 shows synthetic straingrams for one event time-history at two different distances—both in the near field because the strain step is not negligible compared with the radiated pulse. In the extreme near field (Fig. 25a), only the strain step is observed. As distance increases (Fig. 25b), the radiated pulse becomes more dominant because it drops off less rapidly with distance than does the strain step.

In Fig. 26, waveforms for both normal and slow earthquakes are compared with synthetics. The known location and focal mechanism were used for the normal earthquake, and the time history used was a parabolic ramp with a duration of 0.5 seconds. This type of time function is obtained by matching two sections of curves (parabolas) in order to produce a smooth, physically reasonable representation of the relative motion across the fault. Because the slow earthquake was detected on only one in-

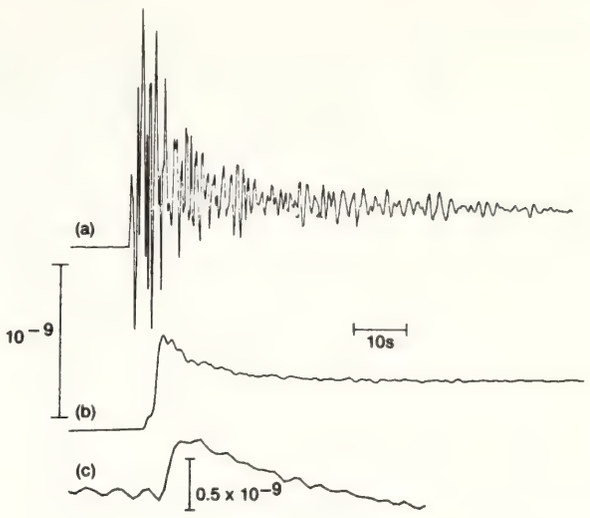


Fig. 24. Records of normal and slow earthquakes. (a) $m = 4.0$ normal earthquake on 19 Sep 1973 at a distance of 15 km from MAT, the recording station. (b) result of low-pass filtering trace (a); frequencies above 1 Hz are highly attenuated. (c) a small slowquake recorded at Irako on 25 Aug 1976. Notice the similarity between (b) and (c).

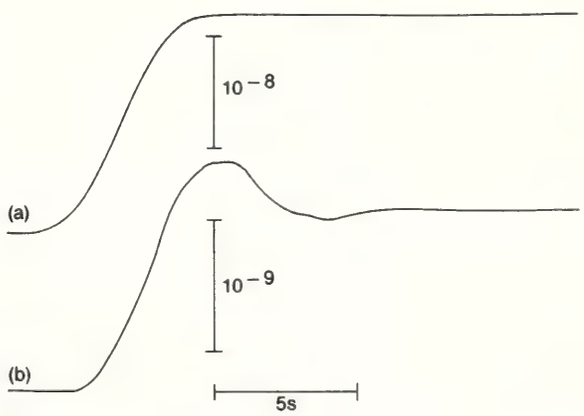


Fig. 25. Theoretical waveforms of dilatant strain vs. time for two different distances. (b) is for a distance four times that for (a). The source time function is a parabolic ramp with a duration of 6 seconds. The difference between the final and initial strain levels is the strain step produced by the earthquake. The magnitude of the step is inversely proportional to the cube of the distance between source and observation. The radiated pulse consists of the strain changes which take place during the arrival of seismic waves and which decrease less rapidly with distance than does the strain step. At greater distances, the radiated pulse dominates and in the far field the strain step is negligible.

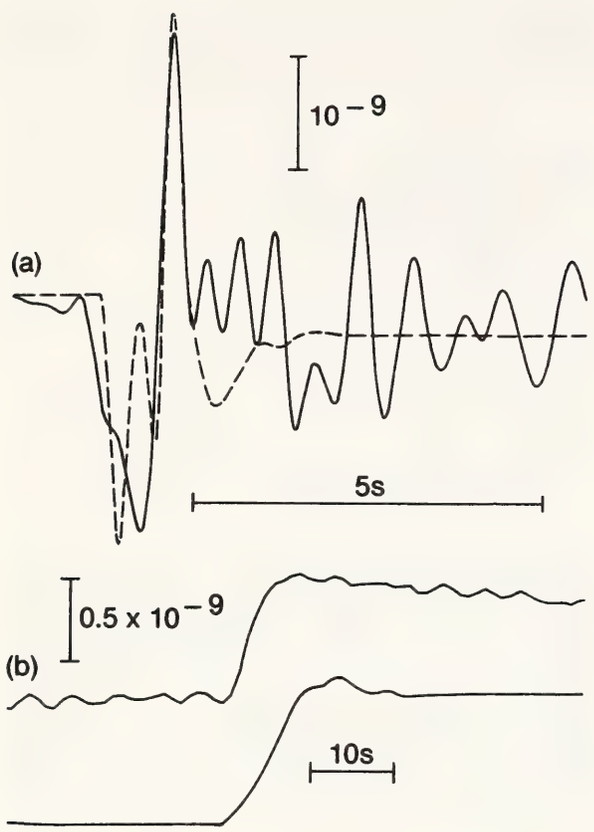


Fig. 26. Comparison of data and model waveforms for (a) a normal earthquake and (b) a slowquake. The first cycle of the earthquake (MAT, depth 3 km, 0.05 degrees, $m = 3.4$, 9 Jun 1973) is matched by a rise time of 0.24 seconds. The slowquake, upper trace in (b) (IRA, 25 Aug 1976), is modeled with a rise time of 8 seconds. Both events are modeled as vertical strike slip events.

strument, its location, depth, and radiation pattern were not known. An adequate fit is obtained by assuming a strike-slip event with a 16-second duration. As discussed more fully by Sacks *et al.* (1978), for such observations on a single instrument there is an unresolvable ambiguity, whether an event is near, slow, and of a certain size, or further, slower, and larger.

Slowquakes: Foreshocks and Aftershocks

Normal earthquakes are often accompanied by foreshocks and aftershocks with magnitudes about 2 smaller than the main shock. Archambeau (1977) reports that, compared with aftershocks of the same magnitude, foreshocks have characteristically higher stress drops and, accordingly, relatively higher high-frequency content.

Figure 27a shows a main slowquake accompanied by a foreshock-aftershock sequence of slowquakes. Examination of these events (Fig. 27b) reveals that the character of the waveform changes after the main event. Relative to strain step size, the foreshocks have larger radiated pulses than the aftershocks. While multiple station observations are required to eliminate ambiguities (as mentioned above), the data are consistent with a reduction in the general stress level caused by the main slowquake.

A Coseismic Slowquake—the Izu-Oshima Earthquake of 1978

On January 14, 1978, a large earthquake ($m = 7.0$) occurred under the sea between Oshima Island and Izu Peninsula. Fault parameters for this earthquake, determined from seismograph recordings of the radiated field, show that the earthquake was confined to the area between the island and the coast of Izu (Shimazaki and Somerville, 1978). Crustal deformation observations, however, require motion on a fault extending well inland (Inouchi and Sato, 1979). These observations indicate that the length and dislocation for the on-land fault are about half those for the submarine fault. Because of the small amount of vibration damage to nearby houses, Umeda and Murakami (1978) suggest that the on-land faulting motion was accompanied only by low accelerations.

The three nearest borehole strainmeters (20–60 km distance) recorded static field changes resulting from motion on the two faults. Figure 28 shows the location of these three in-

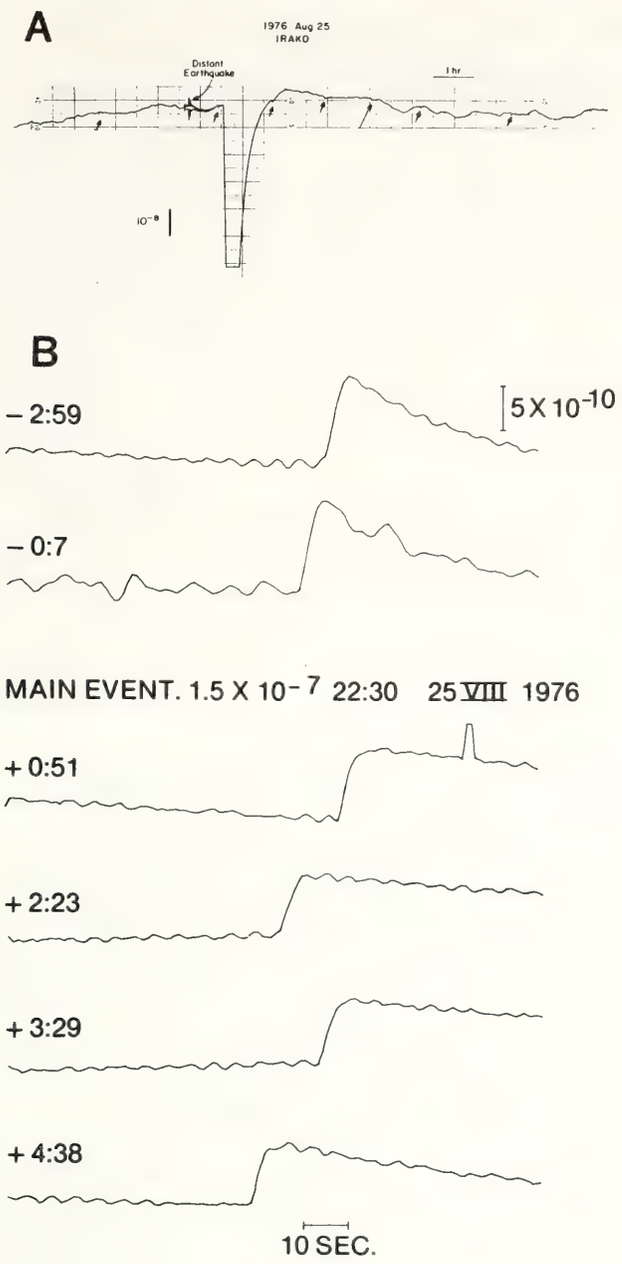


Fig. 27. Irako borehole strainmeter record for 25 Aug 1976, showing (a) a main slowquake, strain = 7×10^{-8}, and its associated foreshocks and aftershocks (shown by arrows) with strains less than 10^{-9}. (b) shows events from the foreshock-aftershock sequence selected on the basis of comparable pulse height (equivalent magnitude). The times (given in hours and minutes) are relative to that of the main slowquake. These are replayed at higher gain and expanded time scale. (The blip on the +0:51 trace is due to a digital transmission error.) Note the distinctive change in waveform with time: foreshocks have a small residual step (moment) compared with events immediately after the main slowquake.

struments and the aftershock region of the earthquake. Also shown are the positions of the faults, as determined from seismic radiation and from crustal deformation. The strain field changes coincident with and following the earthquake are shown in Fig. 29. Because of the filtering of the data and the following signal due to the on-land fault motion, the strain steps due to the earthquake (the upward excursions for SHI and AJI) are highly attenuated. These strain steps are of order 10^{-7}, and their magnitudes and polarities are consistent with the fault parameters determined from the seismological data by Shimazaki and Somerville (1978).

For approximately an hour following these steps, slow strain changes were recorded on these widely spaced ($\sim$60 km) instruments. The magnitudes of the slow strain changes are comparable to the strain steps due to the earthquake. Thus the source of this strain redistribution must have been of dimensions similar to those of the earthquake. These data, together with the crustal deformation observations (Inouchi and Sato, 1979) lead us to conclude that this source was a slowquake with a moment of the same order as that of the normal earthquake. All the data (slow strain changes, crustal deformation, aftershocks) provide strong evidence that this slowquake occurred on the Izu Peninsula (Fig. 29). Not until this slowquake redistributed the stress did the first large (normal) aftershock (m = 5.1, 77 minutes after the main normal earthquake) occur in central Izu.

Conclusions

We have shown data for strain events which have characteristics similar to those of shallow earthquakes except for longer time scales. The interpretation of such events as slow earthquakes is corroborated by observations of associated crustal deformation. These slowquakes may have large moments

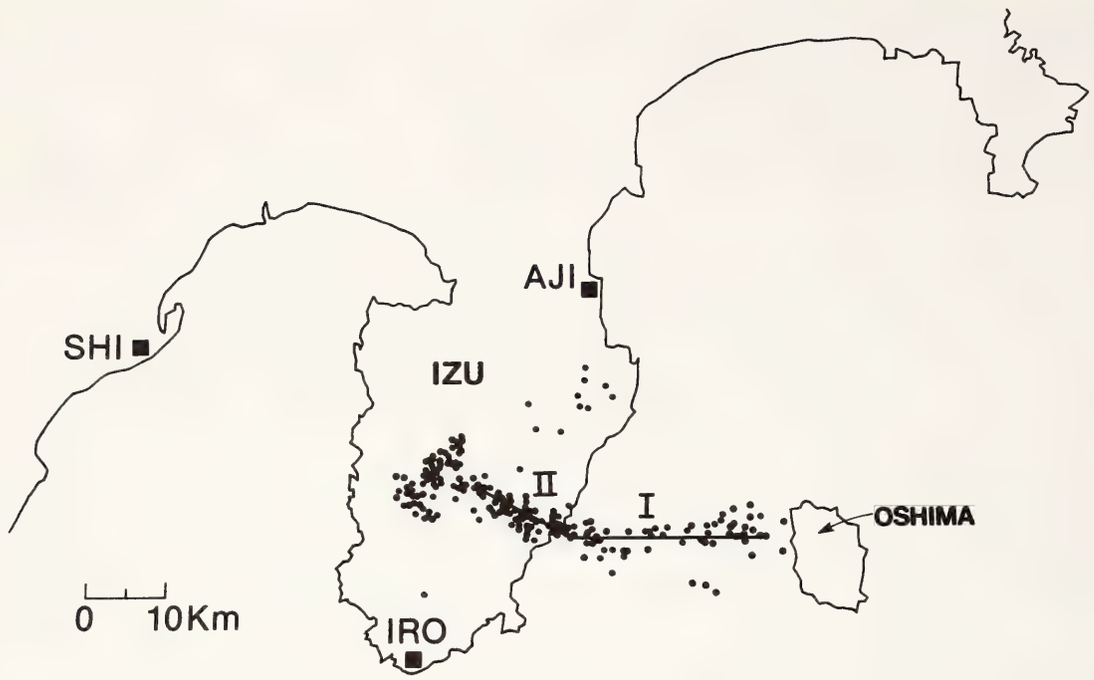


Fig. 28. Map of southern-central Honshu. Borehole strainmeters IRO, AJI, and SHI recorded strain changes due to I, a normal earthquake (m = 7.0, 14 Jan 78) and due to II, an inferred slow-quake. Epicenters of normal aftershocks of these events are also shown.

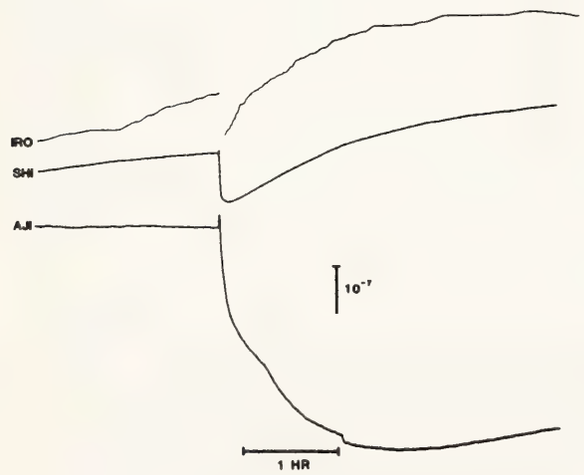


Fig. 29. Records from the three borehole strainmeters at locations shown in Fig. 28. The strain steps (the rapid upward excursions) are due to the earthquake (I in Fig. 28). These steps are significantly attenuated by filtering before recording. Slow strain changes of comparable magnitude occur over the following hour. We associate these slow changes with motion on the fault II (Fig. 28).

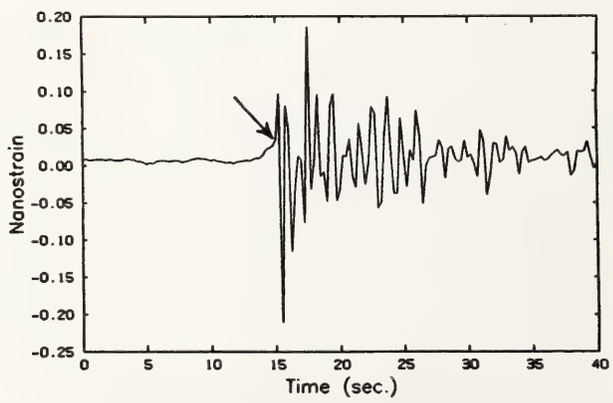


Fig. 30. Straingram of a magnitude 3.8 earthquake (24 July 1974), recorded at a distance of 11.9 km. The arrow indicates the onset of the normal earthquake. Notice the slow strain change starting a few seconds before the earthquake.

and, as evidenced by migration of aftershocks, play a significant role in the redistribution of stress in tectonically active regions.

Slowquakes may occur as independent events or may be associated with a normal earthquake. Here we have given examples of independent events and of a slowquake immediately following a normal quake. In Paper 1, we reported on a slowquake starting at least 20 minutes before the Izu earthquake

of 1974. Figure 30 shows an example of a slow strain change immediately preceding a small earthquake in the Matsushiro region.

As mentioned above (and documented more fully by Rikitaki [1976] and Sacks *et al.* [1978]), large and temporally nonlinear strain changes have been observed preceding some earthquakes. It is thus possible that high stresses may not be concentrated in a source region until a few days (or less) before even large earthquakes. This would set the effective upper limit to the warning period wherein a specific prediction could be made. Great or large slow earthquakes could affect free earth oscillations and even the Chandler wobble.

Acknowledgments

We thank Miss K. Sato for help with the data preparation. This work was partially supported by a grant from the Sloan Foundation and by National Science Foundation Grant EAR 78-01786.

References

Archambeau, C. B., and C. Salvado, Seismically inferred nonhydrostatic stresses in the earth's lithosphere, *Trans. Amer. Geophys. Soc., 58,* 494, 1977.

Inouchi, N., and H. Sato, Crustal deformation related to the Izu-Oshima Kinkai earthquake of 1978, *Bull. Geograph. Surv. Inst., 23,* 14–24, 1979.

Rikitaki, T., Developments in solid earth geophysics, in *Earthquake Prediction, 9,* pp. 112–119, T. Rikitaki, ed., Elsevier, New York, 1976.

Sacks, I. S., S. Suyehiro, D. W. Evertson, and Y. Yamagishi, Sacks-Evertson strainmeter, its installation in Japan and some preliminary results concerning strainsteps, *Pap. Meteorol. Geophys., 22,* 195–208, 1971.

Sacks, I. S., S. Suyehiro, A. T. Linde, and J. A. Snoke, Slow earthquakes and stress redistribution, *Nature, 275,* 599–602, 1978.

Sacks, I. S., S. Suyehiro, A. T. Linde, and J. A. Snoke, Extraseismic redistribution of stress, *Carnegie Inst. Wash. Year Book 76,* 888–896, 1977.

Shimazaki, K., and P. Somerville, Summary of the static and dynamic parameters of the Izu-Oshima-Kinkai earthquake of January 14, 1978, *Bull. Earthq. Res. Inst.,* University of Tokyo, *53,* 613–628, 1978.

Umeda, Y., and H. Murakami, Lineament of cracking of roads due to Izu-Oshima earthquake and the area damaged by its largest aftershock (in Japanese), *Programme and Abstracts,* Seis. Soc. of Japan, no. 1, 22, 1978.

Modeling of Near-Field Straingrams Recorded on Sacks-Evertson Borehole Strainmeters

J. A. Snoke, A. T. Linde, I. S. Sacks, and S. Suyehiro†*

Introduction

In order to understand the earthquake process, we need information about the growth of the rupture as a function of space and time. This can best be accomplished by analysis of the earthquake-caused ground motion recorded on nearby instruments which have high sensitivity and a large dynamic range over a broad frequency band. In this report, we show examples of such data and present preliminary comparisons of the data with source models.

At distances less than several times the spatial extent of an earthquake rupture zone, the ground motion resulting from an earthquake can be described as composed of three parts. The first of these parts is the earthquake radiation: The resulting ground motion is relatively rich in higher frequencies and the shape of the waveform is affected by the rupture history and by the source-receiver geometry. The second part is a coda, which is caused by scatterings and reflections resulting from structural heterogeneities. The third part is a permanent offset caused by the total slip associated with the earthquake: the offset is independent of the details of the rupture history and can be used to give a direct

*Department of Geological Sciences, Virginia Polytechnic Institute and State University, Blacksburg.

†Japanese Meteorological Agency, Tokyo.

estimate of the seismic moment. (The seismic moment gives a measure of the size of the earthquake.) As the epicentral distance increases, the offset decreases in magnitude quite rapidly compared with the radiation and coda.

Instrumentation

The data for this study were recorded on a Sacks-Evertson borehole strainmeter (Sacks *et al.*, 1971). These strainmeters have a high sensitivity (better than 10^{-11} in strain), a large dynamic range, and a flat frequency response from zero to a few hertz.

If the response of a seismograph or strainmeter is not sufficiently linear, high accelerations which are likely to be encountered during local earthquakes may cause anomalous strain steps. To test the performance of the Sacks-Evertson borehole strainmeters, the strainmeter together with its surrounding rock was subjected to accelerations as high as a few hundred gals using explosives. No spurious behavior was detected (Sacks *et al.*, 1971). As the explosion-induced accelerations are much higher than those encountered for the earthquakes used in this study, the instrument response can be assumed linear.

Data

In the Matsushiro region (Honshu, Japan), there was an earthquake swarm which peaked in 1966. We have data from a tripartite (15-km) net of Sacks-Evertson borehole strainmeters for the last few years of the swarm-related activity. From the three instruments there were a total of seven channels digitally recorded. The data discussed below are from the most frequently sampled sensor: a bimorph-type Piezoelectric crystal which is sampled four times a second. The response of this sensor is flat in strain from about 2 Hz to periods of many minutes.

Figures 31–33 are plots of nanostrain vs. time, for three of the events in the data suite. The upper trace in each figure represents the raw data; the lower trace is the upper trace data, low-pass filtered to enhance the strain step relative to the radiated pulse. It is apparent from these figures that the radiated pulses are rich in frequencies of 1 Hz and higher. In each of these cases the strain step is clearly visible: it is 0.5 nanostrain for event 35, 0.02 nanostrain for event 37, and −0.3 nanostrain for event 33.

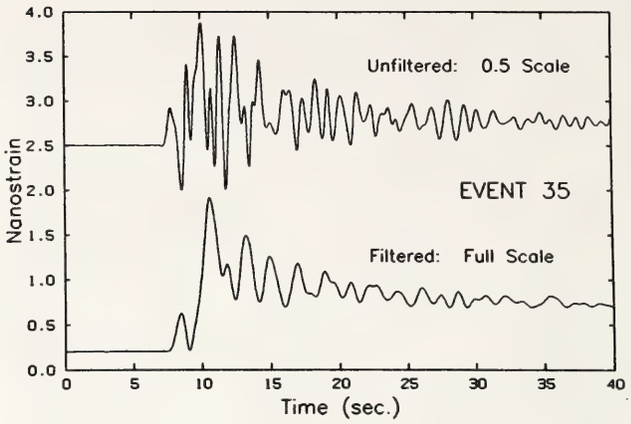


Fig. 31. Straingram for an $m = 4.0$ event on 19 September 1973, recorded at an epicentral distance of 14.5 km and an azimuth of 245°. The upper trace is the raw data with a scale factor of 0.5. The lower trace is the upper trace, low-pass filtered to enhance the strain step relative to the radiated pulse.

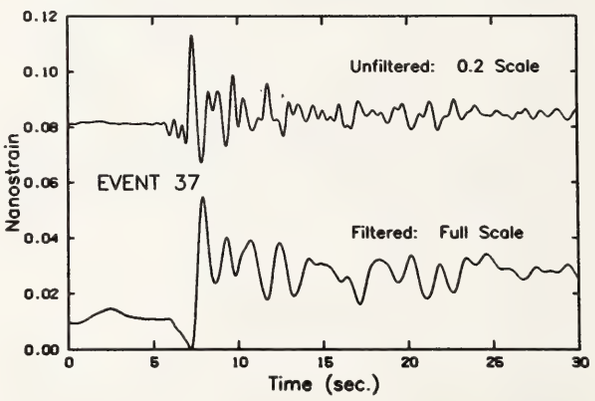


Fig. 32. Straingram as in Fig. 31 for an $m = 3.1$ event on 22 September 1973, recorded at an epicentral distance of 4.8 km at an azimuth of 70°. The (unfiltered) upper trace has a scale factor of 0.2.

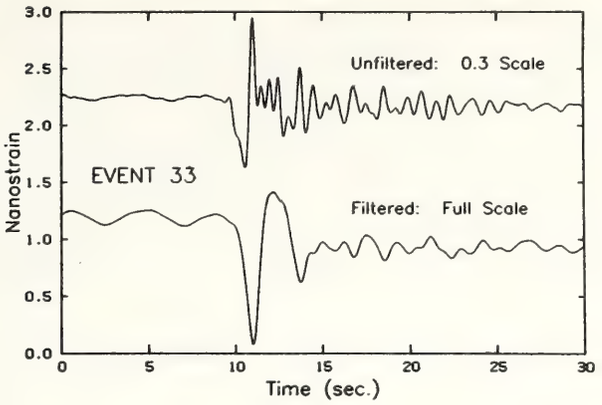


Fig. 33. Straingram as in Fig. 31 for an m = 3.4 event on 9 June 1973, recorded at an epicentral distance of 5.7 km at an azimuth of 177°. The (unfiltered) upper trace has a scale factor of 0.3.

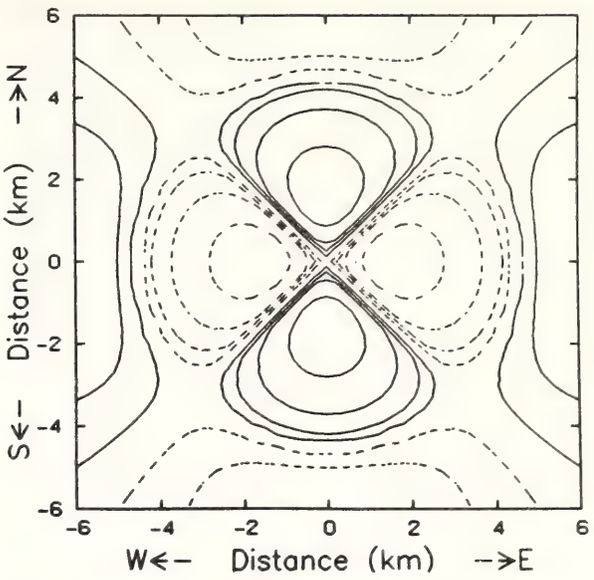


Fig. 34. Volume-strain map for a point source 3 kilometers below the map-coordinate origin. The source is vertical strike slip with a strike direction 45° east of north. For a rigidity of 0.3×10^{12} dyn/cm^2, this event has a moment of 7.5×10^{20} dyn cm. The solid contours represent positive dilatation (expansion). There are two contours per decade: the lowest values contoured are ± 0.1 and -0.1 nanostrain. The strain map for an extended source one kilometer square but of the same moments differs negligibly from the map shown for all epicentral distances greater than about 3 kilometers.

Modeling

It has been shown (R.M.E., 1967; R.M.E.S., 1968) that the events making up the Matsushiro swarm could be fitted with a single focal mechanism: namely, a right-lateral, vertical strike-slip motion with a strike direction of 45° east of north. It was also found that the focal depths were mainly in the range 1–5 km. In both our static and dynamic modeling, we use 5.6 km/sec and 3.3 km/sec for the *P*-wave and *S*-wave velocities, respectively.

Strain Step Modeling. For our strain step modeling we have used a modified version of a program written by Sato and Matsu'ura (1974) to calculate the dilatation for either a point or an extended (rectangular-shaped) double-couple source buried in a uniform, elastic halfspace. For the studied events, the spatial extent of the rupture zone is less than 1.5 kilometers, and we found that for epicentral distances greater than a few kilometers, an extended source is well approximated by a point source.

Figure 34 shows the contoured map view of the strain step pattern for a vertical strike-slip (point-source) event with a focal depth of 3 km. Note that there are three zero-strain-step zones: two are radiation-pattern nulls—along the projections of the fault and auxiliary planes—and the third is a circle (in the point-source limit) of radius r such that

$$r^2 = d^2(4 - 5(v_S/v_P)^2),$$

where d is the focal depth. For near-vertical strike-slip events, this depth-dependent null line changes little with fault orientation, so that for near-field events the sign of an observed strain step places a bound on the focal depth. For events 33, 35, and 37, the focal depths must therefore be less than 3.8, 9.6, and 3.2 km, respectively.

From the observed strain step and the static-model solution for a given location and focal mechanism, it is possible to calculate a seismic moment for the event. Assuming a rigidity of 0.3×10^{12} dyn/cm^2, the calculated moments

for events 33, 35, and 37 are found to be 4.1, 34.3, and 1.0 × 10^{20} dyn cm, respectively.

Dynamical Slip-History Modeling. The method used in this part of the study is the dynamical extension of the Sato and Matsu'ura static point-source model and is patterned after displacement-field programs written by Johnson (1974) and Anderson (1976). We calculate the response of the dilatometer installed at the free surface of a uniform elastic halfspace to a double-couple point source (with a variable time history) buried in the halfspace.

For this study we have used two types of source time functions: the commonly used Ohnaka pulse (Ohnaka, 1973) and a parabolic ramp. The time history for an Ohnaka pulse is characterized by a rapid acceleration followed by a more gradual deceleration. The parabolic ramp is strictly empirical, but it allows flexibility in the choice of rise time for a given duration. (It should be noted that because we are using the point-source approximation, the input "slip" magnitude is in fact the moment divided by the rigidity, and the "slip history" includes both the slip at a point as well as the rupture history.)

The approach we have used in our modeling is first to establish the slip magnitude by using the static model to fit the observed strain step for a given fault-plane solution and hypocenter. We then try to find time histories which give a reasonable fit to the first few cycles of the radiated pulse. Figure 35 shows an example of the results of this procedure for event 33. Superposed on the data are two model curves with the same slip magnitude but with different time histories. One sees that both model curves give a reasonable fit to the frequency of the first couple of oscillations in the data, but the parabolic ramp gives a better fit to the height of the oscillations than the Ohnaka pulse does. The conclusion from this comparison is that the rupture history for this

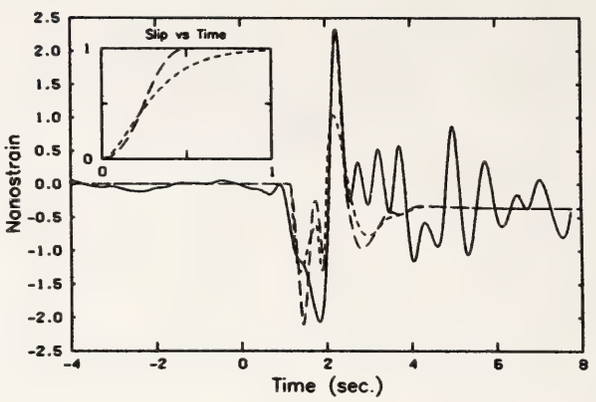


Fig. 35. Comparison between data (solid line) and synthetics (dashed lines) for event 33 (described in the caption for Fig. 33). The slip histories for the synthetics are shown in the insert. The model corresponding to the longer dashes is a symmetric parabolic pulse with a duration of 0.5 seconds, and the model corresponding to the shorter dashes is an Ohnaka pulse with a time constant of 0.16 seconds.

event is fit better by a rapid deceleration than by a gradual one.

The constraint on the modeling imposed by having both the step and the radiation on the same record is illustrated through Fig. 36. Shown in this figure is the straingram for event 33 modeled by a "normal" history (short dashes) and by a slip history having the same first stage as the other but a slower deceleration, resulting in a larger total slip and moment (long dashes). Both histories give reasonable fits to the initial pulse, but in this case the normal history is preferred because of the match with the strain step.

Concluding Remarks

We have shown that straingrams, such as those shown in Figs. 31–33, provide a direct estimate of the seismic moment, place a bound on the focal depth, and provide constraints on the time history of earthquakes. These data will be supplemented by seismograms for the same events from a DTM broadband seismograph (Sacks, 1966) at Matsushiro: This seismograph, with its fre-

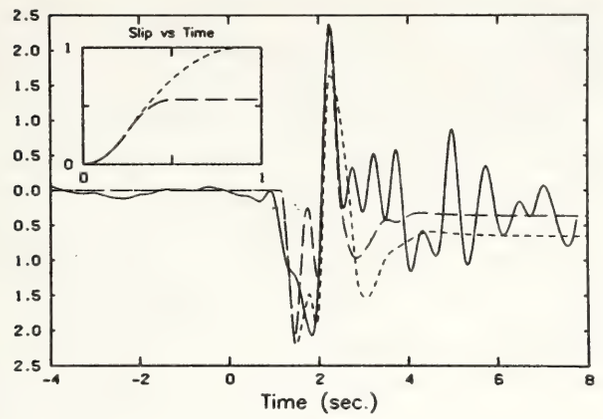


Fig. 36. Comparison between data (solid line) and synthetics (dashed lines) for event 33 (described in the caption for Fig. 33). The slip histories for the synthetics are shown in the insert: both models have the same initial history, but they differ in their deceleration and in the final total slip. Although both synthetics give a reasonable fit to the first part of the data waveform, they differ in their relative magnitude of the strain step.

quency response of up to ten Hz, will provide further information about the earthquake time history and will allow calculation of the radiated energy.

Acknowledgments

This work was partially supported by a National Science Foundation Grant, EAR 78-01786.

References

Anderson, J. G., Motions near a shallow rupturing fault: evaluation of effects due to the free surface, *Geophys. J. Roy. Astron. Soc., 46*, 575–593, 1976.

Johnson, L. R., Green's function for Lamb's problem, *Geophys. J. Roy. Astron. Soc., 37*, 99–131, 1974.

Ohnaka, M., A physical understanding of the earthquake source mechanism, *J. Phys. Earth, 21*, 39–59, 1973.

R.M.E. (Research on the Matsushiro Earthquakes), The party for seismographic observation of Matshushiro earthquakes and the seismometrical section, Matsushiro earthquakes observed with a temporary seismographic network, part 3, Earthquake Research Institute, Tokyo University, 197–223, 1967.

R.M.E.S. (Report of the Matsushiro Earthquake Swarm), August 1965–December 1967, The Japan Meteorological Agency, Tokyo, 77–104, 1968.

Sacks, I. S., A broad-band large dynamic range seismograph, in *The Earth Beneath the Continents: Geophysical Monograph No. 10*, pp. 543–553, John S. Steinhart and T. Jefferson Smith, eds., American Geophys. Union, Washington, D.C., 1966.

Sacks, I. S., S. Suyehiro, D. W. Evertson, and Y. Yamagishi, Sacks-Evertson strainmeter, its installation in Japan and some preliminary results concerning strainsteps, *Pap. Meteorol. Geophys., 22*, 195–208, 1971.

Sato, R., and M. Matsu'ura, Strains and tilts on the surface of a semi-infinite medium, *J. Phys. Earth, 22*, 213–221, 1974.

Installation of a Borehole Strainmeter Array in Iceland

*I. S. Sacks, A. T. Linde, and R. Stefansson**

Generation of new lithosphere takes place at mid-ocean ridges, and thus it is not easy to obtain direct instrumental measurement of the details of this process. Long-term average spreading rates can be determined from sediment ages and magnetic lineations, but we do not know if the spreading is continuous or episodic or whether the rifting results from driving forces applied locally at the ridge or to the plate at some distance from the ridge.

Iceland straddles the North Atlantic ridge and thus provides an opportunity to investigate the character of the spreading process in more detail. As part of a study of such problems, we installed a net of eight Sacks-Evertson borehole strainmeters in southern Iceland during August and September 1979.

Tectonic Setting

The spreading ridge is located under the eastern section of Iceland. Offsets in the form of transform faults occur near both the northern and southern

*The Iceland Meteorological Office, Reykjavik.

coastlines. The seismicity shown in Fig. 37 indicates the extent of these regions. The large earthquakes in the area all occur in association with the transform faults.

Geological and historical evidence seems to indicate that episodic rifting occurs in Iceland about every 100 years. Episodes of correlated volcanic and seismic activity have occurred in 1783 and 1874; in December 1975 a similar series of tectonic events started in northeast Iceland with a minor volcanic eruption in the Krafla caldera. A day later, earthquake swarm activity commenced about 30 km north of the caldera and subsequently migrated northwards. Within a few weeks, subsidence and horizontal extension of about 2 m was observed within the swarm region. On 13 January 1976, a magnitude 6.2 earthquake took place on the northern transform.

The major earthquakes ($M \geq 6$) in the region take place on the transform faults. There are few such big earthquakes and the seismicity before the 1920's is not well known, even for these large events. In 1929, a large earthquake ($M \geq 6$) occurred on the southern transform fault, and this was followed by an event of similar magnitude on the northern transform fault in 1934. Earlier data show that a similar pair of earthquakes occurred in the second decade of this century. Spreading at the ridge results in shear strain buildup at the transform faults. Since the distance between the two faults in Iceland is small, large slip on one fault result-

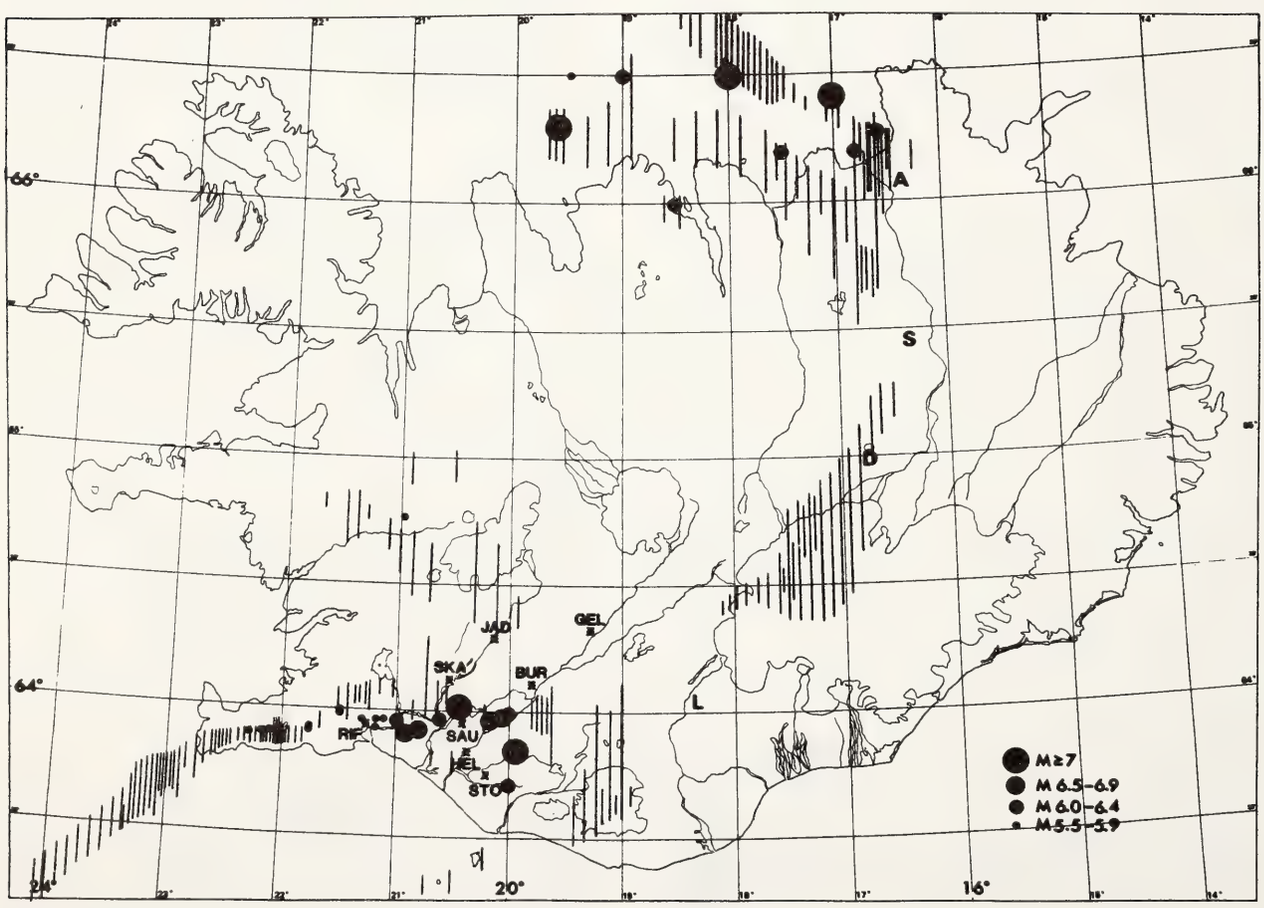


Fig. 37. Map of Iceland showing regions of seismic activity (hatched), major earthquakes (filled circles), and the recently installed strainmeters (crosses). The on-land spreading ridge is in the region ASDL. The activity which began in 1975 is concentrated in region A. The large earthquakes in the south approximately delineate the transform fault. The instrument locations were chosen to monitor activity on this fault as well as on the southern section.

ing in strain accumulation on the other may be sufficient to cause a second large earthquake. From the available data, the time interval between a pair of earthquakes is about five years, but the variation from this could be very large. Thus it appears that we are now in the interval between the January 1976 earthquake on the northern transform and a similar quake on the southern transform.

Location and Installation

The locations of the instruments are shown in Fig. 37, and Table 12 gives the coordinates for the stations. The locations were chosen as a result of our objective to instrument the region of the southern transform such that a comprehensive data set could be obtained before, during, and after a large earthquake. The station distribution is not ideal, since financial constraints limited us to the use of existing holes. Because the holes were primarily of two diameters (6-inch and 3-inch), we developed a smaller version of the strainmeter for use in the narrower holes. Drilling logs and geological mapping information were used to locate the best depth for installation on the basis of a thick competent rock layer; this usually required that the hole be partially filled and sealed.

The instruments were all installed during a seven-week period in August and September 1979. Although the holes were as old as 15 years, we were successful in grouting-in the instruments in all the holes at depths as great as 400 m. Vehicle access was not possible at two of the holes, so that only hand power was used for the installations in those cases. In all holes, loose pebbles from chert bands at various depths presented a threat, since they could lock the instrument or cement container at any depth. This did in fact happen on a number of occasions, but

TABLE 12. Location of Strainmeters

Station	Latitude	Longitude	Depth (m)	Installation Date
RIF	63.956 N	21.27 W	292	10-8-79
HEL	63.84 N	20.41 W	393	13-8-79
STO	63.75 N	20.21 W	401	16-8-79
BUR	64.11 N	19.80 W	181	22-8-79
GEL	64.325 N	19.28 W	233	25-8-79
JAD	63.30 N	20.15 W	58	2-9-79
SAL	63.985 N	20.43 W	180	8-9-79
SKA	64.21 N	20.53 W	125	12-9-79

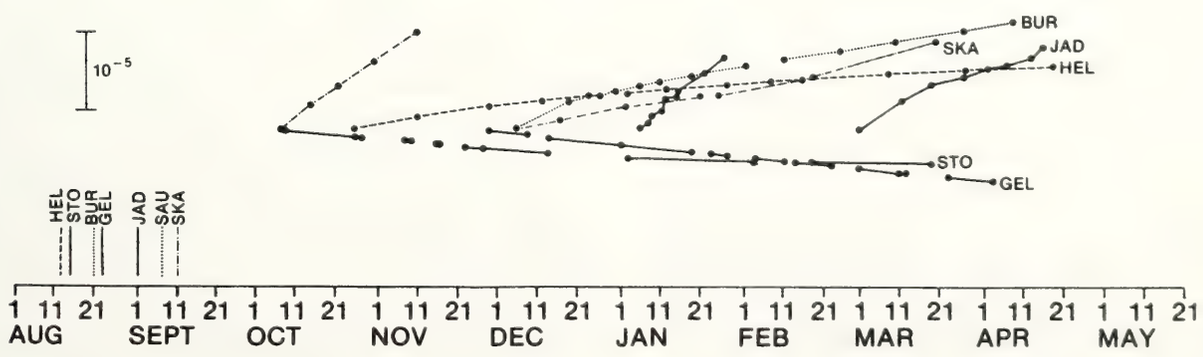


Fig. 38. Preliminary secular strain data. The named vertical coded lines indicate installation times. Data from a much longer time period is required before we can separate installation, seasonal, and tectonic effects.

we were always able to devise a method of freeing the equipment. All but two of the instruments appear to be functioning correctly. RIF behaves as a high-pass-filtered instrument; we suspect that a faulty valve does not completely seal the sensing volume. SAU is currently not operating although further testing is necessary to see if modified above-ground electronics can solve the problem.

Preliminary Results

Our limited budget required that initially we limit our data acquisition to chart recorders at a speed of ½ inch/hr, so we do not fully utilize the frequency response of the instrument. Figure 38 shows some early long-term data. Because of the time required for the expansive grout to cure, we have not plotted the data for the initial period after installation. The six instruments all appear to be operating stably, although it appears that the initial aging is not yet complete. A much longer term data base is obviously required before any conclusions can be drawn.

Preliminary Velocity Structure of Japanese Islands and Philippine Sea from Surface Wave Dispersion

Kiyoji Shiono, I. Selwyn Sacks, and Alan T. Linde

Introduction

There have been few studies of surface wave dispersion in Japan after those of the early 1960's (Aki, 1961; Aki and Kaminuma, 1963; Kaminuma and Aki, 1963; Kaminuma, 1964, 1966; Noponen, 1969; Furuzawa, 1976). With the exception of Noponen, these workers used surface waves of periods less than 50 sec, so they could not discuss fully the upper mantle structure. In the present study, we determined group velocities of Rayleigh and Love waves in NE Japan by using the broad-band seismographs (Sacks, 1966) installed at MAT and KMU (see Fig. 39). The main object of the study was to detect the lithosphere-asthenosphere boundary beneath NE Japan. We also determined surface wave dispersion curves in the West and East Philippine Sea bordered by the Kyushu-Palau Ridge. Many marine surveys have suggested a significant age difference between these regions (e.g., Karig *et al.*, 1973; Tomoda *et al.*, 1975; Sclater *et al.*, 1976; Watts *et al.*, 1977; Hilde *et al.*, 1977).

Method of Analysis

Analogue tape records were digitized at an interval of about 1 sec, to be analyzed either by the single-station method or by the double-station method. In the single-station method, the group velocity between the epicenter and station was measured by applying to the instrumentally corrected signals the multiple-filtering procedure (Dziewonski *et al.*, 1969) modified by the display-equalized filtering technique (Nyman and Landisman, 1977). Because the maximum energy radiation from the source is delayed from the time of initial rupture, a time-lag correction is required for this method. This correction was based on the assumption that the energy radiation becomes maximum when half of the source region is ruptured.

In the double-station method, the group velocity for the path between two stations was determined by applying the multiple-filtering procedure to the cross-correlogram between signals of two stations. It is not necessary to take into account a time-lag correction or an instrumental correction.

Theoretical dispersion curves were calculated using the algorithms by Schwab and Knopoff (1972). Assuming that the region of interest has a horizontally uniform layered structure, we modified a starting model to obtain the best fit to both Rayleigh and Love wave velocities. The starting model for

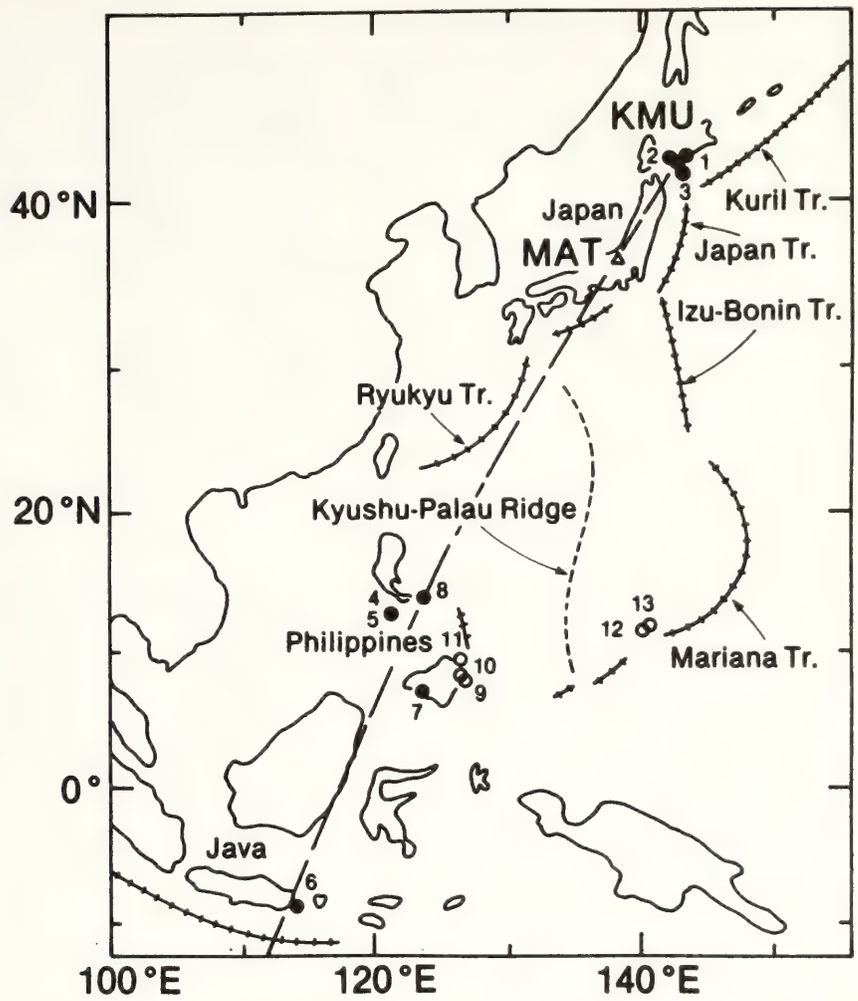


Fig. 39. Map of Japan and the Philippine Sea, showing relationship between locations of studied events and observation stations (MAT and KMU). Numerals give event numbers listed in Table 13. Events Nos. 1–8 and Nos. 8–13 were used for determination of surface wave dispersion curves in NE Japan and in the Philippine Sea, respectively. A broken line shows the great circle passing through MAT and KMU.

NE Japan was constructed on the basis of the crustal structure obtained from explosion data (Yoshii and Asano, 1972; R.G.E.S., 1977) and the J-B model. The starting model for the Philippine Sea was constructed on the basis of the crustal structure by Murauchi *et al.* (1968) and the ARC1 model by Kanamori and Abe (1968), in which velocity structure below 80 km is identical to that of the 8099 model (Dorman *et al.*, 1960).

Observed Dispersion Data

Thirteen events were used to obtain the group velocity in NE Japan (Nos. 1–8) and in the Philippine Sea (Nos. 8–13) (see Fig. 39 and Table 13).

Seismograms recorded at MAT for three events (Nos. 1–3) which occurred near KMU were analyzed by the single-station method (see Fig. 39). As the epicentral distances were short (about seven degrees), a time-lag correction was employed. Three sets of Rayleigh group velocities were obtained in the period range from 8 to 50 sec. Reliable Love velocities were not obtained here because of poor excitation of the waves.

The double-station method was applied to five events (Nos. 4–8), for which epicenters were located within five degrees of the great circle pass-

TABLE 13. Earthquakes Used in This Study*

No.	Date	Origin Time	tc†	Epicenter		m_b	Data‡
1.	20 Jan 70	17:33:03.1	+4.7	42.48°N	143.04°E	6.3	RL
2.	2 Aug 71	13:00:00.0	+2.1	41.32	143.52	5.6	R
3.	30 Oct 75	01:41:32.1	+3.0	42.05	142.60	5.9	R
4.	21 Oct 75	17:12:20.0	...	11.66	121.69	5.5	l
5.	21 Oct 75	23:06:22.0	...	11.65	121.58	5.5	l
6.	14 Jul 76	07:13:23.7	...	−08.21	114.87	6.1	r
7.	16 Aug 76	16:11:05.0	...	06.22	124.10	6.4	r
8.	25 Aug 76	12:29:56.6	+2.3	13.10	124.48	5.7	rRL
9.	10 Jan 70	12:07:08.6	+3.0	06.80	126.75	5.9	RL
10.	26 Oct 75	10:41:33.2	+3.0	06.54	126.81	5.9	RL
11.	27 Oct 75	18:26:43.0	+1.9	07.91	126.96	5.5	RL
12.	27 Feb 68	05:19:03.0	+2.1	12.19	140.69	5.6	RL
13.	27 Feb 68	10:54:42.0	+1.9	12.22	140.74	5.5	RL

*Origin times and locations from ISC bulletin.

†Correction in sec for maximum energy radiation time lag from the origin time, approximated by assuming that the energy radiation becomes maximum at the middle of the focal process and that the time lag is the measure of half-length of the fault divided by rupture velocity. We used a relation between magnitude m_b and fault length L, $\log L = 0.5\, m_b - 2.0$, and rupture velocity of 1.5 km/sec.

‡Types of data obtained from the event. R and L show that group velocities of Rayleigh and Love waves were determined by the single-station method, and r and l show that group velocity of Rayleigh and Love waves were determined by the double-station method, respectively.

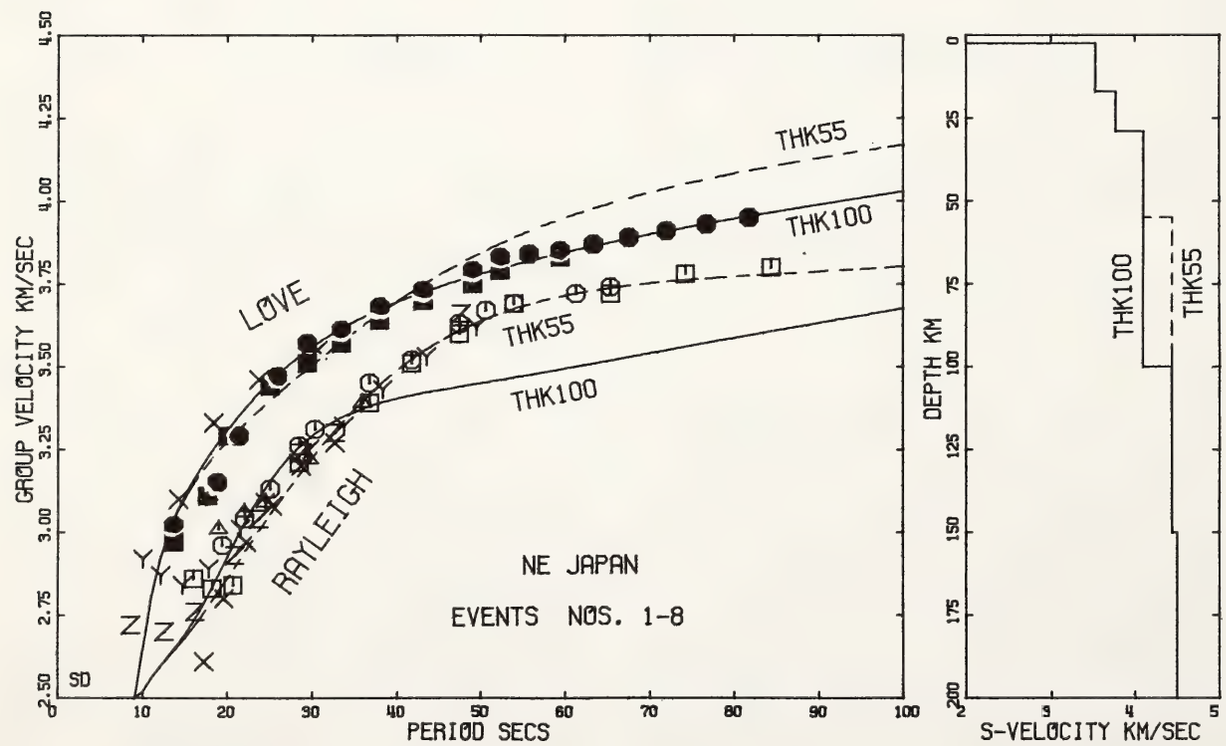


Fig. 40. Observed and theoretical dispersion curves for NE Japan (left), and S-wave velocity structures of the THK100 and THK55 models (right). Group velocities obtained from events Nos. 1–8 are shown by different symbols: *X*, No. 1; *Y*, No. 2; *Z*, No. 3; closed circles, No. 4; closed squares, No. 5; open circles, No. 6; open squares, No. 7; open triangles, No. 8. Solid and broken lines give the theoretical dispersion curves in the left and S-wave velocity structures in the right for the THK100 and THK55 models, respectively.

ing through MAT and KMU. Two and three sets of group velocities were determined for Love and Rayleigh waves, respectively (see Fig. 40). Because no major earthquakes occurred along the northern extension of the great circle, the double-station method could not be used for the reverse path from KMU to MAT.

Seismograms recorded at MAT for four events (Nos. 8–11) and for two events (Nos. 12 and 13) were analyzed to determine group velocities in the West and East Philippine Sea, respectively (see Figs. 41 and 42). The effect of the source time lag was very small, less than 0.03 km/sec. Reliable data were obtained for a wide period range from 10 sec to 80 sec for the West Philippine Sea. Reliability of data for the East Philippine Sea was poorer than that for the West because the available events were of lower magnitude and the excitation of waves was rather weak.

Preliminary Velocity Model for NE Japan

This is a preliminary report on the study, and we have not yet been able to explain the observed group velocities of Rayleigh and Love waves in NE Japan by any single model. We are continuing the investigation in an endeavor to determine a single velocity model which will satisfy all the data. However, we present here, as a preliminary result, two models with different velocities in one depth range: THK55 for Rayleigh and THK100 for Love waves (see Fig. 40 and Table 14). The observed data do not require the existence of a high-velocity lid (a shallow high-wave-velocity layer underlain by material of lower wave velocity) but are best fit by

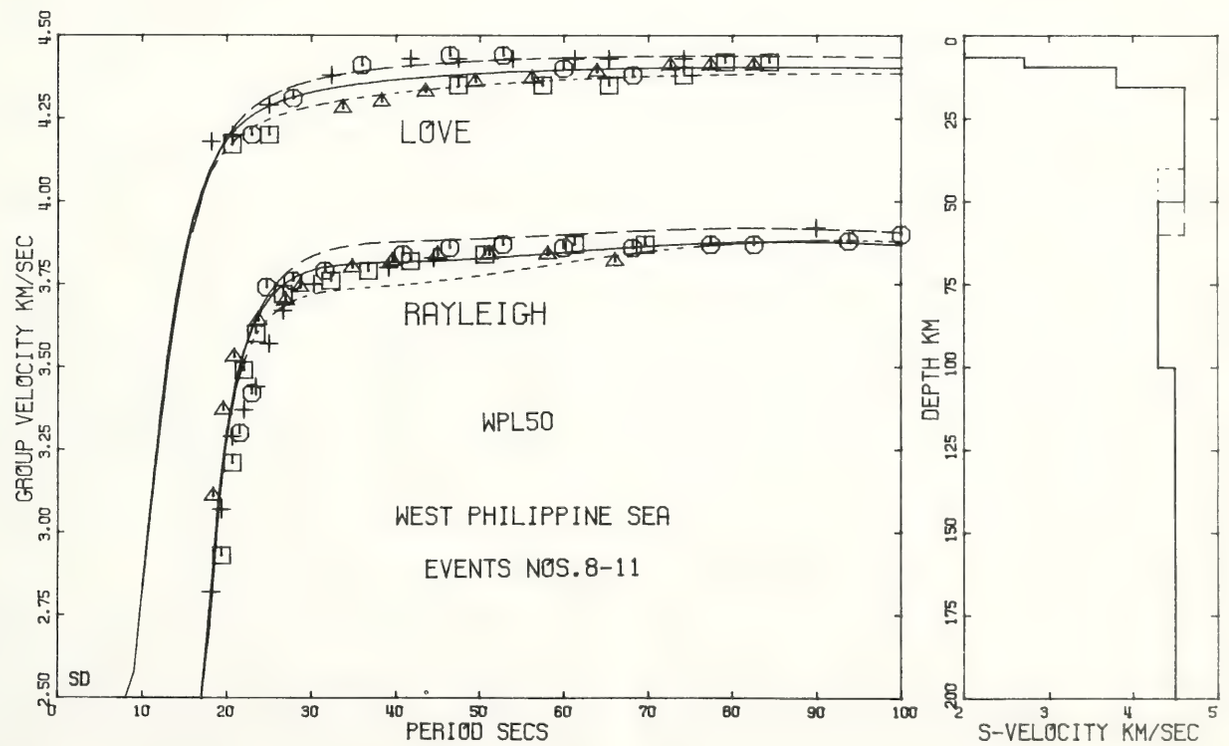


Fig. 41. Observed and theoretical dispersion curves for the West Philippine Sea (left) and velocity models (right). Group velocities obtained from events Nos. 8–11 are shown by different symbols: triangles, No. 8; circles, No. 9; squares, No. 10; plus marks, No. 11. Solid lines show theoretical dispersion curves and S-wave velocity for the WPL50 model; broken and dotted lines are those of models in which the lithosphere is, respectively, thicker and thinner by 10 km than that of the WPL50 model.

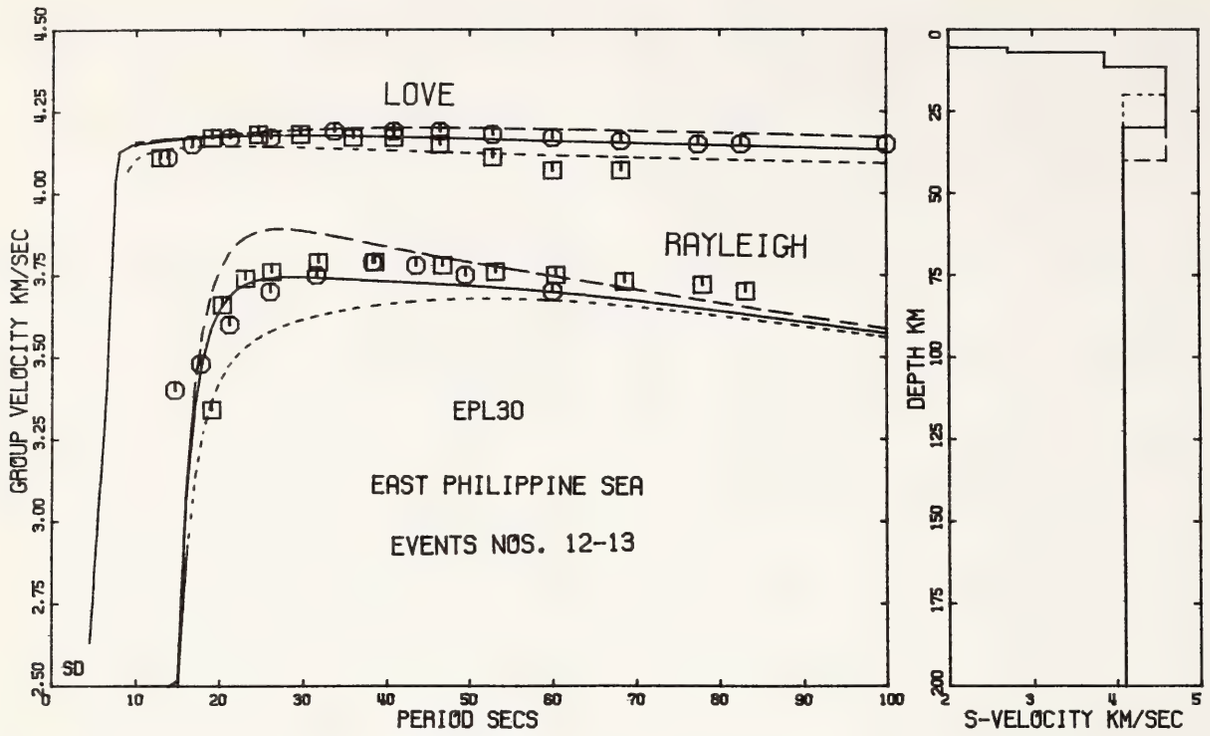


Fig. 42. Observed and theoretical dispersion curves for the East Philippine Sea (left) and velocity models (right). Group velocities obtained from events Nos. 12 and 13 are given by circles and squares, respectively. Solid lines show theoretical dispersion curves and S-wave velocity of the EPL30 model; broken and dotted lines are those of models in which the lithosphere is, respectively, thicker and thinner by 10 km than that of the EPL30 model.

TABLE 14. Representative Shear Velocity–Depth Models

THK 100*		THK 55		WPL 50		EPL 30	
β	h	β	h	β	h	β	h
1.60	2.5	1.60	2.5	0.00	5.5	0.00	5.0
3.53	14.5	3.53	14.5	1.00	1.0	1.00	0.5
3.77	12.0	3.77	12.0	2.70	3.0	2.70	1.5
4.10	71.0	4.10	26.0	3.80	6.0	3.80	4.5
4.40	50.0	4.40	95.0	4.6125	34.5	4.6125	18.5
4.50	50.0	4.50	50.0	4.30	50.0	4.10	190.0
4.70	50.0	4.70	50.0	4.50	120.0	4.60	100.0†
4.83	∞	4.83	∞	4.60	100.0*	...	...

*β: shear velocity (km/sec). h: thickness of the layer (km).
†The distribution of velocity below 220 km is identical to that of the 8099 model.

a low *S*-wave velocity of 4.1 km/sec in the uppermost mantle. Both models have the same structure in the upper 55 km and different velocities in a depth range of 55–100 km, with higher velocity for Rayleigh waves. One possible explanation is that this discrepancy is due to underthrusting of the Pacific plate (see Fig. 43). The model THK55 seems to be required by longer period Rayleigh waves (>50 seconds). We are therefore trying to confirm the velocities at these periods.

Velocity Model for the Philippine Sea

Over two thirds of the length of the wave paths from events Nos. 8–11

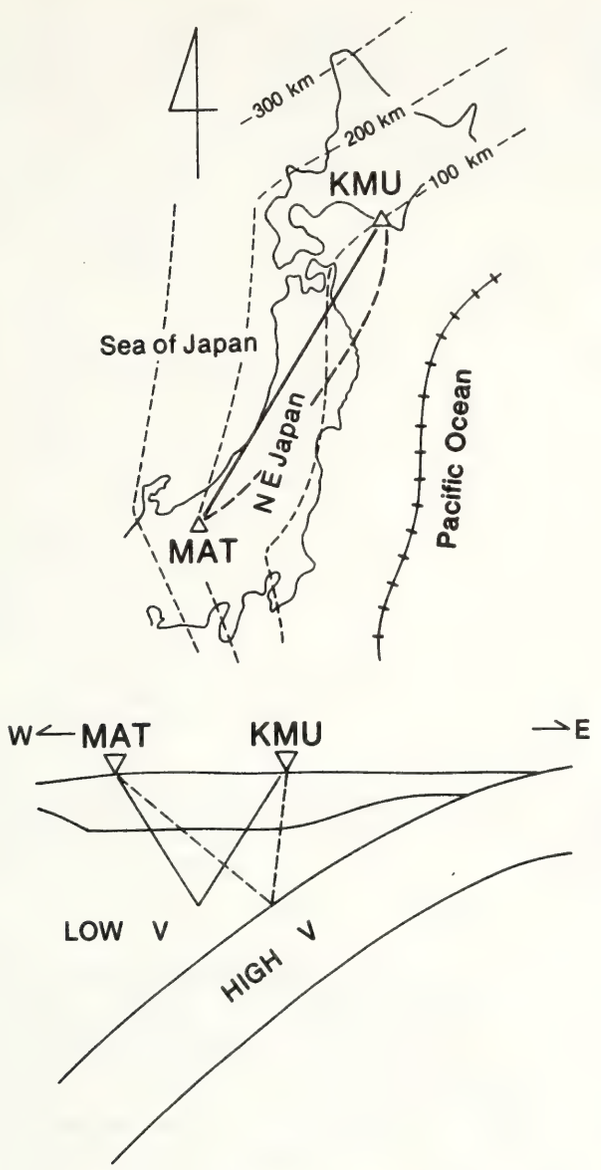


Fig. 43. Schematical illustrations showing spatial relationship between NE Japan and the descending slab of the Pacific plate in horizontal (upper) and vertical (lower) planes. Thin broken lines in the upper subfigure give depth contours of the seismic zone. The existence of the descending slab causes some contortion of wave propagation.

were in the West Philippine Sea. The model WPL50 was derived for this path (see Fig. 41 and Table 14). This model has the crust thicker than that of Murauchi *et al.* (1968). One possible explanation is that the waves traveled through the area of sea mounts such as the Daito Ridge Group and the Kyushu-Palau Ridge, which are considered to have a thick crust (Murauchi *et al.*, 1968; Ludwig *et al.*, 1973).

A lithosphere of 50-km thickness explains the observed data if we take the *S*-wave velocity in the lid to be 4.6125 km/sec, the same as in the 8099 model. However, the trade-off between velocity and thickness of the lid makes it possible to construct other models with lithosphere thickness varying between 40 and 70 km.

The wave paths for events Nos. 12 and 13 were mainly in the East Philippine Sea. Our model EPL30 has a very thin lithosphere and a very low velocity beneath the lid (see Fig. 42 and Table 14), similar to the ARC1 model presented by Kanamori and Abe (1968). A lithosphere of 30-km thickness explains the observed data if we take *S*-wave velocity in the lid to be 4.6125 km/sec. The model is less reliable than WPL50 because of poorer data.

The velocity structure and the theoretical dispersion curves in both regions are compared in Fig. 44, together with those of the 8099 model.

Discussion

A very low *S*-wave velocity of 4.1 km/sec was obtained for the uppermost mantle beneath NE Japan. The value was consistent with a Pn velocity of 7.5 km/sec derived from explosion data (Yoshii and Asano, 1972; R.G.E.S., 1977). From long-period surface wave dispersion in west and central Japan, Noponen (1969) obtained a similar *S*-wave velocity for the depth range from the Moho discontinuity to 70 km.

A velocity change is the traditional indicator of the lithosphere-asthenosphere boundary. In this study, as well as that of Noponen, no velocity change is required between the Moho and some considerable depth. This means either that the asthenosphere starts at the Moho or that because no high-velocity lid has developed beneath Japan, the lithosphere-asthenosphere boundary cannot be detected by velocity structure. We need other types of informa-

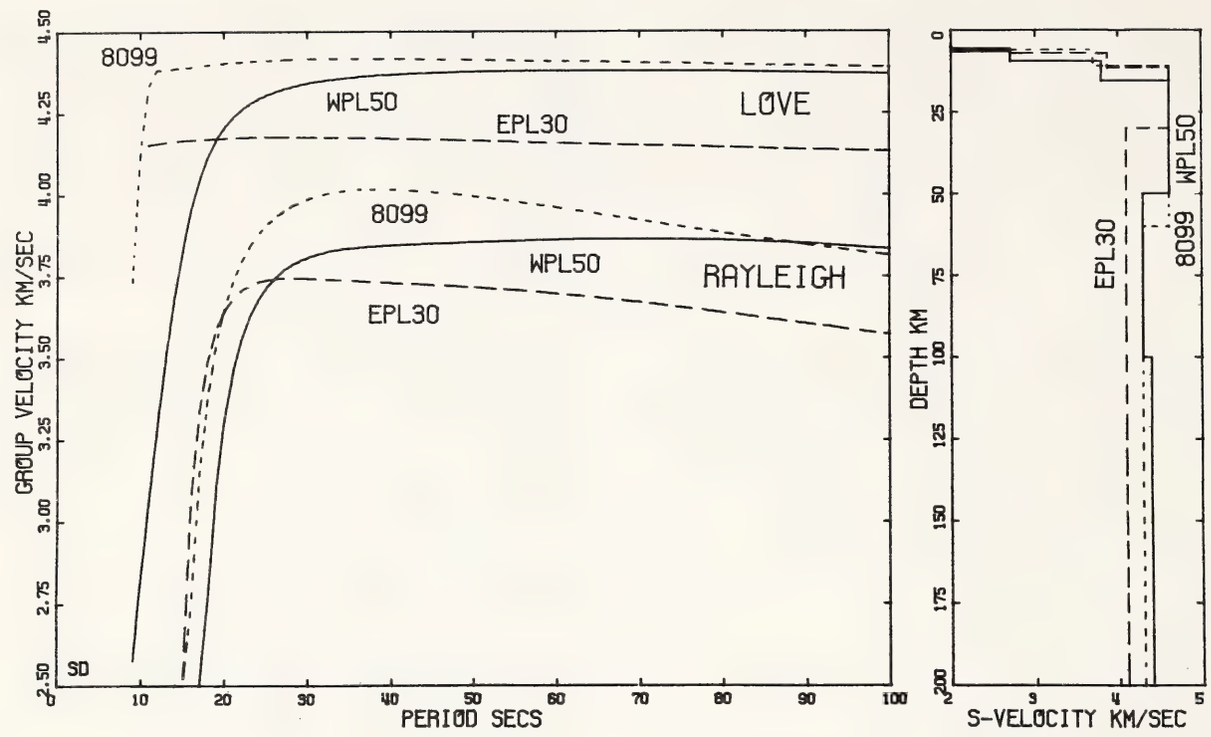


Fig. 44. Comparison of velocity structures and theoretical dispersion curves among three models: WPL50 for the West Philippine Sea (solid lines), EPL30 for the East Philippine Sea (broken lines), and 8099 for normal oceanic regions (dotted lines).

tion to solve the problem; note that Sacks and Okada (1974) found a decrease in anelasticity at a depth of about 70 km.

According to the Deep Sea Drilling Project and surveys of magnetic anomalies, there is a significant difference in age between the West and the East Philippine Sea—early Tertiary in the West and from late Oligocene to early Miocene in the East (Karig *et al.*, 1973; Tomoda *et al.*, 1975; Watts *et al.*, 1977). The difference in thickness of lithosphere between the West Philippine Sea (50 km) and the East (30 km), can be interpreted in terms of the thickening of lithosphere due to cooling, as proposed by Kono and Yoshii (1975) and others. This is consistent with heat flow observations by Sclater *et al.* (1976), who obtained median values of 1.76 and 2.15 μcal/cm^2 sec in the West and East Philippine Sea, respectively.

Seekins and Teng (1977) analyzed surface wave dispersion in the Philippine Sea using records at Guam, and found that most of the Philippine Sea has a thin lithosphere thickness of order of 30 km, while the north part of the West Philippine Sea and the Kyushu-Palau Ridge show some signs of having a typical oceanic structure. The present results are not inconsistent with those by Seekins and Teng (1977).

Conclusion

We have studied the surface wave dispersion of both Rayleigh and Love waves in NE Japan and in the Philippine Sea using the broad-band seismographs at MAT and KMU. The results are summarized as follows:

1. The very low velocity found in the uppermost mantle beneath NE Japan suggests either that the asthenosphere starts at the Moho or that the lithosphere-asthenosphere boundary cannot be detected by study of velocity structure because a high-velocity lid has not developed.

2. Group velocities in the West Phil-

ippine Sea indicated a thick lithosphere (about 50 km), while those in the East were consistent with a thin lithosphere (about 30 km). This difference is interpreted as the result of different cooling times.

References

Aki, K., Crustal structure in Japan from the phase velocity of Rayleigh waves, Part 1, Use of the network of seismological stations operated by the Japan Meteorological Agency, *Bull. Earthq. Res. Inst., 39*, 255–283, 1961.

Aki, K., and K. Kaminuma, Phase velocity of Love waves in Japan, Part 1, Love waves from Aleutian shock of March 9, 1957, *Bull. Earthq. Res. Inst., 41*, 243–259, 1963.

Dorman, J., M. Ewing, and J. Oliver, Study of shear-velocity distribution in the upper mantle by mantle Rayleigh waves, *Bull. Seismol. Soc. Amer., 50*, 87–115, 1960.

Dziewonski, A., S. Bloch, and M. Landisman, A technique for analysis of transient seismic signals, *Bull. Seismol. Soc. Amer., 59*, 427–444, 1969.

Furuzawa, T., Group velocities of surface waves from near earthquakes around Japan, *J. Phys. Earth, 24*, 131–147, 1976.

Hilde, T. W. C., S. Uyeda, and L. Knoenke, Evolution of the western Pacific and its margin, *Tectonophysics, 38*, 145–165, 1977.

Kaminuma, K., Crustal structure in Japan from the phase velocity of Rayleigh waves, Part 3, Rayleigh waves from the Mindanao shock of September 24, 1957, *Bull. Earthq. Res. Inst., 42*, 19–38, 1964.

Kaminuma, K., The crustal and upper mantle structure in Japan, Part 1, Phase velocities of Love and Rayleigh waves in central Japan, *Bull. Earthq. Res. Inst., 44*, 481–494, 1966.

Kaminuma, K., and K. Aki, Crustal structure in Japan from the phase velocity of Rayleigh waves, Part 2, Rayleigh waves from the Aleutian shock of March 9, 1957, *Bull. Earthq. Res. Inst., 41*, 217–241, 1963.

Kanamori, H., and K. Abe, Deep structure of island arcs as revealed by surface waves, *Bull. Earthq. Res. Inst., 46*, 1001–1025, 1968.

Kono, Y., and T. Yoshii, Numerical experiment on the thickening plate model, *J. Phys. Earth, 23*, 63–75, 1975.

Karig, D., J. C. Ingle, A. H. Bouma, N. Haile, I. Koizumi, T. Macgregor, J. C. Moore, H. Ujiie, T. Watanabe, S. M. White, M. Yasui, and H. Yi Ling, Origin of the west Philippine Basin, *Nature, 246*, No. 5434, 458–461, 1973.

Ludwig, W. J., S. Murauchi, N. Den, P. Buhl, H. Hotta, M. Ewing, T. Asanuma, T. Yoshii, and N. Sakajiri, Structure of East China Sea–West Philippine Sea margin off southern Kyushu, Japan, *J. Geophys. Res., 78*, 2526–2536, 1973.

Murauchi, S., N. Den, S. Asano, H. Hotta, T. Yoshii, T. Asanuma, K. Hagiwara, K. Ichikawa, T. Sato, W. J. Ludwig, J. I. Ewing, N. T. Edgar, and R. E. Houtz, Crustal structure of the Philippine Sea, *J. Geophys. Res., 73*, 3143–3171, 1968.

Noponen, I., Wave velocities in crust and upper 300 kilometers of mantle in western and central Japan, *Bull. Intern. Seismol. Earthq. Eng., 6*, 11–37, 1969.

Nyman, D. C., and M. Landisman, The display equalized filter for frequency-time analysis, *Bull. Seismol. Soc. Amer., 67*, 393–404, 1977.

R.G.E.S. (Research Group for Explosion Seismology), Regionality of the upper mantle around northeastern Japan as derived from explosion seismic observations and its seismological implications, *Tectonophysics, 37*, 117–130, 1977.

Sacks, I. S., A broad-band large dynamic range seismograph, *Amer. Geophys. Union Monograph 10*, 543–553, 1966.

Sacks, I. S., and H. Okada, A comparison of the anelasticity structure beneath western South America and Japan, *Phys. Earth Planet. Interiors, 9*, 211–219, 1974.

Schwab, F. A., and L. Knopoff, Fast surface wave and free mode computations, in *Methods in Computational Physics, 11*, pp. 87–180, Academic Press, New York, 1972.

Sclater, J. G., D. Karig, L. A. Lawer, and K. Louden, Heat flow, depth and crustal thickness of the marginal basins of the South Philippine Sea, *J. Geophys. Res., 81*, 309–318, 1976.

Seekins, L. C., and T. L. Teng, Lateral variations in the structure of the Philippine Sea plate, *J. Geophys. Res., 82*, 317–324, 1977.

Tomoda, Y., K. Kobayashi, J. Segawa, M. Nomura, K. Kimura, and T. Saki, Linear magnetic anomalies in the Shikoku basin, northeastern Philippine Sea, *J. Geomagn. Geoelectr., 28*, 47–56, 1975.

Watts, A. B., J. K. Weissel, and R. L. Larson, Sea-floor spreading in marginal basins of the western Pacific, *Tectonophysics, 37*, 167–181, 1977.

Yoshii, T., and S. Asano, Time-term analyses of explosion data, *J. Phys. Earth, 20*, 47–57, 1972.

Explosion Seismology Studies in Southern Peru

L. T. Aldrich, L. Ocola, and A. T. Linde*

In *Year Book 76*, we described an extensive program of observations of

*Instituto Geofísico del Peru, Lima.

seismic arrivals from timed explosions in mines and at sea along the coastline of southern Peru. The work was designed to provide a definitive model of the crustal structure in this region. This structure, as it varies from the Peru-Chile trench to the altiplano, is of some interest because it is the result of the relatively rapid intersection of the Nazca plate of the eastern Pacific and the South American continental plate. This region has been the subject of many previous studies in this Department and by others (Tuve and Tatel, 1958; James *et al.*, 1969; Saa and Sacks, 1969; Okada, 1973; Stauder, 1975; Ocola *et al.*, 1971; Sacks, 1977; James, 1978; Barazangi and Isacks, 1979; Snoke *et al.*, 1979). Because of the tectonic setting of the region, its accessibility, and the long and mutually profitable scientific relationship between the Department and the Instituto Geofísico del Peru, we have been especially active in these studies.

The structural model which will eventually evolve from the work described below will allow more accurate hypocenter locations from the local net operated by the Instituto Geofísico, U. N. San Agustín in Arequipa. In 1957, Tuve and Tatel (*Year Book 57*) led a reconnaissance study using explosions at the Toquepala mine and mill sites and observations in the range 80–260 km. Their findings of strong absorption of seismic energy in directions from east to northeast of the mines and of good transmission along the coast have been confirmed by this and other studies (Ocola *et al.*, 1971). Preliminary travel-time plots have now been assembled by the several groups involved in the 1976 experiment. These plots were compared and discussed during a meeting in March of representatives of all the participants. We present here preliminary results of the Carnegie Institution–Geofísico del Peru efforts.

Figure 45 is a map of the southern half of Peru, showing the locations of the mines and the points at sea at which timed explosions were made.

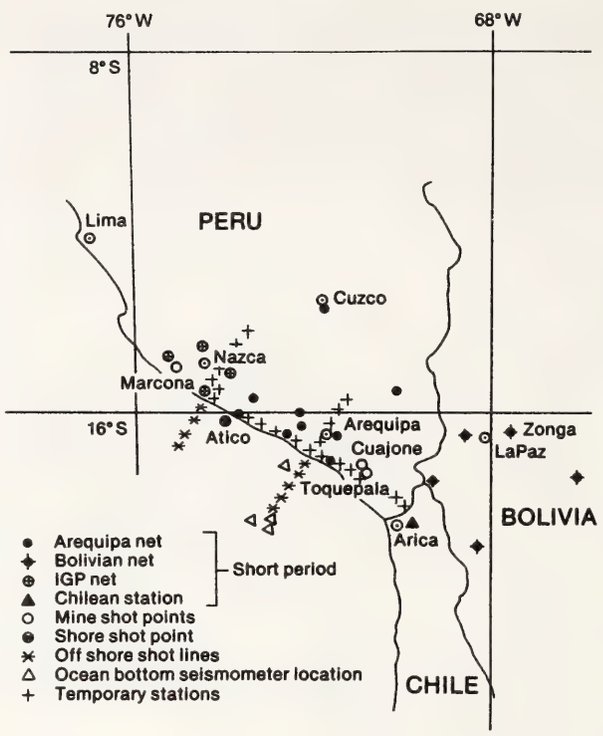


Fig. 45. Map of area in southern Peru for 1976 explosion studies. The legend gives information on locations of shots and observing stations. Data given in this report are all from observations made south of the Atico shot point.

The data shown in this report were obtained using simple, two-channel seismic systems which could be positioned in seismically quiet locations. These locations all lay close to a line drawn between the Atico shot point and the Cuajone-Toquepala mining complex and extended to the Chilean border as indicated. The data were digitized and assembled for the plots shown in Fig. 46. An intensive study of the data of Fig. 46 is under way in which ray-tracing and synthetic seismogram techniques will be used to model the data set. Several qualitative features of the data may be pointed out. These include:

(1) The more frequent occurrence of small-amplitude early arrivals in the records from the Atico shot point in the range 100–200 km. This may be due to the difference in character of mine explosions intended to break up rock and those from an underwater site designed for seismic studies.

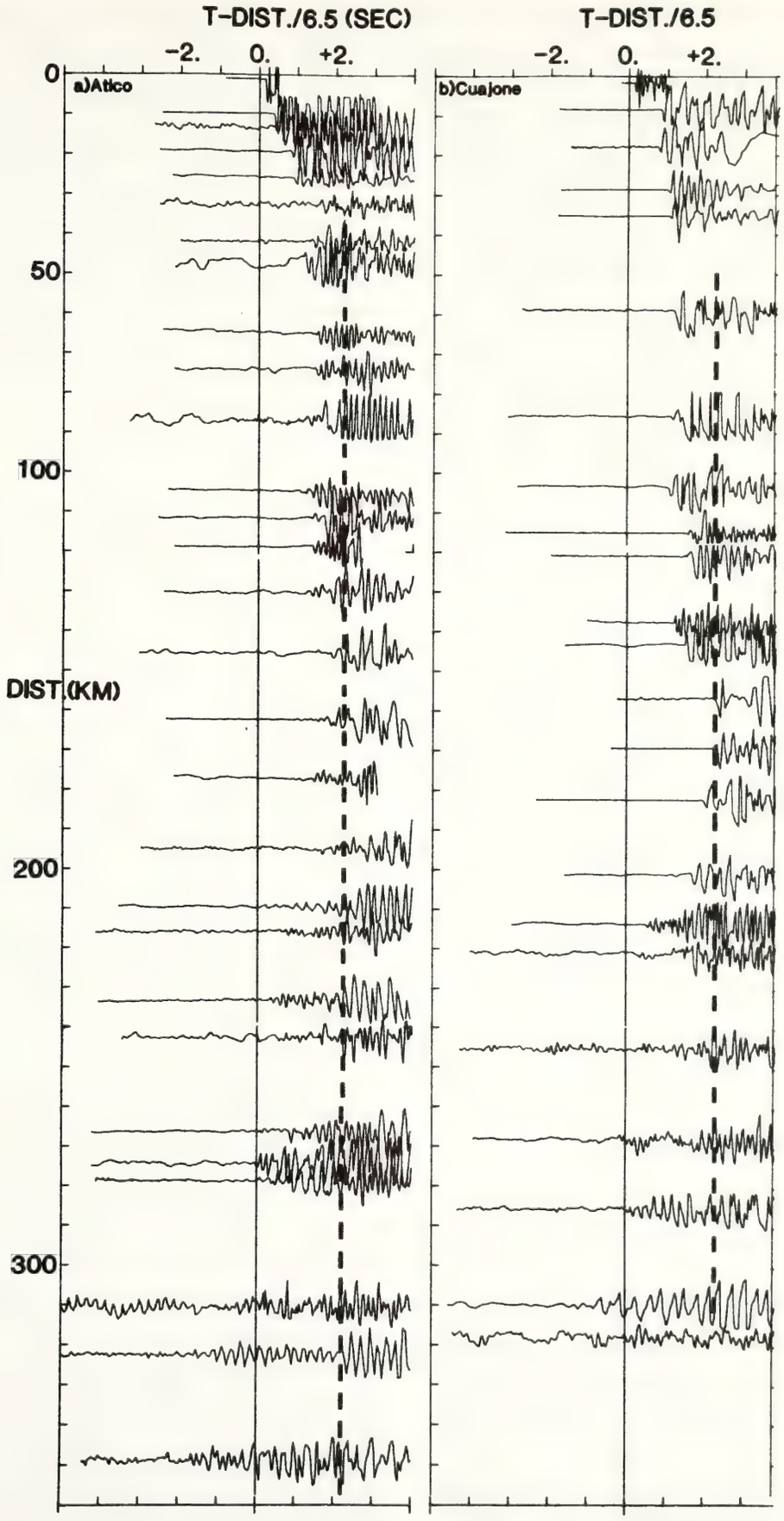


Fig. 46. Reduced time-distance plots obtained from IGP-Carnegie data, for (a) Atico and (b) Cuajone-Toquepala shot points reduced to a velocity of 6.5 km/sec. A segment of the travel-time curve indicative of arrivals with this velocity may be seen as a dashed straight line parallel to the vertical axis. Such a line may be observed in both plots beginning at 30 km from the shot point and extending to about 300 km. These arrivals are thought to be due to wide-angle reflections from the interface between the lower crust and the upper mantle.

(2) A very shallow layer (less than 5 km) with velocity less than 6.5 km/sec.

(3) The presence of material of velocity 6.5 km/sec and a thickness of about 30 km, as manifested by arrivals along the dashed line shown in Fig. 46 in the distance range 50–300 km. These arrivals are interpreted as due to wide-angle reflections from the interface between this layer and the upper mantle. Their large amplitude over this long range is most easily explained by a sharp velocity discontinuity at this interface. Earlier small arrivals are due to rays refracted in this material and in the upper mantle. This thickness is not inconsistent with the 50-km estimate of James *et al.* (1969), in that our line is approximately 100 km SW of the line between Arequipa and Naña.

(4) Material of velocity 8.0 km/sec determined from small-amplitude arrivals in a section of the record in the range 250–350 km at a depth which agrees with that determined from the wide-angle reflections.

(5) Remarkable similarity of two plots. The property of similarity of reversed profiles indicates a simple, nondipping structure along the line between shot points.

We anticipate that the primary objective of determining the crustal structure of southern Peru will be fulfilled.

References

Barazangi, M., and B. Isacks, Subduction of the Nazca Plate beneath Peru: evidence from spatial distribution of earthquakes, *Geophys. J. Roy. Astron. Soc., 57*, 537–555, 1979.

James, D., Subduction of the Nazca Plate beneath central Peru, *Geology, 6*, 174–178, 1978.

James, D., I. S. Sacks, E. Lazo, and P. Aparicio, On locating local earthquakes using small networks, *Bull. Seismol. Soc. Amer., 59*, 1201–1212, 1969.

Ocola, L., R. P. Meyer, L. T. Aldrich, Gross crustal structure under Peru-Bolivia Altiplano, *Earthquake Notes, 42*, 1971.

Okada, H., Converted P phases from the ScS phase at the inclined deep seismic zone, *Carnegie Inst. Wash. Year Book 72*, 238–245, 1973.

Saa, G., and I. S. Sacks, The effect of elevation and region on the P and S waves of some South American seismograph stations (abstract), *Trans. Amer. Geophys. Union, 50*, 237, 1969.

Sacks, I. S., Interrelationships between volcanism, seismicity, and anelasticity in western South America, *Tectonophysics., 37*, 131–139, 1977.

Snoke, J. S., I. S. Sacks, and D. James, Subduction beneath western South America: evidence from converted phases, *Geophys. J. Roy. Astron. Soc., 59*, 219–225, 1979.

Stauder, W., Subduction of the Nazca Plate under Peru as evidenced by focal mechanisms by seismicity, *J. Geophys. Res., 81*, 1053–1064, 1975.

Tuve, M. A., and H. E. Tatel, *Carnegie Inst. Wash. Year Book 57*, 106–111, 1958.

Qs of the Lower Mantle—A Body Wave Determination

I. Selwyn Sacks

Introduction

Since it is likely that whole-mantle convection is involved in the processes which result in phenomena such as plate motion and earthquake activity, it is important to improve our knowledge of mantle structure. One parameter of this structure is the anelasticity. Because the anelasticity gives a measure (indirectly) of the relative difficulty of producing motion in the Earth, many studies have been made of absorption ($1/Q$) of seismic waves and free earth oscillations. These are consistent with other seismic data in that we can subdivide the crust and mantle into a high-Q lithosphere, a low-Q asthenosphere and a high-Q mesosphere. The discussion in this paper is limited to Q_S, the value determined from attenuation of shear waves.

Average values of Q for the whole mantle have been determined from spectral ratios of successive reflections of S waves from the core-mantle boundary. The multiple ScS waves are well recorded and the Q values derived in such studies are mainly in the range 160–290 (e.g., Jordan and Sipkin, 1977; Yoshida and Tsujiura, 1975; Nakanishi, 1979). These values are consistent

with the decay of free earth oscillations, for which a Q of about 240 is obtained (Anderson and Hart, 1978b; Sailor and Dziewonski, 1978). For the upper mantle, the values show a strong regional bias with a global average of about 120 (Anderson and Hart, 1978a, b). Thus Qs for the uppermost mantle is significantly less than that for the average of the whole mantle.

For rays which traverse both the upper and lower mantle, the dominant attenuation will be in the upper mantle. In order to calculate lower-mantle attenuation with a given accuracy, we would need to know the upper-mantle attenuation to a greater accuracy. The difficulty of this situation is increased because the upper-mantle Qs is highly variable laterally due to factors such as lithospheric thickness variations, subduction zones, and spreading regions. In addition, the spectral content of the seismic source is unknown and variable from source to source.

The lower-mantle Q can be inferred from values of upper-mantle and whole-mantle Q. Upper-mantle (600 km) values range from 110 to 170 with a global average of 130. Combining these with the range reported for the whole mantle, 160–290, gives a possible range of lower-mantle values of 200–750. The lower-mantle Qs can also be determined from the decay of free earth oscillations. Depending somewhat on the particular model, these values range up to about 400 (models SL2, SL7, and SL8 of Anderson and Hart, 1978b).

In this paper, use is made of spectral ratio techniques and ray path comparisons such that the problems mentioned above can be eliminated or substantially reduced.

The basic philosophies behind the Q determination are as follows:

(1) By taking the ratio of the spectra of waves traveling two different paths from the same earthquake, the unknown source spectrum is eliminated.

(2) In order to minimize the effects of crustal and other structure, which cause oscillations in the recorded spectra, the widest possible bandwidth is analyzed. While it is possible that Q is frequency dependent, this is not required by the data studied here, over a frequency range from 0.03 to 3 Hz.

(3) A combination of ray paths is studied to isolate the region where Q is required. In particular, the path through the highly attenuative upper mantle is traversed as a P-wave. Compressional waves are less attenuated (by about a factor of seven at the same frequency) than shear waves, and therefore their absorption need not be so accurately known.

Method and Data

There are two phases originating from deep earthquakes which have the property of traversing the lower mantle as S but having a P-wave final path from the base of the mantle to the seismograph.

In *ScP*, S is converted to P at the core-mantle interface and reflected to the surface. It is well observed in the 10–30 degree distance range. While the higher-frequency energy ($\sim$3 Hz) is easily determined, frequencies below about 0.3 Hz are obscured by the coda of S.

The *SKP* arrival (Fig. 47), on the other hand, is not contaminated by nearby strong arrivals. This fact, coupled with the equally broad frequency band allowance for the P part of the path (*P*/*PKPPKP*), make it the preferred phase.

The spectral ratio of the two arrivals (*SKP* and S) will be given by

$$\frac{SKP}{S} = \exp\left[-\Pi f\left(\frac{Tb}{Qb} + \frac{Tc}{Qc} + \frac{Td}{Qd} - \frac{Ta}{Qa}\right)\right], \quad (1)$$

where f is the frequency interval over which the ratio is calculated, and where the travel times and Q values for the paths a, b, c, d in Fig. 47 are Ta and Qa, etc. We are trying to determine Qb, the lower-mantle Q, but Qa, Qc, and Qd must be known first.

Qa has been determined independently for the seismograph-earthquake region used here (Sacks and Okada, 1974). Its ray path is almost entirely within a high-Q subduction plate with $Qs > 500$. Qc and Qd, the outer-core and whole-mantle P-wave paths, are determined by studying the ray paths shown in Fig. 48. Here the spectral ratio may be written as

$$\frac{PKPPKP}{P} =$$

$$= \exp\left[-\Pi f\left(\frac{Tb}{Qb} + \frac{Tc}{Qc} + \frac{Td}{Qd} + \right.\right.$$

$$\left.\left. + \frac{Te}{Qe} + \frac{Tf}{Qf} + \frac{Tg}{Qg} - \frac{Ta}{Qa}\right)\right]$$

$$= \exp\left[-\Pi f\left\{\left(\frac{Tb}{Qb} + \frac{Tg}{Qg} - \frac{Ta}{Qa}\right) + \right.\right.$$

$$\left.\left. + 2\left(\frac{Tc}{Qc} + \frac{Td}{Qd}\right)\right\}\right]. \qquad (2)$$

We now show that the term (Tc/Qc + Td/Qd) dominates. $Ta - (Tb + Tg)$ is about 90 seconds whereas $2(Tc + Td)$ is about 1750 seconds. a, b, d, and g are whole-mantle paths with slightly different geometries and similar Qp values, and the core Qp is rather higher. Substituting reasonable values for these parameters ($Qp = 2000$ for mantle, $Qp = 10{,}000$ for outer-core paths (Sacks, 1971) we calculate that

$$\left(\frac{Tb}{Qb} + \frac{Tg}{Qg}\right) \approx 0.045,$$

and

$$2\left(\frac{Tc}{Qc} + \frac{Td}{Qd}\right) \approx 0.4.$$

Therefore Equation 2 may be reduced to

$$\frac{PKPPKP}{P} =$$

$$\exp\left[-2\Pi f\left(\frac{Tc}{Qc} + \frac{Td}{Qd}\right)\right] \qquad (3)$$

with sufficient accuracy. Referring to Equation 1, ($Tc/Qc + Td/Qd$) is what was required to allow the determinations of lower-mantle Qs without further assumptions.

All the data used were recorded on Department of Terrestrial Magnetism broad-band high-dynamic-range magnetic tape recording seismographs (Sacks, 1966). The instrument range

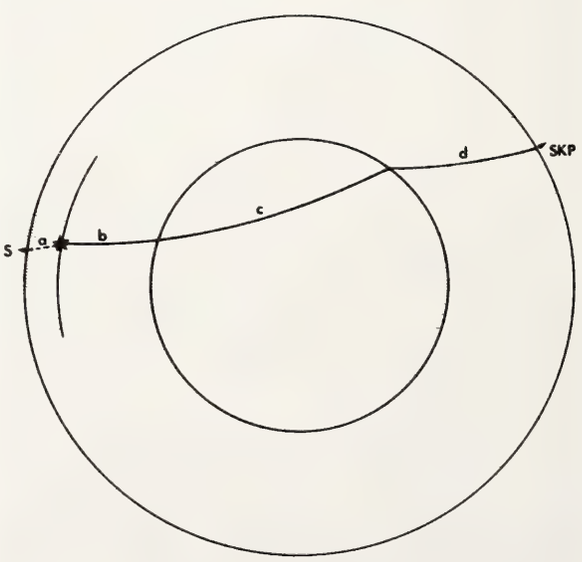


Fig. 47. Ray paths for the S and SKP phases. Portion a is S traveling mainly in the high-Q subducted lithosphere to a seismograph on the surface. Portion b is S traveling from the deep earthquake (star) to the core-mantle interface, where it is converted to P. Energy travels through the core, c, and mantle, d, to the seismograph (SKP) as P waves.

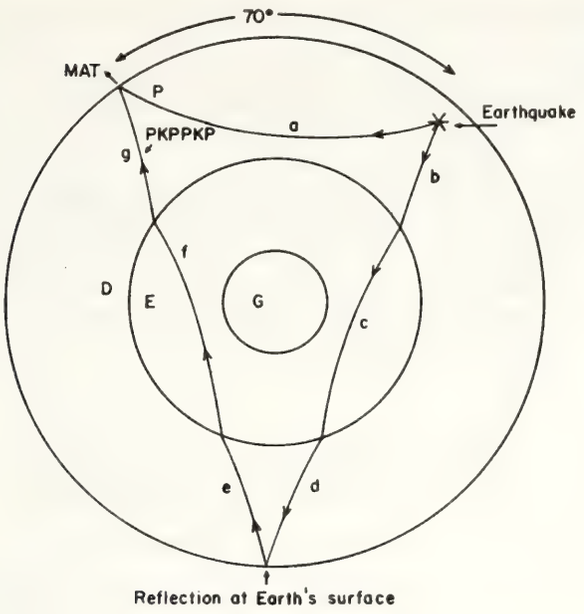


Fig. 48. Ray paths for *P* and *PKPPKP* phase. Energy travels from the earthquake to the seismograph through the mantle only, *a*, as well as through the core and mantle *g, f, e, d, c, b*. All paths are *P*-wave paths.

extends from less than 50-second period to more than 10 Hz.

For the *S/SKP* spectral comparison, the *S* phase of a deep earthquake (600 km) in the Peru-Brazil region of South America was recorded on the CUZ seismograph, and the *SKP* phase was recorded on the PMG, New Guinea, seismograph. For the *PKPPKP/P* comparison, both arrivals were recorded at the MAT seismograph in central Honshu, Japan, as well as at KMU in Hokkaido, Japan. The earthquake was a large, deep event in the Fiji region. These data were selected because they had a particularly good signal-noise ratio over a large frequency range.

Results

The spectral ratio *PKPPKP/P*, which determines the absorption of the *P*-wave paths, is shown in Fig. 49. The frequency range over which the arrivals were above noise was from 0.02 to 3 Hz. Figure 50 shows the *SKP/S* spectral ratio determined over a similar range.

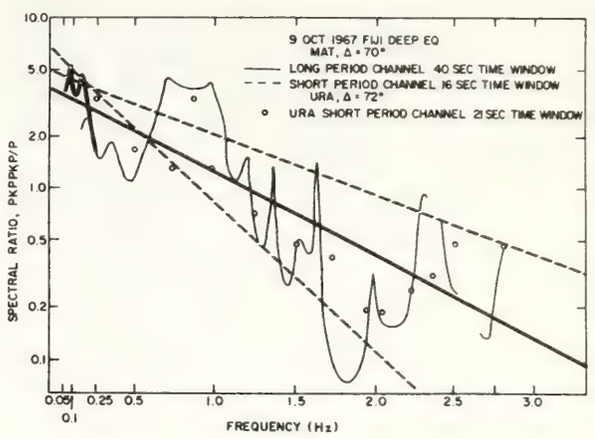


Fig. 49. Spectral ratio of *PKPPKP/P* determined on two different seismographs. MAT is in central Honshu; KMU is in Hokkaido, Japan. Circles are data from KMU. The dashed lines were used to provide values for the limiting cases that illustrate the sensitivity of the final result to this measurement (see text). The full line is the preferred fit to the data.

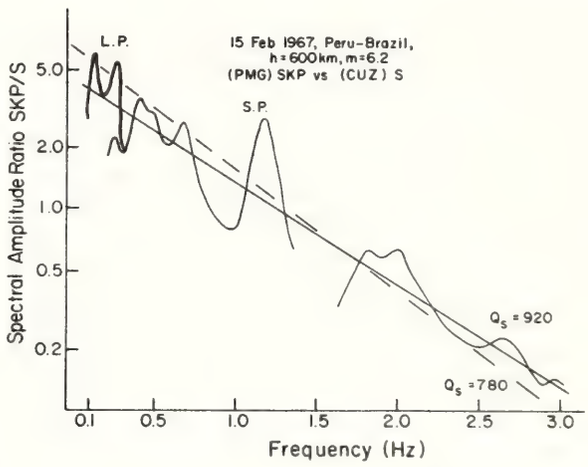


Fig. 50. Spectral ratio *SKP/S* used to determine the *Qs* of the lower mantle (below 600 km). The ratio is plotted only where the signal-to-noise ratio of both phases is greater than 3:1. The noise is determined using an identical window to that for the data and immediately preceding it. The broken line overestimates the low-frequency amplitude and underestimates the high frequencies. Yet the resultant *Q* value only changes 15%. This illustrates the stability of the determination.

The *Qs* value (920) determined for the lower mantle is not particularly sensitive to any assumption made but does depend on attenuation estimates of three paths shown in Fig. 47. For the subducted lithosphere portion of the

path, (*a* in Fig. 47), *Qs* values of 750 and 350 rather than the 500 actually determined (Sacks and Okada, 1974) are consistent with lower-mantle *Qs* values of 800 and 1150.

For the *P* portion of the *SKP* path, the envelope of extreme values is shown in Fig. 49. Minimum *P*-wave attenuation (minimum slope of spectral ratio) is compatible with *Qs* for the lower mantle of 760. Maximum *P*-wave attenuation (maximum slope) yields *Qs* of 1140.

The fundamental ratio, of course, is *SKP/S*. It can be seen in Fig. 50 that a change in *Q* of 15% is precluded by the data. For a *Qs* of 780, for example, all the longer-period amplitudes ($F < 1$ Hz) are too low, and the shorter-period amplitudes are above the calculated values.

The values given above are the extremes; the probable range for *Qs* of the lower mantle (below 600 km) is 900 $\pm$ 100.

The *Qs* for the lower mantle determined from the decay of free earth oscillations (at a frequency ~.001 Hz) is no more than 400, which is significantly less than the value determined in this study. This may imply a frequency-dependent *Q* in the lower mantle.

References

Anderson, D. L., and R. S. Hart, Attenuation models of the earth, *Phys. Earth Planet. Interiors, 16,* 289–306, 1978a.

Anderson, D. L., and R. S. Hart, The *Q* of the earth, *J. Geophys. Res., 83,* 5869–5882, 1978b.

Jordan, T. H., and S. A. Sipkin, Estimation of the attenuation operator for multiple *ScS* waves, *Geophys. Res. Letters 4,* 167–170, 1977.

Nakanishi, I., Attenuation of multiple *ScS* waves beneath the Japanese arc, *Phys. Earth Planet. Interiors, 19,* 337–357, 1979.

Sacks, I. S., A broad-band large dynamic range seismograph, in *The Earth Beneath the Continents: Geophysical Monograph No. 10,* pp. 543–553, John S. Steinhart and T. Jefferson Smith, eds., Amer. Geophys. Union, Washington, D.C. 1966.

Sacks, I. S., Anelasticity of the outer core, *Carnegie Inst. Wash. Year Book 69,* 414–416, 1971.

Sacks, I. S., and H. Okada, A comparison of the anelasticity structure beneath western South America and Japan, *Phys. Earth Planet. Interiors, 9,* 211–219, 1974.

Sailor, R. V., and A. M. Dziewonski, Measurements and interpretation of normal mode attenuation, *Geophys. J., 53,* 559–581, 1978.

Yoshida, M., and M. Tsujiura, Spectrum and attenuation of multiply reflected core phases, *J. Phys. Earth, 23,* 31–42, 1975.

On Small-Scale Convection at the Base of the Mantle

Richard A. Lux and I. Selwyn Sacks

It is generally accepted that some form of thermal convection is occurring within the Earth's mantle. Although the motions of the tectonic plates and the subducting lithosphere are well known, the pattern of flow within the mantle is still a matter of some speculation. Most studies of mantle convection have concentrated on gaining an understanding of the large-scale circulation associated with plate motions. Here, we investigate motions of a much smaller scale which may occur at the base of the mantle.

Several studies (Sacks and Beach, 1974; and Snoke and Sacks, 1976) suggest that there are lateral heterogeneities in the seismic velocity structure at or near the base of the mantle. Contiguous regions (millions of square kilometers in extent) have been found that have significantly different seismic wave transmission properties than normal. Thus some areas at the base of the mantle appear to be laterally homogeneous, while others appear to be laterally heterogeneous. The heterogeneous regions have been modeled by a structure in the lower 150 km of the mantle (the D″ layer) having a periodic velocity variation of about 1.5% and a horizontal wavelength of about 300 km.

Sacks and Beach suggest that the observed lateral velocity variations may be caused by density changes aris-

ing from convection cells of diameter 150 km. These velocity variations could also be caused by chemical differences within the material at this depth, but here we shall only consider whether they are of thermal origin. To investigate the likelihood of small-scale convection at the base of the mantle, we now consider several simple fluid dynamic models for this region.

The dynamics of the D″ layer are controlled by three basic factors: the depth and extent of large-scale mantle motions, the distribution and degree of heating from the core, and the rheology of lower-mantle material. Although none of these factors is well known, we shall assume at the outset that the D″ layer has a lower viscosity (due to the strong dependence of viscosity on temperature) than the material above it and that a substantial amount of the Earth's heat flux comes from the core. Because our focus is on the lower mantle, during this study we will not try to model the lithosphere or asthenosphere.

If mantle convection does not extend to the base of the mantle in the regions where the heterogeneities are found, then small-scale motions may occur as convection confined to the D″ layer if it has a relatively low viscosity. In the next section we present a linear stability analysis in order to predict when convection can be confined to a region of low viscosity. We are interested in determining what contrast in viscosity between the mantle and the D″ layer is required to confine convection to the D″ layer.

Two-Layer Model

We consider the thermal stability of two superposed layers of fluid having identical properties except viscosity. In order to model the D″ layer we shall choose the lower layer of fluid to be thinner than the upper layer and to be of lower viscosity. The layers of fluid are assumed to be Boussinesq and are heated from below. Both the upper and lower boundaries are free-slip with the geometry as shown in Fig. 51. The method used in solving this stability problem follows directly from Davies (1977) and Takeuchi and Sakata (1970) and will not be presented here.

The Rayleigh number is defined to be

$$Ra = \frac{\alpha g \beta d^4}{\kappa \nu},$$

where the length scale d is the depth of the fluid, κ is the thermal diffusivity, ν is the kinematic viscosity, α is the coefficient of thermal expansion, g is the acceleration of gravity, and β is the deviation of the temperature gradient from the adiabatic gradient. Representative values of these parameters for the mantle are shown in Table 15. (Our studies here yield magnitudes for Rayleigh numbers under given conditions; we do not need to determine each of these parameters in order to cal-

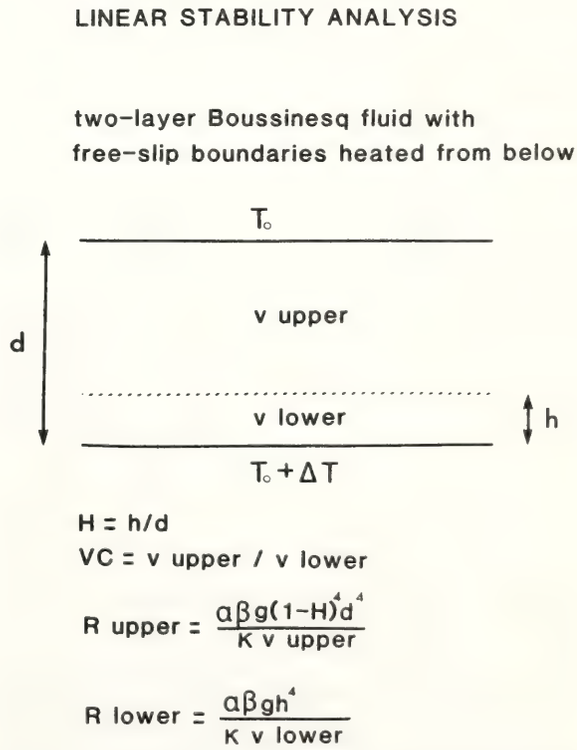


Fig. 51. The model used for the linear stability analysis of two superposed fluids having different viscosities. The dashed line shows the interface between the two layers.

culate the Rayleigh number.) A critical Rayleigh number, Ra_c, is a value of Ra that allows a nontrivial solution to this stability problem. For a given viscosity contrast, $vc = \nu_{upper}/\nu_{lower}$, and a lower layer thickness, $H = h/d$, a wavenumber, A, can be found that minimizes Ra_c. This value of A determines the most unstable mode of convection. Figure 52 shows the streamlines of the most unstable mode at the onset of convection when $H = 0.1$ and the viscosity contrast ranges from 1 to 2×10^6. The critical Rayleigh numbers for these flows are shown in Table 16. For the case $H = 0.1$, Fig. 52 shows that for convection to be confined to the lower layer, the viscosity of that layer must be approximately 10^6 less than the layer above. The thinner a layer is, the greater the viscosity contrast required to confine the convection. This can be understood by noting that the Rayleigh number contains the ratio of the fourth power of the depth to the viscosity. If the instability of the lower layer can be characterized by a local Rayleigh number, of the order of 10^3, then for a thin layer to be unstable the viscosity must decrease by a factor of about H^4 compared to a layer of depth d.

The most unstable cell length (Π/A) also changes with vc. The cell length increases from a value of $1.4d$ for $vc = 1$ to a maximum of $2.6d$ at $vc = 10^5$. As vc is increased still further, the most unstable cell length decreases, until at $vc = 2 \times 10^6$ the cell length is about $0.13d$ or $1.3h$. It is not clear what would maintain such a sharp discontinuity in viscosity in the mantle. Once convection began, the low-viscosity material would tend to penetrate and mix with the upper layer. If core heating were episodic, then such a discontinuity in viscosity might form and allow small-scale convection to occur. Once the small-scale motions start, they could form plumes and remove both heat and low-viscosity material from the D″ region. The process would repeat as new material is warmed to form a new low-viscosity layer. This is only one way in which a low-viscosity layer could form. In the next section, we investigate whether an unstable layer could be formed by whole-mantle convection.

TABLE 15. Typical Values of Mantle Properties

$g = 10^3$ cm s^{-2}	$\Delta T = 10^3$ °C
$\alpha = 10^{-5}$ °C^{-1}	$\nu = 3 \times 10^{21\pm1}$ cm^2 s^{-1}
$\kappa = 10^{-2}$ cm^2 s^{-1}	$d = 3 \times 10^8$ cm

Variable Viscosity Large-Scale Flow

If whole-mantle convection is occurring, then the D″ layer is likely to be the thermal boundary layer of whole-mantle convection cells (Yuen and Peltier, 1980). In this case, small-scale flow might occur as instabilities in this low-viscosity thermal boundary layer. The sharp decrease in viscosity between the mantle and the lower thermal boundary layer of a whole-mantle cell might approximate the layered geometry we are considering. The low viscosity in such a boundary layer would tend to facilitate small-scale convection. To investigate this idea more thoroughly, a finite-amplitude model of the large-scale flow with a temperature-dependent viscosity was developed.

Though convection with temperature-dependent viscosity has been numerically simulated by several investigators (Houston and De Bremaecker, 1975; Mckenzie, 1977; Parmentier and Turcotte, 1978), only Torrance and Turcotte (1971) have done a systematic study. The effects of a strongly temperature dependent viscosity are not fully understood. One effect found in both linear stability analyses (Schubert *et al.*, 1969; McFadden and Smylie, 1968) and by finite-amplitude studies (Houston and De Bremaecker, 1975) is that viscosity

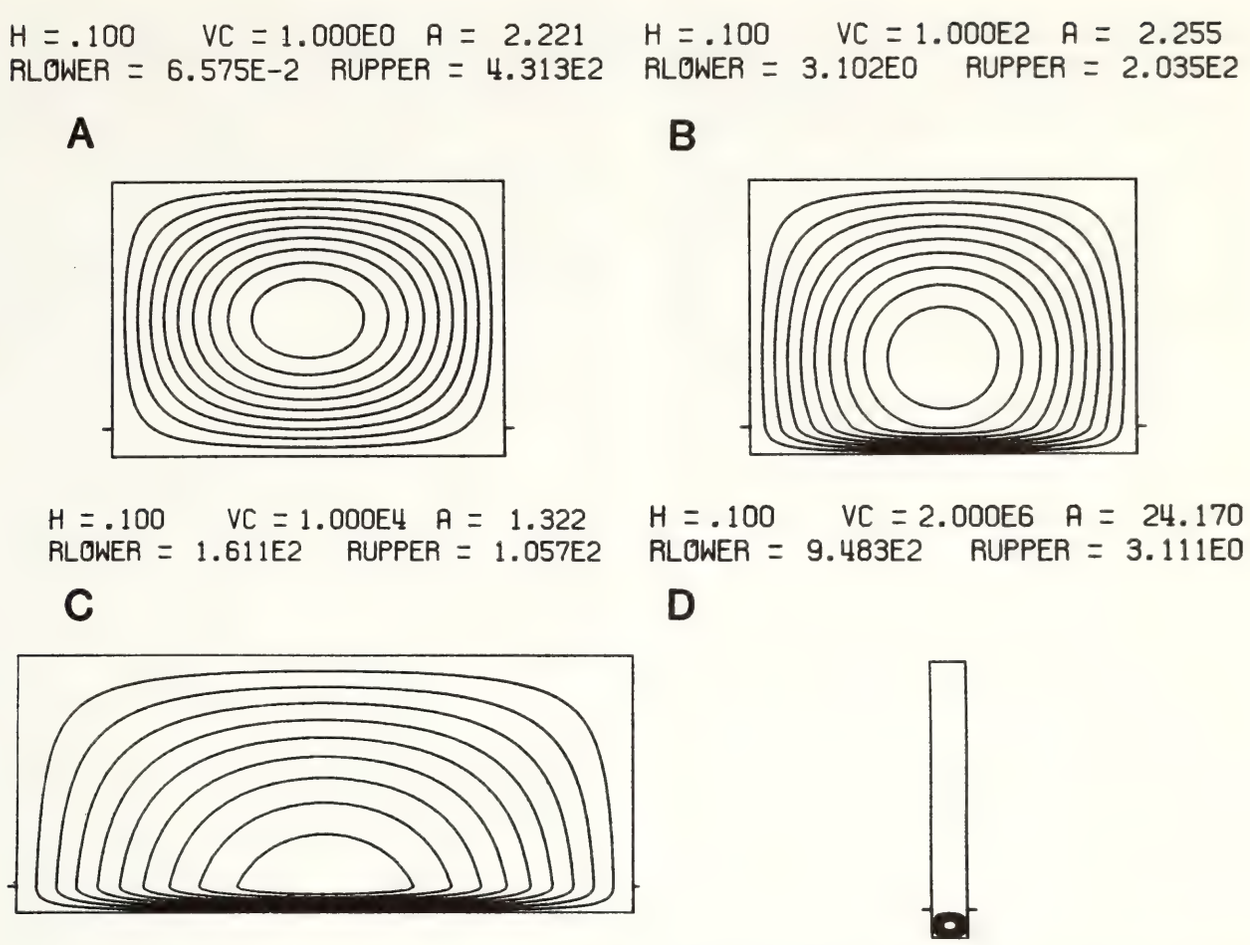


Fig. 52. The streamlines of the most unstable mode of convection in a fluid having two layers of different viscosity. The lower layer is 1/10 the total depth. The tick marks show the interface between the two layers. (A) $vc = 1$; (B) $vc = 10^2$; (C) $vc = 10^4$; (D) $vc = 2 \times 10^6$.

TABLE 16. Critical Rayleigh Numbers and Wavenumbers for a Range of Viscosity Contrasts between the Upper and Lower Layers*

	$H = 0.1$			
Figure	vc	Ra_{upper}	Ra_{lower}	A
52A	1	4.313×10^2	6.575×10^{-2}	2.221
52B	10^2	2.035×10^2	3.102	2.255
52C	10^4	1.057×10^2	1.611×10^2	1.322
52D	2×10^6	3.111	9.483×10^2	2.417×10^1

*The Rayleigh numbers are defined using the thickness and viscosity of each individual layer.

variations have a strong influence on convection cell geometry. In this study we hope to demonstrate the way in which a temperature-dependent viscosity affects the thickness, velocity, and hence the stability of a thermal boundary layer. One motivation for considering a finite-amplitude model was the general expectation that a low-viscosity thermal boundary layer might be inherently unstable and give rise to small-scale motions or plumes.

A model identical to that used by Torrance and Turcotte (1971) has been chosen for this study. It consists of a Boussinesq fluid, having an exponen-

tial viscosity dependence on temperature, contained in a two-dimensional box of length $1.4d$ heated from below. The side walls are insulating and the top and bottom boundaries have a prescribed temperature difference. All the walls of this box are free-slip. Though compressibility, viscous dissipation, spherical geometry, and the third dimension are undoubtedly important for a study of the lower mantle, we have omitted them in order to facilitate our understanding of the model results and to simplify our numerical solution.

The nondimensional variables are defined as:

$$(u', w') = \kappa/d(u, w)$$

$$(x', z') = d(x, z)$$

$$t' = d^2/\kappa t$$

$$T' = T\Delta T + T_o,$$

where primes denote dimensional variables. The velocity components u and w refer to the horizontal (x) and vertical (z) directions, respectively. The temperature scale, ΔT, is the temperature difference maintained across the fluid layer and T_o is a reference temperature. If a streamfunction, Ψ, is introduced and inertial terms are neglected (infinite Prandtl number), the nondimensional fluid equations become

$$\frac{\partial^2}{\partial x \partial z}\left(4\mu \frac{\partial^2 \Psi}{\partial x \partial z}\right) + \left(\frac{\partial^2}{\partial z^2} - \frac{\partial^2}{\partial x^2}\right)\left(\mu \frac{\partial^2 \Psi}{\partial z^2} - \mu \frac{\partial^2 \Psi}{\partial x^2}\right) = Ra \frac{\partial T}{\partial x} \qquad (1)$$

$$u = \frac{\partial \Psi}{\partial z} \qquad v = -\frac{\partial \Psi}{\partial x}$$

$$\frac{\partial T}{\partial t} + u\frac{\partial T}{\partial x} + w\frac{\partial T}{\partial z} = \frac{\partial^2 T}{\partial x^2} + \frac{\partial^2 T}{\partial z^2} \qquad (2)$$

Here the Rayleigh number is defined as

$$Ra = \frac{\alpha g \Delta T d^3}{\kappa \nu_0}.$$

The viscosity scale is normalized to the viscosity at a temperature equal to the average of the boundary temperatures.

Numerical Method

The method of conjugate gradients (Reid, 1971; Concus *et al.*, 1976) was used to solve the biharmonic (Equation 1) directly. This method is iteration-like, since with each successive cycle of the algorithm the error in the solution decreases. Unlike most iterative methods, no estimation of parameters is required and an exact solution (neglecting roundoff error) can be obtained in a finite number of steps. The finite difference formulation used for Equation 1 follows that of Andrews (1972). This finite difference form satisfies the same variational principal as Equation 1 and minimizes the integral of the shear dissipation. This method is not without limitations. The storage requirements are substantial, and thus the maximum number of grid points (and hence the accuracy of the solution) is limited to 21 in each direction.

The energy Equation 2 is solved by the Alternating Direction Implicit Method using upwind differences. The ADI method has been used by Lux *et al.*, (1979) and found to be relatively fast and accurate. To test our numerical scheme, we have repeated some of the calculations done by Torrance and Turcotte (1971). Even though the solu-

tions computed by Torrance and Turcotte use a coarse (6 × 8) finite-difference grid, they agree well with our solutions shown in Fig. 53.

The computer used for these calculations was a PDP 11/34 minicomputer. Since this type of machine has limited memory and is fairly slow, typical convection problems required four or five days of continuous running to reach steady state. The approach to steady state is monitored by noting when the Nusselt number, Nu, and the maximum velocity no longer change with time. The Nusselt number measures the ratio of the heat flux carried by convection relative to the heat flux that would have been carried by conduction alone.

Results

Figure 53 illustrates the primary effects of a strongly temperature dependent viscosity. The exponential viscosity function $\nu = \exp[C(0.5 - T)]$ is the same as that used by Torrance and Turcotte (1971). "C" controls the strength of the viscosity variation. $C = 0$ corresponds to a uniform viscosity. For $C = 3$, the viscosity varies by a factor of 20 from top to bottom. For $C = 6$, the variation is a factor of 400, and for $C = 10$ is a factor of 22,000. Figure 53 shows the streamlines, the horizontal velocity as a function of depth, the isotherms, and the mean temperature as a function of depth for a sequence of flows at the same

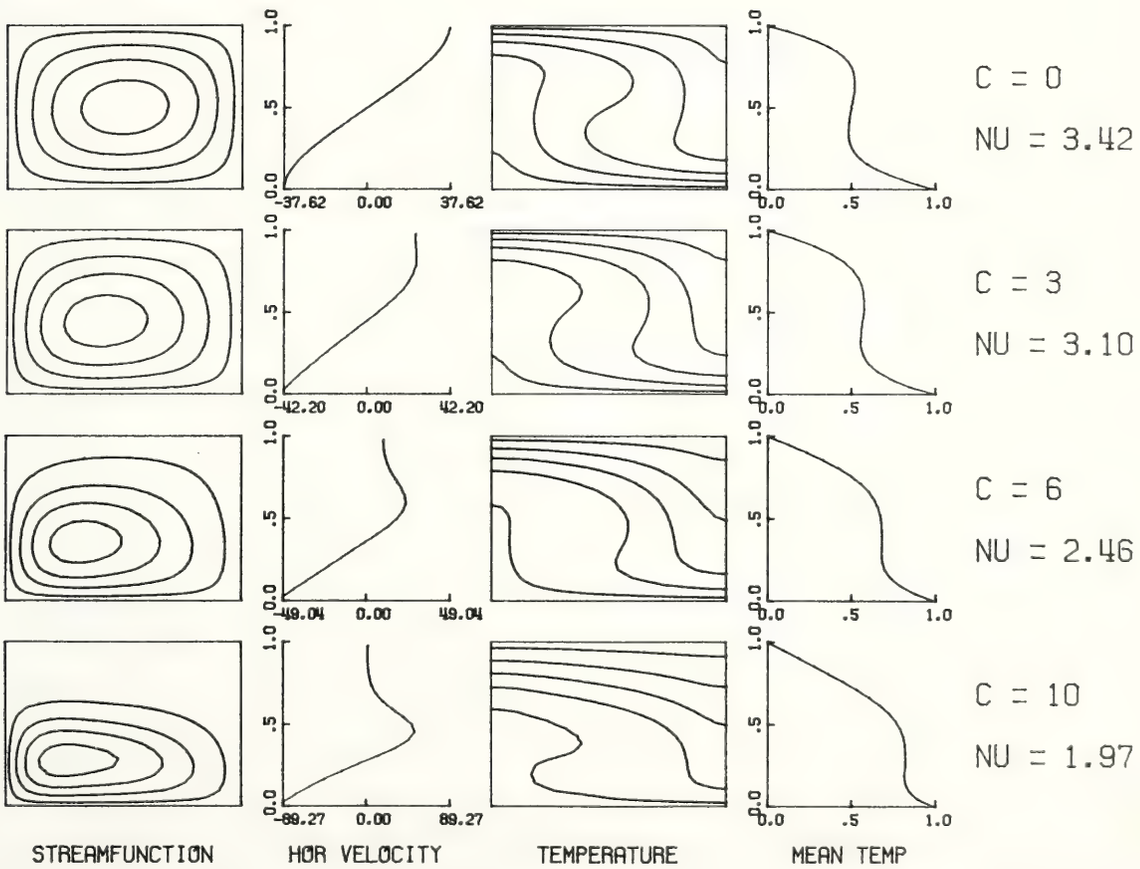


Fig. 53. Steady state streamlines, horizontal velocity as a function of depth, isotherms, and the mean temperature as a function of depth for convection at a fixed Rayleigh number of 3600. The viscosity varies with temperature as exp $\{C(0.5 - T)\}$. C is as shown in the figure. The streamlines are contoured at intervals of 1/8, 3/8, 5/8, and 7/8 the streamfunction minimum. The isotherms are at temperatures of 1/10, 3/10, 5/10, 7/10, and 9/10.

Rayleigh number of 3600 but for increasing viscosity parameter C. Note that the plot of the mean temperature is also equivalent to a plot of the log of the mean viscosity as a function of depth. All flows described here are steady state.

The primary effect of increasing C is geometric. As seen in the streamline plots, the flow is confined to lower in the box as C increases. The hot fluid rises rapidly in a narrow plume while the cold fluid descends more slowly and over a larger area. Heat transport as measured by the Nusselt number Nu also decreases, since the upper thermal boundary layer thickens. Even for the case of $C = 10$, the flow does not seem to be destabilized by this dramatic decrease in viscosity in the lower thermal boundary layer.

The stability of this boundary layer is also evident at higher values of the Rayleigh number. Figure 54 shows a sequence of flows increasing in Rayleigh number but at a fixed value of $C = 10$ corresponding to a viscosity contrast of 22,000. The flow remains stable at a Rayleigh number of 10^5 but at higher Rayleigh numbers it may not be. The local Rayleigh number of the lower thermal boundary layer increases with increasing global Rayleigh number, as shown in Table 17. This suggests that a critical Rayleigh number for the boundary layer (about 10^3) may be exceeded when the global Rayleigh number is 10^6 or 10^7. A more accurate finite-difference grid will be required to investigate this, however.

The flow at a Rayleigh number of 10^5 may be relevant to the mantle even though the Rayleigh number for the mantle could be as large as 10^7. The interior of this flow is nearly isothermal and hence isoviscous. This is consis-

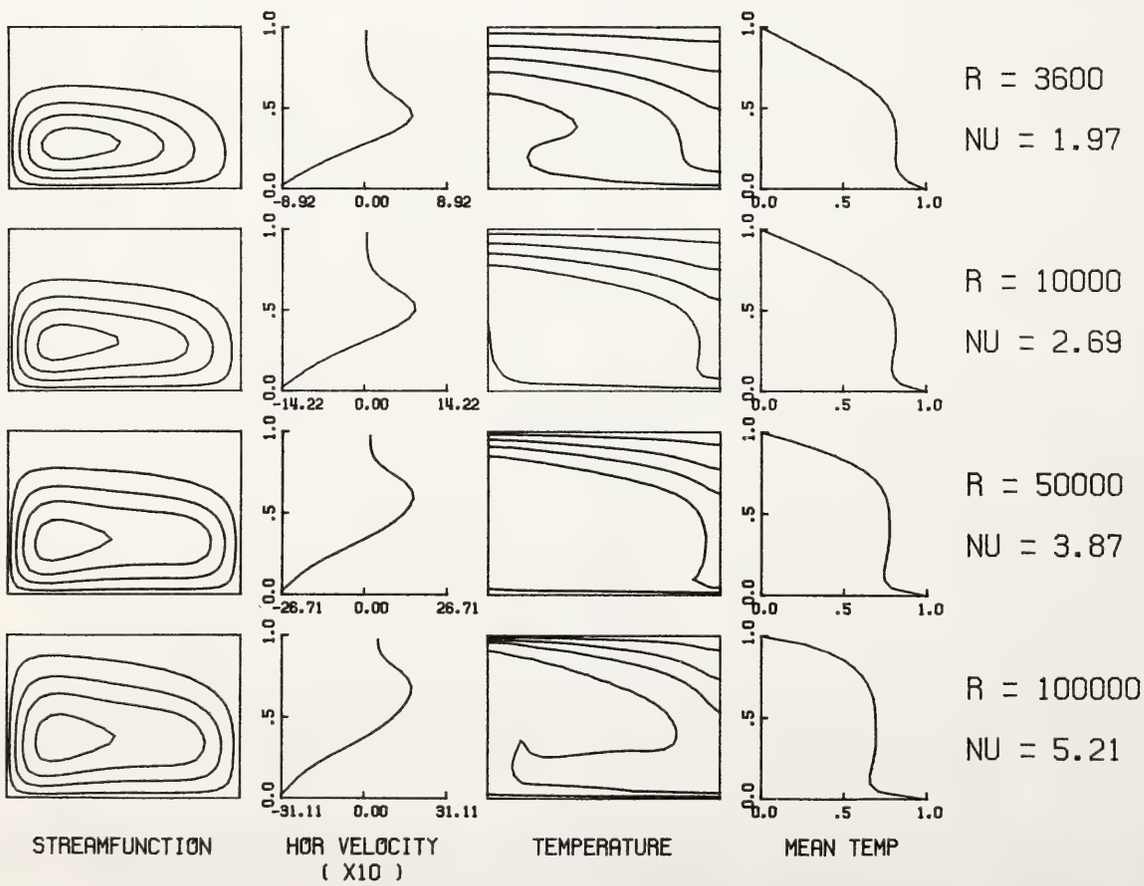


Fig. 54. As in Fig. 53, but for the viscosity parameter C fixed at 10 and for four different values of the Rayleigh number.

TABLE 17. The Local Rayleigh Number for the Lower Boundary Layer as a Function of the Global Rayleigh Number for the Flows Shown in Fig. 54*

Ra	R_{bl}
3600	98
10^4	279
5×10^4	437
10^5	766

*The local Rayleigh number R_{bl} is defined using the thickness of the boundary layer, the temperature drop across it, and the viscosity at the mean temperature within the boundary layer. Ra = global Rayleigh number. $C = 10$.

tent with estimates of mantle viscosity structure determined from glacial rebound studies. The flow also forms a thin low-viscosity lower boundary layer with a large temperature drop across it, simulating perhaps the D" layer. One should also note that the horizontal velocity in the upper thermal boundary layer is much less than the horizontal velocity in the lower thermal boundary layer. Thus plate speeds may severely underestimate convective velocities at depth.

Conclusions

The model displays no secondary instabilities in the plane of the large-scale variable viscosity flow for the range of Rayleigh numbers considered. Note, however, that our model does not address instabilities in the third dimension perpendicular to this flow.

If stabilities do develop in the boundary layer of the large-scale flow, then they will likely occur in the direction perpendicular to the plane of the large-scale flow. The next logical step is to consider the stability of the boundary layers in this two-dimensional model by allowing disturbances in the third dimension. A stability analysis by Yuen and Peltier (1980) indicates that instabilities of this type are very likely. If these transverse instabilities occur, they may not penetrate into the mantle above. The large horizontal velocities within the lower boundary layer will tend to sweep the instabilities away before they grow very large. The relatively higher mantle viscosity may also limit the upward penetration of these instabilities.

In both the linear stability analysis and the finite-amplitude model, for the seismic velocity variations at the base of the mantle to be of thermal origin, the viscosity within the D" layer must be considerably less than the viscosity of the overlying mantle. This condition is likely to be met if the mantle is heated from the core, since we expect mantle viscosity to be strongly temperature dependent.

References

Andrews, D. J., Numerical simulation of sea floor spreading, *J. Geophys. Res., 77*, 6470–6481, 1972.

Concus, P., G. H. Golub, and D. P. O'Leary, A generalized conjugate gradient method for numerical solution of elliptic partial differential equations, in *Sparse Matrix Computations*, pp. 309–332, J. R. Bunch and D. J. Rose, eds., Academic Press, New York, 1976.

Davies, G. F., Whole-mantle convection and plate tectonics, *Geophys. J. Roy. Astron. Soc., 49*, 459–486, 1977.

Houston, M. H., and J. C. De Bremaecker, Numerical models of convection in the upper mantle, *J. Geophys. Res., 80*, 742–751, 1975.

Lux, R. A., G. F. Davies, and J. H. Thomas, Moving lithospheric plates and mantle convection, *Geophys. J. Roy. Astron. Soc., 57*, 209–228, 1979.

McFadden, C. P., and D. E. Smylie, Effect of a region of low viscosity on thermal convection in the mantle, *Nature, 220*, 468–469, 1968.

Mckenzie, D. P., Surface deformation, gravity anomalies and convection, *Geophys. J. Roy. Astron. Soc., 48*, 211–238, 1977.

Parmentier, E. M., and D. L. Turcotte, Two-dimensional flow beneath a rigid accreting lithosphere, *Phys. Earth Planet. Interiors, 17*, 281–289, 1978.

Reid, J. K., On the method of conjugate gradients for the solution of large sparse systems of linear equations, in *Large Sparse Sets of Linear Equations*, pp. 231–254, J. K. Reid, ed., Academic Press, New York, 1971.

Sacks, I. S., and L. Beach, Lateral heterogeneity

at the base of the mantle—an indication of whole mantle convection, *Carnegie Inst. Wash. Year Book 73*, 1020–1032, 1974.
Schubert, G., D. L. Turcotte, and E. R. Oxburgh, Stability of planetary interiors, *Geophys. J. Roy. Astron. Soc., 18*, 441–460, 1969.
Snoke, J. A., and I. S. Sacks, A model for laterally heterogeneous velocity structure at the base of the mantle, *Carnegie Inst. Wash. Year Book 75*, 233–239, 1976.
Takeuchi, H., and S. Sakata, Convection in a mantle with variable viscosity, *J. Geophys. Res., 75*, 921–927, 1970.
Torrance, K. E., and D. L. Turcotte, Thermal convection with large viscosity variations, *J. Fluid Mech., 47*, 113–125, 1971.
Yuen, D. A., and W. R. Peltier, Mantle plumes and the thermal stability of the D″ layer, *Geophys. Res. Lett.*, in press, 1980.

PROPERTIES OF GEOLOGICAL MATERIALS

Diffusion of Ce, Sm, Eu, and Cs in Dehydrated Obsidian Glass and Melt

Albert Jambon and F. J. Ryerson†*

Various observations from igneous rocks, including zoned crystals and concentration gradients in glass adjacent to phenocrysts, indicate that these rocks do not always crystallize under conditions of bulk chemical equilibrium. The extent to which equilibrium is attained depends on the prevailing physical conditions and the diffusivities of chemical species within the coexisting phases. As such, values for these diffusivities are necessary for quantitative evaluation of igneous processes.

In this study we report new data on the diffusivities of Ce, Sm, Eu, and Cs in dehydrated Valles Caldera obsidian glass and melt (for analysis, Magaritz and Hofmann, 1978a, table 1) between 700°–1300°C in air. These data are compared with data from natural and water-saturated obsidians (Magaritz and Hofmann, 1978a,b; Jambon and Carron, 1973; Watson, 1979).

*Laboratoire et Geologie Appliques, Université d'Orléans, France.
†Earth Sciences Division, Lawrence Livermore Laboratory, Livermore, California.

Experimental Techniques

Obsidian was melted in a Pt crucible at 1575 °C for one week. This procedure produced a bubble-free glass, which was extruded into 3-mm Pt tubing for runs above 1100 °C, and cored for slabs (1 cm dia. × 0.25 cm) for runs below 1100 °C. ^{137}Cs, ^{145}Sm, ^{144}Ce, and ^{152}Eu were added as chloride solutions, and a 30-min, 900 °C preannealing step was used to impregnate the tracer. Unreacted tracer was removed by a rinse in 6.0 N HCl, producing a thin source configuration. Run times ranged from 10^3 to 10^6 sec. Runs were analyzed by serial etching, weight loss, and counting for slabs, and serial sectioning and counting for runs in Pt tubes.

Results

The temperature dependence of diffusivities display Arrhenius behavior (Fig. 55). The diffusion coefficients in dehydrated obsidian are given by:

$$D(\mathrm{Ce}) = 4.83 \times 10^6 \exp(-1.17 \times 10^5/RT)$$

$$D(\mathrm{Eu}) = 6.90 \exp(-6.87 \times 10^4/RT)$$

$$D(\mathrm{Cs}) = 2.46 \times 10^{-1} \exp(-5.59 \times 10^4/RT)$$

Shown for comparison are D(Eu) and D(Sr) for natural obsidian (Magaritz and Hofmann, 1978a,b), D(Cs) for natural obsidian (Jambon and Carron, 1973), and D(Cs) in H_2O-saturated granitic melt (Watson, 1979).

Several features of the data stand out:

(1) The diffusivities of Eu and Cs in dehydrated melts are lower than those in the natural glasses. The Valles Caldera obsidian contains 0.38 wt % H_2O, while the Icelandic obsidian of Jambon and Carron (1973) contains 0.65 wt % H_2O. The activation energies, ΔE, increase with decreasing H_2O content. For instance, in dry ob-

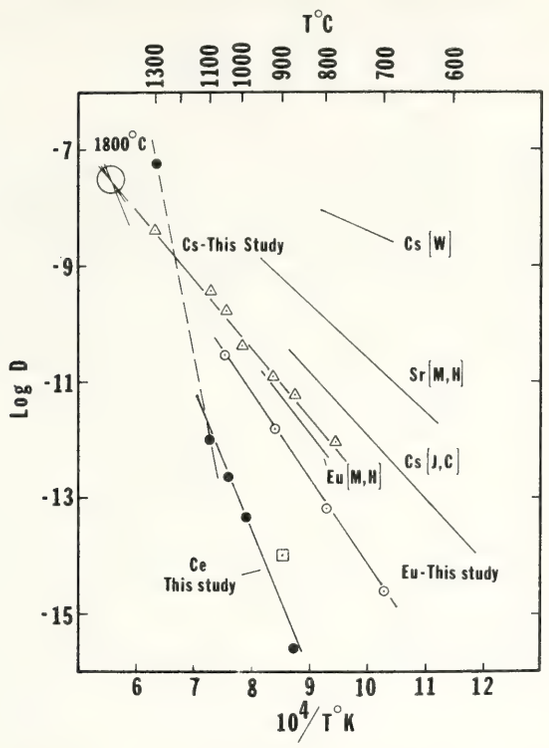


Fig. 55. Arrhenius plot of diffusion results. Solid circles—Ce, open circles—Eu, squares—Sm, triangles—Cs from this study. Eu (M,H) and Sr (M,H) are on natural obsidian from Magaritz and Hofmann, 1978a,b. Cs (J,C) are on natural obsidian from Jambon and Carron, 1973. Cs (W) is on water-saturated granitic melt from Watson, 1979.

sidian $\Delta E(\mathrm{Eu}) = -68.7$ kcal/mole, compared with -59 kcal/mole for the natural obsidian. In dry obsidian $\Delta E(\mathrm{Cs}) = -55.9$ kcal/mole compared to -49.9 kcal/mole in the natural obsidian (Jambon and Carron, 1973). More strikingly, $\Delta E(\mathrm{Cs}) = -19.52$ kcal/mole in H_2O-saturated granitic melt containing 6.1–6.3 wt % H_2O (Watson, 1979).

(2) The temperature dependence of diffusivities of Ce, Eu, Cs in dehydrated obsidian yield a rather precise compensation temperature of 1800 °C at $D = 3.2 \times 10^{-8}$ cm^2 sec^{-1}. For natural obsidians, the temperature is higher (>2500 °C) and less well defined. These data compare with a value of 10^{-6}–10^{-7} cm^2 sec^{-1}, 1500 °C for basalts (Magaritz and Hofmann, 1978).

(3) The 1300 °C data for D(Ce) fall well off the Arrhenius plot developed at lower T. This suggests a change in the diffusion mechanism between 1100 °–1300 °C. More data in this temperature range are required to substantiate this change in diffusion mechanism.

(4) The data for Sm fall close to D(Ce). This is important, as Ce may be either tri- or quadravalent, while Sm is only trivalent. The coincidence of D(Ce) and D(Sm) indicates that cerium is present as Ce^{+3}. D(Eu) is significantly higher than D(Ce,Sm), however. The ionic radii of Sm^{+3} and Eu^{+3} are similar (1.17 Å and 1.18 Å, respectively, for VIII coordination), so ionic radii play no role. However, Eu may be divalent and, as such, comparable to Sr in ionic radius and behavior (1.33 Å for VIII). Hence, the increased diffusivity of Eu is attributed to the presence of some faster diffusing Eu^{+2}. Eu^{+2}/Eu^{+3} can be estimated from the diffusivities by assuming

$$D(\mathrm{Eu}) = X_{\mathrm{Eu}^{+2}} D(\mathrm{Eu}^{+2}) + X_{\mathrm{Eu}^{+3}} D(\mathrm{Eu}^{+3}),$$

where the bulk Eu diffusivity, D(Eu), is the "weighted" (actually mole fractions) sum of the Eu^{+2} and Eu^{+3} diffusivities. $D(Eu^{+2})$ is approximated by D(Sr), and $D(Eu^{+3})$ by D(Ce). At 800 °C, $Eu^{+2}/Eu^{+3} = 5.54 \times 10^{-4}$, and at 900 °C $Eu^{+2}/Eu^{+3} = 1.78 \times 10^{-3}$. This calculation yields the expected reduction with increasing temperature. It should be noted that the concentration of Eu^{+2} is too low to be detected in partitioning behavior by standard analytical techniques, i.e., isotope dilution, electron microprobe. Hence, the value of D(Eu) may be the most sensitive indicator of Eu^{+2} yet developed. It is also important to realize that the Eu-diffusion profiles are identical to those of the single valence cations. A superposition of two profiles, $D(Eu^{+2})$ and $D(Eu^{+3})$, does not and cannot occur as a result of multiple oxidation states.

Discussion

The diffusivities of cations in obsidian are sensitive to changes in H_2O content

and valence. In each case, the decrease in activation energy reflects increased ease in forming activated complexes. It is generally accepted that cations in melts diffuse as cations rather than as parts of large molecules. Hence, the structural change which allows higher diffusivities probably occurs within the cation's immediate coordination polyhedra, and not as a result of gross structural changes in the melt (note the similarities in $D(x)$ for basaltic and granitic compositions [Magaritz and Hofmann, 1978b]). In this regard, it is useful to consider the polarizability of oxygen anions surrounding a given cation. As the cation's valence increases, it draws electrons more efficiently from surrounding oxygen anions, polarizing them toward itself. As such, it becomes more tightly bound to its coordination polyhedra, resulting in increased activation energies. On the other hand, the hydration of a Si-O-M bond complex by H_2O,

$$H_2O + \text{Si-O-M} \rightleftharpoons \text{Si-O-H} + \text{M-O-H}$$

may have the opposite effect. The H^+ cation is highly electronegative and may draw the anion away from the metal cation. Hence, the cation is less tightly bound in its coordination polyhedra, and the activation energy decreases.

References

Jambon, A., and J.-P. Carron, Etude experimentale de la diffusion des elements alcalins K, Rb, Cs dans une obsidienne granitique, *Comptes rendus de seanes de l'Académie des Sciences*, Paris t. *276*, Serie D, 3069–3072, 1973.

Magaritz, M., and A. W. Hofmann, Diffusion of Sr, Ba and Na in obsidian, *Geochim. Cosmochim. Acta*, *42*, 595–605, 1978a.

Magaritz, M., and A. W. Hofmann, Diffusion of Eu and Gd in basalt and obsidian, *Geochim. Cosmochim. Acta*, *42*, 847–858, 1978b.

Watson, E. Bruce, Diffusion of cesium ions in H_2O-saturated granitic melt, *Science*, *205*, 1259–1260, 1979.

Oxide Solution Mechanisms in Silicate Melts

*F. J. Ryerson**

The thermodynamic modeling of silicate melts has received much attention in recent years. Successful models may eventually allow the prediction of phase relations in natural systems, meanwhile aiding in the design of critical experiments. Two choices of components, exist for such models: (1) large molecular components, which allow small-scale primary interactions to be neglected (also missed), or (2) small components (i.e., oxides), which require primary interactions to figure heavily in the formulation of activity coefficients γ. In this report, a set of simple components similar to those of Bottinga and Weill (1972) are used to investigate the primary interactions in $MO\text{-}SiO_2$ systems.

Results and Discussion

The partial molar enthalpies (1600 °C) of SiO_2, $\Delta\overline{H}_{SiO_2}$, have been derived from published phase diagrams (Fig. 56). The data are discussed for three component types: (1) mono- and divalent oxides (network-modifiers) (Fig. 56a), (2) alkali and alkaline earth aluminates (network-formers) (Fig. 56b), and (3) highly charged cations (Fig. 56b).

$\Delta\overline{H}_{SiO_2}$ for network-modifying oxides increases systematically with the electronegativity of the metal cation. At high SiO_2 contents, $\Delta\overline{H}_{SiO_2}$ is positive, yielding γ_{SiO_2}'s greater than unity, i.e., positive deviations from ideality. As these deviations increase, stable liquid immiscibility results. The solution mechanism in such melts is

$$\text{(Si-O-Si)} + \text{M-O-M} \rightleftharpoons 2\text{(Si-O-M)}.$$

*Earth Sciences Division, Lawrence Livermore Laboratory, Livermore, California.

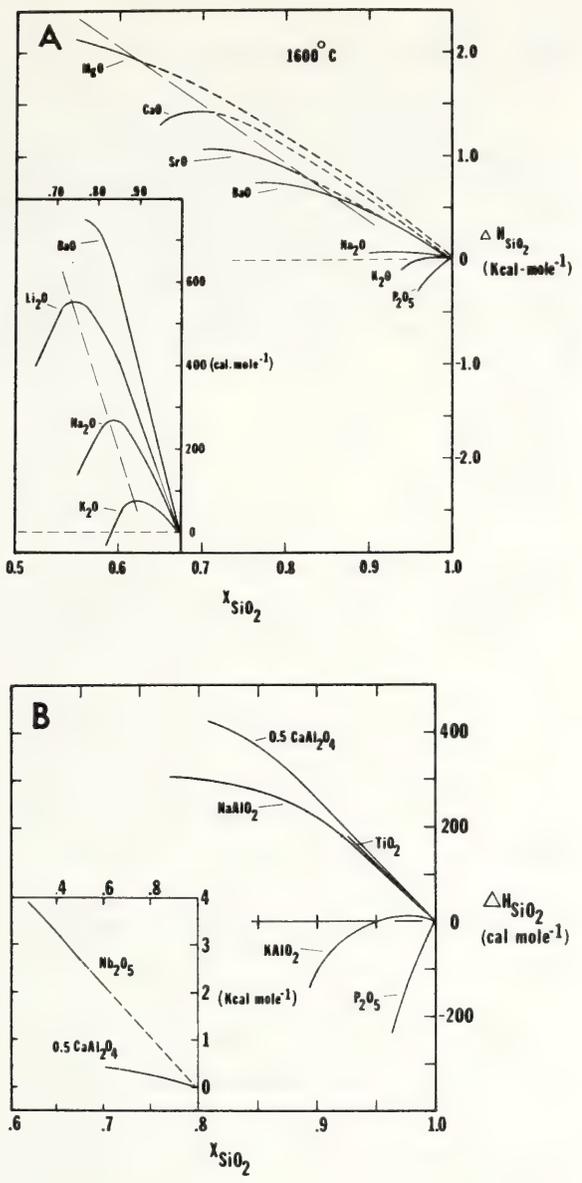


Fig. 56. $\Delta\overline{H}_{SiO_2}$ versus mole fraction SiO_2 at 1600 °C. Calculated from freezing point depression. $\Delta\overline{H}_{SiO_2} = 0$ indicates ideal mixing. For discussion, see text.

Hence, increased $\Delta\overline{H}_{SiO_2}$ reflects the energetics of nonbridging oxygen formation.

The alkali and alkaline earth aluminates have positive deviations from ideality at high SiO_2, but not as great as those of the network-modifiers. These deviations correlate positively with the electronegativity of the alkali or alkaline earth cation. It is generally accepted that such aluminates copolymerize with SiO_2, the alkali or alkaline earth cation providing charge balance. Hence, the correlation between $\Delta\overline{H}_{SiO_2}$ and the electronegativity of the charge-balancing cation reflects the increasing distortion of the aluminosilicate network. Taylor and Brown (1979) have, in fact, shown a structural change in Ab and Or versus An glasses by x-ray derived RDF's. It is interesting to note that the solution of network-forming oxides is more efficient in reducing the activity of SiO_2 than network-modifying oxides.

$\Delta\overline{H}_{SiO_2}$ for P_2O_5-, TiO_2-, and Nb_2O_5-bearing melts yield surprising results. P_2O_5 produces negative deviations from ideality, while the positive deviation produced by TiO_2 is only as large as that of 0.5 $CaAl_2O_4$. Hence, P_2O_5 and TiO_2 must be copolymerizing with the silicate network. This copolymerization has been substantiated by Raman spectra (Mysen *et al.*, 1980a,b). Nb_2O_5, however, produces the largest deviation from ideality of all the oxides investigated, substantiating its role as a pentavalent network-modifier. Its ionic radius is similar to Ti^{+4} and P^{+5}, so IV coordination of oxygen cannot be precluded. However, copolymerization is precluded by the large positive deviation.

The thermodynamic behavior of MO-SiO_2 melts can be rationalized by considering the simple oxide components above. The critical factors are: (1) the electronegativity of network-modifying and charge-balancing cations, and (2) the ability of a cation to copolymerize with the SiO_2 network.

References

Bottinga, Y., and D. F. Weill, The viscosity of magmatic silicate liquids: a model for calculation, *Amer. J. Sci., 272*, 438–475, 1972.

Mysen, B. O., F. J. Ryerson, and D. Virgo, The structural role of P_2O_5 in silicate melts, *Amer. Mineral.*, in press, 1980a.

Mysen, B. O., F. J. Ryerson, and D. Virgo, The structural role of TiO_2 in silicate melts, *Amer. Mineral.*, in press, 1980b.

Taylor, M., and G. E. Brown, Jr., Structure of mineral glasses—I. The feldspar glasses $NaAlSi_3O_8$, $KAlSi_3O_8$, $CaAl_2Si_2O_8$, *Geochim. Cosmochim. Acta., 43*, 61–75, 1979.

EARTH, PLANETS, AND METEORITES

Reassessment of the "Age of the Earth"

F. Tera

In *Year Book 78*, Bugnon, Tera, and Brown (1979) reported on a lead isochron corresponding to 2.64×10^9 years for samples from the Kidd Creek mine near the town of Timmins, Ontario. Subsequent analysis showed that the isochron applies also to samples from the Thompson Bousquet mine located some 400 miles to the east of Timmins (Bugnon *et al.*, 1980). The isochron is defined by data on whole rocks as well as on associated sulfide deposits including galena. The implication of the isochron is that the extrusion of magma (from which the rocks subsequently crystallized) and the deposition of the sulfide minerals could not have been separated in time by more than a few million years.

In terms of Pb isotope systematics, galena has the characteristic, by virtue of excluding uranium and thorium from its lattice, of preserving the Pb isotopic composition that existed in the source at the time of isolation of the galena. Thus in our example the Pb composition of Timmins galena represents the Pb composition of the source 2.64×10^9 years ago. In terms of a single-stage model for the galena, its Pb composition would have evolved (through the decay of ^{235}U to ^{207}Pb and ^{238}U to ^{206}Pb) in a time interval $T - t$ where $t = 2.64 \times 10^9$ y and T is the age of the source which can be calculated from the relationship

$$\left[\frac{^{207}Pb}{^{206}Pb}\right]^* = \left[\frac{^{235}U}{^{238}U}\right]_{today} \frac{e^{\lambda_5 T} - e^{\lambda_5 t}}{e^{\lambda_8 T} - e^{\lambda_8 t}}, \quad (1)$$

where $(^{235}U/^{238}U)_{today} = 1/137.8$ and λ_5 and λ_8 are the decay constants of ^{235}U and ^{238}U, respectively. $(^{207}Pb/^{206}Pb)^*$ is the composition of the radiogenic component of the galena's Pb and is obtained by subtracting primordial Pb, i.e.,

$$\left[\frac{^{207}Pb}{^{206}Pb}\right]^* = \frac{(^{207}Pb/^{204}Pb)_G - (^{207}Pb/^{204}Pb)_P}{(^{206}Pb/^{204}Pb)_G - (^{207}Pb/^{204}Pb)_P}, \quad (2)$$

where G and P stand for galena and primordial, respectively. It is assumed in Equation 2 that the isotopic composition of primordial Pb as determined for meteorites (Tatsumoto *et al.*, 1973; Tilton, 1973) applies for the Earth as well.

From their data, Bugnon *et al.* (1979) have calculated $T = 4.56 \times 10^9$ y. This is one of the oldest calculated ages for a source. In this connection, a method is outlined here which allows, on the basis of the isotopic composition of cognate galenas, the simultaneous calculation of the ages of individual galenas as well as the age of their parental source without the benefit of isochrons. The term cognate is applied here to samples derived from the same homogeneous source or from different sources with identical Pb composition and identical U-Th-Pb relative abundances.

It is clear from Equation 1 that it is not possible to define uniquely the age of the source T or the deposition age t on the basis of the isotopic composition of a given galena alone. However, a simultaneous solution is possible for a group of cognate galenas of different ages, as follows:

(1) $(^{207}Pb/^{206}Pb)^*$ for each galena is calculated from Equation 2.

(2) A series of ages T, T', T'' . . . are assumed for the source and the corresponding deposition ages t, t', t'' . . . are calculated from Equation 1.

(3) For each pair of T and t values the corresponding $\mu_S \equiv (^{238}U/^{204}Pb)_{source}$ is calculated from the relationship:

$$\left[\frac{^{206}Pb}{^{204}Pb}\right]_G = \left[\frac{^{206}Pb}{^{204}Pb}\right]_P + \mu_S(e^{\lambda_8 T} - e^{\lambda_8 t}). \quad (3)$$

Note that μ_S, μ_S', μ_S'' . . . are the present-day values for the sources.

(4) For each μ_S value the present-day composition of the source is calculated from the relationship

$$\left(\frac{^{206}Pb}{^{204}Pb}\right)_S = \left(\frac{^{206}Pb}{^{204}Pb}\right)_P + \mu_S(e^{\lambda_8 T} - 1) \quad (4)$$

$$\left(\frac{^{207}Pb}{^{204}Pb}\right)_S = \left(\frac{^{207}Pb}{^{204}Pb}\right)_P + \frac{\mu_S}{137.8}(e^{\lambda_5 T} - 1) \quad (5)$$

Thus for each galena a profile of imaginary source compositions is obtained by plotting, say, $(^{206}Pb/^{204}Pb)_S$ versus T, T', T'' . . . . The shape of the profile is uniquely dependent on the Pb isotopic composition of its galena. The actual Pb composition of the source is given by a single specific point on the profile, but the location of such a point is undeterminable for any single galena independently. However, if a number of galenas were derived from the same source, the location of the specific point on each profile must be the same; that is, source profiles of cognate galenas intersect each other at a single point.

Figure 57 shows source profiles correlating μ_S with T for four of the oldest known conformable galenas (ranging in age from ~3.4 to ~2.7 × 10^9 y). The Pb composition of the galenas used for the determination of the profiles are shown in Table 18. Because of the close similarity between Manitouwadge (Tilton and Steiger, 1969) and Timmins (Bugnon *et al.*, 1979) the data for both galenas are combined in a single profile. The profiles intersect each other at a point corresponding to 4.53 × 10^9 y. If the model used is correct, this is the age of the source from which the galenas were derived at subsequent times. It could be demonstrated numerically that galenas derived from slightly different sources may still simulate the existence of a common point of intersection. Thus the age of 4.53 × 10^9 y for the source must be considered an approximation to the actual age. There is a degree of inherent ambiguity in the method, and the data seem to reflect some experimental problems which amplify the uncertainty of the age. This is demonstrated by the disagreement in Manitouwadge data obtained first by Tilton and Steiger (1969) and subsequently by Stacey and Kramers (1975). The data of the later workers produce a profile inconsistent with the ones shown in Fig. 57. Because of the close similarity of the data of Timmins with the Manitouwadge data of Tilton and Steiger (both are from the Abitibi belt), it is assumed here that these workers' data are more appropriate for the construction of the source profile of Manitouwadge. This assumption is in harmony with the similarity of the Abitibi belt galenas over a distance of ~600 km, as evidenced by data from Timmins, Bousquet, and Michipicoten (Table 18).

Despite the above equivocations, it is significant that old conformable galenas from several continents appear to define a source with a common age and μ_S; this common age is very close to the age of the solar system primarily defined by meteoritic data. If a major depletion of Pb occurred when the

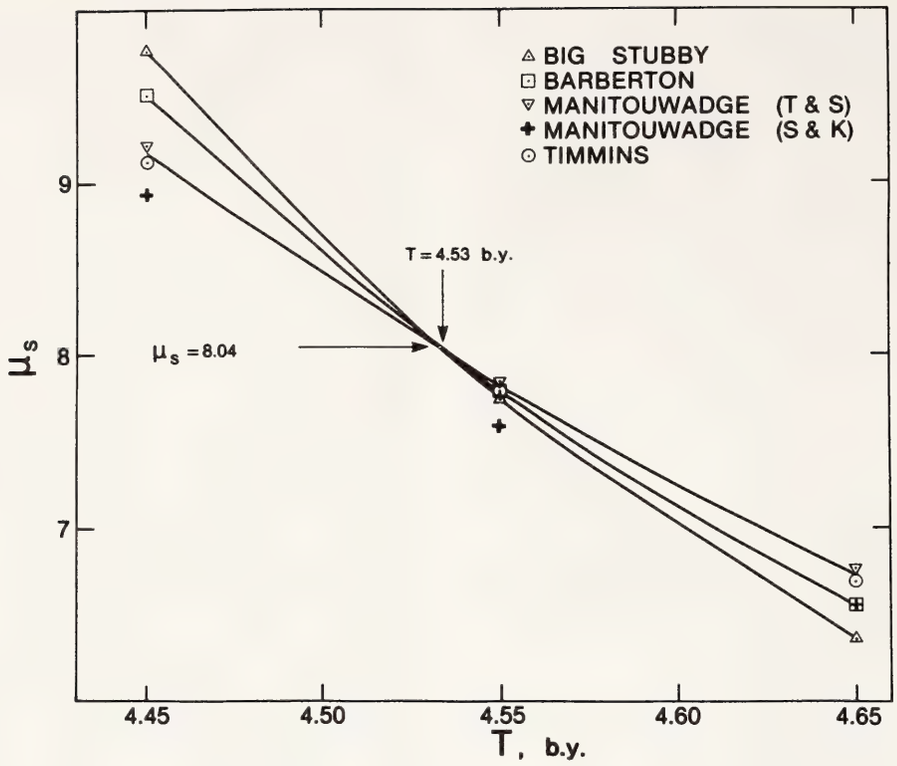


Fig. 57. Source profiles for the four oldest conformable galenas known (deposition ages 3.4–2.64 $\times 10^9$ y). The profiles intersect each other at a congruency point corresponding to a parental source that is 4.53 $\times 10^9$ y old with $\mu_S \sim 8.04$. Consistent with these parameters, the following ages in 10^9 y for the galenas are obtained: Timmins, 2.70; Manitouwadge, 2.71; Barberton, 3.13; and Big Stubby, 3.38. The independently determined ages of Timmins and Manitouwadge are in agreement with the ages obtained from the intersection of the profiles within 2% and 1%, respectively. The so-called "accepted ages" for the other two samples are in agreement within 3%. Because the galenas of the Abitibi belt (to which both Timmins and Manitouwadge belong) seem to be homogeneous with regard to Pb composition (see Table 18), a single profile was constructed for the combined data of Timmins (Bugnon *et al.*, 1979) and Manitouwadge as reported by Tilton and Steiger (1969) (denoted T & S). Stacey and Kramers (S & K) (1975) data on Manitouwadge are inconsistent with the profiles shown.

TABLE 18. Lead Isotopic Composition of Conformable Galenas for which Source Profiles are Shown in Fig. 57*

Sample	Ref.†	Age (10^9 y)	$\frac{^{206}Pb}{^{204}Pb}$	$\frac{^{207}Pb}{^{204}Pb}$	$\frac{^{208}Pb}{^{204}Pb}$
Timmins, Ontario	1	2.64	13.27	14.48	33.18
Bousquet, Ontario	2	. . .	13.29	14.47	33.17
Michipicoten, Ontario	3	. . .	13.28	14.47	33.14
Manitouwadge, Ontario	4	2.68	13.30	14.52	33.58
Manitouwadge, Ontario	5	2.70	13.21	14.40	33.07
Barberton, South Africa	5	3.23	12.46	14.08	32.28
Big Stubby, Australia	6	3.50	11.95	13.72	31.94

*^{235}U and ^{238}U decay constants of Jaffey *et al.* (1971); ^{232}Th decay constant of LeRoux and Glendenin (1963). Primordial Pb of Tatsumoto *et al.* (1973).

†References: (1) Bugnon *et al.* (1979), (2) Bugnon *et al.* (1980), (3) Sinha (1980), (4) Tilton and Steiger (1969), (5) Stacey and Kramers (1975), (6) Sangster and Brook (1977).

Earth's core was formed, then this age refers to some mean time during the course of core formation. Inasmuch as all theories of terrestrial planet formation currently under consideration involve extensive initial melting and core formation during accretion, this time defines the time of formation of the Earth (Wetherill, 1980).

It is also significant that all samples but one of the conformable galenas (Stacey and Kramers compilation, 1975) younger than Timmins yield a point of intersection (T, μ_S) different from the ones shown in Fig. 57. In Fig. 58 are plotted source profiles for four galenas from this second group which define a point corresponding to $\sim 4.46 \times 10^9$ y. In order to be able to project all the data of conformable galenas in one figure without cluttering, the profiles shown in Figs. 57 and 58 (plus profiles for the rest of the galenas) are plotted versus the time of deposition t (Fig. 59). In this presentation the point of intersection is transformed into a line. It is clear from Fig. 59 that the conformable galenas fall into two groups associated with two distinct sources, denoted here as A and B where A, the older and in terms of Pb isotopic composition the less evolved, is the source of conformable galenas 2.65 $\times 10^9$ y or older and B is the source of 2.60 $\times 10^9$ y or younger galenas (down to 2 $\times 10^8$ y ago).

It is premature to speculate about the clear-cut segregation of the samples into two source-associations on the basis of the ages of deposition because further analysis may show an overlap. If this is the case, the sharp time boundary (the interval 2.60–2.65 $\times 10^9$ y) separating the two groups would not exist. Similarly the abrupt jump from line A to line B may not be real and the two lines could be connected by samples derived from hybrid sources. Irrespective of these considerations, however, it seems that the existence of two sources (rather than multiple sources or a single average source) for conformable galenas is reasonably documented by the data at

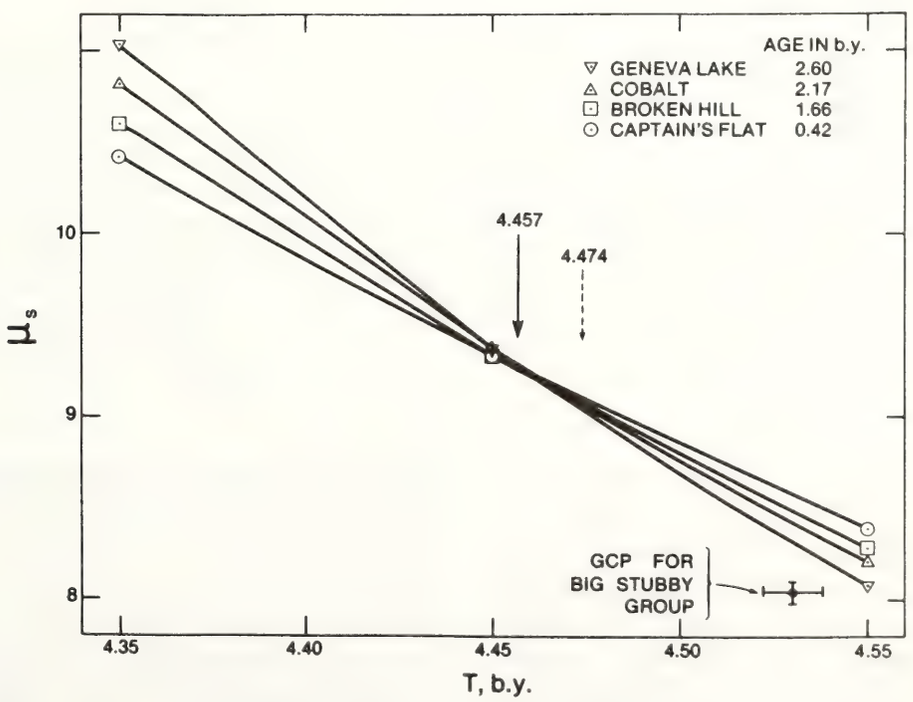


Fig. 58. Source profiles for four conformable galenas ranging in age from 2.6 to 0.42 $\times 10^9$ y. These galenas define a point of intersection corresponding to a 4.46 $\times 10^9$ y parental source (which is distinctly younger than the source of the Big Stubby group shown in Fig. 57) and having $\mu_S \sim 9.3$.

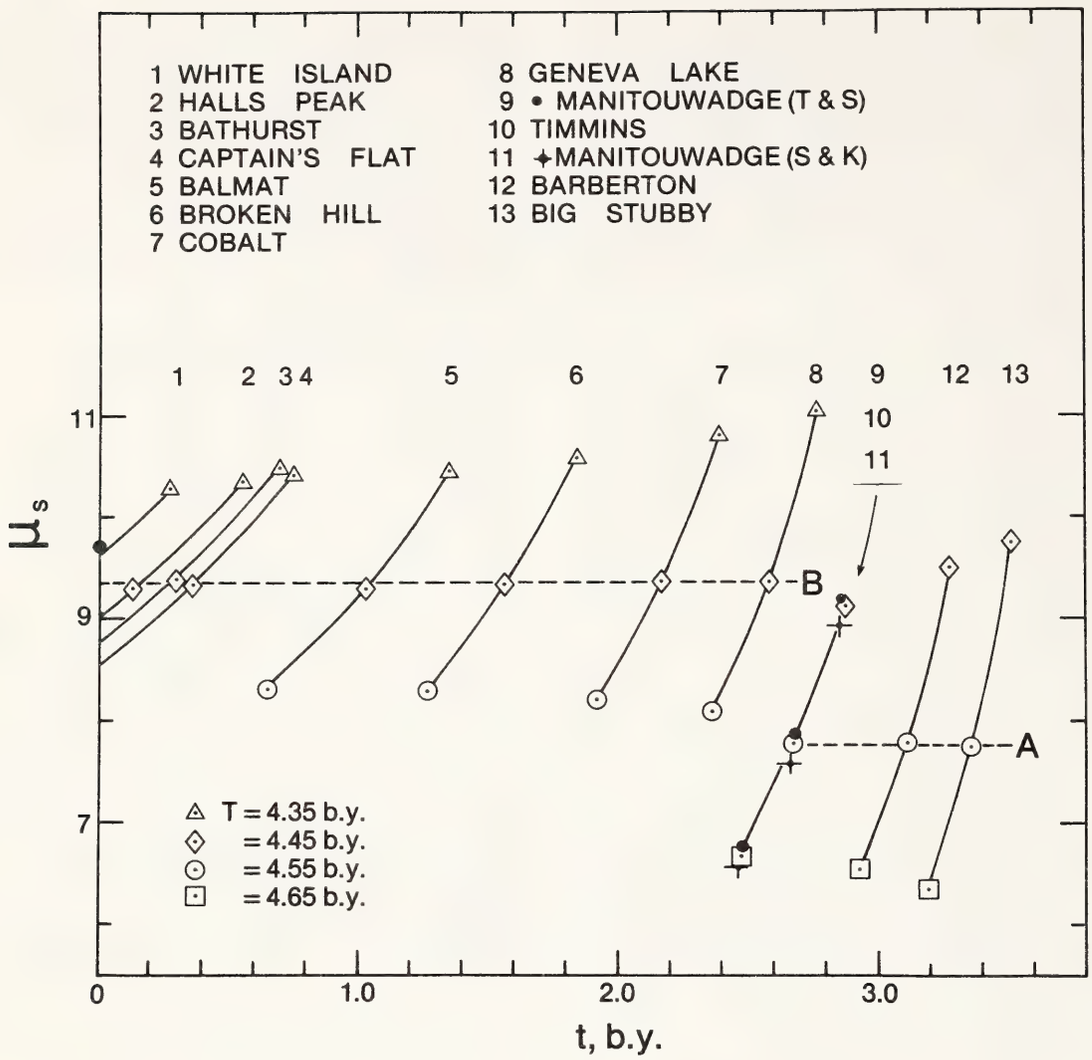


Fig. 59. The source profiles shown in Figs. 57 and 58 (plus profiles for the rest of the conformable galenas in the compilation of Stacey and Kramers [1975]) are plotted versus the calculated deposition age. In this presentation the point of intersection is transformed into a line. That is to say, congruency of the profiles at a point is transformed into alignment at a line. This allows plotting a large number of profiles without cluttering the figure. Notice that conformable galenas are associated with two distinct sources, *A* and *B*, rather than with multiple sources or an average source. Note also that recent oceanic sediments (solid dot) from the Atlantic and the Pacific (Stacey and Kramers [1975]) plot close to source *B*. If oceanic sediments provide a good average for Pb composition in the surface rocks of the continents, then it may be concluded that these rocks are associated with source *B*. Consequently "age of the Earth" calculations based on crustal rocks (or modern sediments) may yield the approximate age of source *B* rather than the age of the Earth.

hand. In addition, the association of galenas 2.6×10^9 y and younger, exclusively with source *B* seems to be unequivocally indicated. The apparent deviation from this strong affinity to source *B* occurs only in very young galenas ($0–10^8$ y ?), as exemplified in Fig. 59 by White Island. This is possibly due to superimposed modern processes in which uranium is enriched relative to Pb in the source. Data for modern oceanic sediments and island arcs (Stacey and Kramers, 1975) plot in the vicinity of the intercept of White Island with the μ_S axis in Fig. 59, indicating a close affinity to source *B*. If one assumes, as Patterson did in his pioneering work (1956), that oceanic sediments represent a reasonable average for Pb in surface rocks, it is reasonable to conclude tentatively that the average rocks on the surface of con-

tinents are closely associated with source *B*. This is further indicated by the fact that the intersection of four isochrons for rocks from widely separated parts of the world indicates a young age of 4.43×10^9 y for the Earth (Stacey and Kramers, 1975).

Table 19 shows a number of "age of the Earth" calculations that were published over the past 25 years. The recurrence of the 4.43×10^9 y age in the first three entries is not surprising, since all three calculations are based dominantly on samples with apparent close affinity to source *B*, as just discussed. The 4.43×10^9 age may or may not have a time meaning. In either case, however, the age has, in the opinion of this author, no direct bearing on the problem of accurate determination of the age of the Earth. It relates rather to a secondary (or higher-order) source which was further fractionated and isolated long ($\sim 10^8$ y) after the more ancient sources were established. It should be pointed out that Stacey and Kramers (1975) *assume* that the Earth is 4.57×10^9 y and that they attribute the apparent age of 4.43×10^9 y to a global U-Pb fractionation event around 3.7×10^9 y ago. The authors seem to preclude or at least underplay the potential of "direct" determination of the age of the Earth from initial Pb, as is demonstrably possible from Timmins (Bugnon *et al.*, 1979) and from old conformable galenas (this work).

The 4.47×10^9 y (fourth entry in Table 19) age is suspect because of the distinct possibility that the initial Pb (of the Amitsôq feldspar) used in the calculation evolved in more than one stage (Gancarz and Wasserburg, 1977). Indeed, when this possibility is taken into account and it is assumed that the feldspar's Pb was modified by a well-documented metamorphism at 2.7×10^9 y, the source's age increases to 4.53

TABLE 19. Summary of "Age of the Earth" Calculations*

Basis of Calculation	Ref.†	Age of Earth (10^9 y)	μ_1
Modern oceanic sediments of zero age.	1	4.43	9.82
Intersection of four isochrons plus some whole-rock data.	2	4.43	9.52
Best-fit growth curve (starting from *P*) to single-stage ages of initial Pb in galenas and feldspars.	3	4.43	9.5
Initial Pb in feldspar and 3.6×10^9 y zircon age for the rocks.	4	4.47	8.5
Assuming that Pb in the above feldspar was modified by a well-documented (4) metamorphism at 2.7×10^9 y.	4	4.53	7.5
Congruency point (see text) of four conformable galenas.	5	4.53	8.04
Initial Pb in feldspar and galena and 2.7×10^9 y zircon age for the rocks.	6	4.55	7.84
Galena, other sulfides and whole-rock isochron of 2.6×10^9 y.	7	4.56	7.49
Open-system model involving linear increase in the value of μ_S since the time of formation of the Earth, or over the past 3.7×10^9 y.	8	4.59	variable

*Initial footnote of Table 18 applies.

†References: (1) Patterson (1956), (2) Stacey and Kramers (1975), (3) Doe and Stacey (1974), (4) Gancarz and Wasserburg (1977), (5) this work, (6) Tilton and Steiger (1969), (7) Bugnon *et al.* (1979), (8) Sinha and Tilton (1973).

$\times 10^9$ y (Gancarz and Wasserburg, 1977).

The last entry in Table 19 is based on an open-system model involving linear increase of the μ_S value at least over the past 3.7×10^9 y. There is no evidence in Fig. 59 for such a process. In addition, the Pb composition of group *A* galena is compatible with its evolution in a single stage in a closed system whose age is close to the age of meteorites. It thus seems reasonable to discount the last entry from the statistics.

The remaining four entries raise in the author's mind the least objections, and on their basis it is concluded that the current best estimate of the age of the Earth is $4.53–4.56 \times 10^9$ y. The μ_S values associated with this age are in the range of 7.5–8.0. This range suggests a mild degree of U/Pb heterogeneity in the ancient sources of the order of ~4%. The evidence for source heterogeneity is more clearly projected from consideration of $K_S \equiv (^{232}Th/^{238}U)_S$. Contrary to μ_S, and as can be seen from Table 20, K_S is insensitive to small changes in the age of the source. For example, K_S for Barberton is constant at 4.19 to within ±0.2% irrespective of whether the source is 4.45 or 4.65×10^9 y. Comparison of K_S values for the sources of the old conformable galenas of group *A* discussed earlier shows clearly that these sources exhibit Th/U heterogeneity of the order of ~3%. It should be mentioned that there exists a serious discrepancy in Manitouwadge K_S data stemming primarily from disagreement on $^{208}Pb/^{204}Pb$ for the galena (see Table 18). Discounting this sample, the average for the source of the three samples is $K_1 = 4.30 \pm 0.13$, as compared with $K = 3.8$ for meteorites (Tilton, 1973). Apparently, very early differentiation processes enhanced the concentration of Th relative to U in the ancient terrestrial sources. In summary, then, the following are, in the author's opinion, the best estimates for the parameters of the ancient terrestrial sources:

Age in 10^9 years: 4.53–4.56

μ_S: 7.5–8.0

K_S: 4.18–4.44

Recently Manhes *et al.* (1979) estimated the age of the Earth to be $4.49 \pm 0.17 \times 10^9$ y. These authors adopted a statistical approach encompassing all available good-quality Pb isochron data, including those of samples as young as 2×10^9 y. Such an approach suffers from two weaknesses: (1) it invariably includes samples which evolved their leads in multiple rather than in two stages, as the calculation generally assumes, and (2) it is a general terrestrial phenomenon that μ_S tends to increase as the magma extrusion age is decreased. The trend becomes quite apparent in samples younger than $\sim 2.7 \times 10^9$ y (Oversby,

TABLE 20. Summary of Calculated* $K_S \equiv (^{232}Th/^{238}U)_{source}$

Galena	Ref.†	K_S‡ for the Assumed Source Age (in 10^9 y)		
		4.45	4.55	4.65
Timmins	1	4.32	4.31	4.29
Manitouwadge	4	4.75	4.74	4.71
Manitouwadge	5	4.25	4.24	4.22
Barberton	5	4.20	4.19	4.18
Big Stubby	6	4.45	4.44	4.43

*Initial footnote of Table 18 applies.
†Same as in Table 18.
‡Calculated from the relationship

$$\left(\frac{^{208}Pb}{^{206}Pb}\right)^* = K_S\left(\frac{e^{\lambda_2 T} - e^{\lambda_2 t}}{e^{\lambda_8 T} - e^{\lambda_8 t}}\right),$$

where λ_2 and λ_8 are the decay constants of ^{232}Th and ^{238}U, respectively. T and t are determined from Equation 1 (see text), and $(^{208}Pb/^{206}Pb)^*$ is obtained from the relationship

$$\left(\frac{^{208}Pb}{^{206}Pb}\right)^* = \frac{(^{208}Pb/^{204}Pb)_G - (^{208}Pb/^{204}Pb)_P}{(^{206}Pb/^{204}Pb)_G - (^{206}Pb/^{204}Pb)_P}.$$

1976). As more of these young samples are included in the statistics, the age is expected to slide downwards. As it stands now, the age obtained is very imprecise because of the nondiscriminating nature of the approach.

Strictly speaking, the average age of $\sim 4.54 \times 10^9$ y dates the last major fractionation process that enriched the source in U and Th relative to Pb as compared with the average solar system material ($\mu \sim 0.3, K \sim 3.8$). If such fractionation took place within the planet and was not a preexisting characteristic of the accreted debris, then the age obtained would be that of the internal event, e.g., core formation. Irrespective of the strict interpretation of the age, the fact that it is very close to the age of meteorites indicates that elemental fractionation took place within $1-3 \times 10^7$ y after the accretion of the primary materials. This result is compatible with current theories of terrestrial planet formation, including those for which complete accretion requires $\sim 10^8$ y (Wetherill, 1980).

If it is further verified that the various classes of meteorites have a constant K_S which is indeed different from that of the Earth, then an element of ambiguity in the meaning of the $\sim 4.54 \times 10^9$ y will be removed. Since both Th and U are refractory, then, rather than appealing as usual to possible Pb loss by volatilization from the primary materials to explain high μ_S and K_S values, magmatic processes (e.g., partial melting, fractional crystallization), in which the individual chemical affinities of the three elements are displayed, would have to be invoked to explain the characteristic terrestrial K_S. Such processes would most plausibly be assumed to have been operative *within* the planet, in which case the $\sim 4.54 \times 10^9$ y age would be dating a planetary event close to the time of accretion of the planet.

References

Bugnon, M.-F., F. Tera, and L. Brown, Are ancient lead deposits chronometers of the early history of Earth?, *Carnegie Inst. Wash. Year Book 78*, 346–352, 1979.

Bugnon, M.-F., F. Tera, and L. Brown, Unpublished data, 1980.

Doe, B. R., and J. S. Stacey, The application of lead isotopes to the problem of ore genesis and ore prospect evaluation: a review, *Econ. Geol., 69*, 757–776, 1974.

Gancarz, A. J., and G. J. Wasserburg, Initial Pb of Amitsôg gneiss, West Greenland, and implications for the age of the earth, *Geochim. Cosmochim. Acta, 41*, 1283–1301, 1977.

Jaffery, A. H., K. F. Flynn, L. E. Glendenin, W. C. Bentley, and A. M. Essling, Precision measurements of half-lives and specific activities of ^{235}U and ^{238}U, *Phys. Rev. C4*, 1889–1906, 1971.

LeRoux, L. J., and L. E. Glendenin, Half-Life of Thorium-232, *Proc. Nat. Conf. on Nuclear Energy*, Pretoria, April, 1963.

Manhes, G., C. J. Allègre, B. Dupré, and B. Hamelin, Lead-lead systematics, the "age of the Earth" and the chemical evolution of our planet in a new representation space, *Earth Planet. Sci. Lett., 44*, 91–104, 1979.

Oversby, V. M., Isotopic ages and geochemistry of Archaean acid igneous rocks from the Pilbara, Western Australia, *Geochim. Cosmochim. Acta, 40*, 817–829, 1976.

Patterson, C., Age of meteorites and the earth, *Geochim. Cosmochim. Acta, 10*, 230–237, 1956.

Sangster, D. F., and W. A. Brook, Primitive lead in an Australian Zn-Pb-Ba deposit, *Nature, 270*, 423, 1977.

Sinha, A. K., Personal communication, 1980.

Sinha, A. K., and G. R. Tilton, Isotopic evolution of common lead, *Geochim. Cosmochim. Acta, 37*, 1823–1849, 1973.

Stacey, J. S., and J. D. Kramers, Approximation of terrestrial lead isotope evolution by a two-stage model, *Earth Planet. Sci. Lett., 26*, 207–221, 1975.

Tatsumoto, M., R. J. Knight, and C. J. Allègre, Time differences in the formation of meteorites as determined from the ratio of lead 207 to lead 206, *Science, 180*, 1279–1283, 1973.

Tilton, G. R., Isotopic lead ages of chondritic meteorites, *Earth Planet. Sci. Lett., 19*, 321–329, 1973.

Tilton, G. R., and R. H. Steiger, Mineral ages and isotopic composition of primary lead at Manitouwadge, Ontario, *J. Geophys. Res., 74*, 2118–2132, 1969.

Wetherill, G. W., Formation of the terrestrial planets, *Annu. Rev. Astron. Astrophys., 18*, 77–113, 1980.

Inert Gases on Venus

G. W. Wetherill

Measurements of the chemical concentrations and isotopic compositions of the inert gases have played a major role in our attempts to understand the record of the early solar system, as preserved in meteorites as well as in lunar and planetary rocks and atmospheres. The reason for this is at first glance paradoxical: these gases are the most minor constituents of these bodies. Whereas chemically reactive volatile elements such as mercury and iodine are depleted on the Earth by a factor of only about 100 relative to solar composition, at the time of its formation the Earth was depleted by factors of about 10^{10} in neon and 10^7 in krypton. A consequence of this enormous depletion is that, after the depletion, it became very easy to "contaminate" the Earth's rare gas inventory by small additions of inert gases from other sources. For example, 99.6% of the argon in the atmosphere is radiogenic ^{40}Ar, produced by the radioactive decay of the rare potassium isotope ^{40}K. The very small initial argon content of the Earth was nearly completely overwhelmed by this later addition of ^{40}Ar. The inert gases are therefore sensitive indicators of events which occurred during Earth history, the effects of which are negligible for the more abundant elements. For this reason, measurements of atmospheric inert gases have been given high priority in spacecraft missions to other planets.

The inert gases in the Venus atmosphere were studied by the U.S. Pioneer Venus atmospheric entry mission and the U.S.S.R. Venera lander missions in December 1978. A surprising discovery was that neon and the nonradiogenic argon isotopes ^{36}Ar and ^{38}Ar were more abundant on Venus than on the Earth by a factor of about 100. (Data summarized by Pollack and Black, 1979; Hoffman *et al.,* 1980.)

In view of the ease with which a planet can be "contaminated" with rare gases, discussed above, one might think that this result could easily be explained in terms of impacts on Venus early in its history by a fairly small number of gas-rich planetesimals. However, dynamical studies (Wetherill, 1975) show that for any source of projectiles in orbit about the Sun subsequent to the accumulation of the planets, the impact rate on the Earth would be very similar to that on Venus, and therefore this explanation cannot produce the observed difference. It seems that this excess gas must date back to the time of formation of Venus.

In the present work an examination is made into the circumstances under which the difference between Earth and Venus (and Mars) fits into theories wherein the terrestrial planets formed by a gradual sweeping-up of planetesimals in an essentially *gas-free* protoplanetary swarm (Safronov, 1969; review by Wetherill, 1980a). It will be proposed that the excess inert gases were implanted by a somewhat enhanced solar wind bombardment (factor of 50–500) during the first 10^5 years of planetesimal growth. During this time the disk-shaped protoplanetary swarm will be opaque to radially directed particles from the Sun, and only the inner edge of the swarm will be irradiated. If this material ultimately is preferentially incorporated into Venus rather than the Earth, then Venus will carry excess solar inert gas. In earlier discussions a solar wind source was rejected on the grounds that in the Sun and solar wind, neon is more abundant than ^{36}Ar by a factor of about 30. This imposes the requirement that some mechanism for preferential retention of argon relative to neon must exist, because on Earth and Venus ^{36}Ar is about twice as abundant as neon. Knowledge of conditions in the protoplanetary swarm is insufficient to *predict* anything about this mechanism. However, it is ob-

served that solar wind neon is depleted relative to argon by a factor of ~5 in the relatively young lunar surface material. Neon can diffuse from the $\sim 10^{-6}$ cm implantation depth of solar wind at temperatures of about 300°C in times of $\sim 10^6$ years, whereas argon is nearly completely retained under these conditions. Therefore the possibility that the necessary neon loss has occurred cannot be readily excluded.

In alternative theories for the origin of the terrestrial planets it is assumed that the entire formation of the planets took place in the presence of a gaseous solar nebula, either as giant gaseous protoplanets (e.g., Cameron, 1978) or by a more gradual sweep-up of planetesimals (Hayashi *et al.*, 1977; Horedt, 1979) in the presence of nebular gas. Theories of this type should certainly be considered seriously, but they do have difficulty in explaining the distinctly nonsolar isotopic composition of neon and xenon in the Earth's atmosphere. If the Earth formed in a gaseous nebula, it seems likely that large amounts of gas of solar composition would be gravitationally bound to the Earth. Even if an adequate mechanism could be found to remove excess gas of this kind (e.g., Sekiya *et al.*, 1979), gas of solar composition would dominate the residual atmospheric composition, and it would be difficult to establish the obviously nonsolar inert gas composition of the Earth's atmosphere, as well as that of the Ne found in glassy rims of basalts (Craig and Lupton, 1976).

For this reason, most attempts to understand the inert gases in the Earth's atmosphere have assumed that these gases were absorbed or weakly chemically bonded in some way to "carrier" dust grains present among those that accumulated to form the planetesimals from which Earth ultimately formed after the dissipation of nebular gas. The inert gases were then incorporated into the Earth and its atmosphere by the sweep-up of these planetesimals. Preferential absorption of the heavier inert gases, as observed in laboratory experiments, would then explain the nonsolar elemental composition of the Earth's inert gases. The observed terrestrial isotopic anomalies in neon and xenon still must be explained, either in terms of some complex mass fractionation events associated with gas loss prior to the Earth's growing large enough to bind the bases gravitationally, or by addition of material with a distinctly different nucleosynthetic history.

A grain accretion theory of this general type has been proposed by Pollack and Black (1979) to explain the observed excess of neon and argon on Venus (as well as the observed deficiency on Mars). In this theory it is assumed that both the Earth and Venus formed from grains which absorbed gas from a solar nebula of the same composition. Pollack and Black also assume that in the region of Venus the grains adsorbed about 50 times as much gas as in the Earth region, because they hypothesize that during the formation of Venus the nebular gas pressure was 50 times greater even though the temperatures were very nearly identical at the position of Earth and Venus. This assumption runs contrary to the usual cosmochemical opinion that the temperature increases rapidly as one approaches the Sun. These authors present qualitative reasons for believing that this constant-temperature condition may have existed at an early stage of star formation. While the reasons for believing that these conditions ever existed are far from compelling, there is the additional problem that such a steep pressure gradient would lead to large relative velocities between the planetesimals, which must be formed before the gas is dissipated if planets are to grow.

As discussed by Kusaka *et al.* (1970) and Whipple (1973), in the presence of a pressure gradient the gas velocity will differ from the Keplerian velocity

because the gas will be partially supported by the pressure gradient:

$$V_g^2 = V_k^2 + \frac{r}{\rho_g}\frac{dP_g}{dr}, \qquad (1)$$

where V_g and V_k are the gas and Keplerian velocities, r is the heliocentric distance, ρ_g the gas density, and dP_g/dr the pressure gradient. An increase in pressure at constant temperature of a factor of 50 between 1.0 A.U. and 0.7 A.U. will cause the velocity of the gas to be about 5 km/sec less than the Keplerian velocity. Small planetesimals will be swept along with the gas, whereas large bodies will move more nearly at the Keplerian velocity. The resulting relative velocities will be far above the escape velocity of any planetesimals which may have formed, and it is hard to see how they could grow, rather than fragment with their collision debris spiraling sunward under the gas drag force.

As mentioned earlier, in the present work another hypothesis is proposed to explain the excess ^{36}Ar and Ne on Venus. It is proposed, not that the inert gas "carriers" contained more gas at the position of Venus in the solar nebula, but that all the carrier material had about the same gas content and that Venus received much more of this material than the Earth. It is suggested that the excess gas was implanted on the surfaces of small fragments and planetesimals by solar wind in the early stage of terrestrial planet formation. During this early stage, most of the planetesimal mass was confined to a disk about 10^5 km thick, determined by the magnitude of the random vertical velocity. Because the range of the solar wind particles is only about 10^{-6} cm, a sufficiently thin disk containing the mass of the terrestrial planets will be opaque to solar wind, and all the implantation will take place on the innermost edge of the disk. Because the gas-rich irradiated material occurs initially in the inner portion of the nebula, one would expect at least qualitatively this material to be preferentially incorporated into Venus and Mercury, rather than into Earth and Mars.

As larger and larger planetesimals grow in the preplanetary disk, the ratio of surface area to mass will decrease, and the disk will become more transparent. Ultimately the solar wind will penetrate the entire disk, as in the present solar system, but if by this time most of the mass is in large planetary embryos, the total cross-sectional area of the planetesimals will be small, and the implantation of solar wind will effectively terminate.

This general scenario has been explored more quantitatively by use of two existing quantitative theories for the early stage of planetary growth: the numerical work of Greenberg *et al.* (1978) and Greenberg (1980), and the analytical theory of Safronov (1969). The differences between the results of these workers are significant, but discussion of the relative merits of their two theories is not the subject of the present discussion. Instead, the magnitude of the implanted argon and the depth of penetration into the swarm has been calculated for both theories. It is found that in either case an adequate quantitity of ^{36}Ar will be implanted during planetesimal growth, provided that the solar wind flux is moderately higher (factor of 50–500) than at present. There is no direct evidence that this was the case, but the enhancement is modest when compared to the 10^6- or 10^7-fold enhancement often attributed to the Sun passing through a "T-Tauri phase" early in its history.

In the case of the Greenberg *et al.* calculations, 10^{25}-g (900 km radius) bodies form within about 10^5 years (Fig. 60). During most of this time most of the mass and an even greater fraction of the area remains in small bodies of relatively large cross-section. Under these conditions the penetration

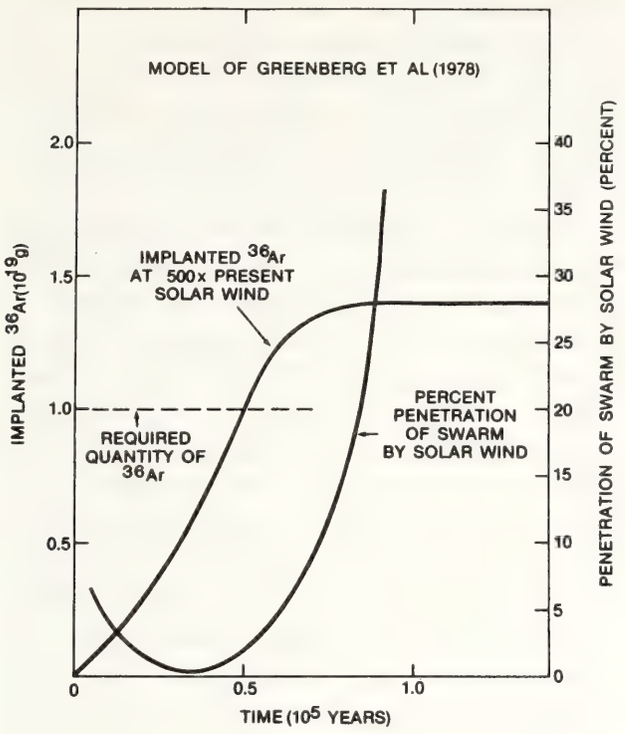


Fig. 60. Calculation of implanted ^{36}Ar on planetesimal fragments during accumulation using the model of Greenberg *et al.* (1978) and Greenberg (1980). Results for the "intermediate material case" were extrapolated beyond 54,000 years by use of the gravitational cross section to calculate the runaway growth of the largest bodies, in accordance with the discussion of Greenberg (1980).

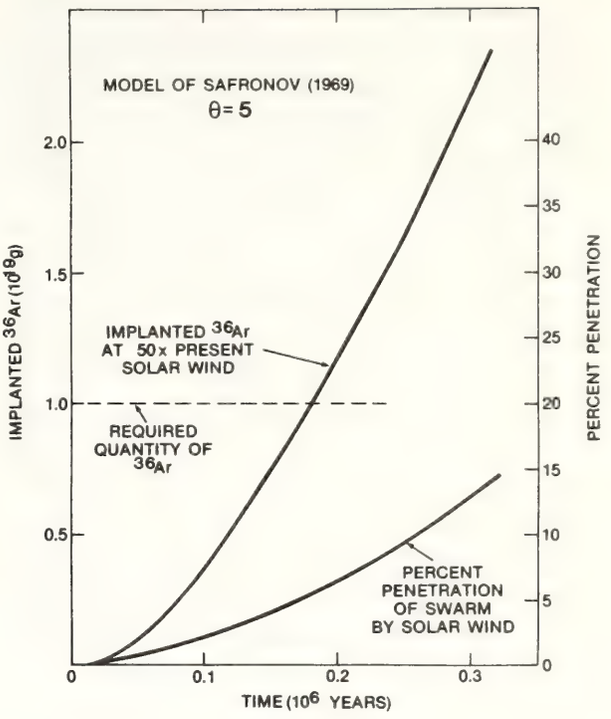


Fig. 61. Calculated implantation of ^{36}Ar on planetesimal fragments using the analytical expressions given by Safronov (1969).

of the swarm remains low, and the irradiation is confined to the inner portion of the disk. In this model, the disk "clears" quite suddenly, and the rate of gas implantation drops sharply. For this model the implantation terminates automatically, and the enhanced solar wind could continue for a while without too much implantation of gas in the Earth zone.

In the case of the Safronov theory (Fig. 61), the mass is always concentrated in the largest bodies of the growing swarm. Relative velocities are higher, and the vertical dimension of the swarm is greater and hence tends to be more transparent. The time scale for growth is about a factor of 10 longer. If the solar wind had been enhanced by a factor of ~ 50 for 2×10^5 years, an adequate supply of ^{36}Ar would be implanted. After this time the solar wind flux would have to drop to near its present value if excessive implantation as deep as Earth and Mars is to be avoided.

As described above and as shown more quantitatively in Figs. 60 and 61, both of these "rival" models for the initial stages of planetary accumulation under gas-free conditions can be compatible with implantation of solar wind gas in the required amount without very strange assumptions about the solar wind flux. In order for the present theory to be complete, two additional requirements must be met:

(1) The implanted ^{36}Ar must be retained by the planetesimals, and at some stage most of the neon must be lost. As discussed earlier, the loss of neon may not pose too serious a problem, but detailed modeling of this is thought premature in view of our lack of knowledge about the thermal history of planetesimals. The $^{20}Ne/^{22}Ne$ ratio in Earth's atmosphere is consistent with diffusive mass loss of Ne, but

the more solar ratio found on Venus (Hoffman *et al.*, 1980) is harder to explain. However, the accuracy of this measurement is not great. Actually, retention of ^{36}Ar could be a greater problem than achieving loss of Ne. Furthermore, this difficulty is common to the grain accretion hypothesis as well as to that described here. The problem is that it is often suggested that the planetesimals from which the Earth was formed were melted by ^{26}Al (Urey, 1955) or by ohmic currents induced by a T-Tauri solar wind (Sonett *et al.*, 1970). This possible early melting has been proposed to account for the iron/silicate difference between the Earth and the Moon (Kaula and Harris, 1975), the well-known early melting of the eucrite parent body (Lugmair, 1974; Birck and Allègre, 1978), the proximity of the presumably differentiated "S" asteroids (Chapman, 1976) to the Sun (Herbert and Sonett, 1978) and to the residual Earth swarm (Wetherill, 1977; Wetherill and Williams, 1979), and the observed deficiency of radiogenic ^{129}Xe in Earth's atmosphere. If these bodies were melted, the carrier bodies required for either the Pollack and Black hypothesis or the present hypothesis must have escaped melting or at least outgassing, and it isn't obvious why this should be the case.

(2) The carrier bodies must be preferentially incorporated into Venus. This problem appears in a different light when one considers recent studies of the late stages of simultaneous multiplanet accumulation (Cox, 1978; Wetherill, 1980b), in contrast to earlier, more qualitative discussions in which each planet has its own "feeding zone." In the earlier models it would seem that the problem is to avoid the collection of most of the carrier bodies by Mercury. In the newer work, it is found that if premature isolation of embryos (and too many terrestrial planets) is to be avoided, there must be considerable mixing of material between the regions of the different planets. To a significant extent, this result is not simply "what the computer tells me," but follows from general considerations of energy and angular momentum conservation (Wetherill, 1978).

Work on simultaneous multiplanet accumulation is not well developed at present, and published work considers only the case of planetesimals of equal size. A calculation of this kind has been carried out in order to determine the ultimate heliocentric distance of the inner 5% of a swarm of one hundred 1.2×10^{26} g bodies; this mass corresponds to the present mass of the terrestrial planet regions (Fig. 62). It is found that about 90% of the innermost material ultimately is collected by the "Venus" embryo. This is short of the required ~100-fold enrichment observed on Venus. A real protoplanetary swarm will consist of a mass spectrum of bodies, and the abundant smaller objects will result in more collisional dissipation of energy of relative motion. This will result in less-eccentric orbits and less mixing between zones, and greater concentration of carrier bodies on Venus. However, it isn't clear whether or not premature isolation of embryos will preclude the nec-

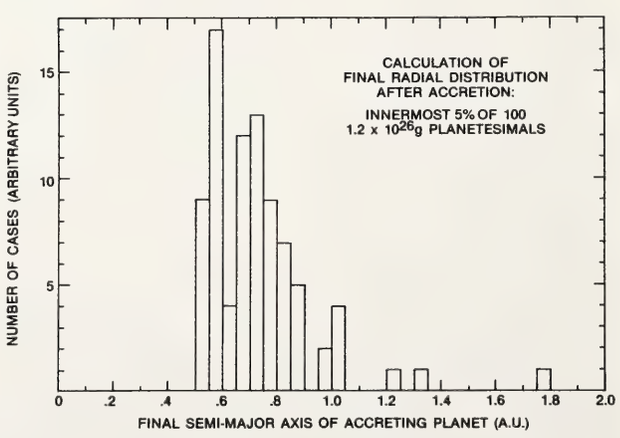


Fig. 62. Results of accumulation calculation of one hundred 1.2×10^{26}g planetesimals using the method of Wetherill (1980b). Final semi-major axis distribution of material initially confined to innermost 5% of swarm.

essary enhancement of carrier impacts on Venus. Special techniques (e.g., "superdamping" [Wetherill, 1980b]) have been developed to deal with this problem, but so far these developments have not proven adequate to the task. It should be noted that this problem is also common to both the grain accretion hypothesis and the present solar wind hypothesis.

Rather than try to do too much with presently inadequate theory, an alternative is to look for observational tests of these hypotheses. Unfortunately we then encounter presently inadequate observations. At least in the most straightforward version of the present hypothesis, it would be expected that Venus' ^{36}Ar/Kr ratio (by volume) would be nearer the solar value of ~2500—much higher than the terrestrial value of 31. The observational results are not clear. Istomin *et al.* (1980) report a ratio of 43 from the Venera 11 and 12 data, whereas Hoffman *et al.* (1980) give only a lower limit for this ratio which is significantly higher than the result of Istomin *et al.* If the present hypothesis is correct, the ratio for Venus should be somewhat less than the solar value because Venus should have received its share of the nonsolar inert gases clearly present on Earth and Mars. However, the Venera result would require that Venus received somewhat more nonsolar Kr than the Earth received ^{36}Ar, which would simply resurrect the original problem of understanding how Venus could receive much more nonsolar gas of some kind than the Earth. On the other hand, since the Pioneer data are only a lower limit, it is compatible with solar Kr on Venus.

The xenon situation is also unclear, inasmuch as no Xe data have been presented. The solar ^{36}Ar/Xe ratio is about 20,000. However, the Pioneer Venus Sounder Probe neutral mass spectrometer did not observe any Xe, and it appears that the lower limit for the ^{36}Ar/Xe ratio (by volume) must be at least 500 (P. R. Hodges and T. M. Donahue, private communication, 1980). Since the terrestrial ratio is about 400, at first glance this lower limit for Venus doesn't appear very useful. However, it is commonly assumed that most of the surficial xenon on the Earth is adsorbed on sedimentary rocks (Fanale and Cannon, 1972) in order to explain the ~10-fold depletion of the terrestrial (and Martian) atmosphere in xenon relative to the so-called "planetary" component found in meteorites. If the terrestrial value is corrected for this adsorbed xenon, the terrestrial value for the ^{36}Ar/Xe ratio becomes 32. It doesn't seem plausible that much Xe at all would be adsorbed on whatever sediments there may be on Venus, in view of the 400°C surface temperature. Therefore, it seems unlikely that Venus can contain "planetary" xenon. Difficulty in interpreting terrestrial xenon in terms of trapped meteoritic Xe was already apparent by the large difference in isotopic composition between terrestrial xenon and the trapped component in meteorites, as well as the complex nature of the latter (Manuel *et al.*, 1972; Srinivisan *et al.*, 1977). If terrestrial xenon is not principally adsorbed on sediments, then xenon on both Earth and Venus could be dominated by the same component, which would be neither solar nor trapped meteoritic. Presence of this anomalous xenon on Earth and Venus would not argue against a solar wind origin for most of Venus' inert gas, because this additional xenon would overwhelm the expected small solar xenon contribution. At least workers in this field should drop the confusing adjective "planetary" when describing the meteoritic inert gases, and reserve this term for the gases actually found on planets.

Neither our theoretical understanding of planet formation nor our measurements of inert gases on Mars and Venus are yet adequate to determine whether the hypothesis proposed

is likely to be correct. The purpose of this article is not to argue the correctness of this hypothesis, but to define the conditions under which Venus' inert gases could come from the solar wind. It is presented in the belief that all possible hypotheses compatible with present knowledge should be developed in order that there be the lively interaction between future theory and observation that is a necessary characteristic of a healthy science.

References

Birck, J. L., and C. J. Allègre, Chronology and chemical history of the parent body of basaltic achondrites by the ^{87}Rb-^{87}Sr method, *Earth Planet. Sci. Lett., 39*, 37–51, 1978.

Cameron, A. G. W., The primitive solar accretion disk and the formation of the planets, in *The Origin of the Solar System*, pp. 49–74, S. F. Dermott, ed., Wiley, New York, 1978.

Chapman, C. R., Asteroids as meteorite parent-bodies: the astronomical perspective, *Geochim. Cosmochim. Acta, 40*, 701–719, 1976.

Cox, L. P., Numerical simulation of the final stages of terrestrial planet formation. Ph.D. dissertation, Department of Earth and Planetary Sciences, Massachusetts Institute of Technology, Cambridge, Massachusetts, 1978.

Craig, H., and J. E. Lupton, Primordial neon, helium, and hydrogen in oceanic basalts, *Earth Planet. Sci. Lett., 31*, 369–385, 1976.

Fanale, F. P., and W. A. Cannon, Origin of planetary primordial rare gas: the possible role of adsorption, *Geochim. Cosmochim. Acta, 36*, 319–328, 1972.

Greenberg, R., J. F. Wacker, W. K. Hartmann, C. R. Chapman, Planetesimals to planets: numerical simulation of collisional evolution, *Icarus, 35*, 1–26, 1978.

Greenberg, R., Numerical simulation of planet growth: early runaway growth, *Lunar Science XI*, 365–367, Lunar and Planetary Institute, Houston, 1980.

Hayashi, C., K. Nakazawa, and I. Adachi, Long-term behavior of planetesimals and the formation of the planets, *Publ. Astron. Soc. Japan, 29*, 163–196, 1977.

Herbert, F., and C. P. Sonett, Primordial metamorphism of asteroids via electrical induction in a T Tauri–like solar wind, *Astrophys. Space Sci., 55*, 227–239, 1978.

Hoffman, J. H., R. R. Hodges, Jr., T. M. Donahue, and M. B. McElroy, Composition of the Venus lower atmosphere from the Pioneer Venus mass spectrometer, preprint, *J. Geophys. Res.*, in press, 1980.

Horedt, G. P., Cosmogony of the solar system, *The Moon and Planets, 21*, 63–121, 1979.

Istomin, V. G., K. V. Grechnev, and V. A. Kochnev, Mass spectrometry of the Venus' lower atmosphere: krypton isotopes and other recent results of processing the data of measurements on-board the Venera 11, 12 spacecraft, preprint, submitted to *J. Geophys. Res.*, 1980.

Kaula, W. M., and A. W. Harris, Dynamics of lunar origin and orbital evolution, *Rev. Geophys. Space Phys., 13*, 363–371, 1975.

Kusaka, T., T. Nakano, and C. Hayashi, Growth of solid particles in the primordial solar nebula, *Prog. Theor. Physics, 44*, 1580–1595, 1970.

Lugmair, G. W., Sm-Nd ages: a new dating method, *Meteoritics, 9*, 369, 1974.

Manuel, O. K., E. W. Hennecke, and D. D. Sabu, Xenon in carbonaceous chondrites, *Nature, 240*, 99–101, 1972.

Pollack, J. B., and D. C. Black, Implications of the gas compositional measurements of Pioneer Venus for the origin of planetary atmospheres, *Science, 205*, 55–59, 1979.

Safronov, V. S., Evolution of the protoplanetary cloud and formation of the earth and planets, Moscow, Nauka; translated for NASA and NSF by Israel Program for Scientific Translations (1972). NASA TT F-677, 1969.

Sekiya, M., K. Nakazawa, and C. Hayashi, Dissipation of the rare gases contained in the primordial Earth's atmosphere, preprint, KUNS 512, 1979.

Sonett, C. P., D. S. Colburn, K. Schwartz, and K. Keil, The melting of asteroidal-sized bodies by unipolar dynamo induction from a primordial T Tauri sun, *Astrophys. Space Sci., 7*, 446–488, 1970.

Srinivisan, B., J. Gros, and E. Anders, Noble gases in separated meteorite minerals: Murchison (C2), Ornans (C3), Karoonda (C5), and Abee (E4), *J. Geophys. Res., 82*, 762–778, 1977.

Urey, H. C., The cosmic abundances of potassium, uranium, and thorium, and the heat balances of the Earth, Moon, and Mars, *Proc. Nat. Acad. Sci. U.S.A., 41*, 127–144, 1955.

Wetherill, G. W., Late heavy bombardment of the Moon and terrestrial planets, *Proc. 6th Lunar Sci. Conf.*, 1539–1559, 1975.

Wetherill, G. W., Evolution of the Earth's planetesimal swarm subsequent to the formation of the Earth and Moon, *Proc. 8th Lunar Sci. Conf., 1*, 1–16, 1977.

Wetherill, G. W., Accumulation of the terrestrial planets, in *Protostars and Planets*, pp. 565–598, T. Gehrels, ed., University of Arizona Press, Tucson, 1978.

Wetherill, G. W., Formation of the terrestrial planets, *Annu. Rev. Astron. Astrophys., 18*, 77–113, 1980a.

Wetherill, G. W., Numerical calculations rele-

vant to the accumulation of the terrestrial planets, *Special Papers, Geol. Assoc. of Canada,* in press, 1980b.

Wetherill, G. W., and J. G. Williams, Origin of differentiated meteorites, in *Origin and Distribution of the Elements,* second symposium, pp. 19–31, L. H. Ahrens, ed., Pergamon Press, New York, 1979.

Whipple, F. L., Radial pressure in the solar nebula as affecting the motions of planetesimals, in *Evolutionary and Physical Properties of Meteoroids,* pp. 355–361, C. L. Hemenway, P. M. Millman, and A. F. Cook, eds., NASA Sp-319, 1973.

Isotopic Anomalies in the Early Solar System

Typhoon Lee and Louis Brown

Nuclides heavier than ^{4}He in the solar system are believed to have been primarily synthesized over a span of billions of years prior to the solar system formation in many galactic sources (e.g. supernovae). Each of these nucleosynthetic sources presumably produces a characteristic set of isotopic compositions reflecting its own physical condition. Material from these sources seems to have been well mixed before the formation of planetary bodies in the solar system, since the Earth, the Moon, and various meteorites all have a nearly uniform, "cosmic" isotopic composition. In the past several years, variations relative to the cosmic composition have been discovered in many elements. These variations (so-called "anomalies") indicate that the mixing was incomplete. Hence the record of distinct nucleosynthetic events may be recoverable. Another type of recently found anomaly is caused by the decay of radioactive nuclides with mean lives of 10^6–10^7 years, which are extinct today but were present in the early solar system. These extinct nuclides give the all-important temporal information about the nucleosynthetic sources. Details of isotopic anomalies can be found in, for example, Lee (1979). We have begun a study of solar system isotopic anomalies.

Search for FUN Mg

The most spectacular example of isotopic anomaly was found in two Ca-Al–rich inclusions of the Allende meteorite, EK1-4-1 and C1. Almost all of their constituent elements show correlated isotopic anomalies due to nuclear processes. In addition, they show large coupled mass-dependent isotopic fractionation in O, Mg, and Si. Thus they have been dubbed "FUN" (for *F*ractionation and *U*nknown *N*uclear). The FUN anomaly is important because the correlated nuclear effects can be compared with the characteristic signatures of nucleosynthetic sources and perhaps can be used to identify the origin of solar system matter. This potential is presently hindered by the paucity of FUN samples. So far, less than one gram of material has been identified. A study of an element with a concentration of 1 ppm (parts per million) would probably consume the entire supply. The difficulty in finding more material is that mineralogically and chemically FUN inclusions are almost indistinguishable from the usual Ca-Al inclusions which do not show correlated nuclear effects. One method is to search for large Mg fractionation, which is a prominent signpost for FUN samples. The advantages of this method are (1) solid sample grains can be directly analyzed for Mg without chemical processing, (2) very little material ($\sim 1\mu$g) is needed for the analysis, and (3) the anticipated effect is large. (The fractionation effects in EK1-4-1 and C1 are 2% and 3% per unit of mass difference, respectively.) Thus an Mg survey seems to be quite economical in both time and sample consumption. Therefore, as a first step of studying isotopic anomaly we have embarked upon an Mg survey to search for more FUN samples. Out of ~ 100 inclusions studied prior to this study, only two are FUN samples. Obviously, such a search, though potentially highly rewarding, will be a low-yield,

high-risk, and long-term effort. The National Museum of Natural History has kindly permitted us to examine their Allende collection and to select fragments which have many exposed inclusions. The exposed inclusions were further examined optically in our clean room. All inclusions weighing more than ~100 mg were documented and several crystals were picked from each of them. In addition, one fragment was obtained from the Field Museum of Natural History at Chicago, and we have been allowed to explore its interior. Also, one inclusion came from the University of Chicago. These crystals were directly loaded onto flat Re filaments with silica gel and H_3PO_4 (Lee *et al.,* 1977) and analyzed for Mg isotopic composition in the DTM 15-inch mass spectrometer. To save time, we spent typically five hours per analysis to obtain intermediate precision data, instead of the ten hours required for high-precision data. The measured Mg ratios are grouped into blocks of ten ratios each. The blocks with standard deviations of the mean $^{25}Mg/^{24}Mg$ better then 0.2% were accepted. Typically, we accumulate ten such blocks per analysis. Figure 63 summarizes the data for terrestrial standards, Allende inclusions, and the reported values for the two FUN inclusions. Percentage deviations of $^{25}Mg/^{24}Mg$ ratios relative to the reference value $(^{25}Mg/^{24}Mg)_o$ = 0.12475 (Lee *et al.,* 1977) are plotted. The average of the grand means of all our Ceylon spinel analyses, which is our primary standard, agrees with this value to within 0.07%, so we use this reference value to facilitate comparison. The data point is the grand mean of accepted blocks, and the error bar covers the range of *all* block means. The results from 11 Ceylon spinel analyses are between the two extreme cases plotted. Judging from the two terrestrial standards, effects above 2% per mass unit level can be resolved. The reproducibility of the analyses is poor. Repeated runs sometimes differ by more than 1%. This is in contrast to the reported range of 0.3% by Lee *et al.* (1977), where only blocks with standard deviations of better than 0.05% were accepted. Although the scattered ^{27}Al ions do produce rugged background bumps near mass 25, we do not think the large spread in our data is

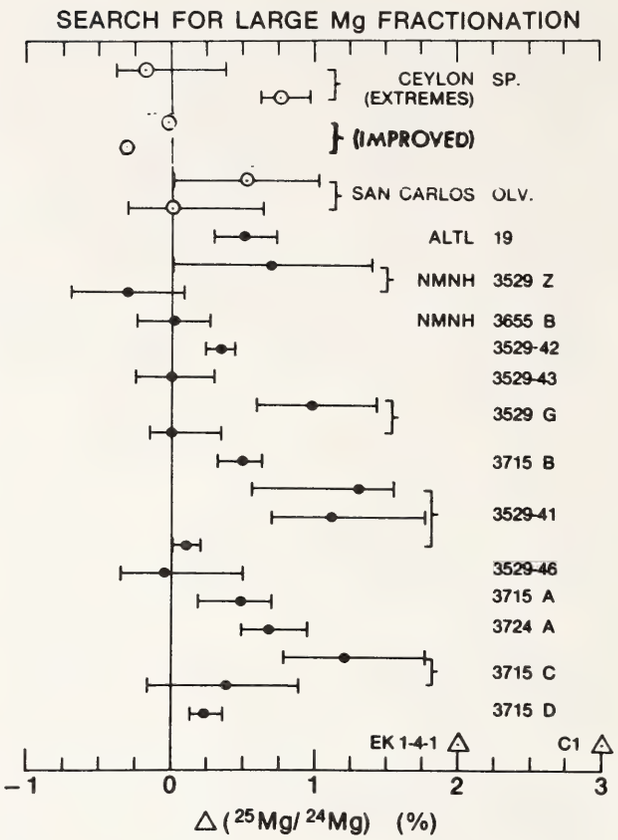


Fig. 63. The percentage deviations of measured $^{25}Mg/^{24}Mg$ ratios ($\Delta\ ^{25}Mg/^{24}Mg$) are plotted relative to the reference value ($\equiv 0$) $(^{25}Mg/^{24}Mg)_0$ = 0.12475. This reference value represents the mean of the measured $^{25}Mg/^{24}Mg$ ratios for normal terrestrial samples (Ceylon spinel and San Carlos olivine). The effect to be searched for is large $\Delta^{25}Mg/^{24}Mg \gtrsim 2\%$, similar to those reported for FUN Allende inclusions EK1-4-1 and C1, which are also plotted. Note that the error bars cover all the measured ratios during one analysis and the two Ceylon spinels analyses represent extreme cases for 11 analysis. No large $\Delta^{25}Mg/^{24}Mg$ above 2% has been detected among the 13 Allende inclusions studied so far. High-precision data for two extreme cases of six new analyses of Ceylon spinel using the V-filament and the new detector are also plotted (labeled "IMPROVED"). The error bars for these two analyses are of the same size as the circles. Evidently we can now resolve fractionation effects beyond 0.5% per amu. No sample has yet been analyzed using this improved method.

due to interferences. The reason is that the variation in $^{26}Mg/^{24}Mg$ correlates with that in $^{25}Mg/^{24}Mg$ but has a magnitude twice as large. This is the signature of mass fractionation whose effect is proportional to mass differences. Thus we believe that the spread in our data is caused by fractionation in the mass spectrometer. It is possible that the good stability during the high-precision analysis always happens at the same fractionation condition. It is also possible that the fractionation depends on the geometry of the filament. Lee *et al.,* (1977) used V-shaped Re filaments instead of the flat ones used in this study. We have finished a jig to manufacture V-shaped filaments based on the Caltech design. So far the Ceylon spinel standard has been analyzed six times using the V filament and the new detector described below. The range of $^{25}\Delta$ for those blocks with standard deviations less than 0.05% is typically 0.1% for one analysis and is from −0.35% to +0.06% for all six analyses. Two extreme cases are plotted in Fig. 63 ("Improved"). It appears that we will be able to resolve fractionation effects above 0.5% per amu using the improved method. So far, none of the 13 inclusions studied show Mg fractionation above 2% per amu, and therefore no new FUN inclusion similar to EK1-4-1 or C1 has been found. During this study we have also looked for mineralogically peculiar inclusions such as the hibonite-rich inclusion HAL studied by Lee *et al.,* (1979). None has been found.

Mass Spectrometer Improvement

It has been said, "When isotopic anomalies are expected, they are usually found" (Podosek, 1978). Confronted with the recent flurry of new anomalies, one must be doubly careful in guarding against systematic errors. In this regard, the DTM 15-inch mass spectrometer (Brown, 1979) had two shortcomings. Its source and detector slits were not adjustable from outside, thus preventing the narrowing of the slits during an analysis to search for interfering species with high resolution. Further, the scattered ions, produced when a nearby intense beam hit the flight tube, interfered with the analysis. For example, as mentioned above, the scattered ^{27}Al ions generated rugged background features near ^{25}Mg so that high-precision Mg data were unobtainable. A new detector assembly for the 15-inch mass spectrometer was recently designed, machined, and installed. It has an entrance slit shielded by two razor-blade baffles from scattered ions, all adjustable from outside by micrometers. In addition, the Faraday cup is mounted on an elevator so that it can be raised to allow the beam to enter the ion multiplier which is mounted behind the elevator. The scattering effect is greatly reduced using the new detector assembly. Figure 64 (upper trace) shows the mass spectrum of the potassium region using the old system. Features *A* and *B* were due to scattered ^{39}K ions while *D* and *E* were due to scattered ^{41}K ions on the opposite side of the tube. The maximum intensity of these features was 280 ppm of the primary beam. Figure 64 also shows (lower trace) the same region scanned using the new system. Some small ripples of yet-unexplained origin still persist, but the scattering anywhere in the flight tube has been reduced to below 5 ppm of the primary beam. This factor-of-56 improvement considerably reduces the danger of possible systematic errors due to scattering. In the new system, the detector slit can be narrowed. Since the source slit is still fixed at 0.2 mm, the maximum usable resolving power is now ~1000. This should permit us to resolve many hydrocarbon molecules.

Cr Anomaly and ^{53}Mn

Among a dozen or so elements in which isotopic anomalies have been found, most were selected for study because of the availability of analytical

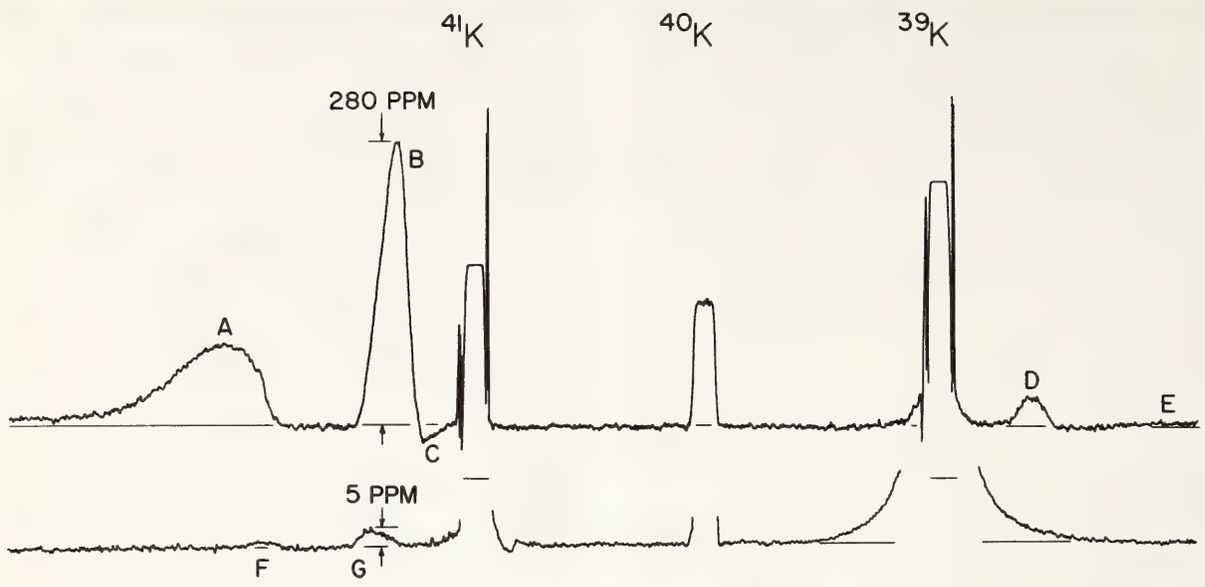


Fig. 64. The mass spectrum of potassium taken with the 15-inch spectrometer both with and without the adjustable baffles for reducing the current of scattered ions entering the detector. The upper part shows a potassium spectrum taken before mass spectrometer modification. Except for ^{39}K and ^{41}K, the electrometer gain is the same as that used for ^{40}K, whose amplitude is 6.6×10^{-14} A; ^{39}K has an amplitude of about 5.3×10^{-10} A and ^{41}K about 3.8×10^{-11} A. Features *A* and *B* result from ^{39}K striking the tube wall; the indicated height of 280 ppm is relative to ^{39}K. Feature *C* results from negative ions produced in the scattering and is not reproducible, as it depends strongly on the wall surface conditions. Features *D* and *E* result from scattering by ^{41}K and correspond to *B* and *A*. A thin line indicates the position of the electrometer base line when there is no beam present. Note the displaced base lines for ^{39}K and ^{41}K. The lower spectrum shows the low-level portion after modification. The electrometer gain is the same but the beam is 3.3 times more intense. The reduction of scattering is evident from the magnitudes of *F* and *G*.

techniques of high precision and sensitivity. The next step, clearly, is to analyze elements of astrophysical significance. Since it will take at least six months to develop such technique for a new element in the most favorable case, the choice of element has to be made very carefully. Element Cr seems to be a good candidate, for several reasons:

(1) It is a member of the iron-group elements, which are thought to be produced in the deepest interior of massive stars and hence are our best probe for the stellar core. None of the iron-group elements have yet been analyzed.

(2) The neighboring elements Ca and Ti have been found to be anomalous and to exhibit a fascinating correlation pattern which is currently under active theoretical study. The addition of Cr to this pair may yield definitive clues to the nucleosynthesis in this region, which is not now well known.

(3) ^{53}Cr is the decay product of ^{53}Mn, whose mean life is $\sim 5 \times 10^6$ years. Since two other extinct nuclides with mean lives 10^6–10^7 years have already been found, it is quite possible that ^{53}Mn was present in the early solar system. Therefore, a Cr study may yield not only stable isotope anomalies but also evidence for a new extinct nuclide.

(4) Cr is relatively abundant with a chondritic abundance of ~ 3000 ppm, so that many samples will be accessible for analysis.

We have just started the Cr isotopic study. A loading and running technique for the mass spectrometry of Cr has been devised. A microgram-sized sample may be analyzed with high precision ($\sim 0.3‰$ for the $^{50}Cr/^{52}Cr$ and $^{54}Cr/^{52}Cr$ ratios). This is about thirty times more sensitive and three times more precise than the conventional technique (Shield *et al.*, 1966). The sensitivity and precision needs to be im-

proved further, and there are still problems due to scattered ions. Using the new V-shaped filament and the new detector assembly, we hope to overcome these difficulties. A chemical procedure for separating Cr from rock samples is also being developed. Because Cr has multiple valence states and because many Cr compounds are volatile, some difficulty is anticipated.

Acknowledgements

The gracious help of B. Mason and R. Clark of the National Museum in providing the Allende fragments is appreciated. We thank E. Olsen of the Field Museum, and E. Anders and R. Clayton of the University of Chicago for additional samples. We acknowledge the skillful construction of the new detector assembly by J. Emler, and of the filament jig by M. Taylor. M. Zeff assisted some of the mass spectrometer analyses. G. J. Wasserburg and D. A. Papanastassiou of Caltech generously provided the design of the jig.

References

Brown, L., The 15-inch Mass Spectrometer, *Carnegie Inst. Wash. Year Book 78,* 419–421, 1979.

Lee, T., New isotopic clues to solar system formation, *Rev. Geophys. Space Phys., 17,* 1591–1611, 1979.

Lee, T., D. A. Papanastassiou, and G. J. Wasserburg, Mg and Ca isotopic study of individual microscopic crystals from the Allende Meteorite by the direct loading technique, *Geochim. Cosmochim. Acta, 41,* 1473–1485, 1977.

Lee, T., W. A. Russell, and G. J. Wasserburg, Ca isotopic anomalies and the lack of ^{26}Al in an unusual Allende inclusion, *Astrophys. J. Lett., 228,* 693–698, 1979.

Podosek, F., The isotopic structure in solar system materials, *Annu. Rev. Astron. Astrophys., 16,* 293–334, 1978.

Shield, W. K., T. J. Murphy, E. J. Catanzaro, and E. L. Garner, Absolute isotopic abundance ratios and the atomic weight of a reference sample of chromium, *J. Res. Nat. Bur. Stand., Sect. A, 70,* 192–197, 1966.

Meteorites from Beyond Jupiter?

*G. W. Wetherill and D. O. ReVelle**

In earlier work (Wetherill *et al.,* 1978; ReVelle and Wetherill, 1978) criteria were described for identifying certain photographically observed bright meteors (fireballs) with the recovered stony meteorites in museum collections. As presently formulated, these criteria are as follows:

1. The final altitude (end height) of the meteor agrees with that calculated from single-body meteor theory (e.g. ReVelle, 1979), taking into consideration the meteor's entry angle, measured velocity, and mass, as calculated from its deceleration in the atmosphere.

2. The meteor survives deceleration from its entry velocity of 14–22 km/sec to $\lesssim$ 8 km/sec, below which the effects of ablation are greatly diminished.

3. The light curve (photographic magnitude vs. altitude, scaled for mass, entry angle, and velocity) resembles that of the photographed meteorites Pribram, Lost City, and Innisfree.

4. The dynamic mass, calculated from deceleration data, is similar in value to the photometric mass. In calculating photometric mass, the luminous efficiency (fraction of dissipated energy emitted as light) was based on comparison with photometric data for recovered fireballs (ReVelle and Rajan, 1979).

These criteria should be regarded as semi-empirical. The two recovered meteorites for which an adequately photographed trajectory exists (Lost City, Innisfree) satisfy the criteria, although when studied in detail there remain unresolved differences in the meteor phenomena exhibited by these two physically very similar objects. Lost City and Innisfree were among the brightest fireballs photographed by meteor camera networks. Experimental and theoretical studies of collisional fragmentation strongly indicate that these

*Department of Physics, Northern Arizona University, Flagstaff.

large bodies should be accompanied by a retinue of smaller objects which, because of their small mass, would be unlikely to be recovered on the ground. The number of smaller fireballs satisfying the criteria is in good agreement with this expectation, and it is plausible to identify these fireballs with strong meteorites. Since most stony meteorites with physical properties similar to Lost City and Innisfree are of the type termed "ordinary chondrites," most of the fireballs satisfying the selection criteria should also be ordinary chondrites.

In the present work, the question is raised whether or not any of these selected fireballs could be derived from comets. It is commonly believed that all meteorites are derived from asteroids (e.g., Anders, 1975). However, inasmuch as there are significant unsolved problems associated with this interpretation (Wetherill, 1974, 1976; Wasson and Wetherill, 1979), the alternative possibility that some meteorites might be of cometary origin should not be abandoned prematurely.

In most cases, the observed solar system orbit of a bright meteor or meteorite does not strongly constrain the nature of its parent body to be either asteroidal or cometary. This is a consequence of the fact that the Earth-impact probability of a comet is greatly enhanced for those few comets (such as Encke) that evolve into more asteroid-like orbits. However, meteors are known in peculiarly cometary orbits (e.g. those in retrograde orbits, or with orbits extending to or beyond the orbit of Jupiter). Do any of these presumably cometary meteors ever fulfill the criteria established for selection as meteorites?

The tentative answer to this question appears to be yes. Table 21 gives data on two fireballs with very large aphelia and which, based on the above

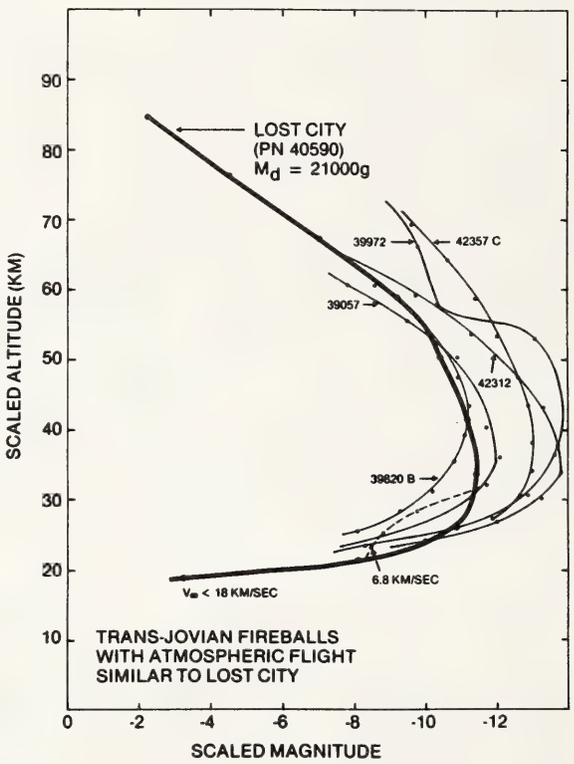


Fig. 65. Light curves of five bright meteors in Jupiter-crossing orbits with atmospheric trajectories similar to the recovered photographic meteorites Lost City and Innisfree.

TABLE 21. Trans-Jovian Fireballs Potentially Recoverable as Meteorites

Prairie Network number	orbit				velocity (km/sec)		scaled end height (km)	est. initial mass (g)
	a (A.U.)	*e*	*i* (deg)	aphelion (A.U.)	final	entry		
39057	4.17	0.76	0	7.3	6.8	14.7	22.3	140
39972	5.55	0.84	3	10.2	6.3	18.1	23.3	20
42357C	2.94	0.67	12	4.9	10.3	16.0	27.7	50
42312	3.03	0.69	14	5.1	8.7	17.5	24.4	40
39820B	3.12	0.69	11	5.3	8.3	16.7	25.5	150
39878A	2.94	0.68	22	4.9	11.1	20.0	25.8	20
42532	9.1	0.89	23	17.2	13.2	21.3	25.5	40

criteria, appear to have had a very good chance of surviving their passage through the atmosphere (McCrosky *et al.*, 1978, 1979). Except for their small mass, it seems likely that they could have been recovered as meteorites. Five others are listed which showed some, but less, success in surviving atmospheric passage, but were nevertheless identified as Type I (ordinary chondrites) by Ceplecha and McCrosky (1976).

The light curves for five of these meteors (with entry velocities < 18.1 km/sec) are compared in Fig. 65 with the light curve of the recovered fireball Lost City. Although these light curves are by no means identical, they are as similar to one another as those of the two bona fide recovered meteorites Lost City and Innisfree (Fig. 66). In contrast, more typical trans-Jovian fireballs with similar atmospheric entry velocity have very different light curves (Fig. 67).

All five of the fireballs shown in Fig. 65 are classified by Ceplecha and McCrosky as Type I, which they identify with ordinary chondrites. The first two objects listed in Table 21 have scaled end heights 1–2 km higher than those we have previously identified with ordinary chondrites. The others have even higher values of this quantity. The higher scaled end heights probably result from increased friability of the objects toward the end of their atmospheric trajectory. It is quite possible that the first two objects are actually ordinary chondrites. However, it seems at least as likely that all of these bodies are somewhat weaker than ordinary

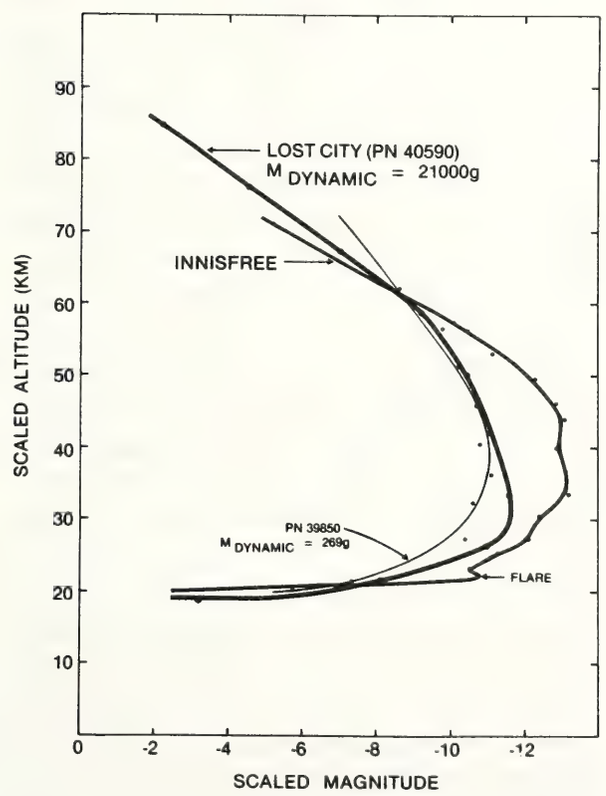


Fig. 66. Light curves of the two ordinary chondrites, Lost City and Innisfree, for which adequate atmospheric trajectories are available. PN39650 is an unrecovered Prairie Network fireball of the type previously identified as stone meteorites (Wetherill *et al.*, 1978).

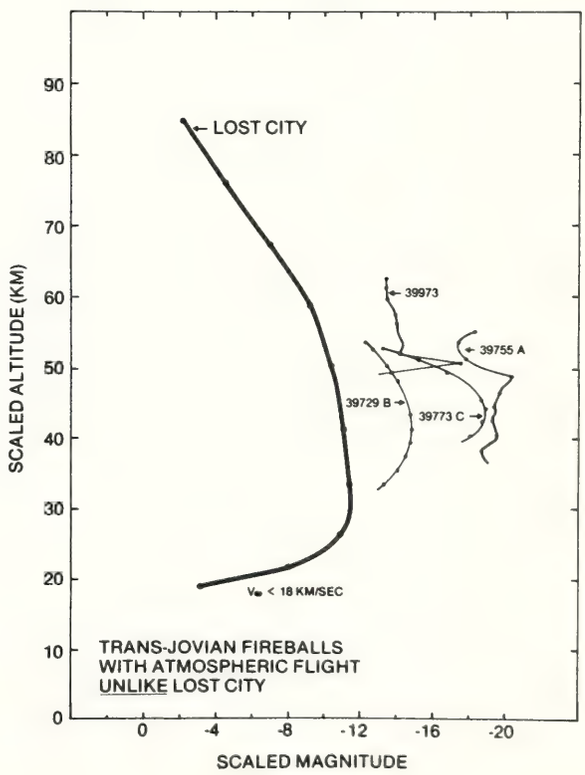


Fig. 67. Comparison of Lost City light curves with those of more typical Jupiter-crossing fireballs, exhibiting little similarity. Note that the magnitude scale of Fig. 67 is twice that of the other figures. The apparent excessive brightness of these fireballs is probably a consequence of their dynamic mass, used in scaling, being much less than their true mass. This would be expected for friable low-density objects.

chondrites, but may be carbonaceous chondrites of varying strength. A chemical association between carbonaceous chondrites and comets is usually thought to be more likely than between ordinary chondrites and comets. However, this identification does little to mitigate the problem of the near absence of main-belt asteroids with photometric properties of ordinary chondrites (Gaffey and McCord, 1978). In either case, it appears that at least the first two objects in Table 21 survived passage through the atmosphere. Because of their small entry mass, only about 25 g of 39057 and 1 g of 39972 would be expected to reach the ground. More massive objects in similar orbits should also exist, since no obvious relationship between meteor masses and orbits is observed. Based on these data, trans-Jovian meteorites could constitute several percent of the meteorites in museum collections.

References

Anders, E., Do stony meteorites come from comets?, *Icarus, 24,* 363–371, 1975.

Ceplecha, Z., and R. E. McCrosky, Fireball end heights: a diagnostic for the structure of meteoric material, *J. Geophys. Res., 81,* 6257–6275, 1976.

Gaffey, M. J., and McCord, J. B., Asteroid surface materials: Mineralogical characterizations from reflectance spectra, *Space Sci. Rev., 21,* 555–628, 1978.

McCrosky, R. E., C. Y. Shao, and A. Posen, Prairie network fireball data I. Summary and orbits. *Meteoritika, 37,* 44–59, 1978.

McCrosky, R. E., C. Y. Shao, and A. Posen, Prairie network fireball data II. Trajectories and light curves, *Meteoritika, 38,* 106–159, 1979.

ReVelle, D. O., A quasi-simple ablation model for large meteorite entry: Theory vs. observations. *J. Atmos. Terr. Phys., 41,* 453–473, 1979.

ReVelle, D. O., and R. S. Rajan, On the luminous efficiency of meteoritic fireballs, *J. Geophys. Res., 84,* 6255–6262, 1979.

ReVelle, D. O., and Wetherill, G. W., Which fireballs are meteorites? A study of the large meteor deceleration data, *Meteoritics, 13,* 612–613, 1978.

Wasson, J. T., and G. W. Wetherill, Dynamical, chemical and isotopic evidence regarding the formation locations of asteroids and meteorites, in *Asteroids,* pp. 926–975, T. Gehrels, ed., University of Arizona Press, Tucson, 1979.

Wetherill, G. W., Solar system sources of meteorites and large meteoroids, *Annu. Rev. Earth Planet. Sci., 2,* 303–331, 1974.

Wetherill, G. W., Where do the meteorites come from? A reevaluation of the earth-crossing Apollo objects as sources of chondritic meteorites, *Geochim. Cosmochim. Acta, 40,* 1297–1317, 1976.

Wetherill, G. W., D. O. ReVelle, and R. S. Rajan, Identification of bright meteors with meteorites, *Carnegie Inst. Wash. Year Book 77,* 482–490, 1978.

Multiple Cosmic Ray Exposure Ages of Meteorites

G. W. Wetherill

During a meteorite's flight in interplanetary space, it is bombarded by high-energy cosmic rays, mainly protons, of galactic origin that usually penetrate the entire meteorite. These protons produce a multitude of nuclear reactions in the interior of the meteorite. The record of this cosmic ray exposure is preserved in the meteorite by the accumulation of the nuclear reaction products. This permits calculation of a "cosmic ray exposure age" of the meteorite. This is usually interpreted as the time in the past when the relatively small fragment of meteorite, recovered on the Earth, was broken away from a larger parent body in space, usually assumed to be an asteroid. Measurements of this kind have shown that typical stony meteorites have been in space for only a few million years, whereas most iron meteorites have been exposed to cosmic rays for hundreds of millions of years. Inferences based on this accumulated record of cosmic ray exposure have played a central role in attempts to understand mechanisms for derivation of meteorites from parent bodies (e.g., Arnold, 1965; Opik, 1965; Wetherill, 1968, 1974; Wetherill and Williams, 1979), the collisional history of meteorites (Wetherill, 1967; Dohnanyi, 1969), and

the degree of their atmospheric ablation (Bhandari *et al.,* 1980).

In these theories, interpretation of the meaning of the cosmic ray exposure age would be different if the measured age referred not to the time the present meteorite fragment was formed, but to an earlier cosmic ray exposure in an earlier body from which the fragment was derived. This alternative interpretation would in some cases remove puzzling discrepancies, but would in other cases complicate interpretation. In the absence of discrepancies it is usually assumed that only a single exposure has occurred, even though the data are usually inadequate to establish this.

An analytical theory for the statistical expectation of multiple exposure has been developed. In this work the usual assumption is made that meteorites result from collisional fragmentation of chemically similar larger objects, and that all material within a given "shielding depth" of the surface of these larger objects has been preirradiated in the larger object. The two principal modes of collisional destruction are (1) "cratering," whereby a surface impact excavates an impact crater on the larger body and meteoritic fragments are ejected from the crater into space, and (2) "catastrophic disruption," whereby a more energetic projectile completely breaks the larger object into a number of fragments.

The present theory calculates the relative importance of cratering and catastrophic disruption. Contrary to much common belief, it is found that cratering is comparable in importance ($\sim$30%) to catastrophic disruption in the production of meteorites.

This same theory gives the fraction of meteorite fragments derived from objects small enough to be themselves entirely pre-irradiated, as well as the fraction obtained by surficial cratering of larger objects. For a 2-meter shielding depth and experimental values of the parameters of fragmentation, the calculated incidence of multiple exposure for both modes of fragmentation is given in Table 22.

TABLE 22. Predicted Frequency of Multiple Cosmic Ray Exposure

Pre-atmospheric Meteorite Mass (g)	Multiple Exposure (percent)	
	catastrophic	cratering
10^6	27	25
10^5	50	44
10^4	67	57
10^3	79	68
10^2	87	77

Although the detailed quantitative results will change when different parameters are used, the general result that multiple exposure should be a common phenomenon is very insensitive to plausible variations in the fragmentation parameters, to the meteorite mass distributions, or to the size distribution of the larger bodies $\gtrsim$ 100 m in diameter.

This work predicts that multiple-exposure history should be a common occurrence. This prediction can be tested by appropriate measurements of cosmic ray reaction products in meteorites. If the prediction is confirmed, the effects of multiple exposure will have to be explicitly recognized in the interpretation of exposure age data. If it is not confirmed, this would call into question some of the fundamental assumptions about the manner in which meteorite fragments are produced.

References

Arnold, J. R., The origin of meteorites as small bodies. II. The model, III. General considerations, *Astrophys. J., 141,* 1536–1556, 1965.

Bhandari, N., D. Lal, R. S. Rajan, J. R. Arnold, K. Marti, and C. B. Moore, Atmospheric ablation in meteorites: an experimental study based on cosmic ray tracks and neon isotopes, in press, *Nuclear Track Detection,* 1980.

Dohnanyi, J. W., Collisional model of asteroids

and their debris, *J. Geophys. Res., 74,* 2531–2554, 1969.
Öpik, E. J., The stray bodies in the solar system. Part II. The cometary origin of meteorites, *Advan. Astron. Astrophys., 4,* 301–336, 1965.
Wetherill, G. W., Collisions in the asteroid belt, *J. Geophys. Res., 72,* 2429–2444, 1967.
Wetherill, G. W., Dynamical studies of asteroidal and cometary orbits and their relation to the origin of meteorites, in *Origin and Distribution of the Elements,* pp. 423–443, L. H. Ahrens, ed., Pergamon, Oxford, 1968.
Wetherill, G. W., Solar system sources of meteorites and large meteoroids, *Annu. Rev. Earth Planet. Sci., 2,* 303–331, 1974.
Wetherill, G. W., and J. G. Williams, Origin of differentiated meteorites, in *Origin and Distribution of the Elements,* Second Symposium, pp. 19–31, L. H. Ahrens, ed., Pergamon, Oxford, 1979.

Brecciation Chronology of Three Xenolithic Chondrites using Fission Tracks

B. K. Kothari and R. S. Rajan

Introduction

Binns (1967) discovered that 20% of about 383 chondrites which he analyzed contain clasts that must have formed somewhere other than within the host sample. Most of these clasts had the same chemical composition as the host but had different metamorphic grade and ranged in size from several mm to several cm. These meteorites he called xenolithic chondrites.

About 7% of xenolithic chondrites are rich in solar gases, solar-flare tracks, and other characteristic features, which suggest that they formed in asteroidal regoliths as a result of collisional mixing of asteroidal material. Gas-poor xenolithic chondrites presumably also formed in regoliths.

Recent studies on isolated clasts have shown the existence of young clasts in the basaltic achondrite Kapoeta (Rajan *et al.,* 1979) and in the chondrites, St. Mesmin (Schultz and Signer, 1977) and Plainview (Bogard, 1979). They range in age from 1.3 to 3.9 b.y., suggesting that brecciation is an ongoing process in meteorite parent bodies. It should, however, be mentioned that young clasts are relatively rare and that the bulk of the regolith is often substantially older (~4 b.y.), as in the case of St. Mesmin (Minster and Allègre, 1979). Since the brecciation process in gas-rich meteorites is gentle and does not reset radiometric clocks, the measured ages in clasts are only upper limits to the time of brecciation.

Our group has carried out a combined study of metal and phosphates in these chondrites to determine the thermal history and brecciation chronology of xenolithic chondrites. Based on metal studies, Scott and Rajan (1980) concluded that the xenolithic chondrites can be subdivided into two groups depending on whether the brecciation took place before slow cooling (through ~700 K to ~500 K) or after. Our studies of fission tracks in phosphates would help in understanding when the metallographic cooling and brecciation events occurred. In this report, we discuss our results on three xenolithic meteorites: two gas-rich chondrites (Weston and Fayetteville), and one gas-poor chondrite (Bhola).

The use of phosphates for chronology has two advantages over other radiometric techniques. First, it has low track retention temperature. About 50% of tracks in phosphates—apatites and presumably whitlockites—will be erased in one day if heated to ~620 K compared to >700 K needed to reset the radiometric clocks in similar time scales. Second, each phosphate grain is a chronometer and is thus capable of providing information on a very fine scale (as small as 10^{-6} g), whereas in radiometric methods bigger samples (≥50 mg) and elaborate methods are required. However, the fission-tracks technique has the disadvantage that the Pu/U ratio is not uniquely known for each crystal.

Experimental Details

Phosphates occur in chondrites at the 0.1–0.5 wt % level and were enriched for the present work using a Frantz magnetic separator. For track studies, grains were mounted in epoxy, polished, and etched in HNO_3. For Weston, enrichment in phosphate was found to be rather poor.

For uranium measurements, samples were prepared by covering the grain mounts with mica detectors. Samples together with standards were irradiated at the NBS reactor to a total fluence of $\sim 2 \times 10^{17}$ neutrons/cm^2. Neutron-induced tracks were counted on mica detectors.

Results and Discussion

Our track results on whitlockites from Bhola, Weston, and Fayetteville are shown in Table 23. About 10% of the phosphates analyzed were apatites; their track data are not reported here because U measurements are not complete. The chemical compositions of phosphates from these meteorites were determined by microprobe and found to be in the range expected from chondrites.

Track densities in 20 Bhola crystals are found to cluster tightly ($3.7–6.3 \times 10^6$ cm^{-2}), with a mean of about 5×10^6 cm^{-2}. The track densities reported in Table 23 were corrected for spallation recoils, which constitute half of the observed tracks. The measured track densities exceed those expected from U fission in 4.55 b.y. (age of chondrites) and the cosmic ray–produced track densities by more than a factor of two (see Table 23); the excess tracks are due to extinct decay of Pu^{244}. Phosphates from other chondrites have similar excesses of fission tracks due to Pu^{244} (e.g., Pellas and Storzer, 1980). For calculating an age, we have taken a Pu/U = 0.045 at 4.55 b.y. as the best mean of chondritic whitlockites, even though the ratio can vary by as much as a factor of four in chondrites of the same chemical class (Pellas *et al.*, 1979). It should be mentioned that a factor of two uncertainty in Pu/U ratio for a fixed concentration of U will change the track retention age by ± 82 m.y. (half-life of Pu^{244}) for ages >4 b.y. However, a factor of two variation in U content for a fixed Pu concentration will not significantly change the ages in the >4 b.y. range.

After normalizing the track densities for varying U contents, five crystals show a factor of two spread which must be due to variations in Pu/U ratio of the different crystals because metal in this chondrite is equilibrated and, hence, the phosphates must be reset. From the mean of fission track densities we get a track retention age of 4.01 b.y. The brecciation in Bhola meteorite itself must have clearly happened at >4.01 b.y., since sometime after brecciation the temperature was greater than 700 K (to account for equilibration of the metal) and fell slowly to the track retention temperature of ~ 300 K at 4.01 b.y.

The track data in conjunction with metal data can be used to constrain the cooling rate of the Bhola meteorite during the brecciation event. The mean track retention age of Bhola (4.01 b.y.) corresponds to a maximum of ~ 550 m.y. for the various metamorphic processes to occur; however, most of the time must be spent in cooling from >700 K (equilibration temperature of metal) to the track retention temperature of the phosphate (~ 300 K). The minimum average cooling rate of $0.7\ ^{+0.2}_{-0.1}$ K/m.y., inferred from the present track data, is higher by at least a factor of six than the deduced metallographic rate of 0.1 K/m.y. Similar discrepancies in metallographic cooling rates of other meteorites have been noted by Wood (1979).

In the gas-rich chondrites Weston

TABLE 23. Summary of Track Data in Whitlockite Crystals

Meteorite	Wt of sample (g)	U content§ (ppb)	U fission track contribution in 4.55 b.y. (10^6 cm^{-2})	Cosmic ray track density (10^6 cm^{-2})	Measured track densities§ (10^6 cm^{-2})	Track retention age‖ (b.y.)
Bhola (LL)*						
NMNH 1806	0.9	140–560(11)	0.7–2.8	~0.4	3.7–6.3(20) (Mean = 5.0)	4.01 ± 0.1
Weston (H)†						
Yale	1.8	. . .	. . .	~0.5	23–58(8)	4.10–4.24
NMNH 1180	1.3	270–650(4)	1.4–3.2	~0.5	25–75(35)	4.15–4.30
Fayetteville (H)‡						
NMNH 1734	1.3	125–575(11)	0.6–2.9	~2.6	50–88(11)	4.26–4.50

*Can be classified as LL4-7 (Fredriksson *et al.*, 1975).

†Matrix has been classified approximately as H4, with most of the xenoliths ranging from H3 to H7 (Noonan and Nelen, 1976).

‡Matrix has been described as H4, but the clasts have different metamorphic grades.

§Numbers in parentheses refer to crystals studied.

‖Assuming $(Pu/U)_{4.55\ b.y.} = 0.045$ (Pellas *et al.*, 1979).

and Fayetteville, 43 and 11 whitlockite crystals, respectively, were analyzed for track density measurements. The track densities of phosphate grains in these meteorites are higher and show much more spread than the Bhola chondrite (Table 23). Also, the contribution of Pu^{244} to the observed track densities in whitlockite crystals is more in both the Weston and Fayetteville chondrites than in the Bhola meteorite (see Table 23). This is reflected in old ages for these meteorites: 4.10–4.30 b.y. for Weston and 4.26–4.50 b.y. for Fayetteville. Because each phosphate is a potential chronometer, it is significant that none of the ages are < 4.10 b.y.

What do these ages mean? If the phosphates were reset during a single brecciation event, then they all should have the same age (or the same track density after correcting for U and Pu concentrations). Because the expected spread in ages due to uncertainty in Pu/U ratios (Pellas *et al.*, 1979) are of the same order as that in the measured ages, it is difficult to distinguish between the following two significant results from our limited data. (1) The phosphates are reset in a single brecciation event, the track density spread being due to Pu/U variation of individual crystals. This would imply brecciation ages of ~4.2 b.y. for Weston and ~4.3 b.y. for Fayetteville. These are higher than the upper limits of brecciation ages of two gas-rich chondrites: 1.4 b.y. for St. Mesmin (Schultz and Signer, 1977) and 3.6 b.y. for Plainview (Bogard, 1979), measured by dating individual clasts. (2) The phosphates are indeed dating different metamorphic or brecciation events; the fission track ages are then upper limits to the times of brecciation. This is consistent with metal being not equilibrated in both the chondrites. The fission track ages of phosphates are in the same range as that expected from the metallographic cooling rates (Scott and Rajan, 1980), suggesting that most of them have been reset by metamorphic events. The time of final brecciation itself can be obtained if a large number of phosphates from widely different lithologies are studied.

Summary

The application of fission track dating in understanding the brecciation of xenolithic chondrites has been quite useful. The major conclusions from the present studies are as follows:

(1) The track retention age of Bhola whitlockites is 4.01 ± 0.1 b.y. Brecciation of the Bhola meteorite must have occurred at >4.01 b.y.

(2) A minimum cooling rate of 0.7 $^{+0.2}_{-0.1}$ K/m.y. is derived from the track data. This result strongly suggests that the metallographic cooling rate for Bhola (0.1 K/m.y.) is too low by at least a factor of six.

(3) Both gas-rich chondrites yield old track retention ages: 4.10–4.30 b.y. for Weston and 4.26–4.50 b.y. for Fayetteville. The unique interpretation of these ages, namely whether they are due to brecciation or metamorphism, must await further study.

Acknowledgements

We would like to thank Roy S. Clarke, Jr., K. Fredricksson, and A. Noonan for samples, and E. R. D. Scott for discussions.

References

Binns, R. A., Structure and evolution of non-carbonaceous chondritic meteorites, *Earth Planet. Sci. Lett., 2,* 23–28, 1967.

Bogard, D. D., Chronology of asteroid collisions as recorded in meteorites, in *Asteroids,* pp. 558–578, T. Gehrels and M. S. Matthews, eds., University of Arizona Press, Tucson, 1979.

Fredriksson, K., A. Noonan, and J. Nelen, The Bhola stone—a true polymict breccia?, Abstract, *Meteoritics, 10,* 87–88, 1975.

Minster, J. F., and C. J. Allègre, ^{87}Rb-^{87}Sr age of Saint Mesmin chondrite and dating of gas-rich polymict breccia, *Nature, 278,* 732–734, 1979.

Noonan, A. F., and J. A. Nelen, A petrographic and mineral chemistry study of the Weston, Connecticut, chondrite, *Meteoritics, 11,* 111–130, 1976.

Pellas, P., D. Storzer, T. Kirsten, J. Jordan, and H. Richter, Pu-244/U-238 ratios in whitlockites of ordinary chondrites: a possible chronological tool, *Lunar and Planet. Sci., 10,* 969–971, 1979.

Pellas, P., and D. Storzer, ^{244}Pu fission track thermometry and its application to stony meteorites, *Phil. Trans. Roy. Soc. London, Ser. A,* in press, 1980.

Rajan, R. S., J. C. Huneke, S. P. Smith, and A. J. Wasserburg, Argon 40-Argon 39 chronology of lithic clasts from the Kapoeta howardite, *Geochim. Cosmochim. Acta, 43,* 957–971, 1979.

Schultz, L., and P. Signer, Noble gases in the St. Mesmin chondrite: implications to the irradiation history of a brecciated meteorite, *Earth Planet. Sci. Lett., 36,* 363–371, 1977.

Scott, E. R. D., and R. S. Rajan, Metallic minerals, thermal histories and parent bodies of some xenolithic, ordinary chondrite meteorites, *Geochim. Cosmochim. Acta,* in press, 1980.

Wood, J. A., Review of the metallographic cooling rates of meteorites and a new model for the planetesimals in which they formed, in *Asteroids,* pp. 849–891, T. Gehrels and M. S. Matthews, eds., University of Arizona Press, Tucson, 1979.

Variation of Fission Track Densities on Olivines from Murchison Carbonaceous Chondrite

R. S. Rajan, T. R. Watters, and B. K. Kothari

In a recent study, Macdougall and Kothari (1976) found evidence for ^{244}Pu fission tracks on the surfaces of olivine crystals. They interpreted the mean of the observed track densities as compaction ages, assuming a mean $(Pu/U)_{4.55\ b.y.}$ ratio = 0.015. It is the purpose of the present work to understand the huge scatter in the observed fission track densities within a single meteorite, and to learn what the deduced "compaction ages" really mean.

We have studied approximately 200 crystals from gently disaggregated Murchison samples, for both surface tracks and side tracks. These grains were carefully mounted in epoxy to expose a single crystal face of the olivine. The mounts were then etched and the grains observed for tracks on the surface of the exposed face. They were then polished to remove approximately 20

μm and etched again. After this procedure, the sides of the grains were examined for tracks on and near the polished surface. Side tracks can thus be defined as those originating on other faces of the grain that intersect the polished surface within nine μm of the edge.

Our surface track density measurements on 31 crystals show a range from 1.4×10^4 cm^{-2} to 1×10^6 cm^{-2}, with a mean of $\sim 1 \times 10^5$ cm^{-2}. The side tracks are observed only up to a distance of $R(\sim 9\ \mu m)$, where R is half the mean range of fission tracks due to ^{244}Pu spontaneous fission. It is interesting to note that side track measurements of comparable quality were possible on 67 crystals (about twice as many as for surface track measurements), and are reported here. The track densities derived from side tracks range from 2.2×10^4 cm^{-2} to 1.2×10^6 cm^{-2}, and have a mean of 3.4×10^5 cm^{-2}, corresponding to $\rho_{Pu}/\rho_U = 22$. Figure 68 shows the measured side track densities on 140 sides observed on 67 crystals. By studying the side tracks on different faces of a single crystal, we have established that the fission track den-

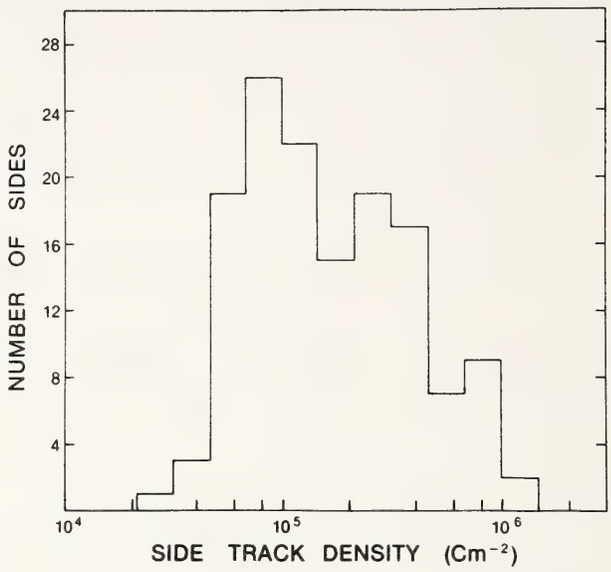


Fig. 68. Histogram of side track densities measured on 140 sides observed on 67 olivine crystals, from the Murchison carbonaceous chondrite.

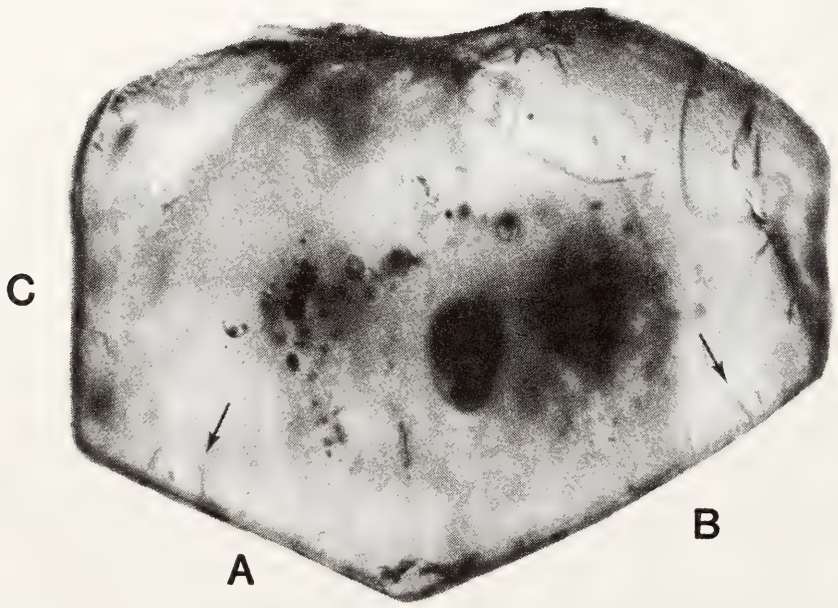


Fig. 69. A 120-μm olivine from Murchison carbonaceous chondrite. Side tracks are visible on sides *A* and *B*. The arrows indicate two tracks in sharp focus due to their nearness to the polished surface. Other tracks are also visible in different degrees of focus because of their variable distance from the surface. While two sides are too irregular to observe, side *C* is clearly devoid of tracks, demonstrating the heterogeneity.

sities vary by up to a factor of 20. In fact, of the 14 crystals that had observable tracks on three sides or more, six had side track densities that varied by at least a factor of ten. Figure 69 shows a typical olivine crystal with side tracks. While two sides, marked *A* and *B*, clearly have side tracks, side *C* has none.

There are three possible explanations for our results that need to be considered. (1) It is possible that C_U (and by inference C_{Pu}) varies in the matrix by as much as a factor of ten or more, on a ten-μm scale. Very high fluence neutron irradiations ($\sim 5 \times 10^{18}$ n cm^{-2}) are needed to check this point. (2) It is unlikely that geometric factors relating to the contact of the matrix and olivine can produce such large variations, though they cannot be rigorously excluded. Again, study of the olivine crystals themselves, after the high irradiation mentioned above, will resolve this problem. (3) If uranium is indeed homogeneous, then the typical variation of track densities on single crystals surfaces, from $\sim 5 \times 10^5$ cm^{-2} to 5×10^4 cm^{-2}, (which correspond to $\rho_{Pu}/\rho_U = 34$ and 2.7, respectively) must refer to actual time differences of up to ~ 270 m.y. One possibility is that aggregates which were in contact with the matrix at 4.55 b.y. were subsequently broken, placing individual crystals into contact with the younger matrix as much as 270 m.y. later.

The present data support the possibility that the bulk of the olivines were previously part of inclusions or aggregates that were subsequently broken. Studies on selected euhedral olivines are in progress, to better understand their origin.

References

Macdougall, J. D., and B. K. Kothari, Formation chronology for C2 meteorites, *Earth Planet. Sci. Lett., 33*, 36–44, 1976.

Occurrences and Formation of Tetrataenite, Ordered FeNi, in Meteorites

Edward R. D. Scott and Roy S. Clarke, Jr.†*

Tetrataenite is a new tetragonal mineral with ideal formula FeNi which forms by the ordering of Fe and Ni atoms in taenite (face-centered cubic γ-Fe,Ni). The name and mineral have been approved by the Commission on New Minerals of the International Mineralogical Association. It has the CuAu structure (Albertsen *et al.*, 1978), contains 48–57 wt % Ni, and has been observed in over 60 chondrites, mesosiderites, irons, and pallasites (Scott and Clarke, 1979; Clarke and Scott, 1980; Danon *et al.*, 1979). Last year (see *Year Book 78*, 409–413) we described occurrences of ordered FeNi in 1–20 μm wide rims on zoned taenite grains, and in 10–60 μm grains in kamacite (α-Fe,Ni). (The latter were called "clear taenite" by Taylor and Heymann [1971].) We report here optical and electron probe studies of new occurrences, and discuss their implications for the origin of tetrataenite.

Metal in LL chondrites is less abundant than in the H and L groups of chondrites but is richer in Ni (25–50%). In Appley Bridge, which has one of the highest metallic Ni concentrations, *all* the metal is tetrataenite with 52.9% Ni, 2.0% Co, and 0.18% Cu. The largest grain observed was 1.2 mm in size. Metal in Manbhoom, which has a slightly lower Ni concentration, consists of tetrataenite with minor kamacite, but no taenite. Most LL chondrites, like Bhola, contain kamacite, "cloudy taenite," and tetrataenite. Thus the relative abundances of these phases in LL chondrites reflect the bulk composition of the metal.

Tetrataenite also forms large grains

*Institute of Meteoritics, University of New Mexico, Albuquerque.

†National Museum of Natural History, Smithsonian Institution, Washington, D.C.

in a 4 × 5 cm sample (USNM 3256, mislabeled Copiapo), which displays a fine octahedral pattern in what was once polycrystalline taenite with a crystal size of 5–10 mm. Troilite nodules are aligned along former taenite grain boundaries and contain silicates. The compositions of silicates, phosphides, and metal suggest that this sample may be a metallic nodule from a mesosiderite (possibly Vaca Muerta), although its bulk Ni content of 10% is high for mesosiderites. Tetrataenite forms grains up to 400 μm wide, which partly coat troilite nodules, and 5–80 μm wide plates and blebs between the oriented kamacite crystals. Only a few large grains of tetrataenite contain residual blebs of cloudy taenite. Thus the Widmanstätten pattern is composed almost entirely of tetrataenite pseudomorphing taenite, and kamacite.

Large tetrataenite grains in LL chondrites and USNM 3256 display very clearly the optical properties common to other occurrences. Crossed polars reveal three different orientations of intergrown crystals, which show polarization colors of orange-brown, bluish-green, or khaki, and an intricate pattern of magnetic domains (Fig. 70). We see no evidence in these occurrences for fine intergrowths of taenite and tetrataenite, as proposed by Mehta *et al.* (1980) from their electron microscopy study. We suggest that they misidentified tetrataenite crystals with [101] and [011] parallel to the electron beam

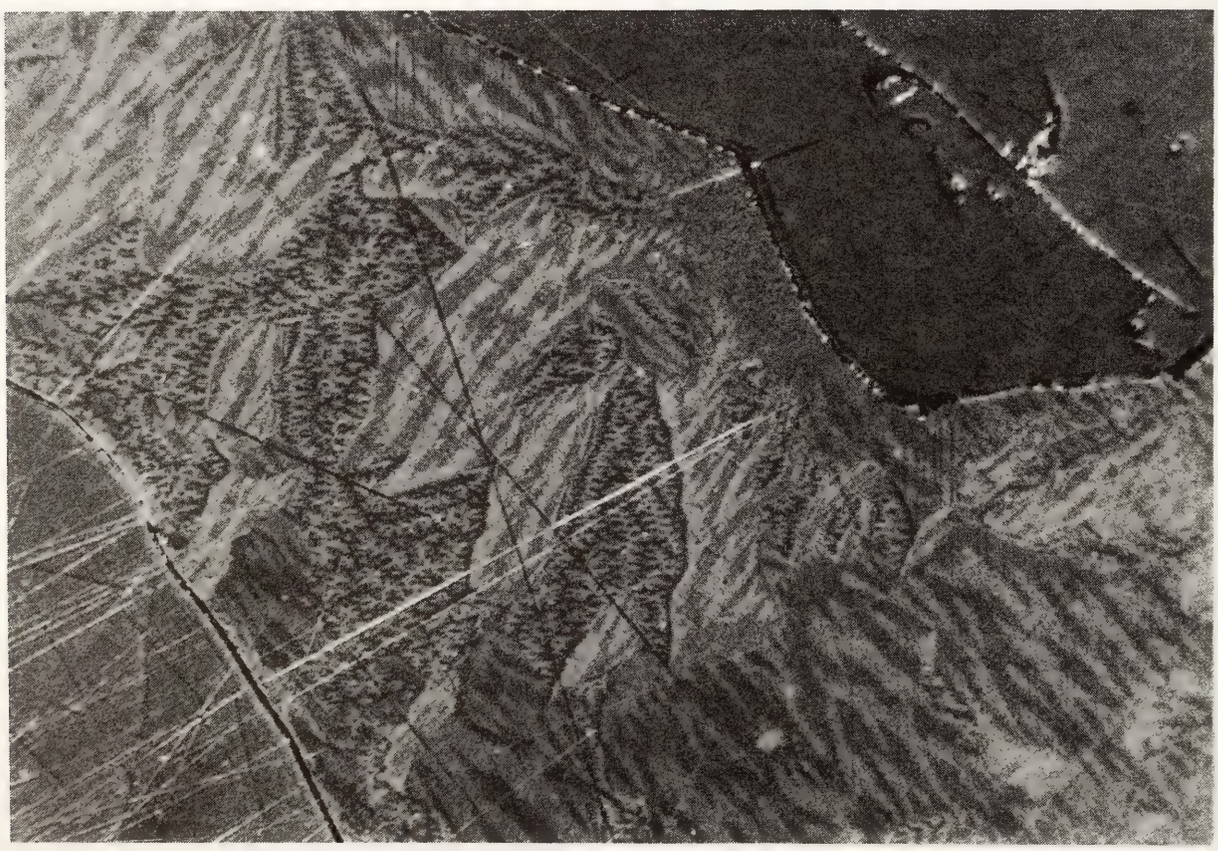


Fig. 70. Reflected-light photomicrograph of tetrataenite in the meteorite USNM 3256 under crossed polars and oil immersion; top right troilite, bottom left kamacite. Tetrataenite, which is white and featureless when polars are uncrossed, shows an array of interlocking crystals, which are oriented in three directions and show vivid polarization colors. Superimposed on these crystals are intricate magnetic domain patterns. Width of field: 220 μm.

as taenite; in these orientations extra diffraction spots due to ordering are not visible.

We have also identified tetrataenite optically in "cloudy taenite," which contains 30–40% Ni and forms cores or borders in zoned taenite. In the Estherville mesosiderite, we observed μm-sized crystals of tetrataenite with the same orientation and polarization colors as rim crystals of tetrataenite, confirming the suggestion of Albertsen *et al.* (1978) that ordered FeNi is a component of "cloudy taenite." Mesosiderites have the slowest cooling rates and the coarsest intergrowths in "cloudy taenite"; in most meteorites the crystals are too small for optical identification. If the second phase in "cloudy taenite" is kamacite, as electron microscopy indicates, the term is a misnomer, as taenite is no longer present.

Heating experiments on synthetic ordered FeNi indicate an ordering temperature of 320 °C (Paulevé *et al.*, 1962). Our observations on the distribution of tetrataenite in meteorites confirm the conclusion of Albertsen *et al.* (1978) that tetrataenite forms at these low temperatures during slow cooling. Figure 71 shows the equilibrium phase relationships of kamacite and taenite in the Fe-Ni system for the temperature range 350–600 °C (Romig and Goldstein, 1980). We believe that below these temperatures, kamacite and tetrataenite are the stable phases for metal of meteoritic compositions, and we have drawn schematic phase boundaries to illustrate this.

Tetrataenite (or its precursor γ phase) appears to form on preexisting taenite by the inward and outward growth of Ni-rich rims. In general, we believe that tetrataenite does not nucleate in kamacite grains, as Taylor and Heymann (1971) proposed, but its growth is aided by the rejection of Ni from kamacite below 500 °C, as they suggested. Outward growth of taenite requires only

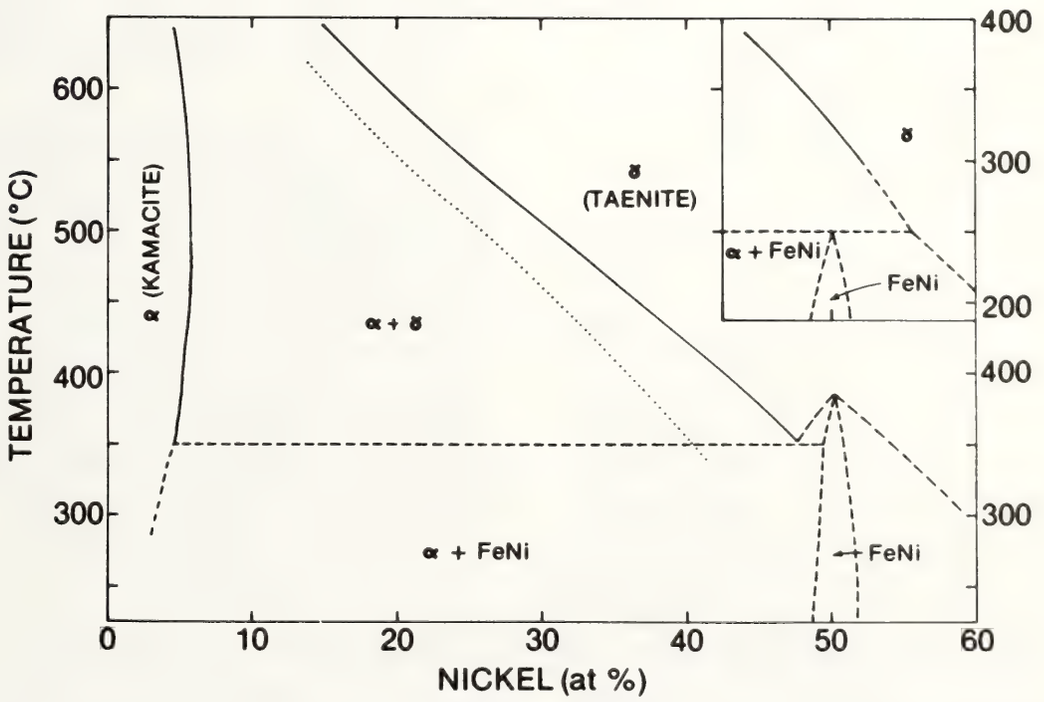


Fig. 71. Equilibrium phase diagram for the Fe-Ni system showing the stability fields of kamacite and taenite (solid lines); the dotted line marks the $(\alpha + \gamma)/\gamma$ boundary for P-saturated alloys (Romig and Goldstein, 1980). The dashed lines show postulated phase relationships for tetrataenite (ordered FeNi); the inset shows how the diagram might look if tetrataenite were not stable above 250 °C.

diffusion through kamacite (which is more rapid than in taenite) assisted by rapid diffusion along kamacite grain boundaries. However, where the bulk (or local bulk) concentration of Ni exceeds about 10%, the equilibrium ratio of kamacite to taenite does not decrease below 500 °C, and tetrataenite growth must rely on inward diffusion of Ni through taenite. In USNM 3256, for example, Ni must have diffused up to 40 μm in taenite (or tetrataenite) below 400 °C. Since the maximum calculated diffusion distance in taenite below 400 °C is < 5 μm, the calculated diffusion rates and consequently metallographically derived cooling rates (Wood, 1979) may be too low.

References

Albertsen, J. F., G. B. Jensen, and J. M. Knudsen, Structure of taenite in two meteorites, *Nature, 273*, 453–454, 1978.

Clarke, R. S., Jr., and E. R. D. Scott, Tetrataenite—ordered FeNi, a new mineral in meteorites, *Amer. Mineral.*, in press, 1980.

Danon, J., R. B. Scorzelli, I. S. Azevedo, and M. Christophe Michel-Lévy, Iron-nickel superstructure in metal particles of chondrites, *Nature, 281*, 469–471, 1979.

Mehta, S., P. M. Novotny, D. B. Williams, and J. I. Goldstein, Electron-optical observations of ordered FeNi in the Estherville meteorite, *Nature, 284*, 151–153, 1980.

Paulevé, J., D. Dautreppe, J. Laugier, and L. Neel, Établissement d'une structure ordonnée FeNi par irradiation aux neutrons, *Compt. Rend. Acad. Sci. Paris, 254*, 965–968, 1962.

Romig, A. D., Jr., and J. I. Goldstein, Determination of the Fe-Ni and Fe-Ni-P phase diagrams at low temperatures (700–350 °C), *Met. Trans.*, in press, 1980.

Scott, E. R. D., and R. S. Clarke, Jr., Identification of clear taenite in meteorites as ordered FeNi, *Carnegie Inst. Wash. Year Book 78*, 409–413, 1979.

Scott, E. R. D., and R. S. Clarke, Jr., Identification of clear taenite in meteorites as ordered FeNi, *Nature, 281*, 360–362, 1979.

Taylor, G. J., and D. Heymann, The formation of clear taenite in ordinary chondrites, *Geochim. Cosmochim. Acta, 35*, 175–188, 1971.

Wood, J. A., Review of the metallographic cooling rates of meteorites and a new model for the planetesimals in which they formed, in *Asteroids*, pp. 849–891, T. Gehrels and M. S. Matthews, eds., University of Arizona Press, Tucson, 1979.

STARS AND GALAXIES

Neutral Hydrogen Shells in the Galaxy

Esther M. Hu

Recent studies of the interstellar gas have shown a high degree of structure on large scales, suggestive of a medium dominated by energetic events. Of special interest are the observed shells of gas, whose systematic expansion, combined with the mass of gas attributed to the shell, indicate that large amounts of energy are required for their production. A careful study of the distribution and properties of shells will allow us to identify the energetic events which produce them, and to study the manner in which this energy propagates into the interstellar medium (ISM).

Neutral hydrogen at 21 cm has been one of the prime tracers of interstellar gas. As part of a doctoral thesis at Princeton, and now continuing at DTM, we began a program of searching for shells in the radio survey of the Galaxy at 21 cm by Heiles and Habing (1974). The survey covers the entire sky visible from the Hat Creek telescope at latitude $\sim 40°$, excluding the portion within 10° of the galactic equator, with a resolution of 0°.6. Velocity coverage for these regions extends from -92 to $+72$ km/sec with a resolution of 2 km/sec. A sample shell, seen at successively different velocities in the Heiles-Habing survey, is displayed in Fig. 72.

The most severe obstacle to identifying shells is the problem of distinguishing them from unrelated background

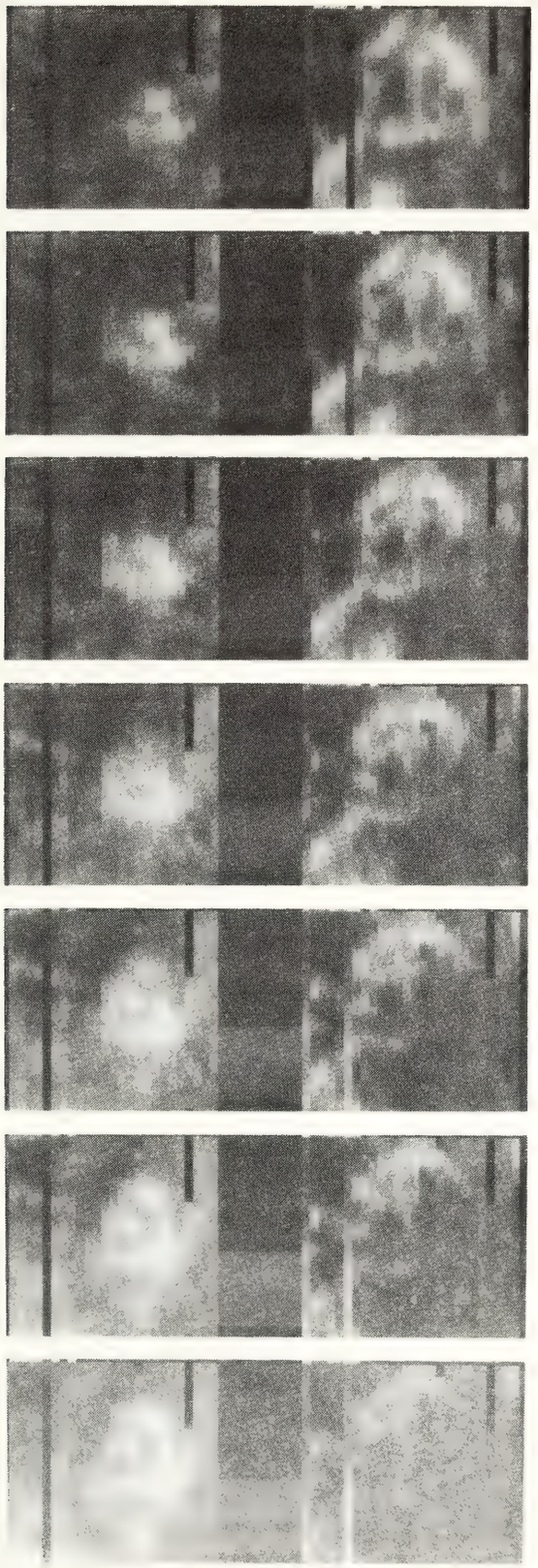


Fig. 72. A shell seen at a succession of velocities in the interstellar gas. Each picture is 15° × 15° in size. The pictures span about 20 km/sec. Note the persistence of ordered structure over this range and the changing size of the feature. For an expanding shell, this corresponds to sampling different regions of the shell at different projected expansion velocities. Also note the presence of substructures in the shell.

gas. The prevalence of hydrogen, which allows us to explore nearly all portions of our Galaxy, combined with our long lines of sight, produces an overwhelming background of gas emission which obscures individual features. While at higher galactic latitudes this problem is negligible (which is the case for our sample shell in Fig. 72), the strong concentration of gas towards the plane of the Galaxy makes it nearly impossible to distinguish structures against the background gas near the galactic equator.

We have solved this problem by designing a filter which makes use of the velocity behavior of shells to distinguish them from the background gas. In Fig. 73, the signal from a beam positioned on the edge of a shell is represented as a function of velocity. We note that the signal due to the shell is strongly peaked in comparison with the more slowly varying background emission. We can approximate the background contribution to the signal over the velocity range of the shell by sampling an adjacent velocity range which does not include the shell feature. By taking the difference between these two quantities, we obtain the emission due to the shell.

In a search procedure, we do not know beforehand the velocity at which a shell feature will appear. However, if the same procedure described above were applied to a region showing only background gas, the difference in the two samplings would be close to zero. This suggests that we can apply our differencing scheme (in extended form) over a large range of velocities. Any peaked feature contributes strongly to our succession of sums and differences. The background contribution cancels out to zero. This differencing technique is represented in Fig. 73 by a square-toothed filter. Its teeth alternate between positive and negative values. To apply the technique, the filter is positioned over some range of velocities we wish to sample, and the emission at

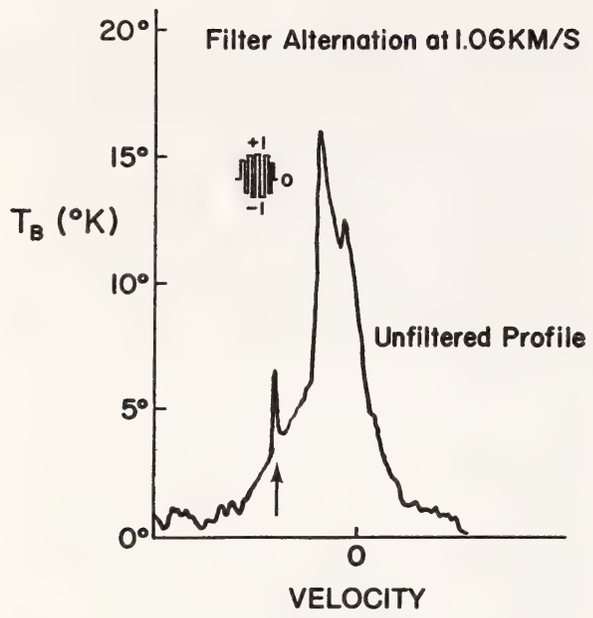


Fig. 73. Sample velocity profile from a single position on a shell. The filter, which extends over a velocity range including a feature (arrow), is an alternating square tooth. A filtered signal is obtained by multiplying the data by the filter, and summing the result over its channels. By combining filtered signals over a region of sky, shell structures are enhanced.

each velocity is multiplied by the corresponding filter-tooth value and summed. Thus, the filtered value F, sampling a range from v_1 to v_4 could be

$$F = (1)\times I(v_1) + (-1)\times I(v_2) + \\ + (1)\times I(v_3) + (-1)\times I(v_4).$$

Each position in the sky is filtered in velocity, and a filtered signal is obtained. If we translate these values to a photographic gray scale with white corresponding to large negative numbers, gray to zero, and black to large positive numbers, a filtered picture will show shells as either light or dark rings against a background gray.

For the sample shell in Fig. 72, we show in Fig. 74 a succession of filtered photographs with the filter centered at various velocities partially overlapping the velocity range of the shell.

The filter technique was developed to eliminate the problems of background gas, but it also has two other useful features: It produces a composite which combines information from several velocities simultaneously, and it allows changes in velocity to be easily viewed. Since gradients in velocity can mean a shift of a feature from a "+" tooth of the filter to a "−" tooth, they can be shown in photographic representation as zebra-striped progressions of light and dark regions. A rapidly expanding shell would show up as a series of concentric light and dark circles, reflecting the change in projected line-of-sight velocity across the shell.

This procedure shows up any feature with enhanced emissions compared to that of background gas over a narrow velocity range. For the purpose of our study, we are concerned only with those shells that have ring-like features. The technique loses information on the exact velocity centers of shells, but that data can be determined in more detailed studies of the data once a shell has been located.

From the filtered photographs we discovered 50 shells, of which 36 are main shells and the rest substructures. Their distribution in the plane is shown in Fig. 75. Many of the shells show structure at various scales. General properties are expansion velocity ~ 8 km/sec, diameter ~ 20 pc, mass $\sim 10^3$ $M_\odot$, and kinetic energy $\sim 10^{48}$ ergs. Except for expansion velocity, determinations of all these values depend on the distance to the shell. Since our survey extends to high latitudes, we can use the extent of the gas to set an upper limit on the distance of shells above the plane of several hundred pc. Assuming that shells consist of swept-up gas, we determine the distance by requiring that the swept-up gas (computed from a general expression for the gas density as a function of height above the Galactic plane and the assumed distance) accounts for the observed emission.

The observed kinetic energies must be accounted for by energetic events.

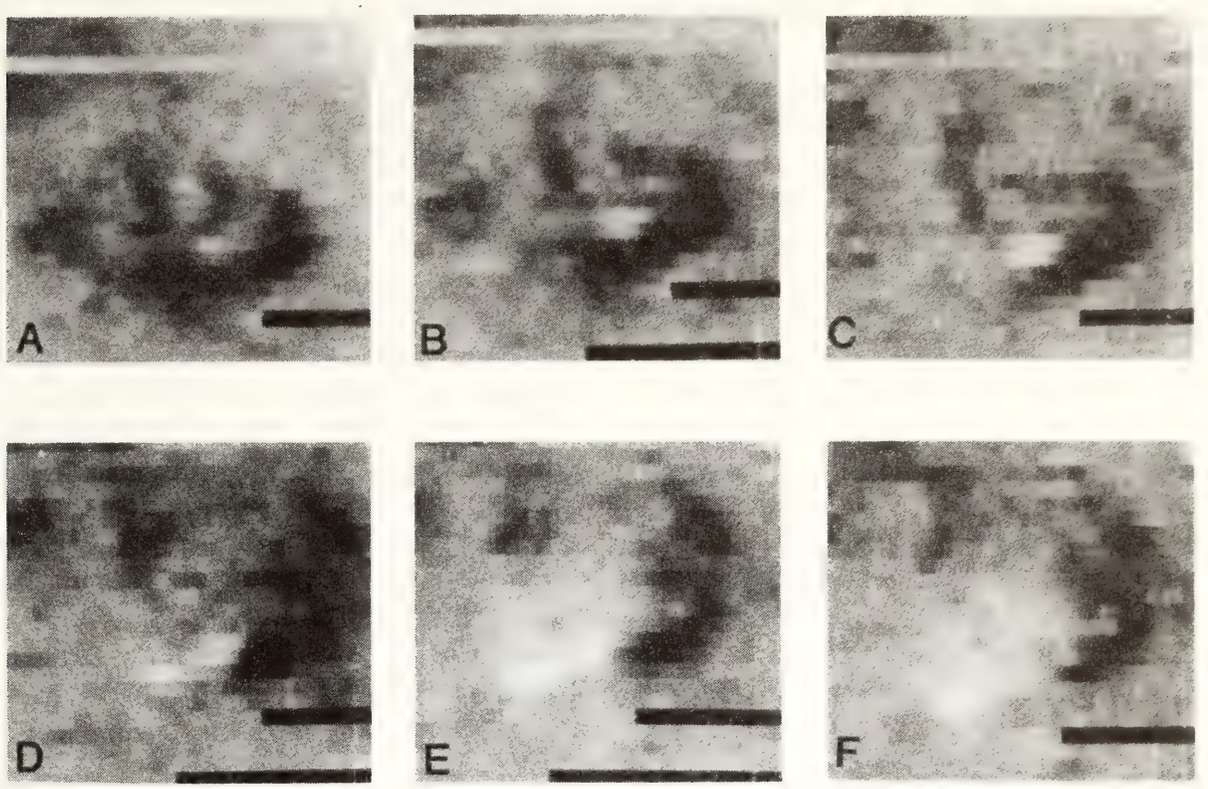


Fig. 74. The shell displayed in Fig. 72 has been processed through the filter. Pictures resulting from six different filter centers, each overlapping the range of velocities occupied by the shell, are shown. Substructures which persist are highlighted. The light feature most prominently seen in (F) peaks at a velocity distinct from the main shell. Similar pictures can be obtained for shells with highly obscured backgrounds.

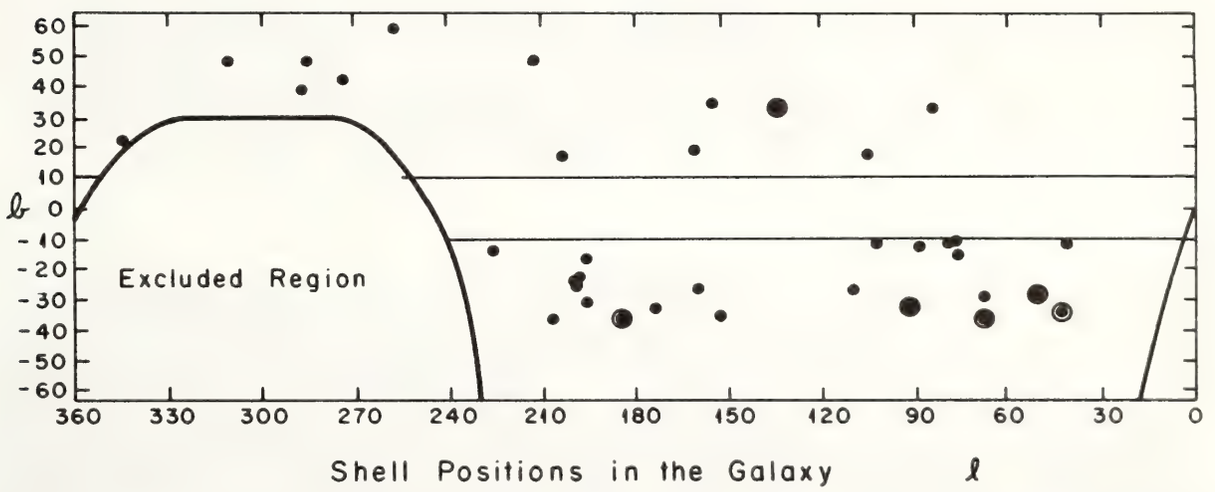


Fig. 75. Distribution of shells in the Galaxy. The observed range is delineated by the heavy black lines. Shells found to have multiple components are denoted by the circled dots.

The most frequently proposed events to produce expanding shells are supernovae and OB stars. Superposing the distribution of OB stars over filtered photographs of shells shows that the number of coincidences does not exceed those of chance superpositions. Also, it is clear that even though OB stars could be energy sources for some shells, there are far too many high-

latitude shells for these to account for most of the shells observed.

Radio continuum loops have been observed and are thought to have been produced by supernovae. In Fig. 76 we show that corresponding features can be seen in the HI gas, not only for loop I (reported by Heiles and Jenkins, 1976), but also for loops II and III. Loop IV is located in the low-density region adjacent to loop I; and there is probably insufficient gas to outline its structure.

We have ruled out OB stars as an energy source, and shown some relation to supernovae sources. Calculations based on Chevalier's (1974) supernova models indicate that the current distribution of shells and their observed mass, size, kinetic energy, and expansion velocity are consistent with supernova origins. Figure 77 shows three possible ways by which this could occur: (a) supernova explosions within a dense cloud, (b) imploded clouds, placed within the overpressured cavities behind the shock wave, and (c) large-scale motions imparted to clouds by the explosion. The results of these models indicate that all three possibilities can account for the data.

The sensitivity limit of our survey is such that we only detect shells with column densities typical of those for interstellar clouds. A shell, if produced by a supernova, must be produced either within a cloud (with typical density of ~ 100 atoms/cm^3, compared to the mean galactic density of 1 atom/cm^3) or by the systematic motion of

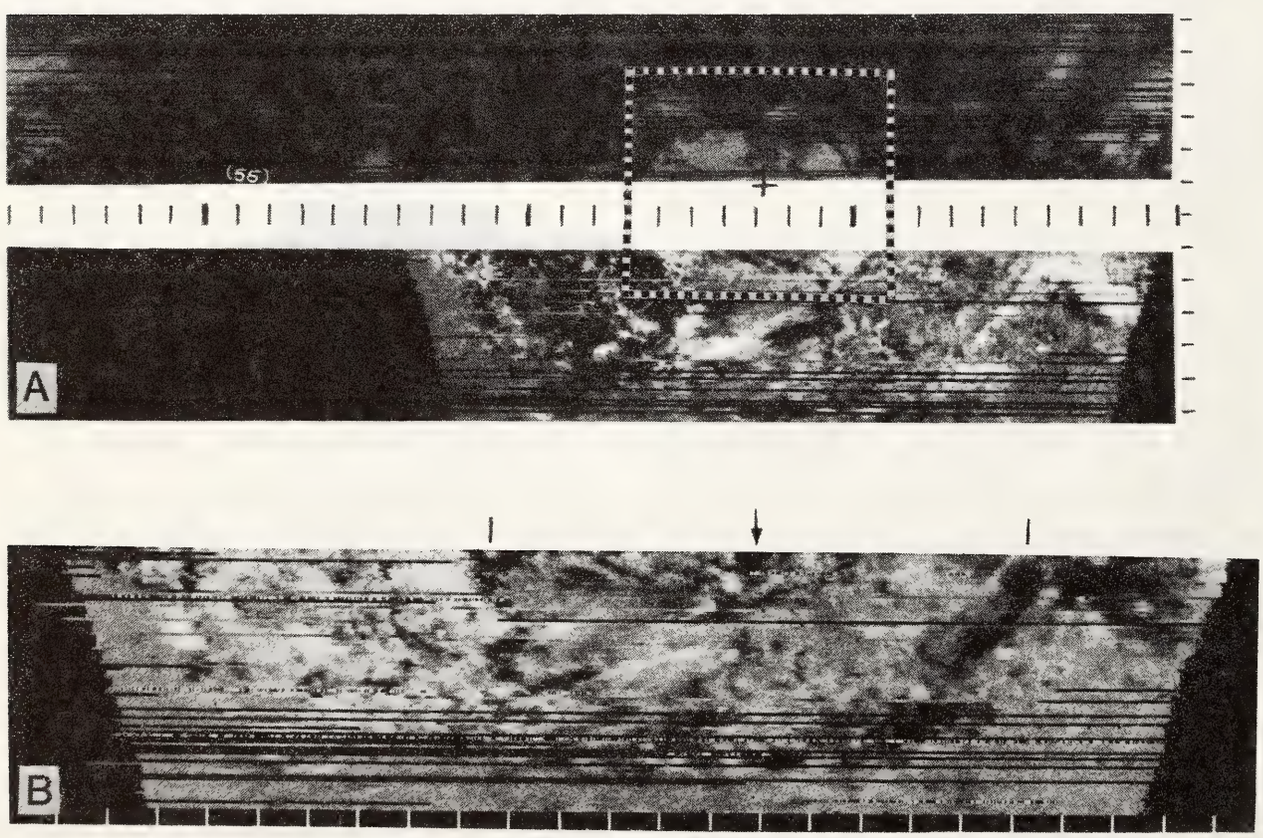


Fig. 76. Filtered pictures of the Galaxy showing features which correspond to radio continuum structures. Coverage extends from 0° to 360° longitude, and from −64° to +64° latitude. The filter has been applied with coarse teeth and over a large velocity range, to bring out large-scale features at the expense of the shells. Radio continuum loop III is contained within the dotted box of (A), and has its center slightly above the plus sign. Loop II is shown in the enlargement of a negative latitude picture (B), and extends between the two tick marks with center below the arrow. These loops are distinguished by the abrupt changes in the velocity properties of gas within them, indicating disruptions in the gas, rather than by the thin sharp boundaries seen for shells.

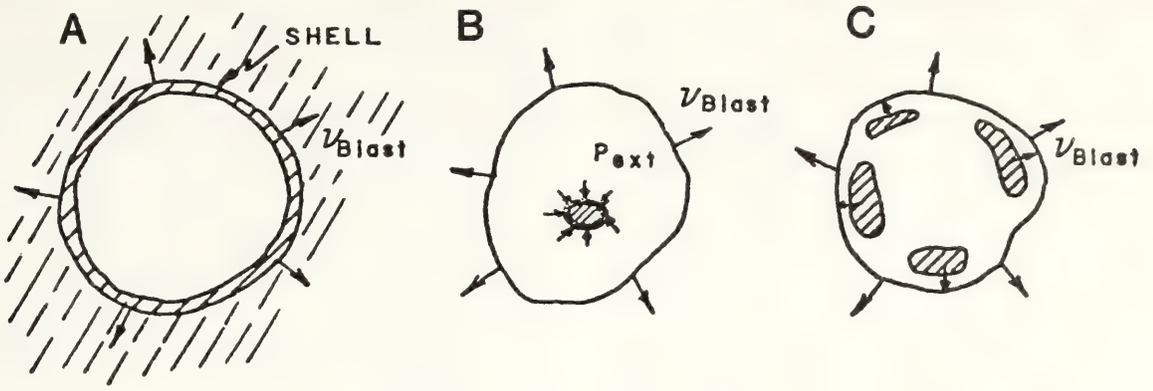


Fig. 77. Three possible mechanisms for forming the shells in our survey. The large observed column densities for these shells, typical of the values seen in diffuse interstellar clouds, suggest that they are formed by material swept out within a cloud (A), or by large-scale motions of clouds following a blast wave (C). If the cloud is caught up by the blast wave at an early stage in the explosion, a third possibility is that the pressure in the cavity drives a shock wave in from the surface of the cloud (B).

clouds. If a cloud were situated near the site of a supernova explosion, it might be left behind as the blast wave swept outwards. In the early stage of the remnant, the cavity is extremely hot and at high pressure. A cloud caught inside would have a shock wave driven inwards from the surface. This imploding region would be indistinguishable in our velocity studies from an expanding shell. Clouds caught up at a late stage of the explosion could be driven outwards and flattened to appear like a patchy shell. Supernovae within clouds could produce the smaller shells (~ 8 pc; typical cloud diameters are 14 pc), and the swept-up clouds could account for the larger ones. A calculation of the volume density of clouds, combined with the volume of remnants, indicates that on average one cloud would be swept out per remnant. This can account for the observed patchiness of some shells. Because there is a maximum extent at which their cloud components can be recognized as part of a shell, these shells have an upper limit to their size. Also, a combination of models (2) and (3) is possible, with a shell produced by swept-out clouds whose imploded surfaces show subshells of the sort seen in Fig. 72.

Further studies of the interstellar gas are being continued at DTM. This procedure will be applied to the low-latitude gas, where its properties will be of even greater value in identifying and studying shell structure.

References

Chevalier, R. A., The evolution of supernova remnants. I. Spherically symmetric models, *Astrophys. J.*, *188*, 501–516, 1974.

Heiles, C., and Habing, H. J., An almost complete survey of 21-cm line radiation for $|b| > 10°$. I. Atlas of contour maps, *Astron. Astrophys. Suppl.*, *14*, 1–555, 1974.

Heiles, C., and Jenkins, E. B., An almost complete survey of 21-cm line radiation for $|b| > 10°$. V. Photographic presentation and qualitative comparison with other data, *Astron. Astrophys.*, *46*, 333–360, 1976.

Abundances of Remote Galactic Halo Subdwarfs

*Bruce W. Carney and Ruth C. Peterson**

The distant edges of our Galaxy have probably evolved in a manner different from the solar neighborhood. We infer this from observed metallicity (i.e.,

*Lockheed Palo Alto Research Laboratory, Palo Alto, California.

abundance of elements with $Z > 2$, especially iron, relative to hydrogen) gradients in the disk of our Galaxy (D'Odorico, *et. al.*, 1976; Janes, 1979; Talent and Dufour, 1979), in those of other galaxies (Searle, 1971), in the galactic halo (Harris and Canterna, 1979), and in the unusual color-magnitude morphologies of the most distant (from the galactic center) globular clusters (see Kraft, 1979, for references). We wish to address the question of the chemical composition and enrichment of halo stars.

The stars in the remote halo are simply too faint to permit high-resolution spectroscopic studies. However, we know of several nearby stars whose velocities are so extreme that they must be in highly eccentric and/or inclined orbits, and must therefore belong to the remote halo and only happen to be passing by the Sun. Using the 4-meter telescope and its echelle spectrograph at Cerro Tololo, we have obtained high-resolution spectrograms for four of these stars. For three of them the data reduction and model atmosphere composition analyses are complete. Table 24 lists the velocities of these three stars in the rotating galactic frame (U = toward $l = 180°$, $b = 0$; V = toward $l = 90°$, $b = 0°$; W = toward $b = 90°$), with respect to the Local Standard of Rest (LSR). Assuming that the LSR is rotating at 220 km/sec toward $l = 90°$, $b = 0°$, we also give v_{gal}, the speed of each star in the rest frame of our Galaxy. All three stars are moving at almost twice the LSR speed, and so are probably remote halo objects. Abundances of several elements have been obtained for these stars, but we consider here only three of the most important—iron, magnesium, and aluminum. Astronomical elemental abundances are denoted by a bracket notation, such that the abundance ratio of element X to element Y is $[X/Y] \equiv \log (X/Y)_{star} - \log (X/Y)_{sun}$, so that stars with compositions equal to the Sun's have [X/Y] = 0. All three stars are metal deficient, as is expected for halo objects, but even though our sample size is small there are a couple of surprises. First, there is the extraordinarily low iron abundance of G64-12. This is the most metal-poor star now known. Second, the spread in metallicity is interesting. The distant ($r_{gal} \gtrsim 25$ kpc) globular clusters and dwarf spheroidal companions to our galaxy seem to have [Fe/H] ~ −1.5 to −2.3 (Harris and Canterna, 1979), whereas we are seeing a spread of from −1.5 to −3.5. An additional surprise from G64-12 is its aluminum-to-magnesium ratio. Explosive nucleosynthesis calculations (Arnett, 1971) predict that metal-poor supernovae will produce less aluminum relative to magnesium than metal-rich supernovae. Peterson (1978, 1980) has provided a general observational confirmation of this prediction in her abundance analyses of subdwarfs, and CD-29°2277 adheres to the relation, in that at [Fe/H] ~ −1.6, [Al/Mg] ~ −0.7. At [Fe/H] ~ −3.5 however, an extrapolation of the relation predicts [Al/Mg] ~ −2, whereas G64-12 has [Al/Mg] ~ −0.7. This discrepancy could have resulted from one or both of two possible causes. First, the production of aluminum relative to magnesium might depend on more than the metallicity of the

TABLE 24. Properties of Remote Halo Stars

Star	U	V	W	gal	[Fe/H]	[Al/Mg]
CD-29°2277	+82	−664	−45	454	−1.63	−0.7
G64-12	−37	−342	+392	412	−3.52	−0.7
HD 134439	−311	−515	−73	435	−1.57	...

supernova. Second, the degree to which the supernova products blend with primordial material (which has near-zero abundances of elements with $Z > 5$) might differ. This blending or dilution is important because the mixing will not alter the Al/Mg ratio but will lower the Fe/H ratio. If dilution is the sole cause, we note that the supernova(e) that produced the heavy elements of G64-12 were metal rich in order to produce a high Al/Mg ratio. Since it is generally thought that metal-rich supernovae occurred more recently than metal-poor ones, G64-12 would then be younger than most of the known metal-poor subdwarfs, which in turn would suggest that star formation in at least some distant parts of the galactic halo occurred more slowly than in the solar vicinity. We need more data to adequately address these problems.

References

Arnett, W. D., Galactic evolution and nucleosynthesis, *Astrophys. J., 166*, 153-173, 1971.

D'Odorico, S., M. Peimbert, and F. Sabbadin, Pregalactic helium abundance and abundance gradients across our Galaxy from planetary nebulae, *Astron. Astrophys., 47*, 341-344, 1976.

Harris, W. E., and R. Canterna, On the abundance gradient in the galactic halo, *Astrophys. J. Lett., 231*, L19-L23, 1979.

Janes, K. A., Evidence for an abundance gradient in the galactic disk, *Astrophys. J. Suppl. 39*, 135-156, 1979.

Kraft, R. P., On the nonhomogeneity of metal abundances in stars of globular clusters and satellite subsystems of the Galaxy, *Annu. Rev. Astron. Astrophys., 17*, 309-343, 1979.

Peterson, R. C., Relative abundances in metal-poor stars. I. The aluminum-to-iron ratio, *Astrophys. J., 222*, 595-599, 1978.

Peterson, R. C., Relative abundances in metal-poor stars. III. Sodium through copper, *Astrophys. J.*, submitted, 1980.

Searle, L., Evidence for composition gradients across the disks of spiral galaxies, *Astrophys. J., 168*, 327-341, 1971.

Talent, D. L., and R. J. Dufour, Spectrophotometry of four H II regions in the Perseus arm and a reassessment of galactic abundance gradients, *Astrophys. J., 233*, 888-905, 1979.

Blue Stragglers

*Bruce W. Carney and Ruth C. Peterson**

An open or globular cluster color-magnitude diagram (Fig. 78; Sandage, 1970) is approximately a temperature-luminosity plot, and one of its salient features is the main sequence turn-off (labelled TO). Since stars in a cluster are thought to be roughly the same age, the turn-off temperature and luminosity measure a cluster's age, with both parameters decreasing for older clusters. The fact that most if not all clusters have well-defined turn-offs supports the coeval hypothesis. However, in several open and globular clusters, stars have been observed at positions in color-magnitude diagrams appropriate to main sequence stars but hotter and brighter than the cluster turn-off. Known for over twenty years, such stars are called blue stragglers (labeled "BS" in Fig. 78), and their cause remains unknown.

Various proposals explaining the phenomenon have appeared over the past twenty years, and these proposals may be grouped into four broad classes. (I) Delayed formation. The blue stragglers really are younger than the other stars in the cluster. The usual signposts of recent star formation have not yet been seen in any cluster containing blue stragglers, so this is unlikely. (II) Highly evolved. Some stars only seem to be on the main sequence but could be very evolved, such as horizontal branch stars (core He and shell H burning phase). The photometrically deduced gravities of blue stragglers are not consistent with this. (III) Reborn. One member of a binary expands during its normal later evolution and transfers material to a less-evolved dwarf, thus increasing the latter's mass, after which it should relocate to a hotter and more luminous state appropriate to a higher-mass

*Lockheed Palo Alto Research Laboratory, Palo Alto, California.

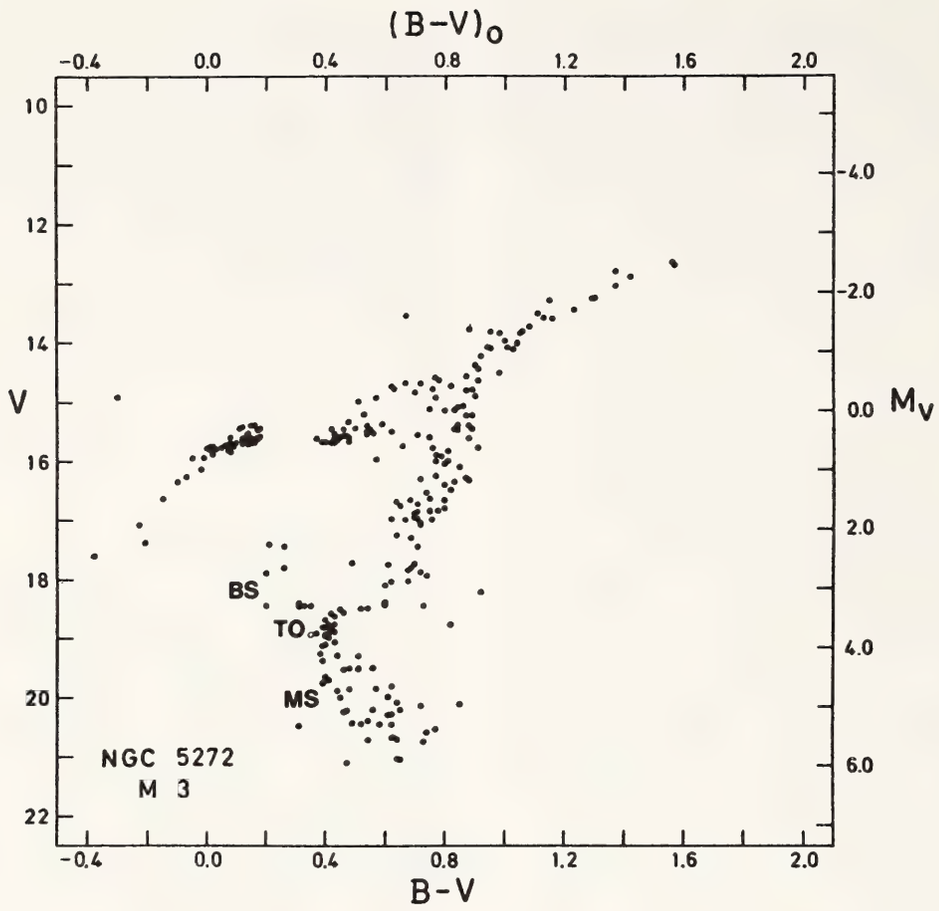


Fig. 78. The color-magnitude diagram of the globular cluster M3, taken from Sandage (1970). BS = blue stragglers; TO = turn-off; MS = main sequence.

dwarf. Circumstantial evidence supporting this idea is that in some clusters, blue stragglers have variable radial velocities, indicating a binary system. In an extreme version of this mass transfer idea, two members of a binary coalesce. At least in some cases, mass transfer or coalescence appears unlikely, since photometrically deduced blue straggler masses exceed twice the turn-off mass and thus exceed the mass available in an unevolved binary. (IV) True stragglers. The normal course of stellar evolution is slowed down somehow, perhaps through mixing of fresh H fuel to the core or through lowered central pressure via rotation.

We have begun a program of high-dispersion, high-resolution spectroscopy of blue stragglers to investigate questions associated with Class IV. Blue stragglers are relatively faint, which is why studies done to date have either been done via low-dispersion spectroscopy or intermediate-band photometry (uvby). We chose to begin with the brighter examples. These stars are not in clusters but are in the general field population. Since the disk population contains stars of almost all ages, it is very difficult to be certain that a star with kinematic properties typical of the disk population is a blue straggler and not a younger, normal dwarf. However, the halo population is quite old, and no known globular cluster main sequence turn-off is bluer than $B - V \sim 0.35$. Thus, if we can find stars whose kinematics are those of the halo population, with gravities typical of dwarfs (obtained via photometry) and

colors bluer than $B - V \sim 0.35$, we will have a sample of halo blue stragglers. Abundance analyses can strengthen the halo nature and rule out "runaway" disk stars, since halo stars are generally very metal poor ([Fe/H] < -0.7). Our first survey was done with a sample of five stars—two "control" stars whose observed properties indicate they are exactly at the main sequence turn-off (BD +1°234lp and HD 84937), and three halo blue stragglers (HD 100363, BD −12°2669, and BD +25°1981). High-dispersion spectrograms of the first four stars were obtained with the CTIO 4-m telescope and echelle spectrograph. The data for BD +25°1981 were similarly obtained at Kitt Peak. *UBVRI* photometry for all stars was acquired at CTIO, and stellar temperatures were derived by comparing model-atmosphere surface-flux distributions against 40-Å bandpass scanner spectrophotometric data obtained at Kitt Peak.

Our basic result is that the blue stragglers rotate faster than the control stars. In fact, the latter have $V_{rot} \sin i \leq 5$ km/sec while BD +25°1981, BD −12°2669, and HD 100363 have $V_{rot} \sin i = 15$, 35, and 65 km/sec. Figure 79 compares line widths in two of our blue stragglers and three metal-poor stars judged to be at or near the main sequence turn-off. Each profile represents the co-addition in velocity space of several metallic lines from one or more spectrograms for each star. The two blue stragglers BD −12°2669 and HD 100363 have much broader lines, as would be caused by rotation. For these last two stars, we have three separate spectrograms, and no radial velocity variations were seen. Instead, we feel these results suggest rotation to be the cause of the blue straggler phenomenon, via either the lowered central pressure or induced meridional circulation-mixing of hydrogen into the stellar core. The results are summarized in Table 25. A sample of three

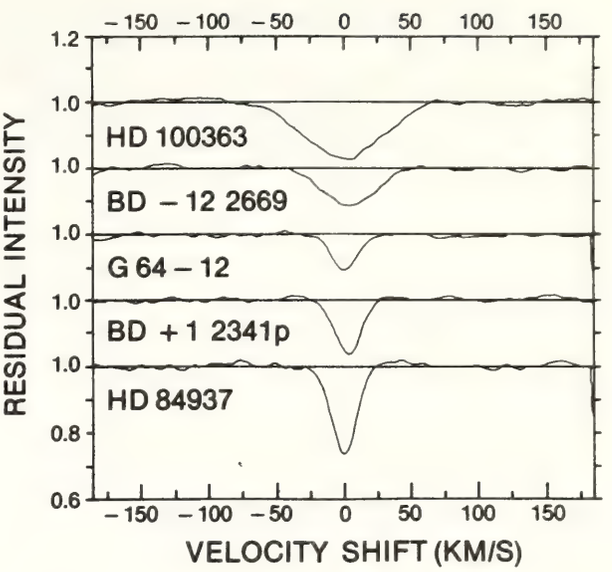


Fig. 79. Metal line profiles co-added in velocity space for two blue stragglers (top) and three normal subdwarfs near the turn-off (lower). Note the broader lines of the blue stragglers.

TABLE 25. Rotation Properties of Blue Dwarf Halo Stars

Star	*Te*	$V_{rot} \sin i$ (km s^{-1})	Nature
HD 84937	6220	<5	Normal Pop II Dwarf
BD+1°2341p	6300	<5	Normal Pop II Dwarf
BD+25°1981	6850	15	Blue straggler
BD−12°2669	6950	35	Blue straggler
HD 100363	7050	65	Blue straggler

does not allow proper accounting for the sin *i* effect, so we hope to study more such stars. Further, to test our ideas, we are now observing blue stragglers in the old, open cluster M67, and comparing those stars with normal dwarfs in the much younger Hyades and Pleiades clusters. Again, we are finding much broader lines in the blue stragglers, but quantitative results are not yet available. We are also looking for various elemental abundance differences that might indicate mixing of CNO-cycle material to the stellar surface.

References

Sandage, A., Main sequence photometry, color-magnitude diagrams, and ages for the globular clusters M3, M13, M15, and M92, *Astrophys. J., 162*, 841–870, 1970.

Systematic Variations of Dynamical Properties along the Hubble Spiral Sequence

*Vera C. Rubin, W. Kent Ford, Jr., Norbert Thonnard, and David Burstein**

For the past several years, our observing has been directed toward learning about both the mass distribution in the universe and the systematic dynamical properties of spiral galaxies. Early in this century, it was reasonable for astronomers to assume that the distribution of luminous matter, i.e., stars and galaxies, was a valid measure of the distribution of mass. However, almost fifty years ago, Sinclair Smith (1936) and Fritz Zwicky (1937) made an amazing discovery: Individual motions of galaxies in a cluster of galaxies are so large that the gravitational attraction of all cluster galaxies is not sufficient to keep the cluster from flying apart. Galaxy clusters should thus be dissolving, although apparently they are not. This observation leads to the suspicion that unseen matter is present to bind the clusters. Very recent work has strengthened this conclusion; the dynamics of individual galaxies, of double galaxies, of groups, and of clusters all point to this unobserved but ubiquitous mass component. As much as 90% of the mass in the universe may be presently unseen. Its form is unknown, although its luminosity per unit mass must be significantly smaller than that of conventional stellar matter. It might consist of very low luminosity stars, or planets, or comets, or neutrinos, or even mini-black holes.

We have chosen to learn about the mass distribution in the universe by studying the mass distribution within individual galaxies. We have asked the question, "What is the distribution of matter in spiral galaxies?" The answer has been clear and unambiguous: At least some fraction of the nonluminous matter of the universe is distributed about individual galaxies. In every galaxy we have studied, the rotational velocities remain high completely across the optical galaxy, and do not decrease as would be expected for galaxies with high central mass concentrations. In spiral galaxies of all types, the mass is not as centrally condensed as the light. Instead, the integrated mass increases approximately linearly with increasing radius. Significant mass exists at large nuclear distances, at least some of it beyond the optical image. The rotational velocities remain high in response to the gravitational attraction of this distant but unseen matter. Thus, although we cannot observe directly the light from this material, we have detected its presence by studying the motions of the stars and gas clouds whose motions it influences.

En route to this conclusion, we have accumulated a body of systematic dynamical data concerning spiral galaxies of various morphologies and luminosities. We discuss some of this material below.

Astronomers group spiral galaxies into three operationally useful classes, following the early work by Hubble (1926): Sa galaxies, with large nuclear bulges surrounded by tightly wound, smooth arms which are barely resolved into knots; Sb galaxies, with moderate-sized bulges, arms more open, and increasingly resolved into emission regions; and Sc galaxies, with small nuclear bulges, arms wide open, and composed of discrete luminous segments. To date, we have obtained spectra of 21

*National Radio Astronomy Observatory, Charlottesville, Virginia, which is operated by Associated Universities, Inc., under contract with the National Science Foundation.

Sc, 18 Sb, and 11 Sa galaxies; these span the range from high luminosity to low luminosity within each Hubble class. Our observing this year has been directed toward completing observations of the Sa and Sb samples. The galaxies were observed with the 4-meter telescopes of the Kitt Peak National Observatory and the Cerro Tololo Inter-American Observatory, and the 2.5-meter du Pont telescope of the Carnegie Institution of Washington at Las Campanas, Chile. A few typical spectra are shown in Fig. 80. In all cases, a spectrograph incorporating a Carnegie image tube was used. We use these spectra to map, at high spatial and high velocity resolution, the velocity of the gas clouds in the galaxies as they orbit the center of each galaxy. From the observed velocities, we deduce the entire mass— luminous and nonluminous alike—whose gravitational attraction is responsible for producing the velocities. We now understand for the first time, even though at an elementary level, what role the variation of parameters such as density, radius, luminosity, mass, and velocity play in locating a galaxy along the Hubble sequence.

One valuable method for characterizing the large-scale dynamical properties of a galaxy is to produce a rotation curve, i.e., a plot showing the rotational velocities in the galaxy (V) as a function of distance from the center of the galaxy (R). We show in Figs. 81 and 82 typical rotation curves and mass distributions for high- and low-luminosity Sa, Sb, and Sc galaxies. Sa galaxies exhibit rotation curves which rise steeply from the origin and level off at high (>300 km/sec) maximum rotational velocities, V_{max}. In contrast, Sc galaxies show lower nuclear velocity gradients, and lower (~ 200 km/sec) maximum rotational velocities. Within a given Hubble type, Sc for example, the lower-luminosity (smaller) galaxies have lower nuclear velocity gradients and lower maximum rotational velocities; the Sc galaxies of highest luminosity (i.e., the largest galaxies) have steep velocity gradients and high maximum rotational velocities.

For all galaxies whose velocities we have measured to date, we show in Fig. 83a the values of V_{max} as a function of Hubble type. Maximum rotational velocities decrease systematically from types Sa through Sc, i.e., with decreasing prominence of the bulge. In general, the lowest observed values of V_{max} for Sa galaxies are equal to the highest observed V_{max} in Sc galaxies. This difference in V_{max} values is the major dynamical difference between galaxies of different morphologies, and reflects a higher mass density in Sa galaxies than in Sc galaxies at the same nuclear distances. But because any classification scheme is an attempt to fit into a few meaningful classes galaxies which actually come in a continuum of types, it is not surprising that the Sb galaxies have values of V_{max} generally spanning the range intermediate between Sa and Sc.

Notwithstanding this difference in maximum rotational velocities along the Hubble sequence, it is important to note that there are similarities in the forms of the rotation curves even for galaxies of different morphologies. Given a rotation curve with no velocity scale, it would be difficult to identify the Hubble class to which that galaxy belongs. In general, a curve rising rapidly from the nucleus followed by a slightly rising (or, less often, flat) portion would be a good characterization of rotation curves of all isolated spiral galaxies, regardless of Hubble class.

In Figures 83b, c, and d, we show the variation of three other parameters as a function of Hubble type. Note that while there is a significant progression from Sa through Sc for each parameter, the ranges are large and the overlaps considerable. The median density in solar masses per cubic parsec at a fixed

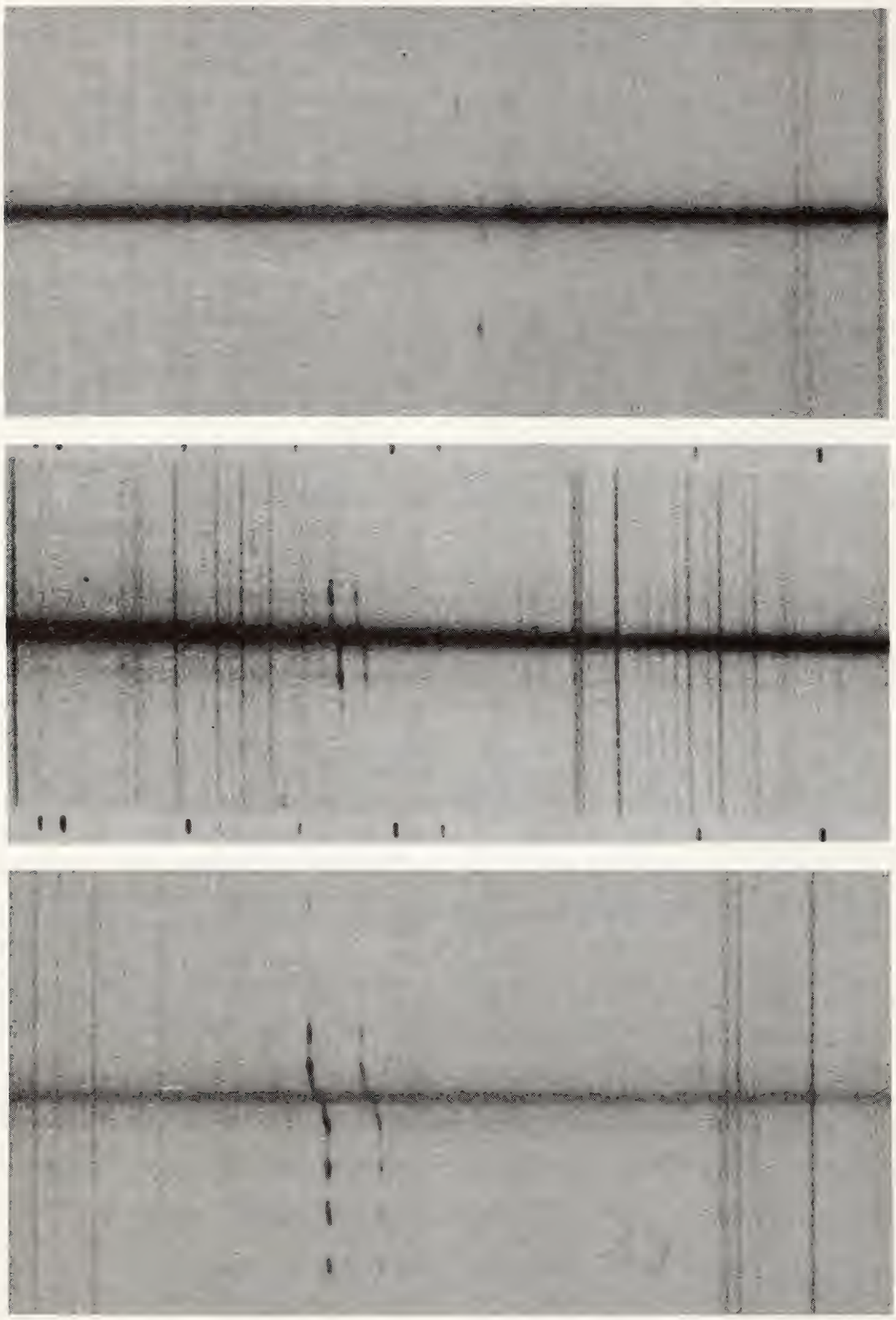


Fig. 80. Image tube spectra of three galaxies of high luminosity. (upper) IC 724, type Sa; (middle) NGC 7083, type Sb; and (lower) NGC 2998, type Sc. The hydrogen emission from each galaxy is recorded as the strongest broken vertical line on each spectrum; the displacement of this line is a measure of the rotational velocity of the galaxy. The strong central horizontal line is the combined spectra of all the stars in the nucleus. Note how the intensity ratio of hydrogen emission to nuclear emission increases from types Sa to Sc. The straight vertical lines completely crossing the spectra are emission (principally OH) from the Earth's atmosphere. The upper and lower spectra were taken with the Kitt Peak National Observatory 4-m spectrograph; the middle spectrum was obtained with the 2.5-m du Pont telescope at Las Campanas, Chile.

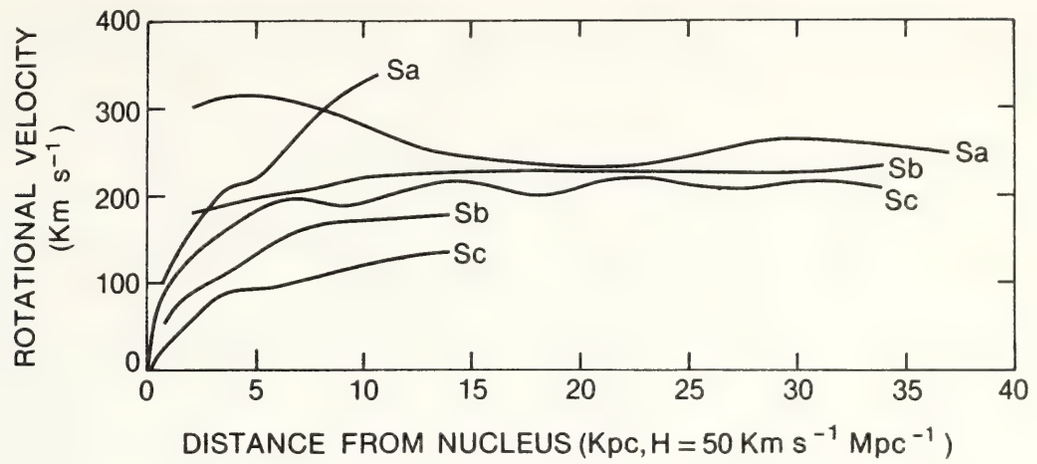


Fig. 81. Rotational velocity as a function of nuclear distance for galaxies of various Hubble types. In general, rotation velocities are constant or rise with large nuclear distances. For galaxies of the same Hubble type, the galaxy of smaller radius is the galaxy of lower luminosity. The galaxy of lower luminosity usually has a maximum rotational velocity smaller than that of the higher-luminosity galaxy.

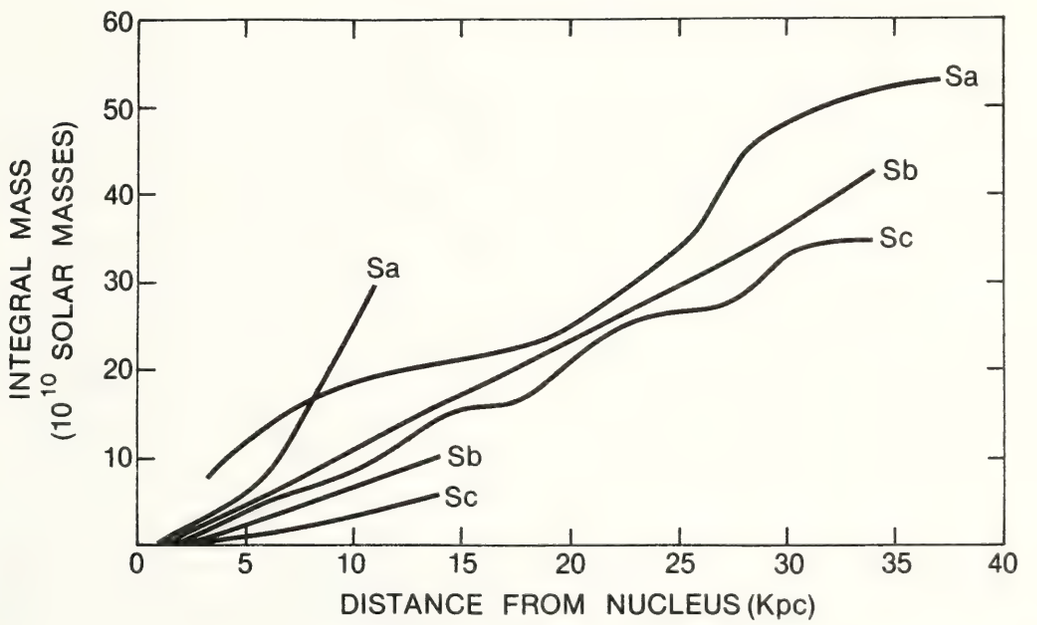


Fig. 82. Integral mass to the indicated radial distance, derived from rotation curves shown in Fig. 80. Because mass is a function of both radius and velocity, a small Sa galaxy (with a large rotational velocity) has a mass larger than that of a small Sb or Sc galaxy, but smaller than that of a large galaxy of type Sb or Sc.

nuclear distance (here chosen as 8.5 kpc) shown in Fig. 83b, decreases by a factor of about two or three from Sa through Sc galaxies. The total range in density across the Hubble spiral sequence is only a factor of ten. This density variation follows directly from the observed velocities, for in the region of the flat rotation curves, the density at every R is proportional to V^2/R^2. Hence at the same R, the density in an Sa is greater than the density in an Sc, for $V(\text{Sa}) > V(\text{Sc})$. Thus the morphology of a galaxy may be determined early in its history and may be related to the density of the gas cloud from which the

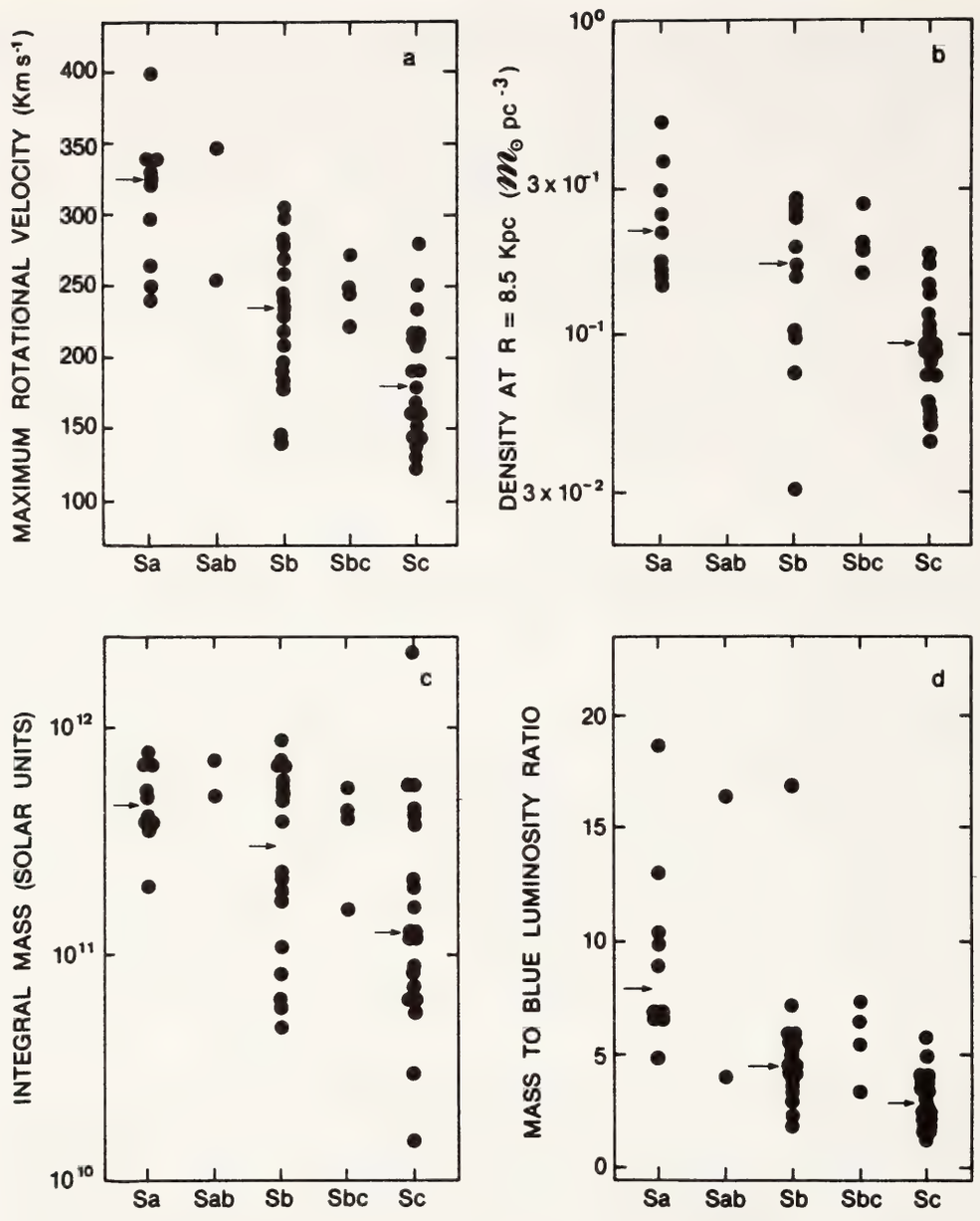


Fig. 83. Distribution of various parameters for spiral galaxies, separated according to Hubble type. In each case, the arrow marks the midpoint of distributions. Sa galaxies systematically have higher rotational velocities, higher masses, higher mass densities, and higher ratios of mass to blue luminosity than do Sb or Sc galaxies, although there is considerable overlap among the distributions for the various galaxy types.

galaxy condensed. In regions of initial high density, Sa galaxies (high density, large bulge) may preferentially have formed; in regions of low initial density, Sc galaxies (low density, small bulge) may have formed. Although much work remains to be done before the relative importance of such factors can be integrated into a comprehensive picture of galaxy formation and evolution, these observations should put interesting constraints on various models.

The integrated mass of a spiral galaxy (here, the mass enclosed within the isophote equal to 25 mag/[arc sec]^2) is a function both of its rotational velocities and its radius, $\int M(R) = V^2R$. An Sc galaxy of large radius may have an integrated mass greater than an Sa of small radius, even though the rotational velocities are lower in the Sc.

This is apparent in Fig. 82, where the large galaxies have masses larger than the small galaxies, independent of type. The distribution of integral masses as a function of Hubble type is shown in Fig. 83c. In the mean, masses of Sa's are higher than Sc's. However, an upper limit to a spiral mass of 10^{12} solar masses is observed, independent of morphology. This limit is undoubtedly real, for galaxies of highest luminosity are well represented in our sample. The principal difference in the mass distributions is the large range of masses (10^{10}–10^{12} solar masses) exhibited by Sc galaxies, compared with the smaller range of Sa masses. The demands of the classification scheme, that Sa galaxies have prominent bulges, apparently restricts Sa galaxies to large masses.

The three parameters discussed so far—maximum rotational velocity, density, and integral mass—are all strictly correlated with luminosity within each Hubble class. That is, in Figures 83a, b, and c, the distribution along any line follows the distribution in luminosity. Large-mass Sc's are high luminosity; small-mass Sc's are low luminosity. This is not true of the distribution of mass-to-luminosity ratio, shown in Fig. 83d. This ratio, $\int M/\int L_B$, measures the average amount of mass per unit luminosity within a galaxy. The distribution indicates that Sa galaxies have more mass per unit luminosity than Sc galaxies. This result is contrary to earlier studies which showed that $\int M/\int L$ was independent of galaxy type. This earlier conclusion arose from calculating galaxy masses based on rotational velocities, which decrease with increasing nuclear distance. Thus, the presently observed flat rotation curves invalidate these early mass values. Our result offers a clue to the types of stellar populations which make up each morphological class. Curiously, small Sc galaxies have the same value of $\int M/\int L$ as large Sc's, although locally in all Sc's the $\int M/\int L$ value is increasing with increasing radial distance. Therefore, to maintain the same average population, in small Sc galaxies the stellar population varies rapidly over a small distance range, while in large Sc's this variation occurs gradually over a very large distance range.

The ranges of properties shown in Fig. 83 do not represent those of galaxies in a fixed volume of space, for we have made considerable effort to study galaxies of all luminosities and Hubble types. For example, low-luminosity Sc galaxies are common, but we must search a larger volume of space to find an extremely high luminosity Sc. Figure 83 does delineate the wide range of properties of Sa, Sb, and Sc galaxies. All the distributions shown in Fig. 83 contain information about fundamental properties of galaxies, properties of the interstellar medium from which they condensed, the mass and density distributions of galaxies, and their present stellar and nonstellar constituents. One important relation which emerges is that of maximum rotational velocity to galaxy luminosity within a single Hubble class (Fig. 84).

The correlation of the maximum rotational velocity with the intrinsic luminosity of a galaxy has been discussed by Tully and Fisher (1977), and is called the Tully-Fisher relation. It is an important astronomical tool, for it makes it possible to deduce the intrinsic brightness of a galaxy if its maximum rotational velocity is known. Then, by comparing the true brightness with the observed brightness, the distances of the galaxy can be inferred. Hence the Tully-Fisher relation, once calibrated on nearby galaxies, serves as an independent yardstick for measuring extragalactic distances. In its previous applications, rotational velocities have come from 21-cm radio observations (which generally obtain values of V_{max} but no details of the rotation curve), and galaxies of all Hubble classes have been used in a single relation.

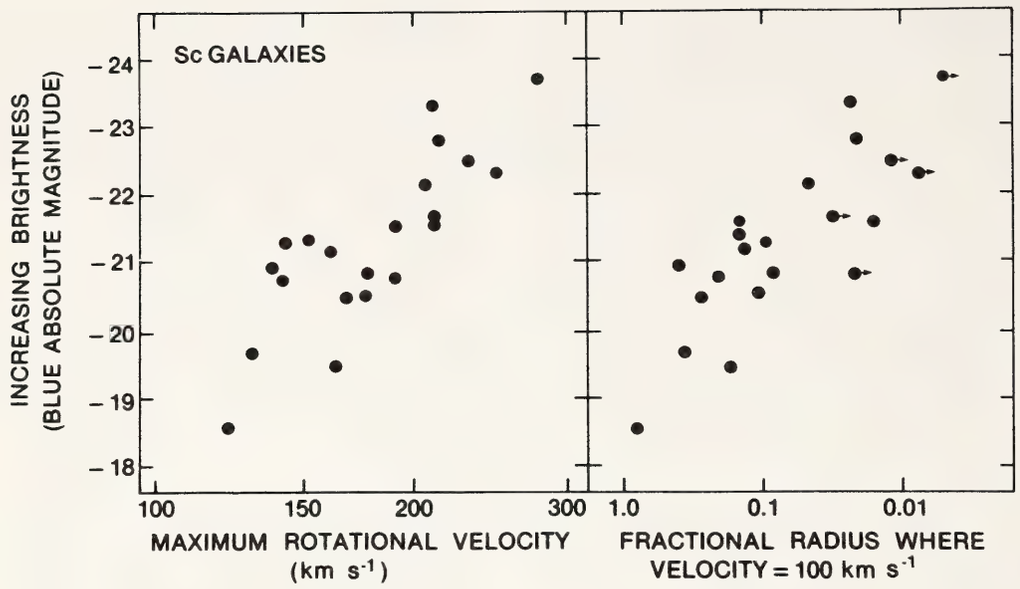


Fig. 84. (left) Correlation of maximum rotational velocity with intrinsic galaxy luminosity; the Tully-Fisher relation. (right) The correlation of radial distance where the rotational velocity reaches 100 km/sec, in fractions of the optical radius, as a function of galaxy luminosity. Note the striking similarity of these two plots, which we attribute to the smooth progression of galaxy rotational properties with luminosity.

In Fig. 84 (left) we show for Sc galaxies the correlation of absolute magnitude with maximum rotational velocity determined from our optical rotation curves; higher-luminosity Sc galaxies have higher rotational velocities. However, the slope is significantly steeper than that deduced by Tully and Fisher for their sample of all Hubble types together. However, the corresponding plot for Sb galaxies in our set shows a similarly good correlation, but is displaced with respect to that for the Sc's. An Sb galaxy is more than one magnitude brighter than an Sc galaxy with the same V_{max}; an Sa galaxy is several magnitudes brighter. The low slope found by Tully and Fisher results from fitting a single line through the very separate distributions. Present attempts to use the Tully-Fisher relation to map the distribution and velocities of galaxies in our region of the universe must take into account the effects of galaxy morphology on the correlation. Aaronson, Huchra, and Mould (1979) have extended the use of the Tully-Fisher relation by using infrared galaxy magnitudes, where the difficulties due to galactic extinction and internal extinction are minimized; the effects of galaxy morphology at these wavelengths must still be assessed.

During our study, we discovered a new relation between dynamics and luminosity of spiral galaxies, one which should find wide use as a distance indicator. We very early noted that in galaxies of low luminosity (i.e., small galaxies), rotational velocities increase slowly with increasing nuclear distance; in galaxies of high luminosity (i.e., large galaxies), velocities increase steeply (see Fig. 81). In fact, for the high-luminosity Sa and Sb galaxies in Fig. 81, the velocity gradient just off the nucleus is too steep to measure, for the rotational velocity is already high at the first measured velocity off the nucleus. Thus, some measure of the nuclear velocity gradient, as measured on the sky, is a measure of the intrinsic luminosity of the galaxy. One such measure is the radius of the galaxy where the rotational velocities have reached 100 km/sec, with the radius expressed

in fractions of the total optical radius. We show in Fig. 84 (right) a plot of absolute magnitude against the fractional radius where the rotational velocity is equal to 100 km/sec. Its similarity to the conventional Tully-Fisher diagram is striking. For Sc galaxies of lowest luminosity, this velocity is reached only near the edge of the optical galaxy, i.e., fractional radius = 1. For high-luminosity galaxies, the rotational velocities reach 100 km/sec at less than 1% of galaxy radius. High-luminosity galaxies are valuable in cosmology as distance indicators. Hence in order to use this correlation, it is necessary to determine rotational velocities of high-luminosity galaxies only near their central regions, where high light levels make the observations relatively straightforward. Moreover, we expect that rotational velocities can be obtained from absorption lines in spectra of gas-poor galaxies for which 21-cm or emission line velocities cannot be found. Thus, this correlation of nuclear velocity gradient with intrinsic luminosity, after calibration for different Hubble type, should be applicable for determining distances to a wide range of galaxies, wider even than the spiral set for which we have established it.

We conclude on a speculative note. Various pieces of evidence, especially the flat rotation curves, lead to the conclusion that low-luminosity mass must exist in large quantities in the universe. If positive evidence for this material (other than its gravitational attraction) does not accrue, then astronomers may be forced to an alternative explanation of the observed dynamical effects. One such explanation might be that the inverse square law of gravitation becomes invalid at large distances.

References

Aaronson, M., J. Huchra, and J. Mould, The infrared luminosity/HI velocity-width relation and its application to the distance scale, *Astrophys. J., 229,* 1-13, 1979.

Hubble, E., Extra-galactic nebulae, *Astrophys. J., 64,* 321-369, 1926.

Smith, S., The mass of the Virgo cluster, *Astrophys. J., 83,* 23-30, 1936.

Tully, R. B., and J. R. Fisher, A new method of determining distances to galaxies, *Astron. Astrophys., 54,* 661-673, 1977.

Zwicky, F., On the masses of nebulae and of clusters of nebulae, *Astrophys. J., 86,* 217-246, 1937.

The Shape of 21-cm Velocity Profiles from Spiral Galaxies; Correlations with Luminosity and Optical Rotation Curves

*N. Thonnard, V. C. Rubin, W. K. Ford, Jr., and M. S. Roberts**

Complementing optical spectroscopy for studying the systematic properties of spiral galaxies are 21-cm neutral hydrogen observations, obtained from the same galaxies studied at optical wavelengths. The emission observed in the optical spectrogram, from which the dynamical studies reported in the previous section were derived, come principally from ionized hydrogen and nitrogen in regions where active star formation is in progress and where temperatures are $\sim 10^4$ K. The slit of the spectrograph is usually aligned along the major axis and samples less than 1% of the surface of the galaxy. In contrast, the 21-cm hydrogen line comes from neutral atomic gas at temperatures between ~50K and ~1000K, most of which is at a few hundred kelvins. The beam of the radiotelescope is typically a few times larger than the galaxies observed. In addition, the 21-cm radiation is not attenuated by dust either in the galaxies or in our own Galaxy, and in most cases the emitting regions appear to be optically thin. Therefore, an observed intensity-velocity profile represents the integral of all neutral atomic hydrogen in a galaxy.

*National Radio Astronomy Observatory, Charlottesville, Virginia.

As an aid in comparing the dynamical information derived from the optical spectroscopy with the observed neutral hydrogen profiles, we have parameterized the optical data for 21 Sc galaxies studied earlier (Rubin, Ford, and Thonnard, 1980) in the following manner. The major-axis spectrogram was divided into 12 intervals, each of which represented a fraction of the corrected optical radius of the galaxy; six of these regions were on the oncoming side of the galaxy and six on the receding side. For each radius interval r_n to r_{n+1}, integrating the observed radial velocity by

$$\int_{r_n}^{r_{n+1}} V(r)dr / \int_{r_n}^{r_{n+1}} dr$$

gave a smoothed, weighted radial velocity for each interval. This resulted in a tabulation of up to 12 radial velocities representing the same fraction of the galaxy radius for each of the 21 Sc galaxies. In addition, we identified regions with no detected emission and noted the farthest measured point from each side of the nucleus.

To emphasize the systematic differences in the shape of the rotation curves as a function of the luminosity of the galaxy, we have normalized the rotational velocities derived from the above smoothed data to the rotational velocity at 60% of the optical radius. This point was far enough from the nucleus for most rotation curves to be close to the maximum rotational velocity, while still close enough for all galaxies to have measurable Hα emission. In Fig. 85 we have plotted the mean normalized rotation curve for the three most-luminous Sc galaxies in our sample, the three median luminosity, and the three least-luminous galaxies. It is immediately apparent that the rotational velocity in the most-luminous galaxies rises very rapidly with radius and reaches 90% of the maximum velocity within the first 10% of the radius. The least-luminous galaxies, on the other hand, have rotation curves that rise slowly as a function of fractional galaxy radius.

As the observed neutral hydrogen profile is the integral over the entire velocity field of the galaxy convolved with the neutral hydrogen surface density, it follows that the shape of the 21-cm hydrogen line profile should depend

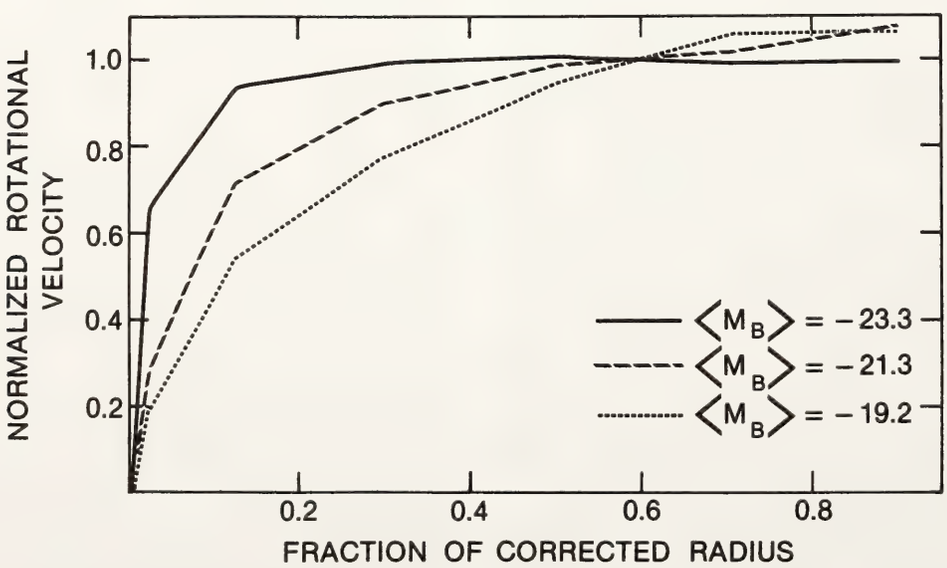


Fig. 85. Mean rotational velocity for the three most-luminous, the three median-luminosity, and the three least-luminous galaxies in our Sc sample. The rotation curves have been normalized both in radius and in velocity to illustrate the change in the shape. We note that the maximum rotational velocity ranges from 122 to 300 km/sec, while the radius ranges from 4 kpc to 122 kpc in this sample.

on the shape of the rotation curve. Since the earliest days of extragalactic hydrogen observations, synthetic profiles have been generated to compare with observation (see, for instance, Epstein, 1964; Gordon, 1971). Unfortunately, except for low-luminosity galaxies, even very recently (Roberts, 1978) the lack of accurate and high-resolution rotation curves that extend out to the entire optical image forced workers to use model rotation curves. These curves decreased in velocity beyond 10–30% of the radius, which we now know is incorrect.

To illustrate the effect of the rotation curve on the 21-cm profile, we plot in Fig. 86 synthetic profiles derived from extremely simple models that nonetheless show the effects of realistic rotation curves. For Sc galaxies, we note that the neutral hydrogen mass is usually less than 10% of the total mass of the galaxy. Therefore, the neutral hydrogen acts only as a tracer for the mass distribution in the galaxy, and large changes in hydrogen distribution will have very small effects on the mass distribution, which, of course, determines the rotation curve. Three neutral hydrogen surface density distributions, convolved with a rotation curve that rises linearly with increasing radius to the outer edge of the galaxy (a limiting approximation to low-luminosity galaxies), were used to generate the profiles shown in Fig. 86a. The solid line represents a constant surface density over the entire observed disk of the galaxy. The dashed line represents a disk whose inner half has twice the surface density of the outer half. Both of these profiles exhibit slowly rising edges and no central minimum, a characteristic of very low luminosity galaxies. Some galaxies of low-to-moderate luminosity have rotation curves that rise slowly with increasing

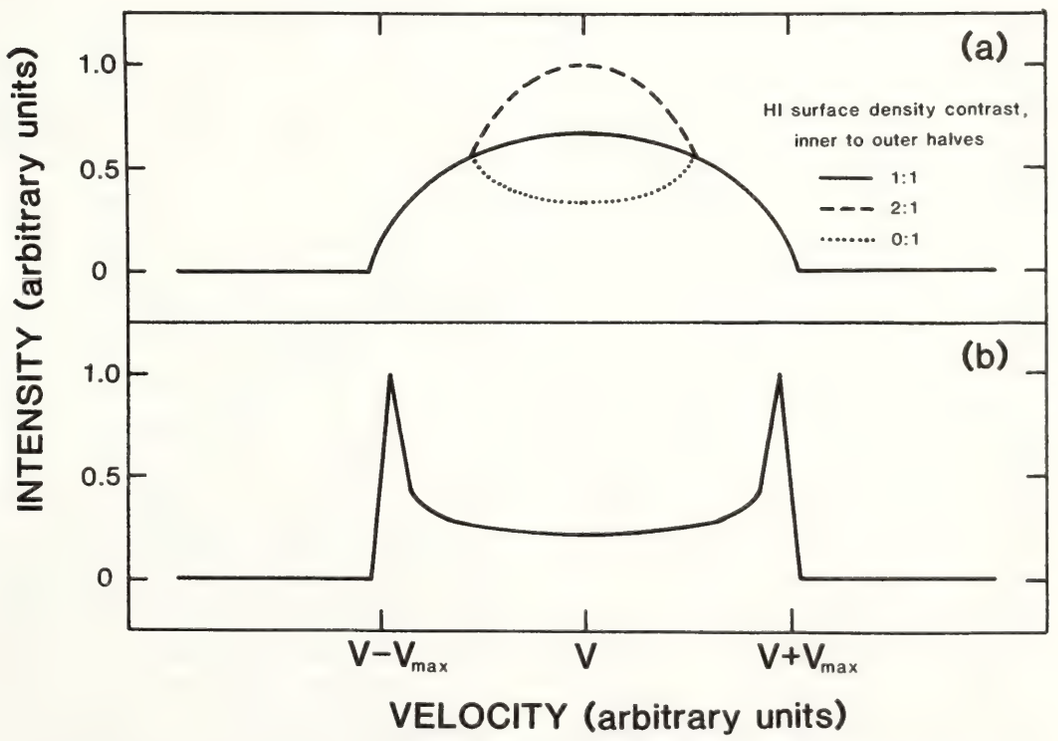


Fig. 86. Model 21-cm velocity profiles. V is the systemic velocity of the galaxy and V_{max} is the peak rotational velocity. In (a), the rotation curve used in the model rises linearly with radius and reaches V_{max} at the outer edge. Three HI surface densities were used: constant over the entire disk of the galaxy, with the inner half twice as dense, and with no hydrogen in the inner half. In (b), the rotation curve used has a constant rotational velocity of V_{max} over the entire disk of the galaxy. Under these conditions, any axi-symmetric density distribution will produce the identical profile.

radius, but their velocity profile does show a central minimum. This is approximated with the dotted profile in Fig. 86a, in which the hydrogen surface density has a hole in the inner half of the galaxy and is constant thereafter to the outer edge.

A rotation curve that changes discontinuously at the nucleus and is constant to the outer edge of the galaxy is a good approximation for the rotation curve of the highest-luminosity galaxies. With this type of rotation curve, the shape of the profile shown in Fig. 86b is independent of hydrogen distribution, as long as the distribution is axi-symmetric. This profile is remarkably similar to that observed in 21-cm profiles of high-luminosity galaxies.

By using realistic density functions that are combinations of gaussians and exponentials, including some random motions in the neutral hydrogen, and using the parameterized optical rotation curves, we should be able to reproduce the observed profiles and learn something about random motions and density distribution as a function of luminosity in galaxies. But qualitatively, as we see from Fig. 86a, for galaxies with rising rotation curves, by varying the hydrogen surface density we can generate profiles with shapes ranging from having strong peaks in the center to having significant dips; yet for high-luminosity galaxies with rotational velocities that are constant as a function of radius, there is only one possible profile shape.

In Fig. 87 we present 21-cm hydrogen line profiles superimposed on their parameterized optical rotation curves for four Sc galaxies. A number of correlations between the optical and 21-cm data are evident.

NGC 4605, the intrinsically faintest galaxy in our sample, has an optical rotation curve that rises slowly with radius. As expected, the neutral hydrogen profile is single-peaked. The profile is also asymmetric. Interestingly, the high-velocity side of the profile—the side having the least amount of neutral hydrogen—is also the side on which the optical spectroscopy extended least in radius.

NGC 3495 is approximately two magnitudes more luminous than NGC 4605, has a rotation curve that is rising a little faster, and has a pronounced dip in the center of its 21-cm profile. For this case, the rotation curve rises slowly such that the only way to make peaks at the high- and low-velocity extremes is by a lower hydrogen surface density at the center of the galaxy than at the edges. A crude 21-cm map of the galaxy seems to confirm this. Also, the two peaks are broad and closer in from the edges of the profile. A smoothed version of the dotted curve in Fig. 86a would not be a bad approximation.

NGC 3672—one magnitude brighter than NGC 3495—has a rotation curve that rises close to its maximum by 40% of the radius, but the 21-cm profile shows no central dip, implying that it has a centrally peaked hydrogen distribution. Figure 87 also shows that on the high-velocity side, where the rotational velocity is constant over a large range of radius, the 21-cm profile edge is steep, whereas on the low-velocity side, where the rotational velocity is more variable with radius, the 21-cm profile edge is less steep.

UGC 2885, the most luminous galaxy in our sample, is five magnitudes brighter than NGC 4605, the faintest. The rotational velocity for this galaxy is essentially constant over its entire radius. The 21-cm profile has the limiting model shape shown in Fig. 86b. In fact, by normalizing the model to the same area and half-power width of the observed profile, the similarity between galaxy and model is remarkable, as shown in Fig. 88. The addition to the model of a small component of random motion in the gas would probably make the profiles coincident. But even in this limiting case, the dynamics of the rotational velocities are evident in the 21-cm profile. On the high-velocity side of

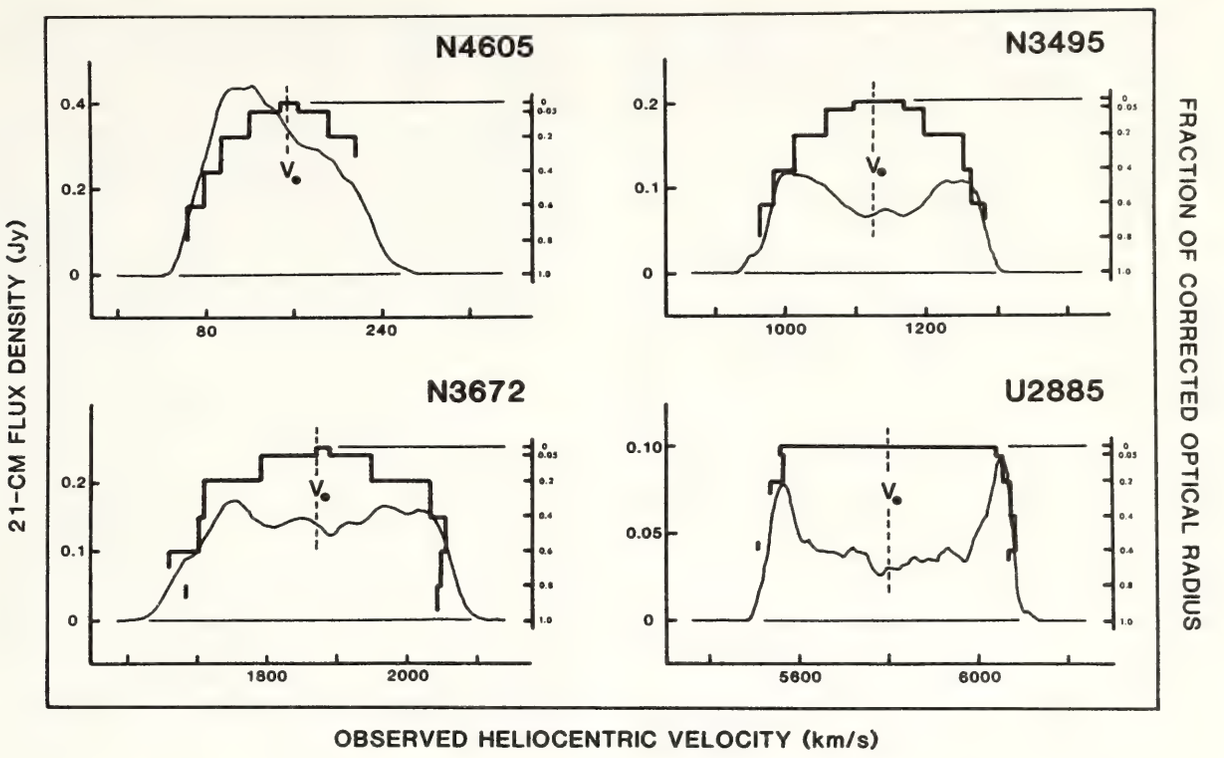


Fig. 87. Comparison of 21-cm neutral hydrogen profiles (thin line) with the optical rotation curves (heavy line) for four galaxies arranged by increasing luminosity: NGC 4605, NGC 3495, NGC 3672, and UGC 2885. The dashed vertical line marks the systemic velocity, $V_{\odot}$. The scale on the left side of the figures denotes the neutral hydrogen flux density, increasing upward. The scale on the right side gives the fractional radius, increasing downward. Both the receding and oncoming sides of the rotation curves are given for the radial distances at which HII was detected.

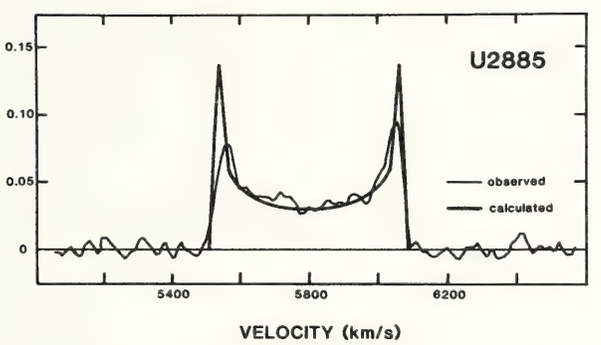


Fig. 88. Comparison of the model using a rotation curve with constant rotational velocity with the observed profile for UGC 2885, the most luminous galaxy in our Sc sample. The model profile was normalized to the area and velocity width of the observed profile.

the profile, the optical rotation curve could be measured over a large range in radius with very small differences in observed velocity; the 21-cm profile edge is very steep. But on the low-velocity side, the optical rotation curve was spottier and covered a slightly larger velocity range, and the 21-cm profile edge is less steep.

Even though much remains to be done to understand the relationships between the 21-cm and optical observations, we can already draw a number of conclusions. The correlation between the dynamics deduced from the optical spectra, which sample a very small fraction of the galaxy, and the 21-cm profile, which is integrated over the entire galaxy, is remarkably good. This implies that asymmetries seen in the rotation curves between the oncoming and receding sides of the galaxies are large-scale phenomena encompassing a considerable fraction of the entire galaxy. Asymmetries in the neutral hydrogen content between the two sides of the galaxy are also reflected in the Hα emission; namely, the side of the galaxy in which the optical spectrum is less complete over all radii is also the

side with less neutral hydrogen. For galaxies of intermediate luminosity, there is a large range in relative radial neutral hydrogen distribution.

The next step in this analysis will be to use the parameterized rotation curves to synthesize model profiles. By knowing one of the important variables—the rotation curve—a much more definitive understanding of the density distribution will be possible. By extending our analysis to the Sb and Sa galaxies, we hope to deduce the systematic variations in neutral hydrogen properties as functions of Hubble type and luminosity.

References

Epstein, E. E., Preliminary investigations of model distributions of atomic hydrogen in galaxies, *Astron. J., 69,* 521–526, 1964.

Gordon, K. J., A 21-cm study of the spiral galaxy Messier 33, *Astrophys. J., 169,* 235–270, 1971.

Roberts, M. S., Twenty-one centimeter line widths of galaxies, *Astron. J., 83,* 1026–1035, 1978.

Rubin, V. C., W. Kent Ford, Jr., and N. Thonnard, Rotational properties of 21 Sc galaxies with a large range of luminosities and radii, from NGC 4605 (R = 4 kpc) to UGC 2885 (R = 122 kpc), *Astrophys. J., 238,* 471–487, 1980.

Acknowledgements

We thank the directors of Cerro Tololo Inter-American Observatory, the Hale Observatories, Kitt Peak National Observatory, the National Astronomy and Ionosphere Center, and the National Radio Astronomy Observatory for making observing time available.

INSTRUMENTATION

Imaging Detectors*

W. Kent Ford, Jr.

The popular concept of an astronomer is probably still the traditional one: a dedicated scientist sits at the eyepiece of a telescope, searching for something new. This is, of course, a quaint but badly outdated picture. Today, an observational astronomer at work is likely to be preparing for an observing session with a telescope which will be operated with the aid of a low-light-level TV viewing system, or reducing, analyzing, and interpreting data obtained with the aid of an electronic detector. We have spent considerable time this year working on problems related to instrumentation in support of our own astronomical research activities. In particular, we have continued our efforts to develop more efficient detectors both by improving the performance of our image intensifier systems and by investigating the performance characteristics of the newer, rapidly evolving silicon sensors. Also, we have begun work with a system of computer programs that will enable us to analyze digital data more efficiently.

*Supported in part by Grant AST-79-03432 from the National Science Foundation.

Image Tubes

Carnegie image-tube systems are built around RCA two-stage magnetically focused image intensifiers. RCA developed the basic design and fabrication techniques used in building these tubes nearly ten years ago. These devices are useful to the astronomer because they are more sensitive than other detectors, such as the photographic emulsion. The photocathodes in these tubes are made by depositing antimony and cesium and other alkali vapors onto a transparent substrate.

Over the years much effort has been invested trying to optimize the processing techniques to increase the sensitivity. However, the sensitivities achieved in the C33063 image tube are consistently lower than those achieved in the earlier version of the "Carnegie" image tube. Also, there has been increasing interest among astronomers in using more uniform cathodes to increase the usefulness of the tubes for various photometric applications, in particular for intensifier-aided direct photography. New techniques have been developed at RCA for depositing the photocathode material, and have been used extensively, for example, in processing SIT tubes. Clearly, the time was ripe for a fresh approach to the problem.

This year we received a research grant from the National Science Foundation that provides funds to develop at RCA improved techniques for processing photocathodes in magnetically focused tubes used for astronomical applications. A series of single-stage versions have been built at RCA in an attempt to optimize the cathode-forming procedure. These tubes employ a side appendage for generating the alkali vapors and an internal baffle to promote a uniform deposition on the cathode. Measurements of cathode sensitivity and uniformity indicate that the experimental cathodes are substantially improved. The greatest variation in photocathode sensitivity is found in the near infrared on the tail of the spectral response curve. Previous cathodes showed variations at 800 nm of ±50% across the 38-mm diameter. The best of the experimental tubes processed with the new technique has a cathode uniformity of ±15% at 800 nm. This cathode has a quantum efficiency of 20% at 420 nm and 2% at 800 nm—relatively high efficiencies for semitransparent photocathodes. With the experience gained in this study, our colleagues at RCA are now in a stronger position to make the two-stage tubes with the exacting specifications that are required by the astronomical applications.

Silicon Detectors

Solid-state imaging devices offer a number of potential advantages for astronomical use, including high quantum efficiency and an inherent geometric stability. Self-scanned photodiode arrays, charged-coupled devices (CCD's), and charge injection devices (CID's) are all being used at various observatories in various digital imaging systems. (Some of the characteristics of these systems are given in Ford, 1979.) While image intensifier tubes produce an optical output, the silicon imaging devices produce an electrical output directly from the optical input. In some cases the silicon detector is used as a read-out mechanism for a high-gain image intensifier. For other applications, the high quantum efficiency of the silicon makes it essential as the prime sensor. Unfortunately, at low light levels the astronomical signals must compete with the instrumental noise of the sensor itself. Therefore, cooling is required to suppress thermally generated spurious charge, and low-noise preamplifiers are needed to minimize the noise introduced by the read-out process.

A continuing and long-term interest at DTM has been to make use of the improved silicon imaging devices as they become more readily available. This year we have worked on two important peripheral parts of this long-term project. We are developing a reliable, general purpose cooling system in the form of an upward-looking liquid nitrogen dewar suitable for use at the focus of a telescope. The dewar provides a large "work surface" on which the silicon device is attached. Also, we have begun to implement a system of computer software for processing digital data.

Interactive Data Processing

Both image intensifiers and the newer silicon detectors produce large quantities of digital data that must be processed and evaluated. In the case of the image intensifiers, the intermediate storage of the data is in analog form on photographic plates and must be extracted with a digitized microphotometer. As other detector systems are developed, more of our observational data will become directly available in digitized form. Consequently, we have an increasing need for ready interaction with digital data of various sorts.

An elegant and well-documented software system has been developed at the Cerro Tololo Interamerican Observatory for the reduction of data acquired with a SIT vidicon (Albrecht, 1979). This interactive system was designed by S. Schaller (1977); most of the astronomical reduction programs were written by B. Lasker and P. Osmer of CTIO and R. Albrecht of the Institute for Astronomy, Vienna, who was working at CTIO as a consultant. A local colleague, Dr. Peter B. Boyce, informed us that the astronomers at Vienna had adapted this system to the same computer and operating system that is in use at DTM, and that they had broadened the scope of the original system to include the processing of microphotometer data and the IUE satellite spectra. With the generous help of Dr. R. Albrecht of Vienna and Dr. H. Jenkner of Ohio State University and the Institute for Astronomy, Vienna, the Tololo-Vienna Reduction System (TVR) was installed on the DTM PDP 11-34.

Our local data acquisition is based on a Nuclear Data 2400 multichannel analyzer and its associated nine-track magnetic tape recorder. We have developed programs for reading these tapes into the TVR system and for converting the instrumental ADC values into opacity or optical density. Existing programs in the TVR system have been modified to permit the determination from a calibration plate of the nonlinear intensity response of the photo-

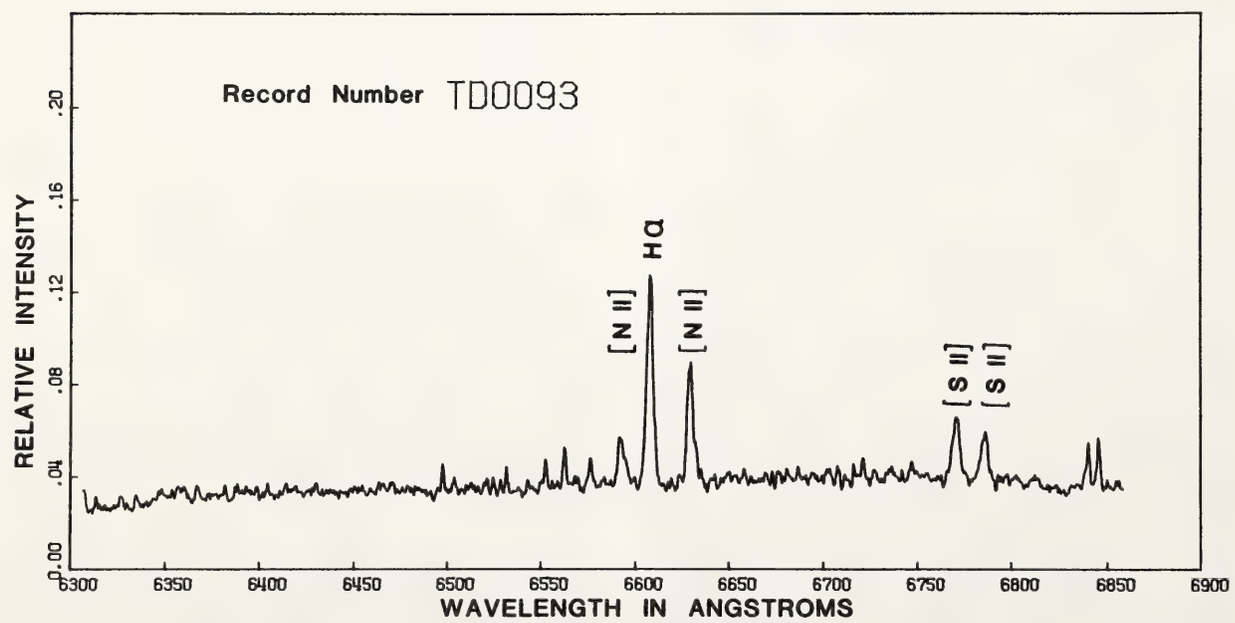


Fig. 89. Relative spectrophotometry of the nucleus of NGC 1421, and Sc spiral galaxy in the Rubin, Ford, and Thonnard sample. The original spectrum was obtained photographically with the aid of a Carnegie image tube on the Kitt Peak National Observatory 4-m telescope. The spectrogram was traced with a digital microphotometer, and the data were reduced with TVR, the Tololo-Vienna Reduction System.

graphic image intensifier system, and the transformation of the measured spectrum into relative intensities. Programs for setting up wavelength scales have been "debugged" to operate on the DTM system. And finally, the procedures for using the TVR programs with our data acquisition system have been documented for other DTM users (see Fig. 89).

As procedures for reducing various types of astronomical data are refined, additional programs will need to be developed. The cost of this software development is enormous; it is to our advantage to participate and share in a growing library of programs for processing astronomical data. We are very much indebted to our colleagues at CTIO and Vienna for developing this system and sharing it with us.

References

Albrecht, Rudolph, Interactive analysis of optical astronomical images, paper given at the "International Workshop for Image Processing in Astronomy," Trieste, Italy, June, 1979.

Ford, W. Kent, Jr., Digital imaging techniques, *Annu. Rev. Astron. Astrophys., 17,* 189–212, 1979.

Schaller, S., *CTIO Facilities Manual,* Chapter 9, La Serena, Chile, 1977.

Installation of the New 21-cm Receiver at the Instituto Argentino de Radioastronomía*

N. Thonnard

An important phase of our longstanding collaboration with the Instituto Argentino de Radioastronomía (IAR) in southern radioastronomy was completed last summer with the installation of a new 21-cm receiver at the IAR. The instrument, which increases the sensitivity and versatility of research at the IAR manyfold, was supported with funds from CIW, IAR, and the National Science Foundation.

*Supported in part by Grant INT-75-19069 from the National Science Foundation.

The receiver was designed and built at DTM with help from our Argentine colleagues, and after careful testing was shipped to Argentina last spring (*Year Book 78,* 414). After the equipment cleared customs and was unpacked at the IAR, Thonnard spent seven weeks last summer in Argentina overseeing the reassembly of the receiver and installation on the CIW-IAR 30-meter antenna.

We were rewarded by the care spent in packing; not a single piece of equipment was damaged in shipment. In fact, after the entire receiver was reassembled, the total system gain was within 10% of its value before packing. As is always the case when a complex piece of equipment is installed, there were numerous mechanical and electrical interfaces that had to be attended to, but finally on Saturday, July 21, 1979, an unusually beautiful day (in contrast to the normally dreary Argentine winter), all preparations had been completed and the receiver front-end box was raised to the focus of the antenna (see Fig. 90).

Before raising the receiver front end to the focus, a number of tests were run. The noise temperature of the receiver at the entrance to the feed was remeasured and confirmed to be 60 K. The value of the calibrating noise source was remeasured very carefully and found to be 6.6 K. This is 0.7 K higher than measured previously, but after performing this delicate test in a number of different ways, we are convinced that the 6.6 K number is correct, and feel that the original value was in error. The stability of the "Cal" is important, as it allows calibrations from many observations, each having some uncertainty, to be easily combined in order to accurately determine the sensitivity of the receiver.

In addition, after hastily building a filter and making various temporary modifications in the front end, we also tested a GASFET amplifier just completed for us by the Radio Astronomy

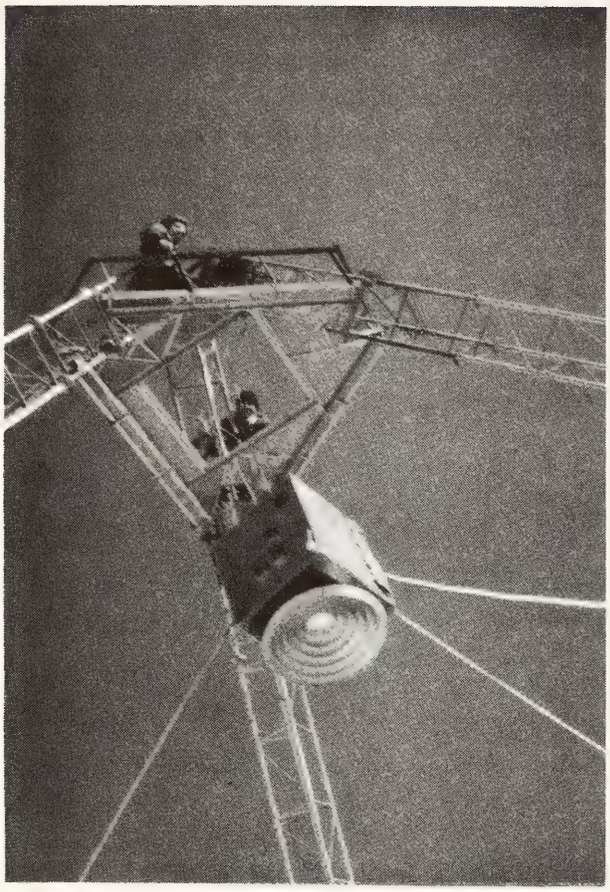


Fig. 90. The new 21-cm receiver (the square box with the circular target-looking feed beneath) being raised to the focus of the CIW-IAR 30-meter radiotelescope antenna.

Laboratory of the University of California, Berkeley. This amplifier was designed for use at the 18-cm wavelength of the hydroxyl radical, but could be easily modified to cover the entire 25- to 17-cm basic tuning range of the receiver. Even though this amplifier occupies a volume of only one fiftieth and its cost is less than one tenth that of a parametric amplifier, the measured noise figure was very close to that of the parametric amplifier. Therefore, for observations outside of the 21-cm band, this amplifier could be easily substituted for the parametric amplifier presently installed in the front end. The possibilities offered by this type of development were exciting indeed.

Before observations could begin, some changes had to be made in the computer hardware and software. Because of the very large line voltage variations encountered, the computer power supplies were modified to keep the system operational. In addition, we encountered a number of problems, some anticipated, some not, due to the 50-Hz operation. Our greatest difficulties occurred with the floppy-disk drives, which in addition to the above-mentioned problems, became unreliable at low ambient temperatures. Fortunately, these troubles are all behind us now. The software was modified to better fit the actual observing conditions and to make the data output more convenient and reliable against power failures by writing the data in a recirculating disk file.

The performance of the receiver has been quite gratifying. As expected, because of the stronger taper in the feed illumination pattern, the HPBW increased from ~30 arc minutes to 34 arc minutes, while the aperature efficiency increased from 52% to 58%. The largest bonus from the tightened illumination pattern was the decrease in spillover contribution and increased immunity to sidelobe interference. The calculated spillover contribution to the system noise temperature by the new feed was 4 K (as compared to 30 K for the old system). This was confirmed in a number of tests. First, the same system temperature, 85 K, was realized both for observations with the front-end box on the ground with the feed pointing upward during tests and with the front end at the focus and the antenna pointing to a region in the sky with no radio emission. Next, no changes in baseline temperature to within 0.5 K could be detected as the antenna was moved around the sky. The old system had variations greater than 5 K. And, most importantly, we found a reduction of many orders of magnitude in the interfering signal from the Buenos Aires airport radar which enters the system via the an-

tenna sidelobes. In the old system, the radar signal was so strong that it would overload the amplifier, cause harmonic distortion, and actually turn off the receiver. In the new receiver, the radar interference is below the saturation level of the amplifier and hence remains linear and can easily be removed after the first few amplifier stages with R.F. filters.

The receiver has now been in operation through a complete winter/summer seasonal cycle. The temperature controller for the front-end box has worked extremely well. Consequently the gain stability has been very good. Unfortunately, because of computer memory size limitations, the Total Power observing mode has not yet been implemented. Therefore, we do not know what the ultimate sensitivity limit will be, as only in this observing mode is stability of utmost importance, while all other instrumental effects cancel out to give the best baselines. Observations to date have mostly used the Load Switched mode. Presently, baselines in the Load Switched mode have curvatures ranging from 2 to 5 K, but we know of a number of adjustments and modifications that should reduce this by at least a factor of four. It is encouraging to note that after 60 minutes of extragalactic hydrogen observations, the RMS noise on the resulting profile is within 20% of the calculated value, indicating that the noise sources are statistical in nature and that sensitivity can be increased with long integrations.

The future looks bright at the IAR. The new receiver has dramatically influenced many facets of the operation, both technological and observational.

As the receiver is computer controlled, using both a PDP-11 minicomputer and the new microprocessors, the scientific and technical staff at the observatory have greatly expanded their visions of what can be done. With the accessibility of the PDP-11, the software for data taking and reduction will be tailored much more to an individual project's needs. The inexpensiveness and versatility of the microprocessors will allow precise and flexible control of observations. The basic simplicity in the design of the GASFET amplifiers, which are inexpensive and for which parts are on hand at the observatory, will allow great flexibility in observing wavelengths. In the past, the complexity and untunability of the first-stage amplifier (usually a parametric amplifier) was the limiting factor. In fact, with a rather simple refrigeration system, these GASFET amplifiers can be cooled with a consequent doubling of sensitivity over the present receiver.

The observational programs possible with the new receiver are numerous. We cannot mention all programs that have been started, but we will describe a few of the major ones.

Under the direction of E. Bajaja, eight members of the IAR staff have started an all-sky, wide-velocity-range (−660 to +660 km/sec), high-sensitivity (0.02 K rms) survey of neutral hydrogen. This will match up with the Northern Hemisphere observations being carried out by Hulsbosch at Dwingeloo, and when complete, should give us a much more sensitive picture of the outer extremities of our Galaxy. Bajaja and C. Martin have also compiled a sample of 180 galaxies of type later than S0 and having apparent magnitudes brighter than 12^m and declinations less than −45°, which they are studying at the 21-cm hydrogen line. F. R. Colomb is heading up a group that will study the H166α recombination line in the direction of southern HII regions and will also look for diffuse H166α emission along the Galactic plane. W. G. L. Pöppel and coworkers have started observing the neutral hydrogen emission at very high resolution (using 3-kHz crystal filters) in the direction of dark optical filaments. These are regions in which the gas is quite cold and where H_2CO and other molecular emissions have been

detected. With the high resolution it is hoped to determine the temperatures of these regions and the relationship of neutral hydrogen to the other constituents.

We feel that the effort expended by many of us on this project is now paying off. Our colleagues at the IAR have undertaken new research projects that would not have been possible with the old equipment. Enough technical expertise and materials are now available at the IAR that will enable the staff to expand their observations to many other wavelength regions at high sensitivity.

Acknowledgments

The author thanks Drs. E. Bajaja, R. Colomb, W. Pöppel, Ing. E. Filloy, and the entire staff of the Instituto Argentino de Radiastronomía for their hospitality during his seven-week stay at the observatory.

BIBLIOGRAPHY

The publications listed below can be obtained at no charge from the Department of Terrestrial Magnetism, 5241 Broad Branch Rd., N. W., Washington, D. C. 20015. When ordering, please give reprint number(s). No reprints are available for titles marked with asterisks.

—— Aaronson, M., *see* Carney, B. W.

4556 Assousa, G. E., and W. Herbst, Supernova-induced star formation, in *Giant Molecular Clouds in the Galaxy,* pp. 275–284, P. M. Solomon and M. G. Edmunds, eds., Pergamon Press, New York, 1980.

—— Beach, L., *see* Sacks, I. S.

4557 Burstein, D., The absorption-line strengths of elliptical and S0 galaxies, *Astrophys. J., 232,* 74–83, 1979.

*4558 Burstein, D., The existence of thick disks in spirals and ellipticals, in *Photometry, Kinematics and Dynamics of Galaxies,* Conference held in Austin, August 6–8, 1979, pp. 81–84, D. S. Evans, ed., University of Texas, Austin, 1979.

4559 Burstein, D., Structure and origin of S0 galaxies. I. Surface photometry of S0 galaxies, *Astrophys. J. Suppl. Ser., 41,* 435–450, 1979.

4560 Burstein, D., Structure and origin of S0 galaxies. II. Disk-to-bulge ratios, *Astrophys. J., 234,* 435–447, 1979.

4561 Burstein, D., Structure and origin of S0 galaxies: III. The luminosity distribution perpendicular to the plane of the disks in S0's, *Astrophys. J., 234,* 829–836, 1979.

4562 Carney, B. W., The main sequence of the globular cluster NGC 6752, *Astron. J., 84,* 515–533, 1979.

4563 Carney, B. W., The subdwarf helium abundance and the rotation of the galactic halo, *Astrophys. J., 233,* 877–887, 1979.

4564 Carney, B. W., Subdwarf ultraviolet excesses and metal abundances, *Astrophys. J., 233,* 211–225, 1979.

4565 Carney, B. W., The ages and distances of eight globular clusters, *Astrophys. J. Suppl. Ser., 42,* 481–500, 1980.

*4566 Carney, B. W., Globular cluster ages and distances, in *Star Clusters* (IAU Symp. 85, Victoria, B. C., Canada, Aug. 27–30, 1979), pp. 329–330, James E. Hesser, ed., D. Reidel Publ. Co., Dordrecht, Holland, 1980.

4567 Carney, B. W., Southern metal-poor stars: UBVRI photometry, *Astron. J., 85,* 38–43, 1980.

4568 Carney, B. W., Spectrophotometry of supernova 1979c in M 100, *Publ. Astron. Soc. Pacific, 92,* 56–59, 1980.

4569 Carney, B. W., and M. Aaronson, Subdwarf bolometric corrections, *Astron. J., 84,* 867–871, 1979.

—— Carney, B. W., *see* Janes, K. A.

—— Clarke, R. S., Jr., *see* Scott, E. R. D.

—— Clayton, R. N., *see* Lee, T.

4570 Echeverría, L. M., Oceanic basaltic magmas in accretionary prisms: The Fran-

ciscan intrusive gabbros, *Amer. J. Sci., 280,* 697–724, 1980.

4571 Echeverría, L. M., Tertiary or Mesozoic komatiites from Gorgona Island, Colombia: Field relations and geochemistry, *Contrib. Mineral. Petrol., 73,* 253–266, 1980.

4572 Erkes, J. W., A. G. D. Philip, and K. C. Turner, Fine structure in the northern extension of the Magellanic Stream, *Astrophys. J., 238,* 546–553, 1980.

4573 Evans, J. R., and I. S. Sacks, Deep structure of the Iceland Plateau, *J. Geophys. Res., 84,* 6859–6866, 1979.

4574 Ford, W. K., Jr., Digital imaging techniques, in *Annual Review of Astronomy and Astrophysics, 17,* pp. 189–212, Geoffrey Burbidge, D. Layzer, and J. G. Phillips, eds., Annual Reviews, Inc., Palo Alto, California, 1979.

—— Ford, W. K., Jr., *see* Rubin, V. C.

—— Hart, S. R., *see* James, D. E.

4575 Herbst, W., and R. S. Rajan, On the role of a supernova in the formation of the solar system, *Icarus, 42,* 35–42, 1980.

—— Herbst, W., *see* Assousa, G. E.

—— Hess, P. C., *see* Ryerson, F. J.

4576 Hofmann, A. W., Diffusion in natural silicate melts: A critical review, in *Physics of Magmatic Processes,* R. B. Hargraves, ed., Princeton University Press, Princeton, New Jersey, in press.

4577 James, D. E., E. R. Padovani, and S. R. Hart, Preliminary results on the oxygen isotopic composition of the lower crust, Kilbourne Hole maar, New Mexico, *Geophys. Res. Lett., 7,* 321–324, 1980.

—— James, D. E., *see* Snoke, J. A.

*4578 Janes, K. A., and B. W. Carney, The SMC cluster NGC330, in *Star Clusters* (IAU Symp. 85, Victoria, B. C., Canada, Aug. 27–30, 1979), pp. 349–350, James E. Hesser, ed., D. Reidel Publ. Co., Dordrecht, Holland, 1980.

*4579 Kothari, B. K., and R. S. Rajan, Irradiation history of Mokoia: Implications for mixing processes in carbonaceous chondrites (ext. abstr.), *Meteoritics, 14,* 456–458, 1979.

*4580 Kothari, B. K., and R. S. Rajan, Brecciation chronology of xenolithic chondrites using fission tracks (ext. abstr.), *Lunar and Planetary Science XI,* pp. 573–575, Lunar and Planetary Institute, Houston, Texas, 1980.

*4581 Kothari, B. K., and J. R. Stephens, Laboratory condensation studies and genesis of chondritic phases (ext. abstr.), *Meteoritics, 14,* 458–460, 1979.

4582 Lee, T., T. K. Mayeda, and R. N. Clayton, Oxygen isotopic anomalies in Allende inclusion HAL, *Geophys. Res. Lett., 7,* 493–496, 1980.

*4583 Lee, T., T. K. Mayeda, and R. N. Clayton, The oxygen isotopic composition in Allende inclusion HAL and the origin of the FUN anomalies (ext. abstr.), *Lunar and Planetary Science XI,* pp. 618–620, Lunar and Planetary Institute, Houston, Texas, 1980.

—— Madden, T. R., *see* Ranganayaki, R. P.

—— Mayeda, T. K., *see* Lee, T.

—— Padovani, E. R., *see* James, D. E.

—— Philip, A. G. D., *see* Erkes, J. W.

—— Rajan, R. S., *see* Herbst, W., Kothari, B. K., ReVelle, D. O., and Scott, E. R. D.

4584 Ranganayaki, R. P., and T. R. Madden, Generalized thin sheet analysis in magnetotellurics: an extension of Price's analysis, *Geophys. J. Roy. Astron. Soc., 60,* 445–457, 1980.

4585 ReVelle, D. O., and R. S. Rajan, On the luminous efficiency of meteoritic fireballs, *J. Geophys. Res., 84,* 6255–6262, 1979.

4586 Rubin, V. C., Stars, galaxies, cosmos: the past decade, the next decade, *Science, 209,* 64–71, 1980.

*4587 Rubin, V. C., UGC 2885, the largest known spiral galaxy, *Mercury, 9,* 78–79, 1980.

4588 Rubin, V. C., Velocities and mass distribution in the barred spiral NGC 5728, *Astrophys. J., 238,* 808–817, 1980

4589 Rubin, V. C., W. K. Ford, Jr., and N. Thonnard, Rotational properties of 21 Sc galaxies with a large range of luminosities and radii, from NGC 4605 (R = 4 kpc) to UGC 2885 (R = 122 kpc), *Astrophys. J., 238,* 471–487, 1980.

4590 Ryerson, F. J., and P. C. Hess, The role of P_2O_5 in silicate melts, *Geochim. Cosmochim. Acta, 44,* 611–624, 1980.

*4591 Sacks, I. S., Interrelationships between volcanism, seismicity, and anelasticity in western South America, in *Oceanic Ridges and Arcs: Geodynamic Processes, 14,* pp. 355–363, M. N. Toksöz, S. Uyeda, and J. Francheteau, eds.,

Elsevier Scientific Publ. Co., Amsterdam, Holland, 1980.

4592 Sacks, I. S., J. A. Snoke, and L. Beach, Lateral heterogeneity at the base of the mantle revealed by observations of amplitudes of PKP phases, *Geophys. J. Roy. Astron. Soc., 59,* 379–387, 1979.

—— Sacks, I. S., *see* Evans, J. R., and Snoke, J. A.

4593 Scott, E. R. D., Origin of anomalous iron meteorites, *Mineral. Mag., 43,* 415–421, 1979.

*4594 Scott, E. R. D., Origin of iron meteorites, in *Asteroids,* pp. 892–925, T. Gehrels and M. S. Matthews, eds., University of Arizona Press, Tucson, 1979.

4595 Scott, E. R. D., and R. S. Clarke, Jr., Identification of clear taenite in meteorites as ordered FeNi, *Nature, 281,* 360–362, 1979.

4596 Scott, E. R. D., and R. S. Rajan, Thermal history of the Shaw chondrite, *Proc. 10th Lunar Sci. Conf.* (Houston, March 19–23, 1979), pp. 1031–1043, R. B. Merrill, ed., Pergamon Press, New York, 1979.

*4597 Scott, E. R. D., and R. S. Rajan, Thermal history of some xenolithic ordinary chondrites (ext. abstr.), *Lunar and Planetary Science XI,* pp. 1015–1017, Lunar and Planetary Institute, Houston, Texas, 1980.

4598 Snoke, J. A., I. S. Sacks, and D. E. James, Subduction beneath western South America: evidence from converted phases, *Geophys. J. Roy. Astron. Soc., 59,* 219–225, 1979.

—— Snoke, J. A., *see* Sacks, I. S.

—— Stephens, J. R., *see* Kothari, B. K.

—— Thonnard, N., *see* Rubin, V. C.

—— Turner, K. C., *see* Erkes, J. W.

4599 Wasson, J. T., and G. W. Wetherill, Dynamical, chemical and isotopic evidence regarding the formation locations of asteroids and meteorites, in *Asteroids,* pp. 926–974, T. Gehrels and M. S. Matthews, eds., University of Arizona Press, Tucson, 1979.

*4600 Wetherill, G. W., Numerical calculations relevant to the accumulation of the terrestrial planets, in *The Continental Crust and Its Mineral Deposits,* J. T. Wilson Symposium held in Toronto, 1979, pp. 3–24, D. W. Strangway, ed., Geological Assn. of Canada, Special Paper No. 20, 1980.

4601 Wetherill, G. W., and C. L. Drake, The earth and planetary sciences, *Science, 209,* 96–104, 1980.

—— Wetherill, G. W., *see* Wasson, J. T.

PERSONNEL

Staff Members

L. Thomas Aldrich
George E. Assousa[1]
Louis Brown
Scott E. Forbush, *Emeritus*
W. Kent Ford, Jr.
Albrecht W. Hofmann
David E. James
Typhoon Lee
Alan T. Linde
R. Sundar Rajan
Richard B. Roberts, *Emeritus*[2]
Vera C. Rubin
I. Selwyn Sacks
Fouad Tera
Norbert Thonnard
George W. Wetherill, *Director*

Distinguished Service Member of Carnegie Institution

Merle A. Tuve

Research Associates (Staff)

Albert Jambon
Rambabu P. Ranganayaki
Frederick J. Ryerson

Research Associate (Nonresident)

Leonidas Ocola, Instituto
Geofísico del Peru
Lima, Peru

Senior Fellow

Edward R. D. Scott

Postdoctoral Fellows

David Burstein
Bruce W. Carney
Lina María Echeverría
W. Daniel Heinze
Esther M. Hu
Emi Ito
Brajesh K. Kothari
Richard A. Lux
Kiyoji Shiono
Robert J. Stern
William M. White

Visiting Investigators

Akira Hasegawa
Douglas G. Mose
Volker von Drach

Student Trainees and Predoctoral Fellows

Marie-France Bugnon
Mark Feigenson
Morgan I. Granger

Collaborators

R. Albrecht, Institute for Astronomy, University of Vienna, Austria
E. Bajaja, Instituto Argentino de Radioastronomía, Villa Elisa, Argentina
J. Bannister P., Universidad de Chile, Santiago, Chile
R. Batiza, Washington University, St. Louis, Missouri
L. D. Bibee, School of Oceanography, Oregon State University, Corvallis
M. Bracamonte, Trujillo, Peru
C. Brooks, University of Montreal, Quebec
D. Burstein, National Radio Astronomy Observatory, Charlottesville, Virginia
R. Cabre, S. J., Observatorio San Calixto, La Paz, Bolivia
M. Casaverde R., Instituto Geofísico del Peru, Lima
T. J. Chow, Scripps Institute of Oceanography, La Jolla, California
R. S. Clarke, Jr., National Museum of Natural History, Smithsonian Institution, Washington, D.C.
F. Colomb, Instituto Argentino de Radioastronomía, Villa Elisa, Argentina
L. P. Cox, Massachusetts Institute of Technology, Cambridge
T. H. Dixon, Jet Propulsion Laboratory, Pasadena, California
E. M. El Shazly, Atomic Energy Establishment, Cairo, Egypt
A. F. J. Engel, Scripps Institute of Oceanography, La Jolla, California
D. W. Evertson, University of Texas at Austin
E. Filloy, Instituto Argentino de Radioastronomía, Villa Elisa, Argentina
K. Fredriksson, Department of Mineral Sciences, Smithsonian Institution, Washington, D.C.
A. A. Geisecke, Instituto Geofísico del Peru, Lima
A. Hasegawa, Tohoku University, Sendai, Japan
C. E. Hedge, U.S. Geological Survey, Denver, Colorado

[1]Through June 1980
[2]Deceased April 4, 1980

C. E. Helsley, University of Hawaii, Honolulu
D. Huaco, Instituto Geofísico del Peru, Lima
I. D. Hutcheon, Enrico Fermi Institute, University of Chicago, Illinois
H. Jenkner, Department of Astronomy, The Ohio State University, Columbus, Institute for Astronomy, University of Vienna, Austria
M. J. S. Johnston, U.S. Geological Survey, Menlo Park, California
J. Klein, Tandem Accelerator Laboratory, University of Pennsylvania, Philadelphia
J. Kormendy, Dominion Astrophysical Observatory, Victoria, British Columbia
I. Kushiro, Geophysical Laboratory, Carnegie Institution of Washington, Washington, D.C.
J. Leutgert, University of Wisconsin, Madison
B. Lewis, University of Washington, Seattle
A. Lindh, U.S. Geological Survey, Menlo Park, California
A. McGarr, U.S. Geological Survey, Menlo Park, California
R. P. Meyer, University of Wisconsin, Madison
R. Middleton, Tandem Accelerator Laboratory, University of Pennsylvania, Philadelphia
K. Muirhead, Australian National University, Canberra
T. Murase, Geophysical Laboratory, Carnegie Institution of Washington, Washington, D.C.
B. O. Mysen, Geophysical Laboratory, Carnegie Institution of Washington, Washington, D.C.
J. Nelen, Department of Mineral Sciences, Smithsonian Institution, Washington, D.C.
H. Okada, Hokkaido University, Sapporo, Japan
G. Olafsson, Akureyri, Iceland
J. Ossaka, Tokyo Kogyo University, Tokyo, Japan
R. C. Peterson, Lockheed Palo Alto Research Laboratory, Palo Alto, California
E. Pimental, Cuzco University, Cuzco, Peru
J. E. Ramirez, S. J., Instituto Geofísico de los Andes Colombiano, Bogotá, Colombia
D. O. ReVelle, Northern Arizona University, Flagstaff
M. S. Roberts, National Radio Astronomy Observatory, Charlottesville, Virginia
A. Rodriquez B., Universidad Nacional de San Agustín, Arequipa, Peru
E. R. D. Scott, Institute of Meteoritics, University of New Mexico, Albuquerque
D. A. Simoni, Arequipa, Peru
R. Sinha, National Radio Astronomy Observatory, VLA, Soccoro, New Mexico
J. A. Snoke, Virginia Polytechnic Institute and State University, Blacksburg
R. Stefansson, The Iceland Meteorological Office, Reykjavik
K. Suyehiro, Tokyo University, Tokyo, Japan
S. Suyehiro, Japanese Meteorological Agency, Tokyo
F. Volponi, Universidad Nacional de Cuyo, San Juan, Argentina

Supporting Staff

Gary A. Bors, Maintenance Technician
Caroline A. Busch, Fiscal Assistant
Richard C. Carlson, Typist
Mary K. Coder, Editorial Assistant
Richard J. Collins, Carpenter
Dorothy B. Dillin, Librarian
John B. Doak, Electronics Research Specialist
Everett T. Ecklund, Design Engineer
John A. Emler, Laboratory Technician
Maura Fitz-Patrick, Receptionist
Esther Gordon, Research Assistant
Bennie Harris, Caretaker
Willis Kilgore, Jr., Caretaker
Glen R. Poe, Electronics Research Specialist
Carl M. Rinehart, Instrument Maker
Michael Seemann, Design Engineer-Mechanical
Terry L. Stahl, Fiscal Officer
Milton T. Taylor, Instrument Maker
Thomas R. Watters, Research Assistant
Marjorie L. Zeff, Research Assistant

Hale Observatories

Operated by Carnegie Institution of Washington
and California Institute of Technology

Pasadena, California

Maarten Schmidt
Director

OBSERVATORY COMMITTEE

Maarten Schmidt, *Chairman*

Halton C. Arp

James E. Gunn

Gerry Neugebauer

George W. Preston

Allan Sandage

Wallace L. W. Sargent

Contents

Introduction 593

Observing Conditions 594

Physics of the Sun 594
- Synoptic observations at Mount Wilson 594
- Large-scale velocity fields 595
- Rotation of the Sun 595
- Coronal x-ray structure and magnetic fields 597
- International cooperation for the solar maximum year 597
- Big Bear Solar Observatory 597
- Thermal phase of flares 598
- Magnetic-field configuration and reconnection in flares 598

Solar System Studies 599
- Orbit of Neptune 599
- The Jovian Magnetosphere 599

Stellar Spectroscopy 601
- Stellar chromospheres 601
- Hot subdwarfs 602
- Lower main sequence 602
- Stellar flares 603
- Stellar coronas 604
- Variable stars 604
- Evolution of contact binary stars . . 604
- Short-period and x-ray binary stars 605
- Degenerate stars 605

Interstellar Matter 607
- Gaseous nebula abundances 607

Globular Clusters 608
- RR Lyrae stars in M15 608
- The Oosterhoff dichotomy 609
- Metallicity of globular clusters . . . 610
- CN/CH anomalies 610

The Galaxy 611
- Survey of low-metal-abundance stars 611
- Embedded stars in the W3-W4 complex 611

Galaxies 611
- Star clusters in the Magellanic Clouds 611
- Carbon stars in the Magellanic Clouds 613
- Metal abundances for supergiant stars in the Magellanic Clouds . 613
- The nucleus of M31 613
- Ultraviolet energy distribution of normal galaxies 614
- Surface photometry of spiral galaxies 614
- Star formation in spiral galaxies . . 615
- Spiral structure in galaxies 615
- Spiral-arm spurs 616
- Carbon monoxide in Magellanic irregulars 616
- Star formation in barred Magellanic irregulars 616
- Morphology of Sa galaxies 616
- Dynamics of early-type galaxies . . 617
- Spectroscopic investigation of companion galaxies 617
- The nucleus of M87 618
- Seyfert galaxies 618
- Binary galaxies 620
- The distribution of galaxies in space 620

Clusters of Galaxies 621
- Virgo cluster survey 621
- Structure and dynamics 623
- Distant clusters of galaxies 623

Quasars and Quasi-Stellar Objects . . 624
- Luminosity effects in QSO's 624
- Spectrophotometry of hydrogen emission lines 624
- QSO-galaxy correlations 626
- Gravitational lenses 627
- New quasars associated with companion galaxies 627

Observational Cosmology 628
- The distance to the Virgo cluster and the use of H II regions as standard candles 628

Theoretical Studies 629
Dynamical models of binary galaxies 629
Dynamics of star clusters containing a black hole 630
Gravitational lenses 630

Instrumentation 630
The du Pont Telescope 630
Infrared spectrometer 630
Multi-Fabry-Perot spectrometer . . 631
60-Foot tower *p*-mode oscillation instrumentation 631
Image processing 632

Guest Investigators 632

Bibliography 641

Personnel 646

INTRODUCTION

This report marks the final year of the Hale Observatories. On July 1, 1980, the joint administration of the four constituent observatories under the name Hale Observatories was terminated. The Carnegie Institution now administers its facilities under the name Mount Wilson and Las Campanas Observatories. The California Institute of Technology has put the management of Palomar Observatory and of Big Bear Solar Observatory in its Division of Physics, Mathematics, and Astronomy.

The original agreement for "Unified Operation of the Mount Wilson and Palomar Observatories" between the Carnegie Institution and the California Institute took effect in 1948. The California Institute had completed the construction of Palomar Observatory from funds provided by the Rockefeller Boards, but most of the astronomical expertise in Pasadena was at the Mount Wilson office at Santa Barbara Street. Under those circumstances, combining the operation of the observatories was beneficial to both institutions.

The agreement was amended in 1969 with the aim of improving the management of the observatories, which were renamed Hale Observatories. Even after the amended agreement took effect, there remained problems of management. Some of these were related to the different operating styles of the parent institutions. Others arose out of the asymmetry of the components of the Hale Observatories, the Carnegie staff being a well-defined group isolated from other Carnegie departments, while the Caltech staff was part of a much larger faculty on the same campus with additional teaching and other responsibilities.

Problems manifested themselves in particular on the occasion of staff appointments. When one of the institutions would consider the appointment of an optical astronomer, the Observatory Committee would evaluate the person in parallel for appointment as staff member of the Hale Observatories. This procedure was a potential source of conflict, since a President would get recommendations for a given appointment from both his institution's faculty and from the Observatory Committee. In practice, this resulted in administrative interference by one institution into the affairs of the other institution.

After reviewing the situation in the early fall of 1979, I concluded that the problems inherent in the administrative system far outweighed its advantages. Accordingly, I proposed the administrative dissolution of the Observatories to the Presidents of Carnegie and Caltech on October 22, 1979. Since the single director was to be replaced by two directors, one for each institution's facilities, I resigned as Director of the Hale Observatories as of July 1, 1980.

The administrative separation of the Observatories was agreed upon by the Presidents of the Carnegie Institution and the California Institute in the spring of 1980. The Carnegie Institution appointed George Preston as Acting Director of Mount Wilson and Las Campanas Observatories. The California Institute named Gerry Neugebauer as Acting Director of Palomar Observatory. Search committees have been formed at both institutions to select permanent directors.

It is expected that collaboration in scientific research and in instrument development between Carnegie and Caltech astronomers will continue. In that connection, it is significant that

the staff of both institutions have recommended to their Presidents that "time on the telescopes of both institutions will be assigned jointly on the basis of scientific merit and without regard to institutional affiliation."

Maarten Schmidt

OBSERVING CONDITIONS

The 2.5-meter Hooker Telescope on Mount Wilson was used for observations on 193 complete nights and 39 partial nights (at least six hours) for a total of 1929 observing hours. The 1.5-meter telescope was in regular use. Two major forest fires threatened the facility in September 1979, making observations impossible for 10 nights. At Mount Wilson, the total rainfall for the year was 1600 mm, and total snowfall was 340 mm.

The 5-meter Hale Telescope on Palomar Mountain was used for a total of 2343 nighttime hours (see Table 1). In addition, 475 hours of daylight or twilight observations were carried out at infrared wavelengths. The Palomar 1.5-meter telescope was in constant use, while the 1.2- and 0.46-meter Schmidt telescopes were in regular use except during the light of the Moon. Total rainfall at Palomar was 1745 mm and total snowfall 500 mm. Maximum temperature was 35 °C in September 1979; minimum was −7 °C in January 1980.

Public visitors at the Palomar Observatory totaled 107,000 for the year.

The 2.5-meter du Pont Telescope at the Las Campanas Observatory was used for 206 full nights and 67 partial nights for a total of 2371 observing hours. The 1-meter Swope Telescope was used on 96 nights for a total of 1034 hours. The maximum temperature during the year was 26 °C; the minimum −1 °C. Total rainfall amounted to 88 mm; total snowfall was 10 mm. The maximum wind velocity was 100 mph.

TABLE 1. Observations with the Hale Telescope

Month	Complete Nights	Partial Nights	Hours of Nighttime Observing
July	20	11	205
August	20	9	199
September	29	0	252
October	19	8	229
November	19	9	236
December	22	4	268
January	8	4	115
February	11	9	156
March	14	8	167
April	17	6	186
May	16	6	136
June	26	4	194
Total	221	78	2343

PHYSICS OF THE SUN

Synoptic Observations at Mount Wilson

Synoptic solar observations continue to provide the basis for the Mount Wilson research effort in solar physics. This long-term program, supervised by Howard, includes the following observations in the interval July 1, 1979, to June 30, 1980:

Direct photographs	261
Hα spectroheliograms, 9-meter focus	425

K2 spectroheliograms, 9-meter focus	454
Full-disk magnetograms	280
Integrated-light magnetic field measurements	170
Sunspot drawings	300
Sunspot magnetic field measurements	282

Observations of the Sun were made on 307 days during this period.

The daily full-disk Mount Wilson magnetograms, along with sunspot data, are published monthly by the National Oceanic and Atmospheric Administration in the bulletin *Solar-Geophysical Data*. Since October 1979, the calcium plage data in this bulletin have been supplied by Adkins from Mount Wilson data. The McMath plage numbers are now the Hale plage numbers, after George Ellery Hale. The start of this work coincided with the closing of the McMath-Hulbert Observatory in Michigan. The published data include latitude, central meridian passage, area, and intensity of the plages.

Partial support for the observing programs, the solar research, and the data reporting comes from the Office of Naval Research, the National Aeronautics and Space Administration, the National Science Foundation, and the National Oceanic and Atmospheric Administration.

The digital magnetograph data from the 150-foot tower telescope have been preserved on magnetic tape since late 1966. A re-reduction program of the whole dataset was completed during the year. One of the features of this and current reductions is that a set of condensed data for each day is stored on a tape. This condensed data tape is proving useful in the analysis of long-term solar activity trends.

Large-Scale Velocity Fields

A systematic search for latitudinally extended, east-west motions in cellular patterns on the Sun has been carried out by Howard and LaBonte. No such patterns were found. The upper limits established by this analysis depend upon the cell size and pattern stability, but in all cases they are $\lesssim 10$ m s^{-1}. A regular low-amplitude pattern that was detected last year is now known to be instrumental in origin.

Howard and LaBonte found longitudinally extended velocity patterns that appear to represent torsional oscillations in the Sun about the rotation axis. The amplitude of this pattern is about 3 m s^{-1}, and it is seen as a symmetric set of waves that travel from the poles to the equator in 22 years. Figure 1 illustrates this effect. At any one place on the Sun, the period of oscillation is 11 years. Howard and LaBonte believe that the effect is a deep-seated one; probably the basic oscillation occurs within the radiative core of the Sun, and the motions are transferred radially upward through the convective zone to the surface. The latitude drift of the drifting shear zone coincides well with the latitude drift of solar activity. The torsional oscillation appears to be related in a fundamental way to the activity cycle. This appears to represent a dynamo effect in the solar core that produces the activity cycle.

Rotation of the Sun

A detailed study of solar rotation and some other large-scale background line-shift effects has been carried out by Howard, Boyden, and LaBonte. Included in this study is a detailed analysis of many potential instrumental effects on the measured line shifts. One line shift effect in particular—the "ears"—has been examined in detail. This effect, which is symmetric about the central meridian of the Sun, has not yet been explained, although none of the instrumental effects examined seemed capable of producing it. Interference fringes at the focus of the

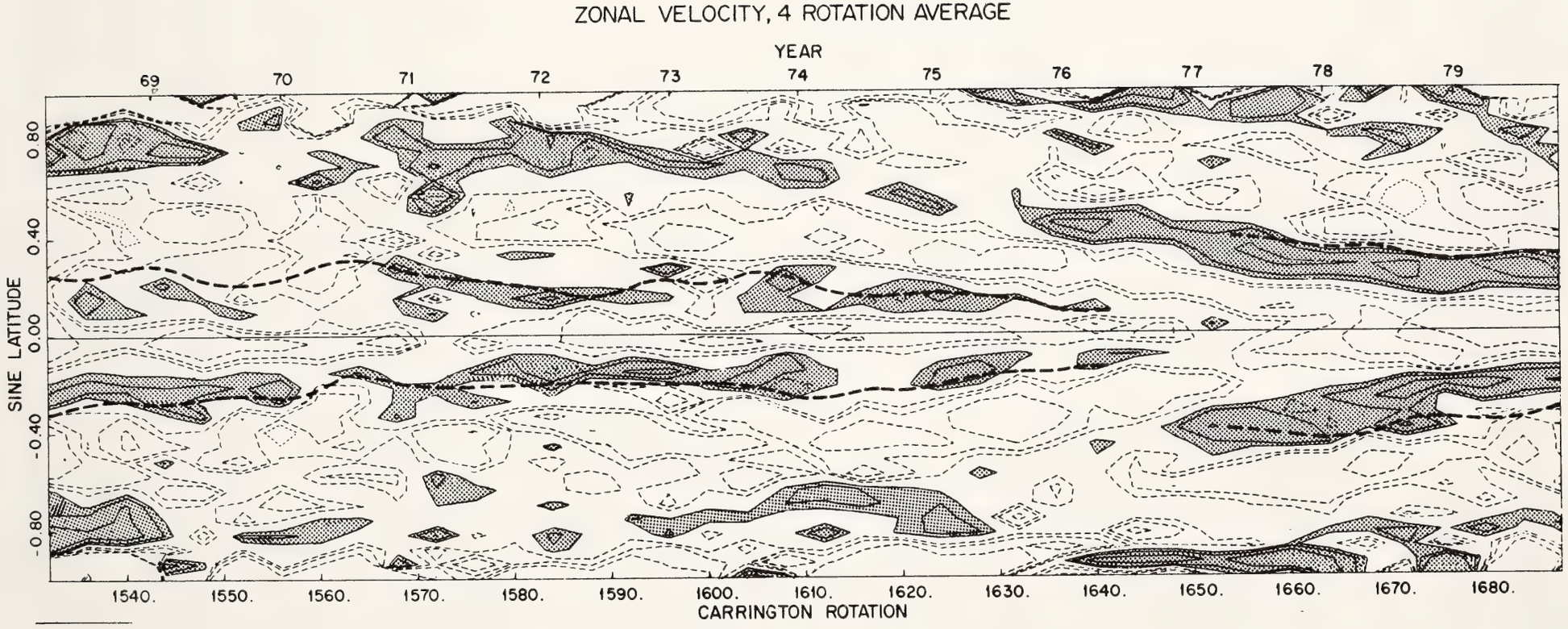


Fig. 1. Contour plot of the zonal excess rotation velocity. This is the rotation in latitude zones minus a smooth curve fitted to all zones. There are 34 independent zones of equal width in sine latitude. The daily values have been averaged over independent intervals of four Carrington rotations (109.1012 days) to reduce the random solar noise level. Contour levels are 1.5, 3, and 6 m s^{-1}. Solid contours and shading represent faster rotation (westward flow); dashed contours represent slower rotation (eastward flow). The heavy dashed lines mark the latitudes of the maxima of the magnetic flux distribution during the activity cycle.

spectrograph represent a potentially serious instrumental difficulty and, for two intervals several years ago, introduced some systematic errors in the measured solar rotational velocity at the 5% level. It has been possible to correct these data for this effect.

Mochnacki has completed a theoretical comparison of data on the rotation of the Sun and of solar-type stars. He finds that the observed proportionality of rotation speed to the inverse square root of the age among solar-type stars is consistent with the open magnetic field being proportional to rotation speed. The field predicted for the Sun is in good agreement with measurements of the radial component of the interplanetary magnetic field, and it is possible that the Sun has been rotating at its present slow rate throughout its entire main-sequence life. The present magnetic braking timescale of the Sun is now estimated to be about $3\text{–}6 \times 10^{10}$ years.

Coronal X-Ray Structure and Magnetic Fields

In collaboration with David F. Webb of American Science and Engineering, Inc., Zirin carried out a study of the connection between x-ray structures observed with the x-ray telescope on Skylab and high-resolution Big Bear observations. The x-ray pictures show the solar corona, and the Big Bear observations show the magnetic-field structures at its base. Webb and Zirin found that there is a reason for the presence of almost every x-ray structure in an active region. They found the most important causes were the existence of a heating source, which most commonly was emerging flux in some area, particularly on the edge of the sunspot penumbra, and the existence of a magnetic trap that kept the material from running away. Most of the x-ray arches crossed over neutral lines in the active region, particularly filaments. But they ran at an angle of 10°–20° to the neutral line, indicating that this was not a simple boundary at all but some sort of a trap boundary. It was found that there was no x-ray emission above sunspots, a result already found with other observations. The long coronal arches connecting different active regions were found to terminate in moderate field regions on the edge of the active region. In almost all cases, the x-ray intensity peaked when the activity at the base of the flux loops was the greatest. And, as a general rule, the peak x-ray emission in the active region occurred above the neutral line.

International Cooperation for the Solar Maximum Year

Magnetic and velocity observations of active regions are being carried out at the 150-foot tower telescope at Mount Wilson in cooperation with the Solar Maximum Year. This program is sponsored by the Scientific Committee on Solar-Terrestrial Physics of the International Council of Scientific Unions. The cooperation is carried out with two different programs—the Study of Energy Release in Flares and the Flare Build-Up Study. These programs will run through February 1981.

Big Bear Solar Observatory

The Big Bear Solar Observatory continued its extensive programs of solar observations. With the return of solar activity, many solar flares were observed. The videomagnetograph, originally built by Leighton, was refurbished and brought into operation again. Magnetic-field changes in solar flares were observed on November 5, 1979, for the first time. These are reported in a paper by Patterson and Zirin, submitted to *The Astrophysical Journal.* Surprisingly, besides a sharp reduction in magnetic-field strength, which was expected, a transient dipole appeared in two solar flares. More observations are being carried out. Extensive observa-

tions of flares were made in a number of wavelengths; these are important both for their own value and through comparison with data obtained in other radio and x-ray wavelength ranges.

Thermal Phase of Flares

Zirin carried out studies of the thermal phase of solar flares in collaboration with Dr. Uri Feldman of the Naval Research Laboratory. By comparing soft x-ray records obtained with an Air Force satellite and Big Bear optical records, they found that the appearance of loop prominences very shortly after the impulsive phase of a flare marked the rise in the thermal soft x-ray component. Zirin and Feldman, along with George Doschek of the Naval Research Laboratory and Dr. Sharad Kane of the University of California, Berkeley, concluded that there is a thermal phase of energy release in flares after the first release that produces a highly compressed thermal plasma at a temperature of about 3×10^7 K and density of about 10^{13} atoms cc^{-1}. In this phase, the soft x-ray emission, including lines of ions such as Fe XXV and the loop prominences that can condense only out of a very dense medium, are produced. Consideration of the physical conditions which permit emission of Hα against the disk again indicated that a high density is required. Why this kind of phenomenon occurs after the first energy release of the flare is not known. The postflare loops have always been a subject of fascination, partly because of their aesthetic beauty and partly because of the mystery of their rapid formation directly after the flare.

Magnetic-Field Configuration and Reconnection in Flares

The x-ray and *EUV* pictures from Skylab have firmly established that the $T \sim 10^7$ K thermal x-ray plasma in flares is contained in closed magnetic-field arches. A key question raised by this result is: What is the configuration of the magnetic field in which or from which the x-ray arches are formed? Most recent flare models are based on one or the other of two possibilities.

1. The closed magnetic arches illuminated in the flare are already present in the preflare configuration. The flare energy is stored in the magnetic arches in the form of a helical twist maintained by electric current flowing along the field lines, and the flare is the result of rapid dissipation of this current.

2. The closed magnetic arches that appear in the flare are not present in the preflare configuration, but are formed by reconnection of field lines at a large-scale current sheet. The electric current in the sheet is the source of the nonpotential component of the magnetic field, and this magnetic energy is rapidly converted to flare plasma energy in the reconnection process.

Moore and co-workers have completed studies of the magnetic-field configuration and its changes in two flares that were especially well observed both in x-ray filtergrams from the American Science & Engineering (AS&E) x-ray telescope on Skylab and in Hα filtergram movies from Big Bear. These were a classic, large two-ribbon flare of July 29, 1973, and another large-scale but much less intense flare of August 29, 1973. The x-ray pictures show the magnetic-field structure in the corona before and after flare onset, and the Hα movies show the magnetic structure, location, and development of the flare in the underlying chromosphere.

Moore collaborated with Stephen W. Kahler and David F. Webb of AS&E on the analysis of the August 29 flare. They concluded that this flare was a four-ribbon flare that resulted from reconnection between two closed-field systems. The deduced preflare and postflare field configurations, the simultaneity of brightenings in all four

Hα ribbons, and the apparent lack of ejection of the filament all support this interpretation. The observations of this flare give perhaps the strongest evidence to date that magnetic-field reconnection does in fact occur in some flares.

The analysis of the July 29 flare was carried out by Moore in collaboration with LaBonte. They concluded that both the filament eruption and the simultaneous onset of the Hα flare were probably triggered by reconnection between closed field lines below the filament.

Considering both flares together, the main conclusions from the studies are as follows.

1. The observations give compelling evidence that large-scale magnetic-field reconnection operated throughout both flares. The two flares were very different, and the July 29 flare was an archetypical two-ribbon flare initiated by a filament eruption; this implies that in a large class of flares the basic energy release is accomplished through large-scale reconnection, as has long been proposed on theoretical grounds.

2. The initial reconnection was between closed field lines in both flares. This suggests that many (perhaps most) flares begin as "four-ribbon" flares and evolve into bona fide two-ribbon flares only if the overlying magnetic field is opened, as in a filament-ejection flare such as that of July 29.

3. Neither flare was triggered by the emergence of new small-scale magnetic flux, as proposed by Heyvaerts *et al.* (*Astrophys. J., 216,* 213, 1977). This indicates that flares can be triggered by the same process that builds up the flare energy, i.e., by evolution of the overall magnetic-field configuration.

SOLAR SYSTEM STUDIES

Orbit of Neptune

Kowal, in collaboration with Mr. Stillman Drake of the University of Toronto, has found that Galileo observed the planet Neptune on two occasions, in 1612 and 1613. Neptune was occulted by Jupiter on January 4, 1613, and both planets were within the same field of view for several weeks. In Galileo's drawings of the Jovian satellites, Neptune is shown as a "fixed star" on the nights of December 28, 1612, and January 28, 1613. On the latter occasion, Neptune happened to be close to a catalogued star. This enabled Kowal to derive a fairly accurate position for Neptune on that date, on the assumption that the separation of Neptune and the star was drawn to the same scale as the Jovian satellites. The resulting position differs from the best available ephemeris of Neptune by about 1′. The nominal error in this determination is about 10″. This early observation of Neptune may significantly improve our knowledge of Neptune's orbit.

The Jovian Magnetosphere

Trauger, with Dr. Guido Münch of the Max-Planck Institute for Astronomy, Heidelberg, and Dr. Frederick L. Roesler of the University of Wisconsin, has extended earlier observations of the Jovian magnetospheric emissions (*Astrophys. J., 236,* 1035, 1980) with new Fabry-Perot observations of [S II] and [S III] near the time of the Voyager I encounter. Representative spectra (Fig. 2) are taken from a sequence of individual spectra; these data constitute the first ground-based observations of Jovian [S III] emissions and extend the

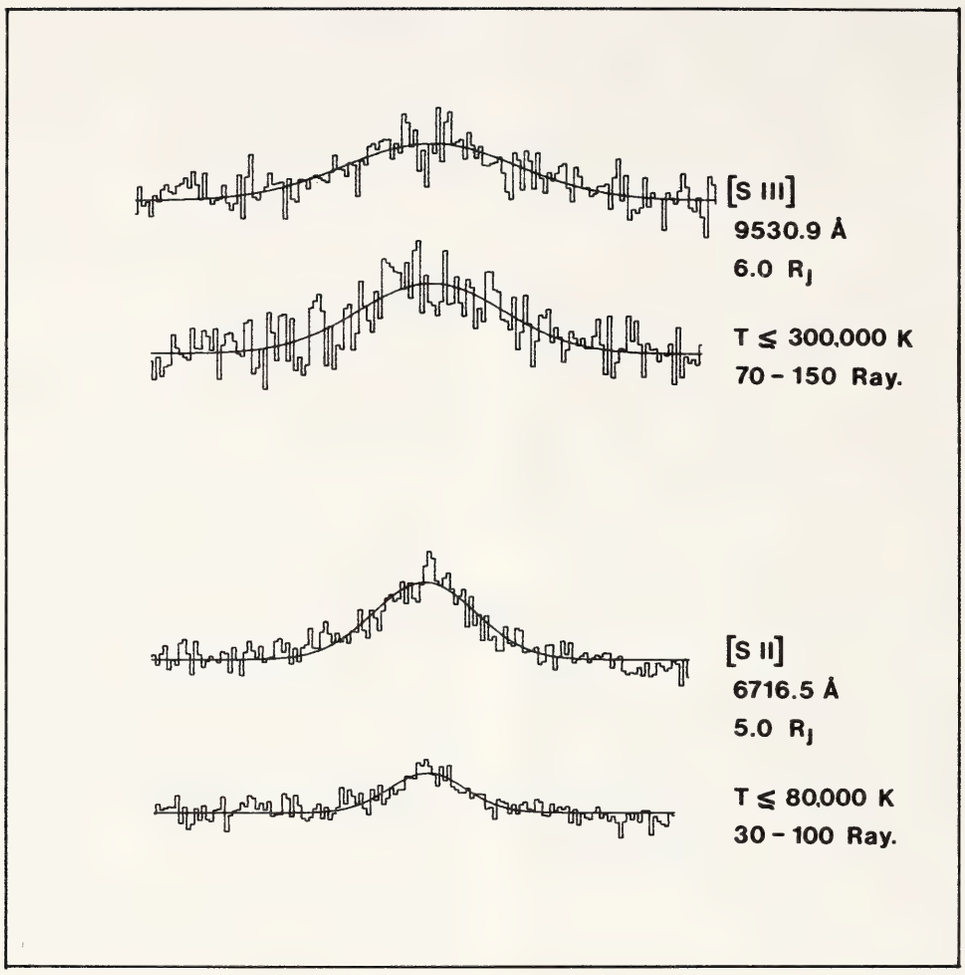


Fig. 2. Representative Jovian [S II] and [S III] spectra obtained near the time of the Voyager I encounter. Emission linewidths at λ9530.9 and λ6716.5 are resolved, allowing a direct estimate of ion temperatures. The observed range of ion temperatures and emission brightnesses are noted.

time base for high-resolution study of the [S II] torus to three years. The observed source of [S II] emissions is confined within 0.5 R_J of a 6 R_J-radius ring concentric with Jupiter and tilted 7° from the rotational equator, as expected for ions confined by Jovian magnetic and centrifugal forces. The [S II] emissions appear within 0.1 R_J of a concentric inner ring 5 R_J in radius. Fitted gaussian curves are shown superimposed upon the raw data in histogram form. Representative spectral widths range from ~8 km s^{-1} in the [S II] spectra to ~25 km s^{-1} in the [S III] emissions. Corresponding ion temperatures are indicated in the figure. Temperature and emission brightness are observed to vary with time and longitude about Jupiter, with the approximate limits noted in the figure. Characteristic parameters for the plasma are: at 6 R_J, S^{++} temperatures ~300,000 K, S^{++} densities ~110 cm^{-3}, S^+ densities <30 cm^{-3}; at 5 R_J, S^+ temperatures variable with longitude, ranging ~20,000 to 80,000 K, S^+ densities ~800 cm^{-3}, electron densities ~2000 cm^{-3}.

Values obtained from this ground-based study are in general agreement with plasma and ultraviolet spectrometer experiments obtained from Voyager I at nearly the same time. These observations suggest that sulfur ions (or parent molecules) cool rapidly to 300,000 K after being swept into corotation with the Jovian magnetosphere in the vicinity of Io's orbit (6 R_J); this is followed by a much slower cooling,

coupled with S^{++} recombination to S^{+} and inward diffusion on a time scale of months. The details of ion production and the eventual demise of magnetospheric ions are subjects of continuing study.

STELLAR SPECTROSCOPY

Stellar Chromospheres

Throughout the past year, Vaughan and Preston have continued a long-term survey (initiated in 1966 by Olin C. Wilson) of stellar activity cycles, monitoring the chromospheric Ca II H and K line emission fluxes in a sample of about 90 main-sequence stars at approximately monthly intervals with the H-K photometer on the 1.5-meter telescope at Mount Wilson. At the same time, the H-K photometer has been used in a second program aimed at gathering data on H-K fluxes in a fairly complete sample of the main-sequence stars within reach of the instrument. Thus far the sample being surveyed has been restricted to the northern half of the Greenwich *Catalogue of Stars Within Twenty-Five Parsecs of the Sun*, of which about 490 stars have, as of June 1980, been observed one or more times. Accounts of these projects have appeared in preceding *Year Book* volumes. Current results of the solar neighborhood survey are described in an article accepted for publication in the *Publications of the Astronomical Society of the Pacific* (*92*, August 1980).

An interesting result that has continued to emerge from this survey (noted earlier in *Year Book 78*, p. 724) is the existence among F- and G-type main-sequence stars of two distinct levels ("high" and "low") of chromospheric H-K emission and a marked deficiency of F-G stars having intermediate levels of H-K flux. The Sun's H-K flux is typical of the "low" branch, along with other main-sequence stars of comparably great age, whereas the "high" branch is composed of young stars similar in H-K flux to members of the Hyades cluster. In an article prepared for the *Publ. Astron. Soc. Pacific* (*92*, August 1980), Vaughan noted that the same "high" and "low" H-K flux levels, separated by a "gap" between them, are manifest in the sample of 90 stars in Wilson's original stellar-cycle survey. Moreover, on the "low" branch (composed of old stars), time variations in H-K flux, when they occur, have the form of smooth, undulating cycles similar in all respects to the solar cycle. In contrast, the behavior of young stars (on the "high" branch of H-K flux) cannot be described as Sunlike. Their behavior consists instead of chaotic variations, fluctuations on a one to two year time scale, and larger excursions of mean flux that are more suggestive of a stochastic process than an aperiodic one. Whether or not these longer-term variations in young stars are actually periodic is a question whose answer will require at least another decade of observations.

The behavioral difference between old and young stars adds to the mystery of the "gap" or bifurcation of stars into chromospherically more active and less active types and has led to speculation that excitation mechanisms of magnetic activity predominating in young stars may differ from those effective in old ones, including the Sun. Resolution of this question is a goal to be sought in the future extension of the stellar-cycle and solar-neighborhood H-K flux surveys.

This work is being greatly aided by the addition of an LSI-11 computer and "floppy disk" data-logging system

and an ISIT television field-viewer to the H-K photometer, made possible by a grant from the National Science Foundation (effective March 1, 1980). This new equipment went into routine operation on the Mount Wilson 60-inch telescope on June 20, 1980. The principal incentive for this advance was a project planned for the summer of 1980 in which a sample of about 50 stars, most of them previously studied in the cycle survey, will be monitored in a nearly uninterrupted series of nightly observations over a span of three months (July through September). These observations will provide a data base from which the nature of short-term time variations can be studied. One of the presumed causes of short-term variability of H-K flux in stars (and an observed effect in the Sun) is the modulation of active regions by rotation; that is, the observed H-K flux rises and falls as magnetically active regions (from which the H-K emission mainly arises) appear and disappear around the limb of the star as the star rotates. Hence, a chief goal is to determine the rotational periods of stars whose long-term chromospheric behavior is known. The planned observational program will be carried out as a collaborative project by a team consisting of Drs. S. L. Baliunas, L. Hartman, and R. W. Noyes of the Harvard-Smithsonian Center for Astrophysics; Mr. Frans Middelkoop, a graduate student of the Astronomical Institute at Utrecht, The Netherlands; Dr. Dimitri M. Mihalas of Sacramento Peak National Observatory; and Preston and Vaughan.

Hot Subdwarfs

Greenstein continued his observations of very hot stars to determine the upper limit to stellar effective temperatures by using the International Ultraviolet Explorer (IUE). In the course of this work, he obtained a most unusual spectrum of the peculiar central star of the planetary nebula Abell 30. This star was previously found by Greenstein and Minkowski to have strong O VI lines. The IUE shows it to have a completely anomalous continuum. At $\lambda < 2500$ Å, the star brightens by nearly 300%; it shows N V and insignificant Lα. There is a region of inner nebulosity within the $20'' \times 10''$ slit in which C IV and [Ne IV] emissions are visible. The ejection velocity indicated by the deep C IV absorption is near -400 km s^{-1}, but the inner nebula C IV absorption is near zero velocity. The nebulosity is a strong infrared source with an internal reddening $E(B - V)$ near 0.3 mag. Correcting for the observed continuum results in a continuum flux, F_ν, steeper than ν^2. If one subtracts a blackbody of 100,000 K from the dereddened F_ν, the residual "added flux" of unknown origin, starting at $\lambda < 2500$, increases roughly as ν^2 (infinite temperature) but is very deficient at $\lambda > 2500$. In fact, the "added flux" increases 30 times from $\lambda\lambda$3300–1450. If the dust absorption has the normal wavelength dependence, the ultraviolet flux is enough to account for the infrared emission. No probable atomic process has been recognized that would account for this "added flux," nor is it known whether it persists into the extreme ultraviolet or x-ray regions. Because Abell 30 is not a known radio source, the synchrotron process is not attractive. The nebula is supposed to have recently ejected two smaller nebulae in a second outburst a few arcseconds from the star. The outer faint nebulosity, $120''$ diameter, was found to have some hydrogen, the inner features none.

Lower Main Sequence

Ake has analyzed the multichannel spectrophotometry of high- and low-velocity late-type dwarfs, and has readied for publication data on 234 parallax stars. Composition-independent luminosities and nearly temperature-independent composition indices

can be derived using measured magnitudes at from five to nine wavelengths. The color-M_v sequences merge for normal and metal-poor stars at late types. Parallaxes and space motions predicted for an additional 119 stars are given. The most extreme metal-poor subdwarfs (sdM) found have galactic orbits with eccentricities exceeding 0.70. These have weak TiO, strong CaH, MgH, and λ4227 at types later than M2. The faintest, most extreme stars studied by Ake and Greenstein are G7-17, LHS 453, 3382, and 489. The faintest subdwarf is LHS 453, $M_v \approx 12.6$. The space motions are, respectively, 391, 681, 524, and 500 km s^{-1}, thereby testing the limiting velocity possible in our Galaxy. All orbits are strongly retrograde; the predicted parallaxes are, unfortunately, quite small. These stars are extremely metal deficient—probably approaching the sdG or M92 giants.

Stellar Flares

Zirin collaborated with Gary J. Ferland of the University of Cambridge in studying the possibility that stellar flares are fairly similar to those on the Sun. They studied an extensive series of flare characteristics—optical, radio, and x-ray—and concluded that although flares are much more frequent on late-type dwarfs, they are essentially the same as those on the Sun. In particular, the flares on a typical UV Ceti star could be explained by the permanent presence of a large sunspot region, such as that of August 1972. However, there are anomalies in the radio emissions from such flare stars.

Following this, Mochnacki and Zirin began a program of photometry of stellar flares with the 32-channel scanner on the 5-meter telescope. They observed a number of flares in UV Ceti, YZ Canis Minoris, Wolf 424, and BD 16°2708, obtaining the most complete records yet of such events. The data, with time resolution of 10–20 seconds, reveal strong Balmer continuum emission, line emission, and a continuum in the visible that can be explained by a bright spot at a temperature of about 10^4 K. By contrast, the continuum from solar flares seldom exceeds 7000–8000 K. Although the first data on the Balmer continuum was restricted by vignetting, the newer data suggests temperatures in the Balmer continuum somewhat higher than the white light continuum, perhaps 15,000–20,000 K. Mochnacki and Zirin confirmed the observation obtained by others that the strongest line in the Balmer series is Hγ. To check whether this was true in solar flares, Zirin and Margaret Liggett measured the Hα/Hβ ratio in 15 solar flares and found it to be approximately 1. So the Balmer increment in solar flares is not as marked as it is in stellar flares.

As part of the program of observations of stellar flares, coordinated observations involving the 5-meter telescope and the 2.5- and 1.5-meter telescopes on Mount Wilson were made by Zirin, Mochnacki, and Horne. Unfortunately, because of the bad winter weather, they observed only one event—a flare on Wolf 424.

This flare was observed by Mochnacki with the 2.5-meter telescope to have a surprisingly narrow Hα profile, about a couple of angstroms wide. Horne, observing the flare with a high-speed photometer on the 1.5-meter telescope, found a rise time of five seconds with the same decay time, followed by a slow second phase. Coordinated observations were also made of flares with the 5-meter telescope and the VLA. A large flare in BD 16°2708 was observed by Zirin, but Dr. David M. Gibson of the New Mexico Institute of Mining, Socorro, New Mexico, observing concurrently with the VLA at 21 cm, could see no radio emission down to about 1 mJy. This left the problem of radio bursts from stellar flares still unresolved; there are not many reports of observations of radio bursts from stars, but they usually occur at differ-

ent times from observations of optical events and do not show the same light curves. It is quite conceivable that most of the reported events are due to interference. There are some plausible detections of a slowly varying component in these stars. The problem is that synchrotron self-absorption strongly limits the flare star emission at higher frequencies, and the short duration of the flare makes it difficult to obtain great sensitivity. The absence of emission from such a strong flare when observed with as powerful an instrument as the VLA renders questionable at least the existence of high-frequency impulsive emission from such events. Incidentally, x-ray bursts from flare stars have definitely been observed.

Stellar Coronas

Zirin has continued his studies of the 10830 helium line in various late-type stars. A new image-tube system installed in 1978 has permitted quite high resolution and good limits of detection. He has been continuing a survey of most of the stars in Olin Wilson's list of K-line emission and also of binaries to find the dependence of helium absorption or emission on period.

The existence of helium absorption in late-type stars may be explained by back radiation of soft x rays from their coronas. Therefore, one might expect that these stars should be detected as x-ray sources. Zirin was accepted as coinvestigator on the HEAO-B spacecraft, and ten stars he detected as having strong 10830 were allocated for the program. In addition, other stars detected as 10830 sources were observed by others or are being observed as part of a cooperative program with Columbia University. HR 7275, η Andromedae, 3 Camelopardalis, and o Draconis were all observed as definite x-ray sources. Collaborative observations with Columbia have also shown the supergiants β Camelopardalis and β Draconis, both stars with huge 10830 absorption, to be x-ray sources as well. One interesting facet of the data is that stars with strong 10830 emission (implying the existence of a shell) are weak x-ray sources, if at all. This suggests that the emission shell cools off whatever corona might be produced in the star. The possibility of confirming a relationship between the x-ray emission and the 10830 strength in single stars is very exciting. It should be noted that most of the strong x-ray sources are, in fact, RS Canum Venaticorum–type stars, where the complex binary behavior is closely related to the x-ray intensity.

Variable Stars

Mochnacki continues to monitor Nova Vulpeculae 1979. As of April 1980, the P Cygni profile of Hα in this very slow eruptive object has changed into a very sharp shell-like absorption with wide absorption wings and narrower but slight emission wings. Many more absorption lines have been seen to develop.

Evolution of Contact Binary Stars

Mochnacki continues his investigation of the evolution of contact binary stars. Stellar wind magnetic braking causes angular momentum loss greater than predicted by the theory of gravitational radiation alone, accounting for the particularly low angular momenta of evolved W Ursae Majoris stars. A new class of W UMa star has been identified, of which OO Aquilae is the prototype; these are systems that have densities too low and angular momenta too large to have existed as contact systems at age zero. Such systems have evolved into contact from an originally detached configuration. Further observations of detached systems which may evolve into contact have been obtained.

Short-Period and X-ray Binary Stars

Schneider and Young have observed several close binary star systems with spectroscopy at 2-Å wavelength resolution and 3-min time resolution.

The prototype magnetic binary AM Herculis was observed in the infrared for five orbits. The Na I λλ8183,8194 absorption lines from the red dwarf companion were discovered, giving a radial velocity amplitude of 175 km s^{-1} with a period of 3.1 hours. This observation allowed a new interpretation of the two sets of emission-line components (broad and sharp) discovered by Greenstein and verified in He I λ7065 emission by the present work. The sharp emission component is phased with the absorption lines and apparently arises from the photosphere of the red dwarf that is forced into emission by *UV* irradiation. The broad emission component is out of phase by 135° and probably arises from an accretion column of gas threaded on the magnetic field of the white dwarf, plunging toward the magnetic pole.

The other three known magnetic binaries (2A0311-227, VV Puppis, and AN Ursae Majoris) have been observed in the spectral region from Hγ to Hβ. The binary 2A0311-227 has only one emission-line component whose profile changes markedly around the orbital cycle. VV Pup and AN UMa have two emission components (broad and sharp) that are out of phase by 50°. The sharp component is eclipsed for half the cycle and is much stronger in VV Pup than in AN UMa. We suspect that the sharp components are, as in the case of AM Herculis, produced in the photosphere of the red dwarf. The emission is forced by a strong ultraviolet flux from the accretion column and white dwarf. The broad components again may be plausibly explained as arising from the magnetic accretion column.

An eclipse of DQ Herculis was observed in the Hβ, He II λ4686, and Hγ emission lines. Eclipse "light curves" of material at specific velocities showed that (1) the He II λ4686 is excited at smaller radii than the Balmer lines, (2) the emission velocities are well explained by a disk of gas in circular Keplerian motion about a white dwarf of mass 0.4 $\mathfrak{M}_\odot$, (3) the eclipse duration gives the mass radio and a red dwarf mass 0.3 $\mathfrak{M}_\odot$, both masses smaller than the values deduced from "standard" analyses, and (4) the red dwarf is not on the main-sequence, mass-radius relation, but is "too large" for its mass.

Degenerate Stars

A final list of degenerates studied with the multichannel or SIT spectrometers was published. It brings to 558 the number of such objects studied by Greenstein with various collaborators. Proper-motion stars as faint as 20 mag, discovered by Dr. Willem J. Luyten of the University of Minnesota with the Palomar Schmidt, yield 13 new red degenerates of mean absolute visual magnitude $M_v = +15.0$. When Greenstein and Dr. Olin J. Eggen of Cerro Tololo Inter-American Observatory began the study of white dwarfs in 1965, only five stars fainter than +14 were known; at present there are 62. The faintest, Gr 536, LP131-66, has $M_v \approx +16.6$, from extrapolation of color-luminosity relations. No parallax is yet known. While red, such stars exhibit few or no spectral features (atomic or molecular); the energy distribution of LP131-66 is fitted moderately well by a blackbody near 3500 K. Its luminosity is $1.8 \times 10^{-5} L_\odot$, i.e., $M_{bol} = 16.5$. Stars of this type are indeed rare in space, and their statistics will be necessary to determine the luminosity function and total space density of degenerate stars. Using observed numbers only, beginning at $M_v = 14.25$, the $N(M_v)$ in 0.5-mag intervals are 18, 17, 13, 12, and 2 ($M_v = 16.25$). The brightest of these

stars may still show weak hydrogen lines, while the faintest are featureless. The accessible volume of space, down to a fixed limiting apparent magnitude, shrinks by a factor of two per 0.5-mag interval, so that the decrease in $N(M_v)$ is largely caused by this volume reduction. The volume density apparently does not steeply increase from M_v = 14–16 mag. The relatively constant numbers stem partly from the selection process used to discover red degenerates. It fails to uncover new objects at $M_v > 16.0$ because of a double selection process; i.e., both proper motion and apparent magnitude must be large to give large reduced proper motion. Of significance is the large mean tangential motion of 110 km s^{-1} for eight red degenerates in this new list, compared to the 55 km s^{-1} for the average degenerate; i.e., we are out on the tail of the velocity distribution of old-disk stars.

Multichannel colors for over 150 degenerates have been measured since Greenstein's 1976 list. These are being prepared for publication. They confirm the general features of the (M_v, color) relations originally derived for parallax stars. In this and in other work, Greenstein has attempted to separate hot degenerate stars from hot subdwarfs. It appears that colors and hydrogen-line equivalent widths, even fit by model atmospheres, are insufficient. But line profiles, at 16-Å resolution, may successfully distinguish subdwarfs, even at 60,000 K, from hot hydrogen white dwarfs.

The helium-atmosphere white dwarfs sometimes show metallic lines in spite of the high efficiency of gravitational diffusion in draining metals from the atmosphere. Cottrell and Greenstein have studied GD 401 (Gr451), which has the strongest Ca II lines known. Spectrum synthesis in a model atmosphere, using Ca I, Ca II, Mg I, and Fe I lines at 8800 K, log g = 8, represents the spectrum moderately well, and yields the abundance Ca/He = 10^{-8}, in contrast to a solar value of 2×10^{-5}. The absence or weakness of Mg and Fe suggests an even greater deficiency. These numbers are sensitive to the opacity (dominantly He^-), which is itself sensitive to the metal-to-helium ratios. The depletion of metals could be overstated if any other source of opacity exists. Figure 3 displays this extraordinary spectrum.

Greenstein unexpectedly discovered an absorption line in the IUE ultraviolet spectrum of 40 Eridani B, one of the

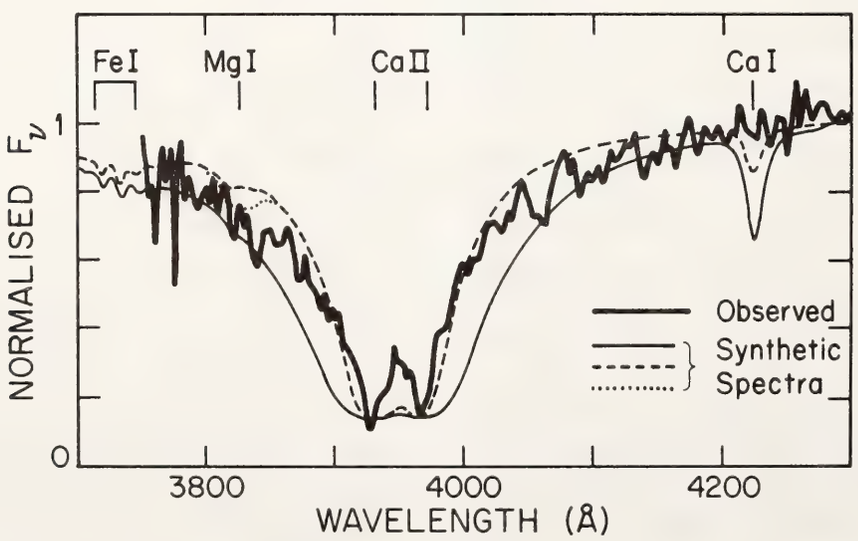


Fig. 3. The observed SIT spectrum of GD 401 compared with predicted synthetic spectra with various calcium abundances, far below those in the Sun. The dotted line shows the effect of increasing magnesium, which is apparently quite deficient.

brightest DA's. The ultraviolet continuum and Lα fit at a temperature near 17,000 K, determined from the optical region. However, three IUE spectra show a shallow, weak line (≈2 Å equivalent width) at λ1392. This lies close to the resonance Si IV doublet seen in quasars, hot B stars, and interacting compact systems. But it requires a temperature near 35,000–45,000 K. If λ1392 is Si IV, possible explanations are an absorbing chromosphere, a stream of hot matter from the K-type companion, or line formation at very large optical depth in a transparent atmosphere. This is the first absorption line other than Lα seen in a hydrogen white dwarf. However, a more reasonable explanation is that molecular hydrogen, H_2, is the absorber. The (0,5) vibrational transition of the Lyman-band system from the ground electronic state is involved; the lower vibrational states, further to the ultraviolet, are those seen in the interstellar medium.

INTERSTELLAR MATTER

Gaseous Nebula Abundances

In collaboration with Dr. Steven Grandi of the University of California, Los Angeles, French has completed a study examining the reliability of the standard procedures for deriving chemical abundances in gaseous nebulae by applying these procedures to model H II regions. They feel that this study is an improvement over previous work because they have incorporated improved atomic parameters in their models (especially with regard to charge-exchange reactions) and because they discuss the reliability of each of the independent steps in the procedure. They find the accuracy of the procedure to be satisfactory, yielding abundances within 50% of the input values, but they point out that it is not clear how adequately any models can represent real nebulae. They also consider the special cases of (1) an H II region photoionized by several stars of differing spectral types (as in an OB association), (2) several H II regions of different ionization levels observed together because of spatial resolution limitations, and (3) the low-abundance, high-ionization H II regions observed in the outer parts of nearby spiral galaxies or isolated in space (i.e., "isolated extragalactic H II regions"). In all cases, the procedure proved satisfactory for situations likely to occur in nature.

Using spectrophotometry obtained with the Lick Observatory 61-cm telescope, French has completed the first part of a study of argon abundances in gaseous nebulae. Argon is of interest because, like sulfur, it represents a more advanced stage of nuclear processing than nitrogen, oxygen, or neon. It has the advantage that most of the important ionization stages have strong lines in the optical portion of the spectrum, whereas sulfur requires a large and increasingly questionable correction for unseen stages. Optical [A III], [A IV], and [A V] collisionally excited lines were used to obtain the abundances of A^{2+}, A^{3+}, and A^{4+} relative to H^+. The observations were of H II regions and planetary nebulae chosen to span a large range in ionization level. It appears that A^{5+} is not an important ionization state in even the highest ionization objects. At low ionization, A^+ can be an important species, but it appears that it correlates well with He^0, so that applying the same correction to argon used to correct helium abundances for neutral helium should yield accurate argon abundances. There is no correlation of the

argon abundances derived in this manner with ionization level, and the derived argon abundances exhibit no more scatter than the oxygen abundances, which are generally the most reliably determined abundances apart from helium. This study is being extended to a larger number of objects with the SIT spectrograph on the Palomar 1.5-meter telescope in order to search for variations among objects and with position. The results will also be used to derive argon abundances for the dwarf emission-line galaxies studied in French's thesis for which sulfur abundance anomalies were found. (Theoretically, sulfur and argon should vary together.)

In another project begun with the Lick 61-cm telescope, French is attempting to derive carbon abundances in planetary nebulae from the very weak optical recombination lines of C II, C III, and C IV. Carbon is of interest because, with no strong optical lines, it is the only previously unobserved member of the CNO group and because it is expected to yield information on the evolutionary state of the progenitor stars of planetary nebulae. Preliminary results suggest that the abundances are rather high (C/H $\sim 10^{-3}$ by number) and, like argon, are relatively constant from object to object. C/O is also rather high (~ 3 by number), but this may reflect a scale factor problem between abundances derived from recombination lines and those derived from collisionally excited lines, which is expected if there are significant temperature fluctuations within a given nebula. This study is being continued with the SIT spectrograph on the Palomar 1.5-meter telescope. The coudé Varo-Reticon on the Mount Wilson 2.5-meter telescope is being used to resolve weak O II lines from some of the carbon lines.

GLOBULAR CLUSTERS

RR Lyrae Stars in M15

Study of the colors, magnitudes, amplitudes, and periods of 61 RR Lyrae stars in the low-metal-abundance cluster M15 has been completed by Sandage, Sandage, and Katem. The work was begun in 1957 when plates in *U, B,* and *V* bandpasses were obtained with the Mount Wilson 2.5-meter reflector. From these data, light curves in three colors have been obtained from measurements of the 61 variables on 39 plates in *U,* 61 plates in *B,* and 64 plates in *V,* relative to a photoelectric sequence, also obtained with the Mount Wilson reflector.

The period distribution of the M15 variables is of the long-period Oosterhoff group II. In an attempt to understand the Oosterhoff period dichotomy, the aim of the work has been to compare the color-amplitude, color-period, and period-amplitude relations for M15 with the same relations for the Oosterhoff group I cluster M3, where the mean period of RR Lyrae stars is shorter. After correcting the M15 colors for reddening by $E(B - V) = 0.08$, obtained from the bluest horizontal-branch stars, it was found that the color-amplitude distributions coincided for the variables in M3 and M15, whereas both the color-period and period-amplitude relations were shifted for variables of *all periods* between M3 and M15 by $\Delta \log P = 0.055$. Both of these facts are consistent with a model of the Oosterhoff problem where the horizontal branch of the group II clusters is brighter than for group I clusters, providing that the temperature boundaries of the instability strip are the same for clusters in each group.

The latter proviso has been shown to be satisfied between M3 and M15 by analysis of the observed colors and reddening in each cluster.

The Oosterhoff Dichotomy

Using the M3–M15 results as a guide, Sandage has studied the available data from the literature on RR Lyrae star light-curve shapes, amplitudes, and periods for 29 globular clusters. From correlations between period and amplitude, and especially between period and light-curve shape, the shift in period could be determined for each cluster so that its period-shape correlation was made coincident with that of M3. The distribution of the resulting Δ log P values is bimodal (which is the Oosterhoff dichotomy), but within each mode the distribution is wide. Hence, the Oosterhoff groups are not as discrete as was once believed, since Δ log P forms a double continuum (Fig. 4).

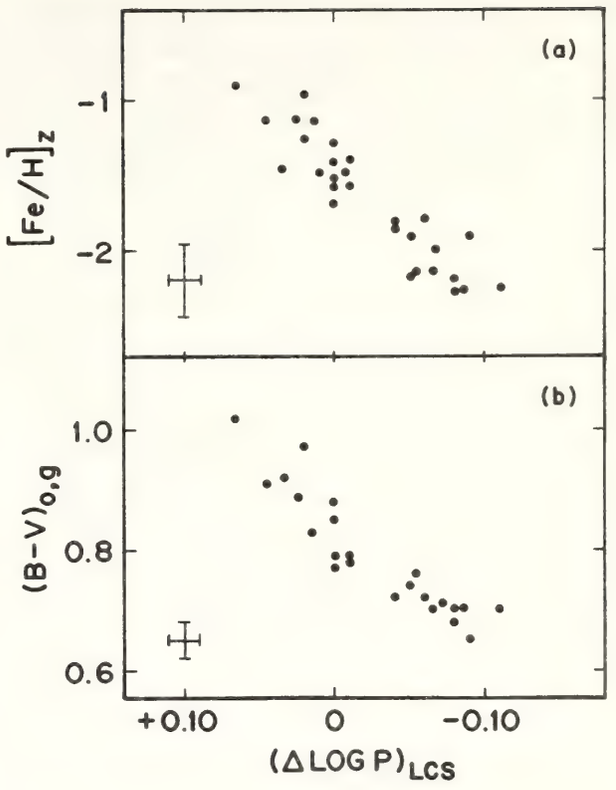


Fig. 4. Correlation of two metallicity indicators $(B - V)_{o,g}$ and [Fe/H] with the period shift Δ log P of the entire distribution of RR Lyrae light-curve shapes in any given globular cluster relative to M3. The Oosterhoff "groups" are seen to be a broad bimodal continuum where the relative period shifts are correlated well with metallicity.

It was then found that Δ log P for a particular cluster is tightly correlated with its metal abundance, in the sense that clusters of low metallicity have longer periods for their RR Lyrae distribution. The correlation between Δ log P (from light-curve shapes) and the metallicity $[Fe/H]_z$ from Zinn (*Year Book 78,* p. 737; *Astrophys. J., Suppl. Ser., 42,* 19), shown in Fig. 4, has a dependence

$$\delta \Delta \log P = 0.11\ \delta[Fe/H]_z.$$

Also shown in Fig. 4 is the correlation between Δ log P and the more directly observable color index $(B - V)_{o,g}$ of the subgiant branch at the level of the horizontal branch—a quantity known itself to be connected with the metal abundance.

If the explanation of the Oosterhoff period ratio among clusters is correct, where Δ log P signals a horizontal-branch luminosity difference Δ log L_{HB}, then the correlation of Δ log P with [Fe/H] requires that $(\Delta \log L)_{HB}$ and [Fe/H] are related. It can be shown from theory (cf. Sweigart and Gross, 1976, *Astrophys. J., Suppl. Ser., 32,* 367) that a change in [Fe/H] cannot cause a difference in the luminosity of the horizontal branch; hence, the tight observed relation between $(\Delta \log L)_{HB}$ and [Fe/H] must be due to an effect where the variation of log L_{HB} and the variation of [Fe/H] between clusters are *both* related to a more common cause.

This relationship could be explained if all globular clusters are the same age, within a small range. The main-sequence turnoff luminosity for a given age depends very strongly on [Fe/H]. As the metallicity is decreased, L_{TO} becomes brighter for constant age. Further, since it is known empirically

that L_{TO}/L_{HB} is constant, independent of [Fe/H], then as L_{TO} increases, so must L_{HB}. As explained earlier, this causes differences in the period distribution of the RR Lyraes and hence gives rise to the apparent correlation of L_{HB} or $\Delta \log P$ with [Fe/H].

The sense of the correlation of $\Delta \log L_{HB}$ with metallicity is of the correct sign and close to the correct slope to balance the $\Delta L_{TO} = f(Z)$ relation for constant age at main-sequence turnoff. These relations seem, then, to point directly to a nearly constant age for all globular clusters and provide a natural explanation for the RR Lyrae period distribution differences.

The calculations on limits to the age spread have not yet been completed, but Sandage believes that when other data on the color-magnitude diagrams are used to determine the helium abundance as well as the differences in [Fe/H] between clusters, the permitted age spread in the globular cluster system will be small (present incomplete analysis gives less than 10%, or two billion years). The properties of the period distribution of RR Lyrae stars now appears to be a new clue making it possible to rediscuss this central problem—the timing of the formation of the system of globular clusters in our Galaxy during the first stages of its formation.

Metallicity of Globular Clusters

Cohen has completed an analysis of echelle spectra obtained with the 4-meter telescopes at Kitt Peak National Observatory and at Cerro Tololo Inter-American Observatory. The iron abundance of M22 is 1/70 that of the Sun, based on three members. A study of high-dispersion spectra of five stars in ω Centauri, chosen to span the giant branch, clearly reveals the large abundance range of all atomic elements within this cluster. An optical and infrared study of Pal 12 by Cohen in collaboration with Dr. Jay A. Frogel of CTIO, Persson, and Zinn shows that this globular cluster in the outer halo is more metal rich than expected; its metallicity is close to that of M71. The four stars studied delineate a well-defined giant branch and hence must be members of this rather distant cluster.

Smith has begun a program to determine metal abundances for the most metal-rich globular clusters possessing RR Lyrae stars. This program is being conducted using the spectroscopic and photographic facilities at Las Campanas Observatory. The metallicity of the so-called "metal-rich" globular clusters is currently in dispute, with some recent results indicating that these clusters are much more metal poor than had been thought. To date, spectra of both RR Lyrae and giant-branch stars have been obtained in the clusters NGC 6712 and NGC 6723.

CN/CH Anomalies

The results of a spectroscopic survey of a large number of giants ($M_V < +0.0$) in the globular cluster NGC 6752 were reported by Da Costa in *Year Book 78* (p. 726). Briefly, the survey showed that on the first giant branch in this cluster the distribution of strengths of the CN molecular band at λ3883 is bimodal; stars appear to be either "CN strong" or "CN weak." Further, the strength of this CN band is anticorrelated with that of the G-band (CH); the CN-weak stars have in general stronger G-bands than the CN-strong stars. This anticorrelation suggests that the CN-strong stars result from the mixing of processed material into the atmospheres of the stars.

During this report year, Da Costa obtained spectra of a number of subgiants ($+2.0 < M_V < 2.5$) in this cluster with the "Shectograph" system attached to the du Pont Telescope at Las Campanas Observatory. These observations show that both the bimodal CN distribution and the CN/CH anti-

correlation are still present at these low luminosities. However, the theoretical meridional circulation-driven mixing mechanism of Sweigart and Mengel (*Astrophys. J., 229,* 624, 1979) predicts that no mixed stars should be seen in this cluster at these luminosities. Consequently, a new mixing mechanism that allows mixing to occur at low luminosities, perhaps even as low as that of the main sequence, is clearly required.

THE GALAXY

Survey for Low-Metal-Abundance Stars

Preston and Shectman have used the 61-cm Curtis Schmidt telescope at Cerro Tololo Inter-American Observatory with its 4° prism and an HK interference filter (bandpass 150 Å at λ3950) to photograph 80 fields distributed over the south galactic hemisphere. The original purpose of the survey, to search for very metal poor stars, continues. In addition, however, the survey has produced large numbers of faint, early-type stars, presumably BHB stars for the most part. Some 2000 such stars have been identified in the 55 fields inspected to date. The integral areal counts decline monotonically from $A = 10$ stars per square degree at α (angular distance from galactic center) = 18° to 1 star per square degree at $\alpha = 130°$. The form of $A(\alpha)$ can be used to derive the density distribution of these objects once the limiting magnitudes of the fields are established. A program of *UBV* photometry at Las Campanas has been initiated for this purpose, in parallel with a spectroscopic program to determine radial velocities and metallicities of a sample of the survey.

Embedded Stars in the W3–W4 Complex

By blinking deep IV-N plates ($\lambda_{eff} \sim$ 8250 Å) with red plates, Elmegreen has discovered 135 stars in the W3–W4 molecular cloud complex that are brighter in the near-infrared than at red wavelengths. The *R* and *I* magnitudes of the bright near-infrared stars were determined from the sizes of their stellar images on the photographic plates. Their positions are well correlated with prominent CO and far-infrared peaks and optical features. Star counts demonstrate that the percentage of bright near-infrared stars in a region increases when the total number of stars in that region decreases. Color-magnitude diagrams that included extinction effects were constructed, and the stars were determined to be primarily embedded pre-main-sequence stars.

GALAXIES

Star Clusters in the Magellanic Clouds

Searle, together with Dr. Althea Wilkinson of the University of Manchester and William G. Bagnuolo (a graduate student at the California Institute of Technology when he participated in this work), completed a study of the integrated light of populous star clusters in the Magellanic Clouds. The statistical distributions of brightness and of spectral characteristics of the

roughly 100,000 stars that make up one of these clusters is expected to depend on two main parameters—the age of the cluster, and the metal/hydrogen ratio of the material from which it formed. If age and composition are uncorrelated, it should prove possible to make a two-dimensional classification scheme for the integrated spectra of the star clusters in a galaxy. Naturally, if age and composition *are* correlated, the integrated spectra of its clusters could be arranged in a one-dimensional classification scheme.

Searle, Wilkinson, and Bagnuolo have shown from observations obtained with the Swope reflector on Las Campanas that the latter situation applies to the clusters of the Magellanic Clouds. They have also shown that their new classification scheme—essentially an ordering of the clusters in an age sequence—makes sense of previously published but not hitherto understood observations of the spectra of these clusters. It is most interesting that the well-established classification scheme appropriate to the clusters of the Galaxy cannot accommodate the spectra of clusters in the Clouds. Evidently the histories of chemical enrichment have been qualitatively different in these systems. A new series of observations, obtained in this report year with Shectman's reticon detector on the spectrograph of the du Pont Telescope, will enable the age-composition relation in the Magellanic Clouds to be put on a quantitative basis.

A program of near-infrared photometry of 84 clusters in the Large and Small Magellanic Clouds was completed by Persson, in collaboration with Dr. Marc Aaronson of Steward Observatory, University of Arizona; Cohen; Dr. Jay A. Frogel of Cerro Tololo Inter-American Observatory; and Matthews. The clusters in the sample range in age from $\sim 10^7$ years, the youngest blue clusters, to 10^{10} years, the old, red globular clusters. The near-infrared data give a picture of the stellar content of the clusters that is complementary to, and quite different from, that revealed by optical observations. Most notable is the importance of carbon stars among the intermediate-age clusters, i.e., those with ages between 2 and 6×10^9 years. Here the cluster energy distributions and narrow-band CO absorption strengths can be understood only if a substantial fraction of the 2-μm light arises from carbon stars. On the average, about 50% of the bolometric luminosity is contributed by such stars. By assuming that the luminosity function of the cluster carbon stars is similar to that observed for carbon stars in several fields of the Magellanic Clouds, one can deduce that, on average, only two or three such stars are required in each cluster. Infrared observations of individual carbon stars in a few clusters support this finding. These few stars, while very important bolometrically, are virtually invisible in the integrated light at 5000 Å because of their extremely red colors. Their bolometric luminosities, which are near -5.5, place them clearly on the upper asymptotic giant branch.

At an age of $\sim 1 \times 10^9$ years, a dramatic change in both the visual and infrared colors occurs. In the younger clusters, the carbon stars appear to die out abruptly, to be replaced by bright M-type giants. This changeover, which may be due mostly to a metal-abundance effect, should be explained by any theory of carbon star production on the asymptotic giant branch.

Among the youngest clusters, which have very blue $U-B$ and $B-V$ colors, the bright red giants and supergiants of the cluster population dominate the infrared energy distributions and bolometric luminosities. Existing synthesis models for the infrared colors and magnitudes of young cluster and galaxy populations fail completely to explain these energy distributions. The authors are working to produce new models that can fit the data.

The most important general result to

come out of the Magellanic Cloud cluster observations is that of the large contribution of the asymptotic giant-branch stars to the energy output of young and intermediate-age stellar systems.

Carbon Stars in the Magellanic Clouds

Cohen, in collaboration with Persson and Drs. Jay A. Frogel and Jonathan H. Elias of Cerro Tololo Inter-American Observatory, has completed infrared observations of a sample of stars from the survey of the most luminous red stars (carbon stars or M giants) in selected fields of the SMC and LMC by Victor M. Blanco and Betty M. Blanco of Cerro Tololo Inter-American Observatory and Dr. Martin F. McCarthy, S. J., of Vatican Observatory. The results are being interpreted with the goal of constructing the luminosity function for the carbon stars in the field of the LMC and SMC and delineating the effects of global galactic properties (e.g., star formation rates, dwarf/giant ratios) on this luminosity function.

Metal Abundances for Supergiant Stars in the Magellanic Clouds

Preston's Δs method has proved very successful in the determination of metal abundances for RR Lyrae stars in the galactic field and in galactic globular clusters. If an analogous method could be adapted to supergiant stars, a useful tool would be available for the study of chemical abundances in the youngest populations of nearby galaxies. Model stellar atmospheres have reached the point where such an adaptation is now possible.

Simple synthetic spectra for A and F supergiants have been calculated by Smith using Dr. Robert Kurucz's (Harvard-Smithsonian Center for Astrophysics) model stellar atmospheres. By applying a variant of the Δs technique, it was possible to determine metal abundances for supergiant stars having $6000 < T_{\rm eff} < 6700$ and $1 < \log g < 2$. Using spectra obtained at Cerro Tololo Inter-American Observatory, Smith determined calcium abundances for six supergiant stars in the Large Magellanic Cloud ([Ca/H] ~ -0.2) and for four supergiant stars in the Small Magellanic Cloud ([Ca/H] ~ -0.6). These values differ significantly from those for young supergiant stars in the solar neighborhood ([Ca/H] ~ 0.0), indicating that the course of chemical evolution has been different for the LMC, SMC, and the Galactic disk. Smith and Dr. Carol Christian of Kitt Peak National Observatory are now employing this method to determine metal abundances for supergiant stars in the outskirts of our Galactic disk.

The Nucleus of M31

Near-infrared observations of the semistellar nucleus of M31 were carried out by Persson in collaboration with Cohen, Sellgren, Dr. Jeremy Mould of Kitt Peak National Observatory, and Dr. Jay A. Frogel of Cerro Tololo Inter-American Observatory. Broad-band *JHK* and narrow-band 2-μm CO and H_2O data were obtained specifically to test a prediction of a recent population synthesis model proposed by Faber and French (*Astrophys. J., 235,* 405, 1980). In their model, the ratio of dwarf-to-giant light increases strongly in going from the nearby bulge onto the semistellar nucleus of M31. In this case, the amount of 2.3-μm CO absorption in the integrated light of the late-type stars should be ~ 0.05 mag weaker on the nucleus than on the surrounding bulge. The new infrared data show, however, that the amount of CO absorption is constant to within ± 0.01 mag in apertures ranging in size from 2.″5 to 100″ in diameter.

The Faber-French model is based on new observations of the Na I 8190 feature, which is also sensitive to the ratio of giants-to-dwarfs. The infrared data

show that their interpretation of the variation of this feature near the nucleus cannot be correct. The resolution of the apparent conflict is not clear, but may involve the luminosity function of the very latest type giants which produce the strong CO-band strengths on the nucleus. Alternatively, the Na I index may be quite sensitive to metal abundance as well as to the relative number of late-type dwarf stars.

Ultraviolet Energy Distribution of Normal Galaxies

Oke and Drs. Francesco Bertola and M. Capaccioli of the Asiago Astrophysical Observatory, Padova, Italy, have now made and analyzed IUE and visual observations of three elliptical galaxies: NGC 3379, NGC 4472, and NGC 4486. In all these objects, and in M31 and M32 observed by Dr. Hugh M. Johnson of Lockheed Missiles & Space Co., Palo Alto, California, the flux F_λ decreases rapidly toward the violet as far as 2200 Å, below which it increases again. The far *UV* radiation can be modeled by a 30,000-K blackbody and is probably produced by hot horizontal-branch stars, although main-sequence OB stars cannot be ruled out. The hot *UV* flux is similar in NGC 3379, NGC 4472, and M31, much weaker in M32, and much stronger in NGC 4486. The spectra in the near *UV* are of sufficient quality to show several broad spectral features in the 2600–3200 Å region, which can be used for redshift determinations. The *UV* fluxes in this region can be compared with those of large redshift galaxies observed from the ground. The agreement is satisfactory if allowance is made for the line-strength difference found between integrated galaxy spectra and nuclear region spectra. The *UV* energy distributions for NGC 3379, NGC 4472, and M31 are very similar to those of the metal-rich globular cluster NGC 6624. If the hot *UV* component becomes significantly brighter in some galaxies, it could perhaps explain the occasional blue galaxies found in faint samples.

Surface Photometry of Spiral Galaxies

Searle, together with Dr. Pieter C. van der Kruit of the Kapteyn Laboratory of the University of Groningen, has completed the observational phase of a study of the light and color distributions in 20 spiral galaxies. The aim of this work is to study the kinematics and population structure of these systems, which were chosen to cover a wide range of morphological types as well as a wide range of intrinsic luminosity. The spatial distribution and motions of the neutral hydrogen gas in these same systems are being obtained with the Westerbork radio synthesis telescope. The optical study is based on two plates in each of three colors obtained with the 1.2-meter Schmidt. The plates are scanned and digitized at the University of Leiden.

As part of this large program, the material on the edge-on spiral NGC 891 was analyzed in detail during this report year. The luminous matter in spiral galaxies belongs to two intermingling subsystems—a usually dominant flattened disk, and a more tenuous spheroidal halo. These components are most cleanly perceived in edge-on systems, and van der Kruit and Searle have studied the three-dimensional light distribution of these two components in NGC 891. To develop a model of the three-dimensional light distribution in a pure disk, they studied the light distribution in two edge-on systems that have negligible halos, NGC 4244 and NGC 5907. They find that this distribution is well described by a model in which the surface density of the disk declines exponentially with galactocentric radius, while the distribution perpendicular to the symmetry plane is that expected for a locally isothermal self-gravitating sheet. An unexpected result is that the temperature

of these disks is quite accurately proportional to the surface density.

Searle and van der Kruit have fitted a disk model of this type to their observation of NGC 891. Subtracting the disk from the total light reveals the structure of the spheroidal halo. This halo becomes strikingly more blue with increasing galactocentric distance, probably because it is made of metal-poor stars, as is the case in our own Galaxy. The spheroidal halo also becomes increasingly flattened with increasing galactocentric distance, as would be expected of an isothermal hot gas of stars moving in the potential field of the disk. The presence of substantial amounts of nonluminous matter in this galaxy is needed to account for its 21-cm rotation curve, but whether this nonluminous matter is located in the disk or in the halo cannot be determined from the present observations.

Star Formation in Spiral Galaxies

Kennicutt has spent much of his observational efforts of the past year in a study of the ionized gas content of normal spiral galaxies in order to establish the global properties of their star formation processes.

The 1-meter Swope Telescope and the 1.5-meter Palomar telescope have been used with large aperture photoelectric photometers to measure integrated Hα + [N II] emission-line strengths in approximately 150 field and Virgo cluster spirals. By using a specially selected set of interference filters and photometric apertures that closely match the diameters of the galaxies measured, Kennicutt has obtained Hα equivalent widths accurate to a few angstroms. These data will be used for a number of purposes: (1) to assess the reliability of earlier small aperture/slit measurements by Cohen, Kent, and Bagnuolo, (2) to obtain the dependence of the ionized gas content and total star formation rate on the H I contents and dynamics of a galaxy, (3) to measure the dispersion in the star formation rates among galaxies of the same type, color, and H I content, and (4) to form a reference set of line strengths in "normal" field galaxies for comparison with other samples of objects such as spirals in rich clusters, interacting spirals, and dwarf galaxies.

To aid in the interpretation of the integrated photometry, detailed studies are also being made of the ionized gas in a number of individual spirals. In collaboration with Dr. Paul Hodge of the University of Washington, Kennicutt is measuring luminosity functions of the H II regions in selected spirals of various Hubble types, and he has obtained broadband surface photometry with the Palomar Schmidt telescope in order to compare the distribution of ionized gas with that of the integrated light and the neutral hydrogen. In a related project, Dr. Robert Schommer of Yerkes Observatory and Kennicutt have obtained SIT imagery in Hα of a number of spirals in rich clusters in order to compare the star formation in these objects with that of field spirals.

Spiral Structure in Galaxies

Kennicutt, in collaboration with Dr. Paul Hodge, is nearing completion of a study of the morphology of the spiral patterns in a large sample of nearby galaxies. Despite considerable theoretical activity in this field, virtually nothing has been done to measure the statistical properties of spiral patterns as a function of galaxy type since Danver's work in 1942. This study is meant to upgrade that work, using when possible deep Hα photographs of late spirals and large-scale blue photographs taken with the 2.5-meter du Pont Telescope for early-type spirals. In addition to establishing empirically how spiral structure evolves along the Hubble sequence, Kennicutt and Hodge have been able to compare the observed patterns of selected spirals with the theoretical predictions of both the density-

wave and stochastic models. They find that while both theoretical pictures adequately account for the qualitative trends observed in spirals of different types, neither agrees on a one-to-one basis with the observed patterns. Moreover, certain properties of the spiral patterns, most notably the pitch angles and widths of the arms, can be best understood in simple kinematic terms independent of the details of any dynamical model of the origin of the spiral structure.

Spiral-Arm Spurs

Elmegreen has studied the properties of spiral-arm spurs in seven galaxies with known rotation curves to determine whether they are material or density-wave features. The time scales for shearing a spur from a spiral arm because of differential rotation or an underlying density wave are on the order of 10^8 years. However, the spurs appear to be as long-lived as spiral arms because both are prominent and smooth in the near-infrared, which emphasizes light from older stars. The pitch angles of the spurs have a very small standard deviation from one galaxy to the next and are always about 50° greater than the pitch angles of the arms. Also, the physical separations between adjacent spurs in the same galaxy vary by factors of 20, but the time scales of separation indicated by a density wave are always a few times 10^7 years. Thus, while a stochastic mechanism for spur formation may not violate the observations, a density-wave origin provides a more viable explanation for the regularity and lifetime of spurs.

Carbon Monoxide in Magellanic Irregulars

Together with Drs. Bruce C. Elmegreen and Mark Morris of Columbia University, Debra Elmegreen has surveyed H II regions, dark clouds, and H I peaks in nearby Magellanic irregular galaxies at 2.7 mm (National Radio Astronomy Observatory 91-cm telescope) for their ^{12}CO content. These irregulars (IC 1613, NGC 1156, NGC 2366, Ho II, IC 2574, and NGC 6822) are found to have upper limits of 0.04 K, although star-forming clouds like those seen in spiral galaxies should be detectable at a level of 0.1–0.3 K. The low level of CO emission in Magellanic irregulars may be due to a variety of factors relating to lower cloud heating rates or to decreased CO abundances. A line of 40 km s^{-1} half-width at a temperature of 0.04 K was discovered in the nucleus of the small Sdm galaxy NGC 7793, making NGC 7793 the least massive galaxy in which CO has been detected.

Star Formation in Barred Magellanic Irregulars

Bruce Elmegreen and Debra Elmegreen have examined all 44 Magellanic spiral and irregular galaxies larger than 4′ and find that nearly half have their most prominent H II regions near their optical peripheries. Almost all such Magellanics are barred, and usually the largest H II regions are at one end of the bar. These galaxies generally are rigidly rotating throughout the barred region. They suggest that the hydrodynamics of the barred regions in the Magellanics may be similar to that in massive barred spirals, where enhanced star formation near bar ends is thought to be due to higher gas compression. The fact that star formation generally is seen at only one end of a bar in Magellanics, but at both ends in massive spirals, may be a result of the bar being displaced from the center of mass in the Magellanic galaxies.

Morphology of Sa Galaxies

Early spiral galaxies have long been known to exhibit an inconsistency in their placement in Hubble's original classification scheme, in the sense that

among galaxies with evolved (i.e., early-type) disks there exists a large range of bulge-to-disk ratio. Sandage, Freeman, and Stokes (*Astrophys. J., 160,* 831, 1970) suggested that this dichotomy arises during the formation of a galaxy; more recently, others argue that it arises from environmental (e.g., stripping) effects.

Unfortunately, most of the above arguments have of necessity been based on qualitative observations of disk and bulge morphology in heavily biased samples. Kennicutt has now obtained blue and red surface photometry for 30 field Sa galaxies, using the Palomar Schmidt and the Las Campanas 2.5-meter and 1-meter telescopes. The Sa galaxies were selected from the *Revised Shapley-Ames Catalog* and possess, by definition, highly evolved unresolved disks. Special care was taken to select galaxies with a variety of apparent bulge-to-disk ratios with special emphasis on the small bulge systems. Those galaxies compose the bulk of van den Bergh's "anemic" class and, in his scheme, are the most likely to have experienced gas depletion.

The initial goal of this program is to ascertain to what degree bulge size *is* decoupled from disk resolution; here the analysis will closely follow that of Burstein's work on S0 galaxies. Subsequent efforts will be made to compare the derived bulge-to-disk parameters with other integrated properties of the galaxies, such as color, H I content, and rotational velocity, in order to ascertain whether the most "anemic" galaxies are better explained in terms of a prenatal or an environmental picture.

Dynamics of Early-Type Galaxies

Dressler and Sandage are continuing their study of the dynamics of S0 galaxies with the 5-meter SIT digital spectrograph. They have measured the rotation curves out to distances of typically 5–10 kpc for NGC 16, 128, 584, 890, 1023, 1175, 1209, 2549, 2732, and 7457. The maximum rotational velocity measured is clearly a function of the absolute magnitude of the galaxy, although the scatter from a mean relation is large. These results will be compared to the Fisher-Tully relationship for spiral galaxies in order to study the continuity of dynamical properties along the Hubble sequence and their possible application to the problem of determining the extragalactic distance scale.

Spectroscopic Investigation of Companion Galaxies

During the first operating period of the du Pont reflector at Las Campanas, Arp began obtaining spectroscopic data on a sample of galaxies and associated companions. During the first year, he used the Image Tube Spectrograph; during the last two years, he used the Varo-Reticon detector designed by Shectman. The objects were drawn from a catalog in preparation by Arp and Dr. Barry Madore of the University of Toronto, entitled *Southern Peculiar Galaxies and Associations*. That catalog represents a systematic search of the entire southern hemisphere from deep, IIIa-J plates taken by the twin of the 1.2-meter Palomar Schmidt in Australia, which was built and is operated by the Royal Observatory at Edinburgh. (After six years in preparation, the catalog will enter the publication process in the fall of 1980.)

The three years of spectroscopic observations of these objects have now been reduced and analyzed by Arp, working at the European Southern Observatory (ESO/Geneva). The results are listed below:

1. Companion galaxies to larger galaxies have more excited emission spectra and younger, stellar-type absorption spectra.

2. Even companions with approximately the same redshift as the central galaxy (± 800 km s^{-1}) show a prepon-

derance of positive redshifts with respect to the central galaxy (36 cases to 15).

3. In addition, there are 34 companions of higher discordant redshift (Δz = 4000–30,000 km s^{-1}) that show strong evidence for being physically associated with the lower redshift central galaxies.

4. Recently published redshifts from radio measurements of neutral hydrogen in companions and central galaxies support the preponderance of positive Δz (12 cases to 4).

Arp's conclusions confirm earlier results showing essentially that all the well-known companions to the local giant spirals M31 and M81 are positively redshifted with respect to these central massive galaxies dominating the group. Arp believes this nonvelocity or intrinsic redshift effect to be a property of the younger, more active physical state of the companions. In any case, the results seem to establish a paradox in terms of conventional physics and hence warrant further investigation.

The Nucleus of M87

Dressler has used the Reticon spectrograph of the du Pont Telescope at Las Campanas to study the central luminosity spike in M87. He found that, contrary to the model of Young *et al.* (*Astrophys. J., 221,* 721, 1978), the spike is actually a star cluster with a K III spectrum (Fig. 5). The velocity dispersion of this star cluster is only slightly higher than that of the stars in the core of M87. This implies that if the cluster is smaller than ~10 pc in diameter, the massive black hole ($M > 10^9\ \mathfrak{M}_\odot$) suggested by Sargent *et al.* (*Astrophys. J., 221,* 731) and Young *et al.* could not be present. Determining the size of the star cluster is thus essential in order to test the mass distribution in the center of M87.

Young and Gunn have investigated the possibility of using the prime-focus CCD camera/spectrograph of the 5-meter Hale Telescope to measure galaxy velocity dispersions. The instrumental profile has a dispersion $\sigma = 180$ km s^{-1}, and galaxian dispersions above this can be measured. A high-resolution diffraction grating has been used to observe the Ca II λλ8498, 8542, 8662 lines in M87. With a signal of 5×10^4 photons per pixel obtained in one hour, the velocity dispersion as a function of radius could be measured to 20 km s^{-1}. The velocity dispersion falls with radius, as observed by Young, Sargent, and collaborators in 1977. In addition, some extra points at small radii showed a continued rise to a central value of 400 km s^{-1}. (The dispersion in the general core is 280 km s^{-1}.)

Preliminary modeling of the dynamics of the core of M87 shows that either a central mass concentration of the magnitude ($2 \times 10^9\ \mathfrak{M}_\odot$) previously found resides in the core of M87 or that the central stellar densities are incredibly high, up to $10^8\ \mathfrak{M}_\odot$ pc^{-3}. The latter possibility is less plausible because the time scale for stars to destroy themselves by physical collisions in such an environment is much less than a Hubble time.

Seyfert Galaxies

Yee has used multichannel spectrophotometric data of 105 quasars, radio galaxies, and Seyfert galaxies to study their optical continua and emission lines. He found a strong continuity between broad-line active galactic nuclei and quasars in terms of the correlations between line luminosities and nonthermal luminosity. There is a tight correlation between line luminosities and nonthermal luminosity for all objects, suggesting that radiative recombination is the dominant mechanism and that physical parameters, such as overall spectral index and covering factor, are similar. Relative to the nonthermal continuum, the forbidden lines of the broad-line objects are approximately one order of magnitude weaker

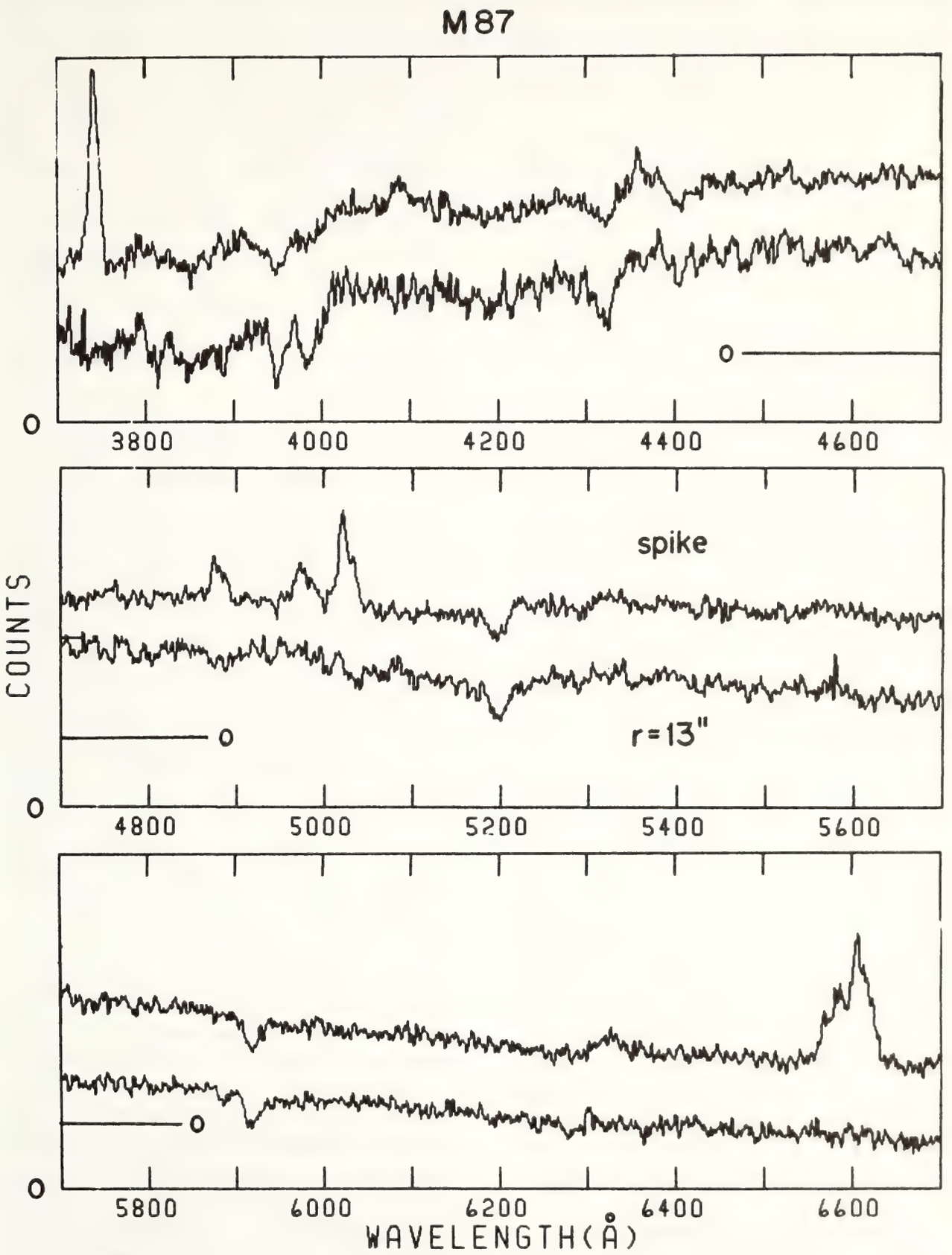


Fig. 5. The spectra of the M87 central spike and the region at $r = 13''$. The similarity of the two spectra at Mg b and Na D indicate that very little nonthermal continuum is present in the spike. (The M87 spike spectrum has been offset, and a second baseline is indicated.)

than those of the narrow-line objects. This is consistent with the view that forbidden lines are suppressed in the dense broad-line region of the broad-line objects.

Yee and Oke have used multichannel scans covering the period between 1969 and 1979 to study the variability of the optical continua and emission lines of the N-galaxies 3C382 and 3C390.3. The decomposition of the continua into galactic and nuclear components is accomplished by assuming that the spectral shape of the nuclear component is unaltered when it varies. This produces consistent decomposition from epochs of different luminosity. The apparent visual magnitude in a 10″ aperture of the underlying galaxy component is 15.2 for 3C382 and 16.1 for 3C390.3. The constancy of the spectral shape of the nuclear component suggests that the 3000-Å bump observed in objects such as N-galaxies and Seyfert I galaxies is very closely related to the continuum source in size and origin. While the narrow forbidden lines such as [O III] λλ5007 and 4959 remain unchanged as the continuum luminosity varies by as much as a factor of ten, the broad permitted Balmer lines vary with the continuum. The variations, however, are not proportional but follow the relation $L_{\text{line}} \propto L_{NT}{}^{\beta}$, where L_{line} is the line intensity and L_{NT} is the integrated optical luminosity of the nuclear component. For 3C390.3, β is approximately 0.4 for both Hα and Hβ. For 3C382, β is 0.4 for Hα but nearly 0 for Hβ, indicating a definite change in the Balmer decrement. These results suggest that processes other than radiative recombination play a significant role.

Oke and Robert W. Goodrich, Caltech undergraduate student, have completed a study of IUE and visual spectra of three type I Seyfert galaxies, Markarian 9 and 10, and 3C390.3. In Markarian 9, the λ2175 interstellar feature is well enough measured to show that the reddening of 0.14 mag in E_{B-V} is in the galaxy. The same absorption feature is present in Markarian 10 and may be present in 3C390.3. After correction for reddening, the Lα/Hβ ratios remain a factor 2–4 times smaller than predicted by recombination theory, whereas the He II λλ1640/4686 ratio is approximately consistent with recombination. A comparison of absolute line strengths and the *UV* ionizing flux suggests that Hβ is enhanced rather than Lα depressed. Changing the reddening does not produce line ratios that can be explained by simple models for the line-emitting region.

Binary Galaxies

An observational investigation of the tidal effects in binary galaxies has been undertaken by Borne. He has observed about 70 pairs of elliptical galaxies and about ten isolated elliptical galaxies (the control sample) with the SIT direct area photometer on the Palomar 1.5-meter telescope. A comparison of these two data sets, an individual analysis of each binary system, and an appraisal of the results in terms of dynamical models (described elsewhere in this report) will help to determine the present state and the future evolution of such pairs.

The Distribution of Galaxies in Space

While matter appears to be distributed evenly throughout the universe at the very largest scales, local matter distribution is characteristically clumped into galaxies and groups, clusters, and even superclusters of galaxies. A group of observers, including Shectman, Dr. Robert Kirshner of the University of Michigan, Dr. Augustus Oemler, Jr., of Yale University, and Dr. Paul L. Schechter of Kitt Peak National Observatory, in an effort to characterize the clumpiness of the galaxy distribution, have discovered a volume conspicuously empty of galaxies—the largest

feature yet found in the distribution of matter in the universe.

Three fields, each 2 □° in area, were studied near the north galactic pole, to avoid the patchy dust obscuration of the galactic plane. The fields were separated from each other on the sky typically by 35°. In each field, a complete list of galaxies brighter than a red magnitude of 17 was derived by scanning photographic plates taken at the Palomar 1.2-meter telescope with the computerized microdensitometer at Yale.

For each of the galaxies on the list, a redshift was measured spectroscopically. More than 100 galaxies were observed, roughly half with the Palomar 5-meter telescope. From the redshift, the distance of each galaxy follows from the Hubble law of universal expansion. Since the limit of the sample is 2 mag fainter than those of previous magnitude-limited surveys of galaxy redshifts, the typical distance of the galaxies is more than twice that of earlier work. The greater distances surveyed make it possible to delineate larger features in the galaxy distribution.

The striking result is that not a single galaxy is observed in the redshift range 12,500 km s^{-1}–18,500 km s^{-1}. This is in spite of the fact that, if galaxies were smoothly distributed, the most likely redshift for a galaxy in the range of brightness surveyed would be 15,000 km s^{-1}. The feature is common to all three fields, so that the angular extent of the gap in the galaxy distribution is comparable to the size along the line of sight.

The gap spans a diameter 100 times the distance to the nearest major galaxy, Andromeda, and six times the distance to the nearest major cluster of galaxies, Virgo. While it is thought that the Milky Way is an outlying member of a supercluster of galaxies associated with the Virgo, the extent of the gap is equal to the distance of the very rich Coma cluster of galaxies. A supercluster associated with the Coma cluster appears to be responsible for a clear peak in the distribution of sampled redshifts on the near side of the gap, while an equally striking peak in the galaxy distribution occurs on the far side of the gap.

The random motions of galaxies relative to the Hubble expansion are not sufficient to carry galaxies out of the empty volume at the present time. Earlier in the expansion of the universe, the volume was smaller and the random velocities may have been higher. A volume of the universe that begins slightly depleted in matter tends to grow and become more empty because the lower mass density is less effective in gravitationally slowing the expansion of the volume compared to neighboring regions. In addition, the gravitational attraction of the concentrations of galaxies on the boundaries of the gap may have served to deplete the region of matter.

Radial velocities for nearly 150 galaxies in three similar fields in the south galactic polar cap have been obtained with the 2.5-meter telescope at Las Campanas Observatory. The analysis of the entire set of data will permit an improved understanding of the clustering of galaxies at such large scales.

CLUSTERS OF GALAXIES

Virgo Cluster Survey

A photographic survey of the Virgo cluster was begun in 1979 by Sandage in collaboration with Dr. Gustav A. Tammann of the Astronomical Institute of the University of Basel, Switzerland, using the du Pont 2.5-meter

reflector at Las Campanas. The region photographed is a circle of radius 5° centered on NGC 4390, covered by 60 plate centers. After two observing seasons, Sandage and Brucato have obtained 30 of the required 50 × 50 cm plates, each of 75 min exposure on 104aO emulsion.

A catalog of all possible members of the cluster in these 30 fields is nearing completion, with a principal goal of studying the distribution of dwarf galaxies. The brighter dwarfs had been studied previously by Dr. Gibson Reaves of the University of Southern California in 1950 using the Carnegie astrographic refractor of the Lick Observatory and, more recently, during 1975–1978 using IIIaJ plates taken by Sandage with the Palomar 1.2-meter Schmidt as a preliminary step of the current survey.

The dwarfs are generally of type dE, with a smooth luminosity profile and no suggestion of recent Population I star formation. They are distributed throughout the cluster region outlined by the bright galaxies. They do not extend southward into the so-called Southern Extension. Hence, this heretofore possible appendage to the Virgo cluster proper is not a part of the cluster core and does not form a dynamical unit with it.

The number of dwarfs per unit magnitude interval in the central cluster region continues to rise to the plate limit, which for these extended low-surface systems is estimated to be $B \simeq 19$. Hence, since $m - M = 31.7$ for the cluster, the differential luminosity function is still increasing for galaxies as faint as $M_B \simeq -13$.

The plates have been traced by Shaw for all possible cluster members using the large microphotometer at the European Southern Observatory headquarters in Geneva. Total magnitudes, accurate to $\sim \pm 0.2$ mag, are expected to be obtained from the data. Preliminary results show that the surface brightness is a decreasing monotonic function of absolute luminosity and has very small scatter about the regression line. Hence it is the very low surface brightness of the dwarfs that is the diagnostic permitting separation of the faint cluster members from the numerous distant E galaxies in the background field. Spectra, described in the next paragraphs, confirm cluster membership in every case. Therefore, the relation of lower surface brightness for fainter absolute magnitudes appears to be well established.

In preparing the catalog, Shaw has estimated the apparent flattening of the dwarfs. From the distribution of the flattenings, it is well established that these dwarf galaxies are true dE systems rather than disk galaxies like S0's or spirals. Hence, no matter what the formation history was, the collapse from a larger volume must have been much slower than the formation time of the stars because the dissipative formation of a gaseous disk did not occur. The very low surface brightness of the systems requires that the star density be low and, since the collapse time varies as $t \sim \rho^{-1/2}$, the formation infall time must have been longer for the dwarfs than for the higher luminosity E galaxies.

Spectra have been obtained for 43 of the dwarfs by Sandage and Dressler using the Gunn SIT digital spectrograph at the Palomar 5-meter reflector and the software programs written by Zimmerman. All of the dwarfs have velocities smaller than ~ 2000 km s^{-1}, proving cluster membership. The composite spectral type, on the average, changes with absolute magnitude, becoming earlier as the luminosity decreases (i.e., as the surface brightness becomes lower). Evidence for the presence of stars as early as type A exists from the increased strength of the hydrogen lines in absorption and the decreased blanketing and temperature break at λ4000 as the surface brightness decreases. These preliminary indications suggest that the main-se-

quence termination point of the HR diagram for the dwarfs is brighter than at type G ($M_v \simeq +4.5$) for the standard globular clusters and that star formation in these dE systems took place until as recently as $\sim 10^9$ years ago. It is possible to believe that this is due to the slower collapse time of the faintest dwarfs caused by their very low mean density.

The cluster dwarf survey and spectroscopic program is expected to continue for two more seasons with the principal aim of calculating the gravitational potential of the cluster from the dwarf distribution and of obtaining detailed velocity dispersions in various subregions of the cluster. Data now available suggest that the dwarfs are moving in the potential of the entire cluster rather than in the potential of particular bright cluster galaxies. The principal evidence to date is that the dwarfs that are projected on the sky near the Sc member spiral M100 show the full range of the velocity dispersion (i.e., 0–2000 km s^{-1}) rather than a smaller velocity range, as they would show if attached to M100 itself.

Structure and Dynamics

Dressler has completed a study of the dynamics of the cD cluster of galaxies A2029. The 47 redshifts of cluster members indicate that, although the cluster is highly flattened, its shape is not due to rotation of the cluster as a whole. Thus A2029 appears to have an anisotropic velocity field, either frozen in during its formation or resulting from a merging of clusters. The velocity dispersion of the seven galaxies seen projected against the cD envelope is as high as that of the remaining galaxies in the cluster. It seems unlikely, therefore, that most of these companions are spiraling into the cD as a result of dynamical friction. This is in rough agreement with the time scale for the cannibalism process, which predicts that only a couple of victims should be seen at any one time.

Dressler has published his catalog of the morphological types, positions, and approximate magnitudes of ~6000 galaxies in 55 clusters, which formed the data base for his study of galaxy morphology in clusters. He is presently analyzing the structural properties of the clusters in an attempt to evaluate the feasibility of using metrics like cluster core radii as standard rods in cosmological tests.

Dressler and Shectman have obtained radial velocities for ~100 galaxies in each of 11 clusters in the Dressler catalog. They are undertaking an analysis of the degree of subclustering in various clusters to test models of cluster collapse and relaxation.

Distant Clusters of Galaxies

Gunn, Oke, and Hoessel have continued their program to study faint distant clusters of galaxies. Direct pictures taken with IV-N plates at the 4-meter Mayall Telescope of the Kitt Peak National Observatory have been used to extend the sample of clusters already obtained with the 1.2-meter Schmidt and the 5-meter Hale Telescopes to fainter limits. The Prime Focus Universal Extragalactic Instrument (PFUEI) is now being used to measure redshifts of very faint galaxies. The Mayall Telescope survey produces clusters that have redshifts greater than 0.50. The largest certain redshift is 0.756, but one other cluster probably has a redshift of 0.92. In total, 400 clusters have now been found and redshifts of over 80 of these have been obtained. Cooled SIT or CCD pictures have been taken of all clusters with redshifts to provide an accurate magnitude of the first-rank galaxy in the redshifted frame of reference. The data will be used in the immediate future to study the Hubble diagram for first-rank galaxies and to derive a formal value of q_o.

QUASARS AND QUASI-STELLAR OBJECTS

Luminosity Effects in QSO's

French is beginning a study of the effects of luminosity on the observable properties in QSO's, based on good signal-to-noise spectrophotometry at $\lesssim 10$ Å resolution of QSO's having a large range of apparent magnitude within two narrow redshift ranges (0.3 ± 0.02 and 2.3 ± 0.1); if the QSO redshifts are cosmological, apparent luminosity should reflect absolute luminosity within each group. These observations, which are about 40% complete at present, are being obtained with the Cassegrain reticon spectrograph on the Las Campanas 2.5-meter du Pont Telescope and with the SIT digital spectrograph on the 5-meter Hale Telescope. When the observations are completed, it is expected that correlation (or the lack thereof) of such properties as continuum shape, emission line fluxes and profiles, and the incidence of absorption-line systems with luminosity will lead to a better understanding of the geometry and physical processes operating within QSO's. In addition, the data obtained for this study will be useful for a variety of other projects, including studies of line profiles and of the narrow line region.

Spectrophotometry of Hydrogen Emission Lines

A study of the emission lines of active nuclei provides a way of understanding the conditions within the nuclear regions of these objects. Studies of the visual spectra of quasars, especially by Baldwin, have indicated that Lα/Hα ratios are significantly less than predicted on the basis of recombination theory. Baldwin's work suffered, however, since with visual spectroscopy Lα and Hα were not observable in the same objects. The correctness of his conclusions has been confirmed for 3C273, where Davidsen, Hartig, and Fastie measured Lα in the *UV*, and in PKS 0237–23, where Hyland, Becklin, and Neugebauer measured Hα redshifted into the 2-μm atmospheric window, thus permitting a direct measurement of the Lα/Hα ratio in these two objects.

Soifer, Neugebauer, and Matthews have extended the technique of measuring lines redshifted into the infrared atmospheric windows to well over a dozen quasars and ten Seyfert galaxies. They have concentrated on the hydrogen emission lines since these lines presumably are the strongest and are crucial to any understanding of the line-emitting regions. For selected redshifts z between 0.07 and 3.9, the Pα, Hα, or Hβ lines fall within the 1.65- or 2.2-μm atmospheric windows. Thus, by selecting quasars with the appropriate redshifts, they have been able to sample the Lα/Hα, Hα/Hβ, and Pα/Hβ ratios of a significant number of low- and high-redshift quasars. The work was done in collaboration with Oke, who obtained visual spectrophotometry with the multichannel spectrometer on the 5-meter telescope.

Figure 6 shows typical infrared spectra as obtained with 1.2% or 5% continuous variable filter wheel spectrometers. The results of the study are as follows:

1. The Pα/Hα ratios in low-redshift quasars are distributed around the case B value (see Fig. 7) with a tendency toward values lower than that predicted by case B. The Hα/Hβ values in these same quasars are generally greater than the case B value. The trend in the Pα/Hα/Hβ ratios is for the Pα/Hα ratio to decrease as Hα/Hβ increases.

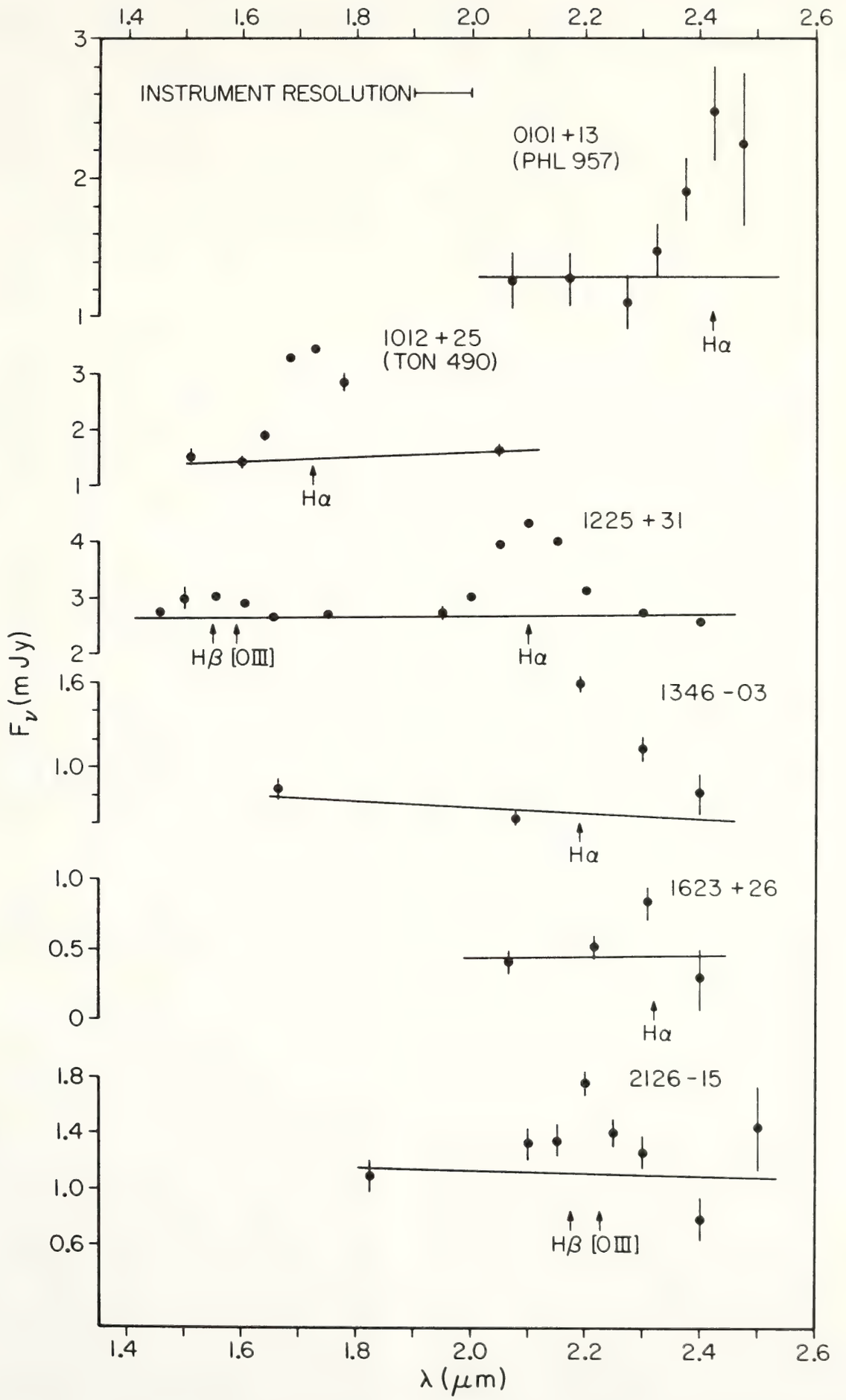


Fig. 6. Near-infrared spectra of high-redshift quasars, showing Hα and/or Hβ + [O III] in the 1.65-μm or 2.2-μm atmospheric window.

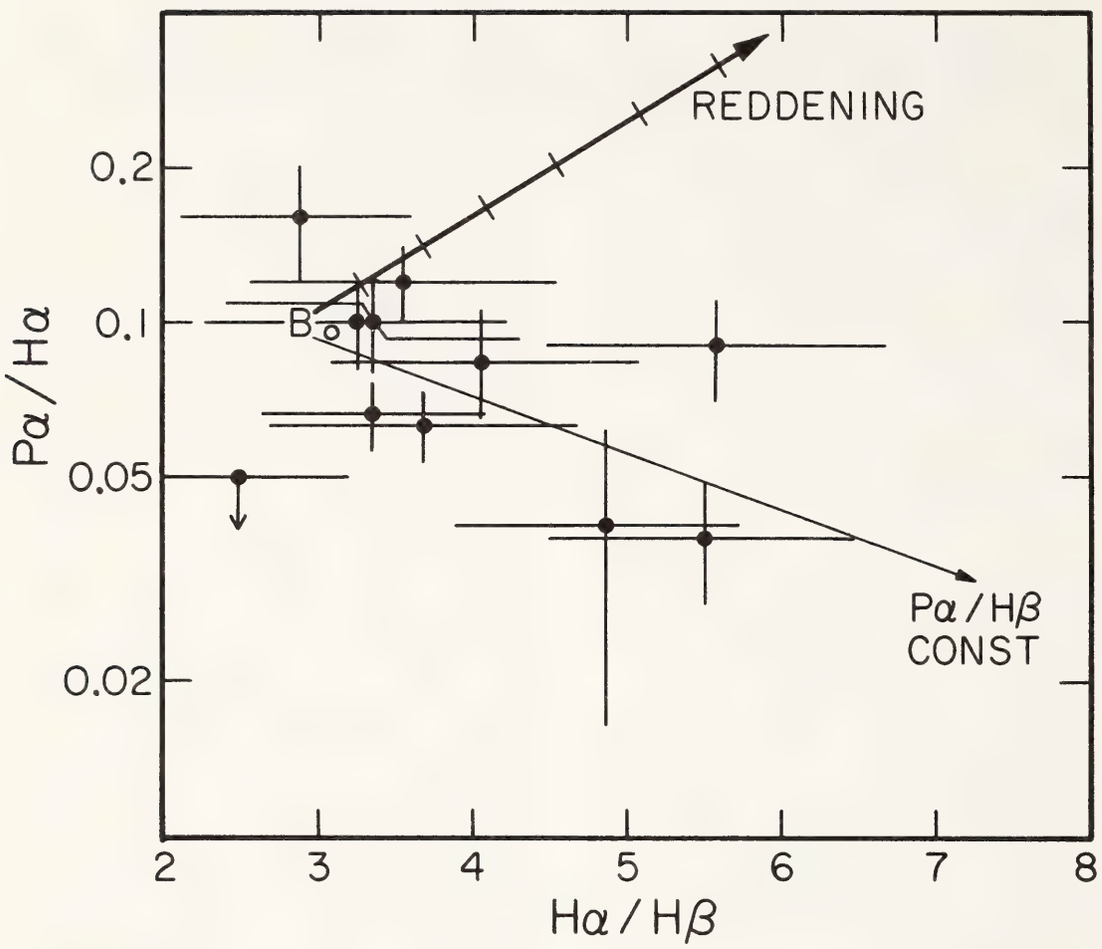


Fig. 7. The Pα/Hα intensity ratio plotted versus the Hα/Hβ intensity ratio in the same quasars, for the low-redshift quasars. The B indicates the location of the pure case B result in this plane. The heavy line indicates the departure expected from case B due to reddening by intervening galactic-type dust. The ticks on this line correspond to $\Delta E(B - V) = 0.1$ mag. The thin line indicates the line of constant Pα/Hβ.

2. The low values of the Lα/Hα ratio compared to the case B value are confirmed for a large sample of high-redshift quasars.

3. Reddening external to the emission-line regions cannot satisfactorily explain the observed hydrogen-line ratios. The current observations also do not support a model of internal dust-destroying resonantly scattered Lα, but such a model cannot be ruled out on the basis of the data. Models of the emission-line regions that apply radiative transfer and collisional excitation effects in the lines appear to be necessary to explain the current observations. The decrease of the Pα/Hα ratio with increasing Hα/Hβ ratio is probably the most significant correlation found from the present data that any valid model of the line-emitting regions must explain.

QSO-Galaxy Correlations

Kristian, Young, and Westphal have investigated the vicinity of QSO's with redshifts from 0.3 to 1.4 in order to search for faint galaxies associated with the QSO's. A total of 16 fields were observed with two-hour red CCD exposures at the 5-meter Hale Telescope. Galaxies were observed to cluster around most of the QSO's, even those with $z > 1$. Objects judged to be stellar on the basis of classification algorithms showed no tendency to cluster around the QSO's. To explain

such a degree of clustering, it is required that the QSO-galaxy correlation function be five times stronger than the local galaxy-galaxy correlation function, or that galaxies at $z = 0.75$ be 4 mag more luminous than nearby galaxies. Out of a total of 16 fields, there was one rich cluster of galaxies ($z = 0.76$) and one poor cluster. The other associations were of loose groups of galaxies.

Gravitational Lenses

In 1979, a pair of QSO's, both with redshifts of 1.41, were discovered by a group at the Steward Observatory. They are only 6″ apart on the sky, aligned north-south, and the spectra are so similar that it was proposed that the two QSO's are gravitationally lensed images of a single object. This hypothesis was strongly contested with VLA observations at 6 cm by an MIT group who showed that the arrangement of sources and radio lobes could not be imaged by an intervening point mass.

Young and Kristian observed the object with the PFUEI CCD system built by Gunn and Westphal. They discovered that Q0957+561 lay behind a cluster of galaxies and that the brightest galaxy in this cluster was only 1″ north of the southern QSO image. Multichannel and CCD spectra by Oke and Gunn gave a redshift of 0.36 for this galaxy, which has a very strong calcium break. The galaxy and cluster of galaxies acting together produced the gravitational lens effect as demonstrated from the theoretical calculations by Young and Gunn. The separation of the images due to the galaxy alone would be only 3″, but the added effect of the mass distribution in the galaxy cluster pries the images apart to the observed 6″. It was further demonstrated from general topological arguments that gravitational lensing by a transparent mass distribution must always produce an odd number of images and that there must be a third image of Q0957+561 somewhere. The most likely solutions make it rather faint and close to the center of the lens galaxy.

The southern QSO was observed to brighten by 0.3 mag in January 1980. The QSO's are being monitored with the CCD in order to detect correlated time variations among the two observed images. If the gravitational lens geometry can be understood well enough, then it will be possible to determine the Hubble constant from the time delays.

In April 1980, a second gravitational lens was discovered at Steward Observatory. This object, Q1115+080, has three images visible at magnitudes 16, 18, and 18½ in a triangle 2″ on each side. Young and Kristian observed the object with the Gunn/Westphal CCD camera/spectrograph in June 1980. All three images have identical spectra and redshifts (to within 100 km s^{-1}). They all have the same, quite blue, color with image B being slightly redder than A and C. No trace of a lens galaxy, to a surface brightness of magnitude 30 per square arcsecond, was found. Some nearby galaxies were seen on a deep CCD picture, apparently forming a small group.

The imaging geometry is strange and has to be formed by a massive spiral galaxy. (That is, if it is a single galaxy; one might postulate multiple galaxies or black holes, or something else!) Five images are found in the configuration, with image A a close double and the fifth image very faint. Image A, in this model, is boosted by a factor of ten in brightness, which might explain the apparent extraordinary luminosity of Q1115+080.

New Quasars Associated With Companion Galaxies

Arp has continued his systematic investigation of areas around companion galaxies in the northern hemis-

phere. This work has been carried out with the 1.2-meter Schmidt telescope and the 5-meter reflector at Palomar. Large spirals with companions have been photographed in ultraviolet and blue wavelengths with the Schmidt telescope. Systematic investigation of spirals between approximately NGC 2400 and NGC 3000 have been completed and are being prepared for publication.

Some results of particular interest are new quasars around companions to NGC 2841 and NGC 2903, two of the brighter nearby spirals in the sky. Of particular interest is a bright quasar of redshift 0.553 near the companion to NGC 2841. At apparent magnitude 16.5, there is only from one chance in a thousand to one chance in ten thousand of finding a quasar this close at any given point in the sky. Additionally, it has two mysterious, unidentified absorption lines at λλ4061, 4116. In another peculiar object near NGC 2841, possibly a transition between a quasar and a galaxy, K and H absorption lines are seen blueshifted by 2800 km s^{-1} with respect to the emission lines, which exhibit a redshift of 0.297.

The "double" quasar (two quasars about 6″ apart and of identical redshift) has been analyzed by Young, Gunn, Kristian, Oke, and Westphal (*Astrophys. J., 241,* 1980 October 1). They have caused considerable excitement by interpreting the phenomenon as a double image of a single quasar caused by the gravitational lens action of a galaxy lying in the foreground and on a line between them. Dr. Geoffrey R. Burbidge, Kitt Peak National Observatory, pointed out that the double quasar lay within a few diameters of the large disturbed galaxy NGC 3079. Arp has now searched the area with ultraviolet blue photographs and reports three (four if Markarian 180 is counted) further bright (~18 mag) quasars within this same area. Spectra of these individual quasars are still being acquired with the Cassegrain spectrograph at the Hale Telescope.

Arp has continued to collaborate with Professor Cyril Hazard of Cambridge University. They report a new pair of quasars, close together and having redshifts of $z = 1.854$ and 2.098. As is usual in such pairs and groups, the redshifts are closer together than would be expected by chance, but are farther apart than velocity differences in a cluster of galaxies at the conventional redshift distance would indicate. Another fairly well aligned, new example of three quasars (this time only approximately aligned) has been found. The data are:

West	$z = 0.912$	$V = 18.5$ mag
Center	$z = 1.752$	$V = 19.8$ mag
East	$z = 2.162$	$V = 18.7$ mag

In one of the previous triplets, redshifts of $z = 1.72$ and $z = 2.15$ were encountered. Unless these numerical coincidences are accidental, there is no apparent explanation for them.

OBSERVATIONAL COSMOLOGY

The Distance to the Virgo Cluster and the Use of H II Regions as Standard Candles

Great controversy currently surrounds the attempts to calibrate the extragalactic distance scale, with factor of two discrepancies common among recent results by different investigators. One of the most fundamental of these calibrations is the Sandage-Tammann distance scale (*Year Book 70,* p. 418), a Population I ladder based on Cepheids, H II regions, and luminosity

classes of late spiral galaxies. Unfortunately, this ladder rests heavily on the giant spiral M101, an abnormal spiral with very abnormal H II regions but the only giant near enough for a direct distance determination. Kennicutt has now taken a step toward eliminating this problem by using H II region luminosities to tie the Virgo cluster directly to the local Cepheid-based distance scale. Calibrated Hα photographs and photometry have been obtained for 20 Sc galaxies in the Virgo cluster, using a Carnegie image tube camera on the Kitt Peak 2.1-meter telescope and the direct SIT camera on the Palomar 1.5-meter telescope. Using software developed at the California Institute of Technology by graduate student William Sebok, absolute fluxes in Hα have been measured for the three brightest H II regions in each galaxy. When these data are compared with similarly determined H II region fluxes in local and M81 group galaxies, a preliminary distance of approximately 20 Mpc is obtained for the Virgo cluster, independent of M101. This corresponds to a local Hubble ratio of 50–55 km s^{-1} Mpc^{-1} in the direction of Virgo, depending on the mean velocity adopted.

Despite the improved distance scale resulting from this work, however, the results also cast serious questions on the general desirability of H II regions as distance indicators. Kennicutt has found that the largest-ranked H II regions possess an enormous dispersion in luminosity—as much as a factor of ten for galaxies of a given type and luminosity. (A comparable dispersion is also present in the H II region diameters, but because of their small angular sizes relative to the seeing disk, quantitative diameters were not measured.) Kennicutt argues that this dispersion is real, arising from two effects: a large stochastic variation in sizes of the largest star-forming regions and a very steep dependence of this mean size on the Hubble type of the parent galaxy. If this interpretation of the observations is correct, it implies that distances for individual galaxies derived from H II regions can only be expected to be accurate to $\pm 50\%$ at best; hence other methods may be more appropriate.

THEORETICAL STUDIES

Dynamical Models of Binary Galaxies

A FORTRAN code has been developed by California Institute of Technology graduate student Kirk Borne for the study of the evolution of interacting binary galaxies. The program essentially performs 1000 concurrent three-body integrations. That is, the primary "galaxy" comprises 1000 particles, each of which interacts gravitationally with the unperturbed mean fields of the primary and secondary "galaxies," where the secondary is a massive point. In this way, the motion of the secondary is determined entirely by its interaction with the 1000 particles. An additional feature of the program is a step that allows the particles to redistribute themselves in the gravitational field of the secondary prior to the investigation of the binary system evolution. It is found that this redistribution is important in those systems of mass ratio = 1. In those cases, the time scale for the "galaxies" to merge is increased by roughly 50% over previous determinations. Galaxies separated by a few times their half-mass radius will merge in about 10^9 years, given typical galaxy parameters. A few cases were run with 2000 particles; no

new behavior was noted. The program output consists of projected surface density maps, distribution functions (energy, velocity, angular momentum), radial distribution functions (torque, velocity dispersion, angular momentum), and many other model diagnostics. It should be noted that the results are similar to those obtained with large N-body codes but are available at a fraction of the expense.

Dynamics of Star Clusters Containing a Black Hole

Young has continued work on stellar dynamics in a star cluster containing a central massive black hole. The black hole was considered to grow adiabatically from gas accretion (i.e., on a slow time scale compared with the dynamical time scale of the star cluster but rapidly compared with the relaxation time scale). Each star in the cluster conserves its adiabatic invariants (the angular momentum and radial action), which leads to the invariance of the distribution function in energy-angular momentum space. If the initial cluster is an isothermal sphere, then a power law cusp $\rho(r) \propto r^{-3/2}$ forms near the black hole. Numerical models have been computed for clusters containing various-sized black holes, each cluster initially being an isothermal sphere.

Gravitational Lenses

Young has investigated the properties of gravitational lensing by an ensemble of point masses. This is designed to discover any differences between the image formed by a real galaxy (composed of stars) and by an idealized galaxy (hydrostatic fluid). Monte Carlo experiments showed that imaging by star fields tends to that for a fluid when there are many stars in the image beam. Young points out that this property is not self-evident, since a fluid focuses the light beam whereas point masses can only shear the beam. For Q0957+561, there are expected to be only 1–10 stars in the image beams. Large statistical fluctuations in the image brightnesses can occur on a time scale of 10–100 years as the light beam drifts through the star fields of the lensing galaxy. Additional perturbations can result if the galaxy cluster is bound by low-mass stars, and these will be on a still shorter time scale, but of low amplitude.

INSTRUMENTATION

The du Pont Telescope

Babcock continued to supervise the project for completion of the coudé optical system. Optical figuring of the tertiary (flat) mirror was completed by Loomis, and the mirror has been delivered to the Santa Barbara Street shop. A cart for handling the half-ton coudé mirror drive mechanism has been built and delivered. Once the electronic drive system is assembled and tested with the mirror, the whole system will be shipped to Las Campanas for installation and testing on the du Pont Telescope.

Infrared Spectrometer

The high-resolution infrared Fabry-Perot and grating spectrometer described in *Year Book 78* (p. 778) successfully underwent initial tests at the Mount Wilson Observatory in May 1980. The spectrometer was built by Geballe and Persson with assistance from several members of the Califor-

nia Institute of Technology Infrared Group.

Tests in the laboratory and on the 2.5-meter telescope show that the instrument can attain the designed resolving power (up to several times 10^4) and has both the low background and the thermal and mechanical stability to be an effective observing instrument. The solid nitrogen-cooled grating spectrometer is complete and achieves, with the present gratings, a resolving power of 500–2000 over the entire 2–5 μm range. Fabry-Perot interferometer mirrors, which increase the resolving power by a factor of 10–30, already exist for the 2-μm region and will be obtained for the other atmospheric windows out to 5 μm.

A computer to operate the spectrometer has been designed and built by Dr. F. Baas of Leiden University and will be delivered this summer. Initially, the computer will be used to scan the Fabry-Perot interferometer, collect and store the spectra, transfer data to magnetic tape, and provide some analytical facility. Eventually, the computer will be used to remotely control several stepping motors that will rotate the gratings and change blocking filters and apertures within the cold grating spectrometer. A further computer function is that of continuously monitoring and automatically aligning the Fabry-Perot interferometer mirrors.

It is intended that the Fabry-Perot and grating spectrometer, together with the computer, function as a complete and independent system usable over a wide range of wavelengths, resolving powers, and aperture sizes, and that it be adaptable to a variety of telescopes. A full observing schedule is planned for the instruments at Mount Wilson, Palomar, Las Campanas, and Mauna Kea Observatories during the coming year. Planned observations relate to problems of the interstellar medium, star formation, stellar evolution, and galactic nuclei—all areas where infrared spectroscopic observations are critical.

Multi-Fabry-Perot Spectrometer

During this past year, a multi-Fabry-Perot spectrometer of 100 mm aperture, designed, fabricated, and made operational by Trauger, was adapted for use as a coudé instrument at both the Palomar 5-meter and the Mount Wilson 2.5-meter telescopes. Fused silica optics throughout the instrument and broad-band Fabry-Perot mirror coatings allow spectral coverage from about 0.33–3 μm. A mechanical arrangement allowing the rapid insertion and interchange of from one to three Fabry-Perots in series in the optical path provides an instrument easily adapted to resolving powers from 20,000 to over 200,000. Software refinements in the data collection and servo-alignment systems will continue this year. Refinements to spectral calibration and interference-filter hardware will be carried out. We hope to complete this year the development of a deposition system for optical multilayer dielectric mirror coatings in support of the Fabry-Perot effort. This instrument development project has been supported through funding from the National Aeronautics and Space Administration.

Astronomical observations, commenced this year, have yielded new spectra of the Jovian magnetospheric S^+, S^{++}, Na, and K species. The use of the spectrometer as a high-spectral resolution imager has been demonstrated in obtaining new images of the faint Jovian [S II] emission nebula with Westphal's CCD camera.

60-Foot Tower p-Mode Oscillation Instrumentation

A Systems Engineering Laboratories (SEL) Model 32/77 32-bit minicomputer has been obtained for the new 60-foot solar tower system at Mount

Wilson. The peripheral equipment for this computer includes a 300-megabyte Ampex disc drive and a CSPI MAP 200 high-speed array processor. The exit slit mechanism for this system has been designed at the Jet Propulsion Laboratory. The design for the CID camera has been completed by Photometric Ltd. in Tucson, Arizona.

Image Processing

The National Aeronautics and Space Administration continues to sponsor Jean Lorre's efforts at the Jet Propulsion Laboratory to develop applications of digital computer image processing for astronomical purposes. A report was issued (JPL publication 79-109) describing the various topics addressed: (1) maximum entropy deconvolution for seeing improvement, (2) polarization in M82, (3) temporal changes in the knots of the M87 jet, and (4) excitation, electron density, and temperature maps of the planetary nebula NGC 6720 from emission-line images. A search for faint nebulosity is under way for Arp on objects 3C120, NGC 450, and NGC 1232.

GUEST INVESTIGATORS

Dr. Lawrence H. Aller of the University of California at Los Angeles and Dr. Stanley J. Czyzak of Ohio State University have used the Mount Wilson 2.5-meter telescope to obtain measurements of the auroral and nebular transitions in the planetary nebulae NGC 7027, 7662, 2440, 6572, and IC 2165, 4997. They conclude that the available values of Ω and A for $3P^3$[Ar IV] ions are incorrect, as the observed auroral/nebular ratio is always larger than the theoretical value.

Dr. Jay T. Bergstralh of the Jet Propulsion Laboratory used the Palomar 1.5-meter telescope to obtain absolute spectrophotometry at 10 Å resolution, from 3390–8080 Å, of Jupiter, Saturn, Titan, Uranus, and Neptune.

Drs. Howard E. Bond and R. Earle Luck of Louisiana State University used the coudé spectrographs of the Palomar 5-meter and Mount Wilson 2.5-meter telescopes, with the Shectman Varo-Reticon detector, to continue their program on chemical abundances in halo red giants, subgiant CH stars, Ba II stars, and supergiants. Perhaps the most significant new result was the discovery that supergiants reveal a pronounced metallicity gradient across the galactic disk. Iron-to-hydrogen ratios determined for 26 supergiants from Mount Wilson scans give a radial gradient of $d[\mathrm{Fe/H}]/dR = -0.24\ \mathrm{kpc}^{-1}$ for the region of the galactic disk between 7.7 and 10.2 kpc from the galactic center. Since this gradient is greater than that generally found from older objects (such as field main-sequence stars, red giants, and open clusters), it is suggested that the metallicity gradients in disk galaxies steepen significantly with age.

Using the 1.2-meter Schmidt telescope, Drs. David Burstein and Vera C. Rubin of the Department of Terrestrial Magnetism, Carnegie Institution of Washington, are continuing their program of obtaining plates suitable for surface photometry of the galaxies for which Rubin and collaborators have obtained extended rotation curves.

Dr. Richard M. Crutcher of the University of Illinois used the Mount Wilson 2.5-meter telescope to carry out studies of interstellar lines. An extensive search for the λ5693 line of NH_2, which is expected to be present in interstellar clouds as a result of the breakup of ammonia, was unsuccessful. Observations were made of the D-lines

of Na I and of the λ7699 line of K I toward B stars behind dark clouds, which have been studied by radio astronomers observing molecular lines. Analysis of these data made it possible to infer the fractional ionization in the clouds and hence to distinguish between two competing cloud models, both of which could account for the radio molecular data. This work has been published in the July 15, 1980, issue of *Astrophysical Journal.*

Da Costa and Dr. Peter L. Cottrell of Mount Stromlo and Siding Spring Observatories used the Varo-Reticon detector at the coudé focus of the 2.5-meter Hooker Telescope on Mount Wilson to observe giants in the open clusters NGC 752 and M67. Spectra were obtained at the blue CN-band, at the G-band, and at the λ6300 [O I] line. These observations will be used to derive the atmospheric carbon, nitrogen, and oxygen abundances of these stars.

Dr. Michael M. Dworetsky of University College London has begun a program of coudé spectroscopy of bright Hg-Mn stars that have also been observed with the International Ultraviolet Explorer satellite. The spectrograms, obtained with the Mount Wilson 2.5-meter telescope, will be used to complement the ultraviolet data.

Dr. Gilles Fontaine of the University of Montreal continued his search for variable white dwarfs, using the Palomar 1.5-meter telescope. The aims of this program are to improve on the statistics of variable white dwarfs of the ZZ Ceti class and to study the light curves of these objects with the help of Fourier techniques. The observations obtained at Palomar so far have led to the discovery of five new variable stars (GR294, GR318, GR277, GR368, and GR404), thereby increasing by some 42% the known number of white dwarfs belonging to this class. These results were independently confirmed by Fontaine's collaborator, Dr. John T. McGraw of the University of Arizona. They were also able to thoroughly study the behavior of GR394 (August 1, 1980, *Astrophysical Journal*). The observations yield estimates of the growth rate of the pulsation amplitude as well as time scales for nonlinear coupling between various modes. These quantities are extremely important in the theory of nonlinear, nonradial stellar pulsations. Finally, the observations have established that the vast majority (if not all) DA white dwarfs go through an instability phase during their evolutionary history. This has important consequences on the nature of the mechanism that makes these stars nonradial pulsators.

Priscilla C. Frisch of the Laboratory for Astrophysics and Space Research, University of Chicago, has started an observing program with the Mount Wilson 2.5-meter telescope to search for previously undetected interstellar molecules, in particular diatomic molecules which may form in the warm regions behind shock fronts moving into diffuse interstellar clouds. No strong features from new molecules were found in the first set of program stars.

Dr. Richard Green of the University of Arizona and graduate student Howard Yee continued to study the association of quasars with groups and clusters of galaxies with the Palomar 1.5-meter telescope. Over 75 quasar-control field pairs have been imaged with the SIT Vidicon camera. The photometric reductions have shown that a conservative limiting magnitude is $R = 21$. Within the 2″ field, an average 90% surface-density enhancement of faint objects is observed around the radio-selected quasars, while only 10% enhancement is detected around the optically selected objects. Both groups show a strong increase in excess faint objects with quasar redshift increase, corresponding to the shrinkage of the core-radius within the fixed angular size field. The other striking effect is that the statistical excess vanishes at $z = 0.5$ for the optically selected objects,

while the radio-selected quasars show a maximum excess of faint objects at that redshift, which doesn't vanish until $z = 0.75$. This effect is consistent with the hypothesis that radio quasars are associated with galaxies of higher average luminosity (ellipticals) than those around radio-quiet quasars, which are perhaps in a more spiral rich population.

Dr. Roger F. Griffin of the Cambridge Observatories, England, continued in collaboration with Gunn to measure radial velocities of individual members of star clusters photoelectrically at the 5-meter Hale Telescope. An observing run in November 1979 was devoted principally to the Hyades; one in June 1980 was concerned with M13, M92, M11, and M15.

Dr. Leif Hansen of the University Observatory, Copenhagen, used the Cassegrain scanner at the Mount Wilson 1.5-meter telescope to obtain spectra of bright standard stars of types γ and K at a bandwidth of 80 Å. The data will be used to develop an intermediate-band filter system for γ- and K-type stars.

Dr. Eduardo J. Hardy of Université Laval, Québec, used the 2.5-meter du Pont Telescope to search for very red objects on infrared and blue exposures of the Fornax system and its globular clusters. In collaboration with Dr. Serge Demers of the University of Montreal and Dr. William E. Kunkel of the National Observatory, Rio de Janeiro, he found strong abundance differences among the clusters. Fitting an M15 giant branch to Hodge clusters 1 and 5 yielded a distance modulus of 20.8. This is the first estimate of the distance to Fornax since Hubble's 1939 determination.

Observations of Saturn were successfully obtained by Dr. Alan W. Harris of the Jet Propulsion Laboratory on March 12–17, 1980, as the Earth passed through the plane of the rings. A coronagraph of a unique design, employing reflecting optics, was used at the 2.5-meter Hooker Telescope at Mount Wilson to remove diffraction from the primary and secondary mirror edges and central support structures, thus minimizing scattered light near Saturn. Five elongations of a satellite interior to Mimas, seen in 1966 by Dollfus, were observed. In addition, two other elongations of satellites not associated with the former body were observed. It is expected that orbits can be derived for at least two more satellites by combining these observations with others from Hawaii, Arizona, Texas, and France.

Dr. Donald S. Hayes of Kitt Peak National Observatory and Dr. A. G. Davis Philip of Dudley Observatory and Union College used the multichannel spectrometer at the 5-meter Hale Telescope to scan horizontal-branch A stars in the field and in the globular clusters M5, M13, and M92. They found a spread of Balmer discontinuities at a given effective temperature in a given cluster, extending the analogous effect found by Oke for horizontal-branch B stars in M92.

Using the Mount Wilson 1.5-meter telescope, Caltech graduate student Keith Horne and Dr. Larry Petro of the Massachusetts Institute of Technology obtained seven nights of high-speed (0.1 sec) broad-band photometry of Scorpius X-1. These data were obtained simultaneously with high-speed (2 sec) spectroscopy at the McGraw-Hill Observatory, high-speed (3 sec) polarimetry at the Steward Observatory, and slow (10 sec) photometry at the Lowell Observatory. The analysis of these data for flare correlations and possible time lags is just beginning and will proceed through the summer of 1980. The originally intended search for x-ray correlation was prevented by the malfunction of the British x-ray satellite, UK-6.

Dr. Roberta M. Humphreys of the University of Minnesota obtained spectra for classification and radial velocities of 65 early-type supergiants

and OB stars in the Small Magellanic Cloud using the image-tube spectrograph on the 2.5-meter du Pont Telescope. These data will be combined with similar information for the late-type supergiants for a study of the evolution of the most massive stars in the Cloud. Preliminary results of the spectral classification reveal a very large number of stars with a strong Balmer series, late B or early A in spectral type, among the population of hot stars observed.

Dr. Robert P. Kirshner of the University of Michigan reports on the dynamics of the Shakbazyan 1 group of galaxies, which he observed with the 5-meter telescope at Palomar in 1977. An earlier investigation had found radial velocities in the group consistent with a zero mass-to-light ratio for the galaxies. This investigation, with Eliot Malamuth, a Michigan graduate student, shows that the new radial velocities obtained with the SIT Vidicon at the 5-meter telescope imply a mass-to-light ratio, in the V band, of 111 ± 15. They were able to measure internal velocity dispersions for three galaxies in the group, and found values that are consistent with those of ordinary galaxies of comparable luminosity. This new spectroscopic evidence, coupled with recent photometric data, points to the conclusion that the group is composed of ordinary galaxies. Although the galaxies are ordinary, the group has the unusual property that it is as dense as the center of the Coma Cluster. Because of this, dynamical interactions that are typical of rich clusters may have been important in the history of Shakbazyan 1.

Using the SIT Vidicon at the 5-meter telescope, Dr. Robert P. Kraft of the Lick Observatory, University of California, Santa Cruz, and Oke obtained 8-Å-resolution blue spectra of stars at the foot of the giant branch in M92 ($M_v \sim +3$, $T_{\rm eff} \sim 5400$ K). Comparison of the strengths of the G-band with predictions from Carbon's (Kitt Peak National Observatory) models suggests carbon abundances [C/Fe] ~ 0 for these stars. A mean value of [C/Fe] ~ −0.5 for SGB stars near $M_v \sim +1.5$ had been determined earlier by Carbon, Kraft, Langer, and their associates at Lick. Comparison of the Lick and Palomar results shows that, contrary to the results of classical evolutionary theory, large-scale mixing of the envelope through the CN-burning shell takes place in M92 soon after the stars leave the main sequence.

Drs. Richard Kron and Andrew Jankevics of the University of Chicago have obtained IIIa-F and IV-N plates to test the hypothesis of red galactic halos around galaxies. The measurement and reduction of the material is awaiting the installation of a microdensitometer and an image-processing system at the University of Wisconsin at Madison.

Drs. John D. Landstreet and Douglas N. Brown of the University of Western Ontario used the 5-meter Hale Telescope to carry out a search for weak longitudinal magnetic fields in cool stars. For this program, the coudé radial-velocity spectrometer was converted to a polarimeter by the addition of a Pockels cell modulator and was used as a multiline Zeeman analyzer. Stars observed included dwarfs with K-line emission, giants with He λ10839, RS Canum Venaticorum, and BY Draconis binary systems, and other cool stellar types that are suspected of harboring magnetic fields. In a few cases, standard errors of less than 10 gauss were achieved, but no definite fields were detected.

Varo-Reticon observations by Mr. Howard Lanning of Mount Wilson Observatory of the unresolved white dwarf-M2e dwarf Case 1 indicate that the system is a short-period spectroscopic binary with a period of about $16^{\rm h}01^{\rm m}.7$. Thirty-six spectra of the Hα emission line in the 14th magnitude star were obtained at the coudé focus of the Mount Wilson 2.5-meter tele-

scope, yielding a sinusoidal velocity curve with eccentricity of zero and a K velocity of ~ 110 km s^{-1}. Although the binary is coincident with the Ursa Major group, it is not a member. The possibility of eclipses in Case 1 seems likely.

Lanning and Dr. Paul Szkody of the University of Washington have examined object number 10 in the list of *UV*-bright stars by Lanning. Profile variations of the broad Hα emission feature (~ 16 Å wide at the base of the line), observed with the Varo-Reticon, suggest that the object may be an accretion disk binary with a period less than eight hours. Centroid velocities of the double-peaked emission line exhibit systematic shifts as large as 500–600 km s^{-1}. While apparently similar to old novae, no *UV* emission lines have been observed with the International Ultraviolet Explorer satellite.

Drs. M. S. Longair, M. A. C. Perryman, and J. M. Riley of the Mullard Radio Astronomy Observatory, Cambridge, England, in conjunction with Gunn, Hoessel, and Westphal, completed their survey of the fields of 3CR radio sources, using the CCD camera at the prime focus of the Hale 5-meter telescope. Identifications have now been found for almost all radio sources in a statistical sample of 166 3CR radio sources. Most of the new identifications are with galaxies. The CCD camera has been used in spectrographic mode and a redshift of 1 has been measured for the faint radio galaxy associated with 3C184. To complement these surveys of sources at high flux densities, the same team, with Drs. J. A. Peacock and J. Allington-Smith of the MRAO, have extended observations to samples of lower flux density. Most of the previously unidentified sources have now been identified, roughly half of the new identifications being with quasars and half with galaxies.

Ms. Phyllis M. Lugger and Dr. William Liller of Harvard College Observatory have obtained plate material with the 1.2-meter Schmidt telescope at Palomar to investigate the properties of galaxies in clusters as a function of Bautz-Morgan type. Lugger is reducing the data, using the Kitt Peak PDS and Interactive Picture Processing System. She is constructing cluster luminosity functions and analyzing galaxy surface-brightness profiles.

The *JHK* photometer attached to the du Pont 2.5-meter reflector was used by Dr. Barry F. Madore of David Dunlap Observatory, Ontario, Canada, to begin a near-infrared calibration of the Cepheid period-luminosity relation. All southern Cepheids in clusters, a number of important field Cepheids, and about a dozen Cepheids in the Small Magellanic Cloud were observed for the first time. The advantages of the new calibration are very exciting, since the effects of metallicity, reddening, and temperature variations are drastically reduced.

Dr. Delbert H. McNamara of Brigham Young University used the 5-meter telescope and both 2.5-meter telescopes to secure spectra of Cepheid variables in the direction of the galactic center, anticenter, and in the Large and Small Magellanic Clouds. The primary aim of the study is to investigate the possible differences in abundances in heavy elements in the various stellar environments. Accurate radial velocities of Magellanic Cloud Cepheids will be obtained. McNamara is also completing an investigation of the dwarf Cepheid XX Cygni, spectra of which were obtained with the 5-meter telescope in 1978. This star apparently has a much lower surface gravity than dwarf Cepheids of similar period and is the only long-period dwarf Cepheid known with a weak metallic-line spectrum.

Drs. Joseph J. Michalsky and Gerald M. Stokes, Batelle Observatory, Washington, used the Palomar 1.5-meter telescope during July 4–7 and October 10–13, 1979, to polarimetrically observe four sources at optical wavelengths. HDE 226868, the companion

of the black hole candidate Cygnus X-1, was observed to show changes in the wavelength dependence of the circular polarization from earlier observations. A significant change at blue wavelengths was found. V Sagittae, a nova-like variable, was observed over its 0.51-day period in each session. A cursory look at data that have not been fully reduced indicates real changes in the orbital phase curve from previous observations. An observation of SS433 confirmed and improved previous polarization observations of this enigmatic source. The data may suggest an intrinsic interpretation of the polarization. Finally, the AM Herculis variable 2A 0311−227 was found to have undergone large changes in its polarization phase curve compared to earlier observations by other observers.

Dr. Hugh R. Miller of Georgia State University obtained spectra of an additional 93 galaxies from the Arakelian list at the Palomar 1.5-meter telescope. Three new Seyfert galaxies have been found in this group; 31 of the galaxies have emission lines associated with their nuclei, and one has an emission-line region offset from the nucleus of the galaxy. In addition, two galaxies in the Arakelian list, which were selected on the basis of suspected optical variability, were found to have slightly broadened Balmer lines of hydrogen. These galaxies may have properties that are intermediate between those of narrow-line, emission-line galaxies and Seyfert galaxies.

Dr. Jeremy R. Mould of the Kitt Peak National Observatory, and Dr. Marc Aaronson of the Steward Observatory, University of Arizona, have continued their study of the Hubble flow with new determinations of cluster distance moduli from the Tully-Fisher relation. Drs. J. A. Dawe (United Kingdom Satellite Tracking Unit), Robert J. Dickens (Royal Greenwich Observatory), and J. B. Murray (Commonwealth Scientific and Industrial Research Organization) report preliminary results for the Fornax and Grus clusters observed in the infrared at Las Campanas and in neutral hydrogen at Parkes, the Australian National Radio Astronomy Observatory. With distance moduli of 30.9 ± 0.2 and 31.1 ± 0.3, respectively, Fornax and Grus are located at distances very similar to that of the Virgo cluster, at an opposing supergalactic longitude. If the clusters were part of an unperturbed Hubble flow, the redshifts of these clusters (~ 500 km s^{-1} larger than that of Virgo) would imply a local infall velocity of between 200 and 300 km s^{-1}. This estimate should be increased by $\sim 30\%$ to account for the retardation of the clusters themselves. A Virgocentric-flow model is being fitted to an all-sky sample of some 300 galaxies within 3000 km s^{-1} to determine the local motion with some precision.

Infrared observations at the 5-meter du Pont Telescope have contributed to Mould's and Aaronson's study of the very red stars in the Fornax dwarf galaxy discovered recently by Demers and Kunkel. For $B - V$ greater than ~ 2.1, the giant branch of Fornax may consist entirely of carbon stars. The luminosities of these stars range from -4.5 to -5.5 in M_{bol}, which places them on the upper asymptotic giant branch, in analogy with carbon stars found in Magellanic Cloud globular clusters. Mould and Aaronson argue that such stars can be produced only by a population of intermediate age. A comparison of the fractional carbon-star light in Fornax and the Magellanic Cloud globulars suggests that roughly 20% of Fornax is of intermediate age (i.e., $2\text{–}8 \times 10^9$ years old). As the most massive dwarf spheroidal known, Fornax seems to have retained longest the gas necessary for continued star formation.

Dr. John Nousek and graduate student Ken Jensen of the California Institute of Technology X-Ray Astronomy Group used the Palomar 1.5-meter telescope to search for optical candidates of x-ray sources discovered by

the HEAO satellites. Positions of 20 sources were observed down to limiting magnitudes as faint as 22 mag. While a number of candidates have appeared, the absence of optical counterparts in some cases suggests objects which radiate ten thousand times higher in the x-ray bands than in the optical.

Dr. Robert W. O'Connell of the Leander McCormick Observatory, University of Virginia, has obtained photographs of the nuclei of 21 nearby radio galaxies obtained in the G-band at the Cassegrain focus of the Mount Wilson 1.5-meter telescope. The purpose of the program is to test models for the origin of strong radio sources by examining the correlation between the optical structure of the parent galaxies and the symmetry axis of the radio source.

Drs. John V. Peach, Jon G. Godwin, and Mr. Adair Butchins of the University of Oxford have begun a program of photometry of diffuse optical intergalactic emission in rich clusters. They are reducing deep 1.2-meter Schmidt plates, accurately calibrated using a 45-spot tube sensitometer, of low-redshift clusters in which they have previously carried out detailed multicolor galaxy photometry.

Drs. Mark M. Phillips and Jack A. Baldwin of Cerro Tololo Inter-American Observatory used the photon-counting image intensifier/reticon scanner on the Las Campanas Observatory du Pont Telescope to observe QSO's and nearby active galaxies. High-dispersion profiles of the Hβ emission lines of several QSO's were obtained as part of a program of ultraviolet, optical, and infrared observations to determine the Lα/Hβ/Hα/Pα intensity ratios in a relatively large sample of QSO's. High-dispersion observations of two of the same QSO's in the region of the mysterious λ3500 continuum bump were also made. These data will be used to investigate the origin of the bump, which has often been suggested to be a Balmer continuum emission. Finally, spectra were taken of the nuclei of 11 nearby galaxies thought to be similar to type 2 Seyfert galaxies. Among the objects studied was the barred spiral NGC 1365, which appears to have a weak Seyfert nucleus embedded in a region undergoing a burst of star formation.

Mr. Bo Reipurth, a graduate student at Copenhagen University Observatory, obtained Hα exposures using the image intensifier of the 1-meter Swope Telescope at Las Campanas, in a program on morphological studies of and a search for Herbig-Haro objects. Assessment of the plates is in progress. It appears that a new riftlike subgroup of Herbig-Haro objects may exist. Also, two new spectacular candidates for Herbig-Haro objects were found in M8. Spectroscopic work is planned.

Dr. Vera C. Rubin of Carnegie Institution's Department of Terrestrial Magnetism used the 2.5-meter du Pont Telescope at Las Campanas to obtain high-dispersion spectra of Sa and Sb galaxies as part of her program to determine rotation curves for galaxies of a wide range of Hubble types and luminosities. In contrast to the more general use of the spectrograph, which employs the Shectograph Reticon system, Rubin imaged the Carnegie image tube directly with photographic plates to obtain two-dimensional (i.e., velocity and position) information. The spectra are centered on the Hα region at a dispersion of 50 Å mm^{-1}, and at a scale perpendicular to the dispersion of 51″ mm^{-1}. Measurements of emission lines of Hα, [N II], and [S II] on the plates indicate that accurate velocity and positional information can be obtained with ease. No problems with stability were encountered, even on exposures as long as three hours. A portion of a spectrum is reproduced in Fig. 8.

Dr. Eugene M. Shoemaker and Mrs. Eleanor F. Helin of the California Institute of Technology continued the photographic search program for new planet-crossing asteroids, using the

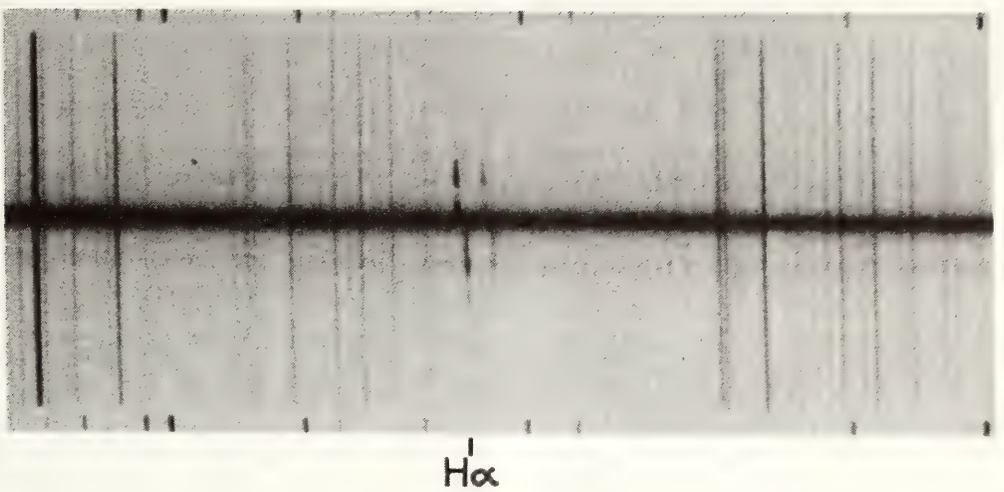


Fig. 8. The Hα region of the spectrum of NGC 7083, taken with the 2.5-meter du Pont Telescope image tube spectrograph. Original dispersion 50 Å mm^{-1} on baked IIIa-J plate; exposure 174 minutes. The lines completely crossing the spectrum are emission lines from the night sky, principally OH. The knots in the galaxy lines arise from structure in the galaxy.

0.45-meter Schmidt telescope at Palomar Mountain. They photographed and examined 328 independent fields. Real-time review of film led to the discovery of asteroid 1979 HA, a high-inclination Phocaea; 1979 VA, an unusual Apollo asteroid with a record high aphelion, which takes it closer to the orbit of Jupiter than any other Apollo; and 1979 XA, another Apollo, rediscovered after being lost for 32 years. From two nights using the 1.2-meter Schmidt, an Apollo (1979 QA), an Amor (1979 QB), and 1979 QC were discovered. Also, 1980 CB was discovered. From a set of plates taken in 1978, 232 asteroids were measured, and orbits were computed and officially designated 1978 VW_1–1978 VP_{11}. Good orbits for 155 new asteroids have been determined. A description and the results of our Palomar Planet-Crossing Asteroid Search Program has been published in *Icarus, 40,* December 1979.

Dr. Jack W. Sulentic of Michigan State University used the SIT spectrograph at the 5-meter Hale Telescope to obtain redshifts of 22 faint galaxies ($m_{pg} \geq 15.0$) near the center of the Virgo cluster. At this magnitude level, 60% of the galaxies had redshifts, indicating cluster membership. Most of the remaining galaxies had velocities near +7500 km s^{-1}, suggesting a thinly populated region of about 80 Mpc extent ($H_0 = 75$ km s^{-1} Mpc^{-1}) between this significant grouping and the Virgo cluster. Re-analysis of all redshifts now available for Virgo cluster members shows that the mean redshift of the lenticular sample (1162 km s^{-1}, $n = 35$) is much closer to that for the spirals (1152 km s^{-1}, $n = 70$) than it is to the ellipticals (890 km s^{-1}, $n = 21$). An unexpected and significant difference in mean redshifts was found between the Sa-Sb cluster members (956 km s^{-1}, $n = 38$) and the Sbc-Scd component (1437 km s^{-1}, $n = 24$). Classifications for galaxies included in the re-analysis were taken from the RC2.

Dr. Paula Szkody of the University of Washington collaborated with graduate student Richard Wade in obtaining coudé spectra with the Shectograph instrument at the Mount Wilson 2.5-meter telescope of the H and He lines in cataclysmic variables in order to ascertain the orbital periods and changes in line structure. Further collaboration with graduate student Graham Berriman on the Mount Wilson 1.5-meter telescope resulted in the study of the 10-micron flux of the brightest cata-

clysmics in order to constrain models of the disks in these systems.

Dr. Richard J. Terrile of the Jet Propulsion Laboratory used the 5-meter Hale Telescope for two programs. First, Jupiter and Saturn were observed with infrared imaging systems in order to continue monitoring the cloud distribution on Jupiter, which was done successfully in conjunction with Voyager, and to search for infrared features in Saturn's atmosphere that could be used as possible targets. The second program consisted of using a 500 × 500 CCD with a coronagraph to image Jupiter's newly discovered ring and close satellites. Images and photometric observations of Saturn's faint E-ring were also made and are being used to determine risk factors for the Voyager ring plane crossings. Cloud cover did not permit a planned search for comet Halley, but this search will be continued at the next opportunity.

Drs. Ian Thompson and Landstreet of the University of Western Ontario and Dr. José Maza of the Universidad de Chile used the 2.5- and 1-meter telescopes at Las Campanas to search for and to study linear polarization in the light from the nuclei of southern Seyfert galaxies. Several Seyfert galaxies were found to show substantial polarization. Searches for magnetic fields in Ap stars located in young clusters and in southern Be stars were also begun.

Dr. Edwin L. Turner of Princeton University, in collaboration with Gunn and Sargent, has completed a redshift survey of galaxies at ~20 mag. Redshifts were determined for 58 objects. Analysis of these data reveals the existence of a population of luminous blue galaxies at redshifts ≥ 0.3 that do not exist at low redshifts.

Turner and Dr. Margaret J. Geller of Princeton University have obtained 1.2-meter Schmidt plates in three bands of fields of unusually high and low cosmic x-ray background brightness (as measured by the HEAO-A2 experiment). These plates are being searched for a population of objects correlated with the x-ray brightness.

Dr. Peter D. Usher from the Pennsylvania State University continued observations with the Palomar 1.2-meter Schmidt telescope. The purpose of this research is to select faint ultraviolet-excess objects in high-latitude fields and to catalog their *B* magnitudes, colors, positions, and morphological properties. Time series are also being established with the view of characterizing the variability of the objects. A study at 5 GHz with the Very Large Array of sources in the 8^h and 15^h survey fields of Sandage and Luyten has been completed.

Dr. Ken-ichi Wakamatsu of Gifu University, Japan, and graduate student Matthew Malkan have undertaken a search for new globular clusters near the galactic center on IV-N plates taken with the 1.2-meter Schmidt telescope at Palomar. Inspection of two thirds of the plates has yielded no new clusters. Some one hundred slightly diffuse objects found at least 8° from the galactic center are probably nuclei of distant galaxies.

Wakamatsu obtained spectra of the nuclear regions of NGC 4314, 5963, and 6951 using the SIT spectrograph of the Palomar 1.5-meter telescope. These galaxies have gigantic H II regions in their nuclear regions and are called hot-spot nucleus galaxies. Metal abundances of the ionized gas will be studied to clarify the nature of bursts of star formation and the origin of the large amount of gas in their nuclear regions.

During November 17–21, 1979, Dr. Gary A. Wegner from The Pennsylvania State University attempted to measure a new, more accurate gravitational redshift of the white dwarf o ^{2}Eridani B, using the coudé spectrograph and Shectograph of the Mount Wilson 2.5-meter telescope. Observations of the three components yield a differential redshift of $+23.9 \pm 1.3$ (s.d.) for the white dwarf. This work

will be published in the November 1980 issue of the *Astronomical Journal.*

Dr. Richard M. West of the European Southern Observatory, Munich, used the Shectman Reticon detector on the spectrograph attached to the Cassegrain focus of the 2.5-meter du Pont Telescope at Las Campanas to obtain spectra of ~100 peculiar and/or interacting galaxies found during the ESO/Uppsala survey of the ESO(B) *Atlas of the Southern Sky.* It was determined that 80% of these galaxies had emission lines. Eleven Shapley-Ames galaxies were observed and their radial velocities measured. Galaxies were observed in eight very distant clusters of galaxies found in the ESO(R) *Atlas;* one of these was at $z = 0.32$ mag. In collaboration with Dr. R. Barbier, ESO, about 40 galaxies with possible emission-line spectra, as seen on ESO Schmidt objective-prism plates, were verified; 90% have strong emission lines. The Third List of Spectroscopic Observation of ESO/Uppsala Galaxies (~300 objects, most of which were observed at Las Campanas) has been submitted for publication in the *Astronomy & Astrophysics Supplement Series.*

Dr. A. E. Whitford of Lick Observatory, University of California at Santa Cruz, is using the Varo-Reticon on the 2.5-meter du Pont Telescope at Las Campanas to obtain spectra of K giants in the Baade window. The objective is to evaluate the metallicity distribution function among members of the stellar population in the nuclear bulge of the Galaxy. Radial velocities will be used to study the kinematics of these stars.

As part of an ongoing study of nucleosynthesis in red giants, Dr. Alma Zook of Hamilton College, New York, observed seven S-type stars, using the Varo-Reticon detector at the coudé focus of the 2.5-meter telescope at Mount Wilson. The spectral features of interest are two band heads of ZrO, one of which is a temperature indicator, while the other permits measurement of the relative abundances of the isotopes of zirconium. Preliminary results suggest that the s-process is the operating nucleosynthetic mechanism in the pure S stars, but has not been taking place long enough to have reached equilibrium.

BIBLIOGRAPHY

Limited reprint supplies are available only for the references that are preceded by an asterisk or a dagger. Requests for reprints preceded by an asterisk should be addressed to Helen S. Czaplicki, Publications Department, Mount Wilson and Las Campanas Observatories, 813 Santa Barbara Street, Pasadena, California 91101, U.S.A. Requests for reprints preceded by a dagger should be addressed to the first author at his present address.

Aaronson, M., J. Mould, and J. Huchra, A distance scale from the infrared magnitude/H I velocity-width relation, I, Calibration, *Astrophys. J., 237,* 655–665, 1980.

Aaronson, M., *see also* Mould, Jeremy; Persson, S. Eric.

Angerhofer, P. E., A. S. Wilson, and Jeremy Mould, The central radio source in the peculiar supernova remnant CTB 80, *Astrophys. J., 236,* 143–152, 1980.

Arnold, S. J., A. Boksenberg, and W. L. W. Sargent, Measurement of the diameter of Pluto by speckle interferometry, *Astrophys. J. (Lett.), 234,* L159–L163, 1979.

*Arp, Halton, Quasars near companion galaxies and the problem of the absolute magnitudes of quasars, *Ann. N. Y. Acad. Sci., 336,* 94–112, 1980.

*Arp, Halton, Ultraviolet excess objects in the region of a companion galaxy to NGC 2639, *Astrophys. J., 236*, 63–69, 1980.

*Arp, Halton, H. R. de Ruiter, and A. G. Willis, A Westerbork 1415 MHz survey of radio sources, V, Spectrophotometric observations of a sample of the stellar identifications, *Astron. J., 77*, 86–92, 1979.

Arp, Halton, *see also* Sulentic, Jack W.

Balick, Bruce, *see* Kennicutt, Robert.

*Beck, S. C., J. H. Lacy, and T. E. Geballe, Ne II emission and galactic dynamics in NGC 253, *Astrophys. J., 231*, 28–31, 1979.

Beck, S. C., H. J. Lacy, and T. R. Geballe, Detection of the 12.28 μm rotational line of molecular hydrogen in the Orion molecular cloud, *Astrophys. J. (Lett.), 234*, L213–L216, 1979.

Becklin, E. E., I. Gatley, K. Matthews, G. Neugebauer, K. Sellgren, M. W. Werner, and C. G. Wynn-Williams, Infrared emission and star formation in the central regions of the galaxy IC 342, *Astrophys. J., 236*, 441–447, 1980.

Becklin, E. E., *see also* Neugebauer, Gerry; Soifer, B. T.; Werner, M. W.; Wynn-Williams, C. G.

*Bertola, F., M. Capaccioli, A. V. Holm, and J. B. Oke, IUE observations of M87, *Astrophys. J. (Lett.), 237*, L65–L69, 1980.

Boksenberg, A., *see* Arnold, J. S.; Briggs, S. A.; Sargent, Wallace L. W.

Boyden, John E., *see* Howard, Robert.

Briggs, S. A., A. Boksenberg, R. F. Carswell, and W. L. W. Sargent, Spectrophotometry of Markarian 3, *Mon. Notic. Roy. Astron. Soc., 191*, 665–673, 1980.

Capaccioli, M., *see* Bertola, F.

Capps, R., *see* Soifer, B. T.

Carswell, R. F., *see* Briggs, S. A.

*Cohen, Judith G., Chemical properties of individual globular clusters, in *Star Clusters, Int. Astron. Union Symp. No. 85*, pp. 385–400, J. E. Hessier, ed., D. Reidel Publishing Company, Dordrecht, Holland, 1980.

*Cohen, Judith G., and A. C. Phillips, FG Sagittae—1975 to 1978, *Astrophys. J., 237*, 99–104, 1980.

Cohen, Judith G., *see also* Horne, Keith; Persson, S. Eric.

*Cottrell, P. L., and J. L. Greenstein, Ultraviolet spectrum synthesis of the helium white dwarf Ross 640, *Astrophys. J., 238*, 941–945, 1980.

Cottrell, P. L., *see also* Da Costa, Gary S.

*Da Costa, Gary S., and P. L. Cottrell, Carbon and nitrogen abundances on the first giant branch of NGC 6752, *Astrophys. J. (Lett.), 236*, L83–L86, 1980.

Daltabuit, E., *see* Neugebauer, Gerry.

de Ruiter, H. R., *see* Arp, Halton.

*Dressler, Alan, The dynamics and structure of the cD galaxy in Abell 2029, *Astrophys. J., 231*, 659–670, 1979.

*Dressler, Alan, Galaxy morphology in rich clusters: implications for the formation and evolution of galaxies, *Astrophys. J., 236*, 351–365, 1980.

*Dressler, Alan, A catalog of morphological types in 55 rich clusters of galaxies, *Astrophys. J., Suppl. Ser., 42*, 565–609, 1980.

Ferland, G., *see* Hazard, C.

Fritzová-Švestková, L., *see* Howard, Robert.

Frogel, Jay A., *see* Persson, S. Eric.

Gatley, I., *see* Becklin, E. E.; Soifer, B. T.; Werner, M. W.

*Geballe, Thomas R., The central parsec of the galaxy, *Sci. Amer., 241*, 60–70, 1979.

Geballe, Thomas R., *see also* Beck, S. C.

Gomer, R., *see* Horne, Keith.

*Green, Richard F., The luminosity function of hot white dwarfs, *Astrophys. J., 238*, 685–698, 1980.

Green, Richard F., *see also* Shipman, Harry L.

*Greenstein, Jesse L., The degenerate stars with hydrogen atmospheres, I, *Astrophys. J., 233*, 239–252, 1979.

†Greenstein, Jesse L., Howard Percy Robertson, 1903–1961, *Biographical Memoirs, 51*, 343–364, 1980.

Greenstein, Jesse L., Hot subluminous stars, in *Highlights of Astronomy, Inter. Astron. Union General Assembly, 1979*, D.

Reidel Publishing Company, Dordrecht, Holland, 1980.

*Greenstein, Jesse L., The evidence for a universal helium and deuterium abundance, in *The Universe at Large Redshifts, Proc. Copenhagen Symp., 1979, Phys. Scripta, 21*, 759–768, 1980.

Greenstein, Jesse L., and Gerard Vauclair, Hydrogen lines in degenerate stars, II, *Astrophys. J., 231*, 491–494, 1979.

†Greenstein, Jesse L., M. A. Kazarian, T. Yu. Maghakian, and E. Ye. Khachikian, A spectrophotometry of NGC 2261 and R Mon, II, *Astrofizika, 15*, 615–628, 1979.

Greenstein, Jesse L., *see also*, Cottrell, P. L.; Schneider, Donald P.; Vauclair, Gerard; Wallerstein, George.

Gunn, James E., Feeding the monster: gas disks in elliptical galaxies, in *Active Galactic Nuclei*, pp. 213–215, C. Hazard and S. Mitton, eds., Cambridge University Press, England, 1979.

*Gunn, James E., The dynamics of galaxies and the "missing mass" problem, *Phil. Trans. Roy. Soc. London, A296*, 313–318, 1980.

*Gunn, James E., G. R. Knapp, and S. D. Tremaine, The global properties of the Galaxy, II, The Galactic rotation parameters from 21-cm H I observations, *Astron. J., 84*, 1181–1188, 1979.

Gunn, James E., J. Kristian, J. B. Oke, J. A. Westphal, and P. J. Young, The double quasar Q0957+561, *Int. Astron. Union Circ., 3431*, December 14, 1979.

Hazard, C., R. Terlevich, D. C. Morton, W. L. W. Sargent, and G. Ferland, Evidence for highly processed material ejected from Abell 30, *Nature, 285*, 463–464, 1980.

Heckman, Timothy, *see* Kennicutt, Robert.

Hoessel, John, *see also* Melnick, Jorge.

Holm, A. V., *see* Bertola, F.

*Horne, Keith, and Richard Gomer, Phase variability in the rapid optical oscillations of SS Cygni, *Astrophys. J., 237*, 845–849, 1980.

Horne, Keith, and Richard Gomer, SS433, *Int. Astron. Union Circ., 3379*, July 20, 1979.

Horne, Keith, J. G. Cohen, J. B. Oke, and S. W. Mochnacki, Stepanyan's star, *Int. Astron. Union Circ., 2462*, March 21, 1980.

Howard, Robert, Large-scale velocity fields on the Sun, in *Proceedings of the Indo-US Workshop on Solar-Terrestrial Physics for Solar Maximum Year 1979–81*, p. 47, A. Bhatnagar, R. V. Bhonsle, and Murray Dryer, eds., Vedhshala Udaipur Solar Observatory, Udaipur, India, 1979.

*Howard, Robert, John E. Boyden, and Barry J. LaBonte, Solar rotation measurements at Mount Wilson, I, Analysis and instrumental effects, *Solar Phys., 66*, 167–185, 1980.

*Howard, Robert, L. Fritzová-Švestková, and Z. Švestka, The birthplaces of active regions and x-ray bright points, *Solar Phys., 63*, 105–112, 1979.

Howard, Robert, *see also* Švestka, Zdeněk.

Huchra, J., *see* Aaronson, M.; Mould, Jeremy.

Humphreys, Roberta M., *see* Sandage, Allan.

Hurford, G. J., *see* Marsh, K. A.

Kazarian, M. A., *see* Greenstein, Jesse L.

*Kennicutt, Robert, Bruce Balick, and Timothy Heckman, A remarkable H II region complex in NGC 2366, *Publ. Astron. Soc. Pacific, 92*, 134–144, 1980.

Khachikian, E. Ye., *see* Greenstein, Jesse L.

Knapp, G. R., *see* Gunn, James E.

Kowal, Charles T., New galaxy of the Local Group, *Int. Astron. Union Circ., 3385*, July 27, 1979.

Kowal, Charles T., Comet Kowal (1979h), *Int. Astron. Union Circ., 3395*, August 27, 1979.

Kowal, Charles T., Two probable comets Kowal, *Int. Astron. Union Circ., 3405*, September 14, 1979.

Kristian, Jerome, *see* Gunn, James E.; Young, Peter J.

LaBonte, Barry J., *see* Howard, Robert.

Lacy, J. H., *see* Beck, S. C.

Lorre, Jean, *see* Sulentic, Jack W.

Maghakian, T. Yu., *see* Greenstein, Jesse L.

*Marsh, K. A., G. J. Hurford, and H. Zirin, VLA observations of spatial structure in the quiet Sun at 6 cm during the October 1977 eclipse, *Astrophys. J., 236*, 1017–1025, 1980.

Matthews, K., *see* Becklin, E. E.; Neugebauer, Gerry; Persson, S. Eric; Soifer, B. T.; Werner, Michael W.; Wynn-Williams, C. G.

Melnick, Jorge, and John Hoessel, Photoelectric surface photometry of the Andromeda nebula, *Astron. Ap., 84*, 317–319, 1980.

*Mochnacki, Stefan W., and Robert A. Schommer, A spectroscopic flare of YZ Canis Minoris, *Astrophys. J. (Lett.), 231*, L77–L81, 1979.

Mochnacki, Stefan W., *see also* Horne, Keith.

Moore, R. L., *see* Zirin, Harold.

Morton, D. C., *see* Hazard, C.; Neugebauer, Gerry.

*Mould, Jeremy, and Marc Aaronson, Carbon stars in the globular clusters of the Magellanic Clouds, *Astrophys. J., 232*, 421–427, 1979.

Mould, Jeremy, Marc Aaronson, and John Huchra, A distance scale from the infrared magnitude/H I velocity-width relation, II, The Virgo cluster, *Astrophys. J., 238*, 458–470, 1980.

Mould, J., *see also* Aaronson, M.; Angerhofer, P. E.

†Neugebauer, Gerry, D. Morton, J. B. Oke, E. E. Becklin, E. Daltabuit, K. Matthews, S. E. Persson, A. M. Smith, B. T. Soifer, S. Torres-Peimbert, and C. G. Wynn-Williams, Recombination spectrum and reddening in NGC 1068, *Astrophys. J., 238*, 502–509, 1980.

Neugebauer, Gerry, *see also* Becklin, E. E.; Soifer, B. T.; Werner, Michael W.; C. G. Wynn-Williams.

Oke, J. B., The Palomar Hale Telescope—the first thirty years, *Sky and Tel., 58*, 505–509, 1979.

*Oke, J. B. and B. Zimmerman, IUE and visual spectrophotometry of 3C120 and Markarian 79, *Astrophys. J. (Lett.), 231*, L13–L17, 1979.

Oke, J. B., *see also* Bertola, F.; Gunn, James E.; Horne, Keith; Neugebauer, Gerry.

*Persson, S. Eric, Jay A. Frogel, J. G. Cohen, M. Aaronson, and K. Matthews, The spread in CO absorption and effective temperature among the giants in Omega Centauri, *Astrophys. J., 235*, 452–469, 1980.

Persson, S. Eric, *see also* Neugebauer, Gerry.

Phillips, A. C., *see* Cohen, Judith G.

*Richstone, Douglas O., and Maarten Schmidt, The spectral properties of a large sample of quasars, *Astrophys. J., 235*, 361–376, 1980.

*Richstone, Douglas O., and Stephen A. Shectman, Rotational velocities in the nuclear bulge of M31, *Astrophys. J., 235*, 30–36, 1980.

*Sandage, Allan, and Roberta M. Humphreys, On the warped optical plane in M33, *Astrophys. J. (Lett.), 236*, L1–L5, 1980.

*Sandage, Allan, G. A. Tammann, and Amos Yahil, The velocity field of bright nearby galaxies, I, The variation of mean absolute magnitude with redshift for galaxies in a magnitude-limited sample, *Astrophys. J., 232*, 352–364, 1979.

Sandage, Allan, *see also* Tammann, G. A.; Yahil, Amos.

*Sargent, Anneila I., Molecular clouds and star formation, II, Star formation in the Cepheus OB3 and Perseus OB2 molecular clouds, *Astrophys. J., 233*, 163–181, 1979.

Sargent, Wallace L. W., Quasar absorption lines and the intergalactic medium, *Phys. Scripta, 21*, 753–758, 1980.

*Sargent, Wallace L. W., Peter J. Young, A. Boksenberg, and David Tytler, The distribution of Lyman-alpha absorption lines in the spectra of six QSOs: evidence for an intergalactic origin, *Astrophys. J., Suppl. Ser., 42*, 41–81, 1980.

Sargent, Wallace L. W., *see also* Arnold, S. J.; Briggs, S. A.; Hazard, C.; Young, Peter J.

Schmidt, Maarten, *see* Richstone, Douglas O.

*Schneider, Donald P., and Jesse L. Green-

stein, High time resolution spectrophotometry of Nova DQ Herculis (1934), *Astrophys. J., 233,* 935–945, 1979.

*Schneider, Donald P., and Peter Young, The magnetic maw of 2A0311−227, *Astrophys. J., 238,* 946–954, 1980.

Schneider, Donald P., *see also* Young, Peter.

Schommer, Robert A., *see* Mochnacki, Stefan W.

†Searle, Leonard, Abundances of the elements in galaxies, in *Les Elements et Leurs Isotopes dans l'Univers, Liège XXII^e Colloque International d'Astrophysique,* June 1978, pp. 347–441, A. Boury, N. Grevesse, and L. Remy-Battiau, eds., Institut d'Astrophysique, Université de Liège, 1979.

Searle, Leonard, *see also* van dur Kruit, P. C.

*Sebok, William A., Optimal classification of images into stars or galaxies—a Bayesian approach, *Astron. J., 84,* 1526–1536, 1979.

Sellgren K., *see* Becklin, E. E.

Shectman, Stephen A., *see* Richstone, Douglas O.

Smith, A. M., *see* Neugebauer, Gerry.

†Soifer, B. T., G. Neugebauer, and I. Gatley, The near-infrared reflectivity of the dark and light faces of Iapetus, *Astron. J., 84,* 1644–1646, 1979.

†Soifer, B. T., G. Neugebauer, and K. Matthews, The 1.5–2.5 μm spectrum of Pluto, *Astron. J., 85,* 166–167, 1980.

Soifer, B. T., G. Neugebauer, K. Matthews, E. E. Becklin, C. G. Wynn-Williams, and R. Capps, Infrared observations of the double quasar 0957+561 A,B and the intervening galaxy, *Nature, 285,* 91–93, 1980.

Soifer, B. T., *see also* Neugebauer, Gerry.

*Sulentic, Jack W., Halton Arp, and Jean Lorre, Some properties of the knots in the M87 jet, *Astrophys. J., 233,* 44–55, 1979.

*Švestka, Zdeněk, and Robert Howard, Transient brightenings of interconnecting loops, I, Morphology of the sudden brightenings, *Solar Phys., 63,* 297–318, 1979.

Švestka, Zdeněk, *see also* Howard, Robert.

†Tammann, G. A., A. Sandage, and A. Yahil, *The Determination of Cosmological Parameters,* Lecture Notes for the 1979 Les Houches Summer School, Preprint of the Astronomical Institute of the University of Basel, No. 1, Switzerland, 1980.

Tammann, G. A., A. Sandage, and A. Yahil, Evidence for local peculiar velocities, *Phys. Scripta, 21,* 630–634, 1980.

*Tammann, G. A., Amos Yahil, and Allan Sandage, The velocity field of bright nearby galaxies, II, Luminosity functions for various Hubble types and luminosity classes: the peculiar motion of the Local Group relative to the Virgo cluster, *Astrophys. J., 234,* 775–784, 1979.

Tammann, G. A., *see also* Sandage, Allan; Yahil, Amos.

Terlevich, R., *see* Hazard, C.

Torres-Piembert, S., *see* Neugebauer, Gerry.

Tremaine, S. D., *see* Gunn, James E.

Tytler, David, *see* Sargent, Wallace L. W.

van der Kruit, P. C., and Searle, Leonard, The Palomar-Westerbork survey of bright northern-hemisphere galaxies, in *Photometry, Kinematics, and Dynamics of Galaxies,* pp. 93–95, David S. Evans, ed., University of Texas, Austin, 1979.

Vauclair, Gerard, *see* Greenstein, Jesse L.

*Wallerstein, George, and Jesse L. Greenstein, The spectrum of the nebulosity around the symbiotic long-period variable R Aquarii, *Publ. Astron. Soc. Pacific, 92,* 275–283, 1980.

*Werner, Michael W., E. E. Becklin, I. Gatley, K. Matthews, G. Neugebauer, and C. G. Wynn-Williams, An infrared study of the NGC 7538 region, *Mon. Notic. Roy. Astron. Soc., 188,* 463–479, 1979.

Werner, Michael W., *see also* Becklin, E. E.

Westphal, James A., *see* Gunn, James E.; Young, Peter J.

Willis, A. G., *see* Arp, Halton.

Wilson, A. S., *see* Angerhofer, P. E.

†Wynn-Williams, C. G., E. E. Becklin, K. Matthews, and G. Neugebauer, Two-micron spectrophotometry of the galaxy NGC 253, *Mon. Notic. Roy. Astron. Soc., 189,* 163–169, 1979.

Wynn-Williams, C. G., *see also* Becklin, E. E.; Neugebauer, Gerry; Soifer, B. T.; Werner, Michael W.

*Yahil, Amos, A. Sandage, and G. A. Tammann, The determination of the deceleration parameter from local data, *Phys. Scripta, 21*, 635–639, 1980.

Yahil, Amos, *see also* Sandage, Allan; Tammann, G. A.

*Young, Peter J., and Donald P. Schneider, Emission-line eclipse phenomena in nova DQ Herculis (1934), *Astrophys. J., 238*, 955–963, 1980.

*Young, Peter J., Wallace L. W. Sargent, Jerome Kristian, and James A. Westphal, CCD photometry of the nuclei of three supergiant elliptical galaxies: evidence for a super-massive object in the center of the radio galaxy NGC 6251, *Astrophys. J., 234*, 76–85, 1979.

Young, Peter J., *see also* Gunn, James E.; Sargent, Wallace L. W.; Schneider, Donald P.

Zimmerman, B., *see* Oke, J. B.

*Zinn, Robert, The globular cluster system of the galaxy, I, The metal abundances and reddenings of 79 globular clusters from integrated light measurements, *Astrophys. J., Suppl. Ser., 42*, 19–40, 1980.

*Zirin, Harold, Three flares with blue continuum, one with a D3 preflare shell, *Astrophys. J., 235*, 618–624, 1980.

*Zirin, Harold, and R. L. Moore, A continuum bright point at the penumbral edge, *Solar Phys., 61*, 79–82, 1980.

Zirin, Harold, *see also* Marsh, K. A.

PERSONNEL

Research Division

Staff Members

Halton C. Arp
Horace W. Babcock
Judith G. Cohen[1]
Jesse L. Greenstein[2]
James E. Gunn[3]
Robert F. Howard
Jerome Kristian
Robert B. Leighton[4]
Gerry Neugebauer,[4] *Technical Assistant Director*
J. Beverley Oke[3]
S. Eric Persson
George W. Preston, *Assistant Director, Mount Wilson*
Allan R. Sandage
Wallace L. W. Sargent[5]
Maarten Schmidt,[3] *Director*
Leonard Searle
Stephen A. Shectman
Arthur H. Vaughan
James A. Westphal[6]
Peter Young[7]
Harold Zirin[8]

Members Engaged in Post-Retirement Studies

Alexander Pogo
Henrietta H. Swope
Olin C. Wilson

[1]Associate Professor of Astronomy, California Institute of Technology
[2]Lee A. DuBridge Professor of Astrophysics, California Institute of Technology
[3]Professor of Astronomy, California Institute of Technology
[4]Professor of Physics, California Institute of Technology
[5]Professor of Astronomy and Executive Officer for Astronomy, California Institute of Technology
[6]Professor of Planetary Science, California Institute of Technology
[7]Assistant Professor of Astronomy, California Institute of Technology
[8]Chief Astronomer of Big Bear Solar Observatory, Professor of Astrophysics, California Institute of Technology

Staff Associates

Robert J. Brucato[9]
Charles T. Kowal[10]
Jean J. Lorre[11]
Keith Matthews[10]
Thomas G. Phillips[4]
B. Thomas Soifer[10]
John T. Trauger[10]
Michael W. Werner[12,13]

Senior Research Fellows

Alan M. Dressler[14]
Thomas R. Geballe[14]
Ronald Moore[15]
Robert J. Zinn[14,16]

Research Fellows

Thomas B. Ake III[17,18]
Peter L. Cottrell[17,19]
Gary S. Da Costa[20,16]
Debra M. Elmegreen[20]
Howard B. French[20]
Richard F. Green[17,21]
John G. Hoessel[17,22]
Frank P. Israel[17,23]
Robert C. Kennicutt[20]
Barry J. LaBonte
Stefan Mochnacki[17]
Jeremy R. Mould[20,24]
Anneila I. Sargent[17]
Horace A. Smith[20]

Carnegie Chilean Fellow

Guido Garay

[9]Scientific Officer, Las Campanas Observatory
[10]Member of the Professional Staff, California Institute of Technology
[11]Scientist/Member of the Professional Staff, Jet Propulsion Laboratory
[12]Assistant Professor of Physics, California Institute of Technology
[13]To August 20, 1979
[14]Las Campanas Observatory Fellow
[15]Senior Research Fellow, California Institute of Technology
[16]Fellowship ended August 31, 1980
[17]Research Fellow, California Institute of Technology
[18]Fellowship ended February 29, 1980
[19]Fellowship ended November 30, 1979
[20]Carnegie Fellow
[21]Fellowship ended December 15, 1979
[22]Graduated June 13, 1980
[23]Fellowship ended December 31, 1979
[24]Fellowship ended September 30, 1979

Predoctoral Fellows

Michael Rich[16]
Robert Shaw[16]

Librarians

Joan Gantz
Helen Z. Knudsen

Senior Research Assistants

Gordon J. Hurford[25]
Grace V. Knox

Research Assistants

John M. Adkins
John E. Boyden
Ken D. Clardy
Basil N. Katem
Margaret Katz
Margaret Liggett
Stephen P. Padilla
Frances C. Tang[26]
Andrew Tomer

Student Observers

Graham Berriman
Kirk D. Borne
Alexi Filippenko
Keith Horne
Stephen M. Kent[22]
Matthew Malkan
Daniel Nadeau
Jeffrey R. Pier
Douglas M. Rabin
Abhijit Saha
Donald P. Schneider
William L. Sebok
Richard A. Wade
Howard K.-C. Yee

Photographic Department

John R. Bedke, Photographer

Instrument Design and Construction

George Avera, Electronics Engineer[27]
Lawrence E. Blakée, Supervisor, Electronic Services
Harvey Crist, Machinist
Earle B. Emery, Senior Research Engineer

[25]Scientist, California Institute of Technology
[26]Associate Scientist, California Institute of Technology
[27]To June 30, 1980

Jerry T. Fridenberg, Senior Electronics Engineer[28]
C. L. Friswold, Head, Design Group
Robert D. Georgen, Machinist
Simon Groesz, Electronics Specialist
Fred H. Harris, Associate Electronics Engineer
Charles E. Hartrick, Engineer
Jeff B. Nenow, Solar Photographer
Nancy A. Newton, Illustrator
Frederick G. O'Neil, Shop Foreman
George Pauls, Electronics Aide
Paul N. Price, Senior Electronics Technician
Edward H. Snoddy, Designer
Merle R. Sweet, Senior Electronics Technician
David A. Tennant, Electronics Technician
David F. Thompson, Senior Technical Assistant

Operation and Maintenance

Mount Wilson Observatory and Offices

Jeanne M. Barton, Bookkeeper
Richard T. Black, Business Manager
Robert E. Cadman, Mountain Superintendent
Herman E. Carpentier, Carpenter[29]
David M. Carr, Night Assistant
Maynard Clark, Electronics Engineer
Helen S. Czaplicki, Editor
Michael Deák, Night Assistant
James Frazer, Night Assistant
Hazel M. Fulton, Head Stewardess
Pamela Gilman, Secretary
Rhea Goodwin, Assistant to the Director
Thomas S. Gregory, Optical Technician
Joseph F. Hacker, Mechanic
Mary Hark, Stewardess
Howard H. Lanning, Night Assistant
José Lopez-Tiana, Purchasing Clerk
Frank Perez, Assistant Mountain Superintendent
William D. Qualls, Chauffeur
Delores Sahlin, Typist-Telephone Operator
Bernard K. Simpier, Electronics Technician
Larry Webster, Night Assistant
Stephen Wilson, Maintenance
Gary Yanik, Electronics Engineer

[28]To October 8, 1979
[29]Retired June 30, 1980

Palomar Observatory and Robinson Laboratory

Albert R. Andrews, Maintenance Mechanic[30]
Pearlene Andrews, Technical Typist
Charles L. D. Beishline, Maintenance Mechanic
Ardith C. Birdsell, Housekeeping Aide
Jan Adriaan Bruinsma, Painter and Senior Custodian
Juan R. Carrasco, Senior Night Assistant
Bruce M. Cuney, Maintenance Mechanic and Relief Night Assistant
Anita Dietz, Housekeeping Aide[31]
Ronald B. Druliner, Safety Assistant
Chrisopher Farmer, Senior Administrative Secretary
Liselotte M. Hauck, Senior Administrative Assistant
Roger Higson, Night Assistant
Helen Holloway, Administrative Secretary
J. Luz Lara, Maintenance Mechanic
Maria Alicia Lara, Housekeeping Aide
Bonnie L. Lobner, Secretary
William H. McLellan, Technical Manager
Charles L. Miller, Senior Custodian
Thomas Murphy, Maintenance Mechanic and Relief Night Assistant
Petra Ornelas, Department Clerk[32]
Ruth E. Rabin, Administrative Aide
Marilynne J. Rice, Senior Administrative Secretary
Barrett A. Staples, Night Assistant
Robert Thicksten, Assistant Superintendent
Michael Thornberry, First Cook
Elsa-Brita Titchenell, Administrative Secretary[33]
Gary M. Tuton, Superintendent
Verdella M. Tuton, Secretary[34]
Paul Van Ligten, Electrician
Linda Waddell, Department Clerk
Dorothy Williams, Cook[35]
Barbara A. Zimmermann, Member Professional Staff

Big Bear Solar Observatory

Alberta R. Altman, Technical Assistant
Richard M. Goeden, Technical Manager

[30]To May 6, 1980
[31]To February 20, 1980
[32]To November 30, 1979
[33]Retired May 31, 1980
[34]To December 16, 1979
[35]To October 31, 1979

Jack R. Klemroth, Solar Observing Assistant
Eugene H. Longbrake, Superintendent
Alan P. Patterson, Scientist in Charge
Owen Phairis, Electronics Technician
Linda P. Zydek, Film Processor and Custodian

Las Campanas Observatory

Ljubomir Papic, Mountain Superintendent
Antonio Urrutia, Administrative Staff Member (part-time)
Manfred Wagner, Administrative Manager

Administrative Reports

Office of Administration

1530 P Street, N.W.
Washington, D.C. 20005

OFFICE OF THE PRESIDENT

James D. Ebert, *President*
Jocelyn M. Bateman, *Secretary*[1]
Montgomery S. Bradley, *Special Assistant, Corporate Sponsors Program*
Barbara F. Deal, *Secretary*[2]
Anne C. Kalicki, *Administrative Assistant*[3]
Robert N. Kreidler, *Vice President*[4]
Franklin H. Portugal, *Historian*
Adrienne K. Powell, *Administrative Assistant*[5]
Julia G. Thompson, *Secretary*[6]
Susan Y. Vasquez, *Assistant to the President*
Christopher Wright, *Staff Member (Science Policy and Institutional Development)*

OFFICE OF THE BURSAR

James W. Boise, *Bursar*
Candace J. Armstrong, *Secretary*[7]
Marvee Campbell, *Secretary*[8]
Mary L. Fones, *Secretary*[9]
Kenneth R. Henard, *Assistant Bursar*
Joseph M. S. Haraburda, *Assistant to the Bursar*
Sherman L. E. Johnson, *Payroll Supervisor*
Richard S. Kuzmyak, *Accountant*
Diep T. Nguyen, *Secretary*
Arnold J. Pryor, *Computer Systems Supervisor*

PUBLICATIONS OFFICE

Ray Bowers, *Editor, Publications Officer*[10]
Sheila McGough, *Editor, Publications Officer*[11]
Barry P. Fay, *Assistant Editor*[12]
Patricia Parratt, *Assistant Editor*[13]

ADMINISTRATIVE OFFICE

Richard E. Hewitt, *Administrative Officer for Services*
Lloyd H. Allen, *Custodian*
Don A. Brooks, *Custodian*
Linda F. Cheek, *Secretary*[14]
Antoinette M. Jackson, *Secretary*[15]
Delinda Tilghman, *Secretary*[16]
Helen R. Wallace, *Secretary*[17]

[1]From October 16, 1979, to January 18, 1980.
[2]From February 4, 1980.
[3]From October 23, 1979.
[4]Effective November 1, 1980.
[5]From October 31, 1979.
[6]To August 3, 1979.
[7]To January 18, 1980.
[8]From February 19, 1980, to May 21, 1980.
[9]From June 23, 1980.
[10]Assistant Editor to January 7, 1980.
[11]To September 18, 1979.
[12]To August 31, 1979.
[13]From September 5, 1979.
[14]From November 19, 1979, to December 10, 1979.
[15]From December 12, 1979.
[16]To July 22, 1979.
[17]To November 30, 1979.

Bibliography

PUBLICATIONS OF THE INSTITUTION

Carnegie Institution of Washington Year Book 78, viii + 47 + 846 pages, 394 figures, December 1979.

Carnegie Institution of Washington Newsletter. Issued in December 1979, March and May 1980.

Ceramics for the Archaeologist. Anna O. Shepard. Publication 609. xxvi + 414 pages, 59 figures. Reprint. May 1980.

PUBLICATIONS BY THE PRESIDENT OF THE INSTITUTION*

James D. Ebert

The importance of basic research to the users of the sea: some biological concerns, in *Marine Sciences and Ocean Policy Symposium, June 17–20, 1979*, University of California, Santa Barbara, David S. Simonett, ed., 1979.

Epidemic of life, Editorial essay in *BioScience, 30*, p. 503, August 1980.

*Scientific publications by Staff Members and Fellows of the Institution are listed in the reports of the several departments.

Report of the Executive Committee

To the Trustees of the Carnegie Institution of Washington

In accordance with the provisions of the By-Laws, the Executive Committee submits this report to the Annual Meeting of the Board of Trustees.

The estimate of expenditures for the fiscal year beginning July 1, 1980, has been reviewed by the Executive Committee.

Five vacancies exist in the membership of the Board of Trustees, resulting from three vacancies which were not filled in 1979, and the resignations of John T. Connor and Michael Ference, Jr., in January 1980. Mr. Connor's resignation also created vacancies on the Executive Committee and Employee Benefits Committee which have not been filled.

The terms of the Chairman of the Board, all Committee Chairmen, and the following members of Committees also expire on May 2, 1980:

Executive Committee
Caryl P. Haskins
William McChesney Martin, Jr.

Finance Committee
Crawford H. Greenewalt

Nominating Committee
Robert C. Seamans, Jr.

Employee Benefits Committee
Carl J. Gilbert
Charles H. Townes

William C. Greenough, *Chairman*

May 2, 1980

Abstract of Minutes

of the Eighty-Third Meeting of the Board of Trustees

The annual meeting of the Board of Trustees was held in the Seminar Room of the Department of Plant Biology, Stanford, California, on Friday, May 2, 1980. The meeting was called to order by Chairman Frank Stanton.

The following Trustees were present: Philip H. Abelson, John Diebold, Carl J. Gilbert, William T. Golden, Crawford H. Greenewalt, Caryl P. Haskins, William R. Hewlett, William McChesney Martin, Jr., Robert M. Pennoyer, Richard S. Perkins, Robert C. Seamans, Jr., and Frank Stanton. James D. Ebert, President, James W. Boise, Bursar, and Marshall Hornblower, Counsel, were also in attendance.

The minutes of the Eighty-Second Meeting were approved.

The resignations of John T. Connor and Michael Ference, Jr., were noted with regret.

The reports of the Executive Committee, the Finance Committee, the Employee Benefits Committee, and the Auditing Committee were accepted. On the recommendation of the latter, it was resolved that Arthur Andersen & Co. be reappointed as public accountants for the fiscal year ending June 30, 1981.

On the recommendation of the Nominating Committee, Edward E. David, Jr., Gerald M. Edelman, Robert G. Goelet, Richard E. Heckert, and Antonia Mörner were elected members of the Board of Trustees.

William R. Hewlett was elected Chairman of the Board for a term ending in 1983.

The following were elected for one-year terms: William C. Greenough, as Chairman of the Executive Committee; Richard S. Perkins, as Chairman of the Finance Committee; Crawford H. Greenewalt, as Chairman of the Auditing Committee; Robert M. Pennoyer, as Chairman of the Nominating Committee; and Carl J. Gilbert, as Chairman of the Employee Benefits Committee.

Vacancies in Standing Committees, with terms ending in 1983, were filled as follows: Caryl P. Haskins, William McChesney Martin, Jr., and Charles H. Townes were elected members of the Executive Committee; Crawford H. Greenewalt was elected a member of the Finance Committee; Lewis M. Branscomb was elected a member of the Nominating Committee; and William T. Coleman, Jr., and Charles H. Townes were elected members of the Employee Benefits Committee. In addition, Frank Stanton was elected a member of the Executive Committee for the unexpired term ending in 1981.

The annual report of the President was accepted.

To provide for the operation of the Institution for the fiscal year ending June 30, 1981, and upon recommendation of the Executive Committee, the sum of $10,258,000 was appropriated.

Financial Statement

for the year ended June 30, 1980

CARNEGIE INSTITUTION OF WASHINGTON

TEN-YEAR FINANCIAL SUMMARY, 1971-1980
(All Figures are Thousands of Dollars)

Fiscal Year ended June 30	Total 1971-80	1980[3]	1979[3]	1978[3]	1977[3]	1976[3]	1975[3]	1974[3]	1973	1972	1971
Receipts											
Interest and dividends	$43,682	$ 6,486	$ 5,256	$ 5,019	$ 4,675	$ 3,958	$ 3,295	$ 3,356	$ 3,647	$ 3,863	$ 4,127
Other	1,362	156	306	80	338	126	83	60	58	65	90
Restricted grants, expended[1]	10,283	2,613	1,805	1,544	1,077	772	447	484	554	470	517
Total	$55,327	$ 9,255	$ 7,367	$ 6,643	$ 6,090	$ 4,856	$ 3,825	$ 3,900	$ 4,259	$ 4,398	$ 4,734
Expenditures											
Terrestrial Magnetism	$10,472	$ 1,030	$ 1,000	$ 1,106	$ 1,209	$ 1,046	$ 1,188	$ 1,025	$ 1,022	$ 937	$ 909
Mount Wilson Observatory	10,834	1,170	1,191	1,168	1,204	1,085	1,027	1,051	1,016	992	930
Las Campanas Observatory	14,660	831	792	700	1,056	1,753	2,138	2,572	2,559	1,075	1,184
Geophysical Laboratory	10,582	1,269	1,284	1,202	1,162	1,032	1,136	964	984	770	779
Embryology	7,559	483	815	818	900	816	851	791	718	699	668
Plant Biology	5,721	602	537	530	636	620	1,270	673	330	271	252
Genetics Research Units	502	21	22	22	23	22	24	70	65	68	165
Research Projects, etc.	792	97	168	85	92	89	51	98	29	22	61
Office of Administration	6,005	791	710	602	577	500	571	520	592	583	559
General Publications	701	66	62	78	59	66	78	57	79	58	98
Consulting fees, insurance, taxes.	1,407	199	175	216	226	158	134	95	62	67	75
Employee benefits, special	1,068	139	143	145	117	102	81	89	97	78	77
Financial advisory, services	2,075	278	308	265	238	205	213	199	195	108	66
Restricted grants	10,283	2,613	1,805	1,544	1,077	772	447	484	554	470	517
Total[2]	$82,661	$ 9,589	$ 9,012	$ 8,481	$ 8,576	$ 8,266	$ 9,209	$ 8,688	$ 8,302	$ 6,198	$ 6,340
Restricted grants, unexpended[1]		$ 2,884	$ (284)	$ 777	$ 95	$ 430	$ 368	$ 21	$ (10)	$ (26)	$ (34)
Gifts received		157	998	637	241	41	146	330	377	354	611
Total market value of investments.		94,359	86,425	84,136	89,287	92,215	93,719	98,200	124,770	128,826	113,042

See Footnotes 1, 2, 3 attached.

CARNEGIE INSTITUTION OF WASHINGTON

Footnotes to the Ten-Year Financial Summary, 1971-1980

[1]Restricted grants for funds received from Federal Agencies, Foundations, etc., in support of specific proposals for scientific research and educational programs.

Many restricted grants received are for the entire grant period which may not coincide with the Institution's fiscal year. Accordingly, the Ten-Year Financial Summary lists separately the portions of the grants expended and unexpended within the fiscal year.

During the report period, significant grants were received from Carnegie Corporation of New York, Helen Hay Whitney Foundation, Andrew W. Mellon Foundation, Alfred P. Sloan Foundation, Charles E. Culpeper Foundation, Inc., Atlantic Richfield Foundation, The Ahmanson Foundation, The Commonwealth Fund, Exxon Educational Foundation, Max C. Fleischmann Foundation, Whitehall Foundation, National Aeronautics & Space Administration, National Science Foundation, Office of Naval Research, Public Health Service, and Department of Agriculture and Interior.

[2]The Institution capitalizes expenditures for land, buildings, telescopes and other significant equipment, and construction projects in progress. Expenditures for other equipment are charged to current operations as incurred, and the cost of such equipment is not capitalized. The Institution follows the policy of not depreciating its buildings, telescopes and significant equipment.

Included in the Expenditures of Appropriated Funds are purchases of capitalized equipment as follows:

1980	$ 50,593
1979	71,994
1978	56,526
1977	316,607
1976	2,133,374
1975	2,806,042
1974	2,048,947
1973	3,078,426
1972	11,987
1971	370,566
Total	$10,945,062

During the report period, significant items of capitalized equipment were:

100" Irenee du Pont Telescope	$7,330,567
Plant Biology Building Annex	952,767
60" Palomar Telescope	800,800
40" Swope Telescope	545,415

[3]In 1974, the financial statements of the Institution were prepared on the accrual basis of accounting. In prior years, the Institution used the cash receipts and disbursements basis of accounting. The purpose of this change was to conform with Audit Guides of the American Institute of Certified Public Accountants which recommend accrual basis accounting for nonprofit institutions. The differences in the financial data on the accrual basis and on the former cash basis are not material.

ARTHUR ANDERSEN & CO.
WASHINGTON, D. C.

To the Auditing Committee of

Carnegie Institution of Washington:

We have examined the statements of assets, liabilities and fund balances of CARNEGIE INSTITUTION OF WASHINGTON (a non-profit corporation chartered by Act of the United States Congress) as of June 30, 1980 and 1979, the related statement of income, expenses and changes in fund balances for the year ended June 30, 1980, and the supplementary schedules, which are presented on the twelve immediately following pages. Our examinations were made in accordance with generally accepted auditing standards and, accordingly, included such tests of the accounting records and such other auditing procedures as we considered necessary in the circumstances.

In our opinion, the financial statements referred to above present fairly the assets, liabilities and fund balances of Carnegie Institution of Washington as of June 30, 1980 and 1979, and the changes in fund balances for the year ended June 30, 1980, and the supplementary schedules referred to above present fairly the information set forth therein, all in conformity with generally accepted accounting principles applied on a consistent basis.

Arthur Andersen & Co.

Washington, D.C.,

August 29, 1980.

CARNEGIE INSTITUTION OF WASHINGTON

Notes to the Financial Statements
June 30, 1980

Note 1

The financial statements of the Institution are prepared on the accrual basis of accounting.

Note 2

The Institution capitalizes expenditures for land, buildings, telescopes and other significant equipment, and construction projects in progress. Expenditures for other equipment are charged to current operations as incurred, and the cost of such equipment is not capitalized. The Institution follows the policy of not depreciating its buildings, telescopes and significant equipment.

Note 3 - Retirement Plan

The Institution has a noncontributory money purchase retirement plan in which all United States personnel are eligible to participate. Voluntary contributions may also be made by employees. Actuarially determined contributions are funded currently by the Institution, and there are no unfunded past service costs. The total contributions made by the Institution were $572,192 in 1980 and $538,299 in 1979. Benefits under the plan upon retirement are dependent upon the investment performance of the Institution's Retirement Trust. After four years participation, benefits are fully vested.

Note 4 - Restricted Grants

Restricted Grants are funds received from Foundations, individuals and Federal Agencies in support of scientific research and educational programs. The Institution follows the policy of reporting only expenditures equal to income. The Restricted Grants Statement shows all of the current grants.

Note 5 - Income Taxes

The Institution is exempt from Federal income tax under Section 501(c)(3) of the Internal Revenue Code. Accordingly, no provision for income taxes is reflected in the accompanying financial statements. The Institution is an educational institution within the meaning of Section 170(b)(1)(A)(ii) of the Code. The Internal Revenue Service has classified the Institution as other than a private foundation as defined in section 509(a) of the Code.

CARNEGIE INSTITUTION OF WASHINGTON

STATEMENTS OF ASSETS, LIABILITIES AND FUND BALANCES
FOR THE YEAR ENDED JUNE 30, 1980 AND 1979

ASSETS

	1980	1979
Current Assets:		
Cash	$ 674,392	$ 569,745
Grants Receivable	278,334	306,982
Accrued Interest	204,755	350,998
Advances	41,352	26,910
	1,198,833	1,254,635
Investments (cost*) Schedule 5:		
United States Government	1,142,001	10,217,990
Corporate Debt Securities	40,837,948	25,149,605
Loan and Collateral Pledge Agreement	200,000	200,000
Mortgage	133,200	166,500
Corporate Stocks-Preferred	150,000	1,051,316
Corporate Stocks-Common	41,948,774	42,311,214
Total Investments	84,411,923	79,096,625
Total Current Assets	85,610,756	80,351,260
Land	869,257	869,257
Buildings	3,924,232	3,884,242
Equipment	10,121,884	10,111,818
TOTAL ASSETS	$100,526,129	$95,217,577

LIABILITIES AND FUND BALANCES

Current Liabilities:		
Appropriated		
Accounts Payable and Accrued Expenses		
Unrestricted	$ 647,500	$ 656,526
Restricted	24,617	126,951
Restricted Grants, received but not expended	1,335,769	369,229
Total Current Liabilities	2,007,886	1,152,706
Fund Balances:		
Appropriated-		
Unrestricted (Schedule 2)	2,280,711	1,977,551
Unappropriated (Schedule 1)	81,322,159	77,221,003
Plant	14,915,373	14,866,317
Total Fund Balances	98,518,243	94,064,871
TOTAL LIABILITIES AND FUND BALANCES	$100,526,129	$95,217,577

*Approximate market value on June 30, 1980: $94,358,627; on June 30, 1979: $86,424,691.

The accompanying notes are an integral part of this statement.

STATEMENT OF INCOME, EXPENSES AND CHANGES IN FUND BALANCES
FOR THE YEAR ENDED JUNE 30, 1980

	Appropriated Funds			Unappropriated	Plant	
	Unrestricted	Restricted	Total	Funds	Fund	Total
Income						
Investment Income						
Interest	$4,022,330	$ 22,510	$4,044,840	$ 33,155	---	$ 4,077,995
Dividend	2,410,350	13,490	2,423,840	19,870	---	2,443,710
Capital Gain Net	---	---	---	4,581,133	---	4,581,133
Grants-Private & Government	---	2,577,150	2,577,150	---	---	2,577,150
Other Income	155,940	---	155,940	---	---	155,940
Gifts	---	---	---	157,080	---	157,080
Total Income	6,588,620	2,613,150	9,201,770	4,791,238	---	13,993,008
Expenses (Schedule 4)	6,975,542	2,613,150	9,588,692	---	---	9,588,692
Income over expenses (Deficit)	(386,922)	---	(386,922)	4,791,238	---	4,404,316
Transfers						
Provision for Operating Deficit	620,082	---	620,082	(620,082)	---	---
Land, Building & Equipment:						
Capitalization	---	---	---	---	$ 50,593	50,593
Retirement	---	---	---	---	(1,537)	(1,537)
Special Fund - Astronomy	70,000	---	70,000	(70,000)	---	---
Total Transfers	690,082	---	690,082	(690,082)	49,056	49,056
Net Change	303,160	---	303,160	4,101,156	49,056	4,453,372
Beginning Balance July 1, 1979	1,977,551	---	1,977,551	77,221,003	14,866,317	94,064,871
Ending Balance, June 30, 1980	$2,280,711	$ ---	$2,280,711	$81,322,159	$14,915,373	$98,518,243

The accompanying notes are an integral part of this statement.

CARNEGIE INSTITUTION OF WASHINGTON

CHANGES IN UNAPPROPRIATED FUNDS
FOR THE YEAR ENDED JUNE 30, 1980

	Balance July 1, 1979	Investment Income	Grants Gifts and Other Income	Capital Gain Net	Appropriations	Transfer	Balance June 30,1980
Endowment Fund							
Andrew Carnegie.....	$22,000,000	---	---	---	---	---	$22,000,000
Sybil & William T. Golden	25,000	---	---	---	---	---	25,000
Anonymous Gifts.....	1,043,250	---	$ 100,000	---	---	---	1,143,250
Realized Capital Gains...	37,650,576	---	---	$3,602,936	---	---	41,253,512
Unrestricted Capital Funds							
Carnegie Corporation.....	10,000,000	---	---	---	---	---	10,000,000
Carnegie Futures.....	201,701	---	45,342	---	---	---	247,043
Vannevar Bush.....	100,000	---	---	---	---	---	100,000
Realized Capital Gains...	4,332,318	---	---	886,038	$ 620,082	---	4,598,274
Working Capital Fund							
Income.....	---	$6,357,580	---	---	6,513,520	$ 155,940	---
Sale of Assets.....	---	---	11,478	---	---	(11,478)	---
Royalties.....	---	---	12,501	---	---	(12,501)	---
Rent.....	---	---	65,497	---	---	(65,497)	---
Refunds.....	---	---	4,079	---	---	(4,079)	---
Sales of Publications....	---	---	34,385	---	---	(34,385)	---
University of Toronto....	---	---	28,000	---	---	(28,000)	---
Restricted Grants.....	---	36,000	2,577,150	---	2,613,150	---	---
Special Funds							
Astronomy.....	144,411	5,813	---	4,170	70,000	---	84,394
Ira S. & Mary Bowen.....	300,894	22,779	---	16,343	12,000	---	328,016
Bush Gift.....	25,102	3,241	---	2,326	---	---	30,669
Colburn.....	260,638	20,745	---	14,884	16,450	---	279,817
Hale Relief.....	7,674	569	---	400	---	---	8,643
Harkavy.....	12,458	905	---	648	650	---	13,361
Lundmark.....	49,818	3,340	---	2,396	2,500	---	53,054
Morganroth.....	41,567	2,406	---	1,726	1,600	---	44,099
Moseley Astronomy.....	127,204	9,406	11,738	6,991	6,900	---	148,439
Special Instrumentation..	127,103	8,372	---	6,007	---	---	141,482
Special Opportunities....	78,926	6,311	---	4,528	---	---	89,765
Wood.....	692,363	44,238	---	31,740	35,000	---	733,341
Total.....	$77,221,003	$6,521,705	$2,890,170	$4,581,133	$9,891,852	$ ---	$81,322,159

The accompanying notes are an integral part of this statement.

CARNEGIE INSTITUTION OF WASHINGTON

SUMMARY STATEMENT OF APPROPRIATED FUNDS
FOR THE YEAR ENDED JUNE 30, 1980

	Unexpended Appropriations July 1, 1979	Appropriations	Transfers and Allotments	Total Expenditures	Unexpended Appropriations June 30, 1980
Terrestrial Magnetism.....	$ 27,623	$1,435,580	$ 20,000	$1,413,601	$ 69,602
Mount Wilson Observatory.....	42,490	1,725,419	87,550	1,785,496	69,963
Las Campanas Observatory.....	9,835	816,611	22,600	846,600	2,446
Geophysical Laboratory.....	36,288	1,582,709	138,450	1,594,679	162,768
Embryology.....	---	1,471,400	30,000	1,444,660	56,740
Plant Biology.....	---	916,677	7,500	913,421	10,756
Research Projects, etc.....	29,835	165,968	(40,100)	117,519	38,184
Office of Administration.....	---	761,267	37,400	791,167	7,500
General Insurance.....	---	162,311	(8,960)	153,351	---
General Publications.....	190	89,841	11,300	65,969	35,362
Consulting Fees.....	---	31,700	8,960	40,660	---
Retiree & Special Employee Benefits.	103,000	126,491	---	139,491	90,000
Financial Advisory Services.....	---	278,684	38,200	277,784	39,100
Real Estate Taxes.....	---	4,294	---	4,294	---
Contingent Operating Fund.....	30,000	322,900	(352,900)	---	---
Unallocated Appropriations.....	1,698,290	---	---	---	1,698,290
Total	$1,977,551	$9,891,852	$ ---	$9,588,692	$2,280,711

The accompanying notes are an integral part of this schedule.

Schedule 3

CARNEGIE INSTITUTION OF WASHINGTON

RESTRICTED GRANTS
FOR THE YEAR ENDED JUNE 30, 1980

	Balance July 1, 1979	New Grants	Expenditures	Balance June 30, 1980
Anonymous Gift	$ ---	$ 70,000	$ ---	$ 70,000
Neva and Philip Abelson Gift.	---	13,000	---	13,000
The Ahmanson Foundation	---	300,000	65,000	235,000
University of Arizona	---	12,300	8,627	3,673
Atlantic Richfield Foundation	25,000	100,000	50,000	75,000
Blue Cross of Maryland	---	500	500	---
California State University Foundation	---	30,825	16,925	13,900
Carnegie Corporation of New York	915	270,000	90,651	180,264
Charles E. Culpeper Foundation, Inc	---	606,000	135,054	470,946
The Commonwealth Fund	---	150,000	22,732	127,268
Exxon Educational Foundation	---	75,000	---	75,000
Max C. Fleischmann Foundation	---	630,000	99,620	530,380
Haruo Ueno	---	100	---	100
The Andrew W. Mellon Foundation	206,430	750,000	202,383	754,047
Mobil Research Development Corporation	---	5,000	5,000	---
Muscular Dystrophy Association	1,994	41,232	26,842	16,384
National Academy of Sciences	14,975	---	13,951	1,024
National Aeronautics and Space Administration	30,074	218,759	119,896	128,937
National Multiple Sclerosis Society	---	500	500	---
National Science Foundation	359,836	1,172,210	839,851	692,195
Office of Naval Research	33,877	99,460	84,000	49,337
New York Community Trust Kenilworth Fund	5,793	---	5,793	
N.L. Industries	---	1,000	---	1,000
Jessie Smith Noyes Foundation, Inc	---	30,000	---	30,000
Public Health Service	368,273	678,530	474,596	572,207
Richard B. T. Roberts	---	2,000	---	2,000
Damon Runyon-Walter Winchell Cancer Fund	---	13,500	5,000	8,500
Alfred P. Sloan Foundation	300,001		200,001	100,000
Helen Hay Whitney Foundation.	10,666	43,750	43,812	10,604
United States Department of Agriculture	41,166	75,000	58,192	57,974
United States Department of Interior	23,469	24,205	44,224	3,450
Whitehall Foundation	---	83,900	---	83,900
Total	$1,422,469	$5,496,771	$2,613,150	$4,306,090

The accompanying notes are an integral part of this statement.

Schedule 4

CARNEGIE INSTITUTION OF WASHINGTON

SCHEDULE OF EXPENSES
FOR THE YEAR ENDED JUNE 30, 1980

	Appropriated Funds		
	Unrestricted	Restricted	Total
Salaries, Fringe Benefits & Payroll Taxes:			
Salaries	$3,602,083	$ 671,884	$4,273,967
Fringe Benefits	676,755	127,822	804,577
Payroll Taxes	258,674	42,325	300,999
Total Salaries Benefits & Payroll Taxes	4,537,512	842,031	5,379,543
Fellowship Grants	135,209	354,140	489,349
Awards, Grants and Honoraria	95,659	5,138	100,797
Equipment:			
Educational & Research	43,650	522,307	565,957
Administrative & Operating	94,644	264	94,908
Library	75,256	1,815	77,071
Building (Improvement)	41,527	---	41,527
Telescopes	---	9,066	9,066
Total Equipment	255,077	533,452	788,529
General Expenses:			
Educational & Research Supplies	291,657	508,154	799,811
Building Maintenance	499,707	---	499,707
Financial Advisory Service	277,784	---	277,784
Administrative	404,863	---	404,863
Travel	170,352	59,898	230,250
Retiree & Special Benefits	139,491	---	139,491
Insurance	153,351	---	153,351
Publications	87,749	18,825	106,574
Consulting Fees	78,373	---	78,373
Commissary	53,110	---	53,110
Entertainment	21,905	---	21,905
Shop	40,129	---	40,129
Rent	20,832	---	20,832
Real Estate Taxes	4,294	---	4,294
Total General Expenses	2,243,597	592,015	2,830,474
Indirect Costs	(291,512)	291,512	---
Total Expenses	$6,975,542	$2,613,150	$9,588,692

The accompanying notes are an integral part of this statement.

CARNEGIE INSTITUTION OF WASHINGTON

INVESTMENTS, JUNE 30, 1980

Description	Par/Shares	Cost	Approximate Market
United States Government Securities			
Federal Home Loan Mortgage Corp., Group #16035, 8.5s, 2007.....	$ 81,433	$ 76,273	$ 70,236
Federal Home Loan Mortgage Corp., Group #17018, 8.5s, 2008.....	84,501	70,162	72,882
United States of America Treasury Notes, 8.625s, 1993 ...	999,000	995,566	895,354
Total United States Government Securities.....	$ 1,164,934	1,142,001	1,038,472
Corporate Debt Securities			
American International Corp., Conv. Sub. Deb. 4s, 1997.....	$ 175,000	147,125	228,813
Banco Mortgage Co. 2nd FHA, 7.33s Insured Project Mtge.....	4,924,156	3,880,547	3,613,099
Digital Equipment Corp., Conv. Sub. Deb., 8.875s, 2005...	1,080,000	1,086,811	1,255,500
Ford Motors Credit Co., 8.25s, 1980	10,000,000	10,000,000	10,000,000
GNMA, Pool #10332, 8s, 2006	730,031	662,960	620,526
GNMA, Pool #10913, 8s, 2006	685,392	622,422	582,583
GNMA, Pool #13912, 8s, 2006	601,630	546,355	511,386
GNMA, Pool #13934, 7.5s, 2006	181,970	141,084	146,486
GNMA, Pool #14728, 7.5s 2007	510,845	461,187	411,230
GNMA, Pool #16544, 7.5s, 2007	541,976	520,728	436,291
GNMA, Pool #16944, 7.5s, 2007	670,207	591,576	539,517
GNMA, Pool #20801, 8s, 2008	378,003	304,411	321,303
GNMA, Pool #34338, 10s, 2009	198,558	176,530	186,645
GNMA, Pool #35390, 10s, 2009	1,017,935	1,015,708	956,859
GNMA, Pool #36788, 11s, 2010	1,997,123	1,906,004	1,957,180

The accompanying notes are an integral part of this schedule.

CARNEGIE INSTITUTION OF WASHINGTON

INVESTMENTS, JUNE 30, 1980

Description	Par/Shares	Cost	Approximate Market
Corporate Debt Securities - Continued			
GNMA, Pool #36953, 11s, 2010	$ 1,997,030	$ 1,905,916	$ 1,907,164
GNMA, Pool #37091, 11s, 2010	399,595	339,406	391,603
GNMA, Pool #37123, 11s, 2009	1,013,511	967,270	993,241
GNMA, Pool #37896, 11s, 2010	494,000	471,461	484,120
GNMA, Pool #37900, 10s, 2009	997,425	997,425	937,580
GNMA, Pool #37907, 11s, 2010	499,169	423,982	489,186
GNMA, Pool #38185, 11s, 2010	1,996,994	1,905,881	1,957,054
GNMA, Pool #38642, 10s, 2010	1,018,748	1,016,519	957,623
Morgan, (J. P.), 7.8s, 1980	2,415,000	2,415,000	2,415,000
Morgan, (J. P.), 9.1s, 1980	3,120,000	3,120,000	3,120,000
Quebec Hydro-Elec Commission SF Deb. 5s, 1988	519,000	509,916	373,680
Teledyne, Inc 10s, 2004.....	2,000,000	1,546,080	1,605,000
United California Bank Prom. Note, 18s, 1980	1,000,000	1,000,644	1,000,644
United States Steel Credit Corp. Prom. Note 8.125s, 1980	2,155,000	2,155,000	2,155,000
Total Corporate Debt Securities...	$43,318,298	40,837,948	40,554,313
Mortgage			
Cold Spring Harbor Laboratory, 1983..	$ 133,200	133,200	133,200
Loan and Collateral Pledge Agreement			
James D. & Alma C. Ebert (non-interest bearing loan to president secured by real estate)	$ 200,000	200,000	200,000
Corporate Stocks--Preferred			
Burlington Northern Inc., 2.85	3,000	150,000	186,000

The accompanying notes are an integral part of this schedule.

CARNEGIE INSTITUTION OF WASHINGTON

INVESTMENTS, JUNE 30, 1980

Description	Par/Shares	Cost	Approximate Market
Corporate Stocks-Common			
Air Products & Chemical Inc.....	26,000	$ 891,302	$ 1,007,500
Alcan Aluminium, Ltd.	14,000	277,193	364,000
Alexander & Alexander Services, Inc...	22,000	623,423	737,000
American Home Products, Corp.....	10,000	280,800	285,000
American International Group, Inc.....	25,000	1,184,400	1,675,000
American Telephone & Telegraph Co.....	50,364	2,982,615	2,644,110
AMP, Inc.....	23,000	590,026	871,125
Avnet, Inc.....	25,000	479,300	693,750
Barnett Banks of Florida, Inc.....	16,000	330,479	384,000
Bearings, Inc.....	12,000	350,550	286,500
Bristol Myers.....	31,500	1,071,402	1,224,563
Chubb, Corp.....	8,000	319,425	320,000
CPC International.....	13,500	686,233	926,438
Coca-Cola, Co.....	19,000	659,092	627,000
Consolidated Edison Company of New York, Inc.....	32,400	773,024	834,300
Continental Corp.....	30,000	756,008	802,500
Continental Illinois Corp.....	19,600	553,174	573,300
Dart Industries, Inc.....	14,000	617,400	593,250
Dominion Bankshares Corp.....	29,700	435,000	423,225
Dover, Corp.....	40,000	898,650	1,540,000
Eckerd (Jack) Corp.....	9,500	237,901	255,313
Exxon Corporation.....	49,020	1,468,904	3,247,575
Farmers Group, Inc.....	60,000	1,393,374	1,672,500
First Kentucky National, Corp.....	12,000	346,875	330,000
Fleming Cosmetics, Inc.....	18,000	305,141	335,250
General Mills.....	26,500	658,435	728,750
General Telephone & Electronics, Corp.	18,000	566,825	504,000
Gulf Oil, Corp.....	37,000	1,003,630	1,493,875
Hewlett-Packard, Co.....	12,800	495,117	798,400
Honeywell, Inc.....	7,500	407,220	587,813
INA, Corp.....	27,000	811,303	951,750
Interco, Incorporated.....	16,550	720,274	719,925
International Business Machines, Corp.	55,076	1,404,785	3,235,715
K Mart.....	40,000	962,335	905,000
McDonalds, Corp.....	24,000	1,061,927	1,158,000
MCA,.....	11,000	544,885	514,250
Malone & Hyde, Inc.....	20,000	511,898	585,000
Marathon Oil, Co.....	12,000	399,057	687,000
Motorola, Inc.....	12,000	553,170	577,500
NCR, Corp.....	16,000	997,134	910,000
Northwest Bank Corp.....	14,000	270,900	343,000
Northwest Industries, Inc.....	25,000	827,904	737,500
Philip Morris, Inc.....	46,500	1,689,044	1,871,625

The accompanying notes are an integral part of this statement.

CARNEGIE INSTITUTION OF WASHINGTON

INVESTMENTS, JUNE 30, 1980

Description	Par/Shares	Cost	Approximate Market
Corporated Stocks-Common Continued			
Procter & Gamble, Co.	16,500	$ 1,275,593	$ 1,216,875
Republic of Texas	16,000	406,994	444,000
Revco, D. S	16,500	335,233	449,625
Richardson Merrell	19,700	485,104	462,950
Schlumberger Limited	9,900	296,150	1,143,450
Security Pacific, Corp	25,000	595,658	753,125
Standard Oil Co. of Ohio	20,280	687,775	1,011,465
Sun Co., Inc	20,000	554,661	765,000
Super Value Stores	28,800	561,896	705,600
Tenneco, Inc	29,000	1,037,455	1,141,875
Texaco, Inc	38,000	1,125,540	1,396,500
Texas Instruments, Inc	8,200	743,273	754,400
Travelers, Corp	18,300	608,742	752,588
Wells Fargo & Co	16,200	524,658	441,450
Whirlpool, Corp	16,500	312,508	319,688
Total Corporate Stocks - Common ...	1,329,390	41,948,774	51,720,893
Forward commitments and stand by options	$ 525,749	---	525,749
Total Investments		$84,411,923	$94,358,627

The accompanying notes are an integral part of this statement.

CARNEGIE INSTITUTION OF WASHINGTON

SUMMARY OF INVESTMENT TRANSACTIONS
FOR THE YEAR ENDED JUNE 30, 1980

Cash awaiting investment, June 30, 1979		$ 114,499

Sales and Redemptions

	Cost	Capital Gain (Net)
Bonds	$425,041,366	$ (596,557)
Preferred stocks	901,316	177,127
Common stocks	30,355,479	5,209,313
Mortgage	33,300	---
Commitment Fees	---	(208,750)
	$456,331,461	$4,581,133

Total sales and redemptions		460,912,594
Gifts of securities at fair market value		69,868
Cash transferred to Operating Fund		319,617
Total		461,416,578

Acquisitions

Bonds	$431,653,720	
Common stocks	29,993,040	
Total acquisitions		461,646,760
Cash awaiting investment, June 30, 1980		$ (230,182)

The accompanying notes are an integral part of this statement.

CARNEGIE INSTITUTION OF WASHINGTON

CONTRIBUTIONS, GIFTS AND GRANTS
FOR THE YEAR ENDED JUNE 30, 1980

Anonymous Gifts
Gordon Allen
Neva and Philip Abelson
The Ahmanson Foundation
University of Arizona
Atlantic Richfield Foundation
Blue Cross of Maryland
California State University Foundation
Carnegie Corporation of New York
Charles E. Culpeper Foundation, Inc.
The Commonwealth Fund
James and Alma Ebert
Exxon Educational Foundation
Max C. Fleischmann Foundation
Crawford Greenewalt
William C. Greenough
William McChesney Martin
The Andrew W. Mellon Foundation
Mobil Research Development Corporation
Francis L. Moseley
Muscular Dystrophy Association
National Aeronautics and Space Administration
National Multiple Sclerosis Society
National Science Foundation
Office of Naval Research
N.L. Industries
Jessie Smith Noyes Foundation, Inc.
Robert M. Pennoyer
Public Health Service
Richard B. T. Roberts
Damon Runyon-Walter Winchell Cancer Fund
Frank and Ruth Stanton
Haruo Ueno
United States Department of Agriculture
United States Department of Interior
Whitehall Foundation
Helen Hay Whitney Foundation

Articles of Incorporation

Fifty-eighth Congress of the United States of America;

At the Second Session,

Begun and held at the City of Washington on Monday, the seventh day of December, one thousand nine hundred and three.

AN ACT

To incorporate the Carnegie Institution of Washington.

Be it enacted by the Senate and House of Representatives of the United States of America in Congress assembled, That the persons following, being persons who are now trustees of the Carnegie Institution, namely, Alexander Agassiz, John S. Billings, John L. Cadwalader, Cleveland H. Dodge, William N. Frew, Lyman J. Gage, Daniel C. Gilman, John Hay, Henry L. Higginson, William Wirt Howe, Charles L. Hutchinson, Samuel P. Langley, William Lindsay, Seth Low, Wayne MacVeagh, Darius O. Mills, S. Weir Mitchell, William W. Morrow, Ethan A. Hitchcock, Elihu Root, John C. Spooner, Andrew D. White, Charles D. Walcott, Carroll D. Wright, their associates and successors, duly chosen, are hereby incorporated and declared to be a body corporate by the name of the Carnegie Institution of Washington and by that name shall be known and have perpetual succession, with the powers, limitations, and restrictions herein contained.

SEC. 2. That the objects of the corporation shall be to encourage, in the broadest and most liberal manner, investigation, research, and discovery, and the application of knowledge to the improvement of mankind; and in particular—

(a) To conduct, endow, and assist investigation in any department of science, literature, or art, and to this end to cooperate with governments, universities, colleges, technical schools, learned societies, and individuals.

(b) To appoint committees of experts to direct special lines of research.

(c) To publish and distribute documents.

(d) To conduct lectures, hold meetings, and acquire and maintain a library.

(e) To purchase such property, real or personal, and construct such building or buildings as may be necessary to carry on the work of the corporation.

(f) In general, to do and perform all things necessary to promote the objects of the institution, with full power, however, to the trustees hereinafter appointed and their successors from time to time to modify the conditions and regulations under which the work shall be carried on, so as to secure the application of the funds in the manner best adapted to the conditions of the time, provided that the objects of the corporation shall at all times be among the foregoing or kindred thereto.

SEC. 3. That the direction and management of the affairs of the corporation and the control and disposal of its property and funds shall be vested in a board of trustees, twenty-two in number, to be composed of the following individuals: Alexander Agassiz, John S. Billings, John L. Cadwalader, Cleveland H. Dodge, William N. Frew, Lyman J. Gage, Daniel C. Gilman, John Hay, Henry L. Higginson, William Wirt Howe, Charles L. Hutchinson, Samuel P. Langley, William Lindsay, Seth Low, Wayne MacVeagh, Darius O. Mills, S. Weir Mitchell, William W. Morrow, Ethan A. Hitchcock, Elihu Root, John C. Spooner, Andrew D. White, Charles D. Walcott, Carroll D. Wright, who shall constitute the first board of trustees. The board of trustees shall have power from time to time to increase its membership to not more than twenty-seven members. Vacancies occasioned by death, resignation, or otherwise shall be filled by the remaining trustees in such manner as the by-laws shall prescribe; and the persons so elected shall thereupon become trustees and also members of the said corporation. The principal place of business of the said corporation shall be the city of Washington, in the District of Columbia.

SEC. 4. That such board of trustees shall be entitled to take, hold and administer the securities, funds, and property so transferred by said Andrew Carnegie to the trustees of the Carnegie Institution and such other funds or property as may at any time be given, devised, or bequeathed to them, or to such corporation, for the purposes of the trust; and with full power from time to time to adopt a common seal, to appoint such officers, members of the board of trustees or otherwise, and such employees as may be deemed necessary in carrying on the business of the corporation, at such salaries or with such remuneration as they may deem proper; and with full power to adopt by-laws from time to time and such rules or regulations as may be necessary to secure the safe and convenient transaction of the business of the corporation; and with full power and discretion to deal with and expend the income of the corporation in such manner as in their judgment will best promote the objects herein set forth and in general to have and use all powers and authority necessary to promote such objects and carry out the purposes of the donor. The said trustees shall have further power from time

to time to hold as investments the securities hereinabove referred to so transferred by Andrew Carnegie, and any property which has been or may be transferred to them or such corporation by Andrew Carnegie or by any other person, persons, or corporation, and to invest any sums or amounts from time to time in such securities and in such form and manner as are permitted to trustees or to charitable or literary corporations for investment, according to the laws of the States of New York, Pennsylvania, or Massachusetts, or in such securities as are authorized for investment by the said deed of trust so executed by Andrew Carnegie, or by any deed of gift or last will and testament to be hereafter made or executed.

SEC. 5. That the said corporation may take and hold any additional donations, grants, devises, or bequests which may be made in further support of the purposes of the said corporation, and may include in the expenses thereof the personal expenses which the trustees may incur in attending meetings or otherwise in carrying out the business of the trust, but the services of the trustees as such shall be gratuitous.

SEC. 6. That as soon as may be possible after the passage of this Act a meeting of the trustees hereinbefore named shall be called by Daniel C. Gilman, John S. Billings, Charles D. Walcott, S. Weir Mitchell, John Hay, Elihu Root, and Carroll D. Wright, or any four of them, at the city of Washington, in the District of Columbia, by notice served in person or by mail addressed to each trustee at his place of residence; and the said trustees, or a majority thereof, being assembled, shall organize and proceed to adopt by-laws, to elect officers and appoint committees, and generally to organize the said corporation; and said trustees herein named, on behalf of the corporation hereby incorporated, shall thereupon receive, take over, and enter into possession, custody, and management of all property, real or personal, of the corporation heretofore known as the Carnegie Institution, incorporated, as hereinbefore set forth under "An Act to establish a Code of Law for the District of Columbia, January fourth, nineteen hundred and two," and to all its rights, contracts, claims, and property of any kind or nature; and the several officers of such corporation, or any other person having charge of any of the securities, funds, real or personal, books or property thereof, shall, on demand, deliver the same to the said trustees appointed by this Act or to the persons appointed by them to receive the same; and the trustees of the existing corporation and the trustees herein named shall and may take such other steps as shall be necessary to carry out the purposes of this Act.

SEC. 7. That the rights of the creditors of the said existing corporation known as the Carnegie Institution shall not in any manner be impaired by the

passage of this Act, or the transfer of the property hereinbefore mentioned, nor shall any liability or obligation for the payment of any sums due or to become due, or any claim or demand, in any manner or for any cause existing against the said existing corporation, be released or impaired; but such corporation hereby incorporated is declared to succeed to the obligations and liabilities and to be held liable to pay and discharge all of the debts, liabilities, and contracts of the said corporation so existing to the same effect as if such new corporation had itself incurred the obligation or liability to pay such debt or damages, and no such action or proceeding before any court or tribunal shall be deemed to have abated or been discontinued by reason of the passage of this Act.

SEC. 8. That Congress may from time to time alter, repeal, or modify this Act of incorporation, but no contract or individual right made or acquired shall thereby be divested or impaired.

SEC. 9. That this Act shall take effect immediately.

J. G. Cannon

Speaker of the House of Representatives.

Fr Frye

President of the Senate pro tempore.

Approved.
April 28. 1904.
Theodore Roosevelt

By-Laws of the Institution

Adopted December 13, 1904. Amended December 13, 1910, December 13, 1912, December 10, 1937, December 15, 1939, December 13, 1940, December 18, 1942, December 12, 1947, December 10, 1954, October 24, 1957, May 8, 1959, May 13, 1960, May 10, 1963, May 15, 1964, March 6, 1967, May 3, 1968, May 14, 1971, August 31, 1972, May 9, 1974, and April 30, 1976.

ARTICLE I

The Trustees

1. The Board of Trustees shall consist of twenty-four members with power to increase its membership to not more than twenty-seven members. The Trustees shall hold office continuously and not for a stated term.

2. In case any Trustee shall fail to attend three successive annual meetings of the Board he shall thereupon cease to be a Trustee.

3. No Trustee shall receive any compensation for his services as such.

4. All vacancies in the Board of Trustees shall be filled by the Trustees by ballot at an annual meeting, but no person shall be declared elected unless he receives the votes of two-thirds of the Trustees present.

5. If, at any time during an emergency period, there be no surviving Trustee capable of acting, the President, the Director of each existing Department, and the Executive Officer, or such of them as shall then be surviving and capable of acting, shall constitute a Board of Trustees *pro tem*, with full powers under the provisions of the Articles of Incorporation and these By-Laws. Should neither the President, nor any such Director, nor the Executive Officer be capable of acting, the senior surviving Staff Member of each existing Department shall be a Trustee *pro tem* with full powers of a Trustee under the Articles of Incorporation and these By-Laws. It shall be incumbent on the Trustees *pro tem* to reconstitute the Board with permanent members within a reasonable time after the emergency has passed, at which time the Trustees *pro tem* shall cease to hold office. A list of Staff Member seniority, as designated annually by the President, shall be kept in the Institution's records.

6. A Trustee who resigns after having served at least five years and having reached age seventy shall be eligible for designation by the Board as a Trustee Emeritus. A Trustee Emeritus shall be entitled to attend the annual meeting of the Board but shall have no vote and shall not be counted for purposes of ascertaining the presence of a quorum. A Trustee Emeritus may be invited to serve in an advisory capacity on any committee of the Board of Trustees except the Executive Committee.

ARTICLE II

Officers of the Board

1. The officers of the Board shall be a Chairman of the Board, a Vice-Chairman, and a Secretary, who shall be elected by the Trustees, from the members of the Board, by ballot to serve for a term of three years. All vacancies shall be filled by the Board for the unexpired term; provided, however, that the Executive Committee shall have power to fill a vacancy in the office of Secretary to serve until the next meeting of the Board of Trustees.

2. The Chairman shall preside at all meetings and shall have the usual powers of a presiding officer.

3. The Vice-Chairman, in the absence or disability of the Chairman, shall perform the duties of the Chairman.

4. The Secretary shall issue notices of meetings of the Board, record its transactions, and conduct that part of the correspondence relating to the Board and to his duties.

ARTICLE III

Executive Administration

The President

1. There shall be a President who shall be elected by ballot by, and hold office during the pleasure of, the Board, who shall be the chief executive officer of the Institution. The President, subject to the control of the Board and the Executive Committee, shall have general charge of all matters of administration and supervision of all arrangements for research and other work undertaken by the Institution or with its funds. He shall prepare and submit to the Board of Trustees and to the Executive Committee plans and suggestions for the work of the Institution, shall conduct its general correspondence and the correspondence with applicants for grants and with the special advisers of the Committee, and shall present his recommendations in each case to the Executive Committee for decision. All proposals and requests for grants shall be referred to the President for consideration and report. He shall have power to remove, appoint, and, within the scope of funds made available by the Trustees, provide for compensation of subordinate employees and to fix the compensation of such employees within the limits of a maximum rate of compensation to be established from time to time by the Executive Committee. He shall be *ex officio* a member of the Executive Committee.

2. He shall be the legal custodian of the seal and of all property of the Institution whose custody is not otherwise provided for. He shall sign and execute on behalf of the corporation all contracts and instruments necessary in authorized administrative and research matters and affix the corporate seal thereto when necessary, and may delegate the performance of such acts and other administrative duties in his absence to the Executive Officer. He may execute all other contracts, deeds, and instruments on behalf of the corporation and affix the seal thereto when expressly authorized by the Board of Trustees or Executive Committee. He may, within the limits of his own authorization, delegate to the Executive Officer authority to act as custodian of and affix the corporate seal. He shall be responsible for the expenditure and disbursement of all funds of the Institution in accordance with the directions of the Board and of the Executive Committee, and shall keep accurate accounts of all receipts and disbursements. Following approval by the Executive Committee he shall transmit to the Board of Trustees before its annual meeting a written report of the operations and business of the Institution for the preceding fiscal year with his recommendations for work and appropriations for the succeeding fiscal year.

3. He shall attend all meetings of the Board of Trustees.

4. There shall be an officer designated Executive Officer who shall be appointed by and hold office at the pleasure of the President, subject to the approval of the Executive Committee. His duties shall be to assist and act for the President as the latter may duly authorize and direct.

5. The President shall retire from office at the end of the fiscal year in which he becomes sixty-five years of age.

ARTICLE IV

Meetings and Voting

1. The annual meeting of the Board of Trustees shall be held in the City of Washington, in the District of Columbia, in May of each year on a date fixed by the Executive Committee, or at such other time or such other place as may be designated by the Executive Committee, or if not so designated prior to May 1 of such year, by the Chairman of the Board of Trustees, or if he is absent or is unable or refuses to act, by any Trustee with the written consent of the majority of the Trustees then holding office.

2. Special meetings of the Board of Trustees may be called, and the time and place

of meeting designated, by the Chairman, or by the Executive Committee, or by any Trustee with the written consent of the majority of the Trustees then holding office. Upon the written request of seven members of the Board, the Chairman shall call a special meeting.

3. Notices of meetings shall be given ten days prior to the date thereof. Notice may be given to any Trustee personally, or by mail or by telegram sent to the usual address of such Trustee. Notices of adjourned meetings need not be given except when the adjournment is for ten days or more.

4. The presence of a majority of the Trustees holding office shall constitute a quorum for the transaction of business at any meeting. An act of the majority of the Trustees present at a meeting at which a quorum is present shall be the act of the Board except as otherwise provided in these By-Laws. If, at a duly called meeting, less than a quorum is present, a majority of those present may adjourn the meeting from time to time until a quorum is present. Trustees present at a duly called or held meeting at which a quorum is present may continue to do business until adjournment notwithstanding the withdrawal of enough Trustees to leave less than a quorum.

5. The transactions of any meeting, however called and noticed, shall be as valid as though carried out at a meeting duly held after regular call and notice, if a quorum is present and if, either before or after the meeting, each of the Trustees not present in person signs a written waiver of notice, or consent to the holding of such meeting, or approval of the minutes thereof. All such waivers, consents, or approvals shall be filed with the corporate records or made a part of the minutes of the meeting.

6. Any action which, under law or these By-Laws, is authorized to be taken at a meeting of the Board of Trustees may be taken without a meeting if authorized in a document or documents in writing signed by all the Trustees then holding office and filed with the Secretary.

7. During an emergency period the term "Trustees holding office" shall, for purposes of this Article, mean the surviving members of the Board who have not been rendered incapable of acting for any reason including difficulty of transportation to a place of meeting or of communication with other surviving members of the Board.

ARTICLE V

Committees

1. There shall be the following Standing Committees, *viz.* an Executive Committee, a Finance Committee, an Auditing Committee, a Nominating Committee, and an Employee Benefits Committee.

2. All vacancies in the Standing Committees shall be filled by the Board of Trustees at the next annual meeting of the Board and may be filled at a special meeting of the Board. A vacancy in the Executive Committee and, upon request of the remaining members of any other Standing Committee, a vacancy in such other Committee may be filled by the Executive Committee by temporary appointment to serve until the next meeting of the Board.

3. The terms of all officers and of all members of Committees, as provided for herein, shall continue until their successors are elected or appointed.

Executive Committee

4. The Executive Committee shall consist of the Chairman, Vice-Chairman, and Secretary of the Board of Trustees, the President of the Institution *ex officio*, and, in addition, not less than five or more than eight Trustees to be elected by the Board by ballot for a term of three years, who shall be eligible for re-election. Any member elected to fill a vacancy shall serve for the remainder of his predecessor's term. The presence of four members of the Committee shall constitute a quorum for the transaction of business at any meeting.

5. The Executive Committee shall, when the Board is not in session and has not given specific directions, have general control of the administration of the affairs of the cor-

poration and general supervision of all arrangements for administration, research, and other matters undertaken or promoted by the Institution. It shall also submit to the Board of Trustees a printed or typewritten report of each of its meetings, and at the annual meeting shall submit to the Board a report for publication.

6. The Executive Committee shall have power to authorize the purchase, sale, exchange, or transfer of real estate.

Finance Committee

7. The Finance Committee shall consist of not less than five and not more than six members to be elected by the Board of Trustees by ballot for a term of three years, who shall be eligible for re-election. The presence of three members of the Committee shall constitute a quorum for the transaction of business at any meeting.

8. The Finance Committee shall have custody of the securities of the Institution and general charge of its investments and invested funds and shall care for and dispose of the same subject to the directions of the Board of Trustees. It shall have power to authorize the purchase, sale, exchange, or transfer of securities and to delegate this power. So long as the Institution is the trustee under any retirement or other benefit plan for the staff members and employees of the Institution, it shall be responsible for supervision of matters relating to investments thereunder and for the appointment or removal of any investment manager or advisor. It shall also be responsible for reviewing the financial status and arrangements of any employee benefit plan for which the Institution is not the trustee and for appointment or removal of any plan trustee or insurance carrier. It shall consider and recommend to the Board from time to time such measures as in its opinion will promote the financial interests of the Institution and improve the management of investments under any retirement or other benefit plan. The Committee shall make a report at the annual meeting of the Board.

Auditing Committee

9. The Auditing Committee shall consist of three members to be elected by the Board of Trustees by ballot for a term of three years.

10. Before each annual meeting of the Board of Trustees, the Auditing Committee shall cause the accounts of the Institution for the preceding fiscal year to be audited by public accountants. The accountants shall report to the Committee, and the Committee shall present said report at the ensuing annual meeting of the Board with such recommendations as the Committee may deem appropriate.

Nominating Committee

11. The Nominating Committee shall consist of the Chairman of the Board of Trustees *ex officio* and, in addition, three Trustees to be elected by the Board by ballot for a term of three years, who shall not be eligible for re-election until after the lapse of one year. Any member elected to fill a vacancy shall serve for the remainder of his predecessor's term, provided that of the Nominating Committee first elected after adoption of this By-Law one member shall serve for one year, one member shall serve for two years, and one member shall serve for three years, the Committee to determine the respective terms by lot.

12. Sixty days prior to an annual meeting of the Board the Nominating Committee shall notify the Trustees by mail of the vacancies to be filled in membership of the Board. Each Trustee may submit nominations for such vacancies. Nominations so submitted shall be considered by the Nominating Committee, and ten days prior to the annual meeting the Nominating Committee shall submit to members of the Board by mail a list of the persons so nominated, with its recommendations for filling existing vacancies on the Board and its Standing Committees. No other nominations shall be received by the Board at the annual meeting except with the unanimous consent of the Trustees present.

Employee Benefits Committee

13. The Employee Benefits Committee shall consist of three members to be elected by the Board of Trustees by ballot for a term of three years, who shall be eligible for re-election and the Chairman of the Finance Committee *ex officio*. Any member elected to fill a vacancy shall serve for the remainder of his predecessor's term.

14. The Employee Benefits Committee shall, subject to the directions of the Board of Trustees, be responsible for supervision of the activities of the administrator or administrators of any retirement or other benefit plan for staff members and employees of the Institution, except that any matter relating to investments or to the appointment or removal of any trustee or insurance carrier under any such plan shall be the responsibility of the Finance Committee. It shall receive reports from the administrator or administrators of the employee benefit plans with respect to administration, benefit structure, operation, and funding. It shall consider and recommend to the Board from time to time such measures as in its opinion will improve such plans and the administration thereof. The Committee shall submit a report to the Board at the annual meeting of the Board.

ARTICLE VI

Financial Administration

1. No expenditure shall be authorized or made except in pursuance of a previous appropriation by the Board of Trustees, or as provided in Article V, paragraph 8, hereof.

2. The fiscal year of the Institution shall commence on the first day of July in each year.

3. The Executive Committee shall submit to the annual meeting of the Board a full statement of the finances and work of the Institution for the preceding fiscal year and a detailed estimate of the expenditures of the succeeding fiscal year.

4. The Board of Trustees, at the annual meeting in each year, shall make general appropriations for the ensuing fiscal year; but nothing contained herein shall prevent the Board of Trustees from making special appropriations at any meeting.

5. The Executive Committee shall have general charge and control of all appropriations made by the Board. Following the annual meeting, the Executive Committee may allocate these appropriations for the succeeding fiscal year. The Committee shall have full authority to reallocate available funds, as needed, and to transfer balances.

6. The securities of the Institution and evidences of property, and funds invested and to be invested, shall be deposited in such safe depository or in the custody of such trust company and under such safeguards as the Finance Committee shall designate, subject to directions of the Board of Trustees. Income of the Institution available for expenditure shall be deposited in such banks or depositories as may from time to time be designated by the Executive Committee.

7. Any trust company entrusted with the custody of securities by the Finance Committee may, by resolution of the Board of Trustees, be made Fiscal Agent of the Institution, upon an agreed compensation, for the transaction of the business coming within the authority of the Finance Committee.

8. The property of the Institution is irrevocably dedicated to charitable purposes, and in the event of dissolution its property shall be used for and distributed to those charitable purposes as are specified by the Congress of the United States in the Articles of Incorporation, Public Law No. 260, approved April 28, 1904, as the same may be amended from time to time.

ARTICLE VII

Amendment of By-Laws

1. These By-Laws may be amended at any annual or special meeting of the Board of Trustees by a two-thirds vote of the members present, provided written notice of the proposed amendment shall have been served personally upon, or mailed to the usual address of, each member of the Board twenty days prior to the meeting.

Index of Names

Aaronson, M., 612, 637
  publications, 641
Abelson, P. H., v, vi, 659
Adkins, J. M., 647
Ake, T. B., III, *42*, 603, 647
Albrecht, R., 580, 587
Aldrich, L. T., *41*, 586
  studies, 505–508
Aller, L. H., 632
Allington-Smith, J., 636
Alonso, M., 223
Anders, E., 543
Anderson, D. M., 223
  publications, 223
  studies, 215–216, 216–217
Anderson, M. J., *40*, 98
  studies, 19–28
Anderson, R. G., 426
Anderson, R. O., v
Argon, Y., *40*, 98
  studies, 37, 38–41
Armond, P. A., *40*, 202, 206
  publications, 200
  studies, 191–193
Arp, H. C., *39, 42,* 617–618, 627, 628, 646
  publications, 641–642
Assousa, G. E., *41*, 586
  publications, 584

Baas, F., 631
Babcock, H. W., *42*, 630, 646
Badger, M. R., 200–201, 202
Bagnuolo, W. G., *14–15*, 611–612, 615
Bajaja, E., 583, 584, 587
Bakken, A., 99
  studies, 70–72
Baldwin, J. A., 638
Balivnas, S. L., 602
Balliett, F., 223
Bannister P., J., 587
Bassett, W., 355–358
Batiza, R., 587
Bayne, E. K., *40*, 98
  studies, 19–28
Beach, L., 441, 512, 584
Belford, H. S., 202
  publications, 201
Bell, P. M., *28, 41,* 232–233, 241, 242, 243, 246, 376, 419, 425
  publications, 423
  studies, 348–351, 351–355, 355–358, 358–364, 374–376, 380–384, 409–411, 411–415
Benjamin, T. M., *41*, 425
Bergstralh, J. T., 632
Berriman, G., *42*, 639, 647
Berry, J. A., *32, 40*, 108, 109, 111, 112, 202–203, 205
  publications, 201
  studies, 141–143, 143–145, 146–147, 147–150, 157–160
Bibee, L. D., 439, 465–472, 587
Björkman, O., *9, 32, 40,* 109, 160–164, 187, 189, 203, 205
  publications, 201
  studies, 150–157, 157–160
Blake, A. E., 223
Blanco, B. M., 613
Blanco, V. M., 613
Blatt, M. R., *41*, 107, 203, 206
  publications, 201
  studies, 123–126
Boctor, N. Z., *41*, 232–233, 234, 239, 240, 419, 425
  studies, 302–304, 304–307, 337–340, 340–345, 345–348
Bogenhagen, D., *40*, 98
  publications, 95
  studies, 72, 79–80, 89–92
Boise, J. W., vii, 653, 659
Bond, H. E., 632
Borne, K. D., *42*, 620, 629, 647
Böving, B., 98
Bowers, R., vii, 653
Boyd, F. R., Jr., *41,* 233, 234, 291, 370, 419, 423, 425
  publications, 423
  studies, 296–302, 302–304
Boyden, J. E., 595, 647
  publications, 642
Bracamonte, M., 587
Bradley, M. S., 653
Brady, J. B., *41*, 425
Brandle, J., 426
Branscomb, L. M., v, 659
Briggs, W. R., *31–32, 39, 40,* 123, 125, 203, 205
  report of the Director, Department of Plant Biology, 105–112
  publications, 201
  studies, 126–128, 128–131, 131–134, 134–136, 136–138, 138–141

Britten, R. J., vii, 95, 223
publications, 224
studies, 212, 213, 214, 215
Britz, S. J., 132
publications, 201
Brody, E. M., 241, 419, 355–358
Brooks, C., 587
Brown, D. D., *4–5, 33, 40*, 7, 73, 98
report of the Director, Department of Embryology, 7–9
publications, 95–96
studies, 79–80, 80–82, 82–85
Brown, D. N., 635
Brown, J. S., *30, 40*, 110, 112, 203, 205
publications, 201
studies, 172–175, 176–179, 200
Brown, L., *23, 41*, 439, 443, 444, 586
studies, 463–465, 539–543
Brucato, R. J., *15, 42*, 647
Bugnon, M.-F., *42*, 524, 526, 529, 587
Burbridge, G. R., 628
Burke, D., *40*, 98
studies, 37
Burstein, D., *42*, 445, 587, 632
publications, 584
studies, 566–573
Busby, S., 99
studies, 70–72
Butchins, A., 638

Cabre, R., 587
Cabrera, C. V., 223
studies, 223
Callaway, S., *37*
Capaccioli, M., 614, 642
Carey, J., 426
Carney, B. W., *42*, 445, 587
publications, 584
studies, 561–563, 563–566
Carpentier, H., *37*, 648
Casaverde, M., 587
Caubergs, R., *32*, 108, 203
publications, 201
studies, 134–135
Cebra, J., 49, 96, 99
Chamberlin, M. E., 223
studies, 218
Chayes, F., *41*, 232, 419–420, 425
publications, 423
studies, 285–287, 287–288, 289–290
Chow, T. J., 587
Christian, C., 613
Clardy, K. D., 647
Clark, R., 543
Clarke, R. S., Jr., 444, 551, 553–556, 584, 587
Clayton, R., 543
Clegg, K. B., 219
Coe, E. H., 53, 54, 99
Cohen, J. G., *42*, 610, 613, 615, 647
publications, 642
Coleman, W. T., Jr., v, *37*, 659
Colomb, F. R., 584, 587
Connor, J. T., v, *36*, 657, 659
Costantini, F., 223
publications, 224
studies, 217
Cottrell, P. L., *42*, 606, 633, 647
publications, 642
Cox, L. P., 587
Cronin, D., 236, 315–318
Crutcher, R. M., 632
Cuellar, R. E., *29, 41*, 106, 203, 206
publications, 201
studies, 119–120
Cummings, M., 213
publications, 224
Czyzak, S. J., 632

Da Costa, G. S., *42*, 610, 633, 647
publications, 642
Dabrowski, H., *41*, 244, 426
studies, 388–391
David, E. E., Jr., v, *38*, 659
Davidson, E. H., 95, 223
publications, 224
studies, 212, 213, 214, 216, 216–217, 217, 217–218, 218, 218–219, 219, 220, 221, 222, 223
Davie, J., 47
Davis, G. L., *41*, 425
Dawe, J. A., 637
Dawid, I. B., 98
Day, F. E., *37*
DeHaan, R. L., 98
Demers, S., 634
Dickens, R. J., 637
Diebold, J., v, *12*, 659
Digan, M. E., 75, 76, 96
Dixon, T. H., 587
Donner, M. W., 93, 96
Dooner, H., 55, 56
Doschek, G., 598
Downton, W. J. S., *32*, 108, 109, 111, 112, 203, 206
publications, 201
studies, 141–143, 143–145, 191–193
Dressler, A. M., *15, 38, 42*, 617, 618, 622–623, 642, 647
Dworetsky, M. M., 633

Ebert, J. D., v, vii, 653, 659
report of the President, *3–39*
publications, 655
Echeverría, L. M., *21, 42*, 437, 587
publications, 584–585
studies, 447–452
Eckmann, S. T., 223
Edelman, G. M., v, *38*, 659
Efstratiadis, A., 214
Eggen, O. J., 605
Eichler, Hj., 165
Elias, J. A., 613
Elliott, E., *36, 40*, 98
studies, 9–11, 13–15, 15–16

Ellison, J. W., 223
studies, 222
Elmegreen, B. C., 616
Elmegreen, D. M., *42,* 611, 616, 647
El Shazly, E. M., 587
Elthon, D. L., *41,* 231, 239, 420, 423, 426
studies, 277–281
Emerson, C., *40,* 99
Emerson, S., *40,* 99
Emler, J., 543, 588
Engel, A. F. J., 587
Engelke, D., 79, 88, 99
studies, 80–82
Ernst, S. G., 223
publications, 224
studies, 220
Estep, M. L. F., *41,* 244, 419, 423, 425
studies, 388–391, 391–394
Evertson, D. W., 440, 486, 495, 587

Fambrough, D. M., *35, 40,* 8, 98
publications, 96
studies, 19–28
Fedoroff, N. V., *40,* 8, 98
studies, 51–61
Feigenson, M., *42,* 439, 587
studies, 472–476
Feldman, U., 598
Ference, M., Jr., v, *36,* 657, 659
Ferland, G. J., 603
publications, 642
Ferry, J. M., 426
Field, C., 112, 146–147
Filippenko, A., *42,* 647
Filloy, E., 584, 587
Finger, L. W., *26, 28, 41,* 241, 242, 245, 373, 420, 425
publications, 423–424
studies, 348–351, 364–367, 406–409
Fontaine, G., 633
Forbush, S. E., *41,* 586
Ford, W. K., Jr., *18, 41,* 445, 586
publications, 585
studies, 566–573, 573–578, 578–581
Fork, D. C., *30–31, 40,* 110, 111, 203, 205
publications, 201
studies, 179–184, 184–186, 187–189, 189–190, 191–193, 193–197, 198–200
Frantz, J. D., *41,* 240, 420, 425
publications, 424
studies, 340–345, 345–348
Fredriksson, K., 551, 587
French, C. S., *40,* 204, 205
French, H. B., *42,* 607–608, 613, 624, 647
Frisch, P. C., 633
Frogel, J. A., 610, 612, 613
publications, 642
Fukuyama, H., *41,* 234, 425
studies, 307–310

Gao, B., 223
studies, 220
Garay, G., *42,* 647
Garcia, J. A., Jr., 223
Gardner, J. M., *40,* 98
studies, 19–28
Gavis, E., *40,* 98
studies, 62–70
Gearhart, P., *40,* 8, 98
publications, 96
studies, 46–51
Geballe, T. R., *42,* 630, 647
publications, 642
Geisecke, A. A., 587
Geller, M. J., 640
George, D. J., 420, 426
Gibson, D. M., 603
Gil-Av, E., 426
Gilbert, C. J., v, 657, 659
Giugni, T., 223
studies, 213
Gize, A. P., *25–26, 41,* 244, 426
studies, 384–388
Godwin, J. G., 638
Goelet, R. G., v, *38,* 659
Golden, W. T., v, *14,* 659
Goldsmith, M. H., *32,* 108
publications, 201
Goodrich, R. W., 620
Gorton, H. L., *41,* 107, 204, 206
publications, 201
studies, 128–131
Govindjee, *30,* 111, 204, 206
studies, 189–190, 191–193, 198–200
Graham, G. J., 223
Grandi, S., 607
Granger, M. I., *42,* 587
Green, R. F., *42,* 633, 647
publications, 642
Greenewalt, C. H., v, 657, 659
Greenough, W. C., v, 657, 660
Greenstein, J. L., *42,* 602, 605, 606, 646
publications, 642–643
Griffin, R. F., 634
Grula, J. W., 223
publications, 224
studies, 212, 214
Gunn, J. E., *17, 42,* 618, 623, 627, 636, 646
publications, 643
Gurdon, J., *4,* 70

Hadidiacos, C. G., 291, 407, 426
Hall, T. J., 223
publications, 224
studies, 213, 215
Hamilton, T. S., 237, 284, 318–320
Hansen, L., 634
Haraburda, J. M. S., vii, 653
Hardy, E. J., 634
Hare, P. E., *8–9, 41,* 244–245, 420, 423, 425
studies, 394–399, 403–406
Harris, A. W., 634
Harrison, W. J., *41,* 237, 311, 389, 426
publications, 424
studies, 320–322

Hart, R. W., *30*, 112, 206
studies, 170–172
Hart, S. R., 438, 455–458
Hartman, L., 602
Harvey, G. W., *40*, 109, 110, 204, 206
publications, 201
studies, 160–164, 179–184
Hasegawa, A., *42*, 587
Haskins, C. P., v, vi, 657, 659
Hayes, D. S., 634
Hazard, C., 628
publications, 643
Hazen, R. M., *26, 28, 41,* 241, 242–243, 245, 373, 420, 425
publications, 424
studies, 348–351, 364–367, 380–384, 406–409
Heckert, R. E., v, *38*, 659
Hedge, C. E., 587
Heinze, W. D., *42*, 587
Helin, E. F., 638
Helsley, C. E., 588
Henard, K. R., vii, 653
Hertig, A. T., 98
Hewitt, R. E., vii, 653
Hewlett, W. R., v, 659
Hiesey, W. M., *40*, 205
Hoch, G. E., 206
Hodge, P., 615
Hoekstra, D., *40*, 98
studies, 28–29
Hoering, T. C., *8, 25–26, 41,* 244–245, 420, 425, 465
studies, 384–388, 391–394, 394–399, 399–403
Hoessel, J. G., *42*, 623, 636, 647
publications, 643
Hofmann, A. W., *22, 41,* 437, 439, 440, 586
publications, 585
studies, 447–452, 472–476, 477–483
Hogan, M. E., 99
studies, 37, 41–42
Hood, L., 47, 95, 99
Hornblower, M., vii, 659
Horne, K., *42*, 603, 634, 647
publications, 643
Hough-Evans, B. R., 223
publications, 224
studies, 218–219, 219, 220
Howard, R. F., *10, 14, 42*, 594, 595, 646
publications, 643
Hu, E. M., *42*, 444, 587
studies, 556–561
Huaco, D., 588
Humphreys, R. M., 634
publications, 643
Hurford, G. J., 647
Hurwitz, J., 47, 49
Hutcheon, I. D., 588

Irvine, T. N., *41,* 230, 232, 238, 239, 308, 332, 420–421, 423, 425
publications, 424
studies, 247–251, 251–256, 257–262, 332–337
Israel, F. P., *42*, 647
Ito, E., *42*, 438, 587
studies, 459–462, 486

Jacobs-Lorena, M., 218, 223
publications, 224
Jambon, A., *42*, 586
studies, 520–522
James, D. E., *22–23, 41*, 438, 586
publications, 585
studies, 452–455, 455–458
Jankevics, A., 635
Jeanloz, R., 243, 376, 426
publications, 424
Jenkner, H., 580, 581
Johnson, H. M., 614
Johnson, N., 47, 99
Johnston, M. J. S., 588
Jordan, E., 99
studies, 79–80, 85–88
Jorgensen, R. A., *29, 40,* 106, 204, 205
studies, 116–119

Kahler, S. W., 598
Karabinos, P., 426
Katem, B. N., 608, 647
Katz, M., 647
Kauffman, D., 236
studies, 315–318
Keith, D. W., 232, 426
Kennicutt, R. C., *42*, 615, 617, 629, 647
publications, 643
Kent, S. M., *42*, 615, 647
Kingsbury, R. C., 62–70
Kingsley, R. H., *41*, 426
Kirshner, R. P., *16*, 620, 635
Klein, J., *23,* 439, 463–465, 588
Knox, G. V., 647
Konigsberg, I. R., *34*, 98
Kormendy, J., 588
Korn, L. J., 90, 96
Kothari, B. K., *20, 42,* 444, 587
publications, 585
studies, 548–551, 551–553
Kotra, R. K., 426
Kowal, C. T., *42*, 599, 647
publications, 643
Kraft, R. P., 635
Kreidler, R., vii, *12, 38*, 653
Kriausakul, N., 426
Kristian, J., *16–17, 42,* 626, 627, 646
publications, 643
Kron, R., 635
Kunkel, W. E., 634
Kushiro, L., *41*, 231, 235, 275, 276, 279, 280, 291, 309, 313, 315, 321, 418, 425, 588
publications, 424
studies, 267–271, 310–311

LaBonte, B. J., *10, 14, 42,* 595, 599, 647
  publications, 643
Landstreet, J. D., 635, 640
Lanning, H. H., 635, 636
Lasky, L. A., 223
  publications, 224
  studies, 212, 214, 215, 221, 222
Leahy, P. S., 223
  studies, 217
Lee, T., *41,* 418, 443, 444, 586
  publications, 585
  studies, 539–543
LeFevre, G., 75, 76
Leighton, R. B., *42,* 597, 646
Leong, T.-Y., *32, 40,* 107–108, 204, 206
  studies, 131–134, 134–135
Leutgert, J., 588
Lev, Z., 223
  publications, 224
  studies, 221
Levitt, J., 204, 205
Lewin, Y., 223
Lewis, B., 588
Liggett, M., 647
Liller, W., 636
Linde, A. T., *7, 41,* 441, 586
  studies, 486–491, 491–495, 495–498, 498–505, 505–508
Lindh, A., 588
Longair, M. S., 636
Lonker, S. W., *41,* 421, 425
Lorre, J. J., *42,* 632, 647
  publications, 643
Luck, R. E., 632
Lugger, P. M., 636
Lusby, M., 223
Lux, R. A., *42,* 587
  studies, 512–520
Luyten, W. J., 605, 640

Macagno, E., 99
Madon, M., 243
Madore, B. F., 617, 636
Mahowald, A., 73, 75
Malkan, M., *42,* 640, 647
Malkin, S., *30,* 111, 204, 206
  studies, 187–189
Mammone, J. F., *41,* 237–238, 243, 244, 246, 426
  publications, 424
  studies, 367–369, 369–374, 415–417
Mandoli, D. F., *31, 41,* 106, 204, 206
  studies, 126–128
Mao, H. K., *28, 38, 41,* 232–233, 241, 242, 243, 246, 340, 376, 379, 407, 421, 425
  publications, 424
  studies, 348–351, 351–355, 355–358, 358–364, 374–376, 380–384, 409–411, 411–415
Margolis, S. A., 426
Martin, C., 583
Martin, O. C., 99
  studies, 28–29, 32–34
Martin, W. M., v, 657, 659
Mason, B., 543
Matthews, K., *42,* 624, 647
  publications, 644
Mauvais, J., 99
  studies, 51–61
Maza, J., 640
McAllister, L. B., 223
  studies, 215–216, 216–217
McCarthy, M. F., 613
McClintock, B., vii, *4,* 51, 53, 54, 57, 60, 99
McCormick, S., *40,* 98
  studies, 51–61, 61–62
McGarr, A., 588
McGough, S., *37,* 653
McGraw, J. T., 633
McKinney, B., 426
McKnight, S., *40,* 8, 98
  publications, 96
  studies, 62–70
McNamara, D. H., 636
Melis, A., *30, 40,* 110, 112, 204, 206
  publications, 201
  studies, 170–172, 172–175
Meyer, R. P., 588
Michalsky, J. J., 636
Middlekoop, F., 602
Middleton, R., *23,* 439, 463–465, 588
Mihalas, D. M., 602
Miller, G. H., 245
  studies, 403–406
Miller, H. R., 637
Miller, O. L., Jr., 223
  studies, 219
Mochnacki, S., *42,* 597, 603, 604, 647
  publications, 644
Mooney, H. A., 109, 146, 150–157
  publications, 201
Moore, G. P., 223
  publications, 224
  studies, 221
Moore, R., *42,* 598–599, 647
  publications, 644
Morgan, G., 99
  studies, 70–72
Morgan, H. S., v
Mörner, A. J., v, *38,* 659
Morris, M., 616
Mose, D. G., *42,* 587
  studies, 483–485
Mould, J. R., *42,* 613, 637, 647
  publications, 644
Mueller, J., 223
Muirhead, K., 588
Muller, K. J., *35–36, 40,* 9, 98
  publications, 96
  studies, 9–11, 11–12, 12–13, 15–16, 16–19
Münch, G., 599
Murase, T., *41,* 234, 319, 425, 588
  studies, 307–310
Murphy, F. D., v
Murray, J. B., 637

Murray, M. G., *30, 40,* 105, 114, 116, 120, 204, 205
publications, 201
studies, 112–114
Myers, J., 426
Mysen, B. O., *38, 41,* 235–236, 237, 238, 239, 275, 276, 309, 319, 421, 425, 588
publications, 424
studies, 310–311, 312–313, 313–314, 314–315, 320–322, 326–327, 337–340

Nadeau, D., *43,* 647
Nathans, B., 99
studies, 37
Nelen, J., 588
Nelson, G. A., *40,* 98
publications, 96
studies, 37, 37–38, 38–41
Nelson, O., 56, 60
Neuffer, M. G., 53, 99
Neugebauer, G., *17, 42,* 624, 646
publications, 644
Nichols, J. W., *40,* 98
studies, 28–29, 29–30
Nivera, N., 99
studies, 46–51
Nixon, P. H., 233, 234, 296–302
Nobs, M. A., *40,* 110, 204, 205
studies, 164–170
Noonan, A., 551
Norton, G., v
Nousek, J., 637
Noyes, R. W., 602

Ocola, L., *42,* 587
studies, 505–508
O'Connell, R. W., 638
Oemler, A., Jr., *16,* 620
Okada, H., 506, 510, 588
Oke, J. B., *42,* 614, 620, 623, 635, 646
publications, 644
Ölsen, E., 543
Öquist, G., *31,* 111, 204, 206
studies, 193–197
O'Rahilly, R., 98
publications, 96
studies, 93–94
Osborn, E. F., *41,* 231, 421–422, 425
publications, 424
studies, 281–285

Padilla, S. P., 647
Padovani, E. R., 438, 455–458, 585
Pagano, R. E., *35, 40,* 8, 43, 98
publications, 97
studies, 28–29, 32–34
Palmer, J. D., *29, 41,* 106, 206
studies, 120–122
Papanastassiou, D. A., 543
Patterson, A. P., 597, 649
Pauls, G., 223
Peach, J. V., 638
Peacock, J. A., 636
Pedersen, L., 73
Pelham, H., *40,* 98
studies, 79–80, 82–85
Pennoyer, R. M., v, 659
Perkins, R. S., v, 659
Perryman, M. A. C., 636
Persson, S. E., *42,* 610, 612–613, 630, 646
publications, 644
Peters, D. L., *30,* 105, 206
publications, 202
studies, 112–114
Peterson, R., *40,* 98
publications, 97
studies, 79–80, 89, 92
Peterson, R. C., 445, 561–563, 563–566, 588
Petro, L., 634
Phillips, M. M., 638
Phillips, T. G., *42,* 647
Pier, J. R., *43,* 647
Pike, C. S., 109, 204
publications, 202
Pikó, L., 223
studies, 219–220
Pimental, E., 588
Pogo, A., 646
Poirier, J. P., 243
Pollock, H. E. D., vii, *37*
Ponnamperuma, R., *41,* 426
Popp, R. K., *41,* 240, 425, 426
publications, 424
studies, 340–345
Pöppel, W. G. L., 583, 584
Portugal, F. H., vii, 653
Posakony, J. W., 223
publications, 224
studies, 216, 217–218
Possolo, A. M. G., *41,* 419, 426
Powles, S. B., *40,* 109, 204, 205
studies, 157–160
Preisler, R. S., *41,* 105, 205, 206
studies, 114–116
Preston, G. W., *17, 42,* 601, 611, 613, 646

Quail, P. H., *40,* 205, 206
publications, 202

Rabin, D. M., *42,* 647
Rajan, R. S., *20, 41,* 444, 586
publications, 585
studies, 548–551, 551–553
Ramirez, J. E., 588
Ramsey, E. M., *34,* 93, 98
publications, 97
Ranganayaki, R. P., *42,* 586
publications, 585
Rawson, S. A., *41,* 231, 238, 426
studies, 281–285, 332–337
Ray, P. M., 148
Reaves, G., 622
Reeder, R. H., 98, 99
studies, 70–72

Reipurth, B., 638
ReVelle, D. O., *21*, 443, 543–546, 585, 588
Reynolds, S. R. M., *39*
Rich, M., 647
Rigg, J., 223
Riley, J. M., 636
Roberts, J. K. M., *32*, 108
  studies, 147–150
Roberts, J. W., 223
  studies, 212, 214
Roberts, M. S., *18*, 445, 573–578, 588
Roberts, R. B., *36, 41,* 586
Roberts, T., *40*, 98
  studies, 37, 41–42, 42–45
Rodriquez B., A., 588
Roeder, R. G., 79, 99
  studies, 80–82
Roesler, F. R., 599
Rotundo, R., *40*, 98
  publications, 97
  studies, 19–28
Rubin, A., *41*, 426
Rubin, G., *38*, 9
Rubin, V. C., *18, 41,* 445, 586, 632, 638
  publications, 585
  studies, 566–573, 573–578
Rumble, D., III, *24, 41,* 238, 418, 422, 423, 425
  studies, 328–332
Ryerson, F. J., *42*, 235–236, 586
  publications, 585
  studies, 313–314, 314–315, 520–522, 522–523

Sacks, I. S., *7, 23, 41*, 439, 441, 586
  publications, 585–586
  studies, 463–465, 486–491, 491–495, 495–498, 498–505, 508–512, 512–520
Saha, A., *43*, 647
Sakonju, S., *40*, 64, 98
  publications, 97
  studies, 79–80, 80–82
Sandage, A. R., *15, 38, 42,* 563, 608–611, 617, 621–623, 640, 646
  publications, 644
Sargent, A. I., *42*, 647
  publications, 644
Sargent, W. L. W., *42*, 618, 646
  publications, 644
Scarfe, C. M., 231, 233, 235, 236–237, 311, 422, 426
  studies, 277–281, 290–296, 312–313, 315–318, 318–320, 320–322
Schaeffer, H., *40*, 99
Schechter, P. L., *16*, 620
Scheller, R. H., 223
  studies, 215–216, 216–217
Schmidt, M., *17, 36, 38, 42,* 646
  report of the Director, Hale Observatories, 593–594
  publications, 644
Schneider, D. P., *43*, 647
Schommer, R., 615
Schroit, A., *40*, 98
  publications, 97
  studies, 28–29, 34–37
Scott, E. R. D., *20, 42,* 444, 551, 587, 588
  publications, 586
  studies, 553–556
Scott, S., *40*, 98
  publications, 97
  studies, 9–11, 12–13, 16–19
Seamans, R. C., Jr., v, 657, 659
Searle, L., *15, 42,* 611–612, 614–615, 646
  publications, 645
Sebok, W. L., *43*, 629, 647
  publications, 645
Seeman, J. R., *32, 41,* 108, 112, 147, 205, 206
  publications, 202
  studies, 141–143, 143–145, 146–147
Sellgren, K., 613
  publications, 645
Sharkey, T. D., *40*, 205
Sharma, S. K., *41*, 237–238, 240, 241–242, 246, 349, 422, 425
  publications, 424–425
  studies, 322–326, 351–355, 358–364, 367–369, 369–374, 415–417
Shaw, R., *15*, 622, 647
Shectman, S. A., *16, 38, 42,* 611, 620, 623, 646
  publications, 645
Shieh, Y. N., 426
Shimizu, H., 241, 355–358
Shin, H., *40*, 99
  studies, 79–80, 88–89
Shiono, K., *42*, 441, 587
  studies, 498–505
Shoemaker, E. M., 638
Shure, M., *40*, 98
Sigleo, A., *8*, 244–245, 426
  studies, 394–399
Simoni, D. A., 588
Simons, B. A., *41*, 237–238, 240, 243, 425
  studies, 322–326, 376–380
Sinha, R., 588
Smith, B., *37*, 9, 99
Smith, C. M., *41*, 206
Smith, H. A., *42*, 610, 613, 647
Smith, N. L., 223
  studies, 213
Snoke, J. A., *7,* 441, 486–491, 491–495, 586, 588
Soifer, B. T., *42*, 624, 647
  publications, 645
Sollner-Webb, B., *40*, 98
  studies, 70–72, 72
Somerville, D., 99
  studies, 19–28
Spector, M., 198–200, 205
Spradling, A., *5, 33, 40*, 7, 98
  publications, 97
  studies, 73–79

Stanton, F., v, 659
Stefansson, R., 495–498, 588
Stern, R. J., *42*, 439, 587
  studies, 465–471, 486
Stokes, G. M., 636
Struck, D., *40*, 98
  publications, 97
  studies, 28–29, 30–32
Sulentic, J. W., 639
  publications, 645
Summers, W., 64
Sundqvist, C., *40*, 107, 108, 205, 206
  studies, 136–138, 138–141
Suyehiro, S., 441, 486–491, 491–495, 588
Suzuki, Y., *5*, 98
Swope, H. H., *36, 39*, 646
Szkody, P., 636, 639

Taft, C. P., v
Takahashi, E., *41*, 231, 233, 239, 426
  studies, 271–276, 290–296
Tammann, G. A., *15*, 621–622
  publications, 645
Tang, F. C., 647
Taylor, E., 426
Tera, F., *19, 41*, 439, 442, 586
  studies, 463–465, 524–531
Terrile, R. J., 640
Thomas, B. E., 99
  studies, 9–11, 11–12, 12–15, 16–19
Thomas, T. L., 223
  publications, 224
  studies, 212, 213, 214
Thompson, I., 640
Thompson, W. F., *29–30, 40*, 105, 106, 205
  publications, 202
  studies, 112–114, 114–116, 116–119, 119–120, 120–122
Thonnard, N., *18, 41*, 445, 586
  publications, 586
  studies, 566–573, 573–578, 581–584
Todd, S. R., 232, 426
Tomer, A., 647
Townes, C. H., v, 657, 659
Trabert, S. W., 223
  studies, 215–216
Trauger, J. T., *42*, 599, 631, 647
Trippe, J. T., v
Turner, E. L., 640
Tuve, M. A., *41*, 586

Unan, C., 426
Usher, P. D., 640

Van Baalen, C., 391
van der Kruit, P.C., 614–615
  publications, 645
van Ginkel, G., *40*, 110, 205, 206
  studies, 179–184, 184–186
Van Valkenburg, A., 422
Vaughan, A. H., *42*, 601, 646
Vasquez, S. Y., vii, 653
Velde, D., 242
Vierstra, R., *32*, 108, 135
Virgo, D., *41*, 235–236, 237, 238, 242, 422, 425
  publications, 425
  studies, 310–311, 312–313, 313–314, 314–315, 320–322, 326–327, 374–376
Volponi, F., 588
von Drach, V., *42*, 587

Wade, R. A., *43*, 647
Wakamatsu, K., 640
Wakshull, E., *40*, 98
  studies, 19–28
Ward, S., *35, 40*, 7, 98
  publications, 97
  studies, 37, 37–38, 38–41, 41–42, 42–45
Waring, G., 73
Wasserburg, G. J., 543
Watters, T. R.,
  studies, 551–553
Watson, T. J., 426
Webb, D. F., 598
Wegner, G. A., 640
Weisblat, D., 99
Weisenseel, M., 107, 123–126
Wendlandt, R., 389, 425
Wenzel, J., 236, 315–318
Werner, M. W., *42*, 647
Wessler, S., *40*, 98
West, R. M., 641
Westphal, J. A., *16–17, 42*, 626, 636, 646
  publications, 645
Wetherill, G. W., *7, 17, 19, 21, 41*, 443, 527, 531, 586
  report of the Director, Department of Terrestrial Magnetism, 433–446
  publications, 586
  studies, 532–539, 543–546, 546–548
White, J. N., v
White, W. M., *42*, 440, 587
  studies, 477–483
Whitford, A. E., 641
Wilkinson, A., *14–15*, 611–612
Williams, W. E., *41*, 206
Wilson, O. C., 601, 604, 646
Winget, G. D., 198–200, 205
Wittig, J., 243, 426
  studies, 380–384
Wormington, M., *40*
  studies, 79–80, 85–88
Wright, C., vii, 653
Wyckoff, R. W. G., 426
Wydrzynski, T., 198–200, 205

Xin, J.-H., 223
  studies, 221, 222

Yee, H. K.-C., *43*, 618–620, 633, 647
Yoder, H. S., *6, 23, 41*, 230, 233, 234, 271, 276, 308, 326, 422–423, 425
  report of the Director, Geophysical Laboratory, 229–246

publications, 425
studies, 263–267, 290–296, 304–307
Young, P., *16–17, 42*, 618, 626–627, 630, 646
publications, 646

Zeff, M., 543, 588
Zies, E. G., *41*, 425
Zinn, R. J., *42*, 609, 610, 647
publications, 646
Zirin, H., *42*, 597, 603, 604, 646
publications, 646
Zook, A., 641
Zoon, K., 426
Zou, G., 242, 379, 426
studies, 374–376